



# Phase I Transport Model of Corrective Action Units 101 and 102: Central and Western Pahute Mesa, Nevada Test Site, Nye County, Nevada



Revision No.: 1

February 2009

Prepared for U.S. Department of Energy under Contract No. DE-AC52-03NA99205.

Approved for public release; further dissemination unlimited.

Available for sale to the public from:

U.S. Department of Commerce  
National Technical Information Service  
5285 Port Royal Road  
Springfield, VA 22161  
Phone: 800.553.6847  
Fax: 703.605.6900  
Email: [orders@ntis.gov](mailto:orders@ntis.gov)  
Online ordering: <http://www.ntis.gov/ordering.htm>

Available electronically at <http://www.osti.gov/bridge>

Available for a processing fee to U.S. Department of Energy and its contractors  
in paper, from:

U.S. Department of Energy  
Office of Scientific and Technical Information  
P.O. Box 62  
Oak Ridge, TN 37831-0062  
Phone: 865.576.8401  
Fax: 865.576.5728  
Email: [reports@adonis.osti.gov](mailto:reports@adonis.osti.gov)

*Reference herein to any specific commercial product, process, or service by  
trade name, trademark, manufacturer, or otherwise, does not necessarily  
constitute or imply its endorsement, recommendation, or favoring by the United  
States Government or any agency thereof or its contractors or subcontractors.*





**PHASE I TRANSPORT MODEL OF  
CORRECTIVE ACTION UNITS 101 AND 102:  
CENTRAL AND WESTERN PAHUTE MESA,  
NEVADA TEST SITE, NYE COUNTY,  
NEVADA**

Revision No.: 1

February 2009

Stoller-Navarro Joint Venture  
c/o U.S. DOE  
P.O. Box 98952  
Las Vegas, NV 89193-8952

Reviewed and determined to be UNCLASSIFIED.

Derivative Classifier: Joseph Johnston SNJV Classification Officer  
(Name/personal identifier and position title)

Signature: *Joseph Johnston*

Date: 2/11/2009

Prepared for U.S. Department of Energy under Contract No. DE-AC52-03NA99205.

Approved for public release; further dissemination unlimited.

**PHASE I TRANSPORT MODEL OF CORRECTIVE ACTION UNITS 101  
AND 102: CENTRAL AND WESTERN PAHUTE MESA,  
NEVADA TEST SITE, NYE COUNTY, NEVADA**

Approved by:



---

Sam Marutzky, UGTA Project Manager  
Stoller-Navarro Joint Venture

Date:

2-11-09

## TABLE OF CONTENTS

List of Figures.....	x
List of Tables.....	xxv
List of Acronyms and Abbreviations.....	xxx
List of Symbols for Elements and Compounds.....	xxxiv
List of Stratigraphic Unit Abbreviations and Symbols.....	xxxvi
Executive Summary.....	ES-1
1.0 Introduction.....	1-1
1.1 Purpose and Scope.....	1-4
1.2 Project Participants.....	1-6
1.3 Regulatory Background - FFACO and Safe Drinking Water Act.....	1-6
1.3.1 Summary of the FFACO UGTA Project Corrective Action Strategy.....	1-10
1.4 Pahute Mesa Background.....	1-10
1.4.1 Underground Nuclear Testing on Pahute Mesa.....	1-13
1.5 Major Supporting Reports Documenting CAU-Specific Data Analysis and Evaluation.....	1-15
1.6 Report Organization.....	1-20
2.0 Review of Background for the Pahute Mesa Phase I Transport Model.....	2-1
2.1 Introduction.....	2-1
2.2 Preliminary Groundwater Flow System Understanding.....	2-2
2.3 Regional Scale Flow and Tritium Transport Modeling.....	2-2
2.4 Characterization Data and Studies.....	2-4
2.5 Corrective Action Investigation Plan.....	2-5
2.6 Pahute Mesa CAU-Scale Modeling Approach.....	2-7
2.7 Pahute Mesa CAUs 101 and 102 Groundwater Flow Model.....	2-8
2.7.1 Conceptualization.....	2-9
2.7.2 Hydrostratigraphic Framework Models.....	2-9
2.7.3 Recharge.....	2-10
2.7.4 Lateral Boundary Fluxes.....	2-10
2.7.5 Discharge.....	2-10
2.7.6 Hydraulic Heads.....	2-10
2.7.7 Hydraulic Conductivity.....	2-11
2.7.8 Groundwater Geochemistry.....	2-11
2.7.9 Flow Model Uncertainties.....	2-11
2.8 Hydrologic Source Term.....	2-12
2.9 Summary.....	2-13
3.0 Alternative Calibrated Flow Models.....	3-1
3.1 Introduction.....	3-1
3.2 Pahute Mesa-Oasis Valley HFM.....	3-2
3.2.1 Hydrostratigraphic Unit Model Development.....	3-3

**TABLE OF CONTENTS (CONTINUED)**

3.2.2	Hydrogeologic and Hydrostratigraphic Units of the PM-OV HFM . . . . .	3-4
3.2.2.1	Hydrogeologic Units of PM-OV HFM . . . . .	3-5
3.2.2.2	Hydrostratigraphic Units of the PM-OV HFM . . . . .	3-6
3.2.3	Pahute Mesa HFMs . . . . .	3-16
3.2.3.1	Structural Features . . . . .	3-17
3.2.3.2	Stratigraphy . . . . .	3-23
3.2.4	Boundary Conditions . . . . .	3-23
3.2.4.1	Alternative Recharge Models . . . . .	3-25
3.2.4.2	Discharge . . . . .	3-26
3.2.4.3	Boundary Heads . . . . .	3-27
3.2.4.4	Lateral-Boundary Fluxes . . . . .	3-27
3.2.5	Summary of Flow Model Calibration and Flow System Behavior. . . . .	3-29
3.2.5.1	Data Components of Calibration Targets . . . . .	3-30
3.2.5.2	Head and Flow Paths . . . . .	3-31
3.2.5.3	Purse Fault . . . . .	3-35
3.2.6	Geochemical Screening and Selection of HFMs for Transport Analysis . . . . .	3-37
3.3	Selected Fault Permeability Adjustments . . . . .	3-44
3.3.1	Background. . . . .	3-44
3.3.1.1	Geochemical Mixing at ER-EC-6 . . . . .	3-45
3.3.1.2	Geochemical Mixing at UE-18r . . . . .	3-47
3.3.2	Alternative HFM Adjustment. . . . .	3-49
3.3.2.1	Analysis of HSU and Fault Permeability . . . . .	3-49
3.3.2.2	Adjustment of HSU and Fault Permeability . . . . .	3-54
3.4	Development of Alternative HFMs . . . . .	3-56
3.4.1	Preferential Flow in the TCM and Contiguous HSUs . . . . .	3-59
3.4.2	Development of the LCCU1-MME-TMD Alternative Model . . . . .	3-64
3.4.3	Development of the LCCU1-MME-TMCM Alternative Model . . . . .	3-66
4.0	Pahute Mesa Simplified Source Model . . . . .	4-1
4.1	Model Representation . . . . .	4-1
4.1.1	Approach . . . . .	4-2
4.1.2	Conceptualization and Dimensions of the Source Region . . . . .	4-2
4.1.3	Inventory. . . . .	4-4
4.1.4	Porosities, Pore Volumes, and Density . . . . .	4-13
4.1.5	Sorption . . . . .	4-13
4.1.6	Nuclear Melt Glass Dissolution . . . . .	4-17
4.1.7	Hydrologic/Transport Model Description . . . . .	4-18
4.1.8	Quantitative Assessment of Uncertainty . . . . .	4-24
4.1.8.1	Inventory Uncertainty . . . . .	4-25
4.1.8.2	Radionuclide Partitioning Uncertainty . . . . .	4-26

**TABLE OF CONTENTS (CONTINUED)**

	4.1.8.3	Source Region Dimensions Uncertainty .....	4-26
4.2		Pahute Mesa SSM Analysis Model .....	4-28
	4.2.1	Introduction .....	4-28
	4.2.2	Pahute Mesa Results for Six HFMs .....	4-28
	4.2.3	Fixed Inputs .....	4-30
	4.2.4	Probabilistic Inputs .....	4-33
	4.2.5	Pahute Mesa Results by HGU and Radionuclide .....	4-34
	4.2.6	Summary .....	4-36
5.0		Transport Conceptual Model .....	5-1
5.1		Introduction .....	5-1
5.2		Release .....	5-2
5.3		Migration .....	5-5
	5.3.1	Source Release .....	5-7
	5.3.2	Advective and Dispersive Transport .....	5-7
	5.3.3	Matrix Diffusion .....	5-8
	5.3.4	Matrix Sorption .....	5-9
	5.3.5	Colloid-Facilitated Transport .....	5-10
	5.3.6	Radioactive Decay Chains .....	5-11
	5.3.7	In Situ Concentrations .....	5-11
	5.3.8	Integrated Transport Model .....	5-11
5.4		Reactive Mineral Model .....	5-12
	5.4.1	Mineralogy of HSUs .....	5-12
	5.4.1.1	Data Sources and Evaluation .....	5-12
	5.4.1.2	Reactive Mineral Characterization of Volcanic and Sedimentary Rock .....	5-13
	5.4.1.2.1	Lithologic Character of PM-OV Rocks ...	5-13
	5.4.1.2.2	Post-Depositional Alteration Processes ...	5-14
	5.4.1.2.3	Reactive Mineral Categories .....	5-15
	5.4.2	Reactive Mineral Model .....	5-15
	5.4.2.1	Model Area .....	5-30
	5.4.3	Reactive Mineral Model Construction .....	5-30
5.5		Reactive Mineral Categories .....	5-32
	5.5.1	Alluvial Aquifer (AA) .....	5-32
	5.5.2	Younger Volcanics Composite Unit (YVCM) .....	5-34
	5.5.3	Thirsty Canyon Volcanic Aquifer (TCVA) .....	5-35
	5.5.4	Detached Volcanics Composite Unit (DVCM) .....	5-36
	5.5.5	Detached Volcanics Aquifer (DVA) .....	5-37
	5.5.6	Fortymile Canyon Composite Unit (FCCM) .....	5-37
	5.5.7	Fortymile Canyon Aquifer (FCA) .....	5-39
	5.5.8	Timber Mountain Composite Unit (TMCM) .....	5-39
	5.5.9	Tannenbaum Hill Lava-Flow Aquifer (THLFA) .....	5-41
	5.5.10	Tannenbaum Hill Composite Unit (THCM) .....	5-41

**TABLE OF CONTENTS (CONTINUED)**

5.5.11	Timber Mountain Aquifer (TMA) . . . . .	5-42
5.5.12	Subcaldera Volcanic Confining Unit (SCVCU). . . . .	5-43
5.5.13	Fluorspar Canyon Confining Unit (FCCU) . . . . .	5-44
5.5.14	Windy Wash Aquifer (WWA) . . . . .	5-44
5.5.15	Paintbrush Composite Unit (PCM) . . . . .	5-45
5.5.16	Paintbrush Vitric-Tuff Aquifer (PVTA). . . . .	5-46
5.5.17	Benham Aquifer (BA) . . . . .	5-46
5.5.18	Upper Paintbrush Confining Unit (UPCU) . . . . .	5-47
5.5.19	Tiva Canyon Aquifer (TCA) . . . . .	5-47
5.5.20	Paintbrush Lava-Flow Aquifer (PLFA) . . . . .	5-48
5.5.21	Lower Paintbrush Confining Unit (LPCU) . . . . .	5-48
5.5.22	Topopah Spring Aquifer (TSA) . . . . .	5-50
5.5.23	Yucca Mountain Crater Flat Composite Unit (YMCFCM) . . . . .	5-51
5.5.24	Calico Hills Vitric-Tuff Aquifer (CHVTA). . . . .	5-51
5.5.25	Calico Hills Vitric Composite Unit (CHVCM) . . . . .	5-52
5.5.26	Calico Hills Zeolitic Composite Unit (CHZCM). . . . .	5-53
5.5.27	Calico Hills Confining Unit (CHCU). . . . .	5-53
5.5.28	Inlet Aquifer (IA) . . . . .	5-54
5.5.29	Crater Flat Composite Unit (CFCM) . . . . .	5-54
5.5.30	Crater Flat Confining Unit (CFCU) . . . . .	5-55
5.5.31	Kearsarge Aquifer (KA). . . . .	5-56
5.5.32	Bullfrog Confining Unit (BFCU). . . . .	5-56
5.5.33	Belted Range Aquifer (BRA). . . . .	5-57
5.5.34	Pre-Belted Range Composite Unit (PBRCM) . . . . .	5-57
5.5.35	Caldera-Related Intrusive Confining Units . . . . .	5-58
5.5.35.1	Black Mountain Intrusive Confining Unit (BMICU) . . . . .	5-61
5.5.35.2	Ammonia Tanks Intrusive Confining Unit (ATICU) . . . . .	5-61
5.5.35.3	Rainier Mesa Intrusive Confining Unit (RMICU) . . . . .	5-62
5.5.35.4	Claim Canyon Intrusive Confining Unit (CCICU) . . . . .	5-62
5.5.35.5	Calico Hills Intrusive Confining Unit (CHICU) . . . . .	5-63
5.5.35.6	Silent Canyon Intrusive Confining Unit (SCICU) . . . . .	5-63
5.5.36	Pre-Tertiary Hydrostratigraphic Units . . . . .	5-64
5.5.36.1	Mesozoic Granite Confining Unit (MGCU) . . . . .	5-64
5.5.36.2	Upper Clastic Confining Unit (UCCU) . . . . .	5-65
5.5.36.3	Lower Carbonate Aquifer (LCA and LCA3) . . . . .	5-66
5.5.36.4	Lower Clastic Confining Unit (LCCU and LCCU1) . . . . .	5-67
5.6	Relationship of Hydrostratigraphic Units and the Water Table . . . . .	5-67
6.0	Pahute Mesa Transport Model . . . . .	6-1
6.1	Introduction. . . . .	6-2
6.2	Particle Tracking. . . . .	6-3
6.3	PLUMECALC . . . . .	6-4
6.4	Transport Parameters . . . . .	6-5



**TABLE OF CONTENTS (CONTINUED)**

6.4.1	Fracture Porosity, Spacing, and Aperture . . . . .	6-7
6.4.1.1	Data Sources . . . . .	6-10
6.4.1.2	Borehole Data . . . . .	6-11
6.4.1.3	Fracture Porosity . . . . .	6-14
6.4.1.4	Fracture Spacing . . . . .	6-15
6.4.1.5	Fracture Aperture . . . . .	6-18
6.4.2	Matrix Porosity . . . . .	6-20
6.4.3	Matrix Diffusion . . . . .	6-25
6.4.4	Dispersivity . . . . .	6-27
6.4.5	Mass Transfer Coefficient . . . . .	6-30
6.4.6	Sorption Coefficient . . . . .	6-32
6.4.7	$K_d$ Upscaling . . . . .	6-35
6.4.7.1	Mechanistic $K_d$ Distributions . . . . .	6-37
6.4.7.2	$K_d$ Distributions . . . . .	6-41
6.4.7.2.1	Summary . . . . .	6-48
6.5	Evaluation Based on $^{14}\text{C}$ Considerations . . . . .	6-48
6.5.1	Summary of $^{14}\text{C}$ Data Evaluation . . . . .	6-49
6.5.2	Numerical Simulation Considerations . . . . .	6-50
6.5.3	Converting Time History Distributions into Apparent $^{14}\text{C}$ Ages . . . . .	6-53
6.6	Consideration of Fracture Parameters Using Calibrated Permeabilities . . . . .	6-58
6.7	Colloidal Transport Parameters . . . . .	6-61
6.7.1	Plutonium-Colloid Source-Release Function . . . . .	6-61
6.7.2	Colloid Filtration . . . . .	6-63
6.7.3	Colloid Transport Parameters . . . . .	6-64
6.8	Parameters Sampling Approach . . . . .	6-64
6.8.1	Distribution Selection . . . . .	6-64
6.8.2	Fitting a Distribution . . . . .	6-66
6.8.3	Checking the Goodness of Fit . . . . .	6-67
7.0	Transport Analysis: Methodology and Results . . . . .	7-1
7.1	Introduction . . . . .	7-1
7.2	Monte Carlo Uncertainty Analysis . . . . .	7-2
7.3	Transport Analysis Metrics . . . . .	7-4
7.3.1	Radionuclides and MCLs . . . . .	7-5
7.3.2	Probability of MCL Exceedance . . . . .	7-7
7.3.3	Exceedance Volume . . . . .	7-7
7.3.4	Regulatory-Based Contaminant Boundary . . . . .	7-9
7.3.5	Probabilistic Exceedance Map . . . . .	7-10
7.3.6	Fractional Exceedance Volume . . . . .	7-10
7.4	Statistical Stability . . . . .	7-13
7.5	Radionuclide Source Reduction . . . . .	7-13
7.6	Transport Analysis Results: Alternative Flow Models . . . . .	7-14
7.6.1	LCCU1-MME . . . . .	7-18

**TABLE OF CONTENTS (CONTINUED)**

7.6.2	LCCU1-MME-TMD .....	7-22
7.6.3	LCCU1-USGSD .....	7-24
7.6.4	DRT-DRIA .....	7-26
7.6.5	PZUP-MME .....	7-31
7.6.6	LCCU1-MME-TMCM .....	7-35
7.6.7	SCCC-MME .....	7-39
7.6.8	High-Dispersion Transport in Alternative Flow Models .....	7-43
7.6.9	Integrated Transport Results .....	7-46
8.0	Transport Parameter Uncertainty and Sensitivity Analysis .....	8-1
8.1	Introduction .....	8-1
8.2	Global Sensitivity Analysis .....	8-2
8.2.1	Classification Tree .....	8-4
8.2.2	Entropy Analysis .....	8-6
8.2.3	Stepwise Regression .....	8-8
8.2.4	Sensitivity Analysis, Transport Parameters, and HFMs .....	8-9
8.2.4.1	LCCU1-MME .....	8-11
8.2.4.2	LCCU1-USGSD .....	8-15
8.2.4.3	LCCU1-MME-TMD .....	8-19
8.2.4.4	LCCU1-MME-TMCM .....	8-23
8.2.4.5	PZUP-MME .....	8-27
8.2.4.6	DRT-DRIA .....	8-31
8.2.4.7	SCCC-MME .....	8-35
8.2.5	Sensitivity Analysis by Method .....	8-39
8.2.5.1	Classification Tree .....	8-39
8.2.5.2	Entropy Analysis .....	8-40
8.2.5.3	Stepwise Regression .....	8-41
8.2.6	Composite Analysis .....	8-42
8.2.7	Summary .....	8-44
8.3	Transport Sensitivity to Flow Model Uncertainty .....	8-46
8.3.1	Previous Analysis of TMCM Permeability Uncertainty .....	8-47
8.3.1.1	Timber Mountain Recharge Mound .....	8-47
8.3.1.2	TMCM Subdivision Local Permeability Perturbation .....	8-50
8.3.1.3	Fortymile Canyon Alternative Model .....	8-50
8.3.2	Null Space Monte Carlo Analysis .....	8-54
8.3.2.1	Transport Modeling .....	8-60
8.3.3	Depth-Decay Reduction .....	8-64
8.3.4	Alternative Dispersivity Scenarios .....	8-70
9.0	Model Uncertainty, Integration, and Assessment .....	9-1
9.1	Introduction .....	9-1
9.2	Pahute Mesa Bench Complexity .....	9-2
9.3	Specific Discharge .....	9-4
9.4	Transport in Fractured Media .....	9-4

**TABLE OF CONTENTS (CONTINUED)**

9.4.1	Fracture Properties .....	9-4
9.4.2	Fracture Pathways .....	9-7
9.4.3	Fault Zones .....	9-7
9.4.4	Confirmation .....	9-9
9.5	Heterogeneity .....	9-10
9.6	Depth Decay .....	9-14
9.7	Recharge .....	9-15
9.8	Boundary Flow .....	9-17
9.9	Source Term .....	9-18
10.0	Summary, Conclusions, and Data Needs .....	10-1
10.1	Data Needs .....	10-9
10.1.1	Pahute Mesa Bench Complexity .....	10-9
10.1.2	Specific Discharge .....	10-10
10.1.3	Fracture Properties .....	10-10
10.1.4	Fracture Pathways .....	10-10
10.1.5	Fault Zones .....	10-10
10.1.6	Heterogeneity .....	10-11
10.1.7	Depth Decay .....	10-11
10.1.8	Recharge .....	10-12
10.1.9	Boundary Flow .....	10-12
10.1.10	Simplified Source Model .....	10-12
11.0	References .....	11-1
 <b>Appendix A - Reactive Mineral Model</b>		
A.1.0	Reactive Mineral Model .....	A-1
 <b>Appendix B - <math>K_d</math> Distributions</b>		
B.1.0	Sorption Coefficients .....	B-1
B.1.1	Stochastic Realizations of Permeability .....	B-1
B.1.1.1	Stochastic Simulation of Permeability .....	B-1
B.1.1.2	Definition of Reactive Mineralogical Zone Permeability .....	B-2
B.1.1.3	Identification of Porous- and Fracture-Flow Dominated RMCs .....	B-3
B.1.2	RMC Permeability .....	B-6
B.1.3	Incorporation of Porous Media and Fracture Properties into RMC Permeability .....	B-11
B.1.4	Results and Verification .....	B-13
B.1.4.1	ECDF Reproduction .....	B-13
B.1.4.2	Variogram Reproduction .....	B-15
B.1.4.3	Flowing Fracture Spacing .....	B-15
B.1.4.4	Transport Simulations for Upscaling .....	B-17

## TABLE OF CONTENTS (CONTINUED)

B.1.4.4.1 Introduction .....	B-17
B.1.5 Yucca Mountain Project $K_d$ Distributions .....	B-21
B.2.0 References .....	B-32
<b>Appendix C - Mechanistic Field-Scale Reactive Transport Modeling</b>	
C.1.0 Introduction .....	C-1
C.2.0 Flow and Transport in Fractured Rock .....	C-3
C.2.1 Background .....	C-3
C.2.2 Generalized Dual-Porosity Model .....	C-4
C.2.2.1 Validation of GDPM with Column Experiment Data .....	C-4
C.2.2.2 Verification of the GDPM for Field-Scale Application .....	C-6
C.3.0 Radionuclide Transport and Reaction Processes .....	C-10
C.3.1 Summary of the Radionuclide Chemical Reactions .....	C-10
C.3.2 Transport Parameters .....	C-12
C.3.2.1 Porosity of Matrix and Fractures .....	C-12
C.3.2.2 Matrix Sorption Coefficients .....	C-12
C.3.2.3 Colloid Load .....	C-13
C.3.2.4 Rate Constants for Plutonium Sorption onto Colloids .....	C-14
C.3.2.5 Rate Constants for Colloid Filtration .....	C-15
C.4.0 Field-Scale Radionuclide Reactive Transport Modeling .....	C-16
C.4.1 TYBO .....	C-17
C.4.1.1 TYBO Radionuclide Source Terms .....	C-17
C.4.1.2 Streamtube from TYBO Source Area .....	C-17
C.4.1.3 Radionuclide Transport without Colloids .....	C-19
C.4.1.4 Colloid-Facilitated Radionuclide Transport .....	C-21
C.4.1.5 Plutonium Isotopes and Daughter Products .....	C-25
C.4.2 PURSE .....	C-27
C.4.2.1 Source Terms of PURSE .....	C-27
C.4.2.2 Streamline from PURSE Sources Area .....	C-29
C.4.2.3 Colloid-Facilitated Radionuclide Transport .....	C-31
C.4.3 Summary of Deterministic Transport Simulations .....	C-33
C.5.0 Scale Dependence of Radionuclide Sorption: Kinetics versus Equilibrium .....	C-35
C.5.1 Identifying Sorption Processes from Column Experiments .....	C-35
C.5.2 Identifying Sorption Processes for Field-Scale Modeling .....	C-42
C.6.0 Pu-Colloid Source Reduction: Monte Carlo Simulation .....	C-45
C.6.1 Framework of Monte Carlo Simulation .....	C-45
C.6.2 Parameters Created with Latin Hypercube Sampling .....	C-46
C.6.2.1 Colloid Mobility .....	C-46

**TABLE OF CONTENTS (CONTINUED)**

C.6.2.2 Monte Carlo Parameters . . . . . C-48  
C.6.3 Results of Monte Carlo Simulations . . . . . C-50  
C.6.4 Summary . . . . . C-53  
C.7.0 References . . . . . C-54

**Appendix D - Evaluation of Groundwater Travel Times in the PM-OV  
Flow System from <sup>14</sup>C Data**

D.1.0 Introduction . . . . . D-1  
D.1.1 Data Limitations . . . . . D-6  
D.1.2 Carbon-14 Data . . . . . D-8  
D.1.3 Estimation of Groundwater <sup>14</sup>C Ages . . . . . D-10  
D.1.4 Effects of Unsaturated-Zone Thickness and Sampling Depths  
on <sup>14</sup>C Ages . . . . . D-18  
D.1.5 Groundwater Travel Time Calculations . . . . . D-22  
D.1.6 Travel Time Results . . . . . D-24  
D.1.7 Flow Path #1 . . . . . D-25  
D.1.8 Flow Paths #2 and #4 . . . . . D-35  
D.1.9 Flow Path #5 . . . . . D-48  
D.2.0 Summary and Conclusions . . . . . D-53  
D.3.0 References . . . . . D-55

**Appendix E - Nevada Division of Environmental Protection Comments**

**LIST OF FIGURES**

<b>NUMBER</b>	<b>TITLE</b>	<b>PAGE</b>
1-1	Location of the Pahute Mesa Corrective Action Units. . . . .	1-2
1-2	Map Showing Location of the Pahute Mesa Model Area . . . . .	1-7
1-3	Process Flow Diagram for the Underground Test Area Corrective Action Units . . . . .	1-9
1-4	Geophysically Inferred Geologic Features of the Pahute Mesa Area . . . . .	1-11
1-5	Features of the NTS Regional Groundwater Flow System . . . . .	1-14
3-1	Generalized Surface Geologic Map of the NTS Area . . . . .	3-10
3-2	Hydrostratigraphic Unit Surface Map for the PM-OV Model Area. . . . .	3-11
3-3	Map Showing HSUs at the Water Table within the PM-OV Model Area. . . . .	3-12
3-4	Southwest-to-Northeast Hydrostratigraphic Cross Section A-A' through the Western Portion of the Timber Mountain Caldera Complex and Southwestern Portion of the SCCC . . . . .	3-13
3-5	West-to-East Hydrostratigraphic Cross Section B-B' through the Black Mountain Caldera and the SCCC. . . . .	3-14
3-6	West-to-East Hydrostratigraphic Cross Section C-C' through the Southern Portion of the Timber Mountain Caldera Complex at Myjo Coffe #1 . . . . .	3-15
3-7	Pahute Mesa Base HFM Described by HSU . . . . .	3-18
3-8	Fault Numbering Key - Base HFM . . . . .	3-19
3-9	Comparison of Silent Canyon Caldera Margins in the Base-HFM Model and SCCC Alternative Model. . . . .	3-22
3-10	Calibrated CAU-Model Boundary Heads and Difference from UGTA Regional Model Viewed from the Northeast. . . . .	3-28
3-11	Groundwater Levels across the Pahute Mesa Flow Model Domain in Western Area 19, Area 20, and West of Area 20. . . . .	3-32
3-12	Simulated Head along B-B' and J-J' with Simulated Flow Path for the SCCC-MME-SDA HFM . . . . .	3-33

**LIST OF FIGURES (CONTINUED)**

<b>NUMBER</b>	<b>TITLE</b>	<b>PAGE</b>
3-13	Simulated Head along B-B' and J-J' with Simulated Flow Path for the BN-MME-SDA HFM. ....	3-34
3-14	Simulated Head near the Purse and Boxcar Faults from the BN-MME-SDA Alternative (top) and SCCC-MME-SDA Alternative (bottom). ....	3-36
3-15	Zones Used To Identify Sources of Groundwater Recharge and Inflow . . . . .	3-38
3-16	Geochemical Residual Means for Each Cluster . . . . .	3-41
3-17	Components of the Total Geochemical Residual for Each Alternative Model . . . . .	3-42
3-18	Flow Model Calibration Metric (Objective Function) per HFM, Sorted by Geochemical Residuals within Clusters (Shown in Figure 3-17) . . . . .	3-43
3-19	LCCU1-MME and SCCC-MME Alternative HFMs from ER-EC-6. ....	3-46
3-20	LCCU1-MME and SCCC-MME Alternative HFMs from UE-18r . . . . .	3-48
3-21	Area 20 Discrepancies in Particle Streamlines. ....	3-50
3-22	Revised Section of Purse Fault. ....	3-52
3-23	Revised Section of Boxcar Fault (Boxcar[42]) . . . . .	3-53
3-24	Particle Streamlines Showing Advective Transport for the Initial Calibrated Case (left) and the Recalibrated Case (right) . . . . .	3-55
3-25	Well Head (m) Residuals before (left) and following (right) Recalibration of the LCCU1-MME Model after Fault Permeability Adjustments. . . . .	3-57
3-26	HSU Permeabilities for the Initial (2006) and Revised (2007) Fault Assignment. . . . .	3-58
3-27	Hydrogeologic Subdomains of the TMCM in the Pahute Mesa Flow Model Area. . . . .	3-60
3-28	Convergent Flow Paths in the TMCM as Particles Exit Areas 19 and 20 . . . . .	3-62
3-29	Convergent Flow (Particle Pathlines) and Transport (Plume) Paths in the TMCM as Particles Exit Areas 19 and 20 . . . . .	3-63
3-30	Plume Convergence upon Northern Entrance of the TMCM as Tracer Particles Exit Areas 19 and 20 . . . . .	3-65

**LIST OF FIGURES (CONTINUED)**

<b>NUMBER</b>	<b>TITLE</b>	<b>PAGE</b>
3-31	Streamlines through the LCCU1-MME-TMD Alternative HFM . . . . .	3-67
3-32	Comparison of Head (m) Residuals and Calibration Metrics between the LCCU1-MME and LCCU1-MME-TMD Alternative HFMs. . . . .	3-68
3-33	Comparison of Head (m) Residuals and Calibration Metrics between the LCCU1-MME and LCCU1-MME-TMCM Alternative HFMs. . . . .	3-71
3-34	LCCU1-MME-TMCM Head (m) Residuals with Well Names . . . . .	3-72
3-35	Primary HSUs Reparameterized for Development of the LCCU1-MME-TMCM Alternative HFM . . . . .	3-73
4-1	Schematic Diagram of the Source Term Regions in the HST Model and the SSM. . . . .	4-3
4-2	Temperature Decay with Time for Nuclear Melt Glass . . . . .	4-19
4-3	Schematic of the SSM Conceptual Model . . . . .	4-21
4-4	HFM Normalized Fluid Flux for all Pahute Mesa Nuclear Tests . . . . .	4-29
4-5	HFM <sup>3</sup> H Solute Mass Flux for TYBO . . . . .	4-30
4-6	Mass Flux Release from TYBO for LCCU1-USGSD . . . . .	4-35
4-7	Mass Flux Release from CHESHIRE for LCCU1-USGSD. . . . .	4-35
5-1	Nuclear Test Cavity Formation Collapse . . . . .	5-3
5-2	Cross Section through TYBO, BENHAM, and ER-20-5. . . . .	5-6
5-3	3-D Display from EarthVision of the Reactive Mineral Model for the PM-OV Model. . . . .	5-31
5-4	West-East Model Profile through the PLFA Showing the RMC Subdivisions in the Northern PM-OV Model Area . . . . .	5-49
5-5	Physiographic Features of the PM-OV Model Area . . . . .	5-60
6-1	Three Characteristic Regions Qualifying the Impact of $D_m$ on Mean Solute Transport Time. . . . .	6-9



**LIST OF FIGURES (CONTINUED)**

<b>NUMBER</b>	<b>TITLE</b>	<b>PAGE</b>
6-2	Dual-Porosity Transport Characteristics Highlighted with Simulated Breakthrough Curve of an Instantaneously Released Source . . . . .	6-10
6-3	Fracture Porosity Distribution for the Monte Carlo Transport Simulations. . . . .	6-16
6-4	Fracture Spacing Distribution for the Monte Carlo Transport Simulations. . . . .	6-17
6-5	Fracture Spacing Parameter Combinations for DMP/R and ML in the Monte Carlo Transport Simulations. . . . .	6-17
6-6	Fracture Spacing and Porosity Parameter Combinations in CAU Monte Carlo Runs. . . . .	6-18
6-7	Fracture Spacing and Porosity Combinations with Aperture in CAU Monte Carlo Runs. . . . .	6-19
6-8	Fracture Aperture Distribution for the Monte Carlo Transport Simulations . . . . .	6-20
6-9	Crossplots of Geophysical Log-Derived and Core-Derived Porosity Values . . . . .	6-21
6-10	Log( $\phi_m D_m$ ) Values as a Function of Matrix Porosity (Fraction) and a Logarithmic Fit to the Data. . . . .	6-26
6-11	NTS Data as Compared to Non-NTS Data for Longitudinal Dispersivity. . . . .	6-29
6-12	MTC and Aperture Combinations in Monte Carlo Simulations . . . . .	6-31
6-13	MTC and Fracture Porosity Combinations in Monte Carlo Simulations. . . . .	6-31
6-14	MTC and $D_m$ Combinations in Monte Carlo Simulations . . . . .	6-32
6-15	YMP Pu $K_d$ Distributions for Volcanic Tuff . . . . .	6-34
6-16	UGTA Pu $K_d$ Distribution for Devitrified Tuff and Zeolite (Shaw, 2003) Compared with YMP Pu $K_d$ Distribution. . . . .	6-35
6-17	UGTA Np $K_d$ Distribution for Devitrified Tuff and Zeolite (Shaw, 2003) Compared with YMP Composite Np $K_d$ Distribution for Saturated Volcanic Tuffs . . . . .	6-36
6-18	Mechanistic Model $K_d$ Distributions for DMP Compared with Laboratory Data . . . . .	6-39

**LIST OF FIGURES (CONTINUED)**

<b>NUMBER</b>	<b>TITLE</b>	<b>PAGE</b>
6-19	Mechanistic Model $K_d$ Distributions for DMP .....	6-39
6-20	Mechanistic Model $K_d$ Distributions for DMR Compared with Laboratory Data .....	6-40
6-21	Mechanistic Model $K_d$ Distributions for ZEOL Compared with Laboratory Data .....	6-40
6-22	Mechanistic Model $K_d$ Distributions for VMP/R.....	6-41
6-23	Estimated Variograms from Mechanistic Model $K_d$ Estimates for YMP Samples in Tc and Tp Groups.....	6-42
6-24	Fitting Np for a DMP Realization .....	6-44
6-25	Distribution of $K_d$ , Upscaled for DMP.....	6-45
6-26	Distribution of $K_d$ , Upscaled for DMR .....	6-45
6-27	Distribution of $K_d$ , Upscaled for ML .....	6-46
6-28	Distribution of $K_d$ , Upscaled for ZEOL.....	6-46
6-29	Distribution of $K_d$ , Upscaled for VMP/R.....	6-47
6-30	Comparison of Mechanistic and Upscaled $K_d$ for Pu.....	6-47
6-31	Locations of ER-EC-5 and ER-OV-3c for $^{14}\text{C}$ Comparisons .....	6-51
6-32	Fracture Aperture Sensitivity: Simulated Travel Time Distributions between Two Wells .....	6-52
6-33	(a) Converting a Sample Age Distribution into a $^{14}\text{C}$ Sample Age Using the (b) $^{14}\text{C}$ Decay Curve .....	6-54
6-34	Simulated $^{14}\text{C}$ Ages between ER-EC-5 and ER-OV-3c for Spacing versus Fracture Porosity .....	6-56
6-35	Simulated $^{14}\text{C}$ Ages between ER-EC-5 and ER-OV-3c for Aperture versus Fracture Porosity .....	6-57
6-36	Simulated $^{14}\text{C}$ Ages between ER-EC-5 and ER-OV-3c for Spacing versus Fracture Porosity .....	6-59

**LIST OF FIGURES (CONTINUED)**

<b>NUMBER</b>	<b>TITLE</b>	<b>PAGE</b>
6-37	Simulated <sup>14</sup> C Ages between ER-EC-5 and ER-OV-3c for Aperture versus Fracture Porosity . . . . .	6-60
7-1	Non-specific Example of a Probability of MCL Exceedance Map for Alpha Particles, Beta Emitters, or Uranium . . . . .	7-8
7-2	Non-specific Example of an FEV Chart Showing the Contribution of Each Radionuclide, at Multiple Timesteps, to the Time-Specific EV . . . . .	7-12
7-3	Comparison of EV ECDFs for Transport Simulation of the LCCU1-MME-TMCM Model for 1,000- and 2,000-Realization Parameter Sets . . . . .	7-14
7-4	Source-Reduction Analysis of Particles Crossing South of the Transect at Northing 4,110,000 m . . . . .	7-15
7-5	Groundwater Flux, Normalized by Model Cell Volume, at an Elevation of 750 m in the LCCU1-MME Model. . . . .	7-19
7-6	LCCU1-MME Probability of MCL Exceedance Map for Alpha Particles, Beta Emitters, and Uranium at 50, 500, and 1,000 Years . . . . .	7-20
7-7	LCCU1-MME Probabilistic MCL Exceedance Map for Discrete Time . . . . .	7-21
7-8	Fractional Exceedance Volumes Based on LCCU1-MME Transport Simulation. . . . .	7-21
7-9	LCCU1-MME-TMD Probability of MCL Exceedance Map for Alpha Particles, Beta Emitters, and Uranium at 50, 500, and 1,000 Years . . . . .	7-23
7-10	LCCU1-MME-TMD Probabilistic MCL Exceedance Map for Discrete Time . . . . .	7-25
7-11	Fractional Exceedance Volumes Based on LCCU1-MME-TMD Transport Simulation . . . . .	7-25
7-12	LCCU1-USGSD Probability of MCL Exceedance Map for Alpha Particles, Beta Emitters, and Uranium at 50, 500, and 1,000 Years . . . . .	7-27
7-13	LCCU1-USGSD Probabilistic MCL Exceedance Map for Discrete Time . . . . .	7-28
7-14	Fractional Exceedance Volumes Based on LCCU1-USGSD Transport Simulation . . . . .	7-28
7-15	DRT-DRIA Probability of MCL Exceedance Map for Alpha Particles, Beta Emitters, and Uranium at 50, 500, and 1,000 Years . . . . .	7-30

**LIST OF FIGURES (CONTINUED)**

<b>NUMBER</b>	<b>TITLE</b>	<b>PAGE</b>
7-16	Probability of MCL Exceedance Based on DRT-DRIA Transport Model . . . . .	7-31
7-17	Comparison of Flux across the Model Domain at a Single Elevation (750 m amsl) between the DRT-DRIA (left) and LCCU1-MME (right) HFMs . . . . .	7-32
7-18	PZUP-MME Probability of MCL Exceedance Map for Alpha Particles, Beta Emitters, and Uranium at 50, 500, and 1,000 Years . . . . .	7-33
7-19	PZUP-MME Probabilistic MCL Exceedance Map for Discrete Time. . . . .	7-34
7-20	Fractional Exceedance Volumes Based on PZUP-MME Transport Model Simulation. . . . .	7-34
7-21	LCCU1-MME-TMCM Probability of MCL Exceedance Map for Alpha Particles, Beta Emitters, and Uranium at 50, 500, and 1,000 Years . . . . .	7-36
7-22	LCCU1-MME-TMCM Probabilistic MCL Exceedance Map for Discrete Time . . . . .	7-37
7-23	Comparison of Flux across the Model Domain at a Single Elevation (750 m amsl) between the LCCU1-MME-TMCM (left) and LCCU1-MME (right) HFMs . . . . .	7-38
7-24	Fractional Exceedance Volumes Based on LCCU1-MME-TMCM Transport Model Simulation. . . . .	7-39
7-25	SCCC-MME Probability of MCL Exceedance Map for Alpha Particles, Beta Emitters, and Uranium at 50, 500, and 1,000 Years . . . . .	7-41
7-26	SCCC-MME Probabilistic MCL Exceedance Map for Discrete Time . . . . .	7-42
7-27	Fractional Exceedance Volumes Based on SCCC-MME Transport Simulation . . . . .	7-43
7-28	EV Cumulative Probability Distributions for the Alternative Transport Models Using the Low (top) and High-Dispersivity (bottom) Tensors . . . . .	7-44
7-29	Probabilistic Exceedance Map for Four Alternative Transport Models Using the High-Dispersivity Tensor. . . . .	7-45
7-30	Probability of MCL Exceedance at Four Exceedance Thresholds for the LCCU1-MME Transport Model at 50 Years . . . . .	7-49
7-31	1,000-Year Time-Invariant Exceedance Map at Three Certainty Levels, with Certainty Represented by the Probability of MCL Exceedance, for the LCCU1-MME and LCCU1-MME-TMCM Transport Models. . . . .	7-52

**LIST OF FIGURES (CONTINUED)**

<b>NUMBER</b>	<b>TITLE</b>	<b>PAGE</b>
8-1	Classification Tree Analysis for LCCU1-MME. . . . .	8-5
8-2	Bubble Plots from Entropy Analysis for LCCU1-MME . . . . .	8-13
8-3	Stepwise Regression Analysis Plot for LCCU1-MME . . . . .	8-14
8-4	Classification Tree for LCCU1-USGSD . . . . .	8-16
8-5	Bubble Plots from Entropy Analysis for LCCU1-USGSD . . . . .	8-17
8-6	Stepwise Regression Analysis Plot for LCCU1-USGSD. . . . .	8-18
8-7	Classification Tree for LCCU1-MME-TMD . . . . .	8-20
8-8	Bubble Plots from Entropy Analysis for LCCU1-MME-TMD . . . . .	8-21
8-9	Stepwise Regression Plot for LCCU1-MME-TMD. . . . .	8-22
8-10	Classification Tree for LCCU1-MME-TMCM . . . . .	8-24
8-11	Bubble Plots from Entropy Analysis for LCCU1-MME-TMCM . . . . .	8-25
8-12	Stepwise Regression Plot for LCCU1-MME-TMCM . . . . .	8-26
8-13	Classification Tree for PZUP-MME . . . . .	8-28
8-14	Bubble Plots from Entropy Analysis for PZUP-MME. . . . .	8-29
8-15	Stepwise Regression for PZUP-MME . . . . .	8-30
8-16	Classification Tree for DRT-DRIA . . . . .	8-32
8-17	Bubble Plots from Entropy Analysis for DRT-DRIA . . . . .	8-33
8-18	Stepwise Regression for DRT-DRIA. . . . .	8-34
8-19	Classification Tree for SCCC-MME . . . . .	8-36
8-20	Bubble Plots from Entropy Analysis for SCCC-MME . . . . .	8-37
8-21	Stepwise Regression for SCCC-MME. . . . .	8-38
8-22	Hydrogeologic Subdomains of the TMCM in the Pahute Mesa Model Area . . . . .	8-48

**LIST OF FIGURES (CONTINUED)**

<b>NUMBER</b>	<b>TITLE</b>	<b>PAGE</b>
8-23	Weighted Well and Spring Head (m) Residuals for TMD Permeability of 10x (top) and 100x (bottom) .....	8-49
8-24	Simulated Water Tables for TMD Permeability Increases of 10x (top) and 100x (bottom) .....	8-51
8-25	Particle Tracks for TMD Permeability Increases of 10x (top) and 100x (bottom) .....	8-52
8-26	Particle Tracks for the BN-MME-SDA Fortymile Canyon Alternative Model.....	8-53
8-27	Boxplots Define the Sampled Range of Permeability Uncertainty before Assessing Their Insensitive Components .....	8-56
8-28	Flow Simulation Objective Functions for Each of the NSMC Permeability Realizations.....	8-57
8-29	Boxplots Define the Calculated Range of Permeability Insensitivity .....	8-58
8-30	Head Residuals for the LCCU1-MME-TMCM HFM Showing Boreholes at Which Head Measurements Are Exclusive to Either the TMCM, FCCM, or Both.....	8-60
8-31	Radionuclide Migration for Four of Nine NSMC Flow Models .....	8-62
8-32	Scatterplot Matrix of NSMC Realization Permeabilities and Resultant EVs .....	8-63
8-33	Subzones in the FCCM for Recalibration with Reduced Depth-Decay Coefficient ...	8-65
8-34	Comparison of Calibrated $k_0$ for TMCM and FCCM Subzones in the LCCU1-MME-TMCM.....	8-66
8-35	Postplot of Weighted Residuals in Recalibrated LCCU1-MME-TMCM-dd Flow Model.....	8-67
8-36	Transect for Comparing Simulated Permeability for Depth-Decay Coefficient Equal to 0.001 and 0.0027.....	8-68
8-37	Comparing Simulated Permeabilities ( $m^2$ ) for Two Depth-Decay Coefficients in TMCM and FCCM HSUs .....	8-68

**LIST OF FIGURES (CONTINUED)**

<b>NUMBER</b>	<b>TITLE</b>	<b>PAGE</b>
8-38	Comparing Time at Which Standard Exceeded for Single Realization of Identical Transport Parameters in Flow Field Calibrated with Two Depth-Decay Coefficients, 0.0027 (left) and 0.001 (right) . . . . .	8-69
8-39	Comparing Time at Which Standard Exceeded for Single Realization of Identical Transport Parameters in LCCU1-MME-TMCM Flow Field with Different Dispersion Tensors (Part 1) . . . . .	8-71
8-40	Comparing Time at Which Standard Exceeded for Single Realization of Identical Transport Parameters in LCCU1-MME-TMCM Flow Field with Different Dispersion Tensors (Part 2) . . . . .	8-72
8-41	Comparing Time at Which Standard Exceeded for Single Realization of Identical Transport Parameters in LCCU1-MME-TMCM Flow Field with Different Dispersion Tensors (Part 3) . . . . .	8-73
8-42	Monte Carlo Simulation Results for Different Dispersion Tensors . . . . .	8-75
B.1-1	Bar Chart Showing the Percentage of HGU per RMC. . . . .	B-5
B.1-2	DMP/R RMC ECDF on y-Axis at Left (black) with Thresholds (red) and PDF (vertical bars) Shown on y-Axis at Right . . . . .	B-7
B.1-3	VMP/R RMC ECDF on y-Axis at Left (black) with Thresholds (red) and PDF (vertical bars) Shown on y-Axis at Right . . . . .	B-7
B.1-4	Permeability ECDF Region for ZEOL RMC (minimum and maximum bounds in black) and 100 Randomly Generated ECDFs (varied colors) with Thresholds (colored solid symbols) . . . . .	B-8
B.1-5	Permeability ECDF (y-axis on left) for Each of the Three RMCs. . . . .	B-11
B.1-6	Selected Permeability Realizations for (from left to right) the DMP/R, VMP/R, and ZEOL RMCs. . . . .	B-14
B.1-7	Comparison of the Discrete ECDFs from (all 100) Realizations of the DMP/R RMC Plotted against the Sample ECDF Described in Table B.1-2 . . . . .	B-14
B.1-8	Comparison of x- and y-Direction Variograms from (100 total) Realizations of the VMP/R RMC Plotted against the Input Variogram at the $k = -11.52 \text{ m}^2$ Threshold. . . . .	B-16

**LIST OF FIGURES (CONTINUED)**

<b>NUMBER</b>	<b>TITLE</b>	<b>PAGE</b>
B.1-9	Vertical Flowing Interval Spacing Histogram for 100 DMP/R Permeability Realizations.....	B-18
B.1-10	Permeability Distribution and Simulated Head for a DMP Realization.....	B-18
B.1-11	Simulated Particle Paths in a 3-D DMP Model.....	B-19
B.1-12	Fitting the Non-reactive Breakthrough Curve (physical dispersion).....	B-20
C.2-1	Schematic Illustration of Column Experiments for Fracture Transport System and the GDPM Grid.....	C-5
C.2-2	Comparison of the GDPM against the Relap Semianalytical Solution for Interpreting the Column Experiments Conducted by Ware et al. (2005).....	C-5
C.2-3	Model Domain and Flow Boundary Conditions for the Verification of the GDPM Algorithm against Analytical and Particle-Tracking Results Solutions.....	C-7
C.2-4	Comparison of the GDPM against the Particle-Tracking Results for the Synthetic Model of Dash (2003).....	C-7
C.2-5	Comparison of Breakthrough Curves for the GDPM against the Particle-Tracking Method with Reactive Tracers in the Pahute Mesa LCCU1-MME Flow Model with Releases at TYBO.....	C-9
C.3-1	Conceptual Model of Pu Reactive Transport in Fractures.....	C-10
C.4-1	Mean Radionuclide Source Flux Functions for $^3\text{H}$ , $^{14}\text{C}$ , $^{237}\text{Np}$ , and $^{239}\text{Pu}$ from TYBO.....	C-17
C.4-2	Mean Radionuclide Source Flux Functions for Pu Isotopes from TYBO.....	C-18
C.4-3	3-D Streamline for the Non-reactive and Non-diffusing Particle Migrating from the TYBO Source Area (in XY plan view).....	C-19
C.4-4	Schematic Illustration of the GDPM Numerical Model with Heterogeneous Rock Properties.....	C-20
C.4-5	Computed Concentration Breakthrough Curves for $^3\text{H}$ , $^{14}\text{C}$ , $^{239}\text{Pu}$ , and $^{237}\text{Np}$ at a Distance of 5 km Away from the TYBO Source Location.....	C-20
C.4-6	Computed Concentration Breakthrough Curves for $^3\text{H}$ , $^{14}\text{C}$ , $^{239}\text{Pu}$ , and $^{237}\text{Np}$ at a Distance of 15 km Away from the TYBO Source Location.....	C-21



**LIST OF FIGURES (CONTINUED)**

<b>NUMBER</b>	<b>TITLE</b>	<b>PAGE</b>
C.4-7	Radionuclide Concentration Distributions at Different Transport Time . . . . .	C-22
C.4-8	Computed Concentration Breakthrough Curves for <sup>239</sup> Pu at a Distance of 5 km Away from the TYBO Source Location . . . . .	C-23
C.4-9	Computed Concentration Breakthrough Curves for <sup>239</sup> Pu at a Distance of 15 km Away from the TYBO Source Location . . . . .	C-24
C.4-10	Simulated Total Pu Concentration (Aqueous and Colloidal) Distributions for the Colloid-Facilitated Radionuclide Transport Model at Different Times . . . . .	C-24
C.4-11	Concentration Breakthrough Curves of Pu Isotopes for Colloid-Facilitated Transport at 5 km Away from the TYBO Source Area . . . . .	C-26
C.4-12	Concentration Breakthrough Curves of Pu Isotopes for the Colloid-Facilitated Transport at 15 km Away from the TYBO Source Area . . . . .	C-26
C.4-13	Concentration Breakthrough Curves of Am, Np, and U for the Colloid-Facilitated Transport at 5 km Away from the TYBO Source Area, by Considering and Omitting the Two Decay Chains . . . . .	C-28
C.4-14	Concentration Breakthrough Curves of Am, Np, Pu, and U for the Colloid-Facilitated Transport at 5 km Away from the TYBO Source Area, by Considering the Decay and In-growth Processes . . . . .	C-28
C.4-15	Concentration Breakthrough Curves of Am, Np, Pu, and U for the Colloid-Facilitated Transport at 15 km Away from the TYBO Source Area, by Considering the Decay and In-growth Processes . . . . .	C-29
C.4-16	Mean Radionuclide Source Flux Functions for PURSE . . . . .	C-30
C.4-17	3-D Streamline for the Non-reactive and Non-diffusing Particle Transport from the PURSE Source Area . . . . .	C-30
C.4-18	Concentration Breakthrough Curves of <sup>14</sup> C, Np, and Pu for Colloid-Facilitated Transport at 5 km Away from the PURSE Source Area, by Considering the Decay and In-growth Processes . . . . .	C-32
C.4-19	Final Concentration Distributions for Radionuclide Transport from PURSE along a GDPM Streamtube Model at 1,000 Years. . . . .	C-32
C.5-1	Fitting Four <sup>3</sup> H Breakthrough Curves from Four Fractured Tuffaceous Rock Experiments . . . . .	C-37

**LIST OF FIGURES (CONTINUED)**

<b>NUMBER</b>	<b>TITLE</b>	<b>PAGE</b>
C.5-2	Fitting Two Np Breakthrough Curves from Two Fractured Tuffaceous Rock Experiments .....	C-39
C.5-3	Fitting Two U Breakthrough Curves from Two Fractured Tuffaceous Rock Experiments under (a) Kinetic and (b) Equilibrium Conditions.....	C-42
C.5-4	Flow Velocity Distribution along the 1-D Streamline Starting from the TYBO Source Area .....	C-43
C.5-5	(a) Computed Residence Time at Each Numerical Node and the Half Reaction Time and (b) Computed Damköhler Number for Np Sorption and Transport .....	C-43
C.5-6	(a) Computed Residence Time at Each Numerical Node and the Half Reaction Time and (b) Computed Damköhler Number for U Sorption and Transport.....	C-44
C.6-1	YMP Cumulative Probability Distribution for Colloid Sorption Retardation Factors Converted to Sorption Coefficients.....	C-47
C.6-2	Sensitivity Analysis of Colloid Sorption Coefficient on Field-Scale Mobility .....	C-48
C.6-3	Distribution of 1,000 Realizations of the Parameters Created with LHS.....	C-49
C.6-4	Simulated Breakthrough Curves of <sup>239</sup> Pu from the First 100 Realizations of the Monte Carlo Simulation of Scenario Two (aperture = 0.001 m) at 5 km .....	C-51
C.6-5	<sup>239</sup> Pu Source-Reduction Factor (f <sub>sr</sub> ) Distribution at 5 km Using a Fracture Porosity of 0.0001 m .....	C-52
C.6-6	<sup>239</sup> Pu Source-Reduction Factor (f <sub>sr</sub> ) Distribution at 5 km Using a Fracture Porosity of 0.001 m .....	C-52
D.1-1	Topographic Features near the PM-OV Area.....	D-2
D.1-2	Well Groups and Key Wells in the PM-OV Flow System.....	D-3
D.1-3	Tracers Used in the PM-OV Geochemical Modeling Analysis: (a) Chloride, (b) Sulfate, (c) δ <sup>18</sup> O, and (d) δD.....	D-4
D.1-4	δD versus Cl with Thirsty Canyon Mixing Line .....	D-5
D.1-5	Map with Groundwater <sup>14</sup> C Data and Flow Paths Interpreted from Groundwater Mixing Model .....	D-9

**LIST OF FIGURES (CONTINUED)**

<b>NUMBER</b>	<b>TITLE</b>	<b>PAGE</b>
D.1-6	Groundwater $\delta^{13}\text{C}$ and Inverse Alkalinity Data from PM-OV Flow System . . . . .	D-11
D.1-7	$^{14}\text{C}$ versus $\delta^{13}\text{C}$ Data from the PM-OV Flow System . . . . .	D-13
D.1-8	Comparison of $\delta^{13}\text{C}$ - and DIC-Corrected Groundwater $^{14}\text{C}$ Ages . . . . .	D-16
D.1-9	Average of the $\delta^{13}\text{C}$ - and DIC-Corrected Groundwater $^{14}\text{C}$ Ages Superimposed on Flow Paths . . . . .	D-17
D.1-10	Average of the $\delta^{13}\text{C}$ - and DIC-Corrected Groundwater $^{14}\text{C}$ Ages as a Function of Depth to Water . . . . .	D-19
D.1-11	Average Corrected $^{14}\text{C}$ Age as a Function of Sample Depth below the Water Table (WT) (a) Pahute Mesa and Thirsty Canyon Wells and (b) Other Wells . . . . .	D-20
D.1-12	Map Summarizing Mixing Models for Flow Path #1 . . . . .	D-26
D.1-13	Inverse Model Results for ER-EC-6: (a) Mixing Fractions, (b) Reactions, and (c) Composite Travel Times . . . . .	D-27
D.1-14	Inverse Model Results for ER-OV-01: (a) Mixing Fractions, (b) Reactions, and (c) Composite Travel Times . . . . .	D-29
D.1-15	Inverse Model Results for ER-EC-2A (shallow): (a) Mixing Fractions and (b) Reactions . . . . .	D-32
D.1-16	Inverse Model Results for ER-EC-2A (deep): (a) Mixing Fractions and (b) Reactions. . . . .	D-33
D.1-17	Inverse Model Results for ER-EC-8 (shallow): (a) Mixing Fractions and (b) Reactions. . . . .	D-34
D.1-18	Map Summarizing Geochemical Inverse Model Results for Flow Path #2 . . . . .	D-36
D.1-19	Inverse Model Results for UE-18r: (a) Mixing Fractions, (b) Reactions, and (c) Composite Travel Times . . . . .	D-37
D.1-20	Inverse Model Results for ER-EC-5: (a) Mixing Fractions, (b) Reactions, and (c) Composite Travel Times . . . . .	D-38
D.1-21	Inverse Model Results for ER-OV-03c: (a) Mixing Fractions, (b) Reactions, and (c) Composite Travel Times . . . . .	D-40

**LIST OF FIGURES (CONTINUED)**

<b>NUMBER</b>	<b>TITLE</b>	<b>PAGE</b>
D.1-22	Travel Times from ER-EC-5 to ER-OV-03c Calculated Assuming Zero Travel Times for Recharge Component to ER-OV-03c .....	D-42
D.1-23	Inverse Model Results for ER-OV-04a with ER-OV-03c as an Upgradient Source: (a) Mixing Fractions, (b) Reactions, and (c) Composite Travel Times .....	D-43
D.1-24	Inverse Model Results for ER-OV-04a with UE-18r as an Upgradient Source: (a) Mixing Fractions, (b) Reactions, and (c) Composite Travel Times .....	D-44
D.1-25	Map Summarizing Geochemical Inverse Model Results for Flow Path #4 .....	D-46
D.1-26	Inverse Model Results for CRWW: (a) Mixing Fractions, (b) Reactions, and (c) Composite Travel Times .....	D-47
D.1-27	Map Summarizing Geochemical Inverse Model Results for J-13 .....	D-49
D.1-28	Inverse Model Results for J-13: (a) Mixing Fractions, (b) Reactions, and (c) Composite Travel Times .....	D-50
D.1-29	Inverse Model Results for J-12: (a) Mixing Fractions, (b) Reactions, and (c) Composite Travel Times .....	D-52

**LIST OF TABLES**

<b>NUMBER</b>	<b>TITLE</b>	<b>PAGE</b>
1-1	Major Supporting Documents . . . . .	1-16
3-1	Hydrogeologic Units of the PM-OV Model Area . . . . .	3-5
3-2	Hydrostratigraphic Units of the PM-OV Model Area Included in the UGTA Project Regional HFM. . . . .	3-7
3-3	Base HFM Fault Indices and Names . . . . .	3-19
3-4	Summary of Alternative HFMs Considered in the PM Flow Model. . . . .	3-21
3-5	Correlation of HSUs between the SCCC HFM and the Base HFM . . . . .	3-24
3-6	k-Means Clusters of Flow Models Based on Geochemical Residuals . . . . .	3-39
3-7	Initial and Recalibrated Objective Function for the Alternative HFMs . . . . .	3-59
3-8	HSU Permeability . . . . .	3-64
3-9	LCCU1-MME and Recalibrated LCCU1-MME-TMCM Permeabilities . . . . .	3-69
4-1	Cavity Geometry Parameters . . . . .	4-3
4-2	Underground Shaft Nuclear Tests Conducted in Central Pahute Mesa (CAU 101) . . . . .	4-5
4-3	Underground Shaft Nuclear Tests Conducted in Western Pahute Mesa (CAU 102) . . . . .	4-8
4-4	Sum of Radionuclide Inventory in Areas 19 and 20 . . . . .	4-9
4-5	Estimated Accuracies for Radionuclide Groups . . . . .	4-11
4-6	Partitioning of the Inventory into Glass, Rubble, Gas, and Water . . . . .	4-11
4-7	CHESHIRE Test Volume, Porosity, and Pore Volume of Source Regions . . . . .	4-13
4-8	Average Log Retardation Ratios for Heterogeneous Mineral Distributions . . . . .	4-14
4-9	Digitized Temperature Time History in the Melt Glass for the SSM . . . . .	4-19
4-10	Probabilistic Distributions for Melt Glass/Exchange Volume Partitioning Coefficients in Terms of Melt Glass Fraction . . . . .	4-27
4-11	HGU-Specific Matrix Porosity . . . . .	4-31

**LIST OF TABLES (CONTINUED)**

<b>NUMBER</b>	<b>TITLE</b>	<b>PAGE</b>
4-12	Porosity Assignments for Components for BENHAM . . . . .	4-31
4-13	Data Defining Cavity Geometry for BENHAM . . . . .	4-32
4-14	Grain Density Assignments for BENHAM . . . . .	4-32
4-15	Hydrologic Parameter Assignments for BENHAM . . . . .	4-33
4-16	Glass Dissolution Parameters for BENHAM . . . . .	4-33
5-1	Reactive Mineral Categories for the PM-OV Model. . . . .	5-16
5-2	Reactive Mineral Summary for RMCs in the PM-OV Model. . . . .	5-18
5-3	Hydrostratigraphic and Reactive Mineral Units of the PM-OV Model. . . . .	5-19
6-1	Fracture Porosity of Volcanic Aquifers Estimated Using Parallel Plate Models . . . . .	6-12
6-2	Fracture Properties for WTA . . . . .	6-13
6-3	Fracture Properties for LFA. . . . .	6-13
6-4	Pahute Mesa - Effective Porosity - Dominant Lithology for Two HSUs . . . . .	6-14
6-5	Lithologic Groups, HGUs, and RMCs. . . . .	6-22
6-6	Pahute Mesa - Matrix Porosity - Dominant Lithology for Each HSU. . . . .	6-23
6-7	Dispersivity Information Summary from the NTS and Vicinity . . . . .	6-28
6-8	Computer Fracture Porosity from Permeability Spacing and Aperture. . . . .	6-61
6-9	Distribution Types and Applicable Data Restrictions . . . . .	6-65
7-1	Maximum Contaminant Levels for Regulatory Groups . . . . .	7-6
7-2	Source-Reduction Analysis . . . . .	7-16
8-1	Input Parameters . . . . .	8-10
8-2	Ranked Entropy Analysis for LCCU1-MME . . . . .	8-12
8-3	Ranked Stepwise Regression Analysis for LCCU1-MME . . . . .	8-14

**LIST OF TABLES (CONTINUED)**

<b>NUMBER</b>	<b>TITLE</b>	<b>PAGE</b>
8-4	Ranked Entropy Analysis for LCCU1-USGSD. ....	8-16
8-5	Ranked Stepwise Regression Analysis for LCCU1-USGSD .....	8-18
8-6	Ranked Entropy Analysis for LCCU1-MME-TMD .....	8-20
8-7	Ranked Stepwise Regression for LCCU1-MME-TMD. ....	8-22
8-8	Ranked Entropy Analysis for LCCU1-MME-TMCM. ....	8-24
8-9	Ranked Stepwise Regression for LCCU1-MME-TMCM. ....	8-26
8-10	Ranked Entropy Analysis for PZUP-MME. ....	8-28
8-11	Ranked Stepwise Regression for PZUP-MME .....	8-30
8-12	Ranked Entropy Analysis for DRT-DRIA. ....	8-32
8-13	Ranked Stepwise Regression for DRT-DRIA .....	8-34
8-14	Ranked Entropy Analysis for SCCC-MME. ....	8-36
8-15	Ranked Stepwise Regression for SCCC-MME .....	8-38
8-16	Classification Tree of Splits for Each HFM .....	8-39
8-17	Classification Tree Transport Parameters .....	8-40
8-18	Ranked Entropy Analysis for the Top Five Parameters for Each HFM .....	8-40
8-19	Entropy Analysis Transport Parameters .....	8-41
8-20	Ranked Stepwise Regression Parameters .....	8-41
8-21	Stepwise Regression Transport Parameters. ....	8-42
8-22	Composite Analysis Transport Parameters .....	8-42
8-23	Grouping of Sensitive Transport Parameters Based on the EV for Each HFM .....	8-43
8-24	Range of Permeability Uncertainty for the TMCM and FCCM Derived from Field Measurement .....	8-55

**LIST OF TABLES (CONTINUED)**

<b>NUMBER</b>	<b>TITLE</b>	<b>PAGE</b>
8-25	Range of Permeability Insensitivity across Realizations. . . . .	8-59
8-26	Average Transport Parameters Used for the Single Transport Simulation of Each NSMC Flow Model . . . . .	8-61
8-27	Dispersivity Tensors for Single Parameter Set Sensitivity Runs. . . . .	8-70
B.1-1	HGU-RMC Crosswalk. . . . .	B-4
B.1-2	ECDF Threshold Descriptors for the DMP/R RMC Including Permeability, CDF, and Directional Variogram Parameters . . . . .	B-8
B.1-3	ECDF Threshold Descriptors for the VMP/R RMC Including Permeability, CDF, and Directional Variogram Parameters . . . . .	B-9
B.1-4	Minimum- and Maximum-ECDF Threshold Descriptors for the ZEOL RMC Including Permeability, CDF, and Directional Variogram Parameters. . . . .	B-10
B.1-5	Small-Scale Probability Distribution Functions for $K_d$ in the Saturated Zone Developed on the Basis of Laboratory Data from Core Samples . . . . .	B-21
B.1-6	Recommended Composite Distribution for $K_d$ in Volcanics and Alluvium . . . . .	B-23
B.1-7	Carbonate Sorption $K_d$ Ranges . . . . .	B-24
B.1-8	Summary of Distributions Fit for Pu Sorption Using YMP Data - Minimum and Maximum of Dataset Listed in Parentheses When Different from Distribution . . .	B-25
B.1-9	Summary of Distributions Fit for Np Sorption Using YMP Data. . . . .	B-26
B.1-10	Summary of Distributions Fit for Sr Using YMP Data. . . . .	B-27
B.1-11	Summary of Distributions Fit for Cs Using YMP Data. . . . .	B-27
B.1-12	Summary of Distributions Fit for U Using YMP Data . . . . .	B-28
B.1-13	Distribution Coefficients Statistics and Shape Parameters for Laboratory Measurement of Radionuclide Sorption on Vitric Tuff. . . . .	B-29
B.1-14	Distribution Coefficients Statistics and Shape Parameters for Laboratory Measurement of Radionuclide Sorption on Devitrified Tuffs. . . . .	B-30



**LIST OF TABLES (CONTINUED)**

<b>NUMBER</b>	<b>TITLE</b>	<b>PAGE</b>
B.1-15	Distribution Coefficients Statistics and Shape Parameters for Laboratory Measurement of Radionuclide Sorption on Zeolitic Tuffs .....	B-31
C.2-1	Inverse Modeling of <sup>3</sup> H Breakthrough Curves from Two Fractured Tuffaceous Rock Experiments.....	C-6
C.3-1	Radionuclide-Related Reactions Included in the Field-Scale Simulations .....	C-11
C.3-2	Statistics of the Porosity Data for the GDPM .....	C-12
C.3-3	Mean Sorption Coefficients for Am, Np, and Pu (cm <sup>3</sup> /g) from Mechanistic K <sub>d</sub> Estimates (Section 6.0) .....	C-13
C.3-4	Statistical Results of Forward and Reverse Rate Constants of Pu Sorption onto Colloids .....	C-14
C.3-5	Statistics of Rate Constants of Colloid Attachment and Detachment to/from Fracture Walls .....	C-15
C.5-1	Inverse Modeling of Four <sup>3</sup> H Breakthrough Curves from Four Fractured Tuffaceous Rock Experiments.....	C-37
C.5-2	Inverse Modeling of Two Np Breakthrough Curves from Two Fractured Tuffaceous Rock Experiments .....	C-38
C.5-3	Inverse Modeling of Two U Breakthrough Curves from Two Fractured Tuffaceous Rock Experiments .....	C-41
C.6-1	Statistics of the Five Most Sensitive Parameters.....	C-50
C.6-2	Summary of the Two Monte Carlo Simulations with Variable Fracture Porosities .....	C-53
D.1-1	Travel Times from Individual Wells to ER-EC-6 .....	D-28
D.1-2	Travel Times from Individual Wells to ER-OV-01.....	D-30
D.1-3	Travel Times from Individual Wells to ER-OV-03c.....	D-41
D.1-4	Travel Times from Individual Wells to the CRWW .....	D-45
D.1-5	Travel Times from Individual Wells to ER-OV-04a.....	D-48

## **LIST OF ACRONYMS AND ABBREVIATIONS**

1-D	One-dimensional
2-D	Two-dimensional
3-D	Three-dimensional
amsl	Above mean sea level
bmsl	Below mean sea level
BN	Bechtel Nevada
CADD	Corrective action decision document
CAI	Corrective action investigation
CAIP	Corrective action investigation plan
cal/mol	Calories per mole
CAP	Corrective action plan
CAS	Corrective action site
CAU	Corrective action unit
CBPT	Convolution-based particle tracking
CD-ROM	Compact disc-read-only memory
CDF	Cumulative distribution function
Ci	Curie
CI	Confidence interval
cm	Centimeter
cm <sup>3</sup> /g	Cubic centimeters per gram
CR	Closure Report
CRWW	Coffer Ranch Windmill Well
CT	Contaminant transport
DEM	Digital elevation model
dEV	Discrete-time maximum contaminant level exceedance volume
D <sub>m</sub>	Matrix diffusion
DOB	Depth of burial
DOE	U.S. Department of Energy
DQO	Data quality objective
DRI	Desert Research Institute
DTN	Data tracking number
ECDF	Empirical cumulative distribution function
EPA	U.S. Environmental Protection Agency

## **LIST OF ACRONYMS AND ABBREVIATIONS (CONTINUED)**

ERP	Environmental Restoration Project
ET	Evapotranspiration
EV	Exceedance volume
FEHM	Finite element heat-mass
FEV	Fractional exceedance volume
FFACO	<i>Federal Facility Agreement and Consent Order</i>
FGE	Forced-Gradient Experiment
ft	Foot
g/cm <sup>3</sup>	Grams per cubic centimeter
g/mol	Grams per mole
GDPM	Generalized dual-porosity model
GWTT	Groundwater travel time
HFM	Hydrostratigraphic framework model
HGU	Hydrogeologic unit
HRMP	Hydrologic Resources Management Program
HST	Hydrologic source term
HSU	Hydrostratigraphic unit
IAEA	International Atomic Energy Agency
IT	IT Corporation
K	Hydraulic conductivity
kcal/mol	Kilocalories per mole
K <sub>d</sub>	Distribution coefficient
kg/m <sup>3</sup>	Kilograms per cubic meter
kg/s	Kilograms per second
km	Kilometer
km <sup>2</sup>	Square kilometer
k <sub>0</sub>	Reference permeability
kt	Kiloton
LANL	Los Alamos National Laboratory
LEA	Local equilibrium assumption
LHS	Latin hypercube sampling
LLNL	Lawrence Livermore National Laboratory
m	Meter

**LIST OF ACRONYMS AND ABBREVIATIONS (CONTINUED)**

m/s	Meters per second
m <sup>2</sup>	Square meter
m <sup>2</sup> /g	Square meters per gram
m <sup>2</sup> /s	Square meters per second
m <sup>3</sup>	Cubic meter
m <sup>3</sup> /yr	Cubic meters per year
Ma	Million years ago
masl	Meters above sea level
MCL	Maximum contaminant level
meq/L	Milliequivalents per liter
mg/L	Milligrams per liter
MGZ	Melt glass zone
mi <sup>2</sup>	Square mile
mL/g	Milliliters per gram
mL/hr	Milliliters per hour
mi	Mile
mm	Millimeter
mm/yr	Millimeters per year
MME	Modified Maxey-Eakin recharge model
mol/L	Moles per liter
mol/m <sup>2</sup> /s	Moles per square meter per second
mrem/yr	Millirem per year
MTC	Mass transfer coefficient
MWAT	Multiple-well aquifer test
N/A	Not applicable
NAD	North American Datum
NDEP	Nevada Division of Environmental Protection
nm	Nanometer
NNSA/NSO	U.S. Department of Energy, National Nuclear Security Administration Nevada Site Office
NSMC	Null Space Monte Carlo
NSTec	National Security Technologies, LLC
NTS	Nevada Test Site
PCC	Partial correlation coefficient

**LIST OF ACRONYMS AND ABBREVIATIONS (CONTINUED)**

pCi/L	Picocuries per liter
PDF	Probability distribution function
PEST	Parameter estimation
PM	Pahute Mesa
PM-OV	Pahute Mesa-Oasis Valley
pmc	Percent modern carbon
QA	Quality assurance
QC	Quality control
RF	Retardation factor
RMC	Reactive mineral category
RMU	Reactive mineral unit
RNM	Radionuclide Migration
RST	Radiologic source term
s	Sample standard deviation
SD	Standard deviation
SDWA	<i>Safe Drinking Water Act</i>
SNJV	Stoller-Navarro Joint Venture
SRC	Standardized regression coefficient
SSM	Simplified source model
SVD	Singular value decomposition
TWG	Technical Working Group
UGTA	Underground Test Area
USGS	U.S. Geological Survey
UTM	Universal Transverse Mercator
XRD	X-ray diffraction
XRF	X-ray fluorescence
YMP	Yucca Mountain Project
°C	Degrees Celsius
δ	Delta value
μg/L	Micrograms per liter
$\bar{x}$	Sample mean

## **LIST OF SYMBOLS FOR ELEMENTS AND COMPOUNDS**

Al	Aluminum
Am	Americium
Ar	Argon
C	Carbon
Ca	Calcium
CaCO <sub>3</sub>	Calcite
CaMgCO <sub>3</sub>	Limestone
Cd	Cadmium
Cl	Chlorine
Cm	Curium
CO <sub>2</sub>	Carbon dioxide
Cs	Cesium
DIC	Dissolved inorganic carbon
Eu	Europium
F	Fluoride
Fe	Iron
<sup>3</sup> H	Tritium
HCO <sub>3</sub> <sup>-</sup>	Bicarbonate
Ho	Holmium
I	Iodine
K	Potassium
Kr	Krypton
Mg	Magnesium
Mn	Manganese
MnO <sub>2</sub>	Manganese oxide
Na	Sodium
Nb	Niobium
Ni	Nickel
Np	Neptunium
Pa	Protactinium
Pb	Lead
Pd	Palladium
Pu	Plutonium

**LIST OF SYMBOLS FOR ELEMENTS AND COMPOUNDS (CONTINUED)**

Ra	Radium
S	Sulfur
Se	Selenium
Si	Silicon
SiO <sub>2</sub>	Silica
Sm	Samarium
Sn	Tin
SO <sub>4</sub> <sup>2-</sup>	Sulfate
Sr	Strontium
Tc	Technetium
Th	Thorium
U	Uranium
Zn	Zinc
Zr	Zirconium

## **LIST OF STRATIGRAPHIC UNIT ABBREVIATIONS AND SYMBOLS**

AA	Alluvial aquifer
ADA	All hydrostratigraphic unit depth decay and anisotropy
ARG	Argillic
ATCE	Ammonia Tanks eastern subdivision
ATCF	Ammonia Tanks caldera structural margin fault
ATCW	Ammonia Tanks western subdivision
ATICU	Ammonia Tanks intrusive confining unit
BA	Benham aquifer
BAQ	Basal aquifer
BCU	Basal confining unit
BFCU	Bullfrog confining unit
BMICU	Black Mountain intrusive confining unit
BRA	Belted Range aquifer
BRCU	Belted Range confining unit
BRT	Belted Range thrust
CA	Carbonate aquifer
CC	Reactive mineral category for carbonate rocks
CCICU	Claim Canyon intrusive confining unit
CCU	Clastic confining unit
CFCM	Crater Flat composite unit
CFCU	Crater Flat confining unit
CHCU	Calico Hills composite unit
CHICU	Calico Hills intrusive confining unit
CHVCM	Calico Hills vitric confining unit
CHVTA	Calico Hills vitric-tuff aquifer
CHZCM	Calico Hills zeolitized composite unit
DMP	Devitrified mafic-poor
DMR	Devitrified mafic-rich
DRIA	Desert Research Institute Chloride Mass-Balance Alluvial and No Elevation Screen Recharge Model
DRIAE	Desert Research Institute Chloride Mass-Balance Alluvial and Elevation Screen Recharge Model
DRT	Deeply rooted belted range thrust fault
DVA	Detached volcanics aquifer
DVCM	Detached volcanics composite unit



**LIST OF STRATIGRAPHIC UNIT ABBREVIATIONS AND SYMBOLS (CONTINUED)**

DVRFM	Death Valley regional flow model
FCA	Fortymile Canyon aquifer
FC-BH	Fluorspar Canyon-Bullfrog Hills
FCCM	Fortymile Canyon composite unit
FCCU	Fluorspar Canyon confining unit
GCU	Granite confining unit
IA	Inlet aquifer
ICU	Intrusive confining unit
IICU	Intra-caldera intrusive confining unit
KA	Kearsarge aquifer
LCA	Lower carbonate aquifer
LCA3	Lower carbonate aquifer-thrust plate
LCCU	Lower clastic confining unit
LCCU1	Lower clastic confining unit - thrust plate
LFA	Lava-flow aquifer
LPCU	Lower Paintbrush confining unit
LTCU	Lower tuff confining unit
LVTA	Lower vitric-tuff aquifer
MGCU	Mesozoic granite confining unit
ML	Mafic lava
NTME	Northern Timber Mountain Eastern subdivision
NTMW	Northern Timber Mountain Western subdivision
PBRCM	Pre-Belted Range composite unit
PCM	Paintbrush composite unit
PLFA	Paintbrush lava-flow aquifer
PVTA	Paintbrush vitric-tuff aquifer
PZUP	Raised Pre-Tertiary surface
RIDGE	Basement Ridge model
RMICU	Rainier Mesa intrusive confining unit
SC	Reactive mineral category for silicic rocks
SCCC	Silent Canyon caldera complex
SCICU	Silent Canyon intrusive confining unit
SCVCU	Subcaldera volcanic confining unit

---

**LIST OF STRATIGRAPHIC UNIT ABBREVIATIONS AND SYMBOLS (CONTINUED)**

SDA	Selected hydrostratigraphic unit depth decay anisotropy
SEPZ	Contiguous imbricate thrust sheet
SWNVF	Southwestern Nevada Volcanic Field
Tb	Belted Range Group
Tbg	Grouse Canyon tuff
Tbgs	Commendite of Split Range
Tbq	Commendite of Quartet Dome
Tc	Crater Flat Group
TC	Tuff cone
TCA	Tiva Canyon aquifer
TCL	Thirsty Canyon lineament
TCU	Tuff confining unit
TCVA	Thirsty Canyon volcanic aquifer
Th	Calico Hills Formation
THCM	Tannenbaum Hill composite unit
THLFA	Tannenbaum Hill lava-flow aquifer
Tma	Ammonia Tanks tuff
TMA	Timber Mountain aquifer
Tmab	Bedded Ammonia Tanks tuff
Tmap	Mafic-poor Ammonia Tanks tuff
Tmar	Mafic-rich Ammonia Tanks tuff
TMCM	Timber Mountain composite unit
TMCU	Timber Mountain confining unit
TMD	Timber Mountain dome
Tmr	Rainier Mesa tuff
Tmrp	Mafic-poor portion of Rainier Mesa tuff
Tmrr	Mafic-rich portion of Rainier Mesa tuff
Tn	Tunnel Formation
Tor	Redrock Valley tuff
Tot	Tuff of Twin Peaks
Toy	Yucca Flat tuff
Tp	Paintbrush Group
Tpt	Topopah Spring tuff

**LIST OF STRATIGRAPHIC UNIT ABBREVIATIONS AND SYMBOLS (CONTINUED)**

TSA	Topopah Spring aquifer
Tt	Thirsty Canyon
Tub	Tub Spring tuff
TUBA	Tub Spring aquifer
Tw	Wahmonie Formation
UCCU	Upper clastic confining unit
UPCU	Upper Paintbrush confining unit
USGSD	U.S. Geological Survey Redistribution Recharge Model
USGSD	U.S. Geological Survey No Redistribution Recharge Model
VMP	Vitric mafic-poor
VMR	Vitric mafic-rich
VTA	Vitric-tuff aquifer
VU	Volcanics undifferentiated
WTA	Welded-tuff aquifer
WWA	Windy Wash aquifer
YMCFCM	Yucca Mountain Crater Flat composite unit
YVCM	Younger volcanics composite unit
ZEOL	Zeolitic

## **EXECUTIVE SUMMARY**

This executive summary is a synopsis of the report entitled *Phase I Transport Model of Corrective Action Units 101 and 102: Central and Western Pahute Mesa, Nevada Test Site, Nye County, Nevada*, prepared for the U.S Department of Energy (DOE). As prescribed in the Pahute Mesa Corrective Action Investigation Plan (CAIP) (DOE/NV, 1999) and Appendix VI of the *Federal Facility Agreement and Consent Order* (FFACO) (1996, as amended February 2008), the ultimate goal of transport analysis is to develop stochastic predictions of a contaminant boundary at a specified level of uncertainty. However, because of the significant uncertainty of the model results, the primary goal of this report was modified through mutual agreement between the DOE and the State of Nevada to assess the primary model components that contribute to this uncertainty and to postpone defining the contaminant boundary until additional model refinement is completed. Therefore, the role of this analysis has been to understand the behavior of radionuclide migration in the Pahute Mesa (PM) Corrective Action Unit (CAU) model and to define, both qualitatively and quantitatively, the sensitivity of such behavior to (flow) model conceptualization and (flow and transport) parameterization.

## **INTRODUCTION**

The DOE, National Nuclear Security Administration Nevada Site Office (NNSA/NSO) initiated the Underground Test Area (UGTA) Project to assess and evaluate the effects of underground shaft and tunnel nuclear weapons tests on groundwater at the Nevada Test Site (NTS) and vicinity through the FFACO (1996, as amended February 2008). The processes that will be used to complete UGTA Project corrective actions are described in the Corrective Action Strategy in the FFACO Appendix VI, Rev. 1 (December 7, 2000). The groundwater modeling advances in two stages: (1) development of a regional scale model from which is developed a continuous flow field over the entire NTS site and (2) development of a subregional scale model that provides a refined view of each of five CAUs. The objective of the strategy is to analyze and evaluate each UGTA Project CAU through a combination of data and information collection and evaluation, and modeling groundwater flow and contaminant transport. For the UGTA Project, the corrective action strategy comprises two major parts: (1) a regional evaluation addressing all CAUs and (2) a corrective action investigation (CAI) process for each of the individual CAUs. The first major part was completed with the development of

the model and report entitled *Regional Groundwater Flow and Tritium Transport Modeling and Risk Assessment of the Underground Test Area, Nevada Test Site, Nevada* (DOE/NV, 1997b). The second part of the process focuses on acquisition and analysis of CAU-specific data and development of CAU-scale flow and transport models. The CAU-specific objectives are to estimate the movement of contaminants using CAU-specific hydrogeologic and transport parameter data, and to define the regulatory contaminant boundaries.

Underground nuclear tests at Pahute Mesa were conducted in deep vertical boreholes drilled into the volcanic rocks of the Silent Canyon caldera. A total of 82 underground nuclear tests were conducted in shafts on Pahute Mesa. Sixty-four of the tests were detonated on Central Pahute Mesa (CAU 101), and 18 tests were detonated at Western Pahute Mesa (CAU 102) (DOE/NV, 1999). Most of the tests were detonated at or near the water table, which serves as the primary medium through which radionuclide contamination migrates out of the underground nuclear test sites.

Pahute Mesa is an elevated plateau of about 500 square kilometers (200 square miles) located in the northwestern part of the NTS. The area of interest for the PM flow model is defined by the potentially affected portion of the regional groundwater flow system, which includes a region stretching from the northern side of Pahute Mesa south and southwestward to Oasis Valley.

Pahute Mesa geology is dominated by the deposition of rock units from volcanic eruptions from nested calderas of the Southwestern Nevada Volcanic Field (SWNVF). The Silent Canyon caldera is the oldest series of calderas and consists of at least two nested calderas: the Area 20 caldera and the older Grouse Canyon caldera. Both calderas were formed, and subsequently filled, by voluminous eruptions of tuff and lava of generally rhyolitic composition. The youngest caldera complex of hydrologic significance is the Timber Mountain caldera. This caldera collapse and its filling with volcanic materials affect the southern portion of the Pahute Mesa CAU.

Groundwater beneath Pahute Mesa generally flows in a southwest direction, primarily through fractures in the lava-flow and tuff aquifers. Zeolitized bedded and nonwelded tuffs act as confining units that inhibit the flow of groundwater. Because of the paucity of data, the spatial distribution of permeable aquifers relative to the confining units is not well understood. Thickness variations within the aquifers and confining units, and their connectivity across faults or caldera boundaries, are important hydrostratigraphic relationships that are also uncertain. A number of wells provide

water-level information in the areas of Pahute Mesa and Oasis Valley, but water levels in the area between Pahute Mesa and Oasis Valley are less well-defined. However, what data are available suggest that groundwater elevations generally gently mimic the topography. Some groundwater discharges to the surface within the Oasis Valley discharge area in the form of springs. Groundwater recharge occurs locally from precipitation and by underflow from areas north of Pahute Mesa. Groundwater then flows south-southwestward to the Oasis Valley and then southwest to Death Valley.

Specific objectives of the PM CAU transport model (including revisions to the flow model) are to:

- Superimpose three-dimensional (3-D) transport model properties onto the PM CAU groundwater model domain through development of reactive mineral categories (RMCs).
- Develop contaminant mass flux for underground nuclear test sites using one-dimensional (1-D) simplified source models (SSMs) that represent flow and transport through the test cavity and disturbed rock zone adjacent to the cavity that is then input to the PM CAU model.
- Simulate transport from the underground test sites using a stochastic approach that provides multiple, equally probable realizations of plume migration and calculation of the spatial extent of the contaminant plume for all model nodes that exceed the regulatory limit of 4 millirem per year (mrem/yr), projected out to 1,000 years.
- Quantify the radionuclide spread and flow path due to uncertainty in parametric values and alternative conceptual models (geology and RMCs).
- Identify data needs for Phase II field data collection and further refinement of the numerical model.

## **PREVIOUS STUDIES**

Before the regional flow and transport model was released, Lacznia et al. (1996) summarized the scientific understanding about groundwater flow beneath the NTS region and highlighted uncertainties in knowledge of hydrogeologic conditions in the complex regional flow system, further furnishing the basis for a conceptual model for flow and transport at both regional and smaller scales.

*The Regional Groundwater Flow and Tritium Transport Modeling and Risk Assessment of the Underground Test Area, Nevada Test Site, Nevada* (DOE/NV, 1997b) provides the initial rationale to determine the magnitude of risk from possible groundwater contamination at various underground

nuclear tests on the NTS to potential downgradient receptors such as the public and the environment. The steps in the regional evaluation consisted of data analysis, model development, and model predictions. Results of the regional evaluation of groundwater flow, tritium ( $^3\text{H}$ ) migration, and risk assessment performed for the underground test areas are presented in that report. The regional evaluation was used during the planning of the Pahute Mesa CAI and served as the basis for developing the CAU conceptual model and constraining CAU model boundary flow rates.

The Pahute Mesa CAIP (DOE/NV, 1999), a document required by the FFACO (1996, as amended February 2008), summarizes previously available site-specific data for Central and Western Pahute Mesa CAUs 101 and 102, and describes the CAI to be conducted at the Pahute Mesa CAUs to identify information that will better define the extent of contamination in groundwater due to the underground nuclear testing. The CAIP constitutes an overall plan to address CAU-scale groundwater flow and contaminant transport modeling activities to be conducted during the CAI, including the assessment and incorporation of existing and newly acquired data. The purpose of the Pahute Mesa CAIP is to structure the data collection and modeling strategy to facilitate understanding the groundwater system such that contaminant boundary uncertainty is reduced. Key uncertainties identified in the Pahute Mesa CAIP (DOE/NV, 1999) were:

- The subsurface for the area southwest of Pahute Mesa between the underground test area and the Oasis Valley discharge area is not well characterized.
- Estimates of precipitation and recharge available for the Pahute Mesa groundwater flow system are highly uncertain.
- Knowledge of contaminant transport processes and associated parameters is limited.
- Understanding of the release of contaminants from nuclear tests is limited.

The strategy for flow and transport modeling is described in the *Modeling Approach/Strategy for Corrective Action Units 101 and 102, Central and Western Pahute Mesa* (SNJV, 2004c). The objective of the strategy is to analyze and evaluate each UGTA Project CAU through a combination of data and information collection and groundwater flow and transport modeling. The strategy report describes the current conceptual model of radionuclide migration from test cavities on Pahute Mesa to the accessible environment, and maps the flow of information from data collection through process model development to the CAU model. The data collection activities culminated in the publication of

the reports *Hydrologic Data for Groundwater Flow and Contaminant Transport Model of Corrective Action Units 101 and 102: Central and Western Pahute Mesa, Nye County, Nevada* (SNJV, 2004b) and *Contaminant Transport Parameters for the Groundwater Flow and Contaminant Transport Model of Corrective Action Units 101 and 102: Central and Western Pahute Mesa, Nye County, Nevada* (Shaw, 2003).

The groundwater flow model that directly supports the PM CAU transport model is the subject of *Groundwater Flow Model of Corrective Action Units 101 and 102: Central and Western Pahute Mesa, Nevada Test Site, Nye County, Nevada* (SNJV, 2006a). That report presents a framework for the PM CAU flow model that incorporates data and information related to multiple component models of the Pahute Mesa hydrogeologic system. The PM CAU flow model is then used to simulate hydrologic response based on flow system characteristics. The system is adjusted to achieve a best-fit scenario to observed data through an automated calibration process. Based on the hydrologic response during calibration, conceptual and parametric uncertainty within the PM CAU flow model can be assessed. The hydrostratigraphic framework model (HFM) is the fundamental building block upon which the PM CAU flow and transport models are built. The HFM consists of a 3-D arrangement of rock depositional sequences, referred to as hydrostratigraphic units (HSUs), and structural features that include basin-and-range fault structures and caldera ring fractures. The PM CAU flow model is then superimposed onto the HFM model domain through definition of groundwater flow system characteristics that comprise:

- Lateral boundary fluxes
- Recharge estimates
- Discharge estimates
- Hydraulic head measurements
- Hydraulic conductivity
- Geochemical mixing targets

The hydrologic source term model (HST) is another of the component models that supplies the radionuclide solute flux from underground test sites for use in the PM CAU transport model. Inputs and conceptual design for this model are defined in *Unclassified Source Term and Radionuclide Data for the Groundwater Flow and Contaminant Transport Model of Corrective Action Units 101 and 102: Central and Western Pahute Mesa, Nye County, Nevada* (SNJV, 2004e). The HST model was initially developed for a 3-D domain at a single underground test site, which in this case was selected



at the underground nuclear test designated CHESHIRE. Because of limited knowledge and computational burden, a 1-D simplified version of the HST, designated the SSM, was developed using the GoldSim simulation software. Results from the SSM were matched to the 3-D model calculations for the CHESHIRE test to check the validity of using the simpler model as a surrogate for the higher-dimensional model.

## ***PAHUTE MESA CAU FLOW MODEL ALTERNATIVES***

The PM CAU flow model was created and calibrated before PM CAU transport modeling for multiple alternative HFMs. Steady-state velocity fields are extracted from the PM CAU flow model for use by the PM CAU transport model. Initial transport simulations using particle-tracking methods for those velocity fields showed distinctive spreading patterns of particle distributions that indicated anomalous flow paths through faults and HSUs. In addition, exploration of additional alternative HFMs was deemed necessary to expand the range of responses that are possible from the model. The PM CAU flow model as provided at the end of the phase I groundwater flow modeling described in Stoller-Navarro Joint Venture (SNJV) (2006a) is used as a starting point to facilitate development of the new alternative models. Development of two additional HFMs from the previous PM CAU flow model are implemented through: (1) permeability adjustment across the Purse and Boxcar faults, and (2) permeability adjustments to select HSUs for the preferred HFM from among the subset of alternatives models investigated during the PM CAU flow model task.

There are two distinct configurations that the HFM can take: (1) the base model (LCCU1) and (2) the Silent Canyon caldera complex (SCCC) alternative. Of these configurations, there are variants of the base model that differ in the location of discrete HSU and permeability features.

The base HFM comprises 47 structural elements that represent either faults or calderas. Only faults with significant displacement (greater than 60 meters [m]) were included in the model. Six calderas were identified in the PM CAU model area, two of which are buried. Of particular interest was the SCCC, an investigation of which led to development of an alternative conceptualization and associated HFM. The SCCC comprises two calderas: the Grouse Canyon and Area 20 calderas. The SCCC alternative HFM includes 20 faults and structural zones in addition to the caldera-forming faults. The faults of the base HFM tend to be steeply dipping normal faults that penetrate the full

thickness of the model, while the SCCC alternative HFM faults have a shallow dip that is often concave and only partially penetrate the PM CAU model domain in the vertical direction.

The base HFM includes considerable structural detail and stratigraphic enhancement over the UGTA regional model HFM (IT, 1996d). The total number of HSUs increased from 20 to 46, with most of the increase affecting the Tertiary volcanic section.

The SCCC alternative HFM differs hydrostratigraphically from the base in the number of HSUs, their definition, and their distribution (BN, 2002a). Principally, whereas in the base HFM the Silent Canyon caldera area includes 25 HSUs, it includes only 12 in the SCCC alternative. Other differences include increased detail in the hydrostratigraphic layers and more irregular contacts within the base HFM HSUs. The SCCC alternative model has thicker, lenticular units that are thick in the middle and include smooth, undulating surfaces.

The groundwater flow and transport discussed in this report refers to the PM CAU (subregional) model domain in contrast to the NTS regional model domain. The PM CAU model covers the geographical area of the site that includes Pahute Mesa, Timber Mountain, Thirsty Canyon, Fortymile Canyon, and Oasis Valley. Through the course of the modeling activities, variants of the naming convention have been used. These names include the PM model, Pahute Mesa-Oasis Valley (PM-OV) model, PM flow model, PM transport model, and PM CAU model. Unless specifically identified as the regional scale model, all references to the groundwater model are synonymous with the PM CAU model. The model can be further categorized as flow or transport. Where neither category is explicitly identified, the model is assumed to refer to both the flow and transport categories.

The PM CAU flow model accounts for regional inflow and outflow across all four lateral edges, internal flow from precipitation recharge, and internal discharge at Oasis Valley. Three approaches were used to develop alternative recharge models for the NTS area (which include the PM CAU flow model area). Each of the recharge alternatives was assumed for at least one of the calibrated PM CAU model alternatives selected for transport simulation. The alternative recharge models are:

- Maxey-Eakin estimation techniques
- Net infiltration-recharge distributed parameter modeling
- Chloride mass-balance modeling

The only internal discharge sources represented in the PM CAU model are the Oasis Valley springs and evapotranspiration outflow. Boundary heads are represented as fixed hydraulic heads at the perimeter of the model domain. By fixing the boundary heads, flow through the PM CAU flow model becomes invariant or otherwise steady state. Boundary heads from the UGTA Project regional model analysis described in SNJV (2004b) were interpolated onto the edge nodes of the PM CAU model. These boundary heads represent a mass conservative calibrated solution to the groundwater flow equation from the UGTA regional model. During calibration, these heads were reviewed and, in spots, revised based on further examination of measured heads and heads determined from the UGTA regional model.

The PM CAU flow model considered seven HFMs (the base case plus six alternatives) and five recharge models. In the interest of brevity, the following shorthand was defined: the first part of the name is the HFM, and the second is recharge condition. The HFMs are distinguished from one another by the geometric location of stratigraphic or structural features. The recharge condition refers to the method used to infer how much water infiltrates at the surface across the PM CAU model domain.

The HFMs are:

- SCCC - Silent Canyon Caldera Complex
- PZUP - Raised Pre-Tertiary/Surface
- DRT - Deeply Rooted Belted Range Thrust Fault
- RIDGE - Basement Ridge
- TCL - Thirsty Canyon Lineament
- SEPZ - Contiguous Imbricate Thrust Sheet
- LCCU1 - Lower Clastic Confining Unit

The five recharge models, summarized in [Section 3.2.4.1](#), are:

- MME - Modified Maxey-Eakin
- USGSD - USGS recharge with redistribution
- USGSND - USGS recharge without redistribution
- DRIA - DRI recharge with alluvial mask
- DRIAE - DRI recharge with alluvial and elevation mask

Four other strategies were applied only to the base model to test the impact of the concepts of permeability depth decay and anisotropy. Depth decay is the condition where the permeability of the

rock decreases as a function of increased lithostatic pressure with increased depth. Anisotropy reflects preferential flow direction within a 3-D space as a function of structural controls and depositional orientation.

The four strategies are:

- No depth decay, no anisotropy
- Selected HSU depth decay
- Selected HSU depth decay and anisotropy (referred to as SDA)
- All HSU depth decay and anisotropy (referred to as ADA)

Calibration targets consisted of four categories of hydraulic observations:

- Hydraulic head from wells
- Estimated spring head in and near Oasis Valley
- Oasis Valley discharge
- Edge flows estimated from regional model analysis

Hydraulic heads at wells comprised the bulk (between about 50 to 60 percent) of the calibration objective function, followed by Oasis Valley discharge (about 25 percent), estimated regional edge flow (about 15 percent), and finally estimated spring heads (5 to 10 percent). Groundwater levels throughout the PM CAU flow model domain taken from Fenelon (2000) imply southwest flow from northern Area 19 and more southerly flow from northern Area 20 across the entire model domain. The gradient is principally derived from elevation gain in the north.

A key characteristic of calibrated flow model behavior involves the measured hydraulic discontinuity across the Purse fault, a feature more pronounced in the HFM alternatives than in the SCCC HFM. There is approximately 100 m of head difference across the fault with flow directed subparallel to the fault (e.g., the fault may act as a no-flow barrier). The hydraulic head on either side of the Boxcar fault also shows a pronounced offset of approximately 40 m of head difference with flow subparallel to the Boxcar fault.

The alternative HFMs were evaluated against independently developed groundwater mixing targets determined from geochemical analyses. The purpose of these comparisons was to determine whether the sources of groundwater at certain wells within the domain (as modeled) were

consistent with the geochemical interpretation, thereby identifying HFM alternatives appropriate for transport simulation.

Based upon the different types of source water identified by Kwicklis et al. (2005), zones are grouped into six categories identified as Northwest, Local Recharge West of Timber Mountain, North Central, Northeast, East (flow in from Rainier Mesa), and East of Timber Mountain. As described in SNJV (2005), differences between simulated mixing ratios from upgradient zone groups and the values measured by Kwicklis et al. (2005) for contributions from wells in those zones constitute a geochemical mixing residual. The geochemical verification approach is applied for calibrated PM CAU models with alternative water-balance conditions and alternative HFMs.

For all of the PM CAU flow model combinations considered, apparent similarities in the errors among the various models motivated a formal cluster analysis in order to identify models with similar geochemical residuals. The clusters were developed with the objective of minimizing the intervariance within each cluster while maximizing the intervariance between clusters. The analysis was achieved with a k-means clustering algorithm, which entails an iterative process for assigning models to different clusters and then testing the objective. The analysis highlights four distinct clusters of the models considered and shows the mean geochemical residual for the models identified in each of the clusters plotted against the errors considered.

Considering the hydraulic data alone, SNJV (2006a) showed that HFMs were able to equitably match measured fluxes and pressures, indicating that the spatial distributions of HSUs between the alternatives were (approximately) insensitive to measured hydraulic data. However, the analysis of flow paths and mixing among the calibrated models indicated an appreciably greater sensitivity to steady-state geochemical targets. Among the seven PM CAU flow models advanced for transport, systematic discrepancies between hydraulic and geochemical targets for all models were identified.

Well ER-EC-6 is southeast of the Purse fault and west of the southern Boxcar fault. The geochemical interpretation suggests that equal ratios of water flowing south from both sides of the Purse fault mix at ER-EC-6. The geochemical signature of the waters on either side of the fault is distinctly different (Kwicklis et al., 2005). In contradiction, the PM flow model results for all selected alternative models, with the exception of the SCCC-MME alternative, show that the large majority of groundwater at ER-EC-6 originates west of the Purse fault primarily as inflow along the northern

boundary. To match the observed and simulated hydraulic and geochemical targets at ER-EC-6 requires either the decrease/redirection of flow from the northwest or the increase/redirection of flow from east of the Purse. The solution to reconcile the PM CAU model with the observations was to decrease permeability of the southern extension of the Purse fault to decrease flow from the northwest.

Borehole UE-18r is just north of Timber Mountain and reflects mixing of groundwater from Areas 19 and 20 of Pahute Mesa, from Timber Mountain, and from flow into the model domain across the eastern boundary near Rainier Mesa. Geochemical interpretation indicates that most of the water originates in the northeast (central and northern Area 19), with only a small component resembling a deep source found (in ER-18-2) on the east flank of Timber Mountain. A high-permeability gap in the Boxcar fault north of UE-18r was adjusted to a lower permeability that then redirected more flow from the northeast through UE-18r.

A preliminary assessment of PM CAU flow model behavior revealed that basin-scale convergent flow paths appreciably impact transport behavior. Specifically, particle flow paths originating from Areas 19 and 20 sources converge when entering the extensive, high-permeability Timber Mountain composite unit (TMCM) HSU, thereby increasing velocity and the rate of plume migration, and impacting related transport mechanisms such as matrix diffusion. Convergent flow was observed for all of the base model alternatives. This behavior is a direct result of how the model permeability is assigned to individual, large-scale HSUs using a single value. To mitigate this behavior, alternative conceptual models were then developed such that flow through the system is spread over a larger area. To achieve this end, two alternative HSUs are developed from the base model. These alternative HSUs were developed from the LCCU1-MME, which exhibited the greatest plume extent based on simulation results, and therefore any change to the model would provide the most conservative result relative to the other model alternatives.

Development of the LCCU1-MME-TMD involved increasing the permeability beneath Timber Mountain (i.e., the TMCMTMD subdivision) relative to the calibrated LCCU1-MME, PM CAU flow model, by two orders of magnitude and then performing minor recalibration. The goal of the LCCU1-MME-TMD alternative was therefore to assess the impact on transport based on flow paths that are more diffuse through the Timber Mountain area as a result of a diminished recharge

mound and the higher permeability. Although the groundwater mound is reduced and there is more flow through the TMCMTMD, the preferential flow path along the west side of Timber Mountain in the TMCM is still seen as a major conduit to flow and transport.

The fundamental purpose behind development of the LCCU1-MME-TMCM alternative was to homogenize permeability, to the extent possible, within the TMCM subdivisions and adjacent HSUs to reduce modes of preferential flow. For development of a new alternative, the general strategy was to enable flow through each of these zones and then to recalibrate, maintaining such flows while honoring hydraulic targets. When the permeability in the confining units is relaxed to allow flow to occur in addition to the existing high-permeability units, flow is spread over a larger front, the volume of rock available for reaction increases, and flow velocities decrease.

## ***PAHUTE MESA SIMPLIFIED SOURCE MODEL***

The purpose of the SSM is to estimate the HST and radiological source term (RST), which provides the source of contaminants introduced to the PM CAU transport model. The HST refers to the radionuclide load in solution within the model domain. The RST is the radionuclide load in the water and entrained in the solid phase that is leached slowly by the groundwater. The SSM is a 1-D representation used in place of a more detailed, 3-D process model that is more computationally demanding and hence unsuitable for wide application as input to the PM CAU transport model, particularly for purposes of sensitivity and uncertainty analysis. This simplification constitutes a parallel computational technique that provides valuable insight into the important processes and uncertainty of the source term.

The source region is conceptualized as two volumes: an exchange volume and a nuclear melt glass zone (MGZ). The exchange volume consists of the cavity zone (i.e., the cavity excluding the nuclear MGZ) and the disturbed zone around the cavity. The nuclear MGZ consists of the nuclear melt glass along with in-fallen alluvium at the bottom of the cavity. The cavity and disturbed zones are idealized as spherical volumes, with the cavity centered on the working point (location of the test in the subsurface) but the disturbed zone center somewhat higher.

A comprehensive unclassified inventory of the RST for the NTS is provided in Bowen et al. (2001). This inventory provides an estimate of radioactivity remaining underground at the NTS after nuclear

testing. The inventory was subdivided into five areas roughly corresponding to the UGTA Project CAUs and comprises  $^3\text{H}$ , fission products, unspent fuel materials, and activation products. This list includes 43 radiological contaminants with half-lives greater than 10 years (with the exception of  $^{154}\text{Eu}$ ). This inventory also includes naturally occurring radioactive isotopes ( $^{40}\text{K}$ ,  $^{232}\text{Th}$ ,  $^{234}\text{U}$ ,  $^{235}\text{U}$ , and  $^{238}\text{U}$ ) and represents the amount in the rock that was melted during the detonation.

The total inventory of each radionuclide is partitioned into glass, rubble, gas, and water in the percentages listed in Bowen et al. (2001). It is assumed that any gas phase radionuclides would be completely dissolved in the aqueous phase. The inventory in the glass, rubble, and water is distributed evenly into the pores of the nuclear MGZ and the exchange volume. In contrast, the inventory in the glass is distributed into the nuclear MGZ and becomes available for release only as the melt glass dissolves.

The SSM incorporates the simplified temperature dependent nuclear melt glass dissolution model described in Pawloski et al. (2001) for use in the HST model. The glass reaction rate is based on a moderate rate at 25 degrees Celsius ( $^{\circ}\text{C}$ ) that represents a conservative estimate of the glass dissolution rate at near-ambient chemical conditions (Pawloski et al., 2001).

Groundwater flows through the far-field rock (a distance greater than two cavity radii) at a flux that is a function of the effective permeability of the formation and of the hydraulic gradient. When groundwater encounters the underground test region, flow will occur through the exchange volume and the nuclear melt glass at different rates because of the different permeabilities of those two regions and the hydraulic conductivity of the undisturbed host rock of the formation.

Source term uncertainty is propagated through the SSM through insufficient data and natural variability of the system. As stated in the modeling objectives set forth in the FFACO (1996, as amended in 2008), quantification of model uncertainty is necessary to evaluate the model results in a meaningful way. Therefore, uncertainty for each component model that contributes to the analysis is required so that uncertainty can be adequately represented. Some of the features of the SSM that are subject to uncertainty propagation include:

- Inventory of radionuclides
- Partitioning of the radionuclide source



- Source region dimensions
- Hydrologic setting of a test

## ***TRANSPORT CONCEPTUAL MODEL***

The transport conceptual model is divided into three general categorical subjects: (1) release, (2) migration, and (3) assignment of RMCs. The release mechanism for underground nuclear test sites at Central and Western Pahute Mesa consists of multiple-point sources. The source term that contributes to the PM CAU model is initially developed at a local scale to capture structural and temporal characteristics that regulate release rate. Migration from the source area is controlled through physical processes that are a function of the hydrogeologic and geochemical properties of the rocks. The role of these processes on groundwater transport serves to control the mechanics by which contamination migrates and spreads. As contaminants migrate through the rocks, they are prone to react with mineral assemblages that are specific to certain rock types. The RMCs identify these mineral types, their distribution, and their affinity to adsorb radionuclides as the contaminant plume moves through the porous structure.

Release of radionuclides from underground nuclear test sites is a function of both the design criteria of the test as well as the hydrogeologic setting in which the test is conducted. These aspects of each test must be adequately captured for an accurate assessment of the source term and release rate from the site. The explosive yield of the nuclear device is critical in assessing the extent of the disturbed and altered geologic material into which the radionuclides are distributed and the estimation of source term inventory. The hydrogeologic nature of the rocks serves to identify the fluid flow rate and geochemical reaction potential for each radionuclide identified in the inventory.

Radionuclide migration away from subsurface nuclear tests is affected by multiple physical and chemical processes that depend either on the hydrogeologic system and its properties, or on the specific properties of the radionuclides. These processes include radioactive decay of the species, advection in both porous and fractured media, diffusion from fracture water into matrix water, sorption onto immobile minerals, sorption onto mobile colloidal minerals, and attachment and detachment of colloids from immobile surfaces. The conceptual model requires specification and parameterization of a limited set of processes that affect migration of solutes evolving from spatially separated source locations.

In general, the HFM focuses on hydraulic properties of the geologic units, as determined by lithology, alteration, and structure. The reactive mineral model is an analogous construct for the transport that addresses the mineralogy of the units, particularly the presence and abundance of minerals known to have absorptive/reactive attributes with regard to radionuclides.

Transport parameters are closely related to the chemical environment in which transport occurs. For example, matrix sorption (a factor in controlling the mobility of contaminants), as discussed is a function of the chemistry of both the solid components (i.e., rock) and water. The nature and distribution of reactive mineral phases in groundwater systems can exert a significant influence on water composition (e.g., major ion chemistry, pH) and the mobility of contaminants of concern. Reactive minerals are expected to occur in four distinct settings within the Pahute Mesa CAU. These are minerals in alluvial deposits, minerals within volcanic and carbonate rock matrices, minerals occurring as coatings on fracture surfaces in fractured volcanic and carbonate rocks, and colloids (fine-grained mineral particles) mobile in groundwater.

After evaluating the occurrence of these reactive minerals to geologic processes relevant to the rocks at the NTS, several natural categories emerge. The RMCs for NTS volcanic rocks are vitric mafic-poor (VMP), vitric mafic-rich (VMR), devitrified mafic-poor (DMP), devitrified mafic-rich (DMR), mafic lavas (ML), zeolitic (ZEOL), and silicic/argillic (SC/ARG), the last of which is not present in the PM CAU model.

The overall process used to construct the reactive mineral model for Pahute Mesa paralleled the HFM construction process. The first step in constructing the PM reactive mineral model was to characterize the mineralogy of each HSU. Information used for this step included X-ray diffraction (XRD) data (whole rock mineralogy data specific to Pahute Mesa and XRD data for correlative units in the adjacent Yucca Mountain area and for the other UGTA Project CAUs); detailed lithologic descriptions from drill holes and outcrops; the petrographical and geochemical database for the SWNVF (Warren et al., 2003); and geophysical logs. Major chemical constituents (X-ray fluorescence [XRF] data) and phenocrysts (petrographic data) were also considered. The XRD dataset was assigned an RMC based on reactive mineral content, and the distribution of RMCs within each HSU was then evaluated. These were then grouped in a stratigraphic context into

reactive mineral units (RMUs) for modeling, similar to how hydrogeologic units (HGUs) are grouped into HSUs for the HFM. The 46 HSUs in the Pahute Mesa HFM have been subdivided into RMUs.

## ***PAHUTE MESA CAU TRANSPORT MODEL***

The PM CAU transport model consists of four model simulation components: (1) steady-state groundwater flux derived from 3-D simulation using the FEHM flow model, (2) transient radionuclide mass flux calculated using the 1-D GoldSim SSM, (3) contaminant release into the groundwater flow field through particle tracking using the FEHM code, and (4) calculation of the flux average solute concentration using the convolution-based particle-tracking method contained within the PLUMECALC code. The CAU-scale groundwater flow for each select HFM was calculated through calibration of the PM CAU flow model (SNJV, 2006a) by minimizing the calculated and measured head residuals through adjustment of the permeability. The source term is a local-scale, time-averaged release for multiple realizations using the Monte Carlo approach. The Monte Carlo method allows sampling of the parameter space and provides a quantitative measure of the source-release uncertainty. Using the flow vector data from the PM CAU model, the FEHM code is used to simulate particle release from each test location in the PM CAU model. The particles move with the water and are assigned a dispersivity value to account for spreading due to sub-CAU-scale heterogeneity. The flux-averaged solute concentration is then calculated from the particle distribution using the output from the flow, SSM, and particle-tracking models, and assignment of RMUs to the model domain that are all incorporated into the PLUMECALC code. Solute retardation and decay are accounted for in this latter modeling activity. A full Monte Carlo simulation is conducted using PLUMECALC for which each realization represents a unique set of the transport parameters drawn from previously calculated parameter distributions. The simulation software, as described above, are:

- FEHM
- PLUMECALC
- GoldSim

Transport parameters of interest for the PM CAU transport model simulation are:

- Fracture porosity, spacing, and aperture
- Matrix porosity

- Matrix diffusion
- Dispersivity
- Mass transfer coefficient
- Sorption coefficient
- $K_d$  upscaling
- Colloid facilitated transport

The FEHM code simulates 3-D, time-dependent, multiphase, nonisothermal flow, and multicomponent reactive groundwater transport through porous and fractured media. The FEHM finite-element formulation allows for representation of complex 3-D geologic media and structures and their effects on subsurface flow and transport. The HST, recharge, lateral boundary conditions, and parameter values are inputs to FEHM. The FEHM output consists of spatial distribution of head and particle distributions. The transport processes of interest are advection, dispersion, sorption, matrix diffusion, radioactive decay, colloid-facilitated transport, and daughter product in-growth.

The PLUMECALC software (Robinson and Dash, 2005) is a convolution-based particle-tracking (CBPT) method for simulating flux-averaged solute concentrations in the PM CAU model. The PLUMECALC method is valid for steady-state flow and linear transport processes, including sorption with linear sorption isotherms, diffusion into a rock matrix, and first-order decay. From a single FEHM particle-tracking run, source term variability, decay, and spatially variable sorption and diffusion are all simulated rapidly without rerunning the more time-consuming particle-tracking model except when the flow field or dispersion parameters are changed. Thus, for each steady-state flow field considered, and for a fixed set of dispersivities, a full Monte Carlo simulation is conducted using PLUMECALC only.

After development of the flow and transport conceptual model and assignment of the source term, the final component necessary to complete the model domain is assignment of the transport parameters, which are mapped to the previously defined RMCs. The process of assigning transport parameters is similar to the procedure used to assign flow parameters to the HSUs.

The input transport parameters are typically derived from field-scale and laboratory-scale data collection programs or through literature review of other sites that possess a similar geologic and hydrostratigraphic origin. Ideally, the parameters are collected to provide information about hydrologic or geochemical properties within the model. For each parameter, a statistical distribution

can be derived. Assuming the central limit theorem is true (the sampled data for each parameter adequately represent a normal distribution and the full range of variability), the parameter distribution should be representative of that parameter range. Once these parameter distributions are defined, multiple combinations of parameters can be selected through random sampling of the distribution. Each sampling event represents a unique realization for the model. Simulation of an adequate number of realizations should capture the full spectrum of the possible transport parameter configurations that are possible given the parametric variation. Analysis of the resulting simulation output for all realizations is then used to identify levels of parametric uncertainty and output sensitivity that results from the parameter influence.

Porosity is classified as either matrix or fracture porosity. The assumption is that effective porosity (as previously defined) will simulate the properties of fracture porosity if the rock is a welded tuff or lava where flow occurs primarily in fractures and matrix water is assumed immobile. It is assumed that the effective porosity will simulate the characteristics of matrix porosity for a zeolitic or porous confining unit and vitric aquifers. A detailed discussion of the fracture porosity in terms of fracture spacing and aperture size is pursued to better quantify mass transfer between the fracture and matrix medium. Mass transfer in the fracture/porous medium is also explored in the context of  $^{14}\text{C}$  migration rates recorded at observation wells located in the PM CAU model domain. Matrix sorption and fracture sorption are addressed together in terms of the sorption coefficient ( $K_d$ ), which is defined by radionuclide and RMC (mineralogy). Analysis of the colloidal-facilitated transport for Pu is performed through the assignment of a Pu reduction factor. This term represents the fraction of the aqueous SSM Pu inventory that is mobilized via sorption to colloids.

## ***TRANSPORT ANALYSIS METHODS AND RESULTS***

A Monte Carlo approach is used to propagate uncertainty in the parameterization of the PM CAU transport model (PLUMECALC) into corresponding output uncertainty. The method entails multiple simulations, each with a randomly selected set of input parameters, to generate an equal number of output metrics that collectively capture the full behavior of the transport system. The metrics used to describe PM CAU transport model predictions are derived from simulated radionuclide concentrations through time. When considered in the context of regulatory standards, or maximum contaminant levels (MCLs) at specified time intervals, radionuclide plumes may be conceptualized as

a contaminant boundary as described in the FFACO (1996, as amended February 2008). However, based on unacceptable uncertainty within the PM CAU model as demonstrated by variability of the results, no attempt will be made to quantify a regulatory contaminant boundary for the current model at this time.

Several different metrics and results maps are used to describe transport model behavior. These are used to understand individual model runs (i.e., using a single set of transport parameters) and collective model (i.e., global) runs with respect to individual radionuclide behavior, the behavior of regulatory-defined groups of radionuclides, and the integrated behavior of all radionuclides. Further, these metrics and results maps are used to compare radionuclide behavior between the alternative PM CAU flow models, thus permitting some measure of the influence of hydrogeologic conceptualization on transport. The metrics used, described in their order of development, are:

- Radionuclide concentrations
- MCLs and MCL groups
- Probability of MCL exceedance
- Exceedance volume (EV)
- Regulatory-based contaminant boundary
- Probabilistic exceedance map
- Fractional EV

The *Safe Drinking Water Act* (SDWA) (CFR, 2007) defines drinking water standards based on MCLs corresponding to a human dose of 4 mrem/yr, or its equivalent depending on the radionuclide, for regulatory groups that may include multiple contaminants. The UGTA Project Technical Working Group (TWG) (IT, 1999) selected seven radioactive contaminants for transport simulation based on observed concentrations in groundwater, inventory estimates, health effects, and fate and transport information. These were  $^{14}\text{C}$ ,  $^{129}\text{I}$ ,  $^{239/240}\text{Pu}$ ,  $^{137}\text{Cs}$ ,  $^{90}\text{Sr}$ ,  $^3\text{H}$ , and  $^{238}\text{U}$ . This set of alpha-particle emitters, beta emitters, and uranium was considered to be the most significant for prediction of regulatory compliance metrics over an approximately 1,000-year period. The PM CAU transport model assumes these seven radionuclides as a standard set for simulation scenarios. In addition to these seven radionuclides,  $^{36}\text{Cl}$ ,  $^{237}\text{Np}$ , and  $^{99}\text{Tc}$  are included in all simulations based on high mobility, longevity, and available inventory.

The Pahute Mesa CAIP (DOE/NV, 1999) and FFACO (1996, as amended February 2008) define the regulatory contaminant boundary as the maximum extent of radionuclide contamination

corresponding to a human dose of 4 mrem/yr for radionuclides, or a concentration equal to drinking water standards (i.e., MCLs) for other contaminants, at the 95 percent confidence level within a 1,000-year interval. The 4 mrem/yr dose regulatory limit is based on the SDWA (CFR, 2007) and may include multiple contaminants, with the total dose equal to the sum of the doses of all contributing radionuclides.

As an alternative to the contaminant boundary, the exceedance map used in this analysis is defined as the set of nodes at which any MCL is exceeded, at any time within a 1,000-year interval, in at least 5 percent of the Monte Carlo runs. Only one probabilistic exceedance boundary is constructed from the full suite of Monte Carlo simulations. It is time invariant in that the map includes nodes at which any MCL is exceeded at any time within 1,000 years.

It is more informative to assess radionuclide migration behavior from a probabilistic perspective that captures the spatial variability in migration as a function of transport parameter uncertainty. Radionuclide migration is therefore presented as a probability map of MCL exceedance that shows, per model node, the percentage of Monte Carlo simulations in which an MCL is exceeded for alpha particles, beta emitters, or uranium.

While the probability map provides qualitative information pertaining to the global behavior of radionuclide migration over all Monte Carlo simulations, a map is inherently difficult to characterize quantitatively because it represents a spatial geometry. Rather than mapping these nodes, the total volume of all such nodes is calculated in order to provide a scalar metric per Monte Carlo run that, when combined over all runs, defines a probability distribution. The EV is the summed volume of all nodes at which the MCL is exceeded for any regulatory group, at any time within a 1,000-year interval from the time of source release, per Monte Carlo run.

The EV is the metric used to quantitatively describe the time-invariant behavior of radionuclide migration in terms of MCLs. Consequently, the EV is used to confirm the statistical stability of Monte Carlo results, ensuring that sufficient realizations are considered to provide stability in the first and second moments (at least) of the continuous metric.

The fractional exceedance volume (FEV) permits a general assessment of the influence of individual radionuclides on plume growth and decay through time. An FEV is computed per radionuclide, per

output timestep, and per realization. It is a scalar metric ranging from 0.0 to 1.0 that approximates the volume fraction of an MCL-exceedance plume, at each simulation timestep, that is accounted for by an individual radionuclide. The volume of the MCL-exceedance plume is computed as the summed volume of all nodes at which an MCL is exceeded at a snapshot in time for the current realization. It is therefore similar to the EV but is not a time-invariant metric as is the EV.

Of the 82 total radionuclide sources (shaft nuclear tests) in the PM CAU model domain, a reduced set was selected in all transport simulations in the interest of reducing computational time. The method of selection involved identifying whether simulated source-release particles cross a specific transect along a southwest flow path, defined at the Universal Transverse Mercator (UTM) northing coordinate that transects 4,110,000 m.

Monte Carlo transport simulation was performed for six alternative, calibrated PM CAU flow models developed during the PM CAU flow model analysis (SNJV, 2006a). The alternatives span a large range of geologic (e.g., structure) and hydrologic (e.g., boundary flow rates) uncertainty. Of the six, five are variations of the base HFM, and one is constructed from the SCCC geologic conceptualization. Transport simulation was also performed for a seventh HFM named the LCCU1-MME-TMCM, developed during this analysis from the LCCU1-MME base alternative, to investigate the effect of hydraulic parameterization on transport.

Of the five base-derived alternatives developed during the PM CAU flow modeling task, three modes of transport behavior became evident, reflecting the hydrostratigraphic, hydraulic, and material property variations among models that matter the most for transport. These modes involve the rate of radionuclide migration, the path of migration, and the relative contribution of individual species to the migration. The remaining two HFMs (SCCC-MME and LCCU1-MME-TMCM) showed considerably different behavior in radionuclide migration rates and paths; however, the predominant species contributing to transport did not differ from the others.

The persistence in preferential flow and transport in channels at material interfaces, despite the improved homogenization of permeability (LCCU1-MME-TMCM) and simplification of hydrostratigraphy (SCCC-MME), indicates that PM CAU flow model zonation is a critical component of PM CAU transport model behavior. Namely, all models are conceptualized as single-property HSUs that can provide 1-kilometer (km)- to 10-km-scale continuous pathways. An



increase in boundary inflows or a decrease in transmissivity, both of which were incorporated across the alternative HFMs, only enhances the effect. The net result is that a lack in heterogeneity, between HSUs (i.e., hydrostratigraphy) and within HSUs (i.e., properties), results in preferential flow and transport. When considered collectively, PM CAU transport model behavior demonstrates that the effects of preferential flow determine the degree of sensitivity of radionuclide migration to transport parameters.

## ***PAHUTE MESA UNCERTAINTY AND SENSITIVITY ANALYSIS***

The method by which the Pahute Mesa transport analysis was performed adheres to a systematic framework that acknowledges uncertainty in both the conceptualization and parameterization of the PM CAU transport model. The influence of parameter uncertainty on sensitivity analysis shows how the sensitivity methods applied capture the influence of parameter uncertainty as it is propagated through the model. Such methods assume a global, as opposed to local, approach that permits the full range of input-output relationships to be assessed.

Identification of parameters that control global output sensitivity includes (1) stepwise regression, (2) classification tree, and (3) entropy analysis.

The stepwise regression model performs a forward regression such that at each step in the process, a parameter is sequentially added to the model starting with the parameter that is most likely to reduce the variability in the model output. The stepwise regression model assumes that the input/output relationship is linear and, therefore, can be fit to the regression model.

Classification tree analysis can provide useful insights into what variable or variables are most important in determining whether outputs fall in one particular category. The decision tree is generated by recursively finding the variable splits that best separate the output into groups where a single category dominates. The tree-building methodology used is based on a probability model approach. Tree-based models are attractive because: (1) they are adept at capturing non-additive behavior, (2) they can handle more general interactions between predictor variables, and (3) they are invariant to monotonic transformations of the input variables.

The information-theoretic concept of entropy is a useful metric for the characterization of uncertainty (or information) in the univariate case, and redundancy (or mutual information) in the multivariate case (Press et al., 1992). Because mutual information is a natural measure of input variable relevance, it is also being used as an indicator of variable importance in many areas of science (Moddemeijer, 1989). The entropy method is suitable for use with nonlinear and non-monotonic data. This information can also be compactly organized in terms of a contingency table – a table whose columns are labeled by the values of the independent variable,  $x$ , and whose rows are labeled by the values of the dependent variable,  $y$ . The contingency table can also be visualized using a “bubble plot,” where the entries of the contingency table are shown as bubbles of varying sizes.

Sensitivity analysis is performed by observing the response of the output given the variability in the input parameters. For this analysis, the output response function is represented by the EV, and the input is a list of transport parameters that are sequentially compared with the EV. There are 35 possible input parameters that when varied may elicit a response from the EV. Analyses were performed for the five modified HFMs advanced from the PM CAU flow model, and two models were developed during the PM CAU transport model evaluation.

Sensitivity analysis proceeded in three stages. First, each HFM was evaluated using the three global sensitivity analysis methods described above. From this analysis, the principal transport parameters that contribute the most to output sensitivity are identified for each of the seven HFMs. After this initial evaluation, all the results for each method are composited for all of the seven HFMs. The result of this approach produces a table of the most sensitive parameters for each of the three methods used, arranged by HFM. The final activity was to group all of the HFMs such that the three most sensitive parameters are identified for all cases. Through this exercise, the HFM models naturally separated into two distinct categories for which a limited number of parameters repeatedly appeared and dominated the uncertainty among each of the groups. Group 1 models included the four HFMs: LCCU1-MME, LCCU1-UDGSD, LCCU1-TMD, and PZUP-MME. Group 2 were the remaining models: SCCC-MME, LCCU1-DRIA, and LCCU1-TMCM. The dominant transport parameters for group 1 corresponded to flow systems that were synonymous with connected, high-permeability flow paths and also represented the contaminant plumes that possess the greatest EVs. The group 2 models, by contrast, represented flow paths that were interrupted by lower-permeability rocks or were

subject to high recharge and possess the smallest EVs. This analysis highlights the importance that the conceptual model construct exerts on plume migration rate and extent.

The identification of basin-scale preferential transport paths within subdivisions of the TCMC provoked a reanalysis of the PM CAU flow model conceptualization through the reparameterization (i.e., hydraulic conductivity adjustment) of selected HSUs. This reanalysis led to the development of the LCCU1-MME-TCMC alternative model in the attempt to better homogenize flow and transport through HSUs south of the Moat fault. Three methods were applied to assess transport sensitivity to PM CAU flow model parameter uncertainty. The first, called the Null Space Monte Carlo (NSMC) approach, defines the range of TCMC/Fortymile Canyon composite unit (FCCM) permeability insensitivity and exploits this to develop multiple, equally probable PM CAU flow models for transport simulation. The second method investigates alternative scenarios for depth decay in the TCMC, and the third investigates the effect of dispersivity on transport. The standard global sensitivity analysis methods are generally able to be applied in these cases.

Before the NSMC analysis, the TCMC permeability uncertainty was evaluated in SNJV (2006a) during PM CAU flow model conceptualization and calibration of the base-HFM alternative PM CAU flow models. Three analyses were performed, one investigating the effect of a recharge mound under Timber Mountain, a second investigating permeability variation within the TCMC subdomains through a local (individual parameter perturbation) sensitivity analysis, and the third inducing flow down Fortymile Canyon through permeability adjustment.

The NSMC analysis permits the quantitative identification of the overlap of uncertainty and insensitivity regions in the parameter space. The results of the analysis serve two purposes. First, a discrete range of permeability insensitivity is defined that honors both field observation of permeability (i.e., the range of uncertainty) and field observation of hydraulic calibration targets, the latter implying that the range of insensitivity is governed by how well observations constrain the parameter estimation problem. Second, multiple equally probable PM CAU flow models may be defined for use in a Monte Carlo transport analysis and subsequent assessment of PM CAU transport model sensitivity to TCMC permeability. In this study, the NSMC analysis is used to assess the general influence of permeability uncertainty (in the TCMC and FCCM) on radionuclide migration

(location and travel time), and not to define an exact, statistically significant range of permeability insensitivity for the HSUs in question.

In general, the NSMC results not only demonstrate that transport is sensitive to flow model parameter uncertainty but also that conceptual model uncertainty is significant to a greater degree than parameter uncertainty. Clearly, the conceptualization of the TMCM is fundamental to its parameterization. Nevertheless, the basic point of this parametric uncertainty exercise is to show that hydraulic observations used to constrain the TMCM/FCCM permeability estimation problem are limited. Due to the large extent of these HSUs, such uncertainty leads to both large variability in plume extent (EV) and location within the model domain.

In all of the models considered so far, a depth-decay coefficient of 0.0027 is applied to the TMCM (SNJV, 2005). This coefficient results in simulations that favor flow in the more shallow parts of the TMCM, which can be as much as 3 km thick. This coefficient in the TMCM was set because the HFM does not have the structural resolution to provide features leading to surface discharge in Oasis Valley when flow in the TMCM is allowed to fully penetrate the HSUs' depth. Rather than eliminating the depth-decay model completely, the coefficient is reduced from 0.0027 to 0.0010 in the TMCM and FCCM HSUs of the LCCU1-MME-TMCM flow model. In the reduced depth-decay model, plume migration is substantially reduced as a result of less shallow convergent flow paths.

A series of semiquantitative sensitivity analyses was conducted to examine model behavior for increased dispersivity. The hypothesis was that increased dispersivity might lead to more dilution, lower concentrations, and reduced plume migration. With the larger longitudinal value, exceedances occur earlier and the size of the boundary is larger. Thus, the increased dispersion considered in this sensitivity study does not lead to reduced contaminant migration through spreading and dilution. The impact is that the method of "random walk" displacement of particles to represent dispersion can move particles many cells away when grid resolution is fine relative to the lack of property variability, such as in the TMCM. This serves to put particles into other flow paths, which may be valid, but also to cause particles to essentially jump into new regions.

## **MODEL UNCERTAINTY INTEGRATION AND ASSESSMENT**

The primary role of this analysis has been to understand the behavior of radionuclide migration in the PM CAU model and to define, both qualitatively and quantitatively, the sensitivity of such behavior to (flow) model conceptualization and (flow and transport) parameterization. Based on this objective and the subsequent modeling and analysis activities, a list of components was assembled to identify key features and processes that require further investigation with the goal to reduce conceptual and parametric uncertainty during a second phase of numerical modeling activities. The components identified through this analysis are:

- Bench characterization for the purpose of hydrogeologic refinement of the region south of Silent Canyon caldera and north of Timber Mountain caldera, which is hypothesized to control migration of radionuclides from source locations to downgradient receptors.
- Transport through fractures, which is a significant factor in the control of radionuclide migration. Proper definition of fracture aperture, spacing, and matrix porosity determines the velocity and exchange potential of the contaminants and rocks.
- Heterogeneity as it applies to the spatial variability of hydrologic and geochemical properties within and between HSUs. The inability to capture sub-CAU-scale heterogeneity was observed to artificially enhance or restrict potential flow paths.
- Specific discharge, which is treated as a function of the simulated groundwater gradient and estimated permeability. This simplistic approach does not adequately capture potential complexity in the groundwater velocity variability that could signal changes in the current gross system behavior.
- Depth decay applied such that observed downgradient discharges are replicated by the simulated model for the specified boundary fluxes. However, there are no measured data to support this conceptualization. Similar outflows may be achieved with a less restrictive depth decay as other contributing properties are varied.
- Recharge over much of the site, which appears to be overestimated for the groundwater flow system. Of particular interest is the effect that enhanced recharge at the flanks of Timber Mountain has on groundwater flux and dilution.
- Boundary flows, currently estimated at the CAU boundaries based on the coarse grid scale of the UGTA regional scale model. Revision of these boundaries to reflect changes in the form of the Death Valley regional flow model and to better match observation well heads and expert elicitation of potential boundary conditions may resolve boundary definitions.

- Source term, currently described by a 1-D representation of a 3-D process. The justification of the 1-D construct is to curve match to the 3-D model at one site. The validity of this approach as it is applied to match processes and application to other sites is not clearly demonstrated.

# 1.0 INTRODUCTION

During Pahute Mesa (PM) corrective action unit (CAU) transport modeling, the Pahute Mesa application of the *Federal Facility Agreement and Consent Order* (FFACO) (1996, as amended February 2008) process (Appendix VI, FFACO) was streamlined by an agreement between the U.S. Department of Energy (DOE), National Nuclear Security Administration Nevada Site Office (NNSA/NSO) and the Nevada Division of Environmental Protection (NDEP) to acknowledge that a Phase II Corrective Action Investigation (CAI) would be required for additional data collection. Consequently, formal determination of the contaminant boundary was superseded by a focus to use the flow and transport modeling process to identify issues and uncertainties in the model that require additional information to resolve and reduce uncertainty. As a prelude to the specific topics discussed in this report, background information is provided regarding project development; regulatory framework; and purpose, scope, and objectives of the modeling effort. The geographic and geologic setting of the site, and operational history of the Pahute Mesa nuclear testing program are summarized. General supporting work that has contributed to the evolution and development of this report are identified and summarized. Finally, the structure and content of the report is outlined.

The NNSA/NSO initiated the Underground Test Area (UGTA) Project to assess and evaluate the effects of the underground shaft and tunnel nuclear weapons tests on groundwater at the Nevada Test Site (NTS) and vicinity. The framework for this evaluation is provided in Appendix VI, Revision No. 1 (December 7, 2000) of the FFACO (1996, as amended February 2008). Appendix VI of the FFACO, “Corrective Action Strategy,” describes the processes that will be used to complete corrective actions, including those in the UGTA Project. The objective of the strategy is to analyze and evaluate each UGTA Project CAU (Figure 1-1) through a combination of data and information collection and evaluation, and groundwater flow and contaminant transport simulation.

The FFACO corrective action process for Central and Western Pahute Mesa was initiated with the Corrective Action Investigation Plan (CAIP) (DOE/NV, 1999). This Pahute Mesa CAIP identified a three-step model development process to evaluate the impact of underground nuclear testing. The

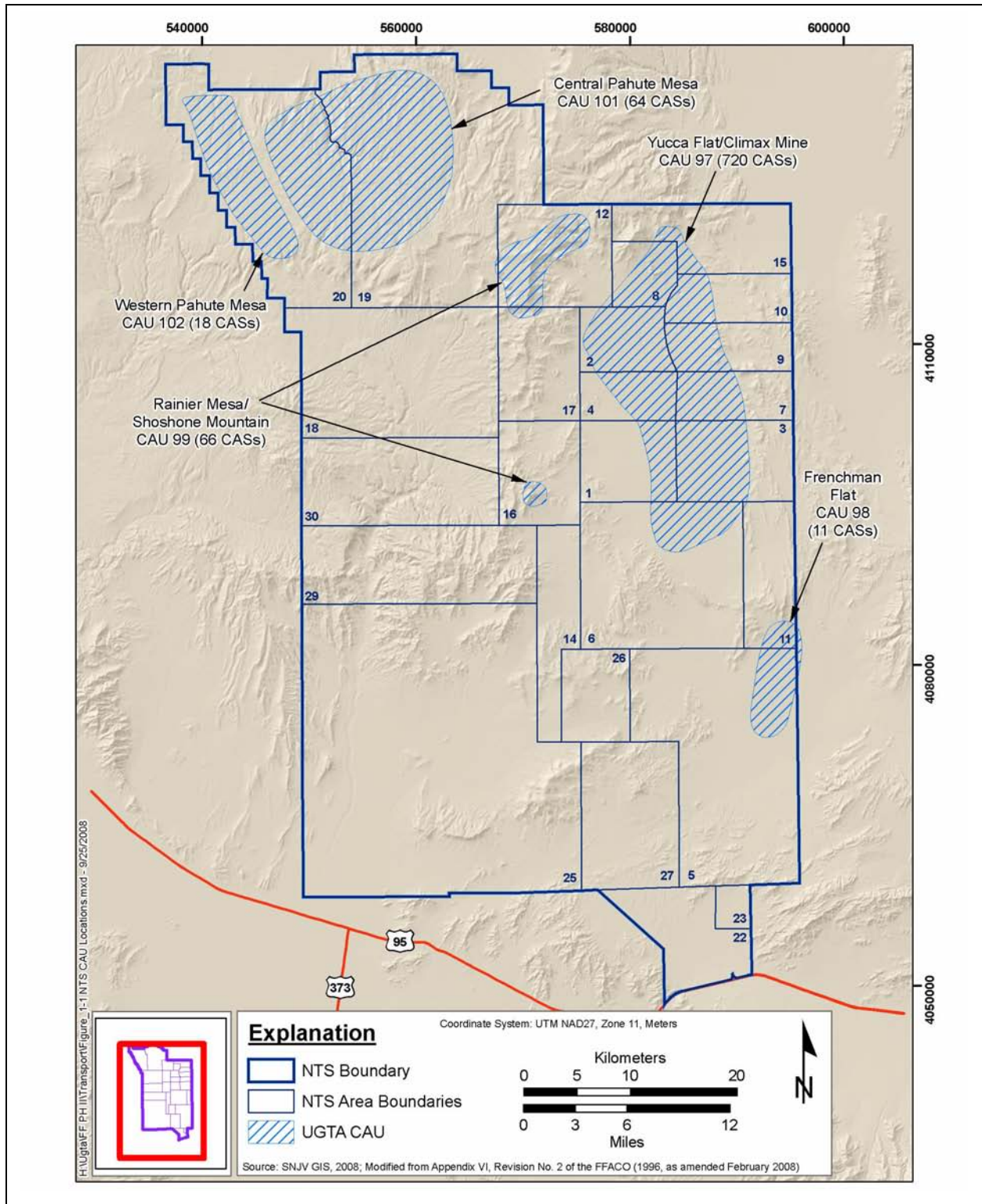


**Figure 1-1**  
**Location of the Pahute Mesa Corrective Action Units**



first step is the data analysis task to compile and evaluate existing and new data for use in the model. The second step is the development of the PM CAU flow model. The third step is the development of the PM CAU transport model.

The first step has been completed and is documented in a series of data compilation and analysis reports, including the *Hydrologic Data for Groundwater Flow and Contaminant Transport Model of Corrective Action Units 101 and 102: Central and Western Pahute Mesa, Nye County, Nevada* (SNJV, 2004b) and the *Contaminant Transport Parameters for the Groundwater Flow and Contaminant Transport Model of Corrective Action Units 101 and 102: Central and Western Pahute Mesa, Nye County, Nevada* (Shaw, 2003).

The second step also has been completed and documents the development of the PM CAU flow model that will be used to assess the migration of radionuclides away from underground nuclear test cavities on Pahute Mesa. The PM CAU flow model is reported in *Groundwater Flow Model of Corrective Action Units 101 and 102: Central and Western Pahute Mesa, Nye County, Nevada* (SNJV, 2006a). The present document addresses the third step, which includes development of the PM CAU transport model for the purpose of bounding the extent of the contaminant plume at the 95<sup>th</sup> percentile confidence level after 1,000 years of migration.

This third step incorporates an additional iteration of the PM CAU flow model development to modify structural and hydrostratigraphic features. This effort deviates from the intent of the third step to simply simulate transport and is intended to further reduce PM CAU flow model uncertainty and provide a better fit to observed geochemical markers. The geochemical markers represent similarity of anion and cation species measured at hydraulically connected observation wells located in the PM CAU model domain. These markers provide an independent check of the model flow paths and are used to screen alternative models. Although a stochastic contaminant boundary is the ultimate objective, the purpose of the present study has been modified to understand the behavior of radionuclide migration in the PM CAU model and to define, both qualitatively and quantitatively, the sensitivity of such behavior to (flow) model conceptualization and (flow and transport) model parameterization. Therefore, the contaminant boundary was not calculated to meet the regulatory requirement but rather for further analysis of system behavior.

Consequently, this report is a combination of the revised PM CAU flow model and implementation of the PM CAU transport model. As with the previous PM CAU flow model, flow and transport are treated separately. That is, the PM CAU flow model is calibrated using an inverse approach that adjusts the flow parameters to match the measured flow observations to the calculated values. The PM CAU transport model is then run in forward mode using the calibrated, steady-state flow field. The observed fit of simulated to measured geochemical markers is performed, but geochemical mixing is not used as a calibration metric.

### **1.1 Purpose and Scope**

The stated purpose of the PM CAU transport model is to support the FFACO UGTA Project corrective action strategy objective of providing an estimate of the vertical and horizontal extent of contaminant migration for each CAU in order to predict contaminant boundaries. A contaminant boundary is the model-predicted perimeter that defines the extent of radionuclide-contaminated groundwater from underground nuclear testing above drinking water standards set by the *Safe Drinking Water Act* (SDWA) standards (CFR, 2007). The contaminant boundary will be composed of both a perimeter boundary and a lower hydrostratigraphic unit (HSU) boundary.

For this report, the exceedance volume (EV), which is a scalar equivalent of the contaminant boundary, is calculated rather than a contaminant boundary perimeter (probability map). While the probability map, which represents the perimeter of the model nodes that exceed the maximum contaminant level (MCL), provides qualitative information pertaining to the global behavior of radionuclide migration over all Monte Carlo simulations, a map is inherently difficult to characterize quantitatively because it represents a spatial geometry. The EV is a metric more amenable to quantitative analysis while retaining a probabilistic perspective of radionuclide migration. The EV is calculated as the total volume of model nodes for which the MCL for all radionuclides per realization for 1,000 realizations for up to 1,000 years is exceeded. The output from the EV calculation provides a range of volume data for 1,000 realizations from which the statistical properties can be computed. The PM CAU flow model (SNJV, 2006a) and the PM CAU transport model described in this report are an integration of the processes required to compute the EV. Other components include the simplified source model (SSM), which incorporates uncertainty and variability in the factors that control radionuclide release from an underground nuclear test (SNJV, 2004b), and the transport

model parameters that incorporate parameter uncertainty as described in Shaw (2003). The uncertainty in all the above model components will be evaluated to produce the final EV.

This report documents PM CAU transport model development, supplementary analysis of the PM CAU flow model, and incorporation of the PM CAU flow model results into the PM CAU transport model analysis for the Central and Western Pahute Mesa CAUs.

Objectives of the Central and Western Pahute Mesa revised flow and transport model as stated in the strategy and approach document are to:

- Develop a CAU model that integrates a wide variety of data into a mass conservative description of contaminant migration in groundwater from underground nuclear test locations in a CAU.
- Simulate, as output, the concentration of individual contaminants downgradient of underground test locations over a time period of 1,000 years. These concentrations will be used to define a contaminant boundary based on a 4 millirem per year (mrem/yr) composite dose.
- Serve as a tool to evaluate impacts of future flow system changes on the migration of contaminants in the CAU.

Specific objectives of the PM CAU flow model (SNJV, 2006a) are to:

- Develop a three-dimensional (3-D), mathematical flow model that incorporates the important physical features of the flow system and honors CAU-specific data and information.
- Simulate the groundwater flow system to determine the direction and magnitude of groundwater fluxes based on calibration to Pahute Mesa hydrogeologic data.
- Quantify the uncertainty in the direction and magnitude of groundwater flow due to uncertainty in parameter values and alternative component conceptual models (e.g., geology, boundary flux, and recharge).

The specific objectives for the PM CAU transport model are to:

- Superimpose 3-D transport model properties onto the PM CAU model domain through development of reactive mineral categories (RMCs).

- Develop contaminant mass flux for underground nuclear test sites using one-dimensional (1-D) SSMs that represent flow and transport through the test cavity and disturbed rock zone adjacent to the cavity, which is then input to the CAU-scale model.
- Simulate transport from the underground test sites using a stochastic approach that provides multiple, equally probable realizations of plume migration and calculation of the EV, which is the quantification of the statistical distribution for the cumulative MCL of 4 mrem/yr from each realizations, projected out to 1,000 years.
- Quantify the radionuclide spread and flow path due to uncertainty in parametric values and alternative conceptual models (geology and RMCs).
- Identify data needs for Phase II field data collection and further refinement of the numerical model.

Figure 1-2 shows the model area that encompasses the Pahute Mesa CAUs, including Timber Mountain, the eastern edge of Oasis Valley, the northern part of Fortymile Canyon, and the northern portion of Yucca Mountain (DOE/NV, 1999). This area was selected to better define the regional groundwater flow system of the lower carbonate aquifer (LCA) in the vicinity of Pahute Mesa.

## **1.2 Project Participants**

The UGTA Project is a component of the NNSA/NSO Environmental Restoration Program (ERP). The UGTA Project CAIs are managed by the NNSA/NSO UGTA Project Manager. A Technical Working Group (TWG) has been established to assist the NNSA/NSO UGTA Project Manager with technical management issues. Tasks assigned to the TWG include providing expert technical support to plan, guide, and monitor UGTA Project technical work, and serving as internal peer reviewers of UGTA Project products. The TWG consists of representatives from National Security Technologies, LLC (NSTec), Desert Research Institute (DRI), Lawrence Livermore National Laboratory (LLNL), Los Alamos National Laboratory (LANL), Stoller-Navarro Joint Venture (SNJV), and the U.S. Geological Survey (USGS).

## **1.3 Regulatory Background - FFAO and Safe Drinking Water Act**

Since 1996, NDEP has regulated the NNSA/NSO corrective actions through the FFAO (1996, as amended February 2008). The individual locations covered by the agreement are known as corrective action sites (CASs), and these are grouped into CAUs. The UGTA Project CAUs are Frenchman Flat,

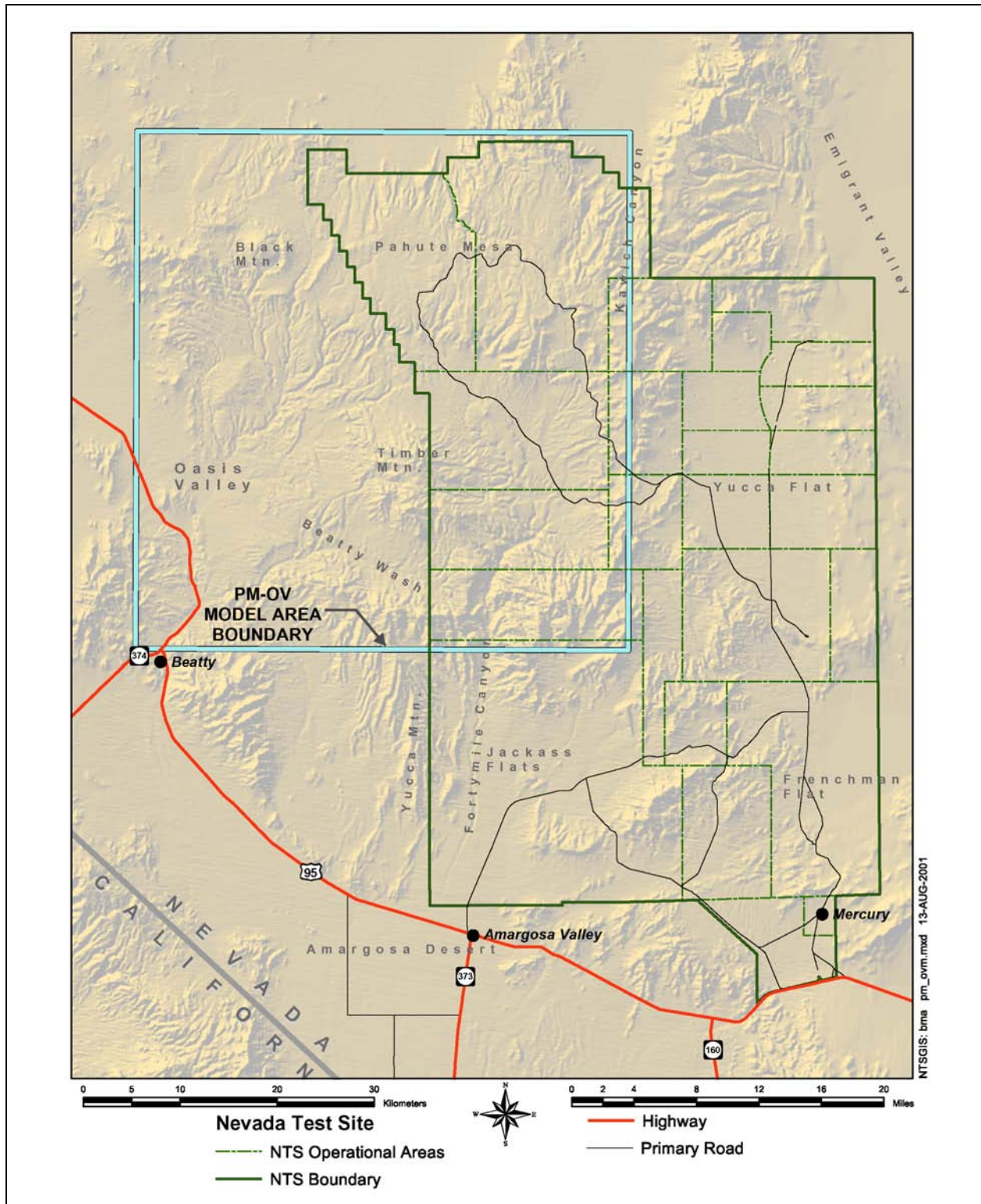


**Figure 1-2**  
**Map Showing Location of the Pahute Mesa Model Area**  
 Source: BN, 2002a

Central and Western Pahute Mesa, Yucca Flat, and Rainier Mesa/Shoshone Mountain (Figure 1-1). Central Pahute Mesa (CAU 101) and Western Pahute Mesa (CAU 102) are addressed together due to their adjacent locations and common groundwater regime as well as similarities in testing practices, geology, and hydrology (SNJV, 2004b).

Appendix VI, Revision No. 1 (December 7, 2000) of the FFACO (1996, as amended February 2008), “Corrective Action Strategy,” describes the processes that will be used to complete corrective actions, including those in the UGTA Project, which provides the current regulatory guidance on the UGTA Project corrective action strategy and is incorporated into this document. All references in this document to the FFACO or its appendices will refer to the Appendix VI, December 2000 revision.

The CAU-specific corrective action process comprises six major components: CAIP, CAI, Corrective Action Decision Document (CADD), Corrective Action Plan (CAP), Closure Report (CR), and long-term monitoring. The purpose or contents of these documents are summarized as follows:

- The CAI planning is documented in the CAIP, an FFACO-required document that provides or references all specific information for planning investigation activities associated with CAUs or sites.
- The CAI includes the collection of new data, the evaluation of new and existing data, and the development and use of CAU-specific groundwater flow and transport model(s).
- The CADD is an FFACO-required report that documents the CAI. It describes the results of the CAI, the corrective action alternatives considered, the results of their comparative evaluation, the selected corrective action, and the rationale for its selection.
- The CAP is an FFACO-required document describing how the selected remedial alternative is to be implemented. The CAP will contain the engineering design and all necessary specifications to implement the selected remedial alternative.
- The UGTA Project strategy has provisions for CAU closure only if the long-term-monitoring alternative is selected. Closure activities include the preparation of a CR, a review of the CR by NDEP, and long-term closure monitoring by NNSA/NSO.
- The long-term, post-closure monitoring is designed to ensure the compliance boundary is not violated (SNJV, 2004b).

Figure 1-3 presents the decision process used to implement the strategy for the PM CAU flow model.

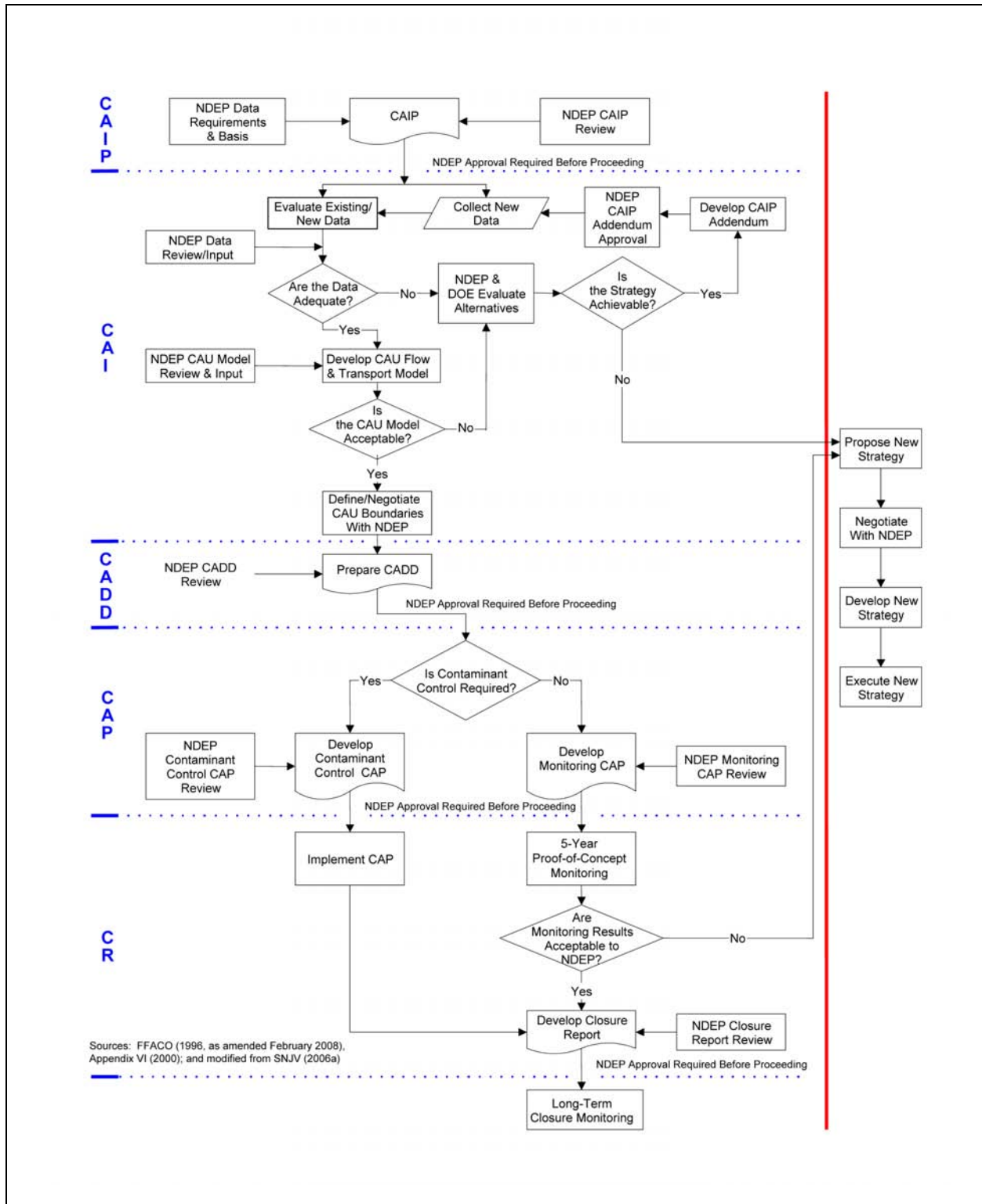


**Figure 1-3**  
**Process Flow Diagram for the Underground Test Area Corrective Action Units**

### **1.3.1 Summary of the FFACO UGTA Project Corrective Action Strategy**

The UGTA Project corrective action strategy consists of two major phases: developing a regional flow model for use in evaluation and coordination for all the UGTA Project CAUs, and developing a corrective action process for each of the CAUs. A model of regional flow encompassing the NTS and the groundwater flow systems extending to downgradient discharge has been completed and is documented in *Regional Groundwater Flow and Tritium Transport Modeling and Risk Assessment of the Underground Test Area, Nevada Test Site, Nevada* (DOE/NV, 1997b). Regional modeling is a cross-cutting activity, supporting the entire UGTA Project, which provides the initial basis for assessing flow paths from CAUs, determining potential receptors, evaluating isolation or interaction of CAUs, and creating a consistent hydrogeologic framework across the CAUs. Regional transport modeling provided the initial basis for determining the magnitude of risk from the source to potential receptors and for scaling individual CAU work (FFACO, 1996; as amended February 2008).

The second phase of the CAI process focuses on developing CAU-specific models that include CAU-specific data. The CAU-specific modeling objectives are to determine boundaries that encompass the extent of contamination, as defined in the FFACO (1996, as amended February 2008). Thus, this second phase is the basis for the analysis of relevant hydrologic data, and the development of the PM CAU flow and transport model. Further refinement of the PM CAU flow model and development of the PM CAU transport model is presented in this report.

## **1.4 Pahute Mesa Background**

Pahute Mesa is located in the northwestern part of the NTS that includes Areas 19 and 20 (Figure 1-1). Pahute Mesa is an elevated plateau of about 500 square kilometers (km<sup>2</sup>) (200 square miles [mi<sup>2</sup>]) over 2,134 meters (m) (7,000 feet [ft]) above mean sea level (amsl) throughout the eastern range (Blankennagel and Weir, 1973). The area of interest for the Pahute Mesa CAU is defined by the potentially affected portion of the regional groundwater flow system, which includes a region stretching from the northern side of Pahute Mesa south and southwestward to Oasis Valley (Figure 1-2).

Pahute Mesa geology is dominated by deposition of rock units from volcanic eruptions from nested calderas of the Southwestern Nevada Volcanic Field (SWNVF) (Figure 1-4). All rocks known to



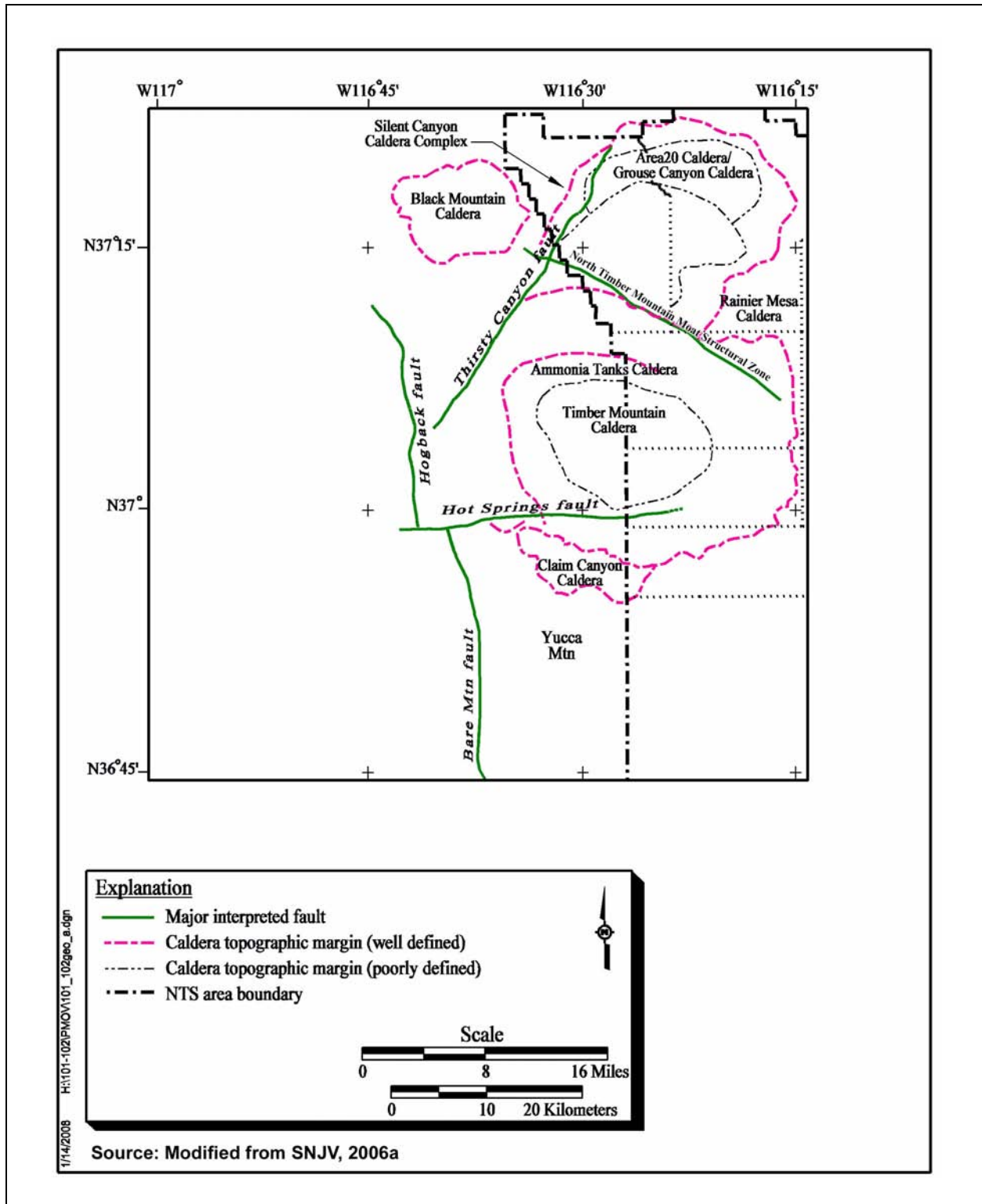


**Figure 1-4**  
**Geophysically Inferred Geologic Features of the Pahute Mesa Area**

underlie Pahute Mesa are volcanic. The younger caldera complex of hydrologic significance is the Timber Mountain caldera. This caldera collapse and its filling with volcanic materials affect the southern portion of the Western Pahute Mesa CAU. The Timber Mountain caldera erupted volcanic ash flows that covered much of Pahute Mesa to the north.

On Pahute Mesa, the rocks from Timber Mountain caldera cover an older series of calderas that make up the Silent Canyon caldera complex (SCCC). This caldera complex consists of at least two nested calderas: the Area 20 caldera and the older Grouse Canyon caldera (Sawyer and Sargent, 1989). Both calderas were formed and subsequently filled by voluminous eruptions of tuff and lava of generally rhyolitic composition. Total thickness of volcanic rocks beneath Pahute Mesa approaches 5 kilometers (km) (Ferguson et al., 1994).

The volcanic rocks that control groundwater flow beneath Pahute Mesa can be grouped into four volcanic hydrogeologic units (HGUs) based mainly on lithology and secondary alteration. These units are lava-flow aquifers (LFAs), welded-tuff aquifers (WTAs), vitric-tuff aquifers (VTAs), and tuff confining units (TCUs).

Groundwater beneath Pahute Mesa generally flows in a southwest direction, primarily through fractures in the lava-flow and tuff aquifers. Zeolitized bedded and nonwelded tuffs act as confining units that inhibit the flow of groundwater. The spatial distribution of permeable aquifers relative to the confining units is not well understood. Thickness variations of aquifers and confining units and their connectivity across faults or caldera boundaries are important hydrostratigraphic relationships that are also not well understood at Pahute Mesa (SNJV, 2006a).

Groundwater-elevation data in the area of interest are at variable spatial density. A number of wells provide water-level information in the area of Pahute Mesa and Oasis Valley, but water levels in the area between Pahute Mesa and Oasis Valley are less well defined. However, what data are available suggest that groundwater elevations generally mimic the topography (SNJV, 2006a). Groundwater elevations are highest beneath northern Pahute Mesa, ranging in elevation from approximately 1,280 to nearly 1,500 m (4,200 to 4,900 ft). Groundwater elevations drop off gradually to the south and west, ranging from 1,100 to 1,250 m (3,600 to 4,100 ft) in Oasis Valley. Some groundwater discharges to the surface within the Oasis Valley discharge area in the form of springs. [Figure 1-2](#)

shows the regional topography, and [Figure 1-5](#) shows the generalized groundwater flow directions for the regional groundwater flow system.

Groundwater recharge occurs locally from precipitation and by underflow from areas north of Pahute Mesa. Groundwater then flows south-southwestward to the Oasis Valley and Death Valley to the southwest. Several factors are believed to account for the flow around Timber Mountain. Due to its elevation, Timber Mountain receives excess precipitation compared to surrounding areas of lower elevation, which leads to additional groundwater recharge shed from Timber Mountain dome (TMD). The central resurgent dome consists of a welded tuff from which silica precipitation in fractures disallows water migration through the dome structure. Both of these factors are expected to lead to elevated groundwater levels at the flanks of the mountain, which affects groundwater flow paths from Pahute Mesa such that they go around both sides of Timber Mountain (SNJV, 2006a).

The bulk of the groundwater flow from Pahute Mesa to Oasis Valley occurs around the northwest side of Timber Mountain. However, a significant portion flows south along the east side of Timber Mountain and makes an abrupt turn to the west to converge with the remaining flow at Oasis Valley ([Figure 1-5](#)). This westerly turn appears to be caused by a structural high of the lower clastic confining unit (LCCU) associated with the Belted Range thrust system, which forces the groundwater to turn west at this point and flow towards the discharge areas. Pathlines from underground nuclear tests on Pahute Mesa generally move downgradient in volcanic aquifers above the LCA before discharging in Oasis Valley (SNJV, 2006a).

The east-west striking boundary of the Timber Mountain and Claim Canyon calderas may line up with a geophysically inferred east-west structure (Hot Springs fault) ([Figure 1-4](#)) (Grauch et al., 1997). The combination of these structures may inhibit southerly flow of groundwater in the vicinity and impart an east-west gradient to groundwater flow south of Timber Mountain (IT, 1998d).

#### **1.4.1 Underground Nuclear Testing on Pahute Mesa**

Underground nuclear testing on Pahute Mesa began with Operation Whetstone in 1965 and ended with Operation Julin in 1992 (DOE/NV, 2000d). Underground nuclear tests conducted at Pahute Mesa that are of interest to the UGTA Project are those detonated in deep vertical shafts, drilled into volcanic rock near or below the water table. A total of 82 such underground nuclear tests were

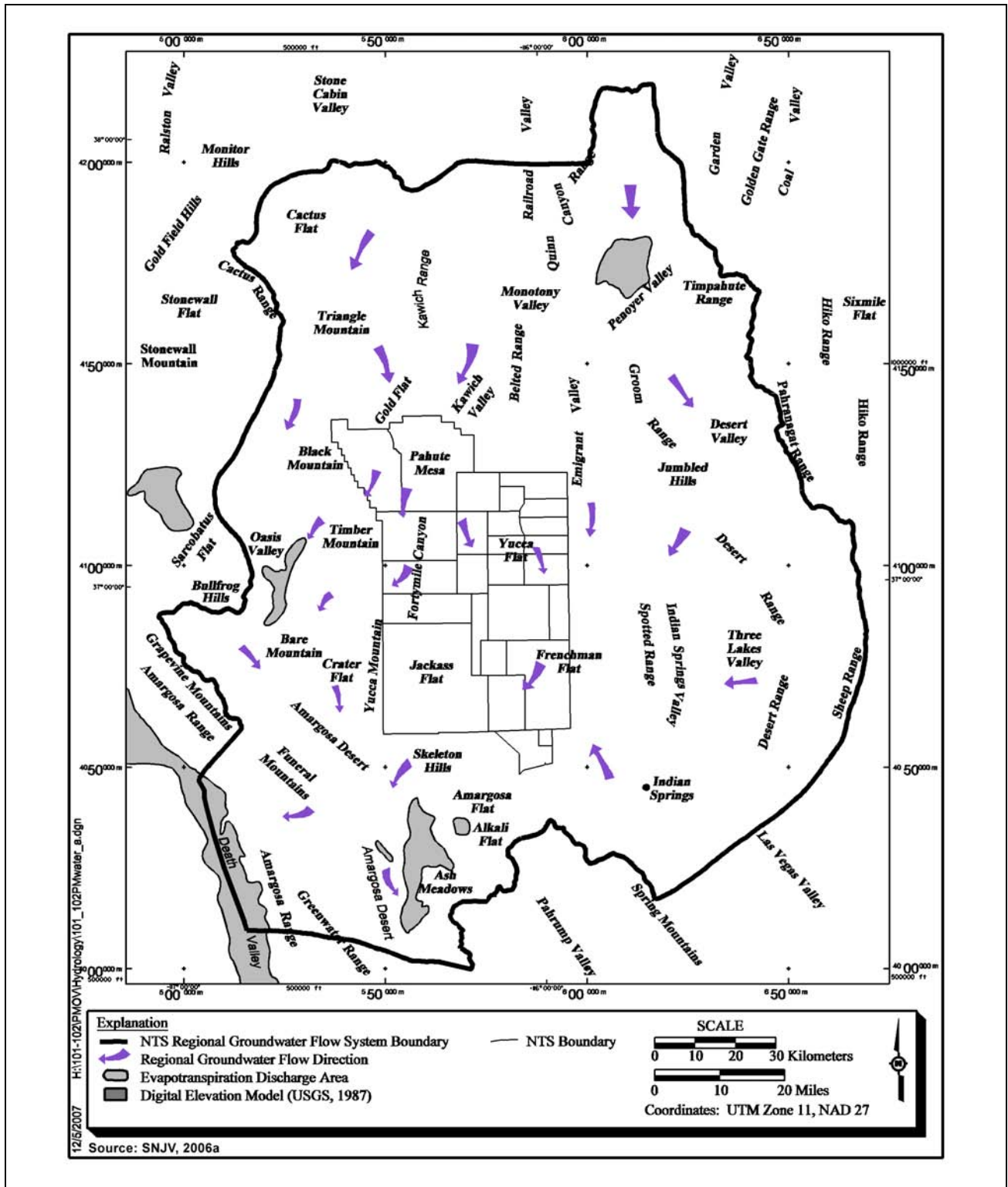


**Figure 1-5**  
**Features of the NTS Regional Groundwater Flow System**

conducted in Pahute Mesa. Sixty-four of these tests were detonated on Central Pahute Mesa (CAU 101), and 18 tests were detonated in Western Pahute Mesa (CAU 102) (DOE/NV, 1999). Media contaminated by the underground nuclear tests on Pahute Mesa are geologic formations within the unsaturated and saturated zones. Transport in groundwater is the primary mechanism of migration for the subsurface contamination away from the Pahute Mesa underground nuclear tests.

### ***1.5 Major Supporting Reports Documenting CAU-Specific Data Analysis and Evaluation***

The PM CAU flow model is supported by a number of major reports that describe a series of data analysis and modeling tasks. [Table 1-1](#) summarizes these reports and identifies their contribution to the development of the PM CAU flow model.

**Table 1-1**  
**Major Supporting Documents**  
 (Page 1 of 4)

Report	Report Synopsis	Contribution to Transport Model
<p><i>Summary of Hydrogeologic Controls on Ground-Water Flow at the Nevada Test Site, Nye County, Nevada</i> (Lacznia et al., 1996)</p>	<p>This report summarizes what is known and inferred about groundwater flow throughout the NTS region. As such, major controls on groundwater flow are identified, some uncertainties about groundwater flow are highlighted, and technical needs are prioritized and identified relative to the ERP.</p>	<ul style="list-style-type: none"> <li>• Conceptual model</li> </ul>
<p><i>Regional Groundwater Flow and Tritium Transport Modeling and Risk Assessment of the Underground Test Area, Nevada Test Site, Nevada</i> (DOE/NV, 1997b)</p>	<p>This report provided the initial rationale to determine the magnitude of risk from various underground nuclear tests on the NTS to potential downgradient receptors, such as the public and the environment from possible groundwater contamination. The regional evaluation consisted of data analysis, model development, and model predictions. Results of the regional evaluation of groundwater flow, tritium (<sup>3</sup>H) migration, and risk assessment performed for the underground test areas are presented in this report. As such, the regional evaluation was used during the planning of the Pahute Mesa CAI and is the basis for the development of the CAU conceptual model.</p>	<ul style="list-style-type: none"> <li>• Conceptual model</li> <li>• Regional model framework</li> <li>• Boundary fluxes</li> </ul>
<p><i>Corrective Action Investigation Plan for Corrective Action Units 101 and 102: Central and Western Pahute Mesa, Nevada Test Site, Nevada</i> (DOE/NV, 1999)</p>	<p>This report is a requirement of the FFACO (1996, as amended February 2008) that summarizes the site-specific historic data for the Pahute Mesa CAUs, and describes the characterization activities implemented to evaluate the extent of contamination in groundwater due to the underground nuclear testing, and the development of a groundwater flow model to predict the perimeter of the regulatory MCL.</p>	<ul style="list-style-type: none"> <li>• Summary of historic data</li> <li>• Background information</li> <li>• CAU model approach</li> </ul>
<p><i>Quality Assurance and Analysis of Water Levels in Wells on Pahute Mesa and Vicinity, Nevada Test Site, Nye County, Nevada</i> (Fenelon, 2000)</p>	<p>This report states that accurate water-level measurements are essential to determine groundwater flow paths that may contain contaminants from underground nuclear tests conducted on Pahute Mesa. As such, quality-assured data can be used to construct flow maps, calibrate steady-state and transient groundwater flow models, locate sites for future remedial monitoring, and identify existing trends that can be used as a means to understand the factors that influence the groundwater flow system.</p>	<ul style="list-style-type: none"> <li>• Supplement water-level targets for flow model calibration</li> </ul>

**Table 1-1**  
**Major Supporting Documents**  
 (Page 2 of 4)

Report	Report Synopsis	Contribution to Transport Model
<i>Evaluation of the Hydrologic Source Term from Underground Nuclear Tests on Pahute Mesa at the Nevada Test Site: The CHESHIRE Test</i> (Pawloski et al., 2001)	This report develops, summarizes, and interprets a series of detailed, unclassified simulations to forecast the nature and extent of radionuclide release and near-field migration in groundwater away from the CHESHIRE test over 1,000 years. The results are referred to as the CHESHIRE Hydrologic Source Term (HST).	<ul style="list-style-type: none"> <li>• Background</li> <li>• Basis for development of the simplified source term</li> </ul>
<i>A Hydrostratigraphic Model and Alternatives for the Groundwater Flow and Contaminant Transport Model of Corrective Action Units 101 and 102: Central and Western Pahute Mesa, Nye County, Nevada</i> (BN, 2002a)	This report presents the evaluation of geologic data and the resulting 3-D hydrostratigraphic framework model (HFM). The framework was built using a collection of stratigraphic, lithologic, and alteration data; a structural model; and results of geophysical, geological, and hydrological studies to formulate the hydrostratigraphic system.	<ul style="list-style-type: none"> <li>• HFM</li> <li>• Alternative HFMs</li> <li>• HSU definition and description</li> </ul>
<i>Geochemical and Isotopic Interpretations of Groundwater Flow in the Oasis Valley Flow System, Southern Nevada</i> (Thomas et al., 2002)	This report summarizes the findings of a geochemical investigation of the Pahute Mesa-Oasis Valley (PM-OV) groundwater flow system in support of the flow and contaminant transport modeling for the Western Pahute Mesa CAU.	<ul style="list-style-type: none"> <li>• Flow paths derived from geochemical analysis used to qualitatively assess flow model</li> </ul>
<i>Ground-Water Discharge Determined from Measurements of Evapotranspiration, Other Available Hydrologic Components, and Shallow Water-Level Changes, Oasis Valley, Nye County, Nevada</i> (Reiner et al., 2002)	This report describes the natural groundwater discharge in the Oasis Valley, an area within the groundwater flow system of the Death Valley region and California. An estimate of groundwater discharge from the Oasis Valley was examined in numerous studies. As a result of these studies, this report refined the estimated groundwater discharge from Oasis Valley by quantifying evapotranspiration (ET), compiling groundwater withdrawal data, and estimating subsurface outflow.	<ul style="list-style-type: none"> <li>• Flow system discharge from ET used as calibration data</li> </ul>
<i>Reconnaissance Estimates of Recharge Based on an Elevation-Dependent Chloride Mass-Balance Approach</i> (Russell and Minor, 2002)	This study describes the DRI evaluation of net infiltration and determination of recharge via the development of recharge models for data gathered from 17 springs located in the Sheep Range and Spring Mountains, and on the NTS. The objective was to improve an existing aquifer-response method based on the chloride mass-balance approach. Results of the recharge estimates are reported.	<ul style="list-style-type: none"> <li>• Recharge models</li> </ul>
<i>TYBO/BENHAM: Model Analysis of Groundwater Flow and Radionuclide Migration from Underground Nuclear Tests in Southwestern Pahute Mesa, Nevada</i> (Wolfsberg et al., 2002)	This report provides a description of an integrated modeling approach used to simulate groundwater flow, radionuclide release, and radionuclide transport near the TYBO and BENHAM underground nuclear test sites.	<ul style="list-style-type: none"> <li>• Test case for finite element heat-mass (FEHM) transfer code model</li> <li>• Results used to help parameterize CAU model</li> </ul>

**Table 1-1**  
**Major Supporting Documents**  
 (Page 3 of 4)

Report	Report Synopsis	Contribution to Transport Model
<i>Contaminant Transport Parameters for Groundwater Flow and Contaminant Transport Model of Corrective Action Units 101 and 102: Central and Western Pahute Mesa, Nye County, Nevada (Shaw, 2003)</i>	This report is a compilation of transport parameters that will be used by the transport model. Parameter values and estimated variability in the parameters is also defined. The data quality is evaluated based on the number and source of data points available to define each parameter.	<ul style="list-style-type: none"> <li>• Transport model parameters and distribution ranges</li> </ul>
<i>Simulation of Net Infiltration and Potential Recharge Using a Distributed Parameter Watershed Model for the Death Valley Region, Nevada and California (Hevesi et al., 2003)</i>	This study reports the development and application of a distributed parameter watershed model to estimate the temporal and spatial distribution of net infiltration for the Death Valley region. As stated, because of uncertainty relative to the input parameters, "averaging results from multiple realizations is more likely to provide a more robust estimate of current climate potential recharge."	<ul style="list-style-type: none"> <li>• Recharge models</li> </ul>
<i>Hydrologic Data for the Groundwater Flow and Contaminant Transport Model of Corrective Action Units 101 and 102: Central and Western Pahute Mesa, Nye County, Nevada (SNJV, 2004b)</i>	This report describes an assessment of hydrologic data and information in support of the CAU groundwater flow model. Relevant information, existing data, and newly acquired data were analyzed for the hydrologic components of the groundwater flow system of Pahute Mesa and vicinity.	<ul style="list-style-type: none"> <li>• Hydraulic head data for calibration</li> <li>• Hydraulic properties data</li> <li>• Discharge due to pumping</li> <li>• Boundary fluxes</li> <li>• Recharge models</li> <li>• Flow paths derived from geochemical analysis</li> </ul>
<i>Modeling Approach/Strategy for Corrective Action Units 101 and 102, Central and Western Pahute Mesa (SNJV, 2004c)</i>	This report summarizes the data and information that are the technical basis for the groundwater flow model. Two approaches are described that propose developing the models to forecast how the hydrogeologic system, which includes the underground nuclear test cavities, will behave over time. One approach is the development of numerical process models to represent the processes that influence flow and transport. The other approach shows how simplified representations of the process models are used to assess the interactions between model and parameter uncertainty.	<ul style="list-style-type: none"> <li>• Numerical code selection</li> <li>• Overall approach</li> </ul>
<i>Unclassified Source Term and Radionuclide Data for Groundwater Flow and Contaminant Transport Model of Corrective Action Units 101 and 102: Central and Western Pahute Mesa, Nye County, Nevada (SNJV, 2004e)</i>	This report identifies the radionuclide inventory; the mechanics of an underground nuclear test, which include changes that occur to the hydrologic properties of the rocks and distribution of the radionuclide source; and description of the approach used to build and simplify the HST process model.	<ul style="list-style-type: none"> <li>• Source inventory at individual test sites</li> <li>• Phenomenology of underground test</li> <li>• Partitioning of radionuclides between water and melt glass</li> <li>• Source term used in the CAU-scale model</li> </ul>



**Table 1-1**  
**Major Supporting Documents**  
 (Page 4 of 4)

Report	Report Synopsis	Contribution to Transport Model
<i>Evaluation of Groundwater Flow in the Pahute Mesa - Oasis Valley Flow System Using Groundwater Chemical and Isotopic Data</i> (Kwicklis et al., 2005)	This report documents the use of groundwater geochemical and isotopic data from the vicinity of the PM-OV flow system to interpret groundwater flow patterns as well as to independently evaluate the groundwater flow model that is currently being developed. A combination of graphical methods and inverse geochemical models form the basis for the PM-OV model area.	<ul style="list-style-type: none"> <li>• Flow paths derived from geochemical analysis</li> <li>• Geochemical verification dataset</li> </ul>
<i>Groundwater Flow Model of Corrective Action Units 101 and 102: Central and Western Pahute Mesa, Nevada Test Site, Nye County, Nevada</i> (SNJV, 2006a)	This report documents the development of the groundwater flow model to assess the migration of radionuclides away from underground nuclear test cavities on Pahute Mesa.	<ul style="list-style-type: none"> <li>• Hydrologic framework models used by the transport model</li> <li>• Flow fields to be used by the transport model</li> </ul>

## **1.6 Report Organization**

This report is organized into the following sections:

**Section 1.0** presents introductory information including regulatory requirements, report purpose, physical setting, related documentation, and document layout.

**Section 2.0** presents previous studies performed that support model flow and transport processes as they pertain to the Central and Western Pahute Mesa CAU flow and transport models.

**Section 3.0** presents changes made to the PM CAU flow model, interpretation of the effects of those changes, and the impact that these changes may have on PM CAU flow model uncertainty.

**Section 4.0** discusses development of the 1-D SSM.

**Section 5.0** explores the phenomenology of a nuclear test, processes that control CAU-scale groundwater flow and transport, and identification of RMCs.

**Section 6.0** presents the numerical models used to simulate CAU-scale flow and describes transport parameters.

**Section 7.0** describes the stochastic method applied to the PM CAU transport model, regulatory based metrics for concentration, methods used to present the data, and analysis of the PM CAU transport models for each alternative HFM.

**Section 8.0** presents uncertainty and sensitivity approaches used to characterize global sensitivity, analysis of uncertainty for each of the seven HFMs, and a composite analysis of the links between parametric and conceptual models.

**Section 9.0** summarizes important components identified through PM CAU modeling, identifies key aspects of uncertainty, and discusses methods to reduce uncertainty for each component.

**Section 10.0** is the summary and conclusions for the preceding modeling effort.

Section 11.0 is the list of references cited in this document.

Appendix A lists the reactive mineral model and corresponding HFM destinations for borehole samples.

Appendix B describes the development of distribution coefficients ( $K_d$ ) and correction of these distributions to account for upscaling and assignment of RMCs.

Appendix C shows how through reactive transport simulations, abstractions are developed to confirm the assumptions invoked by the particle-based transport model.

Appendix D presents an interpretation of groundwater travel times based on carbon-14 ( $^{14}\text{C}$ ) data.

Appendix E contains responses to NDEP comments on the draft version of this document.

## **2.0 REVIEW OF BACKGROUND FOR THE PAHUTE MESA PHASE I TRANSPORT MODEL**

The PM CAU transport model is documented in a set of component reports that define the process requirements and present the content necessary to support the PM CAU transport modeling discussed in this document. This set of documents presents a technically defensible construct that culminates in the transport modeling to predict contaminant migration from nuclear testing sites at Pahute Mesa to potential downgradient receptors. The supporting information includes characterization of multiple, equally probable conceptual models that capture hydrogeologic uncertainty and the range of parametric uncertainty that exists in the available flow and transport data. Initially, a regional scale groundwater model was developed to capture the general flow and transport features for the NTS (DOE/NV, 1997b) and surrounding area. The PM CAU flow and transport models are used to predict transport and to evaluate further data collection and modeling needs to reduce uncertainty. The recommendations from analysis of the regional groundwater model are captured in the Pahute Mesa CAIP (DOE/NV, 1999) that describes data collection activities, data evaluation and analysis needs, and groundwater flow and transport modeling. Further detail about the modeling approach and strategy is presented in SNJV (2004c). Based on these supporting documents the PM CAU flow model was developed and calibrated (SNJV, 2006a). Determination of the HST was treated as a separate, supporting modeling effort described in SNJV (2004e). The solute mass flux that serves as the contaminant source term for the PM CAU transport modeling is calculated by an SSM derived from a detailed process model.

### **2.1 Introduction**

This section provides an overview of the substantial body of work that contributes to the Pahute Mesa flow and contaminant transport task, and identifies how the preceding work is pertinent to this task.

## **2.2 Preliminary Groundwater Flow System Understanding**

Before the regional flow and transport model was released, what was known and inferred about groundwater flow at the regional scale in the NTS region was first described by Winograd and Thordarson (1975). This early work and later studies were compiled and summarized by Laczniaik et al. (1996). That report summarized the scientific understanding about groundwater flow beneath the NTS at that time and highlighted uncertainties in knowledge of hydrogeologic conditions in the complex regional flow system, further furnishing the basis for a conceptual model for flow and transport at both regional and smaller scales. Laczniaik et al. (1996) was, in turn, largely based on (1) reports of earlier hydrologic investigations by the USGS during the 1960s and 1970s; (2) published and unpublished reports documenting complementary work done by other organizations; and (3) published DOE reports through 1992 documenting planning and strategies for environmental restoration at NTS. Additional information from more recent geologic mapping and new structural interpretations in the region by the USGS, the University of Nevada-Reno, and others was also incorporated and cited.

Water-level data presented throughout that report represented measured values through 1991, but these levels were not of equivalent data quality from hole to hole because of differences in hole construction and numerous other factors.

## **2.3 Regional Scale Flow and Tritium Transport Modeling**

Flow models at the CAU scale lack natural boundaries (such as no-flow or constant-head boundaries) to constrain the flow domain. At the CAU scale, flow rates across the somewhat arbitrary boundaries are needed from a larger-scale, regional flow model that extends to such natural flow boundaries and therefore models a largely closed system at the larger scale. This need is met in the report *Regional Groundwater Flow and Tritium Transport Modeling and Risk Assessment of the Underground Test Area, Nevada Test Site, Nevada* (DOE/NV, 1997b). That report also provides the initial rationale to determine the magnitude of risk from various underground nuclear tests on the NTS to potential downgradient receptors, such as the public and the environment from possible groundwater contamination. The regional evaluation consisted of data analysis, model development, and model predictions. Results of the regional evaluation of groundwater flow, <sup>3</sup>H migration, and risk assessment performed for the underground test areas are presented in that report. The regional

evaluation was used during the planning of the Pahute Mesa CAI and served as the basis for the development of the CAU conceptual model and to constrain the boundary flow rates at the scale of a CAU flow model.

Some of the major conclusions derived from the regional groundwater flow modeling, transport modeling, and risk assessment and <sup>3</sup>H transport model (DOE/NV, 1997b) are important to the CAU-scale flow and transport models and are summarized here with indication of the importance of the conclusions to the work in the present report.

With respect to NTS groundwater modeling, several conclusions were drawn. It was found that groundwater flow paths from the Yucca Flat and Frenchman Flat underground test areas discharge either in Death Valley or the Amargosa Desert, but not at Ash Meadows. In contrast, the groundwater flow paths from the Pahute Mesa testing area discharge in Oasis Valley. This information guided and refined the development of the conceptual model for CAU-scale flow and transport modeling.

It was also concluded that simulated water levels and fluxes are very sensitive to the interpretation of major geologic features. This information led to emphasis on alternative geologic interpretations to capture uncertainty associated with this sensitivity.

Another conclusion was that generally, particle travel distances doubled or tripled at specified times in response to a 50 percent increase in recharge and conductivities. The effect was not as significant when recharge and conductivities were decreased. However, the redistribution of recharge to low-lying areas did not have a significant impact on the simulated water levels. The sensitivity analysis performed on 116 hydraulic conductivity values showed that the effect on groundwater flow was small. Emphasis is therefore placed on alternative recharge estimation methods in the CAU-scale flow model to capture uncertainty associated with this sensitivity.

With respect to transport modeling, a regional stochastic numerical transport model was developed to simulate <sup>3</sup>H transport in groundwater along three of the fastest groundwater paths from the underground test areas: the BOURBON, HOUSTON, and TYBO pathlines. The simulated <sup>3</sup>H concentrations along these fastest pathlines were very likely significantly overestimated because lateral dispersion and dilution from adjacent clean water were not considered. It was concluded that for the BOURBON and HOUSTON pathlines, the maximum concentration limit of 20,000 picocuries

per liter (pCi/L) for  $^3\text{H}$  in groundwater would not likely be exceeded outside of the NTS. In contrast, the TYBO pathline maximum concentration limit of 20,000 pCi/L for  $^3\text{H}$  in groundwater could be exceeded outside of the NTS, and may extend as far as Oasis Valley. It was also noted that long-term monitoring of water samples from the Oasis Valley springs and groundwater wells west and south of the Pahute Mesa do not show  $^3\text{H}$  levels above the background levels. This infers the possibility that  $^3\text{H}$  is migrating at a more normal, nonexceptional rate than was simulated in the deliberately conservative flow model that neglected lateral dispersion and dilution from adjacent clean water.

Key uncertainties identified in regional scale flow and transport modeling were the conceptual model for hydrostratigraphy (i.e., interpretation of geologic features), method of estimating areal recharge rates, and multidimensional transport phenomena that were not addressed at the regional scale (e.g., dispersion).

## **2.4 Characterization Data and Studies**

Characterization data and studies that constitute the technical basis for groundwater flow and transport models are identified in the following categories:

- Site-specific historical data (primarily found in DOE/NV [1999])
- Relevant data from other sites (primarily from the Yucca Mountain Project [YMP])
- Documented models of components (the regional groundwater model [DOE/NV, 1997b] and associated inputs; and the integrated radionuclide migration/HST [Tompson et al., 1999; Pawloski et al., 2001])
- Field, laboratory, and modeling investigations:
  - Fracture analyses (Drellack and Prothro, 1997; IT, 1998a and b)
  - Pahute Mesa-Oasis Valley hydrogeologic investigation (IT, 1998d)
  - Geologic investigation (Fridrich et al., 1999a)
  - Pahute Mesa-Oasis Valley hydrostratigraphic model (BN, 2002a)
  - BULLION Forced-Gradient Experiment (FGE) (IT, 1998a)
  - NTS regional recharge study (Russell and Minor, 2002; Hevesi et al., 2002)

- Glass dissolution studies (Bourcier et al., 2000; Pawloski et al., 2001)
- Colloid transport experiments (IT, 1998a; unreferenced Yucca Mountain C-Well test)
- CAMBRIC HST investigation (Tompson et al., 1999)
- CHESHIRE HST investigation (Pawloski et al., 2001)
- TYBO-BENHAM modeling investigation (Wolfsberg et al., 2002)
- Modeling of geochemical transport in the vicinity of Pahute Mesa and Oasis Valley (Thomas et al., 2002; Rose et al., 2006)
- Boundary conditions
- Assessment of fault characteristics (study in progress at time of the report)
- Geochemistry, Hot Well, and Hydrologic Resources Management Program (HRMP) migration data (summarized in DOE/NV [1999])
- Expert elicitations (IT, 1998c)
- Expert review (IT, 1999)

## **2.5 Corrective Action Investigation Plan**

The Pahute Mesa CAIP (DOE/NV, 1999), a document required by the FFACO (1996, as amended February 2008), summarizes previously available site-specific data that were developed for Central and Western Pahute Mesa CAUs 101 and 102, and describes the CAI to be conducted at the Pahute Mesa CAUs to evaluate the extent of contamination in groundwater due to the underground nuclear testing. Several characterization activities to be completed before modeling should be undertaken are included in the CAI to collect new data designed to reduce existing uncertainties in the current conceptual model. As defined using the Data Quality Objective (DQO) process, these activities include:

- Hydrogeologic investigation of the area southwest of Pahute Mesa
- Geologic investigation of the Pahute Mesa area
- Groundwater recharge study
- Isotope- and geochemistry-based investigation
- Groundwater tracer test



- Laboratory study of radionuclide transport parameters
- Near-to-intermediate scale groundwater flow and transport investigation

A description of the Pahute Mesa CAUs is provided in the Pahute Mesa CAIP (DOE/NV, 1999) to define the problem at hand, including the investigative background of the CAUs, their operational history, the CASs of both CAUs, the physical setting based on the available information, the potential contaminants, the conceptual model of the CAU, and the preliminary corrective action levels for the potential contaminants.

The DQO process is discussed and related to the proposed conceptual model and the migration scenarios identified to these results. A plan is presented for CAU-scale groundwater flow and contaminant transport modeling activities to be conducted during the CAI, including the assessment of existing and newly acquired data. The relationship of the CAU-scale model to other models is also discussed. Descriptions are provided of the characterization activities that are either planned or ongoing for the Pahute Mesa CAUs, as part of the CAI. Supporting activities such as waste management, health and safety, and field sampling and analysis are also summarized.

The Pahute Mesa CAIP (DOE/NV, 1999) includes a description of how it is planned in accordance with the requirements of the FFACO (1996, as amended February 2008) and also identifies other applicable or potentially applicable regulations.

Descriptions of the pertinent field and laboratory quality assurance (QA) and quality control (QC) procedures, and a description of the project schedule and records availability are provided in the Pahute Mesa CAIP (DOE/NV, 1999) to guide the CAI.

Key uncertainties identified in the Pahute Mesa CAIP (DOE/NV, 1999) were:

- Subsurface not well characterized for the area southwest of Pahute Mesa between the underground test area and the Oasis Valley discharge area
- Only crude estimates of precipitation and recharge available for the Pahute Mesa groundwater flow system
- Limited knowledge of contaminant transport processes and associated parameters
- Limited understanding of the contamination sources at present

## 2.6 Pahute Mesa CAU-Scale Modeling Approach

The strategy for flow and transport modeling in this effort were developed and described in *Modeling Approach/Strategy for Corrective Action Units 101 and 102, Central and Western Pahute Mesa* (SNJV, 2004c). That report describes the current conceptual model of radionuclide migration from test cavities on Pahute Mesa to the accessible environment, and maps the flow of information from data collection through process model development to the CAU model.

The major assumptions, data inputs, and outputs are listed for each of these CAU model components:

- Geologic framework
- Climate
- Recharge
- Lateral boundary conditions
- Input parameter distributions
- Source term
- Thermal hydrology
- Saturated zone flow
- Saturated zone transport
- Heterogeneity

Two complementary modeling approaches are proposed for developing the models to forecast how the hydrogeologic system, which includes the underground nuclear test cavities, will behave over time. The first approach is the development of rigorous numerical process models (the CAU model) to represent the features, events, and processes that influence flow and transport of contamination from sources in underground nuclear tests at or near the water table on Pahute Mesa. The second approach complements the first by using simplified, computationally efficient representations of those process models in the framework of a total system performance assessment model to support analysis of the interactions between model and parameter uncertainty. The identification and treatment of uncertainty of model components due to parameter values, features, and processes is considered, and an approach is described for determining which uncertain parameters or conceptual models are most significant to model results and for propagating this uncertainty in the CAU model.

Key uncertainties in the PM CAU flow model are addressed in Section 6.0 of SNJV (2006a). Two fundamental types of uncertainty are addressed: parameter uncertainty and conceptual model uncertainty. Parameter uncertainty is treated by using probability distributions for uncertain

parameters rather than single values. The probability distribution selected represents the likelihood of a particular value occurring. The method used to develop the distribution varies depending on the availability of relevant data or other knowledge (Mishra, 2002). In contrast to parameter uncertainty, conceptual model uncertainty is less tractable. The approach adopted to address conceptual model uncertainty is that proposed by Gorelick et al. (1999). In this approach, alternative model components are identified, and for each component, the importance of uncertainty on predicted transport is assessed through hypothesis testing and sensitivity analysis to determine if uncertainties have a significant effect on predictions.

Based on the review of prior work and insight gained from previous NTS modeling, a preliminary list of uncertain model components for the Pahute Mesa CAUs were identified and include:

- Hydrostratigraphic framework
- Hydraulic properties of faults
- Vertical flow (flow-through faults)
- Boundary conditions
- Groundwater discharge
- Recharge
- Focused recharge (Timber Mountain)
- Groundwater-level measurements
- Hydraulic properties of HSUs
- Thermal effects
- Porosity, retardation coefficients, dispersivity
- Matrix diffusion
- Colloid transport
- Partitioning of radionuclides between rubble and melt glass
- Reactive surface area of melt glass

For each of the above components, the nature of the uncertainty was identified, decisions made on whether to explicitly address it and, if so, how it was to be addressed as a parameter or conceptual model uncertainty.

## **2.7 Pahute Mesa CAUs 101 and 102 Groundwater Flow Model**

Two types of numerical hydrologic models are usually used to help understand complex flow systems and predict the movement of contaminants within them. The first of these numerical models predicts only the movement of water, and it is commonly referred to as a “flow model.” The second type of numerical model predicts the concentrations of dissolved radioactive contaminants traveling within

the groundwater flow system, and is usually referred to as a “transport model.” The transport model uses the flow velocity information derived from the flow model and is closely coupled to the flow model. The flow model that directly supports the PM CAU transport model is the subject of *Groundwater Flow Model of Corrective Action Units 101 and 102: Central and Western Pahute Mesa, Nevada Test Site, Nye County, Nevada* (SNJV, 2006a). That report presents a framework for a flow model that incorporates data and information related to multiple component models of the Pahute Mesa hydrogeologic system. The flow model was further refined during transport modeling to modify structural and hydrostratigraphic features that might further reduce flow model uncertainty and improve the fit to observed geochemical markers. These refinements are discussed in this report. Both the flow and the transport models are characterized by uncertainties in both the data and information that characterize the processes described by the respective model, and in the conceptual models that incorporate the data and information.

### **2.7.1 Conceptualization**

The conceptual flow model implemented in SNJV (2006a) derives from another report, *Hydrologic Data for the Groundwater Flow and Contaminant Transport Model of Corrective Action Units 101 and 102: Central and Western Pahute Mesa, Nye County, Nevada* (SNJV, 2004b). That report describes an assessment of hydrologic data and information in support of the PM CAU flow model that in turn is closely coupled to the PM CAU transport model. Relevant information, existing data, and newly acquired data were analyzed in SNJV (2004b) for the hydrologic components of the groundwater flow system of Pahute Mesa and vicinity.

### **2.7.2 Hydrostratigraphic Framework Models**

There are multiple alternative HFMs, presented in *A Hydrostratigraphic Model and Alternatives for the Groundwater Flow and Contaminant Transport Model of Corrective Action Units 101 and 102: Central and Western Pahute Mesa, Nye County, Nevada* (BN, 2002a), accounting for the uncertainty in the geology. These are designated the base HFM and alternative HFMs for the Pahute Mesa area, and provide 3-D spatial discretizations of the geologic stratigraphy grouped in zones of similar hydrologic properties.

### **2.7.3 Recharge**

The uncertainty in recharge was addressed by using three basic alternative approaches in *Groundwater Flow Model of Corrective Action Units 101 and 102: Central and Western Pahute Mesa, Nevada Test Site, Nye County, Nevada* (SNJV, 2006a). These alternative approaches are the Maxey-Eakin empirical approach, the net-infiltration recharge model from a watershed-distributed parameter modeling by the USGS, and the chloride mass-balance modeling by the DRI.

### **2.7.4 Lateral Boundary Fluxes**

A set of boundary fluxes to be used with the PM CAU flow model was developed based on results generated for eight alternate regional-scale flow models using the UGTA Project regional model (SNJV, 2004b). The alternate flux boundary conditions can be used to help evaluate the uncertainty in the PM CAU flow model associated with the choice of HFM and recharge model. The approach used to calculate these fluxes does not specify the locations on the boundary where the flux occurs, just quantifies bounds on the total amount of flow through the CAU-model lateral edges.

### **2.7.5 Discharge**

Within the Pahute Mesa area and vicinity, most natural groundwater discharge to the surface occurs in the form of ET and springs in the Oasis Valley discharge area. The area of interest to this activity includes the Pahute Mesa area and all of the Oasis Valley hydrographic area because the discharge area extends outside of the PM CAU model area. The majority of the groundwater discharge to springs is effectively lost from the groundwater system through ET within the discharge area.

### **2.7.6 Hydraulic Heads**

Hydraulic head data, as well as boundary fluxes estimated from the regional model analysis (SNJV, 2004b), constitute the targets for inverse calibration of the PM CAU flow model. Observed hydraulic heads are derived from depth-to-water measurements and well information and may also be approximated by the land surface elevations of regional springs. The results of the water-level data analysis were used to identify hydraulic head values that are most representative of steady state, predevelopment conditions at specific boreholes and well locations. Each temporal subset of measurements that represents steady-state conditions was reduced statistically to a mean, standard

deviation (SD), and variance of the mean. The hydraulic head data derived from the water-level data were supplemented with land surface elevations of the selected regional springs.

### **2.7.7 Hydraulic Conductivity**

Analysis of hydraulic conductivity data included evaluations of measurement scale (laboratory-scale, slug-test-scale, and constant-rate-scale data), scaling and spatial variability, vertical anisotropy, and the alteration of hydraulic conductivity in nuclear test cavities.

Approximately 300 hydraulic conductivity values were obtained from analyses of constant-rate test data from the NTS area. These tests sample a larger volume of the tested formation than either laboratory or slug-scale tests. Hydraulic conductivity of individual units is assumed to decrease with depth, as was the case for the regional flow model. The treatment of depth decay of hydraulic conductivity is described in SNJV (2004b).

### **2.7.8 Groundwater Geochemistry**

Groundwater geochemistry data are considered during the evaluation of the groundwater flow system because they provide a means for determining the origin, pathway, and timescale of groundwater flow that is independent of estimates based on conventional hydraulic data.

The comparison of PM CAU flow model results to geochemical evaluations was performed as a verification step after model calibration using hydraulic information (heads and fluxes) for comparison against results from an independent study (Kwicklis et al., 2005).

### **2.7.9 Flow Model Uncertainties**

Following the approach identified in the Pahute Mesa CAIP (DOE/NV, 1999), uncertainty is addressed in the PM CAU flow model in terms of parameter and conceptual model uncertainties.

The PM CAU flow model has a large number of parameters that can be changed in order to calibrate the model to observations of hydraulic heads, spring heads, lateral boundary flows, and ET flows. Not all of these parameters have the same influence on the performance of the model. Therefore, it

was necessary to identify those parameters to which the model outputs are most sensitive, and how they relate to the conceptual model.

## **2.8 Hydrologic Source Term**

The HST for radioactive contamination is defined in *Unclassified Source Term and Radionuclide Data for the Groundwater Flow and Contaminant Transport Model of Corrective Action Units 101 and 102: Central and Western Pahute Mesa, Nye County, Nevada* (SNJV, 2004e). That report documents the analysis of available information on the unclassified HST and data on radionuclides relevant to the Pahute Mesa CAUs 101 and 102. The HST of an underground nuclear test is the portion of the total inventory of radionuclides that is released into the groundwater over time following the explosion of an underground nuclear test. In contrast, the total inventory of radionuclides is known as the radiologic source term (RST). The development of an unclassified HST was conducted in direct support of the development of the PM CAU transport model that is the subject of the present report.

Stoller-Navarro Joint Venture (2004e) reviews available information on the sources of radionuclide contamination, which includes: (1) underground nuclear test data, (2) the phenomenology of underground nuclear tests, (3) the unclassified radionuclide inventory, and (4) radionuclide distribution in the nuclear test cavities and vicinity. Relevant detailed process models available include: (1) the CAMBRIC HST model (Tompson et al., 1999); (2) the Frenchman Flat Simplified HST model (Tompson et al., 2004); and (3) the CHESHIRE HST model (Pawloski et al., 2001). A local groundwater flow and transport model of the TYBO-BENHAM area is available to help understand the processes of importance at the intermediate scale (Wolfsberg et al., 2002). This information includes the development of an unclassified SSM to estimate radionuclide source inputs for the PM CAU model to represent the near-field source term releases from the CHESHIRE test. The SSM is developed in the GoldSim software platform to generate cavity source flux terms for use in the PM CAU transport model. The SSM was also tested against the detailed process model calculations for the CHESHIRE test.

Key uncertainties in the SSM are related to the simplifications and assumptions of the model, and are summarized here. First, the total initial mass of each radionuclide at each underground test is based on an average of the unclassified inventory for the sum of all underground tests in the area; this may

be significantly in error for a particular test. Overcoming this uncertainty would require the use of classified, test-specific data; hence, radionuclide concentrations in the near field cannot be expected to match field observations. Second, radionuclides are assumed to be uniformly distributed in the exchange volume and melt glass; this spatial variability could lead to errors when compared against measured cavity data, even if classified source inventories were used. Third, chemical reactions are based on the assumption of linear adsorption isotherms; this will lead to errors in the near field but is expected to have greater validity at larger distances. Finally, solubility limits on melt glass dissolution were ignored in the analysis; this is expected to cause overestimation of melt glass dissolution because limiting factors such as silica solubility were ignored.

## **2.9 Summary**

This section presented an overview of the substantial body of work that contributed to the PM CAU transport model. Historical data and information and data collection provided the technical bases for the development and application of a regional groundwater flow and  $^3\text{H}$  transport model that was used to screen risk from CAUs as well as provide a framework for higher-resolution modeling at the CAU scale. The Pahute Mesa CAIP (DOE/NV, 1999) charted the approach, and identified the data and information available and still needed to construct a groundwater flow and groundwater transport model for CAUs 101 and 102. Data collection and evaluation and construction of a groundwater flow model for CAUs 101 and 102 provided the groundwater velocities and other information needed by the groundwater transport model that is the subject of the present report. An SSM fills the need for an HST to quantify the source of radioactive contaminants from the underground test sites. Uncertainties in all of these supporting documents are summarized and their propagation to downstream modeling efforts identified.



## **3.0 ALTERNATIVE CALIBRATED FLOW MODELS**

The basic structure of the PM CAU flow model (SNJV, 2006a) is the HFM, which is the 3-D representation of the hydrostratigraphy and structural features. Alternate HFMs were constructed to account for geologic uncertainty that potentially could substantially affect groundwater flow. The PM CAU model was defined through assignment of hydraulic properties, boundary conditions, and areal fluxes to the model domain. Flow simulation was performed, calibration targets were fit, and calibration target residuals were evaluated. Hydraulic heads, recharge, discharge, and lateral boundary flows were used to calibrate the PM CAU flow model through an automated calibration process that minimized the residuals between simulated and measured heads.

Geochemical mixing models based on the PM CAU flow model were employed as an independent check for flow patterns and model calibration. The most robust PM CAU flow models would be those that best matched geochemical mixing targets. Specific mismatches to the geochemical data were identified that were attributed to anomalous predicted flow behavior, and guided revisions to the PM CAU flow model conceptualization. Two approaches were pursued to correct observed geochemical mixing model misfits. In the first approach, excessive mixing between east and west sources was mitigated by decreasing flows along targeted segments of the north-south oriented Purse and Boxcar faults. For the second approach, preferential flow and channeling in large, continuous regional blocks was also identified as an artifact of the conceptual model design rather than a real feature of the rocks. By minimizing the permeability difference of all units, more diffuse flow was modeled.

### **3.1 Introduction**

Transport simulation is performed using a convolution-based particle-tracking method that requires particle tracks derived from a steady-state flow field. Each of the PM CAU flow models for which transport is simulated must be conceptualized and parameterized (calibrated) before extracting the particle tracks. The PM CAU flow model report (SNJV, 2006a) discussed 19 alternative models, each

calibrated to hydraulic targets. Each calibrated alternative was screened based on the ability of mixing models based on the PM CAU flow model to simulate observed geochemistry at wells and springs as an independent test of the flow field goodness of fit. Five PM CAU flow models were deemed acceptable, based upon their agreement with observed geochemistry, for use for transport analysis. Additional adjustment of two faults in the SCCC was required to correct for errant geochemical mixing results. Two additional PM CAU flow models, developed from characteristics identified in these selected five, were also considered for transport analysis.

The following subsections present three distinct topics related to the alternative flow fields upon which transport simulations are based. [Section 3.2](#) summarizes general hydrogeologic characteristics of, and differences between, the HFMs selected for transport analysis. [Section 3.3](#) presents a discussion of local-scale fault permeability adjustments, incorporated within all but one of the alternatives, made to improve simulated agreement with geochemical mixing targets. The adjustments and reasons for such are described and the improvements in geochemical mixing metrics are shown, as are the impacts on hydraulic calibration metrics. [Section 3.4](#) discusses the conceptualization and development of two new alternative models based on understanding gained from preliminary transport analysis. These new alternatives retain the same model geologic structure as the previous HFMs but explore the relationship between HSU configuration, permeability, and transport. Most critically, this alternative speaks to the importance of properly defining a conceptual (hydrogeologic) model before its parameterization, a subject that is addressed in depth in [Section 9.0](#).

### **3.2 Pahute Mesa-Oasis Valley HFM**

The PM-OV HFM provided the basic geometric arrangement of model components, including all the structural elements and many of the volume surfaces that define mineralogy subdivisions in the model. Therefore, many of the inherent attributes of the HFM also are integral to the reactive mineral model.

A quick review of the PM-OV HFM is provided in this section as background for the reactive mineral model. The HFM for the PM-OV CAU is fully documented in the report *A Hydrostratigraphic Model and Alternatives for the Groundwater Flow and Contaminant Transport Model of Corrective Action Units 101 and 102: Central and Western Pahute Mesa, Nye County, Nevada* (BN, 2002a).

### **3.2.1 Hydrostratigraphic Unit Model Development**

The general hydrogeologic framework for the NTS and vicinity, established by USGS geoscientists in the 1970s (e.g., Winograd and Thordarson, 1975), provided the foundation for most subsequent hydrogeologic studies at the NTS, including the PM-OV HFM. The hydrostratigraphic framework for the PM-OV area documented in the Bechtel Nevada (BN) report (BN, 2002a) was further enhanced by many field and analytical studies supported by the UGTA Project and conducted over several years. As a result of these studies and the contributions of many experts and organizations associated with the NTS, the hydrogeologic understanding of the model area has become increasingly detailed and refined.

Construction of the PM-OV HFM in EarthVision (Dynamic Graphics, 2002) involved developing a structural model of the area that included the locations and orientations of the relevant faults and calderas in the model area. The structural model of the base HFM incorporates many aspects of structural models of the NTS developed over the years for the weapons testing program at the NTS and recent UGTA Project-sponsored studies (e.g., Warren et al., 2000). These predecessor models integrated data from two-dimensional (2-D) reflection seismic, gravity, aerial and surface magnetic surveys, post-test surface effects, surface geology, and drill-hole data. The structural model for the PM-OV Phase I HFM is a refinement of this earlier work and incorporates new data collected by the UGTA Project program, including drill-hole data (DOE/NV, 1995a and b; Kilroy and Savard, 1996; Robledo et al., 1998; DOE/NV, 2000a, b, and c; NNSA/NV, 2002; NNSA/NSO, 2003); reprocessed gravity data (Maniken et al., 1998 and 1999; Hildenbrand et al., 1999); and aeromagnetic data (Grauch et al., 1997 and 1999). Refer to Section 2.0 in BN (2002a) for more information and specific references.

The base HFM includes 47 structural elements, most of which are basin-and-range-type normal faults. Only faults that were considered to be hydrogeologically significant were included in the model. These include faults with apparent displacement typically greater than about 60 m (200 ft) and those that are thought to form significant structural boundaries. The base HFM for the area also includes 20 faults and structural zones in addition to the caldera-forming faults. Thirteen of these 20 structural features are basin-and-range type faults mapped at the surface that are extended to the bottom of the model. Six calderas have been identified in the PM CAU model area, two of which are buried. The caldera margins are variously modeled as both a high-angle normal fault (shallow) and as

a high-angle (80 degrees) stratigraphic contact containing a subcaldera intrusive. Several older thrust faults, such as the Belted Range thrust (BRT) fault and associated imbricate thrust faults and folds, are also included. However, because the BRT fault is a low-angle feature, it is represented as an HSU contact.

The faults within the HFM form a fault-tree in 3-D space, which provides the structural framework within which the HSUs are located. The HSU classification system, discussed in [Section 3.2.2](#), is the basis for incorporating hydrostratigraphic information. The PM-OV hydrostratigraphic system consists of 46 HSUs that are represented as 3-D volumes in the finite element mesh for the flow model.

To address non-unique aspects of geologic interpretations incorporated in the base model, six alternative interpretations were considered. The alternative HFMs, listed below, are described in detail in BN (2002a).

- Alternative #1 - Silent Canyon Caldera Complex
- Alternative #2 - Area between the Timber Mountain Caldera and the SCCC
- Alternative #3 - Thirsty Canyon Lineament
- Alternative #4 - Depth to the Pre-Tertiary Surface
- Alternative #5 - Contiguous Sheet of Lower Carbonate Aquifer - Thrust Plate (LCA3) Rocks
- Alternative #6 - Deeply Rooted Belted Range Thrust Fault

### **3.2.2 Hydrogeologic and Hydrostratigraphic Units of the PM-OV HFM**

The rocks of the NTS have been classified hydrologically using a two-level classification scheme based on HGUs and HSUs (IT, 1996d; BN, 2002a, 2005, and 2006; NSTec, 2007). Hydrogeologic units are categories of rocks defined according to their ability to transmit groundwater (i.e., aquifers or confining units), which is mainly a function of a rock's primary lithologic properties, degree of fracturing, and secondary mineral alteration. Hydrostratigraphic units are larger, more regional mapping units that group contiguous stratigraphic intervals that have similar hydrogeologic characteristics (i.e., composed of similar HGUs).

**3.2.2.1 Hydrogeologic Units of PM-OV HFM**

The rocks of the PM-OV model area are classified as one of the following nine HGUs: alluvial aquifer (AA), welded-tuff aquifer (WTA), vitric-tuff aquifer (VTA), lava-flow aquifer (LFA), tuff confining unit (TCU), intra-caldera intrusive confining unit (ICCU), granite confining unit (GCU), clastic confining unit (CCU), and carbonate aquifer (CA) (Table 3-1). These HGUs are described in more detail in BN (2002a).

**Table 3-1**  
**Hydrogeologic Units of the PM-OV Model Area**  
(Page 1 of 2)

Hydrogeologic Unit	Typical Lithologies	Hydrologic Significance
Alluvial Aquifer (AA) (AA is also an HSU in the PM-OV hydrogeologic model)	Unconsolidated to partially consolidated gravelly sand, aeolian sand, and colluvium; thin, basalt flows of limited extent	Has characteristics of a highly conductive aquifer, but less so where lenses of clay-rich paleocolluvium or playa deposits are present.
Welded-Tuff Aquifer (WTA)	Welded ash-flow tuff; vitric to devitrified	Degree of welding greatly affects interstitial porosity (less porosity as degree of welding increases) and permeability (greater fracture permeability as degree of welding increases).
Vitric-Tuff Aquifer (VTA)	Bedded tuff; ash-fall and reworked tuff; vitric	Constitutes a volumetrically minor HGU. Generally does not extend far below the static water level due to tendency of tuffs to become zeolitic (which drastically reduces permeability) under saturated conditions. Significant interstitial porosity (20 to 40 percent). Generally insignificant fracture permeability.
Lava-Flow Aquifer (LFA)	Rhyolite lava flows; includes flow breccias (commonly at base) and pumiceous zones (commonly at top)	Generally a caldera-filling unit. Hydrologically complex; wide range of transmissivities; fracture density and interstitial porosity differ with lithologic variations.
Tuff Confining Unit (TCU)	Zeolitic bedded tuff with interbedded, but less significant, zeolitic, nonwelded to partially welded ash-flow tuff	May be saturated, but measured transmissivities are very low. May cause accumulation of perched and/or semi-perched water in overlying units.
Inter-Caldera Intrusive Confining Unit (ICCU)	Highly altered, highly injected/intruded country rock and granitic material	Assumed to be impermeable. Conceptually underlies each of the SWNVF calderas and Calico Hills. Developed for this study to designate basement beneath calderas as different from basement outside calderas.
Granite Confining Unit (GCU)	Granodiorite, quartz monzonite	Relatively impermeable; forms local bulbous stocks, north of Rainier Mesa and Yucca Flat; may contain perched water.

**Table 3-1**  
**Hydrogeologic Units of the PM-OV Model Area**  
 (Page 2 of 2)

Hydrogeologic Unit	Typical Lithologies	Hydrologic Significance
Clastic Confining Unit (CCU)	Argillite, siltstone, quartzite	Clay-rich rocks are relatively impermeable; more siliceous rocks are fractured, but with fracture porosity generally sealed due to secondary mineralization.
Carbonate Aquifer (CA)	Dolomite, limestone	Transmissivity values vary greatly and are directly dependent on fracture frequency.

Source: Table 4-3 in BN (2002a)

### 3.2.2.2 Hydrostratigraphic Units of the PM-OV HFM

One-hundred stratigraphic units in the PM-OV model area were grouped into 46 HSUs that comprise 18 aquifers and 17 confining units, and 11 composite units (units containing both aquifer and confining unit rocks) (Table 3-2). There are 40 Tertiary-age volcanic units comprising 16 aquifers, 13 confining units, and 11 composite units. Composite units contain both aquifer and confining unit rocks which cannot be differentiated into separate HSUs. Pre-Tertiary sedimentary rocks are divided into 6 HSUs, comprising 2 aquifers and 4 confining units (including the Mesozoic granite) (IT, 1996b; SNJV, 2006a).

The hydrostratigraphic classification system is the foundation of the PM-OV HFM. This system was developed by first grouping the rocks within the model area into HGUs based on lithologic character, propensity to fracture, and degree of secondary alteration (Table 3-1). The HGUs of similar character were then grouped into larger HSUs to facilitate mapping and 3-D model construction. A critical component of this step was the careful integration of PM-OV stratigraphy. The integration of stratigraphic concepts is important to ensure that individual HGUs grouped within HSUs and that the HSUs themselves properly correlate within the model.

Hydrostratigraphic units can be thought of as groupings of contiguous stratigraphic units that have a particular hydrogeologic character, such as an aquifer or confining unit. For the PM-OV model, most HSUs consist of a single HGU (e.g., the Windy Wash aquifer [WWA] essentially is 100 percent LFA, and the Paintbrush vitric-tuff aquifer [PVTA] is 100 percent VTA). There are 17 exceptions (the YVCM, TCVA, DVCM, DVA, FCCM, FCA, TMCM, THCM, TMA, PCM, YMCFCM, CHVCM, CHZCM, CHCU, CFCM, BRA, and PBRM; see Section 5.0 for definitions) that may

**Table 3-2**  
**Hydrostratigraphic Units of the PM-OV Model Area Included in the UGTA Project Regional HFM**  
 (Page 1 of 2)

Model HSU Number <sup>a</sup>	Hydrostratigraphic Unit (Symbol)	Dominant Hydrogeologic Unit(s) <sup>b</sup>	Stratigraphic Unit Map Symbols <sup>c</sup>	General Description
20	Alluvial Aquifer (AA) (this term is also used to designate a hydrogeologic unit)	AA	Qay, QTc, Qs, Qam, QTa, QTu, Qb, Tgy, Tgc, Tgm, Tgyx, Tt	Consists mainly of alluvium that fills extensional basins such as Crater Flat. Also includes generally older Tertiary gravels, tuffaceous sediments, and nonwelded tuffs (where thin) that partially fill other basins such as Oasis Valley and the moat of the Timber Mountain caldera complex.
19	Timber Mountain Aquifer (TMA)	Mostly WTA, minor VTA; TCU within the Timber Mountain caldera complex	Tt, Tf, Tm	"The uppermost welded tuffs" in the PM-OV model area. Consists mainly of extra-caldera welded ash-flow tuffs (aquifer-like lithologies). However, the altered intra-caldera equivalent rocks within the Timber Mountain caldera are modeled as confining units.
18	Tuff Cone (TC)	LFA, TCU	Tp, Th (formerly Ta), Tc	Complex 3-D distribution of rhyolite lava and zeolitic nonwelded tuff of the Paintbrush Group (Tp), Calico Hills Formation (Th), or Crater Flat Group (Tc). Present in the northern portion of the PM-OV model area beneath most of eastern and central Area 20.
17	Bullfrog Confining Unit (BFCU)	TCU	Tcb	Major confining unit differentiated within the NTS caldera complex area. Unit consists of thick intra-caldera, zeolitic, mostly nonwelded tuff of the Bullfrog Formation.
16	Belted Range Aquifer (BRA)	LFA and WTA, with lesser TCU	Tub, Tcbs, Tr	Consists of welded ash-flow tuff and lava of the Belted Range Group (Tb) above the Grouse Canyon tuff (Tbg), but may also include the lava-flow lithofacies of the commendite of Split Ridge (Tbgs) and the commendite of Quartet Dome (Tbq) where present. Differentiated within the NTS caldera complex area.
15	Basal Confining Unit (BCU)	TCU	Tn, Tub, To, Tr, Tq	Mostly zeolitized nonwelded tuffs differentiated in the NTS caldera complex area.
14	Basal Aquifer (BAQ)	WTA	To, Tlt, Tqm	Mostly aquifer-like older volcanic rocks. Differentiated within the NTS caldera complex area.
11	Volcanics Undifferentiated (VU)	WTA, TCU, lesser LFA	Potentially includes all Tertiary volcanic units	All Quaternary and Tertiary volcanic units outside the NTS proper and the proximal NTS caldera complex.

**Table 3-2**  
**Hydrostratigraphic Units of the PM-OV Model Area Included in the UGTA Project Regional HFM**  
 (Page 2 of 2)

Model HSU Number <sup>a</sup>	Hydrostratigraphic Unit (Symbol)	Dominant Hydrogeologic Unit(s) <sup>b</sup>	Stratigraphic Unit Map Symbols <sup>c</sup>	General Description
8	Upper Clastic Confining Unit (UCCU)	CCU	MDC, MDe	Late Devonian through Mississippian siliciclastic rocks. Present in the eastern third of the PM-OV model area.
7	Lower Carbonate Aquifer (LCA)	CA	Dg through Cc	Cambrian through Devonian mostly limestone and dolomite. Widespread throughout the PM-OV model area.
6	Lower Clastic Confining Unit (LCCU)	CCU	Cc, Cz, Czw, Zs, Zj	Late Proterozoic through Early Cambrian siliciclastic rocks. Widespread throughout the PM-OV model area.
5	Lower Carbonate Aquifer - Thrust Plate (LCA3)	CA	Dg through Cc	Cambrian through Devonian, mostly limestone and dolomite, rocks that occur in the hanging wall of the Belted Range thrust fault.
4	Lower Clastic Confining Unit - Thrust Plate (LCCU1)	CCU	Cc, Cz, Czw, Zs	Late Proterozoic to Early Cambrian siliciclastic rocks that occur within the hanging wall of the Belted Range thrust fault.
1	Intrusive Confining Unit (ICU)	I	Ti, Kg	Consists of granitic rocks that comprise the Gold Meadows stock along the northeastern margin of the PM-OV model area and intrusives greater than 2 km in size elsewhere in the UGTA regional HFM.

Source: Modified from SNJV (2004b)

<sup>a</sup> UGTA regional model (IT, 1996c; DOE/NV, 1997b)

<sup>b</sup> See [Table 3-1](#) for definitions of HGUs.

<sup>c</sup> Refer to Slate et al. (1999) and Ferguson et al. (1994) for definitions of stratigraphic unit map symbols.



consist of several HGUs, but are defined so that a single general type of HGU dominates (e.g., mostly WTA). These dominant HGUs are noted in the third column of [Table 3-2](#).

Brief descriptions of the HSUs in the PM-OV HFM are provided in [Table 3-2](#). They are generally listed in descending order from the top of the model to the bottom, though some are laterally rather than vertically contiguous, and not all units are present in all parts of the model area. A more detailed description of each HGU can be found in BN (2002a).

A generalized surface geologic map of the NTS area is presented in [Figure 3-1](#). The distribution of HSUs at the surface within the PM-OV HFM area is shown in a block model view in [Figure 3-2](#). The distribution of HSUs at the water table is presented in [Figure 3-3](#).

A southwest-to-northeast hydrostratigraphic profile along the general direction of groundwater flow is provided in Profile A-A' ([Figure 3-4](#)); the west-east hydrostratigraphic Profile B-B' ([Figure 3-5](#)) through central Pahute Mesa is normal to basin structure. Profile C-C' ([Figure 3-6](#)) is a west-east section through the Timber Mountain caldera complex. The profiles illustrate the relationships of the HSUs and structures in various vertical planes. The locations of these profile lines are shown on [Figure 3-3](#). These model profiles are from the PM-OV 3-D framework documentation package (BN, 2002a), where additional model profiles and detailed information regarding this PM CAU model can be found.

The alternative SCCC model is based on the same HGUs as the base HFM. Differences between these two models are a result of the structural model used and the categorizing of HGUs into HSUs. The alternative structural model of the SCCC is simpler than the base HFM, as is the hydrostratigraphy. The SCCC HFM includes an elliptical ring-fracture fault system elongated to the north-northeast. Major structural differences with the base HFM include the margins of this caldera complex, locations of caldera-forming faults, and the number and depth of the faults considered. The SCCC HFM includes the single caldera ring-fracture system and only 11 of the basin-and-range faults mapped at the surface. Another key difference is that the faults in the SCCC HFM end at shallower depths than in the base HFM.

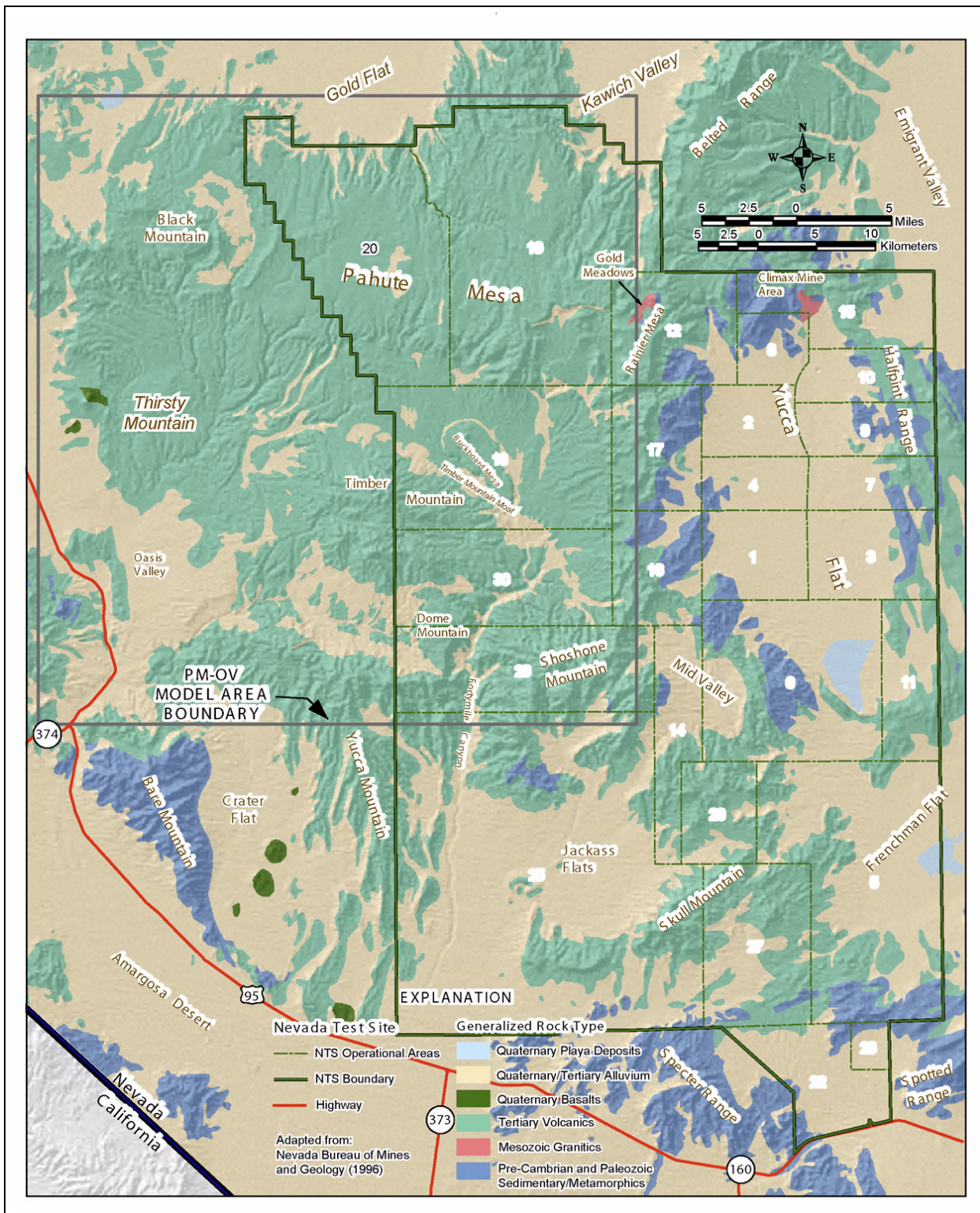


**Figure 3-1**  
**Generalized Surface Geologic Map of the NTS Area**  
 Source: BN, 2002a

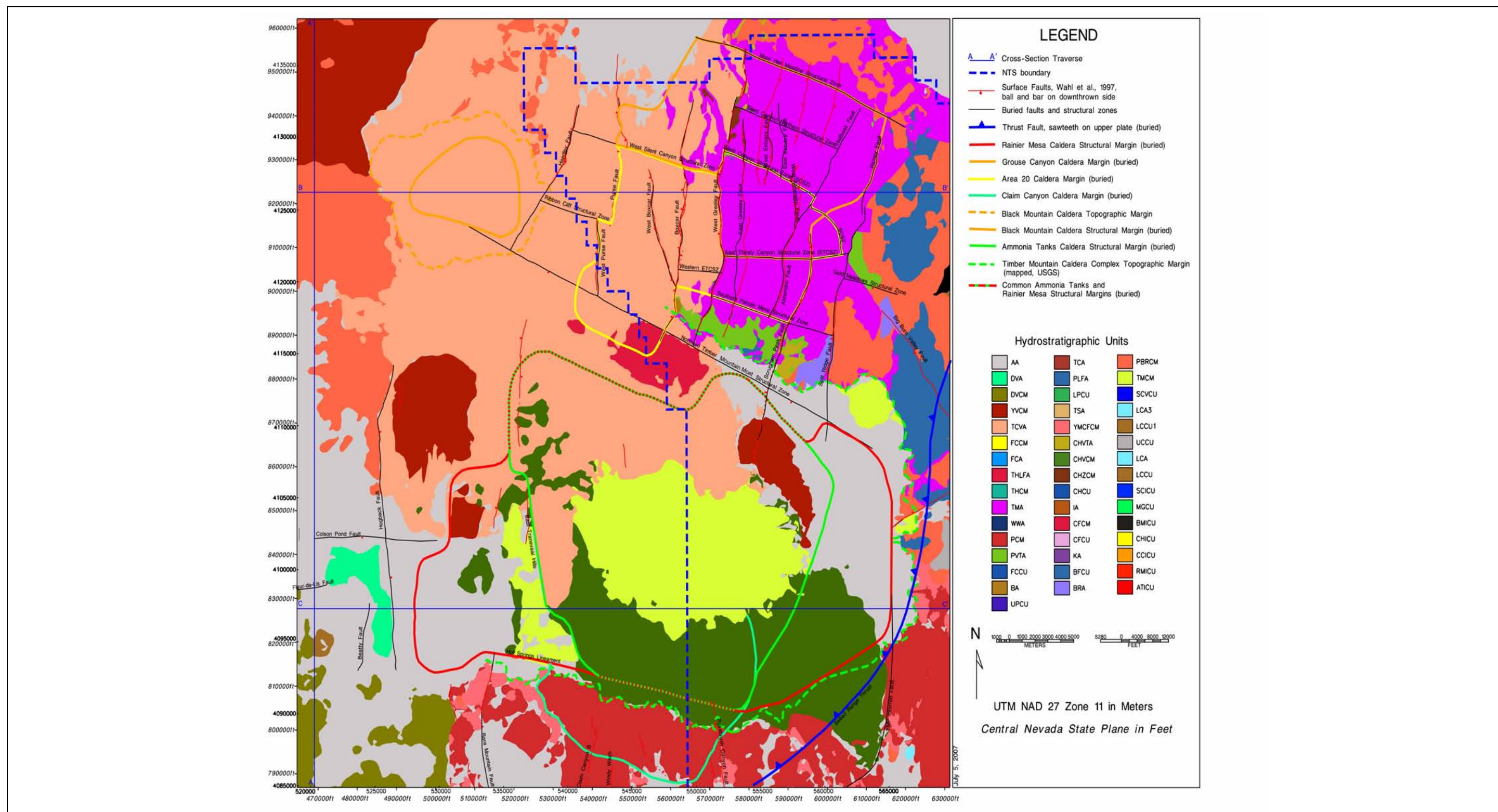


**Figure 3-2**  
**Hydrostratigraphic Unit Surface Map for the PM-OV Model Area**  
Source: BN, 2002a

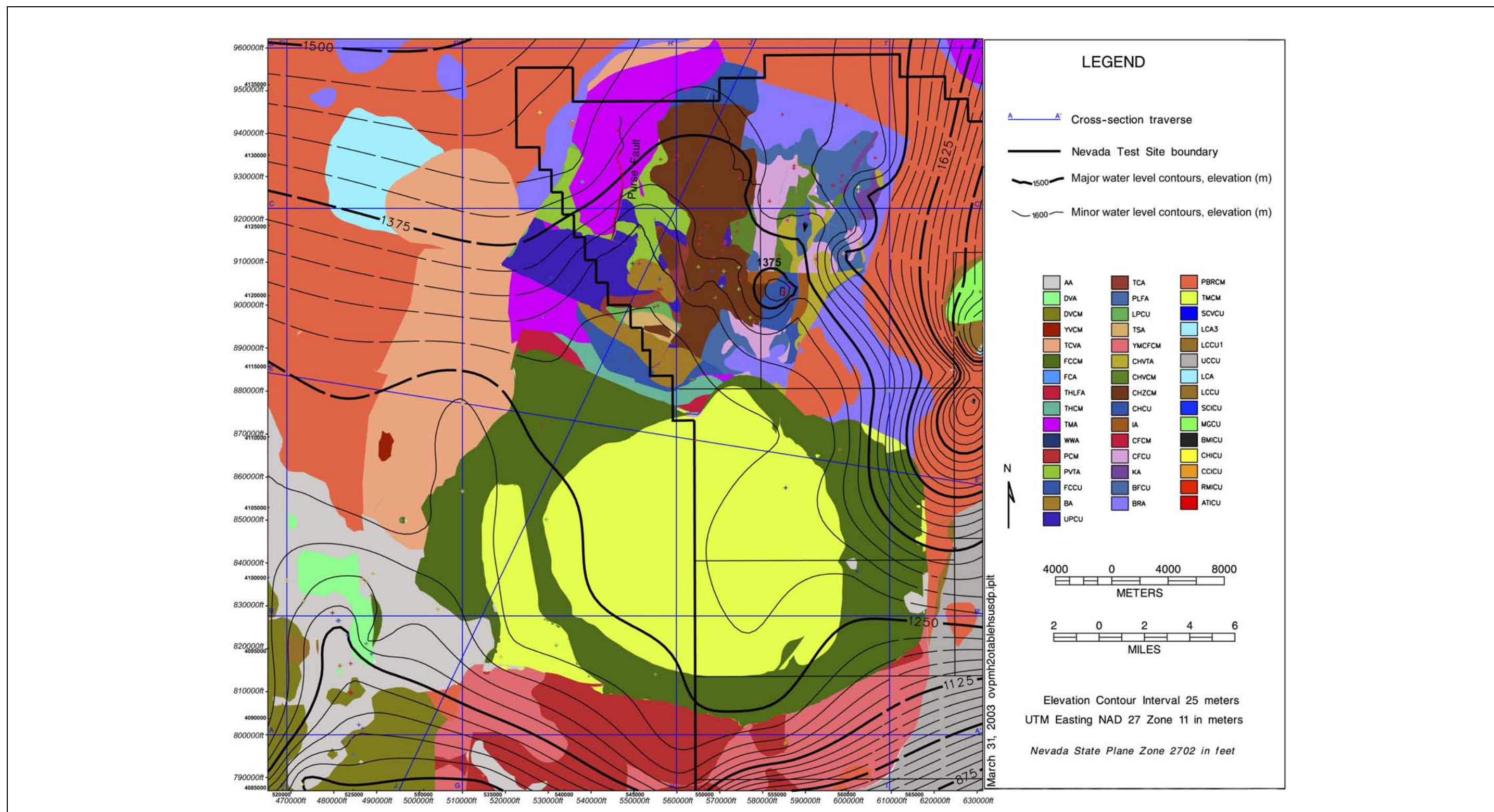


**Figure 3-3**  
Map Showing HSUs at the Water Table within the PM-OV Model Area

Source: BN, 2002a



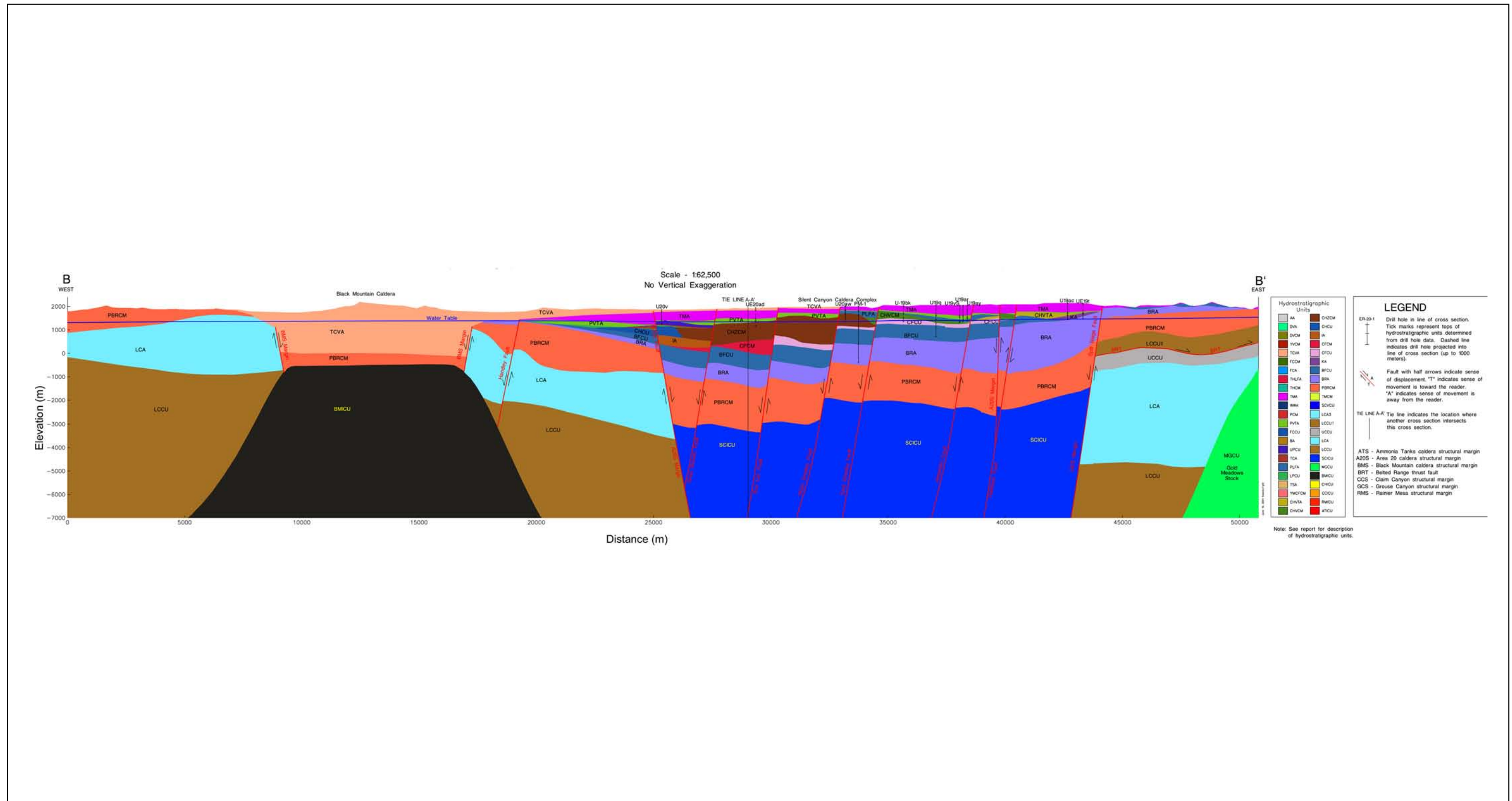


**Figure 3-5**  
**West-to-East Hydrostratigraphic Cross Section B-B' through the Black Mountain Caldera and the SCCC**  
Source: BN, 2002a

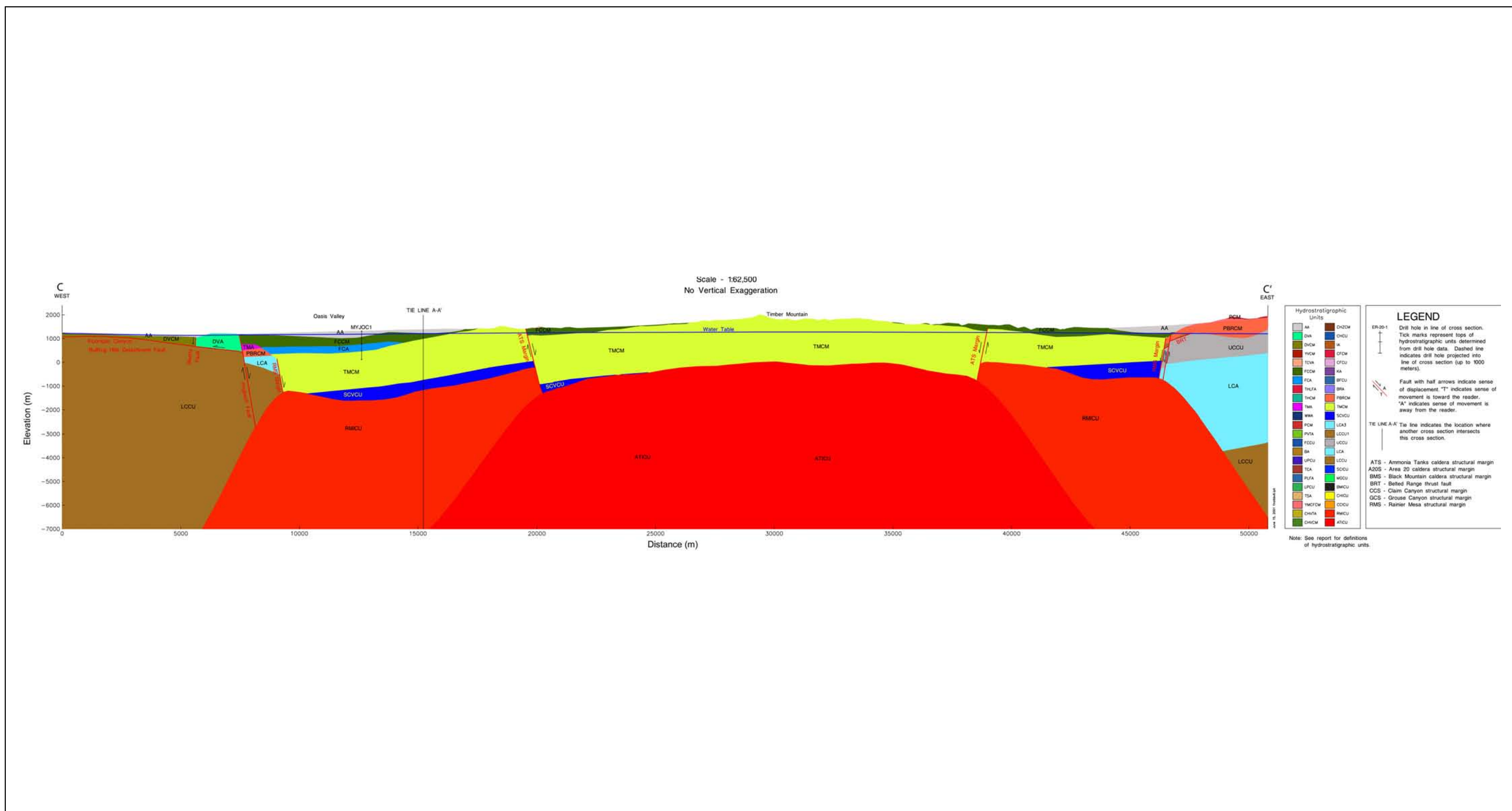


**Figure 3-6**  
**West-to-East Hydrostratigraphic Cross Section C-C' through the Southern Portion of the Timber Mountain Caldera Complex at Myjo Coffer #1**

Source: BN, 2002a

Hydrostratigraphic differences between the two HFMs of the Pahute Mesa area are the number of HSUs, their definition, and their distribution. In the base HFM, the Pahute Mesa area includes 25 HSUs; only 12 are included in the SCCC alternative model. Six post-Paintbrush HSUs are lumped together in the SCCC alternative model. Significant differences also exist in the configuration of the HSU surfaces. The surfaces of the HSUs are less rugged in the SCCC HFM than in the base HFM. The upper surfaces of HSUs in the SCCC HFM are generally bowl-shaped and dip more gently than those in the base HFM. Upper surfaces of HSUs in the SCCC HFM are also higher along the down-thrown sides of faults and lower along the up-thrown sides. The differences in the locations of caldera margins and in structure result in differences in HSU thicknesses. Generally, the thicknesses of HSUs located within the Pahute Mesa area vary to a greater degree in the base HFM. In comparison, in the SCCC HFM, the HSUs are generally lens-shaped. These lenses are thick in the middle and thin out towards the margins of the SCCC. The hydrogeologic importance of the Calico Hills Formation in the SCCC area is recognized in both the base and SCCC HFMs. It is, however, handled differently in the two models. In the base HFM, the Calico Hills Formation is subdivided into four HSUs based on differences in lithologic composition and alteration effects, whereas it is treated as a single composite unit in the SCCC HFM.

### **3.2.3 Pahute Mesa HFMs**

Bechtel Nevada (2002a) presents a best estimate, or what is hereafter referred to as the “base” HFM, of Pahute Mesa and the surrounding area, as well as several base-derived alternative interpretations. Bechtel Nevada also developed the SCCC alternative framework, the only alternative HFM that was fully developed for flow model analysis and calibration in SNJV (2006a). A selected set of the alternative models were applied in transport analysis based on their ability to reproduce measured hydraulic data and aqueous geochemical mixing at wells (Section 3.2.6). This section presents a synopsis of the stratigraphic and hydraulic development of the base HFM and base-derived alternatives, and of the SCCC HFM.

The following provides a brief description of the regional and historical context within which the Pahute Mesa HFMs were developed.

The initial Pahute Mesa CAU HFM was constructed based on the conceptual model of the UGTA hydrologic system described by Winograd and Thordarson (1975). Further developments made by



Laczniak et al. (1996), IT Corporation (IT) (1996a, b, and c), and Drellack and Prothro (1997) were also used to develop the Pahute Mesa CAU base HFM. A revised structural block model for the SWNVF (Warren et al., 2003) and an alternative 3-D model of the SCCC (McKee et al., 1999 and 2001) were incorporated into the information used for development of the base HFM. The hydrologic and geologic information developed for the USGS Death Valley region groundwater flow model (DVRFM) was also included (D'Agnese et al., 1997; Faunt, 1997). Finally, information from the YMP hydrogeologic and flow model was incorporated in assessment of the southern part of the Pahute Mesa CAU.

### **3.2.3.1 Structural Features**

Hydrostratigraphic framework models are differentiated by their defined configuration of HSUs, which are themselves groupings of contiguous stratigraphic units that have a particular hydrogeologic character and upon which material properties are assigned. The BN (2002a) base HFM as characterized by HSU is shown in 3-D perspective in [Figure 3-7](#), and [Figure 3-3](#) shows a planar slice of HSUs at their intersection with the water table, as interpolated from measured heads at observation wells (close in elevation to where the majority of transport occurs). The base HFM includes a total of 47 structural elements that represent either faults or calderas. Only faults with significant displacement (greater than 60 m) were included in the HFM model. Six calderas were identified in the PM model area, two of which are buried. Of particular interest was the SCCC, an investigation of which led to development of an alternative conceptualization and associated HFM. In the base HFM, the SCCC includes two calderas: the Grouse Canyon and Area 20 calderas. The base HFM for the SCCC area also includes 20 faults and structural zones in addition to the caldera-forming faults. Thirteen of these 20 structural features are basin-and-range type faults mapped at the surface.

Fault and caldera margin structural features as they are represented in the base case numerical model are shown in [Figure 3-8](#). Individual structural features are numbered in the figure, and the feature that corresponds to that number is listed in [Table 3-3](#).

Multiple alternative HFMs were considered for their potential structural impact, via variation in HSU structure, on groundwater flow and contaminant transport. A selected subset was developed into numerical models. [Table 3-4](#) summarizes this group.

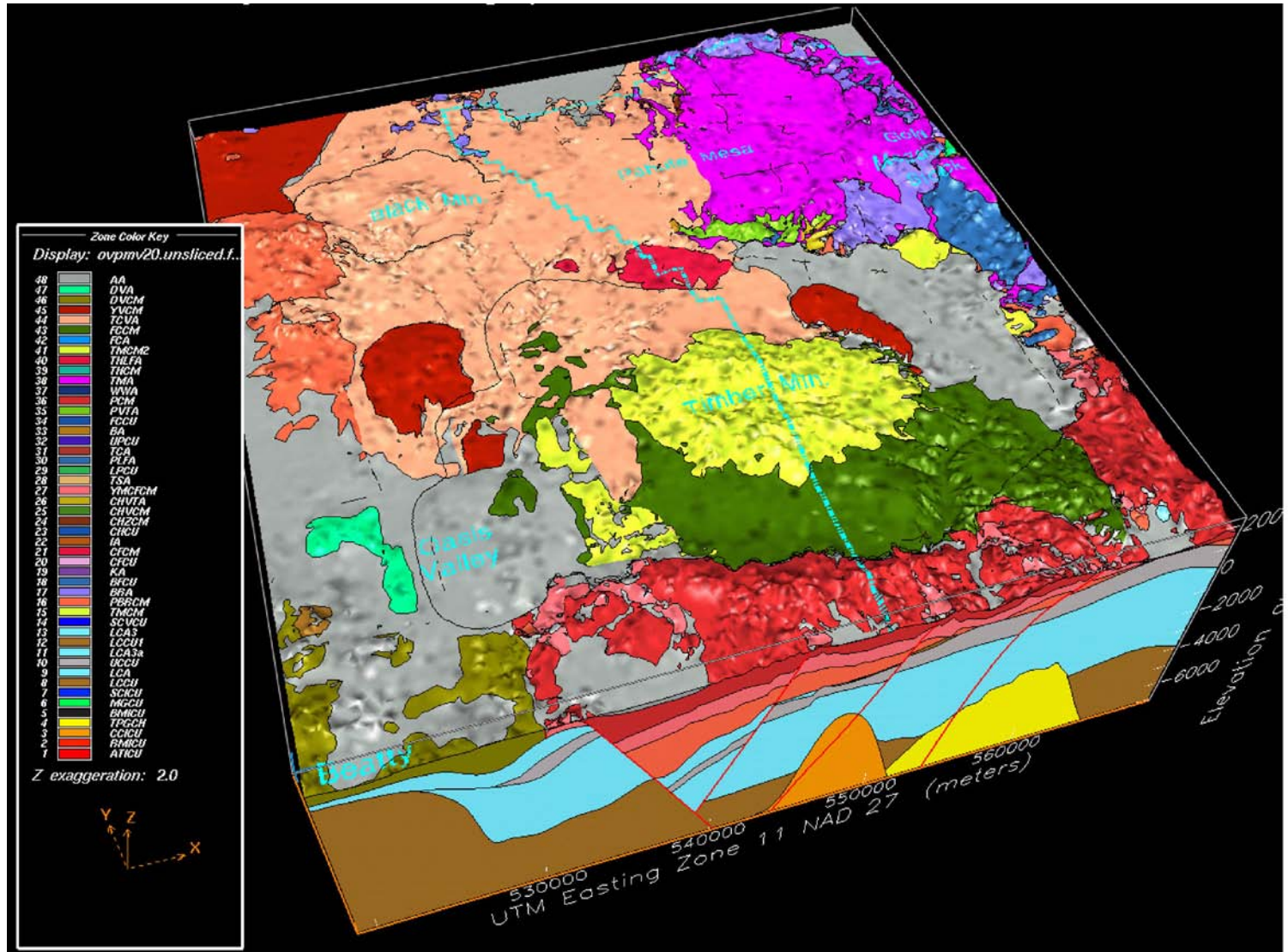


**Figure 3-7**  
**Pahute Mesa Base HFM Described by HSU**  
 Source: BN, 2002a

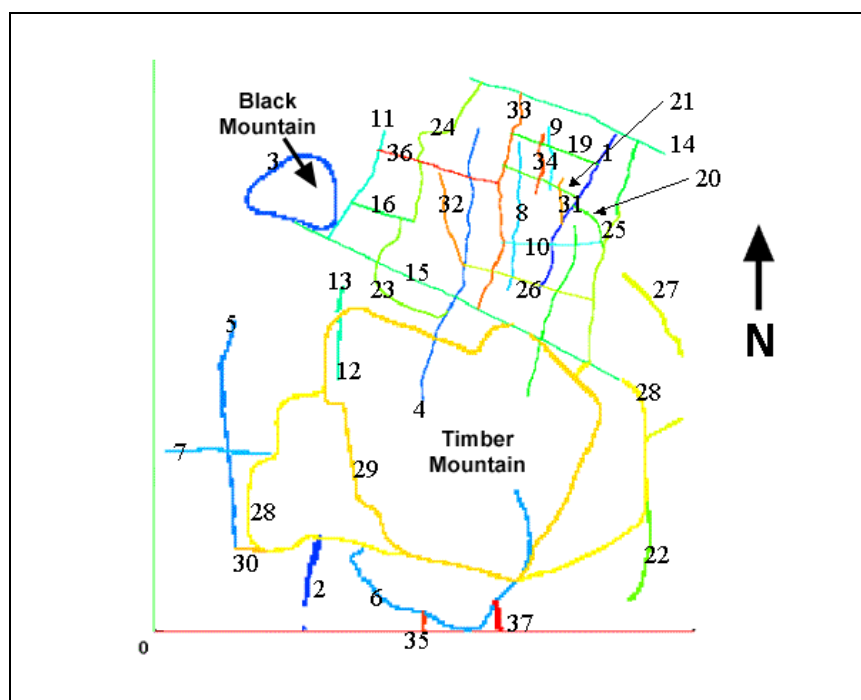


**Figure 3-8**  
**Fault Numbering Key - Base HFM**

Source: SNJV, 2006a

**Table 3-3**  
**Base HFM Fault Indices and Names**  
(Page 1 of 2)

Fault ID	Name
01	Almendo
02	Bare Mountain
03	Black Mountain Caldera Structural Margin
04	Boxcar
05	Hogback
06	Claim Canyon Caldera Structural Margin
07	Colson Pond
08	East Greeley
09	East Estuary
10	East Thirsty Canyon Structural Zone
11	Handley
12	Handley South
13	Handley North
14	Moor Hen Meadow Structural Zone
15	North Timber Mountain Moat Structural Zone
16	Ribbon Cliff Structural Zone
17	Richey

**Table 3-3**  
**Base HFM Fault Indices and Names**  
 (Page 2 of 2)

Fault ID	Name
18	Scrugham Peak
19	Silent Canyon Northern Structural Zone
20	Silent Canyon Structural Zone East
21	Silent Canyon Structural Zone West
22	YMP inferred/CP Thrust
23	Silent Canyon/West Purse
24	Purse North
25	Split Ridge
26	Southern Pahute Mesa Structural Zone
27	Gold Meadows Structural Zone/Big Burn Valley
28	Rainier Mesa Caldera Structural Margin
29	Ammonia Tanks Caldera Structural Margin
30	Hot Springs Lineament extension of Rainier Mesa Caldera Structural Margin
31	West Almendro
32	West Boxcar
33	West Greeley
34	West Estuary
35	Windy Wash/Claim Canyon 1
36	West Silent Canyon Structural Zone
37	Paintbrush Canyon
38	Fault 23 south of North Timber Mountain Moat Structural Zone
39	Fault 16 between faults 23 and 24
40	Extension of Purse Fault to northern edge of model
41	Purse Fault repair where fault 36 crosses

Source: SNJV, 2006a

The single alternative HFM developed with a mesh structure different from the BN (2002a) base model was the SCCC alternative HFM. Its structural model is more simplified than the base HFM. [Figure 3-9](#) shows a comparison of structural features and caldera margins for the base HFM model and the SCCC alternative. This structural model is based on previous models of calderas of the Pahute Mesa region developed by Noble et al. (1968) and Orkild et al. (1969), and also on analogies with other calderas of the world. The SCCC HFM includes an elliptical ring-fracture fault system elongated to the north-northeast ([Figure 3-9](#)). Major structural differences with the base HFM include the margins of this caldera complex, locations of caldera-forming faults, and the number and depth of the faults considered. The number of faults is less than in the base model. The SCCC HFM includes the single caldera ring-fracture system, and only 11 of the basin-and-range faults mapped at

**Table 3-4**  
**Summary of Alternative HFMs Considered in the PM Flow Model**

<b>Alternative HFM</b>	<b>Key Difference(s) Compared to Base HFM</b>	<b>Potential Impacts on Flow Model</b>
Silent Canyon Caldera Complex (SCCC)	The SCCC alternative is stratigraphically and structurally less complex than the base HFM in the vicinity of the Silent Canyon caldera. The SCCC has a reduced number of HSUs, faults, and structural zones. In addition, the eastern and western margins of the SCCC area are different.	Simplifications may impact flow directions and magnitudes in this area of the flow model. Comparisons between flow model results for this HFM and the base HFM will support an evaluation of the impact of faults on groundwater flow.
Basement Ridge Model (RIDGE)	The RIDGE alternative focuses on the bench area between the Timber Mountain caldera and SCCC. For this alternative, the southward distribution of important aquifer units (Benham aquifer [BA], Tiva Canyon aquifer [TCA], Topopah Spring aquifer [TSA], and Crater Flat composite unit [CFCM]) pinch out or truncate against older, less conductive units that, for this HFM, are assumed to form the gravity-high ridge.	Alternate HSU geometries may impact flow through the bench area between the Timber Mountain caldera and SCCC.
Thirsty Canyon Lineament (TCL)	The TCL alternative treats the north-northeast trending linear feature extending from just west of well ER-EC-8 northeastward beneath western Pahute Mesa east of the Black Mountain caldera to the southern edge of Gold Flat as a continuous structural feature. The base HFM treats this feature as a continuous zone of en echelon faults 2 to 3 km wide.	Treating the TCL as a continuous feature (interpreted in this HFM as a normal fault, down to the east) will help explore whether this feature on the west side of the ridge between the Timber Mountain caldera and SCCC acts as a potential hydraulic connection or barrier to groundwater flow.
Raised Pre-Tertiary Surface (PZUP)	The PZUP alternative raises the pre-Tertiary basement surface to its highest geologically permissible elevation (or least possible depth) and raises the basement inside the calderas. Paleozoic rock tops were raised over the entire domain. Under parts of Area 19 and 20, the Silent Canyon intrusive confining unit (SCICU) was raised 750 m.	This alternative examines the impact on groundwater flow from the reduction of the thickness of the transmissive units that results from maximizing the elevation of the basement.
Contiguous Imbricate Thrust Sheet (SEPZ)	The SEPZ alternative models the isolated surface exposure of Paleozoic carbonate rocks that are mapped in the southeast corner of the model area, east of the Belted Range thrust fault, as part of a more extensive imbricate fault. The base HFM considers this outcrop as a small erosional remnant of the hanging wall of an imbricate fault.	This alternative tests the impact of the Paleozoic carbonate rock on the direction of groundwater flow around the east side of Timber Mountain.
Deeply Rooted Belted Range Thrust Fault (DRT)	The DRT alternative considers the Belted Range thrust fault to be more deeply rooted than the base HFM, resulting in a very thick thrust sheet over most of the model area.	This alternative results in the LCA not being a continuous, coherent sheet across the model area. The uppermost pre-Tertiary rock immediately downgradient of Pahute Mesa is the nonconductive LCCC1 rather than the conductive LCA.

Source: SNJV, 2006a

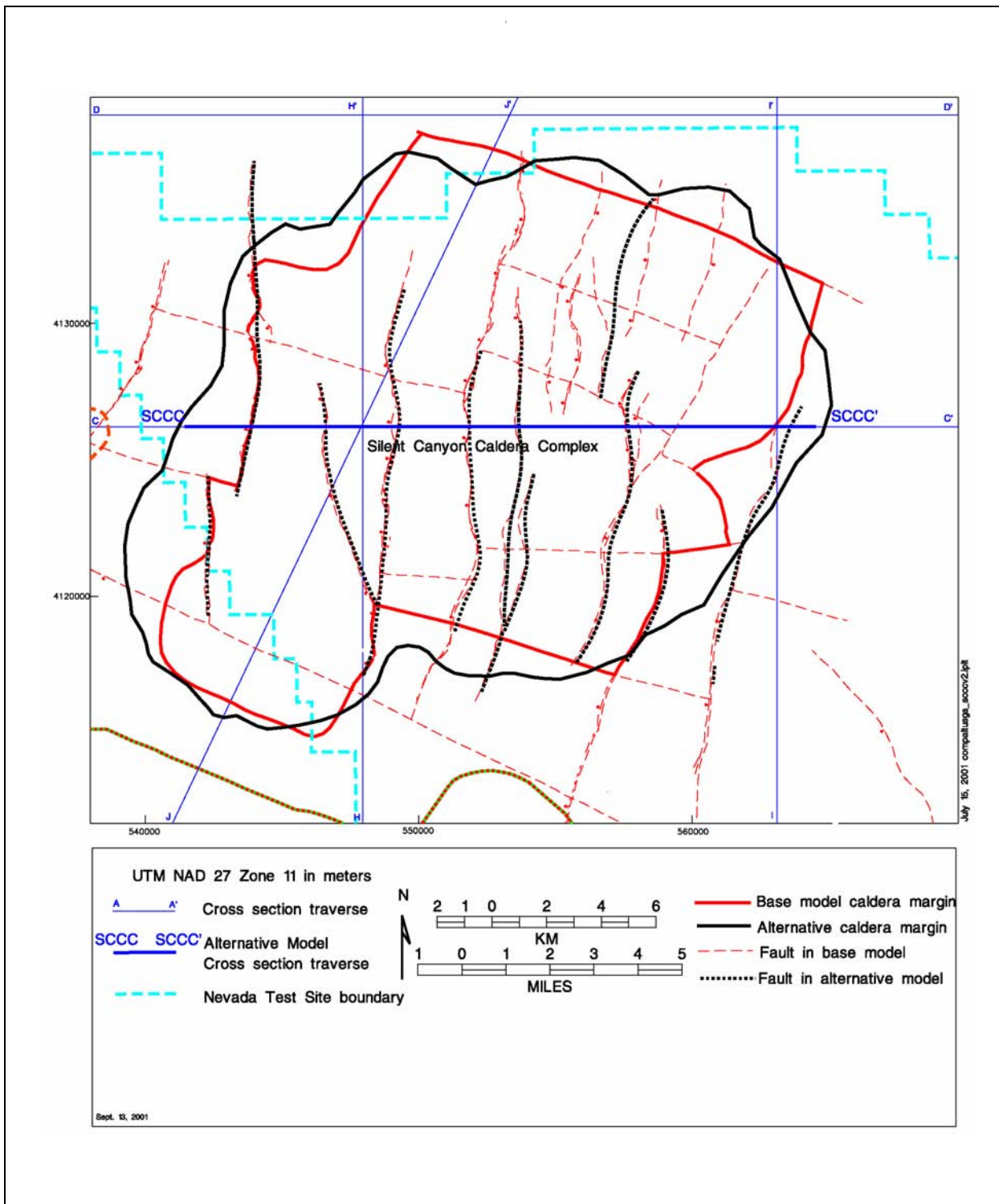


**Figure 3-9**  
**Comparison of Silent Canyon Caldera Margins in the Base-HFM Model**  
**and SCCC Alternative Model**

Source: SNJV, 2006a

the surface. Another difference is that the faults in the SCCC HFM end at considerably shallower depths relative to those for the base HFM.

### **3.2.3.2 Stratigraphy**

The base Pahute Mesa HFM includes considerable structural detail and stratigraphic enhancement over the UGTA regional HFM (IT, 1996d). The total number of HSUs increased from 20 to 46, with most of the increase affecting the Tertiary volcanic section. The six Tertiary volcanic HSUs in the Pahute Mesa and Timber Mountain caldera complex and the single undifferentiated volcanics unit outside the caldera complex (of the UGTA regional HFM) were subdivided into 40 HSUs for the PM CAU model. Except for geometry details, the five pre-Tertiary HSUs remain as initially defined in the UGTA regional groundwater model. Spatial depictions of HSUs in the base HFM are shown in [Figures 3-3 and 3-7](#).

The SCCC alternative HFM differs hydrostratigraphically from the base in the number of HSUs, their definition, and their distribution (BN, 2002a). Principally, whereas in the base HFM the Silent Canyon caldera area includes 25 HSUs, in the SCCC alternative it includes only 12. [Table 3-5](#) compares HSU definitions between the two HFMs. The differences in the locations of caldera margins and in structure result in differences in HSU thicknesses. Generally, the thicknesses of HSUs located within the SCCC area vary to a greater degree in the base HFM. That is, in the SCCC HFM the HSUs are generally lens-shaped, thick in the middle, and thin out towards the margins of the SCCC (BN, 2002a). Other differences, as they are related to flow and transport behavior, are identified and discussed throughout the document as they become relevant.

### **3.2.4 Boundary Conditions**

Solution of the groundwater flow equations requires specification of head and/or flow at the edges and at internal discharge points (e.g., springs in Oasis Valley) of the numerical model. This was particularly important for the PM CAU model because the model boundaries do not coincide with natural hydrologic boundaries. The PM CAU model accounts for regional inflow and outflow across all four lateral edges, internal flow from precipitation recharge, and internal discharge at Oasis Valley. The following sections summarize the implementation of these conditions.

**Table 3-5**  
**Correlation of HSUs between the SCCC HFM and the Base HFM**

UGTA Base Model HSUs	Alternative SCCC Model HSUs
Thirsty Canyon Volcanic Aquifer	Silent Canyon Timber Mountain Composite Unit
Tannenbaum Hill Lava-Flow Aquifer	
Tannenbaum Hill Composite Unit	
Timber Mountain Aquifer	
Fluorspar Canyon Confining Unit	
Windy Wash Aquifer	
Paintbrush Vitric-Tuff Aquifer	
Benham Aquifer	Silent Canyon Benham Aquifer
Upper Paintbrush Confining Unit	
Tiva Canyon Aquifer	Silent Canyon Tiva Canyon Aquifer
Paintbrush Lava-Flow Aquifer	Silent Canyon Lower Paintbrush Confining Unit
Lower Paintbrush Confining Unit	
Topopah Spring Aquifer	Silent Canyon Topopah Spring Aquifer
Calico Hills Vitric-Tuff Aquifer	Silent Canyon Calico Hills Composite Unit
Calico Hills Vitric Composite Unit	
Calico Hills Zeolitic Composite Unit	
Calico Hills Confining Unit	
Inlet Aquifer	Silent Canyon Inlet Aquifer
Crater Flat Composite Unit	Silent Canyon Crater Flat Composite Unit
Crater Flat Confining Unit	
Kearsarge Aquifer	
Bullfrog Confining Unit	Silent Canyon Bullfrog Confining Unit
Belted Range Aquifer	Silent Canyon Belted Range Aquifer
Pre-Belted Range Composite Unit	Silent Canyon Pre-Belted Range Composite Unit
Silent Canyon Intrusive Confining Unit	Silent Canyon Intrusive Confining Unit

Source: SNJV, 2006a

Note: The HSU names used in the alternative model were modified by adding the prefix "Silent Canyon" for differentiation purposes.

The UGTA regional flow model is used to define the lateral boundaries of the CAU-scale groundwater domain. Subsequent to completion of the final PM CAU flow model, the DVRFM was completed (Belcher et al., 2004). However, it is the policy of the UGTA Project not to change the model at the late stages of development. Because the DVRFM is used to define the boundary conditions of the other CAU-scale models, future work with the PM CAU model will include adjustment of the boundary fluxes to maintain consistency among the CAU-scale models.



### 3.2.4.1 Alternative Recharge Models

Three approaches were used to develop alternative recharge models for the NTS area (which include the PM CAU flow model area). Each of the alternatives was assumed for at least one of the calibrated alternative models selected for transport simulation; thus, a brief discussion of these models follows.

The alternative recharge models are:

- Maxey-Eakin estimation techniques
- Net infiltration-recharge distributed parameter modeling
- Chloride mass-balance modeling

The Maxey-Eakin approach (Maxey and Eakin, 1949) is an empirically derived method relating recharge to precipitation zones from a base precipitation map. Several modified versions of this approach were analyzed, including the UGTA regional groundwater flow modeling results and a revised Maxey-Eakin model using a revised base precipitation map. The recharge distribution used in the UGTA regional groundwater flow model (DOE/NV, 1997b) was constructed using a modification of the Maxey-Eakin method. This modification incorporated:

- An updated precipitation map using new and existing data
- The calculation of recharge using modified Maxey-Eakin coefficients
- The calculation of total recharge volumes for individual hydrographic areas
- The redistribution of a percentage of the total recharge within selected subareas to stream channels

Subsequent to the development of the UGTA regional flow model (DOE/NV, 1997b), a revised recharge distribution was generated for the NTS area by updating the original UGTA recharge model. The update included the redigitization and recontouring of the precipitation map, and the redigitization of the hydrographic areas using larger-scale maps. This updated recharge distribution model is designated as the Modified Maxey-Eakin (MME) recharge model.

Two alternative recharge models are derived from the USGS net infiltration/recharge model (Hevesi et al., 2003). The USGS net infiltration/recharge model is a distributed parameter watershed model used to estimate the temporal and spatial distribution of net infiltration for the Death Valley region. The major components of this model include infiltration of rain, snowmelt, or surface water

into the soil or bedrock with subsequent bare-soil evaporation and transpiration from the root zone. All water percolating past the root zone is considered net infiltration. The two alternative USGS recharge models are the recharge model that assumes a runoff/run-on component (USGSD) and the recharge model that does not include the runoff/run-on component (USGSND).

Two alternative recharge models were also developed by DRI for the NTS area using an elevation-dependent chloride mass-balance approach (Russell and Minor, 2002). The DRI chloride mass-balance approach estimates recharge by analyzing the chloride ratios of precipitation and groundwater. Higher chloride concentrations in groundwater discharged from springs result from ET of precipitation that contains low amounts of conservative atmospheric chloride ion, thus providing a relative gauge of recharge. This information, in conjunction with soil chloride profiles in differing recharge locales (wash versus non-wash), allowed DRI to estimate recharge with associated confidence intervals. The alternative recharge models included one model for no recharge in the alluvial areas (DRI alluvial mask alternative [DRIA]), and one model for no recharge in the alluvial areas and no recharge below an elevation of 1,237 m (DRI alluvial and elevation mask alternative [DRIAE]). The data for each model were compiled in a geographic information system and used in a Monte Carlo analysis to determine recharge in the study area. Results of the analysis yielded estimates of the mean and SD of recharge.

In a final comparison of the alternative models, the MME recharge model was chosen as the base recharge model for use in PM CAU flow modeling because, in general, the method yields recharge volumes that are within the ranges of the other models. The other alternative recharge models were incorporated into the PM CAU flow model to evaluate uncertainty associated with recharge. They do in fact contribute to flow scenarios that are found suitable for transport simulation.

#### **3.2.4.2 Discharge**

The only internal discharge sources represented in the PM CAU model are the Oasis Valley springs and ET outflow. Discharge from pumping wells is not included in the model. Spring and ET discharge are represented in a similar manner with FEHM as with the regional model with “drain” boundary conditions. In this condition, a head is set at the elevation of the point of discharge. If the model head at the node is above the specified elevation outflow representing spring or ET, spring discharge or ET loss flows occur. If head is below the set head, no flow of any kind occurs. This is

different than a constant-head boundary condition, which will allow inflow or outflow; the boundary condition used to represent Oasis Valley only allows outflow. Nodes at the top of the model within the areas where Lacznia et al. (2001) mapped ET were identified and drains assigned. In the case of springs, head was assigned at the estimated spring elevation. To represent ET, head equal to land surface elevation less 3 m was used to represent the maximum root depth from which plants could draw water (the effects of extinction depth are examined in Section 6.2.4.1 of SNJV [2006a]). The water table in Oasis Valley is known to vary seasonally from ET (Reiner et al., 2002); thus, the depth of the water table given above is a first approximation of the rooting depth, which ranges from 0 to 6 m. The UGTA regional model (DOE/NV, 1997b) and USGS DVRFM (Faunt et al., 2004) both used values of 10 m.

#### **3.2.4.3 Boundary Heads**

Boundary heads from the UGTA regional model analysis described in SNJV (2004b) were interpolated onto the edge nodes of the FEHM input to the PM CAU model. These heads represent a mass conservative calibrated solution to the groundwater flow equation from the UGTA regional model. During calibration these heads were reviewed and, in spots, revised based on further examination of measured heads and heads determined from the regional model. A description of the revisions is presented in Section 5.3 of SNJV (2006a). So that the reader may conceptualize the general flow behavior over the domain, the calibrated boundary heads for the base HFM, juxtaposed with the head difference as defined initially from the UGTA regional model, are shown in [Figure 3-10](#).

#### **3.2.4.4 Lateral-Boundary Fluxes**

Part of the PM CAU flow modeling strategy was to use the UGTA regional flow model (DOE/NV, 1997b) as a mass conservative integrating model that allows evaluation of water-balance uncertainty around the edges of the PM CAU model. In this analysis, the flows are not directly specified on all edges (to do so creates a numerically unstable problem, see Anderson and Woessner [1992]); head is specified and FEHM computes and reports the flows, which are used as calibration targets. A set of boundary fluxes used with the PM CAU flow model was developed based on results generated for eight alternate regional-scale flow models using the UGTA regional model (DOE/NV, 1997b). The eight models represent combinations of different flow system conceptual models and recharge

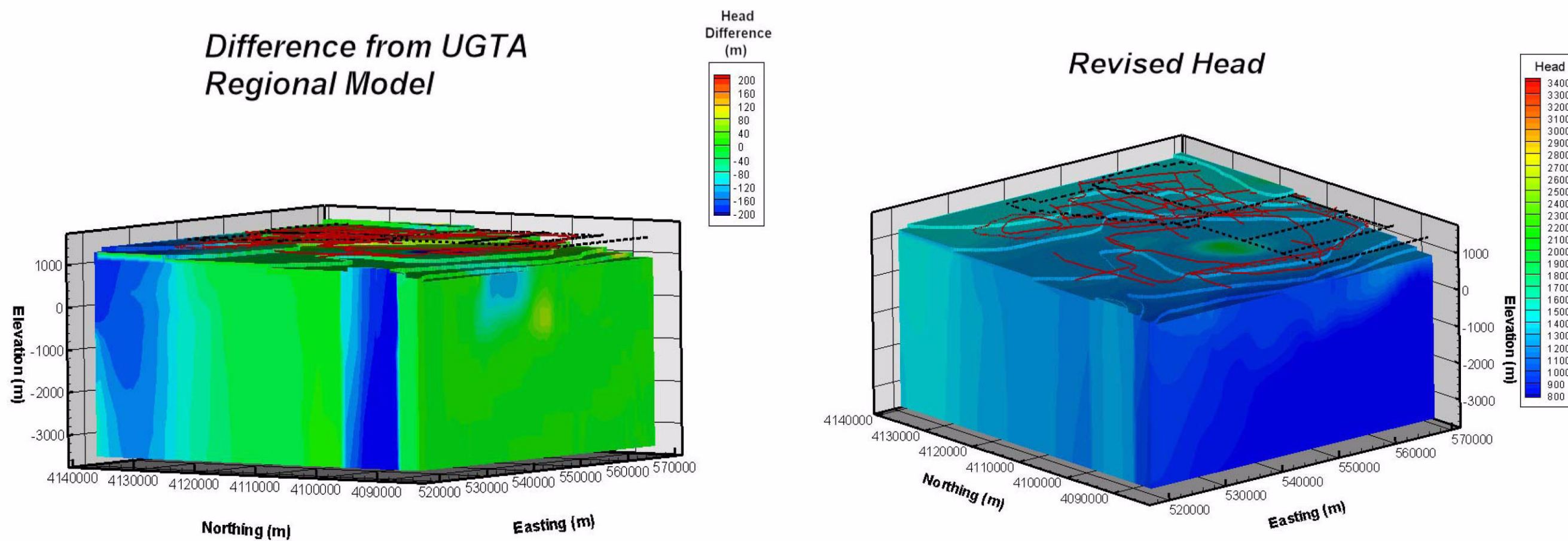


**Figure 3-10**  
 Calibrated CAU-Model Boundary Heads and Difference from UGTA Regional Model Viewed from the Northeast  
 Source: SNJV, 2006a

models. The alternate flux boundary conditions were used to help evaluate the uncertainty in the PM CAU flow model associated with the choice of a flow system conceptual model (and associated HFM) and recharge model. A more detailed discussion of the development of boundary fluxes is provided in Section 9.0 of SNJV (2004b). The approach used to calculate these fluxes does not specify the location or locations on the boundary where the flux occurs, just bounds on the total amount of flow. More specific ranges were developed for the PM CAU model using an interpolation approach and tools developed by LANL (Gable and Cherry, 2001), presented in Section 5.2 of SNJV (2006a).

### **3.2.5 Summary of Flow Model Calibration and Flow System Behavior**

The PM CAU flow model considered seven HFMs (the base case plus six alternatives) and five recharge models. In the interest of brevity, the following shorthand was defined; the first part of the name is the HFM, and the second is the water-balance condition.

Examples of the naming conventions are as follows:

- BN-MME - Bechtel Nevada (or base) HFM with the MME recharge model and boundary flows.
- BN-DRIA - Bechtel Nevada (or base) HFM with the DRI alluvial recharge model and boundary flows.
- BN-USGSD - Bechtel Nevada (or base) HFM with the USGS redistribution recharge model and boundary flows.
- BN-USGSND - Bechtel Nevada (or base) HFM with the USGS no redistribution recharge model and boundary flows.

The other HFMs (Table 3-4) are:

- SCCC - Silent Canyon Caldera Complex
- PZUP - Raised Pre-Tertiary Surface
- DRT - Deeply Rooted Belted Range Thrust Fault
- RIDGE - Basement Ridge
- TCL - Thirsty Canyon Lineament
- SEPZ - Contiguous Imbricate Thrust Sheet

The five recharge models, summarized in [Section 3.2.4.1](#), are:

- MME - Modified Maxey-Eakin
- USGSD - USGS recharge with redistribution
- USGSND - USGS recharge without redistribution
- DRIA - DRI recharge with alluvial mask
- DRIAE - DRI recharge with alluvial and elevation mask

Four other strategies were applied only to the base model to test the impact of the concepts of permeability depth decay and anisotropy:

- No depth decay, no anisotropy
- Selected HSU depth decay
- Selected HSU depth decay and anisotropy (referred to as SDA)
- All HSU depth decay and anisotropy (referred to as ADA)

Due to limitations in computational capability, in all a total of five calibration analyses with the MME recharge model were performed. These were the base HFM with consideration of each of the (four) permeability depth decay and anisotropy strategies, and the SCCC HFM. The alternative HFMs (e.g., DRT-DRIA) were incorporated and calibrated later in an assessment of PM CAU flow model conceptualization uncertainty (Section 6.2.4.1 of SNJV [2006a]).

A summary of calibration results and model behavior follows, with a focus on those features that are relevant to transport analysis.

### **3.2.5.1 Data Components of Calibration Targets**

Calibration targets consisted of the following four categories of hydraulic observations:

- Hydraulic head from wells
- Estimated spring head in and near Oasis Valley
- Oasis Valley discharge
- Edge flows estimated from regional model analysis

The hydraulic targets fall into one of two measurements: head or flow. Weights were developed for each observation from data accuracy and other qualitative considerations. Observation well heads comprised the bulk (between about 50 to 60 percent) of the calibration objective function, followed by Oasis Valley discharge (about 25 percent), estimated regional boundary flow (about 15 percent),

and finally spring heads (5 to 10 percent). Observation well data were given strong consideration because they define the direction and magnitude of the hydraulic gradient, which is directly related to the velocity field used to simulate radionuclide transport. Oasis Valley discharge was the only internal flow constraint for the model and as such had a major control on the effective permeability of the integrated flow path to the accessible environment. Oasis Valley is also the nearest access point for radionuclides to leave Pahute Mesa, thus matching its discharge ensured that the potential for such migration was properly captured in the PM CAU flow model. In addition, matching the spring data also helped to ensure that the heads in Oasis Valley were reasonably matched, and that the combination of head and flow that results is plausible. All of the calibrated models showed similar patterns of error (under/overprediction at individual discharge zones) in fitting Oasis Valley flow.

### **3.2.5.2 Head and Flow Paths**

Measured groundwater levels throughout the PM CAU flow model domain ([Figure 3-11](#), taken from Fenelon [2000]) imply southwest flow from northern Area 19 and more southerly flow from northern Area 20 across the entire model domain. The gradient is principally derived from elevation gain in the north. [Figures 3-12](#) and [3-13](#) show simulated head along geologic model cross-section planes B-B' and J-J' for the SCCC-MME-SDA and BN-MME-SDA models, respectively, along the trajectory of a particle of water released in central Area 20. A striking feature along B-B' is the sharp gradient just west of where J-J' crosses B-B', resulting from a marked head difference across the Purse fault (discussed in [Section 3.2.5.3](#) and shown in [Figure 3-5](#) as the water-level discontinuity). The gradient is more pronounced in the base HFM than in the SCCC HFM. There is also a vertical gradient in the western part of B-B' that is less for the selected HSU depth decay and anisotropy (SDA) than the all HSU depth decay and anisotropy (ADA). This is a consequence of ubiquitously applying depth decay and anisotropy, which tends to continuously reduce permeability with depth and to stratify flow.

Simulated head along J-J' is broadly similar for all calibrated HFMs, with flow down to Oasis Valley driven by gentle horizontal and vertical gradients. Flow paths from central Area 20 have the same basic trajectory with discharge in the Oasis Valley area, but the detailed behavior of the trajectories is quite different. For instance, initially the particle rises in the SDA case, but (justifiably) flows more horizontally in the ADA case (not shown). All particles show a hook behind (to the east of) the plane

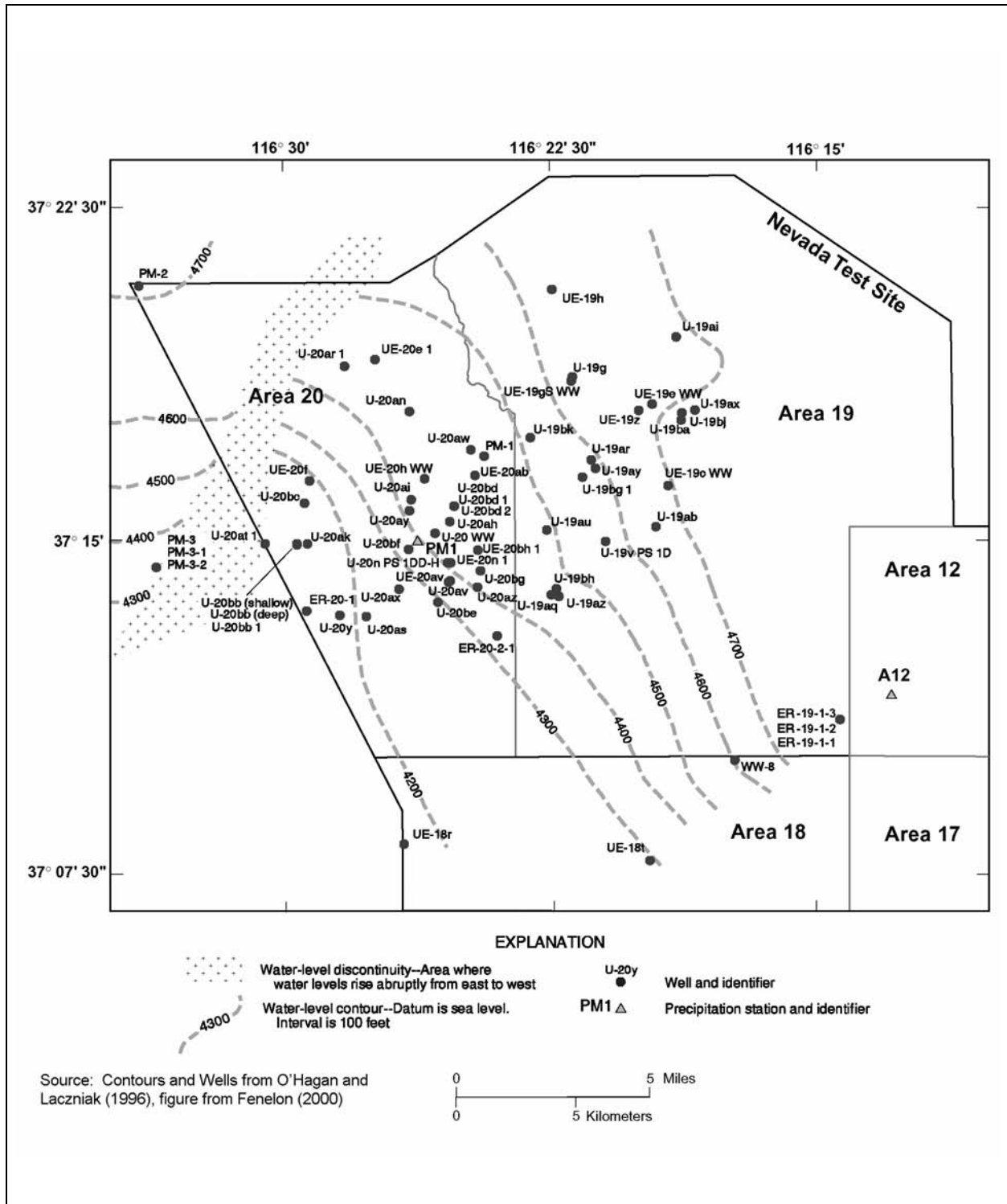


**Figure 3-11**  
**Groundwater Levels across the Pahute Mesa Flow Model Domain**  
**in Western Area 19, Area 20, and West of Area 20**



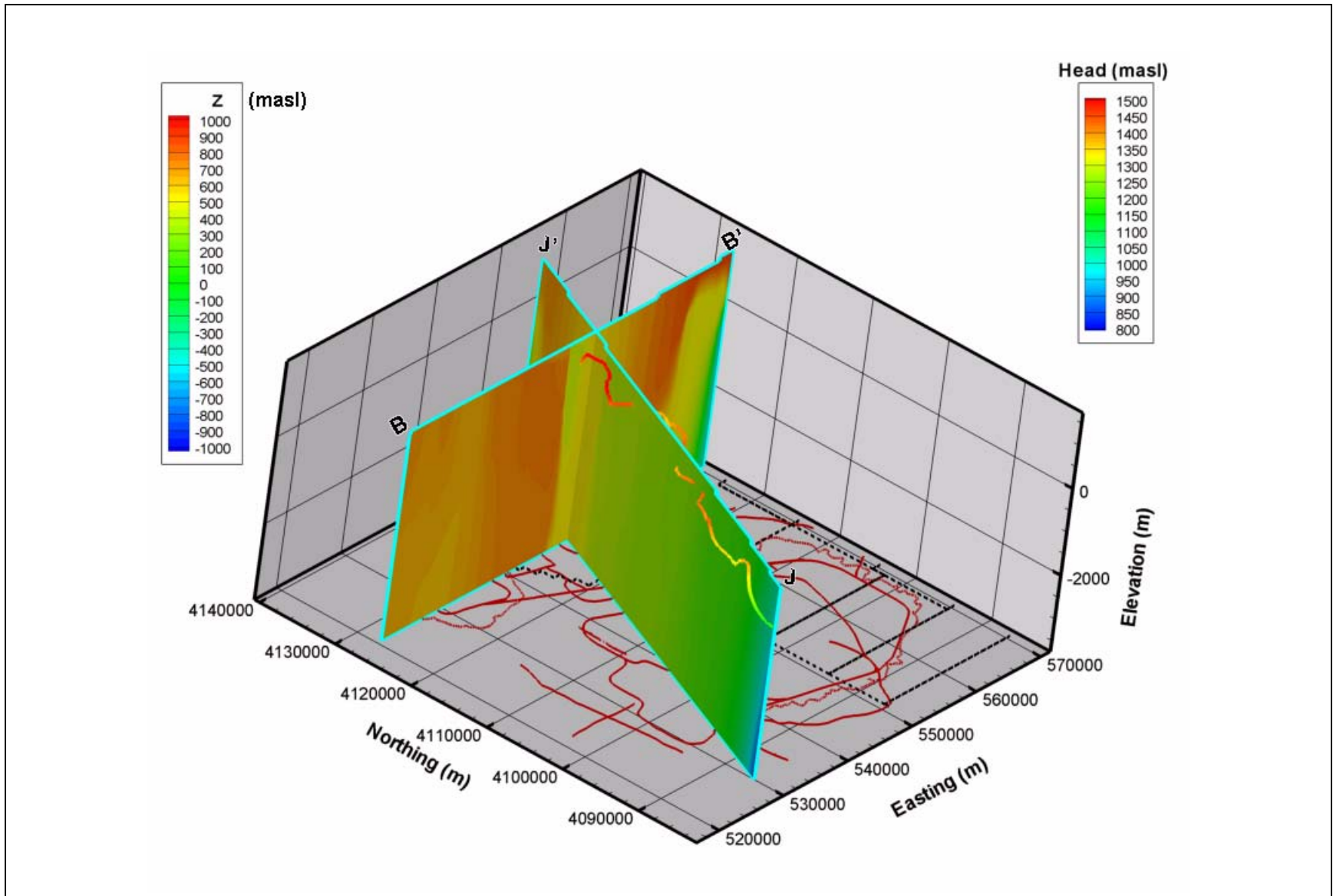


**Figure 3-12**  
**Simulated Head along B-B' and J-J' with Simulated Flow Path for the SCCC-MME-SDA HFM**  
Source: SNJV, 2006a

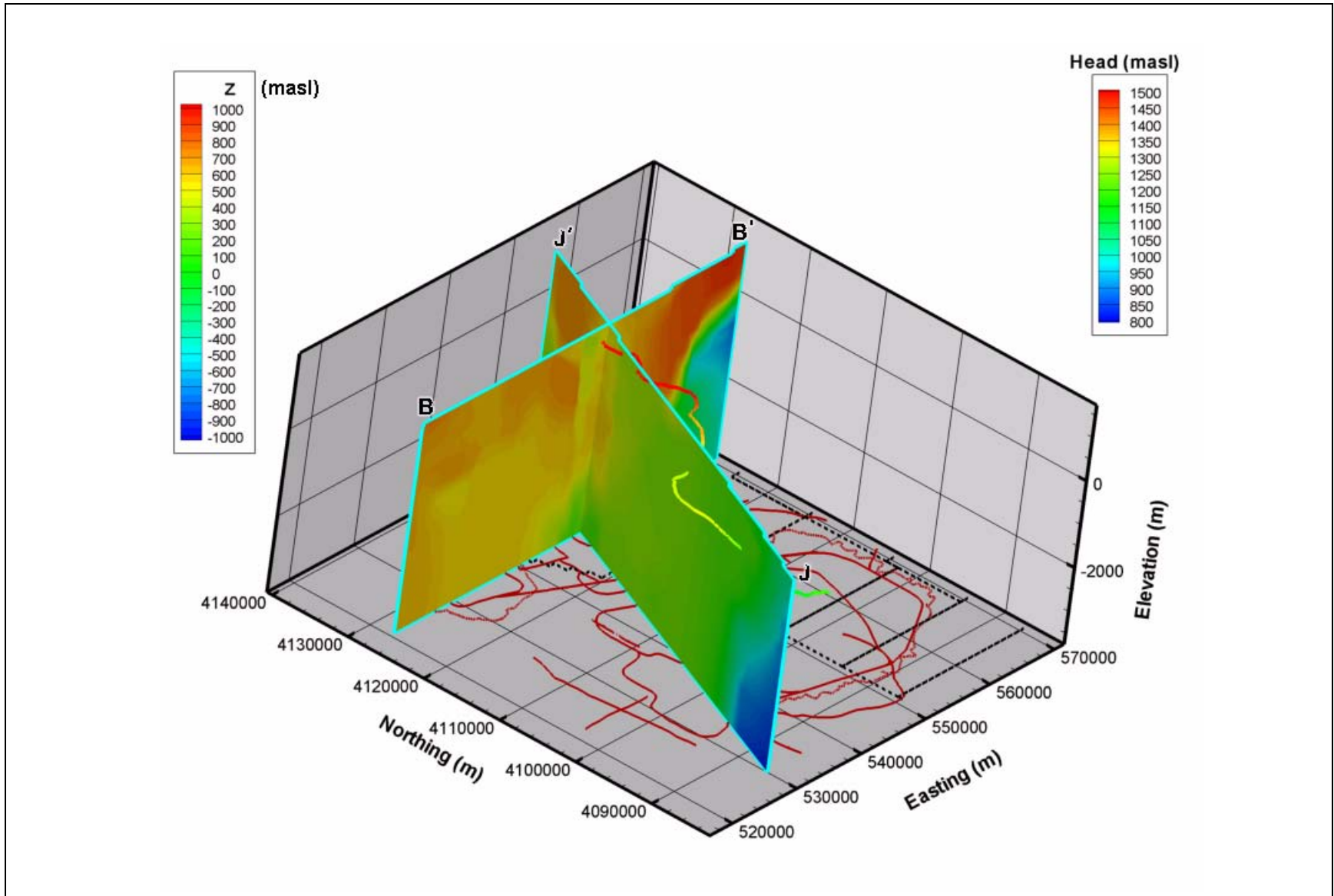


**Figure 3-13**  
**Simulated Head along B-B' and J-J' with Simulated Flow Path for the BN-MME-SDA HFM**  
Source: SNJV, 2006a

of J-J' with a return to the front of the J-J' plane due to the influence of low permeability beneath Timber Mountain. Thus, while the general model characteristics are similar in terms of calibration and boundary flows, the variability in flow paths resulting from alternative parameterization and the major HFMs are noticeable, although not in disagreement with the data that show flow from Pahute Mesa to the south-southwest into Oasis Valley (SNJV, 2004b). Quantitative measures of flow-path match as related to geochemical mixing targets are discussed in [Section 3.2.6](#), and the influence of alternative parameterization approaches on particle trajectories is discussed in [Section 3.4](#).

### **3.2.5.3 Purse Fault**

A key characteristic of calibrated PM CAU flow model behavior involves the measured hydraulic discontinuity across the Purse fault, a feature more pronounced in the base-HFM alternatives than in the SCCC HFM. [Figure 3-14](#) portrays the discontinuity as coincident with the Purse fault, and displays its impact in the simulated heads. There is an approximately 100-m head difference across the fault with flow directed sub-parallel to the fault (e.g., the fault may act as a no-flow barrier). In order to match the head in wells in the base HFM on the western side of the Purse fault and in wells in southwestern Area 20, the Purse fault permeability had to be reduced by a factor of 10,000 relative to the surrounding HSUs to maintain the 100-m or so difference between the two areas. It is important to note that multiple fault segments comprise the Purse fault as defined in the base HFM, a point that is made apparent in [Section 3.3](#). In contrast, the SCCC HFM does not have a Purse fault geometry that allowed connection or that goes as deep (whereas the base HFM has faults projected to the bottom of the model). Thus, simulated head at wells in southwestern Area 20 are too high because the fault did not separate the two areas to sufficiently reproduce the hydraulic discontinuity. However, the SCCC does incorporate juxtaposition across the caldera margins with low-permeability nodes of Black Mountain confining units, so an actual explanation of the offset may correspond with an amplification of this feature.

Whether or not the Purse fault alone is the source of the observed discontinuity is unclear, but its configuration in the base HFM does allow the observed head to be reproduced, while juxtaposition alone does not. The UGTA regional model used lower permeability from alteration between Black Mountain and the Purse fault to try to generate the observed

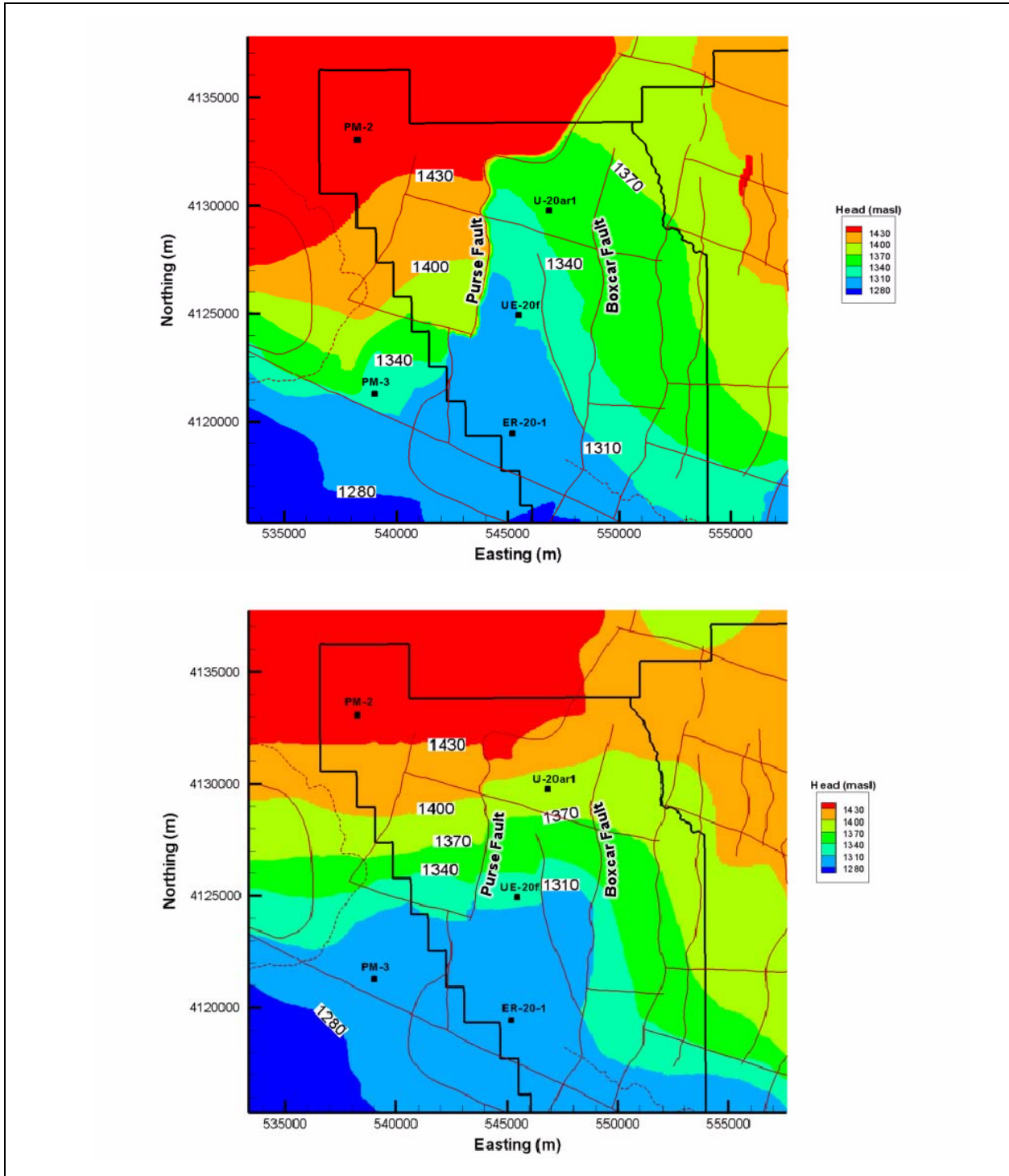


**Figure 3-14**  
**Simulated Head near the Purse and Boxcar Faults from the BN-MME-SDA**  
**Alternative (top) and SCCC-MME-SDA Alternative (bottom)**

Source: Modified from SNJV, 2006a

differences. Hydraulic testing of PM-3 (DOE/NV, 1996) showed relatively low permeabilities in this area, but little other information is available.

The effects of the Boxcar fault can also be seen in [Figure 3-14](#), and both the BN-MME-SDA and SCCC-MME-SDA calibrations improved as its permeability multiplier decreased. Wolfsberg et al. (2002) also noted similar model performance as the West Boxcar and southern part of the main Boxcar fault permeability decreased. Heads to the east of the fault are higher than those to the west and require some portion of the Boxcar faults to have a lower permeability. Thus, these results are consistent with observations and previous analysis.

### **3.2.6 Geochemical Screening and Selection of HFMs for Transport Analysis**

The alternative HFMs were evaluated with respect to independently developed groundwater mixing targets determined from geochemical analyses. The purpose of these comparisons was to determine whether the sources of groundwater at certain wells within the domain (as modeled) were consistent with the geochemical interpretation, thereby identifying HFM alternatives appropriate for transport simulation. In the comparisons, the sources of groundwater in the models were determined with reverse-particle simulations. In reverse mode, particles are started at a downgradient observation well and projected back to exit points in the groundwater flow system, from which the source location is documented. The top of the model was discretized into eight unique recharge zones and the side boundaries were discretized into seven unique inflow zones, the entire set of which comprised the 15 groundwater source zones ([Figure 3-15](#)). Following this method, the fraction of geochemically unique water from each of the recharge and boundary inflow zones that is present in the groundwater at the downgradient mixing target wells is computed. These fractions are then compared with the mixing ratios estimated by interpreting geochemical compositions (Kwicklis et al., 2005).

The residual is the difference between calculated mixing targets based on calibration of well-to-well measured data and the mixing targets calculated for the broader groundwater source zones represented by the zones of [Figure 3-15](#). For example, Kwicklis et al. (2005) indicate that samples from ER-EC-6 appear to be approximately 50/50 mixtures of upgradient water looking like that found in ER-EC-1 and UE-20WW. The implication is that ER-EC-1 water represents groundwater originating north and west of the well, primarily to the west of the Purse fault, while UE-20WW water represents Pahute Mesa groundwaters, hence a major mixing zone near ER-EC-6. In the model

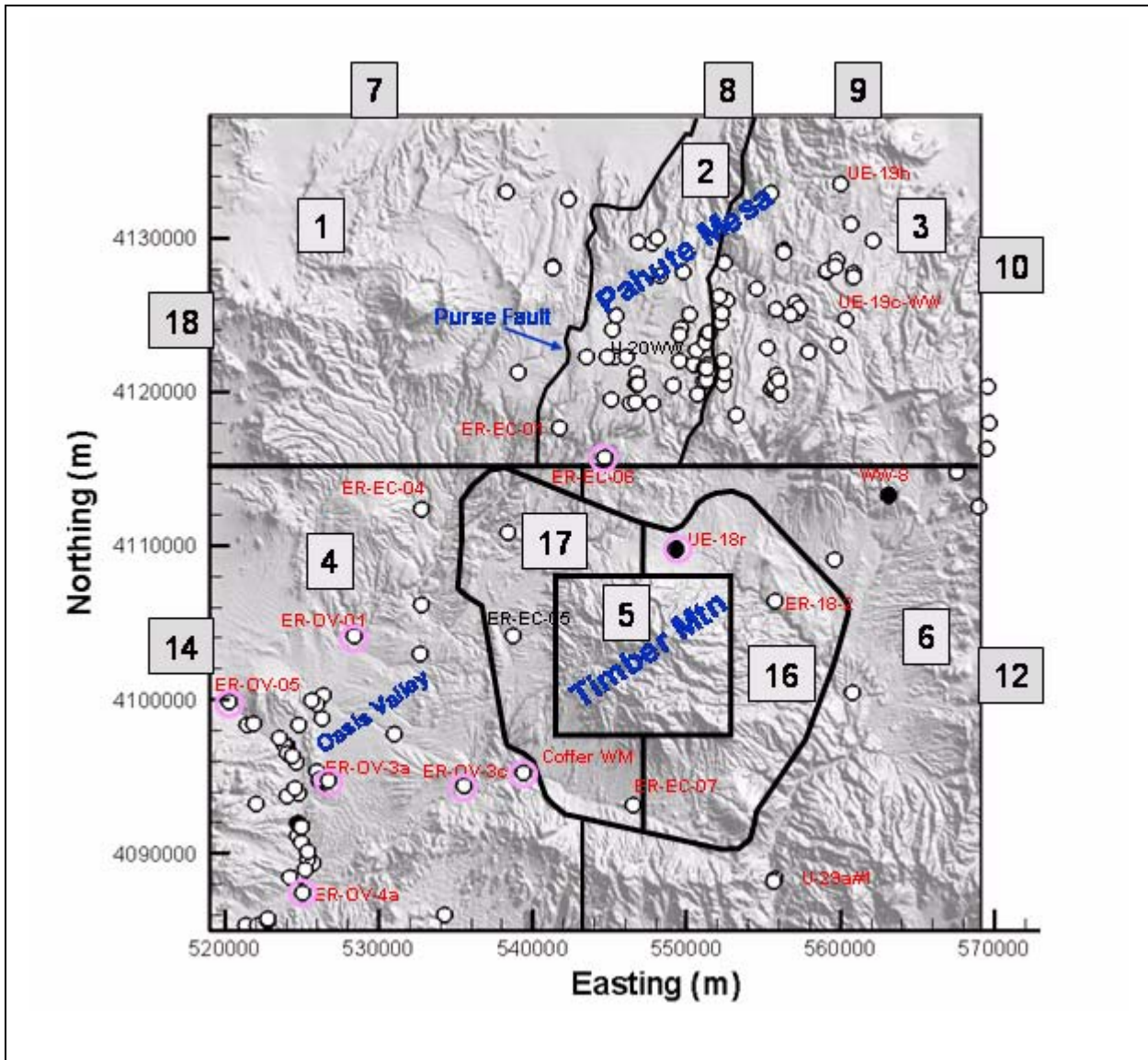


**Figure 3-15**  
**Zones Used To Identify Sources of Groundwater Recharge and Inflow**  
 Source: SNJV, 2006a

(Figure 3-15), the northwest water is identified by sources in zones 1, 7, and 18. The Pahute Mesa water, on the other hand, either enters from above in zones 2 and 3 or from lateral inflow in zones 8, 9, and 10 (greater weight is placed on zones 2 and 8 for the ER-EC-6 mixing analysis). Zones are grouped, based upon the different geochemical signature of source water identified by Kwicklis et al. (2005), into six categories identified as Northwest, Local Recharge West of Timber Mountain, North Central, Northeast, East (flow in from Rainier Mesa), and East of Timber Mountain. As described in SNJV (2005), differences between simulated mixing ratios from upgradient zone groups and the

values calculated by Kwicklis et al. (2005) for contributions from wells in those zones constitutes a geochemical mixing residual. Eighteen total residuals are considered for each PM CAU flow model, which can be grouped into four characteristic flow types:

1. RM: Too much inflow across the eastern boundary from Rainier Mesa. Although the gradients suggest such flow might be possible, the geochemistry rules it out at several wells.
2. NW: Too much inflow across the northern boundary west of the Purse fault (zone 7 in [Figure 3-15](#)).
3. NCNE: Not enough flow from the north-central and northeast areas east of the Purse fault.
4. Rech: Too much local recharge (lower Thirsty Canyon, Beatty Wash, and Oasis Valley).

The geochemical comparison approach is applied for calibrated models with alternative water-balance conditions and alternative HFMs. The alternative HFMs evaluated were the base model, SCCC, PZUP, DRT, RIDGE, TCL, and SEPZ as described in [Table 3-6](#). This approach is then extended to consider the fault correction alternatives described in [Section 3.3](#) and finally the base model modification to reduce channeling in the TCM in [Section 3.4.3](#). Each of the HFM/water-balance alternative combinations represent conceptual model uncertainty; therefore, they are compared with each other and to the BN-MME-SDA (base case) results for each of the target geochemical mixing wells.

**Table 3-6**  
***k*-Means Clusters of Flow Models Based on Geochemical Residuals**

Cluster	4	3	2	1
Models	SCCC-DRIA SCCC-USGSD DRT-USGSD BN-DRIA-LCCU1	BN-USGSD RIDGE-MME BN-MME SEPZ-MME TCL-MME	PZUP-USGSD BN-DRIA BN-MME-ADA PZUP-DRIA	DRT-MME DRT-DRIA BN-MME-LCCU1 PZUP-MME BN-USGSD-LCCU1 SCCC-MME

Source: Modified from SNJV (2006a)

For all of the model combinations considered, apparent similarities in the errors among various models motivated a formal cluster analysis in order to identify models with similar geochemical residuals. The clusters were developed with the objective of minimizing the intravariance within each cluster while maximizing the interviance between clusters. The analysis was achieved with a

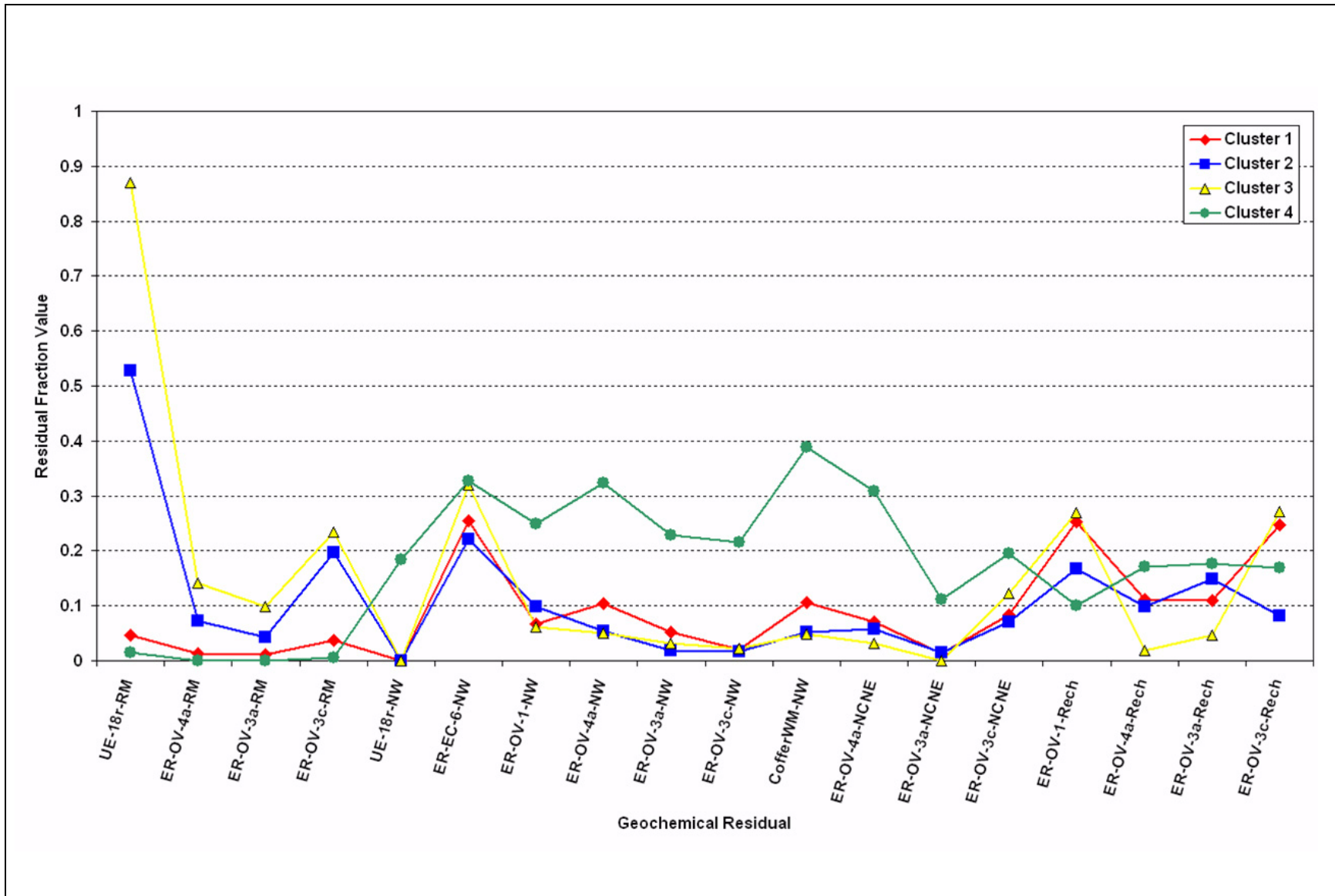
k-means clustering algorithm, which entails an iterative process for assigning models to different clusters and then testing the objective.

The analysis highlights four distinct clusters of the 19 PM CAU flow models considered (Table 3-6). Figure 3-16 shows the mean geochemical residual for the models identified in each of the clusters plotted against the errors considered. Cluster 1 shows the strongest performance in total geochemical residual. These models do not exhibit oversimulated inflow from the NW boundary or from Rainier Mesa, two characteristics that were identified as detrimentally affecting global model behavior. The misfits in Cluster 1 are tied to local errors and generally do not have such global flow errors. The Cluster 1 errors are dominated by excessive local infiltration as a direct result of the specified infiltration maps, an error term that is similar in all four clusters. Specifically, the recharge models apply more recharge in the washes than is consistent with the geochemistry. The impacts on flow and transport are local and generally downgradient from the sources.

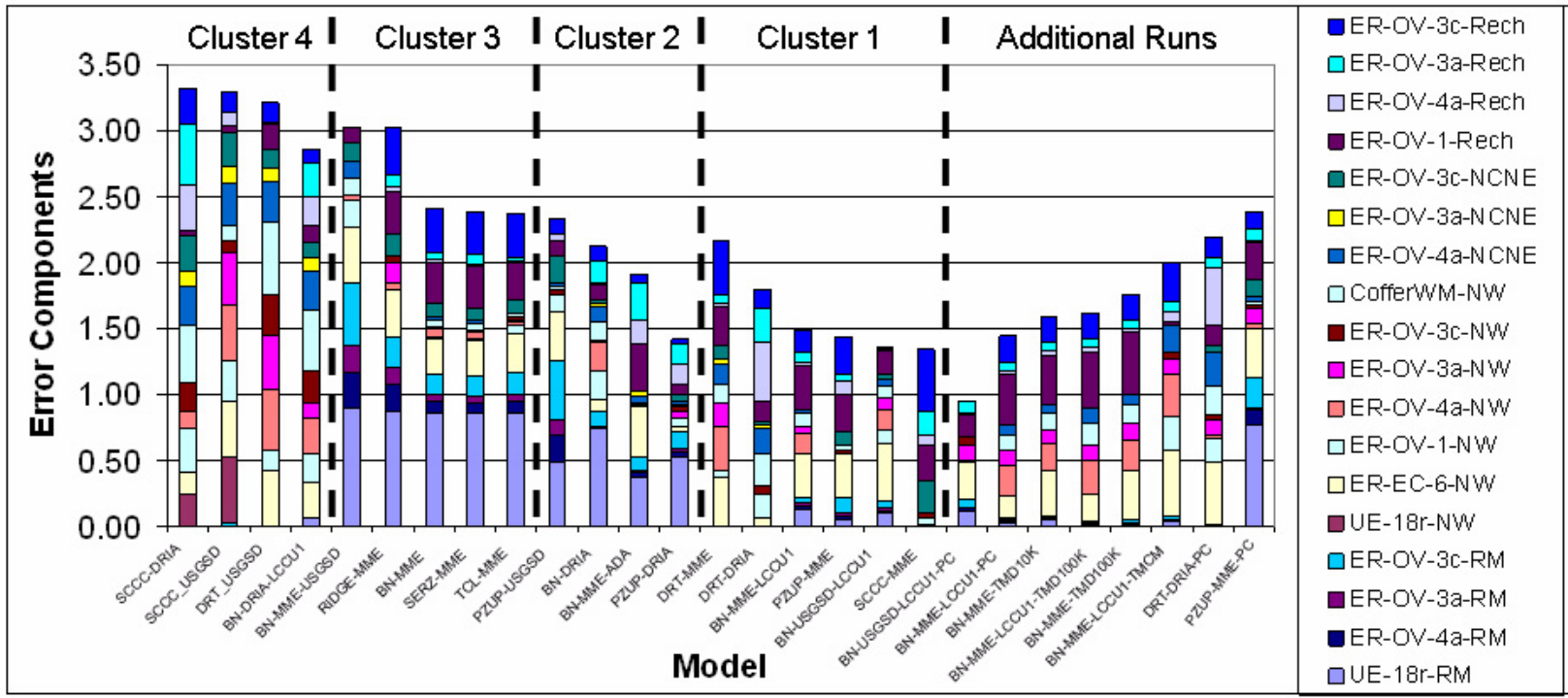
Figure 3-17 shows the individual residual components of the total geochemical residual for each model, grouped by cluster. Figure 3-17 also shows the geochemical residuals for PM CAU flow models developed subsequent to the cluster analysis described here.

Figure 3-18 shows the PM CAU flow model calibration metric (sum of squared residuals) sorted by geochemical residual (Figure 3-17). The total geochemical residual does not correspond with the objective function because PM CAU flow model calibration incorporated head/flux observations only. Because Cluster 1 is the only group to incorporate predominantly local, rather than global, geochemical misfits when simulated mixing ratios are compared with those observed at wells, it was determined that five of the six Cluster 1 models warranted development of PM CAU transport models. The DRT-MME case was excluded due to its particularly high flow model calibration objective function and its poor geochemical error. Before advancement for transport analysis, minor parameterization adjustments, including recalibration and fault property adjustments in southern Area 20, are made to the Cluster 1 models in order to address local flow considerations. These are identified with “FC” in the additional runs shown in Figure 3-17. Also, two additional flow models were added to the suite for consideration. The first, named LCCU1-MME-TMD, involves increasing the permeability of the TMCM subdomain directly under the dome, TMD, by 100 times in order to reduce recharge mounding and flow obstruction in this central portion of the TMCM. The second





**Figure 3-16**  
**Geochemical Residual Means for Each Cluster**  
 Note: Residuals are defined as well-name-error type and are grouped by cluster to highlight differences.  
 Source: SNJV, 2006a



**Figure 3-17**  
**Components of the Total Geochemical Residual for Each Alternative Model**

Note: The models are grouped by the four clusters, and the residuals are grouped by error type.

Source: SNJV, 2006a

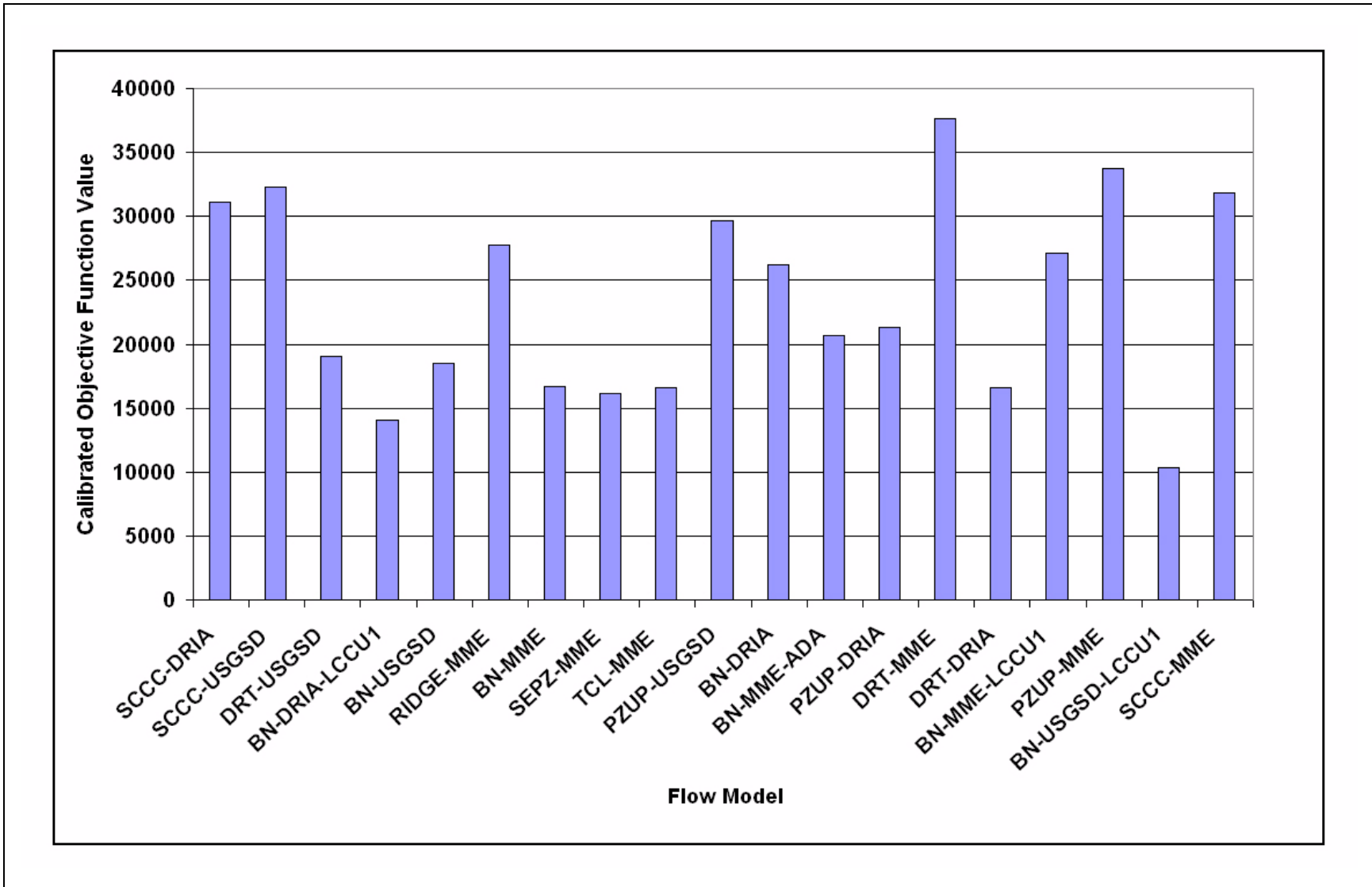


**Figure 3-18**

**Flow Model Calibration Metric (Objective Function) per HFM, Sorted by Geochemical Residuals within Clusters (Shown in Figure 3-17)**

Source: SNJV, 2006a

new model, named LCCU1-MME-TMCM, involves recalibrating the LCCU1-MME with an emphasis to reduce channeling along the TMCM/FCCM boundary discussed later in this report. The effect of this model is to increase the spread of flow coming off of Pahute Mesa westward toward Thirsty Canyon, with less flux per unit volume along any flow path. This is the subject of [Section 3.3](#).

### **3.3 Selected Fault Permeability Adjustments**

In four of the five Cluster 1 flow models ([Section 3.2.6](#)) selected for transport analysis, with the SCCC-MME alternative excluded, analysis of geochemical mixing targets showed systematic discrepancies in southwest Area 20 boreholes related to local fault properties to which flow model calibration was insensitive. Recall that the geochemical comparison study was conducted after flow model calibrations were completed during that stage of model development. This subsequent analysis led to local fault permeability (i.e., permeability multiplier) adjustments resulting in local redirection of flow in the areas of the southern limbs of the Purse and Boxcar faults. Following fault property adjustments, the alternative PM CAU flow models were recalibrated, ensuring that the hydraulic data were matched well. The geochemical residuals were checked (because they were the motivation for the fault property modifications) and were found to be within the range of Cluster 1 values. This property modification in Area 20 maintains the fundamental characteristics (i.e., HSU and fault geometry properties) that characterize and distinguish each of the alternatives. The recharge and boundary flux conditions are not changed in the PM CAU models, so concerns that affect geochemical mixing such as inflow across the western half of the northern boundary are not addressed in these local structural changes.

#### **3.3.1 Background**

Through comparison of model flow metrics with hydraulic and geochemical targets, a subset of five calibrated alternative PM CAU flow models was selected that best represents the target data given the hydrogeologic conceptualization, or spatial distribution of HSUs, for each. Considering the hydraulic data alone, SNJV (2006a) showed that 19 HFMs were able to equitably match measured fluxes and pressures, indicating that the spatial distributions of HSUs between the alternatives were (approximately) insensitive to measured hydraulic data. However, the analysis of flow paths and mixing among the calibrated models indicated an appreciably greater sensitivity to steady-state

geochemical targets. The geochemical analysis, as summarized above, ranked the quality of alternatives relative to how well inflow sources were represented at downgradient wells. It was used to screen the 19 PM CAU flow models to pick a subset for advancement into full transport simulations and analysis. The criteria were:

- Only a limited number of models can be advanced for the full transport analysis.
- The models need to be among the best for matching geochemical mixing targets.
- The models need to be appreciably different in both HFM and recharge/water balance so as to span the range of conceptual uncertainty.

Five PM CAU flow models were chosen, with two additional calibrated PM CAU flow models subsequently added to the set, to address conceptual uncertainty not included in the initial 19 PM CAU flow models (described in [Section 3.4](#)). Among those PM CAU flow models advanced for transport, systematic discrepancies between hydraulic and geochemical targets for all models were identified. Those of concern primarily involved flow in southern Area 20 and were based upon observations at ER-EC-6 and UE-18r. [Sections 3.3.1.1](#) and [3.3.1.2](#) summarize these discrepancies as reported in Sections 7.2 and 7.3 of SNJV (2006a).

### **3.3.1.1 Geochemical Mixing at ER-EC-6**

Well ER-EC-6 is southeast of the Purse fault and west of the southern Boxcar fault ([Figure 3-19](#)), on the southern side of the North Timber Mountain Moat structural zone fault ([Figures 3-3](#) and [3-7](#)) (hereafter referred to as the Moat fault) beneath the southwestern Area 20 wells. The geochemical interpretation suggests that equal ratios of water flowing south from both sides of the Purse fault mix at ER-EC-6, both of which are distinctly different (Kwicklis et al., 2005). In contradiction, the hydraulic model results for all selected alternative PM CAU flow models, with the exception of the SCCC-MME alternative, show that the large majority of groundwater at ER-EC-6 originates west of the Purse fault primarily as inflow along the northern boundary. In the SCCC-MME model, flow to ER-EC-6 is directly from the north and mixing from either side of the fault is nearly even (the Purse fault does not provide a distinct hydraulic barrier in that model). [Figure 3-19](#) exemplifies this difference between the LCCU1-MME and SCCC-MME alternative models. Source locations for water identified by reverse particle tracking from origin ER-EC-6 are shown in color, and flow paths for forward-in-time particle streamlines are shown in gray.

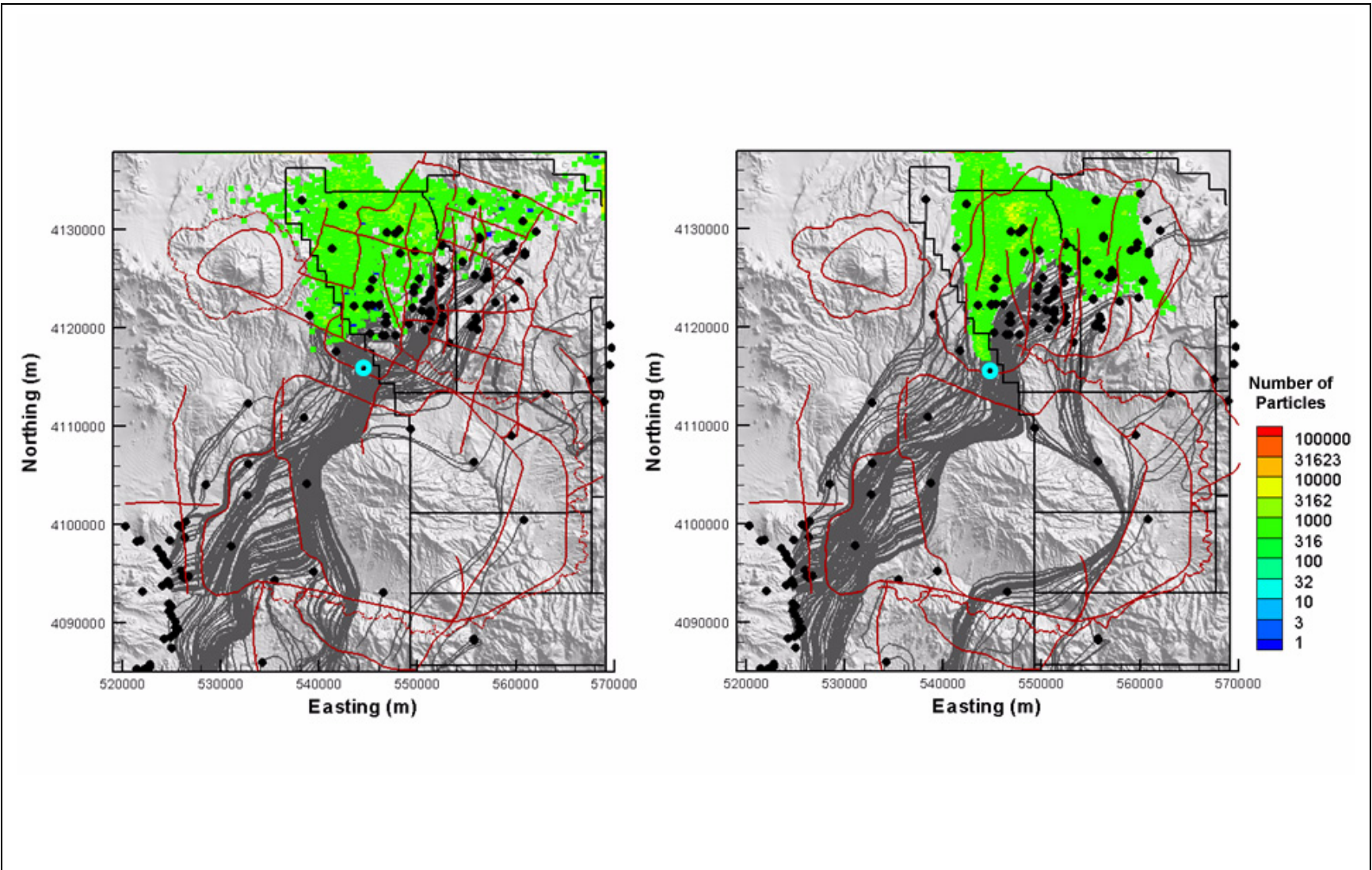


**Figure 3-19**

***LCCU1-MME and SCCC-MME Alternative HFMs from ER-EC-6***

For the LCCU1-MME (left) and SCCC-MME (right) alternative models, flow paths from forward simulation particle tracks originating at wells are shown in gray, and source recharge locations identified by reverse particle tracking from origin ER-EC-6 are shown as colored squares.

Source: Modified from SNJV, 2006a, Figures 7-14 (left) and 7-43 (right)

Because of the systematic excess contributions to mixing at ER-EC-6 from west of the Purse fault, structural control in this area was reexamined. Boundary conditions along the northern boundary are also recognized as potentially having a significant impact on this model discrepancy and are highlighted for consideration in future modifications and improvements to this model. Steady-state flow trajectories are complex in upper Thirsty Canyon due to the convergence of northwest and northeast flows. Although most of the water (in the PM CAU flow models) at the exact location of ER-EC-6 is arriving from the northwest (Figure 3-19), only a short distance to the east of ER-EC-6 flow paths from the northeast enter this zone and result in convergence in upper Thirsty Canyon. That is, the PM CAU flow models display the correct trends in convergence and honor the hydraulic targets, but narrowly miss the geochemical target which was not a model calibration target. To satisfy both hydraulic and geochemical targets at ER-EC-6 requires either the decrease/redirection of flow from the northwest or the increase/redirection of flow from east of the Purse, either adjustment being directly related to the other. In the present extension on PM CAU flow models developed by SNJV (2006a), this was done with local hydraulic properties in southwest Area 20. A broader approach for future consideration will be to revise boundary conditions in the global calibration as well.

### **3.3.1.2 Geochemical Mixing at UE-18r**

Borehole UE-18r is just north of Timber Mountain and reflects mixing of groundwater from Areas 19 and 20 of Pahute Mesa, from Timber Mountain, and from flow into the model domain across the eastern boundary near Rainier Mesa. Geochemical interpretation indicates that most of the water originates in the northeast (central and northern Area 19), with only a small component resembling a deep source found (in ER-18-2) on the east flank of Timber Mountain. Most of the selected PM CAU flow models advanced for transport are consistent with this interpretation; the geochemical error associated with inflow from Gold Meadows stock at the western edge of Rainier Mesa is reflected in the first error bar in Figure 3-17 (UE-18r-RM, lavender). Other PM CAU flow models developed by SNJV (2006a) have much larger chemical residuals at UE-18r related to inflows from the east. Yet, these models calibrated equally well to hydraulic data (see the first error bar in Cluster 2 and 3 models in Figure 3-17).

Given that multiple alternative models permit such varied groundwater sources at UE-18r while honoring the same hydraulic target, it is evident that the hydraulic target is insensitive to the direction of flow from the north (clockwise) to the east. Figure 3-20 exemplifies the range of modeled UE-18r

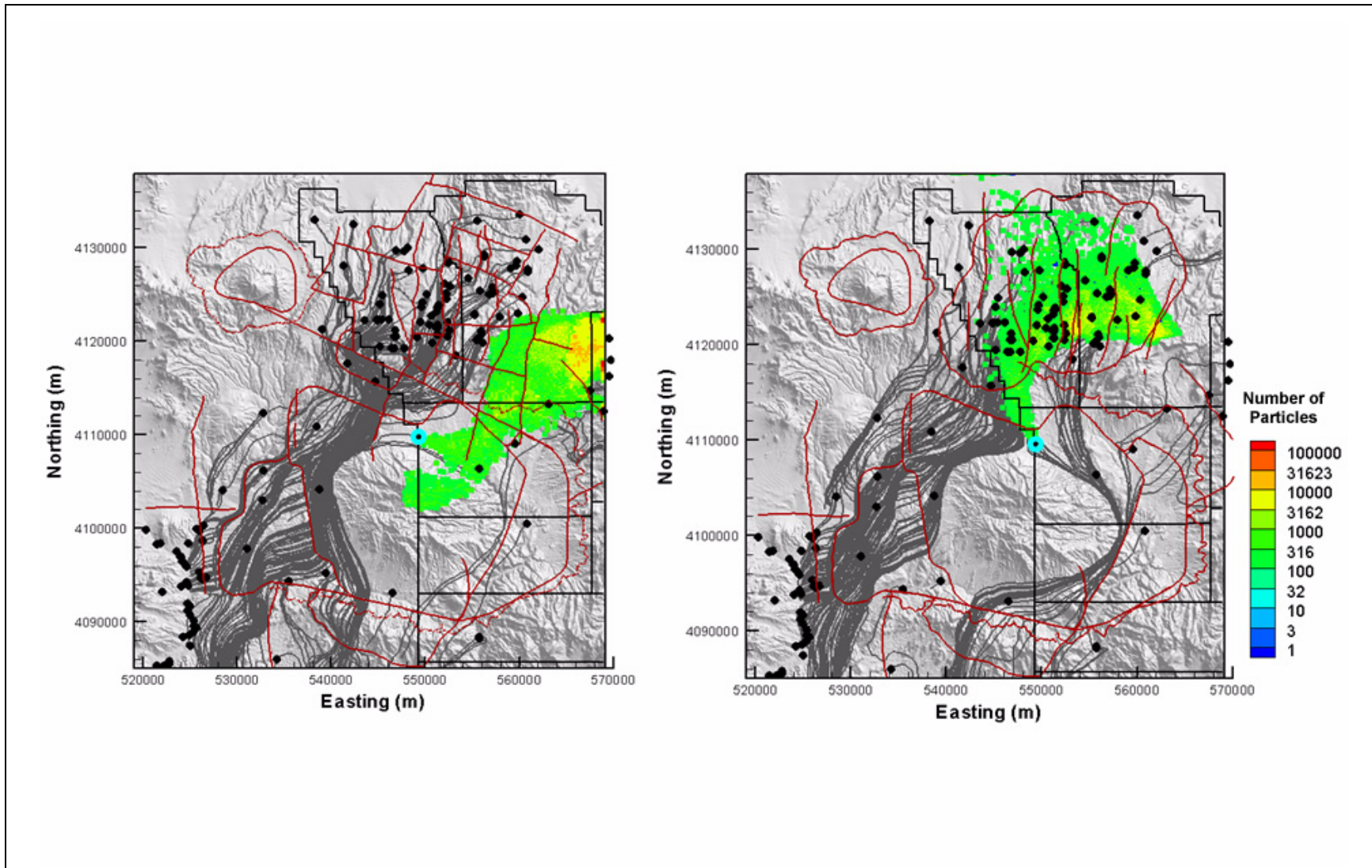


**Figure 3-20**

***LCCU1-MME and SCCC-MME Alternative HFMs from UE-18r***

For the LCCU1-MME (left) and SCCC-MME (right) alternative HFMs, flow paths, from forward simulation particle tracks originating at wells are shown in gray, and source recharge locations identified by reverse particle tracking from origin UE-18r are shown as colored squares.

Source: Modified from SNJV, 2006a, Figures 7-11 (left) and 7-32 (right)



(north)eastern groundwater source locations comparing the LCCU1-MME (a base-derived alternative) and SCCC-MME models. Eastward flow across the eastern boundary is, in fact, a genuine effect of the boundary condition reflecting the regionally high head at Gold Meadows and, hence, the large gradient into the PM model domain. Therefore, in order to satisfy both hydraulic and geochemical targets at UE-18r, the solution does not require that flow from the east is redirected, but that flow from the north(east) is enhanced.

### **3.3.2 Alternative HFM Adjustment**

#### **3.3.2.1 Analysis of HSU and Fault Permeability**

Two specific flow geometries are identified as responsible for the geochemical misfits at ER-EC-6 and UE-18r. [Figure 3-21](#) shows pathlines for single particles released from each test cavity. These pathlines assist in the interpretation because their convergence (and divergence) indicate hydraulic property heterogeneity without observing the properties themselves. The first area of interest is at the intersection of the West Purse fault (yellow and green in [Figure 3-21](#)) and Moat fault (light gray in [Figure 3-21](#)). Particles are shown passing through from west to east, thereby increasing the geochemical signature of northwestern groundwater at ER-EC-6. The second area of interest is at the Boxcar fault just south of where it joins with the West Boxcar fault. Flow paths are shown crossing that fault from east to west and into the adjacent TSA and BA HSUs, diverting flow from UE-18r to the south. The areas of geochemical inconsistency are associated with the merging of discontinuous fault zones. The following describes the influence of fault zonation on flow relative to the permeability heterogeneity of HSUs within which the faults (via permeability multipliers) are embedded.

The LCCU1-MME steady-state flow field was analyzed to identify the origins of differences between observed and simulated geochemical data at ER-EC-6 and UE-18r. In southern Area 20 at elevations amsl, the primary high-permeability HSUs between the Purse and Boxcar faults are the TSA and BA. The depth of interest is relatively shallow as the test working points and the majority of permeable (fractured-flow dominated) aquifers are amsl. The TSA and BA together serve as a high-permeability flow conduit that channels local-area flow (recharge) off of Pahute Mesa. The groundwater from Area 20 flows into the TSA from the north and groundwater from Area 19 flows into the BA from the northeast. All of the outflow is to the south where pathlines converge. Thus, all particles originating

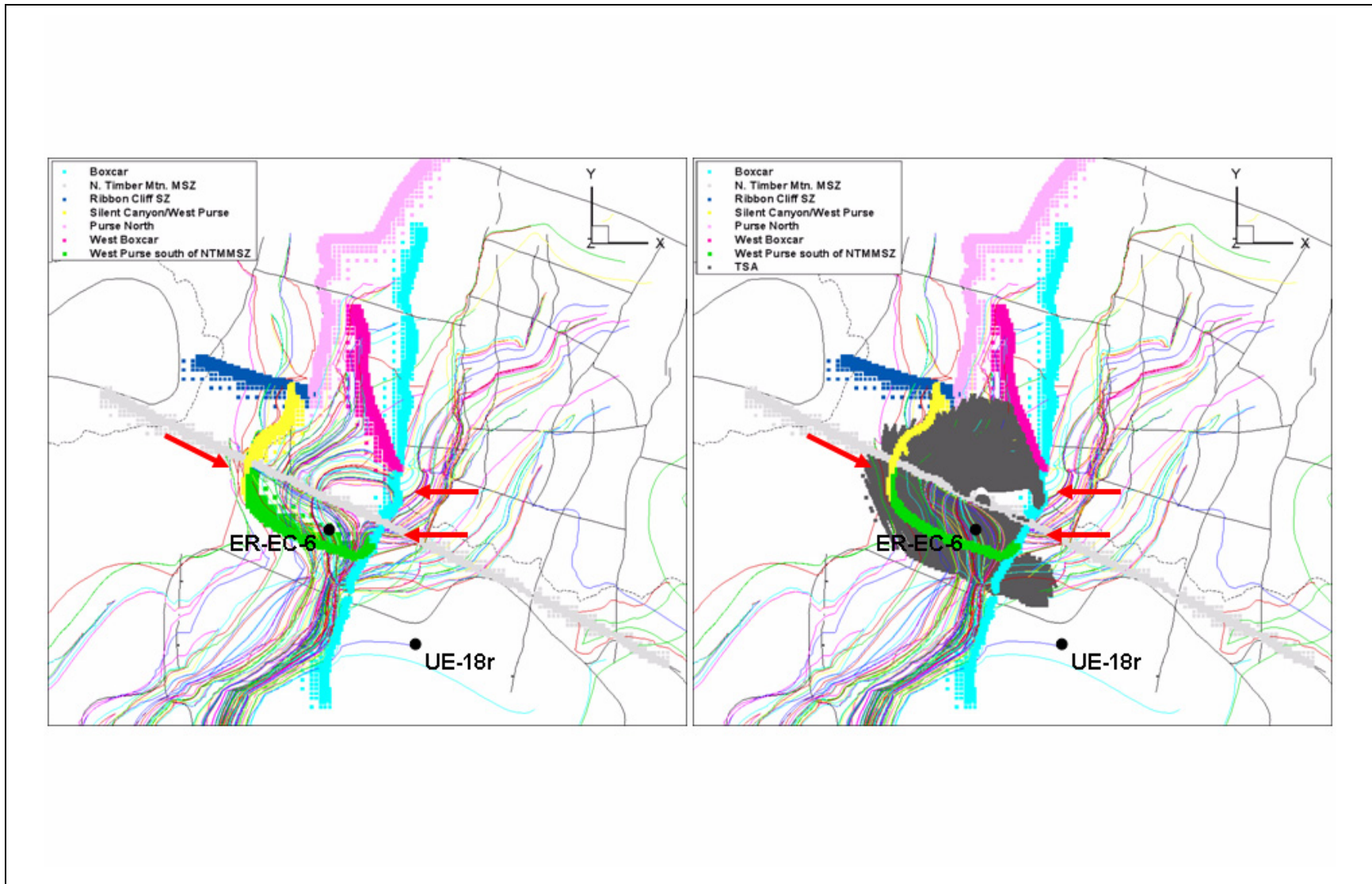


**Figure 3-21**

**Area 20 Discrepancies in Particle Streamlines**

In southern Area 20, areas of flow (red arrows) identified by particle streamlines indicate the sources of discrepancy between hydraulic and geochemical targets.

Note: The figure on the right shows the TSA HSU.

in Area 20 and the large majority from Area 19 pass through the TSA and BA before passing south across the Moat fault and into the extensive TCMC HSU.

The hydraulic properties of the fault zones were redefined to reduce geochemical inconsistencies between simulated and observed values. The merging of local fault zones within the larger Purse and Boxcar faults zones, with each local zone having a unique permeability multiplier (as described below), creates variations in the velocity field at the scale of individual model nodes that permit flow to pass through faults defined (during PM CAU flow model calibration) as low-permeability flow barriers. To correct for the unintended effects of fault zonation and to improve geochemical target estimates at ER-EC-6, minor adjustments were made to Area 20 fault permeabilities that immediately surround the measured geochemical targets (i.e., borehole measurements), with minimum impact to the model calibration metric (which is based on hydraulic targets). Because the source of inconsistency was identified as an artifact of fault zonation within the (base HFM) numerical model, and not as a natural consequence of flow within the LCCU1-MME alternative, the following fault adjustments were made to all base-derived alternative models (i.e., all models excluding the SCCC-MME).

A suite of combined fault adjustments to redirect flow were designed. The most efficient and plausible combination involved (1) adjusting the extent of the West Purse while leaving its original permeability, and (2) adjusting the permeability along a subsection of the south Boxcar fault.

Figures 3-22 and 3-23 show these adjustments and are described as follows:

1. The southern leg of the West Purse fault, labeled “West Purse south of NTMMSZ” in Figure 3-22 (left), is decreased in length such that it now spans only the east-to-west-trending section of the West Purse (Figure 3-22 [right]). As permeabilities remain unmodified, the “West Purse south of NTMMSZ” retains its initial multiplier of 1.0, effectively eliminating its effect on flow (i.e., its permeability is the same as the background HSU permeability). However, by decreasing the extent of the “West Purse south of NTMMSZ,” the segment of the West Purse labeled “Silent Canyon/West Purse” is naturally extended. The “Silent Canyon/West Purse” multiplier is less than unity (decreasing permeability) and therefore extends its flow-impeding influence along the entire north-to-south-trending section of the West Purse fault.

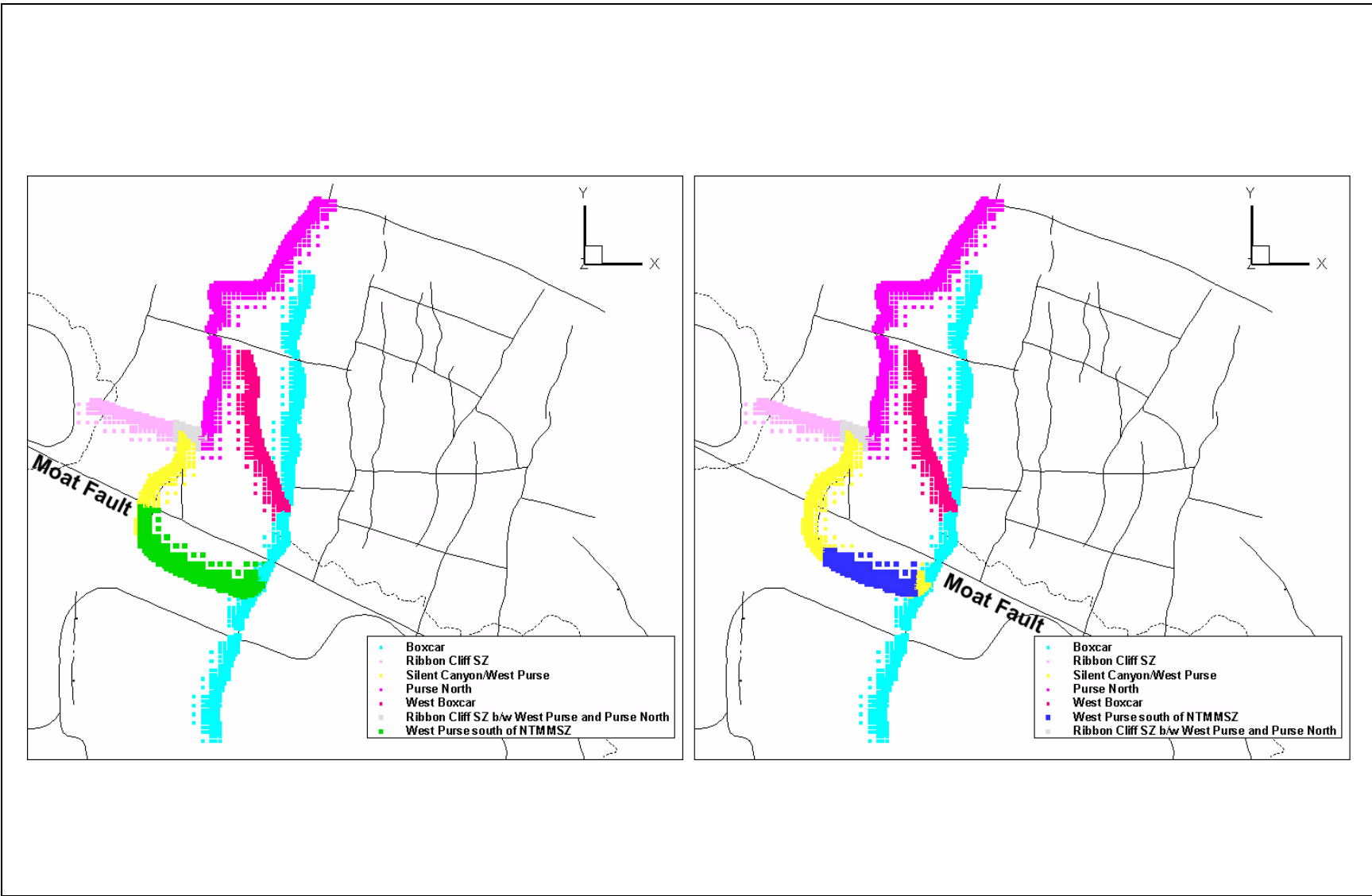


**Figure 3-22**  
**Revised Section of Purse Fault**

To improve the simulated reproduction of geochemical targets, the low-permeability section of the “Silent Canyon/West Purse” fault is extended south, truncating the “West Purse south of NTMMSZ” fault. Note: Before and after images are shown on the left and right, respectively.

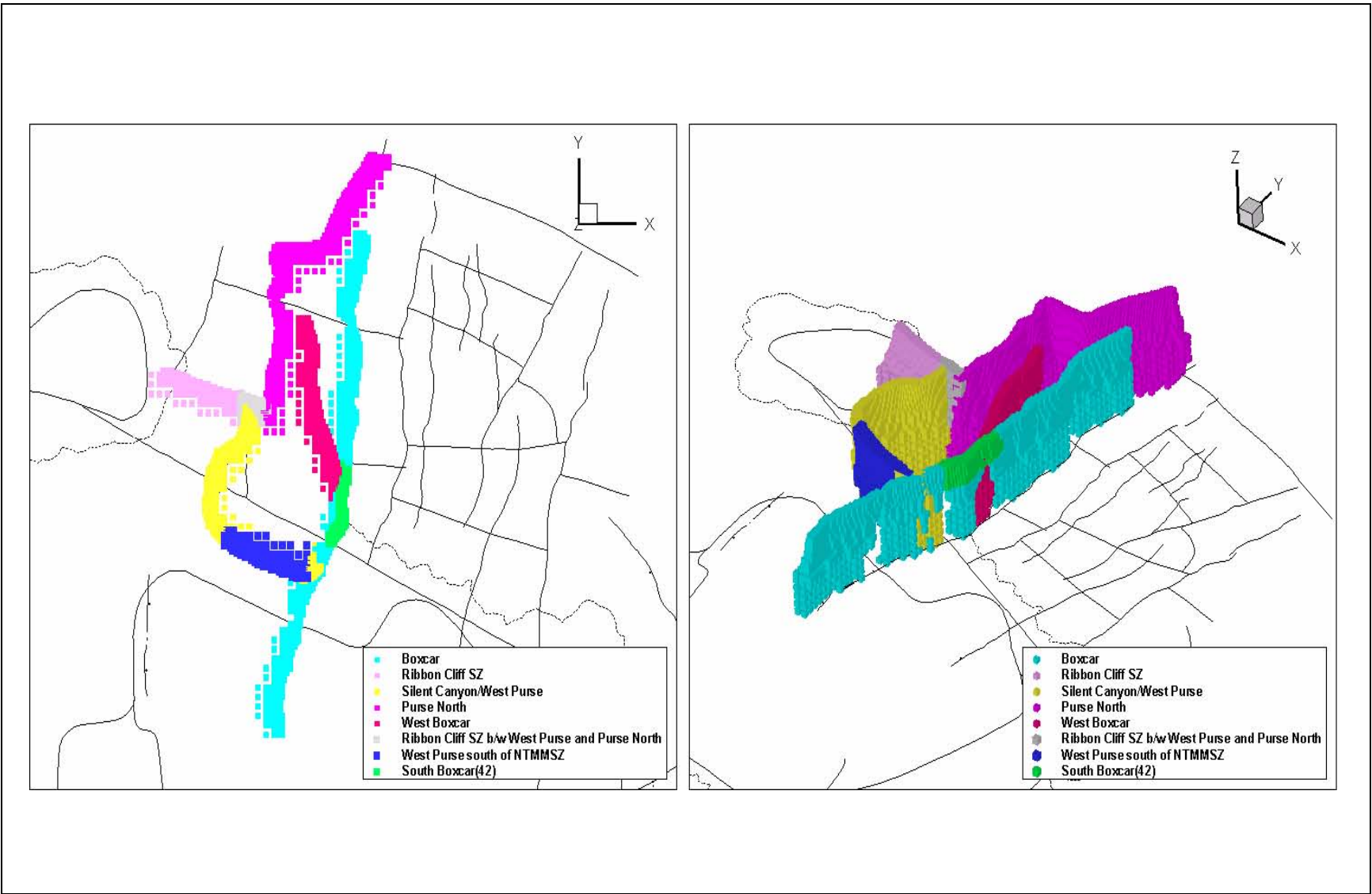


**Figure 3-23**

**Revised Section of Boxcar Fault (Boxcar[42])**

To improve the simulated reproduction of geochemical targets, a subsection of the southern Boxcar fault, labeled “Boxcar42z,” is isolated and assigned a unique permeability multiplier to reduce east-to-west flow across this section of the Boxcar fault (two perspectives are shown).

2. In [Figure 3-23](#) a southern segment of the Boxcar fault, spanning just beyond the eastern edge of the TSA/BA complex and amsl, is shown isolated from the Boxcar. This subsection, labeled “South Boxcar(42)” in the figure, is assigned a unique permeability multiplier. Its permeability was lowered until particle flow paths from Areas 19 and 20 ceased to cross the Boxcar from east to west (where they would subsequently circulate counterclockwise within the TSA as shown in [Figure 3-21](#)).

### **3.3.2.2 Adjustment of HSU and Fault Permeability**

Having adjusted the model node definitions to reflect the West Purse and Boxcar fault adjustments, a sequential process was completed in which the southern Boxcar fault permeability was incrementally decreased until flow along its eastern flank was directed north-to-south and particles no longer crossed over into the TSA. Each step involved an adjustment to the permeability, reanalysis of the local flow field and hydraulic target residuals, and re-computation of particle pathlines to ensure that the impact on the calibrated model was minimal. Before modification of the Boxcar fault, its permeability multiplier was set to between 1.0 and 2.0, effectively enhancing permeability. A smaller permeability multiplier of  $1.0 \times 10^{-3}$  was found sufficient to restrict flow across it.

Although fault adjustments were minor, several hydraulic targets in Area 20 were found sensitive to the flow adjustments such that their agreement with observations worsened. Therefore, a localized recalibration effort was completed to reattain the target fit statistics achieved in the initial calibration. The method entailed identifying all hydraulic head measurements and corresponding HSUs most sensitive to the fault adjustments, and then adjusting those HSU permeabilities until the simulated heads were in improved agreement with the measured target data. The PEST code (Watermark, 2004), using the Levenberg-Marquardt algorithm, was used to automate this procedure. Care was taken such that (relatively) small perturbations were applied to the defined set of model parameters during the estimation procedure, minimizing the impact of the net permeability adjustments on the CAU-scale flow field while maximizing their influence on the hydraulic targets. Results were positive in both efforts. In two of the three cases, the calibration statistics were in fact improved over the initial calibrated model, corroborating the driving assumption behind this analysis that, based on geochemical interpretation, sections of the Area 20 flow field were incompletely defined.

The post-recalibration fault adjustments and model fit metrics are compared with those of the initial calibrated model for the LCCU1-MME alternative. Particle streamlines showing advective transport for the initial calibrated case are shown on the left in [Figure 3-24](#). Again, eastward flow across the

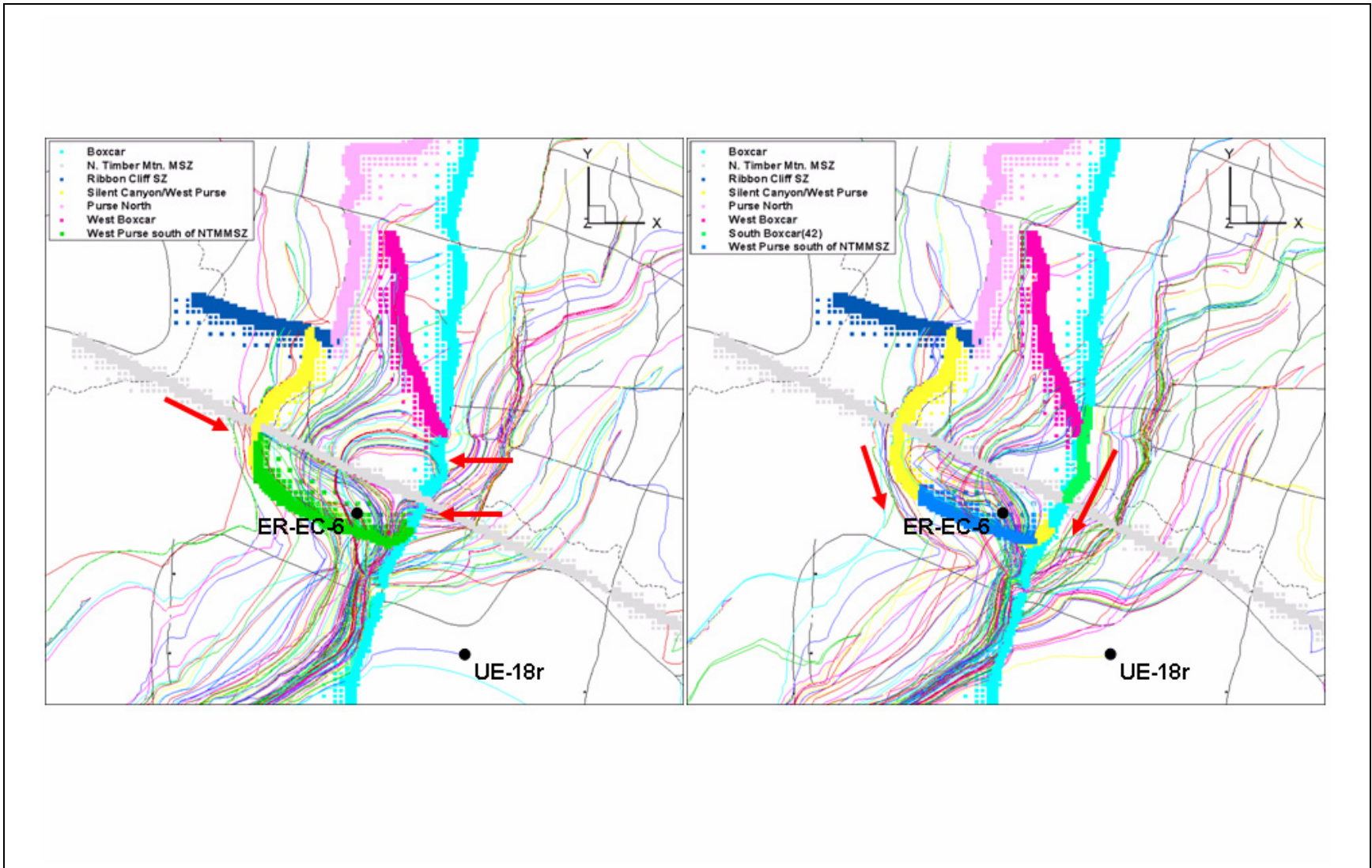


**Figure 3-24**  
**Particle Streamlines Showing Advective Transport for the Initial Calibrated Case (left) and the Recalibrated Case (right)**

West Purse into the TSA, and westward flow across the south Boxcar into the BA, is apparent. At the right in [Figure 3-24](#) are pathlines for the recalibrated model. Recalibration, or the minor adjustment of HSU permeabilities, does not affect the basin-scale pathline orientations. In the same sequence described above, model head residuals are shown in [Figure 3-25](#), and other hydraulic residuals are listed. The equivalence in fit following recalibration is visually apparent and confirmed by the objective function. The HSU permeabilities and their adjustments are plotted in [Figure 3-26](#). The adjustments are clearly minimal and imply that the recalibration effort did not appreciably alter the flow geometries that fundamentally characterize this alternative model.

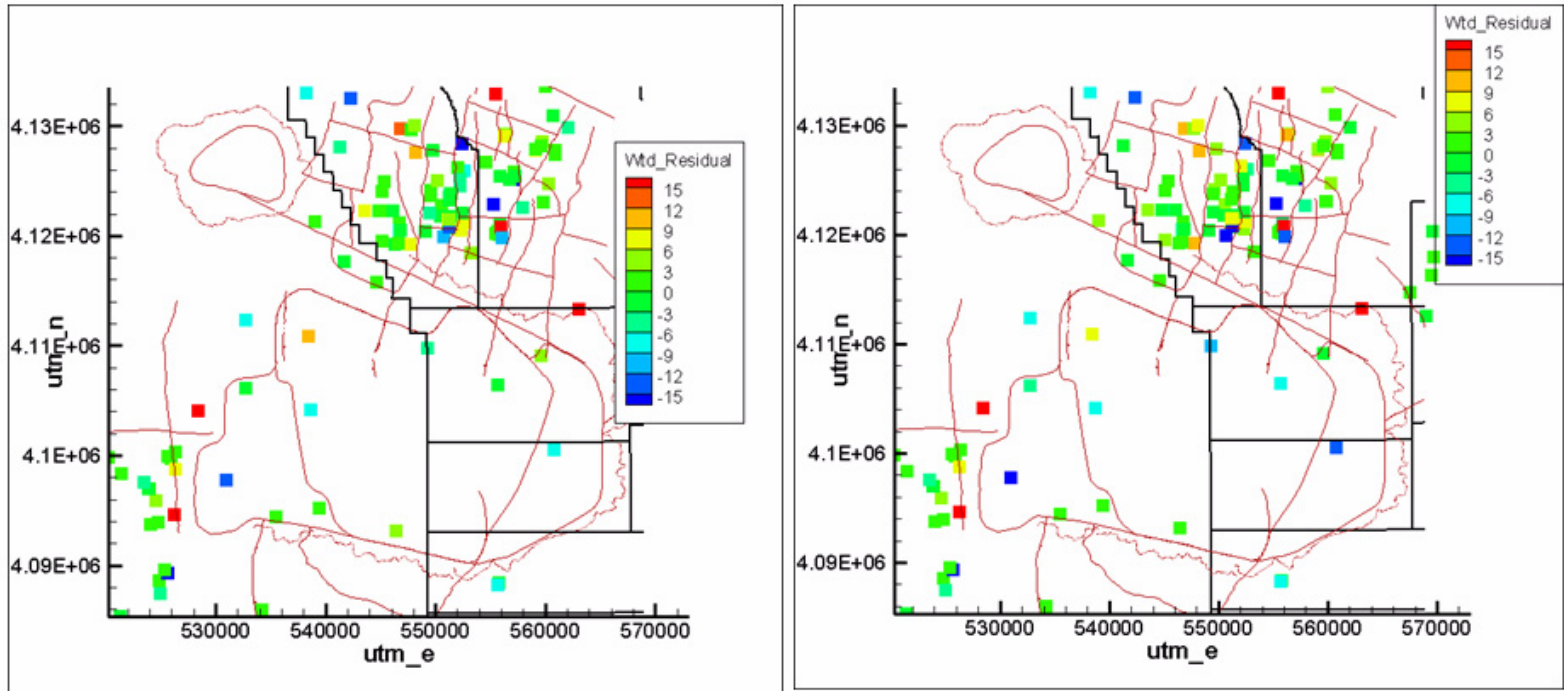
[Table 3-7](#) lists the initial and recalibrated objective function for the alternative PM CAU flow models on which the fault adjustments and recalibration was performed. Recall that fault permeability adjustments were not applied to the SCCC-MME alternative due to its considerably different conceptualization of fault geometry across Pahute Mesa.

Up to this point in the assessment of PM CAU flow model appropriateness for use in transport, five alternatives were selected: LCCU1-MME, PZUP-MME, DRT-DRIA, LCCU1-USGSD, and SCCC-MME. In addition to these five PM CAU models, two new revisions were developed, each based upon the LCCU1-MME (effectively the base case model). These new PM CAU flow models are presented in [Section 3.4](#).

### **3.4 Development of Alternative HFMs**

A preliminary assessment of PM CAU flow model behavior revealed that basin-scale convergent flow paths appreciably impact transport behavior. Specifically, particle flow paths originating from Area 19 and 20 sources converge when entering the extensive TMCM HSU, thereby increasing velocity and the rate of plume migration, and impacting related transport mechanisms such as matrix diffusion ( $D_m$ ). This section investigates the source and plausibility of the km-scale preferential flow, both of which are ultimately determined by hydrogeologic conceptualization and parameterization of the HFMs. These findings prompted the development of two new alternative PM CAU flow models, based on the LCCU1-MME alternative, named the LCCU1-MME-TMD and LCCU1-MME-TMCM alternatives for TMD and TMCM material property changes, respectively.





**Flow Model Calibration Metrics:**

Sum of squared weighted residuals (i.e., phi)  
 phi from observation well head  
 phi from observation spring head  
 phi from observation ET flux  
 phi from observation boundary edge flux

**Initial Calibration (SNJV, 2006a):**

= 16,594  
 = 8,069  
 = 1,302  
 = 3,441  
 = 3,780

**Recalibration:**

= 16,752  
 = 8,598  
 = 1,309  
 = 3,101  
 = 3,742

**Figure 3-25**  
**Well Head (m) Residuals before (left) and following (right) Recalibration of the LCCU1-MME Model after Fault Permeability Adjustments**

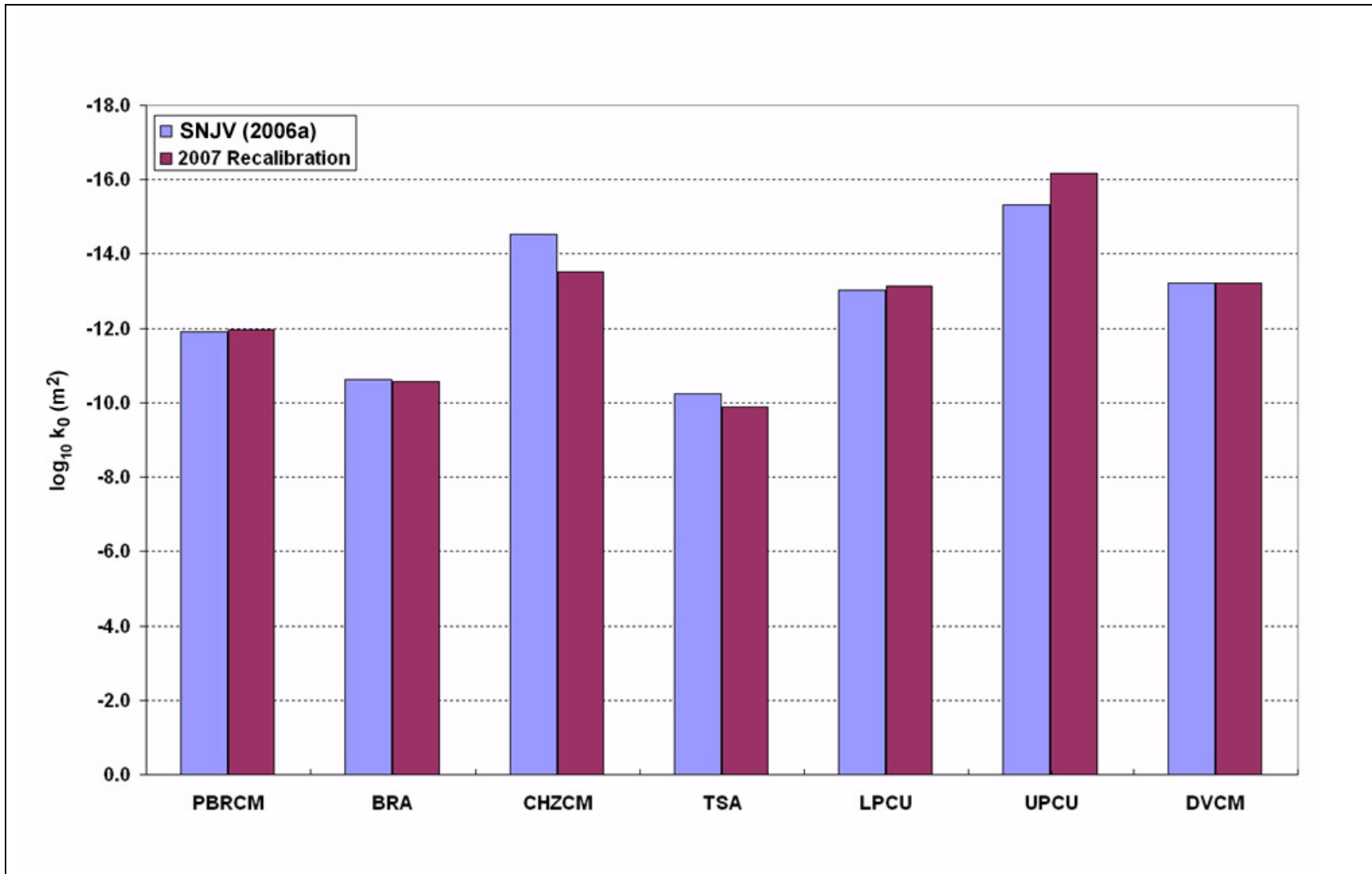


**Figure 3-26**

***HSU Permeabilities for the Initial (2006) and Revised (2007) Fault Assignment***

For the LCCU1-MME alternative model, HSU permeabilities are compared from the initial calibration (2006) versus those from the recalibration (2007) following the adjustment of southern Area 20 fault permeabilities.

Note: Only HSUs updated between the two calibrated versions are shown.

**Table 3-7**  
**Initial and Recalibrated Objective Function for the Alternative HFMs**

Alternative HFM	Initial Calibrated HFM Objective Function (-)	Fault-Adjusted, Recalibrated Objective Function (-)
LCCU1-MME	16,594	16,752
PZUP-MME	27,118	16,399
DRT-DRIA	38,205	32,892
LCCU1-MME-TMD	N/A	17,549
LCCU1-USGSD	10,303	10,472

N/A = Not applicable

### 3.4.1 Preferential Flow in the TMCM and Contiguous HSUs

Stoller-Navarro Joint Venture (2006a) reported that during model calibration the base flow model was particularly sensitive to the properties of the regionally extensive TMCM, comprised of TCU (altered tuffs and lavas), unaltered WTA, and a minor component of LFA. In order to better address the geologic heterogeneity that exists in the unit, the TMCM was areally subdivided within the base numerical model. Bechtel Nevada (2002a) suggested subdivision into eight hydrogeologic subdomains (Figure 3-27). While increasing the dimensionality of the parameter estimation problem permitted a better fit to observed data in the TMCM and beyond, the likelihood of parameter estimate uniqueness consequently decreased. The TMCM permeability insensitivity is quantitatively addressed in Section 8.0, and only alluded to in this section. However, PM CAU transport modeling before development of this alternative shows strong preferential flow and solute migration in the TMCM that is not necessarily supported by data and may be caused by TMCM parameter insensitivity.

Preferential pathways through the TMCM were identified during preliminary transport analysis. A comprehensive presentation of transport theory, analysis methodology and results are presented throughout the remainder of the document. In the preliminary transport analysis, the movement of a time-released conservative tracer from the complete set of Areas 19 and 20 sources was observed throughout the model domain over a 1,000-year interval. The LCCU1-MME alternative was selected for modification because of its high source (cavity) fluxes (described in Section 4.2) relative to the other models, thus making it the conservative choice.

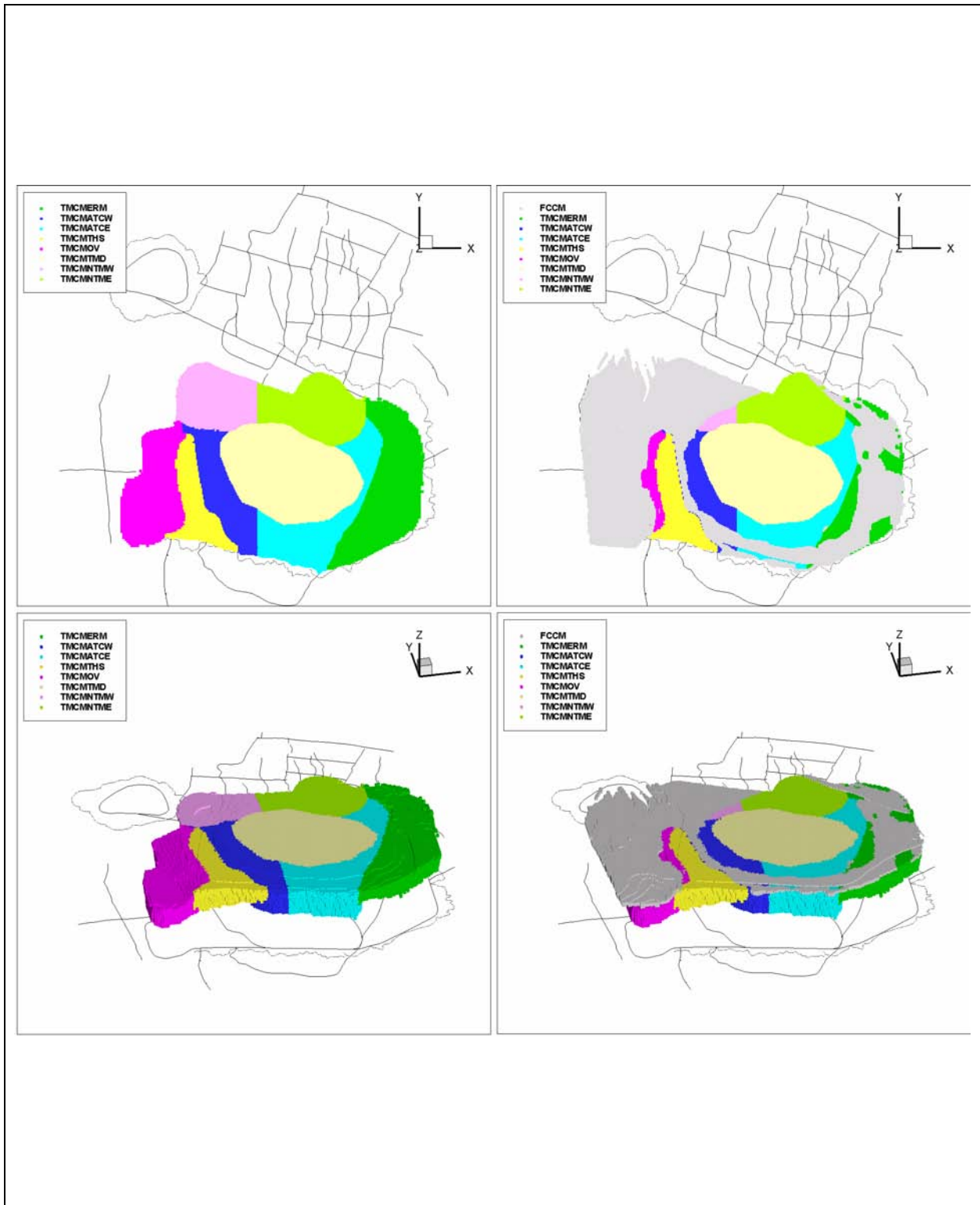
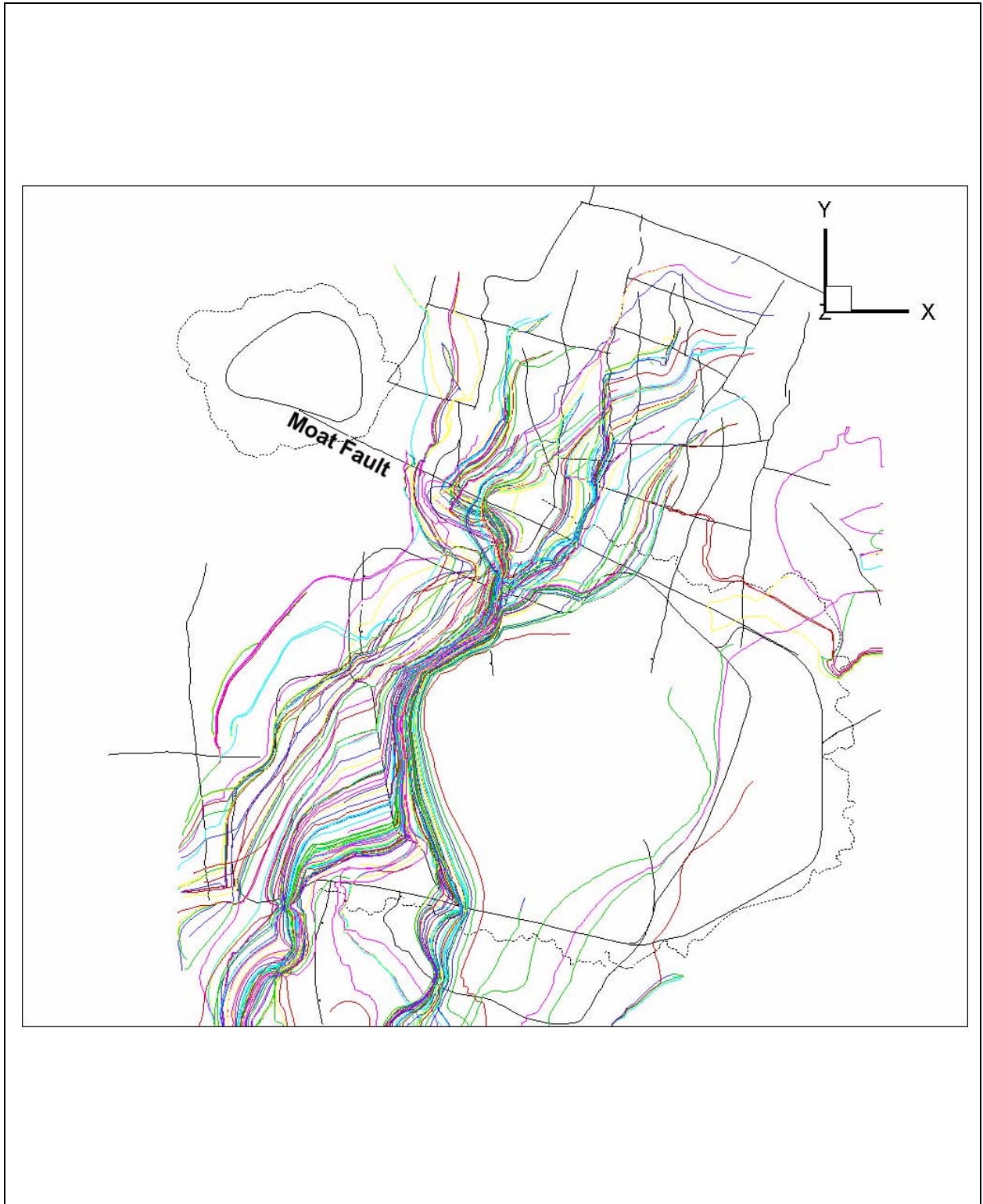


**Figure 3-27**  
**Hydrogeologic Subdomains of the TCMC in the Pahute Mesa Flow Model Area**  
 The subdomains exclude (left) and include (right) the FCCM HSU.

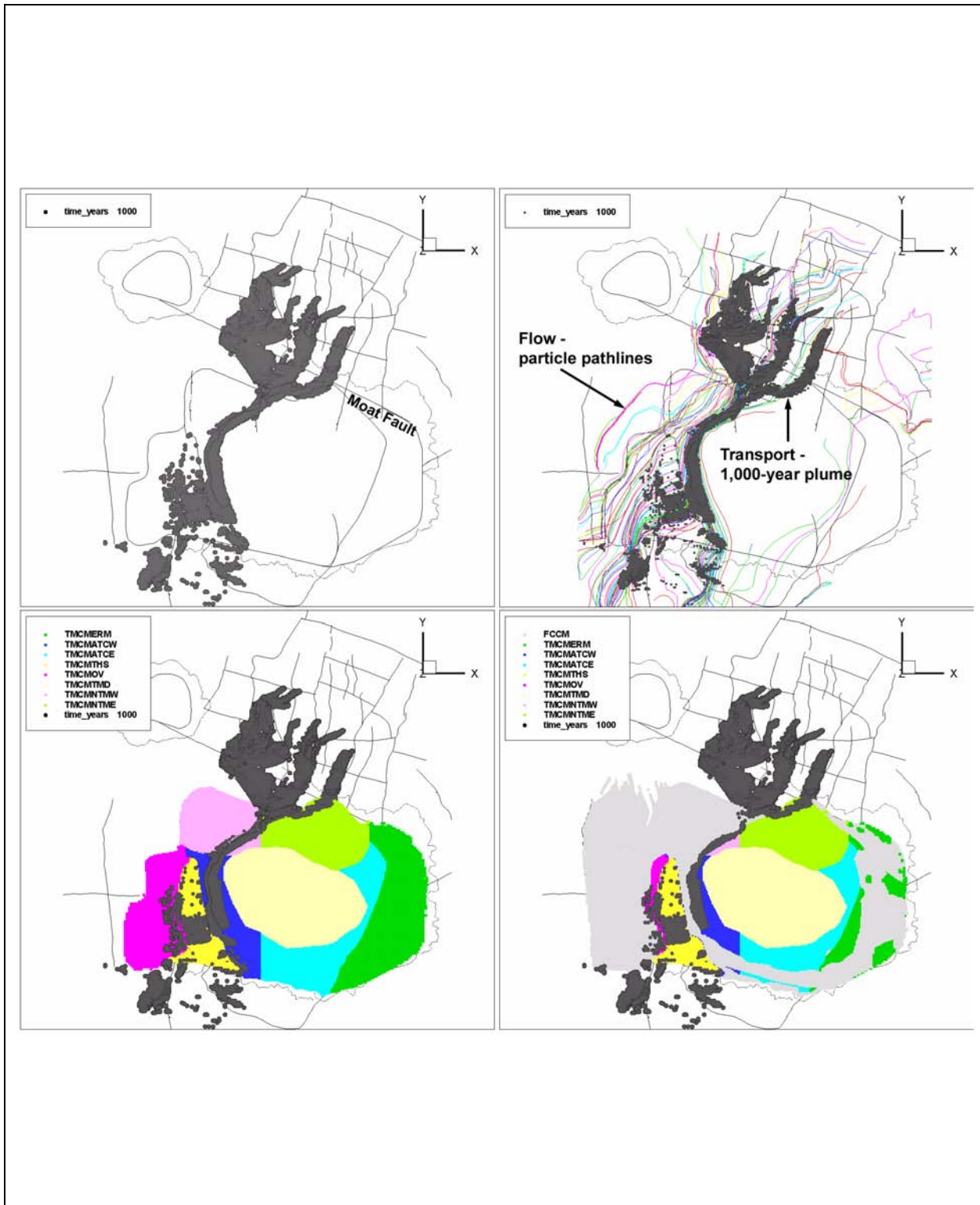
Figure 3-28 shows pathlines for particles released from each source HSU. Pathlines regionally converge just south of the Moat fault as they enter the TCMC. Looking to Figure 3-29, the convergence occurs directly north of the TCMCNTMW subdomain and the northwest corner of the overlying FCCM. Figure 3-29 also shows the 1,000-year tracer plume (in this case, defined as any model node with non-zero concentration) superimposed over both the flow pathlines and HSUs. The plume appropriately replicates the general flow paths, converging in the TCMC and entirely entering the TCMTCW, wherein it begins to disperse to the west.

Table 3-8 lists the permeability for each of the HSUs in Figure 3-29. Channelized flow results from the combined effect of low permeability in the FCCM (one of the dominant HSUs first encountered by the tracer once crossing the Moat fault), high permeability in the TCMATCW (which serves as the local conduit), recharge off of Timber Mountain, and depth decay in the FCCM and TCMC. Observe also that the plume bends east around the TCMCNTMW despite its high permeability, suggesting that some feature north of this HSU (such as inflow from the northwest) impacts flow. Regardless, the occurrence of such locally dominant preferential flow through such an extensive HSU, given its geologic and parametric uncertainty, raises the question of its plausibility when the geologic structure above the Timber Mountain caldera is expected to be as or more complex than on Pahute Mesa above the Silent Canyon caldera (Byers et al., 1989).

Continuing with this noted anomaly, Figure 3-30 shows that additional HSUs, local only to the area near southern Area 20, have a large impact on transport as a result of their geometry and location downgradient of the sources. The Fluorspar Canyon confining unit (FCCU) has a somewhat lens-shaped geometry, concave up with higher elevation, which appears to funnel the tracer plume eastward and then to the south almost directly north of Timber Mountain. The influence of its confining permeability is compounded by at least three additional HSUs. Partially enclosed as local, high-permeability flow conduits within the FCCU from the north are the TSA and BA. Thus, the permeability contrast between the FCCU and TSA/BA complement each other with respect to channeling of the plume. Further, the northern edge of the extensive, low-permeability TMA abuts the southwest edge of the FCCU, not only preventing flow/transport directly to the south into the TCMCNTMW as particles flow directly from the north, but also preventing flow/transport to the southwest down Thirsty Canyon. The permeabilities for these HSUs are listed in Table 3-8.



**Figure 3-28**  
**Convergent Flow Paths in the TCM as Particles Exit Areas 19 and 20**



**Figure 3-29**  
**Convergent Flow (Particle Pathlines) and Transport (Plume) Paths in the TMCM as Particles Exit Areas 19 and 20**

**Table 3-8**  
**HSU Permeability**

HSU ID	HSU	$\log_{10} k_0$ (m <sup>2</sup> )	HSU ID	HSU	$\log_{10} k_0$ (m <sup>2</sup> )	HSU ID	HSU	$\log_{10} k_0$ (m <sup>2</sup> )
25	TSA	-9.88	37	THCM	-12.88	73	TMCMOV	-10.76
26	LPCU	-13.14	38	THLFA	-11.78	74	TMCMTMD	-12.00
29	UPCU	-16.17	41	FCCM	-13.09	75	TMCMNTMW	-9.12
30	BA	-11.12	70	TMCMERM	-12.08	91	TMCMATCE	-10.54
34	FCCU	-12.98	71	TMCMATCW	-9.90	95	TMCMNTME	-10.65
36	TMA	-14.53	72	TMCMTHS	-11.68			

The occurrence of locally controlled preferential flow through an HSU as extensive as the TMCM, given its geologic and parametric uncertainty, certainly raises the question of its uniqueness.

Sections 3.4.2 and 3.4.3 explore two alternative HFMs that were developed to address geologic conceptualization through reparameterization of HSUs.

### **3.4.2 Development of the LCCU1-MME-TMD Alternative Model**

The first alternative developed addresses permeability beneath Timber Mountain, hence its name of the LCCU1-MME-TMD alternative. In all prior conceptualizations of Pahute Mesa flow, to some degree and by design, the effect of a recharge mound under Timber Mountain is incorporated. This feature is inferred and is only suggested by the observation well data; therefore, it is important to understand its impact on both the PM CAU flow and transport models. The impact on flow was addressed in SNJV (2006a) and is reiterated in Section 8.0 during discussion of transport sensitivity to TMCM permeability uncertainty. The preliminary analysis in SNJV (2006a) supported development of an alternative HFM in which an assumed recharge mound does not appreciably influence flow through the TMCM.

Development of the LCCU1-MME-TMD involved increasing only the permeability beneath Timber Mountain (i.e., the TMCMTMD subdivision) (Figure 3-27), relative to the calibrated LCCU1-MME flow model, by two orders of magnitude and then performing minor recalibration. Note that the fault permeability adjustments described in Section 3.3 were incorporated in this model. In all prior PM CAU flow models, including those based on the SCCC conceptualization, flow paths in the TMCM are focused on the northwest and northeast corners of Timber Mountain as they circumvent the subdomain. The goal of the LCCU1-MME-TMD alternative was therefore to assess the impact on



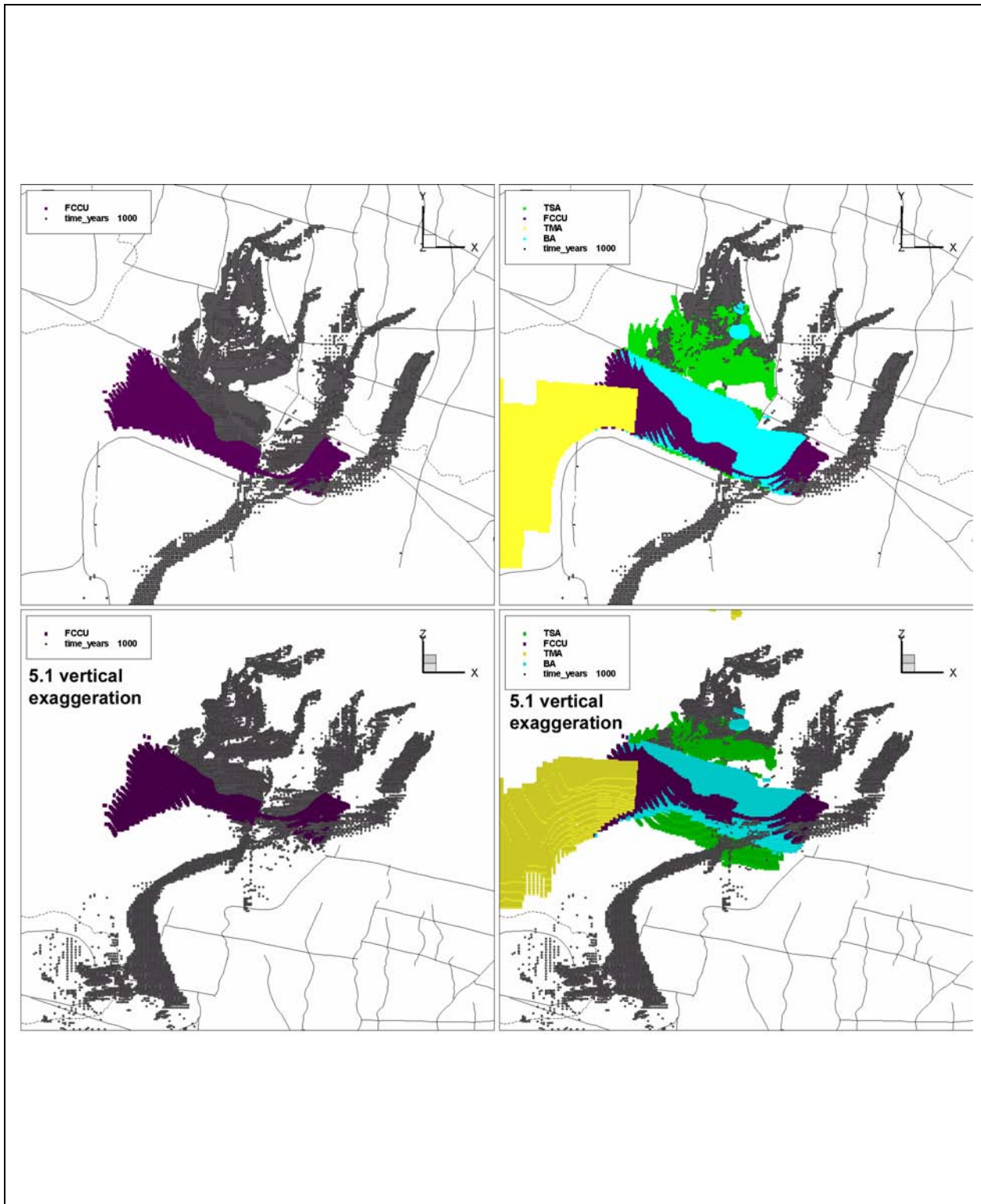


**Figure 3-30**  
**Plume Convergence upon Northern Entrance of the TCM**  
**as Tracer Particles Exit Areas 19 and 20**

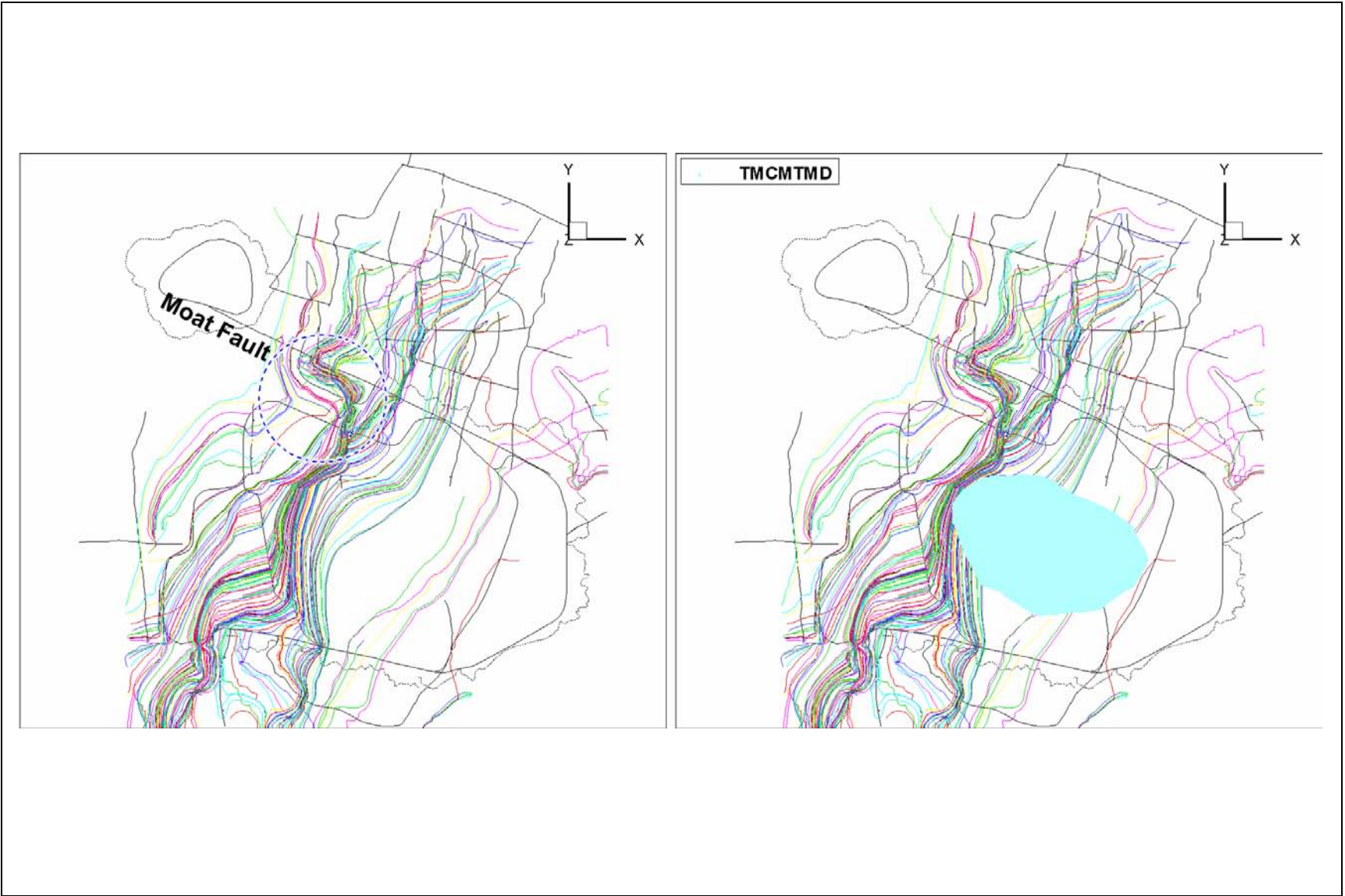
transport based on flow paths that are more diffuse through the Timber Mountain area as a result of a diminished recharge mound.

Figure 3-31 shows particle pathlines for the LCCU1-MME-TMD with the location of the TMCMTMD subdomain. The recharge mound appears completely diminished by the permeability increase; however, the influence of high recharge on the mountain may remain to a slight extent. Notice that convergent flow still occurs in the northwest corner of the TMCM, a feature addressed in Section 3.4.3, proving insensitive to TMCMTMD permeability given the global parameterization. Head residuals and related calibration metrics, shown in Figure 3-32, are approximately equivalent to those for the other alternatives.

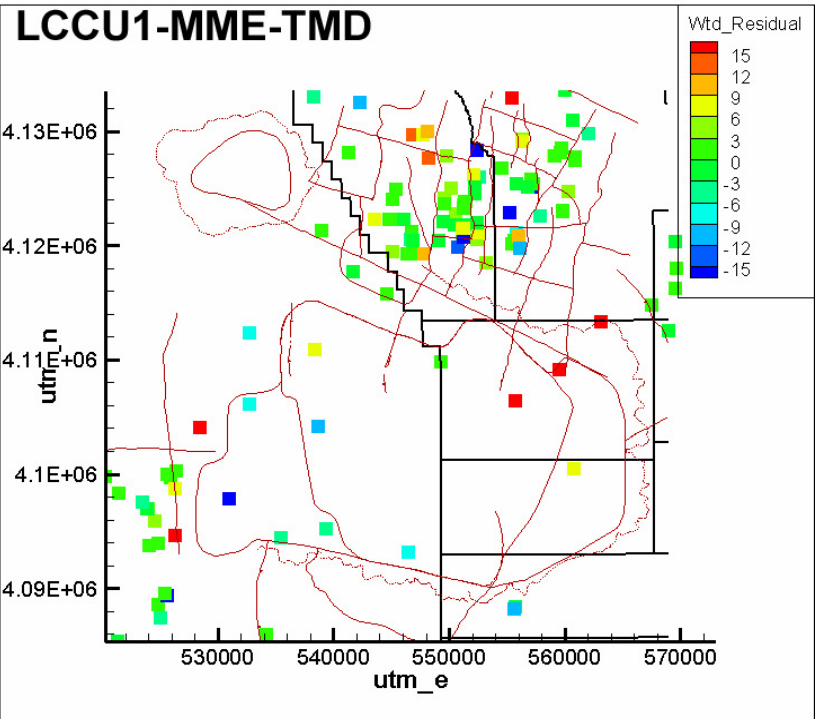
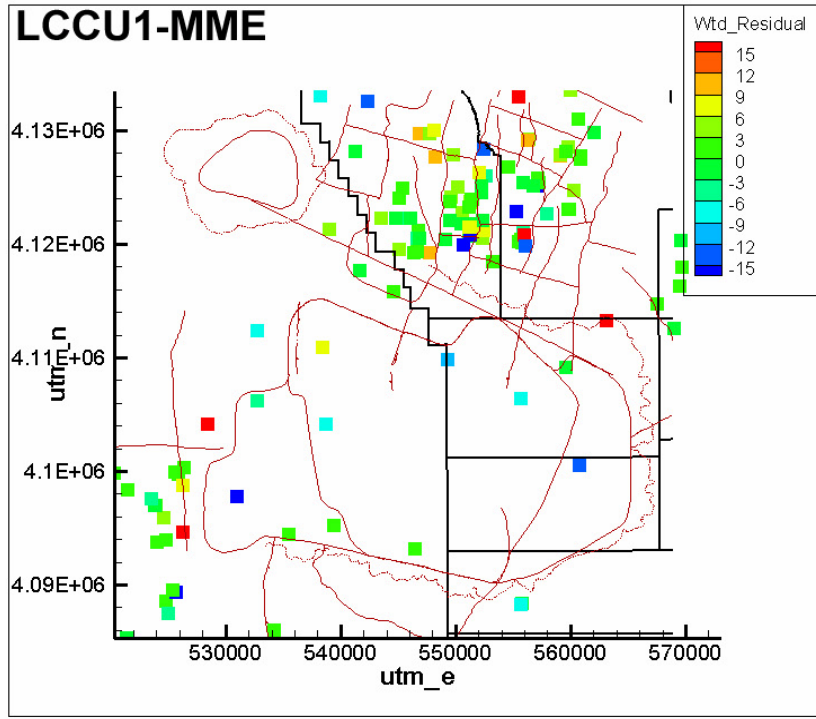
### **3.4.3 Development of the LCCU1-MME-TMCM Alternative Model**

The fundamental purpose behind development of the LCCU1-MME-TMCM alternative was to homogenize permeability, to the extent possible, within the TMCM subdivisions and adjacent HSUs to reduce modes of preferential flow. Section 3.4.1 describes the influence of HSU geometry (conceptualization) and permeability (parameterization) on plume migration. The features controlling flow and transport in the TMCM HSUs are poorly constrained through the process of flow model calibration and are instead almost totally derived from geologic interpretation. Therefore, outside of geologic judgment, there is little additional information available to determine whether these features are accurate. Because of their uncertainty and dominating influence on CAU transport, the affects of HSU parameterization were more closely examined through evaluation of this alternative PM CAU flow model.

Once crossing the Moat fault along some south-tending course, a tracer should move down one of three primary zones: southwest down Thirsty Canyon into Oasis Valley, south to the west of or below Timber Mountain into Oasis Valley or Beatty Wash, or to the east of Timber Mountain into Beatty Wash or down Fortymile Canyon. There is no evidence to argue that one path is favorable over another other than geographic location of the source term relative to each. In fact, the geochemical analysis (Kwicklis et al., 2005) indicates that ER-OV-1 in southern Thirsty Canyon has a component (up to 40 percent) of Area 20-type water. For development of a new alternative, the general strategy was to enable flow through each of these zones and to then recalibrate, maintaining such flows while honoring hydraulic targets. This involved, as shown in Section 3.4.1, permeability adjustment in the TMCM subdomains and adjacent HSUs, the set of which is listed in Table 3-9.



**Figure 3-31**  
**Streamlines through the LCCU1-MME-TMD Alternative HFM**



Flow Model Calibration Metrics:

Sum of squared weighted residuals (i.e., phi)  
 phi from observation well head  
 phi from observation spring head  
 phi from observation ET flux  
 phi from observation boundary edge flux

LCCU1-MME

= 16,752  
 = 8,598  
 = 1,309  
 = 3,101  
 = 3,742

LCCU1-MME-TMD

= 17,549  
 = 8,743  
 = 1,356  
 = 2,965  
 = 4,483

Figure 3-32

Comparison of Head (m) Residuals and Calibration Metrics between the LCCU1-MME and LCCU1-MME-TMD Alternative HFMs

**Table 3-9**  
**LCCU1-MME and Recalibrated LCCU1-MME-TMCM Permeabilities**

HSU	HSD ID	HSU Abbreviation	log <sub>10</sub> k <sub>0</sub> (m <sup>2</sup> )	
			LCCU1-MME	LCCU1-MME-TMCM
Calico Hills Vitric Composite Unit	22	CHVCM	-13.39	-14.12
Topopah Spring Aquifer	25	TSA	-9.88	-10.41
Lower Paintbrush Confining Unit	26	LPCU	-13.14	-11.02
Upper Paintbrush Confining Unit	29	UPCU	-16.17	-12.01
Benham Aquifer	30	BA	-11.12	-10.13
Fluorspar Canyon Composite Unit	34	FCCU	-12.98	-10.98
Timber Mountain Aquifer	36	TMA	-14.53	-10.61
Tannenbaum Hill Composite Unit	37	THCM	-12.88	-10.58
Tannenbaum Hill Lava-Flow Aquifer	38	THLFA	-11.78	-10.48
Timber Mountain Composite Unit Subdivision	70	TMCMERM	-12.08	-13.06
	73	TMCMOV	-10.76	-12.59
	75	TMCMNTMW	-9.12	-10.94
	90	TMCMATCE	-10.54	-9.77

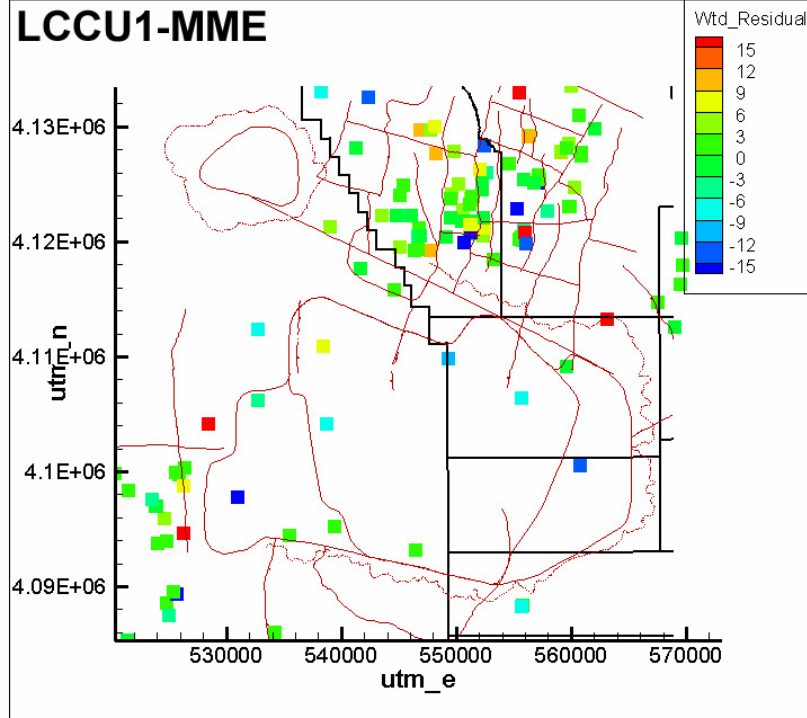
Of the HSUs listed, the FCCU, THCM, LPCU, UPCU, and TMA were identified as aquitards/confining units that required a significant increase in permeability to permit less channelized flow through the southern half of the model domain. The data that express hydraulic properties are of limited spatial density to support the parameterization of these HSUs as defined in the calibrated LCCU1-MME model. Therefore, their reparameterization is not unjustified. The following lists head observations, each unique to a single HSU, that were available for constraint during the recalibration:

- FCCU and THCM: No head observations.
- LPCU: U-20av provides water-level measurements exclusive to this unit.
- UPCU: Water-level measurements exclusive to the UPCU are collected at four boreholes, PM-3 (and piezometer PM-3-2), U-20as, U-20at, and U-20bc.
- TMA: Water-level measurements exclusive to the TMA are collected at ER-EC-4 (lower) near Thirsty Canyon and ER-OV-03c (and ER-OV-03c2).

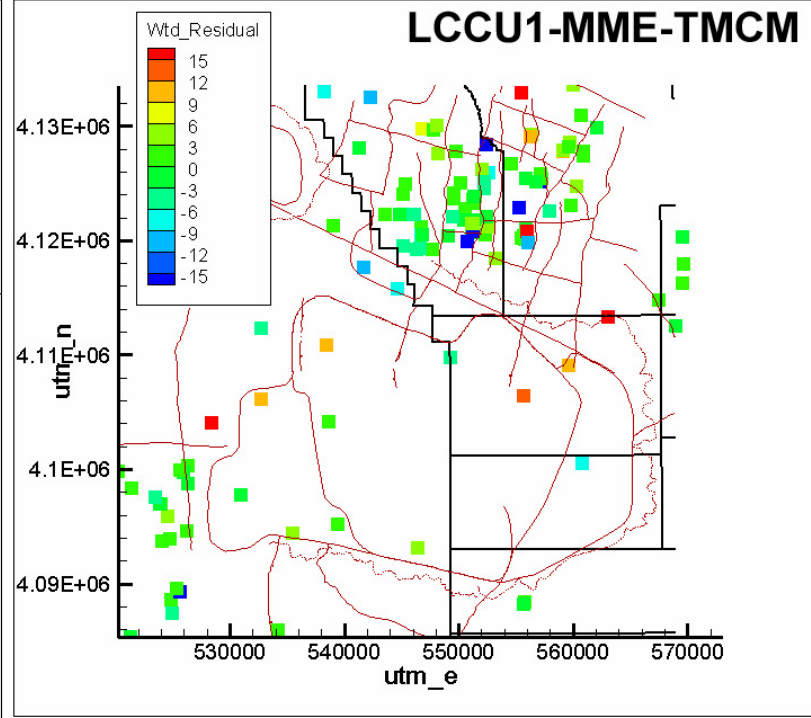
Several other composite-HSU water-level measurements were collected at boreholes intersecting these units. While useful in model calibration, the head contribution from each unit intersected cannot be isolated for the purpose of uniquely differentiating low- from high-permeability units (see SNJV [2006a] for permeability weighting in composite wells). [Table 3-9](#) lists the LCCU1-MME and recalibrated LCCU1-MME-TMCM permeabilities for those HSUs found sensitive in the area of the TMCM. [Figure 3-33](#) compares (weighted) head residuals and calibration metrics between the two alternatives. Components of the objective function between models are effectively equivalent with the exception of edge flows from the regional model, which deteriorated in the LCCU1-MME-TMCM, without appreciably affecting the previously calibrated head residuals. Residuals are small, within about  $\pm 5$  m, with the exception of U-20av in the LPCU ([Figure 3-34](#)). In this case, the increased LPCU permeability cannot support the high water level observed. However, given that such significant permeability adjustments (made initially to a calibrated model) have a negligible detrimental impact on head residuals, this indicates either a nontrivial region of parameter insensitivity or improper conceptualization of HSU location/geometry. For example, the UPCU, conceptualized as a confining unit, has a calibrated log permeability of -13.14 m<sup>2</sup> and -11.02 m<sup>2</sup> in the LCCU1-MME and LCCU1-MME-TMCM alternatives, respectively. This range is shown to span the threshold of a porous- to fracture-flow-dominated flow regime (see [Section 6.0](#)). Therefore, either insufficient data are available to accurately constrain this range, or the UPCU geometry relative to adjacent HSUs is improperly captured.

Particle pathlines, representing single particles released from each of the 82 sources, are shown in [Figure 3-35](#) for the calibrated LCCU1-MME-TMCM. Convergence is limited as particles cross the Moat fault and move through the FCCM and TMCM, still diverging around Timber Mountain because of its low permeability and high recharge. Note that there is flow down Thirsty Canyon and Fortymile Canyon, as well as across the width of the TMCM area. Note also those HSUs, previously defined as confining units, through which particles now flow. However, distinct channels still exist at FCCM-TMCM interface. This is because the FCCM, modeled as a single continuous material, requires lower permeability to maintain water levels at the few FCCM wells for which head data exist. Heterogeneity in this extensive unit is likely large in reality. Capturing components of hydrologic property variability within the FCCM zone could result in substantially less distinct

**LCCU1-MME**



**LCCU1-MME-TMCM**



Flow Model Calibration Metrics:

Sum of squared weighted residuals (i.e., phi)  
 phi from observation well head  
 phi from observation spring head  
 phi from observation ET flux  
 phi from observation boundary edge flux

LCCU1-MME

= 16,752  
 = 8,598  
 = 1,309  
 = 3,101  
 = 3,742

LCCU1-MME-TMCM

= 19,848  
 = 9,074  
 = 1,543  
 = 3,440  
 = 5,789

**Figure 3-33**

**Comparison of Head (m) Residuals and Calibration Metrics between the LCCU1-MME and LCCU1-MME-TMCM Alternative HFMs**

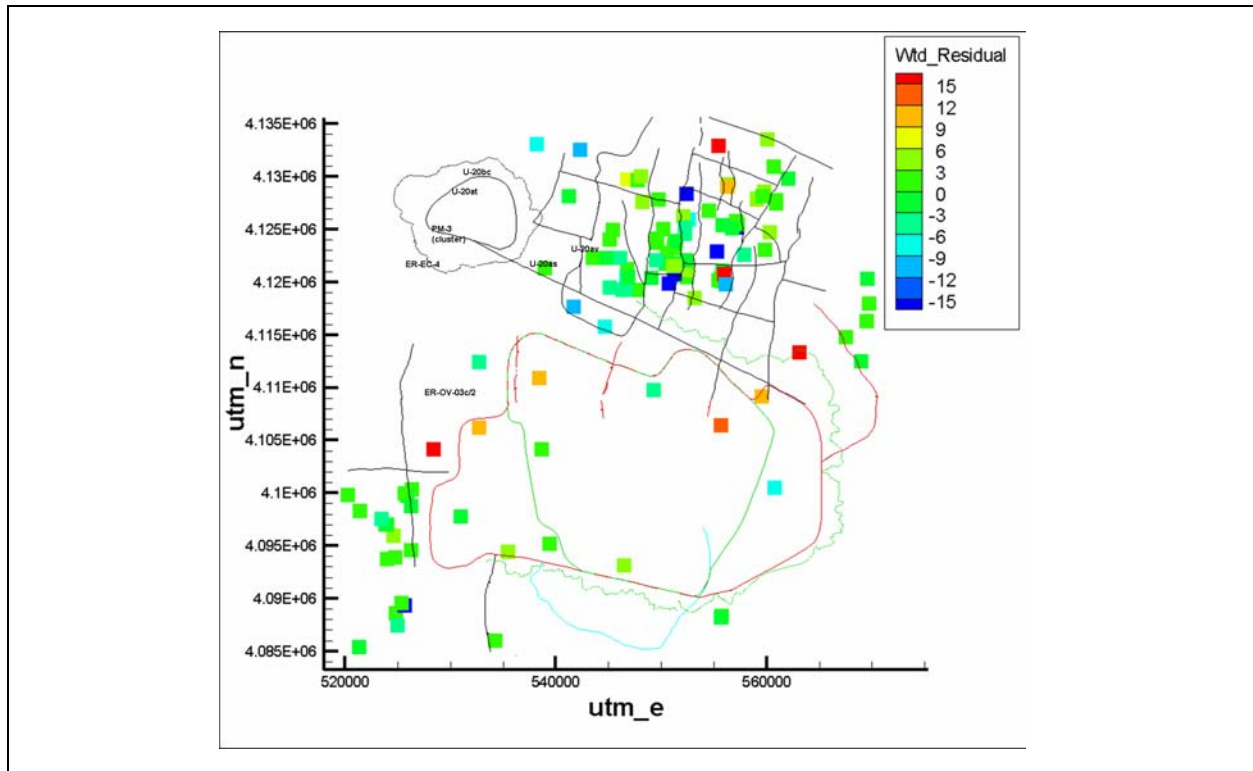


**Figure 3-34**  
**LCCU1-MME-TMCM Head (m) Residuals with Well Names**

boundaries between the TMCM and FCCM, which would then result in even less channeling. As will be shown in [Section 7.0](#), the reparameterized flow field that defines the LCCU1-MME-TMCM alternative proves to have a strong impact on radionuclide transport, naturally leading to a discussion of transport sensitivity to flow model uncertainty in [Sections 8.0](#) and [9.0](#).



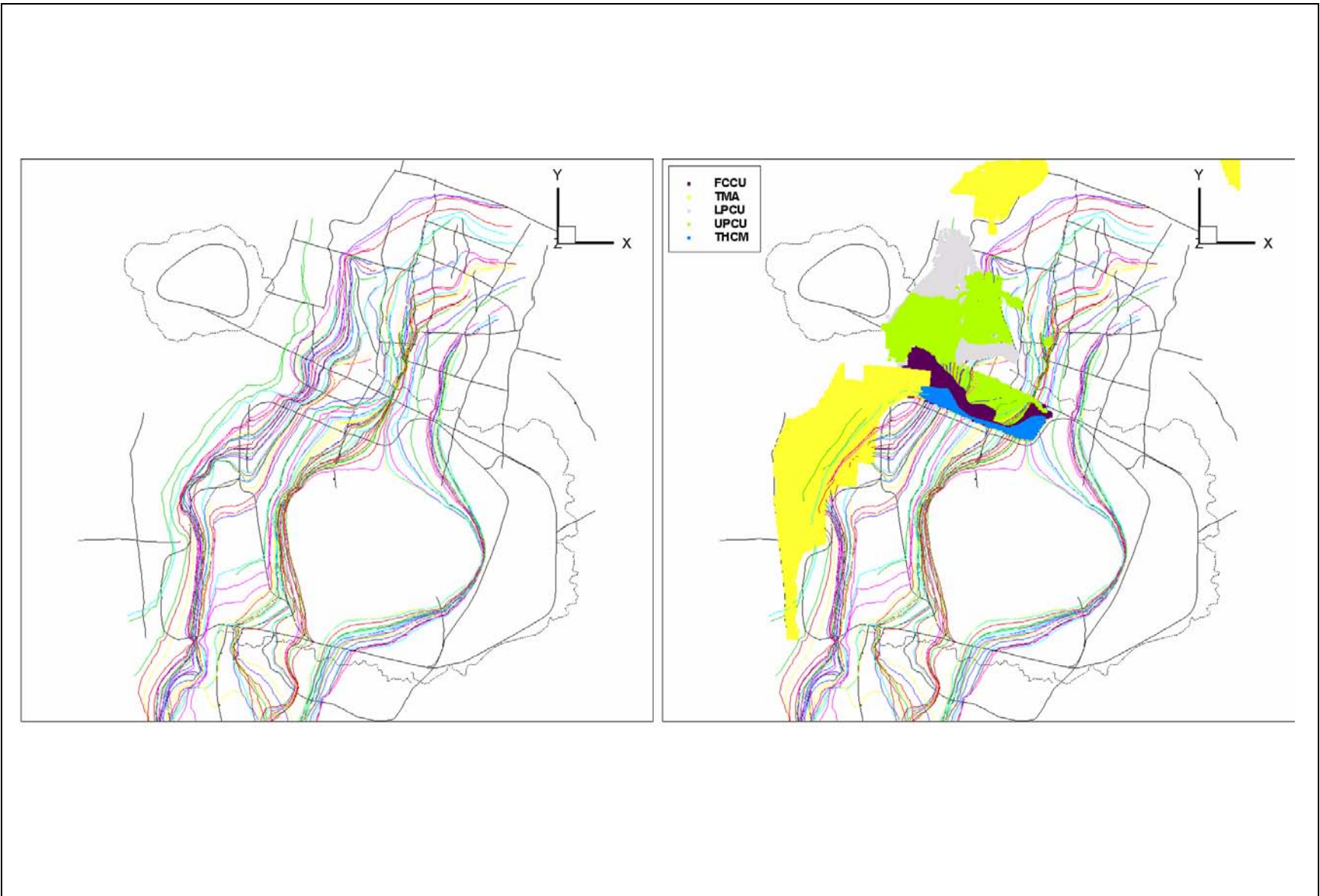


**Figure 3-35**  
**Primary HSUs Reparameterized for Development of the LCCU1-MME-TMCM Alternative HFM**

## **4.0 PAHUTE MESA SIMPLIFIED SOURCE MODEL**

The solute flux used by the PM CAU transport model was calculated through implementation of an SSM. A detailed discussion of the rationale for the SSM model, source term conceptualization, model design, component uncertainties, and verification of results through comparison with a detailed process model is provided in SNJV (2004e). The basic conceptual model is developed from phenomenological processes and relates to cavity size, disturbed zones, and distribution of radionuclides in the melt glass and cavity zones. Radionuclide mass for each test is based on total inventory for the CAU, as specified in Bowen et al. (2001), and the maximum reported yield for each test. The phenomenological model and inventory are used to construct a numerical, 1-D model of the processes of radionuclide mass flux from the cavity, melt glass, and disturbed zone to the outflow face that corresponds to the CAU-scale model cell face. Uncertain parameters are handled stochastically by sampling the parameter space for multiple realizations from which a statistical distribution of the system response can be derived. Fluid flux for each of the test cavities is calculated from groundwater flux derived from the PM CAU flow model, for each HFM. Matrix porosity and the sorption coefficient are both a function of the HGU, which is linked to mineralogy. Consequently, predicted radionuclide releases are integrally linked to the HGUs within which each test is performed.

### **4.1 Model Representation**

The SSM is used to estimate the RST, which provides the source of contaminants introduced to the PM CAU transport model. The SSM is used in place of a more detailed, 3-D process model that provides more detailed information but is also more computationally demanding and hence unsuitable for wide application as input to the PM CAU transport model, particularly for purposes of sensitivity and uncertainty analysis. This simplification constitutes a parallel computational technique that provides valuable insight into the important processes and uncertainty of the source term.

#### 4.1.1 Approach

Available information was reviewed and a methodology developed to estimate HSTs for Central and Western Pahute Mesa CAUs 101 and 102 in SNJV (2004e). This estimate was based on a process model representation of the near-field source term releases from the CHESHIRE test (Pawloski et al., 2001). The process model was further abstracted to provide a more tractable source term for the PM CAU transport model that is the subject of this report. The process of model abstraction is defined as “a methodology for reducing the complexity of a simulation model while maintaining the validity of the simulation results with respect to the question that the simulation is being used to address” (Frantz, 1995). Model abstraction reduces the complexity of the system to be simulated to its essential components and processes. This section provides a summary of the important components of the SSM.

#### 4.1.2 Conceptualization and Dimensions of the Source Region

The source region is conceptualized as two volumes: an exchange volume and a nuclear melt glass zone (MGZ). The exchange volume consists of the cavity zone (i.e., the cavity excluding the nuclear MGZ) and the disturbed zone around the cavity (Figure 4-1). The nuclear MGZ consists of the nuclear melt glass along with collapsed rock at the bottom of the cavity. The cavity and disturbed zones are idealized as spherical volumes, centered on the working point.

The radii of the cavity and the disturbed zone are often determined as a function of yield. Pawloski (1999) gives a standard equation for calculating the spherical cavity zone radius  $R_C$  in meters as a function of test yield:

$$R_C = \frac{70.2(Y)^{1/3}}{(\rho_b DOB)^{1/4}} \quad (4-1)$$

where:

$Y$  = Yield, kilotons

$\rho_b$  = Bulk density of the overlying rock, grams per cubic centimeter (g/cm<sup>3</sup>)

$DOB$  = Depth of burial, meters

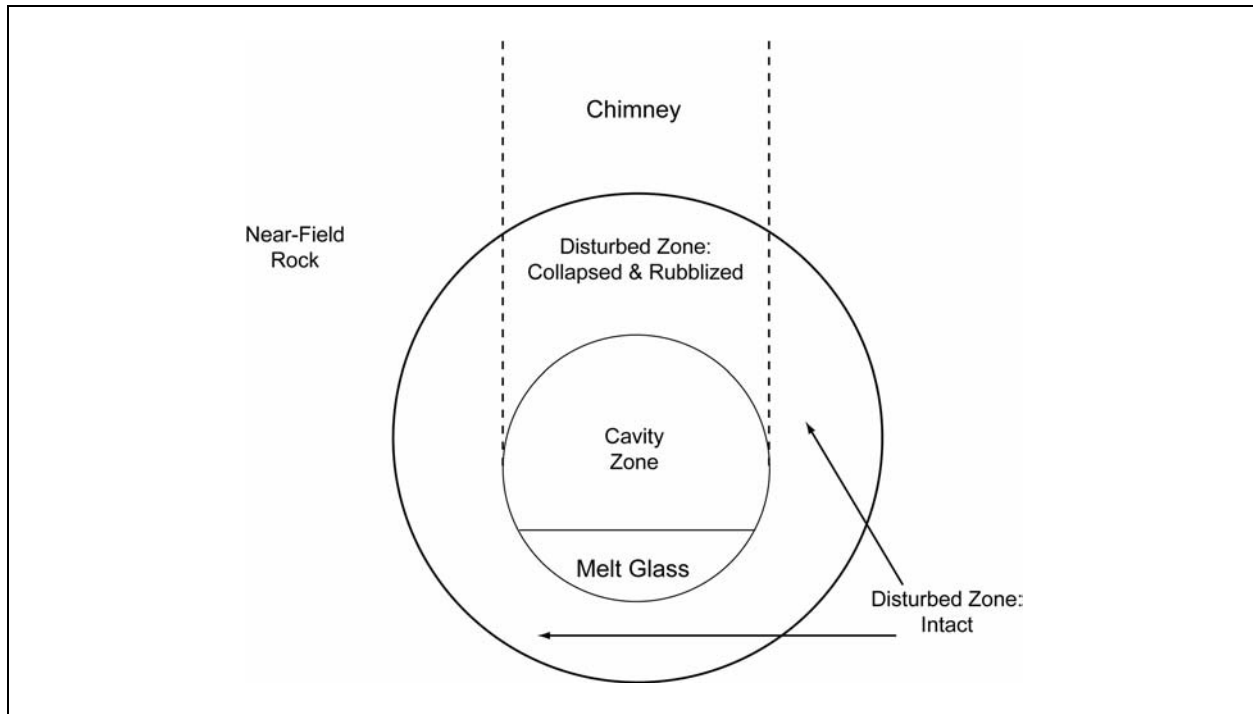


**Figure 4-1**  
**Schematic Diagram of the Source Term Regions in the HST Model and the SSM**  
 Source: SNJV, 2004e

The spherical disturbed zone radius  $R_{EV}$  is estimated from the expression:

$$R_{EV} = MR_C \quad (4-2)$$

where  $M$  is the exchange volume multiplier. The values of the cavity radius and the exchange volume multiplier are uncertain with parameter distributions from SNJV (2004e) and defined in [Table 4-1](#).

**Table 4-1**  
**Cavity Geometry Parameters**

Parameter	Distribution	Mean	SD	Lower Limit	Upper Limit
Cavity Radius (impacts exchange volume, cavity volume, and melt glass volume) <sup>a</sup>	Truncated Normal	1.5	0.2	1.3	2.0
Melt Glass Multiplier <sup>b</sup>	Uniform	--	--	700	1,300

<sup>a</sup> Source: Borg et al., 1976

<sup>b</sup> Source: Tompson et al., 1999

-- = Not applicable

The volume of the melt glass remaining on the bottom of the cavity zone is estimated on the basis of 700 metric tons of melt glass produced per kiloton of yield. The volume of the melt glass is calculated, based on a density of 2,500 kilograms per cubic meter ( $\text{kg/m}^3$ ) and a porosity of 20 percent, as:

$$V_{MG} = \frac{M_{MG}}{(1 - \phi_{MG})\rho_{MG}} = 1.75 \times 10^5 \text{ m}^3 \quad (4-3)$$

where:

$M_{MG}$  = Mass of melt glass, kilograms

$\phi_{MG}$  = Porosity, 0.20 (dimensionless)

$\rho_{MG}$  = Density of the melt glass, 2,500  $\text{kg/m}^3$

The melt glass parameters are identical for the process model and for the SSM. Finally, the process model assumes that the cavity is centered 16 m below the center of the disturbed zone. This shift affects the volumes of the intact disturbed zone and the rubblized disturbed zone, but not that of the cavity or of the melt glass.

### 4.1.3 Inventory

Characteristics of the underground nuclear shaft tests conducted in Areas 19 and 20 on Central and Western Pahute Mesa are listed in [Tables 4-2 and 4-3](#), including test names, dates, locations, yield range, water level, and working point information. A comprehensive unclassified inventory of the RST for the NTS is provided in Bowen et al. (2001). This inventory provides an estimate of radioactivity remaining underground at the NTS after nuclear testing. The inventory was subdivided into five areas roughly corresponding to the UGTA CAUs and includes  $^3\text{H}$ , fission products, unspent fuel materials, and activation products. This list consists of 43 radiological contaminants with half-lives greater than 10 years (with the exception of  $^{154}\text{Eu}$ ).

This inventory also includes naturally occurring radioactive isotopes ( $^{40}\text{K}$ ,  $^{232}\text{Th}$ ,  $^{234}\text{U}$ ,  $^{235}\text{U}$ , and  $^{238}\text{U}$ ) and represents the amount in the rock that was melted during the detonation. The source of  $^{40}\text{K}$  is natural, whereas the others ( $^{232}\text{Th}$ ,  $^{234}\text{U}$ ,  $^{235}\text{U}$ , and  $^{238}\text{U}$ ) are naturally occurring as well as a device component (Bowen et al., 2001). From this information, a total inventory for Areas 19 and 20 is

**Table 4-2**  
**Underground Shaft Nuclear Tests Conducted in Central Pahute Mesa (CAU 101)**  
 (Page 1 of 3)

Test Name <sup>a</sup>	Hole Name <sup>a</sup>	CAS No. <sup>b</sup>	Easting <sup>c</sup> (m)	Northing <sup>c</sup> (m)	Test Date <sup>a</sup>	Yield Range <sup>a</sup> (kt)	Calculated Cavity Radius <sup>d</sup> (m)	Land Surface Elevation <sup>c</sup> (m amsl)	Water Level Elevation <sup>e</sup> (m amsl)	Working Point		
										Elevation <sup>f</sup> (m amsl)	HGU <sup>g</sup>	HSU <sup>h</sup>
ALAMO	U19au	19-57-014	555278.488	4122855.75	07/07/1988	<150	61	1,992	1,366	1,369	LFA	CHVCM
ALMENDRO	U19v	19-57-033	558003.07	4122055.1	06/06/1973	200-1,000	101	2,096	1,389	1,029	TCU	BFCU
AMARILLO	U19ay	19-57-016	557311.377	4125422.57	06/27/1989	20-150	61	2,046	1,398	1,406	LFA	PLFA
BACKBEACH	U19x	19-57-034	556020.555	4120757.93	04/11/1978	20-150	60	2,067	1,361	1,395	LFA	PLFA
BARNWELL	U20az	20-57-026	552392.361	4120468.47	12/08/1989	20-150	62	2,003	1,340	1,403	TCU	CHZCM
BEXAR	U19ba	19-57-019	560899.236	4127735.55	04/04/1991	20-150	61	2,145	1,454	1,515	LFA	KA
BODIE	U20ap	20-57-018	552166.918	4124002.43	12/13/1986	20-150	61	2,018	1,359	1,383	TCU	CHVCM
BOXCAR	U20i	20-57-039	548242.936	4127580.93	04/26/1968	1,300	108	1,942	1,356	776	LFA	CFCM
BULLION	U20bd	20-57-030	551420.292	4123847.44	06/13/1990	20-150	60	1,977	1,356	1,303	TCU	CHZCM
CABRA	U20aj	20-57-012	547855.419	4128161.88	03/26/1983	20-150	63	1,934	1,358	1,391	LFA	CHZCM
CAMEMBERT	U19q	19-57-030	555976.596	4125798.46	06/26/1975	200-1,000	96	2,060	1,401	748	TCU	BFCU
CHANCELLOR	U19ad	19-57-004	557182.928	4125122.57	09/01/1983	143	60	2,040	1,396	1,416	LFA	PLFA
CHARTREUSE	U19d	19-57-022	560056.499	4133488.76	05/06/1966	73	47	2,091	1,450	1,424	WTA	BRA
CHESHIRE	U20n	20-57-041	551424.352	4121743.06	02/14/1976	200-500	78	1,974	1,344	807	LFA	CHZCM
COLBY	U20aa	20-57-003	546837.431	4128745.18	03/14/1976	500-1,000	96	1,931	1,362	659	TCU	CFCM
COLWICK	U20ac	20-57-005	551226.464	4122384.41	04/26/1980	20-150	61	1,973	1,348	1,340	LFA	CHZCM
COMSTOCK	U20ay	20-57-025	549562.425	4123673.3	06/02/1988	<150	61	1,988	1,355	1,367	LFA	CHZCM
CONTACT	U20aw	20-57-024	552097.886	4126211.4	06/22/1989	20-150	63	2,007	1,364	1,463	LFA	CHZCM
CYBAR	U19ar	19-57-012	557127.293	4125777.83	07/17/1986	119	57	2,044	1,401	1,417	LFA	PLFA
DURYEA	U20a1	20-57-002	550480.647	4121740.04	04/14/1966	70	49	1,987	1,329	1,443	LFA	CHZCM
EGMONT	U20aL	20-57-014	544546.024	4124748.04	12/09/1984	20-150	63	1,867	1,323	1,320	VTA	PVTA
EMMENTHAL	U19t	19-57-031	562271.495	4126843.29	11/02/1978	<20	32	2,131	1,461	1,554	LFA	KA
ESTUARY	U19g	19-57-025	556340.474	4129243.99	03/09/1976	200-500	84	2,052	1,430	1,196	TCU	BFCU
FARM	U20ab	20-57-004	552284.421	4125160.47	12/16/1978	20-150	60	2,006	1,368	1,317	TCU	CHVCM
FONDUTTA	U19zs	19-57-036	559673.51	4128120.36	04/11/1978	20-150	61	2,099	1,449	1,466	TCU	BFCU
GALVESTON	U19af	19-57-006	556079.061	4121450.46	09/04/1986	<20	33	2,045	1,365	1,558	LFA	PLFA

**Table 4-2**  
**Underground Shaft Nuclear Tests Conducted in Central Pahute Mesa (CAU 101)**  
 (Page 2 of 3)

Test Name <sup>a</sup>	Hole Name <sup>a</sup>	CAS No. <sup>b</sup>	Easting <sup>c</sup> (m)	Northing <sup>c</sup> (m)	Test Date <sup>a</sup>	Yield Range <sup>a</sup> (kt)	Calculated Cavity Radius <sup>d</sup> (m)	Land Surface Elevation <sup>c</sup> (m amsl)	Water Level Elevation <sup>e</sup> (m amsl)	Working Point		
										Elevation <sup>f</sup> (m amsl)	HGU <sup>g</sup>	HSU <sup>h</sup>
GIBNE	U20ah	20-57-010	551224.787	4123206.53	04/25/1982	20-150	63	1,964	1,351	1,395	TCU	CHZCM
GREELEY	U20g	20-57-037	552440.188	4128343.51	12/20/1966	870	93	1,972	1,368	756	TCU	BFCU
HALFBEAK	U19b	19-57-018	562117.382	4129932.93	06/30/1966	365	77	2,070	1,448	1,251	WTA	BRA
HARDIN	U20av	20-57-023	551172.747	4120677.79	04/30/1987	20-150	61	1,970	1,326	1,345	TCU	LPCU
HARZER	U19aj	19-57-008	559768.325	4128539.07	06/06/1981	20-150	61	2,100	1,446	1,463	TCU	BFCU
HOSTA	U19ak	19-57-009	560573.909	4133490.59	02/12/1982	20-150	61	2,102	1,443	1,463	LFA	BRA
HOUSTON	U19az	19-57-017	555779.157	4120082.43	11/14/1990	20-150	62	2,058	1,355	1,464	LFA	PLFA
HOYA	U20be	20-57-031	550733.503	4119853.2	09/14/1991	20-150	60	1,979	1,315	1,321	TCU	CHZCM
INLET	U19f	19-57-024	556107.38	4119811.47	11/20/1975	200-1,000	108	2,053	1,352	1,234	TCU	CHCU
JEFFERSON	U20ai	20-57-011	549637.352	4124115.4	04/22/1986	20-150	62	1,982	1,356	1,375	LFA	CHZCM
JORUM	U20e	20-57-035	547789.21	4129655.07	09/16/1969	<1,000	99	1,925	1,365	766	TCU	CHZCM
JUNCTION	U19bg	19-57-020	556762.545	4125085.14	03/26/1992	20-150	61	2,040	1,394	1,418	LFA	PLFA
KAPPELI	U20am	20-57-015	552255.845	4124536	07/25/1984	20-150	61	2,010	1,361	1,369	LFA	CHVCM
KASH	U20af	20-57-008	548415.607	4126054.29	06/12/1980	20-150	61	1,938	1,349	1,294	LFA	CHZCM
KASSERI	U20z	20-57-046	552160.289	4127007.85	10/28/1975	200-1,000	97	1,984	1,366	719	TCU	BFCU
KEARSARGE	U19ax	19-57-015	561462.535	4127859.12	08/17/1988	100-150	61	2,129	1,454	1,514	LFA	KA
KERNVILLE	U20ar	20-57-020	546832.3	4129681.86	02/15/1988	20-150	63	1,926	1,373	1,384	VTA	PVTA
LABQUARK	U19an	19-57-010	561381.251	4128183.06	09/30/1986	20-150	61	2,127	1,453	1,511	LFA	KA
LOCKNEY	U19aq	19-57-011	555471.477	4120144.12	09/24/1987	20-150	61	2,072	1,354	1,458	LFA	PLFA
MAST	U19u	19-57-032	560207.323	4133751.35	06/19/1975	200-1,000	105	2,095	1,444	1,184	LFA	BRA
MONTELLO	U20bf	20-57-032	549522.46	4122042.6	04/16/1991	20-150	61	1,988	1,341	1,346	TCU	CHZCM
MUENSTER	U19e	19-57-023	559100.938	4127774.92	01/03/1976	200-1,000	93	2,109	1,442	657	WTA	BRA
NEBBIOLO	U19ae	19-57-005	555867.135	4121059.06	06/24/1982	20-150	61	2,065	1,361	1,426	LFA	PLFA
PANIR	U19ys	19-57-035	556975.703	4125472.58	08/31/1978	20-150	60	2,040	1,398	1,359	LFA	PLFA
PEPATO	U20ad	20-57-006	548286.316	4126944.52	06/11/1979	20-150	60	1,940	1,356	1,258	TCU	CHZCM
PIPKIN	U20b	20-57-027	549594.537	4123294.03	10/08/1969	200-1,000	115	1,992	1,354	1,368	LFA	CHZCM

**Table 4-2**  
**Underground Shaft Nuclear Tests Conducted in Central Pahute Mesa (CAU 101)**  
 (Page 3 of 3)

Test Name <sup>a</sup>	Hole Name <sup>a</sup>	CAS No. <sup>b</sup>	Easting <sup>c</sup> (m)	Northing <sup>c</sup> (m)	Test Date <sup>a</sup>	Yield Range <sup>a</sup> (kt)	Calculated Cavity Radius <sup>d</sup> (m)	Land Surface Elevation <sup>c</sup> (m amsl)	Water Level Elevation <sup>e</sup> (m amsl)	Working Point		
										Elevation <sup>f</sup> (m amsl)	HGU <sup>g</sup>	HSU <sup>h</sup>
POOL	U19p	19-57-029	559541.604	4123266.91	03/17/1976	200-500	84	2,103	1,413	1,222	TCU	BFCU
REX	U20h(e)	20-57-038	550196.529	4124975.16	02/24/1966	19	30	1,999	1,357	1,327	TCU	CHZCM
RICKEY	U19c	19-57-021	560769.426	4124276.51	06/15/1968	20-200	66	2,143	1,435	1,460	VTA	CHVTA
SCOTCH	U19as	19-57-013	555856.824	4125370.82	05/23/1967	155	55	2,061	1,395	1,083	TCU	CFCU
SCROLL	U19n	19-57-028	555314.008	4132315.3	04/23/1968	<20	40	2,059	1,456	1,833	CHVCM	VTA
SERENA	U20an	20-57-016	549804.18	4127791.81	07/25/1985	20-150	62	1,970	1,359	1,372	LFA	CHZCM
SERPA	U19ai	19-57-007	560675.009	4130919.1	12/17/1980	20-150	63	2,055	1,444	1,482	TCU	BFCU
SHEEPSHEAD	U19aa	19-57-001	556415.668	4120269.64	09/26/1979	20-150	61	2,060	1,361	1,420	LFA	PLFA
SLED	U19i	19-57-026	557922.096	4122637.74	08/29/1968	20-200	65	2,084	1,396	1,355	TCU	CFCU
STINGER	U19l	19-57-027	561067.775	4131788.33	03/22/1968	20-200	66	2,062	1,442	1,394	LFA	BRA
TIERRA	U19ac	19-57-003	561575.056	4126107.67	12/15/1984	20-150	61	2,145	1,459	1,505	LFA	KA
TOWANDA	U19ab	19-57-002	559842.413	4122993.41	05/02/1985	20-150	60	2,112	1,415	1,451	TCU	BFCU

Source: SNJV, 2004e

<sup>a</sup> Source: DOE/NV, 2000d

<sup>b</sup> Source: FFACO (1996, as amended February 2008)

<sup>c</sup> Source: UGTA Borehole Project Index (in UTM, Zone 11, NAD 27)

<sup>d</sup> Calculated Cavity Radius =  $[70.2 * (y)^{1/3}] / (\rho_b * DOB)^{1/4}$  where y = yield of the test (kt),  $\rho_b$  = bulk density of the overburden (g/cm<sup>3</sup>), and DOB the working point (m) (taken from Pawloski, 1999); cavity radius calculation uses maximum yield of the yield range.

<sup>e</sup> Source: BN, 2002a

<sup>f</sup> Working Point Elevation = Land Surface Elevation - Working Point Depth (taken from Pawloski, 2004)

<sup>g</sup> Hydrogeologic unit (see [Appendix A](#)); BN, 2002a

<sup>h</sup> Hydrostratigraphy (see [Appendix A](#)); BN, 2002a

g/cm<sup>3</sup> = Grams per cubic centimeter

kt = Kiloton



**Table 4-3**  
**Underground Shaft Nuclear Tests Conducted in Western Pahute Mesa (CAU 102)**

Test Name <sup>a</sup>	Hole Name <sup>a</sup>	CAS No. <sup>b</sup>	Easting <sup>c</sup> (m)	Northing <sup>c</sup> (m)	Test Date <sup>a</sup>	Yield Range <sup>a</sup> (kt)	Calculated Cavity Radius <sup>d</sup> (m)	Land Surface Elevation <sup>c</sup> (m amsl)	Water Level Elevation <sup>e</sup> (m amsl)	Working Point		
										Elevation <sup>f</sup> (m amsl)	HGU <sup>g</sup>	HSU <sup>h</sup>
BELMONT	U20as	20-57-021	547764.676	4119233.62	10/16/1986	20-150	62	1,898	1,289	1,293	TCU	UPCU
BENHAM	U20c	20-57-033	546698.659	4120477.68	12/19/1968	1150	99	1,914	1,285	512	TCU	CHZCM
BUTEO	U20a	20-57-001	550480.647	4121740.04	05/12/1965	<20	30	1,987	1,339	1,292	TCU	CHZCM
CHATEAUGAY	U20t	20-57-043	545866.189	4122030.04	06/28/1968	20-200	68	1,903	1,287	1,296	LFA	BA
DARWIN	U20aq	20-57-019	544396.119	4124138.08	06/25/1986	20-150	63	1,876	1,315	1,327	TCU	UPCU
DELAMAR	U20at	20-57-022	543533.91	4122280.83	04/18/1987	20-150	63	1,902	1,297	1,358	TCU	UPCU
FONTINA	U20f	20-57-036	545355.123	4124900.2	02/12/1976	200-1,000	98	1,864	1,326	646	TCU	CHZCM
GOLDSTONE	U20ao	20-57-017	546767.795	4121180	12/28/1985	20-150	63	1,914	1,287	1,365	LFA	BA
HANDLEY	U20m	20-57-040	541289.565	4128104.3	03/26/1970	>1,000	98	1,799	1,041	590	TCU	PBRCM
HORNITOS	U20bc	20-57-029	545158.173	4123977.74	10/31/1989	20-150	63	1,873	1,306	1,309	VTA	PVTA
KNICKERBOCKER	U20d	20-57-034	546102.61	4122300.85	05/26/1967	76	49	1,906	1,293	1,273	LFA	BA
MOLBO	U20ag	20-57-009	547671.959	4119690.06	02/12/1982	20-150	61	1,900	1,290	1,262	LFA	BA
PURSE	U20v	20-57-044	544266.773	4126168.56	05/07/1969	20-200	68	1,856	1,351	1,257	TCU	UPCU
SALUT	U20ak	20-57-013	545315.269	4122286.8	06/12/1985	20-150	62	1,900	1,288	1,292	LFA	BA
STILTON	U20p	20-57-042	542263.782	4132499.92	06/03/1975	20-200	65	1,695	1,423	963	UNK	PBRCM
TAFI	U20ae	20-57-007	546343.106	4123232	07/25/1980	20-150	60	1,886	1,302	1,206	VTA	PVTA
TENABO	U20bb	20-57-028	544857.893	4122285.19	10/12/1990	20-150	62	1,898	1,289	1,298	VTA	PVTA
TYBO	U20y	20-57-045	546651.338	4119290.95	05/14/1975	200-1,000	110	1,907	1,283	1,142	WTA	TSA

Source: SNJV, 2004e

<sup>a</sup> Source: DOE/NV, 2000d

<sup>b</sup> Source: FFACO (1996, as amended February 2008)

<sup>c</sup> Source: UGTA Borehole Project Index (in UTM, Zone 11, NAD 27)

<sup>d</sup> Calculated Cavity Radius =  $[70.2*(y)^{1/3}]/(\rho_b*DOB)^{1/4}$  where y = yield of the test (kt),  $\rho_b$  = bulk density of the overburden (g/cm<sup>3</sup>), and DOB the working point (m) (taken from Pawloski, 1999); cavity radius calculation uses maximum yield of the yield range.

<sup>e</sup> Source: BN, 2002a

<sup>f</sup> Working Point Elevation = Land Surface Elevation - Working Point Depth (taken from Pawloski, 2004)

<sup>g</sup> Hydrogeologic unit (see [Appendix A](#)); BN, 2002a

<sup>h</sup> Hydrostratigraphy (see [Appendix A](#)); BN, 2002a

derived and decay-corrected to September 23, 1992 (date of the last nuclear test) using the exponential decay expression:

$$A = A_o e^{-(0.693t/T_{1/2})} \quad (4-4)$$

where:

$A$  = activity at time  $t$ , curies (Ci)

$A_o$  = initial activity, Ci

$t$  = time, years

$T_{1/2}$  = half life, years

The resulting total inventory for Areas 19 and 20 is listed in [Table 4-4](#).

**Table 4-4**  
**Sum of Radionuclide Inventory in Areas 19 and 20**  
 (Page 1 of 2)

Radionuclide	Curies <sup>a</sup>	Atoms <sup>a</sup>	Curies <sup>a</sup>	Atoms <sup>a</sup>
	Area 19	Area 19	Area 20	Area 20
<sup>3</sup> H	1.778E+07	3.689E+26	5.903E+07	1.225E+27
<sup>14</sup> C	2.193E+02	2.111E+24	4.693E+02	4.518E+24
<sup>26</sup> Al	8.975E-04	1.073E+21	8.370E-03	1.001E+22
<sup>36</sup> Cl	9.108E+01	4.618E+25	1.573E+02	7.973E+25
<sup>39</sup> Ar	6.398E+02	2.899E+23	1.247E+03	5.652E+23
<sup>40</sup> K	1.588E+02	3.398E+29	3.171E+02	6.783E+29
<sup>41</sup> Ca	5.050E+02	8.763E+25	1.273E+03	2.208E+26
<sup>59</sup> Ni	1.596E+01	2.043E+24	2.976E+01	3.810E+24
<sup>63</sup> Ni	1.724E+03	2.904E+23	3.126E+03	5.266E+23
<sup>85</sup> Kr	4.981E+04	9.028E+23	5.706E+04	1.034E+24
<sup>90</sup> Sr	5.804E+05	2.814E+25	6.835E+05	3.314E+25
<sup>93</sup> Zr	1.887E+01	4.767E+25	2.372E+01	5.993E+25
<sup>93m</sup> Nb	2.969E+03	8.053E+22	5.100E+03	1.383E+23
<sup>94</sup> Nb	7.938E+01	2.674E+24	9.852E+01	3.319E+24
<sup>99</sup> Tc	1.344E+02	4.821E+25	1.782E+02	6.394E+25
<sup>107</sup> Pd	5.957E-01	6.523E+24	1.002E+00	1.097E+25
<sup>113m</sup> Cd	5.017E+02	1.192E+22	7.469E+02	1.774E+22
<sup>121m</sup> Sn	1.782E+03	1.651E+23	2.667E+03	2.470E+23
<sup>126</sup> Sn	8.085E+00	3.405E+24	1.188E+01	5.002E+24
<sup>129</sup> I	4.153E-01	1.098E+25	5.596E-01	1.480E+25
<sup>135</sup> Cs	1.393E+01	5.397E+25	1.838E+01	7.120E+25
<sup>137</sup> Cs	6.971E+05	3.531E+25	8.957E+05	4.537E+25

**Table 4-4**  
**Sum of Radionuclide Inventory in Areas 19 and 20**  
 (Page 2 of 2)

Radionuclide	Curies <sup>a</sup>	Atoms <sup>a</sup>	Curies <sup>a</sup>	Atoms <sup>a</sup>
	Area 19	Area 19	Area 20	Area 20
<sup>151</sup> Sm	2.307E+04	3.498E+24	3.568E+04	5.409E+24
<sup>150</sup> Eu	7.805E+01	4.733E+21	1.069E+03	6.483E+22
<sup>152</sup> Eu	1.151E+04	2.626E+23	2.970E+04	6.774E+23
<sup>154</sup> Eu	7.099E+03	1.028E+23	1.327E+04	1.921E+23
<sup>166m</sup> Ho	3.083E+01	6.231E+22	2.892E+01	5.846E+22
<sup>232</sup> Th	1.147E+01	2.706E+29	2.319E+01	5.468E+29
<sup>232</sup> U	8.730E+01	1.026E+22	1.738E+02	2.044E+22
<sup>233</sup> U	6.508E+01	1.745E+25	1.176E+02	3.154E+25
<sup>234</sup> U	1.421E+02	5.888E+25	1.179E+02	4.885E+25
<sup>235</sup> U	1.293E+00	1.533E+27	1.343E+00	1.592E+27
<sup>236</sup> U	2.213E+00	8.730E+25	2.647E+00	1.044E+26
<sup>238</sup> U	6.826E+00	5.140E+28	1.250E+01	9.411E+28
<sup>237</sup> Np	1.196E+01	4.310E+25	2.476E+01	8.923E+25
<sup>238</sup> Pu	2.857E+03	4.220E+23	4.768E+03	7.043E+23
<sup>239</sup> Pu	7.684E+03	3.119E+26	1.262E+04	5.123E+29
<sup>240</sup> Pu	2.041E+03	2.256E+25	4.405E+03	4.867E+25
<sup>241</sup> Pu	2.946E+04	7.145E+23	6.952E+04	1.686E+24
<sup>242</sup> Pu	1.367E+00	8.637E+23	2.279E+00	1.440E+24
<sup>241</sup> Am	1.299E+03	9.468E+23	3.567E+03	2.600E+24
<sup>243</sup> Am	1.203E-02	1.493E+20	1.772E-01	2.200E+21
<sup>244</sup> Cm	1.190E+03	3.629E+22	2.197E+03	6.700E+22
Total	1.920E+07	6.646E+29	6.086E+07	1.324E+30

Source: Bowen et al., 2001

<sup>a</sup> Decay-corrected to September 23, 1992 (date of last underground nuclear test).

Because the inventory is an estimate based on unclassified data, there is an inherent limit to the accuracy of the radionuclide inventories listed. The accuracy varies with the source of the radionuclides, and the accuracy ranges are given for radionuclide groups in [Table 4-5](#).

The inventory of 37 radionuclides at the CHESHIRE test site is partitioned into glass, rubble, gas, and water (Pawloski et al., 2002) in the percentages listed in [Table 4-6](#). Exclusion of six additional radionuclides was based on a lack of inventory or there is insufficient activity to warrant inclusion. It is assumed that any gas phase radionuclides would be completely dissolved in the aqueous phase.

**Table 4-5**  
**Estimated Accuracies for Radionuclide Groups**

Radionuclide Group	Accuracy	Radionuclides	Distribution Type	Range Multiplier for Upper and Lower Bounds <sup>a</sup>
Fission Products	~ 10 to 30 percent	<sup>85</sup> Kr, <sup>90</sup> Sr, <sup>93</sup> Zr, <sup>93m</sup> Nb, <sup>94</sup> Nb, <sup>99</sup> Tc, <sup>107</sup> Pd, <sup>121m</sup> Sn, <sup>126</sup> Sn, <sup>129</sup> I, <sup>135</sup> Cs, <sup>137</sup> Cs, <sup>151</sup> Sm, <sup>166m</sup> Ho, <sup>39</sup> Ar, <sup>59</sup> Ni, <sup>63</sup> Ni, <sup>113m</sup> Cd	Uniform	0.7 - 1.3
Unspent Fuel Materials	~ 20 percent or better	<sup>232</sup> Th, <sup>232</sup> U, <sup>233</sup> U, <sup>234</sup> U, <sup>235</sup> U, <sup>236</sup> U, <sup>238</sup> U, <sup>238</sup> Pu, <sup>239</sup> Pu, <sup>240</sup> Pu, <sup>241</sup> Pu, <sup>242</sup> Pu, <sup>241</sup> Am, <sup>243</sup> Am, <sup>244</sup> Cm	Uniform	0.8 - 1.2
Fuel Activation Products	~ 50 percent or better	<sup>233</sup> U, <sup>238</sup> Pu, <sup>239</sup> Pu, <sup>237</sup> Np	Uniform	0.5 - 1.5
Residual <sup>3</sup> H	~ 300 percent or better	<sup>3</sup> H	Uniform	0.33 - 3
Activation Products	~ a factor of 10	<sup>14</sup> C, <sup>36</sup> Cl, <sup>41</sup> Ca, <sup>94</sup> Nb, <sup>150</sup> Eu, <sup>154</sup> Eu, <sup>152</sup> Eu, <sup>166m</sup> Ho	Uniform	0.1 - 10

Source: Bowen et al., 2001

<sup>a</sup> Range based on maximum percent uncertainty.

**Table 4-6**  
**Partitioning of the Inventory into Glass, Rubble, Gas, and Water**  
(Page 1 of 2)

Radionuclide	Half-Life (Years)	Radionuclide Amount <sup>a</sup> (Curies)		Partitioning of Total Inventory (Percent)			
		Pahute Mesa Area 19	Pahute Mesa Area 20	Melt Glass	Rubble	Gas	Water
<sup>3</sup> H	1.23E+01	1.778E+07	5.903E+07	0	0	2	98
<sup>14</sup> C	5.730E+03	2.193E+02	4.693E+02	0	10	80	10
<sup>36</sup> Cl	3.01E+05	9.108E+01	1.573E+02	50	40	0	10
<sup>39</sup> Ar	2.69E+02	6.398E+02	1.247E+03	0	10	80	10
<sup>41</sup> Ca	1.03E+05	5.050E+02	1.273E+03	70	30	0	0
<sup>59</sup> Ni	7.6E+04	1.596E+01	2.976E+01	95	5	0	0
<sup>63</sup> Ni	1.00E+02	1.724E+03	3.126E+03	95	5	0	0
<sup>85</sup> Kr	1.070E+01	4.981E+04	5.706E+04	0	10	80	10
<sup>90</sup> Sr	2.91E+01	5.804E+05	6.835E+05	40	60	0	0
<sup>93</sup> Zr	1.5E+06	1.887E+01	2.372E+01	95	5	0	0
<sup>93m</sup> Nb	1.61E+01	2.969E+03	5.100E+03	95	5	0	0
<sup>94</sup> Nb	2.0E+04	7.938E+01	9.852E+01	95	5	0	0

**Table 4-6**  
**Partitioning of the Inventory into Glass, Rubble, Gas, and Water**  
 (Page 2 of 2)

Radionuclide	Half-Life (Years)	Radionuclide Amount <sup>a</sup> (Curies)		Partitioning of Total Inventory (Percent)			
		Pahute Mesa Area 19	Pahute Mesa Area 20	Melt Glass	Rubble	Gas	Water
<sup>99</sup> Tc	2.13E+05	1.344E+02	1.782E+02	80	20	0	0
<sup>107</sup> Pd	6.5E+06	5.957E-01	1.002E+00	70	30	0	0
<sup>121m</sup> Sn	5.5E+01	1.782E+03	2.667E+03	60	40	0	0
<sup>126</sup> Sn	1E+05	8.085E+00	1.188E+01	70	30	0	0
<sup>129</sup> I	1.57E+07	4.153E-01	5.596E-01	50	40	0	10
<sup>135</sup> Cs	2.3E+06	1.393E+01	1.838E+01	20	80	0	0
<sup>137</sup> Cs	3.020E+01	6.971E+05	8.957E+05	20	80	0	0
<sup>151</sup> Sm	9.0E+01	2.307E+04	3.568E+04	95	5	0	0
<sup>150</sup> Eu	3.6E+01	7.805E+01	1.069E+03	95	5	0	0
<sup>152</sup> Eu	1.350E+01	1.151E+04	2.970E+04	95	5	0	0
<sup>154</sup> Eu	8.59E+00	7.099E+03	1.327E+04	95	5	0	0
<sup>166m</sup> Ho	1.2E+03	3.083E+01	2.892E+01	95	5	0	0
<sup>232</sup> U	7.0E+01	8.730E+01	1.738E+02	90	10	0	0
<sup>233</sup> U	1.590E+05	6.508E+01	1.176E+02	90	10	0	0
<sup>234</sup> U	2.46E+05	1.421E+02	1.179E+02	90	10	0	0
<sup>235</sup> U	7.04E+08	1.293E+00	1.343E+00	90	10	0	0
<sup>236</sup> U	2.340E+07	2.213E+00	2.647E+00	90	10	0	0
<sup>238</sup> U	4.47E+09	6.826E+00	1.250E+01	90	10	0	0
<sup>237</sup> Np	2.14E+06	1.196E+01	2.476E+01	95	5	0	0
<sup>238</sup> Pu	8.77E+01	2.857E+03	4.768E+03	95	5	0	0
<sup>239</sup> Pu	2.410E+04	7.684E+03	1.262E+04	95	5	0	0
<sup>240</sup> Pu	6.56E+03	2.041E+03	4.405E+03	95	5	0	0
<sup>241</sup> Pu	1.44E+01	2.946E+04	6.952E+04	95	5	0	0
<sup>241</sup> Am	4.330E+02	1.299E+03	3.567E+03	95	5	0	0
<sup>244</sup> Cm	1.81E+01	1.190E+03	2.197E+03	95	5	0	0

Source: Tompson et al., 2004 (adapted from IAEA, 1998)

<sup>a</sup> Radionuclide summary in curies decay-corrected to September 23, 1992 (Bowen et al., 2001).

The inventory in the rubble and water is distributed evenly into the pores of the cavity and disturbed zones of the exchange volume. In contrast, the inventory in the glass is distributed into the nuclear MGZ and becomes available for release only as the melt glass dissolves.

#### 4.1.4 Porosities, Pore Volumes, and Density

The saturated pores of the exchange volume and the nuclear MGZ represent the volume into which the aqueous phase radionuclide fraction is initially distributed. The test initially vaporizes all water in the cavity (and possibly the compressed zone), but where the test cavity is below the water table, it is anticipated that the cavity will rapidly refill to become fully saturated with groundwater. Table 4-7 lists the volumes and pore volumes of the cavity, intact disturbed zone, rubblized disturbed zone, and exchange volume for the CHESHIRE test SSM. The pore volumes are based on constant porosity for the various regions, consistent with values defined in Table 4-2 of Pawloski et al. (2001). The pore volumes (Table 4-7) are assumed fully saturated because the cavity represented in the SSM is below the water table.

**Table 4-7**  
**CHESHIRE Test Volume, Porosity, and Pore Volume of Source Regions**

Region	Volume (m <sup>3</sup> )	Porosity (%)	Volume (m <sup>3</sup> )
Melt Glass	1.75 × 10 <sup>5</sup>	0.20	3.5 × 10 <sup>4</sup>
Cavity Zone <sup>a</sup>	1.97 × 10 <sup>6</sup>	0.10	1.97 × 10 <sup>5</sup>
Disturbed Zone – Rubblized	1.55 × 10 <sup>6</sup>	0.10	1.55 × 10 <sup>5</sup>
Disturbed Zone – Intact	5.09 × 10 <sup>6</sup>	0.01	5.09 × 10 <sup>4</sup>
Exchange Volume <sup>b,c</sup>	8.61 × 10 <sup>6</sup>	0.0468	4.03 × 10 <sup>5</sup>

Source: SNJV, 2004e

<sup>a</sup> Cavity zone is the region within the cavity, excluding the melt glass.

<sup>b</sup> Exchange volume is the sum of the cavity zone volume and the disturbed zone volumes.

<sup>c</sup> Porosity of the exchange volume is the effective porosity of its three component parts.

#### 4.1.5 Sorption

The SSM represents near-field transport through a 1-D “pipe,” assuming a linear isotherm with a constant value of the sorption coefficient ( $K_d$ ) at ambient conditions assuming groundwater chemistry is constant. This is an abstraction of the more complex, 3-D treatment of sorption found in the process models upon which the SSM is based.

The retardation ratios (i.e., the ratio of moles sorbed to moles in aqueous solution) used in the SSM for 11 elements (Am, Ca, Cm, Cs, Eu, Ho, Np, Pu, Sm, Sr, and U) are listed in Table 4-8 for three media: fracture linings, cavity/chimney, and the rock matrix. The values in this table are based on the average log retardation ratios in Table K.8 of Pawloski et al. (2001). The partition coefficients for fracture lining and cavity/chimney conditions are based on the presence or absence of five possibly sorbing minerals: smectite, calcite, Fe oxide, zeolite, and illite/mica. For matrix flow, the selected minerals are always present, so the partition coefficient for the matrix is constant, without spatial variability. The use of the average log retardation ratios for the SSM is similar to the approach for the process model, except that a single  $K_d$  value is sampled for each realization without spatial variability.

**Table 4-8**  
**Average Log Retardation Ratios for Heterogeneous Mineral Distributions**  
 (Page 1 of 3)

Mineralogy	Fracture Lining		Cavity/Chimney Rubble		Rock Matrix
	1 = On	0 = Off	1 = On	0 = Off	
<b>Am</b>					
Smectite	2.06	1.42	0.92	-0.52	3.67
Calcite	2.77	-3.84	1.73	-4.84	-3.00
Fe Oxide	0.99	-0.05	-0.08	-1.99	2.20
Zeolite	--	--	--	--	--
Illite/mica	--	--	--	--	--
<b>Ca</b>					
Smectite	2.15	1.52	1.01	-0.43	1.75
Calcite	0.85	-5.77	-0.19	-6.76	-6.93
Fe Oxide	--	--	--	--	--
Zeolite	2.65	-26.81	1.61	-26.81	-26.81
Illite/mica	0.07	0.07	-1.87	-1.87	0.31
<b>Cs</b>					
Smectite	1.16	0.52	0.02	-1.42	0.76
Calcite	--	--	--	--	--
Fe Oxide	--	--	--	--	--
Zeolite	2.71	-26.76	1.67	-26.76	-26.76
Illite/mica	2.48	2.48	0.53	0.53	2.71

**Table 4-8**  
**Average Log Retardation Ratios for Heterogeneous Mineral Distributions**  
 (Page 2 of 3)

Mineralogy	Fracture Lining		Cavity/Chimney Rubble		Rock Matrix
	1 = On	0 = Off	1 = On	0 = Off	
<b>Eu, Ho, and Cm</b>					
Smectite	2.04	1.41	0.90	-0.54	3.02
Calcite	3.26	-3.35	2.23	-4.34	-3.14
Fe Oxide	1.57	0.54	0.50	-1.41	2.15
Zeolite	--	--	--	--	--
Illite/mica	--	--	--	--	--
<b>Np</b>					
Smectite	0.37	-0.27	-0.77	-2.21	-0.02
Calcite	2.12	-4.50	1.08	-5.49	-5.66
Fe Oxide	1.48	0.45	0.41	-1.50	0.69
Zeolite	--	--	--	--	--
Illite/mica	--	--	--	--	--
<b>Pu</b>					
Smectite	1.14	0.51	0.00	-1.44	0.80
Calcite	2.04	-4.57	1.00	-5.56	-5.68
Fe Oxide	1.84	0.80	0.76	-1.14	1.09
Zeolite	--	--	--	--	--
Illite/mica	--	--	--	--	--
<b>Sm</b>					
Smectite	2.05	1.41	0.91	-0.53	3.18
Calcite	3.64	-2.97	2.60	-3.97	-2.60
Fe Oxide	1.58	0.54	0.50	-1.40	2.31
Zeolite	--	--	--	--	--
Illite/mica	--	--	--	--	--
<b>Sr</b>					
Smectite	2.15	1.52	1.01	-0.43	1.75
Calcite	-0.90	-7.52	-1.94	-8.51	-8.68
Fe Oxide	-0.55	-1.58	-1.62	-3.52	-1.35
Zeolite	2.80	-26.67	1.76	-26.67	-26.67
Illite/mica	0.07	0.07	-1.87	-1.87	0.30



**Table 4-8**  
**Average Log Retardation Ratios for Heterogeneous Mineral Distributions**  
 (Page 3 of 3)

Mineralogy	Fracture Lining		Cavity/Chimney Rubble		Rock Matrix
	1 = On	0 = Off	1 = On	0 = Off	
<b>U</b>					
Smectite	0.62	-0.02	-0.52	-1.96	0.23
Calcite	-1.74	-8.36	-2.78	-9.35	-9.51
Fe Oxide	2.13	1.10	1.06	-0.85	1.34
Zeolite	--	--	--	--	--
Illite/mica	--	--	--	--	--

Source: Modified from Pawloski et al., 2001 (Table K.8)

-- = Not applicable

The SSM represents the potential variability in the retardation ratio for each of the 11 elements in the fracture lining and cavity/chimney by using a distribution for the retardation ratio that is based on the presence or absence of the five minerals. For example, Am can be sorbed on smectite, calcite, and Fe oxide (zeolite and illite/mica play no role in sorption of Am). The presence or absence of these minerals leads to eight possible states with eight discrete values of the retardation ratio, each of which is assumed equally likely for the SSM.

The discrete distribution of  $K_d$  values for Am in the SSM is essentially bimodal, with four lower values between 27 and 125, four upper values between 616 and 713, and no intermediate values. This feature arises because one mineral tends to have the dominant contribution to the retardation ratio, so that turning it on or off leads to a bimodal response. In the case of Am for fracture flow, this dominant mineral is calcite, but similar behavior is observed for all other elements. This bimodal behavior means that the SSM transport calculations are sampling the extremes of the  $K_d$  values, rather than the full range of effective  $K_d$  values that would likely occur with the 3-D, spatial distribution for the particle code. In other words, developing a 3-D spatial distribution will tend to average out the differences in the sampled  $K_d$  values, while the SSM picks only a single value for each realization.

The retardation ratio  $RR$  is defined as the ratio of moles sorbed to moles in aqueous solution (Pawloski et al., 2001, Table K.8). Because the retardation factor,  $RF$ , is defined as the ratio of total moles to moles in aqueous solution,  $RF = RR + 1$ . The value of the  $K$  can then be determined from:

$$RF = RR + 1 = 1 + \frac{\rho_b K_d}{\phi} \quad (4-5)$$

rearranging:

$$K_d = \frac{\phi RR}{\rho_b} \quad (4-6)$$

where:

$\phi$  = Porosity (dimensionless)

$RR$  = Retardation ratio (dimensionless)

$\rho_b$  = Bulk density of the material, kg/m<sup>3</sup>

Section 6.2.2.3 of Pawloski et al. (2001) provides a detailed development of the fracture morphology in the near-field rock. Based on the requirement to match the porosity in the near-field hydrology and geochemistry process models, each side of a fracture has a 0.1-millimeter (mm)-thick fracture lining atop a 2.5-mm-thick matrix lining. Groundwater can flow through the fracture lining.

The SSM directly represents the fracture lining and matrix lining in the near-field transport pathway. The flow area in the fractures in the near-field rock is set to provide 1 percent porosity, so the matrix lining is a diffusive zone but not an advective zone. In each realization of the SSM, the model samples the distributions for retardation ratio for each element. The retardation ratios for the fracture lining and the retardation ratios for the matrix are applied as  $D_m$  zones for the media lining the transport pathway. The constant values for retardation ratio for the cavity/chimney are applied throughout the exchange volume in the SSM.

#### 4.1.6 Nuclear Melt Glass Dissolution

The SSM incorporates the simplified temperature dependent nuclear melt glass dissolution model described in Pawloski et al. (2001) for use in the HST model. The glass reaction rate is based on a moderate rate at 25 degrees Celsius (°C) that represents a conservative estimate of the glass dissolution rate at near-ambient chemical conditions (Pawloski et al., 2001, Section 6.4.5.1 and Figure 6.20). The value of this rate per reactive surface area of glass is  $6.693 \times 10^{-12}$  moles per square

meter per second (mol/m<sup>2</sup>/s) (Pawloski et al., 2001, Section 6.4.5.1.2). To calculate the bulk rate of dissolution for the melt glass, this rate is multiplied by the reactive surface area, defined as 0.001 square meters per gram of melt glass (Pawloski et al., 2001, Section 6.4.4.4.3); the molecular weight of the glass is defined as 100 grams (Pawloski et al., 2001, Figure 6.20). The Arrhenius equation (Pawloski et al., 2001, Section 6.4.5.2) is then used to calculate the dissolution rate at temperature  $T$ :

$$\ln\left(\frac{k_2}{k_1}\right) = \frac{E_a}{R} \frac{T_2 - T_1}{T_2 T_1} \quad (4-7)$$

where:

- $k_1$  = Dissolution rate at temperature  $T_1$
- $T_1$  = Temperature in degrees Kelvin
- $k_2$  = Dissolution rate at temperature  $T_2$
- $T_2$  = Temperature in degrees Kelvin
- $E_a$  = Activation energy of 20 kilocalories per mole (kcal/mol)
- $R$  = Universal gas constant

The temperature of the melt glass varies between 160 °C at early time to approximately 39 °C at 1,000 years after the test (Pawloski et al., 2001, Figure E.5). Because the dissolution rate from Equation (4-7) is sensitive to the value of temperature, a lookup table based on the digitized temperature time history is included in the SSM. The values for this digitized history are given in Table 4-9, and a corresponding plot of the temperature decay with time is shown in Figure 4-2.

#### 4.1.7 Hydrologic/Transport Model Description

Groundwater flows through the far-field rock at a flux that is a function of the effective permeability of the formation and of the hydraulic gradient. When groundwater encounters the underground test region, flow will occur through the exchange volume and the nuclear melt glass at different rates because of the different permeabilities of those two regions and the hydraulic conductivity of the undisturbed host rock of the formation. Mobilized radionuclides from the nuclear melt glass and exchange volume are transported as dilute species and/or colloids through the near-field rock to the release boundary downgradient. In the case of the CHESHIRE test SSM, this boundary is set at 305 m from the center of the cavity, a distance envisioned as the location where the SSM intersects the PM CAU transport model. When applying the SSM as part of the Pahute Mesa source term evaluation, the distance to this boundary may be revised to reflect the distance to the cell face of the PM CAU model.

**Table 4-9**  
**Digitized Temperature Time History in the Melt Glass for the SSM**

Time (Years)	Temperature (°C)
0.001	160
0.01	160
0.02	159.3
0.05	158
0.1	154.7
0.2	149.7
0.5	132
1	118.7
2	94.7
5	70.7
10	56
20	48
50	41.7
100	39.3
200	39
500	38.7
1,000	38.7

Source: SNJV, 2004e

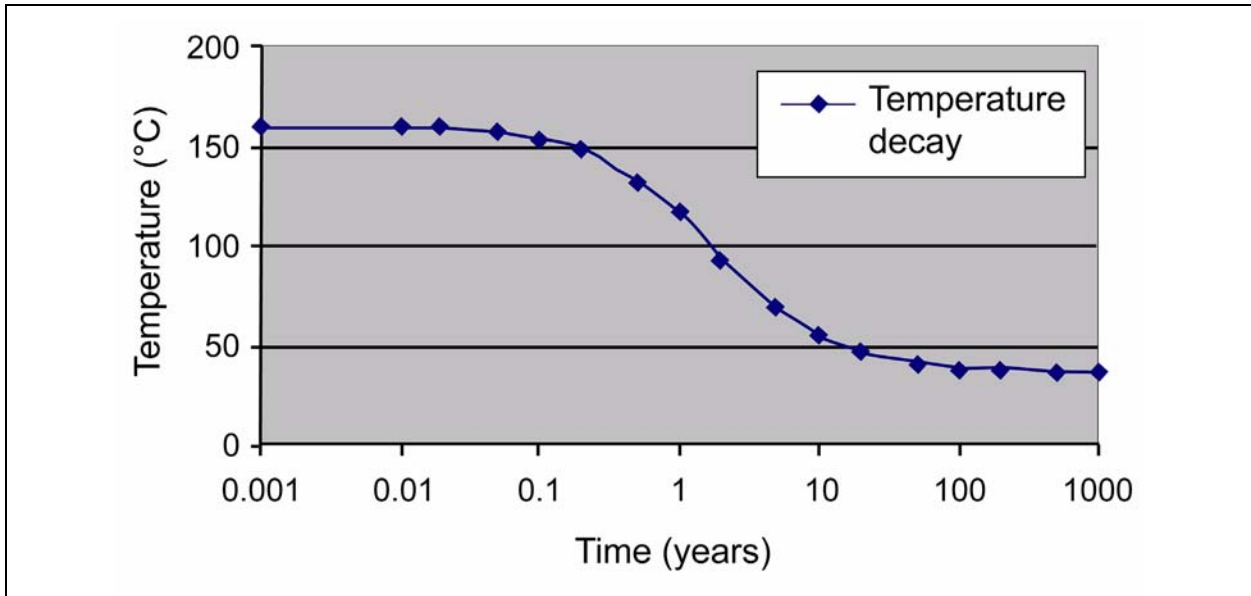


**Figure 4-2**  
**Temperature Decay with Time for Nuclear Melt Glass**

The hydrologic process model simulates the individual regions within the cavity and the disturbed zone. The permeability ( $k$ ) and porosity ( $\phi$ ) of the individual regions in the process model are defined based on data in Table 5-3 of Pawloski et al. (2001). For hydrological purposes, the cavity zone is divided into an upper cavity zone and a lower cavity zone, distinguished by unique physical flow properties. In addition, the permeability of the near-field rock is sampled from four distinct values:  $7.2 \times 10^{-13}$ ,  $1.4 \times 10^{-14}$ ,  $2.6 \times 10^{-15}$ , or  $2.5 \times 10^{-16} \text{ m}^2$ . The two high-permeability values represent fracture flow with a porosity of 0.01, while the two smaller permeability values represent matrix flow with a porosity of 0.15.

The SSM represents this groundwater flow system with three basic components: the exchange volume, the melt glass, and the near-field transport pathway. It is reasonable within the context of the SSM to combine the multiple regions in the cavity and the disturbed zone into the exchange volume. First, the permeability of the cavity zones (ranging from  $1 \times 10^{-12}$  to  $5 \times 10^{-11} \text{ m}^2$ ) and the disturbed zones ( $4 \times 10^{-12} \text{ m}^2$ ) lies within a reasonably narrow range. If the lower cavity zone, with a permeability of  $1 \times 10^{-12} \text{ m}^2$ , is ignored because it has a relatively small volume compared to the other regions, then the range of permeability is reduced to  $4 \times 10^{-12}$  to  $5 \times 10^{-11} \text{ m}^2$ . Second, the range of permeability in the cavity zones and disturbed zones is greater than the permeability of the melt glass,  $4 \times 10^{-14} \text{ m}^2$ , by a factor of at least 250 for the upper cavity zone and the disturbed zones. In this situation, the melt glass is a small, low-permeability kernel that is embedded within a much larger volume of higher-permeability rock that has been disturbed or rubblized by the underground test. It is then reasonable to represent the source regions as the melt glass and the exchange volume for the SSM.

When the SSM is implemented in a GoldSim model framework, the exchange volume and melt glass are represented as cell pathways with volume and porosity that were defined in Table 4-7. The near-field rock is represented as a GoldSim pipe pathway. Figure 4-3 illustrates the conceptual model for the SSM within the GoldSim framework.

Conceptually, the water flux through the melt glass and the exchange volume occur in parallel, each feeding a “streamtube” that represents flow in the aquifer, as described in Tompson et al. (2004). In this manner, the different time scales of radionuclide release from the melt glass and the exchange volume are accounted for.

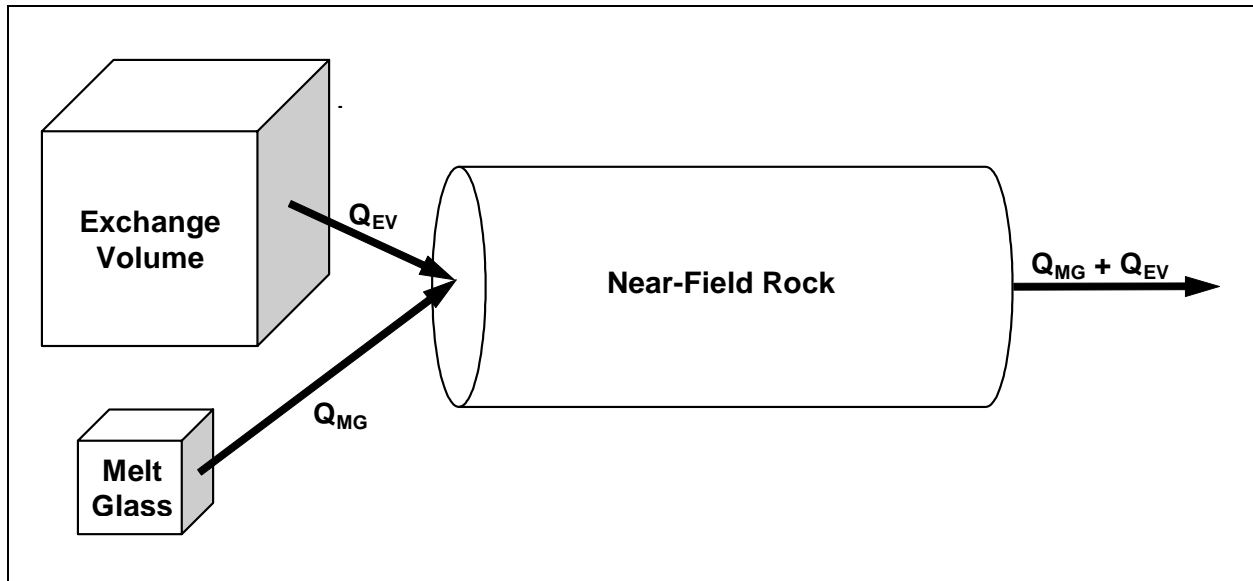


**Figure 4-3**  
**Schematic of the SSM Conceptual Model**

Source: SNJV, 2004e

Each cell pathway (melt glass or exchange volume) is represented as an equivalent cubical volume. For a cube of volume  $V$ , the characteristic length of each cubical volume is given by  $V^{1/3}$  (the length of an edge). The characteristic area of each face of the cube is given by  $V^{2/3}$ . Based on the values in [Table 4-7](#) for the CHESHIRE test, the characteristic area and length of the exchange volume in the SSM are 42,007 m<sup>2</sup> and 205.0 m, respectively, and the characteristic area and length of the melt glass are 3,129 m<sup>2</sup> and 55.9 m, respectively. The concentration within each cell pathway is based on homogeneous conditions in chemical equilibrium with the sorption coefficients for the various radionuclides. Cell pathways also apply solubility and inventory constraints, although solubility constraints are not defined in the SSM (or in the process model). The area of the pipe pathway is assigned to be equal to the area of the exchange volume, or 42,007 m<sup>2</sup>.

The fundamental output from the GoldSim's Contaminant Transport (CT) Module is the predicted mass flux time history at specified locations within the hydrological system. The CT Module is a mass transport model, not a flow model, and so does not directly solve for the movement of groundwater through the hydrological system. The steady-state fluxes between the exchange volume and the near-field pipe pathway,  $Q_{EV}$ , and between the melt glass and near-field pipe pathway,  $Q_{MG}$ , must be defined in an appropriate manner. In a sense, the quantities  $Q_{EV}$  and  $Q_{MG}$  are the fundamental inputs to the SSM, rather than the permeability of the various hydrologic media.

The approach to defining water fluxes  $Q_{EV}$  and  $Q_{MG}$  is to use an analytic solution for the conceptual model to define the initial ranges for these parameters, and to follow up with computational testing for nonsorbing, or tracer, radionuclides. The analytic solution for release of any tracer with no inventory in the melt glass matrix from the exchange volume and cell pathways is very straightforward. Because there is no inventory in the melt glass matrix, the mass in each cell pathway is given by:

$$\frac{dM_i(t)}{dt} = \frac{dM_i(t)}{V_{p,i}} Q_i \quad (4-8)$$

where:

- $i$  = Melt glass (MG) or exchange volume (EV)
- $M_i(t)$  = Mass at time  $t$  (dimension M)
- $Q_i$  = Outward flux (dimension  $L^3$ )
- $V_{p,i}$  = Pore volume in the  $i^{\text{th}}$  cell pathway (dimensionless)

This relationship assumes a well-mixed condition that may or may not exist at the downgradient control plane in the geostatistically based process model. Assuming that the flux  $Q$  is constant, the mass in the cell pathway is given by:

$$M_i(t) = M_i(0)e^{-\left(\frac{Q_i t}{V_{p,i}}\right)} \quad (4-9)$$

The time-dependent mass flux from the cell pathway  $F_i(t)$  is:

$$F_i(t) = \frac{M_i(t)}{V_{p,i}} Q_i \quad (4-10)$$

Because both the melt glass and exchange volume contribute to the flux, the total flux,  $F(t)$ , from the melt glass and exchange volume is the sum:

$$F(t) = F_{EV}(t) + F_{MG}(t) \quad (4-11)$$

Each of the cell pathways contributes over a different time scale to the flux. At early times (less than 100 years), the first (EV) term is dominant. By 1,000 years, the second (MG) term dominates. The relative magnitudes of  $Q_{EV}$  versus  $Q_{MG}$  can be estimated from the formula for steady-state flow in a saturated medium:  $Q = KiA$ , where  $K$  is the conductivity,  $i$  is the head gradient, and  $A$  is the cross-sectional area of the flow for the CHESHIRE test. The cross-sectional area of the exchange

volume, 42,007 m<sup>3</sup>, is more than a factor of 13 greater than the cross-sectional area of the melt glass, 3,129 m<sup>2</sup>. The hydraulic conductivity of the disturbed zone and upper cavity zone is more than a factor of 250 greater than the hydraulic conductivity in the melt glass, based on the permeabilities involved and considering that conductivity is proportional to permeability. Finally, the local head gradients should be similar in magnitude because the melt glass is physically embedded in the larger exchange volume. While this simple analysis is an approximation for a complex source, it is clear that  $Q_{EV}$  will be several orders of magnitude greater than  $Q_{MG}$ . In this situation, radionuclides in the exchange volume are rapidly advected out of the exchange volume and transported to the release boundary shortly after the test, while the radionuclides in the melt glass leak out more slowly and dominate releases near 100 years and beyond.

Tracer radionuclides do not sorb in the exchange volume melt glass or near-field rock. Neglecting dispersion in the near-field pathway, the mass flux from the pipe pathway will be identical to Equation (4-11) except for a temporal shift due to the relatively brief delay in mass advecting through the pipe pathway.

The goal of this testing was to determine appropriate ranges of  $Q_{EV}$  and  $Q_{MG}$  that provide the best fits to the peak fluxes at time zero and to the fluxes at 1,000 years for the tracers considered (<sup>14</sup>C, <sup>3</sup>H, and <sup>59</sup>Ni). As a result of this testing, as documented in SNJV (2004e), the final range of  $Q_{EV}$  is 60,000 to 140,000 cubic meters per year (m<sup>3</sup>/yr), and the final range of  $Q_{MG}$  is 1 to 250 m<sup>3</sup>/yr (SNJV, 2004e). These ranges define the upper and lower bounds of the uniform distributions when sampling values for these parameters. A uniform distribution was deemed appropriate for these parameters because the analysis defined the upper and lower bounds, but offered no insights into the distribution of  $Q_i$  from the 3-D process model (SNJV, 2004e). These distributions are sampled once during each realization of the SSM, providing a single, constant value for  $Q_{EV}$  and a single constant value for  $Q_{MG}$ .

The SSM conceptual model is a simplification (an abstraction) of the flow system in the source region and in the near field compared to a more detailed process model. For example, the process model for the SSM discretizes the individual source components (melt glass, cavity zone, and disturbed zone) with 10-m zones, generating a complex, time-dependent flow field throughout the source. Similarly, the process model for the CHESHIRE test also creates 10 realizations of the near-field permeability, based on a geostatistical approach that is calibrated with the measured thermal response in monitoring



wells. The SSM assumes uniform conditions in each source zone (melt glass and exchange volume). In addition, the initial results reported here are based on a constant flux through the pipe pathway (i.e., a steady-state flow system as opposed to a transient flow system induced by thermal buoyancy effects). Thermal convection from the melt glass is not currently represented, although some initial testing was performed with a time-dependent flux from the melt glass. Similarly, the single transport pipe does not represent the multiple pathways for flow and transport in the 3-D process model for the CHESHIRE test. In effect, the spatial variability of flow in a single realization of the process model for the CHESHIRE test is averaged into a single, randomly sampled value for the flux from the exchange volume.

#### **4.1.8 Quantitative Assessment of Uncertainty**

The approach to assess uncertainty is to develop the GoldSim-based abstraction of the SSM and use it to simulate the transport system for a range of select sampled parameters in multiple realizations. GoldSim is a graphically based (object-oriented programming) Monte Carlo simulator that allows quantitative characterization of uncertainty and produces probabilistic distributions of outputs in response to probabilistic input parameter distributions. The abstraction of the SSM represented in the GoldSim model is a simplification designed to provide speed in execution to support a stochastic analysis. Features and processes that are not represented in this abstraction include the 3-D aspect of the domain, chimney flow (convection), transient flux, reactive transport (nonlinear sorption), and colloidal transport.

There are a number of sources of uncertainty that could be considered, including uncertainty in these aspects:

- Inventory of radionuclides
- Partitioning of the radionuclide source
- Source region dimensions
- Hydrologic setting of a test

Further detail on the treatment of uncertainty is discussed in [Sections 4.1.8.1 through 4.1.8.3](#).

#### 4.1.8.1 Inventory Uncertainty

The inventory was presented in Table 4-4 for 43 radionuclides reported for Areas 19 and 20, with the total estimated inventory of each radionuclide for each area (Bowen et al., 2001) in Table 4-4. Each of these radionuclides is individually considered within the inventory for the SSM. The uncertainty in inventory quantities and distributions is discussed in this section.

The total (initial) amount of each radionuclide in Table 4-4 is presented separately for Areas 19 and 20. The total estimated inventory of atoms of each radionuclide is taken directly from Bowen et al. (2001). The values for moles and grams are calculated as indicated in Section 4.1.6. The total inventory in Table 4-4 must be divided among all the tests in an area (either 19 or 20) to provide an unclassified average source term for each specific test.

The total mass of radionuclide  $j$  ( $MT_j$ ) for any specific underground nuclear test is classified information and not available for analysis. As such, estimates of total mass are used in the modeling. An estimate for  $MT_j$  for each underground test was made from the total inventory data in Bowen et al. (2001) as the average of all the tests in Area 19 or Area 20, as appropriate. The equation for  $MT_j$  for Areas 19 is:

$$MT_j(\text{Area 19}) = MT_{\text{all}}(\text{Area 19})/Nt(\text{Area 19}) \quad (4-12)$$

where:

$MT_{\text{all}}(\text{Area 19})$  = Total radionuclide inventory in Area 19

$MT_j(\text{Area 19})$  = Averaged radionuclide inventory for any test in Area 19

$Nt(\text{Area 19})$  = Total number of tests in Area 19

The same equation is used for Area 20, where the total inventory and total number of tests are specific to Area 20. The number of tests in each area is from the published list of *United States Nuclear Tests, July 1945 through September 1992* (DOE/NV, 2000d). The number of underground nuclear tests conducted in Area 19 is 36, and 49 in Area 20.

The total inventory is subject to some uncertainty as described by Bowen et al. (2001) and shown in Table 4-5. Thus, the inventory uncertainty is accounted for in the HST by defining a uniform distribution that represents a multiplicative factor defining the range of inventory uncertainty for the radionuclide types, as shown in Table 4-5. When a radionuclide is present in more than one

radionuclide group, its inventory is sampled from the category with the greatest uncertainty. For each realization of the HST, the range factor for each radionuclide is sampled and multiplied by the initial radionuclide mass shown in [Table 4-4](#) to incorporate inventory uncertainty directly into the HST.

#### **4.1.8.2 Radionuclide Partitioning Uncertainty**

The partitioning of the radionuclides between glass, rubble, water, and gas is taken from Tompson et al. (2004) and summarized in [Table 4-6](#). For the SSM analysis, the partitioning is simplified by combining the percentages from rubble, gas, and water into one value designated the exchange volume; the percentage in the glass defines the inventory in the melt glass matrix. The melt glass partitioning used is that presented by Tompson et al. (2004). Both the exchange volume and melt glass partitioning are uncertain. As noted in the work of Pawloski et al. (2001), the partition percentages are taken primarily from an International Atomic Energy Agency (IAEA) report (IAEA, 1998) describing the distribution of radionuclides underground at the atolls of Mururoa and Fangataufa in the southern Pacific Ocean. The extrapolation of the IAEA data to the NTS, and to radionuclides not addressed in the IAEA report as noted by Pawloski et al. (2001), means that the percentages shown in [Table 4-6](#) are to be treated as “best estimates.” A range of uncertainty exists but is unknown.

To account for this uncertainty, the percentage of radionuclide partitioned in the melt glass is allowed to vary according to [Table 4-10](#). The corresponding exchange volume percentage is calculated as 100 percent minus the melt glass percentage. The range of partition percentages is an approximation used to assign additional variability to the calculations. Each of these distributions is sampled once per realization, and the resulting value defines the initial distribution of radionuclides between the exchange volume and the melt glass. The ranges in [Table 4-10](#) are estimates based on the IAEA report (IAEA, 1998).

#### **4.1.8.3 Source Region Dimensions Uncertainty**

The cavity volume is calculated from the maximum announced yield, the bulk overburden density, and the DOB (see [Equation \[4-1\]](#)). The yield is not allowed to vary outside the announced range, and all unclassified calculations are performed using the maximum announced yield. Hence, the only way to introduce uncertainty in the cavity volume is via the bulk overburden density or DOB.

**Table 4-10**  
**Probabilistic Distributions for Melt Glass/Exchange Volume**  
**Partitioning Coefficients in Terms of Melt Glass Fraction**

Statistical Distribution Type	Lower Limit	Distribution Fraction <sup>a</sup>	Upper Limit	Radionuclides
Uniform	0.0	0.0	0.05	<sup>3</sup> H, <sup>14</sup> C, <sup>39</sup> Ar, <sup>85</sup> Kr
Uniform	0.1	0.2	0.3	<sup>135</sup> Cs, <sup>137</sup> Cs
Uniform	0.3	0.4	0.5	<sup>90</sup> Sr
Uniform	0.4	0.50	0.6	<sup>36</sup> Cl, <sup>129</sup> I
Uniform	0.5	0.60	0.7	<sup>121</sup> Sn
Uniform	0.6	0.70	0.8	<sup>41</sup> Ca, <sup>107</sup> Pd, <sup>113</sup> Cd, <sup>126</sup> Sn
Uniform	0.7	0.80	0.9	<sup>99</sup> Tc
Uniform	0.85	0.90	0.95	<sup>232</sup> U, <sup>233</sup> U, <sup>234</sup> U, <sup>235</sup> U, <sup>236</sup> U, <sup>238</sup> U
Uniform	0.9	0.95	1.0	<sup>59</sup> Ni, <sup>63</sup> Ni, <sup>93</sup> Zr, <sup>93m</sup> Nb, <sup>94</sup> Nb, <sup>1512</sup> Sm, <sup>150</sup> Gd, <sup>152</sup> Gd, <sup>150</sup> Eu, <sup>152</sup> Eu, <sup>154</sup> Eu, <sup>166</sup> Ho, <sup>237</sup> Np, <sup>238</sup> Pu, <sup>239</sup> Pu, <sup>240</sup> Pu, <sup>241</sup> Pu, <sup>241</sup> Am, <sup>244</sup> Cm

Source: SNJV, 2004e

<sup>a</sup> Source: Pawloski et al., 2001

Pawloski (2004) gives a single value for DOB for each test; no uncertainty is declared although some could be assumed to exist from survey or other measurement. Overburden bulk density has some uncertainty associated with it as well. In SNJV (2004e), it was demonstrated that the SSM reasonably replicated the CHESHIRE test HST process model results as well as its 5 and 95 percent confidence limits without considering any variation in cavity radius. This result is consistent with the process-level calculations for the CHESHIRE test (Pawloski et al., 2001), which also assumed constant values for the cavity volume.

The radius of the exchange volume is a function of the calculated cavity radius and is defined as the product of the calculated cavity radius and a multiplier reflecting the amount of volume around the cavity immediately affected by the underground test and the subsequent radionuclide emplacement [Equation \(4-2\)](#). The exchange volume multiplier accounts for the uncertainty in the estimate of the mixing volume outside the test cavity. It is expected that in some cases, the volume associated with radionuclides will be larger than the exchange volume itself due to prompt injection and other mechanisms. The probabilistic distribution reflecting the uncertainty in the exchange-volume multiplier was shown in [Table 4-1](#). The mass of the melt glass ( $M_{MG}$ ) is estimated to be 700 tons

per kiloton of yield. To account for the uncertainty associated with this parameter, a range of 700 to 1,300 tons per kiloton of yield (Tompson et al., 1999) is used in the SSM, as shown in [Table 4-1](#).

## **4.2 Pahute Mesa SSM Analysis Model**

### **4.2.1 Introduction**

Solute flux that is input to the PM CAU transport model is calculated in the SSM and is reported in units of moles per year for each select radionuclide. The phenomenological construct described in [Section 5.2](#) documents cavity formation and radionuclide distribution from an underground nuclear test. Interpretation of the phenomenological construct as a mathematical analog is described in [Section 4.1](#). These two components are incorporated into a numerical model and combined with Pahute Mesa site-specific information from which the solute flux is then calculated.

### **4.2.2 Pahute Mesa Results for Six HFMs**

The SSM is a 1-D transport model with properties assigned based on the HSU that possesses the highest permeability that intercepts each test cavity. Therefore, the physical properties are the same at individual test sites for all HFMs. Flows calculated by the PM CAU model for each HFM are assigned as flow to the SSM model. Flow through the cavity is different for each HFM and reflects effects of conceptual model changes that are the basis of the HFMs. Fluid flux through the SSM is both a function of the hydrostratigraphic configuration of the conceptual model as well as the recharge applied to the model domain.

[Figure 4-4](#) shows a relative flow rate on the Y-axis, for each of the 82 Pahute Mesa CAU 101 and 102 test sites represented along the X-axis. The flow along the Y-axis is normalized to the flow rate from the LCCU1-MME HFM. Using this approach, all LCCU1-MME sites plot as 1. The PZUP-MME and DRT-DRIA flows exhibit higher flows, and the SCCC-MME, LCCU1-USGSD, and LCCU1-TMD HFMs generally have lower fluxes than those of the LCCU1-MME model. Higher fluxes through the PZUP-MME model are a function of the hydrostratigraphic conceptual model and those for the DRT-DRIA are largely from the higher recharge. The LCCU1-USGSD has the same hydrostratigraphic model, but a lower recharge; SCCC-MME has a radically different hydrostratigraphic model, but the same recharge; and the LCCU1-TMD model has the same recharge, but an expanded area affected by the high-permeability field.

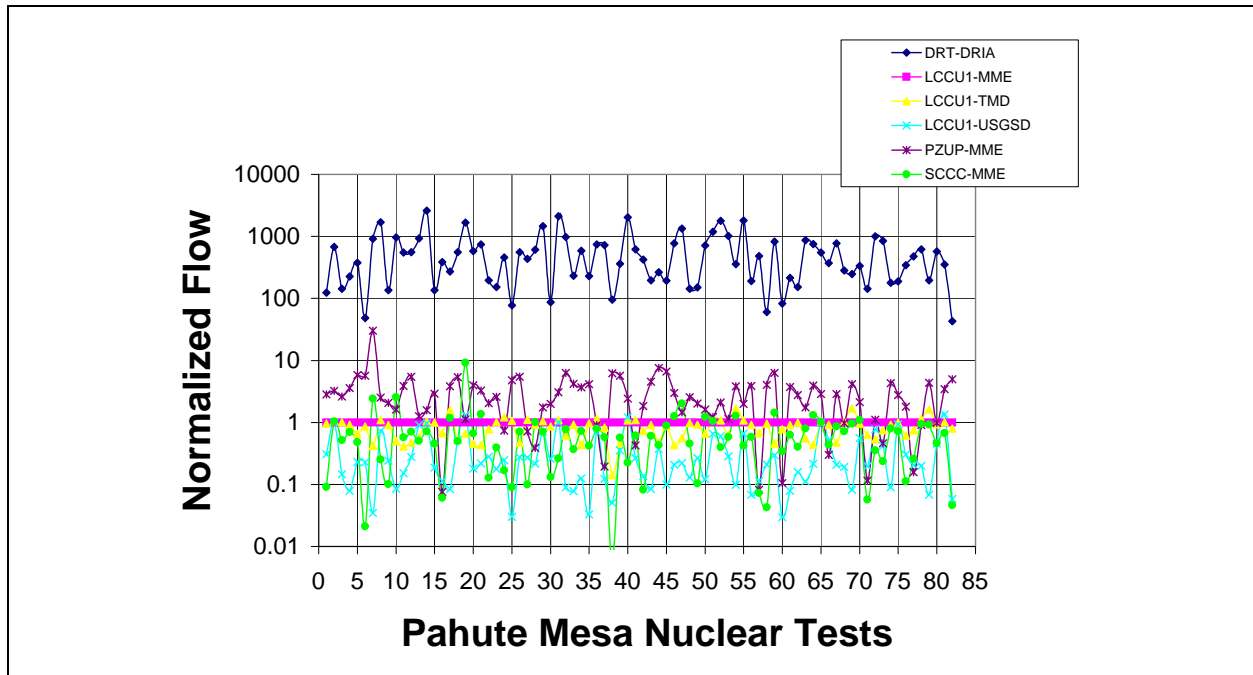


**Figure 4-4**  
**HFM Normalized Fluid Flux for all Pahute Mesa Nuclear Tests**

Figure 4-5 shows the time-series  $^3\text{H}$  plume for each of the six HFMs at the TYBO test site in CAU 102. Examination of Figure 4-5 shows that the DRT-DRIA and PZUP-MME models have a rapid initial release and steep drop off of the solute mass. At the intermediate level, LCCU1-MME and LCCU1-TMD show a slightly later peak arrival time and slightly lower concentration. The time-series decline in mass also shows a more gentle decline allowing  $^3\text{H}$  to persist at higher levels for longer. The SCCC-MME and LCCU1-USGSD HFMs show a delayed response at still lower concentration after which there is a prolonged increase in mass that levels out and then shows a moderate decline relative to the first four HFM responses. The only feature to change in this analysis is the HFM, and therefore the flow moving through the cavity. The solute mass flux results for each HFM match the order observed for the normalized fluid flux.

Based on these analyses, the radionuclide flux is proportional to the fluid flux through the cavity. For the case of highest fluid flux, solute release is at the highest concentration and moves out of the cavity

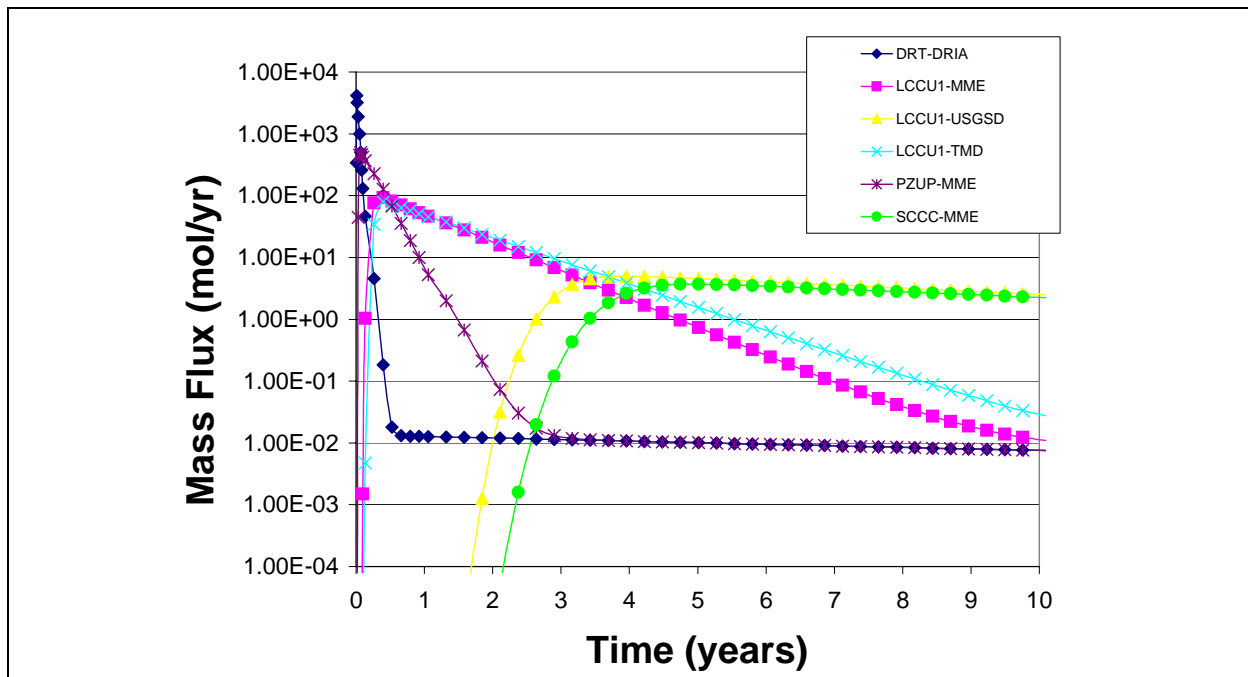


**Figure 4-5**  
**HFM<sup>3</sup>H Solute Mass Flux for TYBO**

faster than the lower fluid flux cases. Given this condition, the order in which the HFMs are expected to contribute an initial high-mass flux pulse to the PM CAU model (in descending order) is:

- DRT-DRIA
- PZUP-MME
- LCCU1-MME
- LCCU1-TMD
- LCCU1-TMCM
- SCCC-MME

### 4.2.3 Fixed Inputs

The groundwater velocity through the model domain is a function of the groundwater flow rate and is inversely related to matrix porosity for specific HGUs. Three initial porosity values are assigned to the HGUs listed in Table 4-11. The higher-porosity units will result in a lower velocity through the rocks. Additionally, the higher porosity also allows higher diffusion rates for the radionuclides in the flow field and exposes more surface area onto which reactive species can attach. Therefore, contaminant migration decrease out of the SSM is expected for those rocks that have increasingly higher porosities.

**Table 4-11**  
**HGU-Specific Matrix Porosity**

HGU	Porosity
WTA/LFA	0.175
VTA2	0.280
TCU	0.405

Source: Shaw, 2003

Porosity input to the SSM includes zones identified as cavity zone, disturbed zone, melt glass, near field, matrix, and fracture lining. Of these porosities, the matrix changes based on the HGUs and matrix porosity values listed in [Table 4-11](#). All other porosities are fixed across the HGUs and the HFMs. The porosity values for the BENHAM test are listed in [Table 4-12](#). These porosities signify the changes along the flow path from the cavity and melt glass through the disturbed zone into the near-field rocks outside of the disturbed zone that extend to the SSM-CAU interface.

**Table 4-12**  
**Porosity Assignments for Components for BENHAM**

Name	Description	Value
Porosity_CZ	Porosity of the cavity zone, above melt glass	0.1
Porosity_DZRubble	Porosity of the collapsed disturbed zone, in the chimney	0.1
Porosity_DZIntact	Porosity of the intact disturbed zone	0.01
Porosity_MG	Porosity of the melt glass	0.2
Porosity_NF	Porosity of the near field - fractures	0.01
Porosity_Matrix	Porosity of the near field - matrix	0.175
Porosity_Lining	Porosity of the fracture lining	0.15

The nuclear test phenomenology parameters that contribute to the model include cavity radius, yield, tons of melt glass, disturbed zone radius multiplier, and rubble volume in the disturbed zone.

[Table 4-13](#) shows these values for the BENHAM test site. These properties are invariant for each test through all HFMs. The cavity radius is listed in [Table 4-13](#) and is a function of yield. The disturbed zone multiplier follows the recommendation of Pawloski et al. (2001).



**Table 4-13**  
**Data Defining Cavity Geometry for BENHAM**

Name	Description	Value	Units
Cavity_Radius	--	99	m
Yield	Maximum reported yield	1,150	kt
Glass_Multiplier	Melt glass produced per kiloton	700,000	kg/kt
DZ_Multiplier	Ratio of disturbed zone to cavity zone radii	1.6	--
Volume_DZ Rubble	Volume of the collapsed disturbed zone, in the chimney	2403445.35	m <sup>3</sup>

-- = Not applicable

Grain densities are necessary to calculate sorption and diffusion exchange rates between the rock-water interface. Table 4-14 lists the grain density used throughout all of the SSM models for all HFMs. The grain density for the melt glass, exchange volume, and near-field are all the same at 2,500 kg/m<sup>3</sup>.

**Table 4-14**  
**Grain Density Assignments for BENHAM**

Name	Description	Value	Units
Density_MG	Grain density of the melt glass	2,500	kg/m <sup>3</sup>
Density_EV	Grain density of the exchange volume	2,500	kg/m <sup>3</sup>
Density_NF	Grain density of the near field	2,500	kg/m <sup>3</sup>

Hydrologic parameter inputs that affect flow through the model domain include fracture density of the near-field, fracture lining thickness, matrix thickness, minimum and maximum flow rates in the melt glass and exchange volumes. Table 4-15 lists the hydrologic parameters for the BENHAM site. The path length is assigned a value of two times the cavity radius. The minimum and maximum flow rate through the exchange volume is the flow rate calculated for the PM CAU model. All other parameters are assigned from literature sources and are consistent for all sites and all HFMs.

Glass dissolution parameters are listed in Table 4-16 and are generic for all sites and all HFMs. All of these parameters are derived from the report of Pawloski et al. (2001).

**Table 4-15**  
**Hydrologic Parameter Assignments for BENHAM**

Name	Description	Value	Units
FractureDensity_NF	Fracture density in the near field and intact disturbed zone	1.5	1/m
PathLength_NF	Length from the center of the cavity to the release plane	198	m
Lining_Thickness	Thickness of the fracture lining	0.1	mm
Matrix_Thickness	Thickness of the rock matrix behind the fracture	2.5	mm
FlowRate_MG_Min	Minimum flow rate through the melt glass	1	m <sup>3</sup> /yr
FlowRate_MG_Max	Maximum flow rate through the melt glass	250	m <sup>3</sup> /yr
FlowRate_EV_Min	Minimum flow rate through the exchange volume	16085838.7	m <sup>3</sup> /yr
FlowRate_EV_Max	Maximum flow rate through the exchange volume	16085838.7	m <sup>3</sup> /yr

**Table 4-16**  
**Glass Dissolution Parameters for BENHAM**

Name	Description	Value	Units
Temperature_Ref	Reference temperature for glass dissolution rate	25	°C
RateConstant_kRef	Moderate glass rate constant, k, at the reference temperature of 25 °C	6.693E-12	mol/m <sup>2</sup> /s
Activation_Energy	Activation energy for melt glass dissolution	20,000	cal/mol
SpecificArea_MG	Specific surface area of the melt glass	0.001	m <sup>2</sup> /g
MolWeight_MG	Molecular weight of the melt glass	100	g/mol

#### 4.2.4 Probabilistic Inputs

Simulation of the SSM follows a stochastic approach for which multiple realizations are performed from which the statistical distribution of output and quantification of uncertainty can be derived. Parameters that are represented in the input file by distribution to be sampled include inventory, sorption coefficient ( $K_d$ ), and matrix porosity for vitrified and devitrified rocks.

An initial inventory for each radionuclide is read as input for each test site. The radionuclides are then assigned to radionuclide groups that correlate to those listed in [Table 4-5](#). The uncertainty of each radionuclide as listed in [Table 4-5](#) is used as the basis to sample a distribution for the radionuclide. This sampled parameter value is then partitioned among lava, rubble, water, and gas phases as per [Table 4-6](#). This cycle is repeated for 100 realizations, the data from which define a distribution of the possible model responses.

The sorption coefficient for each radionuclide is represented as an empirical distribution from which the  $K_d$  is sampled using the Monte Carlo method. Each sampling event is then mapped back to one of the 100 realizations and contributes to the simulated outputs. The  $K_d$  distributions are specific to HGUs that, in turn, can be mapped to corresponding RMCs. (See [Table B.1-1](#) for a crosswalk table that identifies the HGUs and related RMCs.) The  $K_d$  values for the WTA/LFA HGUs are of lower value than those of the VTA/TCU HGUs. The lower  $K_d$  translates to less retardation and consequently a greater potential for migration.

Matrix porosity is sampled from a distribution for the WTA/LFA and VTA HGUs. The porosity for the TCU is fixed to a specific value. As with the  $K_d$  and inventory parameters, the porosity is sampled for each of the 100 realization, and the parameter is included as an additional source of uncertainty for the simulation.

#### **4.2.5 Pahute Mesa Results by HGU and Radionuclide**

Radionuclide releases for the SSM were observed for multiple radionuclide at the CHESHIRE and TYBO nuclear test sites. The TYBO site was selected because it is located in a WTA that has a low porosity and  $K_d$ , and consequently is expected to show minimum retardation and diffusion effects. The CHESHIRE test is located in a TCU that has the highest potential for retardation and diffusion. The expectation is that a comparison of radionuclide release will show a significant difference in release time and rate, with the TYBO site showing a greater potential to release radionuclides at higher concentrations for a shorter duration. Three radionuclides are evaluated for this effort:  $^3\text{H}$ ,  $^{14}\text{C}$ , and  $^{239}\text{Pu}$ . The radionuclide were selected for the following reasons: (1)  $^3\text{H}$  is a conservative species that contributes the most inventory to groundwater, (2)  $^{14}\text{C}$  is also a conservative species with a much longer half-life that also has a higher inventory relative to most other radionuclides, and (3)  $^{239}\text{Pu}$  is a moderately retarded species with a very long half-life and also a moderately high inventory relative to other species.

[Figures 4-6](#) and [4-7](#) show the mean radionuclide release rates for a stochastic simulation of 100 realizations and concentration for TYBO and CHESHIRE, respectively. Observe that the TYBO release is fairly rapid for all species and all peak in less than 10 years. For the CHESHIRE site, release occurs much later, at about 25 years, for the conservative species and does not occur at any time for the retarded radionuclide. The conservative radionuclide concentrations from CHESHIRE

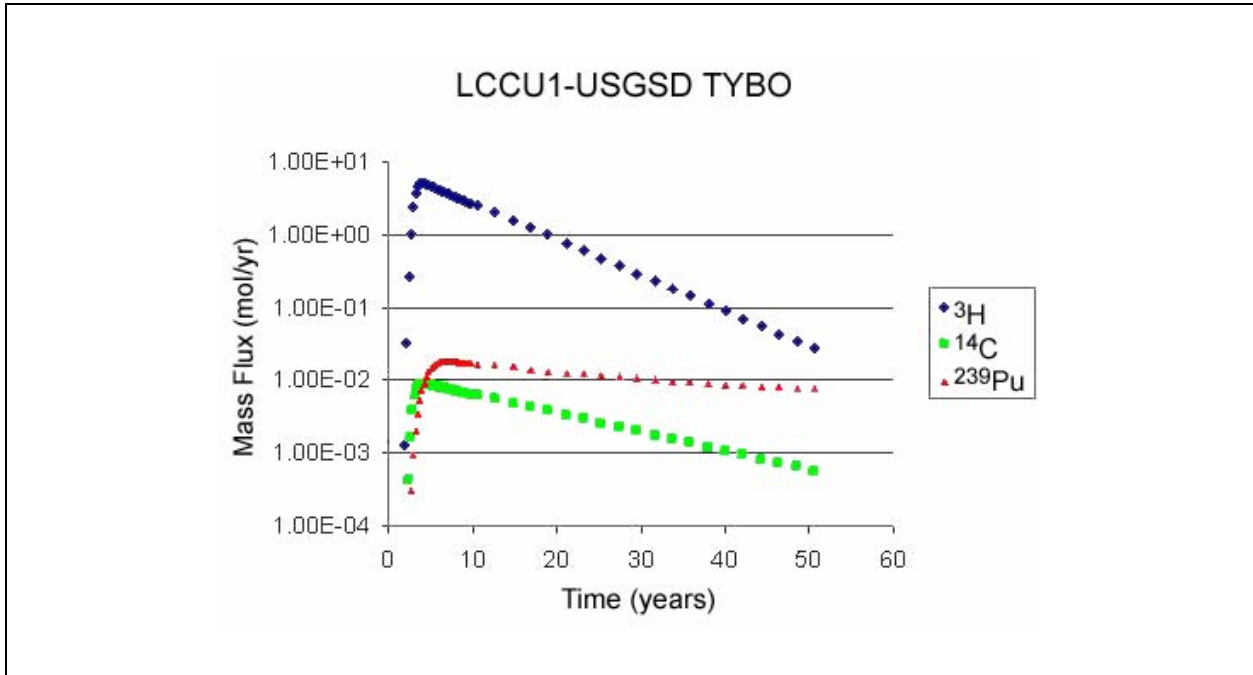


**Figure 4-6**  
**Mass Flux Release from TYBO for LCCU1-USGSD**

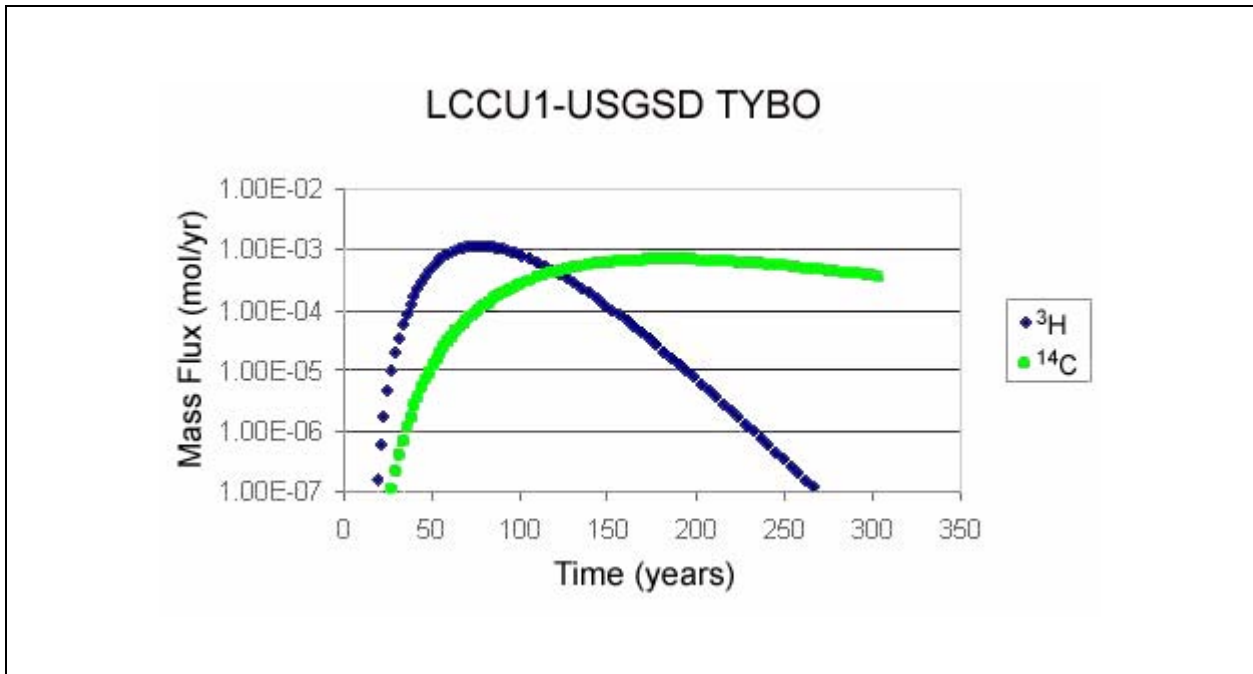


**Figure 4-7**  
**Mass Flux Release from CHESHIRE for LCCU1-USGSD**

are lower than those from TYBO and the plume persists longer, suggesting that inventory is released much more slowly from CHESHIRE than it is from TYBO. This finding is consistent with expected behaviors for the respective sites given the HGU, matrix porosity, and  $K_d$  characteristics of the rocks.

#### **4.2.6 Summary**

Output from the SSM provides the solute mass flux of radionuclides that are input to the PM CAU transport model. Fluid fluxes through the nuclear test cavity for each of the 82 Pahute Mesa shaft nuclear tests are derived from the PM CAU flow model. Observation of the relative fluid flux for each HFM show a clear ordering of fluid flux rates based on the HFM. Additionally, observation of the solute mass flux out of the SSM shows a direct correlation of results with the fluid flux. Based on these observations, the hydrostratigraphic and recharge assignments appear to control fluid and solute flux behavior.

Observation of solute flux from two hydrostratigraphically dissimilar test location for one HFM is used to assess release as a function of the radionuclide,  $K_d$ , and matrix porosity. The CHESHIRE site is a zeolitic, TCU that has a high porosity and high  $K_d$ . The TYBO site consists of a devitrified mafic, WTA unit that has a low porosity and low  $K_d$ . Simulation results for these two sites were evaluated for the LCCU1-USGSD HFM. Results show that the CHESHIRE site retards and prolongs release of conservative radionuclide species and does not allow release of a moderately retarded species from the SSM. The TYBO site allows for a faster release of contaminants that peaks and then declines rapidly. Consequently, it would be expected that the greatest contribution of a large mass flux release would correspond to the high fluid flux HFM through test cavities that are hydrostratigraphically characterized by lower end-member matrix porosity/low  $K_d$ .

## **5.0 TRANSPORT CONCEPTUAL MODEL**

The conceptual model and physical processes of groundwater flow and transport are the framework upon which the numerical transport model is built. The numerical model is the simplified mathematical analog of the spatially distributed processes and properties, translated into model space. The transport model is comprised of three distinct models: (1) the release of radionuclides (based on the phenomenological model of the cavity, melt glass, and disturbed zone) to the flow system; (2) the migration of radionuclides from the source location; and (3) the reactive mineral model (identifies the RMC for each model node) that determines the applied transport properties (similar in nature to hydrostratigraphic properties for the PM CAU flow model).

Phenomenology refers to the processes affecting the subsurface as a result of nuclear testing, and determines the resulting distribution of radionuclides in the cavity and near-cavity material. Processes of concern during migration include advection, radioactive decay, sorption, diffusion, and colloidal transport. Reactive mineral categories are subdivisions of HGUs based on mineralogical properties of the rocks. However, RMCs do not necessarily map to the HGUs as a one-to-one relationship. Rather, RMCs can be uniquely partitioned based on the particular HSU. The properties of RMCs are reflected in the sorption coefficient and the porosity of the respective units. Eight RMCs are defined for Pahute Mesa rocks (see [Section 5.4.1.2.3](#)).

### **5.1 Introduction**

The model conceptualization refers to the understanding of the processes that define system behavior and the geometric arrangement of these processes in a 3-D space. Conceptualization can be understood in the context of the physical processes that are derived from spatial and temporal laboratory and field tests of the physical domain. The second type of conceptualization refers to the translation of the physical conceptualization to a numerical analog. This section focuses on the former definition of the physical conceptualization. Physical conceptualization of the groundwater system entails identification of the 3-D hydrogeologic domain and, in particular, the arrangement of

rock units, flow and transport properties of the individual units, and source and sink terms, in the form of hydrologic sources (recharge), contaminant sources (point releases), boundary fluxes (inflow and outflow), and initial conditions (hydraulic head and contaminant distribution). The conceptualization of the hydrostratigraphic arrangement of the domain in 3-D space is described in BN (2002a). The superposition of the hydrologic properties, boundary fluxes, source and sink terms, and hydrogeologic properties are discussed in SNJV (2006a).

Discussion of the transport conceptual model is divided into three general categorical subjects: (1) release, (2) migration, and (3) assignment of RMCs. The release mechanism for this location consists of multiple-point sources that represent the locations of underground nuclear tests. The source term that contributes to the PM CAU model is initially developed at a local scale to capture structural and temporal characteristics that regulate release rate. Migration from the source area is controlled through physical processes that are a function of the hydrogeologic and geochemical properties of the rocks. The role that these processes have on transport is briefly discussed. As contaminants migrate through the rocks, they are prone to react with mineral assemblages that are specific to certain rock types. The RMCs identify these mineral types, their distribution, and their affinity to adsorb radionuclides as the contaminant plume moves through the porous structure that characterizes each of the HGUs.

## **5.2 Release**

Release of radionuclides from underground nuclear test sites is a function of both the design criteria of the test as well as the hydrogeologic setting in which the test is conducted. These aspects of each test must be adequately captured for an accurate assessment of the source term and release rate from the site. The explosive yield of the nuclear device is critical in assessing the extent of the disturbed and altered geologic material into which the radionuclides are distributed and the estimation of source term inventory. The hydrogeologic nature of the rocks serves to identify the fluid flow rate and geochemical reaction potential for each radionuclide identified in the inventory.

Conceptualization of the pre- and post-test geologic conditions in rocks at Pahute Mesa is based on information available during hole construction, emplacement, post-test data collection (Pawloski, 1999), and numerical simulation for two focused studies at the TYBO-BENHAM (Wolfsberg et al., 2002) and CHESHIRE (Pawloski et al., 2001) sites in Area 20. Additional

pertinent literature that describes underground nuclear testing phenomenology includes Germain and Kahn (1968), Butkovich and Lewis (1973), Butkovich (1976), and the U.S. Congress/OTA (1989).

When a nuclear device is detonated, the surrounding rock is vaporized at the extremely high temperatures produced, and a cavity is formed. The rock beyond the vaporized zone is fractured by the concussion from the blast out to some distance, after which the rock properties are unaffected by the blast. Shortly after the explosion, the vaporized rock will condense and coalesce into a glass that forms at the bottom of the cavity zone. Also some time after the explosion, the high pressure in the cavity dissipates to less than the lithostatic pressure, at which point the rocks above collapse into the cavity, filling the void and creating a rubble chimney above the cavity. This collapsed zone may or may not extend to the surface, depending upon the competence of overlying rocks. The general process of cavity formation and overburden collapse is depicted in Figure 5-1.

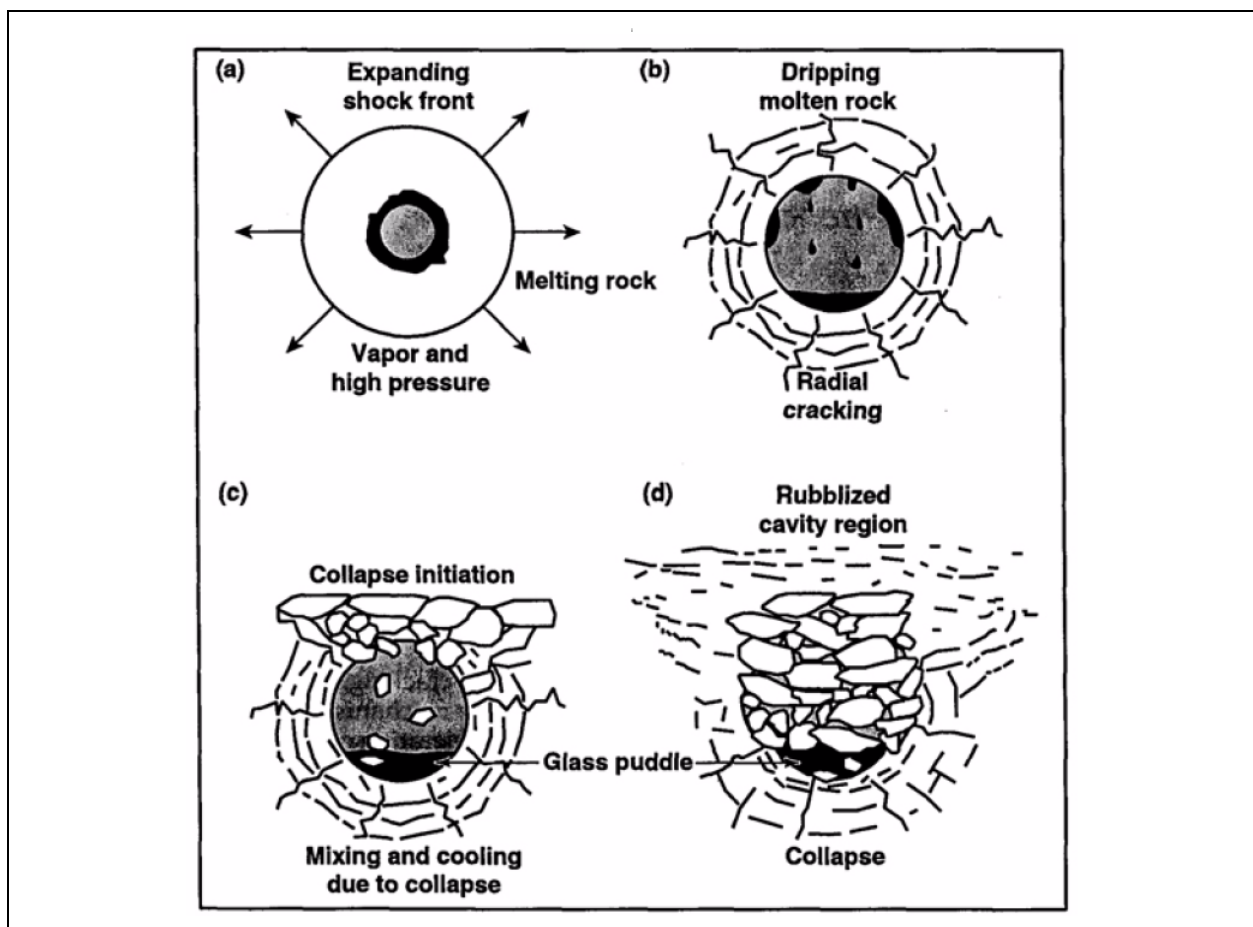


**Figure 5-1**  
**Nuclear Test Cavity Formation Collapse**

Source: Pawloski, 1999



Contaminant products from the nuclear explosion are non-uniformly deposited in different sections of the blast affected volume based on the chemical traits of the radionuclides that are produced during the blast. The high melting point, low vapor pressure, refractory species (Pu, Eu, Am, Np) will predominantly precipitate with the molten rock and become locked into the glass matrix. These species will only become available for release as a dissolved phase upon dissolution of the glass. Glass dissolution is a function of temperature. Therefore, melt glass release is expected to be greatest soon after the test and decrease at later time as the glass cools. The species with a low melting point and high vapor pressure ( $^3\text{H}$ ,  $^{129}\text{I}$ ,  $^{36}\text{Cl}$ ) are volatilized and injected into the rubble or surrounding fractured rock. These species can travel in either a vapor or liquid phase. The volatile species are available for release immediately as a vapor or liquid phase, and are expected to be flushed from the cavity as one pore volume moves through.

Additional processes that are active during the cavity formation and collapse and that affect radionuclide availability and release rates include the following:

- Hydrodynamic fracturing is a process by which high-pressure gas is injected into the existing fractures in the rocks. The injected gas causes the fractures to expand, thereby increasing the permeability of the rocks and allowing faster migration of contaminants. Reduction of cavity pressure after the initial explosion can cause the fractures to close over time.
- Prompt injection of radionuclides directly into the surrounding rock moves contaminants out from the cavity area, and has the potential to advance the contaminant front and accelerate the arrival at a downgradient receptor. This mechanism will most likely be more prominent for the volatile species, particularly those in the gas phase.
- Groundwater mounding and pressurization occurs when the pressure from the blast compression wave is slow to dissipate at later time. The high-pressure front can work to keep contaminants contained in the cavity or drive those species ahead of the front out faster.
- Movement of pre-existing structural features, such as faults, can either result in closing off the feature to flow or opening it up. Closing off the feature may restrict migration out of that feature, but then focus flow elsewhere. Opening up a fault could create a preferential flow path for contaminant species.

Heterogeneity within the source rocks can have a significant effect of release potential from a cavity or rubblized zone. If the test is conducted at or below the water table in a rock unit that is classified as high porosity/confining or geochemically reactive, there is a potential conduit for flow out of the location via embedded high-permeability beds that are distributed through the lower-permeability

media. This phenomenon was inferred from field testing at the CHESHIRE site in Area 20 (Pawloski et al., 2001). At this location, wells drilled near the chimney showed a reduced thermal signature near embedded high-permeability rock layers, which suggest that cooler water moving through these units is mixing with the hotter water in the chimney.

Thermal convective transport of radionuclides in the chimney is also possible where the chimney is in the saturated zone. If the contaminants in the water move up the chimney and intercept a high-permeability layer, this layer could serve as a preferential, high-flux pathway downgradient. This phenomenon was reported by Wolfsberg et al. (2002) at the TYBO-BENHAM sites. High levels of Pu were measured in ER-20-5 near the TYBO test, but the chemical signature matched that of the BENHAM test 1,300 m upgradient. The inference is that the Pu was moved into an overlying permeable unit through thermal convection, where it is then released into a higher-permeability unit that is intercepted by the well near TYBO. The conceptual model of the TYBO-BENHAM system is shown in [Figure 5-2](#). The path from the BENHAM test through the WTA to the downgradient well, ER-20-5, at TYBO is depicted.

### **5.3 Migration**

Radionuclide migration away from subsurface nuclear tests is affected by multiple physical and chemical processes that depend either on the hydrogeologic system and its properties, or on the specific properties of the radionuclides. These processes include radioactive decay of the species, advection in both porous and fractured media, diffusion from fracture water into matrix water, sorption onto immobile minerals, sorption onto mobile colloidal minerals, and attachment and detachment of colloids from immobile surfaces. All of the processes may be modeled and characterized differently depending upon the scale of interest, and additional modeling constructs may be invoked to account for processes that occur at scales smaller than that of the PM CAU transport model scale, processes are averaged and represented on grid blocks with length dimensions between 62 and 500 m. Thus, the processes of dispersion are also included in the PM CAU model to represent the spreading of solutes due to property changes at scales smaller than the PM CAU model grid block. The components of the conceptual model are listed below, with discussion regarding assumptions, simplifications, and scaling as related to the development of the PM CAU transport model. The parameterization of the processes associated with the conceptual model is discussed in [Section 6.4](#).

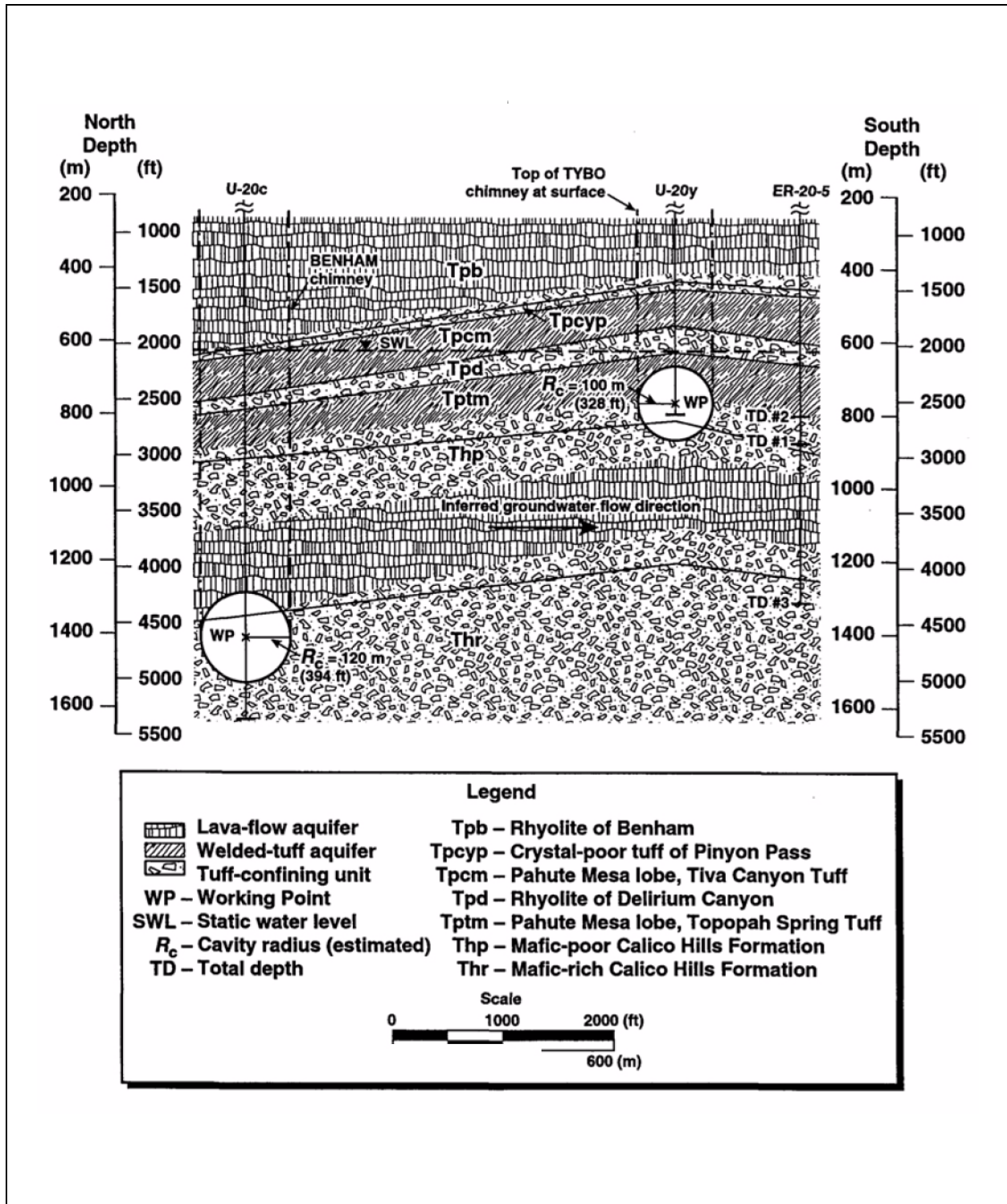


**Figure 5-2**  
**Cross Section through TYBO, BENHAM, and ER-20-5**

Source: DOE/NV, 1997a

### 5.3.1 Source Release

Radionuclides enter the PM CAU transport model as a mass flux versus time function at the interface of the cavity-chimney system with the CAU framework model. This function is developed as an SSM described in Section 4.0, and there are unique SSM release functions for all 82 Pahute Mesa sources. The relationship between the SSMs and the PM CAU transport model is that the groundwater flux through the cavity-chimney systems, a critical parameter in each SSM, is the same as in the PM CAU transport model at the source locations, thus ensuring groundwater flux continuity at the model interface from the SSMs to the PM CAU transport model. Thus, CAU transport begins at each of the Pahute Mesa source locations and is modeled with instantaneous swarm releases of particles at each source location. The spatially and temporally varying transient source-release functions are accommodated by convolution and superposition as described in Section 6.0.

### 5.3.2 Advective and Dispersive Transport

Radionuclides advect and disperse in the flow system as they move through porous and fractured media. The advection at any location is governed by the groundwater flux estimates developed during flow model calibration, with the velocity,  $v$ , being a linear scaling of the flux,  $Q$ , by effective porosity,  $n_{eff}$ , and area,  $A$ , as:

$$v = Q / (A * n_{eff}) \quad (5-1)$$

In porous media such as VTAs and confining units, the effective porosity is the matrix porosity. Fractures are not considered in these zones because fractures do not form in these rocks. In fractured media such as welded tuff and lava, the effective porosity used for advection is the fracture volume. Thus, for the same flux, simulated velocities are much higher for fractured rock than they are for porous media due to the small fracture volume. The advective flow paths correspond with the groundwater flux; the velocity simply determines the rate of movement along flow paths.

The PM CAU transport model includes the HSUs and RMCs as zoned in the framework model. However, these zones are coarse, and it is recognized that material heterogeneities and features not explicitly zoned in the framework model exist at smaller scales. These heterogeneities can cause divergence and/or convergence of flow paths within the zones of single material properties. For example, not every fault in the model domain is represented explicitly. The presence of faults within

an otherwise homogeneous zone could increase the tortuous nature of flow within that zone over the scale of hundreds of meters to kilometers. Likewise, lava beds within a zeolitic confining unit can change the local nature of flow paths. At the very small scale, velocities differ along flow paths between the grains or within fractures. None of these processes are accounted for explicitly in the PM CAU transport model. Rather, dispersion coefficients are assigned that create spreading along and transverse to the advective flow paths as described by Shaw (2003). This is practically accomplished with random walk displacements in the particle-tracking simulations. The values for dispersion are treated as uncertain as described in [Section 6.0](#).

### **5.3.3 Matrix Diffusion**

In fractured rock zones, it is assumed that fluid flow occurs only in fractures and that stagnant fluid resides in the saturated rock matrix. This assumption enables using the dual-porosity simulation methodology in which solutes interact between fracture and matrix water through  $D_m$ . Numerous theoretical, laboratory, and field studies support the validity of the  $D_m$  conceptual and numerical model, showing that single effective material properties cannot adequately capture the complex transport behavior of a solute that advects in fractures, but is retarded via  $D_m$  (e.g., Sudicky and Frind, 1981; Maloszewski and Zuber, 1985; BSC, 2004; and Reimus and Callahan, 2007). Matrix diffusion is conceptualized with a model of uniform flow and transport in a system with equally spaced fractures. Solutes diffuse out of fractures and into the matrix according to concentration gradients and the surface area to volume ratio of the fractures from which they diffuse. Diffusion is limited by the volume of matrix material into which diffusion occurs, which is determined by the spacing between fractures. Over time, the concentrations of solute in the matrix increase, thus reducing the concentration gradient driving diffusion out of the fractures, if they still have higher concentration. For limited-duration source releases, the fractures are flushed of solute first and then the concentration gradient is reversed, causing diffusion back into the fractures from matrix storage. This behavior is often seen in laboratory and field experiments in long contraction tails of breakthrough curves, well after peak arrival times.

This conceptual model is a considerable simplification of the actual processes that occur in complex fracture networks. In reality, fractures intersect and are of variable length and aperture. Diffusion out of some fractures can actually lead to interference of diffusion or enhancement of concentrations in

other fractures. However, at the CAU scale, an abstraction is appropriate and designed to capture the net effect of fracture-matrix interactions with CAU gridblock-scale parameters. The parameters are uncertain, which is addressed in stochastic sampling of fracture properties in the Monte Carlo simulation approach invoked here.

#### **5.3.4 Matrix Sorption**

The conceptual and numerical models allow for reactions between solutes and matrix material. In porous media, the reactions occur as the solute comes into contact with the immobile minerals along the flow paths between the grains. In fractured media, the solute must first diffuse out of the fracture and into the matrix. Then the reactions occur as the diffusing solute comes into contact with immobile minerals. A key assumption here is that sorption reactions do not occur on mineral surfaces coating fractures. Although this assumption is conservative, supporting data for the existence and abundance of fracture coating minerals and their specific role in retarding reactive solutes have not yet been explored. Further, the reactive surface area that would be available for sorption reactions before diffusion out of the fracture is quite small, relative to the reactive surface area a solute encounters once it diffuses out of the fracture. This is also discussed in [Section 6.4.1.5](#).

Sorption reactions can be characterized with both thermodynamic and kinetic formulations. The processes may involve surface complexation and ion exchange. These are discussed in great detail in Zavarin et al. (2002a and b), Shaw (2003), and SNJV (2006a). In the PM CAU transport model, all sorption reactions are assumed to occur under equilibrium conditions and are characterized with distribution coefficients,  $K_d$ . Therefore, the process of sorption of solutes to immobile minerals can be converted into a retardation factor (done internally in the PLUMECALC model), resulting in reduced mobility. [Appendix C](#) considers sorption processes at scales ranging from laboratory columns to the field scale and demonstrates that although kinetic reaction rates are necessary to explain transport at the 20-centimeter (cm) scale, the equilibrium formulation is sufficient at the 100-m to 1-km scale. This is not a surprising conclusion given that the distinction between equilibrium and kinetic formulation of the sorption process can be made on a resident-time contact basis. At the field scale, the solutes have more time to come into contact with the reactive minerals than they do in short-time laboratory experiments.

### 5.3.5 Colloid-Facilitated Transport

Whereas  $D_m$  of all solutes and matrix sorption of reactive species serves to reduce their mobility, colloidal processes can increase the mobility of a reactive solute. The conceptual model for colloid-facilitated transport in the PM CAU transport model is that reactive species entering the PM CAU transport model domain from the source region can be partitioned irreversibly onto naturally occurring mobile colloids. Those colloids then migrate experiencing only the reversible processes of attachment and detachment to immobile surface in fractures, or on grains for porous media-only zones. Colloids do not diffuse out of fractures, and the species sorbed onto them do not desorb and then react with immobile minerals. Colloids onto which reactive species are partitioned at the source region are also never removed irreversibly from the flow system. This conceptual model, therefore, is highly sensitive to the amount of solute that partitions onto mobile colloids.

The conceptual model for CAU-scale colloid facilitated transport is a highly abstracted simplification of far more complex processes that are included in a detailed model to support the abstraction, as documented in [Appendix C](#). Whereas the conceptual model holds that solutes that sorb onto colloids are irreversibly sorbed, the process model investigates the complex competitive reactions between the solute, mobile colloidal surface minerals, and immobile minerals. Recognizing that the reactions are reversible, the process modeling seeks to identify what portion of the SSM aqueous release behaves as if it were irreversibly sorbed to mobile colloids at substantial distances from the source. Thus, identifying what portion of the measured colloidal load is actually mobile over large distances is an additional component of the process model upon which the PM CAU model is abstracted. The process model addresses uncertainty in reaction rates between the solute and the colloids, in the amount of colloid available for large-distance migration, and the reaction coefficients for the solutes onto immobile minerals. Additional, field-scale process simulations are conducted for fractured media in which the fracture aperture and  $D_m$  coefficient are also uncertain. Conducting a suite of Monte Carlo simulations with the process model yields a distribution of fractions, representing the component of source-released solute that migrates to distances away from the source of concern. The fractions, multiplied by the source-release function of aqueous solute, yield the abstracted colloidal source-release function, thus informing the conceptual model for CAU transport.

### 5.3.6 **Radioactive Decay Chains**

Most of the species emanating from the source locations experience radioactive decay. Kersting et al. (2003) examined all of the potential decay chains associated with the radiologic source term for underground nuclear tests and identified the most important chain to be  $^{241}\text{Pu} \rightarrow ^{241}\text{Am} \rightarrow ^{237}\text{Np}$ . The field-scale process model described above for colloid-facilitated transport model abstraction was also used to investigate the importance of including this decay chain. Field-scale simulations led to the conclusion that due to the large quantity of Np in the source, coupled with its high mobility and low activity, inclusion of this decay chain did not change predictive results when compared to simply eliminating mass as a result of decay. Therefore, decay chains and their daughter products are not included in the radioactive decay process, as simulated in CAU-scale transport.

### 5.3.7 **In Situ Concentrations**

One of the great difficulties addressed by this study is simulating *in situ* concentration at any location in space that account for transient source releases as spatially distributed sources. This is accomplished, as described in [Section 6.3](#) (PLUMECALC), with a novel convolution integral method coupled with the principle of superposition. Superposition enables efficient additive impacts of multiple sources to be represented at a single location in space. Invoking superposition entails assuming that species' concentrations do not interfere with each other and that the concentrations are small enough that immobile sorption site concentration far exceeds the concentrations of the aqueous reactive species.

### 5.3.8 **Integrated Transport Model**

The conceptual model requires specification and parameterization of a limited set of processes that affect migration of solutes evolving from spatially separated source locations. For non-reactive species, they emanate from the source as specified by the SSM. Then, they experience advection, dispersion,  $D_m$ , decay, and their concentrations are diluted as groundwaters mix. No other processes affect simulated groundwater concentrations. Reactive species' concentrations are affected by the same processes with the additional reactions to immobile minerals and mobile colloids and then the process of retarded, reversible colloid migration. The processes are considered at all locations for all sources, with the concentrations simulated at any time being converted into contaminant levels for



comparison with standards. The methods, parameters, and integrated results are described in subsequent sections.

#### **5.4 Reactive Mineral Model**

This section provides an overview of how the reactive mineral model for the PM CAU model was developed and presents brief summaries of the processes, methods, and data used to construct the model. The PM-OV HFM, presented in [Section 3.2](#), provides the basic framework for the reactive mineral model and is included along with a brief description of each of the HSUs with their reactive mineral subunits that cumulatively constitute the 3-D model volume.

In general, the HFM focuses on hydraulic properties of the geologic units, as determined by lithology, alteration, and structure. The reactive mineral model addresses the mineralogy of the units, particularly the presence and abundance of minerals known to have absorptive/reactive attributes with regard to radionuclides.

##### **5.4.1 Mineralogy of HSUs**

Transport parameters are closely related to the chemical environment in which transport occurs. For example, matrix sorption (a factor in controlling the mobility of contaminants, as discussed in [Section 6.4](#)) is a function of the chemistry of both the solid components (i.e., rock) and water. The nature and distribution of reactive mineral phases in groundwater systems can exert a significant influence on water composition (e.g., major ion chemistry, pH) and the mobility of contaminants of concern. Reactive minerals are expected to occur in four distinct settings within the PM CAU model. These are minerals in alluvial deposits, minerals within volcanic and carbonate rock matrices, minerals occurring as coatings on fracture surfaces in fractured volcanic and carbonate rocks, and colloids (fine-grained mineral particles) mobile in groundwater. This section addresses the mineralogy of alluvial, volcanic, and carbonate rock matrices and mineral coatings on fracture surfaces.

###### **5.4.1.1 Data Sources and Evaluation**

A large effort was made to compile the available mineralogy data from X-ray diffraction (XRD) analyses for the PM CAU model, much of it from historical sources related to the weapons testing

program. Evaluation of these data took into account various sampling biases. These include different sampling objectives of the weapons testing program, and operational limitations such as the difficulty of sampling hard units (WTAs and LFAs) and incompetent zones with the standard sampling tools. The location and distribution of boreholes is also a biasing factor.

The XRD data are presented in [Appendix A](#). Much of the data in [Appendix A](#) were collected for the weapons testing program, which had specific objectives. For example, of particular concern in Pahute Mesa were intervals of argillic alteration within generally unaltered rocks that may indicate the presence of a fault that could cause operational or containment problems. Thus, the weapons testing program downhole sampling programs tended to sample and analyze anomalous zones. Although these samples provide information on the heterogeneity within a particular unit, they could result in an overestimation of the amount of clay and/or zeolite unless properly weighted.

#### **5.4.1.2 Reactive Mineral Characterization of Volcanic and Sedimentary Rock**

##### **5.4.1.2.1 Lithologic Character of PM-OV Rocks**

Most of the volcanic rocks within the PM CAU model area are pyroclastic rocks composed of ash-flow tuffs and ash-fall deposits of generally rhyolitic composition, and lesser rhyolitic lava flows and fewer occurrences of basaltic rocks. The silica-rich rocks (e.g., rhyolite ash-flow or ash-fall tuffs) can be composed of more than 80 percent glass when originally deposited (the remainder is a mixture of original phenocrysts and lithic fragments). Reactive minerals such as zeolite, clay, carbonate, mica, and hematite are rare in these vitric rocks of rhyolitic composition.

Post-depositional processes such as welding, devitrification, zeolitization, and argillization, however, can significantly alter not only the mineralogy but also hydraulic properties of volcanic rocks. On average, volcanic units in the SWNVF show fairly consistent mineralogy that tends to vary only as a function of type and intensity of alteration (Warren et al., 2003).

Zeolitic and argillic alteration is commonly observed in the volcanic rocks at the NTS (Hoover, 1968; Prothro, 2005). Argillic alteration commonly is characterized by the presence of the clays smectite and lesser kaolinite. In addition to decreasing the hydraulic conductivity of the rock, these secondary alteration minerals are reactive with respect to radionuclide transport (Tompson et al., 1999).

Clinoptilolite (a zeolitic mineral) and smectite, for example, have a strong sorptive affinity for certain radionuclides (Zavarin et al., 2004). The confining unit HSUs in the PM CAU model (e.g., the upper and lower Paintbrush confining units) contain a significant amount of zeolite minerals, typically more than 30 percent (Prothro, 2005). In addition to the zeolite and clay minerals mentioned above, reactive minerals relevant for radionuclide transport includes Fe oxides (hematite), certain mafic minerals such as biotite, and calcite. These reactive minerals are found in the rock matrix, in lithic fragments, as phenocrysts, or in the fracture fillings and fracture coatings.

#### **5.4.1.2.2 Post-Depositional Alteration Processes**

Devitrification, which is typically associated with welded ash-flow tuffs and the interior portions of lava flows, occurs during cooling of these volcanic deposits shortly after emplacement. This post-depositional process results in the conversion of the original glass to micro-crystalline quartz and feldspar, and thus yields a rock composed almost entirely of non-reactive quartz and feldspar that is resistant to other post-depositional processes such as zeolitization and argillization. Devitrified welded ash-flow tuffs and lava flows form important aquifers in the PM CAU model area (e.g., the Topopah Spring WTA and the Benham LFA).

Volcanic rocks that remain vitric after emplacement — such as nonwelded ash-flow tuffs, ash-fall deposits, and the outer or pumiceous portions of lavas — are susceptible to diagenetic alteration processes. Zeolitization is common in volcanic rocks at the NTS, including the PM area, and results in the original glass being converted to clinoptilolite, with lesser amounts of other zeolite minerals such as mordenite and analcime at the deeper levels. Because of the high percentage of glass in the original rocks, zeolitization results in volcanic rocks composed predominantly of zeolite, with very low effective permeability. Other reactive minerals such as carbonate, mica, and hematite are typically rare in zeolitic rocks (though there are a few stratigraphic exceptions that can be both mafic-rich and zeolitic). Clay in the form of mainly smectite is usually a minor constituent. Large portions of the volcanic section beneath PM-OV are pervasively zeolitic, and form important confining units (e.g., Calico Hills zeolitic composite unit, BFCU).

Unaltered volcanic rocks and tuffaceous alluvium are also susceptible to argillization. In this post-depositional process the original glass is converted to clay minerals such as smectite and lesser kaolinite. The basal portion of the volcanic section is commonly pervasively argillic, and forms a

confining unit that directly overlies the regional CA (e.g., the argillic TCU, as is well documented in Yucca Flat [Prothro, 2005]).

Alteration of the Pre-Tertiary carbonate rocks mainly results in deposition of Fe oxides, carbonaceous clays, and carbonate minerals in fractures and other openings.

#### **5.4.1.2.3 Reactive Mineral Categories**

After evaluating the occurrence of these reactive minerals to geologic processes relevant to the rocks at the NTS, several natural categories emerge. The RMCs for NTS volcanic rocks are vitric mafic-poor (VMP), vitric mafic-rich (VMR), devitrified mafic-poor (DMP), devitrified mafic-rich (DMR), mafic lavas (ML), zeolitic (ZEOL), and argillic (ARG). The RMCs for Paleozoic sedimentary rocks are calcic (CC) for the carbonate rocks and silicic (SC) or ARG for the siliciclastic rocks. In general, the volcanic confining units relate to the ZEOL RMC, the welded-tuff aquifers relate to the DMR or DMP, the VTAs relate to VMR or VMP, and the argillic TCU relates to the ARG RMC. The CAs relate to the CC and the siliciclastic confining units relate to the SC if mostly quartzite or the ARG if mostly shale. Mineralogical criteria used to establish RMCs for the PM-OV HFM are provided in [Table 5-1](#). The amount of the four primary reactive mineral groups (zeolite, clay, carbonate, and mafic minerals) for the RMCs, as determined by XRD analyses, is summarized in [Table 5-2](#). [Table 5-3](#) provides the reactive mineral unit (RMU) assignments for each HSU, or a subdivision of, in the PM-OV HFM.

#### **5.4.2 Reactive Mineral Model**

As mentioned above, the HFM provided the basic framework for the reactive mineral model. By starting with the HFM, most of the geometric arrangements for the geologic component of the model were already established and developed into an EarthVision 3-D model. It was only necessary to define the HSUs mineralogically and make a few additional subdivisions. As discussed in [Section 5.4.1.2](#), alteration not only has a profound effect on the hydraulic conductivity of the volcanic rocks, but it also determines to a large extent if, and what, reactive minerals will be

**Table 5-1**  
**Reactive Mineral Categories for the PM-OV Model**  
 (Page 1 of 2)

Reactive Mineral Category (RMC)	Typical Lithologies	Major Alteration	Reactive Minerals Present in Significant Quantities	UGTA Criteria
Zeolitic (ZEOL)	Bedded tuffs, nonwelded tuffs, pumiceous lavas, alluvium	Primarily zeolitic, also includes argillic	Dominant clinoptilolite, lesser mordenite, analcine; if argillic includes smectite, kaolinite	>20% zeolite and/or clay; zeolite > clay typically <10% glass
Vitric, mafic-rich (VMR)	Ash-flow tuffs (typically nonwelded to partially welded or vitrophyres), bedded/ash-fall tuffs (unaltered), vitrophyric and pumiceous lava	None (vitric/glassy)	Biotite, hematite/Fe oxide, hornblende, glass, feldspars	<u>vitric</u> >30% glass <10% clay <20% zeolite <u>mafic-rich</u> >1.0% biotite or >1.5% biotite and hornblende
Vitric, mafic-poor (VMP)	Ash-flow tuffs (typically nonwelded to partially welded or vitrophyres), bedded/ash-fall tuffs (unaltered), vitrophyric and pumiceous lava, alluvium	None (vitric/glassy)	Glass, feldspars	<u>vitric</u> >30% glass <10% clay <20% zeolite <u>mafic-poor</u> <1.0% biotite or <1.5% biotite and hornblende
Devitrified, mafic-rich (DMR)	Ash-flow tuff (typically moderately to densely welded), dense/stony lava, granite	Devitrification, vapor-phase mineralization, quartzo-feldspathic, albitic	Biotite, hematite/Fe oxide, hornblende, feldspars	<u>devitrified</u> <20% glass >60% quartz and feldspars <u>mafic-rich</u> >1.0% biotite ("mica") or >1.5% biotite and hornblende
Devitrified, mafic-poor (DMP)	Ash-flow tuff (typically moderately to densely welded), dense/stony lava, some granitic intrusives	Devitrification, vapor-phase mineralization, quartzo-feldspathic, albitic	Feldspars	<u>devitrified</u> <20% glass >60% quartz and feldspars <u>mafic-poor</u> <1.0% biotite or <1.5% biotite and hornblende

**Table 5-1**  
**Reactive Mineral Categories for the PM-OV Model**  
 (Page 2 of 2)

Reactive Mineral Category (RMC)	Typical Lithologies	Major Alteration	Reactive Minerals Present in Significant Quantities	UGTA Criteria
Mafic lavas (ML)	Lava flows; basalt, andesite, dacite	None (vitric) to devitrified	Hematite/Fe oxide, hornblende, magnetite, olivine, pyroxene	>1.5% mafic minerals (as noted in the reactive mineral column to the left) <10% zeolite
Carbonate rocks (CC)	Limestone and dolomite	None, recrystallization	Calcite, dolomite	>50% carbonate
Silicic rocks (SC)	Sandstone, siltstone, some argillite and conglomerate	None, silica	Silica	>50% silica/quartz

Source: Drellack, 2007

Note: Alluvium sediments and granitic intrusives treated like volcanic units.

Modifiers (e.g., DMP-Z or DMR-C)

A (argillic) if > 5%, but < 20%, clay

Z (zeolitic) if > 5%, but < 20%, zeolite

C (calcic) if > 3%, but < 50%, calcite/dolomite

**Table 5-2**  
**Reactive Mineral Summary for RMCs in the PM-OV Model**

RMC	Statistics	Zeolite	Smectite	Illite	Calcite	Hematite
<b>DMP All</b>	<b>Mean %</b>	1.6	7.1	0.7	1.3	0.9
	Min %	0.0	0.0	0.0	0.0	0.0
	Max %	17.0	70.0	20.0	23.0	2.5
	Std	3.5	11.8	2.4	4.2	0.7
	# of samples	207.0	199.0	207.0	187.0	73.0
<b>DMR All</b>	<b>Mean %</b>	1.5	9.3	1.0	2.5	2.1
	Min %	0.0	0.0	0.0	0.0	0.0
	Max %	15.0	40.0	11.4	18.0	50.0
	Std	3.4	10.3	2.5	4.6	8.0
	# of samples	92.0	92.0	92.0	70.0	38.0
<b>ML All</b>	<b>Mean %</b>	0.0	7.6	0.0	0.4	1.1
	Min %	0.0	0.0	0.0	0.0	0.5
	Max %	0.0	20.0	0.0	3.0	3.0
	Std	0.0	6.1	0.0	1.1	1.0
	# of samples	7.0	7.0	7.0	7.0	6.0
<b>VMP All</b>	<b>Mean %</b>	1.8	6.2	0.0	0.5	0.1
	Min %	0.0	0.0	0.0	0.0	0.0
	Max %	19.0	70.0	1.5	10.0	1.0
	Std	4.0	11.3	0.2	1.8	0.2
	# of samples	96.0	95.0	96.0	83.0	20.0
<b>VMR All</b>	<b>Mean %</b>	1.7	6.3	0.0	5.8	0.5
	Min %	0.0	0.0	0.0	0.0	0.0
	Max %	8.0	20.0	0.0	20.0	1.0
	Std	2.5	5.9	0.0	7.8	0.7
	# of samples	12.0	12.0	12.0	8.0	2.0
<b>ZEOL All</b>	<b>Mean %</b>	48.3	4.5	0.1	0.2	0.1
	Min %	0.0	0.0	0.0	0.0	0.0
	Max %	93.0	55.0	8.0	25.0	7.0
	Std	26.6	8.2	0.7	1.7	0.8
	# of samples	318.0	306.0	318.0	271.0	88.0

Source: Drellack, 2007

Note: Based on available XRD data for samples (outcrop and drill hole) in the PM-OV model area.

**Table 5-3**  
**Hydrostratigraphic and Reactive Mineral Units of the PM-OV Model**  
 (Page 1 of 11)

HSU Layer No. <sup>a</sup>	Hydrostratigraphic Unit (HSU) <sup>b</sup>	HSU Symbol	Reactive Mineral Unit (RMU)	RMU Symbol	Dominant RMCs <sup>c</sup>	Typical Stratigraphic Units <sup>d</sup>
46	Alluvial aquifer	AA	Alluvium Vitric	AA V	VMP, minor VMPZ	Tgc, QTa, Tgs, Qa, Tg, Tyo, Tt
			Alluvium DMP	AA DMP	DMP, minor V	Ttt, Ttp
			Alluvium Zeolitic	AA ZE	ZEOL, VMP-Z	QTa, Qa
45	Younger volcanics composite unit	YVCM	Younger Mafic Lava	Y ML	ML	Tpy
			Younger Volcanics DMP	Y DMP	DMP	QTa, Tgs, Tg, Ts
44	Thirsty Canyon volcanic aquifer	TCVA	Thirsty Canyon Upper Vitric	Tt UV	VMP, minor DMP	Ttt, Ttp, Ttr, QTa, Ttg
			Thirsty Canyon DMP	Tt DMP	DMP, minor VMP, DMPZ	Ttp, Ttr, Tmap, Ttcm, Ttcl, Tfbr
			Thirsty Canyon Lower Vitric	Tt LV	VMP	Ttp, Ttr, Tfbr, Tfbw, Tmap, Tfb
			Thirsty Canyon Zeolitic	Tt ZE	ZEOL	Ttr, Tfbr
			Thirsty Canyon Lower Mafic Lava	Tt LML	ML	Ttc
43	Detached volcanics aquifer	DVA	Detached Volcanics DMP	DV DMP	DMP	Tf, Tma
42	Detached volcanics composite unit	DVCM	Detached Volcanics Composite Vitric	DVC V	VMP, VMR	Tf through Tq
			Detached Volcanics Composite DMP	DVC DMP	DMP	Tf
			Detached Volcanics Composite Zeolitic	DVC ZE	ZEOL, minor DMPZ	Tf, Tma



**Table 5-3**  
**Hydrostratigraphic and Reactive Mineral Units of the PM-OV Model**  
 (Page 2 of 11)

HSU Layer No. <sup>a</sup>	Hydrostratigraphic Unit (HSU) <sup>b</sup>	HSU Symbol	Reactive Mineral Unit (RMU)	RMU Symbol	Dominant RMCs <sup>c</sup>	Typical Stratigraphic Units <sup>d</sup>
41	Fortymile Canyon composite unit	FCCM	Fortymile Canyon Composite Upper Mafic Lava	FCC UML	ML	Tfdb, Tte
			Fortymile Canyon Composite Upper DMP	FCC UDMP	DMP, minor DMPZ	Tfbw, Qay
			Fortymile Canyon Composite Upper Zeolitic	FCC UZE	ZEOL	Tfu, Tfbw
			Fortymile Canyon Composite Upper Vitric	FCC UV	VMP, minor DMP	Tfbw, Tf
			Fortymile Canyon Composite Middle Zeolitic	FCC MZE	ZEOL, minor DMPZ	Tfbw, Tg, Tfbr, Tgc, Tfb, Tf, Tfu
			Fortymile Canyon Composite Middle DMP	FCC MDMP	DMP, minor VMPZ	Tfbw, Tfb, Tfbr, Tfl
			Fortymile Canyon Composite Lower Mafic Lava	FCC LML	ML	Tfbb
			Fortymile Canyon Composite Lower DMP	FCC LDMP	DMP	Tfbc, Tfl, Tff
			Fortymile Canyon Composite Lower Zeolitic	FCC LZE	ZEOL	Tf
			Fortymile Canyon Composite Lower DMP	FCC LDMP	DMP	Tfbc, Tfl, Tff
40	Fortymile Canyon aquifer	FCA	Fortymile Canyon DMP	FC DMP	DMP	Tff

**Table 5-3**  
**Hydrostratigraphic and Reactive Mineral Units of the PM-OV Model**  
 (Page 3 of 11)

HSU Layer No. <sup>a</sup>	Hydrostratigraphic Unit (HSU) <sup>b</sup>	HSU Symbol	Reactive Mineral Unit (RMU)	RMU Symbol	Dominant RMCs <sup>c</sup>	Typical Stratigraphic Units <sup>d</sup>
39	Timber Mountain composite unit	TMC	Timber Mountain Composite Upper Vitric	TMC UV	VMP	Tmay, Tmaw
			Timber Mountain Composite Upper Zeolitic	TMC UZE	ZEOL	Tmawr
			Timber Mountain Composite Upper DMP	TMC UDMP	DMP, minor VMP	Tmawr, Tmaw, Tmx, Tmap
			Timber Mountain Composite Middle Zeolitic	TMC MZE	ZEOL	Tmawp
			Timber Mountain Composite Middle DMR	TMC MDMR	DMR, minor ZEOL, DMRZ	Tmar
			Timber Mountain Composite Middle DMP	TMC MDMP	DMP, minor VMP	Tmap
			Timber Mountain Composite Lower DMR	TMC LDMR	DMR	Tmrr
			Timber Mountain Composite Lower DMP	TMC LDMP	DMP	Tmrp
38	Tannenbaum Hill lava-flow aquifer	THLFA	Tannenbaum Hill Vitric	THLF V	VMP	Tmat
			Tannenbaum Hill DMP	THLF DMP	DMP, minor VMP, DMPZ	Tmat
37	Tannenbaum Hill composite unit	THCM	Tannenbaum Hill Composite DMP	THC DMP	DMP	Tmat
			Tannenbaum Hill Composite Zeolitic	THC ZE	ZEOL	Tmat, rarely Tmrp

**Table 5-3**  
**Hydrostratigraphic and Reactive Mineral Units of the PM-OV Model**  
 (Page 4 of 11)

HSU Layer No. <sup>a</sup>	Hydrostratigraphic Unit (HSU) <sup>b</sup>	HSU Symbol	Reactive Mineral Unit (RMU)	RMU Symbol	Dominant RMCs <sup>c</sup>	Typical Stratigraphic Units <sup>d</sup>
36	Timber Mountain aquifer	TMA	Ammonia Tanks Upper Vitric	AT UV	VMR, minor VMPZ, ZEOL	Tmar, Tmap, Ttt, Ttp, Ttl, Tfbr, Tfbw
			Ammonia Tanks DMR	AT DMR	DMR	Tmar
			Ammonia Tanks DMP	AT DMP	DMP, minor VMP	Tmap, Tmay, Tma
			Timber Mountain Middle Vitric	TM MV	VMP, VMR	Tmab, Tmrr, Tmap, Tmrbr, Tg
			Timber Mountain Middle Zeolitic	TM MZE	ZEOL, minor VMPZ	Tmab, Tmarb
			Rainier Mesa DMR	RM DMR	DMR	Tmrr, Tmr
			Rainier Mesa DMP	RM DMP	DMP	Tmrp, Tmr
			Rainier Mesa Lower Vitric	RM LV	VMP, minor VMR, VMPZ	Tmrr, Tmrp, Tmg, Tmra
35	Subcaldera volcanic confining unit	SCVCU	Subcaldera Zeolitic	SC ZE	ZEOL, lesser DMP, DMPZ	Tm, Tp, Tc, older undifferentiated tuffs
34	Fluorspar Canyon confining unit	FCCU	Fluorspar Canyon - Zeolitic	FL ZE	ZEOL	Tmrf
33	Windy Wash aquifer	WWA	Windy Wash - DMP	WW DMP	DMP, minor VMP	Tmw

**Table 5-3**  
**Hydrostratigraphic and Reactive Mineral Units of the PM-OV Model**  
 (Page 5 of 11)

HSU Layer No. <sup>a</sup>	Hydrostratigraphic Unit (HSU) <sup>b</sup>	HSU Symbol	Reactive Mineral Unit (RMU)	RMU Symbol	Dominant RMCs <sup>c</sup>	Typical Stratigraphic Units <sup>d</sup>
32	Paintbrush composite unit	PCM	Paintbrush Composite Upper DMP	PC UDMP	DMP, minor VMP	Tmr, Tmrf, Tmn, Tp, Tpc, Tpy
			Paintbrush Composite Middle Vitric	PC MV	VMP, minor DMP, ZEOL	Tpg, Tpy
			Paintbrush Composite Lower Zeolitic	PC LZE	ZEOL	Tpg, Tpp
			Paintbrush Composite Lower DMP	PC LDMP	DMP	Tptr, Tptp
31	Paintbrush vitric-tuff aquifer	PVTA	Paintbrush Vitric	P V	VMP, VMPZ	Tmrf, Tpb, Tpcm, Tpr, Tpd, Tmrh, Tpe, Tm, Tmt, Tptb
30	Benham aquifer	BA	Benham Upper Zeolitic	B UZE	ZEOL	Tpb
			Benham DMP	B DMP	DMP, minor VMP, ZEOL, DMPZ	Tpb
29	Upper Paintbrush confining unit	UPCU	Upper Paintbrush Zeolitic	UP ZE	ZEOL, minor VMPZ	Tpb, Tpcyp, Tpd, Tmrp, Tmrf, Tmrh, Tmw, Tpcx, Tpcy, Tp
28	Tiva Canyon aquifer	TCA	Tiva Canyon DMP	TC DMP	DMP	Tpcm

**Table 5-3**  
**Hydrostratigraphic and Reactive Mineral Units of the PM-OV Model**  
 (Page 6 of 11)

HSU Layer No. <sup>a</sup>	Hydrostratigraphic Unit (HSU) <sup>b</sup>	HSU Symbol	Reactive Mineral Unit (RMU)	RMU Symbol	Dominant RMCs <sup>c</sup>	Typical Stratigraphic Units <sup>d</sup>
27	Paintbrush lava-flow aquifer	PLFA	Paintbrush Lava-Flow Upper Vitric	PLF UV	VMP	Tpe
			Paintbrush Lava-Flow Upper DMP	PLF UDMP	DMP	Tpe
			Paintbrush Lava-Flow Middle Vitric	PLF MV	VMP, minor ZEOL, DMP	Tpe, Tptb, Tpr
			Paintbrush Lava-Flow Middle DMP	PLF MDMP	DMP, minor VMP	Tpe, Tpr
			Paintbrush Lava-Flow Middle Zeolitic	PLF MZE	ZEOL	Tpe, Tpr
			Paintbrush Lava-Flow Lower DMP	PLF LDMP	DMP	Tpr
			Paintbrush Lava-Flow Lower Vitric	PLF LV	VMP	Tpr
			Paintbrush Lava-Flow Lower Zeolitic	PLF LZE	ZEOL	Tpr
26	Lower Paintbrush confining unit	LPCU	Lower Paintbrush Zeolitic	LP ZE	ZEOL	Tp, Tpe, Tpcm, Tpd, Tptx, Tptm
25	Topopah Spring aquifer	TSA	Topopah Spring DMP	TS DMP	DMP, minor ZEOL	Tptm
			Topopah Spring Zeolitic	TS ZE	ZEOL	Tptm

**Table 5-3**  
**Hydrostratigraphic and Reactive Mineral Units of the PM-OV Model**  
 (Page 7 of 11)

HSU Layer No. <sup>a</sup>	Hydrostratigraphic Unit (HSU) <sup>b</sup>	HSU Symbol	Reactive Mineral Unit (RMU)	RMU Symbol	Dominant RMCs <sup>c</sup>	Typical Stratigraphic Units <sup>d</sup>
24	Yucca Mountain Crater Flat composite unit	YMCFCM	Yucca Mountain Crater Flat Composite Upper Zeolitic	YMCF UZE	ZEOL	Thp, Tptp, Thr
			Yucca Mountain Crater Flat Composite Upper DMP	YMCF UDMP	DMP	Tcp
			Yucca Mountain Crater Flat Composite Middle Zeolitic	YMCF MZE	ZEOL	Tcp, Tcby
			Yucca Mountain Crater Flat Composite Middle DMP	YMCF MDMP	DMP	Tcby
			Yucca Mountain Crater Flat Composite Lower Zeolitic	YMCF LZE	ZEOL	Tcby, Tct
			Yucca Mountain Crater Flat Composite Lower DMP	YMCF LDMP	DMP	Tct
23	Calico Hills vitric-tuff aquifer	CHVTA	Calico Hills Upper Vitric	CHV UV	VMP, minor VMP-Z, DMP, ZEOL	Thp, Tpe, Tcu, Tcj
			Calico Hills Zeolitic	CHV ZE	ZEOL, minor VMP	Thp
			Calico Hills Lower Vitric	CHV LV	VMP	Thp, Tcu, Tcj
22	Calico Hills vitric composite unit	CHVCM	Calico Hills Vitric Composite Upper Vitric	CHVC UV	VMP, minor VMPZ	Thp
			Calico Hills Vitric Composite DMP	CHVC DMP	DMP	Thp
			Calico Hills Vitric Composite Lower Vitric	CHVC LV	VMP	Thp
			Calico Hills Vitric Composite Zeolitic	CHVC ZE	ZEOL	Thp

**Table 5-3**  
**Hydrostratigraphic and Reactive Mineral Units of the PM-OV Model**  
 (Page 8 of 11)

HSU Layer No. <sup>a</sup>	Hydrostratigraphic Unit (HSU) <sup>b</sup>	HSU Symbol	Reactive Mineral Unit (RMU)	RMU Symbol	Dominant RMCs <sup>c</sup>	Typical Stratigraphic Units <sup>d</sup>
21	Calico Hills zeolitic composite unit	CHZCM	Calico Hills Zeolitic Composite Upper Zeolitic	CHZC UZE	ZEOL	Tpr, Thp, Tcu
			Calico Hills Zeolitic Composite Upper DMP	CHZC UDMP	DMP	Thp, Thr
			Calico Hills Zeolitic Composite Upper Vitric	CHZC UV	VMP	Thp
			Calico Hills Zeolitic Composite Middle Zeolitic	CHZC MZE	ZEOL	Thp
			Calico Hills Zeolitic Composite Middle DMP	CHZC MDMP	DMP	Thp
			Calico Hills Zeolitic Composite Middle Zeolitic 2	CHZC MZE2	ZEOL	Thp
			Calico Hills Zeolitic Composite Lower DMP	CHZC LDMP	DMP	Thp
			Calico Hills Zeolitic Composite Lower Zeolitic	CHZC LZE	ZEOL	Thr
20	Calico Hills confining unit	CHCU	Calico Hills Zeolitic	CHZ ZE	ZEOL, minor DMP	Thr, Tpe, Tcg, Thp, Tci, Tcps, Tptb,
19	Inlet aquifer	IA	Inlet DMP	I DMP	DMP, ZEOL, minor VMPZ	Tci
18	Crater Flat composite unit	CFCM	Crater Flat Composite Upper Zeolitic	CFC UZE	ZEOL	Tcpe
			Crater Flat Composite DMP	CFC DMP	DMP	Tcpe, Tcpk
			Crater Flat Composite Lower Zeolitic	CFC LZE	ZEOL	Tcpe, Tci, Tcj
17	Crater Flat confining unit	CFCU	Crater Flat Zeolitic	CFZ ZE	ZEOL, minor VMPZ	Tcu, Tcps
16	Kearsarge aquifer	KA	Kearsarge Upper Zeolitic	K UZE	ZEOL	Tcpk
			Kearsarge Upper Vitric	K UV	VMP	Tcpk
			Kearsarge DMP	K DMP	DMP	Tcpk
			Kearsarge Lower Vitric	K LV	VMP	Tcpk
			Kearsarge Lower Zeolitic	K LZE	ZEOL	Tcpk

**Table 5-3**  
**Hydrostratigraphic and Reactive Mineral Units of the PM-OV Model**  
 (Page 9 of 11)

HSU Layer No. <sup>a</sup>	Hydrostratigraphic Unit (HSU) <sup>b</sup>	HSU Symbol	Reactive Mineral Unit (RMU)	RMU Symbol	Dominant RMCs <sup>c</sup>	Typical Stratigraphic Units <sup>d</sup>
15	Bullfrog confining unit	BFCU	Bullfrog Upper Zeolitic	BF UZE	ZEOL, minor DMP	Tcblr, Tcblp, Tcbx, Tct, Tcbs
			Bullfrog DMP	BF DMP	DMP	Tcbs, Tcbx
			Bullfrog Lower Zeolitic	BF LZE	ZEOL	Tcbr, Tcbx, Tbcs, Tct, Tcblr, Tcblp
14	Belted Range aquifer	BRA	Belted Range Upper DMP	BR UDMP	DMP	Tdbl, Tbdk, Tqj, Tbq, Trl, Trr, Trg, Ton2
			Belted Range Upper Zeolitic	BR UZE	VMP	Trl, Tbdk, Tbgb, Tqh, Tdbl, Tct,
			Belted Range Upper Vitric	BR UV	VMP	Tbd
			Belted Range Middle DMP	BR MDMP	DMP, minor DMPZ	Tbgr, Tbgp, Tbg, Tbdb, Tbdc, Tbds
			Belted Range Middle Zeolitic	BR MZE	ZEOL	Tdbl, Tcl
			Belted Range Middle DMP 2	BR MDMP2	DMP	Tdbl, Tbdk, Tbgm, Tbgs, Tn4JK, Tbq
			Belted Range Lower Zeolitic	BR LZE	ZEOL	Tbq, Tbgp, Tbgb
			Belted Range Lower DMP	BR LDMP	DMP	Tbdc, Tbgb, Tbgs, Trr, Tbq, Tbg



**Table 5-3**  
**Hydrostratigraphic and Reactive Mineral Units of the PM-OV Model**  
 (Page 10 of 11)

HSU Layer No. <sup>a</sup>	Hydrostratigraphic Unit (HSU) <sup>b</sup>	HSU Symbol	Reactive Mineral Unit (RMU)	RMU Symbol	Dominant RMCs <sup>c</sup>	Typical Stratigraphic Units <sup>d</sup>
13	Pre-Belted Range composite unit	PBRM	Pre-Belted Range Zeolitic	PBR UZE	ZEOL, minor DMP	Tbgb, Tqh, Tbq, Tqu
			Pre-Belted Range Upper DMR	PBR UDMR	DMR	Trpd
			Pre-Belted Range Upper DMP	PBR UDMP	DMP	Trl, Trr, Trg, Ton2, Tbgb, Tn, Tub, Toy, Tbj, Tqj
			Pre-Belted Range Middle Zeolitic	PBR MZE	ZEOL	Tn3, Tn4, Ton2, Tor, Tqh, Tbgb, Tqj, Tbj
			Pre-Belted Range Middle DMP	PBR MDMP	DMP	Tbj, Tqc, Toy
			Pre-Belted Range Middle Zeolitic 2	PBR MZE2	ZEOL	Toy, Tor, Tbj, Tqc
			Pre-Belted Range Middle DMP 2	PBR MDMP2	DMP	Tqj
			Redrock Valley DMP	RV DMP	DMP	Tor
			Pre-Belted Range Lower Zeolitic	PBR LZE	ZEOL	Tqj, Tot, Toa, To, Tor
			Pre-Belted Range Lower DMP	PBR LDMP	DMP	Tot
			Pre-Belted Range Lower Zeolitic 2	PBR LZE2	ZEOL	Tot, Tln
12	Black Mountain intrusive confining unit	BMICU	Black Mountain Intrusive	BM DMP	DMP	Tti
11	Ammonia Tanks intrusive confining unit	ATICU	Ammonia Tanks Intrusive	ATI DMR	Mostly DMR, lesser DMP	Tmai
10	Rainier Mesa intrusive confining unit	RMICU	Rainier Mesa Intrusive	RMI DMR	Mostly DMR, lesser DMP	Tmri
9	Claim Canyon intrusive confining unit	CCICU	Claim Canyon Intrusive	CCI DMP	DMP	Tpi
8	Calico Hills intrusive confining unit	CHICU	Calico Hills Intrusive	CHI DMP	DMP	Thi
7	Silent Canyon intrusive confining unit	SCICU	Silent Canyon Intrusive	SCI DMP	DMP	Tc, Tb

**Table 5-3**  
**Hydrostratigraphic and Reactive Mineral Units of the PM-OV Model**  
 (Page 11 of 11)

HSU Layer No. <sup>a</sup>	Hydrostratigraphic Unit (HSU) <sup>b</sup>	HSU Symbol	Reactive Mineral Unit (RMU)	RMU Symbol	Dominant RMCs <sup>c</sup>	Typical Stratigraphic Units <sup>d</sup>
6	Mesozoic granite confining unit	MGCU	Granitic Unit	GU	DMR	Kg
5	Lower carbonate aquifer-thrust plate	LCA3	Thrusted LCA	LCA3	CA	Dg through Cc
4	Lower clastic confining unit-thrust plate	LCCU1	Thrusted Lower Clastic Siliceous	LCCU1	SC	Cc, CZ, CZw, Zs
3	Upper clastic confining unit	UCCU	Eleana	CSCU	SC	MDe
			Chainman Shale	CCCU	ARG	MDc
2	Lower carbonate aquifer	LCA	LCA	LCA	CA	Dg through Cc
1	Lower clastic confining unit	LCCU	Lower Clastic Siliceous Unit	LCCU	SC	Cc, CZ, Czw, Zs, Zj

<sup>a</sup> Refer to BN (2002a) for description of the PM-OV 3-D HFM.

<sup>b</sup> See Table 4-2 in BN (2002a) for explanation of HSU nomenclature.

<sup>c</sup> See Table 4-3 in BN (2002a) for explanation of RMC nomenclature.

<sup>d</sup> See Table 4-1 and 4-2 in BN (2002a) for explanation of stratigraphic nomenclature.

DMP = Devitrified mafic poor

DMR = Devitrified mafic rich

VMP = Vitric mafic poor

VMR = Vitric mafic rich

AA = Alluvium

CA = Carbonate rocks

ML = Mafic lavas

SC = Silicic clastic rocks

ZEOL = Zeolitic volcanic rocks

present. Consequently, many of the HSUs consist of rocks in just one RMC (e.g., the FCCU, UPCU, and LPCU are ZEOL RMCs), and many of the HSUs can be assigned in their entirety to a single RMU (e.g., the UPCU HSU equates to the UP ZE, and the LPCU HSU equates to the LP ZE).

#### **5.4.2.1 Model Area**

The reactive mineral model area is the same as for the HFM and is shown in [Figures 3-3 and 3-7](#). The former testing area on Pahute Mesa (NTS Areas 19 and 20) is included. The underground nuclear shaft tests in Pahute Mesa are grouped into two CAUs: Western and Central Pahute Mesa. Structural features that could possibly control groundwater flow through the area are also included. Discharge areas in Oasis Valley are also included in the southwest corner of the model area. The 3-D model block as depicted in EarthVision is presented in [Figure 5-3](#).

#### **5.4.3 Reactive Mineral Model Construction**

In general, the overall process used to construct the PM reactive mineral model paralleled the HFM construction process. (See Section 2.0 in BN [2002a] for more information on constructing the PM-OV HFM.) The first step in constructing the PM reactive mineral model was to characterize the mineralogy of each HSU. Information used for this step included XRD data (whole rock mineralogy data specific to Pahute Mesa presented in [Appendix A](#), and XRD data for correlative units in the adjacent Yucca Mountain area and for the other UGTA CAUs); detailed lithologic descriptions from drill holes and outcrops; the petrographical and geochemical database for the SWNVF (Warren et al., 2003); and geophysical logs. Major chemical constituents (X-ray fluorescence [XRF] data) and phenocrysts (petrographic data) were also considered. However, the XRD data proved to be the best indicator of reactive mineral attributes.

Each sample in the XRD dataset was assigned an RMC based on reactive mineral content (according to [Table 5-1](#)). The distribution of RMCs within each HSU was then evaluated. These were then grouped in a stratigraphic context into RMUs for modeling, much like how the HGUs were grouped into HSUs for the HFM.

Stratigraphy was factored into this reactive mineral modeling process in two ways: (1) as input for mafic-rich versus mafic-poor units (i.e., the upper portions of the Rainier Mesa tuff [Tmr] and

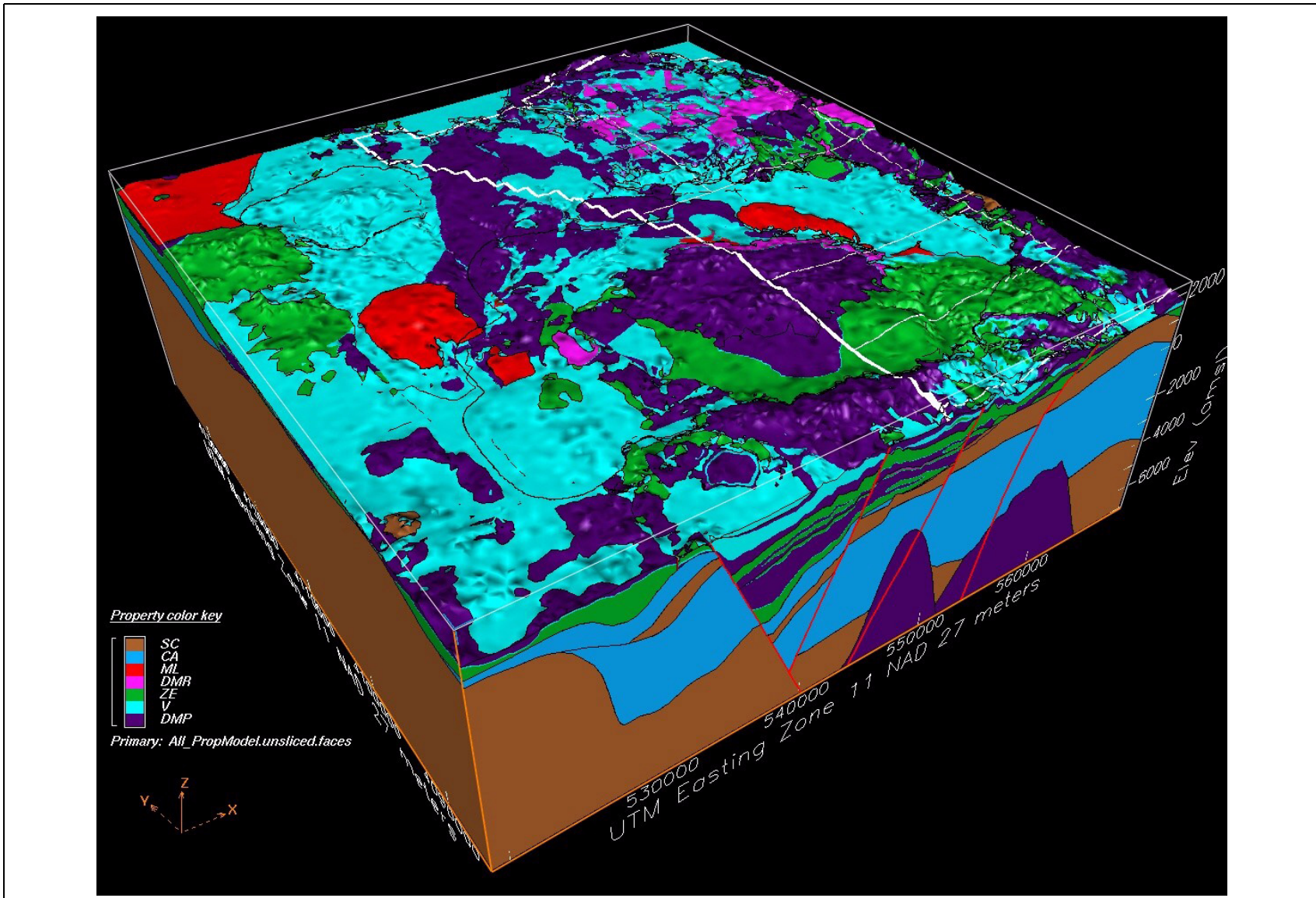


**Figure 5-3**  
**3-D Display from EarthVision of the Reactive Mineral Model for the PM-OV Model**

Source: Drellack, 2007

Ammonia Tanks tuff [Tma] are mafic-rich), and (2) as input to relative position in the total potential stack of RMUs.

Hydrostratigraphic units that show a predictable arrangement of RMCs (e.g., mostly DMP with some ZEOL on bottom, or DMR in upper portion and DMP in lower portion) were subdivided into two or more RMUs. Refer to, for example, the THLFA and THCM HSUs in [Appendix A](#).

The HSU drill-hole database was expanded to include RMC and RMU contacts ([Appendix A](#)). It is important to note that each HSU, or its subdivisions, is based on the average mineralogy of the RMCs ([Appendix A](#)). The RMU name was used to distinguish RMCs within the different HSUs ([Appendix A](#)) and to facilitate model construction.

Input to the EarthVision model consisted of the RMU drill-hole database and unit extent maps, supplemented with conceptual profiles for the more complex HSUs. Additionally, instructions for subdividing some RMUs were composed, especially in areas with insufficient drill-hole control. For example, the EarthVision technician was instructed to subdivide the xxx HSU in areas away from drill-hole control so that the upper 40 percent was yyy (RMU) and the lower 60 percent was zzz (RMU).

The final step took place after EarthVision created a preliminary framework model. This 3-D visualization was an iterative process of checking for geologic reasonableness, adjusting, and then rechecking. Additional details about how some of the RMUs were defined are included in the following individual RMU subsections.

## **5.5 Reactive Mineral Categories**

The 46 HSUs in the PM-OV HFM, have been subdivided into RMUs listed in [Table 5-3](#). The RMC/RMU subdivisions for each of the HSUs in the PM CAU model, mineralogical composition and depositional environment are described below.

### **5.5.1 Alluvial Aquifer (AA)**

This HSU consists of Quaternary- and Tertiary-age basin-filling alluvium such as that mapped at the surface in the southern portions of Gold Flat and Kawich Valley, and eastern Sarcobatus Flat (Qay,

Qam, and QTa in Slate et al., 1999) (Figure 3-2). It also includes generally older Tertiary gravels, tuffaceous sediments, and nonwelded tuffs (caldera moat-filling sediments and younger landslide and sedimentary breccias in Slate et al., 1999) that partially fill other basin areas such as Oasis Valley basin and the moat of the Timber Mountain caldera complex (BN, 2002a). Although the AA is considered the highest HSU in the model, stratigraphically, it consists of alluvial debris as young as recent alluvium found in active drainages and as old as tuffaceous gravels that may correlate time-stratigraphically with the youngest units of the Volcanics of Fortymile Canyon, approximately 11 million years ago (Ma) (Sawyer et al., 1994; Warren, 1999).

Lithologically, the AA is generally composed of poorly sorted, moderately to poorly bedded, unconsolidated to moderately indurated, angular to rounded sand and gravel in a locally tuffaceous matrix (Slate et al., 1999). Where lesser intervals of the older gravels and tuffaceous sediments are intercalated within the upper volcanic section, the gravels and sediments are grouped with a volcanic HSU. Conversely, where thin volcanic units are intercalated within significant thicknesses of older gravels or alluvium, the lesser volcanic beds may be grouped with the AA.

The mineralogy of the alluvium mainly reflects the lithologic composition of the constituent clasts. Though typically tuffaceous, volcanic clasts will contribute feldspars, quartz, and mafic minerals of biotite, hornblende, and magnetite, which may be oxidized to hematite. The mafic minerals are generally in very small amounts, approximately on the order of 1 or 2 percent by volume. The volcanic fragments may also contribute a significant percent, but usually less than 10 to 20 percent, of zeolite and clay minerals, though some clay minerals may be of sedimentary origin. Disseminated calcite from alluvial, eolian, and diagenetic processes is also common. Unlike the alluvial deposits in Yucca and Frenchman Flats, the alluvium in the PM CAU model area does not contain a significant amount of carbonate clasts (e.g., calcite [CaCO<sub>3</sub>] and dolomite [CaMgCO<sub>3</sub>]).

In general, most of the AA HSU can be classified as a VMP RMC reflecting relatively low percentages of the reactive minerals zeolite, clay and mica. However, two minor subdivisions (volumetrically) were created to address known variability. A DMP interval represents the interbedded Thirsty Canyon tuffs in the Timber Mountain moat area (i.e., in the vicinity of ER-18-2), and a ZEOL for the lowermost alluvium that is zeolitic in places (e.g., at ER-18-2, ER-30-1, and

ER-OV-03a2/3 [[Appendix A](#)]). For continuing RMUs laterally away from drill-hole control, all alluvium not contained within drill-hole data is considered alluvium vitric (AA V).

Fracture-filling minerals in the AA HSU, as reported in various lithologic logs (Benedict et al., 2001; Orkild and Jenkins, 1978), include calcite. Of the caldera moat-filling sediments, the calcite consists of loose, typically single crystals.

### **5.5.2 Younger Volcanics Composite Unit (YVCM)**

This minor unsaturated HSU consists of Pliocene and youngest Miocene basaltic rocks such as those composing Thirsty Mountain and Buckboard Mesa ([Figures 3-2](#) and [3-3](#)). It also consists of welded ash-flow tuff and nonwelded tuff erupted approximately 7.5 Ma from the Stonewall Mountain caldera located approximately 22 km (14 miles [mi]) northwest of the Black Mountain caldera (Noble et al., 1984; Slate et al., 1999). Older basaltic rocks ranging in age from 9.9 and 6.3 Ma (Crowe et al., 1995; Slate et al., 1999) are also included within this HSU (BN, 2002a).

The YVCM is present at Thirsty Mountain, Buckboard Mesa, and northwest of the Black Mountain caldera, where alluvium and some isolated exposures of older units have been grouped with the HSU (BN, 2002a). The unit is relatively thin, mainly because it consists of thin out-flow sheets of ash-flow tuff and younger basaltic lava flows. At ER-EC 4, on the eastern flank of Thirsty Mountain, the HSU is 15.2 m (50 ft) thick. At ER-18-2 on Buckboard Mesa, the HSU is 36.0 m (118 ft) thick.

The HSU is designated a composite unit because of the varied lithologic (and hydrogeologic) composition of the unit, though aquifer-type lithologies appear to be most common. The HSU is likely everywhere unsaturated, but is designated a separate HSU because of the conspicuous occurrences of the HSU at Thirsty Mountain and Buckboard Mesa, and the complex and poorly understood distribution of the unit in the northwest portion of the area northwest of Black Mountain, where it overlies much older volcanic units.

The YVCM HSU is subdivided into two RMUs: the younger mafic lavas (Y ML), and the younger volcanics devitrified mafic-poor (YV DMP) ([Appendix A](#)). Clinopyroxene and olivine are relatively abundant, and biotite and hematite occur in lesser amounts in the Y ML. Reactive minerals are rare in the YV DMP (DMP All in [Table 5-2](#)).

For continuing RMUs laterally away from drill-hole control, all units were thinned out in the northwest corner except YV DMP.

Fracture-filling minerals in the YVCM HSU, as reported in various lithologic logs (Benedict et al., 2001), include potassium feldspar, quartz, chalcedony, and smectite/illite.

### **5.5.3 Thirsty Canyon Volcanic Aquifer (TCVA)**

The TCVA consists mainly of peralkaline welded tuff and lava of the Thirsty Canyon Group erupted from the Black Mountain caldera between 9.4 and 9.15 Ma (Noble et al., 1984; Slate et al., 1999). It includes the stratigraphic units comendite of Ribbon Cliff, Pahute Mesa and Rocket Wash tuffs; Trail Ridge tuff; trachytic rocks of Pillar Spring and Yellow Cleft; trachyte of Hidden Cliff; and Gold Flat tuff (BN, 2002a). Outcrop patterns of these rocks suggest that the tuffs flowed mainly east onto Pahute Mesa, south into the northern half of the Oasis Valley basin, and southeast around Timber Mountain and into the northern and western portions of the moat of the TMCC. The more distal portions of the TCVA on Pahute Mesa and in the Timber Mountain moat consist mostly of welded ash-flow tuff and lesser nonwelded tuff of Pahute Mesa and Rocket Wash tuffs and Trail Ridge tuff. Closer to the source of these rocks, in the vicinity of Black Mountain, the tuffs overlie a thick section of lava of the comendite of Ribbon Cliff. Within the Black Mountain caldera, a considerable thickness of post-caldera lavas assigned to trachytic rocks of Pillar Spring and Yellow Cleft, and trachyte of Hidden Cliff overlie the older tuffs and lavas. Welded ash-flow tuff of Gold Flat tuff is the youngest unit within the TCVA and appears to be limited to isolated exposures within the caldera, an area just north of the caldera, and in the northern portion of the Oasis Valley basin just south of the caldera. The TCVA also includes minor deposits of overlying alluvium and older gravels, particularly in the moat of the Timber Mountain caldera complex. On Pahute Mesa, the TCVA includes relatively thin (typically less than 30 m [100 ft]) vitric nonwelded tuffs of the underlying Volcanics of Fortymile Canyon. Because the rocks that make up the TCVA are widely exposed within the model area, and numerous drill holes penetrate the HSU, the lateral extent of the TCVA is well constrained (Figure 3-2).

Because of its high structural position, the TCVA is nowhere completely saturated. Only where the base of the unit is structurally low, such as in the northern portion of the Oasis Valley basin and in the



vicinity of the Black Mountain caldera, does the lower portion of the HSU become saturated (see data from well ER-EC-4 [DOE/NV, 2000b] and drill hole PM-3 [Kilroy and Savard, 1996]).

The TCVA is subdivided into five RMUs: the Thirsty Canyon upper and lower vitric (Tt UV and Tt LV), Thirsty Canyon devitrified mafic-poor (Tt DMP), Thirsty Canyon zeolitic (Tt ZE), and the Thirsty Canyon lower mafic lava (Tt LML) ([Appendix A](#)). For continuing laterally away from drill-hole control, the edges of the TCVA and areas away from drill holes, the TCVA was equally divided into the Tt UV, Tt DMP, and Tt LV.

Fracture-filling minerals in the TCVA HSU, as reported in various lithologic logs (Benedict et al., 2001; Orkild and Jenkins, 1978), include calcite, chalcedony, clinoptilolite, mordenite, and smectite/illite.

#### **5.5.4 Detached Volcanics Composite Unit (DVCM)**

The DVCM consists of a very complex distribution of lavas and tuffs that form a relatively thin, highly extended interval above the Fluorspar Canyon-Bullfrog Hills (FC-BH) detachment fault of Maldonado (1990) and Fridrich et al. (1999b). This HSU comprises only Tertiary volcanic rocks because the surface of the detachment fault is assumed to have developed along the upper surface of the pre-Tertiary rocks (see west end of Profile C-C' [[Figure 3-6](#)]). Except for a thin veneer of AA that overlies the DVCM in some places, this HSU can include all rocks from the surface to the top of the pre-Tertiary rocks (BN, 2002a).

The DVCM consists of a variety of rock types, including rhyolitic lava, welded and nonwelded tuff, and landslide breccia (Slate et al., 1999; Fridrich et al., 1999b). Intense hydrothermal alteration and mineralization of the rocks are present locally, particularly in the Bullfrog Hills (Noble et al., 1991).

The DVCM underlies most of the Oasis Valley discharge area, where many springs and wells produce water directly from this HSU. Rocks of the DVCM observed at the surface are welded- and LFAs and TCUs. The unit is designated a composite unit because complex structural deformation in the area makes predictions of the distribution of subsurface HGUs highly speculative and uncertain. The presence of intense hydrothermal alteration not only complicates estimates of the hydrogeologic character, but also its mineralogical composition of the HSU.

The DVCM is subdivided into three RMUs: the Detached Volcanics Composite vitric (DVC V), the Detached Volcanics Composite devitrified mafic-poor (DVC DMP), and the Detached Volcanics Composite zeolitic (DVC ZE) ([Appendix A](#)). For continuing RMUs laterally away from drill-hole control, the DVCM was subdivided into the upper 75 m consisting of DVC DMP, with the remainder consisting of DVC ZE.

Fracture-filling minerals in the DVCM HSU, as reported in various lithologic logs (Benedict et al., 2001; Orkild and Jenkins, 1978), include Fe oxides, Mn oxides, chalcedony, smectite, and Zn oxide. Fractures typically are irregular and discontinuous.

### **5.5.5 Detached Volcanics Aquifer (DVA)**

The DVA consists mainly of welded ash-flow tuff and lava assigned to the Ammonia Tanks tuff and units of the Volcanics of Fortymile Canyon (BN, 2002a). These units, which are exposed on Oasis Mountain and the Hogback ([Figures 3-2 and 3-3](#)), were originally deposited within the TMCC, but were later detached and transported westward along the FC-BH detachment fault (Fridrich et al., 1999b). Although like the DVCM, the DVA also overlies the FC-BH detachment fault (Profile C-C' [[Figure 3-6](#)]), it is considered a separate HSU because of the preponderance of welded-tuff and LFAs that compose the HSU and much lower degree of alteration present.

Based on the mineralogy of these rocks, the dominant RMC for the DVA is DMP. For tracking purposes, the DVA is given the RMU name of detached volcanics DMP ([Appendix A](#)).

Fracture-filling minerals in the DVA HSU, as reported in various lithologic logs (Benedict et al., 2001, Orkild and Jenkins, 1978) include Fe oxides, Mn oxides, chalcedony, smectite, and Zn oxide. Fractures typically are irregular and discontinuous.

### **5.5.6 Fortymile Canyon Composite Unit (FCCM)**

This HSU consists of a complex and poorly understood 3-D distribution of lava and associated tuff of the Volcanics of Fortymile Canyon of Ferguson et al. (1994). Stratigraphic units that make up the FCCM include (generally from oldest to youngest) rhyolite of Fleur-de-lis Ranch, tuff of Leadfield Road, Beatty Wash Formation (with subunits, rhyolite of Beatty Wash, tuff of Cutoff Road, and rhyolite of Chukar Canyon), rhyolite of Rainbow Mountain, lavas of Dome Mountain, and rhyolite of

Shoshone Mountain (BN, 2002a). Together, these stratigraphic units compose an interval containing a variety of interfingering lithologic units, including rhyolitic and mafic lava, welded and nonwelded ash-flow tuff, bedded tuff, and tuffaceous gravels. The Volcanics of Fortymile Canyon were erupted from various vent sources in the area of the TMCC between approximately 11.4 and 9.5 Ma (Slate et al., 1999), and deposits of significant thickness are largely confined within the moat of the TMCC, where they form a ring around Timber Mountain, and in areas to the southwest of the TMCC (Figures 3-2 and 3-3).

The FCCM is lithologically variable, and information from outcrops and drill holes suggests that its lithologic composition varies geographically. Mafic and rhyolitic lava and nonwelded and bedded tuff appear to be the main components in the southeastern portion of the FCCM, with mafic lava more prevalent than in other areas. The northeastern portion of the FCCM, in the vicinity of drill hole UE-18t, is dominated by nonwelded and bedded tuffs. The northern, western, and southern portions of the HSU include significant deposits of rhyolitic lava and generally lesser nonwelded and bedded tuff and mafic lava. Welded ash-flow tuff becomes significant in the southwestern portion of the FCCM, with rhyolitic lava and nonwelded and bedded tuff also present. Because welded ash-flow tuff is so prevalent in the lower portion of the Volcanics of Fortymile Canyon in the southwestern portion of the TMCC, these rocks have been grouped into a separate HSU called the Fortymile Canyon aquifer that directly underlies the southwestern extent of the FCCM. In the northern portion of the Oasis Valley basin, around ER-EC-4, the FCCM is exclusively nonwelded and bedded tuff. Fortymile Canyon units that are present west of the Hogback fault and occur in the hanging wall of the FC-BH detachment fault are grouped with the DVCM, as described in Section 5.5.4.

The FCCM is designated a composite unit because of the complex distribution of lithologic units with considerably different hydrogeologic characters. The welded ash-flow tuffs and lavas within the HSU form welded-tuff and lava-flow aquifers. Where nonwelded and bedded tuffs are altered to zeolite, such as at wells ER-EC-4 and ER-EC-8 (DOE/NV, 2000b; BN, 2002b), they form confining units. The FCCM is typically unsaturated in the northern moat area of the TMCC (based on stratigraphic and hydrologic data from drill holes UE-18r, UE-18t, and ER-18-2), but becomes progressively more saturated to the west and southwest as the level of saturation rises stratigraphically towards the discharge area in Oasis Valley, based on data from ER-EC-4, ER-EC-8, MyJo Coffey #1, and ER-OV-06a (Profile A-A' [Figure 3-4]).

The FCCM in the PM-OV HFM can be subdivided into 9 RMUs based on the distribution of lithologic facies ([Appendix A](#)). Where nonwelded and bedded tuffs are altered to zeolite, the RMUs are the Fortymile Canyon Composite upper zeolitic (FCC UZE), Fortymile Canyon Composite middle zeolitic (FCC MZE), and the Fortymile Canyon lower zeolitic (FCC LZE). Devitrified mafic rocks of the FCCM are divided into the Fortymile Canyon Composite upper devitrified mafic-poor (FCC UDMP), middle devitrified mafic-poor (FCC MDMP), and lower devitrified mafic-poor (FCC LDMP). Mafic lavas that comprise the FCCM are the Fortymile Canyon Composite upper mafic lava (FCC UML) and lower mafic lava (FCC LML). One vitric component is the Fortymile Canyon Composite vitric (FCC UV).

Fracture-filling minerals in the FCCM HSU, as reported in various lithologic logs (Benedict et al., 2001; Orkild and Jenkins, 1978), include calcite, chalcedony, Mn oxides, and Fe oxides. Calcite is void-filling and consists of secondary cement.

#### **5.5.7 Fortymile Canyon Aquifer (FCA)**

Welded ash-flow tuff that occurs in the lower portion of the Volcanics of Fortymile Canyon in the Oasis Valley area forms an HSU designated as the FCA (BN, 2002a). This HSU is composed mainly of welded ash-flow tuffs and lesser amounts of rhyolitic lava assigned to the tuff of Cutoff Road and rhyolite of Fleur-de-lis Ranch. The FCA is designated an aquifer HSU because of the abundance of welded tuff and lava which form welded-tuff and LFAs. The FCA is completely saturated within the PM CAU model area.

Mineralogically, these rocks are DMP and are given the RMU name of Fortymile Canyon DMP ([Appendix A](#)).

Fracture-filling minerals in the FCA HSU, as reported in various lithologic logs (Benedict et al., 2001; Orkild and Jenkins, 1978), include calcite, chalcedony, Mn oxides, and Fe oxides.

#### **5.5.8 Timber Mountain Composite Unit (TMCM)**

The TMCM consists mainly of intra-caldera units of the Timber Mountain Group, most notably the Rainier Mesa and Ammonia Tanks tuffs (BN, 2002a). The eruption of these two units resulted in the formation of the Rainier Mesa and Ammonia Tanks calderas 11.6 and 11.45 Ma, respectively (Sawyer

et al., 1994). These two nested calderas comprise the Timber Mountain caldera complex (Byers et al., 1976a). The TMCM also includes units related to the Ammonia Tanks tuff, such as tuff of Buttonhook Wash, tuff of Crooked Canyon, and trachyte of East Cat Canyon, which erupted shortly after the Ammonia Tanks tuff (Slate et al., 1999). The TMCM is prominently located in the south-central portion of the model area (Figure 3-2). The HSU is confined within the margins of the Timber Mountain caldera complex where it is mostly saturated.

Lithologically, the TMCM consists mainly of densely welded ash-flow tuff that ponded to great thicknesses within subsiding calderas. Densely welded tuff is typically fractured, and thus assumed to behave as an aquifer. However, the TMCM is designated a composite unit because of the possibility that hydrothermal alteration within this deep intra-caldera setting has altered the hydraulic properties of the rocks, in particular, filling fractures with secondary minerals such as quartz.

The TMCM is subdivided into eight RMCs (Table 5-1). The Ammonia Tanks tuff and underlying Rainier Mesa tuff can both be subdivided into DMR and DMP RMCs based on their devitrified and welded tuff lithology, and the presence of both mafic-rich and mafic-poor members of both formations. The DMP are comprised of an upper, middle, and lower (UDMP, MDMP, and LDMP, respectively). The DMR contains a middle and lower (MDMR and LDMR). The Ammonia Tanks and Rainier Mesa tuffs are separated by a thin interval of zeolitic nonwelded and bedded tuff that is categorized as a ZEOL RMC, and consist of an upper and middle zeolitic (UZE and MZE).

For continuing RMUs laterally away from drill-hole control, the area of the Timber Mountain dome outcrop is Timber Mountain Composite middle devitrified mafic-poor (TMC MDMP). The area within the Ammonia Tanks caldera, the dominant RMU is TMC MDMP, with the bottom 300 m consisting of Timber Mountain Composite lower devitrified mafic-rich (TMC LDMR). West of Timber Mountain, in the Oasis Valley segment, the bottom 1,000 m was split equally between TMC LDMR and lower devitrified mafic-poor (TMC LDMP). In the eastern area, the RMU for the bottom 300 m is TMC LDMP. The overlying 500 m is lower devitrified mafic-rich (TMC LDMR).

Fracture-filling minerals in the TMCM HSU, as reported in various lithologic logs (Benedict et al., 2001; Orkild and Jenkins, 1978), include calcite, chalcedony, Fe oxides, Mn oxides, illite/smectite, and apatite. Fracture coatings are typically sparse to thinly coated on irregular surfaces.

### **5.5.9 Tannenbaum Hill Lava-Flow Aquifer (THLFA)**

Rhyolitic lava of the rhyolite of Tannenbaum Hill, a formation of the Timber Mountain Group, is the sole component of this HSU (BN, 2002a). The lava was erupted 11.54 Ma (Slate et al., 1999) between the caldera-forming eruptions of the Rainier Mesa and Ammonia Tanks tuffs. The lava appears to have flowed out on a structural bench formed as a result of late-stage outer collapse of the northwestern portion of the Rainier Mesa caldera.

The thickness of the THLFA is also fairly well constrained. Data from ER-EC-1 and ER-EC-6 indicate that the unit is probably 200 to 300 m (656 to 984 ft) thick (DOE/NV, 2000a and c; [Appendix A](#)).

The THLFA is considered an aquifer because it consists entirely of rhyolitic lava that is assumed to be well fractured. Although the unit is likely unsaturated, it is designated an HSU because of the importance of the rhyolite of Tannenbaum Hill in defining the complex structural relationships in the vicinity of the northwestern portion of the TMCC which is just downgradient from the underground nuclear tests in southwestern Area 20.

Mineralogically, the THLFA is mostly DMP (the Tannenbaum Hill DMP) with a minor amount of ZEOL at the base in some places (the Tannenbaum Hill Zeolite, [Appendix A](#)). Fracture-filling minerals in the THLFA HSU, as reported in various lithologic logs (Drellack et al., 1997), include dominant zeolites, common chalcedony, minor clay, unknown silicates, Fe oxides, and Mn oxides. Above the water table, chalcedony is the primary fracture-coating mineral, followed by zeolites with clay minerals and Fe/Mn oxides. Zeolites are the most abundant fracture-coating mineral below the water table, followed by Fe/Mn oxides.

### **5.5.10 Tannenbaum Hill Composite Unit (THCM)**

The THCM consists of welded and nonwelded tuff of the rhyolite of Tannenbaum Hill (BN, 2002a). These rocks may represent construction of a tuff cone (Warren et al., 1989a) before extrusion of the overlying lava (i.e., THLFA).

The unit is not exposed at the surface and has only been encountered in ER-EC-1 and ER-EC-6 (DOE/NV, 2000a and c). Well ER-EC-6 encountered 122.6 m (402 ft) of zeolitic nonwelded

Tannenbaum Hill tuff. However, ER-EC-1 encountered 84.4 m (277 ft) of THCM consisting of devitrified to partially vitric, nonwelded tuff, overlying vitric and devitrified, moderately welded ash-flow tuff, which overlies zeolitic nonwelded tuff. Thus, the THCM is designated a composite unit because it is composed of several HGUs. Only the lower portion of the THCM may be saturated, and like the THLFA, it is designated a separate HSU mainly because of its importance in defining complex structural relationships in the area.

The mineralogy of the unaltered welded tuff is DMP and given the RMU name of THC DMP. The altered nonwelded tuff component is a ZEOL RMC and given the RMU name of THC ZE ([Appendix A](#)).

Fracture-filling minerals in the THCM HSU, as reported in various lithologic logs (Drellack et al., 1997), include strongly dominant zeolites, minor quartz, Fe/Mn oxides, and clay.

#### **5.5.11 Timber Mountain Aquifer (TMA)**

The TMA consists of rocks that are mostly the extra-caldera equivalent of the rocks that compose the TMCM. Stratigraphically, these include (from oldest to youngest) the Rainier Mesa and Ammonia Tanks tuffs, both formations of the Timber Mountain Group. Lithologically, the TMA consists mostly of welded ash-flow tuff and lesser amounts of vitric (unaltered) nonwelded ash-flow tuff and bedded tuff. These rocks were erupted from the Rainier Mesa and Ammonia Tanks calderas and deposited as outflow sheets and ash-fall deposits in areas outside of the margins of the calderas.

The Tma and Tmr consist of nonwelded to densely welded, rhyolitic ash-flow tuff. The rocks contain abundant phenocrysts of sanidine, quartz, and sodic plagioclase, with less abundant biotite and clinopyroxene, and accessory sphene (Tma only), zircon, apatite, and monazite (Tmr only) (Warren et al., 2003). Both can usually be divided into a mafic-rich upper part and a mafic-poor lower part. In most places, the Tma is separated from the underlying Tmr by a 1.5- to 9.1-m (5- to 30-ft) thick bedded tuff; the bedded Ammonia Tanks tuff (Tmab). The Tmab is typically vitric and slightly calcareous. However, in the vicinity of the northern testing area of PM-OV, around ER-EC-4 (NNSA/NV, 2002), the Tmab is zeolitic.

Reactive minerals within the TMA are typically rare, reflecting the devitrified welded tuff lithology that results in a rock composed mostly of micro-crystalline quartz and feldspar ([Appendix A](#)). Consequently, dominant RMCs for the TMA are DMR, where the mafic-rich Tmar, Tmrr, and Tmr are present, and DMP, for the mafic-poor Tma and Tmr. The vitric Tmab is considered a VMP RMC, and a ZEOL where it is zeolitic. Based on the stratigraphic groupings of these typical RMCs, the TMA HSU can be subdivided into seven RMUs: the Ammonia Tanks DMR (AT DMR), the Ammonia Tanks DMP (AT DMP), the Timber Mountain middle zeolitic (TM MZE), the Timber Mountain middle vitric (TM MV), the Rainier Mesa DMR (RM DMR) and Rainier Mesa DMP (RM DMP), the Ammonia Tanks upper vitric (AT UV) ([Appendix A](#)).

For continuing RMUs laterally away from drill-hole control, in the areas to the north and east, the thin edges consist of Rainier Mesa lower vitric. For the area south-southwest from drill hole ER-EC-4 the TMA is subdivided into the following RMUs: AT DMP at 35 percent; TM MV at 11 percent; TM MZE was thinned out to the south, west, and north from ER-EC-4; RM DMR at 16 percent; RM DMP at 30 percent; and RM LV at 8 percent.

Fracture-filling minerals in the TMA HSU, as reported in various lithologic logs (Benedict et al., 2001; Drellack et al., 1997), include calcite, chalcedony, Mn oxides, Fe oxides, illite and smectite, zeolites, and quartz. Three secondary mineral coatings were observed to occur most often in fractures within the TMA and include calcite, clay, and Fe/Mn oxides.

#### **5.5.12 Subcaldera Volcanic Confining Unit (SCVCU)**

The SCVCU is a highly conjectural unit (BN, 2002a). The unit is exposed nowhere at the surface and has not been encountered in any drill hole. Its existence is based primarily on the presence of deep basement (or low-density regions) beneath the TMCC, as defined by gravity measurements.

If the SCVCU exists beneath the TMCC at the depths depicted in the model (Profiles A-A' [[Figure 3-4](#)] and B-B' [[Figure 3-5](#)]), then the rocks comprising the HSU are likely to be highly altered and intruded. This would probably significantly reduce the ability of these rocks to transmit groundwater, and thus they are considered a confining unit in the model.



There are no XRD analyses specifically of the SCVCU rocks in any of the UGTA CAU datasets. However, based on the type and intensity of alteration, this unit is classified as a ZEOL RMC. Its RMU designation is Subcaldera zeolitic (SC ZE) ([Appendix A](#)).

Fracture-filling minerals in the SCVCU HSU, a conjectural unit modeled as consisting of highly altered volcanic rocks, are likely filled with secondary minerals, such as quartz, due to the circulation of hot, mineral-rich water associated with deep magma bodies (Orkild and Jenkins, 1978).

### **5.5.13 Fluorspar Canyon Confining Unit (FCCU)**

The FCCU consists of zeolitic, nonwelded tuff of the rhyolite of Fluorspar Canyon, a formation of the Timber Mountain Group (BN, 2002a). The rhyolite of Fluorspar Canyon is widespread across western Pahute Mesa and has been encountered in numerous drill holes. Beneath most of western Pahute Mesa, the rhyolite of Fluorspar Canyon is typically vitric and is included within the PVTa described in [Section 5.5.16](#) (BN, 2002a). However, in ER-EC-1 and ER-EC-6, the formation is zeolitic ([Appendix A](#)). This is apparently due to the lower structural position of the formation in this area resulting from down-to-the-south displacement along the Northern Timber Mountain Moat structural zone. The lower elevation of the unit in the vicinity of ER-EC-1 and ER-EC-6 has resulted in most of the unit being saturated, a situation more conducive to zeolitization. The pervasive zeolitization of the unit observed in ER-EC-1 and ER-EC-6 classifies the FCCU as a confining unit, which is consistent with water production measured during drilling of these two wells, both of which produced only very minor amounts of water from the unit (DOE/NV, 2000a and c).

The rocks comprising the FCCU are zeolitic. Other reactive minerals are relatively low in abundance. Because of the dominance of zeolite minerals in the FCCU, the overall RMC is ZEOL or FL ZE for the RMU ([Appendix A](#)).

Fracture-filling minerals in the FCCU HSU, as reported in various lithologic logs (Benedict et al., 2001), include calcite and Mn oxides that consist of very sparse vein fillings.

### **5.5.14 Windy Wash Aquifer (WWA)**

The WWA is composed of a single LFA consisting of rhyolite lava of the rhyolite of Windy Wash, a stratigraphic unit of the Timber Mountain Group (BN, 2002a).

The occurrence of the unit is generally centered around drill hole U-20a #2WW in east-central Area 20. The aquifer has a maximum thickness of approximately 180 m (591 ft) and is very limited in extent.

The WWA is unsaturated beneath Pahute Mesa. It was designated a separate HSU because its lithologic and hydrogeologic character is conspicuously different from that of the units above and below it.

Based on detailed lithologic descriptions from U-20a #2, Windy Wash is categorized as a DMP RMC and given the RMU name of WW DMP ([Appendix A](#)).

Fracture-filling minerals in the WWA HSU, as reported in various lithologic logs (Benedict et al., 2001), include chalcedony, calcite, Fe oxides, and clays.

#### **5.5.15 Paintbrush Composite Unit (PCM)**

This HSU consists mostly of units of the Paintbrush Group that occur south of Pahute Mesa in the vicinity of the Claim Canyon caldera (BN, 2002a). It includes such stratigraphic units as rhyolite of Vent Pass, Tiva Canyon tuff, rhyolite of Delirium Canyon, Pah Canyon tuff, and Topopah Spring tuff. The eruption of the Tiva Canyon tuff 12.7 Ma (Sawyer et al., 1994) formed the Claim Canyon caldera. The PCM also includes isolated exposures of younger Timber Mountain Group units such as Rainier Mesa tuff, rhyolite of Pinnacles Ridge, Rhyolite of Waterpipe Butte, and rhyolite of Windy Wash. At Pahute Mesa, where numerous drill holes penetrate the Paintbrush Group, units of the Paintbrush Group are divided into seven separate HSUs. The extent of the PCM is well constrained in the southern portion of the model area, where there are well-defined surface exposures (BN, 2002a).

Lithologically, the PCM consists of welded ash-flow tuff, rhyolitic lava, and lesser unaltered to altered (i.e., zeolitic) nonwelded tuff. Consequently, the HSU consists hydrogeologically of vitric- and WTAs, LFAs, and TCUs. However, within the Claim Canyon caldera, the Tiva Canyon tuff probably forms a very thick WTA. The PCM is designated a composite unit because of the variety and unknown distribution of HGUs. However, within the Claim Canyon caldera, WTA of the Tiva Canyon tuff probably dominates the HSU.

Within the Claim Canyon caldera, the unit is mostly saturated. Outside of the caldera the HSU is likely to be unsaturated in its upper portion.

The PCM is subdivided into four RMUs: an upper and lower devitrified mafic-poor (PC UDMP and PC LDMP, respectively), a middle vitric (PC MV), and a middle zeolitic unit (PC LZE) ([Appendix A](#)).

Fracture-filling minerals in the PCM HSU, as reported in various lithologic logs (Benedict et al., 2001), include calcite, chalcedony, Fe oxides, Mn oxides, illite/smectite, and apatite.

#### **5.5.16 Paintbrush Vitric-Tuff Aquifer (PVTA)**

The PVTA consists of vitric bedded and non-welded tuffs that occur stratigraphically between the base of the Rainier Mesa tuff and the top of Echo Peak lava (BN, 2002a). For an explanation of the spatial relationships of the various HSUs of the Paintbrush Group, refer to Figure 4-23 of BN (2002a). The PVTA is present within the northeastern portion of the model area, particularly in the Pahute Mesa testing area. East of the West Greeley fault, the PVTA mainly includes the stratigraphic units tuff of Holmes Road, Tiva Canyon tuff, and rhyolite of Delirium Canyon. West of the fault, this HSU mainly includes rhyolite of Fluorspar Canyon and tuff of Holmes Road.

The vitric character and general scarcity of biotite in the included stratigraphic units of the PVTA result in rocks that are likely low in reactive minerals; thus, the PVTA is primarily categorized as a VMP RMC, with a given Paintbrush vitric (P V) RMU label ([Appendix A](#)).

Fracture-filling minerals in the PVTA HSU, as reported in various lithologic logs (Drellack et al., 1997), include zeolites, clay minerals, Fe/Mn oxides, and quartz.

#### **5.5.17 Benham Aquifer (BA)**

Like the WWA, the BA consists of a single LFA composed of rhyolite lava, the rhyolite of Benham (BN, 2002a). The BA occurs mostly west of the intersection of the Boxcar and West Boxcar faults in southwestern Area 20. The BA is limited in extent and generally centered around drill hole U-20c where 347 m (1,138 ft) of this HSU was penetrated (Profile A-A' [[Figure 3-4](#)]). In the southern portion of the BA, in the vicinity of drill hole U-20as, the lava is underlain by thick zeolitic bedded

tuff of rhyolite of Benham, which is included in the underlying upper Paintbrush confining unit (UPCU). The presence of this thick bedded tuff under the lava suggests the formation of a tuff cone before extrusion of lava (Wagoner and Clark, 1986; Warren et al., 1989a). The origin of the tuff cone and related lava was probably a vent or fissure at the intersection of the Boxcar and West Boxcar faults (Warren et al., 1989a). Only the lower portions of the northern and northeastern margins of the aquifer are below the water table.

The mineralogy of the altered bedded tuff is ZEOL and is given the RMU name of B UZE. Unaltered, devitrified BA is given the RMU name of B DMP ([Appendix A](#)).

Fracture-filling minerals in the BA HSU, as reported in various lithologic logs (Benedict et al., 2001; Orkild and Jenkins, 1978), include chalcedony, illite, quartz, potassium feldspar, Fe oxides, and Mn oxides.

#### **5.5.18 Upper Paintbrush Confining Unit (UPCU)**

The UPCU generally consists of zeolitic bedded and nonwelded tuffs that occur below the rhyolite of Benham lava and above the welded Tiva Canyon tuff, including zeolitic nonwelded and bedded Tiva Canyon tuff (BN, 2002a). These rocks are generally the stratigraphic equivalent of the rocks in the lower portion the PVTA. The unit is mostly saturated and occurs mainly in central Area 20 west of the West Greeley fault.

The UPCU is strongly zeolitic. Other reactive minerals are relatively low in abundance. Because of the dominance of zeolite minerals in the UPCU, the overall RMC is ZEOL and is given an RMU name of UP ZE ([Appendix A](#)).

Fracture-filling minerals in the UPCU HSU, as reported in various lithologic logs (Orkild and Jenkins, 1978), include calcite and Mn oxides.

#### **5.5.19 Tiva Canyon Aquifer (TCA)**

The TCA consists of a single WTA composed of welded ash-flow tuff of the Pahute Mesa lobe of the Tiva Canyon tuff (BN, 2002a). The unit is saturated.

The TCA is rare in reactive minerals. This reflects the high degree of devitrification characteristic of the Tiva Canyon tuff that yields a rock predominantly composed of felsic minerals in the form of micro-crystalline quartz and feldspar. Within the model area, biotite is rare in the Tiva Canyon tuff. The TCA is categorized as a DMP RMC, with an RMU name of TC DMP ([Appendix A](#)).

Fracture-filling minerals in the TCA HSU, as reported in various lithologic logs (Orkild and Jenkins, 1978), include calcite, chalcedony, smectite, illite, Fe oxides, and Mn oxides.

#### **5.5.20 Paintbrush Lava-Flow Aquifer (PLFA)**

The PLFA consists of two LFAs and a WTA. These aquifers are composed of lithologies assigned to both the rhyolite of Silent Canyon and the rhyolite of Echo Peak, both of which are caldera-burying units of the Paintbrush Group (BN, 2002a). The PLFA occurs mainly in western Area 19 between the Scrugham Peak and West Greeley faults. The northwestern portion of the PLFA consists mostly of a single LFA composed of an interval of rhyolite lava assigned to the older rhyolite of Silent Canyon. This lava appears to be more pumiceous than others in this area, possibly indicating a higher initial gas content, which would have made the lava more fluid. The PLFA occurs mostly above the water table, however, anomalously high water levels have been measured in this aquifer in several holes in the vicinity of drill hole U-19bh (O'Hagan and Laczniak, 1996).

The PLFA is subdivided into eight RMUs: Paintbrush lava-flow upper, middle, and lower vitric (PLF UV, PLF MV, and PLF LV); and Paintbrush lava-flow upper, middle, and lower devitrified mafic-poor (PLF UDMP, PLF MDMP, and PLF LDMP) ([Appendix A](#)). The lower altered portion of the PLFA is comprised of a middle and lower zeolitic (PLF MZE and PLF LZE).

[Figure 5-4](#) is a model profile through the PLFA HSU in the reactive mineral model showing the RMC/RMU subdivisions.

Fracture-filling minerals in the PLFA HSU, as reported in various lithologic logs (Drellack et al., 1997), include zeolites and chalcedony.

#### **5.5.21 Lower Paintbrush Confining Unit (LPCU)**

The LPCU consists of zeolitic bedded and nonwelded tuffs that occur stratigraphically between the Tiva Canyon tuff and the welded Topopah Spring tuff (BN, 2002a). This mainly includes the rhyolite

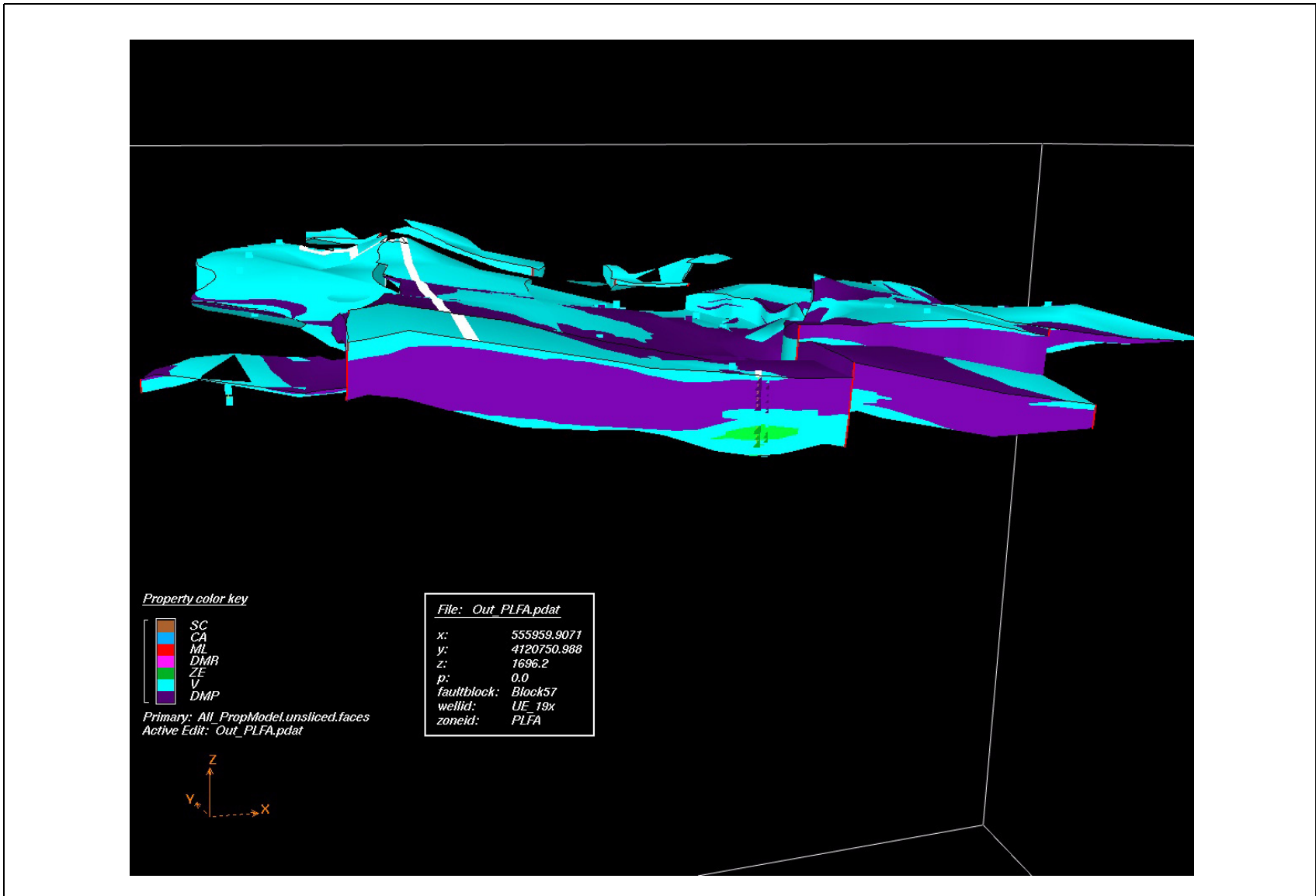


**Figure 5-4**  
**West-East Model Profile through the PLFA Showing the RMC Subdivisions in the Northern PM-OV Model Area**

Source: Drellack, 2007

of Delirium Canyon, and the bedded and nonwelded Topopah Spring tuff. The LPCU occurs mainly west of the West Boxcar fault in the southwestern portion of the model area. A limited occurrence of the unit is present adjacent to the down-thrown side of the West Greeley fault around drill hole U-20n.

The LPCU is composed of zeolitic tuffs similar to the lower tuff confining unit (LTCU), and thus is categorized as a ZEOL RMC and is assigned an RMU name of LP ZE ([Appendix A](#)).

Fracture-filling minerals in the LPCU HSU, as reported in various lithologic logs (Drellack et al., 1997), include zeolite, chalcedony, Fe oxides, and Mn oxides.

### **5.5.22 Topopah Spring Aquifer (TSA)**

The TSA consists of a single WTA composed of welded ash-flow tuff of the Yucca/PM-OV lobe of the Topopah Spring tuff (BN, 2002a). The TSA is highly transmissive but is limited in areal extent. The unit is saturated in Western Area 20 and in Mid Valley.

The Topopah Spring tuff is a densely to moderately welded rhyolitic ash-flow tuff. Phenocrysts include scarce to common sanidine and plagioclase, common biotite, and lesser clinopyroxene. There is a characteristic 5-m-thick black vitrophyre (glassy zone) near the top; a lithophysal zone below the vitrophyre is also common. The lithophysal cavities are generally lined with euhedral cristobalite, tridymite, and feldspar crystals.

The TSA is rare in reactive minerals. This reflects the low amounts of biotite and the high degree of devitrification characteristic of the Topopah Spring tuff that yields a rock predominantly composed of felsic minerals. Therefore, most of the TSA is categorized as a DMP RMC with an RMU name of TS DMP. At some locations on the NTS, however, the relatively thin non- to partially welded basal portion of the TSA may be zeolitic. For these minor occurrences, the basal zeolitic portion is categorized as a ZEOL RMC and is named Topopah Spring zeolitic (TS ZE) in [Appendix A](#).

Fracture-filling minerals in the TSA HSU, as reported in various lithologic logs (Benedict et al., 2001; Orkild and Jenkins, 1978), include chalcedony and calcite.

### **5.5.23 Yucca Mountain Crater Flat Composite Unit (YMCFCM)**

This HSU comprises all units of the Crater Flat Group and Calico Hills Formation that occur in the southern portion of the model area (BN, 2002a). In the northern portion of the area at Pahute Mesa, these stratigraphic units are divided into multiple HSUs. However, due to limited subsurface information on these units in the southern portion of the area, they are grouped together into a single HSU. Stratigraphic units included are Calico Hills Formation, Bullfrog tuff, rhyolite of Prospector Pass, and Tram tuff. Lithologic units include welded and nonwelded tuff and rhyolitic lava.

The YMCFCM is subdivided into six RMUs ([Appendix A](#)). Zeolitized units are divided into upper, middle, and lower zeolitic RMUs (YMCF UZE, YMCF MZE, and YMCF LZE). Devitrified units, rare in reactive minerals and predominantly composed of felsic minerals, are divided into upper, middle, and lower devitrified mafic-poor RMUs (YMCF UDMP, YMCF MDMP, and YMCF LDMP).

For continuing RMUs laterally away from drill-hole control, the following subdivisions are based on drill hole USW G-2: YMCF UZE at 45 percent, YMCF UDMP at 13 percent, YMCF MZE at 11 percent, YMCF MDMP at 7 percent, YMCF LZE at 7 percent, and YMCF LDMP at 17 percent. All the subunits were thinned proportionally until the DMP units were not distinguishable, then the dominant RMU became Yucca Mountain Crater Flat upper zeolitic.

Fracture-filling minerals in the YMCFCM HSU, as reported in various lithologic logs (Benedict et al., 2001; Orkild and Jenkins, 1978), include chalcedony, Mn oxides, Fe oxides, and Pb oxide.

### **5.5.24 Calico Hills Vitric-Tuff Aquifer (CHVTA)**

This aquifer consists of mainly vitric, bedded and nonwelded tuff of the mafic-poor member of the Calico Hills Formation (BN, 2002a). The unit occurs in Area 19 where the Calico Hills Formation is structurally high, and thus mostly vitric ([Figure 3-2](#)). The central and northern portions of the western margin form a vertical boundary (conceptually) that coincides with the approximate location of the pinch-out of the lavas within the adjacent Calico Hills vitric composite unit. The southern portion of the western margin is a vertical boundary (conceptually) coinciding with the approximate position where the tuffs become predominately zeolitic within the adjacent Calico Hills confining



unit. The relationship of the four Calico Hills HSUs is graphically depicted in the schematic cross section Figure 4-32 in BN (2002a).

Overall, the CHVTA is categorized as a VMP based on the unaltered (i.e., glassy) and general mafic-poor character of the constituent rocks ([Appendix A](#)). However, in some areas, a portion of the CHVTA has become zeolitic. To account for these altered zones, the CHVTA has been subdivided into three RMUs: Calico Hills upper and lower vitric (CHV UV and CHV LV) and middle Calico Hills zeolitic (CHV ZE).

Fracture-filling minerals in the CHVTA HSU, as reported in various lithologic logs (Drellack et al., 1997), include zeolites, clay minerals, Fe/Mn oxides, and quartz.

#### **5.5.25 Calico Hills Vitric Composite Unit (CHVCM)**

The CHVCM consists of lava and bedded and nonwelded tuff mostly assigned to the mafic-poor member of the Calico Hills Formation (BN, 2002a). The generally higher structural position of the CHVCM has resulted in much of the bedded and nonwelded tuff remaining vitric, particularly the upper portions of the unit. This may result in somewhat higher overall permeability for this HSU. Limited drill-hole information and the unpredictable occurrence of lava within the unit preclude accurate correlation and mapping of individual HGUs within this HSU. The percentage of LFA within the CHVCM ranges from 20 to 70 percent (by thickness) and appears to average about 50 percent (Prothro and Drellack, 1997).

Overall, the CHVCM is categorized as a VMP based on the unaltered (i.e., glassy) and general mafic-poor character of the constituent rocks. However, in some areas, a portion of the CHVCM has become devitrified and is categorized as a DMP. To account for these altered zones, the CHVCM has been subdivided into four RMUs: Calico Hills upper and lower vitric (CHVC UV and CHVC LV), Calico Hills vitric composite DMP (CHVC DMP), and Calico Hills vitric composite zeolitic (CHVC ZE) ([Appendix A](#)).

Fracture-filling minerals in the CHVCM HSU, as reported in various lithologic logs (Drellack et al., 1997), include zeolites, clay minerals, Fe/Mn oxides, and quartz.

### **5.5.26 Calico Hills Zeolitic Composite Unit (CHZCM)**

The Calico Hills zeolitic composite unit is probably the most important HSU in Area 20. It consists of a complex distribution of rhyolite lava and zeolitized bedded and nonwelded tuff of the mafic-poor and mafic-rich members of the Calico Hills Formation (BN, 2002a). This HSU is dominated by the thicker and more extensive mafic-poor member, which consists of at least three intervals of LFAs separated by TCUs. The percentage of LFAs within the CHZCM appears to be approximately the same as that for the CHVCM (0 to 20 percent; Prothro and Drellack, 1997).

The CHZCM has been subdivided into seven RMUs ([Appendix A](#)). Zeolitized tuffs are subdivided into upper, middle, and lower zeolitic (CHZC UZE, CHZC MZE, and CHZC LZE). Devitrified units with predominantly felsic minerals are divided into upper, middle, and lower devitrified mafic-poor (CHZC UDMP, CHZC MDMP, and CHZC LDMP). A small vitric portion is given the RMU Calico Hills zeolitic composite upper vitric (CHZC UV).

Fracture-filling minerals in the CHZCM HSU, as reported in various lithologic logs (Drellack et al., 1997), include zeolites, clay minerals, Fe/Mn oxides, and quartz.

### **5.5.27 Calico Hills Confining Unit (CHCU)**

The CHCU consists of zeolitic bedded and nonwelded tuff of the mafic-poor and mafic-rich members of the Calico Hills Formation (BN, 2002a). The main occurrence of the CHCU is in the western portion of the study area. In this area, the unit pinches out along its northern and western margins. The eastern margin is a vertical boundary that coincides with the approximate location of the westward pinch-out of the lavas within the adjacent CHZCM. The northern margin of the Timber Mountain caldera complex forms the southern boundary. The CHCU is also present to a limited extent adjacent to the down-thrown side of the Almendro fault in southern Area 19 around drill hole UE-19fS.

Overall, the CHCU is categorized as a ZEOL RMC based on predominantly zeolitized bedded and nonwelded tuff and is assigned an RMU of Calico Hills zeolitic (CHZ ZE) ([Appendix A](#)).

Fracture-filling minerals in the CHCU HSU, as reported in various lithologic logs (Drellack et al., 1997), include zeolites, clay minerals, Fe/Mn oxides, and quartz.

### **5.5.28 Inlet Aquifer (IA)**

The IA consists of lava and minor zeolitic, bedded and nonwelded tuff of the Area 20 caldera-filling rhyolite of Inlet (BN, 2002a). Thus, the IA consists mostly of LFA with only minor TCU lithologies. Only a few drill holes at Pahute Mesa have encountered the rhyolite of Inlet, so estimates of the extent, thickness, and hydraulic character of the IA are highly conjectural.

There appears to be two main occurrences of the IA at Pahute Mesa. One occurrence is in southwestern Area 19 and the adjacent portion of southeastern Area 20 within the outer collapse zone of the Area 20 caldera. This occurrence is defined by drill hole UE-19fS, which encountered 561 m (1,840 ft) of the rhyolite of Inlet, consisting of 99 percent lava ([Appendix A](#)). Lava of the rhyolite of Inlet, and thus the IA, appears to be confined to the outer collapse zone in this area. Maximum thickness for this occurrence may be as much as 610 m (2,000 ft).

The other occurrence of IA is in western Area 20, between the West Boxcar and Purse faults. This occurrence is defined by drill hole UE-20f, which encountered 381 m (1,250 ft) of rhyolite of Inlet, of which 84 percent is lava ([Appendix A](#)).

Based in mineralogy, the IA is categorized as a DMP RMC and is given an RMU name of IA DMP ([Appendix A](#)).

Fracture-filling minerals in the IA HSU, as reported in various lithologic logs (Benedict et al., 2001; Orkild and Jenkins, 1978), include smectite and Fe oxides.

### **5.5.29 Crater Flat Composite Unit (CFCM)**

The CFCM occurs west of the West Greeley fault mainly within the inner collapse zone of the Area 20 caldera (BN, 2002a). This HSU consists of lava-flow and WTAs, and TCUs of the tuff of Jorum and underlying rhyolite of Sled. Like the IA, few drill holes penetrate this HSU, and therefore, depictions of its distribution and hydrologic character are highly conjectural.

The tuff of Jorum appears to be relatively thin and sporadic at Pahute Mesa. However, at drill hole UE 20h, a thickness of more than 488 m (1,600 ft) was encountered, including 239 m (784 ft) of welded tuff and 37 m (121 ft) of lava, in which the hole was terminated (Noto et al., 1999; Prothro

and Warren, 2001). This anomalously thick occurrence of tuff of Jorum suggests that the main site of deposition of this caldera-filling unit is west of the West Greeley fault. This is also the site of thick occurrences of other Area 20 caldera-filling units such as rhyolite of Inlet and Calico Hills Formation. If it is assumed that the lithologic composition of tuff of Jorum is similar to that of other Area 20 caldera-filling units, then tuff of Jorum west of the West Greeley fault is expected to consist of lava and welded tuff interbedded and intercalated with zeolitic bedded and nonwelded tuff. For this reason, this unit is designated a composite HSU.

The lower portion of the CFCM probably consists of lava and bedded and nonwelded tuff of the rhyolite of Sled. Little is known of this formation west of the West Greeley fault. However, because it is a caldera-filling unit, it is assumed to be similar to the tuff of Jorum lithologically, hydrogeologically, and in its distribution.

Overall, the CFCM is categorized as a ZEOL RMC based on predominantly zeolitized bedded and nonwelded tuff and is divided into two RMUs: upper and lower zeolitic (CFC UZE and CFC LZE). The devitrified mafic-poor portion of the CFCM is assigned a DMP RMC and is given the RMU name CFCM DMP ([Appendix A](#)).

Fracture-filling minerals in the CFCM HSU, as reported in various lithologic logs (Benedict et al., 2001; Orkild and Jenkins, 1978), include calcite, smectite, and Fe oxides.

### **5.5.30 Crater Flat Confining Unit (CFCU)**

This HSU occurs mainly within the eastern half of the inner-collapse zone of the Area 20 caldera, east of the West Greeley fault (BN, 2002a). Portions of the unit extend north into the moat of the Grouse Canyon caldera and south into the outer-collapse zone of the Area 20 caldera. The CFCU consists mainly of zeolitic bedded and nonwelded tuff with minor intercalated lava of mostly rhyolite of Sled with lesser tuff of Jorum.

Zeolite is the major mineral component of the CFCU. Other reactive minerals are typically rare. Because of the high zeolite content, the CFCU is categorized as a ZEOL RMC and is given the RMU name of CFZ ZE ([Appendix A](#)).

Fracture-filling minerals in the CFCU HSU, as reported in various lithologic logs (Benedict et al., 2001; Orkild and Jenkins, 1978), include heulandite.

### **5.5.31 Kearsarge Aquifer (KA)**

The KA consists of a single interval of LFA consisting of rhyolite lava of the rhyolite of Kearsarge (BN, 2002a). It is located in north-central Area 19. The unit is limited in extent and relatively thin, having a maximum thickness of approximately 198 m (650 ft).

Although the KA is mostly devitrified, the top and basal portions are glassy to zeolitic. Also, the rhyolite of Kearsarge is mafic rich. To account for these variations, the KA has been subdivided into five RMUs that correspond to the dominant RMCs ([Appendix A](#)). From the top down, these are Kearsarge upper zeolitic (K UZE), Kearsarge upper vitric (K UV), Kearsarge DMP (K DMP), Kearsarge lower vitric (K LV), and Kearsarge Lower Zeolitic (K LZE).

Fracture-filling minerals in the KA HSU, as reported in various lithologic logs (Benedict et al., 2001; Orkild and Jenkins, 1978), include chalcedony, calcite, Fe oxides, and clays.

### **5.5.32 Bullfrog Confining Unit (BFCU)**

The BFCU consists of zeolitic nonwelded ash-flow tuff of the Area 20 caldera-forming Bullfrog tuff (BN, 2002a). The Bullfrog tuff is unusually thick and extensive for a nonwelded ash-flow tuff. It is believed that the abundance of lithic fragments within the formation effectively quenched the ash-flow tuff before welding could occur (Warren et al., 1989b; Ferguson et al., 1994). The BFCU occurs within the northeastern portion of the model area, particularly within the Area 20 caldera, where it has a rather uniform thickness of approximately 610 m (2,000 ft).

Typically, the BFCU is a ZEOL RMC. However, in some areas, it may be devitrified (DMP RMC). To account for this variation, the BFCU was subdivided into three RMUs: from the top down, BF, BF DMP, and the BF lower zeolitic ([Appendix A](#)).

Fracture-filling minerals in the BFCU HSU, were not observed. The poorly fractured TCU HGU comprises much of the BFCU (Drellack et al., 1997).

### 5.5.33 **Belted Range Aquifer (BRA)**

The BRA is composed mainly of lava-flow and WTAs consisting of rhyolite lava and welded ash-flow tuff of the Belted Range Group, which formed and filled the Grouse Canyon caldera (BN, 2002a). Minor amounts of TCU is also intercalated within the unit. The BRA underlies most of Areas 19 and 20. It is very thick, particularly within the inner and outer collapse zones of the Grouse Canyon caldera, where it is as much as 1,981 m (6,500 ft) thick. The BRA is probably completely saturated everywhere except in the northern and eastern portions of Area 19.

Most of the rocks that compose the BRA are devitrified and mafic-poor, and thus the BRA is categorized overall as a DMP RMC ([Appendix A](#)). The occurrence of zeolitic tuff and lava results in some zones better characterized as ZEOL RMC. For the PM reactive mineral model, the BRA was subdivided into eight RMUs ([Appendix A](#)) generally reflecting the occurrence of zeolite minerals within an otherwise DMP stratigraphic package. The DMP units are divided into an upper, middle, and lower DMP, and zeolitized units are divided into an upper, middle, and lower ZEOL. The Belted Range upper vitric is assigned the RMU name of BR UV.

For continuing RMUs laterally away from drill-hole control, in the northern area and in the northeast (north of Model Profile B-B' [[Figure 3-5](#)]), all subunits are pinched out except for the BR UDMP. In the area to the southeast (south of Gold Meadows stock), all subunits are pinched out except for the BR MDMP. In areas to the east and southeast (south of cross section B-B' to the Gold Meadows stock), all subunits are pinched out except for the BR UDMP and MDMP, with the bottom 20 percent comprised of BR MDMP.

Fracture-filling minerals in the BRA HSU, as reported in various lithologic logs (Drellack et al., 1997), include euhedral quartz, zeolite, clay, Fe oxides, and Mn oxides.

### 5.5.34 **Pre-Belted Range Composite Unit (PBRM)**

Thick accumulations of tuff and lava that predate the Belted Range Group are believed to underlie Pahute Mesa. Compared with shallower units, little is known about these deep rocks beneath much of Pahute Mesa, but exposures of these rocks in other areas indicate they consist of lava, welded ash-flow tuff, nonwelded tuff, and bedded tuff (Slate et al., 1999). Beneath Pahute Mesa, these lithologies form an unknown distribution of lava-flow and WTAs, and TCUs that have been grouped

together within a single HSU called the Pre-Belted Range composite unit (BN, 2002a). The PBRCM is believed to underlie almost all of the study area, but is not differentiated within the Timber Mountain or Claim Canyon caldera complex domains or in the detached volcanics domain. The PBRCM is probably up to 1,981 m (6,500 ft) thick within the model area.

Most of the volcanic units within this section consist mostly of zeolitic nonwelded tuff, but also includes several intercalated devitrified to weakly zeolitized, nonwelded to partially welded, ash-flow tuff deposits. Stratigraphically, these older ash-flow tuffs are assigned to the Yucca Flat tuff (Toy), Redrock Valley tuff (Tor) and tuff of Twin Peaks (Tot), all formations of the Volcanics of Oak Spring Butte. Because these ash-flow tuff units were devitrified soon after deposition, there was little glass to be converted to zeolite.

Based on mineralogy the zeolitic nonwelded tuff has been assigned an RMC of ZEOL and has been divided into five zeolitic RMUs (PBR UZE, PBR MZE and MZE2, and PBR LZE and LZE2). A small portion of DMR was assigned a DMR RMC and given the RMU name of PBR UDMR. Devitrified mafic-poor units were further subdivided into upper, middle, and lower DMP RMCs (PBR UDMP, PBR MDMP and MDMP2, and PBR LDMP) (Table 5-3).

For continuing RMUs for the Pre-Belted Range (PBR) laterally away from drill-hole control, the subdivisions were used (Table 5-3); though this scheme is based on outcrop and limited drill-hole logs, this is an extreme simplification.

Fracture-filling minerals in the PBRCM HSU, as reported in various lithologic logs (Drellack et al., 1997), include calcite and zeolite, which were observed in fractures in the basal aquifer of the PBRCM.

Although the basal aquifer was observed to have one of the highest densities of fractures, it also contained the smallest average apertures, with fractures averaging less than 10 percent open.

### **5.5.35 Caldera-Related Intrusive Confining Units**

It is widely accepted that calderas form over shallow magmatic bodies; however, pre-caldera intrusive processes are poorly understood. The intrusive bodies may be stock-like masses, a series of dikes rising up from a larger batholithic intrusion, a lacolithic intrusion, or various combinations of these

types of intrusions. These bodies may consist almost exclusively of igneous intrusive rocks, as modeled here, or consist of a considerable amount of pre-Tertiary and older volcanic rocks that are intruded to varying degrees by igneous rocks.

Intrusive rocks likely behave as confining units due to low primary porosity and permeability for the Cretaceous granitic bodies in the model area. Although near-surface intrusive rocks are typically hard and brittle, and thus commonly fractured, the fractures in deeper bodies are probably filled with secondary minerals, such as quartz, due to the circulation of hot, mineral-rich waters associated with deep magma bodies. It is likely that sedimentary and older volcanic rocks present under and around calderas originally had aquifer-like properties, but now behave as confining units due to contact metamorphism and hydrothermal alteration related to intrusive activity during caldera development.

Intrusive confining units, as defined for the purpose of the PM CAU model, are interpreted to underlie the six calderas of this region ([Figure 5-5](#)) and are critical in understanding the major volcano-tectonic features of the Timber Mountain caldera complex. These intrusive rocks are treated as a separate HGU because they are thought to have hydraulic properties significantly different from those of adjacent and overlying units due to intense magmatic activity related to caldera formation. For ease of modeling, the intrusive rocks underlying each caldera are treated as a separate HSU (BN, 2002a).

Because no drill holes penetrate these intrusives and they are not exposed at the surface, their subsurface extent is poorly constrained. These intrusive units are modeled as underlying the calderas at some depth, with the top of the unit bounded by the caldera margin and with sides that dip outward at approximately 80 degrees to the base of the model at about 9 km (5.6 mi) below ground surface (BN, 2002a). Based on the inferred granitic composition of these intrusive bodies, and their extrusive equivalents (i.e., rhyolitic ash-flow tuffs), these rocks would be classified as either DMR or DMP RMCs ([Appendix A](#)).

The six intrusive confining units defined in the PM CAU model are described, beginning with the youngest, in [Sections 5.5.35.1](#) through [5.5.35.6](#).



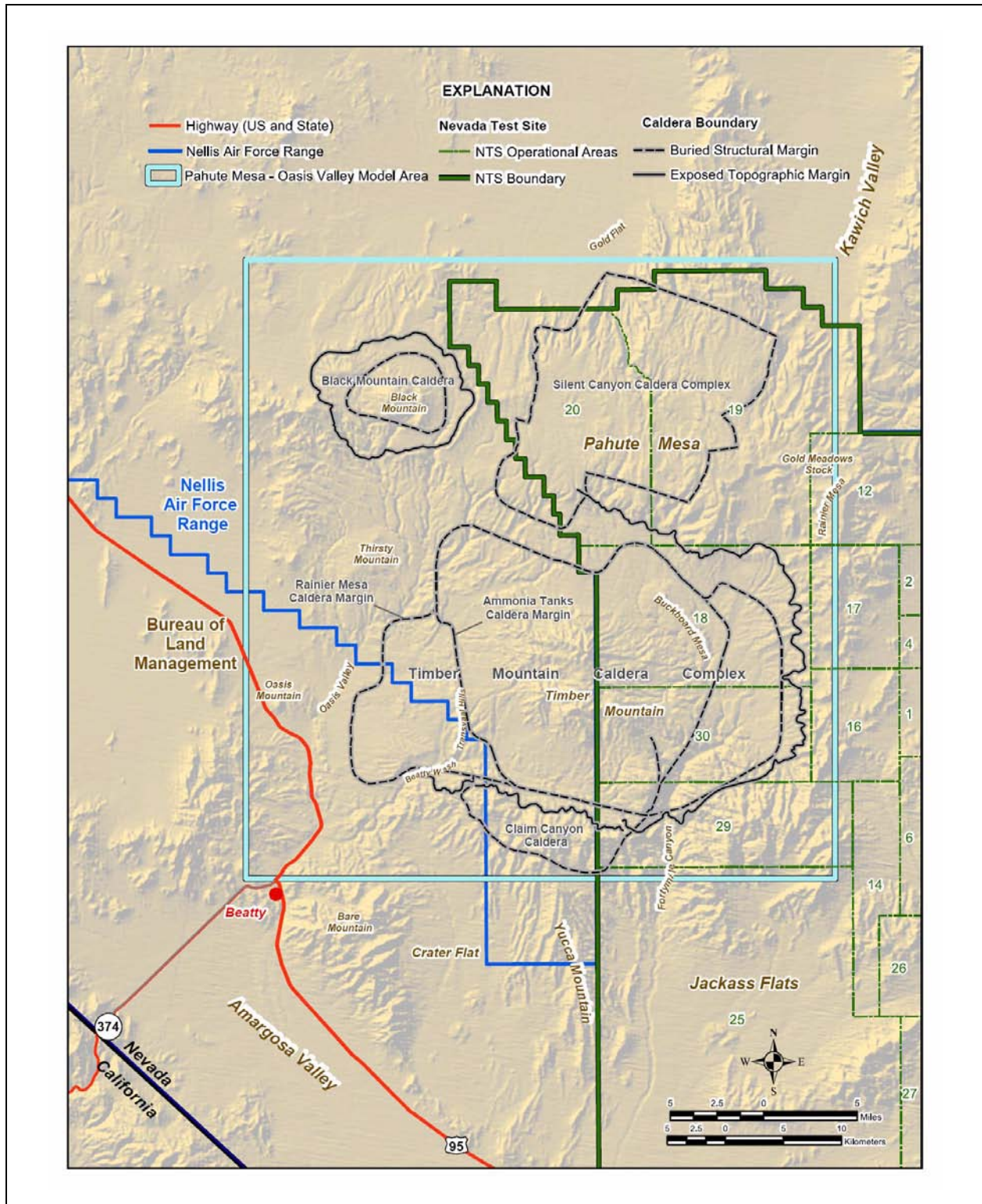


**Figure 5-5**  
**Physiographic Features of the PM-OV Model Area**  
 Source: BN, 2002a

#### **5.5.35.1 Black Mountain Intrusive Confining Unit (BMICU)**

The Black Mountain caldera is a relatively small caldera in the northwest portion of the PM CAU model (Figure 5-5). It is the youngest caldera in the model area, having been formed 9.4 Ma by the eruption of the Thirsty Canyon Group (Sawyer et al., 1994). The topographical margin of the caldera is well exposed, and thus the location of the caldera is well constrained. Although the BMICU is modeled as a single intrusive mass beneath the Black Mountain caldera, the actual nature of the rocks beneath the caldera is unknown.

Because no drill holes penetrate the intrusive and it is not exposed at the surface, the extent (including the depth to the top) of the BMICU is poorly constrained.

Based on the inferred granitic composition of this intrusive body and its extrusive equivalents (i.e., mostly rhyolitic ash-flow tuffs of the Thirsty Canyon Group), the BMICU is a DMP RMC and is assigned an RMU name of BM DMP (Appendix A).

Fracture-filling minerals in the BMICU HSU, a deep-seated intrusive body, are likely filled with secondary minerals, such as quartz, due to the circulation of hot, mineral-rich water associated with deep magma bodies (Orkild and Jenkins, 1978).

#### **5.5.35.2 Ammonia Tanks Intrusive Confining Unit (ATICU)**

The Ammonia Tanks caldera formed 11.45 Ma with the eruption of the Ammonia Tanks tuff (Sawyer et al., 1994). The ATICU has been modeled as a single intrusive mass, similar to the BMICU (BN, 2002a). As is common at many large calderas, the Ammonia Tanks magma chamber surged back toward the surface after caldera collapse and formed a central dome (Timber Mountain resurgent dome) within the caldera-filling rocks.

Because no drill holes penetrate these intrusives and they are not exposed at the surface, the extent of the unit is poorly constrained. Based on the inferred granitic composition of this intrusive body and its extrusive equivalents (i.e., Ammonia Tanks tuff), the ATICU is a DMR RMC. The RMU name for ATICU is ATI DMR (Appendix A).

Fracture-filling minerals in the ATICU HSU, a deep-seated intrusive body, are likely filled with secondary minerals, such as quartz, due to the circulation of hot, mineral-rich water associated with deep magma bodies (Orkild and Jenkins, 1978).

#### **5.5.35.3 Rainier Mesa Intrusive Confining Unit (RMICU)**

This HSU consists of a solidified pluton or magma body associated with the eruption of the lower member of the Timber Mountain Group, the Rainier Mesa tuff (BN, 2002a). The formation of the nested Timber Mountain caldera complex began about 11.6 Ma with the eruption of the Rainier Mesa caldera (Byers et al., 1976a; [Figure 5-5](#)).

Because no drill holes penetrate these intrusives and they are not exposed at the surface, the extent of the unit is poorly constrained. Based on the inferred granitic composition of this intrusive body and its extrusive equivalents (i.e., mostly rhyolitic ash-flow tuffs of the Rainier Mesa tuff), these rocks are a DMR RMC. The RMU name for RMICU is RMI DMR ([Appendix A](#)).

Fracture-filling minerals in the RMICU HSU, a deep-seated intrusive body, are likely filled with secondary minerals, such as quartz, due to circulation of hot, mineral-rich water associated with deep magma bodies (Orkild and Jenkins, 1978).

#### **5.5.35.4 Claim Canyon Intrusive Confining Unit (CCICU)**

The CCICU has been modeled as a single intrusive body beneath the Claim Canyon caldera (BN, 2002a), but as is the case with the other ICUs, the actual nature of these rocks is unknown. The Claim Canyon caldera is believed to be the source of the Tiva Canyon tuff, which has an age date of 12.7 Ma (Sawyer et al., 1994).

A small portion of the resurgent intra-caldera block of the Claim Canyon caldera is exposed south of the Timber Mountain caldera complex (Byers et al., 1976b), but most of the Claim Canyon caldera collapsed into the younger Timber Mountain caldera complex ([Figure 5-5](#)).

Because no drill holes penetrate these intrusives and they are not exposed at the surface, the extent of the unit is poorly constrained. Based on the inferred granitic composition of this intrusive body and

its extrusive equivalents (i.e., rhyolitic ash-flow tuffs of the Tiva Canyon tuff), the CCICU is a DMP RMC. The RMU name for CCICU is CCI DMP (Table 5-3).

Fracture-filling minerals in the CCICU HSU, a deep-seated intrusive body, are likely filled with secondary minerals, such as quartz, due to circulation of hot, mineral-rich water associated with deep magma bodies (Orkild and Jenkins, 1978).

#### **5.5.35.5 Calico Hills Intrusive Confining Unit (CHICU)**

This HSU is located at the southern part of the PM CAU model area and, like the ATICU, constitutes only a small volume of the PM CAU model. The CHICU is modeled here as a deep-seated pluton that intruded rocks of the LCCU and the LCA, and is not associated with a known caldera (BN, 2002a).

As with the caldera-related intrusives, the CHICU does not outcrop, nor is it penetrated by any drill holes. Based on its inferred granitic composition, the CHICU is categorized as a DMP RMC. The RMU name for CHICU is CHI DMP (Table 5-3).

Fracture-filling minerals in the CHICU HSU, a deep-seated intrusive body, are likely filled with secondary minerals, such as quartz, due to circulation of hot, mineral-rich water associated with deep magma bodies (Orkild and Jenkins, 1978).

#### **5.5.35.6 Silent Canyon Intrusive Confining Unit (SCICU)**

The SCICU is modeled as a single highly altered and/or intruded mass that underlies the buried Silent Canyon caldera complex at a depth of about 5 km (3.1 mi) (BN, 2002a; Figure 3-2).

The block model and the piecemeal collapse process suggested in the model interpretation here have resulted in a complex final geometry for the floor of the SCCC (BN, 2002a). The SCICU is conceived to consist of a group of distinct structural blocks (though highly altered and/or intruded) related to basin-and-range faulting or caldera formation.

Drill hole UE-20f, currently the deepest drill hole on the NTS, is located on Pahute Mesa at the western edge of the SCCC. The borehole penetrated 4,171.5 m (13,686 ft) of Cenozoic tuffs and was

terminated within the PBRCM, which overlies the SCICU. This well thus indicates a minimum depth to the SCICU in the western portion of the SCCC (Model Profile B-B' [Figure 3-5]).

Because no drill holes penetrate these intrusives and they are not exposed at the surface, the extent of the unit is poorly constrained. Based on the inferred granitic composition of similar intrusive bodies, and associated extrusive equivalents (i.e., rhyolitic ash-flow tuffs), the SCICU is classified a DMP RMC. The RMU name for SCICU is SCI DMP (Appendix A).

Fracture-filling minerals in the SCICU HSU, a deep-seated intrusive body, are likely filled with secondary minerals, such as quartz, due to circulation of hot, mineral-rich water associated with deep magma bodies (Orkild and Jenkins, 1978).

### **5.5.36 Pre-Tertiary Hydrostratigraphic Units**

The pre-Tertiary stratigraphic units at the NTS have been divided into seven HSUs (BN, 2002a; Table 3-2). Each HSU corresponds to a distinct RMU (Appendix A) discussed separately below.

#### **5.5.36.1 Mesozoic Granite Confining Unit (MGCU)**

The Mesozoic Era is represented only by intrusive igneous rocks in the model area. Cretaceous-age granitic rocks are exposed at Gold Meadows in the eastern part of the model area (Figure 3-2). The Gold Meadows intrusive and the Climax stock, which lies 12.9 km (8 mi) east of the Gold Meadows stock, in northern Yucca Flat, are probably related in both source and time, and may be connected at depth (Snyder, 1977; Jachens, 1999). The Gold Meadows intrusive body consists principally of quartz monzonite (Houser et al., 1961). The Gold Meadows intrusive is grouped into the MGCU (see also the east end of Model Profile B-B' [Figure 3-5]). Because of low intergranular porosities and permeabilities plus the lack of inter-connecting fractures (Walker, 1962), the MGCU is considered to be a confining unit.

This unit is an intrusive stock of quartz monzonite. Primary phenocrysts include plagioclase, potassium feldspar, quartz, and biotite, with a trace of pyrite, sphene, zircon, apatite, and Fe oxides (Maldonado, 1977). Based on this mineralogy, the MGCU is classified as a DMR RMC and is given the RMU name of GU (Table 5-3).

Fracture-filling minerals in the MGCU, as reported in various lithologic logs (Maldonado, 1977), include calcite, quartz, secondary feldspars, clay, chlorite, pyrite, epidote, and Fe oxides.

### **5.5.36.2 Upper Clastic Confining Unit (UCCU)**

Upper Devonian and Mississippian siliciclastic rocks at the NTS and vicinity are assigned to the Eleana Formation and the Chainman Shale (Cashman and Trexler, 1991; Trexler et al., 1996). The Eleana Formation as originally defined by Poole et al. (1961) was partitioned by Cashman and Trexler (1991) on the basis of lithofacies variations and sediment source. The shaley lithofacies (i.e., in western Yucca Flat) was assigned to the Chainman Shale, while the section bearing the non-shaley quartzite, sandstone, and conglomeratic lithofacies retains the original formation name. Both formations are grouped into the UCCU. The subsurface control for this HSU is poor, as no drill holes within the model area penetrate this unit. The UCCU crops out at the eastern edge of the model, in the Eleana Range (Figure 3-3). There are two bedrock exposures just outside the study area, one within the Calico Hills to the southeast and the other at Bare Mountain to the southwest.

The mineralogy of the UCCU varies with lithology. Rocks associated with the Eleana Formation are generally siltstone and sandstone with quartz and chert grains ( $\text{SiO}_2$ ). The Eleana Formation also contains several bioclastic limestones. The Chainman Shale contains significant quartz and smectite/illite; minor feldspar and mica; lesser chlorite, and trace amounts of hematite, limonite, calcite, and manganese oxide ( $\text{MnO}_2$ ). No drill holes penetrate the UCCU in the PM CAU model area. However, there are XRD data for the Yucca Flat model area. The XRD dataset for the UCCU is not large, but the data do show two distinct RMCs (Appendix A). The dominant RMC for the Eleana Formation is SC. The dominant RMC for the Chainman Shale is ARG, with minor SC representing the interbedded quartzite lithologies. The Chainman Shale component of the UCCU is present beneath the eastern portion of the model area (BN, 2002a) and is encountered along the eastern margin of the model at ER-16-1 and ER-12-1 (NNSA/NSO, 2006; Russell et al., 1996). The RMU equivalent for the UCCU in the PM-OV model area is called the UCCU ARG (Appendix A).

Fracture-filling minerals in the UCCU, as reported in various lithologic logs (NNSA/NSO, 2004; Russell et al., 1996), include quartz, calcite, clay and rare pyrite, and trace  $\text{MnO}_2$ .

### 5.5.36.3 Lower Carbonate Aquifer (LCA and LCA3)

The LCA consists of thick sequences of Middle Cambrian-age through Upper Devonian-age carbonate rocks (Table 3-2; Winograd and Thordarson, 1975; BN, 2002a). This HSU serves as the regional aquifer for most of southern Nevada, and locally may be as thick as 5,000 m (16,400 ft) (Winograd and Thordarson, 1975; Cole, 1992 and 1997). The upper 30 percent of the LCA is predominately dolomite, while the lower 60 percent is mostly limestone. Relatively thin intervals of siliciclastic rocks such as the Eureka Quartzite (125 m [400 ft] thick) and Dunderberg Shale (70 m [225 ft] thick) occur within the HSU. Virtually all of the LCA is classified as a CC RMC, with only a few percent of the total thickness being an SC (e.g., Eureka Quartzite) and an ARG (e.g., Dunderberg Shale). Whole rock mineralogy (XRD data) for the LCA is not available for the PM CAU model area. However, similar data for the Yucca Flat model can be applied to the LCA in the PM CAU model area. The HSU name, LCA, is also the RMU name (Appendix A).

Detailed information about fracture geometry and fracture-filling minerals in LCA core samples from ER-6-1 and ER-6-2 in southern Yucca Flat is presented in IT (1996e). These data are also applicable to the PM-OV setting due to hydrogeologic similarities. The IT document (1996e) found that the fractures in the LCA rocks were generally filled or lined with three types of minerals: Fe oxides (limonite and hematite), carbonaceous clays, and carbonate minerals (almost always calcite with rare occurrences of dolomite). It also noted that silica cements are rare and restricted to fractures in quartzite lithologies. Another observation was that most of the fractures are lined or filled with a combination of two or more of these materials.

Deformation related to the east-vergent Belted Range and to the west-vergent CP thrust faults has placed these older LCA rocks over younger rocks of the UCCU ARG, and over stratigraphically equivalent LCA rocks. This geometry is only present in the western portion of the PM-OV. The position of these rocks above the UCCU ARG requires that they be distinguishable (in the model) from the regional aquifer (LCA). These thrust rocks, designated LCA3 (for both HSU and RMU), are stratigraphically equivalent, and therefore are hydrogeologically and chemically similar to the LCA.

#### **5.5.36.4 Lower Clastic Confining Unit (LCCU and LCCU1)**

The Proterozoic to Middle-Cambrian rocks in the vicinity of the NTS are largely quartzite (SiO<sub>2</sub>) and silica-cemented siltstone. Although these rocks are brittle and commonly fractured, secondary silica mineralization seems to have greatly reduced formation permeability (Winograd and Thordarson, 1975). These units make up the LCCU, which is considered to be the regional hydrologic basement (IT, 1996d). Where it is in a structurally high position, the LCCU may act as a barrier to deep regional groundwater flow. The present structural interpretation for the PM CAU model depicts the LCCU at great depth (Model Profile J-J' [Figures 3-12 and 3-13]), except in the western portion of the study area (Model Profiles B-B' and C'C' [Figures 3-5 and 3-6]).

Fracture-filling minerals in the LCCU and LCCU1, as reported from outcrop descriptions and a few lithologic logs, include quartz, calcite, and rare clay. There are no whole rock mineralogy (XRD data) for the LCCU in the PM-OV model area. However, because of the regional scale of this unit, the Yucca Flat data given in SNJV (2007) could be used for the PM CAU model. Nearly all of the LCCU is an SC RMC. The HSU name, LCCU, is also retained as the RMU name ([Appendix A](#)).

The upper plate of the Belted Range thrust fault in the PM-OV area consists of Precambrian siliciclastic rocks thrust over younger siliciclastic (i.e., UCCU) and carbonate (i.e., LCA3) rocks (Model Profile B-B' [Figure 3-5]). These thrust Precambrian rocks are designated LCCU1 to distinguish them from the deeper and unthrust LCCU.

### **5.6 Relationship of Hydrostratigraphic Units and the Water Table**

The EarthVision base framework model was electronically “sliced” along a surface that represents the water table (modified from IT [1996d]) to reveal the distribution of HSUs at the water table ([Figure 3-3](#)). (The perched water zones are not shown in this water table map).

Within most of the model area the water table is within the Tertiary-age volcanic units. Where the UCCU and LCA are structurally high, such as in the southeastern and northwestern portions, the water table is within the UCCU or LCA. In the deepest portion of Oasis Valley, the lower portion of the AA is saturated.



## **6.0 PAHUTE MESA TRANSPORT MODEL**

Two numerical models are used to simulate flow and transport processes: FEHM and PLUMECALC. Groundwater flow is simulated using the FEHM numerical model, which is linked with the parameter estimation (PEST) code through input and output files. During the simulation cycle, uncertain parameters are read from the PEST files into the FEHM model. The FEHM model outputs are compared to the observation data and observation residuals are calculated. Uncertain parameters are updated and the simulation is repeated. This process continues until the residuals do not change at a predefined threshold level. Transport modeling is performed with the FEHM model and with PLUMECALC. The FEHM model uses a particle-tracking algorithm to determine flow path information from the flow model velocity field. PLUMECALC is a convolution-based transport code that uses the particle-track information to calculate flux-average solute concentration by superposition of solute flux over the particles.

The solute flux from each source was calculated using the SSM described previously. Transport parameters include fracture properties (fracture porosity, spacing, aperture), matrix porosity, matrix diffusion ( $D_m$ ), mass transfer coefficient (MTC), dispersivity, sorption coefficient ( $K_d$ ), and colloidal transport. The  $K_d$  was evaluated using a mechanistic model approach, and upscaled from the sample scale to model grid block scale. Knowledge of fracture properties is critical to understanding fracture-matrix transfer functions and flow velocity fields. Additional evaluations of fracture properties were undertaken through evaluation of  $^{14}\text{C}$  concentration changes between observation locations, and fracture property relationships for fixed permeability for specific HGU's. Because of uncertainty of the transport parameters, a stochastic approach was used for simulating transport. The approach defined criteria and procedure for sampling parametric distributions and employed methods to verify that the distributions were valid.

## 6.1 Introduction

The PM CAU transport model was designed to efficiently simulate the movement of reactive and non-reactive solutes in the fractured and porous media of the PM model domain. The following functionality was required:

- Simulate radionuclide concentration histories at all locations in the model domain (not just at a specific location or plane).
- Function in Monte Carlo mode, sampling from distributions of uncertain transport parameters.
- Accommodate up to 82 spatially distributed sources.
- Accommodate uncertain radionuclide release functions at each of the different source locations.
- Accommodate many different radionuclides, each with different source-release functions (mass flux versus time), and each with potentially different transport parameter values such as sorption and  $D_m$  coefficients.
- Simulate transport in zones conceptualized as fractured media as well as zones conceptualized as porous media within the same model domain.

A modeling framework using FEHM (Zyvoloski et al., 1997) and PLUMECALC (Robinson and Dash, 2005) was developed and implemented. The PM CAU flow model is implemented in FEHM, which has particle-tracking capability. Particle-track information from FEHM for the calibrated steady-state flow models for instantaneous particle releases from all source locations provides input to PLUMECALC for transport modeling. The PLUMECALC model uses convolution integrals to convert the transient source-release functions for all radionuclides for all sources, and instantaneous release breakthrough curves, into concentration histories at each model node with the superposition of results from each source; 3-D concentration profiles for all radionuclides are computed through the 1,000-year regulatory time frame of the simulations.

The following sequence describes transport simulation within this framework:

1. FEHM particle tracking for each steady-state flow model (each hydrostratigraphic framework model):
  - Specify longitudinal, transverse, and vertical dispersivities (fixed for each simulation).

- Simulate 10,000 particles per source with FEHM using the flag to output particle information for input to PLUMECALC.

2. PLUMECALC Monte Carlo transport simulations:

- For each Monte Carlo transport simulation, sample uncertain transport parameter values from parameter distributions, including source-release functions for each radionuclide.
- For each radionuclide, simulate transport for 1,000 years, including uncertain release functions, for each source.

This method is efficient because transport simulations with PLUMECALC are fast relative to FEHM simulations, which would have substantial time overhead related to particle-tracking simulations and timestepping. [Sections 6.2](#) and [6.3](#) discuss the details of these two models and the modeling process.

Measured data are used to estimate fracture properties from which transport parameters distributions may be derived. The two approaches used to develop the fracture properties were: (1) independent analysis of  $^{14}\text{C}$  ages in groundwater and (2) fit to HSU permeability data. Starting with a calibrated PM CAU flow model, transport simulations were conducted to assess  $^{14}\text{C}$  loss between two wells in the model domain. The  $^{14}\text{C}$  loss was used to calculate possible fracture porosity, spacing, and aperture ranges ([Section 6.4.1](#)). The other approach calculates fracture aperture with variable spacing for previously defined, HSU-specific permeability ranges ([Section 6.4.1.3](#)).

Finally, the steps used to sample transport parameters from a distribution for multiple realizations, fitting a function to the data and testing of the theoretical and empirical goodness of fit. Proper selection and fitting of the parameter distributions is key to assuring that the resulting parameter sets provide a representative collection of the parameter values that captures the central tendency in the data and the measured range of variability.

## 6.2 Particle Tracking

Particle-track information is determined using FEHM. The particle-tracking method in FEHM is based upon Pollock (1988) and documented in more detail in Robinson and Dash (2005). Although the particle tracking implemented in FEHM is capable of dual-porosity matrix diffusion, linear sorption, and radionuclide decay, those processes are modeled using PLUMECALC as described in [Section 6.3](#), thereby reducing FEHM particle tracking to advective and dispersive processes only.

The random walk dispersion implemented in the particle-tracking module requires longitudinal, transverse, and vertical dispersivities. For each calibrated steady-state flow model, a dispersion tensor is specified and particle tracking is simulated with particles released at each source location. Advection is computed with the minimum flowing porosity for each RMC, which is adjusted in PLUMECALC simulations using the porosity input, resulting in additional residence time, similar to residence time computed for linear sorption isotherms or for  $D_m$ . The PLUMECALC-required output is then read into the Monte Carlo simulator, for which PLUMECALC is run for each transport realization.

### **6.3 PLUMECALC**

The PLUMECALC software, developed for this project (Robinson and Dash, 2005), is a convolution-based particle-tracking (CBPT) method for simulating flux-averaged solute concentrations in groundwater models through superposition of solute flux onto particle-track information. The flux-averaged solute concentration is the flux of solute divided by the flux of groundwater in a control volume. PLUMECALC can also be used to estimate resident concentrations, but that mode was not invoked for the transport modeling. With the dual-porosity formulation, the resident concentration would account for mass in the mobile fracture water as well as the immobile matrix water, providing mass per unit volume of material.

The PLUMECALC method is valid for steady-state flow and linear transport processes, including sorption with linear sorption isotherms, diffusion into matrix rock, and first-order decay. Implementation of these processes and associated assumptions are addressed in Robinson and Dash (2005). The principles of superposition of multiple solute sources and numerical convolution are used to integrate results for multiple time-varying sources. In FEHM particle tracking, a pulse of particles is introduced at each source location, and movement is simulated through time. Particle departure times are recorded from each cell encountered as particles move through the system. The CBPT technique used in PLUMECALC incorporates the time variation of each input source function, taking advantage of the ability of particle-based FEHM simulations to maintain sharp fronts when advection dominates, such as in the high-flux zones of the PM CAU flow models. The algorithm for carrying out the convolution and superposition calculation from the FEHM particle-tracking results is efficient. For each calibrated steady-state flow model (in FEHM), PLUMECALC is used to simulate

transport incorporating source term variability, decay, and spatially variable sorption and matrix diffusion. To change the flow field or dispersion parameters, FEHM must be run to determine new particle-track information. For each steady-state flow field considered and for a fixed set of dispersivities, FEHM is only run once, and the Monte Carlo transport simulation set is conducted using only PLUMECALC.

The theory for the CBPT method in PLUMECALC is discussed in Section 2 of the PLUMECALC user's manual (Robinson and Dash, 2005). The flux-averaged concentration method is described in Sections 2.3.4, the extension for linear sorption in Section 2.3.5, and the extension for dual-porosity matrix diffusion in Section 2.3.6 of the manual.

#### **6.4 Transport Parameters**

Transport parameter information is derived from field-scale and laboratory-scale data collection for the subject formations, ideally from within the model area. Alternately, parameter information may be obtained from literature on other sites with similar geologic and hydrostratigraphic characteristics. For each parameter, a statistical distribution is derived based on the central limit theorem and the assumptions that the parameters are adequately represented by normal distributions (or transformed normal distributions) and that the data used to define the distributions represent the full range of parameter variability. Multiple sets of parameter values are selected for Monte Carlo realizations through random sampling of the parameter distributions. Each parameter set presents a unique realization for the PM CAU transport model. Monte Carlo transport simulation with an adequate number of realizations captures the full spectrum of possible transport parameter configurations given the defined parametric variation. Statistical analysis of the Monte Carlo realizations identifies levels of parametric uncertainty influence and output sensitivity.

Transport parameter data and distribution analysis for those data were initially compiled and published in the *Contaminant Transport Parameters for the Groundwater Flow and Contaminant Transport Model of Corrective Action Units 101 and 102: Central and Western Pahute Mesa, Nye County, Nevada* (Shaw, 2003).

The parameters compiled in Shaw (2003) were:

- Effective porosity
- Matrix porosity
- Dispersivity
- Matrix diffusion
- Matrix sorption
- Fracture sorption
- Colloid-facilitated transport

The discussion of transport parameters in this document presents the information as it was incorporated in the transport modeling. The transport parameter discussion is organized by:

- Fracture porosity, spacing, and aperture
- Matrix porosity
- Matrix diffusion
- Dispersivity
- Mass transfer coefficient
- Sorption coefficient
- $K_d$  upscaling
- Colloid transport parameters

These discussions correlate to the categories used in Shaw (2003) with some explanation. Porosity is classified as either matrix or fracture porosity. Effective porosity, the porosity appropriate to groundwater flow, is assumed to be similar to fracture porosity if the rock is a welded tuff or lava where flow occurs primarily in fractures and matrix water is assumed immobile. Effective porosity is assumed to be similar to matrix porosity for a zeolitic or porous confining unit and for vitric aquifers. A detailed discussion of fracture porosity is presented in terms of fracture spacing and aperture size, as it is incorporated in the transport modeling, to better quantify mass transfer between the fracture and matrix medium.

The MTC is a lumped parameter used in the PLUMECALC model for simulating matrix diffusion mass transfer, taking into account both fracture parameters and matrix diffusion coefficients. Mass transfer in fracture/porous media is also explored in the context of  $^{14}\text{C}$  migration rates recorded at observation wells located in the PM CAU model domain.

Matrix sorption and fracture sorption are addressed together in terms of the sorption coefficient ( $K_d$ ), which is determined by radionuclide and RMC (mineralogy). The  $K_d$  upscaling refers to the approach used to assign  $K_d$  throughout the model domain.

The following sections present a general overview of the transport parameters as they are incorporated in the transport modeling, discussion of supplemental information, and presentation of the parameter distributions used for the transport modeling.

#### 6.4.1 Fracture Porosity, Spacing, and Aperture

Fracture parameters affect predicted solute migration rates through the fracture velocity and mass transfer to immobile matrix water. The fracture parameters sampled in the PM CAU transport model runs include fracture porosity ( $\phi_f$ ), fracture aperture ( $b$ ), and fracture spacing ( $s$ ). Fracture porosity is the primary parameter for converting flux, as simulated in the PM CAU flow model, to velocity:

$$v = Q/(A*\phi_f) \quad (6-1)$$

where  $v$  is velocity,  $Q$  is groundwater flux, and  $\phi_f$  the fracture porosity. The fracture porosity is often called the fracture volume fraction because it is the ratio of fracture void volume to total volume of a unit of material. In the dual-porosity formulation invoked here, the conceptual model is of parallel plate fractures with fracture porosity linked to spacing and aperture by:

$$\phi_f = b/s \quad (6-2)$$

whereas smaller fracture porosity leads to higher groundwater velocity for the same flux, smaller fracture porosity implies to smaller apertures for the same fracture spacing. Smaller apertures, however, lead to larger MTCs:

$$MTC = \frac{\phi_m \sqrt{D_m}}{b} \quad (6-3)$$

where  $\phi_m$  is the matrix porosity. The MTCs are shown later to reflect the ability of solutes to diffuse out of fractures and thus experience an apparent retardation due to residence time in the immobile matrix water before diffusing back into the flowing fractures.

Complicating the relationship between  $\phi_p$ ,  $b$ , and  $s$  further, with respect to their impact on groundwater velocity in fractures and radionuclide diffusion into immobile (assumed) matrix water, the amount of mass that can diffuse out of a fracture depends on the volume of matrix water between fractures and the rate that its concentration approaches that of the solute concentration in the fracture water. If the fractures are sufficiently close together, then the matrix water concentrations and the fracture water concentrations come to equilibrium more quickly and mass transfer from fracture to matrix water decreases. Robinson (1993) provides an insightful non-dimensional comparison (Figure 6-1) of the apparent retardation relationships with changes in fracture spacing, the  $D_m$  coefficient, and velocity. As velocity increases (represented as decreasing groundwater travel time by Robinson, 1993), the  $D_m$  coefficient decreases or fracture spacing increases (with associated increase in fracture aperture), less mass transfer occurs from the fracture to the matrix water, and the solutes move more at the velocity of the groundwater. Conversely, as velocity decreases, the  $D_m$  coefficient increases or fracture spacing decreases (with associated decrease in fracture aperture), more mass transfer occurs from the fracture to the matrix water, the matrix and fracture solute concentrations come closer to equilibrium, and the solutes move more at the velocity of the groundwater multiplied by the matrix porosity – hence, a slower rate.

In Robinson's (1993) analysis, only the mean concentration is considered. Another component of the phenomenon in which mass transfer occurs due to low velocities is associated with large  $D_m$  coefficients and/or small apertures and fracture spacing is large, for which substantial storage occurs in the matrix. In comparing finite-spacing fracture transport models with earlier formulations assuming infinite matrix storage, Sudicky and Frind (1982) refer to this phenomenon as limited solute storage capability. In this case, when considering a distribution of residence times or apparent velocities associated with a breakthrough curve, the apparent velocities span a range from close to the fracture-water velocity to much slower than the velocity of the same flux in a porous media with the matrix porosity. Figure 6-2 shows characteristic breakthrough curves for field-scale solute transport of an instantaneously released pulse of solute. Series 1 represents the fracture-only transport of Zone 1 in Figure 6-1, and Series 4 represents the fracture-matrix equilibrium transport of Zone 3 in Figure 6-1. Series 2 and 3, however, demonstrate that the dual-porosity assumption of immobile matrix water leads to a much broader range of travel times associated with the breakthrough curve, with residence times extending far beyond those of Zone 3.



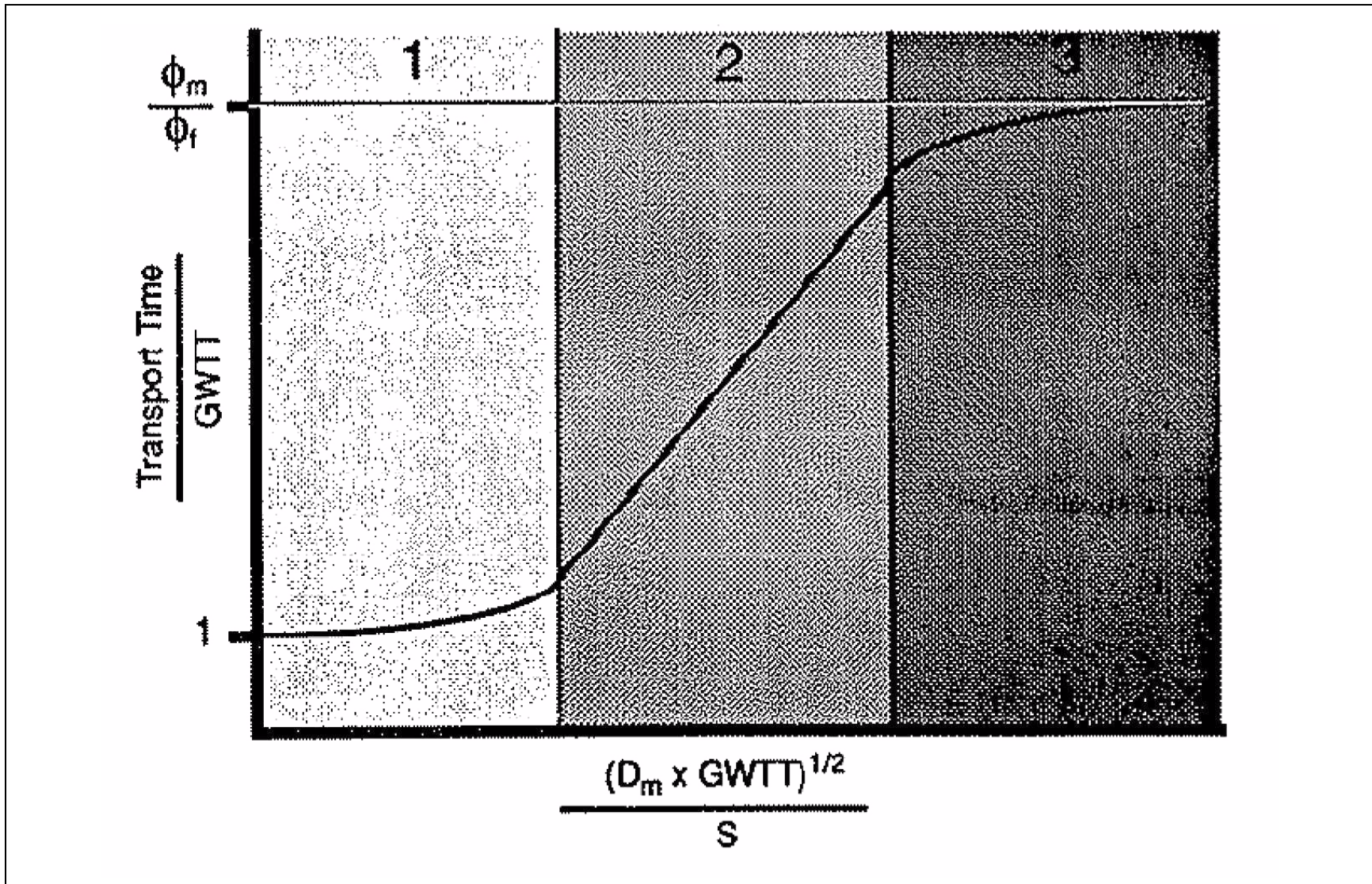


**Figure 6-1**

**Three Characteristic Regions Qualifying the Impact of  $D_m$  on Mean Solute Transport Time**

Note: Groundwater travel time (GWTT) is comparable with the reciprocal fracture velocity for the present study. Zone 1 represents fracture-dominated transport with little  $D_m$ ; Zone 3 represents transport with sufficient  $D_m$  that fracture water and matrix water are in equilibrium.

Source: Robinson, 1993

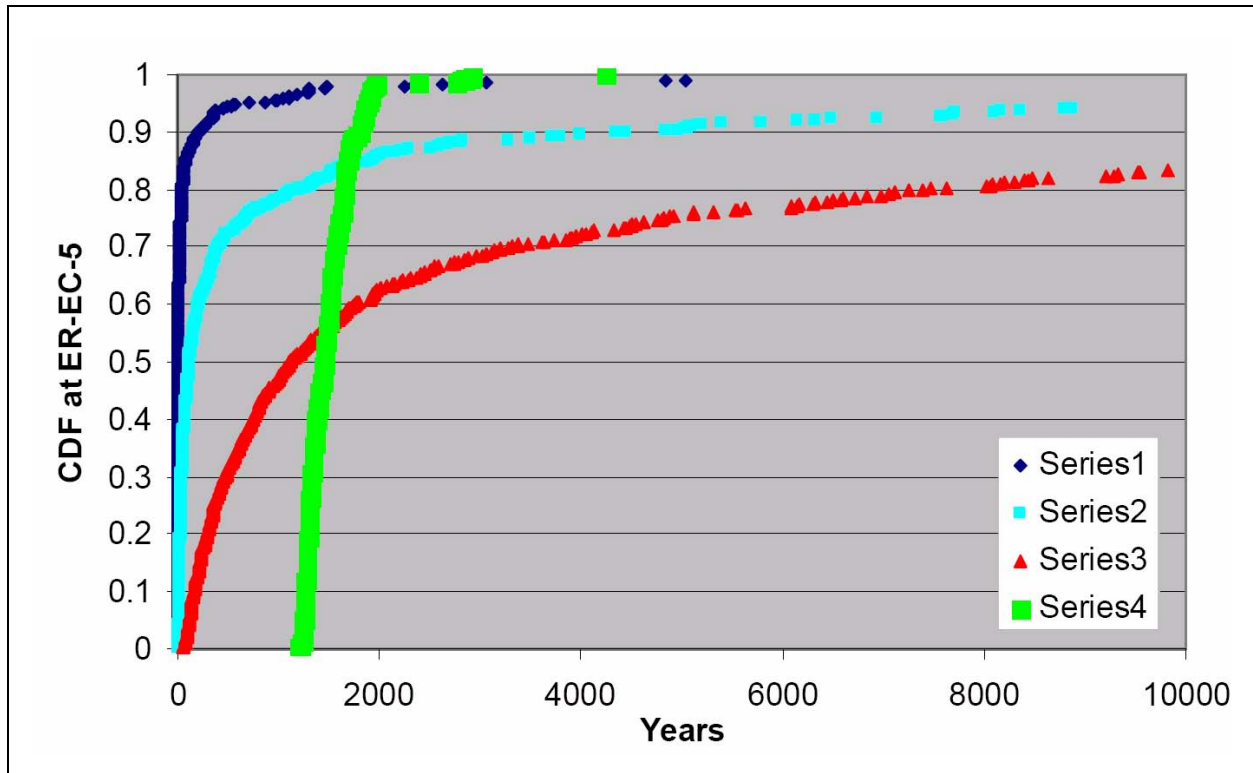


**Figure 6-2**

***Dual-Porosity Transport Characteristics Highlighted with Simulated Breakthrough Curve of an Instantaneously Released Source***

Note: Series 1 - large fracture apertures and spacing, very little  $D_m$ ; Series 2 - reducing aperture, increasing  $D_m$ , still plenty of rapid fracture migration, some tailing; Series 3 - full distribution of travel times, showing characteristic long tails due to diffusion; Series 4 - fractures and matrix in equilibrium because fracture spacing is small. Transport identical to single continuum model (flowing matrix) with matrix porosity.

Given the relationship between  $\phi_p$ ,  $b$ , and  $s$ ,  $\phi_f$  and  $s$  are sampled from uncertainty distributions, and  $b$  is computed. While all three parameters are highly uncertain, the effective field-scale aperture is considered most poorly constrained. In Section 6.5, an independent set of simulations is conducted to evaluate the feasibility of the parameter combinations described below.

**6.4.1.1 Data Sources**

Fracture parameters adhering to the mathematical relationships given above and appropriate for use in RMC zones with lengths of thousands to tens of thousands of meters are, first, only abstractions of processes that occur in far more complex fracture network geometries, and second, highly uncertain. They can only be estimated based upon measurements in individual boreholes or derived from measured or estimated hydraulic conductivities. They can also be evaluated with respect to

observations of natural solute migration such as  $^{14}\text{C}$ . These different lines of evidence provide input to a process that ultimately prescribes fairly broad ranges of uncertainty for the fracture transport parameters. Of these three critical uncertain fracture parameters, Shaw (2003) lumps together fracture porosity and effective porosity for composite units, without distinguishing how they are different. Matrix porosity is discussed in [Section 6.4.2](#). [Table 6-1](#) lists values of fracture porosity in the volcanic aquifers derived from parallel plate models.

#### **6.4.1.2 Borehole Data**

Drellack et al. (1997) provides analysis and interpretation of fractures in volcanic core from Pahute Mesa. Although this report is unable to distinguish actual flowing fracture intervals, it does identify closed and open fractures. Eliminating closed fractures from the interpretation, [Tables 6-2](#) and [6-3](#) summarize fracture aperture and spacing results for the WTA and LFA, respectively. The fracture porosity is computed using [Equation \(6-2\)](#), and the fracture spacing is estimated using the reported spacing between open fractures in the boreholes and assuming 10, 20, and 30 degrees from vertical for the fractures.

Whereas the fracture parameter interpretation based on borehole logs (not hydraulic) from Drellack et al. (1997) indicates closely spaced small aperture fractures, the flowing interval analysis conducted by Yucca Mountain (BSC, 2004) in saturated volcanic tuffs suggests very large distances between actual flowing fractures. Fracture properties for lava were also estimated during the BULLION FGE (IT, 1998a). However, the site-specific nature of that experiment seemed to indicate that a specific fracture dominated the interpretation, and methods for extension to field-scale WTAs were not developed.

In [Section 6.5](#) of this report, a set of independent simulations are represented that evaluate fracture transport parameters in the context of recent  $^{14}\text{C}$  data analyses. The essential question asked was: “What combinations of fracture parameters lead to consistent predictive results with the observations when the PM CAU flow model is used?” To that end, independent Monte Carlo simulations were conducted in which fracture porosity and aperture were chosen from uncertain distributions and fracture spacing was then computed. With the parameter realizations, transport calculations simulating  $^{14}\text{C}$  age differences between two wells were conducted and the results compared with the data interpretation. Simulations having results consistent with the data were used to estimate viable

**Table 6-1**  
**Fracture Porosity of Volcanic Aquifers Estimated Using Parallel Plate Models**

Well	Interval Name	Top of Interval (m)	Bottom of Interval (m)	Hydraulic Conductivity Minimum (m/s)	Hydraulic Conductivity Maximum (m/s)	Fracture Spacing (m)	Aperture Minimum (m)	Aperture Maximum (m)	Fracture Porosity Minimum	Fracture Porosity Maximum	HGU	HSU <sup>a</sup>
ER-20-6#1 <sup>b</sup>	--	701.0	898.0	2.40E-05	--	0.62	2.63E-04	--	4.26E-04	--	LFA	CHZCM
ER-20-6#2 <sup>b</sup>	--	777.0	887.0	1.49E-05	--	3.37	3.95E-04	--	1.17E-04	--	LFA	CHZCM
ER-EC-1	Screen Joint 1	691.9	715.7	1.26E-04	5.41E-04	1.68	6.39E-04	1.04E-03	3.80E-04	6.17E-04	LFA	BA
ER-EC-1	Screen Joint 2	715.7	737.3	2.27E-05	1.23E-04	1.68	3.60E-04	6.34E-04	2.14E-04	3.77E-04	LFA	BA
ER-EC-1	Screen Joint 3	737.3	758.6	8.26E-05	2.71E-04	1.68	5.55E-04	8.24E-04	3.30E-04	4.90E-04	LFA	BA
ER-EC-1	Screen Joint 4	758.6	780.0	3.50E-06	3.70E-05	1.68	1.93E-04	4.24E-04	1.15E-04	2.52E-04	LFA	BA
ER-EC-4	Screen 1	293.2	326.9	1.95E-04	4.76E-04	8.67	1.28E-03	1.72E-03	1.47E-04	1.98E-04	LFA	TCVA
ER-EC-4	Screen 2	326.9	348.5	1.66E-04	7.38E-04	8.67	1.21E-03	1.99E-03	1.40E-04	2.29E-04	LFA	TCVA
ER-EC-4	Screen 3-1	348.5	357.0	1.27E-04	6.90E-03	8.67	1.11E-03	4.19E-03	1.28E-04	4.83E-04	LFA	TCVA
ER-EC-6	Screen 1	489.5	511.7	8.09E-06	2.60E-05	7.02	4.12E-04	6.08E-04	5.86E-05	8.66E-05	LFA	BA
ER-EC-6	Screen 2	511.7	533.2	6.91E-07	2.78E-06	7.02	1.81E-04	2.88E-04	2.58E-05	4.11E-05	LFA	BA
ER-EC-7	Screen 1	278.0	312.1	3.90E-06	2.60E-05	3.21	2.49E-04	4.68E-04	7.75E-05	1.46E-04	LFA	FCCM
ER-EC-7	Screen 2	360.9	399.3	5.84E-05	1.22E-04	2.38	5.55E-04	7.09E-04	2.33E-04	2.98E-04	LFA	FCCM
UE-18-r <sup>b</sup>	--	1,083.3	1,184.5	3.24E-06	--	1.64	1.87E-04	--	1.14E-04	--	LFA	TMCM
UE-18-r <sup>b</sup>	--	897.6	1,027.2	3.24E-06	--	0.82	1.48E-04	--	1.81E-04	--	VTA	TMCM
UE-18-r <sup>b</sup>	--	1,184.5	1,367.0	3.24E-06	--	0.66	1.38E-04	--	2.09E-04	--	VTA	TMCM
ER-18-2	--	411.9	758.0	7.31E-09	1.53E-08	2.65	2.88E-05	3.68E-05	1.09E-05	1.39E-05	WTA	TMCM
ER-EC-5	Screen Joint 1	361.8	389.5	4.61E-06	5.13E-05	2.37	2.38E-04	5.31E-04	1.00E-04	2.24E-04	WTA	TMCM
ER-EC-5	Screen Joint 2	389.5	410.9	7.83E-06	1.06E-04	2.37	2.84E-04	6.76E-04	1.20E-04	2.85E-04	WTA	TMCM
ER-EC-5	Screen Joint 3	410.9	439.8	7.95E-08	8.59E-06	2.37	6.14E-05	2.92E-04	2.59E-05	1.23E-04	WTA	TMCM
ER-EC-5	Screen Joint 4	565.4	601.4	5.58E-05	1.85E-04	2.37	5.45E-04	8.13E-04	2.30E-04	3.43E-04	WTA	TMCM
ER-EC-5	Screen Joint 5	601.4	623.0	7.92E-05	6.52E-04	2.37	6.13E-04	1.24E-03	2.59E-04	5.22E-04	WTA	TMCM
ER-EC-5	Screen Joint 6	623.0	654.1	3.89E-07	2.44E-04	2.37	1.04E-04	8.92E-04	4.40E-05	3.76E-04	WTA	TMCM
ER-EC-5	Screen Joint 7	677.6	699.8	1.09E-05	1.92E-04	2.37	3.17E-04	8.23E-04	1.34E-04	3.47E-04	WTA	TMCM
ER-EC-5	Screen Joint 8	699.8	721.5	1.11E-05	1.57E-04	2.37	3.19E-04	7.71E-04	1.34E-04	3.25E-04	WTA	TMCM
ER-EC-5	Screen Joint 9	721.5	755.9	6.29E-06	1.71E-04	2.37	2.64E-04	7.92E-04	1.11E-04	3.34E-04	WTA	TMCM
ER-EC-8	Screen Joint 9	544.6	566.2	9.14E-07	1.14E-05	2.50	1.41E-04	3.27E-04	5.64E-05	1.31E-04	WTA	TMCM
ER-EC-8	Screen Joint 10	566.2	606.6	2.63E-07	9.15E-06	2.50	9.31E-05	3.04E-04	3.72E-05	1.22E-04	WTA	TMCM
UE-18-r <sup>b</sup>	--	485.0	897.6	3.24E-06	--	0.72	1.42E-04	--	1.97E-04	--	WTA	TMCM
UE-18-r <sup>b</sup>	--	1,027.2	1,083.3	3.24E-06	--	1.19	1.68E-04	--	1.41E-04	--	WTA	TMCM
UE-18-r <sup>b</sup>	--	1,367.0	1,504.0	3.24E-06	--	0.62	1.35E-04	--	2.17E-04	--	WTA	TMCM

Source: Shaw, 2003

Data Sources: See Table 6-2.

<sup>a</sup> See Table A.1-1 for definitions.

<sup>b</sup> Only single values of K were available for these wells; only single values of aperture and porosity were calculated.

-- = Not applicable

**Table 6-2**  
**Fracture Properties for WTA**

		UE-18r	UE-18t	UE-19x	UE-20c/U-20c	UE-20f	All
<b>Aperture (m)</b>		4.00E-05	2.19E-03	2.10E-04	4.20E-04	7.00E-04	3.40E-04
<b>Vertical Spacing (m)</b>		1.02	1.02	0.36	0.36	0.36	0.48
	Degrees from Vertical						
<b>Horizontal spacing (m), corrected for fracture angle</b>	10	0.18	0.18	0.06	0.06	0.06	0.08
	20	0.35	0.35	0.12	0.12	0.12	0.16
	30	0.51	0.51	0.18	0.18	0.18	0.24
<b>Porosity <sup>a</sup></b>	10	2.3E-04	1.2E-02	3.4E-03	6.7E-03	1.1E-02	4.1E-03
	20	1.1E-04	6.3E-03	1.7E-03	3.4E-03	5.7E-03	2.1E-03
	30	7.8E-05	4.3E-03	1.2E-03	2.3E-03	3.9E-03	1.4E-03

Source: Drellack et al., 1997

<sup>a</sup> Estimated with Equation (6-2).

**Table 6-3**  
**Fracture Properties for LFA**

		UE-18r	UE-19x	UE-20f	All
<b>Aperture (m)</b>		2.09E-03	9.80E-04	5.30E-04	9.10E-04
<b>Vertical Spacing (m)</b>		1.32	2.54	2.54	2.17
	Degrees from Vertical				
<b>Horizontal spacing (m), corrected for fracture angle</b>	10	0.23	0.44	0.44	0.38
	20	0.45	0.87	0.87	0.74
	30	0.66	1.27	1.27	1.09
<b>Porosity <sup>a</sup></b>	10	9.1E-03	2.2E-03	1.2E-03	2.4E-03
	20	4.6E-03	1.1E-03	6.1E-04	1.2E-03
	30	3.2E-03	7.7E-04	4.2E-04	8.4E-04

Source: Drellack et al., 1997

<sup>a</sup> Estimated with Equation (6-2).

ranges of parameters. For the limited number of simulations conducted (see [Section 6.5](#)), fracture spacings between 1 and 30 m were estimated to be viable. Smaller fracture spacings led to simulations with fracture and matrix water concentrations in equilibrium due to insufficient matrix storage and results that were outside the range of uncertainty from the data analysis. The viable fracture apertures determined from that study range from being equal to the fracture porosity to being 30 times larger (as per [Equation \[6-2\]](#) and the viable fracture spacings). The simulations were conducted for fracture porosities up to 0.01, so conclusions regarding even larger fracture porosities cannot be drawn from that analysis.

### **6.4.1.3 Fracture Porosity**

The Pahute Mesa contaminant transport parameters data document (Shaw, 2003) develops distributions of effective porosities for all HSUs in the model domain. Subsequent to the development of that document, transport parameters were assigned by RMCs recognizing that the sorption parameters were most appropriately assigned in such a fashion and that the fracture properties and matrix diffusion coefficients tended to be aligned with the RMC distinctions as well. Table 6-15 in the contaminant transport parameters data document (Shaw, 2003) provides distributions for effective porosity for each HSU. For the fractured rock aquifers and the composite units, which have both fractured and porous media, the distributions in Shaw (2003) are listed in [Table 6-4](#).

**Table 6-4  
Pahute Mesa - Effective Porosity - Dominant Lithology for Two HSUs**

	<b>Percent Fractured</b>	<b>Log Triangular</b>	<b>Lower Bound</b>	<b>Mean</b>	<b>Upper Bound</b>
WTA	100	Log triangular	1E-05	1E-03	1E-01
LFA	100	Log triangular	1E-05	1E-03	1E-01
Composite Unit	0.85	Log triangular	1E-05	2.46E-03	5.5E-01
Composite Unit	0.75	Log triangular	1E-05	4.02E-03	4.6E-01
			1E-05	4.47E-03	5.5E-01
Composite Unit	0.7	Log triangular	1E-05	6.03E-03	5.5E-01
			1E-05	5.3E-03	4.6E-01

Source: Modified from Shaw, 2003

In [Table 6-4](#), the composite units each have effective porosities that span the entire range of fracture porosities and matrix porosities. During PM CAU flow model development, some of the composite units were calibrated with high permeabilities, indicative of fracture-dominated flow, while others took on hydraulic properties with lower permeabilities more representative of porous media zones such as confining units. Examination of the RMC model ([Appendix A](#)) confirmed that, short of creating new zones in the PM CAU model, composite units such as the TMCM and FCCM need to be represented as fracture-flow units in the present PM CAU models, while the FCCU needs to be represented as a porous confining unit. The RMCs modeled as fractured include devitrified mafic poor and rich (DMP/R) and mafic lava (ML). The confining units, vitric units, and composite units predominantly composed of confining and vitric units are modeled as porous flow zones.

[Appendix A](#) provides information and a description of the RMC zones used in this model, and compares them with the HSU model zones. [Figure 6-3](#) shows the distribution of fracture porosities used for all fractured zones in the PM CAU model (DMP/R and ML). It is based on the distribution in Shaw (2003), with the exception that the maximum value is set at 0.01 rather than 0.11.

[Section 6.5](#) discusses the viability of fracture parameter combinations in the context of matching  $^{14}\text{C}$  age differences between two wells along a dominant flow path in the PM CAU model. In those simulations, the fracture porosities considered did not extend above 0.01, so the results are inconclusive as to whether fracture porosities as high as 0.1 are feasible. One line of evidence is the BULLION FGE with results documented in Shaw (2003). However, with effective porosities of 0.1, fracture spacings would need to be very small or apertures extremely large, both of which would lead to transport behavior of a single porous media, for which unviable results were obtained (see [Section 6.4.1.4](#)).

#### **6.4.1.4 Fracture Spacing**

The fracture spacing parameter plays two roles in the PM CAU transport model, both of which affect the estimation of mass transfer from fracture water to immobile matrix water. First, it is used to compute the fracture aperture in conjunction with the fracture porosity; second, it defines the volume of storage for solutes that diffuse out of the fractures. The contaminant transport parameters data document (Shaw, 2003) does not specify uncertainty distributions for flowing fracture spacing. Therefore, a distribution was developed seeking to account for uncertainty in this field-scale parameter, recognizing that it is an abstraction of actual processes, because fracture networks are not



**Figure 6-3**  
**Fracture Porosity Distribution for the Monte Carlo Transport Simulations**

actually made up of parallel features. Fracture spacing is only applied to the DMP, DMR, and ML RMCs, as all other zones are modeled as porous media flow units. The fracture spacing distributions used for DMP, DMR and ML are the same in the Monte Carlo transport simulations. The DMP and DMR RMCs use the same value sampled for any realization while the ML fracture spacing is sampled independently from the same distribution. The distribution used is triangular with a most likely value of 3 m, a minimum of 1 m, and a maximum of 30 m. The maximum value was assigned based upon the  $^{14}\text{C}$  analysis in [Section 6.5.1](#). For the porosities considered, as fracture spacing increases, the apertures become excessively large and insufficient matrix diffusion occurs. [Figure 6-4](#) shows the fracture spacing distribution that were sampled, and [Figure 6-5](#) shows the fracture spacing combinations that were used in the Monte Carlo transport simulations.

The fracture spacing distribution is broad due to sparse data and incomplete information regarding field-scale fracture pathways. Comparing the Drellack et al. (1997) findings with those of Kuzio (2004) leads to a range of less than a meter to tens or even hundreds of meters between flowing fractures. Complicating the process of parameterizing fracture spacing is the notion that fractures associated with throughgoing faults could dominate the flow paths, particularly in the TCM and FCCM HSUs where most faults have not been explicitly included in the PM CAU model.



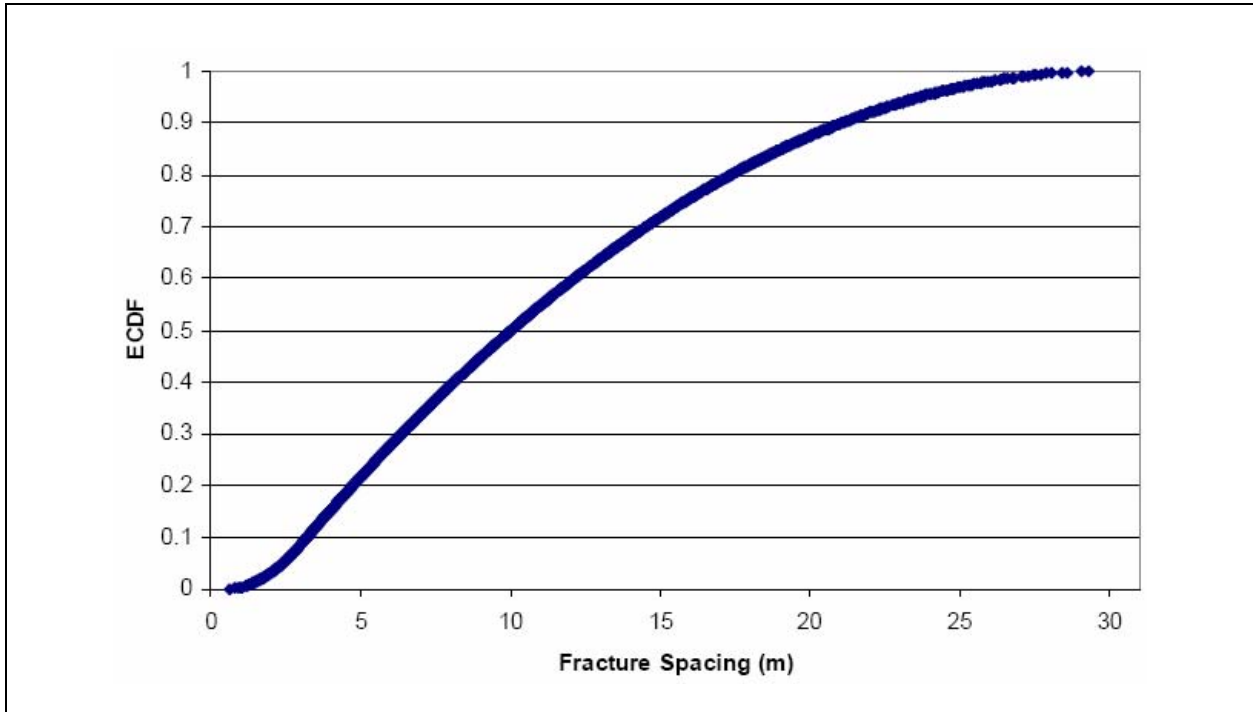


**Figure 6-4**  
**Fracture Spacing Distribution for the Monte Carlo Transport Simulations**

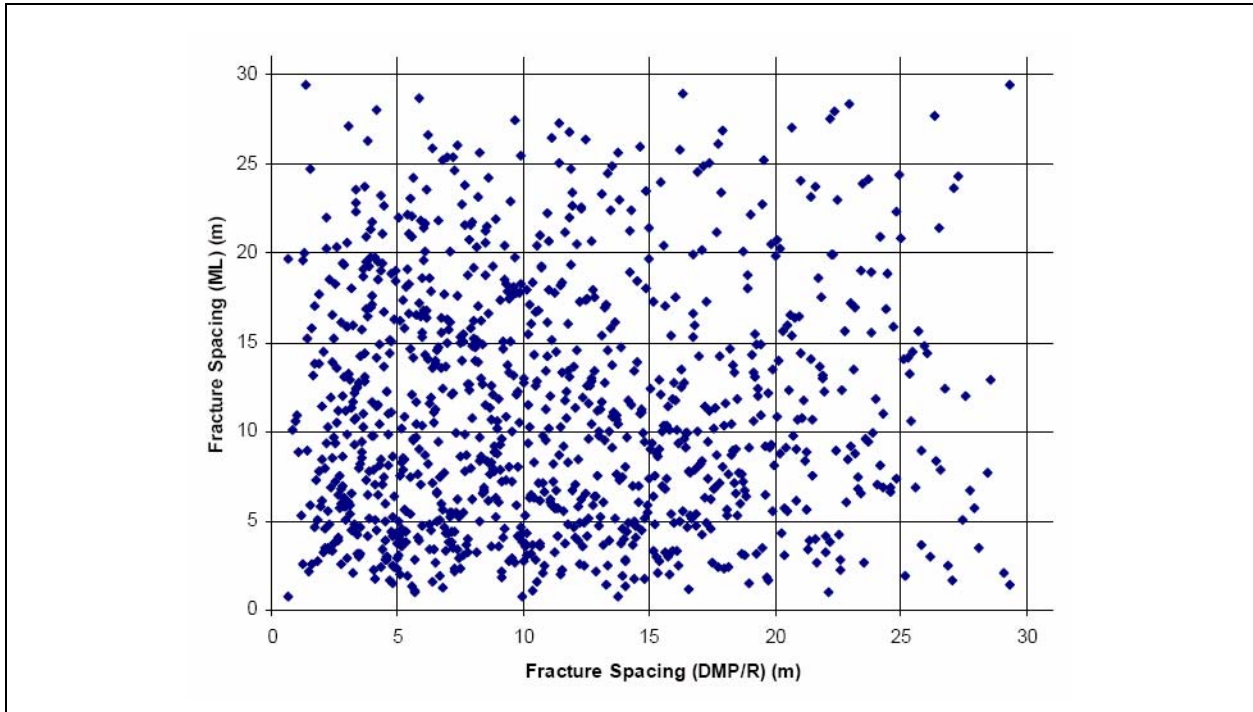


**Figure 6-5**  
**Fracture Spacing Parameter Combinations for DMP/R and ML in the Monte Carlo Transport Simulations**

### 6.4.1.5 Fracture Aperture

The fracture aperture parameter affects matrix diffusion by specifying the wetted surface area per unit area of flow in the PM CAU transport model. In the Monte Carlo simulations, fracture porosity and spacing are selected independently from the distributions and, for each realization, aperture is computed. Figure 6-6 shows the combinations of fracture spacing and porosity that were used to compute the fracture apertures shown in Figure 6-7. The resulting fracture aperture distribution is shown in Figure 6-8. Although there was an attempt to constrain the growth of parameters, the fracture apertures in this distribution clearly extend to values much larger than those observed in boreholes by Drellack et al. (1997). Before initiating the full Monte Carlo transport simulations, fracture apertures as large 10 cm were allowed with the rationale of (1) not knowing what flowing features solutes would actually encounter at the field scale and (2) recognizing that the impact would lead to conservative transport by reducing matrix diffusion. Section 6.4 reconsiders these rules and, as a secondary examination, estimates fracture apertures from PM CAU flow model permeability, rather than as a product of fracture porosity and spacing, similar to the method used to estimate apertures in Table 6-1.

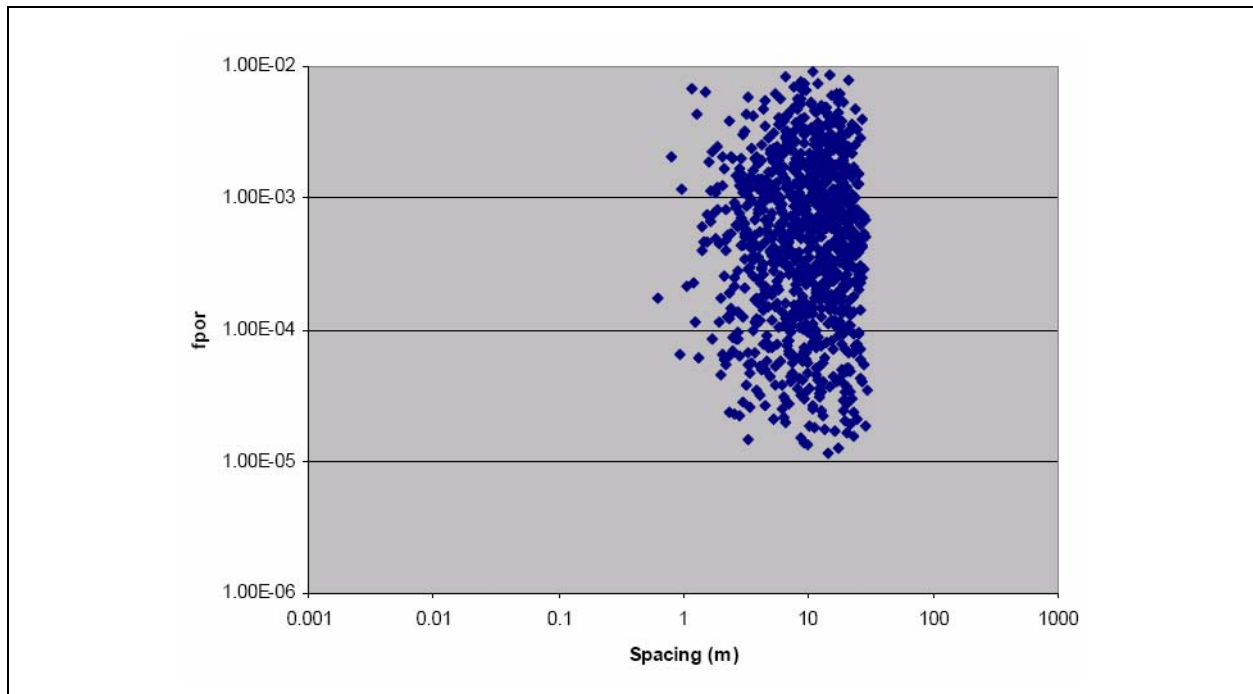


**Figure 6-6**  
**Fracture Spacing and Porosity Parameter Combinations in CAU Monte Carlo Runs**

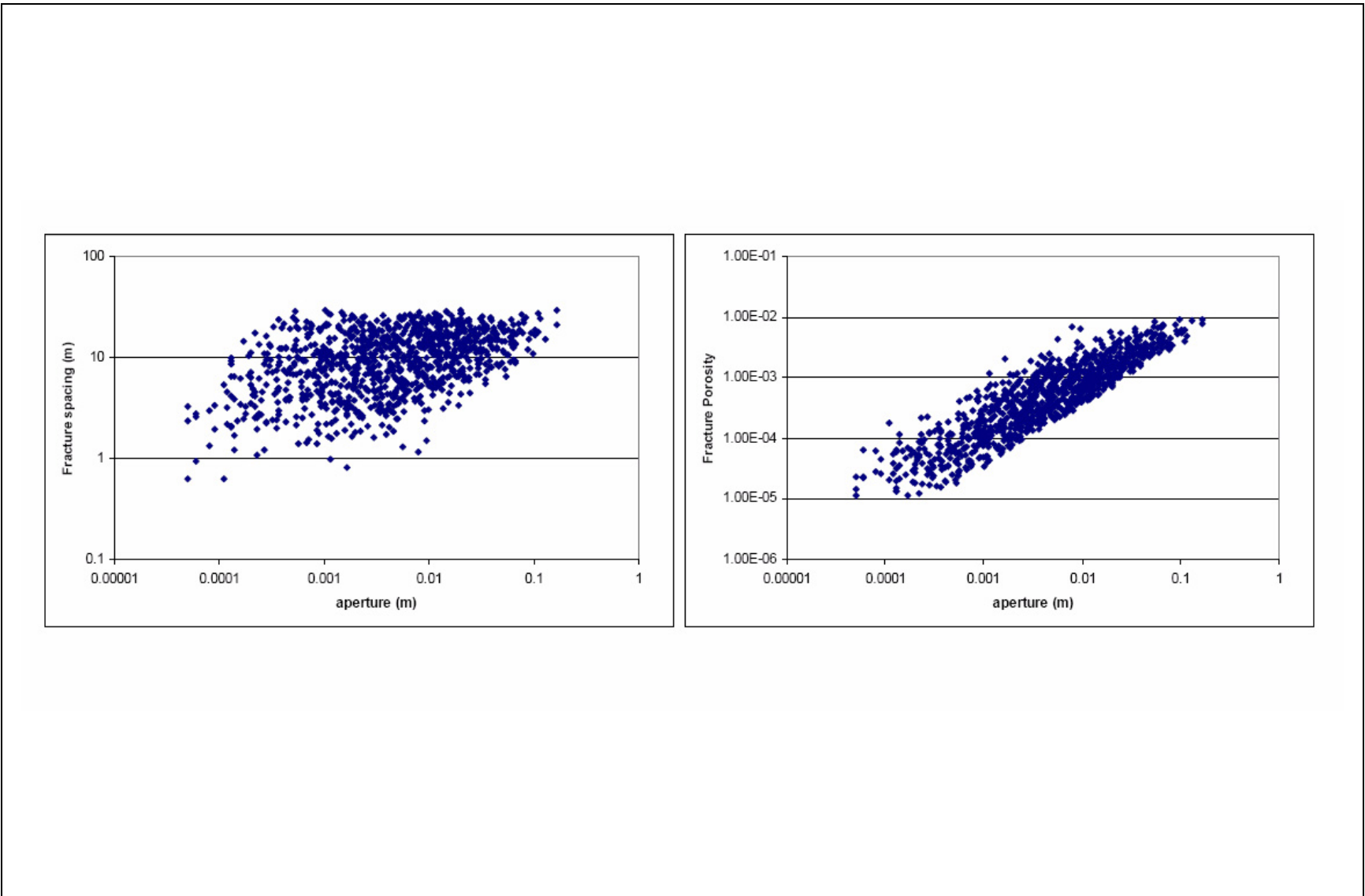


**Figure 6-7**  
**Fracture Spacing and Porosity Combinations with Aperture in CAU Monte Carlo Runs**

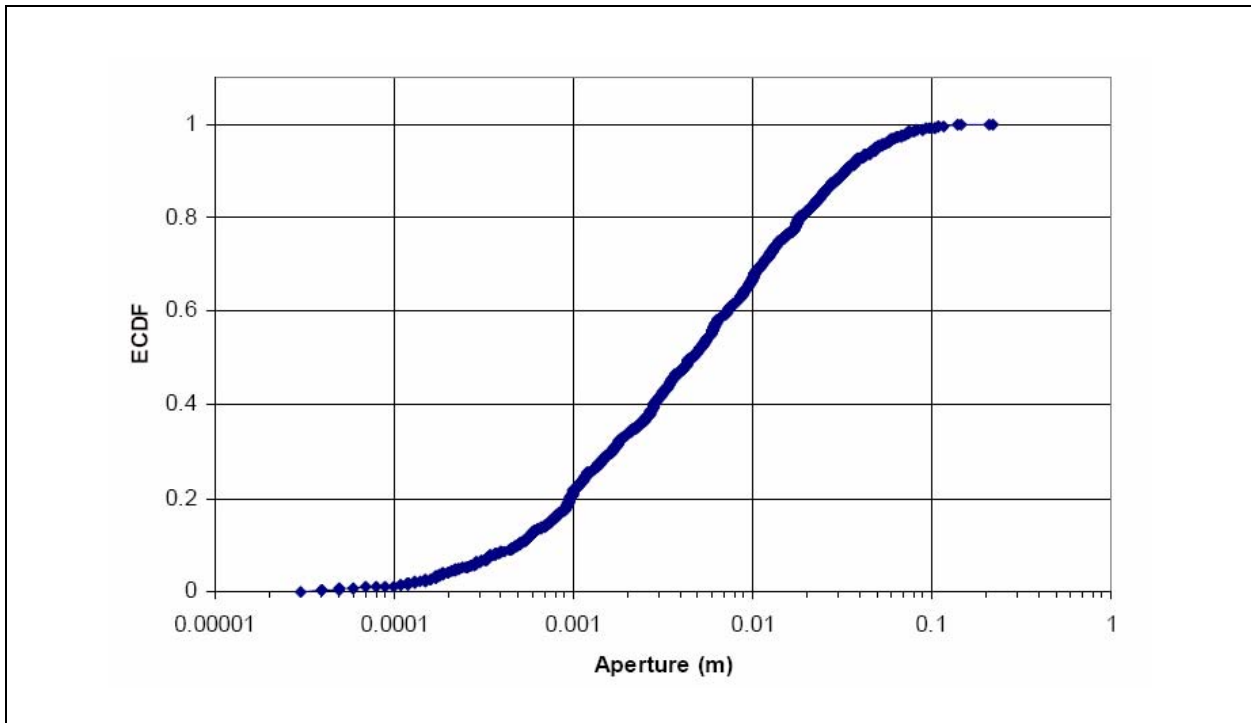


**Figure 6-8**  
**Fracture Aperture Distribution for the Monte Carlo Transport Simulations**

### 6.4.2 Matrix Porosity

The matrix porosity serves to convert flow-model flux to velocity for porous media zones in the transport model and to provide storage in immobile matrix water for diffusing solutes in fractured (dual-porosity) zones. Matrix porosity ( $\phi_m$ ) distributions are taken from Shaw (2003) for the HSUs and converted into distributions for the RMCs for this transport model. The relationship between matrix porosity, groundwater flow, and velocity is represented by the equation:

$$v = \frac{Q}{\phi_m A} \quad (6-4)$$

where  $Q$  is the volumetric flow rate ( $L^3/t$ ),  $v$  is flow velocity ( $L/t$ ),  $A$  is area perpendicular to flow, and  $\phi_m$  is matrix porosity. The relationship between velocity and matrix porosity is such that as matrix porosity increases, the velocity decreases. This effect has two consequences: (1) slower movement downgradient and (2) an increase of the mineral surface area onto which contaminants can adsorb.

A large portion of the data used to determine matrix porosity is, in fact, total porosity. Fracture porosities are typically less than 1 percent, whereas matrix porosity may be 25 percent or more. The total porosity is, therefore, a good estimator of the matrix porosity of fractured rocks in most cases. In the case of porous rocks, matrix porosity is equivalent to total porosity.

Most of the available porosity data for Pahute Mesa were derived from interpretations of geophysical logs. A small subset of the data were derived from core measurements. Such data provide little information about fracture porosity or the effective porosity of fractured media, but are a good source of information for matrix porosity. Five boreholes were identified with both core- and geophysical log-derived porosity values: UE-20ae, UE-20ad, UE-18t, UE-19t/U-19t, and WW-8. A crossplot (Figure 6-9) was constructed to illustrate the relationship between the core-derived and the geophysical log-derived porosity using data from the five boreholes. Inspection of Figure 6-9 reveals that for each of the five boreholes, the data points tend to plot along the bisecting line. The bisecting line is the line at which equal porosity measurements from the two measurement methods would plot.

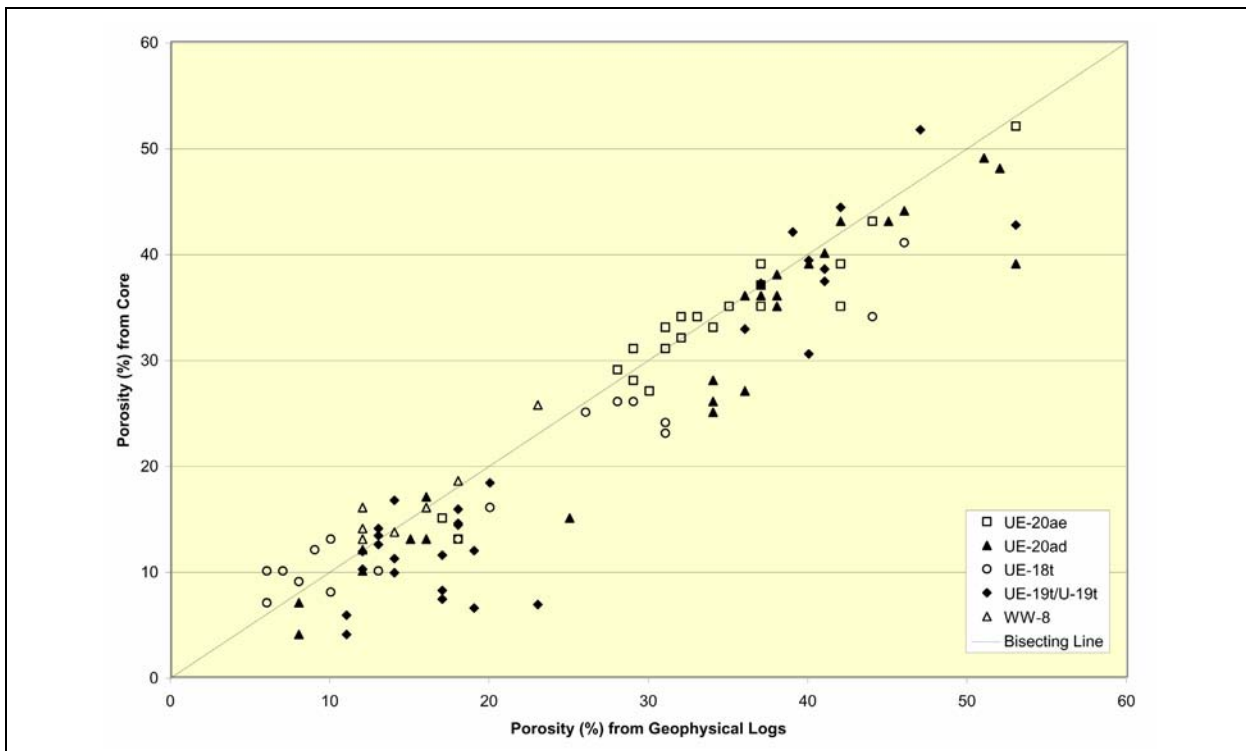


**Figure 6-9**  
**Crossplots of Geophysical Log-Derived and Core-Derived Porosity Values**  
Source: Shaw, 2003

The porosity data come from a wide range of HSUs, alterations, and lithologies. Thus, matrix porosity was investigated by grouping the porosity based on three different classifications. The first classification was based on HSU, the second on alteration, and the third on lithology. The first two approaches did not provide conclusive results for classification of matrix porosity for hydrostratigraphic or alteration applications for all units (Shaw, 2003). The matrix porosity data were plotted as a function of the lithology. Based on these plots and geologic reasoning, the matrix porosity data for volcanic rocks were divided into four groups based on the lithology of the unit.

These groups are:

- Group 1: Welded Tuff, Densely Welded Tuff, Moderately Welded Tuff, Lava, and Vitrophyre
- Group 2: Bedded Tuff and Nonwelded Tuff
- Group 3: Partially Welded Tuff and Pumaceous Lava
- Group 4: Flow Breccia and Tuff Breccia

Of the four groups identified by Shaw (2003), three groups are advanced for use in the current model. The three remaining groups are identified by the hydrogeologic convention, which in turn is cross referenced to an RMC as defined in [Appendix A](#) of this report. Therefore, the three groups are identified in [Table 6-5](#).

**Table 6-5**  
**Lithologic Groups, HGUs, and RMCs**

Group	HGU	RMC
1	WTA, LFA	DMP, DMR
2	VTA	VMP, VMR
3	TCU	ZEOL

The mean matrix porosity for each of the remaining groups is derived from the cumulative distribution function (CDF) described by the matrix porosity measurements published in Appendix D of Shaw (2003) and listed in [Table 6-6](#). The probability distribution from which the matrix porosity is selected during the Latin hypercube sampling (LHS) step is represented by a table of the empirical data rather than as a set of values associated with a fitted distribution.

**Table 6-6**  
**Pahute Mesa - Matrix Porosity - Dominant Lithology for Each HSU**  
 (Page 1 of 2)

Layer Number	Symbol	Name	Dominant HGU	Continuous Lithology	Lower Bound	Mean	Upper Bound	Group Number
45	YVCM	Younger Volcanics Composite Unit	LFA, WTA, VTA	PWT	6	34.1	75	3
44	TCVA	Thirsty Canyon Volcanic Aquifer	WTA, LFA, lesser VTA	WT	14.3	46.4	70.9	N/A
43	DVCM	Detached Volcanics Composite Unit	WTA, LFA, TCU	PWT	6	34.1	75	3
42	DVA	Detached Volcanics Aquifer	WTA, LFA	WT	2	17.5	60	1
41	FCCM	Fortymile Canyon Composite Unit	LFA, TCU, lesser WTA	PWT	6	34.1	75	3
40	FCA	Fortymile Canyon Aquifer	WTA, LFA	WT	2	17.5	60	1
39	TMCM	Timber Mountain Composite Unit	TCU, unaltered WTA, lesser LFA	DWT	2.4	17.4	63	N/A
38	THLFA	Tannenbaum Hill Lava-Flow Aquifer	LFA	LA	2	17.5	60	1
37	THCM	Tannenbaum Hill Composite Unit	TCU, lesser WTA	NWT	4	41.0	70	2
36	TMA	Timber Mountain Aquifer	WTA, minor VTA	WT	4.4	28.6	68.4	N/A
33	WWA	Windy Wash Aquifer	LFA	LA	2	17.5	60	1
32	PCM	Paintbrush Composite Unit	WTA, LFA, TCU	MWT	2	17.5	60	1
31	PVTA	Paintbrush Vitric-Tuff Aquifer	VTA	BED	10	43.5	57	N/A
30	BA	Benham Aquifer	LFA	LA	3.5	20.4	33.6	N/A
28	TCA	Tiva Canyon Aquifer	WTA	WT	2	17.5	60	1
27	PLFA	Paintbrush Lava-Flow Aquifer	LFA	LA	2.0	23.6	45.1	N/A
25	TSA	Topopah Spring Aquifer	WTA	WT	2	17.5	60	1
24	YMCFCM	Yucca Mountain Crater Flat Composite Unit	LFA, WTA, TCU	PWT	6	34.1	75	3
23	CHVTA	Calico Hills Vitric-Tuff Aquifer	VTA	NWT	28	40.7	49	N/A
22	CHVCM	Calico Hills Vitric Composite Unit	VTA, LFA	NWT	0	26.5	44	N/A

**Table 6-6**  
**Pahute Mesa - Matrix Porosity - Dominant Lithology for Each HSU**  
 (Page 2 of 2)

Layer Number	Symbol	Name	Dominant HGU	Continuous Lithology	Lower Bound	Mean	Upper Bound	Group Number
21	CHZCM	Calico Hills Zeolitic Composite Unit	LFA, TCU	NWT	0	9.2	75	N/A
20	CHCU	Calico Hills Confining Unit	TCU, minor LFA	NWT	4	41.0	70	2
19	IA	Inlet Aquifer	LFA	LA	2	17.5	60	1
18	CFCM	Crater Flat Composite Unit	LFA, intercalated TCU	WT	2	17.5	60	1
16	KA	Kearsarge Aquifer	LFA	LA	2	17.5	60	1
14	BRA	Belted Range Aquifer	LFA, WTA, lesser TCU	WT	2.0	22.0	42.0	N/A
13	PBRCM	Pre-Belted Range Composite Unit	TCU, WTA, LFA	PWT	3.2	17.2	29.5	N/A
12	BMICU	Black Mountain Intrusive Confining Unit	IICU	IN	0.24	1.82	10.3	N/A
11	ATICU	Ammonia Tanks Intrusive Confining Unit	IICU	IN	0.24	1.82	10.3	N/A
10	RMICU	Rainier Mesa Intrusive Confining Unit	IICU	IN	0.24	1.82	10.3	N/A
9	CCICU	Claim Canyon Intrusive Confining Unit	IICU	IN	0.24	1.82	10.3	N/A
8	CHICU	Calico Hills Intrusive Confining Unit	IICU	IN	0.24	1.82	10.3	N/A
7	SCICU	Silent Canyon Intrusive Confining Unit	IICU	IN	0.24	1.82	10.3	N/A
6	MGCU	Mesozoic Granite Confining Unit	GCU	IN	0.24	1.82	10.3	N/A
5	LCA3	Lower Carbonate Aquifer - Thrust Plate	CA	DM	1.0	5.0	9.7	N/A
4	LCCU1	Lower Clastic Confining Unit - Thrust Plate	CCU	Quartzite	0.2	3.3	10	N/A
2	LCA	Lower Carbonate Aquifer	CA	DM	1.0	5.0	9.7	N/A
1	LCCU	Lower Clastic Confining Unit	CCU	Quartzite	0.2	3.3	10	N/A

Source: Shaw, 2003



### 6.4.3 Matrix Diffusion

Matrix diffusion has the effect of attenuating the concentration and increasing the travel time of solute contaminants moving through saturated, fractured rock. The  $D_m$  process involves the diffusion of contaminants out of flowing fractures and into the relatively stagnant water in the pores of the surrounding matrix (and vice versa). The  $D_m$  MTC is a lumped parameter that reflects the rate at which solutes may diffuse out of fractures and into the matrix. Discussion of the MTC can be found in [Section 6.4.1](#), a process also limited by the fracture spacing.

One of the most important scaling considerations (and uncertainties) associated with the MTC is the manner in which fracture apertures scale with distance. An additional  $D_m$  scaling consideration is the effective distance into the matrix that solutes can diffuse from fractures before encountering interference from solutes diffusing out of another flowing fracture. The experimental studies are conducted over short time scales relative to field conditions, so the MTC is estimated but not the reduction in diffusion caused by other products.

Diffusion cell tests have been employed to measure  $D_m$  coefficients ( $D_m$  values) for various radionuclides and anions in a large number of volcanic rocks from beneath Pahute Mesa and from the saturated zone near Yucca Mountain in Area 25 of the NTS (Reimus et al., 1999 and 2002). Matrix diffusion coefficients and the product of matrix porosity and  $D_m$  coefficients from both diffusion cell and fracture transport experiments were estimated from model interpretations of the datasets from these tests (Reimus et al., 1999 and 2002). A 1-D numerical diffusion model (DIFFCELL) was used to interpret the diffusion cell tests, and a semi-analytical, dual-porosity transport model (RELAP) was used to interpret the fracture transport experiments. For the intrusive volcanic units, there are no matrix permeability data available. Therefore, an estimate of the log  $D_m$  is derived from the log porosity.

From a modeling perspective, the product of the matrix porosity ( $\phi_m$ ) and  $D_m$  coefficient (in numerical models) or of the matrix porosity and the square root of the  $D_m$  coefficient (in many analytical or semi-analytical models) effectively serves as a lumped parameter to account for  $D_m$ . [Figure 6-10](#) shows how the product of matrix porosity and diffusion coefficient depends on matrix porosity. Obviously, there is a correlation between  $\phi_m D_m$  and  $\phi_m$  because the former is a lumped parameter that includes the latter. [Figure 6-10](#) also shows a logarithmic fit to the data and 95 percent confidence bounds associated with this fit.

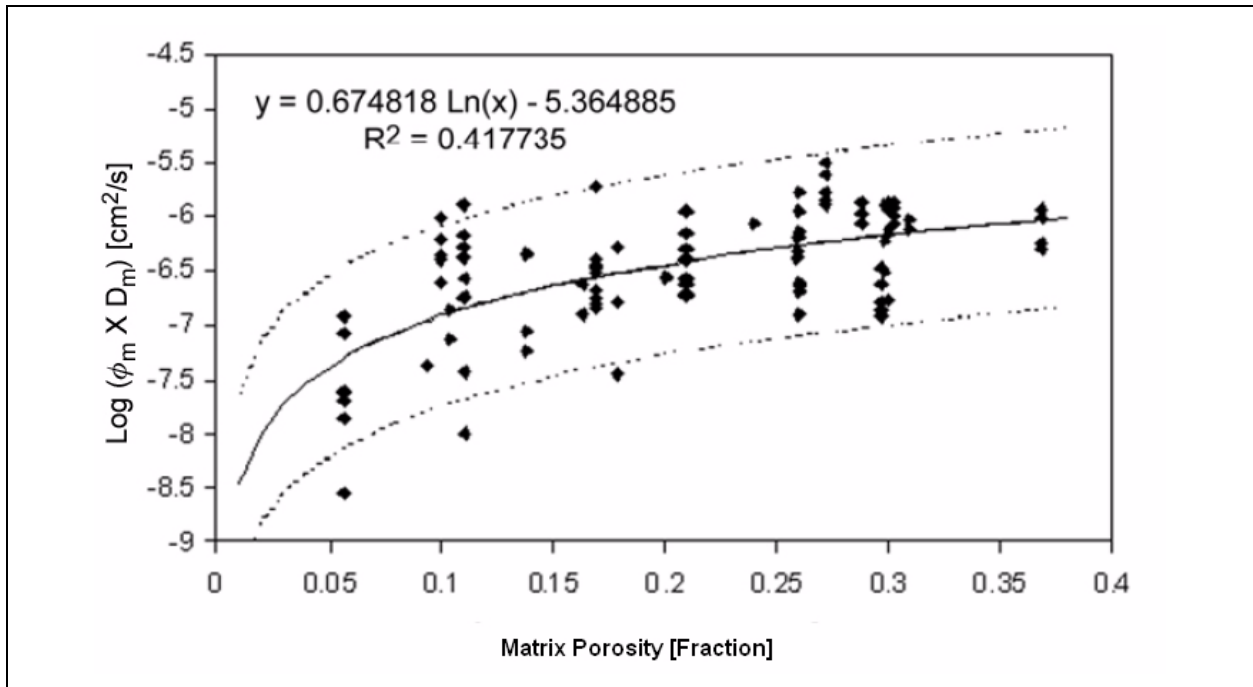


**Figure 6-10**  
 **$\text{Log}(\phi_m D_m)$  Values as a Function of Matrix Porosity (Fraction)**  
**and a Logarithmic Fit to the Data**

Note: The dashed lines represent the 95 percent confidence intervals.  
 Source: Shaw, 2003

The regression equation using  $\log_{10}$  instead of the natural log is as follows:

$$\log(\phi_m D_m) = 1.5538 \log(\phi_m) - 5.3649 \quad (6-5)$$

Using the properties of logarithms, the relationship for  $D_m$  as a function of  $\phi$  becomes:

$$\log(D_m) = 0.5538 \log(\phi_m) - 5.3649 \quad (6-6)$$

Equation (6-5) could be used to obtain an estimate of the mean value of  $\log(\phi_m D_m)$  for any known value of  $\phi_m$ . A normal distribution of  $\log(\phi_m D_m)$  values with this mean and an SD of 0.41 to 0.42 could be randomly sampled to obtain a stochastic estimate of  $\log(\phi_m D_m)$  for that porosity. The SD of  $\log(\phi_m D_m)$  varies slightly over the full range of porosities, with the value being 0.41 at the mean experimental porosity (0.21) and increasing to 0.42 at porosities of 0.015 and 0.405.

Estimated  $D_m$  coefficient distributions for specific HSUs are listed in Table 8-4 of Shaw (2003), although the  $D_m$  coefficient distribution will be directly impacted by the distribution developed from the matrix porosity as per Equations (6-5) and (6-6).

Matrix porosity for the HGUs at Pahute Mesa is assigned by RMCs, each of which is associated with a specific RMC. The correlation between HGU and RMC are discussed in Appendix A of this report. The matrix porosity is discussed in Section 6.4.2.

#### **6.4.4 Dispersivity**

The hydrodynamic dispersion of solutes in groundwater describes the spreading phenomenon at a macroscopic level by the combined action of mechanical dispersion and molecular diffusion. At typical scales of observation, dispersion is a mixing process, the result of which causes dilution of the solute (Freeze and Cherry, 1979). This uncertainty in concentration estimates is related to uncertainty in dispersivity values. The effect of dispersion is commonly quantified and measured in terms of longitudinal and transverse dispersivities. These dispersivities are key input parameters to the governing transport model used to estimate the concentration distribution of a solute in groundwater over time and space. The available dispersivity measurements conducted at or near the NTS were derived from five tracer transport experiments listed in Table 6-7 and are described with regard to the aquifer type and geology, test method, tracer type, analytical method, and the derived dispersivities. Note that these are all forced-gradient tests and therefore do not estimate transverse dispersivities.

Further details about the NTS dispersivity test results are reported in Shaw (2003). The dispersivity scale from which longitudinal dispersivity is derived for the tracer tests performed at the NTS, as listed in Table 6-7, ranges between 29 to 131 m. Additional data available for non-NTS sites were obtained from the literature. An important source of non-NTS dispersivity data is the dispersivity review paper of Gelhar et al. (1992). The analyses indicate a trend of systematic increase of the longitudinal dispersivity with observation scale, but the trend is much less clear when the reliability of the data is considered. The longitudinal dispersivities reported by Gelhar et al. (1992) range from  $10^{-2}$  to 104 m for travel distances ranging from  $10^{-1}$  to 105 m; however, the largest distance with high-reliability data was only 250 m, and the longitudinal dispersivity was only 4 m. Gelhar et al. (1992) also conclude from the data that, overall, dispersivity values did not appear to vary with lithology (porous versus fractured media).

**Table 6-7**  
**Dispersivity Information Summary from the NTS and Vicinity**

Site Location	Test Site Geology	Scale of Test (m)	Test Method	Tracers	Analysis Method	Longitudinal Dispersivity (m)	References
BULLION FGE, Pahute Mesa, Nevada	Fractured Lava-Flow Aquifer, Calico Hills Formation	42.3 to 131.5	Radial converging with monitoring at an intermediate well and the pumped well	Pentafluorobenzoic acid, difluorobenzoic acid, sodium iodide, carboxylate-modified latex polystyrene microspheres	Calibration of numerical 3-D transport model and 2-D analytic	10 (horiz. trans. 3) (vert. trans. 2)	IT, 1998a; Reimus and Haga, 1999
C-Well Complex, Yucca Mountain, Nevada	Bullfrog and Tram Tuffs	90	Radial conversion with two injection wells	Iodide, difluorobenzoic acid, pyridone, pentafluorobenzoic acid, lithium bromide, polystyrene microspheres	1-D and 2-D analytical models	3.3 to 59	Winterle and La Femina, 1999
Amargosa Tracer Calibration Site, Amargosa Desert, Nevada	Cambrian Bonanza King Dolomite (fractured)	122.8	Doublet recirculation ( <sup>3</sup> H, <sup>35</sup> S, Br)	<sup>3</sup> H (pulse)	1-D quasi-uniform Fitting of Grove's curves	15 to 30.5	Leap and Belmonte, 1992
C-Well Site, Yucca Flat, Nevada	Fractured Limestone	29.3	Radial converging (fluorescein) test at Wells C and C-1	Fluorescein dye	2-D analytical Welty and Gelhar (1994)	0.6 to 1.4	Winograd and West, 1962 (calculation not included)
CAMBRIC Test, Frenchman Flat, Nevada	Tuffaceous Alluvium	91.0	Radial converging with monitoring the elutions of <sup>3</sup> H and <sup>36</sup> Cl at pumping Well RNM-2S	Nuclear test radionuclides: <sup>3</sup> H	Welty and Gelhar, 1994	9.6	Thompson, 1991 (calculation not included)
				Nuclear test radionuclides: <sup>3</sup> H	Sauty's Method	2.0	Burbey and Wheatcraft, 1986
				Nuclear test radionuclides: <sup>3</sup> H	Sauty's Method	9.1	Travis et al., 1983
				Nuclear test radionuclides: <sup>3</sup> H, <sup>36</sup> Cl	Sauty's Method	15.1	Thompson, 1988; Ogard et al., 1988

Source: Shaw, 2003

The measured longitudinal dispersivity values for the NTS region are shown in Figure 6-11. It can be clearly seen that the values of dispersivity from tracer tests conducted at the NTS and vicinity are consistent with those derived from tracer tests conducted elsewhere. The longitudinal, transverse, and vertical dispersivities are described by Shaw (2003).

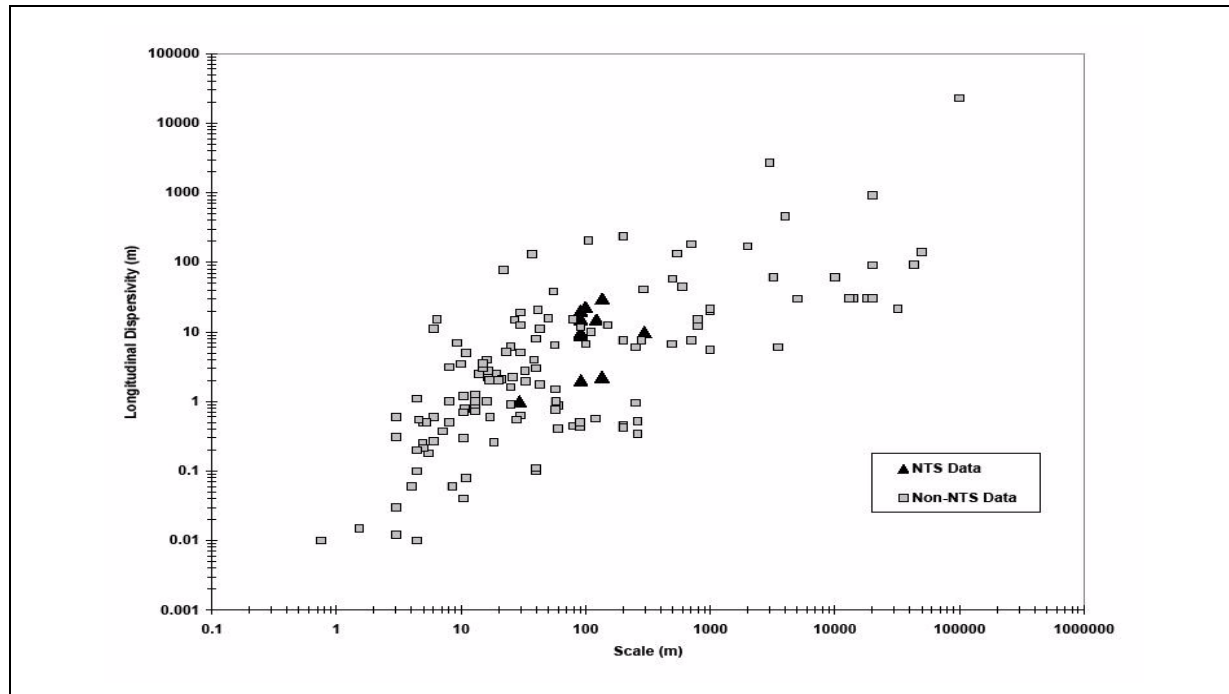


**Figure 6-11**  
**NTS Data as Compared to Non-NTS Data for Longitudinal Dispersivity**  
Source: Shaw, 2003

The following rules were applied to the uncertainty in dispersivity. In the longitudinal direction, at scales greater than 1,000 m, the dispersivity varies between 5 and 500 m. A few outliers of even larger values have been presented in the literature, but these are considered to have a low likelihood of occurrence. The distribution is represented by a log-triangular distribution with a lower bound of 3 m, an upper bound of 2,000 m, and a most likely value of 40 m. This simple distribution represents the observed range of values.

In the horizontal transverse direction, the log triangular distribution of dispersivity is defined with a lower bound of 0.01 m, a most likely value of 1 m and an upper bound value of 200. The vertical transverse dispersivity is assumed to be defined by a log-triangular distribution with a range between 0.001 and 5.0 m and a most likely value of 0.05 m.

Dispersivity is implemented in the PM CAU transport modeling through particle tracking, which is discussed in [Section 6.2](#). Because the particle-tracking results are generated as input to PLUMECALC, which is in turn simulated for 1,000 realizations, it is computationally impractical to sample the dispersivity distribution for a large range of values. Therefore — based on the ranges identified for the NTS site in [Table 6-7](#), the dispersivities derived by Shaw (2003), and the scaled relationship reported by Welty and Gelhar (1989) and SNJV (2004d) — selection of a few discrete dispersivity values provide a reasonable range for the available data.

Three ranges were selected that incorporate varying degrees of dispersivity. For the seven hydrologic framework models, a longitudinal, transverse and vertical dispersivity of 10, 1, and 0.2 were selected. This range incorporates weak dispersive fluxes that tend to reflect conservative transport through limited spread as the contaminant plume migrates downgradient. Consistent with many particle-tracking-based applications, this favors the assumption that the HFM heterogeneity will provide large-scale spreading or focusing of migration pathways. This range is also close to the most likely values of dispersivity identified by Shaw (2003). A subset of four HFMs (LCCU1 models) was assigned a higher dispersivity range of 100, 10, 2, for the respective dispersivities. These values reflect an increase of 10 times over the initial dispersivity. A longitudinal dispersivity of 100 m also corresponds to a travel distance of 1,000 m as reported by Welty and Gelhar (1989) and shown in [Figure 6-11](#). This distance corresponds to the largest horizontal grid dimension used in the numerical model. A single HFM (LCCU1-MME-TMCM) was assigned dispersivities of 300, 50, and 20. This case is intended to show how the plume spreads for very high values of dispersivity relative to the previous cases, probably extending the values beyond what is practical for the scale of permeability variation in the PM CAU model. Based on [Figure 6-11](#), selection of a dispersivity of 300 m corresponds to a longitudinal scale of 10,000 m, which is more representative of the regional scale domain. However, HFM resolution occurs in the PM CAU model often at much smaller scales.

#### **6.4.5 Mass Transfer Coefficient**

The MTC, defined in [Equation \(6-3\)](#), was a highly sensitivity parameter in the sensitivity analyses described in this report. [Figures 6-12](#) through [6-14](#) show the correlation between the MTC and its three defining parameters: fracture aperture, fracture porosity, and  $D_m$  coefficient. It is most strongly

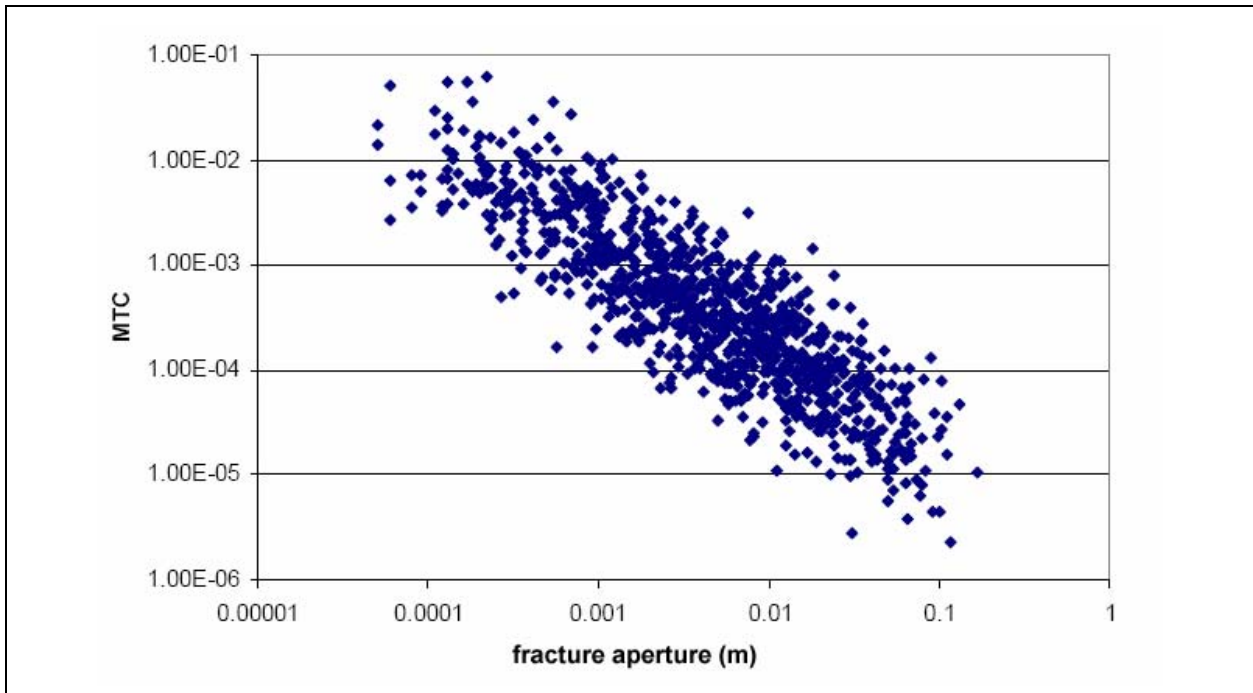


**Figure 6-12**  
**MTC and Aperture Combinations in Monte Carlo Simulations**

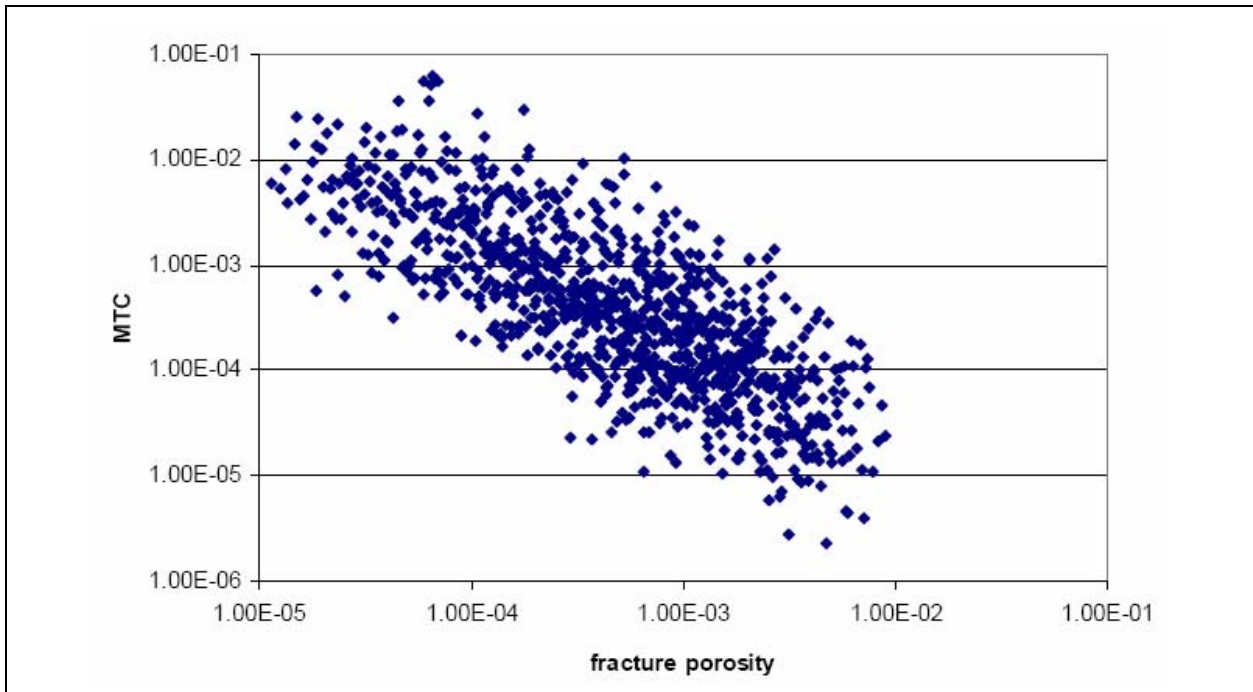


**Figure 6-13**  
**MTC and Fracture Porosity Combinations in Monte Carlo Simulations**

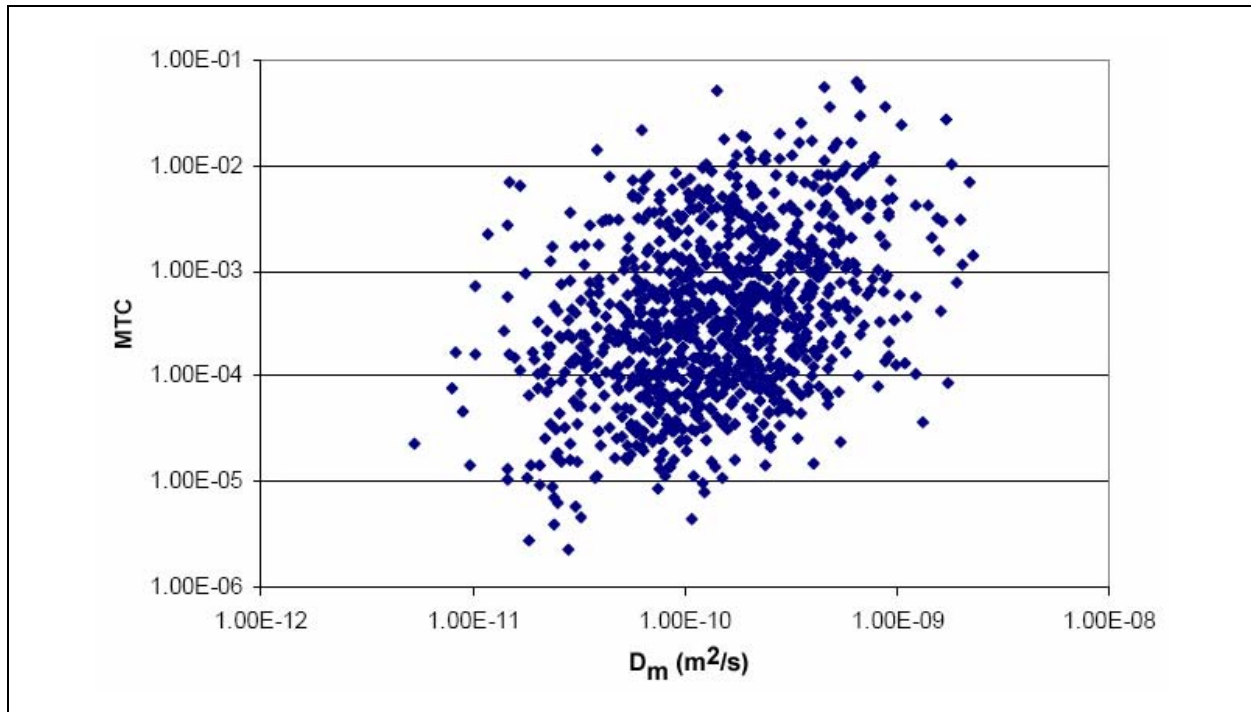


**Figure 6-14**  
**MTC and  $D_m$  Combinations in Monte Carlo Simulations**

correlated with aperture due to the range of variability in aperture. The relationships between MTC and its component parameters are shown in Figures 6-12 through 6-14.

#### 6.4.6 Sorption Coefficient

In the PM CAU transport model, radionuclide retardation via sorption is considered for reactions with immobile minerals in matrix material only. For dual-porosity zones, sorption occurs after solutes diffuse out of the fracture material into the immobile matrix continuum. For porous media zones (e.g., confining and vitric units), sorption occurs on the material through which groundwater flows. For the purposes of CAU-scale transport, only equilibrium sorption is considered and is parameterized by the distribution coefficient,  $K_d$ . Appendix B provides support for the equilibrium assumption by comparing equilibrium and kinetic sorption formulations in field-scale solute transport in the Pahute Mesa domain. Although theoretical fracture sorption coefficients are considered in Shaw (2003) and Wolfsberg et al. (2002), there are no compelling datasets that isolate this process and identify parameters. Therefore, the specific process of sorption onto minerals coating fractures, before diffusion, is not considered in this PM CAU transport model. One line of justification for this



conservative assumption is that the actual reactive surface area for fracture coatings accessible to aqueous solutes in fracture water is extremely small relative to the surface area accessible to solutes that experience even a small amount of diffusion. Further, if the fracture coating minerals are not substantially different than those in the matrix, then distinguishing between fracture sorption and matrix sorption becomes less important. Additional discussion of fracture sorption can be found in Shaw (2003), SNJV (2005), and Wolfsberg et al. (2002).

In support of this study and the related Frenchman Flat Phase II CAU transport model, Shaw (2003) and SNJV (2005) provide detail regarding the sorption process, datasets available at the time of report development, and the development of matrix  $K_d$  distributions for use in transport models. This section identifies three alternative sources of sorption  $K_d$  distributions that are considered in this model report. These are UGTA-developed values for  $K_d$  based upon laboratory measurements (Shaw, 2003; SNJV, 2005); YMP-developed values for  $K_d$  based upon laboratory measurements but then scaled for field-scale considerations (SNL, 2007a and b); and UGTA-upscaled  $K_d$  using mechanistically developed  $K_d$  distributions (this study).

Chapter 9 in Shaw (2003) details the development of  $K_d$  distributions for Pu, Np, U, Cs, and Sr based primarily on YMP laboratory measurements, as reported before 2002. These  $K_d$  distributions are developed for vitric, devitrified, and zeolitic tuff, the primary distinguishing characteristics of the RMCs in the PM CAU transport model. Subsequent to Shaw (2003) and SNJV (2005), YMP reanalyzed their data, focusing on the experimental conditions under which the observations were made, the quality of the data, and scaling considerations for site-scale models. This analysis led to new  $K_d$  distributions, which are currently being used for YMP transport calculations. The new YMP  $K_d$  distributions are documented in SNL (2007a, Tables A-4, C-8, C-12, and C-17) and SNL (2007b, Tables 6-42 and 6-1a). Those reports show laboratory and data distribution fits, as derived for all radionuclides considered as well as field-scale  $K_d$  distributions used in unsaturated zone and saturated zone models as determined through expert judgment. In the present study, radionuclides with large  $K_d$  are demonstrated to be unimportant during the 1,000-year regulatory time frame. Therefore, attention is focused on radionuclides with relatively low  $K_d$ . [Figure 6-15](#) shows the various distributions developed recently by YMP for Pu sorption on volcanic tuff. This plot is shown again in [Figure 6-16](#) with the inclusion of the Pu  $K_d$  distributions for devitrified tuff and zeolitic tuff derived from YMP data in Shaw (2003, Figure 9-6). In the UGTA Project transport model, zeolitic, vitric,

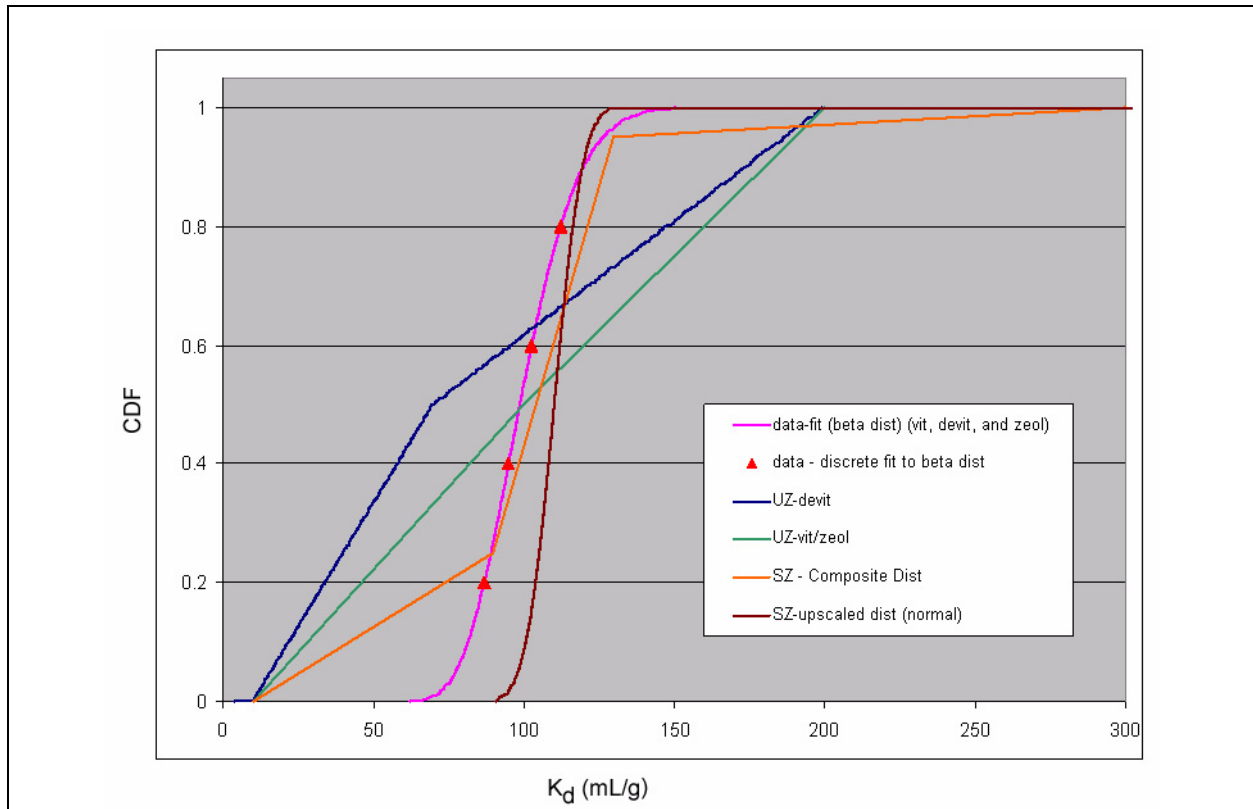


**Figure 6-15**  
**YMP Pu  $K_d$  Distributions for Volcanic Tuff**

Note: The data curve is fit to laboratory-scale  $K_d$  measurements, the UZ curves are used for site-scale transport in the unsaturated zone, and the SZ composite curve is used for site-scale transport in all volcanics in the saturated zone.

and devitrified tuff are separated into different model zones, whereas YMP does not provide that level of separation for volcanic tuff. The Shaw (2003) zeolitic and devitrified  $K_d$  curves for Pu in Figure 6-16 provide a bounding envelope for the composite YMP distribution used for all tuff. For all of the data-based distributions, the  $K_d$  values never go below 4 for Pu and are mostly less than 300. Neptunium, having even smaller measured  $K_d$  than Pu as shown in Figure 6-17 for the Shaw (2003) distributions with the composite volcanic  $K_d$  used by YMP, again shows the similarities discussed for Pu. As demonstrated in the CAU-scale transport simulations in this report, model sensitivity is limited to nuclides with  $K_d$  less than 4. Uranium  $K_d$  are similar to those for Np in Figure 6-17 and all other  $K_d$  distributions are populated by much larger values. Appendix B identifies the  $K_d$  distribution statistics from Shaw (2003), SNJV (2005), and SNL (2007a). Plutonium is the only radionuclide to which the preliminary transport model analysis exhibits sensitivity as a result of the source mass

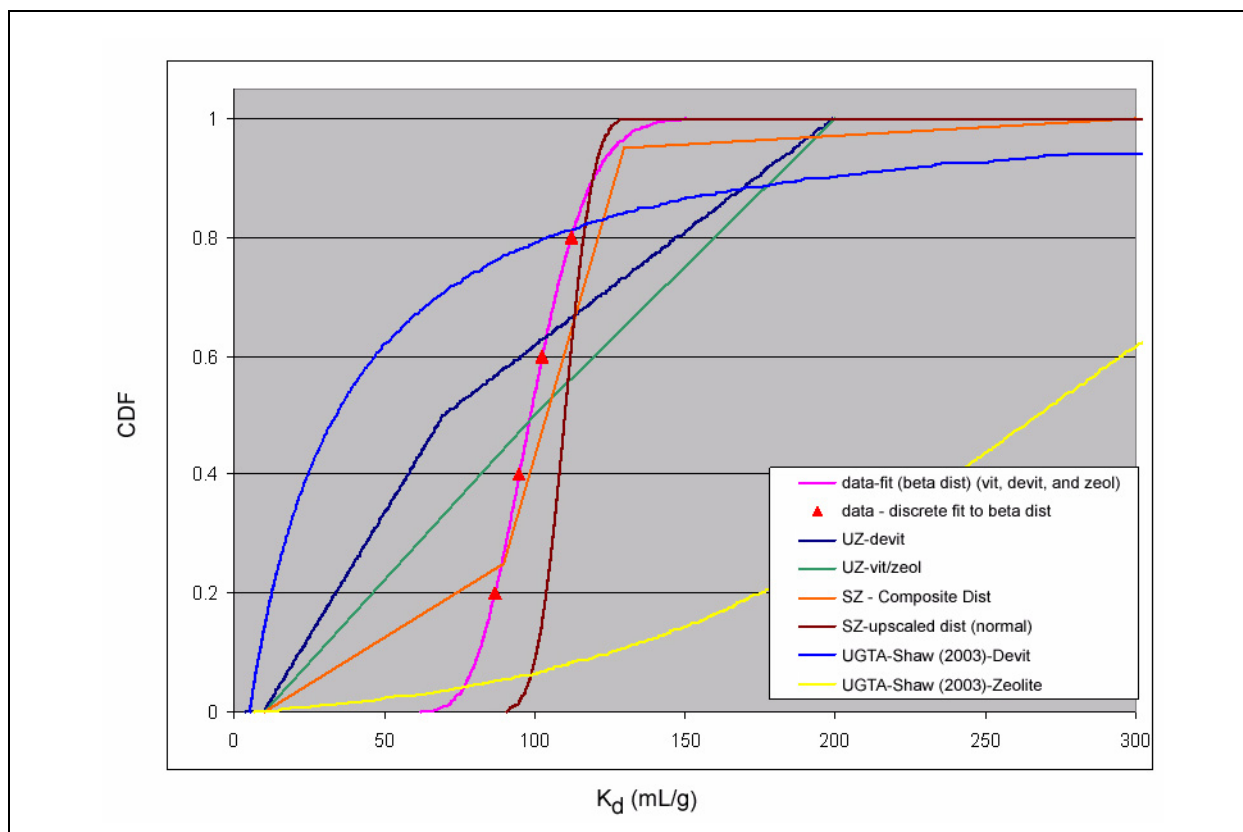


**Figure 6-16**  
**UGTA Pu  $K_d$  Distribution for Devitrified Tuff and Zeolite (Shaw, 2003)**  
**Compared with YMP Pu  $K_d$  Distribution**

Note: The data curve is fit to laboratory-scale  $K_d$  measurements, the UZ curves are used for site-scale transport in the unsaturated zone, and the SZ composite curve is used for site-scale transport in all volcanics in the saturated zone.

release. Alternative forms of the Pu distributions, including the much smaller  $K_d$  values derived, are in [Section 6.4.7](#), where non-sorbing radionuclides dominate the model predictions.

### 6.4.7 $K_d$ Upscaling

In addition to the  $K_d$  distributions developed from laboratory experiments described above, a numerical upscaling exercise was conducted to develop UGTA  $K_d$  distributions that represent sorption at the scale of a PM CAU transport model grid block (approximately 100 m), taking into consideration physical and chemical heterogeneity including fracture distributions that occur at scales smaller than the grid block. This exercise employed alternative methods for estimating  $K_d$  variability using uncertainty in reactive mineral abundance and water chemistry composition. Stoller-Navarro

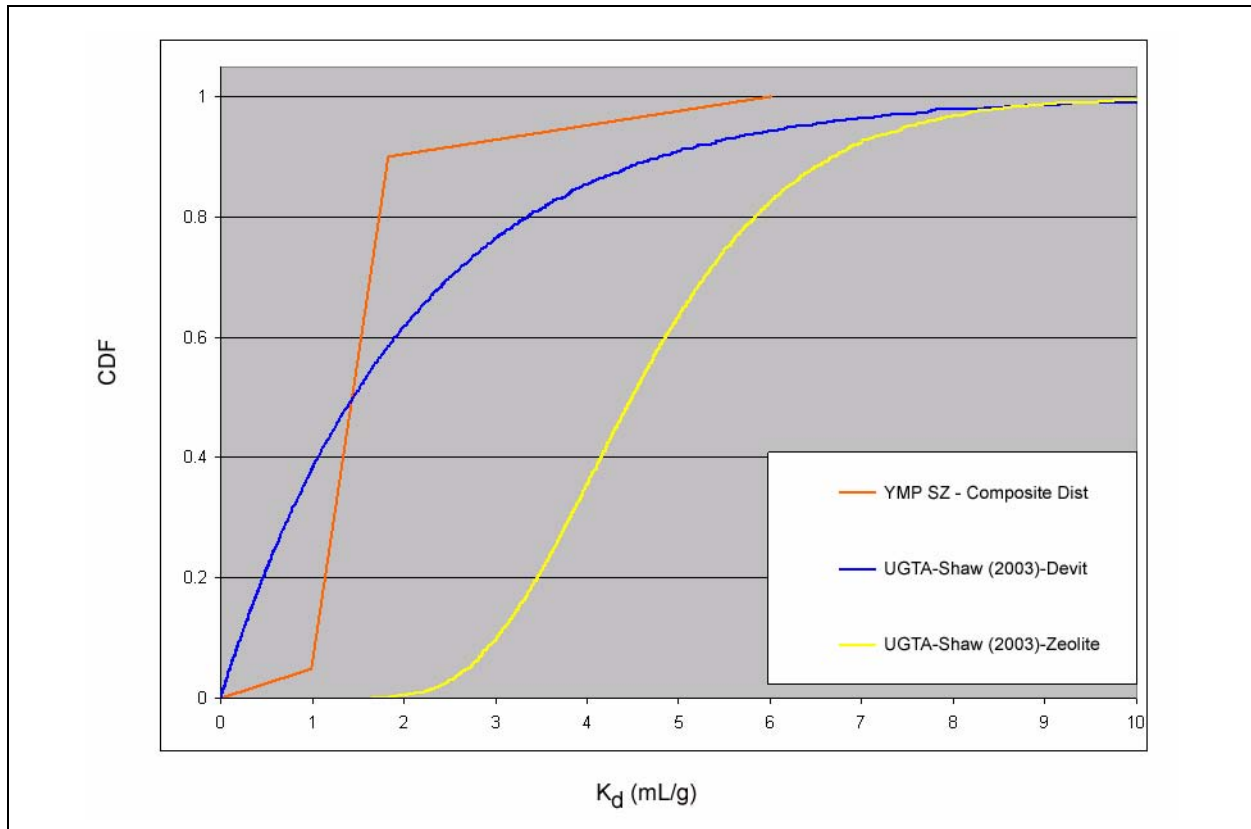


**Figure 6-17**  
**UGTA Np  $K_d$  Distribution for Devitrified Tuff and Zeolite (Shaw, 2003) Compared with YMP Composite Np  $K_d$  Distribution for Saturated Volcanic Tuffs**

Joint Venture (2005) describes the basis for mechanistic  $K_d$  estimates in the context of transport in the Frenchman Flat CAU. The same concepts developed by Zavarin et al. (2004) are applied in this upscaling exercise. As an introductory note, however, it must be pointed out that the mechanistic  $K_d$  span a range much larger than those determined from laboratory measurements, most importantly including a substantial percentage of Pu  $K_d$  values much less than 4 (Figure 6-16). Concerns that YMP datasets, from which previous  $K_d$  distributions were developed, may not necessarily reflect the physical and chemical characteristics of the PM CAU model domain are evaluated.

Measured  $K_d$  represents the ratio of sorbed to aqueous solute in a test-tube scale laboratory experiment under controlled environmental conditions. In the PM CAU transport model,  $K_d$  are specified for grid cell volumes on the order of  $10^6$  or  $10^7$  m<sup>3</sup>. The volume of zones (RMCs) with a single parameter value in a simulation can exceed  $10^{12}$  m<sup>3</sup>. This subsection describes a process for scaling  $K_d$  from the laboratory scale to the CAU model grid-block scale. The mechanistic method

allows development of  $K_d$  distributions for radionuclides not considered in laboratory experiments such as Eu and Sm. Finally, the mechanistic estimation method allows consideration of chemical conditions such as varying redox potentials that may occur in the field but which are not established in the laboratory. Thus, new distributions for  $K_d$  were computed using mechanistic concepts (SNJV, 2005; Zavarin et al., 2004) and then upscaled with the following procedure.

The components of the  $K_d$  upscaling procedure are as follows:

1. Develop RMC-specific  $K_d$  distributions for reactive radionuclides using mechanistic calculations with inputs spanning the range of mineralogic variation and water chemistry in Pahute Mesa samples.
2. For each RMC (DMP, DMR, ML, ZEOL, VMP/R) develop 100 equally probable, high-resolution, stochastic permeability fields representing physical property variations including fractures within a CAU-scale model grid block. Each model is 100 by 100 by 50 m with 500,000 grid blocks.
3. Compute flow on each of the property fields with a simple gradient.
4. Randomly distribute  $K_d$  from (1), assuming no correlation with permeability, on the flow model domain.
5. Compute transport simulations for each of the 500 models described above for seven different sorbing radionuclides (Np, U, Pu, Cs, Sr, Am, and Eu) and for a conservative tracer, recording the solute breakthrough curve at the downgradient boundary.
6. Using inverse model methods and the conservative tracer breakthrough curve from the heterogeneous model, estimate Peclet number and residence time for a single material model (no spatial distribution of parameters).
7. Fixing parameters from (6), use inverse methods to estimate effective  $K_d$  for a single material model by matching the reactive radionuclide breakthrough curves for the heterogeneous model simulations.
8. Combine results from (7) (100 realizations per upscaling run) to create empirical distributions of upscaled  $K_d$  for each radionuclide for each RMC.

#### **6.4.7.1 Mechanistic $K_d$ Distributions**

Using the method of Zavarin and Bruton (2004a and b) described in SNJV (2005, Section 9.6), a mechanistic approach was used to estimate  $K_d$  distributions for Pahute Mesa RMCs. Mechanistic

sorption modeling seeks to capture the fundamental reactions between radionuclides and the rock surfaces with which they come in contact, accounting for aqueous speciation, surface complexation, ion exchange, and precipitation reactions. Model inputs include the ranges of mineralogy and water chemistry observed at Pahute Mesa.

Each RMC was assigned a specific range of felsic minerals, glass, and zeolitic and mafic minerals inferred from XRD measurement (Warren et al., 2003), along with aqueous geochemistry for 958 analyses from Pahute Mesa (SNJV, 2004a; NNSA/NSO, 2004). Water chemistry sample analyses were screened and the dataset corrected for two deficiencies. The average over all samples was used for analyses that excluded ions required for modeling, including  $\text{HCO}_3^-$ ,  $\text{SO}_4^{2-}$ , Ca, K, Mg, Na, and  $\text{SiO}_2$ , or pH, water temperature, and  $\text{F}^-$  concentrations. Analyses that did not meet a charge balance criteria, no greater than 5 percent difference between cation and anion concentrations, were excluded. Mechanistic radionuclide sorption to smectite, zeolite, Fe oxide, calcite, and illite was calculated for Ca, Cs, Sr, Ni, Eu, Sm, Am, Np, Pu, and U, accounting for the varying mineralogic, geochemistry, and groundwater conditions. Mechanistically modeled radionuclide sorption reaction constants and aqueous speciation and were combined using the CRUNCH code (an updated version of the GIMRT code [Steeffel and Yabusaki, 1996]) to predict radionuclide  $K_d$  as a function of mineralogy and water chemistry. For each RMC, multiple simulations using CRUNCH, sampling different permissible combinations of mineral and water composition, provided an empirical distribution of permissible  $K_d$  at the laboratory scale for each radionuclide of interest.

The mechanistic  $K_d$  distributions provide new ranges for consideration. [Figure 6-18](#) shows a comparison between the calculated and the measured values for DMP tuffs. The most important features in this figure are the lower bounds for Pu, Sr, Np and U. These play an important role in the statistical distributions used in Monte Carlo sampling. [Figures 6-19](#) through [6-22](#) show the empirical cumulative distribution functions (ECDFs) for all of the radionuclides for each different RMC. Again, Np, U, Pu, and to some extent Sr have substantial probabilities associated with low  $K_d$ . Comparing [Figures 6-19](#) through [6-22](#) with [Figures 6-15](#) through [6-17](#) suggests entirely different distributions. The differences have not been reconciled and there are little field-scale transport data with which to evaluate. However, using the mechanistic  $K_d$  is conservative with respect to the transport modeling process, especially because non-sorbing radionuclides ( $^3\text{H}$ ,  $^{14}\text{C}$ ,  $^{36}\text{Cl}$ ,  $^{99}\text{Tc}$ , and  $^{129}\text{I}$ ) are in the source term (and shown later to dominate model predictions).

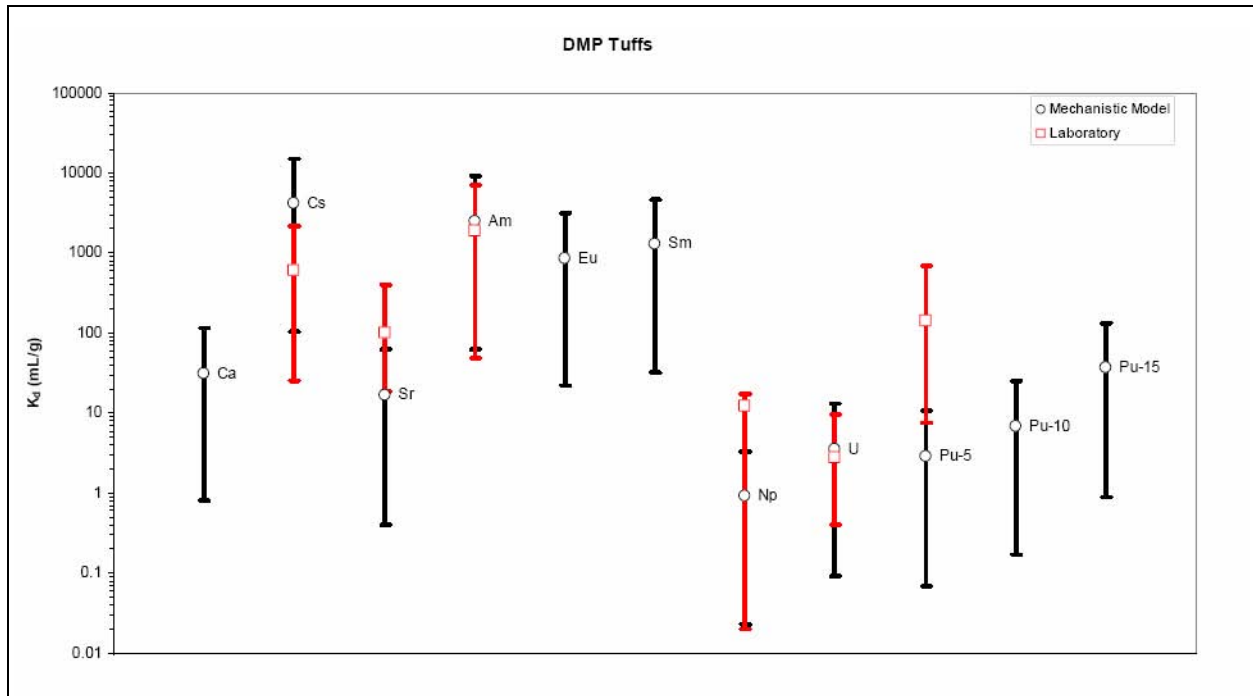


**Figure 6-18**  
**Mechanistic Model  $K_d$  Distributions for DMP Compared with Laboratory Data**  
 Note the low  $K_d$  estimates associated with Pu, U, Np, and Sr.

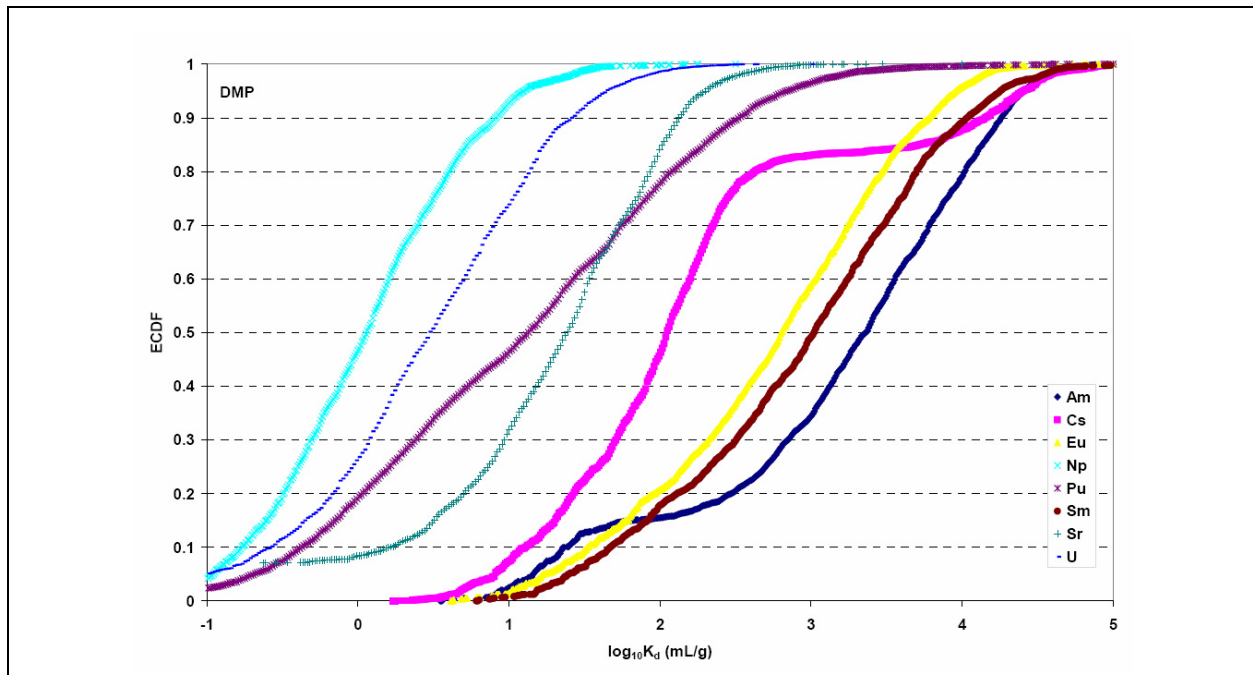


**Figure 6-19**  
**Mechanistic Model  $K_d$  Distributions for DMP**  
 Note the low  $K_d$  estimates associated with Pu, U, Np, and Sr.

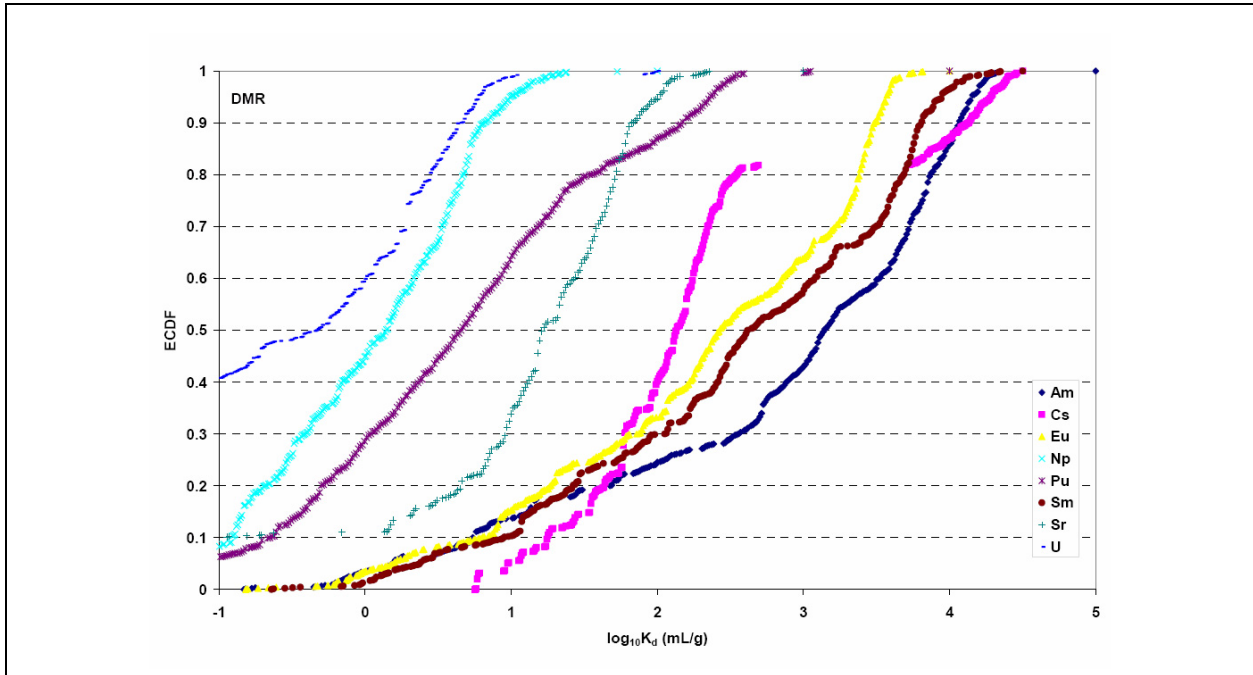


**Figure 6-20**  
**Mechanistic Model  $K_d$  Distributions for DMR Compared with Laboratory Data**  
 Note the low  $K_d$  estimates associated with Pu, U, Np, and Sr.

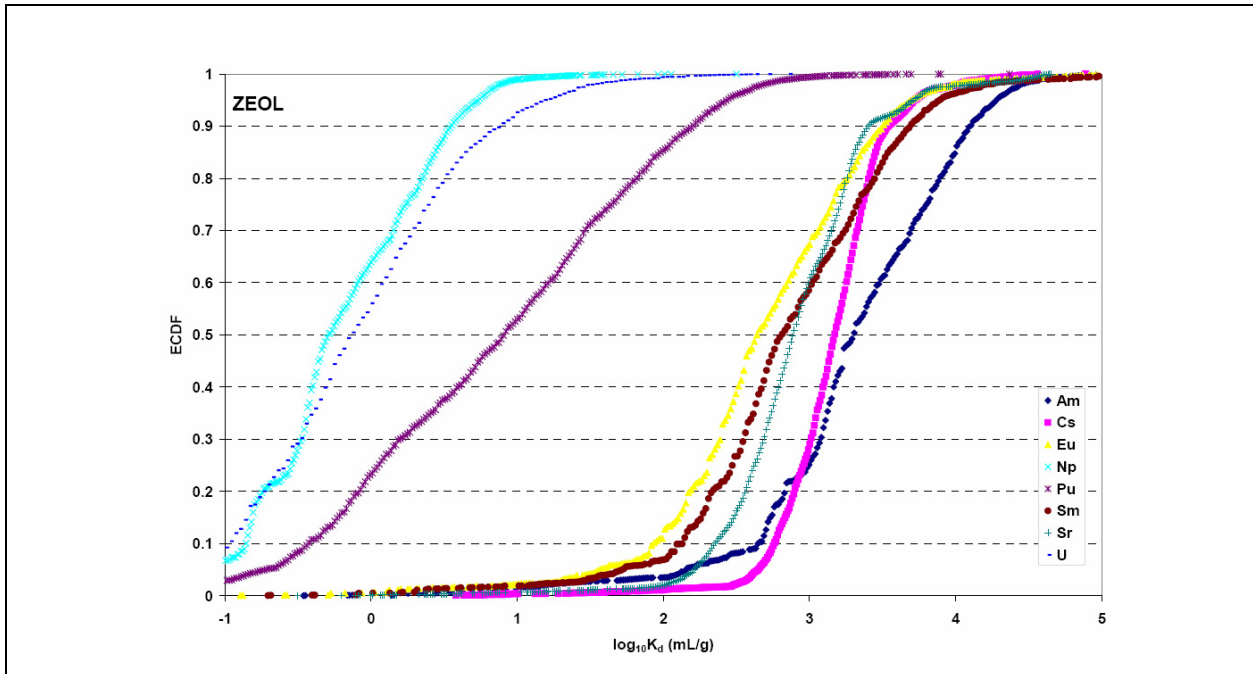


**Figure 6-21**  
**Mechanistic Model  $K_d$  Distributions for ZEOL Compared with Laboratory Data**  
 Note the low  $K_d$  estimates associated with Pu, U, and Np.



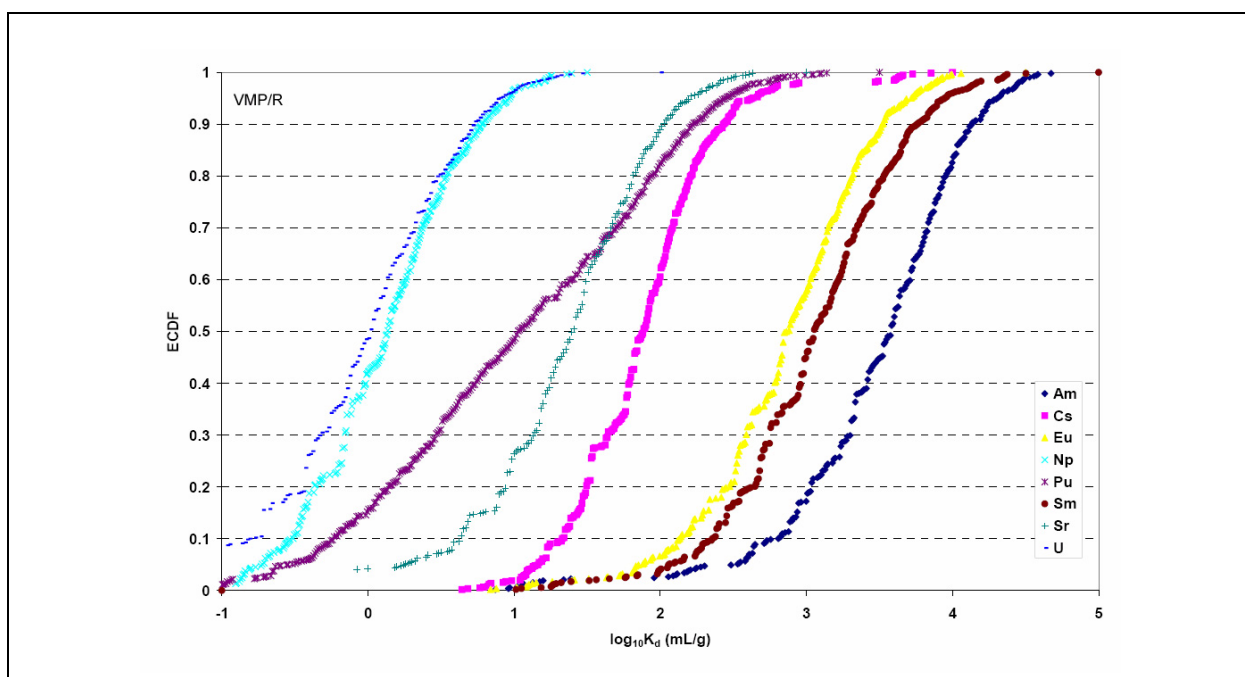


**Figure 6-22**

***Mechanistic Model  $K_d$  Distributions for VMP/R***

Note the low  $K_d$  estimates associated with Pu, U, Np, and Sr.

The  $K_d$  distributions developed using mechanistic estimation techniques are broad. Most noteworthy, this method yields  $K_d$  for Pu, Np, U, and Sr that are substantially smaller than those measured (Figure 6-18). The maximum values in these distributions are also substantially greater than those in the measurement ranges. Therefore, these distributions were adopted for the remainder of the upscaling exercise described next. The results suggest that the low values in these distributions dominate the upscaling procedure, leading to upscaled distributions representing less sorptive capacity than the data distributions in Figures 6-15 through 6-17. Comparison of the mechanistically derived distributions with upscaled data-based distributions has not been conducted.

#### **6.4.7.2 $K_d$ Distributions**

An analysis of spatial  $K_d$  structure based upon mechanistic  $K_d$  estimates was conducted after upscaling study was completed. However, it serves to provide additional information for considering: (1) the spatial distribution of  $K_d$  used in this study as described in this section, (2) how to populate heterogeneous reactive transport models in future studies, and (3) future data collection activities to support upscaling studies. Zavarin et al. (2004) computed  $K_d$  mechanistically for intervals from several Yucca Mountain boreholes using measured mineral abundances and water chemistry. More

than 300  $K_d$  estimates were computed mechanistically by Zavarin et al. (2004) for mineralogic samples from boreholes USWG2, USWG1, UE25P1, UE4A, U20BD, U20AS, PR95/22, J13, and DEB5. Initially, the samples were segregated based upon whether they were from the Crater Flat Group (Tc), or the Paintbrush Group (Tp). For Pahute Mesa, many of the HSUs fall into these two groups. For example, CHZCM (RMC ZEOL) is part of Tc, while TSA (RMC DMP) is part of Tp. For detailed classification of units, see [Appendix A](#) (or BN, 2002a). Noting that any structure identified in these values represents strictly vertical relationships, the data were not sufficient to develop variances and correlation length scales when segregated by Tc and Tp groupings. However, when all of the data were combined, variograms for Np and U  $K_d$  were developed as shown in [Figure 6-23](#). In these cases, the variance of  $\ln(K_{58,d})$  for Np and U are 1.25 and 1.75, respectively, and the correlation length,  $\lambda$ , in the vertical direction is 5 m. These results say nothing about horizontal correlation. The importance of horizontal  $\lambda$  between 5 and 500 m could be investigated through sensitivity analysis.

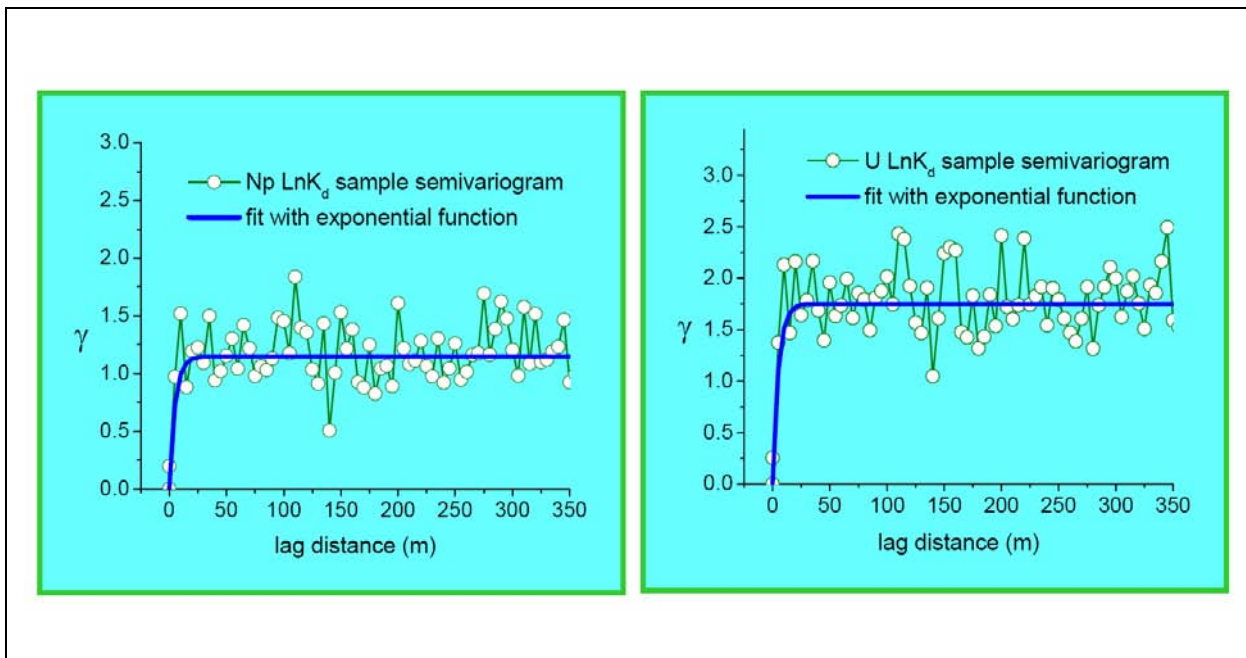


**Figure 6-23**  
**Estimated Variograms from Mechanistic Model  $K_d$  Estimates**  
**for YMP Samples in Tc and Tp Groups**

Note:  $K_d$  estimated by Zavarin et al. (2004).

In the present upscaling analyses, matrix  $K_d$ , sampled from the distributions were randomly distributed throughout the transport model domain. Efforts to correlate structure to  $K_d$  variation were unsuccessful due to sparsity of data within RMCs, and it is not expected that  $K_d$  would correlate with  $k$  because  $k$  is dominated by fracture properties for DMP, not the structure of the reactive minerals as has been suggested for porous media in other studies. This approach will not yield a 100-by-100-by-50-m model domain dominated by either high or low values from the  $K_d$  distribution. However, the analysis of available data described above suggests a very small, if any, correlation length in the vertical direction. Presently, there are no data to indicate whether the reactive minerals that affect  $K_d$  variability are laterally correlated.

With spatial distributions of fracture properties and  $K_d$ , the second set of particle-tracking simulations are conducted for each realization. Again, the particles are released in a high-permeability, low-porosity manifold on the upgradient boundary and breakthrough curves across the downgradient boundary are simulated. Fracture aperture and spacing are computed for each node based upon permeability and the fixed fracture porosity of  $1.8E-04$ . The  $D_m$  coefficient is set to  $1.4E-10$  square meters per second ( $m^2/s$ ), and particles are simulated in dual-porosity mode.

RELAP is again used to fit the particle breakthrough curves with single dual-porosity material properties. In these calculations,  $Pe$  and  $\tau$  are held constant at their values estimated with the non-reactive solute, and matrix  $K_d$  is estimated in the inversion. Upscaling a few single property parameters for this highly complex heterogeneous system leads to imperfect matches. [Figure 6-24](#) shows the particle-tracking breakthrough curve for a DMP Np simulation (symbols) and the match with RELAP. For all of these inversions, more weight was put on the early time and initial curvature of the breakthrough curve than on the tails, focusing on the dominant processes in the regulatory time frame of 1,000 years. This also deweights errors associated with particles initiating in the non-reactive manifold and sorbing to immobile minerals before fully entering flowing fracture pathways in the modeling approximation. An alternative approach would have been to start particles only in fractures with their density being based upon flux, to avoid the processing of releasing particles into flow fractures.

This process of simulating one flow field, two particle-tracking breakthrough curves, and two RELAP inversions per realization is conducted 100 times for each of five RMCs (DMP, DMR, ML,

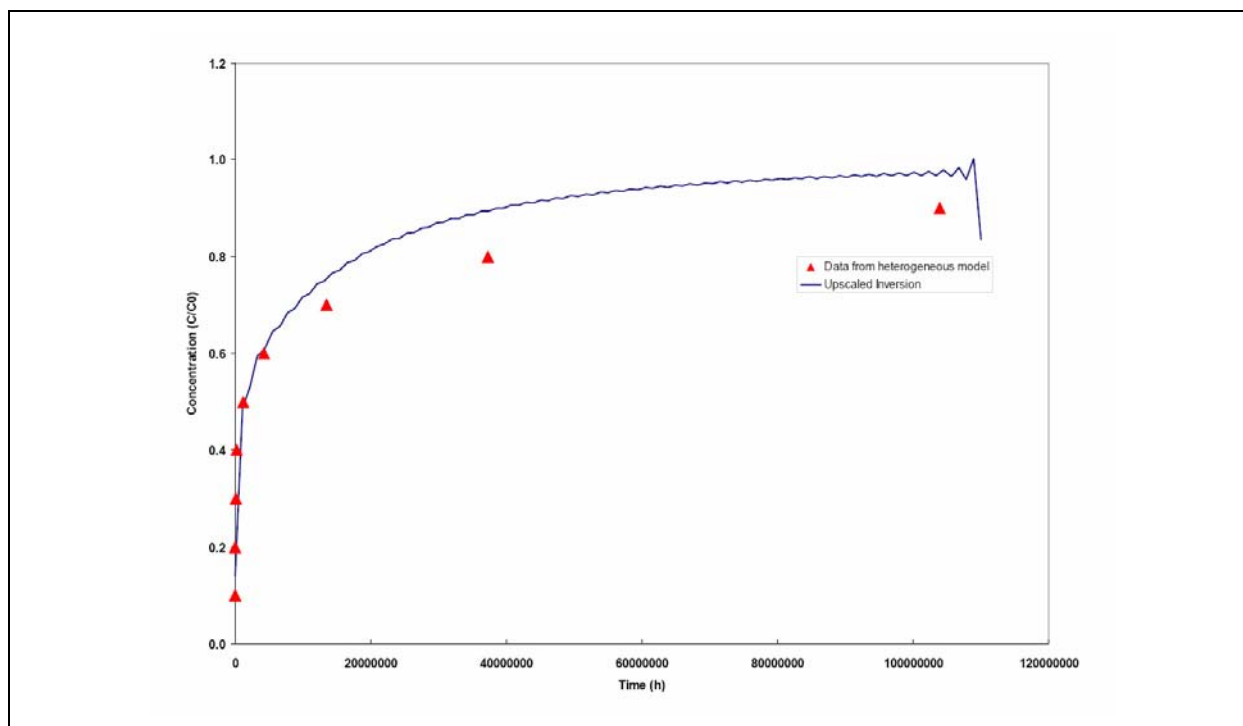


**Figure 6-24**  
**Fitting  $N_p$  for a DMP Realization**

Note:  $K_d$  estimated at 1.26.

ZEOL, VMP/R) for each radionuclide. The calibrated  $K_d$  values are then assigned to a new distribution of upscaled  $K_d$ . Figures 6-25 through 6-29 shows the upscaled distributions computed with this process. These  $K_d$  distributions are compared with the underlying mechanistic  $K_d$  distributions shown in Figures 6-19 through 6-21 as well as with the distributions developed based upon laboratory scale  $K_d$  measurements shown in Figures 6-15 through 6-18.

Comparing these results with the underlying mechanistic  $K_d$  ECDFs, the tails of the mechanistic  $K_d$  distributions are somewhat clipped, with less probability on the lowest  $K_d$ . Figure 6-30 shows a direct comparison for Pu for three of the five RMCs (DMR and ML are similar to DMP). The new distributions eliminate the lowest  $K_d$  from consideration at the 100-m CAU grid block scale, an initial concern with the mechanistic  $K_d$  distributions. However, the large fraction of small  $K_d$  (much smaller than are shown in the data distributions) leads the upscaled distribution to represent small  $K_d$ , by comparison.

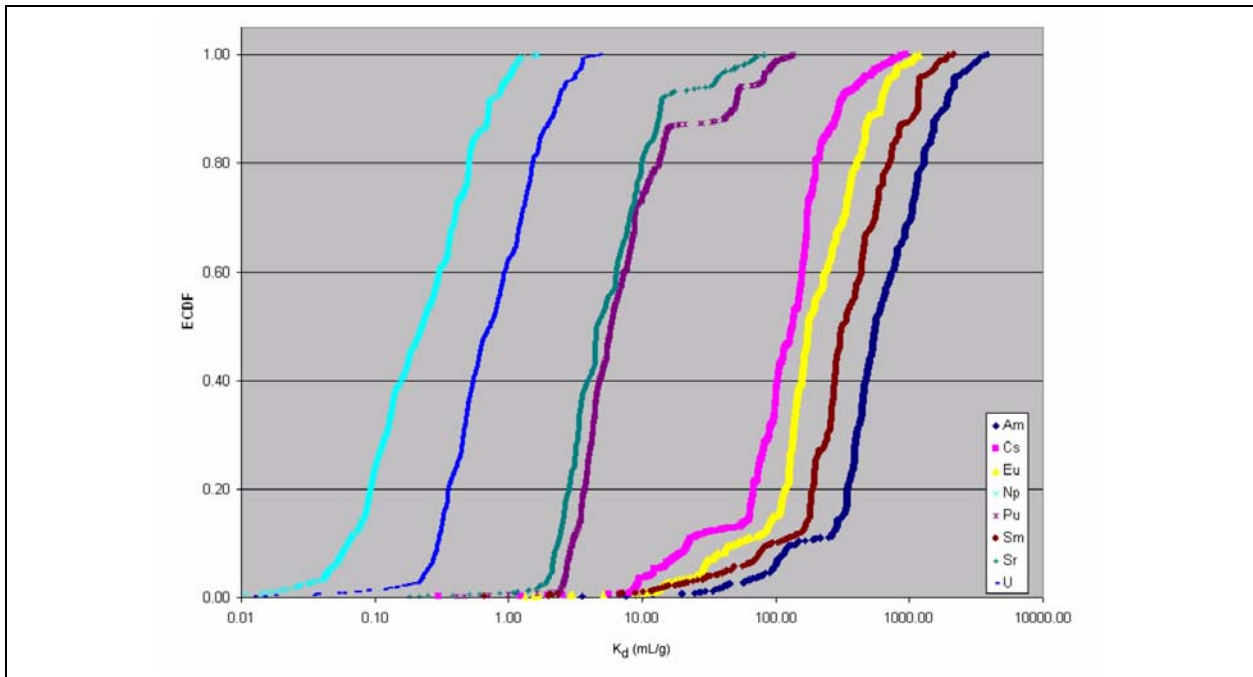


**Figure 6-25**  
**Distribution of  $K_d$ , Upscaled for DMP**

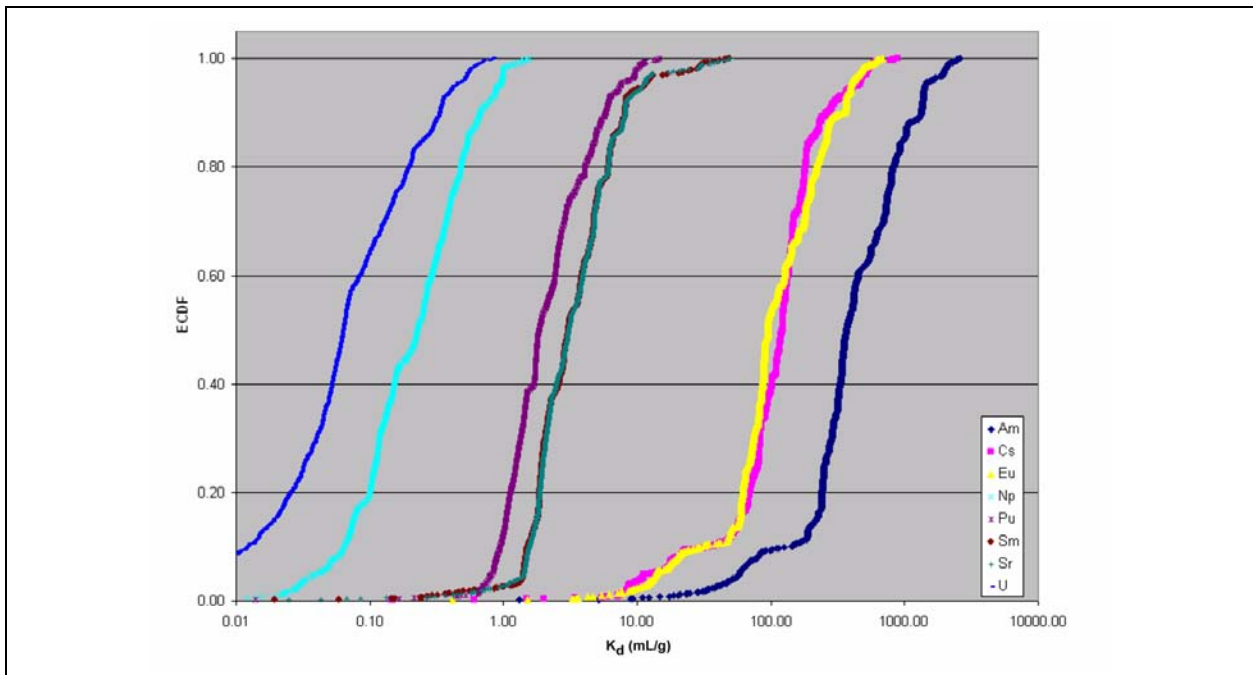


**Figure 6-26**  
**Distribution of  $K_d$ , Upscaled for DMR**

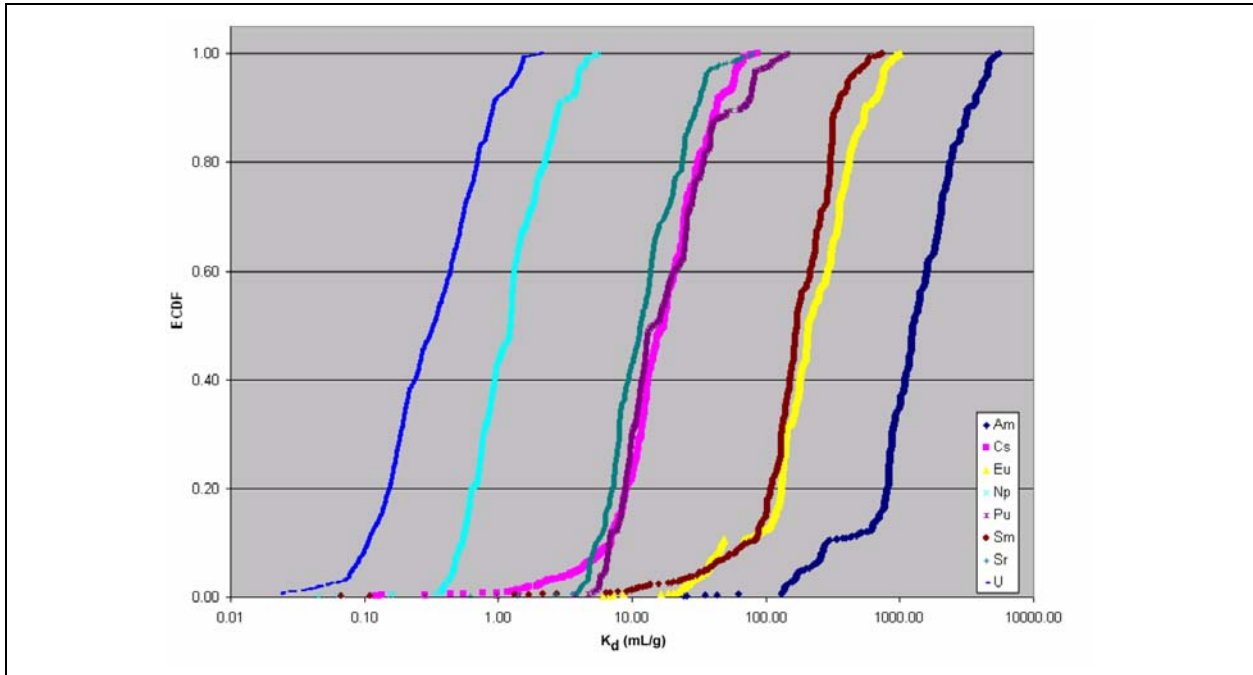


**Figure 6-27**  
**Distribution of  $K_d$ , Upscaled for ML**

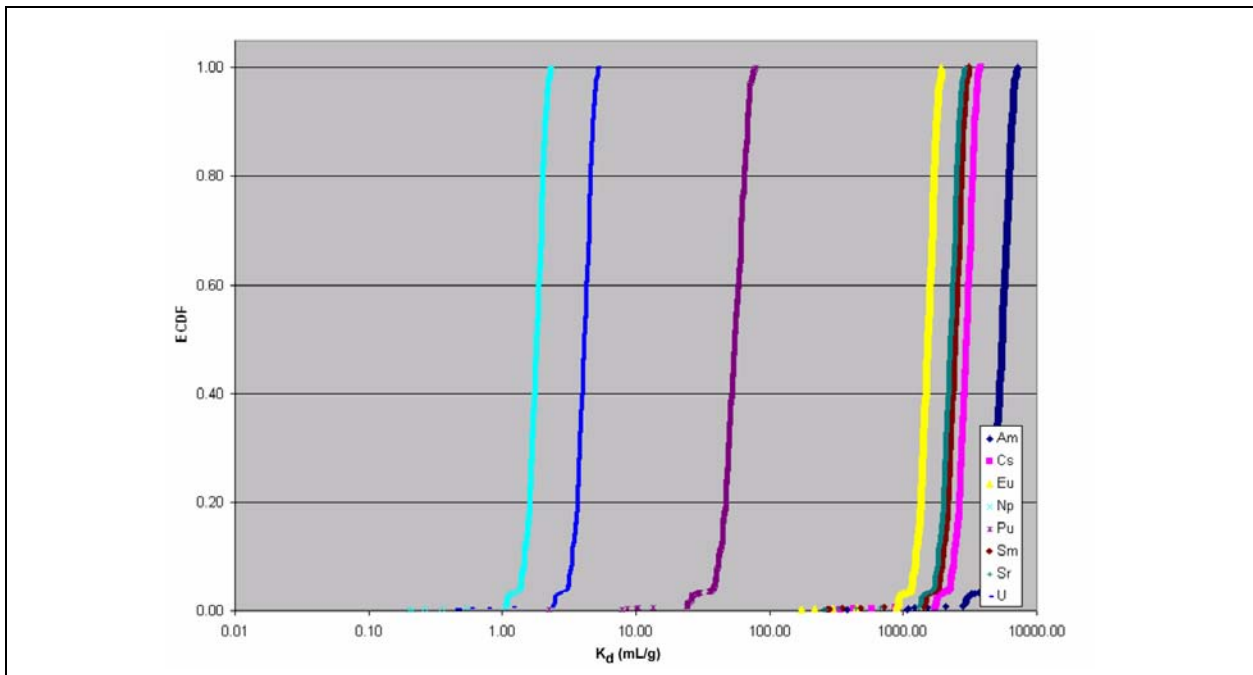


**Figure 6-28**  
**Distribution of  $K_d$ , Upscaled for ZEOL**

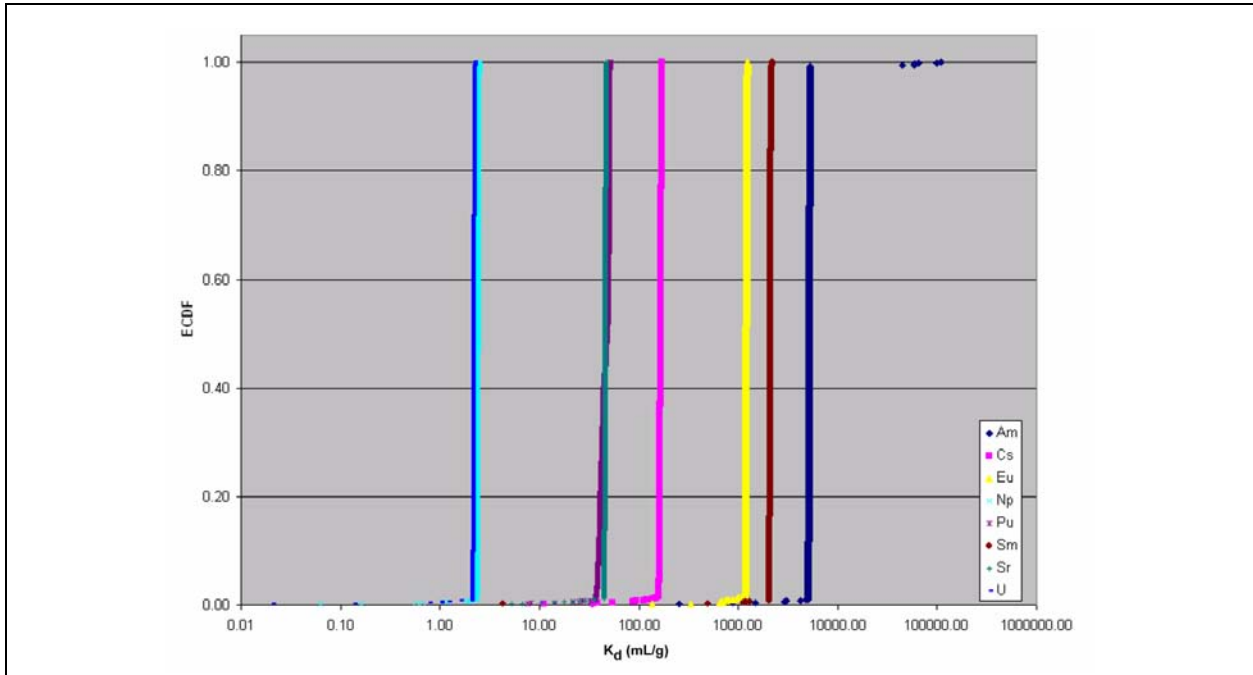


**Figure 6-29**  
**Distribution of  $K_d$ , Upscaled for VMP/R**

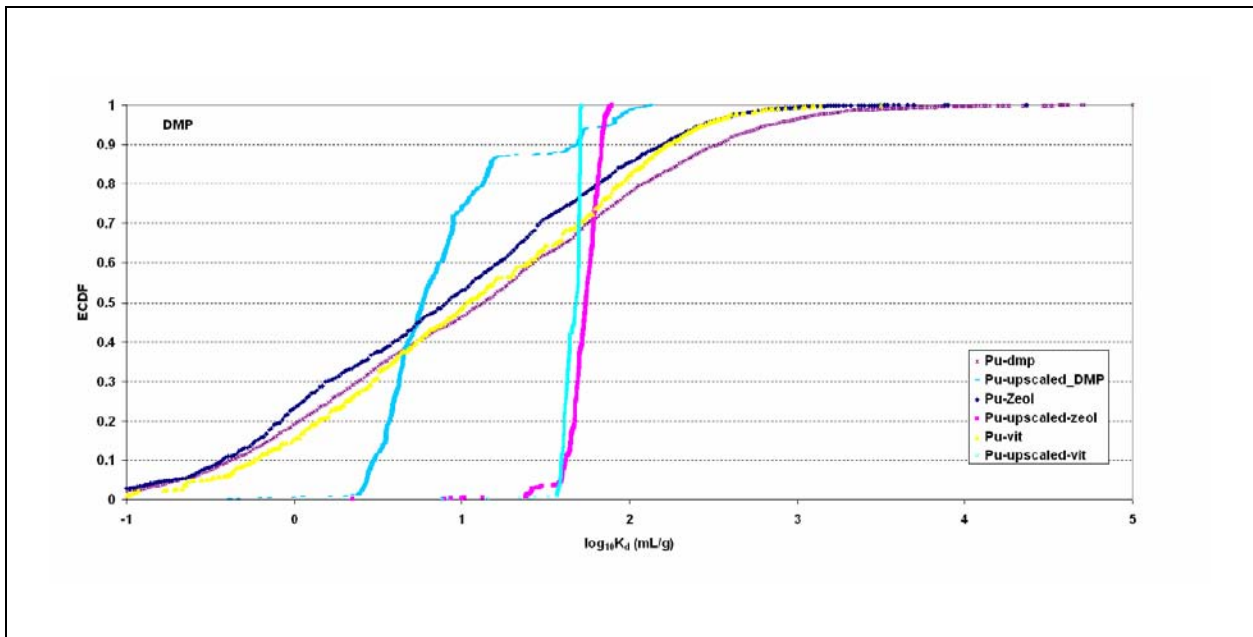


**Figure 6-30**  
**Comparison of Mechanistic and Upscaled  $K_d$  for Pu**

Whereas DMP, DMR, and ML are modeled as fracture-dominated RMCs, ZEOL and VMP/R are matrix-flow dominated. In the permeability distributions developed for these RMCs, throughgoing fractures are far less likely (nearly non-existent), so solutes migrating through the model domain necessarily encounter porous matrix material. In porous material, matrix diffusion does not dominate the ability of a solute to encounter reactive minerals. Therefore, the solutes experience a broader distribution of  $K_d$ . Because the  $K_d$  from the mechanistic distributions are populated randomly in the flow domain, and because preferential paths do not exist as they do in DMP, DMR, and ML, the upscaled values converge near the average. The curves in [Figure 6-28](#) show that less than 5 percent of the breakthrough solute encounters pathways that may be somewhat more channeled than the remaining 95 percent for the zeolitic models. This value decreases to 2 percent for the vitric material models. These results for porous media-dominated upscaling models raise concerns regarding the random distribution of  $K_d$ . For this reason, the data-based distributions described previously are also used in the sensitivity analysis of the PM CAU model.

#### **6.4.7.2.1 Summary**

Two very different approaches for developing  $K_d$  distributions have led to two very different distributions for consideration. The difference is evaluated later in sensitivity analysis where field-scale Monte Carlo analyses are conducted with the mechanistic distributions as well as with a data-based distribution. The results presented in [Section 7.0](#) show that, compared to non-sorbing and relatively high-activity species, the model is insensitive to the  $K_d$  distributions for these sorbing species (the low activity of Np and U contribute to their insensitivity). Thus, regarding the substantial differences between the upscaled  $K_d$  distributions and the data-based distributions, the conclusion is that the model is insensitive to any sorbing aqueous species (see [Section 7.0](#)).

### **6.5 Evaluation Based on $^{14}\text{C}$ Considerations**

An extension of the Pahute Mesa geochemical mixing targets study (Kwicklis et al., 2005) includes evaluation of  $^{14}\text{C}$  ages in various wells on Pahute Mesa. Examining the results of that study led to the development of a simulation study to evaluate transport parameters in the model. Starting with a calibrated PM CAU flow model, transport simulations were conducted to simulate migration of solutes between two wells in the model domain. The distribution of  $^{14}\text{C}$  age simulated with a particle-tracking approach was used to estimate the ensemble sample  $^{14}\text{C}$  age difference, and was



compared with the difference between  $^{14}\text{C}$  age estimates for samples from the two wells considered. In the next subsections, the data interpretation is reviewed and then the model, its assumptions, and the comparative simulations are described.

### **6.5.1 Summary of $^{14}\text{C}$ Data Evaluation**

[Appendix D](#) of this report presents an interpretation of groundwater travel times based upon  $^{14}\text{C}$  data. The study highlights the flow paths from Pahute Mesa toward downgradient locations such as Oasis Valley. Starting with the flow paths and mixing models developed by Kwicklis et al. (2005), the  $^{14}\text{C}$  continuation investigates travel times as estimated from  $^{14}\text{C}$  ages in wells within the model domain. Whereas the mixing model analysis provided a clear context for flow path evaluation, the travel time analysis recognizes greater ambiguities as a result of interpretation of waters that mix with various apparent ages. Complicating the interpretation is the inherent 2-D interpretation of 3-D system. Namely, as a result of large open intervals and differences in formations penetrated by different wells, the samples do not necessarily reflect measurements along actual flow paths. For example, water from Area 20 is characterized by U20-WW, which is screened in the CHCZM. The flow path analysis considers downgradient well ER-EC-6, which is screened in a combination of units including the BA, UPCU, TCA, LPCU, TSA, CHCU, and CFCM. The data are sparse, but the analysis provides substantial insight into  $^{14}\text{C}$  age differences along some of the flow paths.

A process of decomposing apparent age differences between a well and those upgradient with water types found in that well met with mixed success as described in [Appendix D](#). One combination of potential use in characterizing travel times within the TMCM includes ER-EC-5 and ER-OV-3c. Two different methods for estimating the travel time along this path are described in [Appendix D](#), with a range for consideration in the model analysis of 1,500 to 5,000 years. As described in [Section 6.5.2](#), ER-EC-5 and ER-OV-3c penetrate substantially different depths and the screens are in different units. However, most of the flow between the two wells occurs in the TMCM. The initial hypothesis was that the age differences between the two wells reflected groundwater velocities. However, analysis with the flow and transport model highlights the distribution of travel times associated with solutes between the two wells. This reflects the apparent  $^{14}\text{C}$  age measured in any well potentially results from a mixture of waters with different ages. [Section 6.5.2](#) describes a modeling approach used to evaluate fracture properties relative to apparent  $^{14}\text{C}$  age differences of 1,500 to 5,000 years between these two wells.

### 6.5.2 Numerical Simulation Considerations

The PM CAU flow model is a saturated zone-only model and does not account for residence time as recharge percolates to the water table through the overlying vadose zone. It also does not seek to determine the age of water entering at the lateral boundaries. Therefore, this analysis must focus only on the age differences of water, as estimated by  $^{14}\text{C}$  analyses at wells along the same flow path.

Of the wells sampled and analyzed for  $^{14}\text{C}$  as described in [Section 6.5.1](#), the most unambiguous migration pathway is from ER-EC-5 to ER-OV-3c. For this segment of the flow system, the chloride and stable isotope analysis (Kwicklis et al., 2005) indicates that ER-OV-3c may have a very strong component of ER-EC-5-type water as an upgradient source (80 to 90 percent) with a possibility of 10 to 20 percent coming from local recharge. Further, a unique aspect of the geochemical interpretation of this segment is that the  $^{14}\text{C}$  age difference between the ER-EC-5 water and the component of ER-EC-5-type water in the ER-OV-3c sample is estimated to be between 1,500 and 5,000 years. This is quite different from the comparison of ER-EC-5 water with its upgradient sources. The composite  $^{14}\text{C}$  age difference between ER-EC-5 water and potential upgradient source water represented by UE-18r, U-20ww, and ER-EC-1 is estimated at 1,700 years. However, the components could not be separated in the geochemical inversion modeling, so it would be difficult to design a comparative transport model with which to match results. The UE-18r  $^{14}\text{C}$  interpretation, with regard to its upgradient water types, is also not uniquely identified for the comparison. Therefore, this analysis focuses on comparing model results with  $^{14}\text{C}$  differences between ER-EC-5 and ER-OV-3c. [Figure 6-31](#) shows the location of these wells in the model domain.

The simulation design for this analysis involves particle releases at ER-OV-3c in the open interval between 1,127 and 1,113 masl, and then reverse simulations upgradient to the northing coordinate of ER-EC-5, a distance of approximately 10 km. The particle breakthrough curve at a transect through the model 10 km north of ER-OV-3c is *assumed* to represent the distribution of travel times for water starting with an ER-EC-5 signature and traveling to ER-OV-3c. Therefore, the reverse breakthrough curve is referred to as the age distribution between the two wells. This implies that a water sample at ER-OV-3c represents a distribution of water parcels, each with a different aging history because it had a  $^{14}\text{C}$  signature of ER-EC-5-type water. Therefore, all of the different ages need to be considered when computing a single,  $^{14}\text{C}$  age difference between the two wells. Whereas ER-OV-3c samples

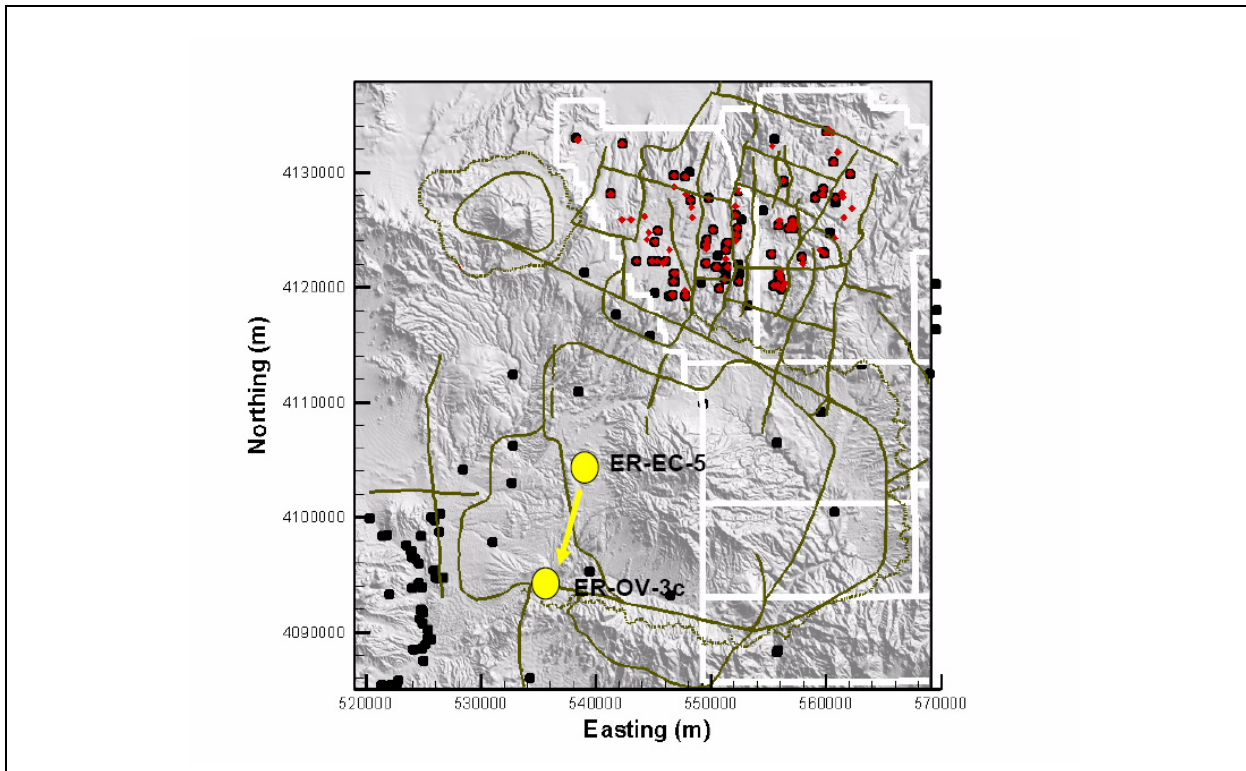


**Figure 6-31**  
**Locations of ER-EC-5 and ER-OV-3c for <sup>14</sup>C Comparisons**

come from a small interval in the TMA, ER-EC-5 samples come from a much larger open interval between 1,191 and 791 masl in the TMCM.

These calculations were conducted before developing the LCCU1-MME-TMCM alternative flow model described in [Section 3.4.3](#); they use the LCCU1-USGSD flow model. Thus, the simulations are characterized by strong channeling at the TMCM-FCCM interface, as discussed in [Section 3.4.3](#).

The first component of this analysis involves identifying the characteristic relationships between fracture parameters and transport behavior in this model. [Figure 6-32](#) shows the reverse particle breakthrough curves (age distribution) as simulated for several different fracture apertures for a fixed fracture porosity value of 0.0001. For each change in fracture aperture, the fracture spacing is recomputed automatically according to [Equation \(6-2\)](#). For the smallest aperture considered, 0.0001 m, the fracture spacing would only be 0.1 m. Thus, with little matrix volume between fractures, concentration equilibrium between the fracture and matrix water is established, and the solute migrates with an effective porosity of the matrix material. The 0.0001-m aperture curve lies on

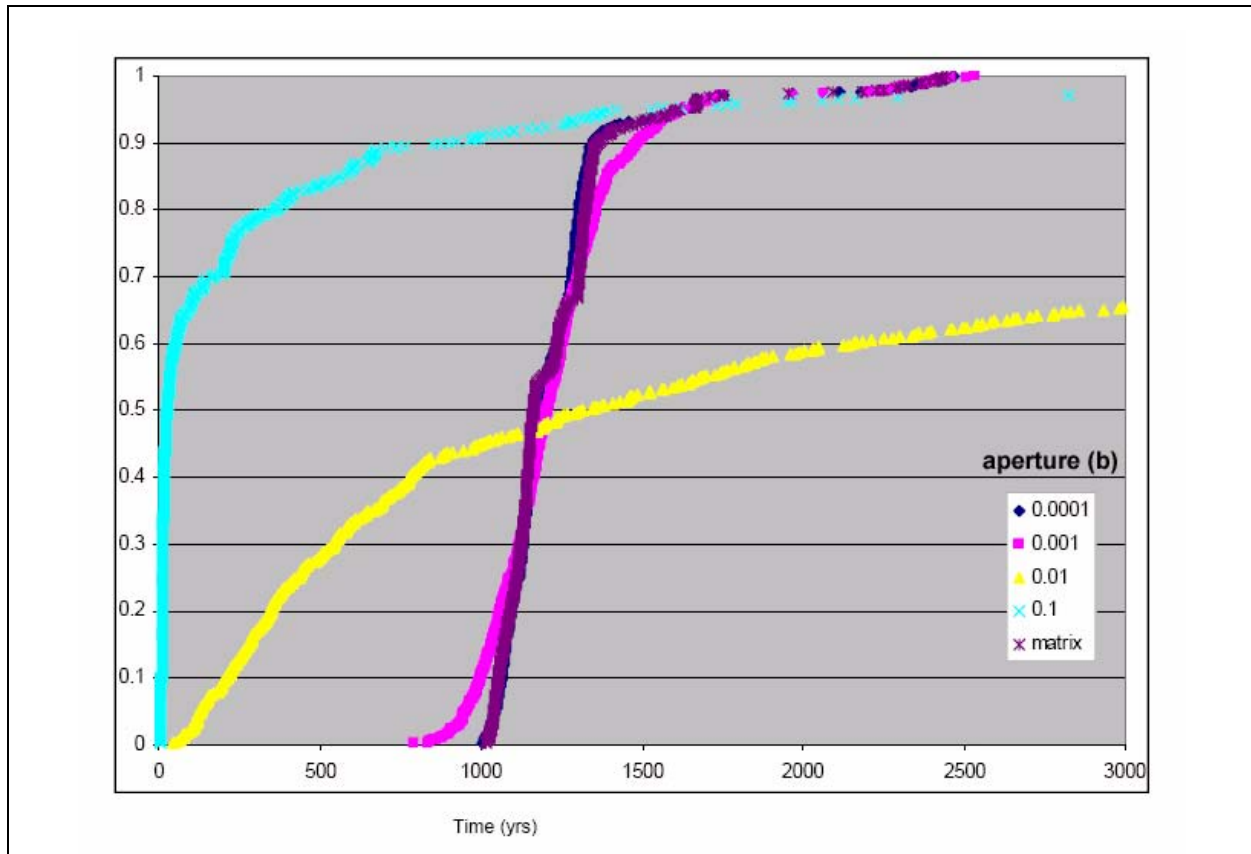


**Figure 6-32**  
**Fracture Aperture Sensitivity: Simulated Travel Time**  
**Distributions between Two Wells**

top of a curve for the simulation in which a single continuum with matrix porosity is assumed. As the aperture increases to 0.001, the spacing increases to 1 m, providing more distance between fractures. The next effect is that with a larger aperture, the wetted surface per fracture decreases, and some of the solute moves at a velocity closer to the fracture water velocity as a result. Offsetting this effect is the portion of the solute that does diffuse, and for which residence time in the matrix is longer as a result of the increased time to reach equilibrium between fracture and matrix water concentrations; hence, the increased residence time is represented by larger tails at the end of the distribution. It is important to note here the difference between the dual-porosity formulation for fractured rock and porous media transport. Once the dual-porosity model is invoked, it is assumed that matrix water is immobile — essentially a storage volume for solutes that diffuse into and out of the matrix; hence, the longer residence time of particles that enter the matrix as compared to porous media flow. As the aperture and spacing increase even further, the effects of rapid fracture migration combined with long

matrix residence times lead first to an increasingly broad distribution (e.g.,  $b = 0.01$ ), which then contracts when the aperture becomes so large that less and less diffusion actually occurs and most of the solute migrates at the velocity of the fracture water. These characteristic behaviors, discussed in [Section 6.4](#), will be identified in multirealization simulations sampling from the uncertain fracture parameter distributions.

### 6.5.3 Converting Time History Distributions into Apparent $^{14}\text{C}$ Ages

Ideally, it would be nice to average the particle ages for breakthrough curves such as in [Figure 6-32](#) to compare with the 1,500- to 5,000-year  $^{14}\text{C}$  age difference between ER-EC-5 and ER-OV-3c water samples. However, the role of  $^{14}\text{C}$  decay must be factored into the interpretation. Starting with a simulated age distribution curve and the  $^{14}\text{C}$  decay function, both plotted in [Figure 6-33](#), we derive the apparent  $^{14}\text{C}$  age difference for a sample of water at ER-OV-3c is derived as compared to water at the northing location of ER-EC-5.

Starting with the following relationship to represent the fraction of  $^{14}\text{C}$  decayed,  $c_i$ , from initial concentration,  $c_o$ , over time  $t_i$ :

$$\frac{c_i}{c_o} = e^{-kt_i} \quad (6-7)$$

where  $k$  is the radioactive decay coefficient,  $1.21\text{E-}04$  for  $^{14}\text{C}$ . If the time from ER-OV-3c to ER-EC-5 for each particle,  $i$ , is  $t_i$ , then the concentration of the entire sample,  $c_a$ , is:

$$\frac{c_a}{c_o} = \frac{\sum_{i=1}^N \frac{c_i}{c_o}}{N} = \frac{\sum_{i=1}^N e^{-kt_i}}{N} \quad (6-8)$$

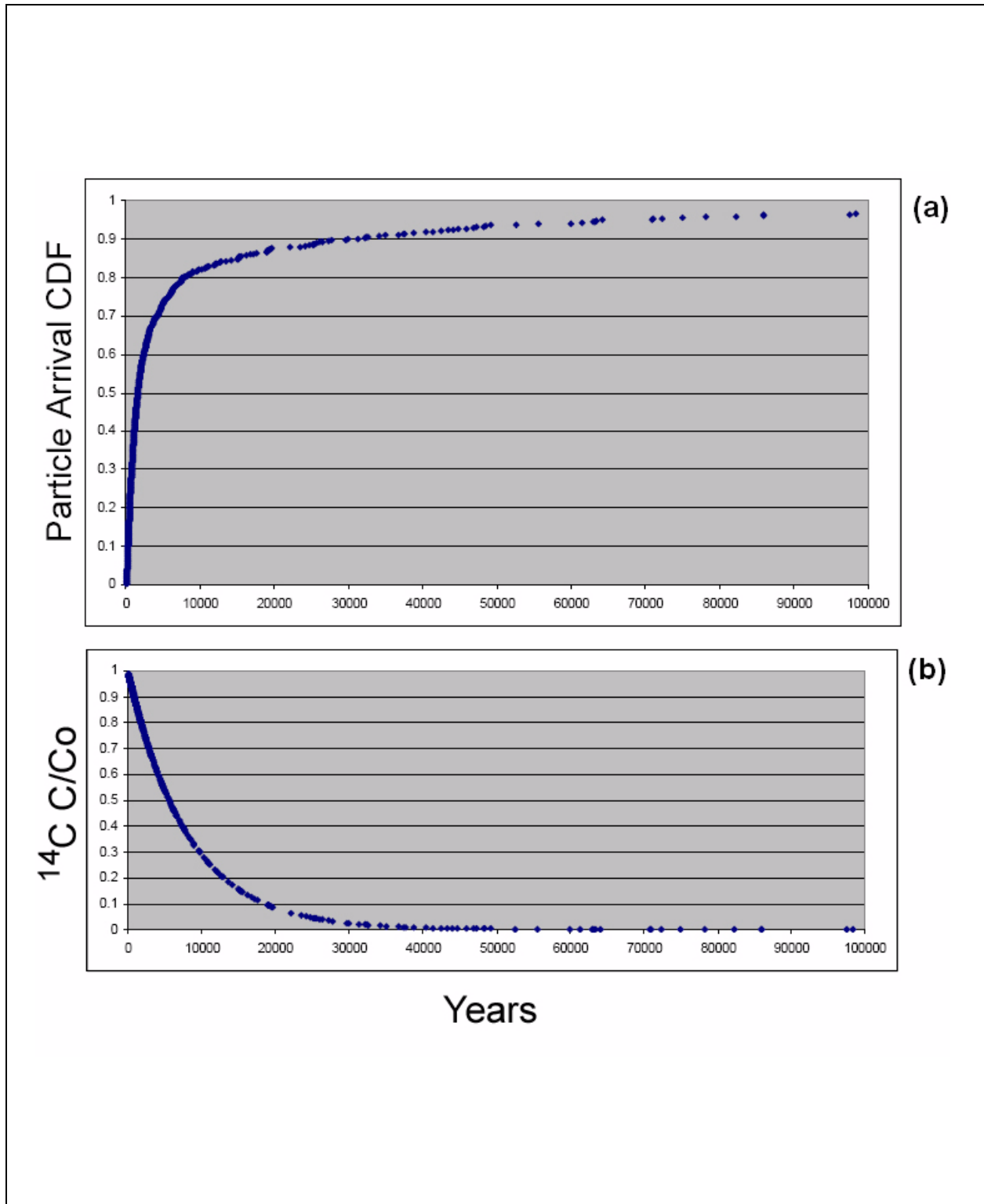


**Figure 6-33**  
**(a) Converting a Sample Age Distribution into a <sup>14</sup>C Sample Age**  
**Using the (b) <sup>14</sup>C Decay Curve**

The average time,  $t_a$ , for the integrated sample can be derived as:

$$\frac{c_a}{c_o} = e^{-kt_a} \quad (6-9)$$

so:

$$t_a = -\frac{1}{k} \ln\left(\frac{c_a}{c_o}\right) \quad (6-10)$$

which leads to:

$$t_a = -\frac{1}{k} \ln\left(\frac{\sum_{i=1}^N e^{-kt_i}}{N}\right) \quad (6-11)$$

This derivation does not apply any weighting to the different ages because the open interval in ER-OV-3c where the integrated, mixed sample was collected is only 13 m long. There is no simulated flux variation at that scale in this flow model. Thus, all reverse particles released in this small interval are assumed to carry equal weights.

Using distributions of fracture porosity, fracture spacing, and fracture aperture (computed from the first two), Monte Carlo simulations are conducted where reverse particles are released at ER-OV-3c and breakthrough curves at the northing location of ER-EC-5 are produced. Then, the ages associated with the particle breakthrough curves are integrated with Equation (6-10) to produce a sample age. This age is then compared with the age difference between  $^{14}\text{C}$  apparent ages in the two wells (1,500 to 5,000 years).

These simulations are conducted for two different  $D_m$  coefficients,  $1\text{E-}10 \text{ m}^2/\text{s}$  and  $10\text{E-}10 \text{ m}^2/\text{s}$ . Figure 6-34 shows the simulated  $^{14}\text{C}$  ages using the method described above for a fixed  $D_m$  coefficient of  $1\text{E-}10 \text{ m}^2/\text{s}$ . The symbols on the plot indicate results for the same parameter combinations considered for fracture spacing and fracture porosity and the colors show the simulated ages. These results are also plotted with a threshold for  $^{14}\text{C}$  ages between 1,500 and 5,000 years, thus showing which parameter combinations are consistent with the data interpretation. Plotted in gray are the parameter combinations that were used in the Monte Carlo runs for radionuclide migration on all of the flow fields considered (Figure 6-34). The same results are shown in Figure 6-35 where the apertures are shown. Increasing the  $D_m$  coefficient to  $1\text{E-}09 \text{ m}^2/\text{s}$ , a value near the upper end of the

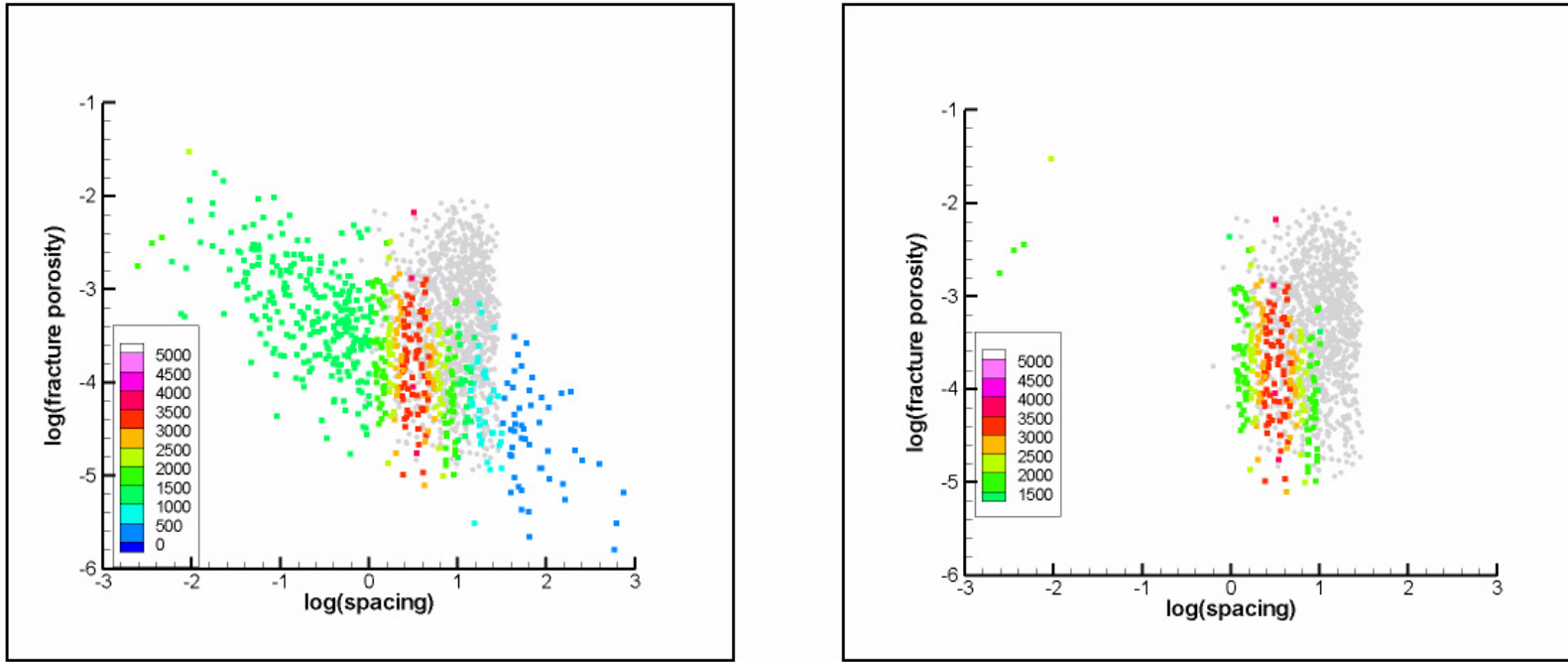


**Figure 6-34**  
**Simulated <sup>14</sup>C Ages between ER-EC-5 and ER-OV-3c for Spacing versus Fracture Porosity**  
Note:  $D_m = 1E-10$  m<sup>2</sup>/s, LCCU1-USGSD flow model.



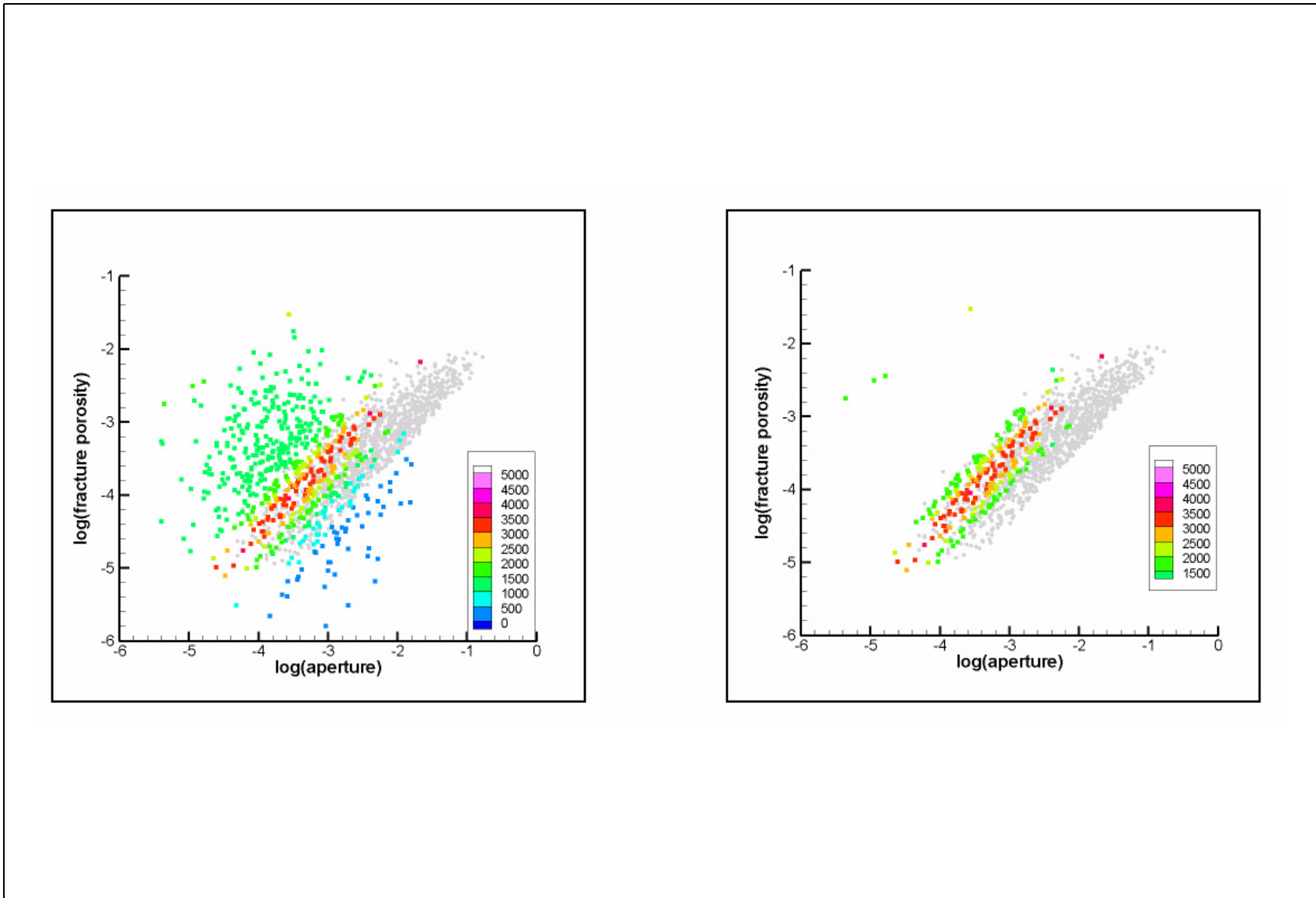


**Figure 6-35**

**Simulated <sup>14</sup>C Ages between ER-EC-5 and ER-OV-3c for Aperture versus Fracture Porosity**

Note:  $D_m = 1E-10$  m<sup>2</sup>/s, LCCU1-USGSD flow model.

Monte Carlo parameter distribution for the transport simulations, the  $^{14}\text{C}$  age calculations were run again, and the results are plotted in [Figures 6-36 and 6-37](#).

These simulations demonstrate that for the flow field considered and for  $D_m$  coefficients between  $1\text{E-}10$  and  $1\text{E-}09$ , the range in fracture spacing used in the Monte Carlo transport models (gray symbols) spans the values consistent with  $^{14}\text{C}$  estimates of 1 to 30 m. However, in the  $^{14}\text{C}$  calculation presented in this section, the LHS density is very sparse for large fracture porosity values combined with large fracture spacing (which requires large fracture apertures, per [Equation \[6-2\]](#)). Thus, whereas the transport model parameter distributions allow for significant parameter combinations with fracture porosities greater than  $1\text{E-}03$  and corresponding apertures greater than 1 cm, such combinations were not considered with this  $^{14}\text{C}$  analysis.

## 6.6 Consideration of Fracture Parameters Using Calibrated Permeabilities

[Section 6.4.1](#) describes estimation of the fracture aperture distribution as a function of sampled fracture porosity and spacing values. Another approach considers fracture aperture using the flow model permeabilities and a range of plausible fracture spacings. At the elevations within the TMCM where radionuclides are simulated to migrate, model log permeabilities range from -10.5 to -12 m. For a specified fracture density, the cubic rule (Freeze and Cherry, 1979) states that:

$$b = (k * 12 * spacing)^{0.333} \quad (6-12)$$

For the range of permeabilities in the TMCM and for fracture spacings between 1 and 10 m, [Table 6-8](#) shows the apertures computed with [Equation \(6-12\)](#) as well as the porosities computed with [Equation \(6-2\)](#).

By this estimation method, the largest fracture aperture, for 30 m spacing, is about 2 mm. This value falls in the lower 20 percent of the ECDF of fracture apertures shown in [Figure 6-8](#). These results are consistent with the aperture estimates in [Table 6-8](#). However, the cubic rule is an empirical estimation that may be no more accurate than the methods described in [Section 6.4.1.5](#). Similarly, the fracture porosity ranges from  $2\text{E-}05$  to  $7\text{E-}04$ .

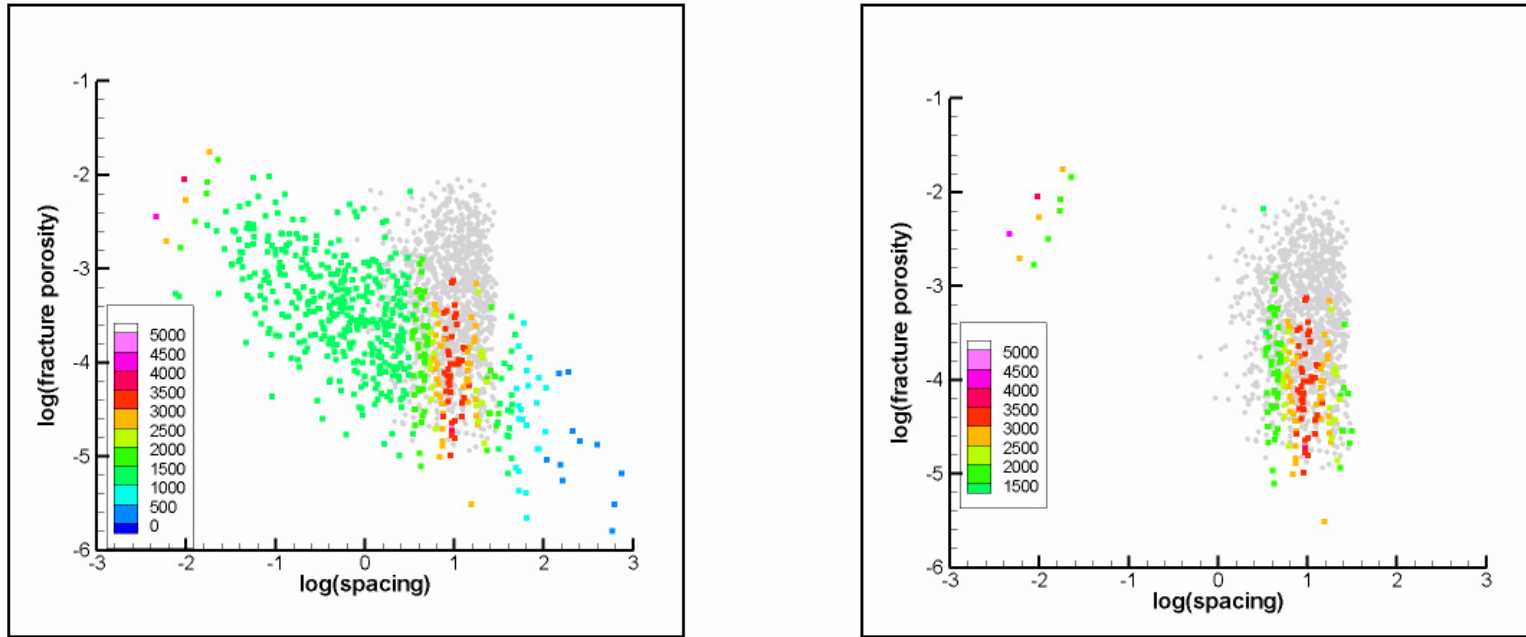


**Figure 6-36**  
**Simulated <sup>14</sup>C Ages between ER-EC-5 and ER-OV-3c for Spacing versus Fracture Porosity**

Note:  $D_m = 1E-09$  m<sup>2</sup>/s, LCCU1-USGSD flow model.

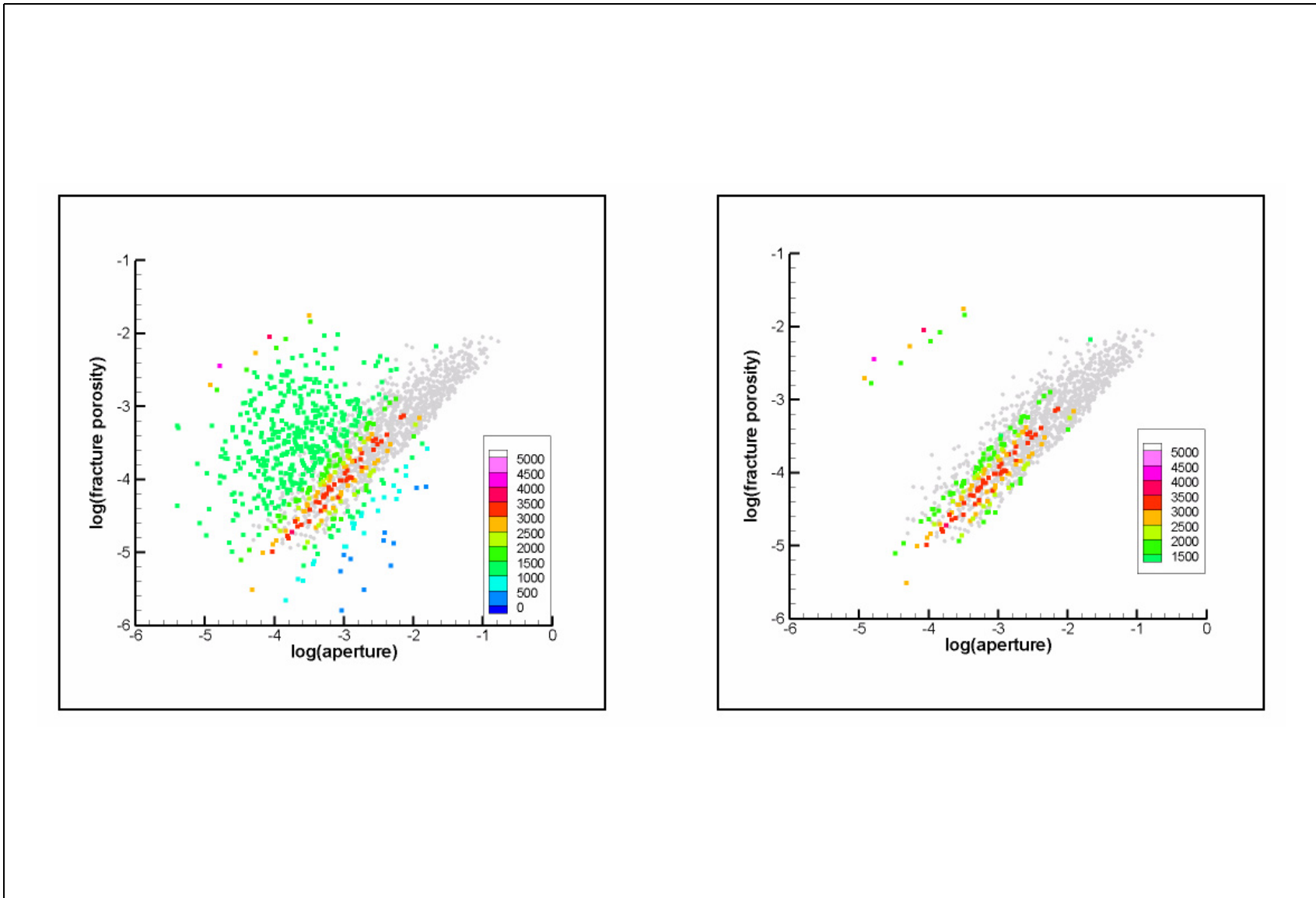


**Figure 6-37**

**Simulated <sup>14</sup>C Ages between ER-EC-5 and ER-OV-3c for Aperture versus Fracture Porosity**

Note:  $D_m = 1E-09$  m<sup>2</sup>/s, LCCU1-USGSD flow model.

**Table 6-8**  
**Computer Fracture Porosity from Permeability Spacing and Aperture**

logk	Fracture Spacing			Aperture (m) (from Cube Rule)			Computed Porosity		
	a	b	c	a	b	c	a	b	c
-10.5	1	10	30	7.24E-04	1.56E-03	2.25E-03	7.24E-04	1.56E-04	7.50E-05
-10.75	1	10	30	5.98E-04	1.29E-03	1.86E-03	5.98E-04	1.29E-04	6.19E-05
-11	1	10	30	4.93E-04	1.06E-03	1.53E-03	4.93E-04	1.06E-04	5.11E-05
-11.5	1	10	30	3.36E-04	7.24E-04	1.04E-03	3.36E-04	7.24E-05	3.48E-05
-12	1	10	30	2.29E-04	4.93E-04	7.11E-04	2.29E-04	4.93E-05	2.37E-05

### 6.7 Colloidal Transport Parameters

Analysis of the colloidal-facilitated transport for Pu is performed through the assignment of a Pu reduction factor. This term represents the fraction of the aqueous SSM Pu inventory that is mobilized via sorption to colloids.

#### 6.7.1 Plutonium-Colloid Source-Release Function

Plutonium migration in Pahute Mesa groundwater has been observed, with the implication of colloid-facilitated transport (Kersting et al., 1998; Wolfsberg et al., 2002). Neither the HST study (Pawloski et al., 2001) nor the SSM (Section 4.1 of this report) provide an assessment or statistical distribution of radionuclide mass flux release functions when associated with natural or test-related colloidal material. Functions of source-released colloidal Pu have been developed based on field-scale mechanistic reactive transport modeling that considers competitive sorption between solutes and both mobile colloids and immobile minerals in fractured and porous media. Laboratory and field experiments investigating colloid-facilitated Pu migration have been conducted for the UGTA Project. Methods and inferences drawn from colloid-facilitated Pu migration developed here can be extended to other radionuclides. Plutonium is an important and interesting species due to its large, radiological source mass, high activity, and sorption coefficient values that lie between the strongly sorbing species such as Am and more weakly sorbing species such as Np. A model developed by Wolfsberg et al. (2002) was used to estimate the percentage of total Pu released that could be considered colloidal in a PM CAU transport model.

The PM CAU transport model used for Monte Carlo simulation and sensitivity analysis is a particle-based process unable to consider multicomponent, competitive reactions and kinetic reaction rates. Therefore, a field-scale reactive transport model, extending upon the TYBO-BENHAM study of Wolfsberg et al. (2002) was developed to evaluate field-scale colloid-facilitated reactive transport and to derive abstractions appropriate for the particle-based CAU-scale transport model. [Appendix C](#) describes the development, testing, and implementation of the field-scale reactive transport model for fractured and porous media and the abstraction used here for particle-based, field-scale colloid-facilitated transport. The model uses a multiscale modeling approach, considering colloid-facilitated Pu transport from the laboratory column experiments of Kersting et al. (1999) to field-scale migration away from an underground nuclear test where multiple different rock properties are encountered (Wolfsberg et al., 2002). This model enables consideration of competitive reactive processes with continuum modeling methods (e.g., finite-volume solutions to partial differential equations instead of particle-tracking-based methods) for fractured rock by invoking the Generalized Dual-Porosity Model (GDPM), also introduced in the TYBO-BENHAM study by Wolfsberg et al. (2002).

[Appendix C](#) outlines the model development and testing for both laboratory and field-scale migration problems. For the purposes of the PM CAU transport model, an abstraction of reactive colloid facilitated transport is developed to estimate a pseudo species representing irreversibly sorbed Pu on naturally occurring colloids. This abstraction entails estimating the portion of the aqueous Pu-release function from the SSM that is mobile in the colloidal phase at some distance of interest away from the source in the PM CAU flow and transport model. Thus, the abstraction seeks to estimate the component of aqueous Pu released at the source that then sorbs irreversibly to colloids and remains mobile over field-scale distances. The mechanistic modeling upon which the abstraction is based uses streamtubes from a calibrated 3-D flow model. Plutonium is released as an aqueous species, per the SSM, and comes in contact immediately with natural colloids as well as immobile minerals. The competitive processes associated with colloid sorption, which mobilize the Pu, and  $D_m$  and sorption to minerals, which immobilize the Pu interact from the source to downgradient locations in the model domain. Colloid filtration is also considered in the simulations, serving to reduce the available surface area of mobile colloids competing with immobile sorption sites.

A series of Monte Carlo field-scale transport simulations were conducted, varying the parameters for colloid load, fracture aperture, forward and reverse reaction rates for Pu onto colloids, and the sorption distribution coefficient for Pu onto immobile minerals. For each parameter combination, transport simulations are conducted and time-history concentration records are developed for locations 5 and 8 km away from the source. Companion simulations for a perfectly colloidal Pu species that includes the entire Pu source-release function and does not diffuse or sorb are also conducted with concentration time histories developed at 5 and 8 km downgradient from the source. At each of these locations, the maximum ratio between the reactive Pu and the perfectly colloidal Pu is used to define the Pu source-reduction factor for that realization's set of parameters. The distribution of reduction factors from the 1,000 Monte Carlo reactive transport simulations then defines an ECDF. Assuming that the Pu that is mobile at 8 km from the source is effectively irreversibly sorbed to colloids, the Pu reduction factor is used to approximate a source-release function for irreversibly sorbed Pu releases from the source location. Sampling values from the ECDF yields values between 0 and 12 percent that are multiplied by the SSM Pu source-release function to generate a Pu-colloid species for particle-based CAU transport model simulations. The Pu-colloid species then migrates as a non-diffusing species, affected only by attachment versus detachment rates in both matrix and fracture media. The full development, testing, and ECDF development are described in greater detail in [Appendix C](#).

### **6.7.2 Colloid Filtration**

Colloid filtration plays two roles in the abstraction model for colloid-facilitated Pu transport. First, it reduces the available load of mobile reactive surface sites for irreversible sorption (as assumed here for large-distance migration). Second, it reduces the mobility of the Pu-colloid species, once formed. As described in [Appendix C](#), colloid retardation is modeled with a kinetic formulation for attachment and detachment rates. These, in turn, are used to approximate retardation factors. A distribution of colloid retardation factors was developed by YMP (SNL, 2008) with values ranging from 1 to more than 1,000 years. Simulations described in [Appendix C](#) show that colloids with retardation factors greater than 300 are incapable of migration to 5 km distance from the Pahute Mesa source considered more than 1,000 years. Thus, they are excluded from consideration. This results in a reduction of available colloid load to less than 2 percent of the values determined from sampling at Pahute Mesa boreholes. Because colloids in the distribution with retardation factors greater than 300 are

excluded from availability in the PM CAU transport model, only values between 1 and 300, with a lognormal distribution, are considered for the Pu-colloid pseudo species approximated as a source-release function.

### **6.7.3 Colloid Transport Parameters**

The previous two sections summarize [Appendix C](#), describing the abstraction of a Pu-colloid species source function and the retardation factor for this species in the CAU particle-based transport model. The load of the Pu-colloid species is a fraction between 0 and 12 percent of the SSM aqueous Pu-release function, drawn randomly for each realization in the CAU Monte Carlo transport model. The mobility of the Pu-colloid species in the PM CAU transport model is affected only by advective processes, with a retardation factor between 1 and 300 (values greater than 300 are already accounted for in load reduction while estimating the source function). The Pu-colloid species in this abstraction does not participate in  $D_m$  processes. Therefore, it is a highly mobile species for which the impact on water quality is mainly determined by the source.

## **6.8 Parameters Sampling Approach**

Parameter sampling is initiated to quantify the level of uncertainty attributed to each parameter of interest. The level of uncertainty depends of the quantity and quality of the available data. Uncertainty is reduced for larger datasets and data that sample a diverse range of the parameters population. The first step in the sampling process is to identify those parameters of interest for which data are required. Then all available data for each parameter must be pooled and evaluated on the basis of appropriateness of representation as a statistical distribution. Distributions are the means to represent uncertainty as ranges and likelihood of occurrence. The sequence of steps required to identify the appropriate distribution, as defined by Mishra (2002), are as follows:

- Select the appropriate distribution type.
- Fit a parametric model to the data.
- Test the quality of the parametric model fit to the empirical model.

### **6.8.1 Distribution Selection**

The selection of a distribution depends upon the amount of data available and the range of possible values that each particular parameter can take on. The definition of the parameter space as a



probabilistic distribution is useful because it allows the interpolation of data between measured data points and also allows extrapolation of the parameter space beyond the end points of the measured data. This approach also facilitates assignment of characteristic values such as mean, high, low, and SD that are a compact and more portable form of representing the datasets. The most common types of distributions, listed in Table 6-9, include a brief description of the data characteristics for which the distribution is best suited.

**Table 6-9**  
**Distribution Types and Applicable Data Restrictions**

Distribution	Useful for Representing
Uniform (log-uniform)	Low state of knowledge and/or subjective judgment
Normal	Errors due to additive processes
Lognormal	Errors due to multiplicative processes
Weibull	Component failure rates
Poisson	Frequency of rare events
Beta	Bounded, unimodal, random variables

A brief description of the distributions used for this report and the general applicability of each distribution are listed below:

- **Uniform Distribution:** The uniform distribution represents a low state of knowledge for which only the upper and lower bounds of the data are known. Data extracted from a uniform distribution are equally probable over the entire range of available possibilities. The log-uniform distribution has the same characteristics as the uniform distribution, except that values range over many orders of magnitude.
- **Triangular Distribution:** The triangular distribution is also used to describe data that possess low knowledge value. However, for this distribution, the mode or most likely value is known as well as the minimum and maximum limits of the distribution. The triangular distribution can be symmetric or asymmetric and can also span a range of many orders of magnitude, in which case a log-triangular distribution is appropriate.
- **Normal Distribution:** The normal distribution typically plots as a bell-shape curve and represents data whose random error term can be represented as an additive process. This method assumes the central limit theory is correct, in that all of the data approach a normal distribution.
- **Lognormal Distribution:** The assumption for the lognormal distribution is the same as the normal distribution, except that the range of the independent, random variables are normal for

ranges spanning many orders of magnitude. Before these data are plotted, the parameter values must be log-transformed from which the normal plot can then be derived.

- Empirical Distribution: In addition to the distributions listed above, the parameters may be sampled directly from the empirical data without further fitting of the data using a mathematical function. Those points that fall between measurements are assigned through interpolation between the bracketing measurements.

The other distributions listed in [Table 6-9](#) are not used to fit to the transport parameters data from the PM CAU modeling effort. Further detail for these other parameter distributions as well as those listed above can be found in Mishra (2002).

### **6.8.2 Fitting a Distribution**

To select the appropriate distribution, the data first must be fit to a probabilistic construct of the general distribution. The fitting process is based on the following criteria:

- Identify the potential distribution to fit.
- Estimate parameter distributions.
- Assess the quality of the fit to the parameters through goodness-of-fit analysis.

This process is not necessary if the data are represented by an empirical distribution. After the distribution has been selected, the next step is to estimate the parameters of the distribution. This process is achieved through one of the following parameter estimation techniques:

- Linear regression
- Method of moments
- Maximum likelihood
- Non-linear least squares

Linear regression interpolates values between the measured data points through a linear function. For this method to work, some distributions may require transformation to get an optimal fit. For some distributions, the parameters may not remain optimal when the value is transformed back to its original form.

The method of moments approach relies on matching the moments of the probabilistic parameter distribution to the distribution model selected. The number of moments required equals the

number of parameters. This method may not adequately represent the distribution in the presence of large outlier data.

The maximum likelihood approach requires definition of a likelihood equation from which the model parameters are adjusted such that the likelihood fit to the observed data is maximized. One potential drawback of this method is that the moments may not always be preserved.

The non-linear least squares method calculates parameters such that the differences in the residuals are minimized.

### **6.8.3 Checking the Goodness of Fit**

The goodness of fit is assessed by mapping the fit parameter distribution over the measured data distribution and observing the level by which the measured data deviate from the expected distribution. The deviation is evaluated as a function of the number of sample points in the data population. Standard tables can be referenced that indicate whether the deviation from the expected distribution is tolerable for a given distribution. In some instances, it may be necessary to transform the original dataset to achieve a fit to the expected distribution. An acceptable fit does not necessarily mean that the selected probabilistic distribution is correct, but rather that the distribution cannot be discounted as a possible match.

Two common goodness-of-fit tests are:

- Chi-square
- Kolmogrov-Smirnov

The chi-square test works best for datasets with more than 25 samples, which are then binned into at least five groups. The groups of the chi-square distribution represent regions of equal probability. The results are compared with tabulated chi-square distribution for a specific confidence interval and degrees of freedom. The Kolmogrov-Smirnov test relies on the stepwise comparison of the ECDF with a theoretical ECDF. The measure of fit for the Kolmogrov-Smirnov method is a function of the maximum deviation of the ECDF from that of the theoretical ECDF.

## 7.0 TRANSPORT ANALYSIS: METHODOLOGY AND RESULTS

Transport modeling culminates in the identification of migration pathways, travel times, and time-series identification of radionuclides that are important to development of the exceedance map at different time intervals. A reduced list of radionuclides was selected to define the source term for modeling transport from nuclear test sites from which the exceedance map can be calculated. Selection was based on total inventory, mobility, and longevity in the groundwater system. The radionuclides selected for inclusion were  $^{14}\text{C}$ ,  $^{129}\text{I}$ ,  $^{239/240}\text{Pu}$ ,  $^{137}\text{Cs}$ ,  $^{90}\text{Sr}$ ,  $^3\text{H}$ , and  $^{238}\text{U}$ ,  $^{36}\text{Cl}$ ,  $^{237}\text{Np}$ , and  $^{99}\text{Tc}$ . Radionuclides are grouped into three categorical classes: alpha emitters, beta emitters, and U. Identification of exceedance of the regulatory radionuclide levels of 4 mrem/yr was used in accordance with the SDWA (CFR, 2007). The quantification of exceedance levels that were used to characterize the contaminant plume was achieved through calculation of the EV, the probability map, and the fractional exceedance volume (FEV). The EV represents the volume of all model nodes for which the MCL (4 mrem/yr) for all radionuclide species is exceeded at any time up to 1,000 years. The probability map is the model predicted perimeter of the contaminant plume at any time out to 1,000 years, defined at the 95 percent confidence level (5 percent probability of exceedance). The FEV identifies the contribution of each individual radionuclide to the total EV at discrete time intervals. Through this metric, the time at which individual radionuclides become dominant is identified. In consideration that the exceedance map was the primary objective, and in the interests of computational efficiency, the number of source locations that were modeled was reduced. Particles were released at each test location and tracked for 1,000 years. Only locations for which particles crossed a predefined datum were included in the transport modeling. Simulations for seven HFMs were performed and transport metrics, as defined above, were used to assess plume migration rates and extent.

### 7.1 Introduction

A Monte Carlo approach is used to propagate uncertainty in the model response of the PM CAU transport model (PLUMECALC) into corresponding output uncertainty. The method entails multiple

simulations, each with a randomly selected set of input parameters, to generate an equal number of output metrics that collectively capture the full behavior of the transport system. The metrics used to describe PM CAU transport model predictions are derived from simulated radionuclide concentrations through time. When considered in the context of regulatory standards, or MCLs at specified time intervals, radionuclide plumes may be conceptualized as an exceedance map, which is equivalent to the contaminant boundary as described in the FFACO (1996, as amended February 2008). Thus, following the routine of Monte Carlo transport simulation, the focus of analysis is on metrics that define the scalar EV, an areal exceedance map, and define their development.

[Section 7.2](#) reports the Monte Carlo simulation methodology, and [Section 7.3](#) describes the metrics applied to characterize radionuclide plume concentrations relative to federal groundwater standard that the State of Nevada uses to regulate. [Section 7.4](#) demonstrates that the Monte Carlo output solution is stable through analysis of these metrics. [Section 7.5](#) describes the method and justification for reduction of the source-release points (tests) considered in the transport analysis for each alternative model, and lastly, [Section 7.6](#) presents simulation output results for the alternative HFMs that are used to define conceptual (rather than parametric) uncertainty in the Pahute Mesa flow and transport system.

## **7.2 Monte Carlo Uncertainty Analysis**

Monte Carlo simulation is a method of uncertainty analysis that captures the full range of input parameter uncertainty as it is propagated through the modeled system as long as the input distributions are sufficiently sampled. Mishra (2007) identifies its two fundamental components, uncertainty characterization and uncertainty propagation, which are described below in the application of Pahute Mesa transport simulation.

Uncertainty characterization entails the definition of a probability distribution for each input (transport) parameter considered uncertain. It is followed by (pseudo-) random sampling of each distribution for the definition of multiple parameter sets that, in total, capture the entire range of parameter uncertainty. [Section 6.4](#) described those parameters required for transport simulation in both porous and fractured media in the PM CAU model domain. [Section 6.4](#) also discussed the assignment of a probability distribution to each parameter and the justification for such assignment. Depending on the data type, availability, and quality for each variable, either a qualitative

(subjective), quantitative, or some combination of these two methodologies was applied for assignment of a distribution.

It is important to note that the dispersivity tensor was the only transport parameter set excluded from Monte Carlo characterization. Dispersivity is incorporated in the particle-tracking step during flow modeling before transport simulation. It was computationally more feasible to perform a discrete number of particle-tracking runs (input to PLUMECALC) for each PM CAU flow model and to then conduct full Monte Carlo simulation on the rest of the transport parameters within PLUMECALC than to sample dispersivity as a random, uncertain parameter. [Section 6.4.4](#) described the selection of a discrete set of dispersivity tensors for the analysis. This section presents transport results using the lowest dispersivity scenario (longitudinal, transverse, vertical = 10, 1, 0.2 m) for each of the seven alternative models. The low scenario was selected because a preliminary analysis showed that radionuclide migration sensitivity to dispersion was at least as great as the sensitivity to the collective parametric uncertainty of all other transport parameters, thereby complicating the isolation of the effect of dispersivity during analysis. [Section 7.6.8](#) presents transport simulation results for the full Monte Carlo analysis using a higher-dispersion scenario (longitudinal, transverse, vertical = 100, 10, 0.2 m) for four models. [Section 8.3.4](#) revisits sensitivity to dispersion by considering values as high as 300, 100, 20 m for longitudinal, transverse, and vertical dispersivity, respectively.

With a probability distribution defined for each input parameter, the LHS scheme was used to generate multiple samples, or realizations, of parameter sets. A good sampling scheme must, in the Monte Carlo context, completely cover the entire range of parameter space with random association between parameters (unless otherwise specified), and also provide a sufficient number of samples such that the output metric(s) are statistically stable. [Section 7.4](#) describes the output metrics adopted for statistical stability tests. The LHS scheme is a stratified random approach in which the distribution range per parameter is equally binned, a random sample is selected from within the range of each bin, and the samples between parameters are randomly combined (McKay et al., 1979). The number of bins, at a minimum, corresponds with the number of realizations (or number of Monte Carlo simulations). Additionally, the restricted pairing technique of Iman and Conover (1982) was used to force zero correlation between parameters, removing the effect of any inadvertent correlation that might result from the random combination of parameters.

Uncertainty propagation, the second component of Monte Carlo uncertainty analysis, involves the translation of parameter uncertainty to output uncertainty via the simulator's use as a transfer function. When an output metric is viewed as a distribution, measures of its uncertainty, or variability, may be directly assessed. A probability distribution also permits an estimate of reliability (e.g., confidence in the expected value). Of course, analysis of output uncertainty relies on the assumption of the statistical stability of the output distribution, which entails the provision of some guarantee that (at least) the first and second moments of the distribution would remain constant if the number of Monte Carlo realizations were to change within reasonable limits. That is, would the transport uncertainty captured by 500 realizations result in output uncertainty equivalent to that from 1,000 or 2,000 realizations? When the distribution tails are of particular interest, as may be expected for a regulatory-based investigation such as this, the stability of the tails should also be examined. [Section 7.4](#) presents the output stability tests performed and demonstrates that the number of realizations advanced in all of the Monte Carlo simulations is appropriate.

### **7.3 Transport Analysis Metrics**

As prescribed in the Pahute Mesa CAIP (DOE/NV, 1999) and Appendix VI of the FFAO (1996, as amended February 2008), the ultimate goal of transport analysis is to develop a stochastic prediction of the contaminant boundary at a specified level of uncertainty. While the stochastic component can be well defined (e.g., using a Monte Carlo approach), uncertainty must be evaluated at a number of different levels within the model. Although the stochastic contaminant boundary is the ultimate objective of the transport modeling, the purpose of the Phase I modeling presented in this document has been to understand the behavior of radionuclide migration in the PM CAU model and to define, both qualitatively and quantitatively, the sensitivity of such behavior to (flow) model conceptualization and (flow and transport) model parameterization.

Several different metrics and results maps are used to evaluate transport model behavior. These are used to understand individual model runs (i.e., using a single set of transport parameters) and collective (i.e., global, stochastic) model runs with respect to individual radionuclide behavior, the distinct behaviors of the regulatory-defined groups of radionuclides, and the integrated behavior of all radionuclides. Further, these metrics and results maps are used to compare radionuclide behavior between the alternative flow models, thus evaluating the influence of hydrogeologic

conceptualization on transport. The metrics used and described in this section, in their order of development, include:

- Radionuclide concentrations
- MCLs and MCL groups
- Probability of MCL exceedance
- Exceedance volume
- Regulatory-based contaminant boundary
- Probabilistic exceedance map
- Fractional exceedance volume

Sections 7.3.1 through 7.3.6 explain the derivation of these metrics and their (typical) presentation as maps depicting the migration of radionuclides from sources (tests). The reader may refer to this section for clarification during discussion of individual and collective model results in Section 7.6.

### **7.3.1 Radionuclides and MCLs**

The migration of radionuclides from sources is considered in terms of regulatory compliance. The development of radionuclide plumes through time is not viewed in terms of concentration but is viewed relative to regulatory limits based on the SDWA (CFR, 2007). The Pahute Mesa unclassified SSM (Section 4.1) identifies three groups of radionuclides of concern based on different regulatory standards: gross alpha (particle emitters), beta emitters, and U. All radionuclides incorporated in the transport analysis fall into one of these groups and are considered within the context of the appropriate standard throughout the analysis. The following discussion identifies the radionuclides selected for transport simulation, their regulatory-based group, and conversion of the modeled radionuclide concentrations to regulatory-based standards.

The UGTA Project TWG (IT, 1999) selected seven radioactive contaminants for transport simulation based on observed concentrations in groundwater, inventory estimates, health effects and fate and transport information. These were  $^{14}\text{C}$ ,  $^{129}\text{I}$ ,  $^{239/240}\text{Pu}$ ,  $^{137}\text{Cs}$ ,  $^{90}\text{Sr}$ ,  $^3\text{H}$ , and  $^{238}\text{U}$ . This set of alpha-particle emitters, beta emitters, and U was considered to be the most significant for prediction of regulatory compliance metrics over an approximately 1,000-year period. The PM CAU transport model assumes these seven radionuclides as a standard set for simulation scenarios. In addition to these seven radionuclides,  $^{36}\text{Cl}$ ,  $^{237}\text{Np}$ , and  $^{99}\text{Tc}$  are included in all simulations. Additionally,  $^{241}\text{Am}$ ,  $^{151}\text{Sm}$ ,  $^{93}\text{Zr}$ , and the isotopes of Eu ( $^{150/152}\text{Eu}$ ) and Ni ( $^{59/63}\text{Ni}$ ) are incorporated in selected simulation



scenarios, for reasons described in Section 5.3.2, as well as a colloidal Pu component (Section 6.7); however, the contribution of these additional species to the collective migration metric is often negligible (see Section 7.5).

The National Primary Drinking Water Regulations for radionuclides were developed for the SDWA (CFR, 2007), and are referred to as the SDWA standard’s MCLs for radionuclides. This version, in practice, divides radionuclides into three categories, each with a different metric for the MCL: total beta/photon emitters (annual dose); [adjusted] gross alpha emitters, excluding U (activity per volume); and U (mass per volume). The radionuclides being evaluated for transport are assigned to their respective MCL regulatory groupings in Table 7-1.

**Table 7-1  
Maximum Contaminant Levels for Regulatory Groups**

Regulatory Group	Radionuclide	MCL
Beta/Photon Emitters	$^3\text{H}$ , $^{14}\text{C}$ , $^{36}\text{Cl}$ , $^{129}\text{I}$ , $^{90}\text{Sr}$ , $^{151}\text{Sm}$ , $^{99}\text{Tc}$ , $^{93}\text{Zr}$ , $^{137}\text{Cs}$ , $^{59/63}\text{Ni}$ , $^{150/152}\text{Eu}$	4 mrem/yr
Gross Alpha Particles	$^{241}\text{Am}$ , $^{237}\text{Np}$ , $^{239/240}\text{Pu}$	15 pCi/L
Uranium	$^{238}\text{U}$	30 $\mu\text{g/L}$

Transport simulation output (Section 6.3) consists of the radionuclide molar concentration (moles per liter [mol/L]) per individual species and per node; therefore, in order to define radionuclide migration in terms of regulatory standards, it is necessary to first convert radionuclide concentrations to the corresponding MCL-group unit metric (each radionuclide is simulated individually in PLUMECALC as a result of non-scalable source-release functions).

The U.S. Environmental Protection Agency (EPA) *Implementation Guidance for Radionuclides* (EPA, 2002) discusses conversion of alpha emitter and U concentrations to their respective MCL metrics; the MCLs are based on activity or concentration, respectively, with activity a direct function of concentration. The conversion for activity (pCi/L) for beta/photon emitters to 4 mrem/yr annual dose is found in EPA (2000). The conversion for alpha activity is obtained directly as a function of concentration using the specific activity for a particular alpha-emitting radionuclide. The MCL for U is a mass per unit volume unit, and no conversion between activity and mass is required. The concentration or dose for all radionuclides in the beta/photon-emitter and alpha-emitter regulatory groups must be summed before comparison to the corresponding MCL. In the context of the

numerical model, this is done on a node-by-node basis. From this point forward in the discussion, radionuclide concentrations are considered only in the context of regulatory, or MCL, groups and metrics. Radionuclide migration is evaluated by individual regulatory group (e.g., the beta plume) and collectively over all three groups.

### **7.3.2 Probability of MCL Exceedance**

Radionuclide migration is evaluated relative to regulatory compliance for the radionuclide regulatory groups using radionuclide concentration converted to the corresponding MCL-group metric (Table 7-1). Consequently, each Monte Carlo realization presents the evolution through time of a plume that is defined as the set of all nodes at which the respective MCL is exceeded for either alpha particles, beta emitters, or U, or any combination of these groups. Each such plume corresponds to a single realization of transport parameters, representing only one of many transport scenarios that taken together constitute the stochastic simulation.

It is more informative to assess radionuclide migration behavior from a probabilistic perspective which captures the spatial variability in migration as a function of transport parameter uncertainty. Radionuclide migration is therefore presented as a probability map of MCL exceedance that shows, per model node, the percentage of Monte Carlo simulations in which an MCL is exceeded for alpha particles, beta emitters, or U. In accordance with the stochastic (i.e., Monte Carlo) approach assumed, the percentage of some outcome over all simulations is equivalent to the probability of that outcome. Figure 7-1 presents a non-specific example of a probability map with the probability of MCL exceedance per node indicated by color contour. The probability map may be constructed for any simulation timestep. Figure 7-1 shows the probability of MCL exceedance at 50 and 500 years. The map for a given PM CAU flow model displays the growth and/or decay of the radionuclide plume, affected by processes such as dilution, decay, and sorption over the duration of simulation.

### **7.3.3 Exceedance Volume**

While the probability map provides qualitative information pertaining to the global behavior of radionuclide migration over all Monte Carlo simulations, a map is inherently difficult to characterize quantitatively because it represents a spatial geometry. Quantitative analysis of the probability map is further complicated because it is comprised of indicator datasets (i.e., per

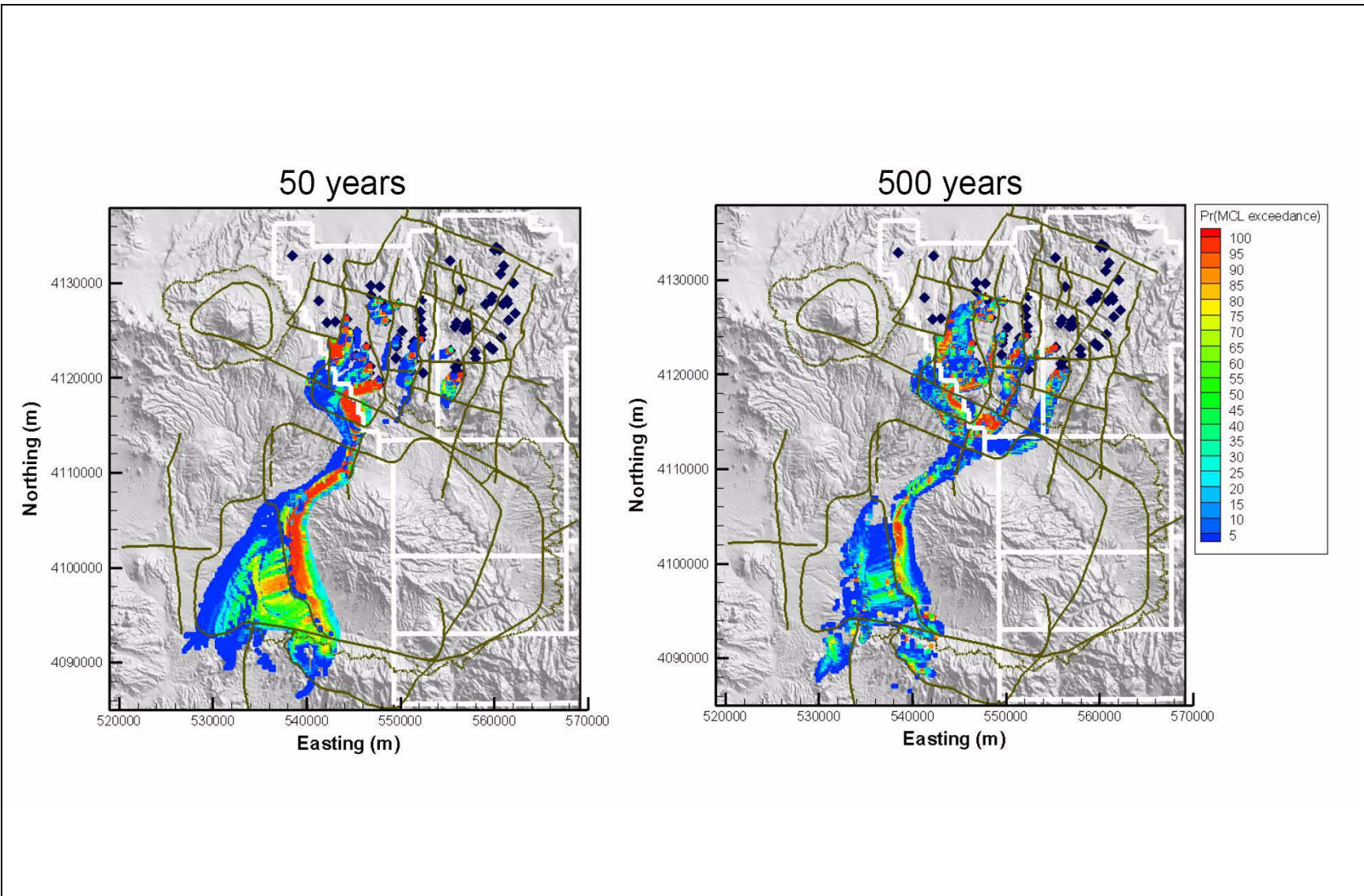


Figure 7-1

**Non-specific Example of a Probability of MCL Exceedance Map for Alpha Particles, Beta Emitters, or Uranium**

Note: Colors define the percentage of times, relative to the total number of Monte Carlo realizations, that an MCL is exceeded per mesh node.

realization); either a node exceeds the MCL for at least one of the regulatory groups and is added to the map, or it does not and is excluded from the map. In order to obtain a metric more amenable to quantitative analysis while retaining a probabilistic perspective of radionuclide migration, the scalar metric of the EV is developed.

Each Monte Carlo simulation results in an evolving radionuclide plume that is defined as the set of all nodes at which an MCL is exceeded for either alpha particles, beta emitters, or U at any time as well as cumulatively over 1,000 years. Rather than mapping these nodes, the total volume of all such nodes is calculated in order to provide a scalar metric per Monte Carlo realization that, when combined over all realizations, defines a probability distribution. The EV is the summed volume of all nodes at which the MCL is exceeded for any regulatory group, at any time within a 1,000-year interval from the time of source release, per Monte Carlo realization. It is important to recognize that the EV is a time-invariant metric. It includes node volumes for which any regulatory-group MCL is exceeded at any time within 1,000 years, whereas a probability map (e.g., [Figure 7-1](#)) reflects only a single snapshot in time. This is important to consider because a contaminant plume may diminish in size through time as a result of dilution of the decay of all radionuclide regulatory groups. For example, the probability of MCL exceedance maps in [Figure 7-1](#) show that the simulated plume adjacent to Timber Mountain is more extensive at 50 years than at 500 years.

When the EV is aggregated over all Monte Carlo simulations, an empirical probability distribution is defined. The EV distribution defines the variability of radionuclide migration in the context of transport parameter uncertainty, permitting a quantitative analysis of the association between input parameters and transport simulation output (i.e., sensitivity analysis). Further, the EV distribution enables quantitative comparison of transport simulation output between the alternative flow models for assessment of the influence of the conceptual model on transport.

#### **7.3.4 Regulatory-Based Contaminant Boundary**

[Sections 7.3.1](#) and [7.3.2](#) present the methods used to qualitatively and quantitatively describe radionuclide migration in terms of regulatory compliance. The Pahute Mesa CAIP (DOE/NV, 1999) states that the goal of transport modeling is to determine a contaminant boundary that meets or exceeds regulatory standards. Because the role of this report is to quantify model uncertainty, the quantification of the contaminant boundary is not formally defined; rather, the EV was used for this

purpose. The EV is a scalar metric derived from the contaminant boundary concept, as defined in Appendix VI of the FFACO (1996, as amended February 2008), describing how such a volume may be defined given the set of results available from this analysis and detailing the nuances of the definition and the data required for its construction. The FFACO was amended subsequent to the Pahute Mesa CAIP (DOE/NV, 1999), and the specific definition for the contaminant boundary was changed to specify the maximum extent of radionuclide contamination per SWDA standards (CFR, 2007) for radionuclides (Table 7-1) at the 95 percent probability that the contaminant boundary exceeds MCLs within a 1,000-year interval.

### **7.3.5 Probabilistic Exceedance Map**

The probabilistic exceedance map used in this analysis is based on the regulatory contaminant boundary concept, interpreted in the context of the probability of MCL exceedance per node. The probabilistic exceedance map is defined by the set of nodes at which any MCL is exceeded, at any time within a 1,000-year interval, in at least 5 percent of the Monte Carlo runs. The specified 95 percent confidence is interpreted as the probability that nodes outside the map would not exceed the MCLs. The probabilistic exceedance map defines a map between uncontaminated and contaminated areas. Only one probabilistic exceedance map is constructed from the full suite of Monte Carlo simulations. It is time invariant in that the map includes nodes at which any MCL is exceeded at any time within 1,000 years. Each node is assigned a color representative of the first time at which a node is added to the map, or at which at least 5 percent of the Monte Carlo simulations exceed a map's MCL. The color contours reflect the growth of the map through time.

### **7.3.6 Fractional Exceedance Volume**

A final tool used for evaluation of radionuclide migration results is the FEV, which permits a general assessment of the influence of individual radionuclides on plume growth and decay through time. An FEV is computed per radionuclide, per output timestep, and per realization. It is a scalar metric ranging from 0.0 to 1.0 that approximates the volume fraction of an MCL-exceedance plume, at each simulation timestep, that is accounted for by an individual radionuclide. The volume of the MCL-exceedance plume is computed as the summed volume of all nodes at which an MCL is exceeded at a snapshot in time for the current realization. It is therefore similar to the EV but is not a time-invariant metric like the EV. For abbreviation, this discrete-time MCL-exceedance volume is

called the “dEV” for the remainder of this section. The FEV is an approximate measure because in some cases it considers fractional node volumes, which is in contradiction to the categorical (indicator) nature of the EV concept (i.e., either the node concentration exceeds an MCL and its entire volume is added to the EV, or it is not in exceedance and has no contribution to the EV). The following describes the method of FEV calculation and provides an example.

Considering only a single Monte Carlo run, contaminated areas are defined in terms of MCL exceedance at multiple timesteps. The fundamental step of FEV calculation is to define the volume of the dEV, which incorporates all regulatory groups (i.e., alpha particles, beta emitters, and U) at each timestep. The dEV differs from the EV because it depicts node volumes at a single snapshot in time; the EV considers all timesteps up to 1,000 years. The dEV later becomes a normalizing constant for the FEV at each timestep. The next step is to loop through all radionuclides, and then all timesteps, defining for each unique radionuclide-time combination the set of nodes that have non-zero concentration in the corresponding MCL unit (Table 7-1). Each node concentration (in MCL units) is divided by the corresponding MCL standard to result in a fraction. A sum of node volumes over all nodes is subsequently computed: if the node MCL fraction is greater than or equal to unity, then the node volume is added to the volume sum; if the node MCL fraction is less than unity, then the node volume is multiplied by that fraction, and the product is added to the volume sum. Finally, for each unique radionuclide-time combination, the resultant volume sum is divided (normalized) by the dEV for that timestep, resulting in a number between 0.0 and 1.0. Conceptually, an upper limit of 1.0 is appropriate because no individual radionuclide plume can be larger than a plume that incorporates all radionuclides. After looping through each radionuclide-time combination for each Monte Carlo run, the result is a suite of FEVs for each combination of Monte Carlo run, radionuclide, and timestep. The final metric used for analysis is the average FEV, with the average taken over Monte Carlo runs.

Figure 7-2 provides a general example of the FEV for a transport simulation considering nine radionuclides and seven timesteps. The growth and decay of long- and short-lived radionuclides becomes apparent. When the FEV for a given radionuclide-time combination is equal to 1.0 (e.g.,  $^3\text{H}$  in Figure 7-2), this indicates that, at that timestep, a single radionuclide alone is able to account for the entire size of the MCL-exceedance area. This observation leads to a final point that must be considered when viewing an FEV chart. At a single timestep, the sum of the FEVs across all

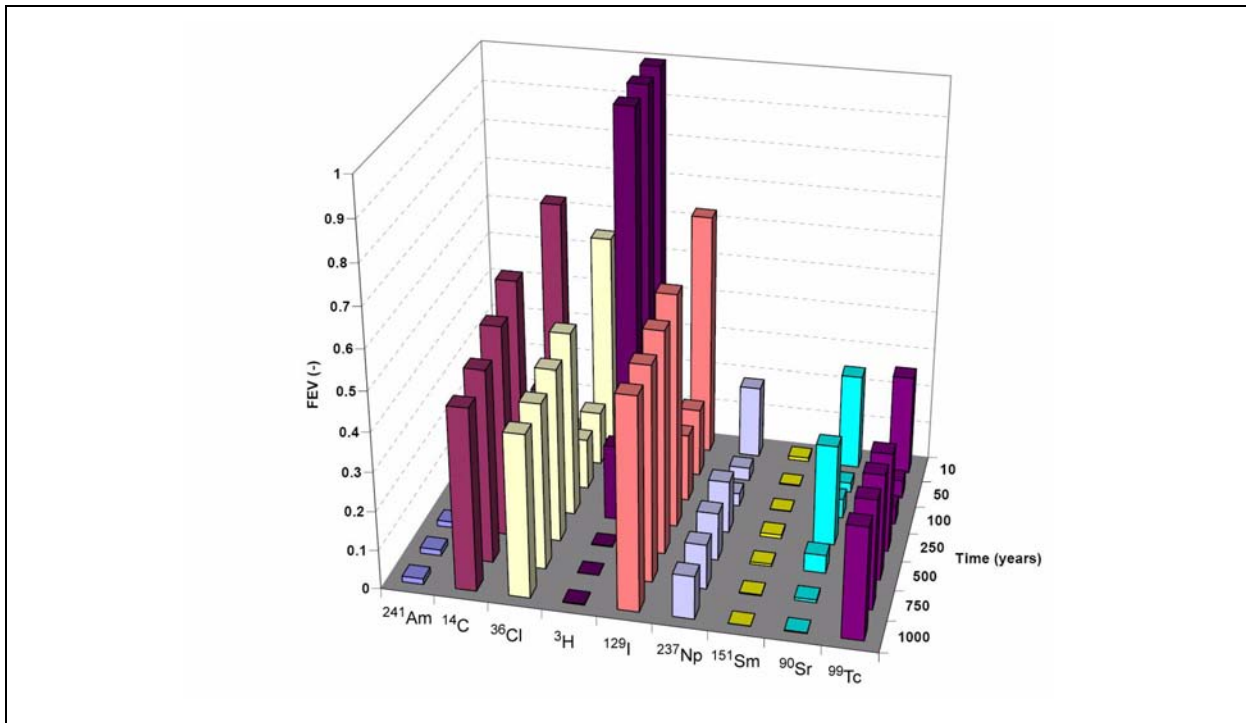


**Figure 7-2**

***Non-specific Example of an FEV Chart Showing the Contribution of Each Radionuclide, at Multiple Timesteps, to the Time-Specific EV***

Note: May be conceptualized as the plume volume comprised of all nodes at which any MCL is exceeded.

radionuclides does not equal 1.0, which results from the categorical character of the dEV, the denominator of an FEV. Namely, the dEV characterizes an area comprised of mesh nodes at which *any* MCL is exceeded. Therefore, although multiple MCL groups may exceed their respective MCL standard, this information is not contained within the dEV (i.e., it only takes a single radionuclide-group MCL exceedance to place a node within the dEV). This is why, at a given timestep, the summed FEVs for multiple radionuclides may exceed unity. The consequence is that the FEV cannot be interpreted as the exact radionuclide contribution to a plume, but only as a tool used to indicate radionuclide contributions relative to each other. However, the FEV can be used to designate radionuclides that do not contribute to a plume. The FEV is therefore used to screen radionuclides that do not contribute to plume volume during the course of simulation. For example, [Figure 7-2](#) shows that  $^{151}\text{Sm}$  accounts for less than 1 percent of the EV at any time (dEV). Because  $^{151}\text{Sm}$  is not a highly mobile species, it is unlikely that it is defining the extent of the plume through additive contributions at the leading edge, as is the case for the mobile beta emitters, none of which completely define the plume volume solely at a later time.

## 7.4 Statistical Stability

The EV ([Section 7.3.3](#)) is the metric used to quantitatively describe the time-invariant behavior of radionuclide migration in terms of MCLs. Consequently, the EV is used to confirm the statistical stability of Monte Carlo results, ensuring that sufficient realizations are considered to provide stability in the first and second moments (at least) of the continuous metric.

The main issue regarding stability of the model results is whether sufficient Monte Carlo runs are performed to adequately characterize the uncertainty in radionuclide migration subject to the given input probability distributions. That is, do the results change significantly between 1,000 and 2,000 realizations? This is of practical concern given the computational time and storage requirements that the Monte Carlo technique requires for large, complex models such as the PM CAU flow and transport model. This issue is addressed practically by comparing empirical EV distributions of 1,000- and 2,000-realization transport parameter sets. [Figure 7-3](#) shows the EV ECDFs for transport simulation of the LCCU1-MME-TMCM model. A two-sample Kolmogorov-Smirnov test was used to test the null hypothesis that both empirical distributions are sampled from the same continuous EV distribution. The resultant p-value or the probability of obtaining such differences as those observed between the two empirical distributions, equals 0.94; therefore, the null hypothesis is not rejected with high confidence. As will be shown in [Section 8.0](#), EV sensitivity distills down to a limited number of radionuclides and parameters, thus reducing the number of realizations needed to adequately sample the sensitive parameter distributions.

## 7.5 Radionuclide Source Reduction

Of the 82 total radionuclide sources (shaft nuclear tests) in the PM CAU model domain, a reduced set was applied in all transport simulations in the interest of reducing computational time. The five base-derived alternative models developed during the flow modeling task (see [Table 3-8](#)) were considered for the identification of sources that would potentially contribute contaminant mass to areas off of the NTS boundary. The method involved identifying whether simulated source-release particles cross a specific transect along a southwest flow path, defined at the northing value of 4,110,000 m ([Figure 7-4](#)). For each PM CAU flow model, a single realization of transport parameters was used for the simulation that assumes non-diffusing and non-sorbing transport through low-porosity media, thus assuming the most conservative flow field. In each flow model, 10,000



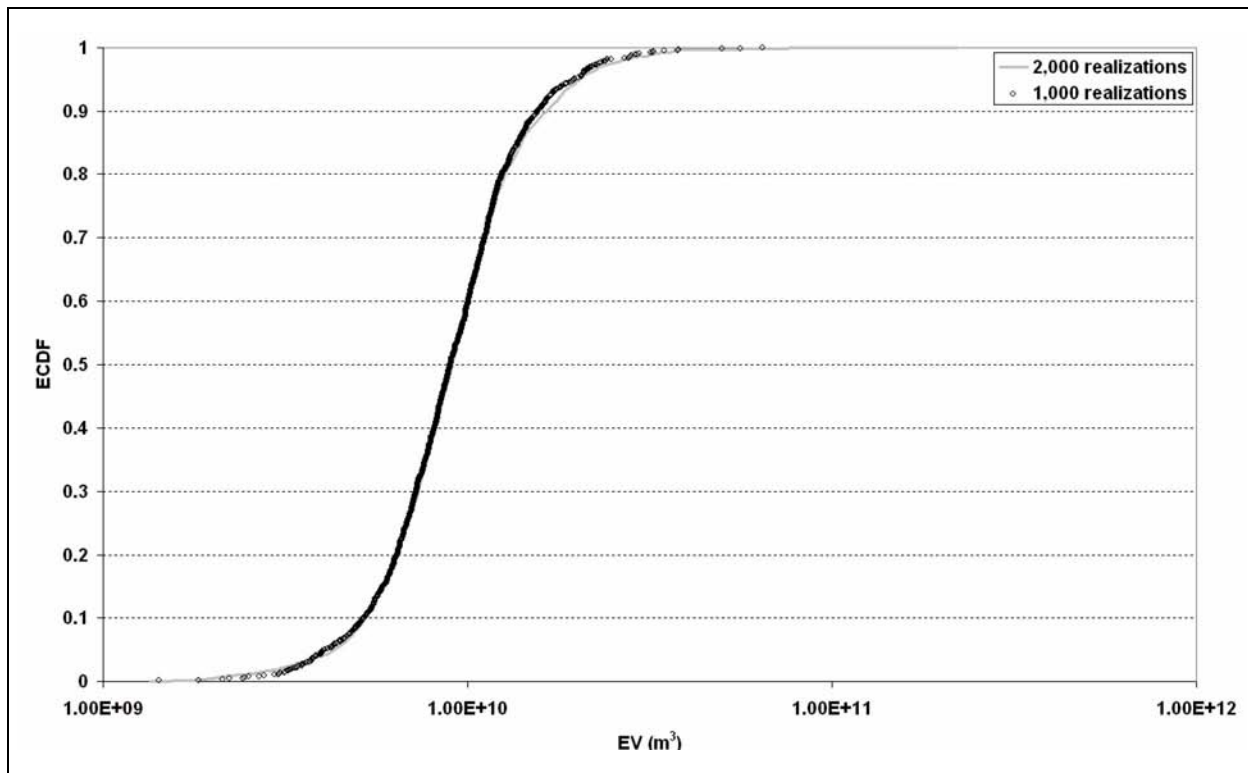


**Figure 7-3**

**Comparison of EV ECDFs for Transport Simulation of the LCCU1-MME-TMCM Model for 1,000- and 2,000-Realization Parameter Sets**

particles were released at each test, and the number of particles crossing south of the transect from each test was counted. Sources that had at least 1 percent of their particles cross the transect were considered for transport. For each of the five flow models, [Table 7-2](#) lists the sources selected for transport and the number of contributing particles (out of 10,000) per source. For the LCCU1-MME-TMCM model, the LCCU1-MME sources were used for transport analysis. This assumption is supported by the high cavity fluxes in the LCCU1-MME, which are the highest of any alternative considered, in concert with the observed rapid radionuclide migration off of Pahute Mesa in this model ([Section 7.6.1](#)). For the SCCC-MME model, all (82) sources were used for transport analysis.

**7.6 Transport Analysis Results: Alternative Flow Models**

This section presents the simulated transport behavior for the seven alternative PM CAU flow models selected in [Section 3.0](#). A constant dispersivity tensor representing the low-dispersion scenario

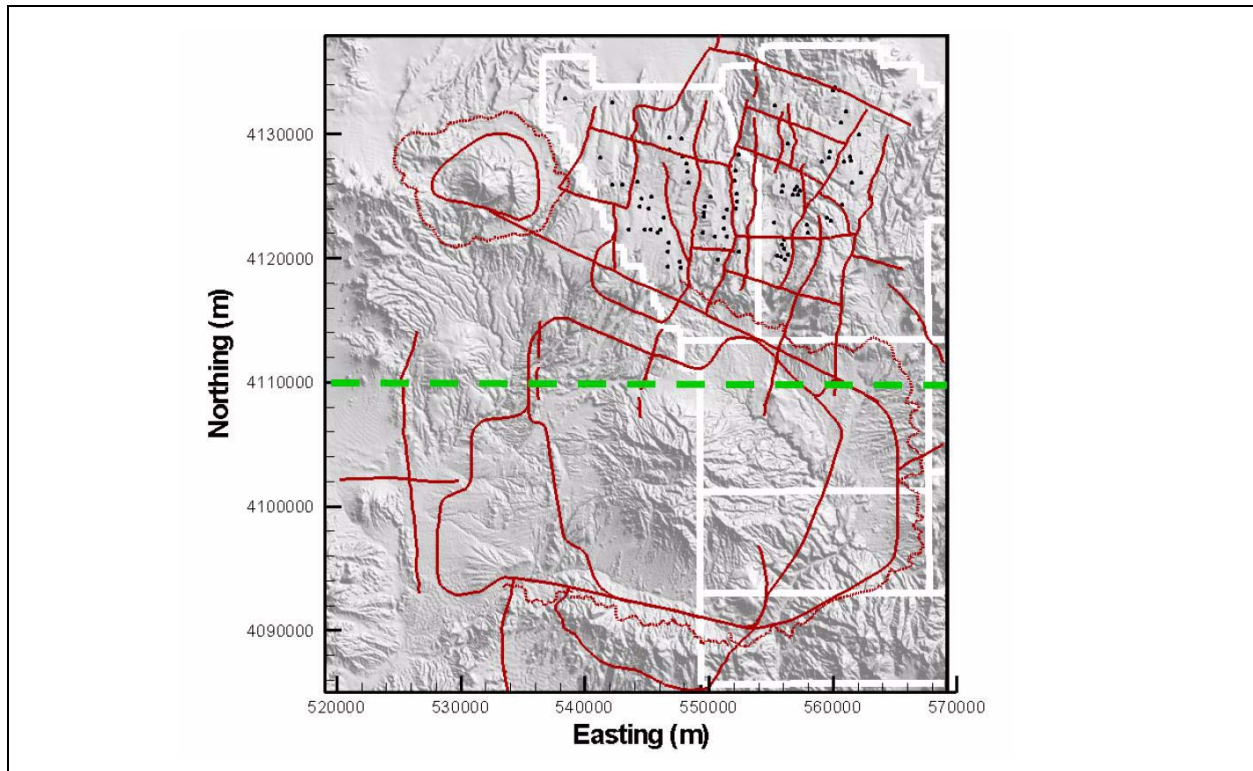


**Figure 7-4**  
**Source-Reduction Analysis of Particles Crossing South**  
**of the Transect at Northing 4,110,000 m**

Note: This indicates that their release source has the potential to contribute to transport off of the NTS boundary.

(Section 7.2) is used for all models. Transport results for simulations using a higher-dispersivity scenario are presented in Section 8.3.4. Results are presented in terms of uncertainty in the spatial and temporal migration of radionuclides from sources in accordance with the Monte Carlo approach to uncertainty analysis. Three sets of results metrics and maps are shown for each model:

1. Probability (of MCL exceedance) maps (defined in Section 7.3.2) at the discrete times of 50, 500, and 1,000 years
2. Probabilistic exceedance map (Section 7.3.5)
3. FEV for all radionuclides considered for the given transport model (Section 7.3.6)

**Table 7-2**  
**Source-Reduction Analysis**  
 (Page 1 of 2)

NAME	Easting (m)	Northern (m)	DRTDRIAFC (28)	LCCU1MMEFC (35)	LCCU1USGSDFC (19)	LCCU1TMDFC (34)	PZUPMMEFC (24)
ALAMO	555278	4122856	--	22	1	9	--
BACKBEACH	556021	4120758	--	2	--	193	37
BELMONT	547765	4119234	150	9216	5	5028	--
BENHAM	546699	4120478	2491	66	--	--	--
BODIE	552167	4124002	--	37	3	6	--
BOXCAR	548243	4127581	--	--	--	9	--
BUTEO	550481	4121740	4593	1	2683	75	--
CABRA	547855	4128162	209	55	1	59	8
CHATEAUGAY	545866	4122030	5164	146	--	820	719
CHESHIRE	551424	4121743	--	5692	4484	3531	--
COLWICK	551226	4122384	3337	114	4517	112	--
COMSTOCK	549562	4123673	9	96	--	--	--
DARWIN	544396	4124138	1190	--	--	--	--
DELAMAR	543534	4122281	8721	5091	224	3503	1890
DURYEY	550481	4121740	4170	--	1793	45	--
EGMONT	544546	4124748	9513	8638	491	7656	5055
FONTINA	545355	4124900	7736	442	--	232	30
GALVESTON	556079	4121450	--	1	817	2492	2
GIBNE	551225	4123207	--	--	3	--	--
GOLDSTONE	546768	4121180	7120	3197	--	3854	4187
HARDIN	551173	4120678	--	30	23	12	--

**Table 7-2**  
**Source-Reduction Analysis**  
 (Page 2 of 2)

NAME	Easting (m)	Northern (m)	DRTDRIAFC (28)	LCCU1MMEFC (35)	LCCU1USGSDFC (19)	LCCU1TMDFC (34)	PZUPMMEFC (24)
HORNITOS	545158	4123978	2022	4	--	4	7
HOUSTON	555779	4120082	2208	346	--	7550	1716
HOYA	550734	4119853	--	7911	4561	4194	662
INLET	556107	4119811	2985	2236	--	3431	2355
JEFFERSON	549637	4124115	--	10	--	--	--
KASH	548416	4126054	8387	289	--	849	45
KNICKERBOCKER	546103	4122301	3968	12	--	175	63
LOCKNEY	555471	4120144	29	155	--	5815	1434
MOLBO	547672	4119690	5222	2441	1	870	16
NEBBIOLO	555867	4121059	--	--	--	13	--
PEPATO	548286	4126945	829	645	--	28	68
PURSE	544267	4126169	8214	6210	345	3277	1144
SALUT	545315	4122287	7242	145	--	1061	801
SERENA	549804	4127792	6080	16	--	3	868
SHEEPSHEAD	556416	4120270	1605	540	--	1737	2180
STINGER	561068	4131788	--	2	--	--	--
TAFI	546343	4123232	8750	7714	55	8684	9126
TENABO	544858	4122285	8129	630	1	1614	1943
TYBO	546651	4119291	9487	8942	2	7929	7831

-- = Not applicable

### 7.6.1 LCCU1-MME

The LCCU1 (thrust plate) lower-permeability alternative was developed principally to reduce northeastern boundary inflow from Gold Meadows. The thrusted LCCU1 permeability, shown as a highly sensitive parameter during flow model calibration, was reduced by approximately one order of magnitude (to  $2.9 \times 10^{-14} \text{ m}^2$ ) from the original BN-MME (base model) calibration, a value that is still relatively high, reflecting assumed pervasive fracturing from thrusting. An SNJV (2006a) report concluded that the LCCU1 was principally acting to support heads in the far east-central part of the model domain (e.g., WW-8). Compensating changes in permeability required to maintain model calibration resulted in an increase of almost four orders of magnitude in the LCA3 (the thrusted eastern portion of the LCA) reference permeability, as well as lesser permeability increases in the CHZCM and PBRCM, both of which are at or near test cavities.

Radionuclide migration in the LCCU1-MME occurs along well-defined preferential pathways once having crossed south of the Moat fault, converging at the northwestern edge of Timber Mountain and moving south along the mountain flank until bleeding off west into Oasis Valley. [Figure 7-5](#) shows groundwater flux, normalized by model cell volume at an elevation of 750 m. The convergent channel along the TCM/FCCM interface is a distinct feature in this figure. The probability (of MCL exceedance) maps in [Figure 7-6](#) show that transport is rapid (e.g., the extent of the contaminated area at 50 years is greater than that at 500 and 1,000 years). However, these probability plots show an increasing number of realizations contributing to migration from southern Area 19 (north of the Moat fault) at later time. The time of first MCL exceedance ([Figure 7-7](#)) highlights the rapid migration of at least 5 percent of the realizations. The rapid migration and subsequent early time decay of  $^3\text{H}$  explain this behavior, evidenced by the early time  $^3\text{H}$  FEV peak in [Figure 7-8](#). The non-sorbing beta emitters  $^{14}\text{C}$ ,  $^{36}\text{Cl}$ ,  $^{99}\text{Tc}$ , and  $^{129}\text{I}$  also move rapidly at early time, although their contributions to the MCL plume is not as large as the  $^3\text{H}$  because their release mass is less. They contribute to the contaminant plume jointly at later time as a result of their longer half-lives.

Alpha emitters begin to appreciably contribute to the plume only at later time as they are delayed at the source and in the media by matrix sorption. As time increases,  $^3\text{H}$  decays, the other beta emitters are flushed from their sources, and the continuous flux of groundwater serves to dilute beta concentrations. Thus, the slower-moving alpha particles begin at later time to migrate into the areas where beta emitters earlier defined MCL exceedance. However, the existence of the alpha emitters

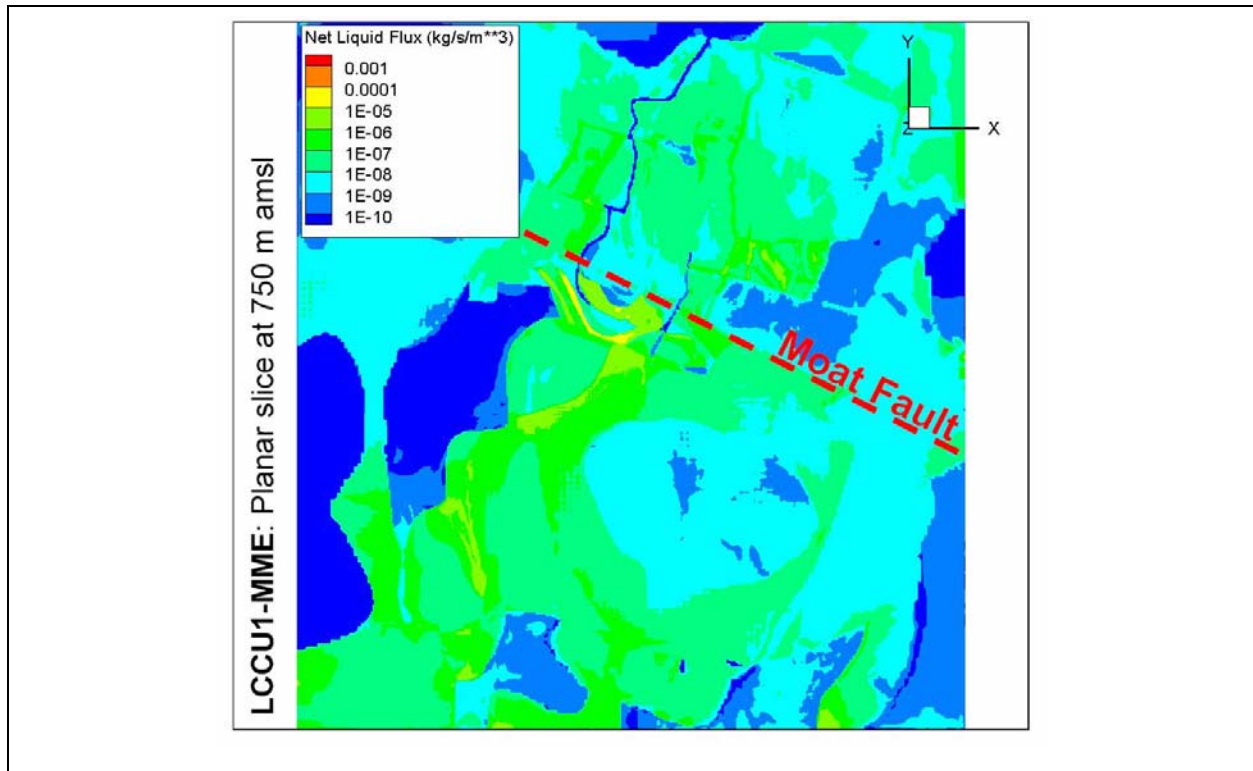


**Figure 7-5**  
**Groundwater Flux, Normalized by Model Cell Volume, at an Elevation of 750 m**  
**in the LCCU1-MME Model**

does not change the site of the MCL exceedance, which is fully defined at earlier times by the beta emitters. In these simulations, only colloidal Pu,  $^{237}\text{Np}$ , and possibly  $^{239}\text{Pu}$  have non-negligible individual MCL EVs relative to the EV of all radionuclides. Their contributions to the contaminated area, however, do not differ from those of the beta emitters; therefore, the influence of alpha emitters is masked, the effect of which is revealed through global sensitivity analysis (see [Section 8.2](#)).

The LCCU1-MME transport simulation indicates that the effect of shallow preferential flow paths may supersede the ability of transport parameters to retard basin-scale contaminant migration. For example, the 1,000-year probability map shows that more than 95 percent of the LCCU1-MME transport realizations exceed MCLs at areas near Oasis Valley and Beatty Wash. This concept is explored in full in [Section 7.6.8](#).

The LCCU1-MME transport results were also used to reduce the number of radionuclides simulated in subsequent PM CAU flow models. This model was the first of all alternatives for which the full Monte Carlo analysis was performed and, as such, incorporated all radionuclides deemed important

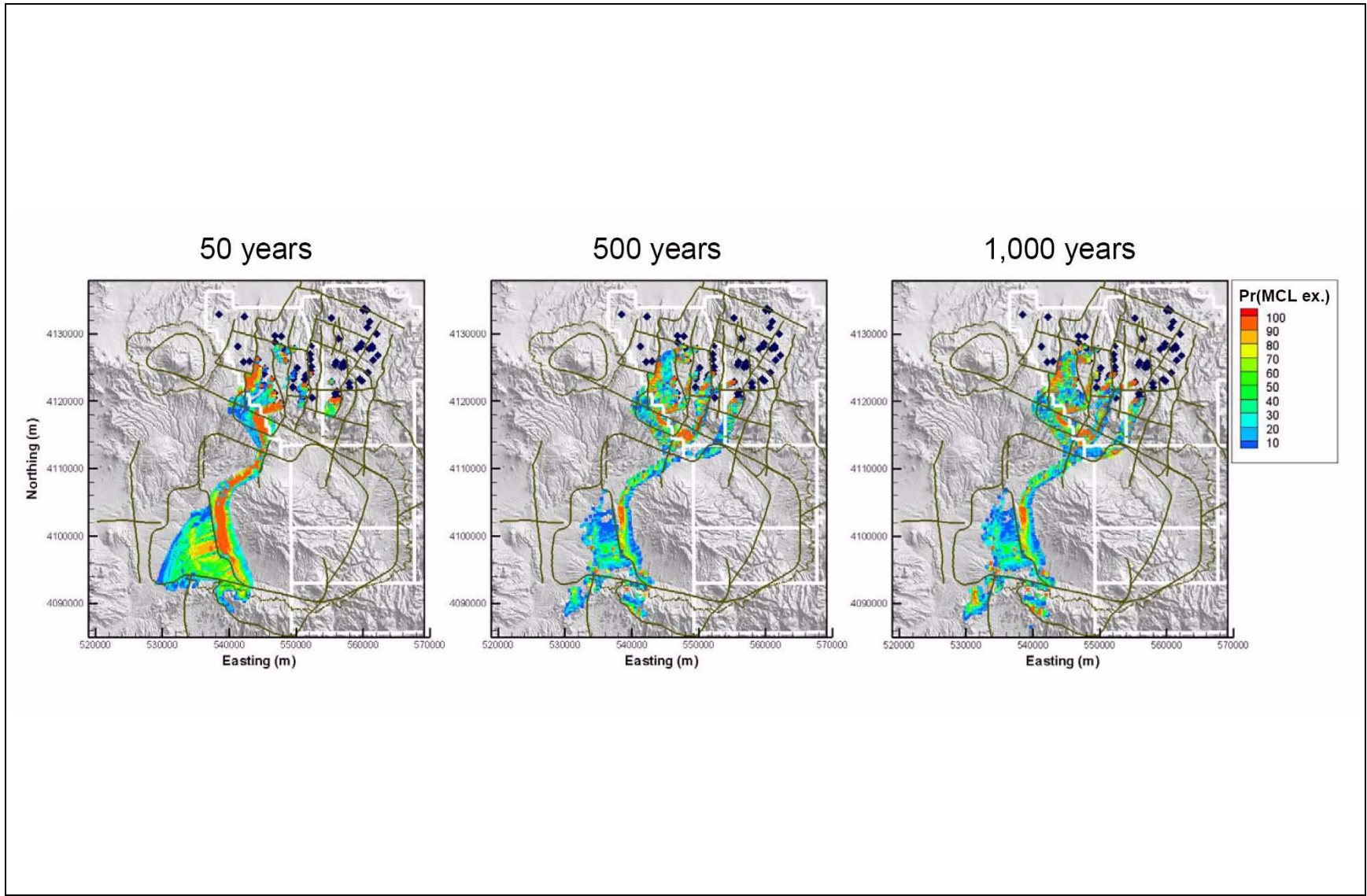


**Figure 7-6**  
**LCCU1-MME Probability of MCL Exceedance Map for Alpha Particles,**  
**Beta Emitters, and Uranium at 50, 500, and 1,000 Years**  
Note: Probabilities less than 5 percent are not shown.

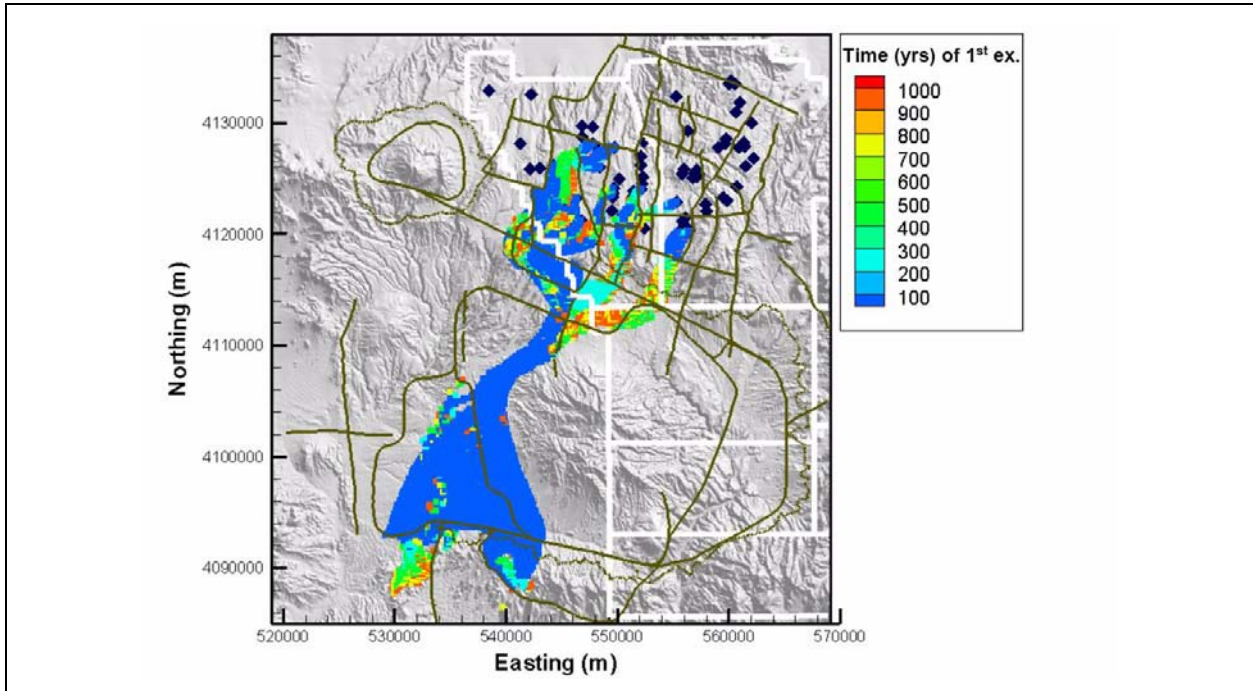


Figure 7-7

**LCCU1-MME Probabilistic MCL Exceedance Map for Discrete Time**

Note: Color contour per model node indicates the time at which at least 5 percent of Monte Carlo simulations exceed an MCL within a 1,000-year interval.

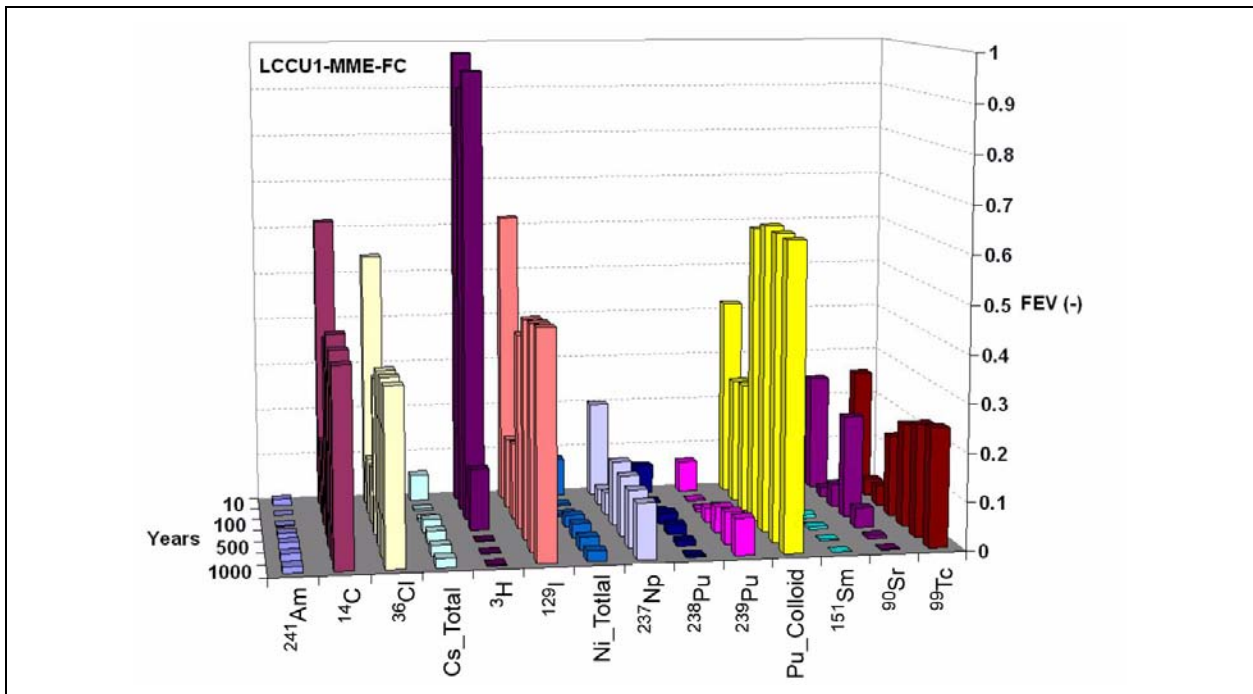


Figure 7-8

**Fractional Exceedance Volumes Based on LCCU1-MME Transport Simulation**



to Pahute Mesa transport (Section 7.3.1). For reasons described in Section 7.3.6, the FEV may be used to select radionuclides that do not contribute to radionuclide migration at any time within 1,000 years. The LCCU1-MME FEV bar chart in Figure 7-8 shows that  $^{241}\text{Am}$ ,  $^{238/239}\text{Pu}$ ,  $^{151}\text{Sm}$ ,  $^{90}\text{Sr}$ , and all isotopes of Ni and Cs do not contribute to migration at any time. In order to considerably reduce computational time, these radionuclides are not considered for transport in all subsequent PM CAU flow models. Because the LCCU1-MME model has the highest cavity fluxes of any of the alternatives, it provides the most conservative source-release rates and justifies the use of this model for radionuclide reduction analysis.

Additionally, the distribution of the sorption coefficients was considered with the LCCU1-MME model. As described in Section 6.4.7, the  $K_d$  distributions were developed through upscaling of mechanistically computed  $K_d$ . Because these distributions vary substantially from data-based distributions (see Figure 6-15), full Monte Carlo transport simulations were run using Pu  $K_d$  from the YMP distributions and compared with those using the upscaled distributions. The resulting EVs were nearly indistinguishable because the aqueous Pu migration never serves to define the EV. Whether Pu is modeled as more or less mobile, according to the two distributions considered, there are always beta emitters present to provide MCLs in exceedance wherever Pu contributes. These simulations with two different Pu  $K_d$  distributions were repeated for the LCCU1-MME-TMD, LCCU1-USGSD, and LCCU1-MME-TMCM models, always with the same conclusion.

### **7.6.2 LCCU1-MME-TMD**

Stoller-Navarro Joint Venture (2006a) developed the LCCU1-MME-TMD alternative by increasing the permeability of the LCCU1-MME Timber Mountain dome (TMD) (a subdomain of the TMCM) by two orders of magnitude, and then recalibrating while holding the dome permeability fixed. The purpose was to assess how the reduction of a recharge mound beneath Timber Mountain would influence flow and transport. The flow model analysis is summarized in Section 8.2.4.3 of this report (during analysis of transport sensitivity to flow model uncertainty).

The 50-, 500-, and 1,000-year probability maps in Figure 7-9 indicate that early time transport is rapid along the western flank of Timber Mountain, effectively replicating the behavior of the LCCU1-MME. By 500 years,  $^3\text{H}$  decay reduces the plume extent south of the Moat fault, and the other beta emitters do not contribute as strongly as in the LCCU1-MME, such that there is less than

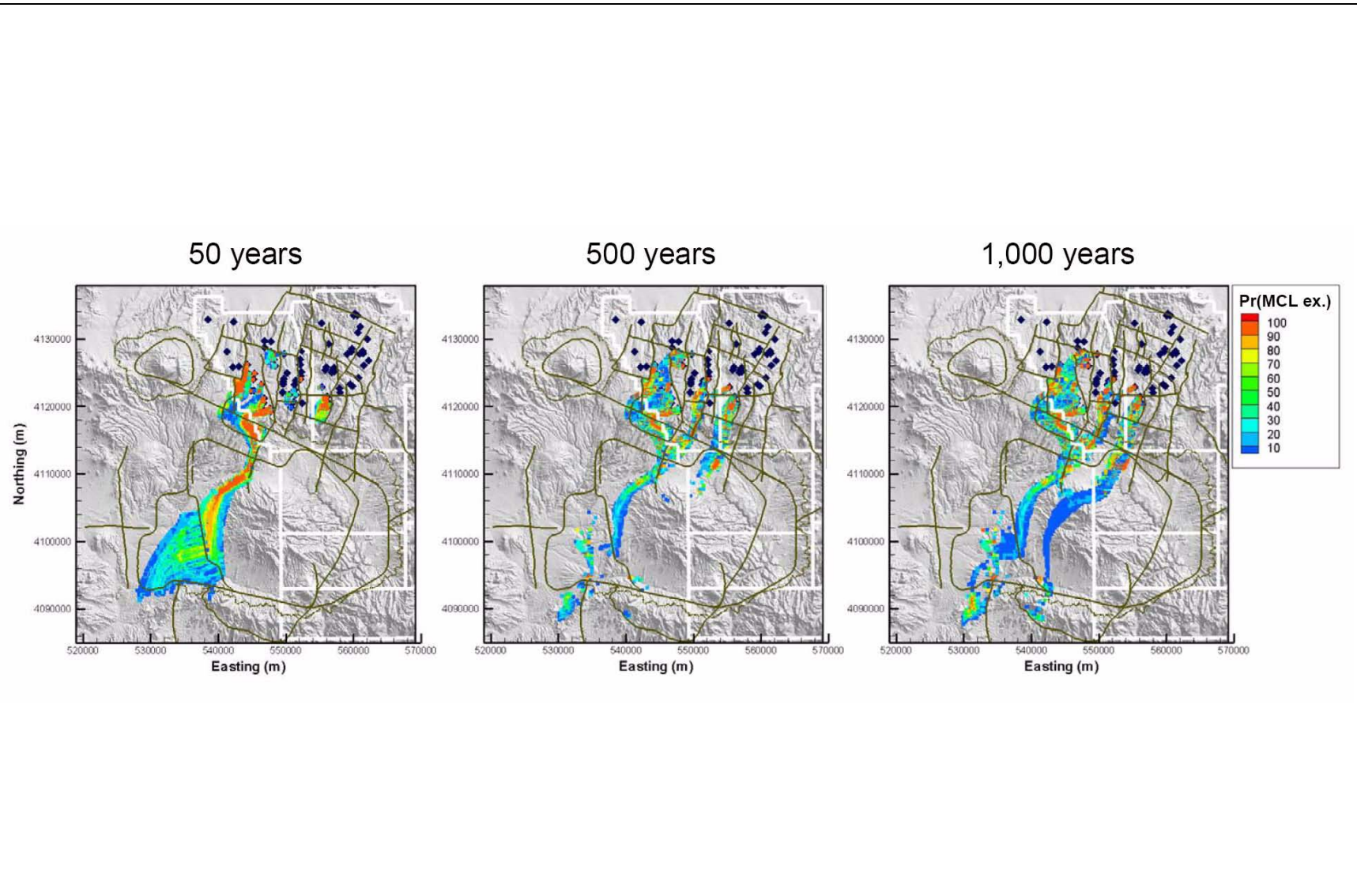


**Figure 7-9**  
**LCCU1-MME-TMD Probability of MCL Exceedance Map for Alpha Particles, Beta Emitters, and Uranium at 50, 500, and 1,000 Years**

Note: Probabilities less than 5 percent are not shown.

about a 50 percent probability that an MCL is exceeded in this region at this time. Although the contamination area along the TMCM/FCCM interface is reduced in size after the  $^3\text{H}$  contribution decays, the area grows again from the arrival of retarded alpha emitters, which are less affected by dilution.

The early radionuclide migration evolving from southwestern Area 20 does not spread into the TMD zone. Even with higher permeability, the contrast with other TMCM zones and the continued recharge pushing outward initially leads to convergent migration near the TMCM/FCCM boundary. It is at later time that radionuclides migrating from southern Area 19 begin to enter the TMD zone, traveling only slightly westward due to the outward flow from recharge, eventually passing below Beatty Wash. The probabilistic exceedance map in [Figure 7-10](#) (showing the time at which at least 5 percent of the realizations exceed an MCL) highlights the difference in travel times between the contaminated areas beneath and to the west of Timber Mountain. Notably, the divergence of radionuclide migration paths coming out from southern Areas 19 and 20 and the offset in arrival times (relative to the LCCU1-MME) begins to reveal the strong influence of permeability, as opposed to transport parameters, on radionuclide migration, an association that cannot be inferred from the analysis of only a single flow and transport model. Lastly, the FEV chart in [Figure 7-11](#) shows that radionuclide contributions to exceedance plumes are generally similar to those of the LCCU1-MME. The similarity in FEVs between models despite the difference in migration paths suggests that transport processes are potentially insensitive to the location of contaminated areas and, therefore, to flow behavior. This concept is expanded upon in [Section 7.6.9](#).

### **7.6.3 LCCU1-USGSD**

The reduced LCCU1 permeability alternative with the USGSD recharge model is the best-calibrated model considered for all flow and transport analyses and has the best geochemical mixing performance (SNJV, 2006a). The USGSD map has the lowest total recharge rate of all models (total recharge mass rate of 318 kilograms per second (kg/s) as opposed to 393 kg/s for the MME model and 633 kg/s for the DRIA model). Optimized HSU permeabilities are consequently lower for this alternative HFM, a consequence required to maintain observed heads in light of lower fluxes, with the BFCU, CFCM, IA, and CHZCM appreciably reduced. These are generally shallow units just south of the mesa near the region of transport.

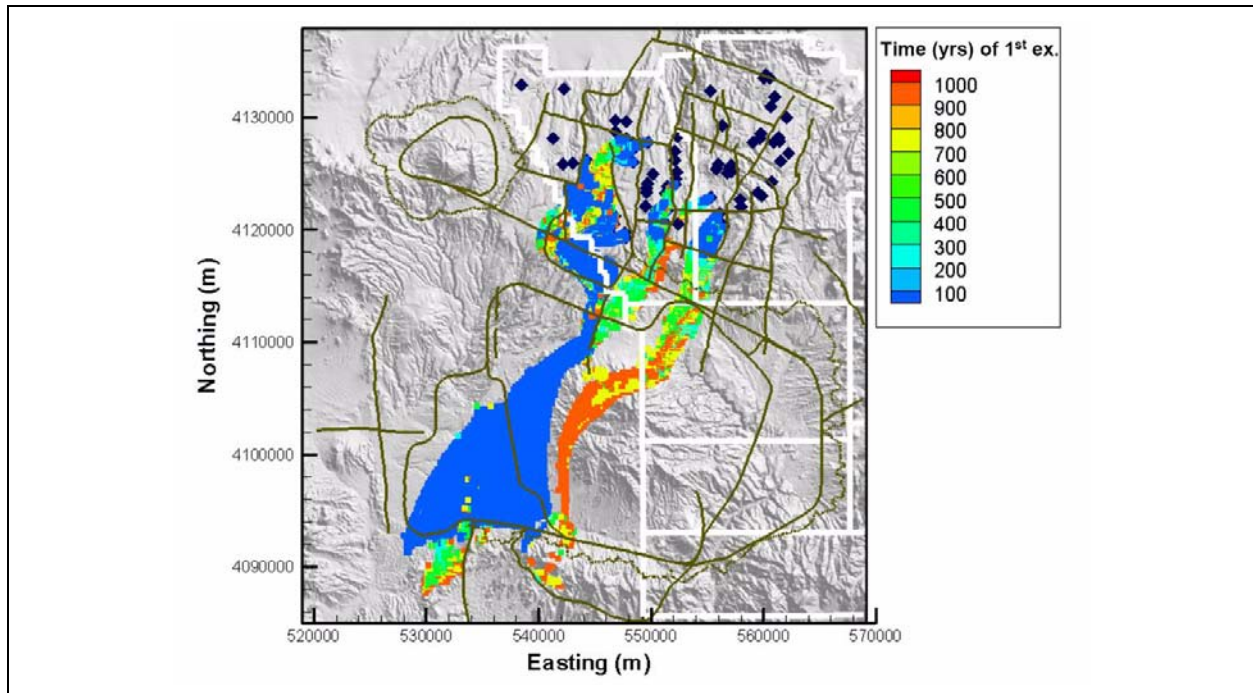


Figure 7-10

**LCCU1-MME-TMD Probabilistic MCL Exceedance Map for Discrete Time**

Note: Color contour per model node indicates the time at which at least 5 percent of Monte Carlo simulations exceed an MCL within a 1,000-year interval.

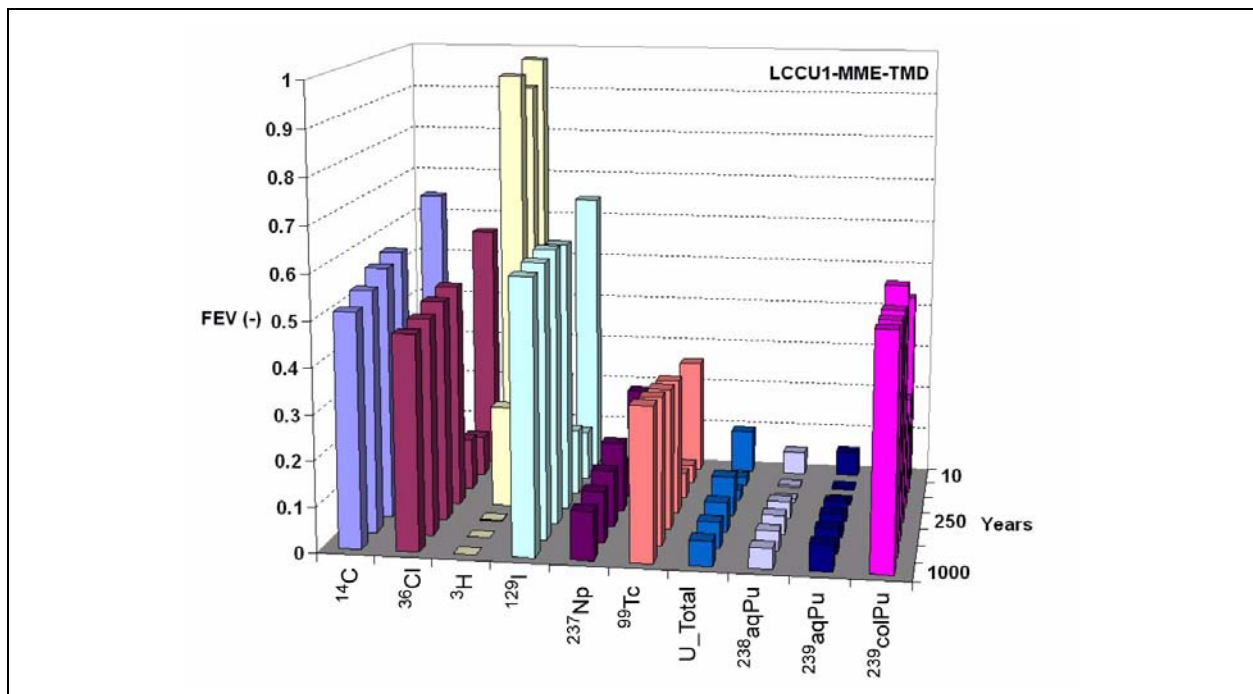


Figure 7-11

**Fractional Exceedance Volumes Based on LCCU1-MME-TMD Transport Simulation**

The MCL-exceedance probability map (Figure 7-12) and MCL exceedance map for discrete time (Figure 7-13) show that the contaminant plume develops generally along the same high-flux path west of Timber Mountain as in the other LCCU1-based alternatives. The lower recharge and corresponding lower HSU permeabilities influence the early time (within 50 years) arrival of radionuclides at Oasis Valley, as indicated by reduced probabilities for MCL exceedance in Oasis Valley as compared to the previous two models. However, with respect to only 5 percent of realizations exceeding MCLs, this model still predicts rapid migration along the TMCM/FCCM interface and to Oasis Valley. The lower recharge rate and groundwater velocity also appear to affect the dispersion of the contaminated area, which is appreciably decreased relative to the previous models. The radionuclide FEVs in Figure 7-14 show similar behavior to the other LCCU1-based models, again pointing to an insensitivity of transport properties to flow behavior.

#### **7.6.4 DRT-DRIA**

The DRT alternative raises the elevation of the low-permeability, basement pre-Tertiary structure in the model region. The thrust fault extends deeper, resulting in a thick sheet of LCCU over most of the model area such that the uppermost pre-Tertiary rock immediately downgradient of Pahute Mesa is the (nonconductive) LCCU1 rather than the (conductive) LCA. The consequence is the focusing of flow at higher elevation in the model from the reduction in the (x-z plane) cross-sectional area of permeable rocks, thus increasing flow velocity.

Calibration of the DRT-DRIA flow model generally resulted in higher HSU permeabilities in several of the larger units that control boundary fluxes. This resulted from the large section of LCCU1 extending westward and northward into the model, greatly reducing transmissivity along these boundaries, as well as the high inflow associated with the DRIA recharge map. Most relevant to the transport system, SNJV (2006a) observed that advective particle paths in the DRT-DRIA alternative were focused particularly along the western flank of Timber Mountain, and that the DRIA recharge model is strongly associated with this behavior. For example, the optimized PBRCM Zone 84 and DVCM permeabilities were appreciably reduced (relative to the base model) to limit flow into Oasis Valley from the north and west boundaries, respectively, because sufficient flux was available from the DRIA-estimated Timber Mountain recharge to account for the southwestern boundary flows.

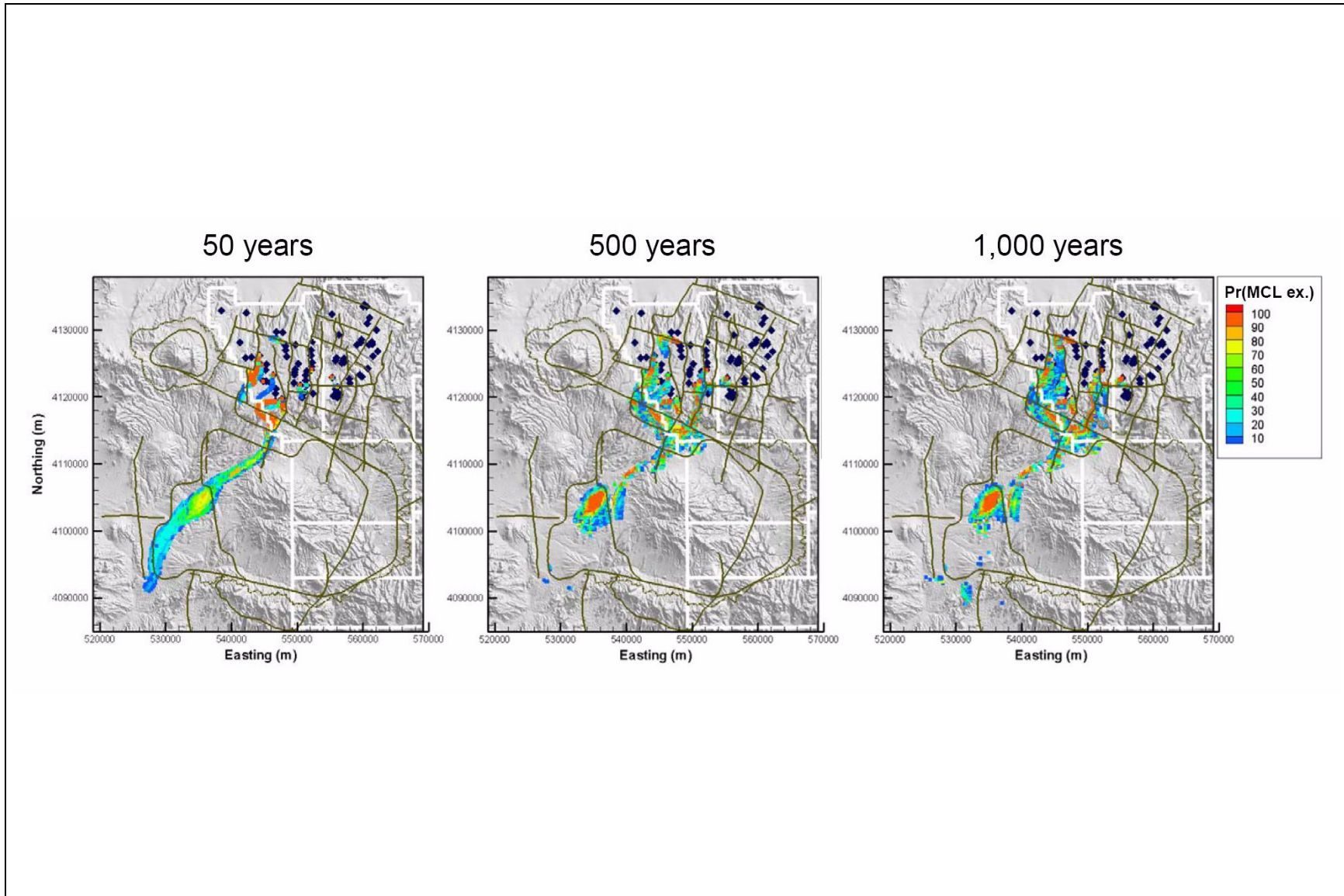


**Figure 7-12**  
**LCCU1-USGSD Probability of MCL Exceedance Map for Alpha Particles, Beta Emitters, and Uranium at 50, 500, and 1,000 Years**

Note: Probabilities less than 5 percent are not shown.

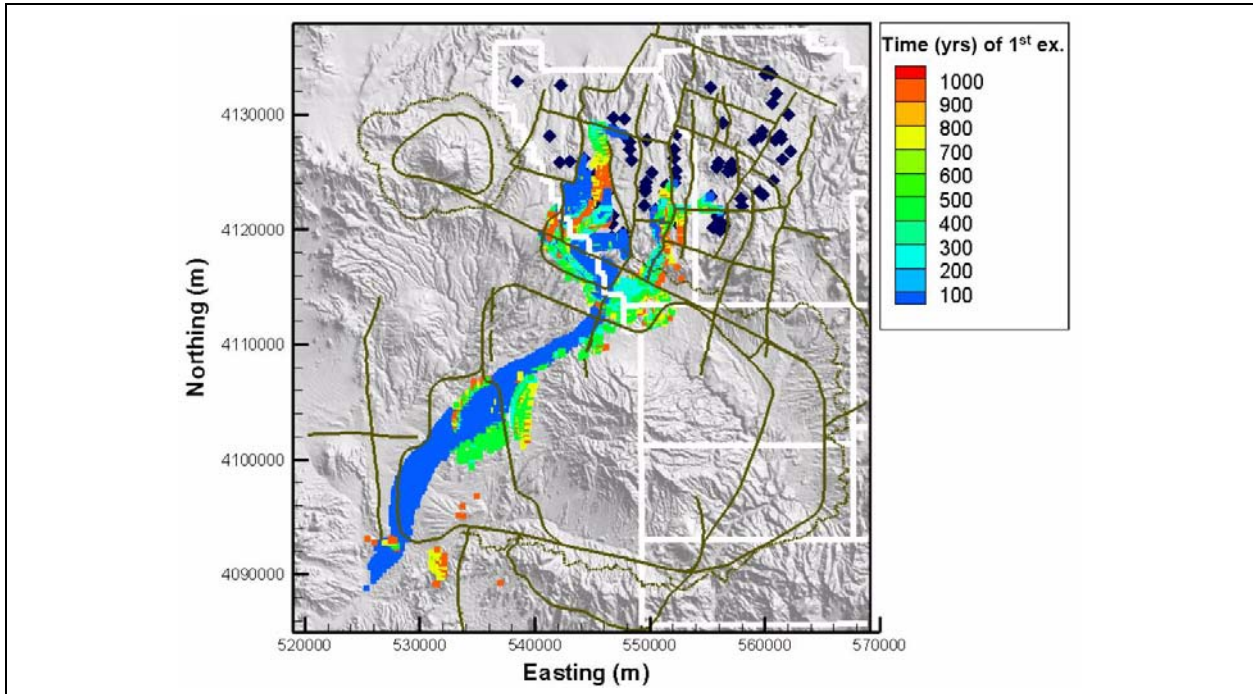


**Figure 7-13**

**LCCU1-USGSD Probabilistic MCL Exceedance Map for Discrete Time**

Note: Color contour per model node indicates the time at which at least 5 percent of Monte Carlo simulations exceed an MCL within a 1,000-year interval.

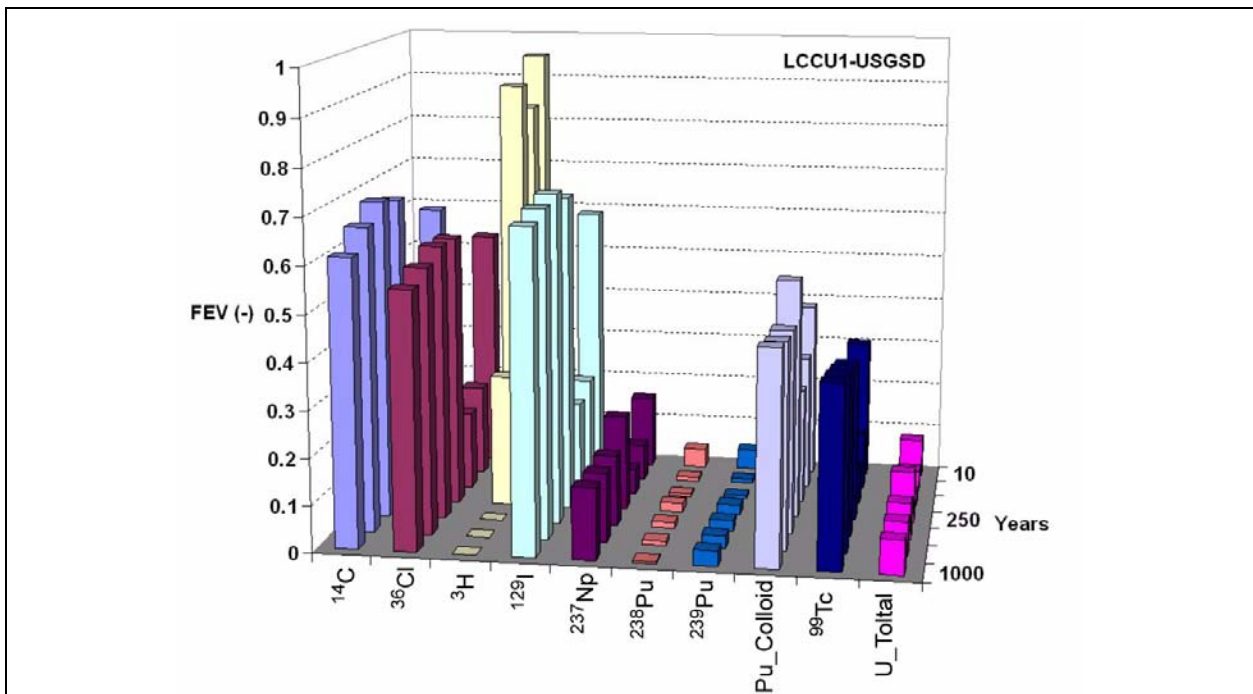


**Figure 7-14**

**Fractional Exceedance Volumes Based on LCCU1-USGSD Transport Simulation**

The MCL exceedance probabilities associated with radionuclide migration in the DRT-DRIA alternative are shown in [Figure 7-15](#). At all time intervals, concentrations fail to exceed the MCL standard equivalents once the plume enters a particularly high-flux pathway through the TMCM. [Figure 7-16](#) illustrates how the combined effect of high Timber Mountain recharge, high TMCM permeability (particularly in the TMCMATCW subdivision), low FCCM permeability, and permeability depth decay in the TMCM and FCCM result in a high-flux channel around the western flank of Timber Mountain, behavior that was more completely described in [Section 3.4.1](#).

A planar cross-section of groundwater flux (normalized per node volume), shown at 750 m in [Figure 7-17](#), confirms the result of high groundwater velocity at this area. The large majority of transport occurs approximately within the 0 to 1,000 m (water table) elevation range, corresponding with the primary interval in which fractured volcanics are located north of the Moat fault. As a point of reference, the contact between the FCCM and underlying TMCM subdivision is at approximately 800 m elevation. The distinct areas of high flux to the northwest of Timber Mountain provide the basis for substantial radionuclide dilution in this simulation. [Figure 7-17](#) also shows the flux at 750 m for the LCCU1-MME model. In the area of dilution directly along the northwest flank of Timber Mountain, the high-flux paths do not appear markedly different between the two models despite both the high DRIA recharge rate and raised pre-Tertiary basement in the DRT model. This slight difference in groundwater flux at the elevation of the plume suggests a strong sensitivity of radionuclide concentration, and therefore of MCL exceedance to flow.

The DRT-DRIA flow model differs from the others because the local high fluxes in the TMCM lead to dilution of radionuclide concentrations and contaminant levels below MCLs. There is little sensitivity to transport parameters in this model because the flux determines the mobility and dilution of radionuclides.



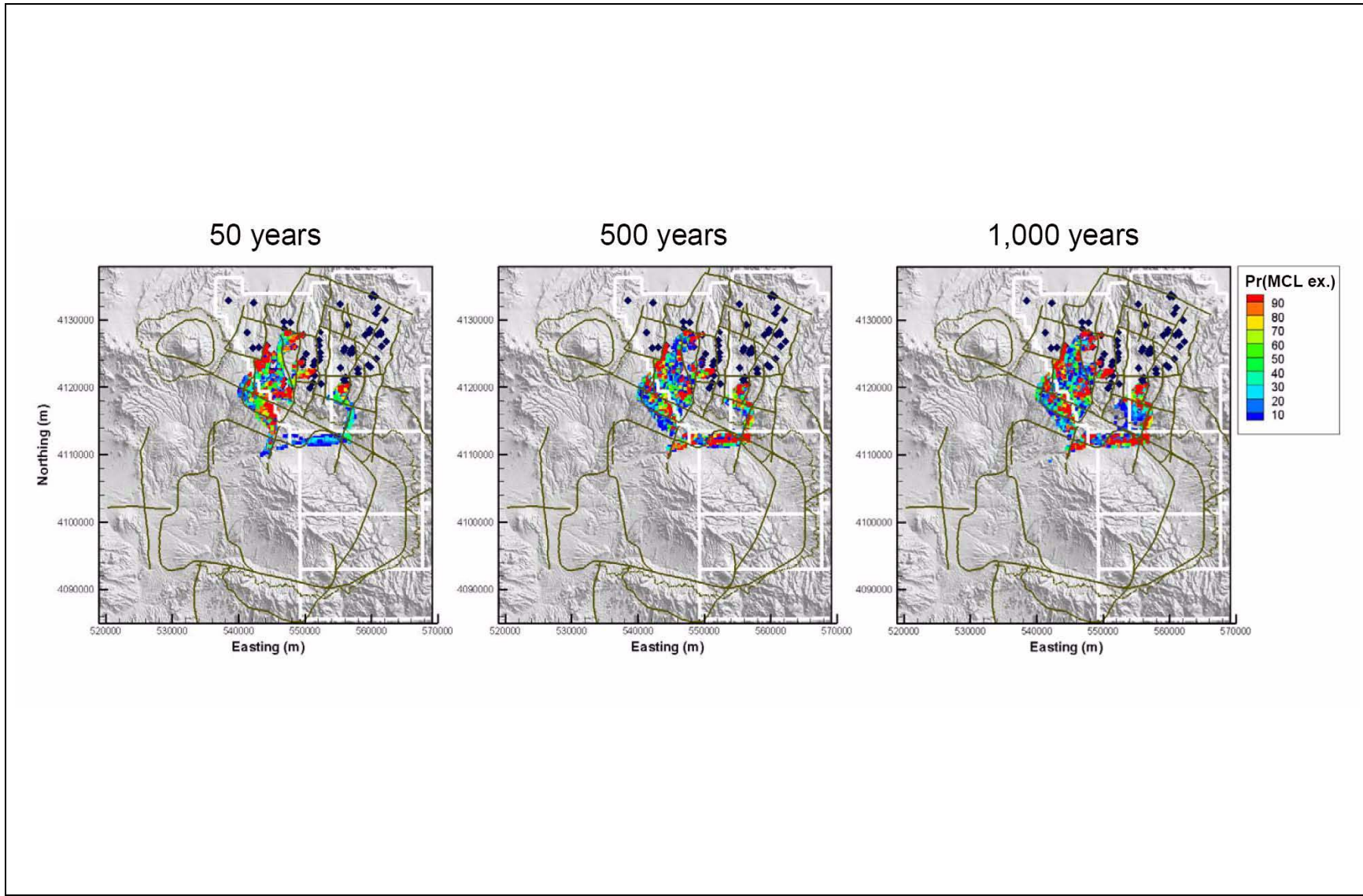


**Figure 7-15**  
**DRT-DRIA Probability of MCL Exceedance Map for Alpha Particles,**  
**Beta Emitters, and Uranium at 50, 500, and 1,000 Years**

Note: Probabilities less than 5 percent are not shown.

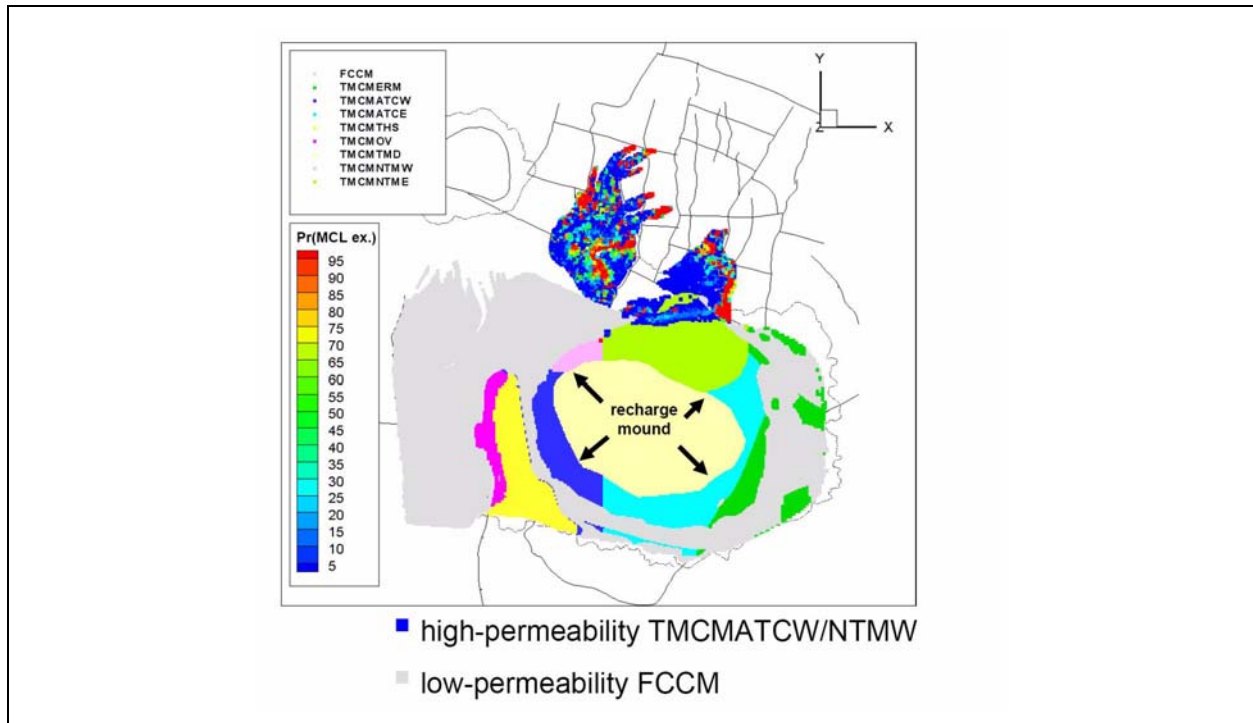


**Figure 7-16**  
**Probability of MCL Exceedance Based on DRT-DRIA Transport Model**

### 7.6.5 PZUP-MME

The raised pre-Tertiary surface model is the second alternative that investigates the effect of raising the elevation of, or otherwise increasing the thickness of, low-permeability rocks through the domain. The PZUP alternative raises the pre-Tertiary basement surface to its highest geologically permissible elevation, with up to 2-km variation from the base model, and raises the basement inside the calderas. The intent was to accentuate the shallow flow system, much like for the DRT alternative, particularly enhancing groundwater flow around the eastern side of Timber Mountain.

Simulated transport through the PZUP-MME flow model is not appreciably different from the prior alternatives. Again, the probability maps (Figure 7-18) and probabilistic exceedance map (Figure 7-19) show that transport to Oasis Valley is rapid (within 50 years) and that a single plume to the west of Timber Mountain reaches its maximum extent within 100 years of release. The radionuclide FEVs in Figure 7-20 confirm that it is the high-mass, non-retarded  $^3\text{H}$  release and its rapid decay that characterize this behavior. Dilution of beta emitters contributes to the decrease in MCL-exceedance plume size through time as well.

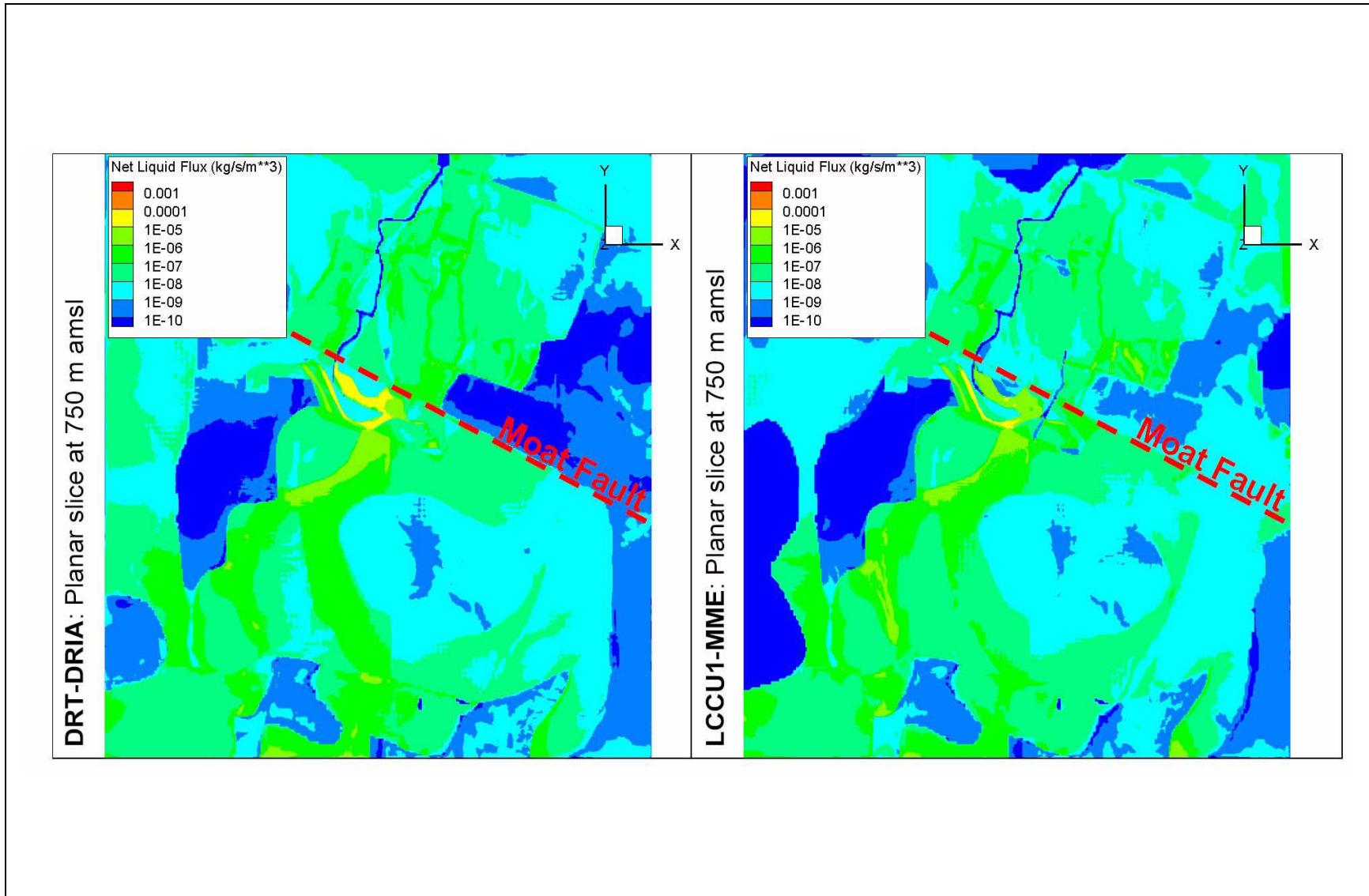


**Figure 7-17**

**Comparison of Flux across the Model Domain at a Single Elevation (750 m amsl)  
between the DRT-DRIA (left) and LCCU1-MME (right) HFM**

Note: In both models, transport is strongly associated with high-flux pathways to the north, west, and south of Timber Mountain.

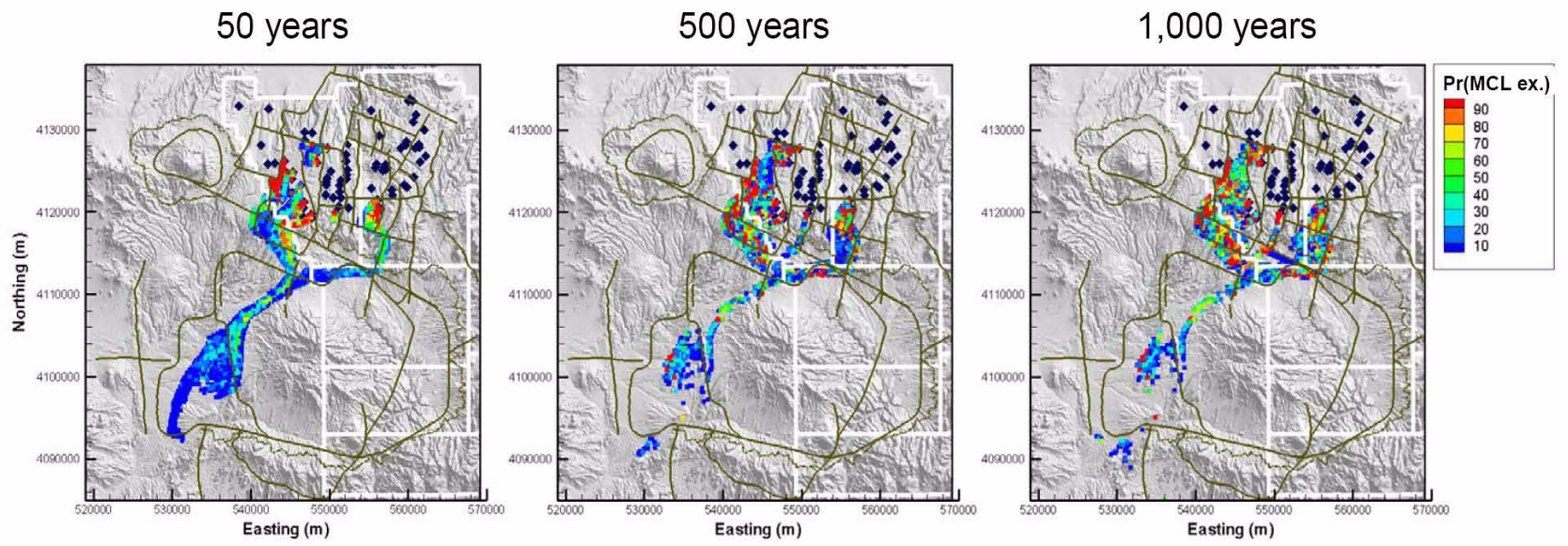


**Figure 7-18**  
**PZUP-MME Probability of MCL Exceedance Map for Alpha Particles, Beta Emitters, and Uranium at 50, 500, and 1,000 Years**

Note: Probabilities less than 5 percent are not shown.

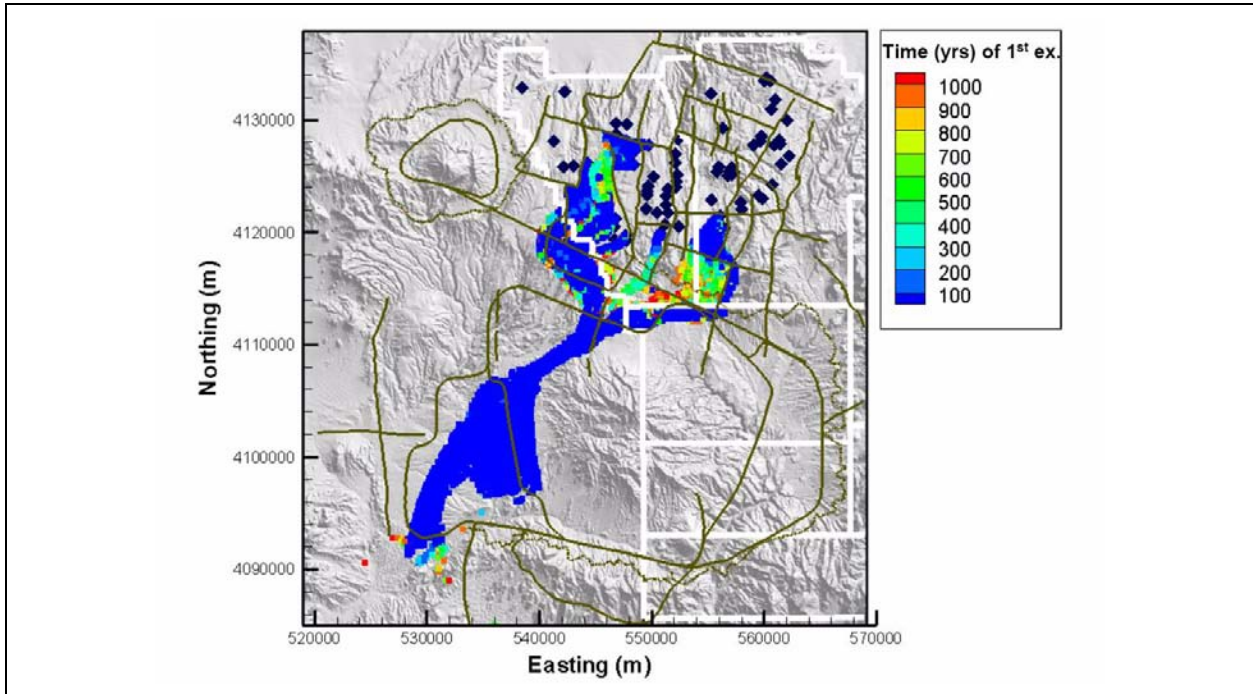


**Figure 7-19**  
**PZUP-MME Probabilistic MCL Exceedance Map for Discrete Time**

Note: Color contour per model node indicates the time at which at least 5 percent of Monte Carlo simulations exceed an MCL within a 1,000-year interval.

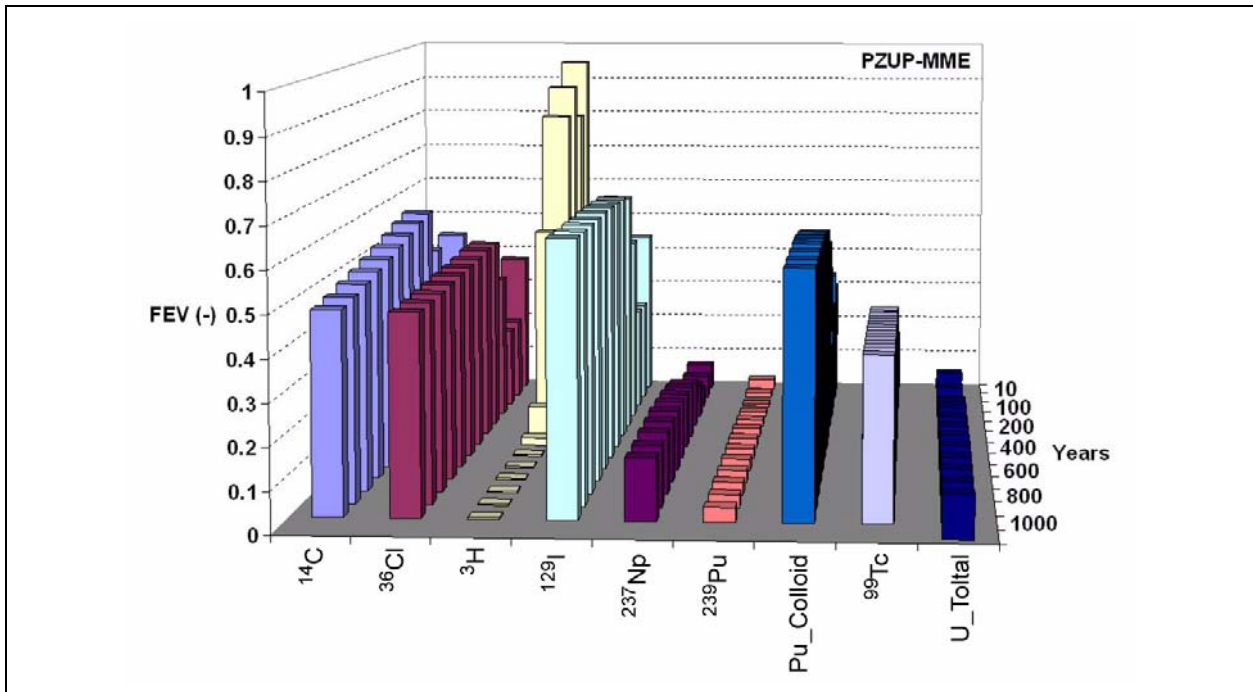


**Figure 7-20**  
**Fractional Exceedance Volumes Based on PZUP-MME Transport Model Simulation**

Similar to migration through the other alternative models, the simulated contaminated area south of the Moat fault is controlled by preferential flow along the western flank of Timber Mountain. While the goal of increasing flow around the mountain's east side was realized, this effect was not realized in transport because a high-permeability (and therefore higher-flux) connection between west and east was not realized north of Timber Mountain. Increased fluxes along the western pathway from raising the pre-Tertiary basement are not sufficiently high to dilute radionuclides to below their MCL standards (as in the DRT-DRIA case) because of the moderate MME recharge rate applied. However, relatively large dispersion of the PZUP-MME plume indicates that preferential-pathway fluxes are generally as high as in the above-described LCCU1-based alternatives.

#### **7.6.6 LCCU1-MME-TMCM**

The influence of HSU geometry (conceptualization) and permeability (parameterization) on radionuclide migration, introduced in [Section 3.4.1](#) and [Sections 7.6.1](#) through [7.6.5](#), demonstrated its effects in the form of preferential-pathway transport through all base-derived alternative models. There are, however, no data to confirm the simulated preferential-flow channels identified in the alternative models, although the geochemical implications of ER-EC-5 water having a strong component of UE-18r-type water and ER-OV-3c water having a strong component of ER-EC-5-type water is important (Kwicklis et al., 2005). In those simulations, the channels form as a result of single-permeability, basin-scale HSUs with contrasting properties at interfaces. Investigating the reduction of preferential flow and transport south of the Moat fault and increasing the influence of transport parameters on plume migration, the LCCU1-MME-TMCM alternative was developed with more homogenous permeability within the TMCM subdomains and adjacent HSUs, and still preserves the geochemical mixing targets.

[Section 3.4.3](#) presented this alternative and showed that improved homogenization of TMCM subdomain permeabilities reduced preferential flow south of the Moat fault. The effect on transport, both temporally and spatially, is considerable although channels still exist as a result of property differences in the coarse zonation of the HFM model. [Figure 7-21](#) shows the resulting 50-, 500-, and 1,000-year probability (of MCL exceedance) maps. Transport rates are significantly reduced, with only minor breakthrough at the Moat fault at 50 years. While radionuclides have reached near Oasis Valley and Beatty Wash at 500 and 1,000 years, the majority of migration (south of the Moat fault)

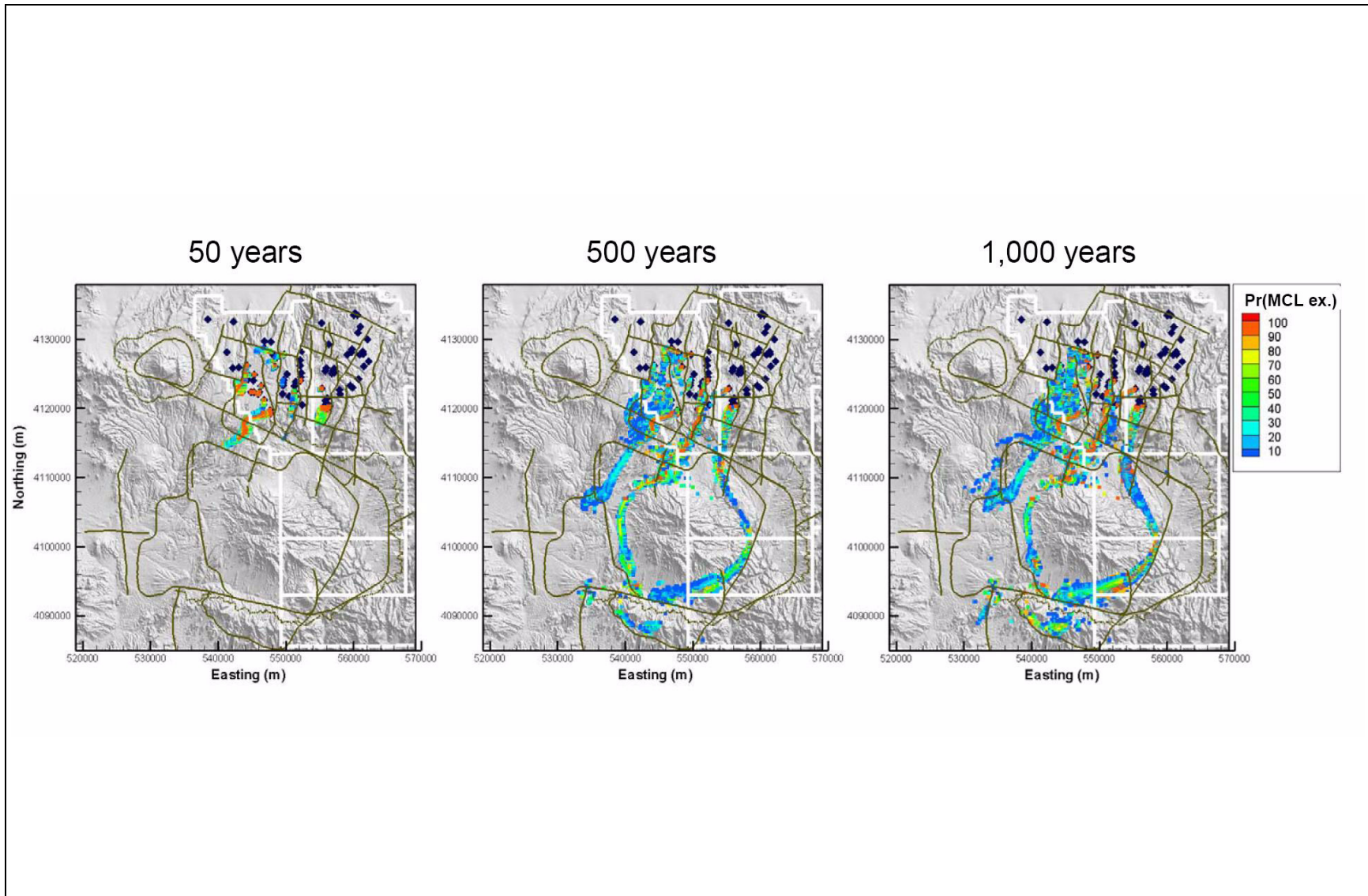


**Figure 7-21**  
**LCCU1-MME-TMCM Probability of MCL Exceedance Map for Alpha Particles, Beta Emitters, and Uranium at 50, 500, and 1,000 Years**

Note: Probabilities less than 5 percent are not shown.

shows less than a 50 percent probability of MCL exceedance. These relatively low probabilities in the southern reaches of the contaminated areas only highlight the fact that the level of certainty prescribed for the subsequent definition of some contaminant boundary is of great importance. The probabilistic exceedance map in [Figure 7-22](#), showing the time of first MCL exceedance for at least 5 percent of the realizations, demonstrates the slowed migration rate relative to the other base-derived alternative models.

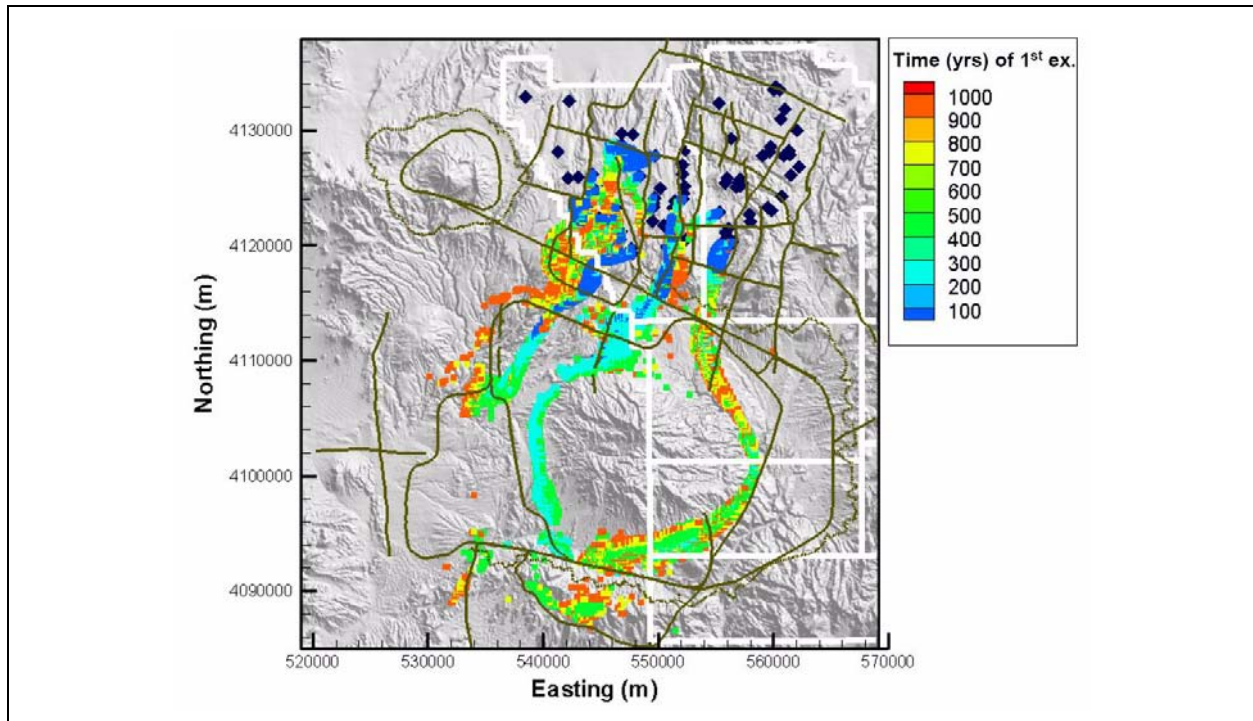


**Figure 7-22**

***LCCU1-MME-TMCM Probabilistic MCL Exceedance Map for Discrete Time***

Note: Color contour per model node indicates the time at which at least 5 percent of Monte Carlo simulations exceed an MCL within a 1,000-year interval.

Of equal importance to the reduced migration rates, [Figure 7-21](#) also shows the inhibition of transport through a single preferential pathway. Although preferential flow still exists, such as along the TMCM/FCCM interface as a result of coarse zonation, the east-west spreading of flow appreciably reduces fluxes along the channels. [Figure 7-23](#) shows a planar slice of normalized flux per node at 750 m, comparing the LCCU1-MME-TMCM with the LCCU1-MME. The effect of increased permeability homogenization is evident as connected flow paths in Thirsty Canyon and to the west and east (Fortymile Canyon) of Timber Mountain are visible in the LCCU1-MME-TMCM.



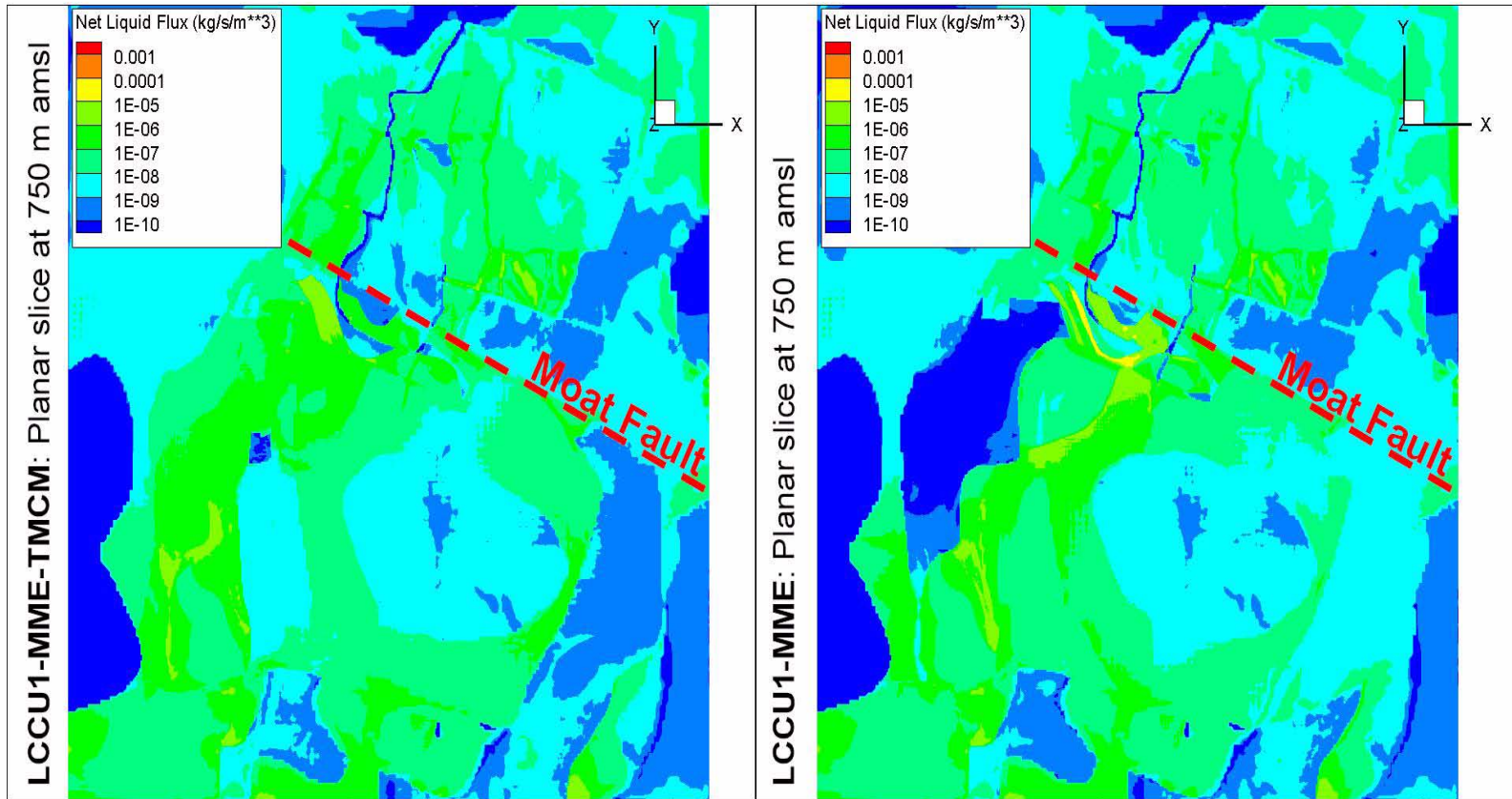


**Figure 7-23**

**Comparison of Flux across the Model Domain at a Single Elevation (750 m amsl) between the LCCU1-MME-TMCM (left) and LCCU1-MME (right) HFMs**

Note: Connected zones of high flux through Thirsty Canyon and Fortymile Canyon lead to transport through these areas in the LCCU1-MME-TMCM that are non-existent in the base LCCU1-MME model.

Lastly, it is worth noting that despite the reduced rate of radionuclide migration, the relative contributions of radionuclides to the exceedance map (in Figure 7-24) did not appreciably differ from those of the other base-derived alternatives. In the LCCU1-MME-TMCM model, non-sorbing species still dominate the contaminated area at any time in the 1,000-year simulation. The exception, again, is colloidal Pu, which migrates even more conservatively than the diffusing beta emitters. Thus, its ultimate sensitivity relates to the source-release function, an uncertain process discussed in Section 4.0. With the lower velocities, the beta emitters experience more  $D_m$ , hence the reduced rate of plume advancement. The reactive species experience similar diffusion and then even more retardation in the matrix material. Therefore, the sensitivities shown in Figure 7-24 are, not surprisingly, similar to those for the other alternative flow models.

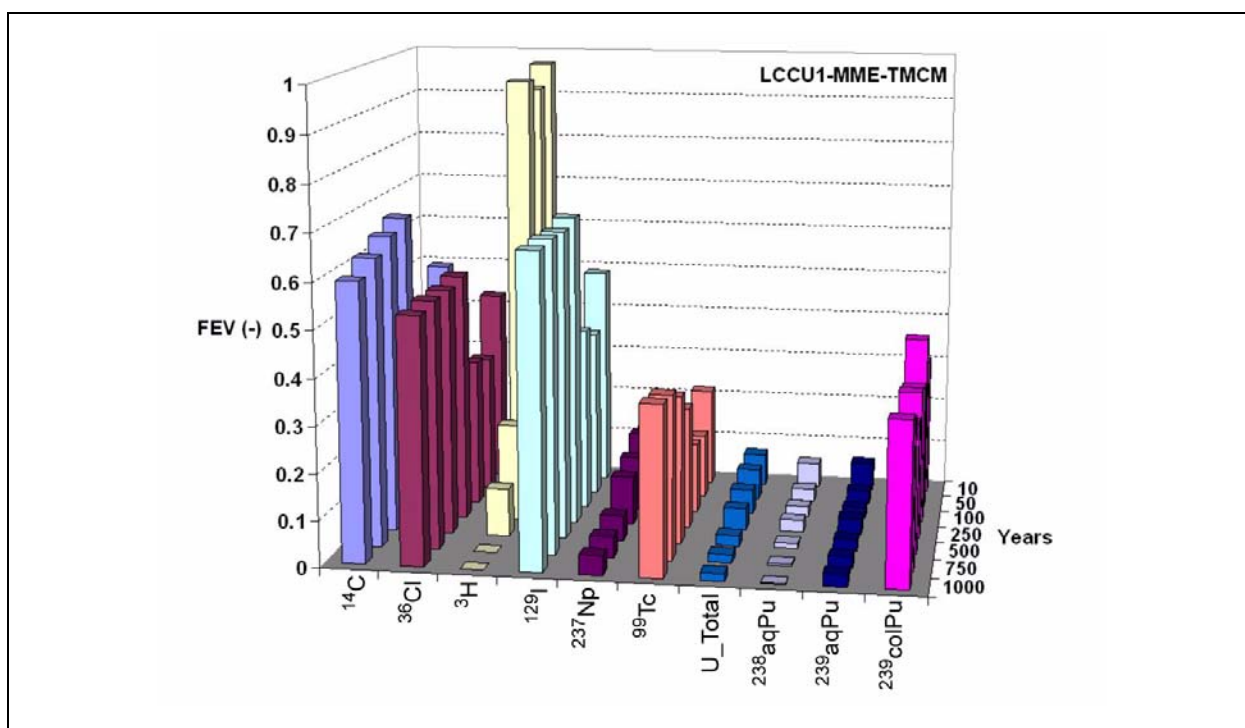


**Figure 7-24**  
**Fractional Exceedance Volumes Based on LCCU1-MME-TMCM**  
**Transport Model Simulation**

### 7.6.7 SCCC-MME

The alternative structural model and hydrostratigraphy of the SCCC HFM are more simplified than the base HFM. Major structural differences include the margins of the caldera complex (the SCCC HFM includes the single caldera ring-fracture system), locations of caldera-forming faults, and the

number and depth of the faults considered. Only 11 of the basin-and-range faults were mapped at the surface, and the majority of faults terminate at shallower depths than in the base HFM.

The SCCC-based alternatives did not perform as well in matching observed heads in key areas of the domain (e.g., the Purse fault) and, in general, did not calibrate as well as the base HFM. Additionally, the poorest-performing HFM considered under all recharge models was the SCCC alternative (see [Figure 3-18](#)). However, the calibration of SCCC-MME proved acceptable and the broad characteristics of the flow system are correct, which is a partial consequence of specifying head around the edges of the PM CAU model. In fact, SCCC-MME performed exceptionally well with regard to geochemical mixing targets. Unlike in the base-derived HFMs, with the exclusion of the LCCU1-MME-TMCM alternative, a considerable portion of flow (observed via particle tracks) is down Fortymile Canyon (see [Figure 3-19](#)). Also, the flow paths in southern Area 20 are nearly due south, in contrast to the base HFM models. Flow paths leaving Area 20 include areas of porous media, rather than fractured aquifer, as a result of the simpler stratigraphy. Therefore, the rapid migration from Pahute Mesa to the TMCM observed in the other alternatives was not expected for the SCCC-MME due to lower velocities.

The probability maps in [Figure 7-25](#) show the delayed development of radionuclide plumes, similar to that observed for the LCCU1-MME-TMCM case. The velocities in Area 20 are much lower, and connected fracture pathways do not exist. The probabilistic exceedance map in [Figure 7-26](#) reveals that not until about 500 years are MCLs exceeded south of the Ammonia Tanks caldera structural margin fault (ATCF, [Section 3.2.3.1](#)), the equivalent of the Moat fault in the base HFM. This is partially a consequence of the larger (relative to the base HFM); composite HSU definitions (see [Table 3-8](#)) of lower effective block permeabilities unique to the SCCC hydrostratigraphy. The resultant lower fluxes further increase the diffusive components of transport and the sensitivity of migration to transport parameterization. [Figure 7-26](#) indicates that slower migration also results from a transport barrier due to decreased permeability (by a factor of 105) at the ATCF relative to the background HSU permeability. This latter observation highlights the competing influence between flow and transport parameterization on transport.

[Figure 7-25](#) also shows that channelization of migration paths occurs south of the ATCF, similar to all other models. This is particularly shown east of Timber Mountain where fluxes are sufficiently high

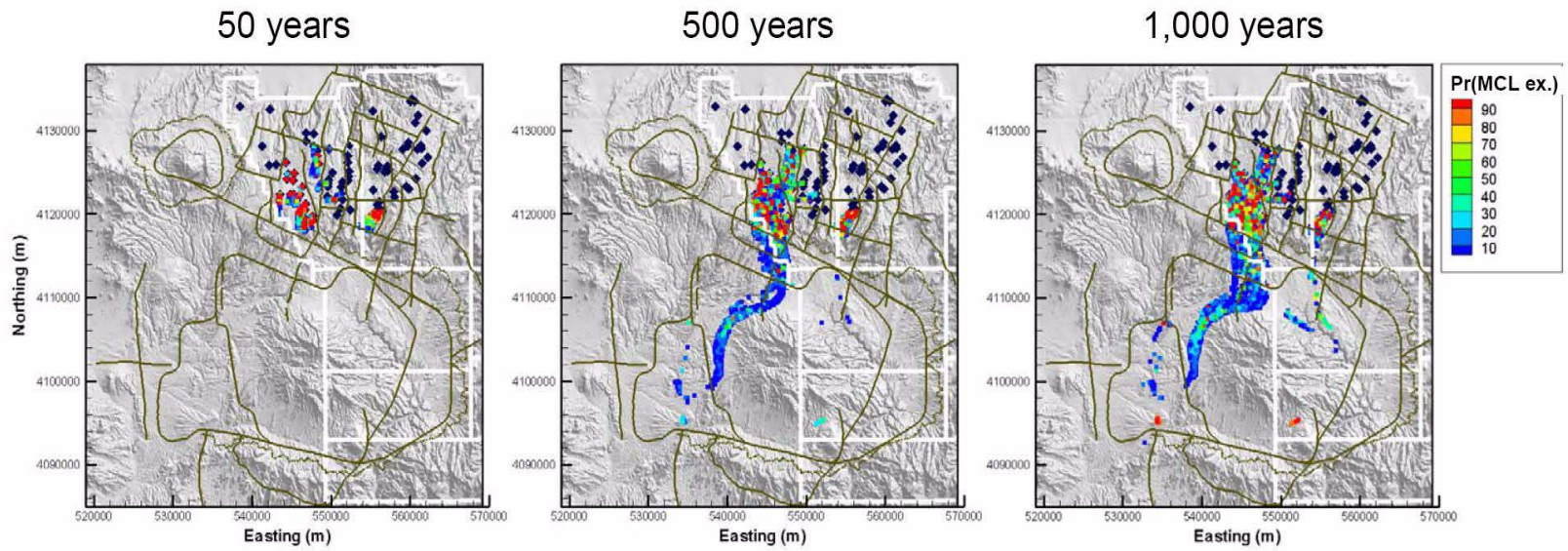


**Figure 7-25**  
**SCCC-MME Probability of MCL Exceedance Map for Alpha Particles,  
Beta Emitters, and Uranium at 50, 500, and 1,000 Years**

Note: Probabilities less than 5 percent are not shown.

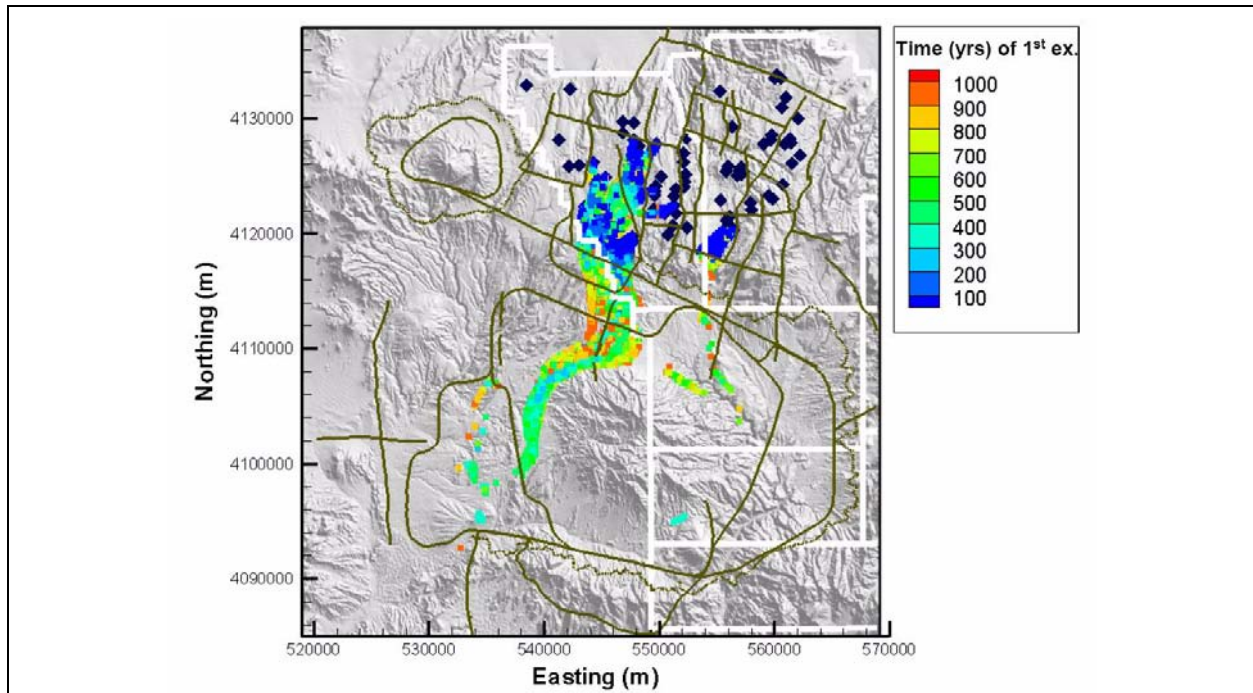


**Figure 7-26**

**SCCC-MME Probabilistic MCL Exceedance Map for Discrete Time**

Note: Color contour per model node indicates the time at which at least 5 percent of Monte Carlo simulations exceed an MCL within a 1,000-year interval.

to dilute concentrations to below MCLs. That channelization persists despite the considerable simplification of hydrostratigraphy indicates that it is the large, single-permeability HSUs (lacking heterogeneity within HSUs) that permit this behavior. Once in a high-velocity path within a single HSU, there is no heterogeneity of (HSU-based) flow properties or (RMC-based) transport properties to delay radionuclide migration or, more importantly, to disperse the flow and reduce local velocities, until the HSU is exited.

Despite reduced transport rates and the channeling of radionuclide migration along multiple paths, the relative contributions of radionuclides to areas of MCL exceedance (in [Figure 7-27](#)) do not differ from those of all other models. For any of the flow models, the conservative species fully prescribe the shape and volume of migration paths. In other words, there are no scenarios where dilution or decay of the beta emitters over 1,000 years is sufficient to permit less mobile but more persistent species to define the shape of the contaminated area.

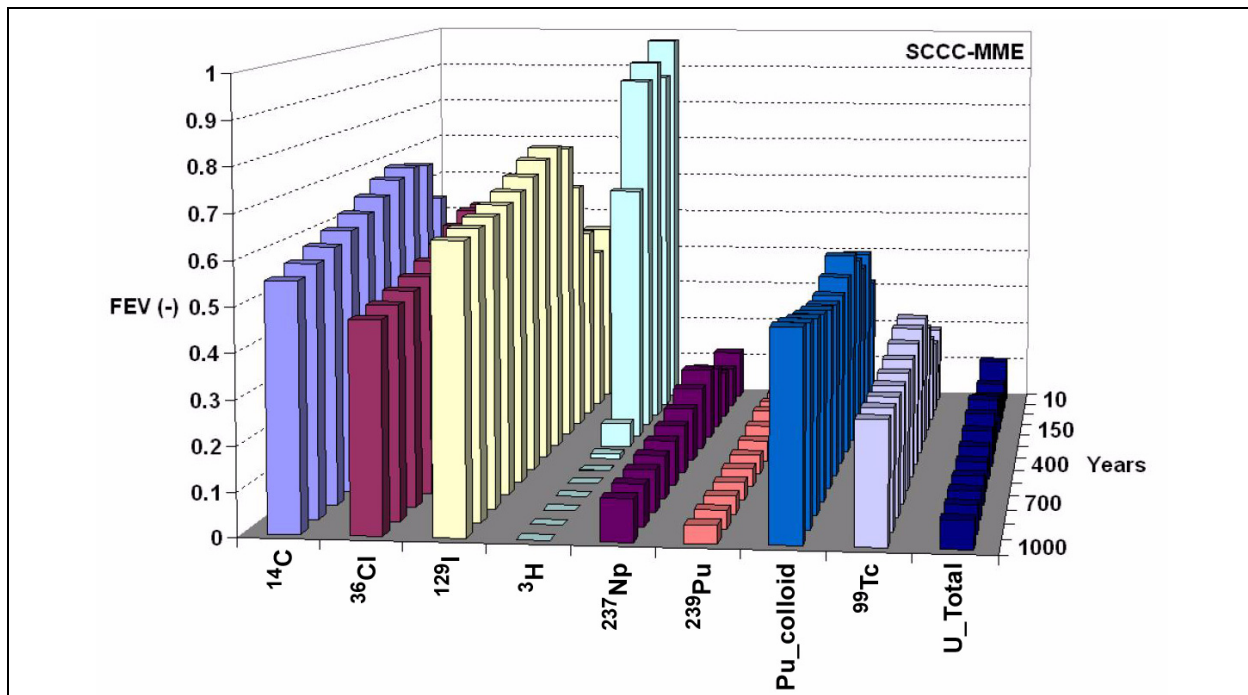


**Figure 7-27**  
**Fractional Exceedance Volumes Based on SCCC-MME Transport Simulation**

### 7.6.8 High-Dispersion Transport in Alternative Flow Models

A full Monte Carlo transport analysis was performed using a higher-dispersion scenario (longitudinal, transverse, vertical = 100 m, 10 m, 2 m) for the four LCCU1-based models. Section 6.4.4 reported the selection of a discrete set of dispersivity tensors for transport analysis. While this analysis was performed to assess the general impact of dispersivity on radionuclide migration, the rapid (i.e., within 50 years) transport associated with basin-scale preferential flow observed in several of the alternative models also motivated the analysis. It was hypothesized that the increased dispersion of radionuclides at Pahute Mesa would permit diffusive and sorptive (when applicable) mechanisms to more retard migration before entering zones of channelized flow primarily south of the Moat fault, thereby slowing migration rates.

Results showed that, contrary to expectation, the effect of higher dispersion was to increase migration rates throughout the domain, as well as to significantly increase the extent of the contaminated area as defined by MCL exceedance (Figure 7-28). Figure 7-29 shows the time at which at least 5 percent of realizations exceed an MCL for the four LCCU1-based alternative models (i.e., LCCU1-MME, LCCU1-MME-TMD, LCCU1-MME-TMCM, LCCU1-USGSD), with color contours depicting the

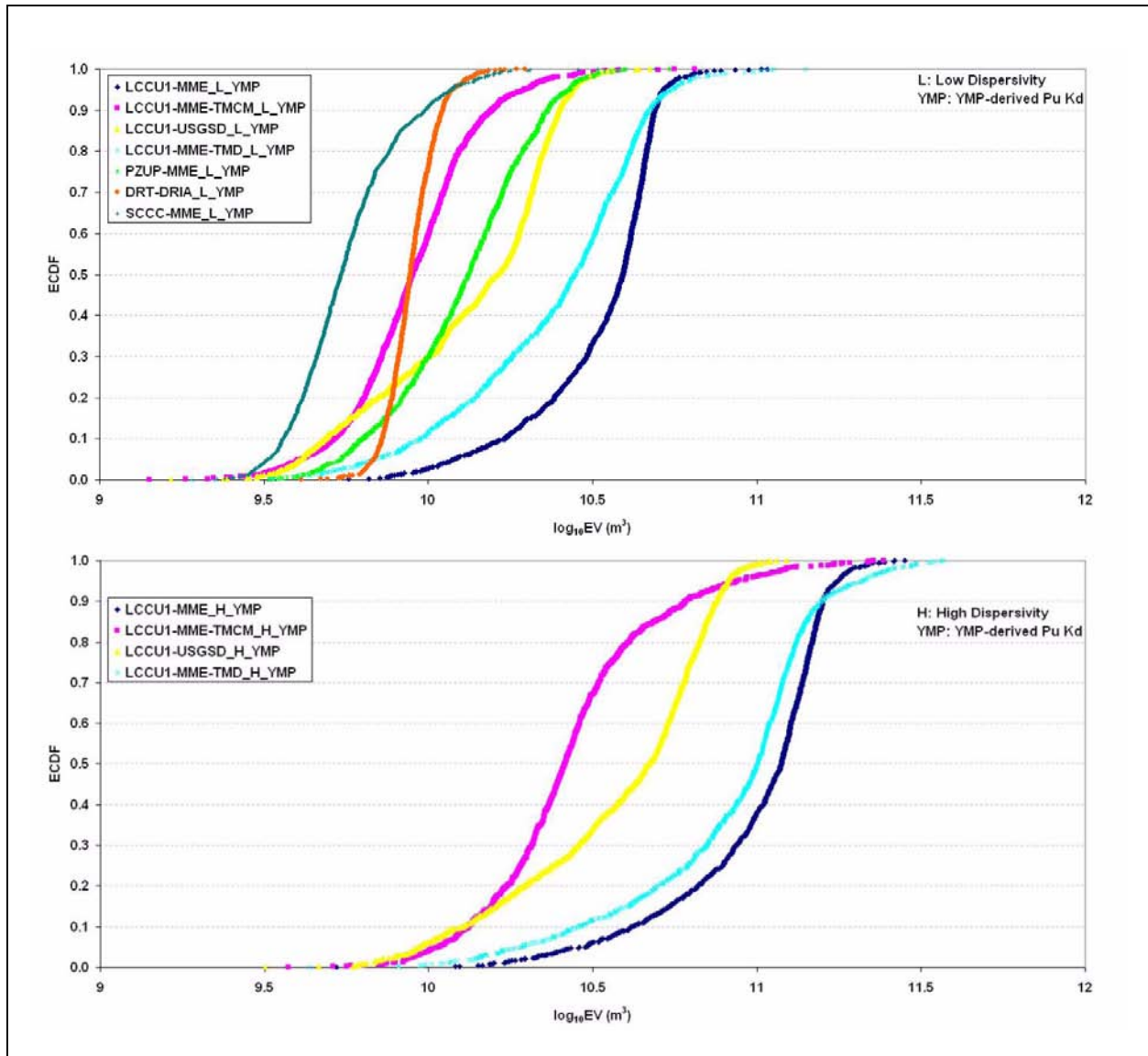


**Figure 7-28**  
**EV Cumulative Probability Distributions for the Alternative Transport Models**  
**Using the Low (top) and High-Dispersivity (bottom) Tensors**

time at which at least 5 percent of the realizations first exceed an MCL. In each model, transport rates to areas near Oasis Valley and Beatty Wash are greatly increased relative to the lower dispersion scenario. This effect is particularly noticeable in the LCCU1-MME-TMCM, which in the lower dispersion scenario did not have migration to the southwest of Timber Mountain until about 300 years (Figure 7-22). Larger longitudinal dispersivity, in concert with high fluxes along flow channels, cause particles (radionuclides) to move downgradient several nodes at a single point in time in the numerical model. Although radionuclide concentrations at individual nodes were consequently

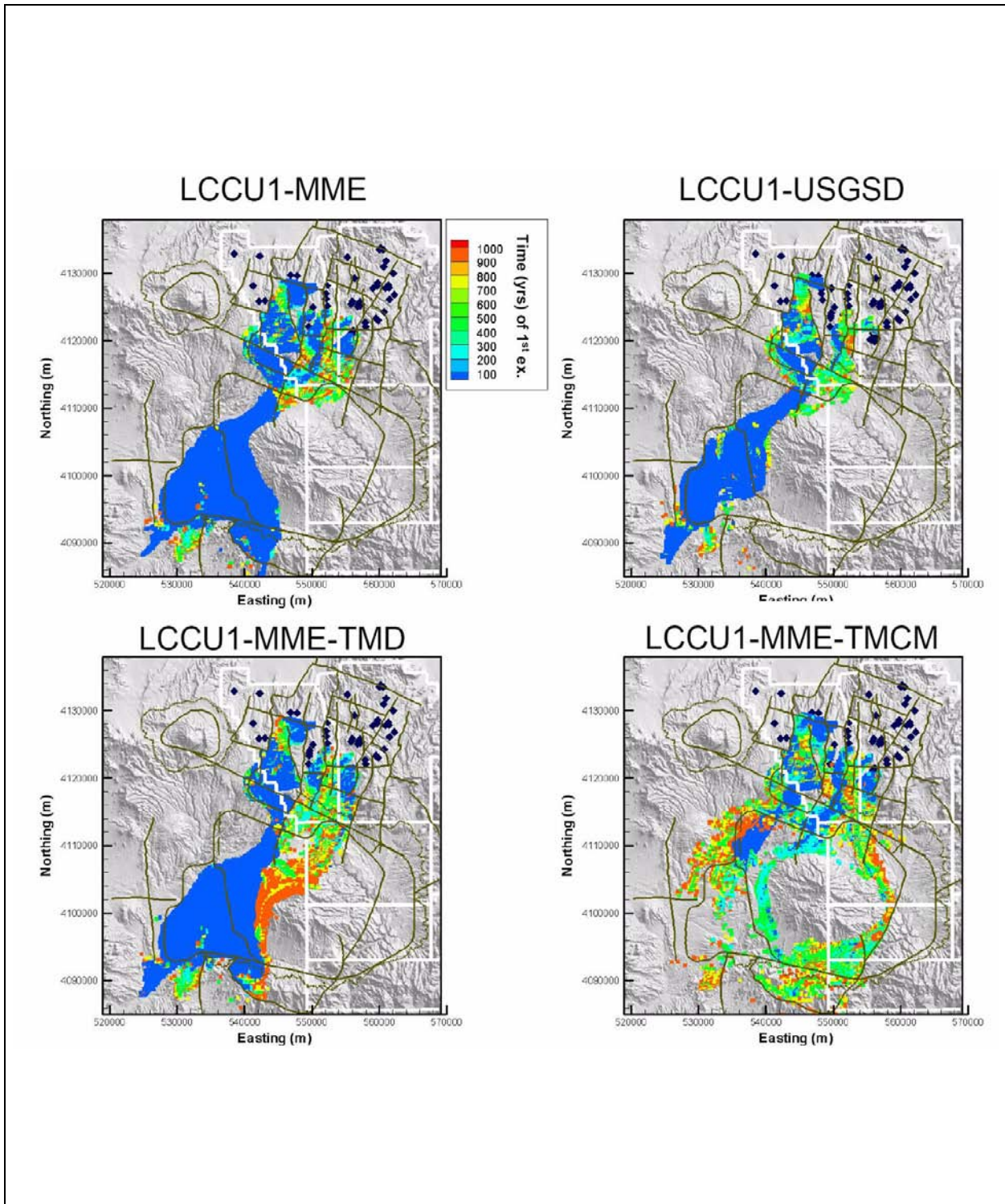


**Figure 7-29**  
**Probabilistic Exceedance Map for Four Alternative Transport Models**  
**Using the High-Dispersivity Tensor**

Note: The color contour per model node indicates the time at which at least 5 percent of Monte Carlo simulations exceed an MCL within a 1,000-year interval.



decreased, the combined effect of large source-release mass and (low) MCL standards nevertheless resulted in MCL exceedance along the extent of migration paths. Dispersion does not serve to reduce concentrations to below standards for these values.

The effect of larger dispersion in the transverse and vertical orientations is also evident. Comparison of the flow model EV ECDFs between the high- and low-dispersion scenarios indicates that the volume of contaminated areas (per realization) is significantly increased in the higher-dispersion flow models. [Figure 7-28](#) shows that the shift in medians between the low- and high-dispersivity ECDFs for respective transport models is between one-half and one order of magnitude, a range that is on the same order as the range of EV variability resulting from transport parameter uncertainty (i.e., within-distribution variability). Although the significance of the EV ECDFs is discussed in the next section, the above result depicts the dominant influence of dispersivity on radionuclide migration relative to the other transport parameters.

### **7.6.9 Integrated Transport Results**

Monte Carlo transport simulation was performed for six alternative, calibrated flow models (see [Table 3-4](#)) developed during the PM CAU flow model analysis (SNJV, 2006a). The alternatives span a large range of geologic (e.g., structure) and hydrologic (e.g., boundary flow rates) uncertainty. Of the six, five are variations of the base HFM, and one is constructed from the SCCC geologic conceptualization. Transport simulation was also performed for a seventh HFM named the LCCU1-MME-TMCM, developed during this analysis from the LCCU1-MME base alternative, to investigate the effect of hydraulic parameterization on transport.

Of the five base-derived alternatives developed during the flow modeling task, three modes of transport behavior became evident, reflecting the hydrostratigraphic, hydraulic, and material property variations among models that matter the most for transport. These modes involve the rate of radionuclide migration, the path of migration, and the relative contribution of individual species to the migration. The remaining two HFMs (SCCC-MME and LCCU1-MME-TMCM) showed considerably different behavior in radionuclide migration rates and paths; however, the predominant species contributing to transport did not differ from the others.

With the exception of the LCCU1-MME-TMCM, transport through all base-derived models is rapid and occurs along a similar, single path that is shown to be associated with material property differences between HSUs in the large model zones in concert with recharge spreading from Timber Mountain. In general, within 50 years from release, a single migration path exits Pahute Mesa through shallow fractured rock aquifers, migrating to the northwest of Timber Mountain, and then following the western flank of Timber Mountain south before arriving in the areas of Oasis Valley, Beatty Wash, or both. This characteristic behavior associated with the original flow models was presented in [Figures 7-7](#) (LCCU1-MME), [7-13](#) (LCCU1-USGSD), and [7-19](#) (PZUP-MME), and is explained from the combined effects of flow and transport parameterization and model zones.

The rapid and preferential transport simulated in these base-derived models is explained by the nature of the hydraulic properties. Particle release locations in southern Areas 19 and 20, are in a geologically complex area comprised of shallow volcanics (between about 500 m and 1000 m), with high-permeability fractured units intermingled with confining units. The model HSUs are defined as such, and flow and transport are rapid in this region as expected. However, south of the Moat fault transecting southern Areas 19 and 20, the majority of hydrostratigraphy is described as large (several km thick in all orientations) composite volcanic units. Because each HSU is assigned constant hydraulic properties, high permeability within these km-scale HSUs result in potentially large, high-velocity flow paths. The TMCM subdivisions, shown to host the primary transport paths, have calibrated permeabilities that are typically high, accommodating the recharge from Timber Mountain, flow off of Pahute Mesa, decreased transmissivity from pre-Tertiary uplift (of various extents depending on the HFM), and depth decay. Basin-scale high-flux zones through the TMCM HSU are demonstrated in [Figure 7-17](#) for the DRT-DRIA and LCCU1-MME models.

While the influence of flow conceptualization (i.e., HSU structure) and parameterization (hydraulic property definition) on transport is strong, the influence of transport parameterization is weaker. In the five base-derived models (again excluding the LCCU1-MME-TMCM from this line of reasoning), there is often greater than 90 percent probability that at least one radionuclide-group MCL is exceeded near Oasis Valley/Beatty Wash. Although the dispersion of the contaminated area varies considerably between transport parameter realizations, the southern extent of the area is almost always geographically similar within a model domain. This indicates that relative to the gross

behavior of some general contaminant boundary, transport parameters play a secondary role behind flow behavior for the base-derived models.

A quantitative comparison of the competing influence of flow characteristics versus transport parameterization on radionuclide migration is demonstrated by comparing EV probability distributions between flow models. [Figure 7-28](#) shows the EV ECDFs for all (seven) flow models considered in transport analysis. Variation between distribution medians has a maximum of about one order of magnitude between the LCCU1-MME and SCCC-MME HFMs, which is a direct consequence of the net groundwater flux through the shallower volcanics. The median shift is not considerable because the probabilistic exceedance maps for the LCCU1-MME ([Figure 7-7](#)) and SCCC-MME ([Figure 7-26](#)) both extend to Oasis Valley/Beatty Wash. Within-distribution variability, which reflects the influence of transport parameter uncertainty on the EV, ranges from about one-half to one order of magnitude if the central 90 percent of the distributions are considered. Rather than affecting the geographic location of a plume, EV distribution variability is a measure of plume dispersion. This result is demonstrated from the 50-year LCCU1-MME radionuclide plume shown at four levels of MCL-exceedance probability in [Figure 7-30](#). A time of 50 years was selected because migration is not yet affected by dilution and  $^3\text{H}$  decay ([Figure 7-6](#)). The first spatial moment of an exceedance map appears associated with flow model behavior while its second moment is associated with transport parameterization. Again, this result applies to the base-derived models, excluding the LCCU1-MME-TMCM, each of which demonstrated rapid and preferential transport to areas southwest of Timber Mountain.

It is appropriate at this point to make a distinction between the DRT-DRIA and all other alternative models. In the DRT-DRIA, the influence of high flux in channelized flow paths to the northwest of Timber Mountain was so strong that dilution prevented MCL exceedance at any model node downgradient of this area. Consequently, there is little sensitivity of radionuclide migration to transport parameters in this model. The combined influence of flow model conceptualization (e.g., recharge model) and parameterization (e.g., high permeability in connected TMCM subdivisions) overshadow the entire range of uncertainty in transport mechanisms.

The LCCU1-MME-TMCM flow model was developed to address the preferential flow paths highlighted in the other flow models ([Section 3.4.3](#)). Preferential flow was reduced by homogenizing TMCM subdivision permeabilities. The SCCC-MME alternative provided similar flow dispersion as

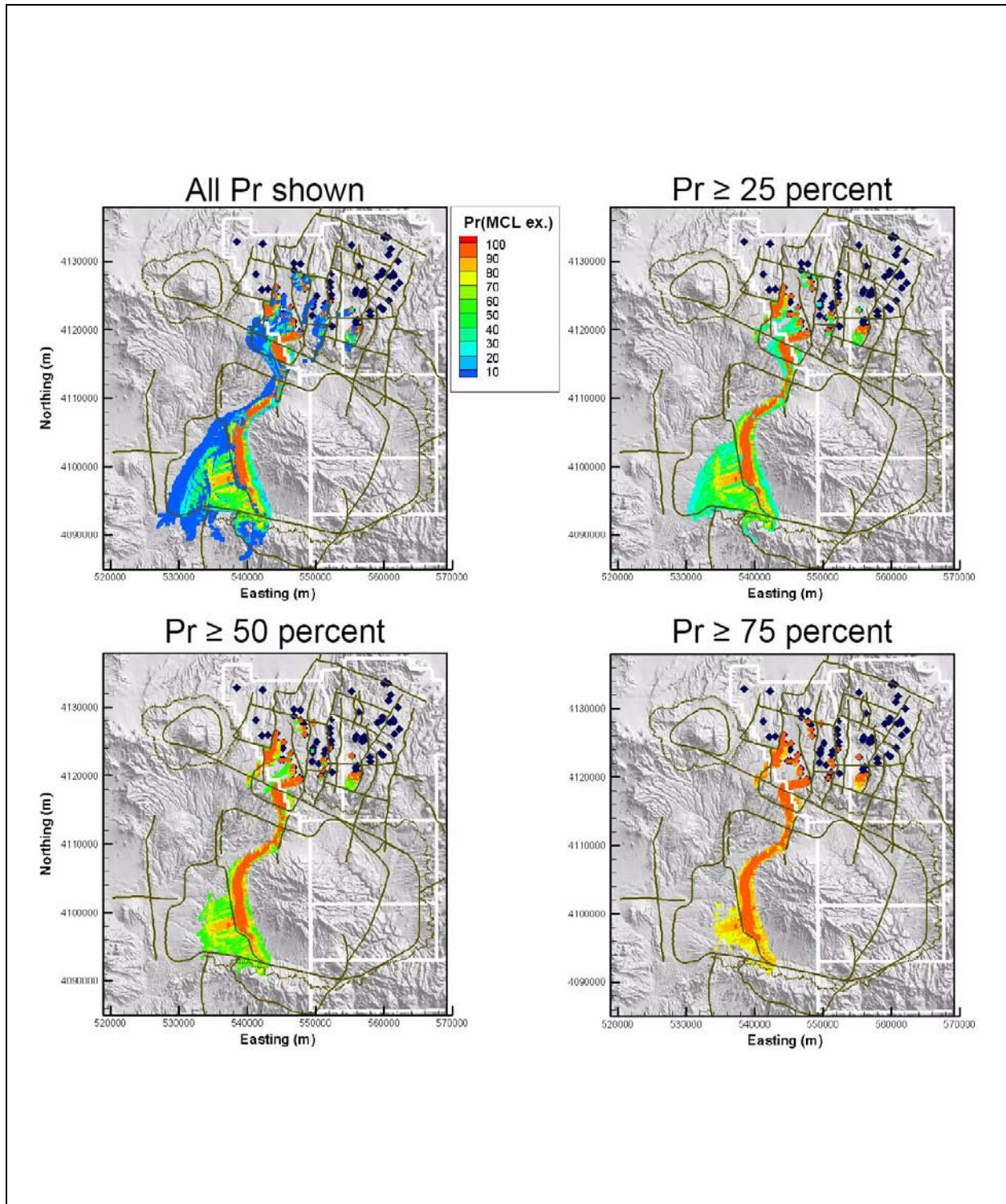


**Figure 7-30**  
**Probability of MCL Exceedance at Four Exceedance Thresholds for the LCCU1-MME Transport Model at 50 Years**

a result of its simplified, single-property hydrostratigraphy (Section 7.6.7). The two models reduce radionuclide migration rates and inhibit transport along a single path. Breakthrough at the Moat fault generally occurred after 200 to 300 years (Figures 7-22 and 7-26), and the probability of MCL exceedance is typically well below 50 percent at nodes south of the Moat fault (which could be a significant factor depending on the certainty level defined for some contaminant boundary).

Although migration still occurs along preferential flow paths, increased permeability homogenization in both models resulted in the development of multiple flow channels and, therefore, transport paths.

The persistence in preferential flow and transport in channels at material interfaces, despite the improved homogenization of permeability (LCCU1-MME-TMCM) and simplification of hydrostratigraphy (SCCC-MME), indicates that flow model zonation is a critical component of transport model behavior. Namely, all models are conceptualized as single-property HSUs which can provide km- to 10-km scale continuous pathways. An increase in boundary inflows or a decrease in transmissivity, both of which were incorporated across the alternative HFMs, only enhances the effect. The net result is that a lack in heterogeneity, between HSUs (i.e., hydrostratigraphy) and within HSUs (i.e., properties), results in preferential flow and transport.

While the above summary describes how the rates of radionuclide migration and migration paths differ between models, the FEV analysis shows that the radionuclide contribution to MCL exceedance areas, regardless of the extent of an area, is generally insensitive to flow behavior. This is partially a result of the categorical nature of the FEV, which is based on MCL exceedance thresholds. That is, any influence of transport processes on plume development once an MCL is exceeded is lost. The similarity of FEVs across models, regardless of the extent of migration, indicates that the radionuclide contribution to plumes is based principally on the total mass release per radionuclide. The source term model applied at cavities distributes the same proportion of radionuclides to each cavity-volume of water across all models; therefore, the low- and high-flux models have proportionately lower and higher mass release.

When considered collectively, transport model behavior demonstrates that the effects of preferential flow determine the degree of sensitivity of radionuclide migration to transport parameters. For example, the DRT-DRIA exemplifies one end-member in that high-flux channelization generally prevents MCL exceedance, thereby denying sensitivity to transport parameters. At the other end, the LCCU1-MME-TMCM and SCCC-MME models showed that the extent of radionuclide migration off

of Pahute Mesa is strongly associated to transport mechanisms. In the context of regulatory-based transport, it can also be demonstrated that the effects of preferential flow determine the degree of sensitivity of radionuclide migration, now in the form of an exceedance map, to the level of certainty with which an exceedance map perimeter is defined. That is, depending on the flow behavior of a model, a stochastically derived exceedance map may or may not be sensitive to the level of certainty. This point is exemplified in [Figure 7-31](#), which shows, for the LCCU1-MME and LCCU1-MME-TMCM models, the 1,000-year time-invariant exceedance map at three levels of certainty, with certainty defined by the probability of MCL exceedance relative to the full Monte Carlo analysis. In the LCCU1-MME, a high-flux model with a single basin-scale preferential flow path, the general behavior of the exceedance map perimeter is insensitive to the level of certainty defined. The boundary consistently reaches areas southwest of Timber Mountain. Conversely, in the LCCU1-MME-TMCM, the map appreciably changes in extent with the level of certainty defined. This result depicts that the sensitivity of regulatory-based transport behavior is a relative term that must be considered in relation to conceptualization and parameterization of the flow model, and also to the level of certainty (relative to MCL exceedance) considered acceptable.

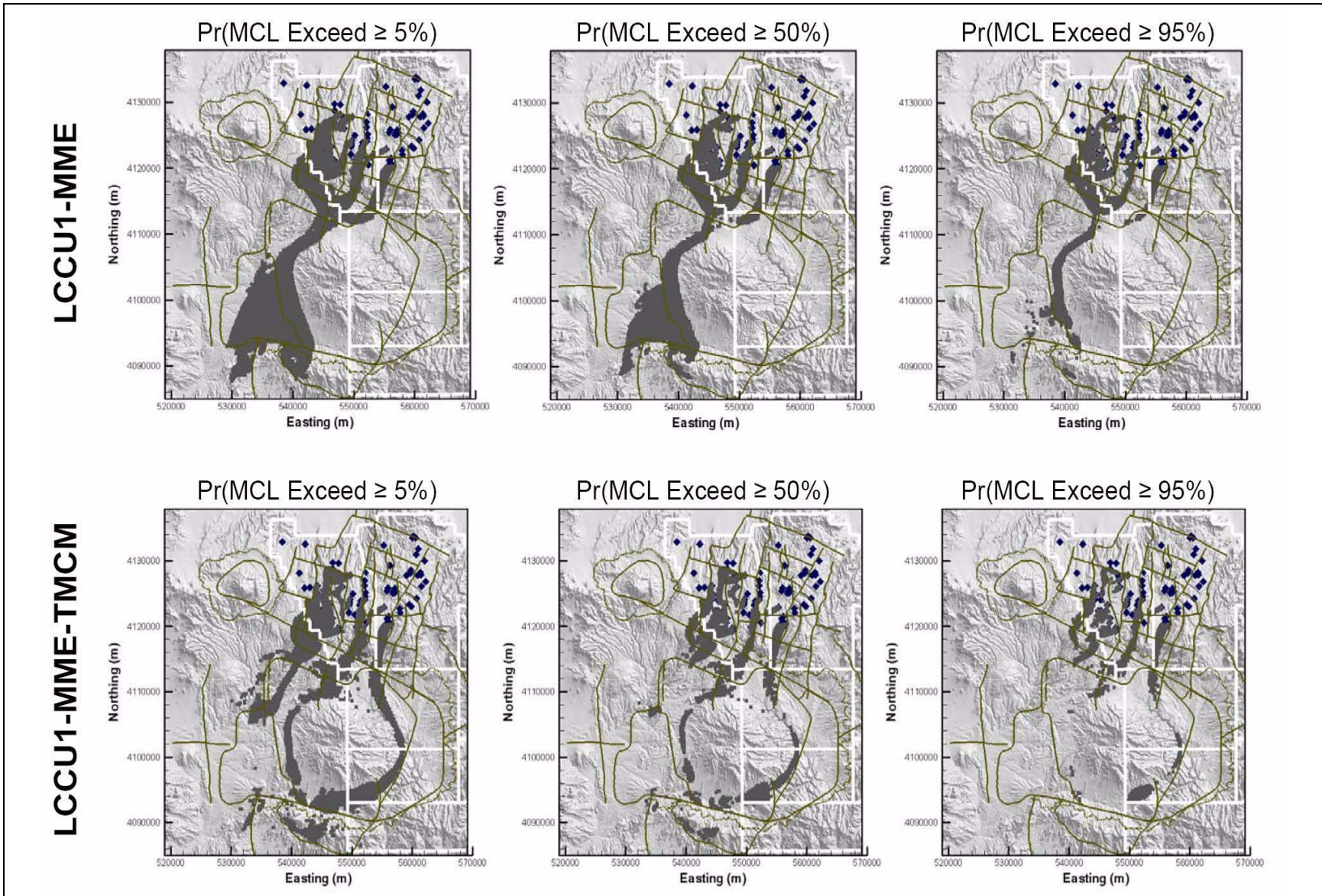


**Figure 7-31**  
**1,000-Year Time-Invariant Exceedance Map at Three Certainty Levels, with Certainty Represented by the Probability of MCL Exceedance, for the LCCU1-MME and LCCU1-MME-TMCM Transport Models**

## **8.0 TRANSPORT PARAMETER UNCERTAINTY AND SENSITIVITY ANALYSIS**

Sensitivity analyses were performed for both flow and transport processes. Three global sensitivity analysis methods were used to gauge the sensitivity of process response to input parameter variability: (1) classification tree, (2) maximum entropy analysis, and (3) linear stepwise regression. Classification tree is a categorical approach that identifies the extreme ends of a behavior. Maximum entropy analysis provides a measure of mutual information and can be applied to non-monotonic, nonlinear problems. Stepwise regression provides a measure of the response sensitivity to each input parameter. This approach is limited to monotonic and linear systems. Sensitivity analysis for each of the seven HFMs was performed using each of these analysis methods, from which the most sensitive inputs were identified. Results for all HFMs and each analysis method were then composited. Evaluation of the results led to grouping of HFMs into two conceptually different transport regimes. Flow model insensitivity was evaluated through the process of Null Space Monte Carlo (NSMC) analysis. Null space analysis for 10 Monte Carlo realizations demonstrated a range of behaviors that were indicative of the variability in transport behavior observed for different conceptual models. Consequently, flow parameterization not only affects sensitivity but also conceptual uncertainty. Additional uncertainty analysis was performed to assess the effect of depth decay and dispersion on plume development. The depth-decay factor controls reduction of permeability with depth. Reducing depth decay was shown to reduce the extent of the EV. Increasing dispersivity was expected to lead to decreasing EV through dilution. However, results showed that the contaminant levels were high enough in the plumes that increasing dispersion caused increasing EV.

### **8.1 Introduction**

The methods by which the Pahute Mesa transport analysis was performed, as explained throughout this document, adhere to a systematic framework that acknowledges uncertainty in both the conceptualization and parameterization of the PM CAU transport model. Transport parameter sensitivity analysis, the subject of this section, is therefore presented in the context of uncertainty in



model conceptualization and parameterization. Regarding the former, the more fundamental of the two, multiple alternative HFMs provide the flow fields on which transport is based. Each flow field provides an alternative (and hypothetically equiprobable) conceptualization of flow, and therefore transport, behavior based on (hydro)geologic considerations and assumptions. Sensitivity analysis is performed for each alternative. Regarding the latter, the influence of parameter uncertainty on sensitivity analysis, this section shows how the sensitivity methods applied capture the influence of parameter uncertainty as it is propagated through the model. Such methods assume a global, as opposed to local, approach that permits the full range of input-output relationships to be assessed.

## **8.2 Global Sensitivity Analysis**

As elucidated by Mishra (2007), what is referred to as “sensitivity analysis” might also be termed “uncertainty importance assessment,” which in this case entails the identification of transport parameters that have the greatest influence on output uncertainty. Sensitivity analysis is the last of three components of model uncertainty assessment, each of which has a direct counterpart in the framework of the PM CAU transport model. The first two components, uncertainty characterization and uncertainty propagation, fall under the general category often referred to as uncertainty analysis. Uncertainty characterization essentially involves the definition of probability models for input parameters, where the degree of uncertainty is related to some measure of a distribution's variability. [Section 5.4](#) of this report discussed the definition of such a model for each transport parameter. Uncertainty propagation involves the translation of input parameter uncertainty to model output uncertainty. [Section 7.3.3](#) presented the EV, a scalar surrogate for the contaminant boundary, which defines the transport model output metric. Over multiple realizations, a discrete EV probability distribution is defined from which model output uncertainty is assessed. The third and final component of modeling uncertainty is uncertainty importance assessment, or (global) sensitivity analysis, which is the topic of this section.

As stated, the goal of sensitivity analysis is to determine the key transport parameter(s) driving transport behavior, in one context or another. Global sensitivity analysis techniques are used for investigating input-output sensitivities that are valid over the entire range of possible parameter variations and not just at or near the reference point (Saltelli et al., 2000). The starting point for global sensitivity analysis is the selection of a strategy for exploring the entire parameter space over

which model calculations will be performed. Section 6.3 presented the approach adopted, a Monte Carlo-simulation-based uncertainty analysis methodology using Latin hypercube sampling (McKay et al., 1979) from each transport parameter distribution. The restricted pairing technique (Iman and Conover, 1979) was used to force zero correlation between all variable pairs.

The Monte Carlo approach provides  $N$  realizations of input (transport) parameter sets that permit discrete uncertainty characterization. Each realization is propagated through the transport simulator to yield  $N$  EV values, the output metric used to characterize transport behavior. This is uncertainty propagation. Global sensitivity analysis entails the comparison of the EV distribution to each of the transport parameter distributions. Here, it is important to note two properties of the global sensitivity methods applied. First, global methods rather than local methods are applied because the latter provide information regarding the relative sensitivities of input parameters valid only in the vicinity of the reference point. That is, the validity of local sensitivity methods would require a linear relationship between input and output over the entire range of input values, a property far from being realized in this case. The global methods applied are generally valid for any (nonlinear non-monotonic) input-output relationship, as will be discussed. Second, the global methods applied inherently consider both the uncertainty in the input variable and the sensitivity of output to input. Therefore, those parameters identified as most sensitive generally have large uncertainty (i.e., large variance) and strongly influence the value of the EV (i.e., large sensitivity coefficient).

Three sensitivity analysis methods are used to analyze the sampling results: stepwise linear regression, mutual information (entropy), and classification tree analysis. Although several methods are available for global sensitivity analysis (e.g., Saltelli et al., 2000), analyzing input-output relationships for a non-monotonic output (i.e., quadratic objective function) requires special consideration. As shown by Mishra and Knowlton (2003), entropy (mutual information) analysis is particularly useful for determining the strength of input-output association for any general non-linear non-monotonic relationship, whereas commonly used sensitivity analysis techniques such as stepwise rank regression are known to fail under such conditions. A second issue is the determination of decision rules that identify which variables or combinations of variables lead to extreme values of the EV distribution. Classification tree analysis has been shown to be a useful tool for analyzing such categorical problems (Mishra et al., 2003).

### 8.2.1 Classification Tree

Classification tree analysis can provide useful insights into what variable or variables are most important in determining whether outputs fall in one particular category. Categories are generally based on meeting some acceptable threshold (e.g., pass versus fail, fit versus misfit).

A binary decision tree is at the heart of classification tree analysis. The decision tree is generated by recursively finding the variable splits that best separate the output into groups where a single category dominates. The degree by which a single category dominates is called the split “purity.” For each successive fork of the binary decision tree, the algorithm searches through the variables one by one to find the purest split within each variable. The splits are then compared among all the variables to find the best split for that fork. The process is repeated until all groups contain a single category, or until a specified level of purity is reached for all groups. In general, the variables that are chosen by the algorithm for the first several splits are most important, with less important variables involved in the splitting near the terminal nodes of the tree.

The tree-building methodology used here is based on a probability model approach. Classifiers at each node are selected based on an overall maximum reduction in impurity for all possible binary splits over all the input variables. The impurity at a given node A ( $I_A$ ) is based on the Gini index:

$$I_A = 2\rho_{1A}\rho_{2A} \quad (8-1)$$

where  $\rho_{1A}$  and  $\rho_{2A}$  are the estimated probabilities of classes 1 and 2, respectively, at node A. The probabilities are estimated from the proportion where  $n$  is the number of observations in a class at a node by:

$$\rho_{1A} = \frac{n_{1A}}{n_A} \quad (8-2)$$

where  $A$  is the total number of observations at node A, and  $1A$  is the proportion belonging to class 1.

The decrease in impurity for a given split of node A into nodes L and R (left and right) is:

$$\Delta I = I_A - \rho_L I_L - \rho_R I_R \quad (8-3)$$

where  $\rho_L$  and  $\rho_R$  are the proportions of the cases that go to L and R, respectively.

The classification tree is built by successively taking the maximum reduction in purity over all the allowed splits of the branch to determine the next split. Termination occurs when the number of cases at a node drops below a set minimum, or when the maximum possible reduction in purity for splitting a particular node drops below a set minimum.

As an example, Figure 8-1 shows the results of a classification tree analysis to variable EV. Here, the category “low” refers to the smallest 10 percent EV values, and the category “high” refers to the largest 10 percent EV values. Each node of the classification tree is labeled with the numbers of each category that have been assigned to that node, with the number of high values comprising the first and the number of low values comprising the second.

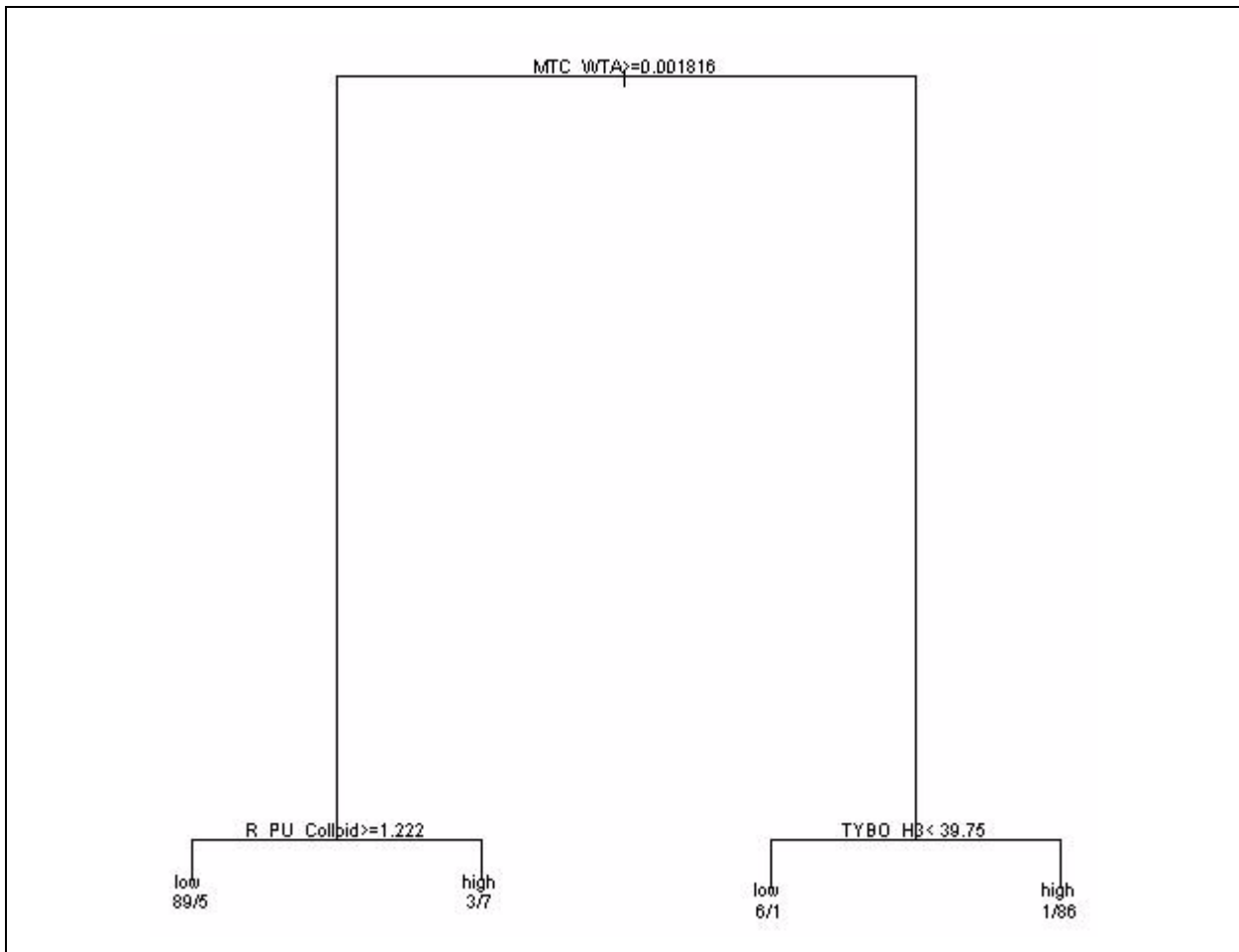


**Figure 8-1**  
**Classification Tree Analysis for LCCU1-MME**

Tree-based models are attractive because: (1) they are adept at capturing non-additive behavior, (2) they can handle more general interactions between predictor variables, and (3) they are invariant to monotonic transformations of the input variables. These attributes make classification trees more suitable for input-output modeling as compared to regression analysis, which is restricted to a linear (or linearized) input-output relationship and where the function for the relationship has to be specified *a priori*.

### 8.2.2 Entropy Analysis

The information-theoretic concept of entropy is a useful metric for the characterization of uncertainty (or information) in the univariate case, and redundancy (or mutual information) in the multivariate case (Press et al., 1992). The concept of mutual information has been used to select key input variables in neural network-based input-output modeling (Bonnländer and Weigand, 1994). Because mutual information is a natural measure of input variable relevance, it is also being used as an indicator of variable importance in many areas of science (Moddmeijer, 1989).

The following theoretical discussion is based on Press et al. (1992). Let the input variable  $x$  have  $I$  possible states (labeled by  $i$ ), and the output variable  $y$  have  $J$  possible states (labeled by  $j$ ). The possible states are represented by a quantile plot, which is an empirical form of the CDF. This metric characterizes the probability that a random variable is smaller than some specified value.

To construct a quantile plot, the data are first ranked in ascending order from smallest ( $X_1$ ) to largest ( $X_n$ ) for the  $i$ -th sample of  $N$  total samples. The quantile (cumulative frequency) is determined as  $q_i = i/(N+1)$ . For the entropy analysis, the samples are assigned to five equally probable bins that represent a quintile (e.g., each bin represents 20 percent of the total).

The probability of outcomes corresponding to both states  $x_i$  and  $y_j$  is  $\rho_{ij} = N_{ij}/N$ , where  $N_{ij}$  denote the number of events occurring when  $x$  takes its  $i$ -th value and  $y$  takes its  $j$ -th value. Let  $N_i$  denote the number of events for which  $x$  takes its  $i$ -th value regardless of the value of  $y$ ; similarly, let  $N_j$  denote the number of events with the  $j$ -th value of  $y$  regardless of  $x$ . The probability of outcomes corresponding to state  $x_i$  alone is:  $\rho_i = N_i/N$ , and the probability of outcomes corresponding to state  $y_j$  alone is:  $\rho_j = N_j/N$ .

The mutual information between  $x$  and  $y$ , which measures the reduction in uncertainty of  $y$  due to knowledge of  $x$  (or vice versa), is defined as:

$$I(x, y) = -\sum_i \sum_j \rho_{ij} \ln \left( \frac{\rho_{ij}}{\rho_i \rho_j} \right) \quad (8-4)$$

Here  $\rho_{ij}$  is the probability outcomes corresponding to both states  $x_i$  and  $y_j$ , while  $\rho_i$  is the probability outcome of state  $x$  alone and  $\rho_j$  is the probability outcome of state  $y$  alone.

The  $R$ -statistic has been proposed as a measure of association based on the concept of entropy or mutual information as follows (Granger and Lin, 1994):

$$R(x, y) = [1 - \exp\{-2I(x, y)\}]^{1/2} \quad (8-5)$$

$R$  takes values in the range  $[0,1]$ , with values increasing with  $I$ .  $R$  is zero if  $x$  and  $y$  are independent, and is unity if there is an exact non-linear relationship between  $x$  and  $y$ . It can also be shown that if  $x$  and  $y$  have a bivariate normal distribution with correlation  $\rho$ , then  $R = |\rho|$  (Cover and Thomas, 1991).

The entropy-based measure  $R$ -statistic can thus be recognized as a very general tool for quantifying the strength of an association. It is applicable to both linear/non-linear and monotonic/non-monotonic relationships, whereas commonly used regression-based measures are restricted to linear and monotonic associations only.

This information can also be compactly organized in terms of a contingency table – a table whose columns are labeled by the values of the independent variable,  $x$ , and whose rows are labeled by the values of the dependent variable,  $y$ . The entries of the contingency table are non-negative integers giving the number of observed events for each combination of row and column.

The contingency table can also be visualized using a “bubble plot,” where the entries of the contingency table are shown as bubbles of varying sizes. Here, the contingency table is organized such that the quintiles of the independent variable (input) increase from left to right, and that of the dependent variable (output) increase from bottom to top. The size of the bubble indicates how many observations fall in each quintile-quintile box.

The notation listed below to describe the assignment of each quintile is taken from Press et al. (1992). The expected number of observations of the  $N_{ij}$  is calculated from row and column totals:

$$n_{ij} = E[N_{ij}] = \frac{(N_{i\cdot} \cdot N_{\cdot j})}{N} \quad (8-6)$$

$$\chi^2 = \sum_{i,j} \frac{(N_{ij} - n_{ij})^2}{n_{ij}} \quad (8-7)$$

A chi-square test is used to determine whether or not the association between input and output variables is non-random. The chi-square statistic is calculated by summing over the difference between observed and expected entries for each binned input-output combination in the table. The larger the chi-square value, the higher the correlation between the dependent and independent variables.

The chi-square probability is the chance that the observed  $\chi^2$  will exceed the calculated value by chance even for a correct model. Therefore, probabilities approaching zero identify a non-random association.

### 8.2.3 Stepwise Regression

The stepwise regression model performs a forward regression such that at each step in the process a parameter is sequentially added to the model starting with the parameter that is most likely to reduce the variability in the model output. In each subsequent step, the next most significant parameter is added to the preceding parameter(s) such that output variance is maximally reduced at each step. The stepwise regression model assumes that the input/output relationship is linear and, therefore, can be fit to the regression model of the form:

$$\hat{y} = b_o + \sum_{j=1}^p b_j x_j \quad (8-8)$$

where  $y$  is the rank-transformed output result,  $x$  is the rank-transformed input variable, and  $b$  is the normal regression coefficient. The  $o$  subscript corresponds to the point where the regression line intercepts the output axis ( $y$ ) and the  $j$  subscript identifies the input variable among all possible variables. For the standardized form of this equation,  $b_o$  reduces to zero. Standardization is necessary

to achieve a direct comparison of the regression coefficients. The standardized regression coefficient (SRC) is used to measure the uncertainty importance and is defined as:

$$SRC = \frac{b_j \sigma(x_j)}{\sigma(y)} \quad (8-9)$$

$$PCC^2(Y, X_{p+1}) = \frac{(R_{p+1}^2 - R_p^2)}{(1 - R_p^2)} \quad (8-10)$$

where  $b_j$  is the normal regression coefficient for the  $j$ -th variable, and  $\sigma(x_j)$  and  $\sigma(y_j)$  are the standard deviation of the input and output, respectively. The square of the SRC ( $R^2$  loss) is approximately equal to the  $R^2$  loss.

The partial correlation coefficient (PCC) is an indication of the strength of a linear relationship between input/output pairs after eliminating the influence of other linear input variables.

#### 8.2.4 Sensitivity Analysis, Transport Parameters, and HFMs

Sensitivity analysis is performed by observing the response of the output given the variability in the input parameters. For this analysis, the output response function is represented by the EV, and the input is a list of transport parameters that are sequentially compared with the EV. There are 35 possible input parameters that when varied may elicit a response from the EV. Of those 35, only 10 will be identified as having any significant affect on the EV. The 10 parameters are listed in the following text in abbreviated form. The abbreviation and the full text explanation are listed in [Table 8-1](#).

The parameter values used to test the EV response are of two categorical types: (1) transport parameters and (2) inventory parameters. Examples of transport parameters include the mass transfer coefficient, effective porosity, and  $K_d$ . These parameters are further divided into properties based on HGU's (WTA, VTA, TCU, LFA). The second category of parameters is the inventory parameters. These correspond to the total time-released inventory for three radionuclides ( $^3\text{H}$ ,  $^{36}\text{Cl}$ ,  $^{14}\text{C}$ ). The three radionuclides selected are those that contribute significantly to model sensitivity. The variability of this parameter is sampled only for the TYBO test. The TYBO test is selected because it is a large test at the southwestern Pahute Mesa/NTS boundary and is located within a



**Table 8-1  
Input Parameters**

Abbreviation	Description
MTC_WTA	Mass Transfer Coefficient for Welded-Tuff Aquifer
EFFPOR_WTA	Effective Porosity for Welded-Tuff Aquifer
EFFPOR_TCU	Effective Porosity for Tuff Confining Unit
EFFPOR_VTA	Effective Porosity for Vitric-Tuff Aquifer
R_Pu_Colloid	Reduction Factor for Pu-Colloid
TYBO_H3	<sup>3</sup> H inventory (TYBO)
TYBO_Cl36	<sup>36</sup> Cl inventory (TYBO)
TYBO_C14	<sup>14</sup> C inventory (TYBO)
FRAC_DMP/R	Fracture Aperture Devitrified Mafic Poor/Rich
K <sub>d</sub> _NP_ZEOL	K <sub>d</sub> for Neptunium in Zeolite

high-permeability, fractured HSU. Therefore, it possesses a great risk of contributing contaminant mass to any downgradient receptor.

The sensitivity analysis is performed on seven variations of the HFM:

- LCCU1-MME
- LCCU1-MME-TMD
- LCCU1-MME-TMCM
- LCCU1-USGSD
- PZUP-MME
- DRT-DRIA
- SCCC-MME

The prefix and suffix for each of these conceptual models are defined in [Section 3.0](#). As previously defined, the prefix of the model represents the conceptual hydrostratigraphic configuration, and the suffix identifies the recharge model used.

The recharge cases are the Modified Maxey-Eakin (MME), distributed watershed model (USGSD), and a chloride flux mass balance with alluvial mask (DRIA). The permeability changes made to the LCCU1 HFM are (1) increasing the TMD permeability by a factor of 100 and (2) modifying the permeabilities to the subunits of the Timber Mountain composite units as well as the FCCU and the FCCM. This model is designated by the suffix, TMCM. The MME recharge is used for all LCCU1 HFMs in this study, except for the USGSD. The transport model fluid fluxes used for each of the seven HFMs are derived from separately calibrated, steady-state flow models.

### 8.2.4.1 LCCU1-MME

The classification tree analysis explores the categorical response of the EV to individual transport parameter distributions. The output response of the EV at the upper and lower deciles of the distribution is compared to the variability of the input parameters. The inputs are evaluated to determine the parameter and its values that provide the best split of high and low EVs. For the LCCU1-MME case, the best split occurs for three parameters as shown in [Figure 8-1](#). The MTC\_WTA is the most important of the parameters. The next two splits are for TYBO\_H3 on the upper decile and for R\_Pu\_Colloid on the lower decile. This tree exhibits a 5 percent misclassification after three splits (e.g.,  $(5+3+1+1)/(89+7+6+86)$ ) listed at the end of each split in [Figure 8-1](#)).

Entropy analysis is used to determine the strength of association between the input variable and output response. For the multivariate case addressed here, a measure of the importance on the basis of mutual information is defined by the R-statistic. The ranking by entropy analysis is shown in [Table 8-2](#). The top three ranked parameters are MTC\_WTA, EFFPOR\_WTA, and TYBO\_H3, respectively. The R statistic shows that the first and second parameter shows a significant association while the remaining parameters are less pronounced. This association can also be seen in the bubble plots of the top four parameters in [Figure 8-2](#). The origin is at the lower left corner such that EV increases upward, and the parameter value increases from left to right. For the MTC\_WTA plot, as the input variable (MTC\_WTA) increases, the output variable (EV) decreases. That is, as mass transfer increases, the size of the EV decreases. This response is reasonable and implies that mass diffusion into the matrix reduces plume migration and, therefore, its size. In the second plot, as effective porosity in the WTA increases, so does the EV. Because larger porosity implies lower groundwater velocity and less migration, the indirect relationship between WTA effective porosity and EV indicates that the enlargement of fracture apertures limits diffusion, thereby permitting enhanced migration and enlargement of the EV. This would suggest that diffusive mechanisms are important to plume migration in the LCCU1-MME. Although the R-statistics for TYBO\_H3 and EFFPOR\_TCU are not as strong, [Figure 8-2](#) shows that there is a perceived increase of EV with an increase of TYBO\_H3, and a decrease of EV with increase of TCU effective porosity. It makes sense that as the total mass of  $^3\text{H}$  increases, so should the EV. The effect of increasing effective porosity of the TCU is opposite to that of the WTA. This is because the primary porosity of the TCU is not fracture porosity, but matrix porosity. Therefore, as porosity increases, so does mass transfer.

**Table 8-2**  
**Ranked Entropy Analysis for LCCU1-MME**

Entropy Analyses		Chi-Square Analyses		
Rank	Variable	R-statistic	Chi-Square	Probability
1	MTC_WTA	0.617316	513.25	0
2	EFFPOR_WTA	0.539836	340.95	0
3	TYBO_H3	0.324077	106.65	1.89E-15
4	EFFPOR_TCU	0.283895	83.4	4.04E-11

Comparison of the preceding results show that classification tree and entropy analysis rank the most important parameter as MTC\_WTA. TYBO\_H3 is second most important from classification tree analysis and third for the entropy analysis. R\_Pu\_colloid, which is the third split for the classification tree, is fifth in importance for entropy analysis.

Stepwise regression analysis was also performed on the input-output data. This analysis identifies those parameters that contribute, in descending order of importance, to output variability through a rank-transformed linear model. For the LCCU1-MME, the top three parameters are MTC\_WTA, TYBO\_H3, and FRAC\_DMP/R. The first two parameters are consistent with observations from classification tree and entropy analysis. The measure of uncertainty importance is represented by the standard regression coefficient in Table 8-3. The square of the SRC is the fractional contribution of variance to the model as each parameter is added. It is expressed as the variance loss (approximately R<sup>2</sup> loss) if a parameter were to be removed from the model. The effect of adding the variance of each parameter to the model is shown in Figure 8-3. In the instance that variables are correlated, the PCC quantifies the strength of the linear relationship between input-output pairs after eliminating the linear influence of these other variables from the output (Mishra, 2007). A total number of eight parameters were identified for variance reduction for the LCCU1-MME case. The total R<sup>2</sup> contribution is 0.48, which suggests there is not a strong linear correlation between the parameters and EV.

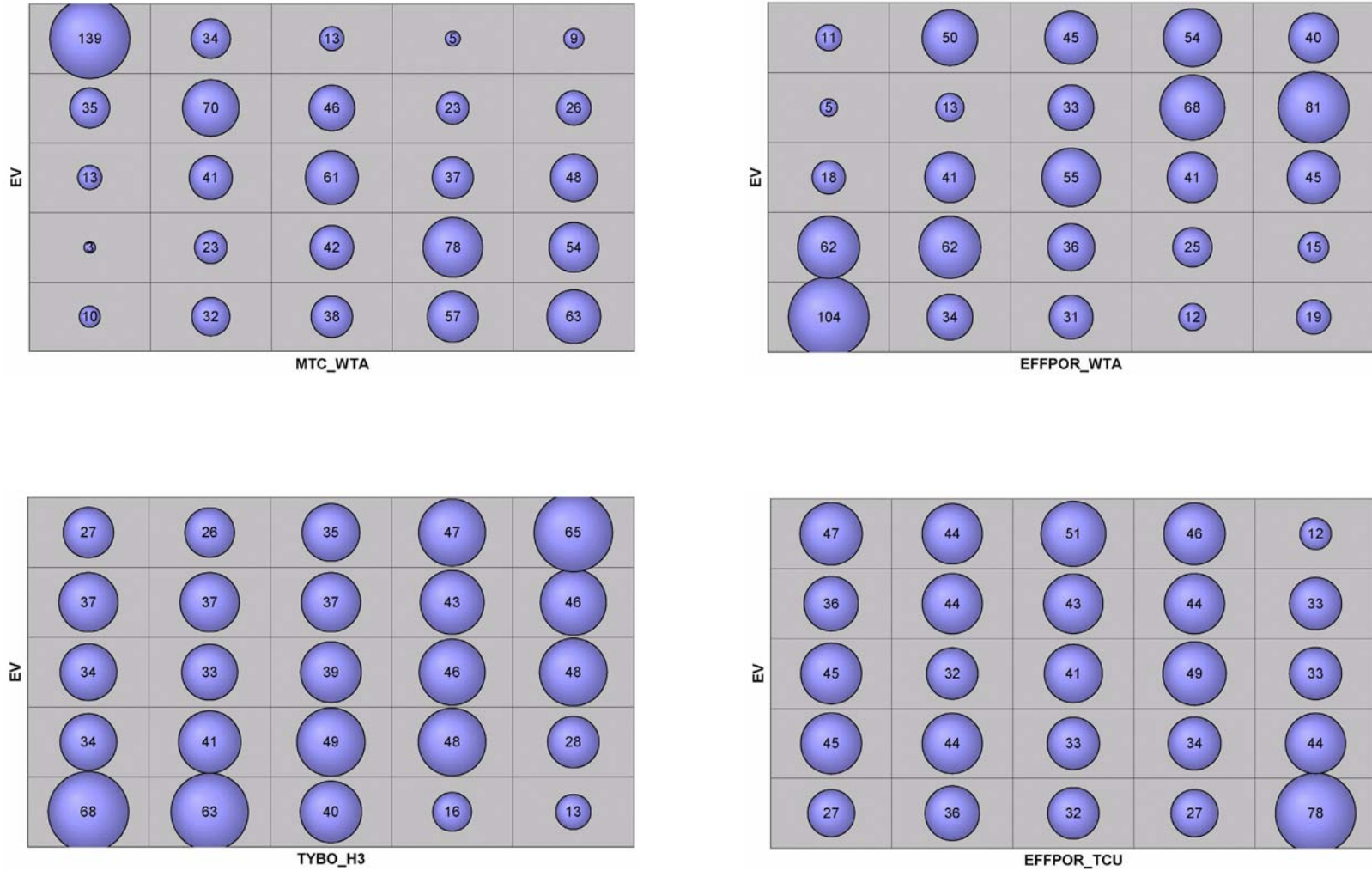


**Figure 8-2**  
**Bubble Plots from Entropy Analysis for LCCU1-MME**

**Table 8-3**  
**Ranked Stepwise Regression Analysis for LCCU1-MME**

Stepwise Regression		SRC	R <sup>2</sup> Loss	PCC
Rank	Variable			
1	MTC_WTA	-0.731	0.1478	-0.47
2	TYBO_H3	0.305	0.0902	0.384
3	FRAC_DMP/R	-0.221	0.033	-0.244
4	R_Pu_Colloid	-0.173	0.0297	-0.232

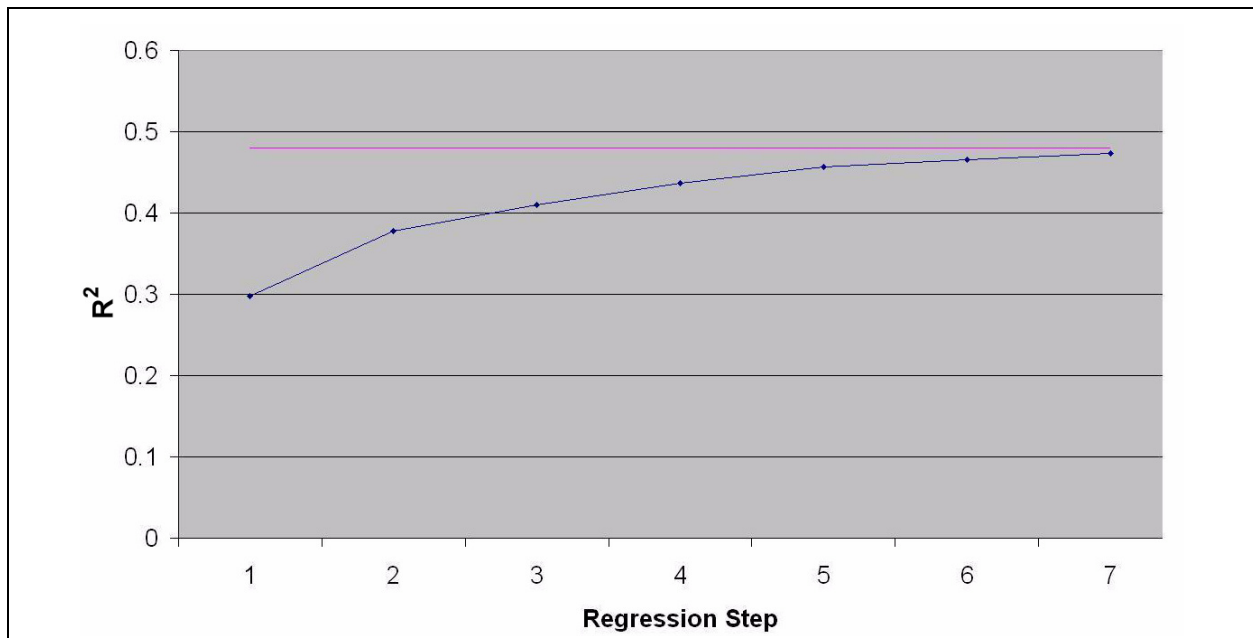


**Figure 8-3**  
**Stepwise Regression Analysis Plot for LCCU1-MME**

#### 8.2.4.2 LCCU1-USGSD

The LCCU1-USGSD is identical to the LCCU1-MME except for the recharge rate applied at the model surface. The lower recharge for the USGSD is expected to produce a smaller flux to groundwater, particularly from Timber Mountain.

The classification tree for the LCCU1-USGSD model in [Figure 8-4](#) shows that the MTC\_WTA adequately classifies all parameters in one split. The split on both the upper and lower deciles correctly classifies 96 realizations and misclassifies three (for a misclassification rate of 3 percent). As with the LCCU1-MME case, the best split is for the mass transfer coefficient of the WTA. This indicates that sensitivity of the EV is highly dependent upon the capacity of the WTA unit to diffuse the contaminant plume. Of the WTA units that are important to the PM CAU model, the most pervasive and dominant unit is the TCM, immediately south of Areas 19 and 20, which extends to downgradient discharge locations at Oasis Valley.

Entropy analysis of the LCCU1-USGSD model for the four most important input parameters listed in [Table 8-4](#) is shown in [Figure 8-5](#). The R-statistic for the parameters MTC\_WTA and EFFPOR\_WTA show that the input/output pairs are strongly associated. The remaining parameters show much less of a trend, as can also be discerned from the third and fourth plots in [Figure 8-5](#). The three most significant parameters for the LCCU1-USGSD case are the same as those identified for the LCCU1-MME case. This is not particularly surprising, because the HFMs are identical. The difference between the models is the recharge rate, with the LCCU1-MME recharge exceeding that of the LCCU1-USGSD. Also as with the previous model, EV is inversely related to MTC\_WTA, and EV is directly related to EFFPOR\_WTA.

The stepwise analysis identifies the same top three parameters that are identified in the entropy analysis. [Table 8-5](#) lists the four most sensitive parameters, and [Figure 8-6](#) shows the variance contribution of each parameter to the model. There are seven parameters identified for variance reduction for the LCCU1-USGSD model. Total  $R^2$  for this model is 0.49, which indicates a weak linear relationship between the parameters and EV.

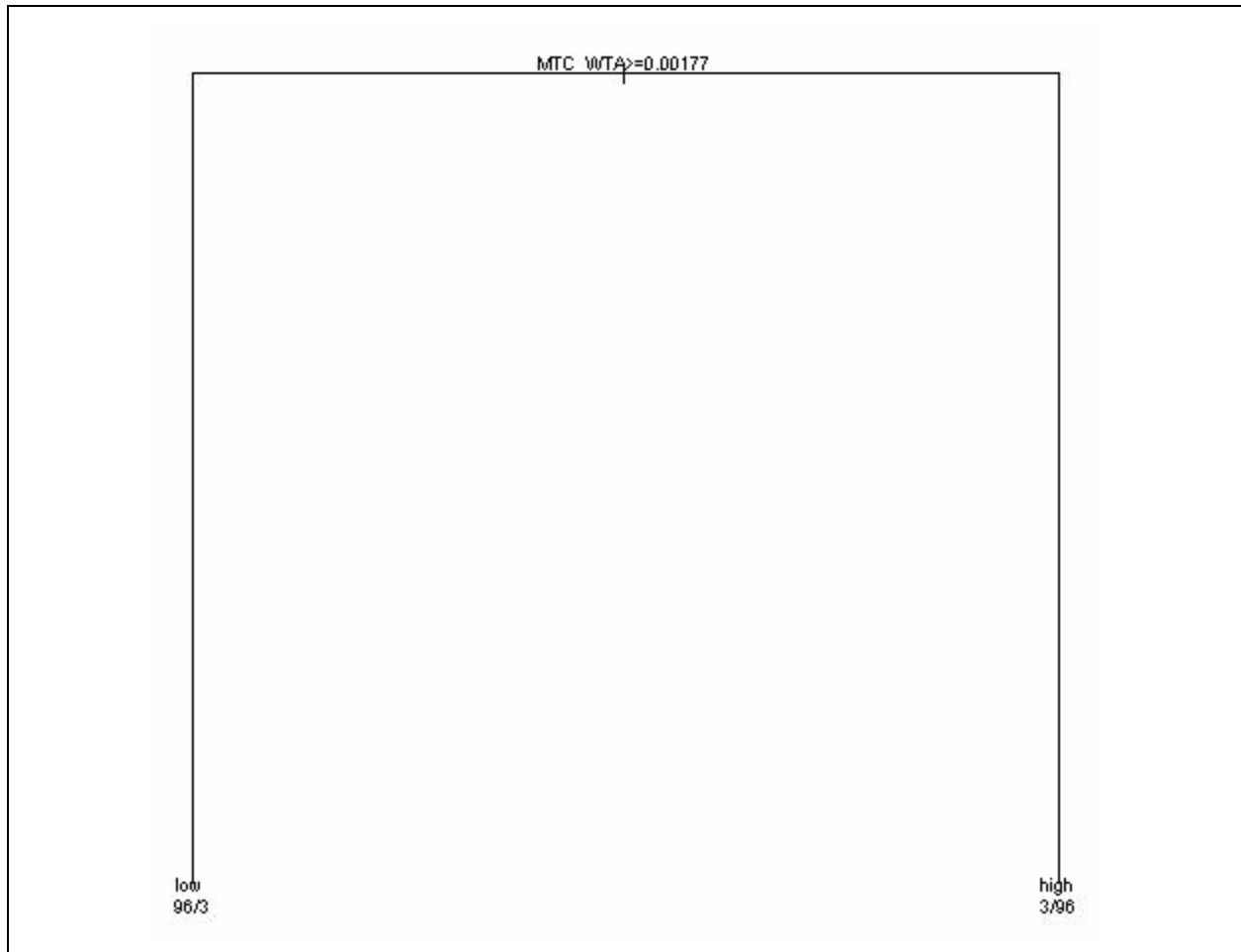


**Figure 8-4**  
**Classification Tree for LCCU1-USGSD**

**Table 8-4**  
**Ranked Entropy Analysis for LCCU1-USGSD**

Entropy Analyses		Chi-Square Analyses		
Rank	Variable	R-statistic	Chi-Square	Probability
1	MTC_WTA	0.635455	537.65	0
2	EFFPOR_WTA	0.547877	350.15	0
3	TYBO_H3	0.353504	122.3	0
4	FRAC_DMP/R	0.190713	35.95	0.00294

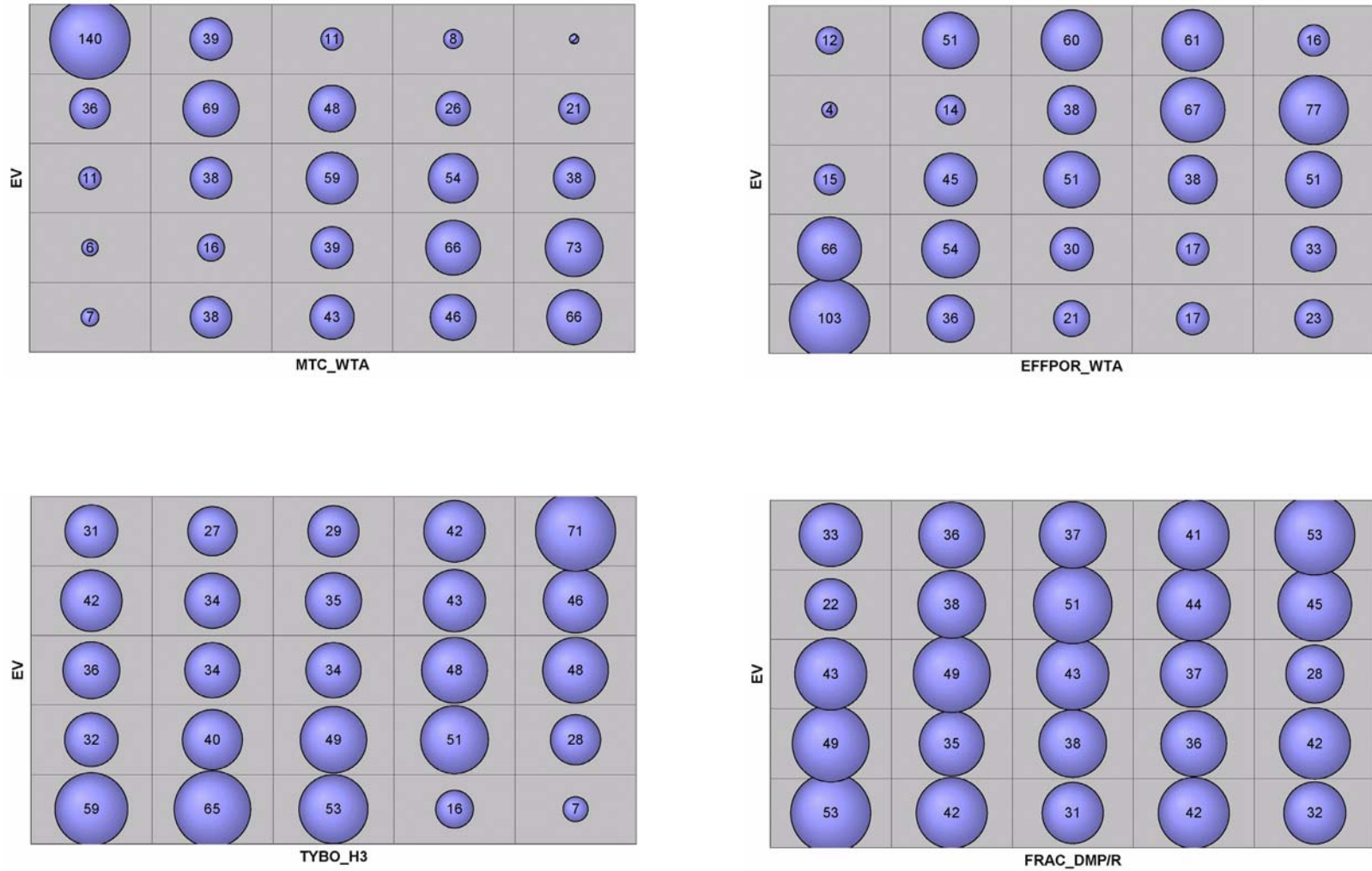


**Figure 8-5**  
**Bubble Plots from Entropy Analysis for LCCU1-USGSD**



**Table 8-5**  
**Ranked Stepwise Regression Analysis for LCCU1-USGSD**

Stepwise Regression		SRC	R <sup>2</sup> Loss	PCC
Rank	Variable			
1	MTC_WTA	-0.966	0.2592	-0.579
2	TYBO_H3	0.273	0.0723	0.352
3	EFFPOR_WTA	-0.399	0.0504	-0.299
4	FRAC_DMP/R	-0.226	0.0348	-0.252

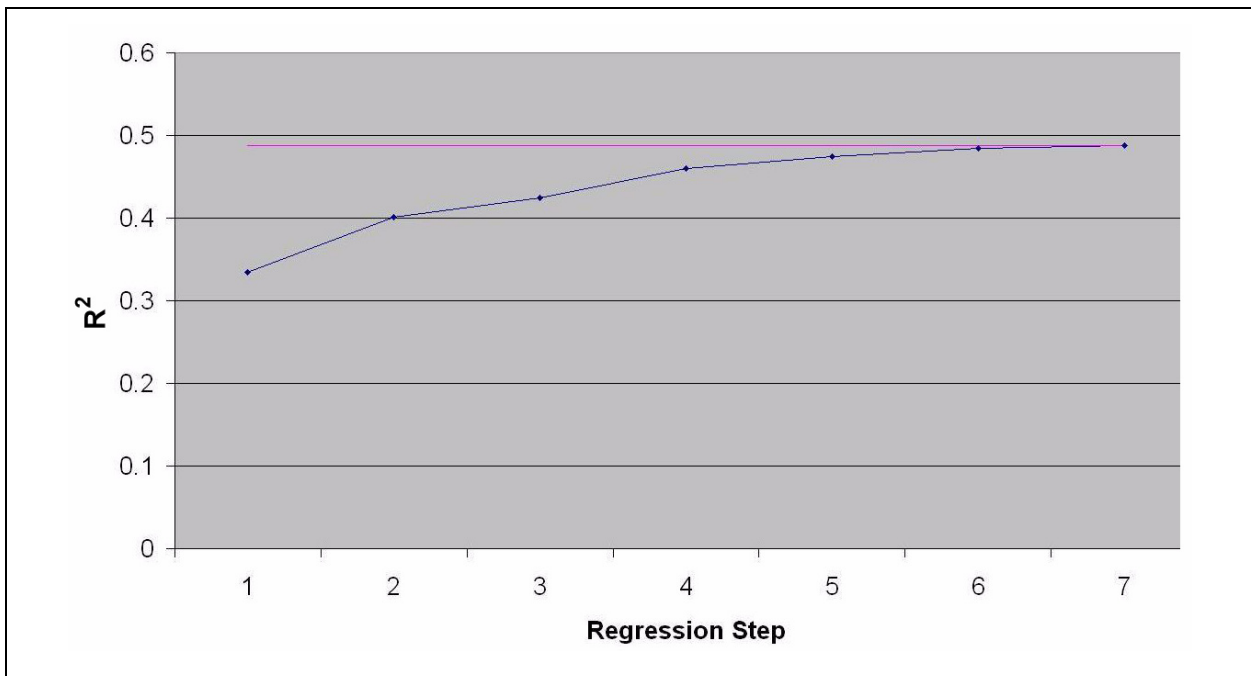


**Figure 8-6**  
**Stepwise Regression Analysis Plot for LCCU1-USGSD**

Each of the three methods applied to the LCCU1-USGSD output identified the MTC\_WTA as the most important parameter that influences output. The second and third most important parameters are the same for the stepwise regression and entropy analysis, although their order of importance is reversed. Two of the top three parameters are transport parameters, while the third is the <sup>3</sup>H inventory.

### 8.2.4.3 LCCU1-MME-TMD

The LCCU1-MME-TMD model is identical to the LCCU1-MME model except that the permeability of the TMD is now increased by a factor of 100. This change would potentially allow southward flow from Pahute Mesa through Timber Mountain rather than diverting flow about its flanks. This option also reduced the height of the recharge mound beneath Timber Mountain, which further reduces the propensity for contaminant migration along the flanks of Timber Mountain.

The classification tree in [Figure 8-7](#) shows four splits of the parameters; in order of importance, MTC\_WTA, R\_Pu\_Colloid, TYBO\_H3, and Kd\_NP\_ZEOL have the greatest influence on output response at the extremes of the EV distribution. Misclassification on the final splits is 4 percent, or  $(2+6+2)/(84+9+7+5+82)$ . As with the previous models, MTC\_WTA is the most important parameter.

The entropy analysis results are shown in [Table 8-6](#) and in [Figure 8-8](#). The first-ranked parameter is again MTC\_WTA, followed by EFFPOR\_WTA, TYBO\_H3, and R\_Pu\_Colloid. The top three parameters identified are identical to those of the LCCU1-MME and the LCCU1-USGSD models.

As with those alternatives, the R-statistics for the first two parameters are appreciably stronger than for the latter two. The bubble plots in [Figure 8-8](#) confirm this trend and also show that the input/output association is consistent with previous results.

The stepwise regression analysis results are listed in [Table 8-7](#), and [Figure 8-9](#) depicts how the addition of parameters explains a progressively higher and higher fraction of variance. The most important parameters are the MTC\_WTA, TYBO\_H3, and R\_Pu\_Colloid. The top two parameters are among the top three identified in the entropy analysis. The third parameter listed corresponds to the fourth in the entropy analysis. Variance reduction for the LCCU1-MME-TMD model resulted in a final  $R^2$  term of 0.46, which indicates a weak correlation between parameters and EV.

From the three sensitivity methods, the parameters MTC\_WTA and TYBO\_H3 appear as significant in all cases. R\_Pu\_Colloid is also among the top three for the classification tree and stepwise regression methods.

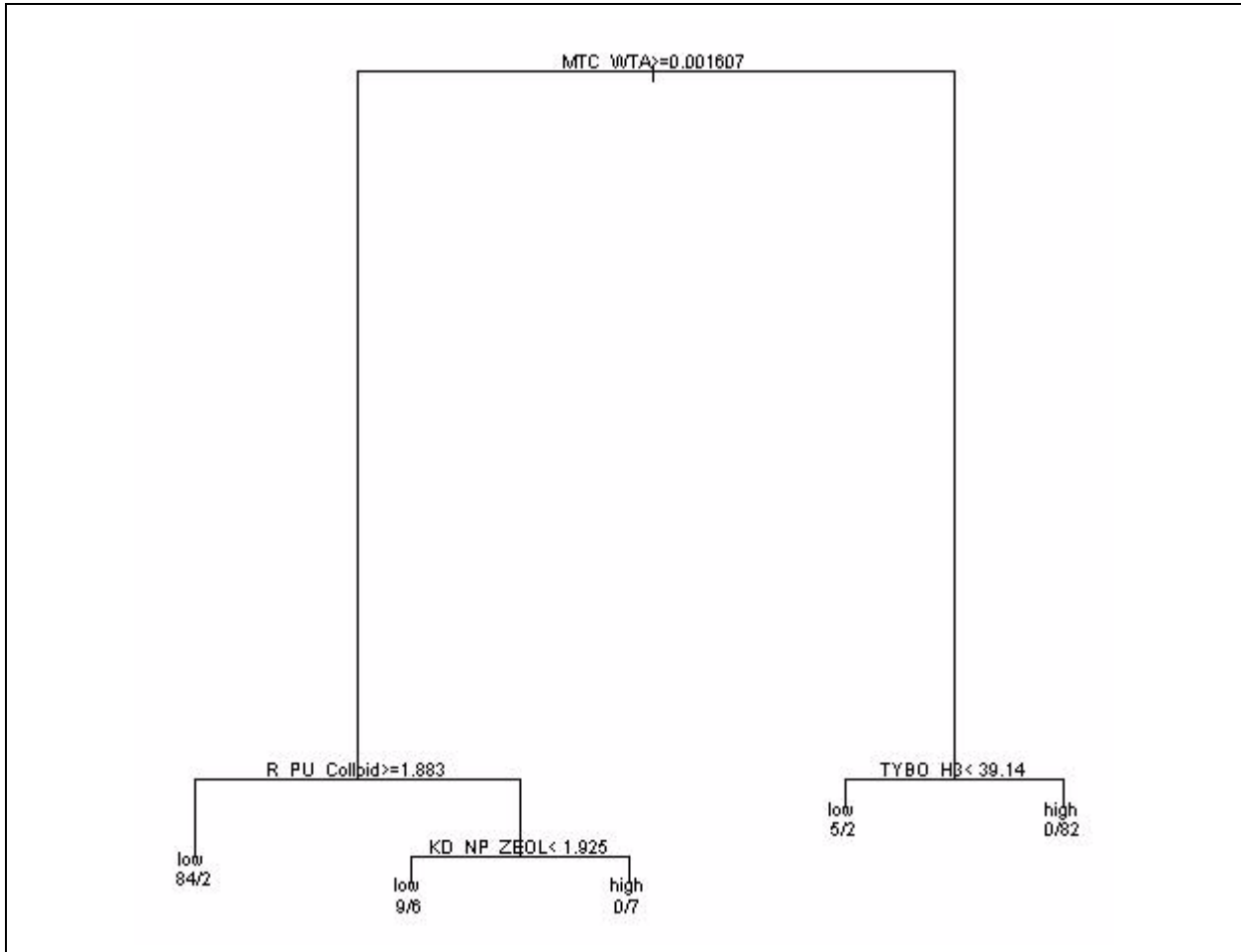


**Figure 8-7**  
**Classification Tree for LCCU1-MME-TMD**

**Table 8-6**  
**Ranked Entropy Analysis for LCCU1-MME-TMD**

Entropy Analyses		Chi-Square Analyses		
Rank	Variable	R-statistic	Chi-Square	Probability
1	MTC_WTA	0.584044	446.3	0
2	EFFPOR_WTA	0.517543	316.7	0
3	TYBO_H3	0.302119	93.5	5.64E-13
4	R_Pu_Colloid	0.268463	72.65	3.41E-09

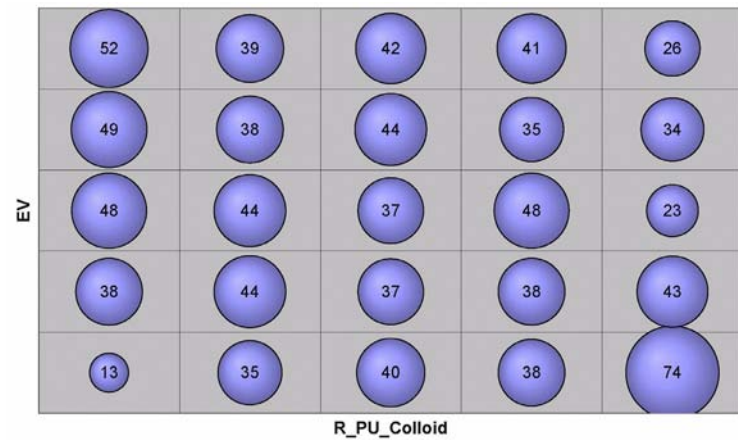
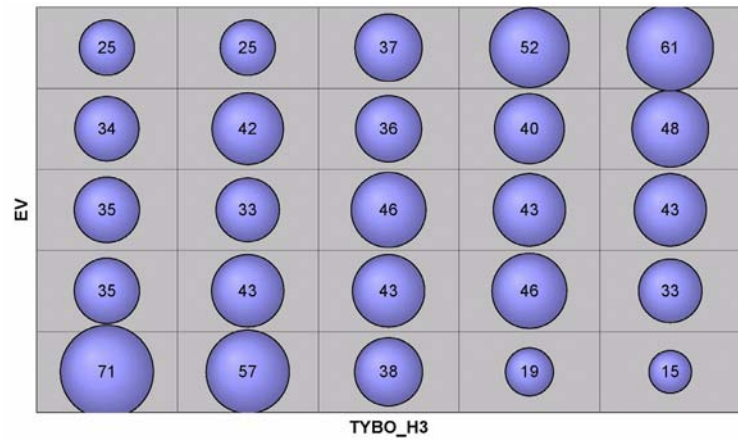
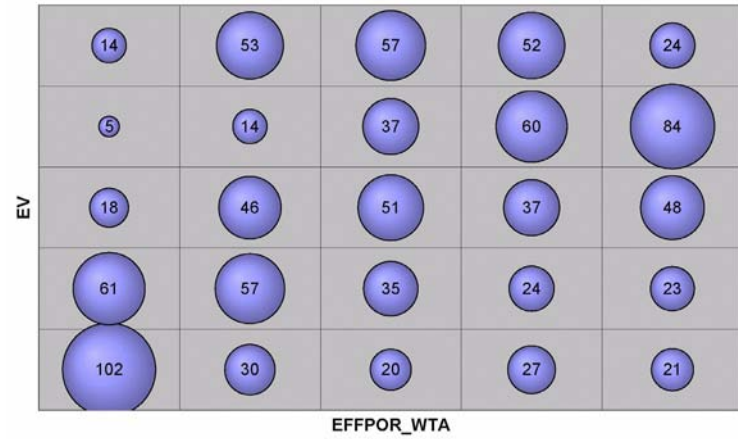
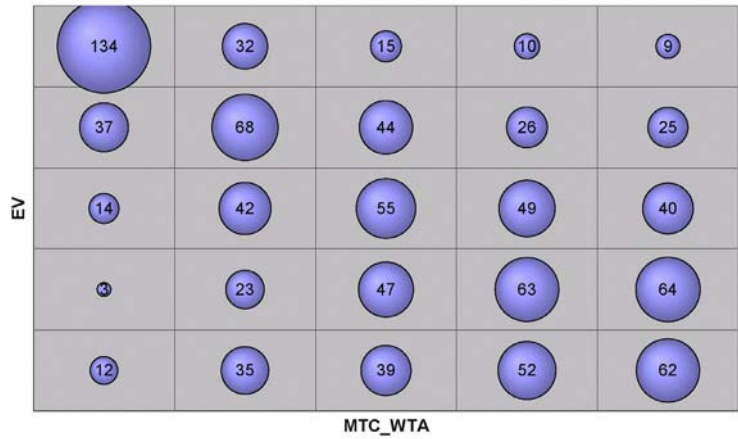


**Figure 8-8**  
**Bubble Plots from Entropy Analysis for LCCU1-MME-TMD**

**Table 8-7**  
**Ranked Stepwise Regression for LCCU1-MME-TMD**

Stepwise Regression		SRC	R <sup>2</sup> Loss	PCC
Rank	Variable			
1	MTC_WTA	-0.833	0.1928	-0.513
2	TYBO_H3	0.291	0.0821	0.363
3	R_Pu_Colloid	-0.22	0.0477	-0.285
4	FRAC_DMP/R	-0.241	0.0393	-0.26

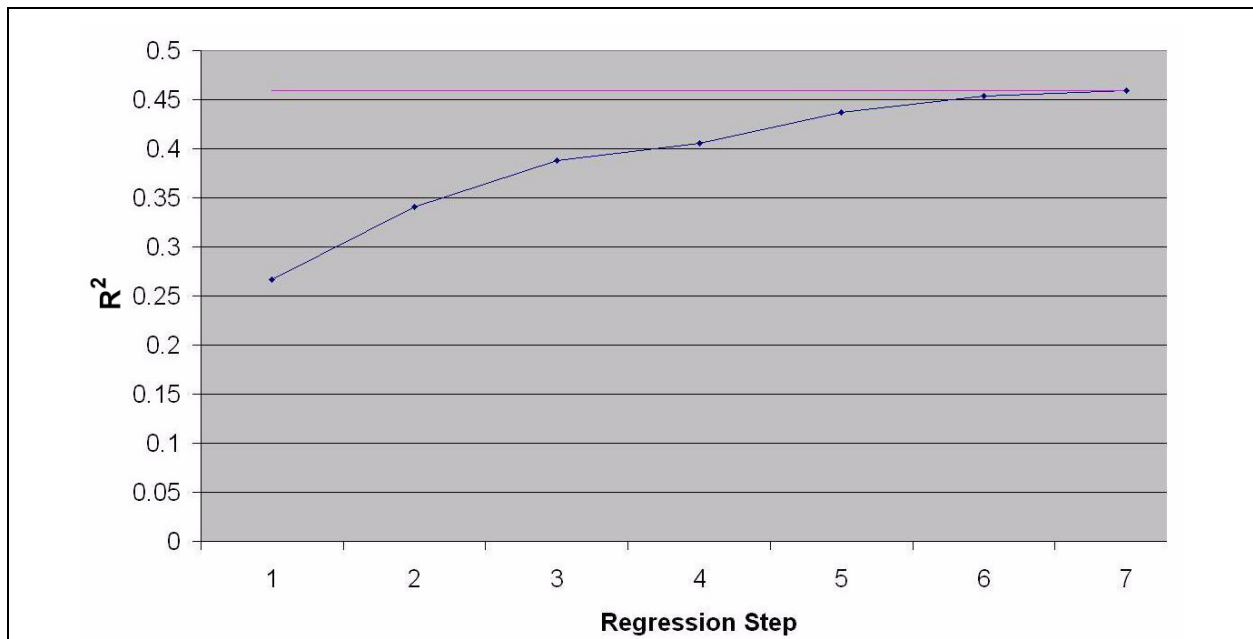


**Figure 8-9**  
**Stepwise Regression Plot for LCCU1-MME-TMD**

#### 8.2.4.4 LCCU1-MME-TMCM

The LCCU1-MME-TMCM is also structurally identical to the LCCU1-MME; however, permeability in HSUs shown influential to flow and transport have been appreciably modified (see [Section 3.4.3](#)).

The classification tree derived from the LCCU1-TMCM flow model is shown in [Figure 8-10](#). The classification tree is defined by three splits. R\_Pu\_Colloid provides the root split, and then EFFPOR\_TCU splits both the high and low branches. The degree of misclassification after the second split is 2 percent. The appearance of the EFFPOR\_TCU on both upper and lower arms of the second split indicates that transport through the TCU is important in all simulations, for small- and large-scale transport alike. The high split is on an EFFPOR\_TCU value greater than or equal to 0.425, and the split on the lower EFFPOR\_TCU decile is greater than or equal to 0.175. The number of realizations greater than 0.425 are 85, between 0.425 and 0.175 is 23, and less than 0.175 is 90. Compared with the previous cases of the LCCU1 models, the impact of the WTA parameters is not represented as most significant for this model.

The entropy analysis ranking of importance for the LCCU1-MME-TMCM model is listed in [Table 8-8](#), and the top four results are shown in [Figure 8-11](#). The top four parameters for this model are EFFPOR\_TCU, R\_Pu\_Colloid, EFFPOR\_WTA, and MTC\_WTA. The top two parameters are the same as those identified in the classification tree analysis, although their order is reversed. [Figure 8-11](#) shows that as EFFPOR\_TCU increases, EV decreases. The TCU describes porous units in which velocity is lower, thus reducing migration. In the case of R\_Pu\_colloid, an increase of this parameter also corresponds to a decrease in EV. As the reduction factor increases, the colloids in the system are less and the EV is smaller. The third and fourth most important parameters show the same trend as seen in previous entropy plots for those parameters.

The top four parameters identified through stepwise regression are EFFPOR\_TCU, R\_Pu\_Colloid, TYBO\_C136, and MTC\_WTA. Except for the third parameter, all others identified as important are identical to the parameters cited in the entropy analysis. The top four parameters and statistical metrics are listed in [Table 8-9](#). [Figure 8-12](#) shows the loss-of  $R^2$  for the listed parameters. The first three parameters are the primary contributors to output variance. There are seven parameters selected for variance reduction for the LCCU1-MME-TMCM model. The final  $R^2$  for this model is 0.67, which although a weak correlation of linearity is much stronger than the previous three HFMs.

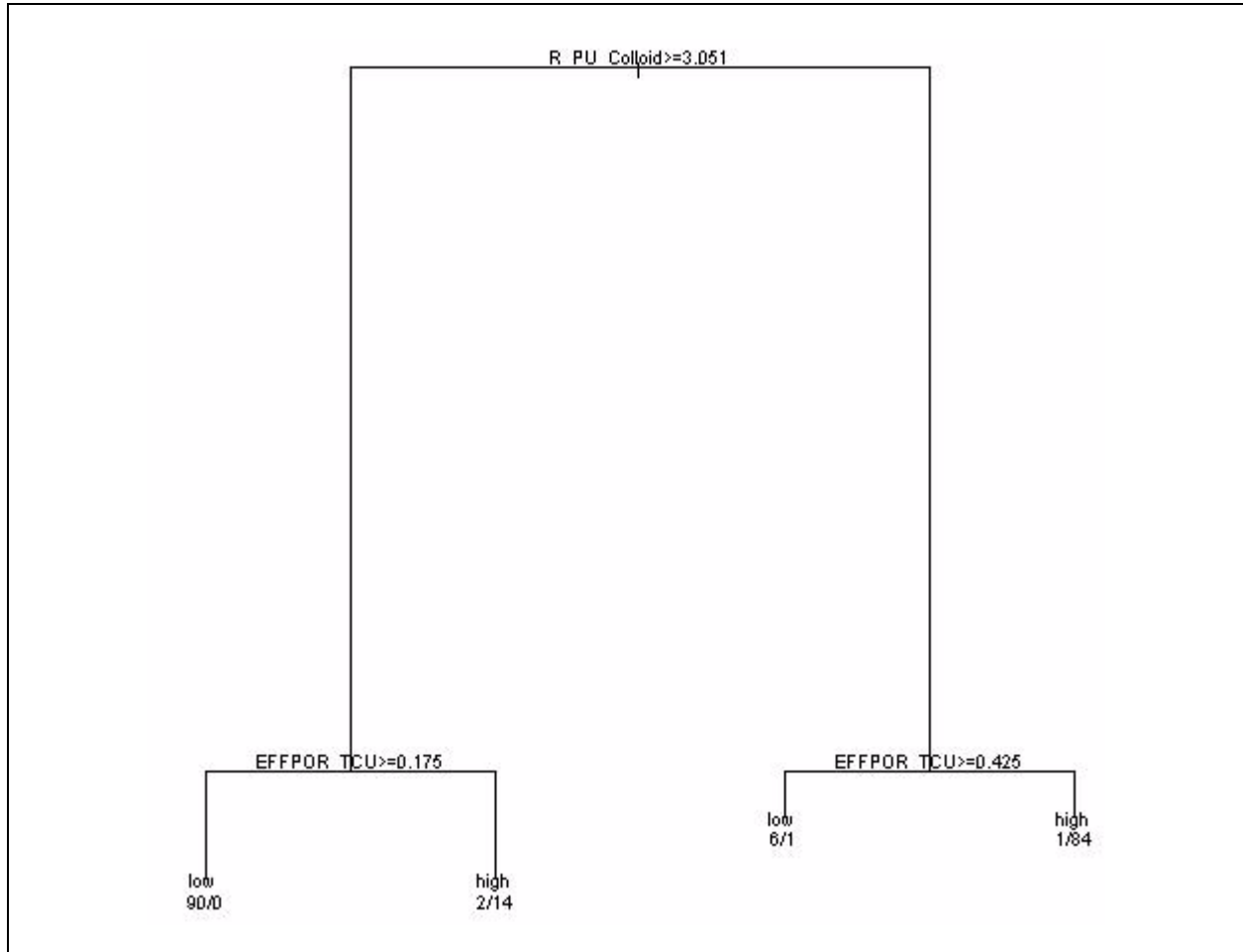


**Figure 8-10**  
**Classification Tree for LCCU1-MME-TMCM**

**Table 8-8**  
**Ranked Entropy Analysis for LCCU1-MME-TMCM**

Entropy Analyses		Chi-Square Analyses		
Rank	Variable	R-statistic	Chi-Square	Probability
1	EFFPOR_TCU	0.536987	336.7	0
2	R_Pu_Colloid	0.487377	277.95	0
3	EFFPOR_WTA	0.397909	179.8	0
4	MTC_WTA	0.389291	178	0

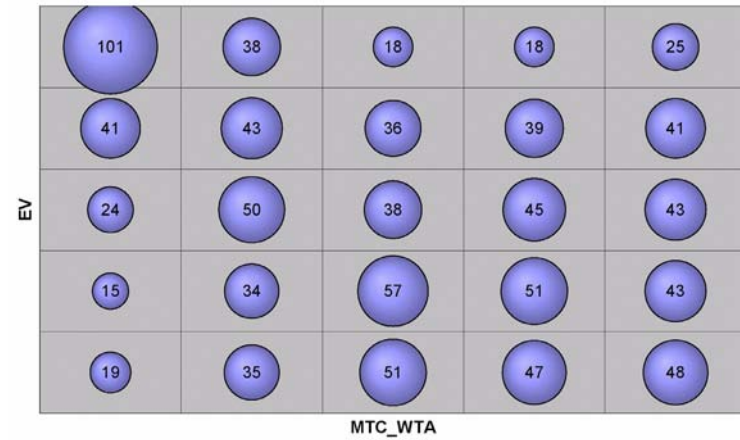
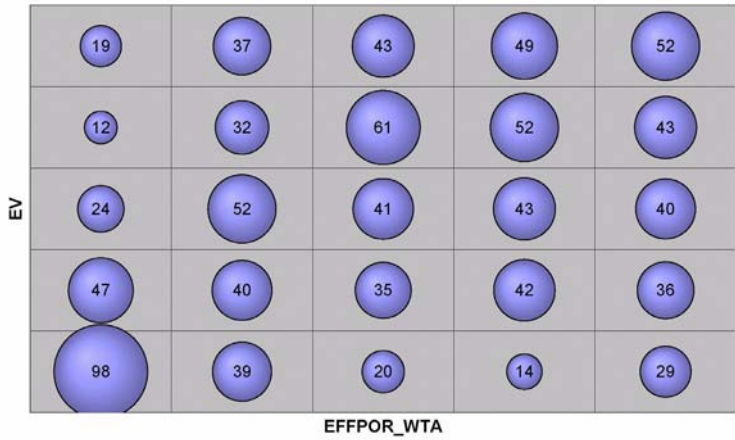
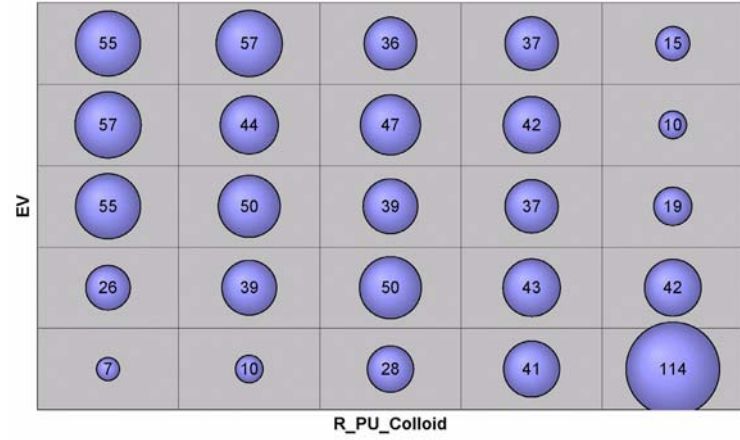
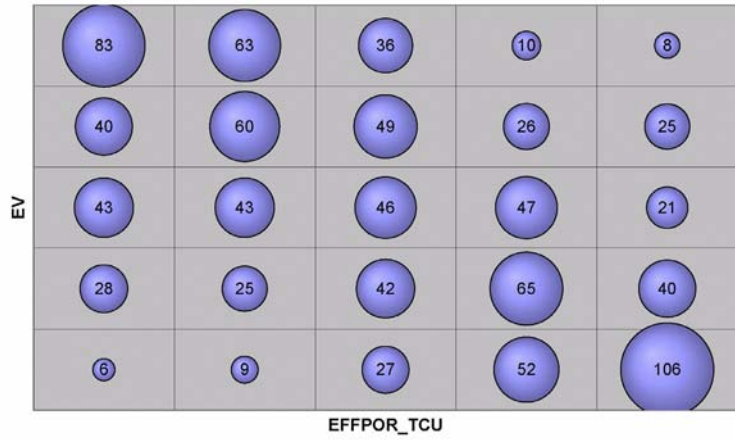


**Figure 8-11**  
**Bubble Plots from Entropy Analysis for LCCU1-MME-TMCM**



**Table 8-9**  
**Ranked Stepwise Regression for LCCU1-MME-TMCM**

Stepwise Regression		SRC	R <sup>2</sup> Loss	PCC
Rank	Variable			
1	EFFPOR_TCU	-0.514	0.2635	-0.668
2	R_Pu_Colloid	-0.42	0.1755	-0.591
3	TYBO_CI36	0.335	0.1116	0.504
4	MTC_WTA	-0.245	0.0167	-0.22

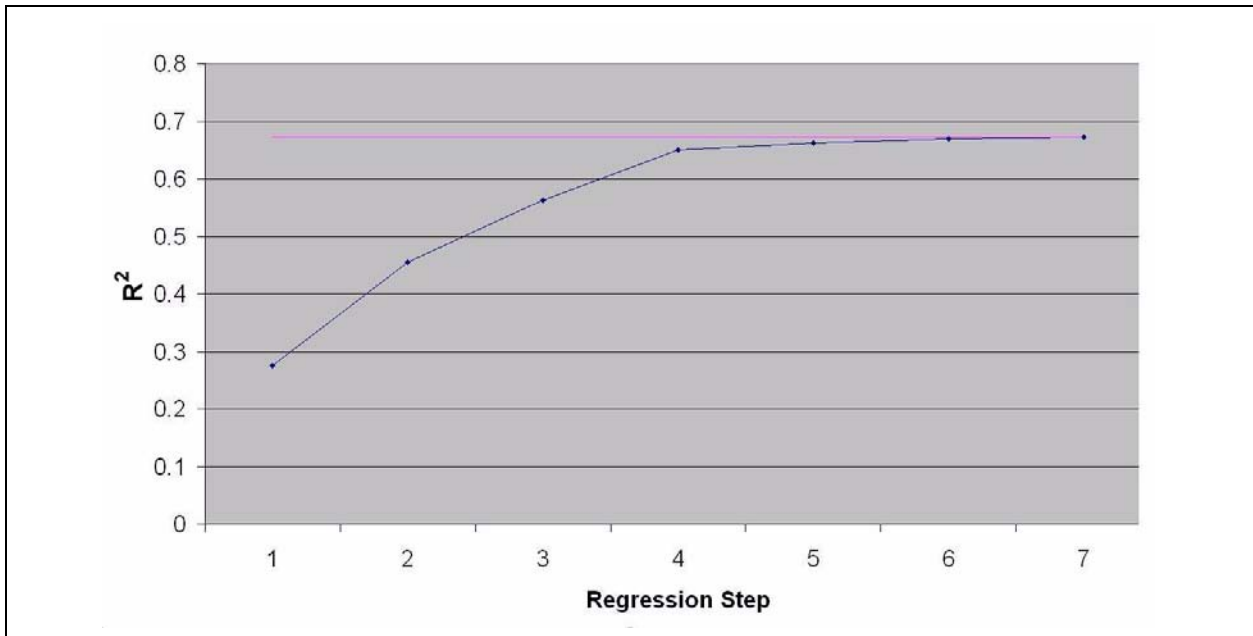


**Figure 8-12**  
**Stepwise Regression Plot for LCCU1-MME-TMCM**

#### 8.2.4.5 PZUP-MME

The PZUP model (Pre-tertiary uplift) differs from the preceding models in that the thickness of permeable units is reduced as the basement elevation is increased. For this case, the classification tree is represented by two splits on the parameters MTC\_WTA and TYBO\_H3. The degree to which the parameters are misclassified is 4 percent. The classification tree split is shown in [Figure 8-13](#). The selected parameters show that the WTA and the <sup>3</sup>H inventory strongly influence the response of EV.

The entropy analysis ranking of importance for the PZUP-MME model is listed in [Table 8-10](#). The four parameters, in order of importance, are MTC\_WTA, EFFPOR\_WTA, EFFPOR\_VTA, and TYBO\_H3. The R-statistic shows the degree of association between the parameters and EV. This association is shown visually in the bubble plots in [Figure 8-14](#). As was the case with most of the LCCU1 models, the top two parameters are properties of the WTA. The relationships also are the same as in previous models. Although showing a lower index of association, a trend can be discerned for EFFPOR\_VTA and TYBO\_H3. In the first case, as EFFPOR\_VTA increases, there is a decrease in the EV. In the second case, as TYBO\_H3 increases, so does the EV. Both results are consistent with expected behavior. An increase in EFFPOR\_VTA is expected to reduce velocity and, therefore, decrease plume size. Conversely, as <sup>3</sup>H inventory increases, more contaminant is available for transport.

The four parameters from the stepwise regression that contribute the most to the output variance are MTC\_WTA, TYBO\_H3, EFFPOR\_VTA, and R\_Pu\_Colloid ([Table 8-11](#)). MTC\_WTA was ranked first by all analyses and three of the four parameters from the stepwise-regression are also represented in the entropy analysis. [Figure 8-15](#) shows the loss of R<sup>2</sup> as the variance of each parameter is incrementally added. There are eight parameters for which variance reduction was performed for the PZUP-MME HFM. The final R<sup>2</sup> for this model is 0.53, which although weak is higher than the first three HFMs.

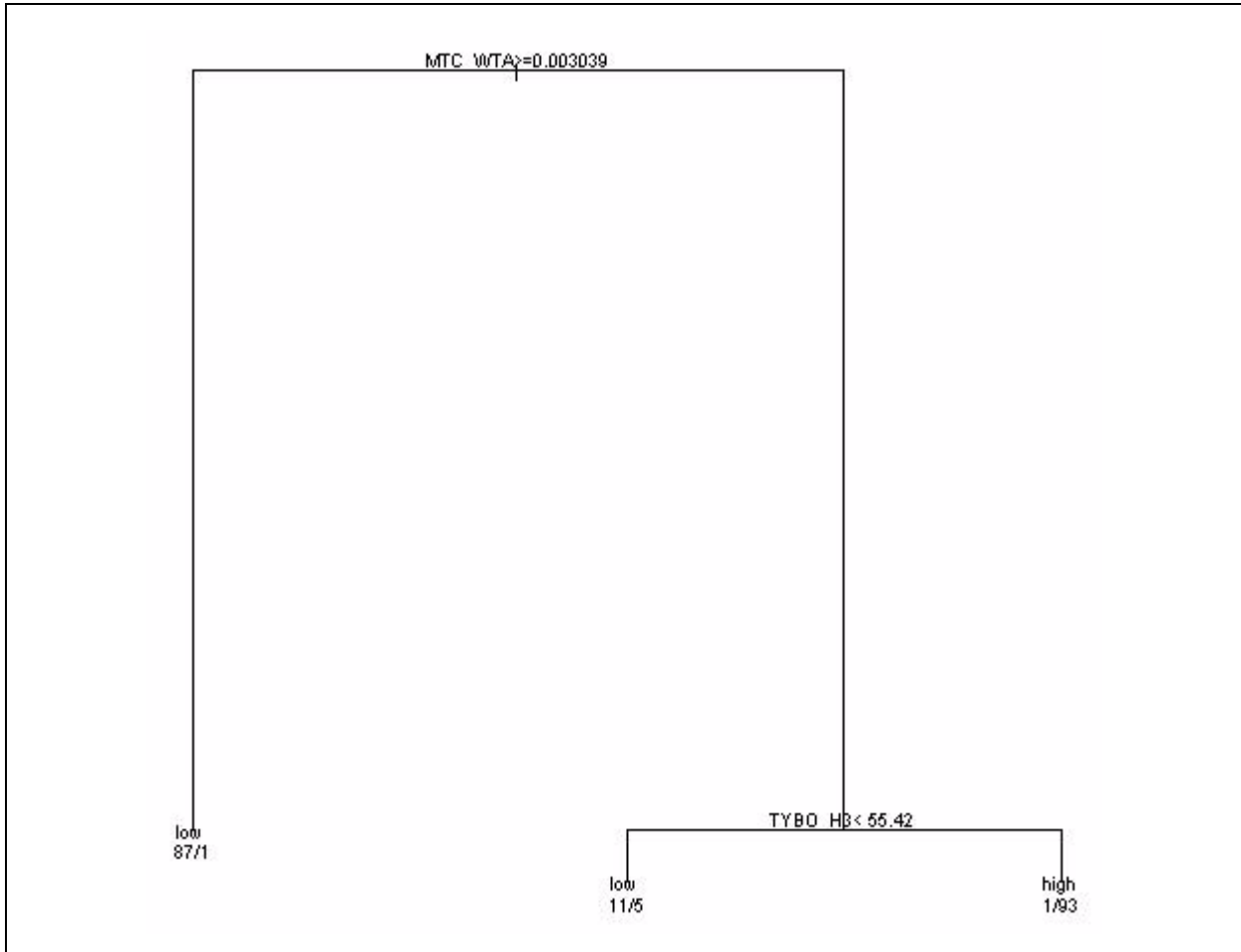


**Figure 8-13**  
**Classification Tree for PZUP-MME**

**Table 8-10**  
**Ranked Entropy Analysis for PZUP-MME**

Entropy Analyses		Chi-Square Analyses		
Rank	Variable	R-statistic	Chi-Square	Probability
1	MTC_WTA	0.561399	392.55	0
2	EFFPOR_WTA	0.485656	279.7	0
3	EFFPOR_VTA	0.349638	133.2	0
4	TYBO_H3	0.310007	93.35	6.02E-13

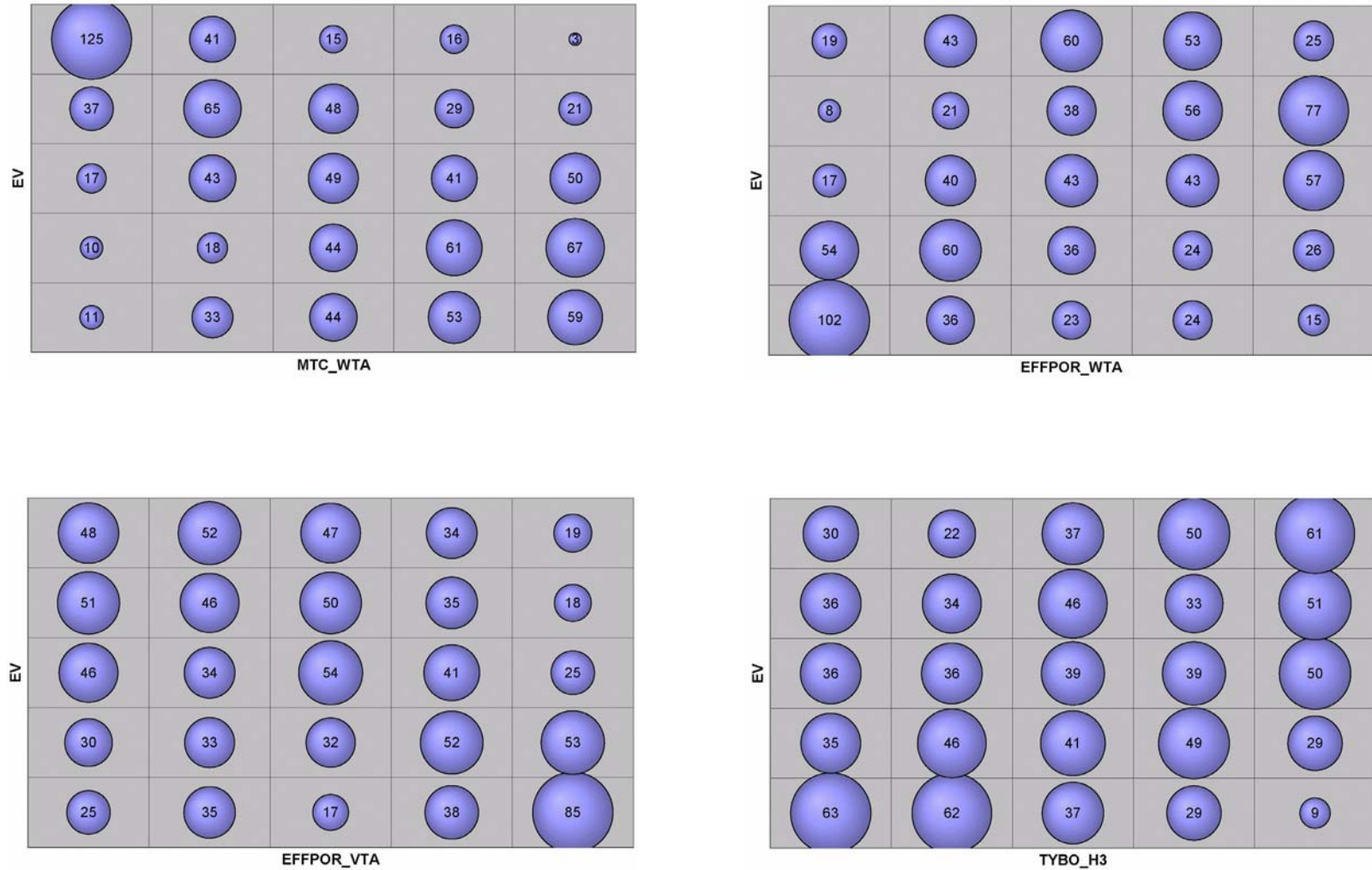


**Figure 8-14**  
**Bubble Plots from Entropy Analysis for PZUP-MME**

**Table 8-11**  
**Ranked Stepwise Regression for PZUP-MME**

Stepwise Regression		SRC	R <sup>2</sup> Loss	PCC
Rank	Variable			
1	MTC_WTA	-0.765	0.1617	-0.508
2	TYBO_H3	0.294	0.0841	0.391
3	EFFPOR_VTA	-0.253	0.0633	-0.346
4	R_Pu_Colloid	-0.216	0.046	-0.3

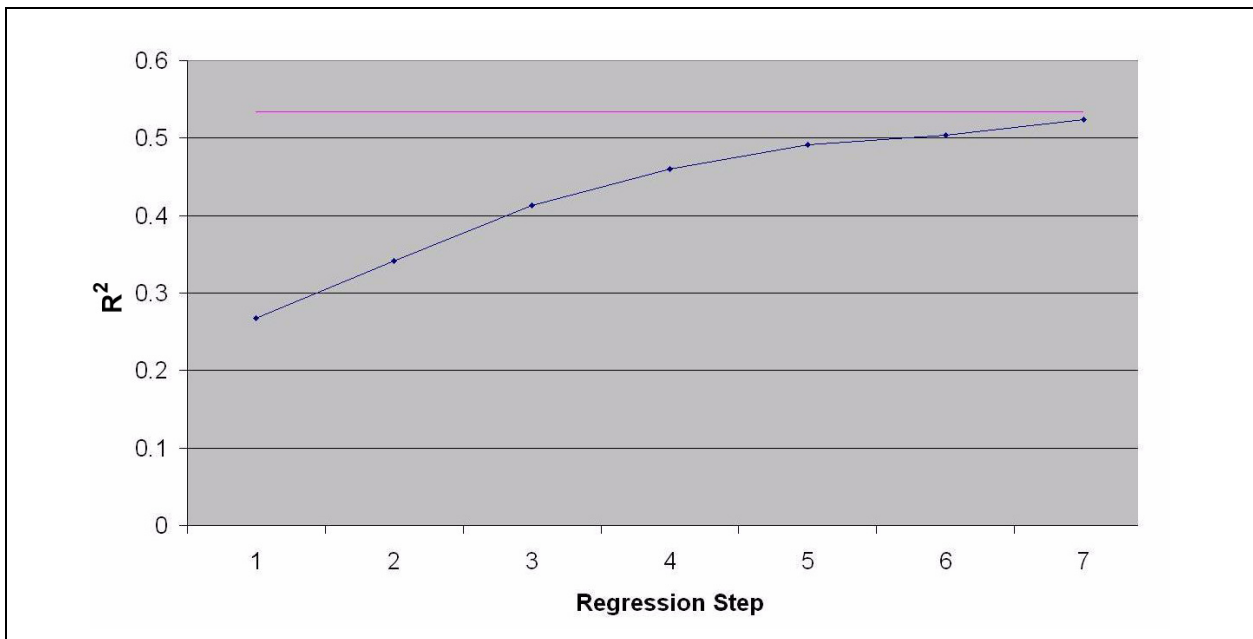


**Figure 8-15**  
**Stepwise Regression for PZUP-MME**

#### 8.2.4.6 DRT-DRIA

The deeply rooted belted range thrust fault (DRT) model assumes that the deeply rooted thrust brings the LCCU higher in the stratigraphic sequence south of Pahute Mesa, thereby cutting off the basal higher-permeability LCA.

The DRT model classification tree is defined by two splits as shown in [Figure 8-16](#). The tree is split first by EFFPOR\_TCU and then by R\_Pu\_Colloid. The level of misclassification for this tree is 3 percent. The parameters identified match those observed from the split of the LCCU1-MME-TMCM model.

Entropy analysis importance rankings for the DRT-DRIA model are listed in [Table 8-12](#). The top four parameters that show non-random association with the EV are EFFPOR\_TCU, R\_Pu\_Colloid, MTC\_WTA, and EFFPOR\_WTA. The corresponding bubble plots are shown in [Figure 8-17](#). In general, this set of parameters indicates that output variability is more dependent on flow behavior in the matrix than in fractures, consistent with the limited extent of contaminant migration observed for this alternative (see [Section 7.6.6](#)).

In the stepwise regression analysis, the top three parameters contributing to output variance are identical to those identified by the entropy analysis. [Table 8-13](#) lists the top four. [Figure 8-18](#) shows by the  $R^2$  loss that the first three parameters explain most of the model variability. There are 10 parameters that require variance reduction for the DRT-DRIA HFM. The final  $R^2$  for this model is 0.72, which indicated that there is a mild correlation between the parameters and the EV. This model exhibits the strongest correlation of any of the preceding models.

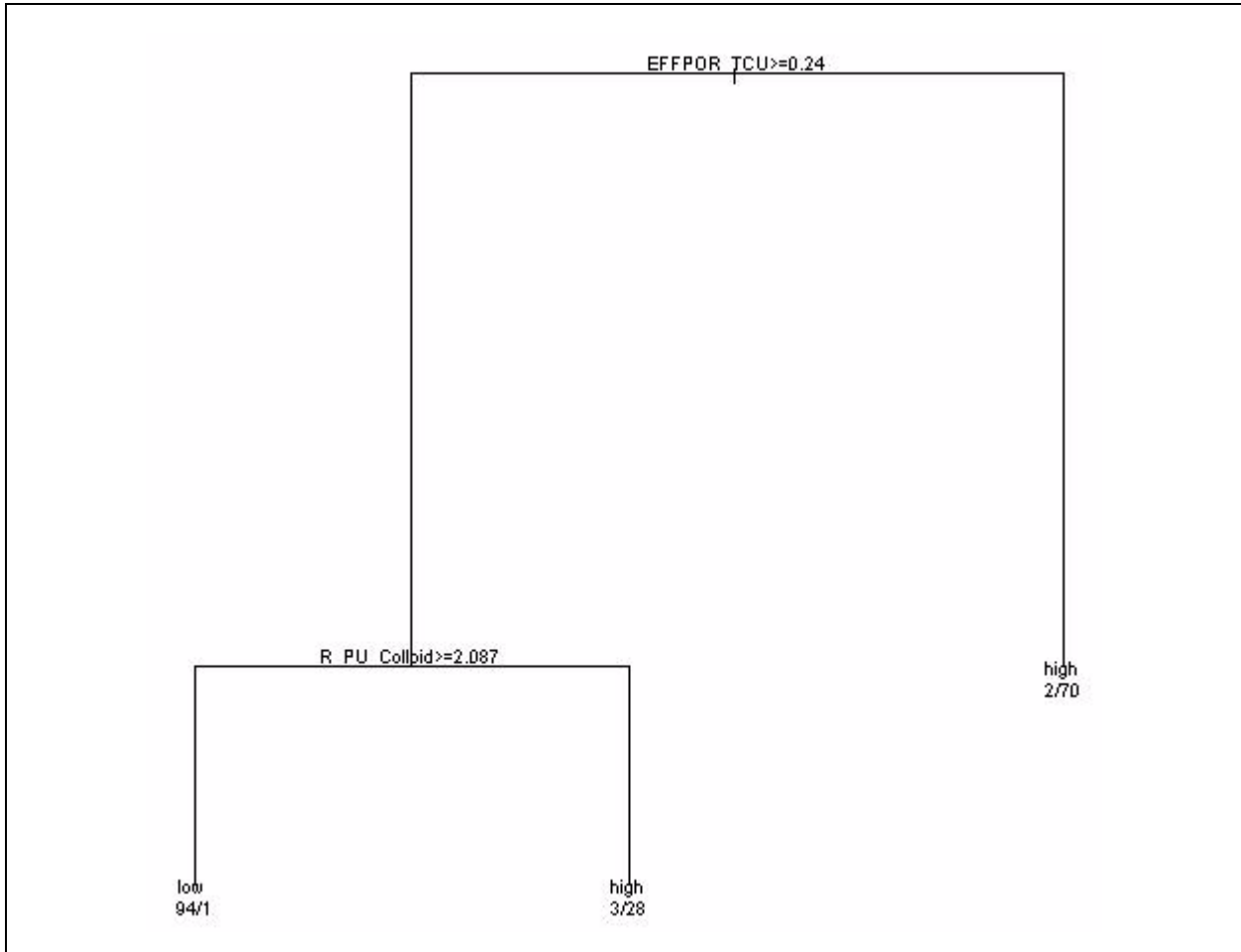


**Figure 8-16**  
**Classification Tree for DRT-DRIA**

**Table 8-12**  
**Ranked Entropy Analysis for DRT-DRIA**

Entropy Analyses		Chi-Square Analyses		
Rank	Variable	R-statistic	Chi-Square	Probability
1	EFFPOR_TCU	0.604717	470.35	0
2	R_Pu_Colloid	0.464971	248.95	0
3	MTC_WTA	0.402554	195.65	0
4	EFFPOR_WTA	0.347811	139.7	0

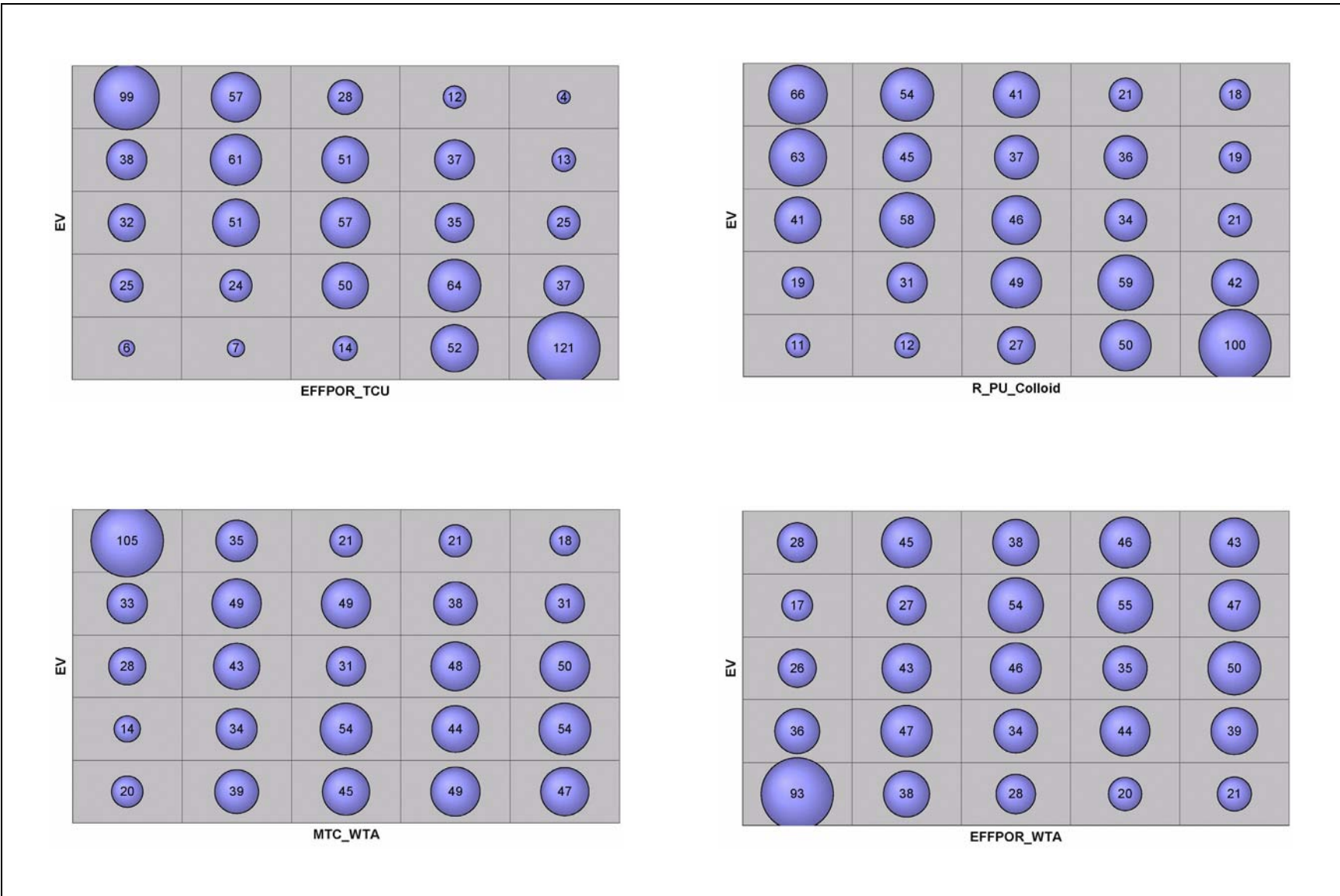


**Figure 8-17**  
**Bubble Plots from Entropy Analysis for DRT-DRIA**



**Table 8-13**  
**Ranked Stepwise Regression for DRT-DRIA**

Stepwise Regression		SRC	R <sup>2</sup> Loss	PCC
Rank	Variable			
1	EFFPOR_TCU	-0.57	0.3222	-0.73
2	R_Pu_Colloid	-0.449	0.1991	-0.643
3	MTC_WTA	-0.429	0.0508	-0.39
4	TYBO_Cl36	0.178	0.0308	0.313

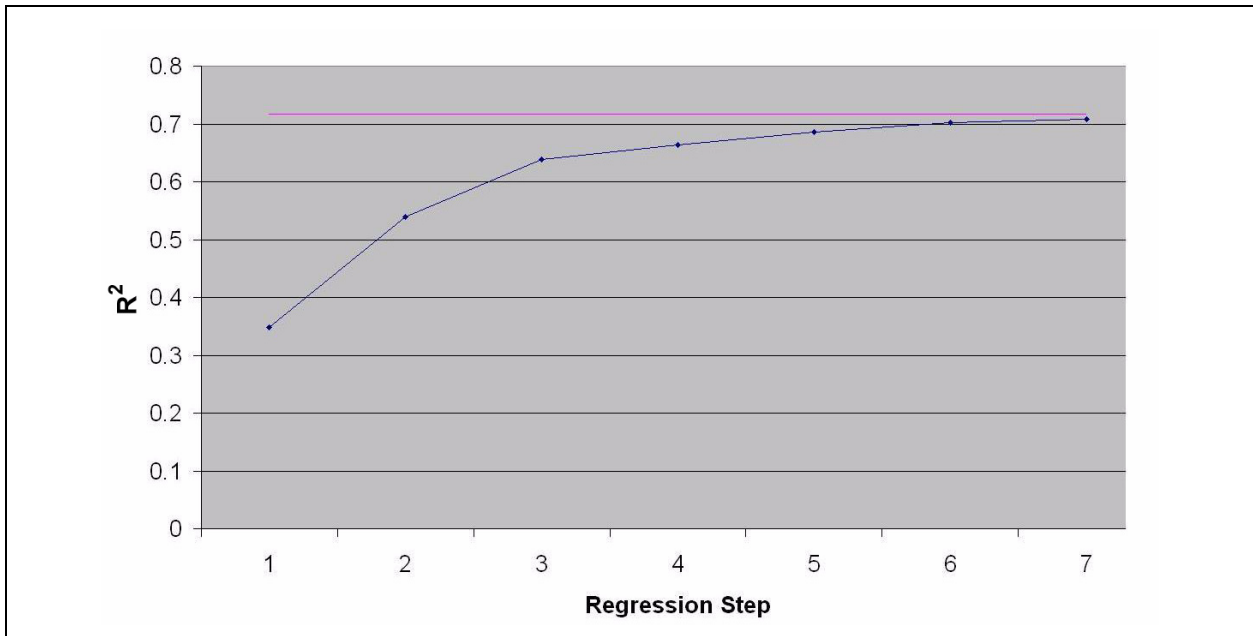


**Figure 8-18**  
**Stepwise Regression for DRT-DRIA**

#### 8.2.4.7 SCCC-MME

The SCCC model is significantly different from all previous models. It is structurally simpler and has fewer faults and HSUs.

The classification tree shown in [Figure 8-19](#) for this model is split on the two parameters R\_Pu\_Colloid and EFFPOR\_TCU. This split excludes the WTA, suggesting that the porous units have more influence on plume size than the fractured units. The level of misclassification for this analysis is 3 percent.

As determined by entropy analysis, the top four parameters associated with EV ([Table 8-14](#)) are R\_Pu\_Colloid, EFFPOR\_TCU, TYBO\_C136, and TYBO\_C14. The first two parameters correspond to those identified by the classification tree. The third and fourth parameters are related to the inventory. The relative strength of association is strong for the first two parameters and moderate for the final two parameters. [Figure 8-20](#) shows that, as is the case for other alternative HFMs, when R\_Pu\_Colloid increases, the EV decreases, and when EFFPOR\_TCU increases, the EV decreases. For both of the inventory parameters, as the parameter increases, so does the EV. Each of the inventory parameters is conservative, so an increase in each translates to an increase of mass in the groundwater system.

The stepwise regression analysis parameters listed in [Table 8-15](#) identify the four most important parameters as EFFPOR\_TCU, R\_Pu\_Colloid, TYBO\_C136, and MTC\_WTA. The top three parameters are the same as those cited in the entropy analysis, although the first and second are reversed in order. The loss in  $R^2$  is of comparable magnitude for the first two parameters and much less for the third parameter. The reduction in the variance as each parameter is added can be observed in [Figure 8-21](#). This indicates that most of the variance is accounted for after the third variable is added, which suggests that the fourth variable may not be important. There are seven parameters that require variance reduction for the SCCC-MME HFM. The final  $R^2$  for this model is 0.68, which shows a mild correlation between parameters and EV.

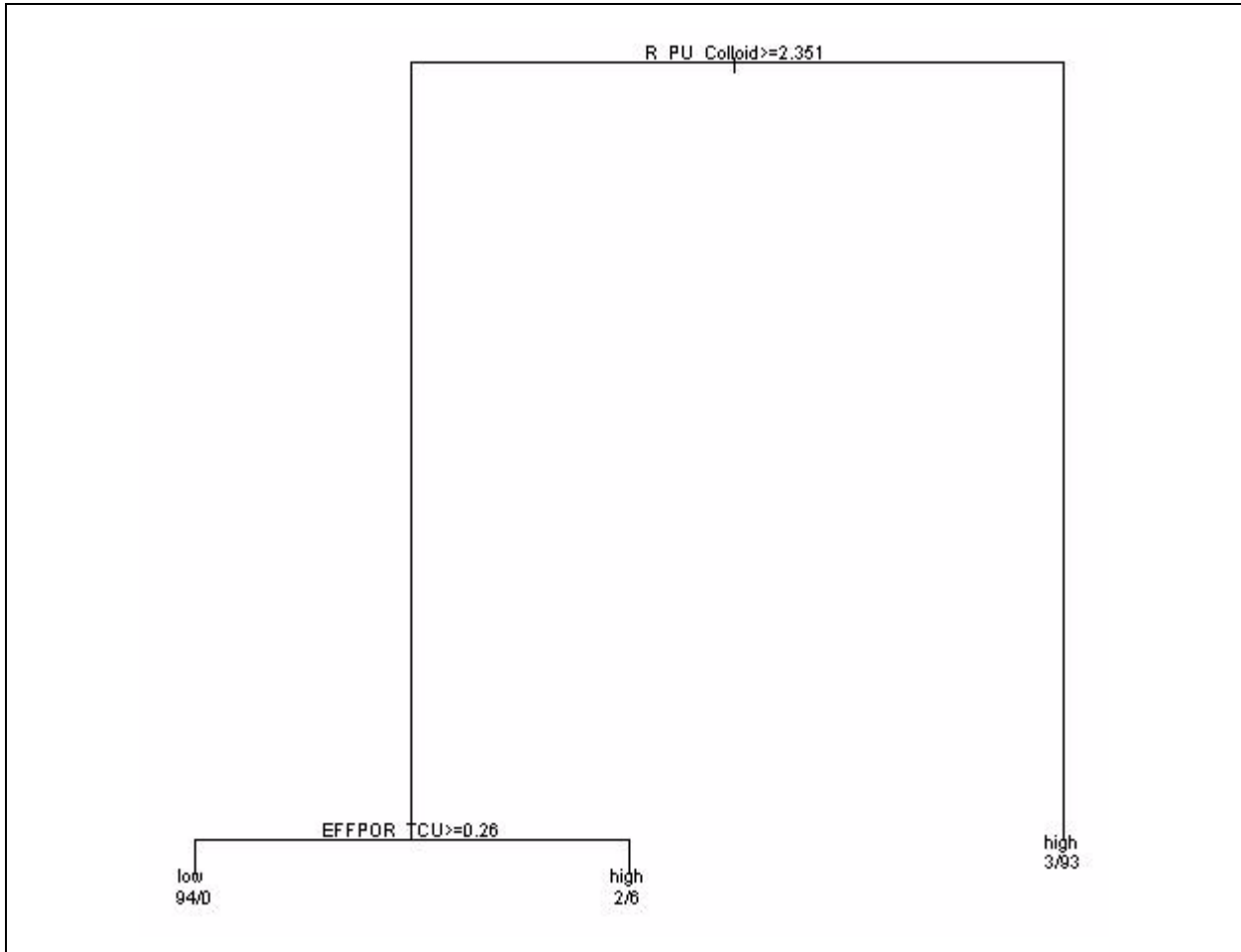


**Figure 8-19**  
**Classification Tree for SCCC-MME**

**Table 8-14**  
**Ranked Entropy Analysis for SCCC-MME**

Entropy Analyses		Chi-Square Analyses		
Rank	Variable	R-statistic	Chi-Square	Probability
1	R_Pu_Colloid	0.558796	388.1	0
2	EFFPOR_TCU	0.550545	348.65	0
3	TYBO_C136	0.396147	180.8	0
4	TYBO_C14	0.395461	179.25	0

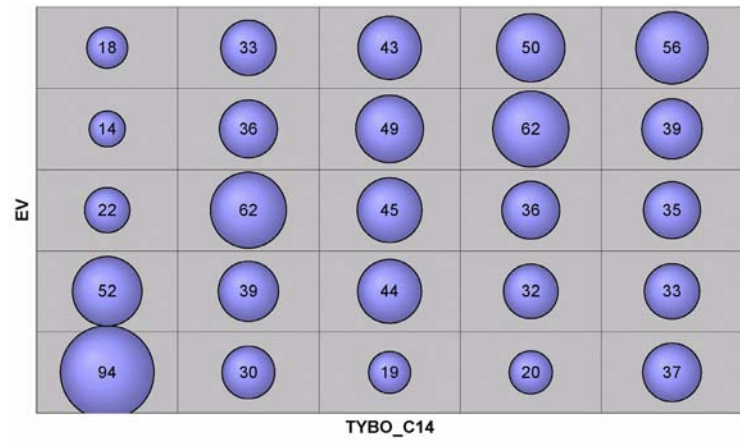
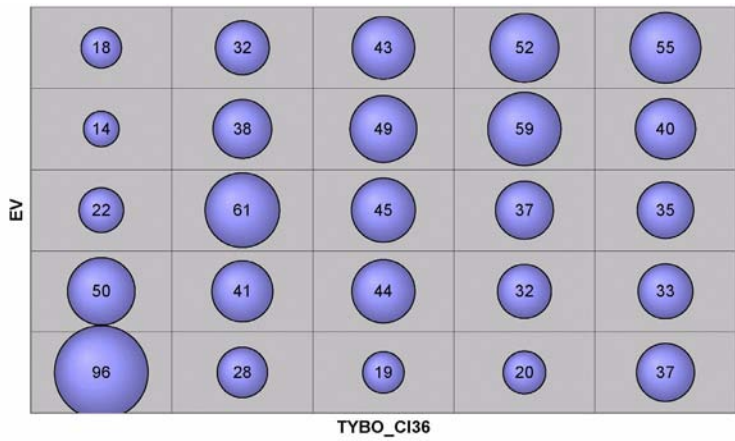
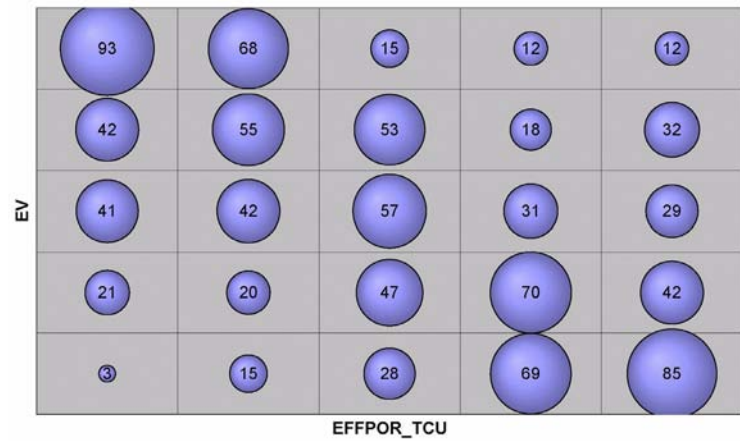
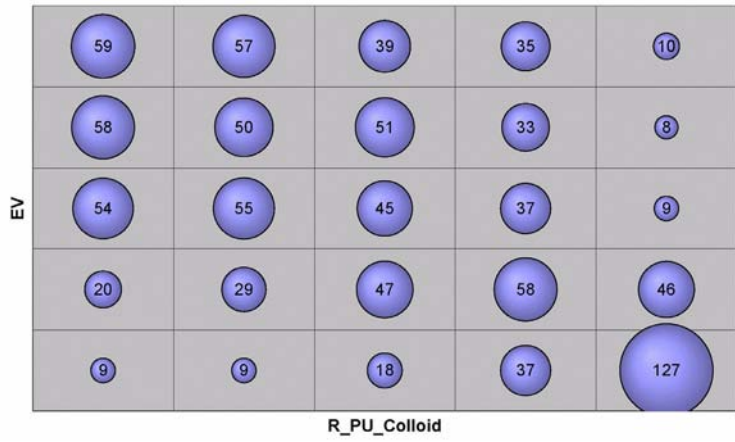


**Figure 8-20**  
**Bubble Plots from Entropy Analysis for SCCC-MME**

**Table 8-15**  
**Ranked Stepwise Regression for SCCC-MME**

Stepwise Regression		SRC	R <sup>2</sup> Loss	PCC
Rank	Variable			
1	EFFPOR_TCU	-0.515	0.2642	-0.67
2	R_Pu_Colloid	-0.493	0.2416	-0.653
3	TYBO_C136	0.324	0.1024	0.49
4	MTC_WTA	-0.236	0.0486	-0.361

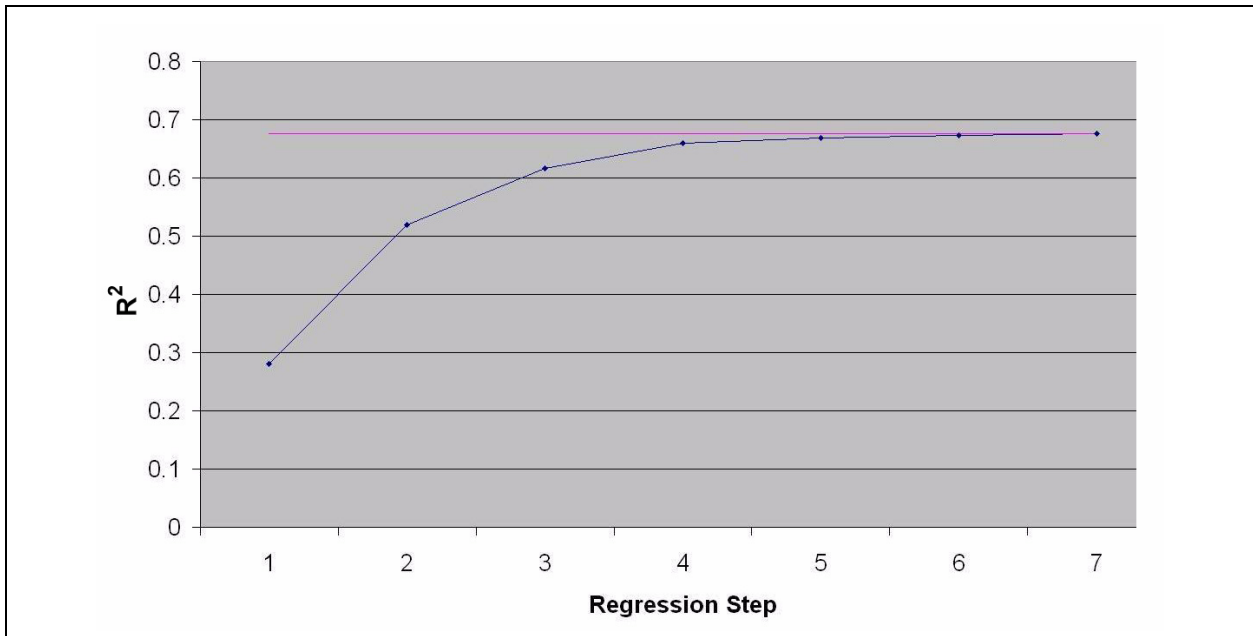


**Figure 8-21**  
**Stepwise Regression for SCCC-MME**

### 8.2.5 Sensitivity Analysis by Method

This section provides a composite analysis of the three global sensitivity methods for all seven of the selected HFMs. Throughout the analysis, a specific subset of the total number of parameters has consistently appeared to impact the EV response. These were identified in Table 8-1. The results for all HFMs are compiled into three tables, one for each method. The progressive increase of the EV for each HFM is one possible metric to identify models that have similar attributes. The ECDF in Figure 7-3 shows the EV ranges calculated for each of the HFMs and provide a preliminary categorization scheme. The purpose of this section is threefold: (1) assess which parameters are most important overall, (2) identify parameters that consistently appear for specific HFMs and/or specific methods, and (3) identify the cause of key parameter sensitivities so that, through further analysis, parameter sensitivity can be reduced.

#### 8.2.5.1 Classification Tree

The classification tree results as listed in Table 8-16 show the splits that occurred for each of the seven HFMs. The higher splits denote the more important parameters that contribute to output uncertainty. For only the first two splits, Table 8-17 shows those parameters that appear, their number of occurrences, and the number of times that a parameter is the first ranked. Of the seven first-split parameters, five are transport parameters and two are inventory (shown shaded in light blue). Of the five second-split parameters, four are inventory and one is a transport parameters.

**Table 8-16**  
**Classification Tree of Splits for Each HFM**

Classification Tree	Split1	Split2hi	Split2low	Split3hi	Split3low
LCCU1-MME	MTC WTA	TYBO H3	R Pu Colloid	X	X
LCCU1-USGSD	MTC WTA	X	X	X	X
LCCU1-TMD	MTC WTA	TYBO H3	R Pu Colloid	K <sub>d</sub> Np Zeol	X
LCCU1-TMCM	R Pu Colloid	EFFPOR TCU	EFFPOR TCU	X	X
DRT-DRIA	EFFPOR TCU	R Pu Colloid	X	X	X
PZUP-MME	MTC WTA	TYBO H3	X	X	X
SCCC-MME	R Pu Colloid	X	EFFPOR TCU	X	X

**Table 8-17**  
**Classification Tree Transport Parameters**

Transport Parameters	Number of Occurrences	Number of First Occurrences
MTC_WTA	4	4
R_Pu_Colloid	3	2
EFFPOR_TCU	2	1
TYBO_H3	3	0

**8.2.5.2 Entropy Analysis**

The entropy analysis method is a measure of the strength of association between the input parameters and output EV. Any non-random association is considered, including those that are non-monotonic and non-linear. The order of ranking for the top five parameters for each of the seven HFMs is listed in [Table 8-18](#). Using this method, the top three parameters typically show a strong to moderate association. For all HFMs, [Table 8-19](#) identifies the parameters ranked in the top three, how many times the parameters appear, and how many times the parameters are ranked first. Of the seven first-ranked parameters, six are transport parameters and one is an inventory. For the second-ranked parameters, five are transport parameters and two are inventory.

**Table 8-18**  
**Ranked Entropy Analysis for the Top Five Parameters for Each HFM**

Entropy Analysis	Rank-by-Importance				
	First	Second	Third	Fourth	Fifth
LCCU1-MME	MTC_WTA	EFFPOR_WTA	TYBO_H3	EFFPOR_TCU	R_Pu_Colloid
LCCU1-USGSD	MTC_WTA	EFFPOR_WTA	TYBO_H3	FRAC_DMP/R	TYBO_C14
LCCU1-TMD	MTC_WTA	EFFPOR_WTA	TYBO_H3	R_Pu_Colloid	EFFPOR_TCU
LCCU1-TMCM	EFFPOR_TCU	R_Pu_Colloid	EFFPOR_WTA	MTC_WTA	TYBO_CI36
PZUP-MME	MTC_WTA	EFFPOR_WTA	EFFPOR_VTA	TYBO_H3	R_Pu_Colloid
DRT-DRIA	EFFPOR_TCU	R_Pu_Colloid	MTC_WTA	EFFPOR_WTA	FRAC_DMP/R
SCCC-MME	R_Pu_Colloid	EFFPOR_TCU	TYBO_CI36	TYBO_C14	EFFPOR_WTA

**Table 8-19**  
**Entropy Analysis Transport Parameters**

Transport Parameter	Number of Occurrences	Number of First Occurrences
MTC_WTA	5	4
R_Pu_Colloid	3	1
EFFPOR_TCU	3	2
EFFPOR_WTA	5	0
TYBO_H3	3	0
EFFPOR_VTA	1	0
TYBO_CI36	1	0

### 8.2.5.3 Stepwise Regression

The stepwise regression method assesses the component of variance that a parameter contributes to the output variance, sequentially adding parameters to the regression model until a significant contribution can no longer be made. Unlike the entropy (mutual information) approach, stepwise regression only applies to input/output pairs that are monotonic and linear. As with entropy analysis, the three top-ranked parameters typically account for the greatest combined variance. Of the parameters in [Table 8-20](#), MTC\_WTA and EFFPOR\_TCU comprise the first ranked parameters across all HFMs. All of the first-ranked parameters are transport parameters, and all second-ranked parameters are inventory. The list in [Table 8-21](#), drawn from the first three ranked parameters across HFMs, identifies how many times the parameters appear in any of the ranks and how many times the parameter is first ranked.

**Table 8-20**  
**Ranked Stepwise Regression Parameters**

Stepwise Regression	Rank-by-Importance				
	First	Second	Third	Fourth	Fifth
LCCU1-MME	MTC_WTA	TYBO_H3	FRAC_DMP/R	R_Pu_Colloid	EFFPOR_TCU
LCCU1-USGSD	MTC_WTA	TYBO_H3	EFFPOR_WTA	FRAC_DMP/R	TYBO_C14
LCCU1-TMD	MTC_WTA	TYBO_H3	R_Pu_Colloid	FRAC_DMP/R	EFFPOR_WTA
LCCU1-TMCM	EFFPOR_TCU	R_Pu_Colloid	TYBO_CI36	MTC_WTA	TYBO_I129
PZUP-MME	MTC_WTA	TYBO_H3	EFFPOR_VTA	R_Pu_Colloid	EFFPOR_TCU
DRT-DRIA	EFFPOR_TCU	R_Pu_Colloid	MTC_WTA	TYBO_CI36	TYBO_H3
SCCC-MME	EFFPOR_TCU	R_Pu_Colloid	TYBO_CI36	MTC_WTA	TYBO_I129



**Table 8-21**  
**Stepwise Regression Transport Parameters**

Transport Parameter	Number of Occurrences	Number of First Occurrences
MTC_WTA	5	4
EFFPOR_TCU	3	3
TYBO_H3	4	0
R_Pu_Colloid	4	0
EFFPOR_WTA	1	0
EFFPOR_VTA	1	0
TYBO_CI36	2	0
FRAC_DMP/R	1	0

### 8.2.6 Composite Analysis

The most dominant parameters across all HFMs are the MTC\_WTA, EFFPOR\_TCU, and R\_Pu\_Colloid. Of secondary importance are TYBO\_H3 and EFFPOR\_WTA. Table 8-22 lists the number of times that each parameter appears and the number of times that it is ranked first over all methods and all HFMs. Transport through four of the seven HFMs appears to be strongly influenced by parameters associated with fracture-flow-dominated (high-permeability/low-porosity) units and indicate that WTA HGU's constitute an appreciable proportion of transport media. The remaining three HFMs promote parameters that are associated with the more porous/lower-permeability units and are grouped as the HFMs that exhibit the lowest EV. The general correspondence between HFMs and parameters is shown in Table 8-23.

**Table 8-22**  
**Composite Analysis Transport Parameters**

Transport Parameters	Number of Occurrences	Number of First Occurrences
MTC_WTA	14	12
EFFPOR_TCU	8	6
R_Pu_Colloid	10	3
TYBO_H3	10	0
EFFPOR_WTA	4	0

**Table 8-23**  
**Grouping of Sensitive Transport Parameters Based on the EV for Each HFM**

HFM	Transport Parameter	EV
LCCU1-MME LCCU1-USGSD LCCU1-TMD PZUP-MME	MTC_WTA EFFPOR_WTA TYBO_H3	High
LCCU1-TMCM DRT-DRIA SCCC-MME	R_Pu_Colloid EFFPOR_TCU	Low

Because the high-permeability units allow passage of the plume without any significant retention of the contamination, the plumes are always large and the output response is high for the HGU because of the size of the plume, although the high-permeability flow parameters tend to be generally insensitive. Conversely, the low-permeability units react with the plume at a smaller scale that results in a more immediate response and therefore higher sensitivity associated with the low-permeability units for a smaller plume. Consequently, the location and size of the HGUs in the form of the conceptual model is a critical component in understanding the flow model dynamics, the spread in the contaminant plume and proper identification of the most uncertain parameters that contribute to model output sensitivity.

In the context of individual HFMs, the four high-permeability cases are dominated by the parameters MTC\_WTA, EFFPOR\_WTA, and TYBO\_H3 because the interconnected flow path from the source area to downgradient receptors is largely uninterrupted and is represented by large, high-permeability blocks within the model domain. The LCCU1-MME is generally considered the base model from which most of the conceptual modifications performed are derived during the transport modeling Phase I task. The EV for this model is larger than any of the other HFMs as depicted in [Figure 7-3](#) (from EV discussion). The larger plume is an artifact of the large, interconnected blocks of high-permeability rock that are common to the high-permeability HFMs. The LCCU1-USGSD model is identical to the preceding model, except that the recharge is now less. The plume is slightly smaller because the lower fluxes from Timber Mountain and, consequently, a lower groundwater gradient. The LCCU1-TMD model is another variation of the LCCU1-MME model for which the permeability through the TMD is increased by two orders of magnitude. The results of this change cause a deflection of the Area 19 plume further to the east, along the flank of Timber Mountain. However, the main plume from Area 20 is largely unaffected. The high-permeability rocks still

dominate flow and cause the extended plume. The PZUP-MME model incorporates a raised pre-tertiary basement over the entire domain. This results in a thinner permeable unit and, therefore, concentration of the plume in the upper formation. This prevents the plume from spreading vertically, which would aid in dilution.

The three low-permeability cases are the result of the different conceptualization relative to the high-permeability cases. The transport parameters that most affect the output sensitivity are EFFPOR\_TCU and R\_Pu\_Colloid. For the LCCU1-TMCM model, increasing the permeability of the FCCU and FCCM units and adjusting the subunits of the TMCM allows the contaminant plume to spread out more and interact with the lower-permeability units. By doing this, the plume is slowed in the lower-permeability units and diluted elsewhere in the model such that the parameters that are more important in these units become the parameters that the output is most sensitive to. The SCCC-MME case consists of a simpler hydrostratigraphic conceptual model that does not incorporate the large and complex interconnections of hydrogeologic blocks such that the high-permeability blocks form a continuous flow path through the model domain. This can be observed at the boundary between the NTS boundary where the high-permeability unit of the Silent Canyon caldera abuts the lower-permeability Calico Hills unit to the south. Because the flows are slowed moving through the Calico Hills unit, the contaminant can react with the high-porosity unit and dilute as the flow re-enters the higher-permeability units. For the DRT-DRIA case, the impact may not be the presence of a lower-permeability flow path as the effects of high recharge off of TMD that effectively dilutes any contaminant to below MCLs that may flow south of the Silent Canyon caldera.

### **8.2.7 Summary**

Parameter sensitivity analysis, as is customary practice and specified in the Pahute Mesa CAIP (DOE/NV, 1999), was performed on seven HFMs in the PM CAU model using a complementary suite of techniques. Global sensitivity analyses were carried out using classification tree, entropy analysis, and stepwise regression to determine parameter importance conditioned over the entire range of parameter variations. For the global sensitivity analysis, a Monte Carlo simulation-based sampling methodology was used to generate multiple parameter combinations to evaluate each model.

In the global sensitivity analysis, the classification tree provided insight into what parameters affect the output over the entire parameter space. The classification tree also showed how particular

combinations of parameters interact to produce a particular result. The entropy analysis not only served to corroborate results from the classification tree analysis, but also quantified the relative importance of particular parameters. The stepwise regression analysis served as an additional confirmation of the results of the two preceding methods. The similarity of the results between the stepwise regression and the other methods suggests that the sensitivity relationship is largely linear for the input/output data pairs. This assumption tends to be supported by the observed trends in the bubble plots that are derived from the entropy analysis.

A compilation of all parameters that are identified by all three sensitivity analysis methods leads to the reduction of the original number of 35 possible parameters to a revised count of 10. Then, by assuming that the most significant parameters are those of the two highest-ranked parameters in each analysis, the number of significant parameters is further reduced to five. Observation of the plume evolution for each of the HFMs indicates that the HFMs can be categorized in terms of the size of the plume and, therefore, by the EV. When the large plume models and the smaller plume models are separated, there is also a separation of the parameters that show up as most sensitive in the analysis step. In the cases of large plume extent, the transport parameters are associated with models that are strongly influenced by the high-permeability rock, while the smaller plumes are associated with transport parameters that identify the lower-permeability rocks as contributing most to sensitivity. For the former case, the very large block of TCM appears to dominate transport out of Pahute Mesa for the high-permeability models. In the flow model, the TCM is largely insensitive. However, because of the large plume sizes, the transport parameters in these units become important. In the latter case, the dominance of the lower-permeability parameters is affiliated with three features of the conceptual model. The features that reduce plume size are (1) migration of the plume through a porous/low-permeability unit such as the CHZCM; (2) removal of confining units that “channel” flow through narrow, high-permeability rocks that then allows the contamination to spread out, dilute, or react over a wider area; and (3) dilution of the plume as a function of higher recharge near the plume.

The above analysis shows that model conceptualization has a strong influence on the results that the model will produce. Also recognition that the flow model and transport models separately identify different HSUs as important would suggest that further modeling should include a calibration and analysis of combined flow and transport parameters. To this end, additional transport data recovered

during a second phase of field data collection could potentially serve to provide insight for the conceptual model and further reduce groundwater model uncertainty.

### **8.3 Transport Sensitivity to Flow Model Uncertainty**

The identification of basin-scale preferential transport paths within subdivisions of the TMCM provoked a reanalysis of flow model conceptualization through the reparameterization (i.e., hydraulic conductivity adjustment) of selected HSUs. As presented in [Sections 3.4](#) and [7.6.6](#), this reanalysis led to the development of the LCCU1-MME-TMCM alternative model in the (justifiable) attempt to more homogenize flow and transport through HSUs south of the Moat fault. This section assesses the influence of parameter (i.e., permeability) uncertainty on transport, observing radionuclide migration paths and times of MCL exceedance with distance. The HSUs of focus are primarily the TMCM and FCCM, two extensive units south of the Moat fault that have been repeatedly shown to strongly influence transport. For example, radionuclide breakthrough near Oasis Valley and Beatty Wash, or otherwise at locations southwest of Timber Mountain, varies between about 250 and 750 years depending solely on differences in TMCM and FCCM parameterization.

Three methods were applied to assess transport sensitivity to flow model parameter uncertainty. The first, called the NSMC approach, defines the range of TMCM/FCCM permeability insensitivity and exploits this to develop multiple, equiprobable flow models for transport simulation. In this analysis, unlike for the global sensitivity methods described in [Section 8.2](#), the Monte Carlo approach is used before transport for development of flow models, and only individual transport simulations are performed for each model using a set of averaged transport parameters. The second method investigates alternative scenarios for depth decay in the TMCM, and the third investigates the effect of dispersivity on transport. The standard global sensitivity analysis methods are generally able to be applied in these cases.

Before relating these analyses, it is appropriate to begin with an attempt at definition of TMCM (and related HSU) parameter uncertainty conditional to the state of a calibrated model. This was spoken to during the initial flow model calibration effort and is summarized before a quantitative assessment of transport sensitivity to flow model uncertainty.

### 8.3.1 Previous Analysis of TMCM Permeability Uncertainty

Timber Mountain composite unit permeability uncertainty was first identified and addressed by SNJV (2006a) during flow model conceptualization and calibration of the base-HFM alternative flow models. Due to high flow model sensitivity to the regionally extensive TMCM when modeled as single-material HSU, BN (2002a) suggested subdivision of the TMCM into eight hydrogeologic domains (Figure 8-22). Three analyses were performed, one investigating the effect of a recharge mound under Timber Mountain, a second investigating permeability variation within the TMCM subdomains through a local (individual parameter perturbation) sensitivity analysis, and the third inducing flow down Fortymile Canyon through permeability adjustment. These cases are summarized below and provide the basis for analysis of transport sensitivity to TMCM permeability in this analysis.

#### 8.3.1.1 Timber Mountain Recharge Mound

In an analysis of the effect of a recharge mound under Timber Mountain, three cases were investigated:

1. A single value for TMCM reference permeability ( $k_0$ ) was used, effectively homogenizing the TMCM subdomains.
2. The Timber Mountain dome subdivision (TMCMTMD in Figure 8-22)  $k_0$  was increased 10 times. The TMCMTMD covers the areal extent with the highest recharge in Timber Mountain and is used to control the height of the mound.
3. The TMCMTMD  $k_0$  was increased 100 times.

In each case, the model was recalibrated following the parameter change. The reduced LCCU1 permeability alternative with MME recharge and selected depth decay was used as the starting point for these analyses.

In general, the differences between cases are mild, with the single TMCM-material case showing the largest errors. The objective functions were 16,690, 18,156, and 24,180 for cases 1 through 3, respectively, noting that the calibration of the case from which these analyses were derived was 16,623. The impact of adjusting the TMD and TMCM is generally the same for all cases; model agreement at WW-8 degrades, Torrance Spring is misfit, west and north boundary flows are misfit, as is ET Zone 3 in Oasis Valley. Figure 8-23 shows the posted weighted head residuals. The most

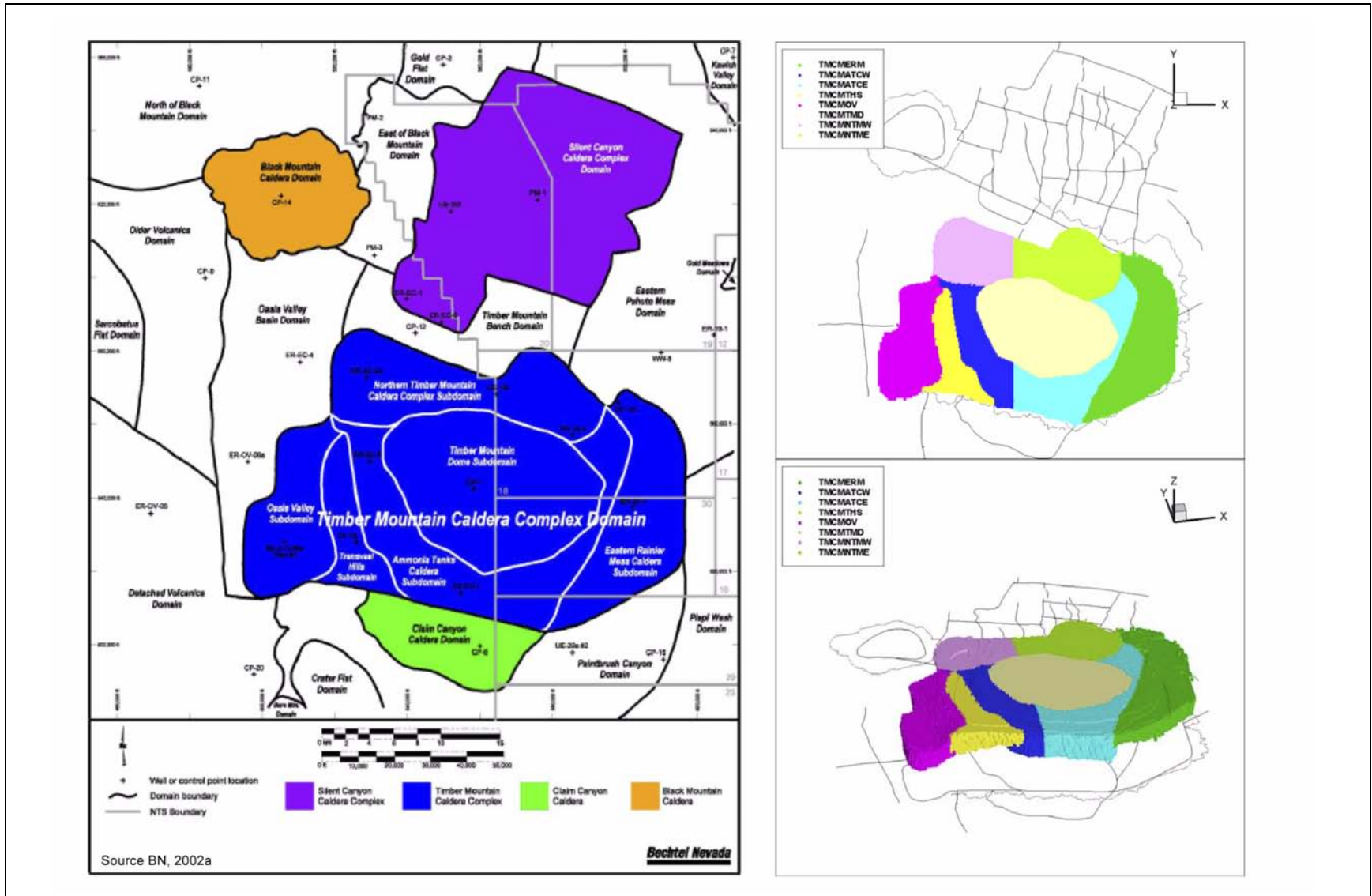
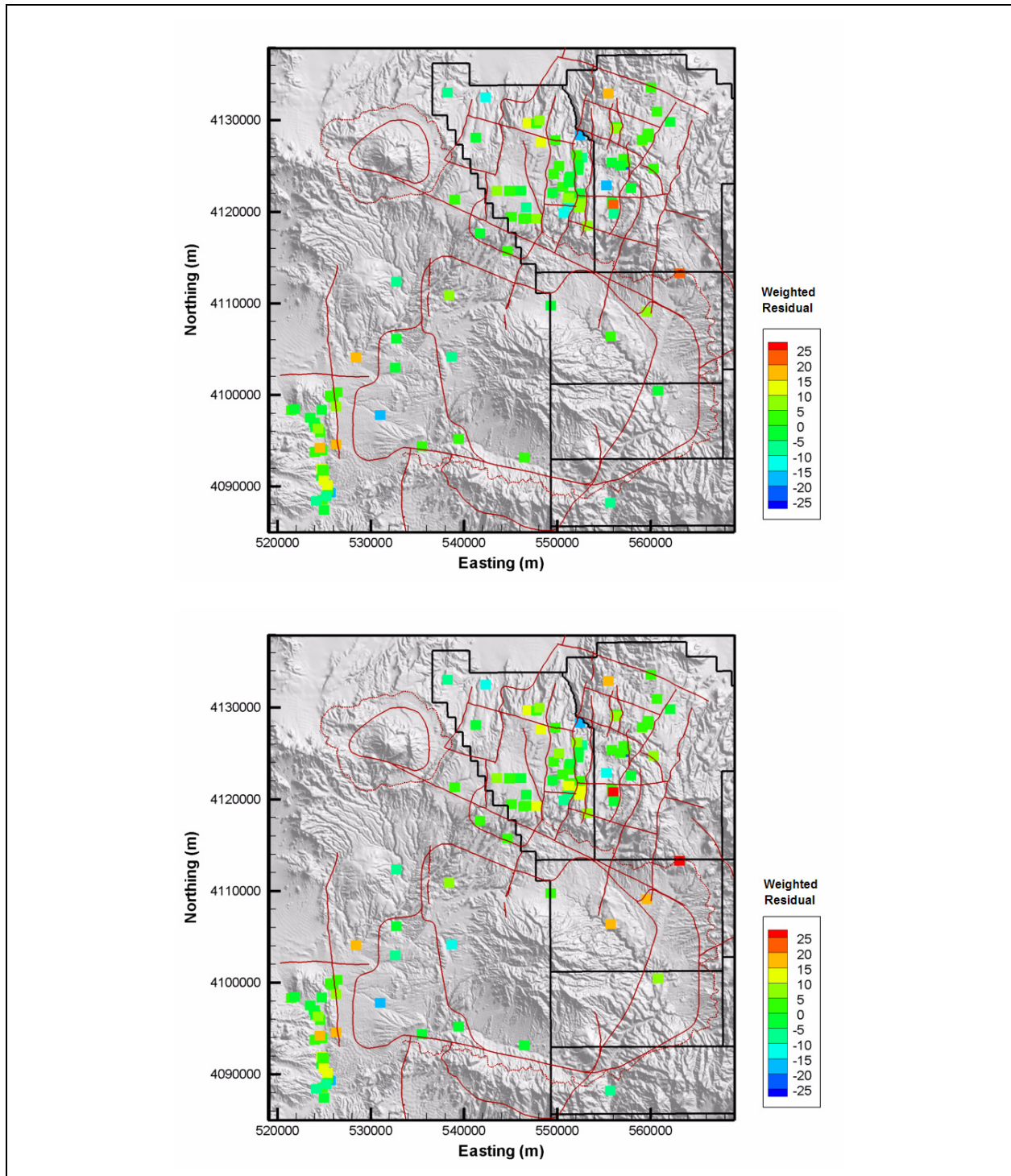


Figure 8-22  
Hydrogeologic Subdomains of the TCMC in the Pahute Mesa Model Area



**Figure 8-23**  
**Weighted Well and Spring Head (m) Residuals for TMD Permeability**  
**of 10x (top) and 100x (bottom)**

Source: SNJV, 2006a



notable change is the increasing underprediction of head in the area of WW-8 as the TMCMTMD  $k_0$  increases. Forming the mound under Timber Mountain clearly has an effect in this area, although less so elsewhere. [Figure 8-24](#) shows the simulated water table, and [Figure 8-25](#) shows the particle tracks. As the TMCMTMD  $k_0$  increases, decreasing the simulated mound, the potentiometric surface grows flatter (as it conceptually should). The flow paths become more diffuse through the Timber Mountain area as the mound diminishes and no longer focuses flow on its northwest and northeast flanks.

### **8.3.1.2 TCMC Subdivision Local Permeability Perturbation**

In the perturbation analysis, the permeability of several dominant HSUs, including the TCMC, was individually increased and decreased while changes in the objective function, heads, and various fluxes were recorded. This analysis was performed on only the base-HFM selected HSU depth-decay and anisotropy parameterization with the MME recharge model. Estimated SDs in HSU permeability (Section 2.0 of SNJV [2006a]) and depth decay were applied to describe the uncertainty in the calibrated values of these parameters. For both the HSU permeability and depth decay, six simulations were completed where the input value was perturbed up and down one-half, one, and two SDs from the calibrated value.

Regarding only the TCMC, results indicate that in general the calibration metrics are insensitive to  $k_0$  variation within subdomains, but sensitive when considered as a single-material unit. Not all subdomains, however, were considered in the analysis. The single-material conceptualization of the TCMC was shown to be the single-most sensitive parameter when considering depth-decay coefficient perturbation ([Section 8.3.3](#) of this report discusses transport sensitivity to the TCMC depth-decay parameter). Although the perturbation analysis was not designed to specifically address TCMC parameter uncertainty, results indicate that a nontrivial region of permeability insensitivity likely exists within the set of subdivision permeabilities.

### **8.3.1.3 Fortymile Canyon Alternative Model**

The Fortymile Canyon conceptualization was designed to test the model sensitivity to increased flow down Fortymile Canyon. The Northern Timber Mountain eastern subdivision (TMCMTME), Timber Mountain dome (TMCMTMD), and Ammonia Tanks eastern subdivision (TMCMTCE) permeabilities each were raised one order of magnitude in an attempt to direct more flow to the southeast down Fortymile Canyon. The LCCU1 HSU permeability was simultaneously dropped one order of magnitude to both remove its influence and to test the ability of recharge in the

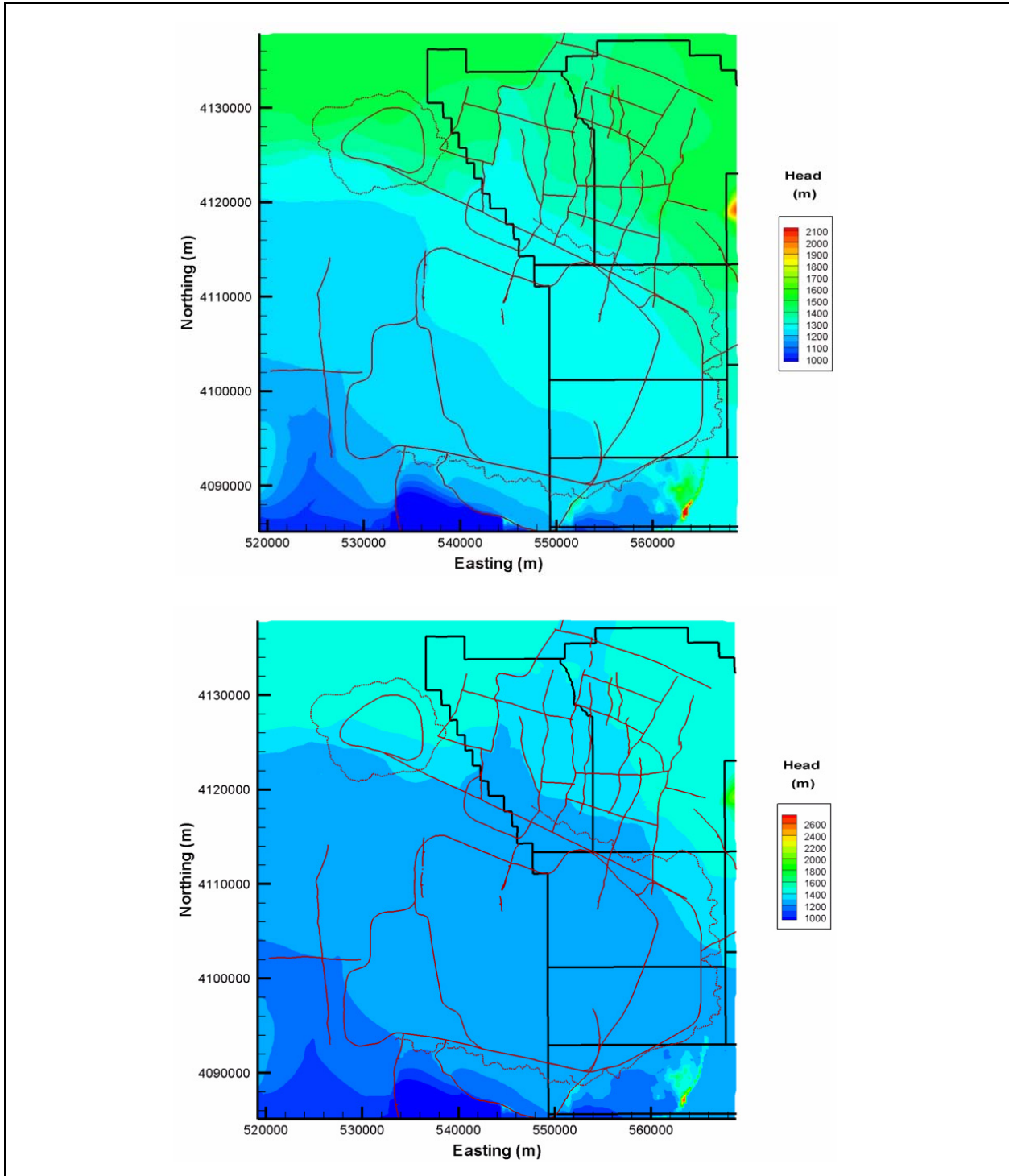


**Figure 8-24**  
**Simulated Water Tables for TMD Permeability Increases**  
**of 10x (top) and 100x (bottom)**

Source: SNJV, 2006a

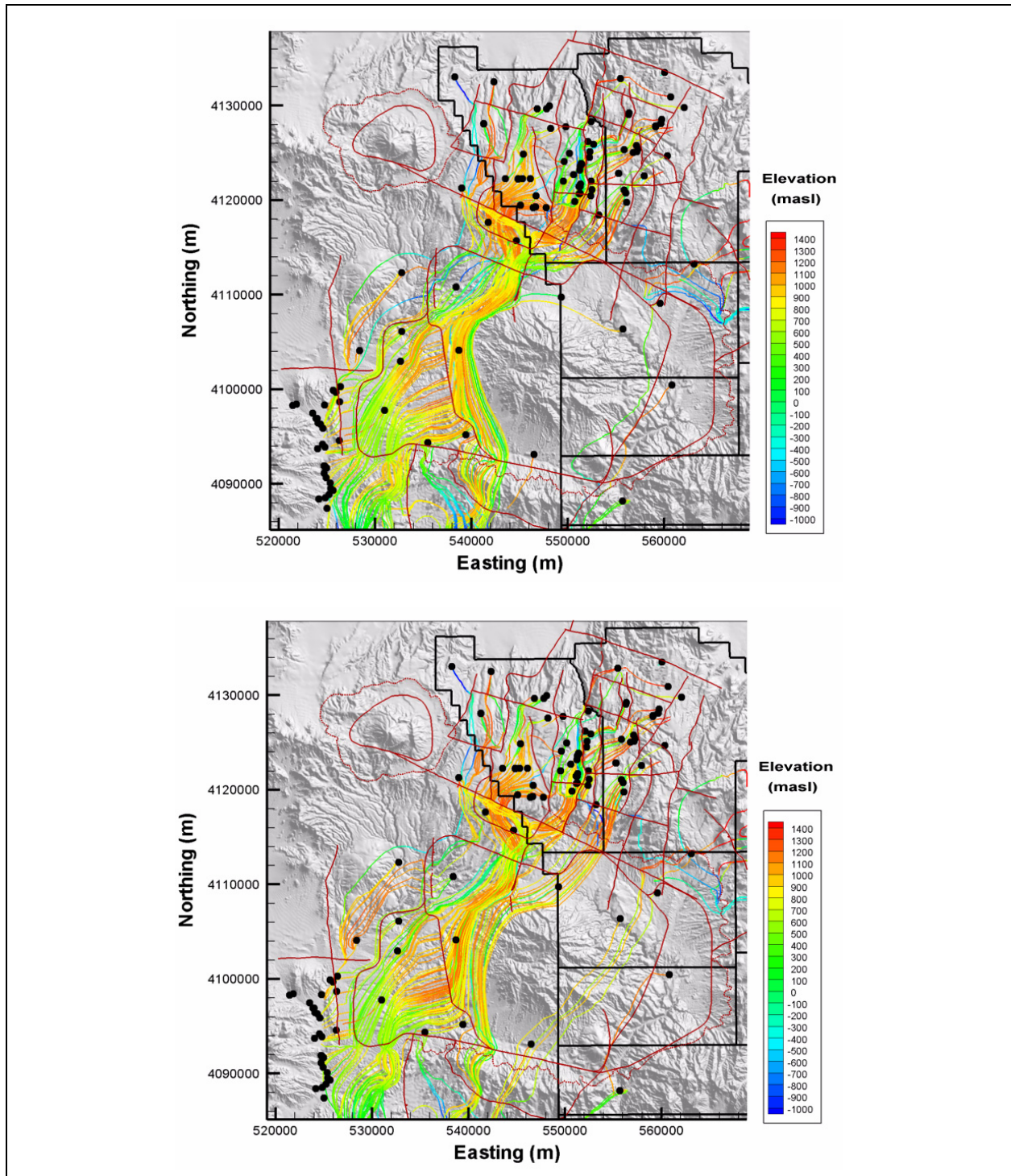


**Figure 8-25**  
**Particle Tracks for TMD Permeability Increases of 10x (top) and 100x (bottom)**

Source: SNJV, 2006a

canyon to support the flow field. This analysis was performed on only the base-HFM selected HSU depth-decay and anisotropy parameterization with the USGSD recharge model (having the best calibration results).

Calibration summary statistics (shown in Table 6-16 of SNJV [2006a]) indicate decreased Oasis Valley discharge (179 kg/s simulated versus 227 kg/s observed) with increased flow down Fortymile Canyon. Simulated well heads, particularly at WW-8, are also underestimated in this area. The calibration objective function deteriorates by about 20 percent for this alternative; however, it remains better than other accepted alternative HFM cases. Particle tracks for this alternative are shown in [Figure 8-26](#). There is clearly a bias in flow through Fortymile Canyon, thought to result from the draining off of water along the canyon from the higher permeabilities. More particle tracks exit Areas 19 and 20 and then flow down Fortymile Canyon than in any other alternative cases, which is consistent with the behavior of undersimulating Oasis Valley discharge as noted.

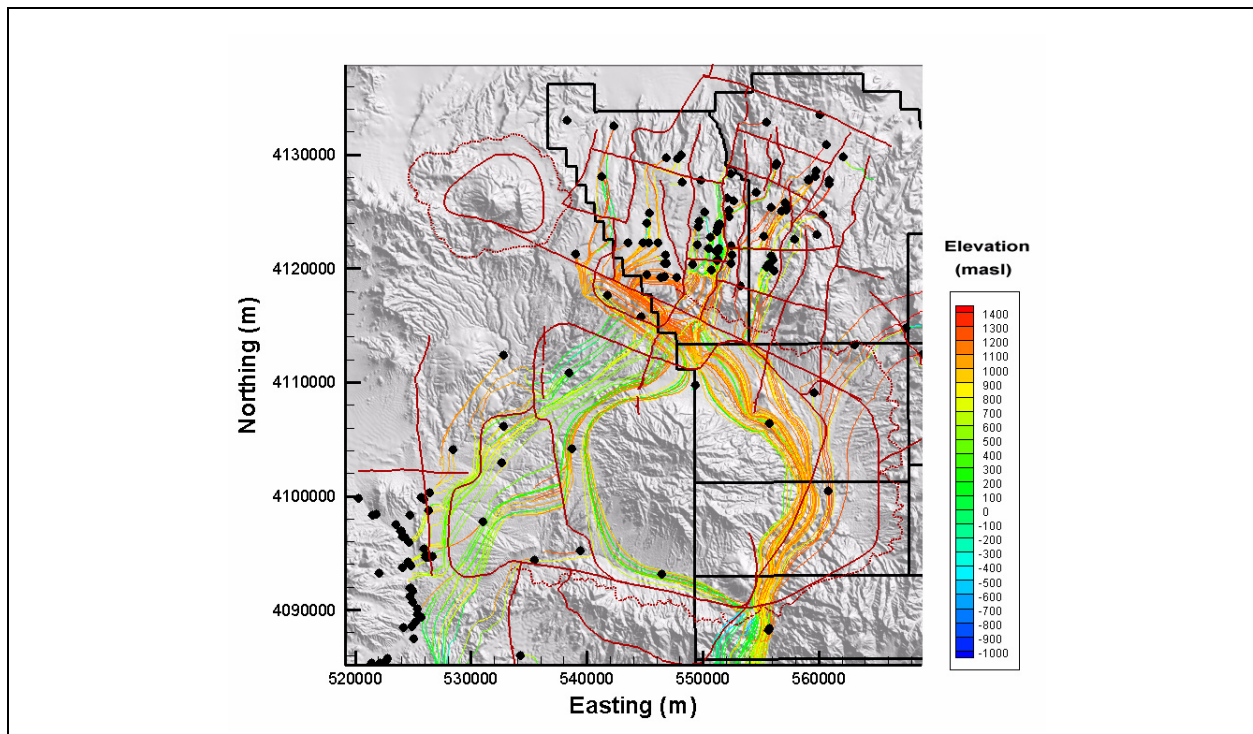


**Figure 8-26**  
**Particle Tracks for the BN-MME-SDA Fortymile Canyon Alternative Model**  
 Source: SNJV, 2006a

### 8.3.2 Null Space Monte Carlo Analysis

Preliminary investigation of the influence of TMCM permeability, when conceptualized as a set of subdivisions, on flow model calibration metrics clearly imply that a nontrivial region of uncertainty and insensitivity exist. Uncertainty implies the range of permeability values plausible at the modeled scale, and insensitivity points to the range of permeabilities for which the model calibration metrics remain constant and/or below some acceptable value. The NSMC analysis permits the quantitative identification of the overlap of both such regions, the results of which serve two purposes. First, a discrete range of permeability insensitivity is defined that honors both field observation of permeability (i.e., the range of uncertainty) and field observation of hydraulic calibration targets, the latter implying that the range of insensitivity is in large part governed by how well observations constrain the parameter estimation problem. Second, multiple equiprobable flow models may be defined for use in a Monte Carlo transport analysis and subsequent assessment of transport model sensitivity to TMCM permeability.

In this study, the NSMC analysis is used to assess the general influence of permeability uncertainty (in the TMCM and FCCM) on radionuclide migration (location and travel time), and not to define an exact, statistically significant range of permeability insensitivity for the HSUs in question. Given this purpose, it was computationally practical to generate 10 realizations of TMC-subdivision and FCCM permeability via the NSMC methodology for the construction of 10 alternative, equiprobable flow models. The base model from which these were developed was the LCCU1-MME-TMCM, conceptualized and calibrated during transport analysis (see [Section 3.4.3](#)) for its reduction of preferential flow and transport paths observed in the prior alternative models. The following summarizes the analysis methodology.

The NSMC approach begins with the identification of the range of permeability uncertainty for the TMCM and FCCM, derived from field measurements and listed in [Table 8-24](#). In the LCCU1-MME-TMCM model, the calibrated (best-estimate) permeability for each of the units is then identified and assumed to reflect the expected value within each HSU/subdivision. Each realization is subsequently generated beginning with the calibrated parameter set in a four-step process that is repeated for each realization. First, for each subdomain, a random permeability datum is sampled from an assumed normal distribution with mean equal to the calibrated value and SD equal to that defined for the TMCM or FCCM ([Table 8-24](#)).

**Table 8-24**  
**Range of Permeability Uncertainty for the TMCM and FCCM**  
**Derived from Field Measurement**

HSU	$\bar{x}$ ( $\log_{10}$ m <sup>2</sup> )	$\bar{x} + 3*s$ ( $\log_{10}$ m <sup>2</sup> )	$\bar{x} - 3*s$ ( $\log_{10}$ m <sup>2</sup> )
FCCM	-12.028	-8.728	-15.328
TMCM	-11.528	-8.228	-14.828

Note: Values originally documented in Table 2-19 of SNJV (2006a).

$\bar{x}$  = Sample mean  
s = Sample SD

Thus, for each realization, there is a vector **p** that comprises the set of sampled TMCM subdivision and FCCM parameter values. Boxplots in [Figure 8-27](#) show the sampled range of uncertainty for each unit. In the second step, a vector of parameter residuals is calculated as **p - p\***, where **p\*** is the set of calibrated permeabilities. Third, the parameter residuals vector is projected onto the parameter null space, identified by the analyst through singular value decomposition (SVD) of the model Jacobian matrix, to generate a vector of parameter residual components **p<sub>d</sub>** that are within the region of permeability insensitivity. Lastly in the fourth step, **p<sub>d</sub>** is added to **p\*** to produce a single NSMC realization.

In the case of a linear flow model that presents a well-posed problem, each of the NSMC permeability realizations would yield equivalent calibration metrics. The PM CAU flow model is, however, clearly a nonlinear system. Additionally, observation of the Jacobian singular values indicated an ill-posed problem in the sense that a clear distinction did not exist between the nonzero and (approximately) zero singular values. Thus, not all of the NSMC flow models were expected to retain the calibrated state. In fact, three of the 10 models deteriorated in calibration. When this occurred, a single recalibration iteration was performed that brought the model back to a calibrated state, corresponding to an objective function at or below a value of 20,000, as shown in [Figure 8-28](#). Only one model, corresponding to realization 7, was not able to be recalibrated and was, therefore, left out of further analysis.

[Figure 8-29](#) shows the discrete range of TMCM and FCCM permeability insensitivity (following NSMC analysis) as opposed to the range of uncertainty (before NSMC analysis) in [Figure 8-27](#). With the exception of a single outlier, FCCM permeability is well bounded within about one-half order of

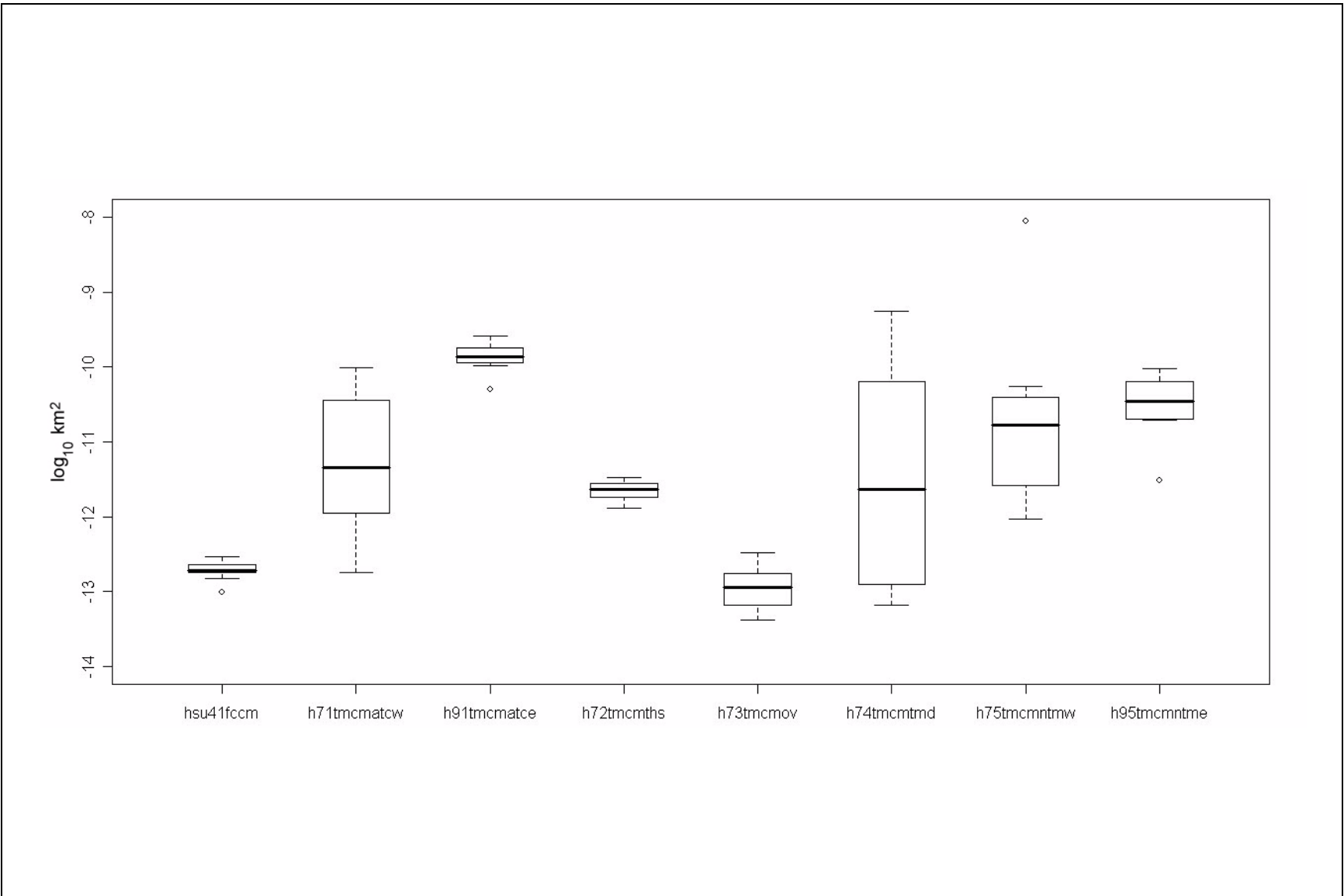


**Figure 8-27**

**Boxplots Define the Sampled Range of Permeability Uncertainty before Assessing Their Insensitive Components**

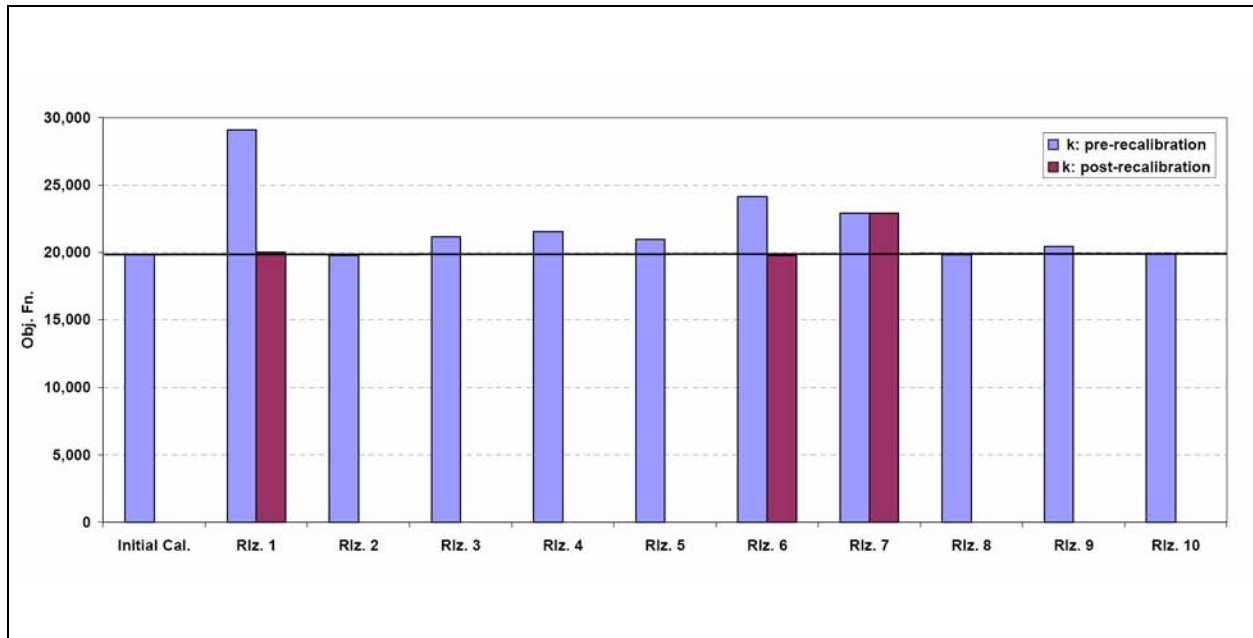


**Figure 8-28**

**Flow Simulation Objective Functions for Each of the NSMC Permeability Realizations**

magnitude. On the contrary, permeability varies about four orders of magnitude across the TCMC subdomains, excluding a few outliers. The range of permeability insensitivity across realizations is shown in Table 8-25. Relative to the initial calibrated model with a permeability range (across HSUs) of 2.8 m<sup>2</sup> and SD of 1.7 m<sup>2</sup>, the range of permeability per NSMC realization is typically larger. Realization 1 has the largest range (5.3 m<sup>2</sup>) and variability (SD of 1.7 m<sup>2</sup>).

The NSMC analysis considers data constraints when defining a range of insensitivity through SVD of the Jacobian. Therefore, under the assumption that the model geologic conceptualization is accurate, it is only through additional calibration targets that the range of insensitivity can be reduced. While natural insensitivity of the model output to TCMC permeability may exist, principally due to its large areal extent and depth, any such effect given the current model construction and data availability is certainly outweighed by the affect of insufficient constraint by field observations. For example, the FCCM, one of the largest HSUs extending east-west across the southern half of the model domain, holds 11 well head observations, some of which reflect composite borehole completions. The TCMC as a single-material HSU holds only six while its volume is at least one order of magnitude larger than that of the FCCM. Figure 8-30 shows boreholes at which head measurements are exclusive to either the TCMC or FCCM or reflect composite HSUs.



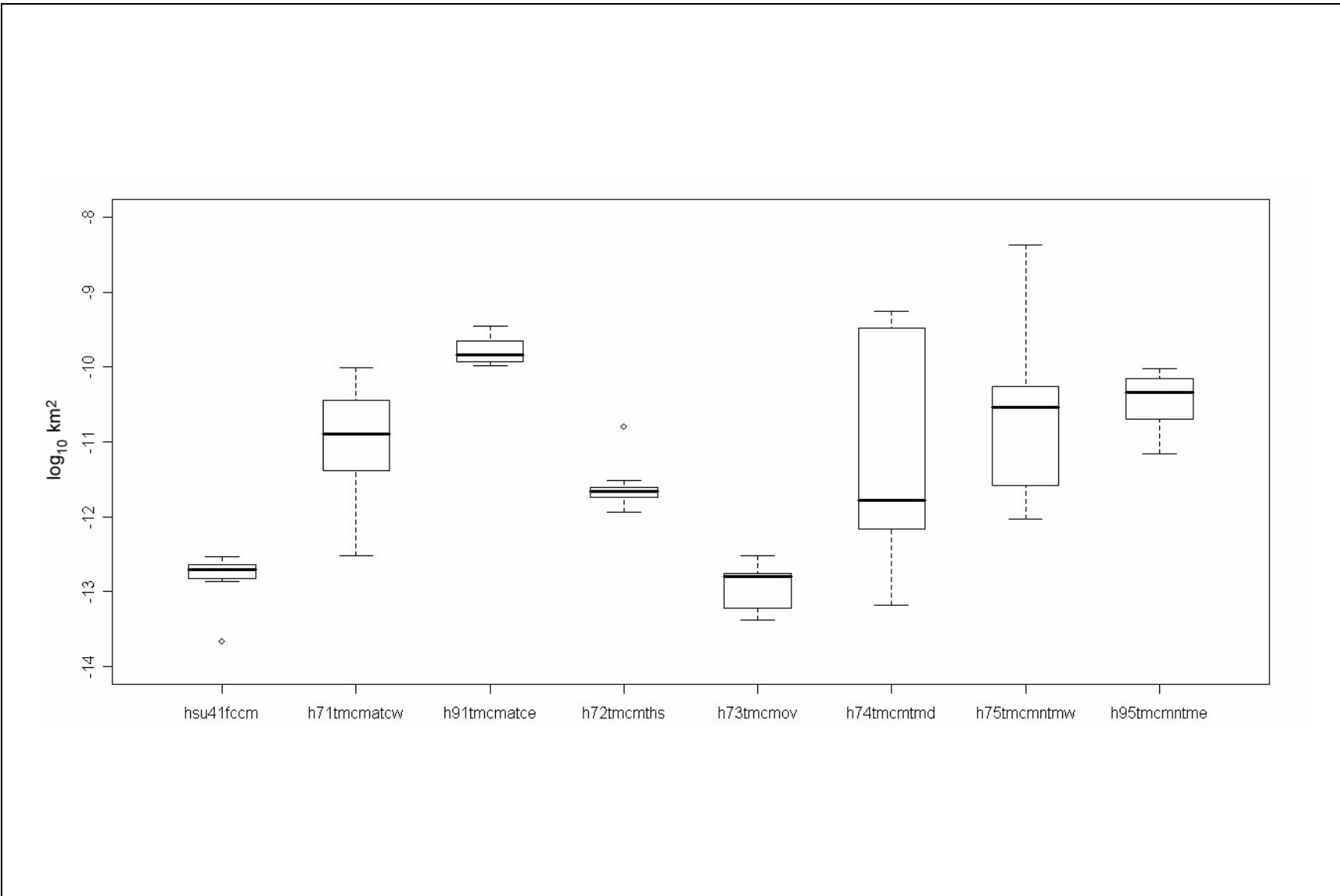


**Figure 8-29**  
**Boxplots Define the Calculated Range of Permeability Insensitivity**

**Table 8-25**  
**Range of Permeability Insensitivity across Realizations**

Realization	TMC and FCCM Permeability ( $\log_{10} m^2$ )								SD ( $m^2$ )	Range ( $m^2$ )
	HSU41FCCM	H71TMCATCW	H91TMCATCE	H72TMCMTS	H73TMCMOV	H74TMCMTD	H75TMCMTMW	H95TMCMTME		
1	-13.676	-10.517	-9.987	-11.945	-12.518	-9.477	-8.366	-11.161	1.73	5.31
2	-12.706	-10.430	-9.645	-11.604	-12.758	-13.180	-11.579	10.150	1.32	3.53
3	-12.640	-11.960	-9.743	-11.521	-13.224	-11.883	-11.565	-10.191	1.16	3.48
4	-12.540	-11.386	-9.838	-11.660	-13.390	-9.247	-11.621	-10.336	1.38	4.14
5	-12.825	-10.896	-9.886	-11.699	-12.663	-12.168	-10.258	-10.651	1.12	2.94
6	-12.869	-12.524	-9.457	-10.808	-14.713	-11.781	-10.065	-10.047	1.78	5.26
7	-12.744	-12.579	-9.788	-11.471	-13.114	-12.974	-11.002	-10.307	1.29	3.33
8	-12.750	-10.443	-9.927	-11.785	-12.769	-10.543	-10.404	-10.704	1.12	2.84
9	-12.682	-11.299	-9.979	-11.741	-13.103	-9.433	-10.536	-10.701	1.28	3.67
10	-12.644	-10.012	-9.583	-11.616	-12.801	-12.903	-12.036	-10.019	1.38	3.32

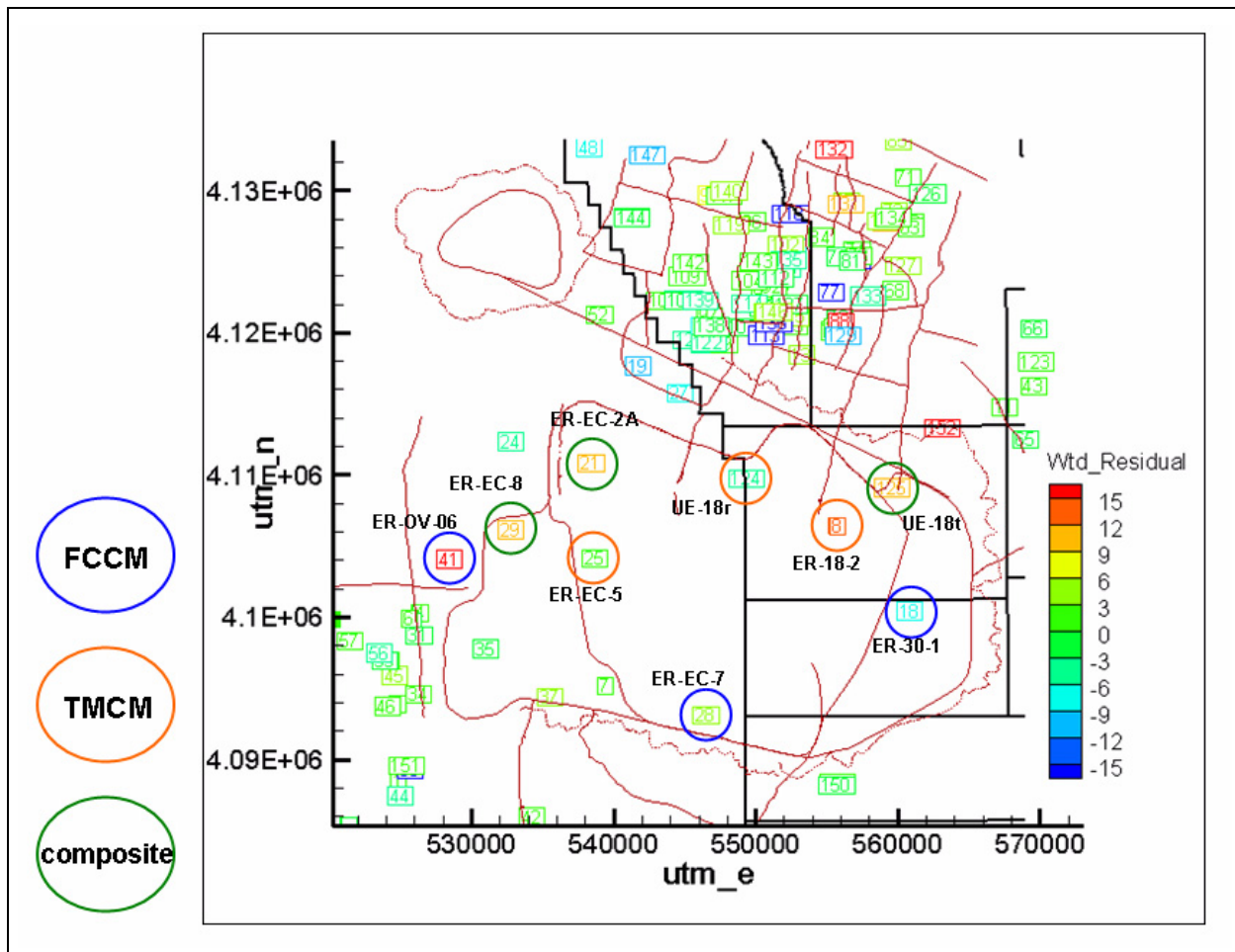


**Figure 8-30**

**Head Residuals for the LCCU1-MME-TMCM HFM Showing Boreholes at Which Head Measurements Are Exclusive to Either the TMCM, FCCM, or Both**

### 8.3.2.1 Transport Modeling

Each of the nine flow fields was applied in transport simulation of radionuclide migration from selected cavity sources. The exercise was designed to capture and differentiate the general transport behavior of each of the alternatives and to observe the association of each with its corresponding permeability realization. Accordingly, a single simulation to a maximum time of 1,000 years was performed using a set of average transport parameters, listed in [Table 8-26](#).

The region of FCCM/TMCM permeability insensitivity presented in [Figure 8-29](#) indeed leads to significant transport uncertainty. It should again, however, be noted that the use of an average set of transport parameters for each simulation provides only the general behavior of radionuclide migration. [Figure 8-31](#) shows the paths of radionuclide migration for four of the nine NSMC

**Table 8-26**  
**Average Transport Parameters Used for the Single Transport Simulation**  
**of Each NSMC Flow Model**

RMC	$n_{matrix}$	$n_{effective}$	$D_m$ (m <sup>2</sup> /s)	Fracture Aperture (m)
DMP	0.14	0.10E-02	0.144E-09	0.0030
VMP/R	N/A	0.19	N/A	N/A
ZEOL	N/A	0.33	N/A	N/A
DMR	0.14	0.10E-02	0.144E-09	0.0030
ML	0.16	0.50E-03	0.152E-09	0.0015

realizations with nodes colored by the time that an MCL is first exceeded. North-to-south-trending preferential flow paths vary significantly across the realizations, from transport down Thirsty Canyon (e.g., Case 3) to transport beneath Timber Mountain (e.g., Case 4) to transport east of Timber Mountain (e.g., Case 6). The time of MCL exceedance at nodes near or at the southern model boundary critically differ with a range of about 100 to 500 years.

To better define the cross-correlation between permeabilities and the correlation between permeability and EV, a scatterplot matrix of the subdomain permeabilities and EV (on the bottom row) is shown in [Figure 8-32](#). Note, however, that the resultant comparisons based on this figure are limited in their robustness because of the small sample size. Several of the subdivision permeability sets maintain a strong correlation and provide justification, given the hydraulic (and not geochemical) observations, for differentiation of these units given that their estimated permeabilities are in fact different as a result of some geologic process(es). Some such cases appear to make conceptual sense (e.g., the TCMATCE and TCMNTME are juxtaposed), while other pairs may not (e.g., TCMATCE and TCMTHS). Conversely, those subdomains showing a weak association may not justify differentiation of the TCM, or may simply serve as insensitive fitting parameters unsupported by observations.

Regarding the association between subdomain permeability and EV, there is clear relationship between a given permeability set, transport path, and EV. From the bottom row of [Figure 8-32](#), a positive correlation between an HSUs permeability and EV, indicates that advective transport in the TCM, as opposed to diffusive mechanisms, strongly influence transport. A negative correlation is involved in only two instances, with the TCMTMD and TCMNTMW. In both cases, low

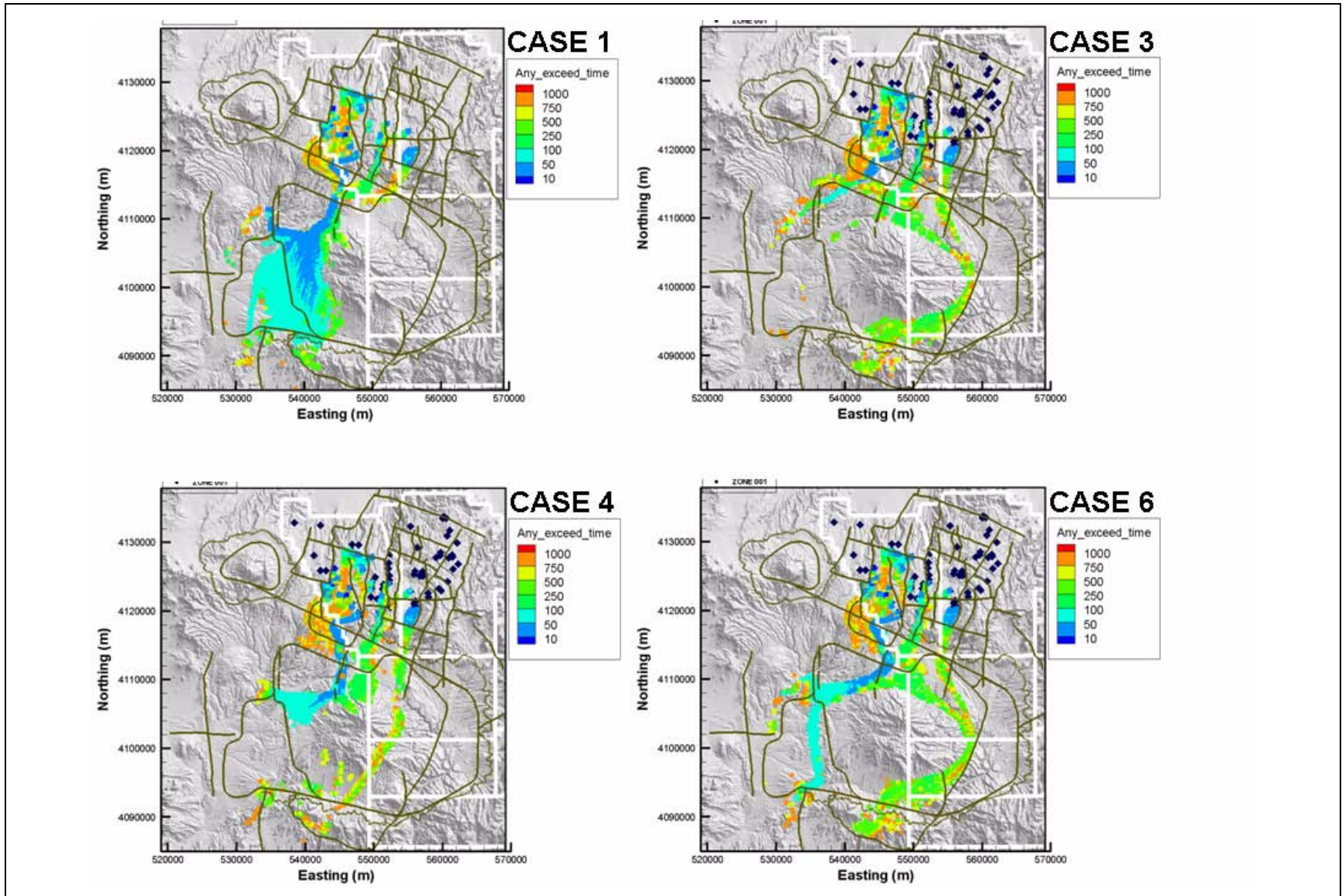


**Figure 8-31**  
**Radionuclide Migration for Four of Nine NSMC Flow Models**  
Note: Color contours indicate the time at which an MCL is first exceeded.

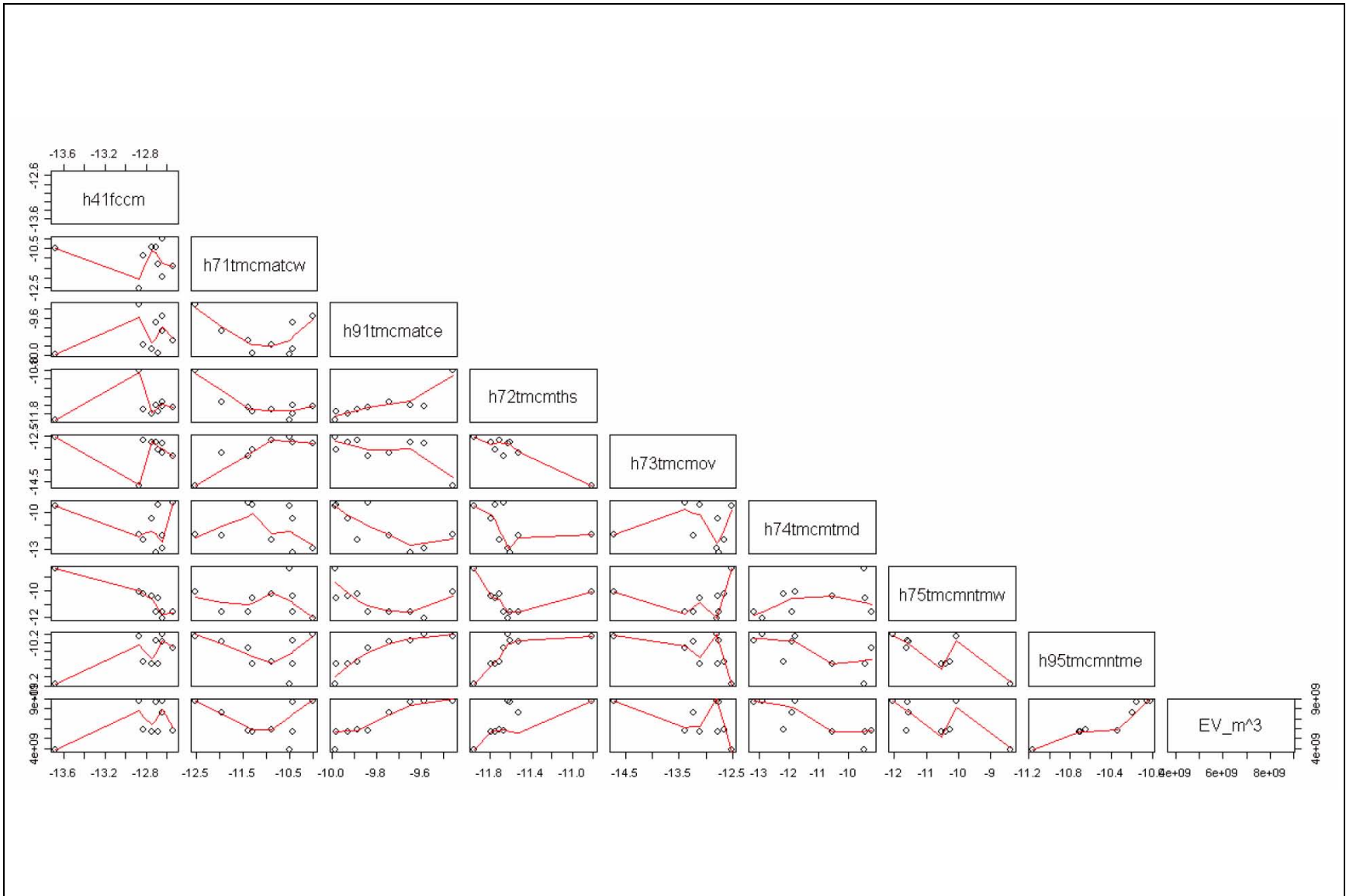


**Figure 8-32**  
**Scatterplot Matrix of NSMC Realization Permeabilities and Resultant EVs**

permeability pushes flow and transport around these units (to the east or west), thereby extending the plume path. Note also the general negative correlation between the TMCMTMD and all other subdomains, indicating that the permeabilities adjacent to Timber Mountain must increase when the TMCMTMD is low in order to dispel recharge off of the mountain.

In general, the NSMC results not only demonstrate that transport is sensitive to flow model parameter uncertainty, but also that conceptual model uncertainty is significant to a greater degree than parameter uncertainty. Clearly, the conceptualization of the TMCM is fundamental to its parameterization. Nevertheless, the basic point of this parametric uncertainty exercise is to show that hydraulic observations used to constrain the FCCM/TMCM permeability estimation problem are limited in their ability. Due to the large extent of these HSUs, such uncertainty leads to both large variability in plume extent (EV) and location within the model domain.

### **8.3.3 Depth-Decay Reduction**

In all of the models considered so far, a depth-decay coefficient of 0.0027 is applied to the TMCM (SNJV, 2005). This coefficient results in simulations that favor flow in the shallower parts of the TMCM, which can be as much as 3 km thick. This coefficient in the TMCM was set because the HFM does not have the structural resolution to provide features leading to surface discharge in Oasis Valley when flow in the TMCM is allowed to fully penetrate the HSUs' depth. However, there was only limited sensitivity analysis to depth-decay coefficient during flow model development. This semiquantitative sensitivity analysis considers reduced depth decay and investigates its impact on transport.

Rather than eliminating the depth-decay model completely, the coefficient is reduced from 0.0027 to 0.0010 in the TMCM and FCCM HSUs of the LCCU1-MME-TMCM flow model. The FCCM is subdivided into five zones capturing the RMCs in that HSU. [Figure 8-33](#) shows that 75 percent of the FCCM volume falls in the zeolitic category, but almost 20 percent of the volume is DMP (e.g., fractured). The TMCM is divided by subdomains described by BN (2002a) and discussed in [Section 3.4](#) of this report. However, more than 95 percent of the volume in all TMCM subzones is DMP or DMR. The depth-decay coefficient of 0.001 is applied to all FCCM and TMCM subzones, and the  $k_0$  values (permeability at depth = 0) are recalibrated.

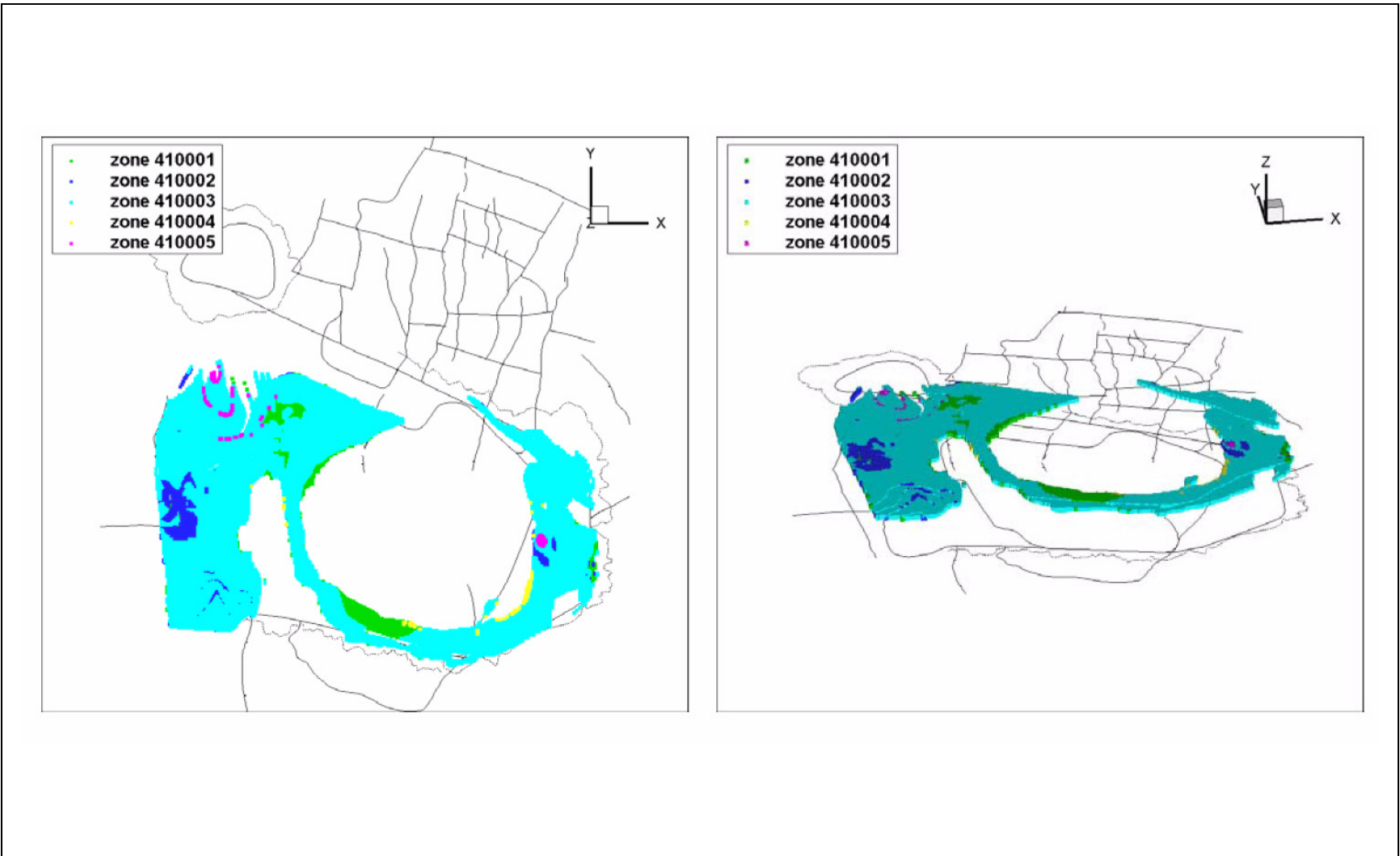


**Figure 8-33**

***Subzones in the FCCM for Recalibration with Reduced Depth-Decay Coefficient***

Note: The trailing numbers for each zone represent 1-DMP, 2-VMP, 3-ZEOL, 4-DMR, 5-ML.



Starting from a well-calibrated model, the new flow field with reduced depth decay is calibrated to the combined head and flux targets nearly as well. The main difference is that  $k_0$  values in the reduced depth-decay model are smaller, thus compensating for the reduced decay rate with depth (Figure 8-34). These new values serve to keep heads adequately high for calibration (increased permeabilities tend to lead to reduced simulated heads at target locations). With the reduced depth decay, three differences are apparent when comparing with the high depth-decay model. The error in estimating discharge at Oasis Valley springs and ET zones increases, and the head residuals deteriorate in the southeastern portion of the model, showing the systematic error of over/underpredicting heads in those wells when depth decay is reduced (Figure 8-35).

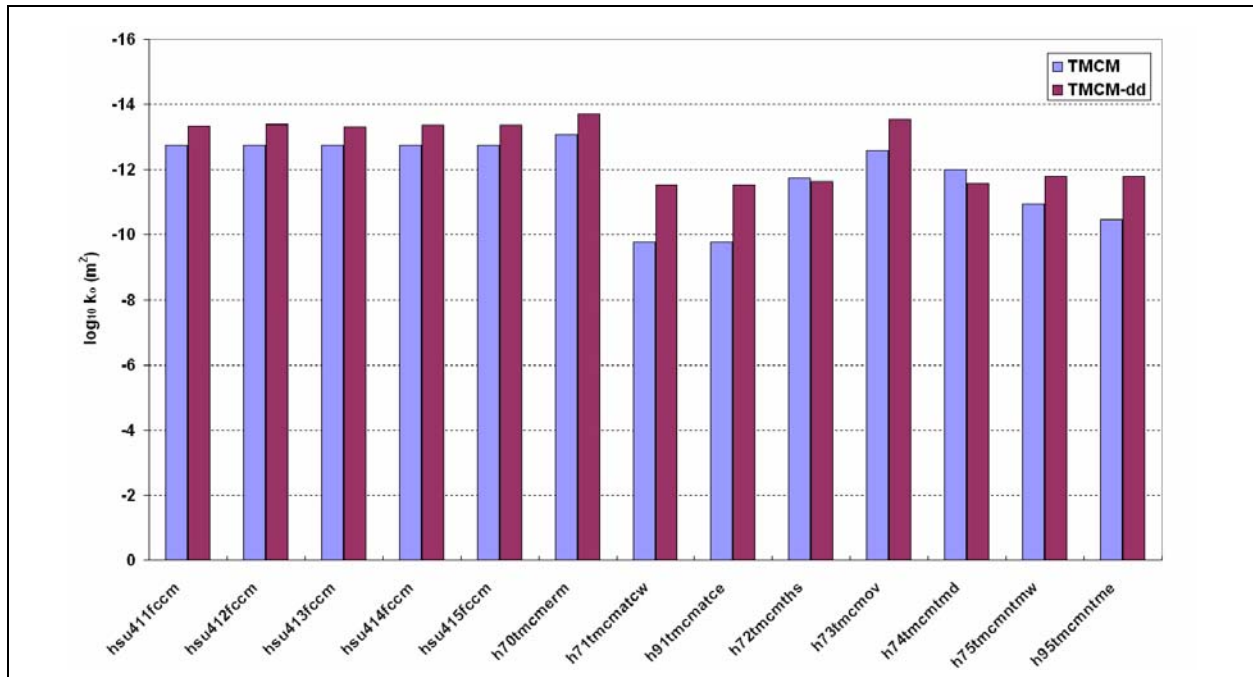


**Figure 8-34**  
**Comparison of Calibrated  $k_0$  for TCMC and FCCM Subzones**  
**in the LCCU1-MME-TMCM**

Note: (Depth Decay = 0.0027) and LCCU1-MME-TMCM-dd (Depth Decay = 0.001) models.

These two types of error led to the decision to invoke depth decay for FCCM and TCMC during flow model calibration (SNJV, 2005). However, the head residuals improve elsewhere in the model with the recalibration such that the sum of all weighted residuals for the entire model is no worse than the flow model with larger depth decay. Thus, this examination sheds light on future calibrations and how depth decay can be considered.

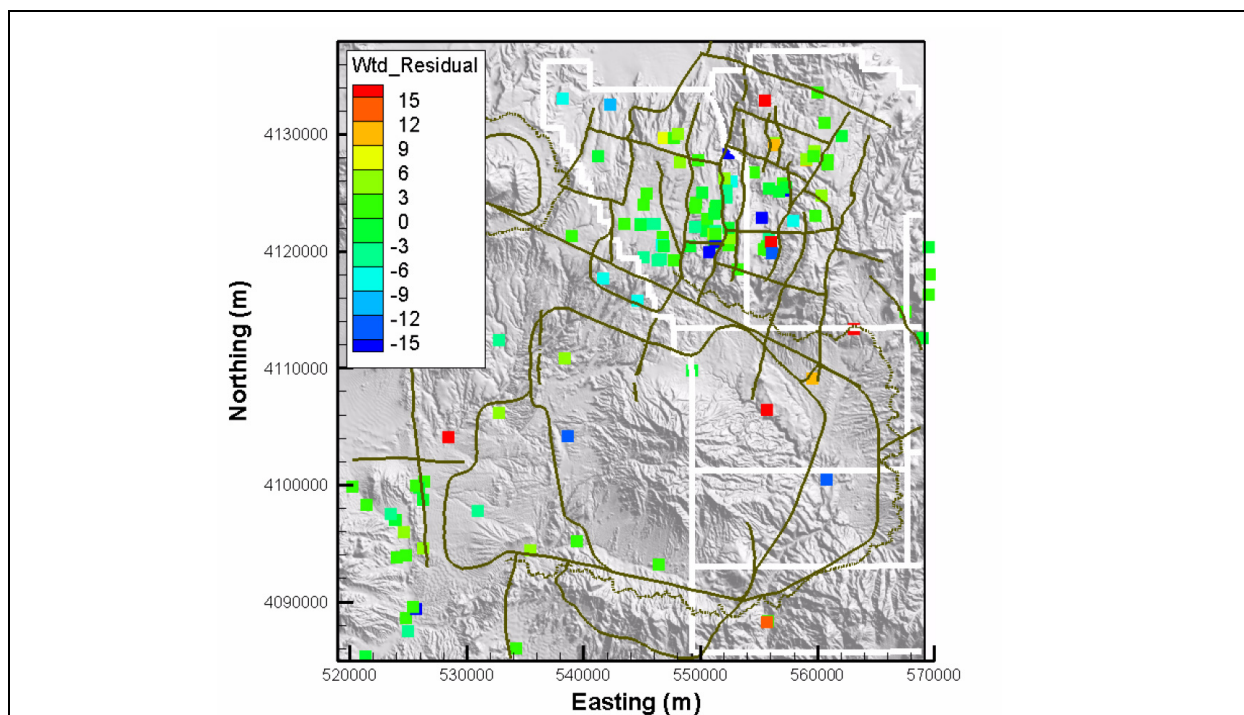


**Figure 8-35**

***Postplot of Weighted Residuals in Recalibrated LCCU1-MME-TMCM-dd Flow Model***

Reducing calibrated permeability to compensate for reduced depth decay does not result in an identical flow system. Figure 8-36 shows the location of a transect for which simulated permeabilities are plotted for calibrated models with depth-decay coefficients of 0.0010 and 0.0027 (Figure 8-37). With the reduced depth-decay model, permeability contrasts with depth are less and flow paths can penetrate deeper in the TMCM and FCCM units. The impact of the revised flow field is highlighted in Figure 8-38, where transport on the two flow models is compared for a single set of transport parameters. In the reduced depth-decay model, plume migration is substantially reduced as a result of less shallow convergent flow paths. With deeper penetration, the plumes migration is reduced for two reasons. First, the velocity at any location is less due to the greater distribution for flux in the vertical direction. With reduced velocities, more  $D_m$  occurs in fractured rock, thus retarding solute migration. Second, with greater spreading of flow paths in the vertical direction, more dilution occurs, thus reducing the local solute concentrations at any time.

Although only semiquantitative, this comparison of two flow models (calibrated with the same HFMs and the same flux boundary conditions, but with different depth-decay coefficients in the TMCM and FCCM) shows the potential large sensitivity of transport model predictions to the depth to which flow

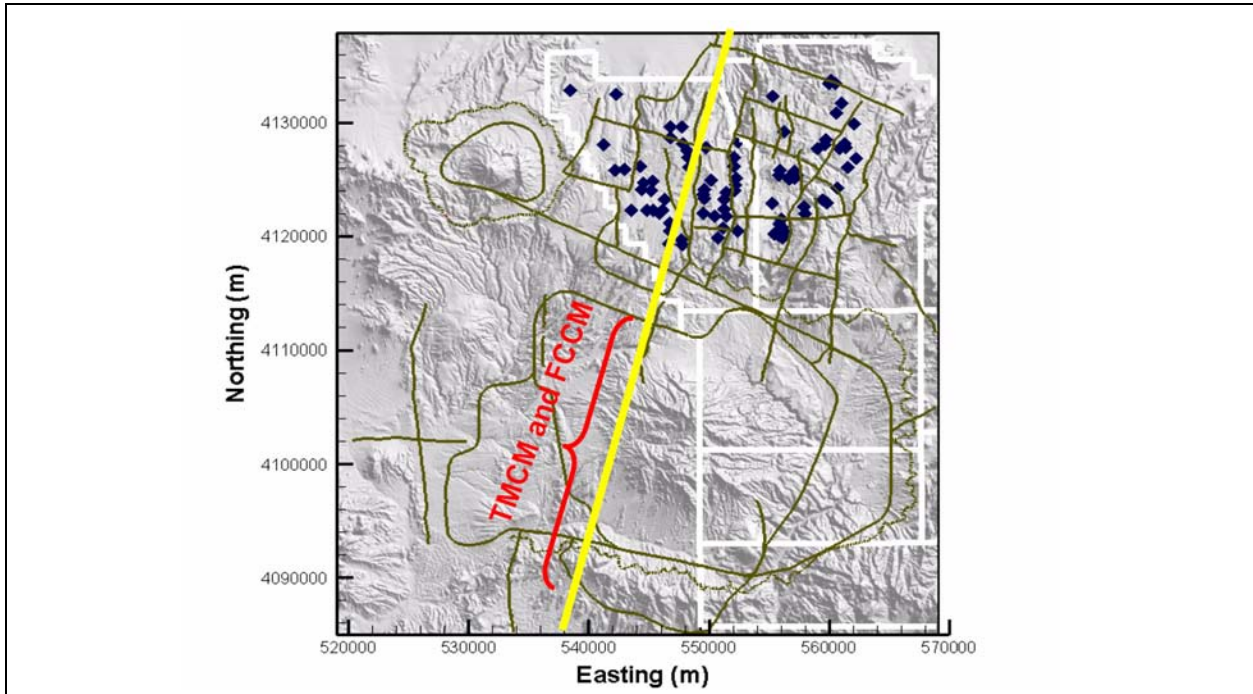


**Figure 8-36**  
**Transect for Comparing Simulated Permeability for Depth-Decay Coefficient Equal to 0.001 and 0.0027**

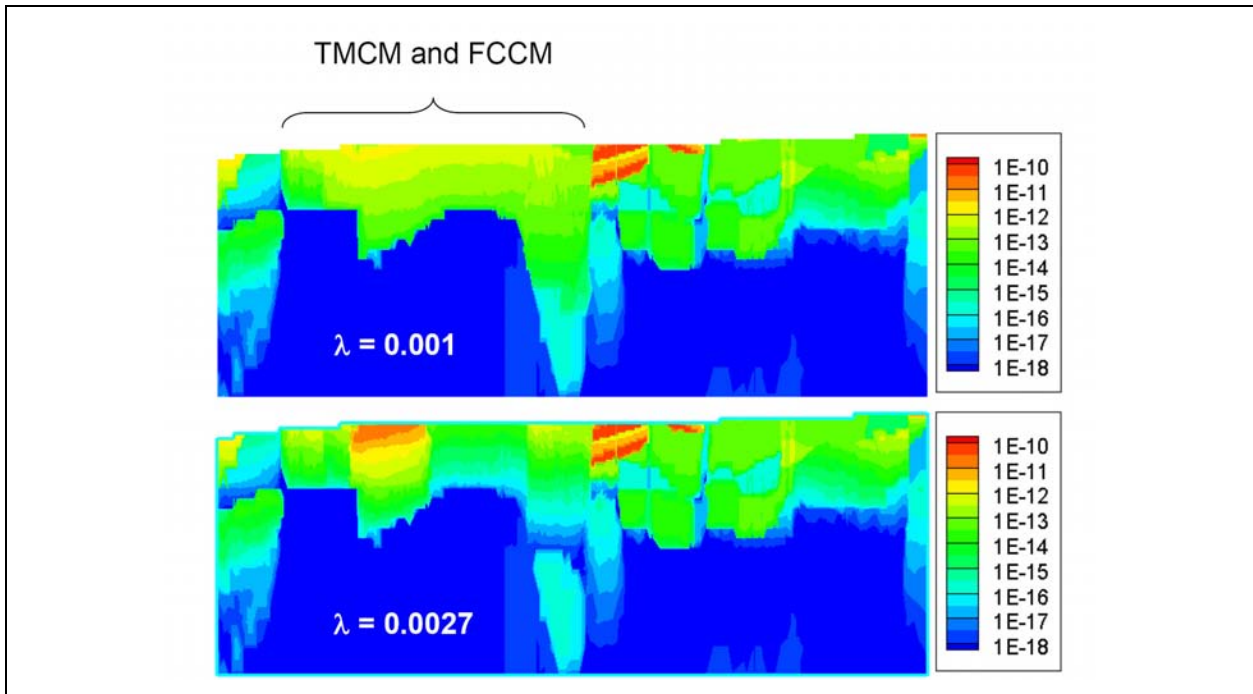


**Figure 8-37**  
**Comparing Simulated Permeabilities ( $m^2$ ) for Two Depth-Decay Coefficients in TMCM and FCCM HSUs**

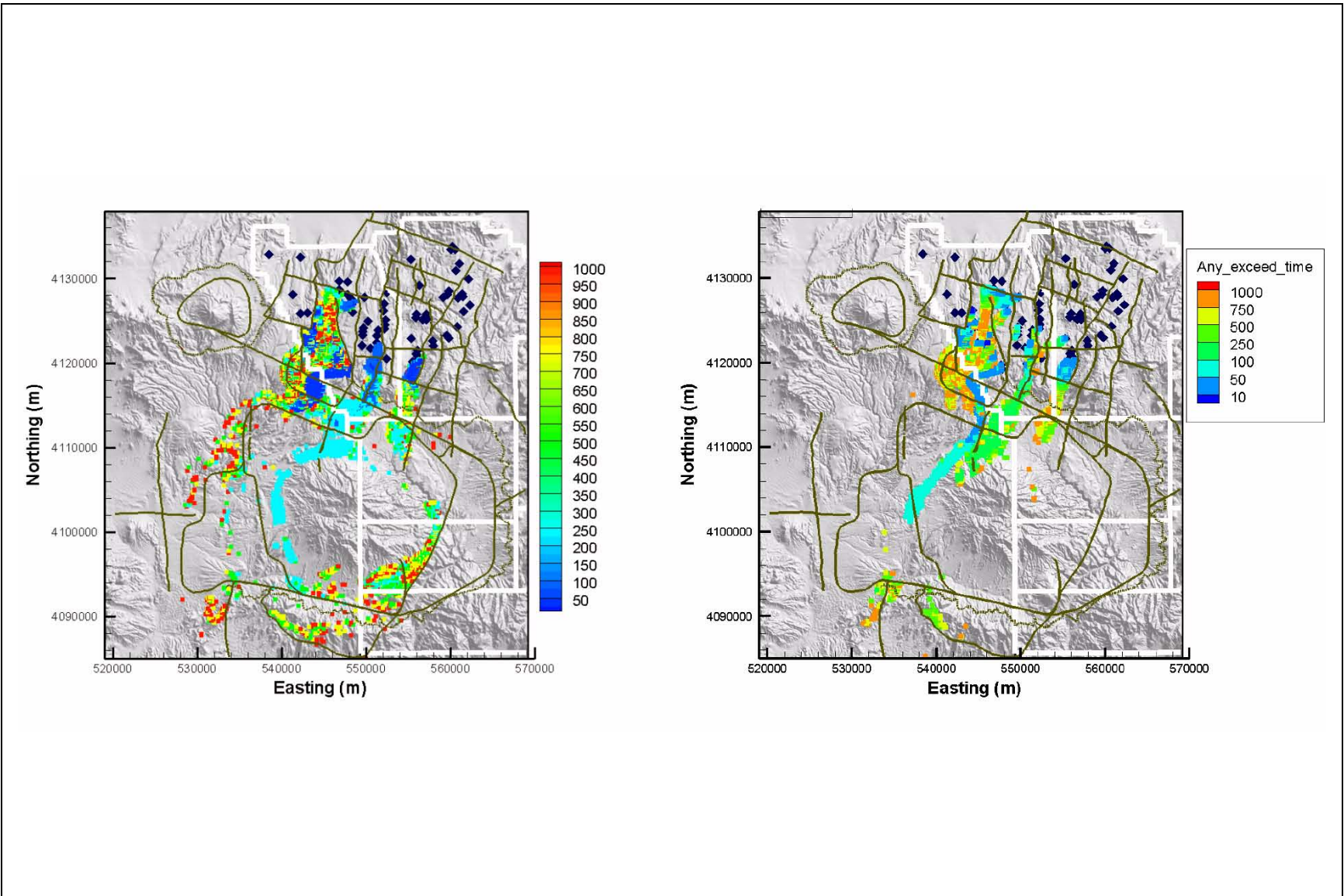


**Figure 8-38**  
**Comparing Time at Which Standard Exceeded for Single Realization of Identical Transport Parameters in Flow Field Calibrated with Two Depth-Decay Coefficients, 0.0027 (left) and 0.001 (right)**

paths penetrate the large units in the southern half of the model. It is likely that a full Monte Carlo simulation on the reduced depth-decay model will result in a distribution of EVs much smaller than those for the LCCU1-MME-TMCM model.

**8.3.4 Alternative Dispersivity Scenarios**

In the Monte Carlo simulations discussed in Section 7.2, dispersivity tensors reflect fairly small values (10, 1, 2) and (100, 10, 2). Stoller-Navarro Joint Venture (2004d) and Shaw (2003) discuss larger values potentially applicable to large extensive units such as the TMCM (in the particle-tracking methodology, it is not appropriate to use such large value when heterogeneity exists over small scales such as in the volcanics of Pahute Mesa). Therefore, a series of semiquantitative sensitivity analyses was conducted to examine model behavior for increase dispersivity. The hypothesis was that increased dispersivity might lead to more dilution, lower concentrations, and reduced plume migration. This hypothesis is examined with respect to simulation results.

Starting with the LCCU1-MME-TMCM flow model and a set of expected value transport parameters, nine transport simulations were conducted, each with a different dispersion tensor. The combinations are listed in Table 8-27.

**Table 8-27  
Dispersivity Tensors for Single Parameter Set Sensitivity Runs**

Model Name	$\alpha_x$	$\alpha_y$	$\alpha_z$
Disp1	10	1	0.2
Disp2	100	10	2
Disp3	100	10	10
Disp4	100	25	25
Disp5	100	50	50
Disp6	100	50	10
Disp7	50	25	25
Disp8	50	50	50
Disp9	100	100	100

Plots of the time at which the standard is exceeded for these single runs are in Figures 8-39 through 8-41. In all of these plots, there are two fundamental behaviors: those that have a plume extending down the west side of Timber Mountain, and those that show more spreading into the Thirsty Canyon flow system. For all dispersivities greater than those used previously in the Monte Carlo runs, the

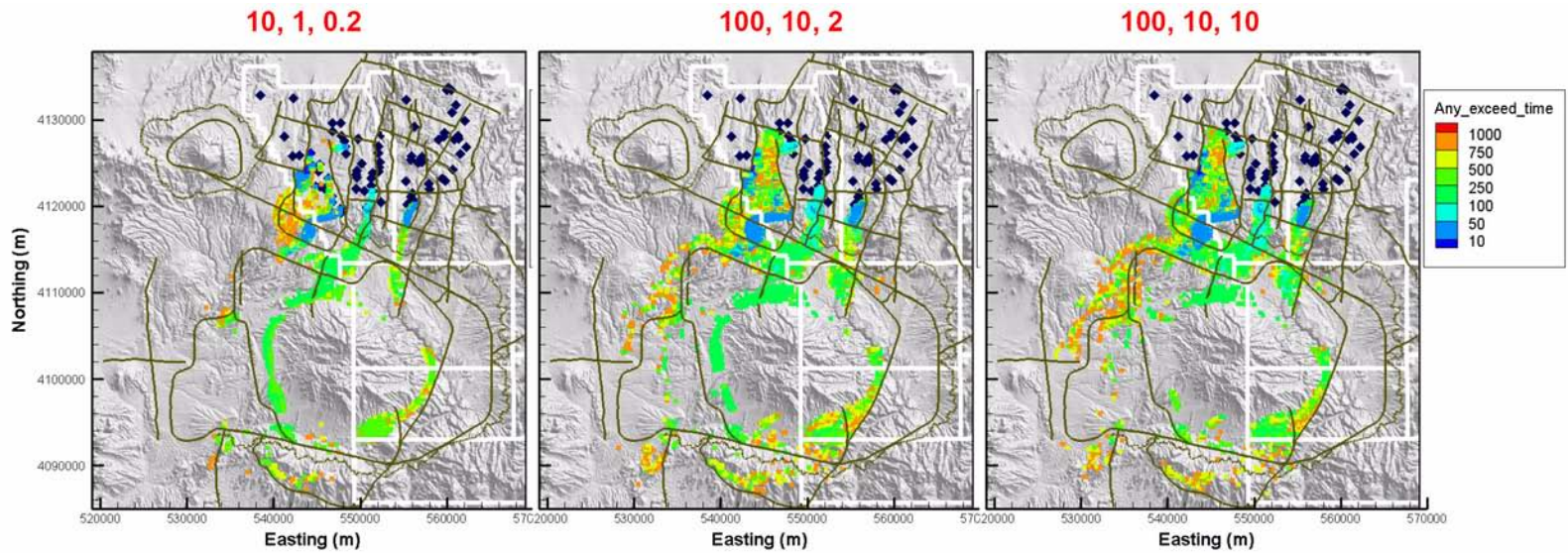


**Figure 8-39**  
**Comparing Time at Which Standard Exceeded for Single Realization of Identical Transport Parameters in LCCU1-MME-TMCM Flow Field with Different Dispersion Tensors (Part 1)**

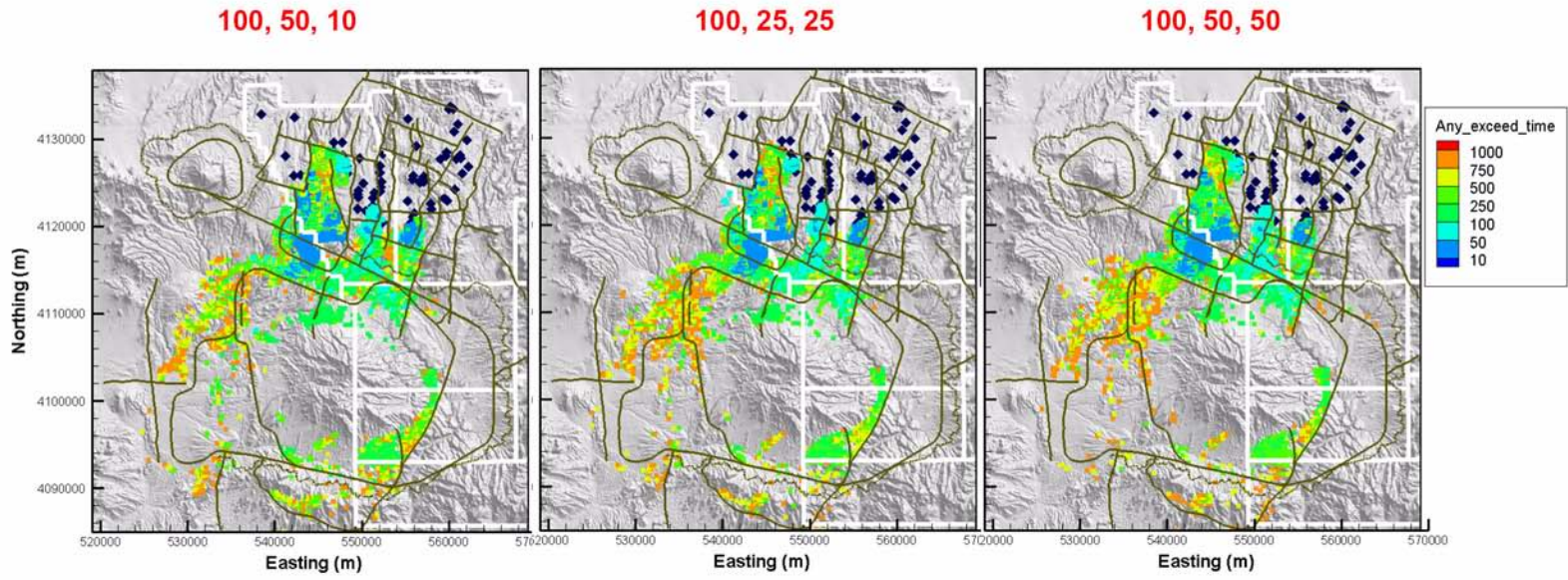


**Figure 8-40**  
**Comparing Time at Which Standard Exceeded for Single Realization of Identical Transport Parameters in LCCU1-MME-TMCM Flow Field with Different Dispersion Tensors (Part 2)**

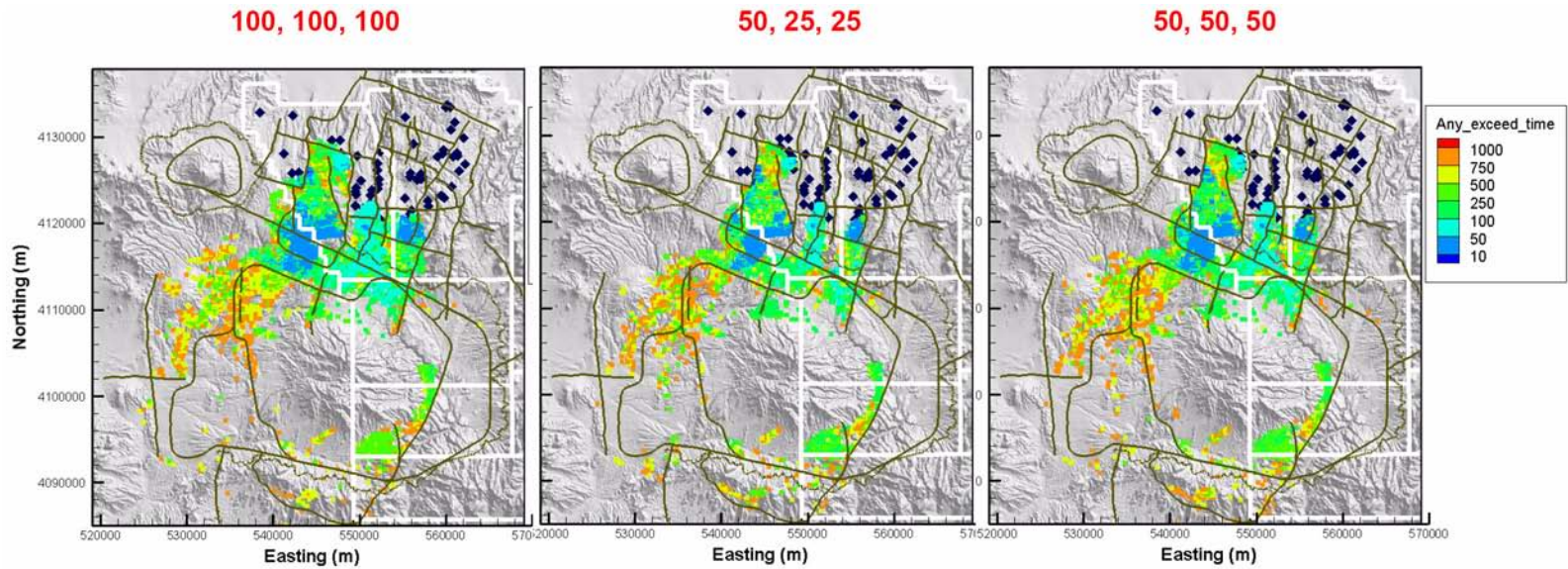


**Figure 8-41**  
**Comparing Time at Which Standard Exceeded for Single Realization of Identical Transport Parameters in LCCU1-MME-TMCM Flow Field with Different Dispersion Tensors (Part 3)**



additional spreading of particles is sufficient to reduce the convergent plume along western Timber Mountain. In most cases, the additional transverse dispersion causes greater spreading and the subsequent later time of standard exceedance in the western half of the model domain. The flow remains strongly channelized in the eastern half of TCMC/FCCM system, thus preserving nearly identical behavior in all cases.

Increasing values of the dispersion tensor to (300, 100, 10), a 1,000-Monte Carlo simulation on the remaining transport parameters was conducted. [Figure 8-42](#) compares the time at which 5 percent of the realizations exceed the standard for the original and increased dispersion cases. With the larger longitudinal value, exceedances occur earlier and the size of the boundary is larger. Thus, the increased dispersion considered in this sensitivity study does not lead to reduced contaminant migration through spreading and dilution. Also shown is the time at which 50 percent of the realizations exceed the standard, representing a reduced size in boundary.

The dispersion analysis presented here is only semiquantitative because the large values considered are not ideal for the particle-tracking method invoked. A governing assumption in the particle-tracking method is that large scale macrodispersion is accounted for with the features and zones. That is true in some locations in the PM CAU model, such as on Pahute Mesa, but not so in the TCMC zone. The impact is that random walk displacement of particles to represent dispersion can move particles many cells away when grid resolution is fine relative to the lack of property variability, such as in the TCMC. This serves to put particles into other flow paths, which may be valid, but also to cause particles to essentially jump into new regions. These issues are not addressed rigorously in this study. Rather, these simulations serve to highlight the need to better understand the continuity, or lack thereof in large models zones such as the TCMC.

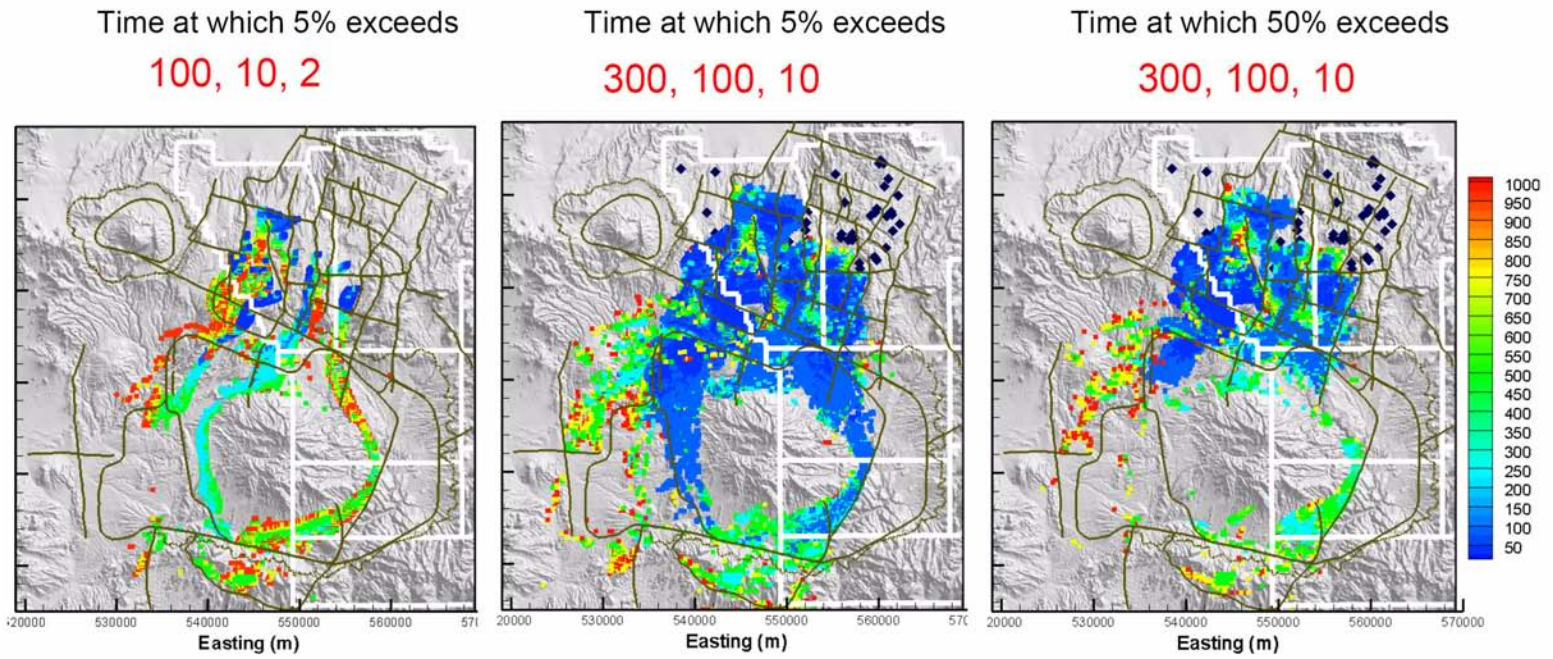


**Figure 8-42**  
**Monte Carlo Simulation Results for Different Dispersion Tensors**  
Note: Plot shows time at which 5 or 50 percent of realizations exceed the standard.

## **9.0 MODEL UNCERTAINTY, INTEGRATION, AND ASSESSMENT**

Observations of predicted transport pathways, plume extent, and migration times provide insight into controlling features and potential weaknesses in the conceptualization and implementation of the PM CAU flow and transport models. Consideration of the features and processes that appeared most important in determining the modeling results leads to the following concerns for further characterization and model development:

- Improved characterization of the “Bench” (HFM feature) located immediately south of Pahute Mesa, which appears to act to channelize flow from source locations toward potential receptor sites.
- Incorporation of sub-CAU-scale heterogeneity into HSUs.
- Improved characterization of fracture properties and their effect on flow and transport processes in the volcanics.
- Further evaluation of the effects of recharge on the migration and evolution of the contaminant plume, particularly recharge on Timber Mountain.
- Improved characterization of the source term and representation in the CAU-scale model.
- Improved determination of appropriate boundary conditions for the flow model.
- Review of the concept and characterization of depth decay.
- Further evaluation of appropriate values for specific discharge for specific HSUs and areal variability.

### **9.1 Introduction**

The focus of this document has been to understand the behavior of radionuclide migration in the PM CAU model and to define, both qualitatively and quantitatively, the sensitivity of such behavior to (flow) model conceptualization and (flow and transport) parameterization. This section summarizes the components of PM CAU transport modeling performed for this analysis, identifies key aspects of

the uncertainties elucidated in this analysis relating to both PM CAU flow and transport models for these components, and concludes with a discussion of each component with the object of reducing its uncertainty from understanding gained through field investigation and/or improved modeling.

## **9.2 Pahute Mesa Bench Complexity**

A critical region when considering flow and transport from Pahute Mesa is the bench area that lies between the SCCC and the TMCC. The arrangement of the HSUs and faults is a primary control on flow and transport to downgradient locations. The bench is particularly important and complex because it represents a transitional zone between the adjacent calderas that have each experienced multiple caldera formation events. Therefore, the lithologic units found in each caldera and across the bench are not necessarily continuously deposited units, but represent unique stacks of rock in each area. In addition to eruptive cycles and deposition of volcanic rock, structural offset along faults can further displace units at the bench and may provide either a conduit or barrier to flow across the bench. Some of the specific issues of concern are juxtaposition of the lithologic units, distribution and role that specific units have on determining flow and transport pathways, location and role of faults in promoting or inhibiting communication between units, and the general flow and transport properties that are attributed to the rocks through designation of HGUs and reactive mineral categories.

Each caldera formed independently of the other and was subject to multiple eruptive events. The older Silent Canyon caldera is filled in by volcanic rocks from SCCC eruptions as well as volcanic rocks from the later Timber Mountain caldera events. In geologic cross sections developed from borehole data, there are more distinct lithologic units stacked in the SCCC, and these units are thinner than the lithologic units south of SCCC. Each unit is discretely categorized as high or low permeability. Additionally, the vertical position of the units for each depositional events controls the rate of flow and plume transport as the plume moves from one depositional unit to an adjacent unit. If a high-permeability unit abuts a low-permeability unit, flow and transport may be inhibited, depending on connectivity to other units. If two high-permeability units abut, flow is rapid and unimpeded. The difference in migration of the plume to downgradient locations for each scenario can be significant relative to the sequence of units along the flow path. Therefore, the ability to

characterize the bench is dependent upon available data collected on the bench. However, within this area, there are only two wells (ER-EC-1 and ER-EC-6) for which there is any lithologic information.

Displacement of units along faults can also reposition HSUs such that travel paths are inhibited or enhanced. Faults may also connect units in the vertical and horizontal directions such that water from a high-permeability unit is diverted along the fault until it intercepts one or more other high-permeability units, depending on the fault's unique properties. If the fault is a conduit, then water may flow downward through the fault, and contamination will migrate to deeper units. If the fault has a lower permeability, such that flow is restricted, it may serve to halt flow from one high-permeability unit to an adjacent unit. The former case may exist along the Moat fault that extends from the northwest to southeast through the bench area. This fault is roughly perpendicular to flow gradient, yet the head at wells on either side of the fault differ only by centimeters.

The location and continuous distribution of HSUs currently dictate flow paths from Pahute Mesa across the bench then south to Timber Mountain. Not only is the spatial extent of these units poorly known, but the connectivity between HSUs is also uncertain. In the current conceptual model, shallow groundwater moves from the TSA through the BA before diving beneath the shallowest part of the THCU and FCCU into a massive TMCM south of the bench. Both of these units are classified as high permeability. Additionally, the low-permeability THCU and the FCCU bracket the high-permeability units and constrict flow, which causes channeling through a narrow segment of the bench. Further characterization of flow through these poorly defined, large blocky units along the bench is required to assess whether channelized flow actually occurs, or whether the units allow more diffuse flow through the low-permeability zones.

For the instance where high-permeability units allow more water to pass through a wider area or where a continuous high-permeability path is not present across the bench, the water velocity is appreciably reduced and the radionuclides are susceptible to spreading through the porous media. The net effect of either case is to significantly reduce migration of the plume and the extent of the exceedance perimeter. Therefore, given the level of uncertainty, the location and size of HSUs require better definition and the properties of the rocks, whether high permeability or low permeability, also need to be defined at higher resolution. This can be achieved by drilling additional wells into those units that are the most uncertain, and through their attributes, are primary drivers of flow and transport dynamics.

### **9.3 Specific Discharge**

The simulations and analyses in this report highlight the important role specific discharge plays in characterizing flow pathways and flux. Specific discharge is calculated as the volumetric flux divided by the area perpendicular to flow and is therefore a measure of the velocity. To date, specific discharge has not been a measurable parameter in the model domain to which PM CAU flow and transport models can be calibrated. Rather, it is simulated based upon flow model matches to groundwater head in which large-scale permeability is estimated. Specific discharge is then the result of combinations of groundwater gradients and the estimated permeabilities. Specific discharge within the model is a highly important quantity because it directly impacts flow velocities, which in turn impact how much  $D_m$  occurs.

The model region where specific discharge appears to be most important to understand is northwest of Timber Mountain, west of UE-18r, where several conceptual models simulate converging flow paths from Areas 19 and 20 that then create a narrow, high-flow zone along the model interface where the TMCM and FCCM units abut at the water table. Methods to measure field-scale groundwater velocities or fluxes in fractured volcanic rock have not been demonstrated at other sites or in the literature. Thus, indirect means must be considered to reduce uncertainty in this area. A large-scale multiple-well aquifer test (MWAT) could potentially serve to quantify the conductance of the material in this portion of the domain. The values obtained from such a test would constrain the permeability in the flow model, leading to reduction of uncertainty in calibrations and clarifying whether convergent flow is possible. If convergent flow is not possible, then the flow models with less convergent flow (e.g., LCCU1-MME-TMCM, where more flow from Area 20 enters the Thirsty Canyon system) will be favored.

### **9.4 Transport in Fractured Media**

#### **9.4.1 Fracture Properties**

Earlier sections in this report (e.g., [Section 6.4](#)) examined the impact of fracture properties and fracture-matrix interaction parameters on the prediction of solute migration rates. It is a complicated process due, in part, to conceptual model formulation and also to offsetting impacts of the model parameters. Model parameters follow with brief descriptions of their roles in enhancing and/or

retarding solute migration. This discussion considers the parameters and their impacts for a fixed groundwater flux (as passed from the flow model to the transport model). However, fracture parameters and their actual impact on flux are also addressed, hence the potential need to consider coupled flow and transport models in future revisions.

A complex relationship exists between fracture porosity ( $\phi_f$ ), aperture ( $b$ ), and spacing ( $s$ ) with regard to their impact on groundwater velocity, solute migration rates in fractures, and mass transfer between fractures and matrix material. For a fixed groundwater flux, fracture porosity decreases lead to fracture velocity increases, just as with porous media relationships. However, fracture porosity is tied in the conceptual model to fracture aperture and fracture spacing by the relationship  $\phi_f = b/s$ . So, if  $\phi_f$  decreases, then either  $b$  must decrease or  $s$  must increase. If  $b$  decreases, then the wetted surface area per unit fracture volume increases and  $D_m$  is enhanced, leading to more retarded net solute migration. If  $s$  increases, the volume of matrix available to store solutes diffusing out of the fracture increases, also leading to increased retardation due to the process of  $D_m$ . Now, if  $b$  and  $s$  both decrease such that  $\phi_f$  remains unchanged, the net  $D_m$  impacts may change substantially, depending on the parameter values and the simulation time. At early time, reducing  $b$  will favor increased  $D_m$ . But, as the fracture concentrations and matrix concentration come closer to equilibrium at later time due to reduced  $s$ , the concentration gradient is reduced, and the matrix no longer serves as immobile storage. Thus, the relationships between fracture properties and how they are parameterized becomes critical to understand better for field-scale simulation over long time periods.

The UGTA Sub-Project has an impressive set of detailed transport experiments in fractures (e.g., Kersting and Reimus, 2003) but only one field-scale tracer experiment in volcanic rocks (IT, 1998a), and that experiment is in fractured lavas that do not reflect the properties of the major welded-tuff flow and transport pathways identified in this study. The laboratory experiments provide valuable insight into the local fracture matrix interactions that occur in a single fracture, but the time scales are very small relative to regulatory interests and the interactions of multiple fractures in a complex network are not addressed in such studies. These experiments shed light on the relationships between single fracture properties and mass transfer processes as well as the reactive processes of sorption to immobile minerals. Additionally, the fracture transport experiments highlight the role colloids can play in facilitating the migration of otherwise immobile species. However, even with column diameters of only a few centimeters, the bench-scale experiments never replicate the

increased matrix concentrations and subsequent decreased concentration gradients that may occur after long times in the field.

The field-scale fracture properties used in sensitivity analyses in this study were chosen to reflect limited field-scale information and substantial uncertainty. The process involved developing distributions of fracture porosities and fracture spacing and then using the relationship written above to compute fracture apertures, asserting that fracture apertures are the least well constrained parameters for field-scale models. The result, as documented in [Section 6.4](#), is that approximately 40 percent of the model realizations include fracture apertures greater than 1 cm. Such large fractures lead to simulations with minimized mass transfer from the fractures to the matrix as a result of small wetted surface areas to fracture volume ratios. Observations of welded-tuff fracture apertures in core and in tunnels conflict with these larger apertures, as do estimates based on other properties (Section 6 of Shaw [2003]). On the other hand, large fracture apertures would be estimated from the large effective porosities that were derived in the BULLION FGE (IT, 1998a; Shaw, 2003). Additionally, the geometry of the fractures that actually conduct water for large distances at the field scale is not well characterized. One conceptual model is that flow in small fractures eventually converges into larger fractures that then serve as the conduit for large-distance migration. Another line of evidence that might support large aperture fractures for large-scale migration is provided in Reimus and Callahan (2007), where observations of reduced effective mass transfer with increasing spatial scales may indicate transport in larger fractures.

With conflicting indirect evidence for actual fracture geometry and properties, the fracture model parameters remain highly uncertain in the simulations conducted in this study. However, due to the porosity-spacing-aperture relationship, certain correlations in parameters exist, as discussed in [Section 6.4.1](#) (e.g., [Figure 6-7](#)). The MTC ( $MTC = (n/b)\sqrt{D_m}$ ) relates the matrix porosity ( $n$ ), the fracture aperture ( $b$ ), and the  $D_m$  to the potential for mass transfer out of fractures into the matrix, but does not consider the impact of fracture spacing on limiting the storage volume for mass in the matrix. The MTC surfaces as a highly sensitive parameter in many of the simulations described in [Section 7.0](#). Thus, reducing uncertainty in the parameters of the MTC will serve to reduce predictive uncertainty substantially. Currently, many of the predictive simulations substantially underestimate the importance of  $D_m$  in retarding migrating solutes, particularly in the TSA, BA, and TMCM. Understanding and quantifying  $D_m$  for field-scale migration in these units is important.



### 9.4.2 Fracture Pathways

The conceptual model for transport in fractured media applied in this study is a classic dual-porosity model. Flow is assumed to occur primarily in fractures, with immobile matrix water providing a reservoir for storage of solutes that diffuse out of the fractures. One of the constraints of the method as applied is that a uniform permeability value is applied to all of the nodes in the zone defining an HSU. This provides full continuity within that zone. Considering this from the perspective of fractures, this conceptualization implies that fracture pathways are fully connected and continuous. In reality, fractures comprise networks with the connectivity of flow paths being dependent on fracture density, length, and orientation. The flux in a fracture network can be very complex, being spatially variable depending on properties such as fracture aperture and gradients (Kwicklis and Healy, 1993). In other words, the location of the dominant pathways can vary as a function of the local gradient. Discrete fracture network modeling studies have considered rocks very similar and of the same origin to the main units in the Pahute Mesa pathway (e.g., Kwicklis and Healy, 1993). However, none of these studies have examined the effect of the tortuous pathway in fracture networks on mass transfer. Permeability can be upscaled, presumably, if the volume is large enough. However, Wolfsberg et al. (2002) discuss issues and limitations of assuming equivalent porous media properties for complex fracture networks. One of the primary issues is that the volume at which a continuum parameter can be applied may be very large, and the effective parameters may change with scale (Wellman and Poeter, 2005 and 2006). In the PM CAU model, where single permeability value is applied to an entire HSU, this is less of an issue. However, all heterogeneity is then lost, and the effective field-scale permeability fails to represent complex processes at smaller scales. At the smaller scales, flow may occur along far more tortuous pathways in the fracture network. These pathways may expose solutes to substantially greater surface area across which  $D_m$  may occur. Thus, while many of the realizations in this study's sensitivity analysis predict limited retardation due to  $D_m$ , the actual process remains highly uncertain. Future field testing activities coupled with a variety of modeling techniques could serve to understand solute migration process in fractured welded tuffs over large scales and thus improve the conceptual model for such transport as currently implemented.

### 9.4.3 Fault Zones

In the current model, fault zone properties are treated as modified values of the unfaulted material adjacent to the fault zone. The framework model has no volume assigned to the fault zones –

materials are simply truncated or offset across a 2-D plane where the fault trace is specified. In the numerical model grid, volume is added to the fault zones; nodes identified as fault-zone nodes are assigned the identity of the HSUs and RMCs from the framework model, but are also made available for property modification because they represent faults. One limitation in the model implementation is that although permeabilities are changed in fault zones, transport parameters (e.g., fracture properties) are not. Note that this is not a limitation of the simulation software. In other words, the transport parameters for an RMC in a fault zone are identical to those in that RMC in non-fault zones. Thus, unfractured porous media is represented as unfractured in fault zones. More importantly, fractured media through which migration rates are high remain as such through faults for which permeabilities are not reduced. This is particularly evident in the Moat fault across which solutes migrate off of Pahute Mesa. There is no observed gradient across that fault (the head difference between ER-20-5 and ER-EC-6 is only 6 cm), so the permeabilities in the fault zone are not reduced. A continuous fracture pathway exists in the BA, so there is no impact of this fault in reducing migration rates. Consequently, migration off of Pahute Mesa is often rapid in the simulations.

Very little is actually known about fault-zone hydraulic and transport properties in the Pahute Mesa system. Where gradients exist across faults, their permeabilities are assumed to be reduced, which also can be a consequence of termination or fully offset units through which groundwater flows. A more complex view of Pahute Mesa fault hydraulics is presented in a highly schematic set of simulations by Kwicklis and Sulley (2005), who concluded that:

1. High-permeability features that are oriented parallel to the regional gradient act as drains, so that hydraulic head contours bend toward the feature in a manner consistent with convergent flow toward the feature.
2. High-permeability features of limited extent that are oriented perpendicular or oblique to the regional hydraulic gradient exert little observable effects on the gradient, although path lines are displaced laterally across obliquely oriented features. Complexly zoned faults in which an outer zone of high-permeability material surrounds an inner low-permeability zone also have little observable effect on the hydraulic gradient when the features are of limited extent and are oriented obliquely to the regional gradient.
3. Low-permeability features of limited extent that are oriented obliquely to the regional gradient result in local hydraulic head contours that intersect the features at high angles and cause the water-level contours to appear to be “discontinuous” across the feature. Complexly zoned faults of similar extent and orientation in which an outer zone of low-permeability material surrounds an inner high-permeability zone exert similar effects.

4. Groundwater flow is diverted around low-permeability features of limited extent that are perpendicular to the regional hydraulic gradient, so that flow diverges upgradient from the barrier and converges downstream of the barrier.
5. Where high-permeability rocks are juxtaposed against low-permeability rocks with no distinct structural feature present, the hydraulic gradient in the high-permeability rocks can be very small and heads decrease linearly through the low-permeability material. This relationship is maintained regardless of whether the low-permeability rocks are the upgradient or the downgradient member. The inclusion of a very low-permeability structural feature between the two rock types causes some of the head loss through the moderately low-permeability rock to occur through the feature instead.
6. Where groundwater flow through layered aquifer/aquitard systems is blocked by low-permeability features, both upward and downward hydraulic gradients exist near the fault as groundwater moves out of the aquifers into the adjacent aquitards and through the faults.

Because the simulations conducted with the alternative flow models tend to provide rapid migration away from Pahute Mesa (for tests from southern Area 20) without considering faults as even more conductive conduits, little emphasis was placed on assessing fault property sensitivity to solute migration. However, there is a potential role for faults to retard migration. This could be considered in future studies in concert with any assessments of the radionuclide plume measured in ER-20-5 #1 and #3 (Table 1-1 of Wolfsberg et al., 2002). If radionuclides are found on the north side of the Moat fault, but not on the south side (they have not been detected in ER-EC-6), then slow porous media-like flow and/or lateral diversion in the fault should be considered. Additionally, there are no faults interior to the TCMC HSU in the framework model, yet a continuous transport pathway exists in that HSU. Future considerations should examine the potential role of faults to spread, retard, focus, and enhance flow in the TCMC and FCCM.

#### **9.4.4 Confirmation**

There are very little field-scale transport data with which to confirm the results of the transport model. [Section 6.5](#) investigated the use of  $^{14}\text{C}$  data but demonstrated that the data were better used, in the current model framework, to evaluate model parameters rather than to assess solute migration rates. It originally was hoped that the distance between two wells divided by the difference in  $^{14}\text{C}$  ages would provide a transport velocity with which to compare model results; instead, the  $^{14}\text{C}$  apparent age was found to represent a mixing of multiple  $^{14}\text{C}$  sources of different ages. Another dataset that was not investigated includes the wells that have not shown contamination along the simulated transport

pathway. Specifically, ER-EC-1, ER-EC-6, UE-18r, and ER-EC-5 have never shown elevated concentrations of  $^3\text{H}$  or other beta emitters. To the north of ER-EC-6, on the other side of the Moat fault, ER-20-5 shows substantial contamination. This information could be used with the current simulation results to screen implausible parameter combinations. However, such an activity inherently assumes that if contamination crosses the Moat fault in the vicinity of ER-EC-6, then it would be detected there. The complexity of flow and transport in fracture networks, as described above, could lead to such migration that is not detected at ER-EC-6, especially if transport occurs in a single feature such as a fault not included in the model. Nevertheless, consideration is currently being given to a process to unarchive existing simulations and to separate model runs for which no contamination is simulated at these wells in less than 50 years. This could shed light on future activities seeking to measure fracture properties and the capacity of the system for  $D_m$  over 1,000-year time frames. Finally, the quantification of specific flux as described in [Section 9.3](#) would serve to assist in confirming predictive transport results.

## **9.5 Heterogeneity**

In a numerical model, the definition of heterogeneity depends on the scale of the process modeled and the variability of the parameter in question at this scale. For example, heterogeneity may be represented adequately at the nominal grid scale used in the simulations, or by the average value defined over a group of grid blocks, or by sub-grid scale considerations. In the PM CAU flow and transport models, heterogeneity is represented at the first two of these scales using variable-sized grid blocks to characterize the local complexity of geologic structure, and the grouping of grid blocks to form homogenous, single-material HSUs (i.e., HSUs for the flow model and RMCs for the transport model). Sub-grid-scale heterogeneity is not addressed in the models with the exception of permeability depth decay in selected HSUs and in the  $K_d$  upscaling exercise described in [Section 6.4.7](#).

The collective analysis of radionuclide migration between alternative Pahute Mesa hydrostratigraphic model/flow combinations showed that transport is sensitive to both flow model and transport model heterogeneity. However, depending on the magnitude of groundwater fluxes as determined in part by flow model heterogeneity, transport behavior may not be sensitive to transport parameter heterogeneity, in any form. This occurs when high groundwater fluxes in preferential flow path(s)

result in rapid, HSU-scale radionuclide migration regardless of transport mechanisms. Consequently, it was determined that the component of flow model heterogeneity that most affects transport is HSU zonation. The HSUs are defined as single-material units. When an HSU is large relative to the modeled scale — such as is defined for the majority of HSUs in the southern half of the PM model domain, where volcanic units are extensive and constraining geologic field data are sparse — the HSU has the potential to become a km-scale preferential flow path if the single-material permeability is high. Rapid and preferential transport occurring through these HSUs was addressed in this analysis by reducing HSU permeability heterogeneity in the flow models (e.g., development of the LCCU1-MME-TMCM model) and by incorporating permeability depth decay within selected HSUs.

The PM CAU transport model heterogeneity is defined by RMC zonations, wherein parameters are assigned a single value to represent the entire zone. Because flow and transport modeling are performed in sequential steps, RMC heterogeneity is superimposed over the prior-defined flow field that reflects flow model heterogeneity. Because only six individual RMCs are defined for the PM CAU transport model, the spatial influence of transport parameter variability on radionuclide migration is not always apparent or significant. Usually, the effect of transport parameters is to retard, disperse, or enhance migration along flow paths that are principally dependent on the flow field. An exception occurs when an RMC for porous media (no fractures) is specified along a flow path with sufficient permeability to define a transport pathway. This occurs in the LCCU1-MME-TMCM flow model, where flow from Area 20 enters upper Thirsty Canyon. The RMC specifies vitric porous media or zeolitic media along that flow path, so rapid fracture transport does not occur and simulated plume extent is minimal.

This analysis determined that the gridding of the framework model and zonation of HSUs represent the variability of hydrogeology at the scale of the PM CAU model domain. When HSUs are large, they are zoned as such only because data are not available to justify their further subdivision. However, transport analysis through each of the alternative models indicates that some form of sub-HSU scale material variability should be incorporated in the flow and/or transport models to address km-scale preferential flow paths that result as an artifact of permeability contrasts along boundaries between HSU zones rather than of observed hydrogeology. Although the flow models are consistent with the geochemistry for large-scale flow paths, there is no data-based justification for HSU-scale focused flow transport paths. The NSMC analysis in [Section 8.3.2](#) documents this result.

Results indicate that it is primarily permeability heterogeneity at the scale of the HSUs, or within HSUs, that can reduce flow channelization through extensive portions of the model domain. Incorporating such heterogeneity would better honor the variability in borehole-measured heads located within individual, single-material HSUs (e.g., see the FCCM in [Figure 8-30](#)). Permeability depth decay was the only mode of within-HSU heterogeneity incorporated in PM CAU flow and transport modeling (for a select set of composite units). [Figure 8.3.3](#) addressed the sensitivity of transport to depth decay and concluded that transport model predictions have potentially large sensitivity to the depth to which flow paths penetrate large HSUs in the southern half of the model. This section discusses the relevance and permissibility of the depth-decay assumption in prospective PM CAU flow modeling.

An additional component of within-HSU permeability heterogeneity evaluated during flow model calibration (SNJV, 2006a) is anisotropy. Anisotropy, of which depth decay is effectively one form, is attractive because it is readily incorporated in the numerical model, is geologically defensible, and does not require the collection of additional field measurement (e.g., borehole flow logging) for its constraint.

For supplementary analysis, there are several easily applied geostatistical methods that would be appropriate for the incorporation of within-HSU heterogeneity. These may be readily incorporated in the modeling process, with parameters that describe the scales of spatial permeability variability defined as either fixed parameters assumed from measured data or as fitting parameters optimized during the flow model calibration process. Several such methods have been applied in previous NTS modeling studies.

In the PM CAU flow model, geostatistical interpolation, and possibly simulation, of permeability is attractive because the models of spatial variability applied permit additional degrees of freedom that result in a better fit to measured hydraulic data, as well as reducing the HSU-scale channeling of flow that dominates transport processes in the higher groundwater flux models. For the PM CAU models, it would be more constructive to use geostatistical parameters describing spatial variability as fitting parameters during flow model calibration, constraining these parameters by the range of uncertainty from measured data at the relevant scale (e.g., pumping test data). The HSUs for which this might be performed, such as the TMCM, are on the order of tens of kilometers and have material properties

poorly constrained by field measurement, supporting the use of geostatistical parameters as fitting parameters rather than as determined from field measurement.

In the Well Cluster ER-6-1 multi-well aquifer and tracer test analysis, SNJV (2006b) used the pilot-point method to allow for continuous permeability variation at the tens-of-kilometers scale within a single-HSU (LCA) model. Although the models and corresponding parameters describing spatial variability were assumed, the permeability at each pilot point was adjusted during model calibration. This was an appropriate method because variability in flow geometry was inferred from hydraulic testing at the well cluster, although no hard data were available for the model domain beyond the well cluster. Although the locations of pilot points were qualitatively assigned in the analysis, a quantitative assignment for optimal placement of pilot points within HSUs is possible using numerically derived sensitivities to permeability (e.g., Lavenue and de Marsily, 2001), although this latter component would require additional capability in the model setup. Lastly, implementation of the pilot-point method within Pahute Mesa HSUs may incorporate scales of spatial correlation, as well as the pilot-point permeability, as fitting parameters during flow model calibration.

A transition probability-based geostatistical method (Carle, 1999; Dai et al., 2007a and b) would also be well suited to define within-HSU permeability heterogeneity. This approach can be used to simulate multiple categorical zones within a single HSU while honoring any available borehole data. The zones may be categorical classes of permeability (e.g., low, medium, high), stratigraphic layers, or some other relevant hydrogeologic characteristic. The strength of the transition probability method over other geostatistical methods is that the juxtapositional tendencies of HSUs as observed in the field (or in theory) can be reproduced, and also that the models of spatial variability and their parameters can be understood in terms of standard geologic descriptions and observations. This allows for better incorporation of subjective, as well as observed, geologic knowledge into the models of spatial variability. Once having defined zones within a single HSU, each can be assigned either a single-material property or randomly assigned properties (possibly via some geostatistical method). Wolfsberg et al. (2002, Appendix G) applied the latter method for the within-HSU simulation of permeability, as well as of other properties, in a sub-CAU-scale modeling analysis of flow and transport near the TYBO and BENHAM tests in Pahute Mesa.

A final readily applied method of characterizing within-HSU heterogeneity, demonstrated in [Section B.1.1.1](#) of this report, uses an indicator geostatistical method to simulate continuous permeability fields at the individual gridblock scale for different HGUs, the building blocks of HSUs. The method is particularly relevant to Pahute Mesa HSUs because it captures the hydraulic discontinuity between fracture and matrix permeability within a single gridblock, which implies that such a discontinuity can be achieved at the larger HSU scale, and also because it applies permeability data at multiple scales, from the core to pumping-test scale. This latter point is particularly important because the primary difficulty in applying any geostatistical method is the reconciliation between the scale of observed data, upon which models of material property spatial variability are defined, and the grid scale being populated. However, given the large uncertainty in geologic structure and permeability in the extensive volcanic units south of Pahute Mesa, the assignment of permeabilities at some scale smaller than the HSU, and possibly the assignment of the scales of spatial correlation, as fitting parameters during flow model calibration is justifiable and removes the difficulty of relating the scale of measured permeability to the grid.

## **9.6 Depth Decay**

If hydraulic conductivity were uniformly distributed vertically in the HSUs of the groundwater model, flow off of Pahute Mesa would penetrate into the lower portions of the TCM and would not produce the observed discharge at Oasis Valley that are necessary to calibrate the flow model. To mitigate this discrepancy, a depth-decay multiplier is incorporated to condition hydraulic conductivity distribution in the vertical direction. The depth-decay coefficient of 0.0027 is used in the PM CAU flow model described in SNJV (2006a). The depth-decay coefficient is derived from observed, depth-dependent hydraulic conductivity measurements described in SNJV (2004b), which are then recalibrated for the flow model. The revised depth-decay coefficient is assigned such that the observed heads at observation wells and the observed fluxes (ET, springs) at discharge locations are preserved. The effect of incorporating depth decay into the model domain is to reduce permeability with depth, which in turn causes higher velocities in the shallower zones of the aquifer where permeabilities are higher. This leads to minimized contaminant mixing with depth, which results in higher concentrations in the shallow portions of the aquifer. However, by incorporating depth decay, the discharge calibration targets are achieved.



In [Section 8.3.3](#), the depth-decay coefficient is relaxed to allow for more vertical penetration into the lower aquifer. The revised depth-decay coefficient selected is 0.001 for the TMCM HSU. To maintain the calibration targets of head at observation wells and discharge locations, it was necessary to reduce the permeability of the TMCM to keep heads high in the TMCM and FCCM and to simulate discharge in Oasis Valley. Reduction of the depth-decay coefficient results in smaller local specific discharge at any location, deeper penetration of radionuclides into the TMCM, increased  $D_m$  (and sorption of reactive species) due to reduced velocities, and dilution in the larger mixing volume. The combined effects of dilution in the larger volume and longer residence time results in a smaller plume relative to the simulations with a larger depth-decay coefficient. This behavior is seen for the transport model results and in the comparison of the two depth-decay scenarios discussed in [Section 8.3.3](#).

The degree to which depth decay is incorporated into the flow and transport model may prove a very important consideration for understanding plume evolution and definition of the regulatory boundary. A possible approach to better define depth decay may include measurement of geochemical tracers and permeability testing at discrete vertical intervals at existing and planned well sites. Most of the wells currently accessible have only been sampled and tested over large open intervals making characterization of attribute changes with depth difficult. Characterization over multiple intervals with depth may provide sufficient information to quantify depth decay and anisotropy, and to map the spatial variability using geostatistical or traditional probability methods.

## **9.7 Recharge**

Recharge applied to the top of the model domain provides significant constraints on the water balance and fluxes, and directly impacts the calibrated permeabilities. Three independent recharge models for the Central and Western Pahute Mesa CAUs were developed as alternative conceptual models for inflow to the top of the saturated zone in the model. These recharge models extend throughout the DVRFM domain and provide inflow boundary conditions to the regional model from which side boundary inflow and outflow calibration constraints are derived for the PM CAU flow model as well. The three models are (1) the MME empirical model, (2) the DRIA chloride mass-balance model and (3) the USGSD watershed model. A detailed discussion of these alternative models is provided by SNJV (2006a). Each of these models is based on a different method by which recharge is measured.

Consequently, the three methods also provide three different potential recharge rates that are then applied as three alternatives during simulation. Of these three alternatives, the DRIA option provides the highest total recharge to the model, and the USGSD option accounts for the lowest total recharge. The MME model has the largest total area where recharge rates exceed 20 millimeters per year (mm/yr).

Radionuclide migration through the system shows a high degree of sensitivity to the recharge rate applied to the model domain. For the model with DRIA and the DRT HFM, simulations of the contaminant plume that emanates from Pahute Mesa plateau predict that the MCL is not exceeded at any time south of the Timber Mountain caldera structural fault zone. This behavior is the result of a combination of factors. However, of all the alternative HFMs, this model is the only one that exhibits truncation of the plume south of Pahute Mesa, which is attributed to the higher recharge rate for the DRIA option. The domain-wide higher recharge is further compounded by enhanced recharge and mounding below TMD. High flows from the west flank of Timber Mountain added to the high flows from Pahute Mesa result in higher water volumes that serve to dilute the contaminants in the groundwater.

The lower recharge of the USGSD option does not dilute the plume to the extent that was observed for the DRIA case, nor does the lower recharge case cause the plume to migrate as far as intermediate recharge case of MME. The head residuals calculated through inverse parameter estimation for the USGSD alternative showed the best fit to measured heads. This result suggests that the recharge rate for the DRIA and MME options may be too high and that the USGSD option is a better approximation of the actual recharge to the system. Even with the reduced head residuals for the USGSD model, another alternative with yet a lower recharge may result in further reduction of the head residuals, which would suggest that perhaps even the low recharge case may be too high.

An additional observation with regard to the high recharge, DRIA option is that the numerical model outputs are most sensitive to parameters associated with the high-permeability rocks. When high flows do not dominate contaminant migration, the lower-permeability HSU transport parameters become more important in defining model output sensitivity. Consequently, the arrangement of the HSUs coupled with the higher recharge applied to the system tends to mask the impact that transport parameters have on contaminant plume migration, particularly in the high-permeability units.

A primary component of recharge adjacent to the primary groundwater flow path from Pahute Mesa is generated by recharge at the flanks of Timber Mountain. Uncertainty in the permeability of the TMD and actual recharge rates at Timber Mountain has not been adequately addressed, so recharge and additional flux at the west flank of Timber Mountain are not well known. Three tasks that may serve to reduce this uncertainty are: (1) measurement of the permeability (assumed to be fracture dominated) of the TMD, (2) measurement of the precipitation accumulation at Timber Mountain, and (3) subsurface measurements of deep percolation below Timber Mountain (such as chloride mass balance or neutron probe) to determine whether unfractured porous media exist in the shallow subsurface. If precipitation and subsequent recharge on Timber Mountain is found to be less than the assumed rate, lower flows could significantly affect flow dynamics and therefore transport. An increase in the permeability of the TMD sub-HSU could result in less outward flow at the flanks of Timber Mountain. The result of either condition could be a reduction in the flow velocities and dilution volume of water, and potential increased interaction of the aqueous phase radionuclides with the reactive minerals in the rocks.

## **9.8 Boundary Flow**

Calibration of the PM CAU flow models is constrained by inflow and outflow across the model's lateral boundaries. These values are estimated from the regional flow model and other studies such as the Yucca Mountain site scale flow model, which overlaps the Pahute Mesa southern boundary. Through the course of this investigation, radionuclides were predicted to migrate primarily in shallow volcanic units, with very little interaction with the deeper carbonate flow system. Nonetheless, a distinction between inflow and outflow in carbonate or volcanic material along model boundaries is not made. Thus, whereas the flow model may calibrate well to net inflow, small changes in the distribution of boundary flux between volcanic and carbonate rock may lead to substantial permeability and flux changes, particularly in the volcanics where radionuclide migration is of concern. Thus, future refinement of inflow distribution and perhaps head variations along key boundaries such as the western half of the northern boundary could serve to constrain the flow model calibration uncertainty. This, in turn, would reduce uncertainty in transport simulations.

## 9.9 Source Term

The purpose of the source term calculation is to provide the radionuclide mass flux from individual nuclear test sites for input into the PM CAU model. The source term is developed from measurement of post-detonation conditions at and near the working point, the data from which are then used to build a conceptual and numerical model of the near-field processes. Simulation of flow and transport from the model and observed fit to data are used to further refine the conceptual model and constrain the system characteristics. Detailed analyses and simulations at the CHESHIRE (Pawloski et al., 2001) site is used to refine the dynamic processes and characteristics that contribute to the radionuclide mass release. The TYBO-BENHAM test (Wolfsberg et al., 2002) is also available to serve as a source of additional detailed data. From these tests and previously published reports that form the basis for understanding physical and geochemical evolution of the post-detonation environment, the configuration and inputs at other sites on Pahute Mesa can also be predicted.

The CHESHIRE and TYBO-BENHAM tests were simulated using a 3-D flow and transport process model. These models require high levels of detail and supporting information, and are computationally demanding. This level of information is not available for all of the test sites, and collection of these data and development of process model is impractical on the basis of cost, time, and computational effort. Therefore, a simplified form of the flow and transport model was developed that would build on the general features described in the process models, is computationally tractable, and incorporates parameter variability that describes the uncertainty in the parameter space that is then reflected by the sensitivity of the output. The utility of the simplified model as a surrogate for the more complex process model is validated through matching of output and observed sensitivity between the simplified and available process models. Once validated, the other sites are simulated by changing out site-specific variables in the input files of the SSM. A description of underground nuclear test phenomenology is located in [Section 5.2](#), and the SSM is described in [Section 4.0](#).

The SSM is a 1-D representation of a 3-D process model domain. As such, some processes that are 3-D in nature, such as dispersivity, cannot be directly represented by the 1-D model. This makes the assignment of parameters a fitting exercise that may not necessarily accurately represent the physical

system. Other underground test features that can be represented by a 3-D model, but are not explicitly represented by the 1-D model include:

- Hydrogeologic heterogeneity
- Vertical convection in the rubble chimney
- Reactive transport
- Transient flow
- Colloidal transport

These features can be incorporated in a general way; for example, if the test working point is located beneath the water table in a confining unit and there is a high-permeability zone above the water table that is assumed to receive radionuclide mass, the working point location can be assigned the properties of the higher-permeability material. However, the convection cell transport may be expected to diminish at later time, resulting in less mass release to the higher-permeability unit. The option of reducing the radionuclide source term for this process is not incorporated into this model. Further comparison of the 3-D features of the process model and the manner in which the 1-D simplified model accounts for these features may be warranted. The question should be asked whether the 3-D process is important and, if so, whether this process is adequately accounted for in the SSM.

Fluid flux out of the test cavities is directly related to the recharge rate assigned to the model. The DRT-DRIA test has the highest recharge of the three alternative recharge rate models. The lowest recharge rates are from the SCCC-MME and LCCU1-USGSD models. The USGSD model is the lowest recharge model option, and the MME model is the intermediate between the other two. However, the hydrogeologic properties of the SCCC, HFM model are very different from all the other HFMs. The fluid flux rate assigned for the SSM is derived from flux through the cavity calculated with the PM CAU flow model. For the case of the SCCC model, lower-permeability rocks along critical flow paths restrict flow rates through source region. From this analysis, it is apparent that not only the recharge rate but also the hydrostratigraphic arrangement of the HFM will affect fluid flux through the source region.

A critical component for definition of the source area for each test site is assignment of an HGU as constraining mass flux out of the test cavity. Those tests that are in or beneath the water table and are located in high-permeability rocks are assigned HGU properties that promote rapid flux out of the

cavity. The same approach does not necessarily apply to low-permeability rocks. For the case where a cavity resides in a low-permeability formation that is overlain by a high-permeability unit, such that the high-permeability unit resides in or beneath the water table, a conduit may exist through the chimney rubble zone that serves as a conduit for radionuclide migration. Another scenario is the case where the test is in a low-permeability unit but is underlain by a high-permeability unit. Does contamination migrate along preferential fractures in the host rock into the higher-permeability aquifer below? A third scenario is that of high-permeability layers in the homogenized lower-permeability host rock. This latter case was observed for the CHESHIRE test as described in [Section 5.2](#). These questions highlight the issue of whether the 1-D SSM captures enough detail about the site for both the 3-D nature of the system dynamics and the resolution of HGU's. The impact of capturing the correct rock type can be a significant factor in determining which radionuclides contribute to the PM CAU model and how rapidly they will migrate to downgradient receptors.

The inventory assigned for each test site is also a key component that will contribute to contaminant distribution and size of the EV at progressive timesteps. The inventory is calculated for each test by adding the unclassified sources for each area (Areas 19 and 20, respectively), then multiplying the total inventory for each radionuclide by the ratio of the maximum yield for each single test by the total yield for all the tests in that area. Although this provides a reasonable distribution of the radionuclide mass, it is still only an approximation and introduces an unknown level of error relative to the validity of the yield reported for each test. In addition to this error in the inventory, there is also uncertainty associated with how much mass is generated for each particular radionuclide. This error term is also incorporated as the variability assigned through the parameter distribution. For the case of radionuclide groups identified by Bowen et al. (2001) and defined by the inventory term, deviation can occur based on an assumed error range. For the case of  $^3\text{H}$ , the error can be as much as 300 percent above or below the selected parameter.

Another question is to what degree model error is attributable to parameter variability (parameter uncertainty) and to what degree the model error is attributable to model error (conceptual model uncertainty). For example, the reduction of a 3-D problem to a 1-D problem introduces uncertainty aside from the inherent uncertainty in the input parameter distributions. What tools or methods

could be employed to separate parametric uncertainty from conceptual model uncertainty, if this distinction can be made?

Although it was not done for this modeling task, sensitivity analysis of the input ranges and output response may further help to quantify the range of uncertainty that each parameters contributes to the total uncertainty for the SSM. In addition, a statistical analysis of the parameters (such as through an analysis of variation) could provide a ranking of the parameters in the order that they contribute to the total system variance.

## **10.0 SUMMARY, CONCLUSIONS, AND DATA NEEDS**

The purpose of this study is to simulate the release and migration (transport) of radionuclides into the groundwater based on the PM flow model developed at the CAU scale (SNJV, 2006a). This task comprises one component of the strategy to characterize the risk associated with radionuclide release from the NTS. The objective of the strategy is to analyze and evaluate each UGTA CAU through a combination of data and information collection and evaluation, and modeling groundwater flow and contaminant transport. This analysis will estimate the vertical and horizontal extent of contaminant migration for each CAU in order to predict exceedance maps. An exceedance map is the model-predicted perimeter that defines the extent of radionuclide-contaminated groundwater from underground testing above background conditions exceeding the SDWA standards (CFR, 2007). The exceedance map will be composed of both a perimeter boundary and a lower HSU boundary. The computer model predicts the location of this boundary within 1,000 years and must do so at a 95 percent probability of exceedance within the contaminant perimeter.

Before performing transport simulations, the previous flow model was revised by adjusting the permeability of selected structural components and modifying permeability fields of select HSUs. The transport model was then developed from the corrected flow fields. As with the previous flow model, conceptual uncertainty is explored through the selection of multiple HFMs. After flow model revision, simulation and parameter estimation were performed such that the calculated residuals at the calibration points of the corrected model were consistent with previous calibration targets. The steady-state flow solution was then used to calculate the transport plume distribution for each of the HFMs. Uncertainty analysis within the transport component of the model was estimated through application of the Monte Carlo method during development of multiple model realizations. Through this process, a quantitative assessment of the conceptual and parametric uncertainty was performed, and output sensitivity was calculated. The metrics identify those parameters and conceptual elements from which the greatest variability in model output results. A composite analysis of all components for both flow and transport provided insight into the critical processes that affect the flow and



transport models, and identify critical elements of the domain that require further review and warrant additional data collection efforts in support of Phase II modeling. This analysis was performed to satisfy the criteria identified in Appendix VI, Revision No. 1 (December 7, 2000) of the FFACO (1996, as amended February 2008) and set forth in the *Corrective Action Investigation Plan for Corrective Action Units 101 and 102: Central and Western Pahute Mesa, Nevada Test Site, Nevada* (DOE/NV, 1999). The results of this study are intended to provide guidance for development of the CAIP addendum that will define Phase II data collection activities.

The HFM is the basic construct upon which the flow and transport models are built. In general, the HFM describes the ensemble arrangement of the hydrologic properties for geologic units. Conceptual uncertainty is explored through the development and simulation of groundwater flow and contaminant transport from multiple alternative HFMs.

Seven alternative HFMs were evaluated with respect to independently developed groundwater mixing targets determined from geochemical analysis. The purpose of these comparisons was to determine whether the source of groundwater at certain wells within the model domain were consistent with the geochemical interpretation, thereby identifying HFM alternatives appropriate for transport simulation.

Revision of the flow model conceptualization was performed to correct observed anomalous flow through the model domain. In the first step, adjustment of fault permeability was necessary to correct for anomalous flow paths through the faults and to improve the geochemical mixing signature at ER-EC-6 and UE-18r. Flow paths were observed to cross the Purse and Boxcar faults at the intersection with other faults. This behavior was attributed to order of assignment of the higher fault permeabilities that intercept the two primary faults. At nodes common to both faults, a higher permeability was estimated, which allowed flow to cross the Purse and Boxcar faults. The gaps in the fault were sealed by reassignment of the permeability in the gap to the lower value. A general reduction in the permeability of the Southern Purse fault and the Central Boxcar was necessary to segregate the flow field into three primary components that take on a more north-to-south orientation parallel to the Purse and Boxcar fault traces.

The second step taken to adjust the groundwater flow model was to revise permeability of HSUs that have a major influence on the groundwater flow path, both as highly permeable conduits and also

low-permeability barriers. Two alternative models were developed from the LCCU1-MME HFM. The LCCU1-MME model directs flow from the northeast Pahute Mesa to the southwest just above the northwest flank of Timber Mountain. Flow from the northwest is directed to the southeast to the same location above the northwest flank of Timber Mountain. Flow from the northwest model quadrant is channeled into the TSA and BA to the southeast by the FCCU. The convergence of the two flows off of Pahute Mesa is then channelized along the western flank of Timber Mountain in the TMCM where flow to the west is constrained by the FCCM, and the central resurgent dome beneath Timber Mountain is a low-permeability unit that bounds groundwater flow along the western flank of Timber Mountain to the east.

The LCCU1-MME-TMD HFM was the first alternative flow model developed and tested to assess the extent to which the flow field changes with a change in the HSU permeability. The permeability of the TMD was increased by a factor of 100 times. The recharge mound that was simulated on Timber Mountain for the lower-permeability dome was appreciably diminished, and the flow was more susceptible to diffusion into the dome rocks. The effect of this change was to shift flow from the Area 19 sources to closer into the dome center on the western flank. The flows from Area 20 sources remain in the previous channel along the western flank of Timber Mountain.

The LCCU1-MME-TMCM alternative model incorporates an increase of the FCCU and the FCCM unit permeabilities to approximately the permeability of the TMCM. The permeability along the eastern slope of Timber Mountain was also increased to approximately match that on the western flank. This alternative allows more diffuse flow along a broader region of northwest Area 20 of Pahute Mesa and opens a path for flow from Area 19 locations along the eastern flank of Timber Mountain. For this scenario, the permeability at the central dome of Timber Mountain is not increased from that defined for LCCU1-MME.

Inputs to the CAU-scale transport model include (1) the source term that is generated through an SSM, (2) the transport parameter distributions that were derived before the modeling task, and (3) the groundwater flow fields that were simulated during the groundwater flow model task. Output metrics from which uncertainty and sensitivity analyses are performed include the EV, the FEV, and the probability map. The SSM is a 1-D representation of the underground nuclear test at the local scale (approximately two cavity radii). A radionuclide mass flux for each radionuclide is generated for

each CAU HFM at each test location. Inputs to this model include the volumetric fluid flux for each of the cavities and the unclassified radionuclide inventory based on inventory totals as a ratio of the maximum reported bomb yield at each site. Output from this model consists of time-varying mass flux. The EV is a scalar measure of the total volume of the PM-OV groundwater model domain that exceeds the regulatory standard at individual nodes by more than 5 percent at any time for each of the 1,000 simulations. This equates to a 95 percent probability that contamination within the plume exceeds the MCL. The distribution of this metric for all 1,000 realizations provides the mean EV and the variance about the mean. The FEV is a measure of exceedance for individual radionuclides per output timestep per realization. It is a scalar metric ranging from 0 to 1 that approximates the volume fraction of an exceedance MCL plume, at each simulation timestep, that is accounted for by each radionuclide. The probability map is a regulatory boundary that is defined such that there is a 95 percent probability of the area external to the boundary is uncontaminated and, conversely, that there is at least a 5 percent probability that a node within the boundary will exceed an MCL any time within a 1,000-year interval.

In the interest of reducing the computational effort for the transport model task, a reduced set of sites was developed from the 82 total radionuclide sources in the PM model domain. Five of the base HFM models were considered for the identification of sources that would potentially contribute contaminant mass at the NTS boundary. The method involved identifying whether simulated source-release particles cross a specific transect along a southwest flow path defined by the 4,110,000 m Northing value. In each model simulation, 10,000 particles were released from each test, and the number of particles crossing the transect were counted. Sources that had at least 1 percent of their particles crossing the transect were included for subsequent transport simulation.

All simulations were performed with a fixed, low-dispersivity value whose purpose was to maximize potential downgradient migration. A higher-dispersion case was also performed for a limited number of HFMs to assess the impact that dispersivity has on the EV. Results show that the effect of higher dispersion was to increase migration rate through the domain and significantly increase the extent of the contaminated area as defined by the MCL exceedance. Large longitudinal dispersivity in concert with high fluxes along flow channels cause particles to move downgradient several nodes at a single point in time in the numerical model. Although the concentration at nodes decrease, the large source release combined with low MCL standard resulted in MCL exceedance along the flow path.

Simulations for seven HFMs were performed for a constant low-dispersivity scenario. The simulations included five that are variations of the base HFM, one that is built from the SCCC geologic conceptualization, and one that is a variant of the base model that investigates the effect of hydraulic parameterization on transport. Uncertainty of the spatial and temporal distribution of radionuclides was included through the Monte Carlo process. Assessment of the simulation results were performed through evaluation of EV, FEV, and probabilistic exceedance map.

Rapid and preferential transport simulated in the base-derived models is explained by the hydraulic properties and connectivity of the HSUs. Flow within high-permeability units that are constricted by low-permeability units result in focusing contaminants. Additionally, interconnected high-permeability flow paths allow rapid downgradient migration.

While the influence of flow conceptualization and parameterization on transport is strong, the influence of transport parameterization was found to be weaker. In the five base-derived models, there is often a 90 percent probability that at least one radionuclide group exceeds the MCL near Oasis Valley or Beatty Wash. This indicates that the gross behavior of the flow model dominates, and transport parameters play a secondary role.

The DRT-DRIA HFM exemplified the high-flow end-member of the set of simulations that is characterized channelized flow path coupled with strong dilution associated with high recharge to the model domain that prevented MCL exceedance at any model nodes downgradient of the Silent Canyon caldera. The low-flow end-member is represented by the LCCU1-MME-TMCM and SCCC-MME models. The LCCU1-MME-TMCM flow model results in dilution caused by homogenization of the TMCM subdivision permeability, and the SCCC-MME model results from dispersion through a single-property hydrostratigraphy. The two models reduce radionuclide migrations rates and inhibit transport along a single flow path.

The FEV analysis shows that the radionuclide contribution to the MCL exceedance areas is generally insensitive to flow behavior. The similarity of the FEVs across models indicates that the radionuclide contribution to plumes is based principally on the total mass release per radionuclide. The source term model applied at cavities distributes the same proportion of radionuclides to each cavity volume of water across all models; therefore low- and high-flux models experience low- and high-mass release, respectively.

The transport model results show the following general trends:

1. Where high-permeability HSUs form a long, continuous flow path and are bracketed by lower-permeability units, radionuclide migration is rapid, and contaminant levels remain at or above the MCLs at long distances from the source. The EVs are greatest for these high-flow cases. The only exception to this phenomenon is for the highest recharge model, which results in dilution of the contaminant plume as it crosses into the Timber Mountain caldera.
2. Where there is not a continuous, constricted high-permeability zone, the plume can spread laterally, thereby slowing the velocity and allowing more time for radionuclides to react or diffuse into the rocks. For the low-flow cases, the EV is smaller, and the time of downgradient arrival is later.
3. In all cases, the FEV shows a similar order as to which radionuclides dominate at discrete time intervals, regardless of the conceptual flow model considered. This suggests that the FEV is solely a function of the initial inventory at each test location.

The Pahute Mesa CAIP (DOE/NV, 1999) requires analysis of parameter sensitivity and conceptual model uncertainty. To this end, the sensitivity of the EV to each input parameter is tested using the methods of stepwise regression, entropy analysis, and classification and regression tree analysis. Each of these methods represents a different approach to quantitatively identifying those inputs for which the output shows the greatest sensitivity (variance). These methods also represent a global sensitivity approach that is valid over the entire range of possible parameter variation and not just near the reference point. Stepwise regression performs a forward regression such that the parameter that shows the greatest reduction in the variance at each regression step is identified. Entropy analysis is a useful metric for characterization of uncertainty (or information) in a univariate case and redundancy (or mutual information) in a multivariate case. Because mutual information is a natural measure of input variance, it is also useful as an indicator of variable importance. The classification and regression tree is generated by recursively finding the input variable split that best separates the output into groups where a single category dominates. For all methods, the first occurrence in the process represents the transport parameter that exerts the greatest variance on the model results.

Sensitivity analysis was performed for 35 input parameters and the output parameter, EV. The analysis was performed for each of the seven alternative HFMs that were developed for the transport model. Sensitivity analysis was performed in three stages: (1) each HFM was evaluated using the three sensitivity methods, (2) the top five results for all seven HFMs were grouped by method, and (3) the top five parameters from all HFMs and all methods were compiled. While going through

these steps, the significant parameters were distilled to five that consistently dominated the top two positions for all methods and all HFMs. The top parameters identified through this analysis are:

- Mass transfer coefficient for the WTA
- Effective porosity for the WTA
- Tritium concentration from the TYBO underground test
- The Pu reduction factor to represent colloidal migration
- Effective porosity of the TCU

Further assessment of the parameters by HFM revealed that the first three parameters listed were dominant among four of the HFMs, and the last two parameters mapped to the remaining three HFMs. Upon examination of the grouping, it became apparent that the first grouping of four HFMs corresponds to the largest EV sizes. These parameters are also characteristic of the higher-flux welded tuff and lava flows. The second grouping of parameters corresponds to the smaller EV sizes that are characteristic of lower flux/high dilution. These observations show that the flow and transport models separately identify different HSUs as important.

In addition to the transport model sensitivity, transport sensitivity to flow model uncertainty was explored. The identification of basin-scale preferential transport paths within subdomains of the TCMC required reanalysis of flow model conceptualization through the reparameterization (i.e., hydraulic conductivity adjustment) of selected HSUs. The HSUs of concern were primarily the TCMC and FCCM, two extensive units south of the Moat fault that have repeatedly shown strong influence on contaminant transport.

Preliminary investigation of the influence of TCMC permeability, when conceptualized as a set of subdomains, on flow model calibration metrics clearly imply that a region of uncertainty and insensitivity exists. Uncertainty implies the range of permeability values plausible at the modeled scale, and insensitivity points to the range of permeabilities for which the model calibration metrics remain constant and/or below some acceptable value. Null Space Monte Carlo analysis permits the quantitative identification of the overlap of both such regions, the results of which serve two purposes. First, a discrete range of permeability insensitivity is defined that honors both field observation of permeability (i.e., the range of uncertainty) and field observation of hydraulic calibration targets. The latter implies that the range of insensitivity is in large part governed by how well observations constrain the parameter estimation problem. Second, nine equiprobable flow

models may be defined for use in a Monte Carlo transport analysis and subsequent assessment of transport model sensitivity to TCMC permeability.

Each of the nine flow fields was applied in transport simulation of radionuclide migration from selected cavity sources. The NSMC results not only demonstrate that transport is sensitive to flow model parameter uncertainty but also that conceptual model uncertainty is more significant than parameter uncertainty. Clearly, the conceptualization of the TCMC is fundamental to its parameterization. Nevertheless, the basic point of this parametric uncertainty exercise was to show that hydraulic observations used to constrain the FCCM/TCMC permeability estimation problem are limited in their ability to define the permeability with any degree of certainty. Due to the large extent of these HSUs, such uncertainty leads to both large variability in plume extent (EV) and location within the model domain.

In all of the models considered so far, a depth-decay coefficient of 0.0027 was applied to the TCMC (SNJV, 2005). This coefficient results in simulations that favor flow in the shallower parts of the TCMC, which can be as much as 3 km thick. Rather than eliminating the depth-decay model completely, the coefficient was reduced from 0.0027 to 0.0010 in the TCMC and FCCM HSUs of the LCCU1-MME-TCMC flow model. Starting from a well-calibrated model, the new flow field with reduced depth decay was calibrated to the combined head and flux targets nearly as well. With the reduced depth-decay model, permeability contrasts with depth were less and flow paths could penetrate deeper in the TCMC and FCCM units. In the reduced depth-decay model, plume migration was substantially reduced as a result of fewer shallow convergent flow paths. With deeper penetration, the plume migration is reduced for two reasons. First, the velocity at any location was less due to the greater distribution for flux in the vertical direction. With reduced velocities, more  $D_m$  occurs in fractured rock, thus retarding solute migration. Second, with greater spreading of flow paths in the vertical direction, more dilution occurs, thus reducing the local solute concentrations at any time.

In the Monte Carlo simulations, X, Y, Z dispersivity tensors reflect fairly small values ([10, 1, 2] and [100, 10, 2]). Shaw (2003) and SNJV (2004d) discuss larger values, potentially applicable to large extensive units such as the TCMC (in the particle-tracking methodology, it is not appropriate to use such large values when heterogeneity exists over small scales such as in the volcanics of Pahute

Mesa). Therefore, a series of semiquantitative sensitivity analyses was conducted to examine model behavior for increase dispersivity. The hypothesis was that increased dispersivity might lead to more dilution, lower concentrations, and reduced plume migration. This hypothesis was examined with respect to simulation results.

Increasing values of the dispersion tensor to (300, 100, 10), a 1,000-Monte Carlo simulation on the remaining transport parameters was conducted. With the larger longitudinal value, exceedances occur earlier, and the size of the boundary is larger. Thus, the increased dispersion considered in this sensitivity study does not lead to reduced contaminant migration through spreading and dilution. The dispersion analysis presented is only semiquantitative because the large values considered are not ideal for the selected particle-tracking method.

## **10.1 Data Needs**

The following identifies key components of the flow and transport model that have a dominant influence on the uncertainty and sensitivity observed in simulation results for the Pahute Mesa CAU. The discussion identifies the nature of each component, its effect on transport model results, and possible data collection activities that could prove useful in developing additional information from which parametric and/or conceptual uncertainty can be further reduced.

### **10.1.1 Pahute Mesa Bench Complexity**

The Pahute Mesa bench is a particularly important and complex region of the model because it represents a transitional zone between the adjacent SCCC and TMCC that has experienced multiple caldera formation events. Discontinuous emplacement of HSUs in each caldera and their complex geometric arrangement compound the inability to conceptualize this region of the model domain. This region also serves as the primary conduit for flow from the test areas to downgradient locations. Better measurement of flow and transport through the rocks may be possible through placement of additional wells such that MWATs can be performed to characterize large-scale permeability. Tracer tests can also be performed from which diffusion processes and effective surface area at the field can be determined. A potential candidate site for the MWATs is between UE-18r and ER-EC-5.



### **10.1.2 Specific Discharge**

Specific discharge was simulated based upon flow model matches to groundwater head in which large-scale permeability was estimated. Specific discharge within the model is highly important because it directly impacts flow velocities, which in turn impacts how much  $D_m$  occurs. The region of the PM flow model where specific discharge is most important is along Northwest Timber Mountain, west of UE-18r, where several conceptual models simulate convergent flow from Areas 19 and 20. A large MWAT could potentially serve to quantify the conductance of the material in this portion of the domain.

### **10.1.3 Fracture Properties**

Understanding and quantifying  $D_m$  for field-scale migration in fractured rocks — particularly the BA, TSA, and TCM — is necessary to adequately predict migration of solutes to downgradient locations. Current understanding of local fracture matrix interactions is derived from laboratory experiments. Field-scale fracture properties used in sensitivity analysis were chosen to reflect limited field-scale information and substantial uncertainty. Because of lack of field-scale measured data, the porosity-spacing-aperture relationship was used to calculate the fracture properties that control mass transfer between the fracture and matrix.

### **10.1.4 Fracture Pathways**

The length and continuity of fracture pathways is another variable that is not well understood and introduces significant uncertainty for the calculation of mass transfer into the rock matrix. For the PM model, the large-scale effective fracture permeability fails to adequately represent complex small-scale features. Future field and modeling studies may help to provide insight into migration in fractures over larger scales and improve the conceptual model.

### **10.1.5 Fault Zones**

Faults may serve as major conduits or barriers to flow of radionuclides released from Pahute Mesa. The Moat fault is one such feature that may provide insight into the role faults play in altering the migration path. Wells ER-20-5 #1 and #3 both show high levels of contamination, while ER-EC-5

south of the Moat fault shows no contamination. Further testing on both sides of the fault may provide insight into how this feature impacts migration off of Pahute Mesa.

### **10.1.6 Heterogeneity**

In a numerical model, the definition of heterogeneity depends on the scale of the process and the variability of the parameters at the scale of interest. Heterogeneity of the flow and transport model is a component of both the HSU and RMC zonations. The HSUs are represented as large, homogeneous blocks in the CAU-scale model. Transport analysis through each of the alternative HFMs indicates that some form of sub-HSU scale variability is necessary to address km-scale preferential flow paths that result as an artifact of permeability contrasts along boundaries between HSU zones rather than observed hydrogeology. Possible forms of supplementary analysis that may provide some means of incorporating heterogeneity into the large HSU blocks include (1) geostatistical methods that describe the scales of permeability variation, (2) development of geostatistical parameters describing spatial variability as fitting parameters during flow model calibration, and (3) deployment of pilot points to allow for continuous permeability variation of the km-scale HSUs simulation of multiple categorical zones within a single HSU while honoring observed borehole data using transitional probabilities, and simulation of continuous permeability fields at the individual grid-block scale through indicator geostatistical methods.

### **10.1.7 Depth Decay**

If hydraulic conductivity were uniformly distributed vertically in the HSUs of the groundwater model, flow off of Pahute Mesa would penetrate into the lower portions of the TMCM and would not produce the observed discharge at Oasis Valley that is necessary to calibrate the flow model. Reducing the depth-decay coefficient, which is a vertical scaling of the permeability, allows deeper penetration of contaminants and requires an increase of the permeability in order to maintain model head calibration. These conditions promote larger mixing volumes, which cause dilution and slower velocities that, in turn, cause longer residence times for  $D_m$  to occur. Testing of discrete vertical intervals in existing and planned wells for permeability changes and geochemical tracers may provide additional insight into the permeability changes with depth. This information can then be used to map spatial variability using geostatistical or transitional probability methods.

### **10.1.8 Recharge**

Recharge applied at the surface of the model domain provides significant constraints on the water balance and fluxes, and directly impacts the calibration permeabilities. Three recharge options were used for the seven HFMs. General observations of the transport model indicate that numerical model output is most sensitive to parameters associated with the high-permeability rocks. When high flows do not dominate contaminant migration, the low-permeability HSU transport parameters become more important for defining output sensitivity. In all cases, recharge to the model has a significant impact on exceedance map perimeter uncertainty. Three potential tasks that could help to reduce this uncertainty are: (1) measurement of the permeability of the TMD, (2) measurement of precipitation at Timber Mountain, and (3) subsurface measurement of deep percolation below Timber Mountain, such as chloride mass balance or neutron probe borehole logging.

### **10.1.9 Boundary Flow**

Through the course of this investigation, radionuclides were predicted to migrate primarily in shallow volcanic units and very little in deeper carbonate flow systems. Thus, whereas the flow model may calibrate well to net inflow, small changes in the distribution of boundary flux between volcanic and carbonate rock may lead to substantial permeability and flux changes, particularly in the volcanics where radionuclide migration is of concern. Thus, future refinement of inflow distributions and head variations along key boundaries could serve to constrain the flow model calibration uncertainty.

### **10.1.10 Simplified Source Model**

The purpose of the source term calculation was to provide the radionuclide mass flux from individual nuclear test sites for input into the CAU-scale model. The source term is developed from measurement of post-detonation conditions at and near the test working point, the data from which are then used to build a 3-D conceptual and numerical model of the near-field processes. Simulation of flow and transport from the model and observed fit to data is used to further refine the conceptual model and constrain the system characteristics. The 3-D model is then extrapolated to a simplified 1-D model of the flow and transport local scale site. Two critical elements of the SSM include groundwater flux through the cavity and the inventory. Future sampling at or near test cavities could provide useful information regarding contaminant migration away from the test location.

Temperature measurements can be used to determine whether formation water is moving through the cavity. Based on temperature decay and inventory estimates, any change in the expected temperature profile could identify the flow rate through the cavity. Sampling of the radionuclide inventory could also identify the extent to which the cavity is exposed to throughflow. An observed reduction in cavity inventory beyond that expected from decay could be used to calculate a flow rate through the cavity.

## 11.0 REFERENCES

- Anderson, M.P., and W.W. Woessner. 1992. *Applied Groundwater Modeling*. San Diego, CA: Academic Press.
- BN, see Bechtel Nevada.
- BSC, see Bechtel SAIC.
- Bechtel Nevada. 2002a. *A Hydrostratigraphic Model and Alternatives for the Groundwater Flow and Contaminant Transport Model of Corrective Action Units 101 and 102: Central and Western Pahute Mesa, Nye County, Nevada*, DOE/NV/11718--706. Las Vegas, NV.
- Bechtel Nevada. 2002b. Written communication. Subject: *Completion and Geology Data for Well ER-EC-8*. Las Vegas, NV.
- Bechtel Nevada. 2005. *A Hydrostratigraphic Model and Alternatives for the Groundwater Flow and Contaminant Transport Model of Corrective Action Unit 98: Frenchman Flat, Clark, Lincoln and, Nye Counties, Nevada*, DOE/NV/11718--1064. Las Vegas, NV.
- Bechtel Nevada. 2006. *A Hydrostratigraphic Model and Alternatives for the Groundwater Flow and Contaminant Transport Model of Corrective Action Unit 97: Yucca Flat-Climax Mine, Lincoln and Nye Counties, Nevada*, DOE/NV/11718--1119. Las Vegas, NV.
- Bechtel SAIC. 2004. *Probability Distribution for Flowing Interval Spacing*, ANL-NBS-MD-000003 REV 01, DOC.20040923.0003. Las Vegas, NV.
- Belcher, W.R., J.B. Blainey, F.A. D'Agnesse, C.C. Faunt, M.C. Hill, R.J. Lacznik, G.M. O'Brien, C.J. Potter, H.M. Putnam, C.A. San Juan, and D.S. Sweetkind. 2004. *Death Valley Regional Model Ground-Water Flow System, Nevada and California - Hydrogeologic Framework and Transient Ground-Water Flow Model*, Scientific Investigations Report 2004-5205. U.S. Geological Survey.
- Benedict, F.C., Jr., T.P. Rose, and X. Zhou. 2001. *Mineralogical, Chemical, and Isotopic Characterization of Fracture-Coating Minerals in Borehole Samples from Western Pahute Mesa and Oasis Valley, Nevada*, UCRL-ID-152919. Livermore, CA: Lawrence Livermore National Laboratory.

- Blankennagel, R.K., and J.E. Weir, Jr. 1973. *Geohydrology of the Eastern Part of Pahute Mesa, Nevada Test Site, Nye County, Nevada*, Professional Paper 712-B. Denver, CO: U.S. Geological Survey.
- Bonnlander, B.V., and A.S. Weigend. 1994. "Selecting Input Variables Using Mutual Information and Nonparametric Density Estimation." In Proceedings of *International Symposium on Artificial Neural Networks (ISANN'94)*, 42-50. Tainan, Taiwan.
- Borg, I.Y., R. Stone, H.B. Levy and L.D. Ramspott. 1976. *Information Pertinent to the Migration of Radionuclides in Ground Water at the Nevada Test Site, Part 1: Review and Analysis of Existing Information*, UCRL-52078. Lawrence Livermore National Laboratory, Livermore, CA.
- Bourcier, W.L., S. Roberts, D.K. Smith, S. Hulsey, L. Newton, A. Sawvel, C. Bruton, C. Papelis, W. Um, C.E. Russell, and J. Chapman. 2000. *Determination of Reactive Surface Area of Melt Glass*, UCRL-ID-145181. Livermore, CA: Lawrence Livermore National Laboratory.
- Bowen, S.M., D.L. Finnegan, J.L. Thompson, C.M. Miller, P.L. Baca, L.F. Olivas, C.G. Geoffrion, D.K. Smith, W. Goishi, B.K. Esser, J.W. Meadows, N. Namboodiri and J.F. Wild. 2001. *Nevada Test Site Radionuclide Inventory, 1951-1992*. Los Alamos, NM: Los Alamos National Laboratory.
- Burbey, T.J., and S.W. Wheatcraft. 1986. *Tritium and Chlorine-36 Migration from a Nuclear Explosion Cavity*, Publication No. 45050. Las Vegas, NV: Desert Research Institute.
- Butkovich, T.R. 1976. *Cavities Produced by Underground Nuclear Explosions*, UCRL-52097. Livermore, CA: Lawrence Livermore National Laboratory.
- Butkovich, T.R., and A.E. Lewis. 1973. *Aids for Estimating Effects of Underground Nuclear Explosions*, UCRL-50929. Livermore, CA: Lawrence Livermore National Laboratory.
- Byers, F.M., Jr., W.J. Carr, P.P. Orkild, W.D. Quinlivan, and K.A. Sargent. 1976a. *Volcanic Suites and Related Cauldrons of the Timber Mountain-Oasis Valley Caldera Complex, Southern Nevada*, Professional Paper 919. U.S. Geological Survey.
- Byers, F.M., Jr., W.J. Carr, R.L. Christiansen, P.W. Lipman, P.P. Orkild, and W.D. Quinlivan. 1976b. *Geologic Map of the Timber Mountain Caldera Area, Nye County, Nevada*, Miscellaneous Geologic Investigation Map, I-891, scale 1:48,000. U.S. Geological Survey.
- Byers, F.M., Jr., W.J. Carr, and P.P. Orkild. 1989. "Volcanic Centers of Southwestern Nevada: Evolution and Understanding." In *Journal of Geophysical Research*, Vol. 94(B5): 5908-5924.
- CFR, see *Code of Federal Regulations*.
- Carle, S.F. 1999. *Transitional Probability Geostatistical Software, Version 2.1*. Livermore, CA: Lawrence Livermore, CA.

- Cashman, P.H., and J.H. Trexler, Jr. 1991. "The Mississippian Antler Foreland and Continental Margin in Southern Nevada: The Eleana Formation Reinterpreted." In J.D. Cooper and C.H. Stevens, eds., *Paleozoic Paleogeography of the Western United States - II: Pacific Section SEPM*, Vol. 67: 271-280.
- Code of Federal Regulations*. 2007. Title 40 CFR Part 141 Subchapter D, "National Primary Drinking Water Regulations." Washington, DC: U.S. Government Printing Office.
- Cole, J.C., U.S. Geological Survey. 1992. Written communication to S.L. Drellack (RSN) regarding thickness of Paleozoic units at the Nevada Test Site.
- Cole, J.C. 1997. *Major Structural Controls on the Distribution of Pre-Tertiary Rocks, Nevada Test Site Vicinity, Southern Nevada*, Open-File Report 97-533. U.S. Geological Survey.
- Cover, T.M., and J.A. Thomas. 1991. *Elements of Information Theory*. New York, NY: John Wiley & Sons, Inc.
- Crowe, B.M., F.V. Perry, J. Geissman, L.D. McFadden, S.G. Wells, M. Murrell, J. Poths, G.A. Valentine, L. Bowker, and K. Finnegan. 1995. *Status of Volcanism Studies for the Yucca Mountain Site Characterization Project*, LA-12908-MS. Los Alamos, NM: Los Alamos National Laboratory.
- DOE/NV, see U.S. Department of Energy, Nevada Operations Office.
- Dynamic Graphics, see Dynamic Graphics, Inc.
- D'Agnese, F.A., C.C. Faunt, A.K. Turner, and M.C. Hill. 1997. *Hydrogeologic Evaluation and Numerical Simulation of the Death Valley Regional Ground-water Flow System, Nevada and California: Water-Resources Investigations Report 96-4300*, p. 124. Denver, CO: U.S. Geological Survey.
- Dai, Z., A. Wolfsberg, Z. Lu, and R. Ritzi. 2007a. "Representing Aquifer Architecture in Macrodispersivity Models with an Analytical Solution of the Transition Probability Matrix." In *Geophysical Research Letters*, Vol. 34.
- Dai, Z., A. Wolfsberg, Z. Lu, and P.M. Reimus. 2007b. "Upscaling Matrix Diffusion Coefficients for Heterogeneous Fractured Rocks, 16 April." In *Geophysical Research Letters*, Vol. 34(7).
- Drellack, S.L., Jr., National Security Technologies, LLC. 2007. Personal communication to E. Freeman (SNJV) regarding the Pahute Mesa Phase I CAU Transport Model report that includes an MS-Word file prepared for Section 4 reactive mineral categories, figures, and tables; and the reactive mineral unit and hydrostratigraphic unit mineralogy table for Appendix D, 29 June. Las Vegas, NV.

- Drellack, S.L., Jr., and L.B. Prothro. 1997. Written communication. Subject: *Descriptive Narrative for the Hydrogeologic Model of Western and Central Pahute Mesa Corrective Action Units*. Las Vegas, NV: Bechtel Nevada.
- Drellack, S.L., Jr., L.B. Prothro, K.E. Roberson, B.A. Schier, and E.H. Price. 1997. *Analysis of Fractures in Volcanic Cores from Pahute Mesa, Nevada Test Site*, DOE/NV/11718-160. Las Vegas, NV: Bechtel Nevada.
- Dynamic Graphics, Inc. 2002. *EarthVision 5.1: Software for 3-D Modeling and Visualization*. Alameda, CA.
- EPA, see U.S. Environmental Protection Agency.
- FFACO, see *Federal Facility Agreement and Consent Order*.
- Faunt, C.C. 1997. *Effect of Faulting on Ground-Water Movement in the Death Valley Region, Nevada and California*, Water-Resources Investigations Report 95-4132. Denver, CO: U.S. Geological Survey.
- Faunt, C.C., F.A. D'Agnesse, and G.M. O'Brien. 2004. *Death Valley Regional Ground-Water Flow System, Nevada and California — Hydrogeologic Framework and Transient Ground-Water Flow Model*, Scientific Investigations Report 2004-5205, Chapter D, Hydrology, pp. 137-163. U.S. Geological Survey.
- Federal Facility Agreement and Consent Order*. 1996 (as amended February 2008). Agreed to by the State of Nevada, the U.S. Department of Energy, and the U.S. Department of Defense. Appendix VI, which contains the Underground Test Area strategy, was last amended December 7, 2000, Revision No. 1.
- Fenelon, J.M. 2000. *Quality Assurance and Analysis of Water Levels in Wells on Pahute Mesa and Vicinity, Nevada Test Site, Nye County, Nevada*, Water-Resources Investigations Report 00-4014. Carson City, NV: U.S. Geological Survey.
- Ferguson, J.F., A.H. Cogbill, and R.G. Warren. 1994. "A Geophysical- Geological Transect of the Silent Canyon Caldera Complex, Pahute Mesa, Nevada." In *Ground Water*, v. 99(B3): 4323-4339. Columbus, OH: Groundwater Publishing Co.
- Frantz, F.K. 1995. *A Taxonomy of Model Abstraction Techniques*. Proceedings of the 27th Conference on Winter Simulation. Washington, DC: IEEE Computer Society.
- Freeze, A.R., and J.H. Cherry. 1979. *Groundwater*. Prentice Hall, NJ.
- Fridrich, C.J., S.A. Minor, and E.A. Mankinen. 1999a. *Geologic Evaluation of the Oasis Valley Basin, Nye County, Nevada*, Open-File Report 99-533-A. U.S. Geological Survey.



- Fridrich, C.J., S.A. Minor, P.L. Ryder, and J.L. Slate. 1999b. *Geologic Map of the Oasis Valley Basin and Vicinity Nye County, Nevada*, Open-File Report 99-533-B, scale 1:62,500. Denver, CO. U.S. Geological Survey.
- Gable, C., and T. Cherry. 2001. *Technical Note on Interpolation of MODFLOW Flux onto a Piecewise Linear Surface*. Los Alamos, NM: Los Alamos National Laboratory.
- Gelhar, L.W., W. Welty, and K.R. Rehfeldt. 1992. "A Critical Review of Data on Field Scale Dispersion in Aquifers." In *Water Resources Research*, Vol. 28(7): 1955-1974.
- Germain, L.S., and J.S. Kahn. 1968. *Phenomenology and Containment of Underground Nuclear Explosions*, UCID-50482. Livermore, CA: Lawrence Livermore National Laboratory.
- Gorelick, S., C. Andrews, and J. Mercer. 1999. *Report of the Peer Review Panel on the Proposed Hanford Site-Wide Groundwater Model*, as accessed at <http://terrassa.pnl.gov:2080/> on 22 November 2007.
- Granger, C.W.J., and J. Lin. 1994. "Using Mutual Information To Identify Lags in Nonlinear Models." In *Journal of Time Series Analysis*, v. 15: 371-384.
- Grauch, V.J.S., D.A. Sawyer, C.J. Fridrich, and M.R. Hudson. 1997. *Geophysical Interpretations West of and Within the Northwestern Part of the Nevada Test Site*, Open-File Report 97-476. Denver, CO: U.S. Geological Survey.
- Grauch, V.J.S., D.A. Sawyer, C.J. Fridrich, and M.R. Hudson. 1999. *Geophysical Framework of the Southwestern Nevada Volcanic Field and Hydrologic Implications*, Professional Paper 1608. U.S. Geological Survey.
- Hevesi, J.A., A.L. Flint, and L.E. Flint. 2002. *Preliminary Estimates of Spatially Distributed Net Infiltration and Recharge for the Death Valley Region, Nevada-California*, Water-Resources Investigations Report 02-4010. Sacramento, CA: U.S. Geological Survey.
- Hevesi, J.A., A.L. Flint, and L.E. Flint. 2003. *Simulation of Net Infiltration and Potential Recharge Using a Distributed Parameter Watershed Model for the Death Valley Region, Nevada and California*, Water-Resources Investigations Report 03-4090. Sacramento, CA: U.S. Geological Survey.
- Hildenbrand, T.G., V.E. Langenheim, E.A. Mankinen, and E.H. McKee. 1999. *Inversion of Gravity Data to Define the Pre Tertiary Surface and Regional Structures Possibly Influencing Ground Water Flow in the Pahute Mesa Oasis Valley Region, Nye County, Nevada*, Open-File Report 99-49. Menlo Park, CA: U.S. Geological Survey.
- Hoover, D.L. 1968. "Genesis of Zeolites, Nevada Test Site. In: Eckel, E.B., editor, Nevada Test Site." In *Geological Society of America*, Memoir 110. Boulder, CO.

- Houser, F.N., R.E. Davis, and W.L. Emerick. 1961. *Geologic Map of the Ammonia Tanks Quadrangle, Nye County, Nevada*, Quadrangle Map GQ-638, scale 1:24,000.
- IAEA, see International Atomic Energy Agency.
- IT, see IT Corporation.
- Iman, R.L., and W.J. Conover. 1979. "The Use of Rank Transform in Regression." In *Technometrics*, Vol. 21(4): 499-509.
- Iman, R.L., and W.J. Conover. 1982. "Controlling Correlations in Latin Hypercube Samples." In *Journal of the American Statistical Association*, Vol. 89: 1994.
- International Atomic Energy Agency. 1998. *The Radiological Situation at the Atolls of Mururoa and Fangataufa, Technical Report, Volume 3: Inventory of Radionuclides Underground at the Atolls*, IAEA-MFTR-3. Vienna, Austria: Proceedings of an IAEA Conference.
- IT Corporation. 1996a. *Groundwater Recharge and Discharge Data Documentation Package (Phase I Data Analysis Documentation, Volume III)*, ITLV/10972-181. Las Vegas, NV.
- IT Corporation. 1996b. *Hydrologic Parameter Data Documentation Package (Phase I Data Analysis Documentation, Volume IV)*, ITLV/10972-181. Las Vegas, NV.
- IT Corporation. 1996c. *Potentiometric Data Documentation Package (Phase I Data Analysis Documentation, Volume II)*, ITLV/10972-181. Las Vegas, NV.
- IT Corporation. 1996d. *Regional Geologic Model Data Documentation Package (Phase I Data Analysis Documentation, Volume I)*, ITLV/10972-181. Las Vegas, NV.
- IT Corporation. 1996e. *Wells ER-6-1 and ER-6-2 Core Fracture Analyses and Geophysical Comparisons*, ITLV/10972-171. Las Vegas, NV.
- IT Corporation. 1998a. *Report and Analysis of the BULLION Forced-Gradient Experiment*, DOE/NV-13052, ITLV/13052-042, UC-700. Las Vegas, NV.
- IT Corporation. 1998b. *Summary of Micrographic Analysis of Fracture Coating Phases on Drill Cores from Pahute Mesa, Nevada Test Site*, DOE/NV/13052--050; ITLV/13052--050. Las Vegas, NV.
- IT Corporation. 1998c. *Value of Information Analysis for Corrective Action Units Nos. 101 and 102: Central and Western Pahute Mesa, Nevada Test Site, Nevada*, ITLV/13052-041. Las Vegas, NV.
- IT Corporation. 1998d. *Western Pahute Mesa – Oasis Valley Hydrogeologic Investigation Wells Drilling and Completion Criteria*, Rev. 0, ITLV/13052-049, p. 439. Las Vegas, NV.

- IT Corporation. 1999. *External Peer Review Group Report on Frenchman Flat Data Analysis and Modeling Task, Underground Test Area Project*, ITLV/13052--077. Las Vegas, NV.
- Jachens, R.C. 1999. Written communication to S.L. Drellack (BN) concerning the inferred subsurface distribution of Cretaceous granitic bodies along the north edge of Yucca Flat, Nevada Test Site. Menlo Park, CA: U.S. Geological Survey.
- Kersting, A.B., and P.W. Reimus, eds. 2003. *Colloid-Facilitated Transport of Low-Solubility Radionuclides: A Field, Experimental, and Modeling Investigation*, UCRL-ID-149688. Livermore, CA: Lawrence Livermore National Laboratory.
- Kersting, A.B., D.W. Efurud, D.L. Finnegan, D.J. Rokop, D.K. Smith, and J.L. Thompson. 1998. "Migration of Plutonium in Groundwater at the Nevada Test Site." In *Hydrologic Resources Management Program and Underground Test Area Operable Unit FY 1997 Progress Report*, UCRL-ID-130792. Livermore, CA: Lawrence Livermore National Laboratory.
- Kersting, A.B., D.W. Efurud, D.L. Finnegan, D.J. Rokop, D.K. Smith, and J.L. Thompson. 1999. "Migration of Plutonium in Groundwater at the Nevada Test Site." In *Nature*, v. 397: 56-59.
- Kersting, A.B., D.L. Finnegan, A.F.B. Tompson, B.K. Esser, D.K. Smith, M. Zavarin, C.J. Bruton, and G.A. Pawloski. 2003. *Radionuclide Decay and In-growth Technical Basis Document*, UCRL-ID-153798. Livermore, CA: Lawrence Livermore National Laboratory.
- Kilroy, K.C., and C.S. Savard. 1996. *Geohydrology of Pahute Mesa 3 Test Well, Nye County, Nevada*, Water-Resources Investigations Report 95-4239. U.S. Geological Survey.
- Kuzio, S. 2004. *Probability Distribution for Flowing Interval Spacing*, ANL-NBS-MD-000003 REV. 01. Las Vegas, NV: Yucca Mountain Project.
- Kwicklis, E.M., and R.W. Healy. 1993. "Numerical Investigation of Steady Liquid Water Flow in a Variably Saturated Fracture Network." In *Water Resources Research*, Vol. 29(12): 4091-4102. Washington, DC: American Geophysical Union, TIC: 226993.
- Kwicklis, E.M., and M. Sulley. 2005. *Effects of Fault Geometry and Properties on Groundwater Flow and Transport: A Simulation Study*, LA-UR-05-3952. Los Alamos, NM: Los Alamos National Laboratory.
- Kwicklis, E.M., T.P. Rose, and F.C. Benedict. 2005. *Evaluation of Groundwater Flow in the Pahute Mesa – Oasis Valley Flow System Using Groundwater Chemical and Isotopic Data*, LA-UR 05-4344. Los Alamos, NM: Los Alamos National Laboratory.
- Laczniak, R.J., J.C. Cole, D.A. Sawyer, and D.A. Trudeau. 1996. *Summary of Hydrogeologic Controls on Ground-Water Flow at the Nevada Test Site, Nye County, Nevada*, Water-Resources Investigations Report 96-4109. Denver, CO: U.S. Geological Survey.

- Laczniak, R.J., J.L. Smith, P.E. Elliott, G.A. DeMeo, M.A. Chatigny, and G. Roemer. 2001. *Ground-Water Discharge Determined from Estimates of Evapotranspiration, Death Valley Regional Flow System, Nevada and California*, Water-Resources Investigations Report 01-4195. Denver, CO: U.S. Geological Survey.
- Lavenue, M., and G. de Marsily. 2001. "Three-Dimensional Interference Test Interpretation in a Fractured-Unfractured Aquifer Using the Pilot Point Inverse Method." In *Water Resources Research*, Vol. 37(11): 2659-2676.
- Leap, D.I., and P.M. Belmonte. 1992. "Influence of Pore Pressure on Apparent Dispersivity of a Fissured Mitic Dolomitic Aquifa." In *Groundwater*, Vol. 30 (1): 87-95. Columbus, OH: Groundwater Publishing Company.
- Maldonado, F. 1977. *Summary of the Geology and Physical Properties of the Climax Stock, Nevada Test Site*, Open-File Report 77-356. Denver, CO: U.S. Geological Survey.
- Maldonado, F. 1990. "Structural Geology of the Upper Plate of the Bullfrog Hills Detachment Fault System, Southern Nevada." In *Geological Society of America Bulletin*, Vol. 102: 992-1006.
- Maloszewski, P., and A. Zuber. 1985. "On the Theory of Tracer Experiments in Fissured Rocks with a Porous Matrix." In *Journal of Hydrology*, Vol. 79: 333-358.
- Maniken, E.A., T.G. Hildenbrand, C.W. Roberts, and J.G. Davidson. 1998. *Principal Facts for New Gravity Stations in the Pahute Mesa and Oasis Valley Areas, Nye County, Nevada*, Open-File Report 98-498. U.S. Geological Survey.
- Maniken, E.A., T.G. Hildenbrans, G.L. Dixon, E.H. McKee, C.J. Fridricch, and R.J. Laczniak. 1999. *Gravity and Magnetic Study of the Pahute Mesa and Oasis Valley Region, Nye County, Nevada*, Open-File Report 99-303. Menlo Park, CA: U.S. Geological Survey.
- Maxey, G.B., and T.E. Eakin. 1949. "Groundwater in White River Valley, White Pine, Nye and Lincoln Counties, Nevada." In *Water Resources*, Bulletin No. 8. Carson City, NV: State of Nevada, Office of the State Engineer.
- McKay, M.D., W.J. Conover, and R.J. Beckman. 1979. "A Comparison of Three Methods for Selecting Values of Input Variables in the Analysis of Output from a Computer Code." In *Technometrics*, v. 21(3): 239-245.
- McKee, E.H., T.G. Hildenbrand, M.L. Anderson, P.D. Rowley, and D.A. Sawyer. 1999. *The Silent Canyon Caldera Complex: Three Dimensional Model Based on Drill-Hole Stratigraphy and Gravity Inversion*, Open-File Report 99-555, p. 38. Las Vegas, NV: U.S. Geological Survey.
- McKee, E.H., G.A. Phelps, and E.A. Mankinen. 2001. *The Silent Canyon Caldera: Three-Dimensional Model as Part of a Pahute Mesa-Oasis Valley, Nevada Hydrogeologic Model*, Open-File Report 01-297. Las Vegas, NV: U.S. Geological Survey.

- Mishra, S. 2002. *Assigning Probability Distributions to Input Parameters of Performance Assessment Models*. Austin, TX: INTERA, Inc.
- Mishra, S. 2007. “Uncertainty and Sensitivity Analysis Techniques for Hydrologic Modeling.” In *International Workshop on Advances in Hydroinformatics*, 4-7 June. Niagara Falls, Canada.
- Mishra, S., and R.G. Knowlton. 2003. “Testing for Input-Output Dependence in Performance Assessment Models.” In *Proceedings of Tenth International High-Level Radioactive Waste Management Conference*, March 30 - April 2. Las Vegas, NV.
- Mishra, S., N.E. Deeds, and B.S. RamaRao. 2003. “Application of Classification Trees in the Sensitivity Analysis of Probabilistic Model Results.” In *Reliability Engineering & System Safety*, v. 73: 123-129.
- Moddemeijer, R. 1989. “On the Estimation of Entropy and Mutual Information of Continuous Distributions.” In *Signal Processing*, v. 16(3): 233-248.
- NNSA/NSO, see National Nuclear Security Administration Nevada Site Office.
- NNSA/NV, see National Nuclear Security Administration Nevada Operations Office.
- NSTec, see National Security Technologies, LLC.
- National Security Technologies, LLC. 2007. *A Hydrostratigraphic Model and Alternatives for the Groundwater Flow and Contaminant Transport Model of Corrective Action Unit 99: Rainier Mesa-Shoshone Mountain, Nye County, Nevada*, DOE/NV/29546--146. Las Vegas, NV.
- Nevada Bureau of Mines and Geology. 1996. *County Digital Geologic Mapping Project - Final Report*, Open-File Report 97-1, scale 1:250,000.
- Noble, D.C., K.A. Sargent, H.H. Mehnert, E.B. Ekren, and F.M. Byers, Jr. 1968. “Silent Canyon Volcanic Center, In Eckel, E.B., ed., Nevada Test Site.” In *Geological Society of America*, Memoir 110: 65-75.
- Noble, D.C., T.A. Vogel, S.I. Weiss, J.W. Erwin, E.H. McKee, and L.W. Younker. 1984. “Stratigraphic Relations and Source Areas of Ash-Flow Sheets of the Black Mountain and Stonewall Mountain Volcanic Centers, Nevada.” In *Journal of Geophysical Research*, Vol. 89(B10): 8593-8602.
- Noble, D.C., S.I. Weiss, and E.H. McKee. 1991. “Magmatic and Hydrothermal Activity, Caldera Geology, and Regional Extension in the Western Part of the Southwestern Nevada Volcanic Field.” In G.L. Raines, R.E. Lisle, R.W. Schaefer, and W.H. Wilkinson, eds., *Geology and Ore Deposits of the Great Basin: Symposium Proceedings, Geological Society of Nevada*, pp. 913-934. Reno, NV.

- Noto, H.M., L.B. Prothro, and R.G. Warren. 1999. *Geology of Drill Holes UE20f, UE20h, UE20j, U20m and TP/AFB1, Pahute Mesa and Vicinity, Nye County, Nevada*. Las Vegas, NV: Bechtel Nevada.
- O'Hagan, M.D., and R.J. Laczniak. 1996. *Ground-Water Levels Beneath Eastern Pahute Mesa and Vicinity, Nevada Test Site, Nye County, Nevada*, Water-Resources Investigations Report 96-4042. Denver, CO: U.S. Geological Survey.
- Ogard, A.E., J.L. Thompson, R.S. Rundberg, K. Wolfsberg, P.W. Kubic, D. Eklmore, and H.W. Bentley. 1988. "Migration of Chlorine-36 and Tritium from an Underground Nuclear Test." In *Radiochimica Acta*, Vol. 44/45: 213-217. Munich, Germany: R. Oldenburg.
- Orkild, P.P., and E.C. Jenkins. 1978. *Report of Exploration Progress, Pahute Mesa, October 1, 1969 to December 31, 1976*, USGS-474-239. Denver, CO: U.S. Geological Survey.
- Orkild, P.P., K.A. Sargent, and R.P. Snyder. 1969. *Geologic Map of Pahute Mesa, Nevada Test Site and Vicinity, Nye County, Nevada*, Map I-567, scale: 1: 48,000. Denver, CO: U.S. Geological Survey.
- Pawloski, G.A. 1999. *Development of Phenomenological Models of Underground Nuclear Tests on Pahute Mesa, Nevada Test Site-BENHAM and TYBO*, UCRL-ID-136003. Livermore, CA: Lawrence Livermore National Laboratory.
- Pawloski, G.A. 2004. Personal communication with B. Deshler (SNJV) regarding a draft report entitled *Categorization of Underground Nuclear Tests on Pahute Mesa, Nevada Test Site, for Use in Radionuclide Transport Models*, 28 July. Livermore, CA: Lawrence Livermore National Laboratory.
- Pawloski, G.A., A.F.B. Tompson, and S. Carle, eds. 2001. *Evaluation of the Hydrologic Source Term from Underground Nuclear Tests on Pahute Mesa at the Nevada Test Site: The CHESHIRE Test*, UCRL-ID-147023. Livermore, CA: Lawrence Livermore National Laboratory.
- Pawloski, G.A., T.P. Rose, and J.W. Meadows. 2002. *Categorization of Underground Nuclear Tests on Pahute Mesa, Nevada Test Site, for Use in Radionuclide Transport Models*, UCRL-TR-208347. Livermore, CA: Lawrence Livermore National Laboratory.
- Pollock, D.W. 1988. "Semianalytical Computation of Path Lines for Finite-Difference Models." In *Ground Water*, v. 26: 743-750.
- Poole, F.G., F.N. House, and P.P. Orkild. 1961. *Eleana Formation of Nevada Test Site and Vicinity, Nye County, Nevada*, Professional Paper 424-D: D104-D111. U.S. Geological Survey.
- Press, W.H., S.A. Teukloksky, W.T. Vetterling, and B.P. Flannery. 1992. *Numerical Recipes in FORTRAN*, LBL-29400. London, England: Cambridge University Press.

- Prothro, L.B. 2005. *Mineralogic Zonation Within the Tuff Confining Unit, Yucca Flat, Nevada Test Site*, DOE/NV/11718--995. Las Vegas, NV: Bechtel Nevada.
- Prothro, L.B., and S.L. Drellack, Jr. 1997. *Nature and Extent of Lava Flow Aquifers Beneath Pahute Mesa, Nevada Test Site*, DOE/NV11718B--156. Las Vegas, NV: Bechtel Nevada.
- Prothro, L.B., and R.G. Warren. 2001. *Geology in the Vicinity of the TYBO and BENHAM Underground Nuclear Test, Pahute Mesa, Nevada Test Site*, DOE/NV11718--305. Los Alamos, NM: Los Alamos National Laboratory and Las Vegas, NV: Bechtel Nevada.
- Reimus, P.W., and T.J. Callahan. 2007. "Matrix Diffusion Rates in Fractured Volcanic Rocks at the Nevada Test Site: Evidence for a Dominant Influence of Effective Fracture Apertures." In *Water Resources Research*, Vol. 43, W07421, doi: 10.29/2006WR005746.
- Reimus, P.W., and M.J. Haga. 1999. *Analysis of Tracer Responses in the BULLION Forced-Gradient Experiment at Pahute Mesa, Nevada*, LA-13615-MS. Los Alamos, NM: Los Alamos National Laboratory.
- Reimus, P.W., A. Adams, M.J. Haga, A. Humphrey, T. Callahan, I. Anghel, and D. Counce. 1999. *Results and Interpretation of Hydraulic and Tracer Testing in the Prow Pass Tuff at the C-Holes, Yucca Mountain Site Characterization Project Milestone Report SP32E7M4*. Los Alamos, NM: Los Alamos National Laboratory.
- Reimus, P.W., S.D. Ware, F.C. Benedict, R.G. Warren, A.R. Humphrey, A.I. Adams, B. Wilson, and D. Gonzales. 2002. *Diffusive and Advective Transport of 3H, 14C, and 99Tc in Saturated Fractured Volcanic Rocks from Pahute Mesa, Nevada, LA-13891-MS*. Los Alamos, NM: Los Alamos National Laboratory.
- Reiner, S.R., R.J. Laczniak, G.A. DeMeo, J. LaRue Smith, P.E. Elliott, W.E. Nylund, and C.J. Fridrich. 2002. *Ground-Water Discharge Determined from Measurements of Evapotranspiration, Other Available Hydrologic Components, and Shallow Water-Level Changes, Oasis Valley, Nye County, Nevada*, Water-Resources Investigations Report 01-4239. Carson City, NV: U.S. Geological Survey.
- Robinson, B.A. 1993. "A Strategy for Validating a Conceptual Model for Radionuclide Migration in the Saturated Zone Beneath Yucca Mountain." In *Radioactive Waste Management and Environmental Restoration*, Vol. 19: 73-96.
- Robinson, B.A., and Z.V. Dash. 2005. *User's Guide for the PLUMECALC Application, V.2.2*. Los Alamos, NM: Los Alamos National Laboratory.
- Robledo, A.R., P.L. Ryder, J.J. Fenelon, and F.L. Paillet. 1998. *Geohydrology of Monitoring Wells Drilled in Oasis Valley Near Beatty, Nye County, Nevada*, Water-Resources Investigations Report 98 4184. U.S. Geological Survey.

- Rose, T.P., F.C. Benedict, Jr., J.M. Thomas, W.S. Sicke, R.L. Hershey, J.B. Paces, I.M. Farnham, and Z.E. Peterman. 2006. *Geochemical Data Analysis and Interpretation of the Pahute Mesa - Oasis Valley Groundwater Flow System, Nye County, Nevada, August 2002*, UCRL-TR-224559. Livermore, CA: Lawrence Livermore National Laboratory; Reno, NV: GeoTrans Inc. and Desert Research Institute; Denver, CO: U.S. Geological Survey; and Las Vegas, NV: Harry Reid Center for Environmental Studies.
- Russell, C.E., and T. Minor. 2002. *Reconnaissance Estimates of Recharge Based on an Elevation-Dependent Chloride Mass-Balance Approach*, DOE/NV/11508-37. Las Vegas, NV: Desert Research Institute.
- Russell, C.E., D. Gillespie, J.C. Cole, S.L. Drellack, L.B. Prothro, P.H. Thompson, R.L. McCall, G.A. Pawloski, and R. Carlson. 1996. *ER-12-1 Completion Report*, DOE/NV/10845-36 UC-703. Las Vegas, NV: Desert Research Institute.
- Shaw, see Shaw Environmental, Inc.
- SNJV, see Stoller-Navarro Joint Venture.
- SNJV GIS, see Stoller-Navarro Joint Venture Geographic Information Systems.
- SNL, see Sandia National Laboratories.
- Saltelli, A., K. Chan, and M. Scott. 2000. *Sensitivity Analysis*. New York, NY: John Wiley & Sons Inc.
- Sandia National Laboratories. 2007a. *Site-Scale Saturated Zone Transport*, MDL-NBS-HS-000010 REV 03. Las Vegas, NV.
- Sandia National Laboratories. 2007b. *Radionuclide Transport Models Under Ambient Conditions*, MDL-NBS-HS-000008 REV 02 ADD 01. Las Vegas, NV.
- Sandia National Laboratories. 2008. Written communication. Subject: *Total System Performance Assessment Model/Analysis for the License Application*, MDL-WIS-PA-000005 REV00G. Los Alamos, NM: Los Alamos National Laboratory.
- Sawyer, D.A., and K.A. Sargent. 1989. "Petrologic Evolution of Divergent Peralkaline Magmas from the Silent Canyon Caldera Complex, Southwestern Nevada Volcanic Field." In *American Geophysical Union, Journal of Geophysical Research*, Vol. 94(B5): 6021-6040.
- Sawyer, D.A., R.J. Fleck, M.A. Lanphere, R.G. Warren, and D.E. Broxton. 1994. "Episodic Caldera Volcanism in the Miocene Southwest Nevada Volcanic Field: Revised Stratigraphic Caldera Framework,  $^{40}\text{Ar}/^{39}\text{Ar}$  Geochronology and Implications for Magmatism and Extension." In *Geological Society of America Bulletin*, Vol. 67(10): 1304-1318.



- Shaw Environmental, Inc. 2003. *Contaminant Transport Parameters for the Groundwater Flow and Contaminant Transport Model of Corrective Action Units 101 and 102: Central and Western Pahute Mesa, Nye County, Nevada*, Rev. 0, Shaw/13052-201-CD. Las Vegas, NV.
- Slate, J.L., M.E. Berry, P.D. Rowley, C.J. Fridrich, K.S. Morgan, J.B. Workman, O.D. Young, G.L. Dixon, V.S. Williams, E.H. McKee, D.A. Ponce, T.G. Hildenbrand, W.C. Swadley, S.C. Lundstrom, E.B. Ekren, R.G. Warren, J.C. Cole, R.J. Fleck, M.A. Lanphere, D.A. Sawyer, S.A. Minor, D.J. Grunwald, R.J. Laczniak, C.M. Menges, J.C. Yount, and A.S. Jayko. 1999. *Digital Geologic Map of the Nevada Test Site and Vicinity, Nye, Lincoln, and Clark Counties, Nevada, and Inyo County, California*, Open-File Report 99-554-A. Denver, CO: U.S. Geological Survey.
- Snyder, R.P. 1977. *Geology of the Gold Meadows Stock, Nevada Test Site*, Open-File Report USGS-474-179, (Area 12-26). Denver, CO: U.S. Geological Survey.
- Steeffel, C.I., and S.B. Yabusaki. 1996. *OS3D/GIMRT, Software for Multicomponent and Multidimensional Reactive Transport: User's Manual and Programmer's Guide*, Version 1.0, PNL-11166. Richland, WA: Pacific Northwest National Laboratory.
- Stoller-Navarro Joint Venture. 2004a. *Geochem04.mdb and Comprehensive Water Quality Database for Groundwater in the Vicinity of the Nevada Test Site*. Las Vegas, NV.
- Stoller-Navarro Joint Venture. 2004b. *Hydrologic Data for the Groundwater Flow and Contaminant Transport Model of Corrective Action Units 101 and 102: Central and Western Pahute Mesa, Nye County, Nevada*, Rev. 0, S-N/99205-002; Shaw/13052-204. Las Vegas, NV.
- Stoller-Navarro Joint Venture. 2004c. *Modeling Approach/Strategy for Corrective Action Units 101 and 102, Central and Western Pahute Mesa*, S-N/99205-008. Las Vegas, NV.
- Stoller-Navarro Joint Venture. 2004d. *The Role of Dispersion in Radionuclide Transport - Data and Modeling Requirements*, S-N/99205-003, Shaw/13052-200, Rev. 1. Las Vegas, NV.
- Stoller-Navarro Joint Venture. 2004e. *Unclassified Source Term and Radionuclide Data for the Groundwater Flow and Contaminant Transport Model of Corrective Action Units 101 and 102: Central and Western Pahute Mesa, Nye County, Nevada*, Rev. 0, S-N/99205--022. Las Vegas, NV.
- Stoller-Navarro Joint Venture. 2005. *Phase II Contaminant Transport Parameters for the Groundwater Flow and Contaminant Transport Model of Corrective Action Unit 98: Frenchman Flat, Nye County, Nevada*, S-N/99205--043. Las Vegas, NV.
- Stoller-Navarro Joint Venture. 2006a. *Groundwater Flow Model of Corrective Action Units 101 and 102: Central and Western Pahute Mesa, Nevada Test Site, Nye County, Nevada*, Rev. 0, S-N/99205--076. Las Vegas, NV.

- Stoller-Navarro Joint Venture. 2006b. *Well ER-6-1 Tracer Test Analysis: Yucca Flat, Nevada Test Site, Nye County, Nevada*, S-N/99205--084, Rev. 0. Las Vegas, NV.
- Stoller-Navarro Joint Venture. 2007. *Phase I Contaminant Transport Parameters for the Groundwater Flow and Transport Model of Corrective Action Unit 97: Yucca Flat/Climax Mine, Nevada Test Site, Nye County, Nevada*, S-N/99205--096, Rev. 0. Las Vegas, NV.
- Stoller-Navarro Joint Venture Geographic Information Systems. 2008. ESRI ArcGIS Software.
- Sudicky, E.A., and E.O. Frind. 1981. "Carbon 14 Dating of Groundwater in Confined Aquifers: Implications of Aquitard Diffusion." In *Water Resources Research*, Vol. 17(4): 1060-1064. Washington, DC: American Geophysical Union. TIC:247712.
- Sudicky, E.A., and E.O. Frind. 1982. "Contaminant Transport in Fractured Porous Media: Analytical Solutions for a System of Parallel Fractures." In *Water Resources Research*, Vol. 18(6): 1634-1642.
- Thomas, J.M., F.C. Benedict, Jr., T.P. Rose, R.L. Hershey, J.B. Paces, Z.E. Peterman, I.M. Farnham, K.H. Johannesson, A.K. Singh, K.J. Stetzenbach, G.B. Hudson, J.M. Kenneally, G.F. Eaton, and D.K. Smith. 2002. *Geochemical and Isotopic Interpretations of Groundwater Flow in the Oasis Valley Flow System, Southern Nevada*, DOE/NV/11508-56; Publication No. 45190. Las Vegas, NV: Desert Research Institute.
- Thompson, J.L., ed. 1988. *Laboratory and Field Studies Related to the Radionuclide Migration Project (October 1, 1986 - September 30, 1987)*, LA-11223-PR. Los Alamos, NM: Los Alamos National Laboratory.
- Thompson, J.L., ed. 1991. *Laboratory and Field Studies Related to the Hydrology/Radionuclide Migration Project (October 1, 1989 - September 30, 1990)*, LA-12100-PR. Los Alamos, NM: Los Alamos National Laboratory.
- Tompson, A.F.B., C.J. Bruton, and G.A. Pawloski, eds. 1999. *Evaluation of the Hydrologic Source Term from Underground Nuclear Tests in Frenchman Flat at the Nevada Test Site: The CAMBRIC Test*, UCRL-ID-132300. Livermore, CA: Lawrence Livermore National Laboratory.
- Tompson, A.F.B., M. Zavarin, C.J. Bruton, and G.A. Pawloski. 2004. *Simplified Hydrologic Source Term for Frenchman Flat Sensitivity Studies*. Livermore, CA: Lawrence Livermore National Laboratory.
- Travis, B.J., H.E. Nuttall, S.W. Hodson, and R.S. Rundberg. 1983. "Section B: Transport of Tritium the Cambrian Cavity Region to RNM-2S: Modeling." In *Laboratory and Field Studies Related to the Hydrology/Radionuclide Migration Project (October 1, 1981 - September 30, 1982)*, LA-9691-PR. Los Alamos, NM: Los Alamos National Laboratory.

- Trexler, J.H., Jr., J.C. Cole, and P.H. Cashman. 1996. "Middle Devonian-Mississippian Stratigraphy On and Near the Nevada Test Site: Implications for Hydrocarbon Potential." In *American Association of Petroleum Geologists Bulletin*, Vol. 80(11): 1736-1762. Tulsa, OK.
- U.S. Congress/OTA, see U.S. Congress Office of Technology Assessment.
- USGS, see U.S. Geological Survey.
- U.S. Congress Office of Technology Assessment. 1989. *The Containment of Underground Nuclear Explosions*, PB90-1561183. Washington, DC.
- U.S. Department of Energy, National Nuclear Security Administration Nevada Operations Office. 2002. *Completion Report for Well ER-EC-2A*, DOE/NV/11718--591. Las Vegas, NV.
- U.S. Department of Energy, National Nuclear Security Administration Nevada Site Office. 2003. *Completion Report for Well ER 18-2*, DOE/NV/11718--388. Las Vegas, NV.
- U.S. Department of Energy, National Nuclear Security Administration Nevada Site Office. 2004. *Well Completion Report for Well ER-12-2*, DOE/NV/11718--846. Las Vegas, Nevada: Bechtel Nevada.
- U.S. Department of Energy, National Nuclear Security Administration Nevada Site Office. 2006. *Completion Report for Well ER-16-1*, DOE/NV--1180. Las Vegas, NV: National Security Technologies, LLC.
- U.S. Department of Energy, Nevada Operations Office. 1995a. *Completion Report for Well ER 19-1*, DOE/NV/11718--410. Las Vegas, NV.
- U.S. Department of Energy, Nevada Operations Office. 1995b. *Completion Report for Well ER 30-1*, DOE/NV--407. Las Vegas, NV.
- U.S. Department of Energy, Nevada Operations Office. 1996. *Recompletion Report and Summary of Well History for Well PM-3*, DOE/NV-437 UC700. Las Vegas, NV.
- U.S. Department of Energy, Nevada Operations Office. 1997a. *Completion Report for Well Cluster ER-20-5*, DOE/NV--466 UC-700. Las Vegas, NV.
- U.S. Department of Energy, Nevada Operations Office. 1997b. *Regional Groundwater Flow and Tritium Transport Modeling and Risk Assessment of the Underground Test Area, Nevada Test Site, Nevada*, DOE/NV--477. Las Vegas, NV.
- U.S. Department of Energy, Nevada Operations Office. 1999. *Corrective Action Investigation Plan for Corrective Action Units 101 and 102: Central and Western Pahute Mesa, Nevada Test Site, Nevada*, DOE/NV--516, Rev. 1. Las Vegas, NV.

- U.S. Department of Energy, Nevada Operations Office. 2000a. *Completion Report for Well ER-EC-1*, DOE/NV/11718--381. Las Vegas, NV.
- U.S. Department of Energy, Nevada Operations Office. 2000b. *Completion Report for Well ER-EC-4*, DOE/NV/11718--397. Las Vegas, NV.
- U.S. Department of Energy, Nevada Operations Office. 2000c. *Completion Report for Well ER-EC-6*, DOE/NV/11718--360. Las Vegas, NV.
- U.S. Department of Energy, Nevada Operations Office. 2000d. *United States Nuclear Tests, July 1945 through September 1992*, DOE/NV-209, Rev. 15. Las Vegas, NV.
- U.S. Environmental Protection Agency. 2000. *Radionuclides Notice of Data Availability Technical Support Document*. March. Washington, DC.
- U.S. Environmental Protection Agency. 2002. *Implementation Guidance for Radionuclides*, Vol. 66(12): 4826. 18 January. Washington, DC.
- U.S. Geological Survey. 1987. *U.S. Geological Data Digital Elevation Models: U.S. Geological Survey, National Mapping Program Technical Instructions, Data User's Guide 5*. Reston, VA.
- Watermark, see Watermark Numerical Computing.
- Wagoner, J.L., and S. Clark. 1986. *U20as Site Characteristics Report*, CP 86-32, 13 June. Livermore, CA: Lawrence Livermore National Laboratory.
- Wahl, R.R., D.A. Sawyer, M.D. Carr, S.A. Minor, J.C. Cole, W.C. Swadley, R.J. Laczniaik, R.G. Warren, K.S. Green, and C.M. Engle. 1997. *Digital Geologic Map Database of the Nevada Test Site, Nevada*, scale 1:120,000, Open-File Report 97-140. Denver, CO: U.S. Geological Survey.
- Walker, G.E. 1962. *Ground Water in the Climax Stock, Nevada Test Site, Nye County, Nevada*, Open-File Report TEI-813. Washington, DC: U.S. Geological Survey.
- Warren, R.G. 1999. Personal communication to L.B. Prothro (BN), regarding volcanic units intercalated within older alluvial deposits in the vicinity of Timber Mountain. Los Alamos, NM: Los Alamos National Laboratory.
- Warren, R.G., F.M. Byers, Jr., D.E. Broxton, S.H. Freeman, and R.C. Hagan. 1989a. "Phenocryst Abundances and Phenocryst Compositions as Indicators of Magmatic Environments of Large-Volume Ash Flow Sheets in Southwestern Nevada." In *Journal of Geophysical Research*, Vol. 94(B5): 5987-6020.

- Warren, R.G., D.A. Sawyer, and H.R. Covington. 1989b. *Distinguishing Characteristics of Stratigraphic Units of Pahute Mesa*, Attachment 2, informal technical report, 26 July. Los Alamos, NM: Los Alamos National Laboratory.
- Warren, R.G., G.L. Cole, and D. Walther. 2000. *A Structural Block Model for the Three-Dimensional Geology of the Southwestern Nevada Volcanic Field*, LA-UR-00-5866. Los Alamos, NM: Los Alamos National Laboratory.
- Warren, R.G., D.A. Sawyer, F.M. Byers, and G.L. Cole. 2003. *A Petrographic, Geochemical, and Geophysical Database, and Stratigraphic Framework for the Southwestern Nevada Volcanic Field*, LA-UR-03-1503. Los Alamos, NM: Los Alamos National Laboratory.
- Watermark Numerical Computing. 2004. *PEST Model-Independent Parameter Estimation Software*. Brisbane, Australia.
- Wellman, T.P., and E.P. Poeter. 2005. "Estimating Spatially Variable Representative Elementary Scales in Fractured Architecture Using Hydraulic Head Observations." In *Water Resources Research*, Vol. 41, W03001, doi:10.1029/2004WR003287.
- Wellman T.P., and E.P. Poeter. 2006. "Evaluating the Uncertainty in Predicting Spatially Variable Representative Elementary Scales in Fractured Aquifers." In *Water Resources Research*, Vol. 42 W08410, doi:10.1029/2005WR004431.
- Welty, C., and L.W. Gelhar. 1989. *Evaluation of Longitudinal Dispersivity from Tracer Test Data*. Massachusetts Institute of Technology.
- Welty, C., and L.W. Gelhar. 1994. "Evaluation of Longitudinal Dispersivity from Nonuniform Flow Tracer Tests." In *Journal of Hydrology*, Vol. 153 (71-102). New York, NY: Elsevier Publishing Company.
- Winograd, I.J., and W. Thordarson. 1975. *Hydrogeologic and Hydrochemical Framework, South-Central Great Basin, Nevada-California, with Special Reference to the Nevada Test Site*, Professional Paper 712-C. Denver, CO: U.S. Geological Survey.
- Winograd, I.J., and L.R. West. 1962. *Preliminary Tracer Experiment to Demonstrate Hydraulic Continuity Between Water Wells C and C-1, Yucca Flat, Nevada Test Site*, Technical Letter NTS-20. Denver, CO: U.S. Geological Survey.
- Winterle, J.R., and P.C. La Femina. 1999. *Review and Analysis of Hydraulic and Tracer Testing at the C-Holes Complex Near Yucca Mountain, Nevada*, Center for Nuclear Waste Regulatory Analyses. San Antonio, TX: U.S. Nuclear Regulatory Commission.

- Wolfsberg, A., L. Glascoe, G. Lu, A. Olson, P. Lichtner, M. McGraw, T. Cherry, and G. Roemer. 2002. *TYBO/BENHAM: Model Analysis of Groundwater Flow and Radionuclide Migration from Underground Nuclear Tests in Southwestern Pahute Mesa, Nevada*, LA-13977. Los Alamos, NM: Los Alamos National Laboratory.
- Zavarin, M., and C.J. Bruton. 2004a. *A Non-Electrostatic Surface Complexation Approach to Modeling Radionuclide Migration at the Nevada Test Site: I. Iron Oxides and Calcite*, UCRL-TR-208673. Livermore, CA: Lawrence Livermore National Laboratory.
- Zavarin, M., and C.J. Bruton. 2004b. *A Non-Electrostatic Surface Complexation Approach to Modeling Radionuclide Migration at the Nevada Test Site: II. Aluminosilicates*, UCRL-TR-208672. Livermore, CA: Lawrence Livermore National Laboratory.
- Zavarin M., S.F. Carle, and R.M. Maxwell. 2002a. *Upscaling Radionuclide Retardation-Linking the Surface Complexation and Ion Exchange Mechanistic Approach to a Linear  $K_d$  Approach*. Lawrence Livermore National Laboratory report attached to a memorandum to files by W. Drici (Shaw Environmental, Inc.), 13 August 2003. Las Vegas, NV.
- Zavarin, M., S.K. Roberts, T.P. Rose, and D.L. Phinney. 2002b. *Validating Mechanistic Sorption Model Parameters and Processes for Reactive Transport in Alluvium*, UCRL-ID-149728. Livermore, CA: Lawrence Livermore National Laboratory.
- Zavarin M., S.F. Carle, and R.M. Maxwell. 2004. *Upscaling Radionuclide Retardation-Linking the Surface Complexation and Ion Exchange Mechanistic Approach to a Linear  $K_d$  Approach*, UCRL-TR-214713. Livermore, CA: Lawrence Livermore National Laboratory.
- Zyvoloski, G.A., B.A. Robinson, Z.V. Dash, and L.L. Trease. 1997. *Summary of Models and Methods for the FEHM Application - A Finite-Element Heat- and Mass-Transfer Code*, LA-13307-MS. Los Alamos, NM: Los Alamos National Laboratory.



## **Appendix A**

### **Reactive Mineral Model**

## **A.1.0 REACTIVE MINERAL MODEL**

The reactive mineral model described the mineralogical distribution of reactive minerals relative to abundance observed in HGUs. Hydrogeologic units are assigned to the HFM based on rock lithology, alteration, and structural elements. Each of the HGUs has a distinctive arrangement of mineral assemblages that are superimposed upon the HGU. These mineral assemblages and their distribution within the HGU constitute the reactive mineral categories. [Table B.1-1](#) is an HGU-RMC crosswalk list that allows co-location of the HGU and RMC categories as described in borehole logs. A detailed discussion of the development and assignment of RMC to HSU is provided in [Section 5.4](#). Discussion of the RMC as it is represented by a mechanistic  $K_a$  distribution is provided in [Appendix B](#).

The reactive mineral model table (Table A.1-1) is included as an electronic attachment on the accompanying compact disc-read-only memory (CD-ROM). Table A.1-1 lists all discrete borehole samples used to describe Pahute Mesa in terms of the HGU and RMC intervals as determined through XRD measurement at each sampling point. There are 4,495 sampling locations identified in this appendix from which the HSU and RMC distribution is derived.

The name of each borehole, located in the first data column, uniquely identifies the content of each row, and the column headings identify the rock properties (mineralogical and hydrostratigraphic) and spatial location of the samples.

The Northing and Easting coordinates of the borehole are tabulated in columns B and C followed by stratigraphic unit, lithologic unit, and major alteration products at each location in columns D through F.


The reactive mineral and hydrostratigraphic classifications for each row are listed in columns G through J. These columns identify HGU, HSU, RMC and RMU, respectively, for each location.



Columns K through N list the depth below surface and elevation amsl at each measurement point in units of feet and meters.

Abbreviations used in the table are defined at the end of the list for lithology, alteration product, and RMC. The abbreviations and description for other categories are located in the following tables:

- HGU definitions are located in [Table 3-1](#).
- HSU definitions are located in [Table 5-3](#).
- RMC definitions are located in [Table 5-1](#).
- RMU definitions are located in [Table 5-3](#).



**Appendix B**  
 **$K_d$  Distributions**

## **B.1.0** *SORPTION COEFFICIENTS*

### **B.1.1** *Stochastic Realizations of Permeability*

This section describes the method of populating a single CAU gridblock-scale (flow and transport) domain with a continuous permeability field that honors the physical properties of a mineralogical unit. The stochastic approach is assumed in which multiple, equiprobable realizations of permeability are generated for each mineralogical unit in order to capture, via numerical flow simulation, the effect of random variation in permeability and its heterogeneity on contaminant transport. The CAU gridblock dimensions for each mineralogical unit are 50 by 100 by 100 m. The sub-gridblock continuum is composed of 1 m<sup>3</sup> blocks for which individual permeabilities are assigned as a constant value. The reason for selection of the CAU gridblock dimensions was twofold. First, and fundamentally, this volume approximately corresponds with the size of a CAU-scale numerical model gridblock. Second, the length of each dimension is sufficiently large to honor spatial constraints related to hydraulic properties, primarily matrix- and fracture-related properties, requisite for the simulation method.

#### **B.1.1.1** *Stochastic Simulation of Permeability*

The sequential indicator approach (Deutsch and Journel, 1992) is used to generate multiple, equiprobable realizations of permeability over a gridblock-scale domain for each of three composite mineralogical units. The method is well suited for this application for the following reasons:

1. The transformation of permeability to indicator data permits the definition of a discrete, nonparametric probability distribution that fully describes the observed permeability data for each unit.
2. The spatial continuity of physical properties of both porous and fractured media may be readily incorporated into the simulation method.
3. The spatial continuity of permeability, as related to physical properties of the medium and at multiple indicator thresholds, may be explicitly defined in each principal direction.

The sequential indicator method requires that two fundamental types of data be provided for each mineralogical class. The first type required is the ECDF of permeability per class. The ECDF is fully defined at 10 thresholds between which the linear interpolation of cumulative probability is applied. The minimum and maximum thresholds define, respectively, the lower and upper distribution bounds beyond which the data are not defined. Factors considered for the assignment of thresholds include fully describing the shape of the ECDF, defining classes of approximately equal frequency, and assigning thresholds to critical parts of the distribution (relative to spatial continuity) for greater precision in those regions. The most critical region of each distribution is located near the matrix- to fracture-flow dominated permeability threshold, described below.

The second type of data required includes the measures of spatial continuity that describe the directional heterogeneity of permeability in each mineralogical class. Spatial continuity is described at each ECDF threshold using a model semivariogram. In an entirely porous mineralogical unit, semivariogram parameters describe the scale of autocorrelation between sub-gridblock (1 m<sup>3</sup>) permeabilities. In a partially to fully fractured mineralogical unit (such as for this application), data are necessary to describe properties of both fractures and porous matrix material. For the higher-permeability (ECDF) thresholds that represent fracture flow, semivariogram parameters are used to define fracture orientation, length, and aperture width. At the lower-permeability thresholds that represent porous or small-scale fracture flow, semivariogram parameters are defined to account for these smaller spatial scales of continuity.

Sections [B.1.1.2](#) through [B.1.1.3](#) present the available data required for simulation of the mineralogical unit permeabilities. These include reactive mineral class permeability measurements, for both porous and fractured media, and fracture properties.

#### ***B.1.1.2 Definition of Reactive Mineralogical Zone Permeability***

Mineralogical zones are presented as RMCs as described in [Appendix A](#). An RMC is defined based upon lithology, alteration, and hydrogeology, the last of which considers whether a unit is a porous or fractured medium, the essential factor affecting RMC permeability. In many cases, multiple RMCs can be defined as equivalent (with respect to permeability) if their effective flow properties are the same or similar. Thus, the identification of individual and/or lumped RMC permeability depends first

on defining those that represent porous or fractured media, and second on the similarity of permeability ranges within those units that are porous and within those that are fractured.

Recall that the simulation method requires that both permeability and fracture properties be defined for each RMC. The permeability data (discussed in [Section B.1.2](#) of this document; Flint, 1998), whether they represent a porous or fractured medium, are explicitly defined at the same spatial scale as the RMC zones, both of which are identified from borehole logs at depth-discrete intervals. On the contrary, fracture properties are typically defined on a depth-averaged basis within boreholes, often over large intervals, and are not readily assigned per RMC. Consequently, it is not practical to define an RMC as a porous or fractured media based upon the co-location of RMC and observed fracturing in boreholes; the spatial scale of characterization is different for each variable. To resolve this scale-related effect, RMCs are (or are not) assigned fracture properties based on the strong relationship, in most cases, between an RMC and an HGU, the physical properties of which are well defined and well documented. Additionally, properties of both porous and fractured media are generally presented in the literature with respect to their association to HGUs.

[Section B.1.1.3](#) describes the rationale for categorizing each RMC as a porous or fractured medium, the precursor to the assignment of RMC permeability and fracture properties (when applicable).

### ***B.1.1.3 Identification of Porous- and Fracture-Flow Dominated RMCs***

From Prothro and Drellack (1997) and Warren (1994), there are four primary volcanic HGUs that control groundwater flow at Pahute Mesa. Based on their lithology and alteration, these units are LFAs, WTAs, VTAs, and TCUs. The following general descriptions were provided for each of the volcanic units at Pahute Mesa by Prothro and Drellack (1997) and Warren (1994):

#### ***LFA***

Lava-flow aquifers at Pahute Mesa are typically devitrified, stony lavas characterized as hard, dense, and highly fractured. Highly fractured vitrophyric zones are present but constitute a small minority of the LFA. The majority of fractures form in response to cooling; however, there is evidence to suggest that post-depositional forces have affected (created and altered pre-existing) fractures.

**WTA**

Welded-tuff aquifers at Pahute Mesa generally consist of thick, moderately to densely welded tuff units. Cooling fractures are generally well developed, particularly in the more strongly welded interior of a unit, and account for the majority of the WTA permeability. The WTA may also consist of thin units of stony and/or vitrophyric lava, both of which are highly fractured.

**VTA**

Vitric-tuff aquifers at Pahute Mesa primarily consist of pumiceous (unaltered) lavas that were deposited as the top unit of a lava flow sequence. Above the water table, the VTA is soft and contains few fractures; the medium is completely porous. Below the water table, pumiceous lavas remain vitric to a depth on the order of a few hundred meters before becoming zeolitized.

**TCU**

Tuff confining units at Pahute Mesa consist of nonwelded and bedded tuffs that have been zeolitized below the water table. Cooling fractures are not observed in zeolitic tuffs. Because matrix permeability is low, hydraulic pathways are defined as faults and joints induced by regional effects.

Provided the qualitative HGU descriptions above, combined with those presented for RMCs in [Appendix A](#), an HGU-RMC crosswalk table is defined in [Table B.1-1](#).

**Table B.1-1  
HGU-RMC Crosswalk**

HGU	RMC
LFA, WTA	DMP (0.92), DMR (0.98), VMP (0.59), VMR (0.29), ML (1.00)
VTA	VMP (0.41), VMR (0.71)
TCU	ZEOL (0.85)

Note: Percentage values correspond to those presented in [Figure B.1-1](#).

Empirical confirmation of these associations is provided by the co-located, interval-specific classifications of RMC and HGU in individual boreholes. Their graphical comparison is shown in [Figure B.1-1](#), which shows the percentage of HGU per RMC. The reader should interpret [Figure B.1-1](#), for example, as “71 percent of the VMR RMC is composed of the VTA HGU.”

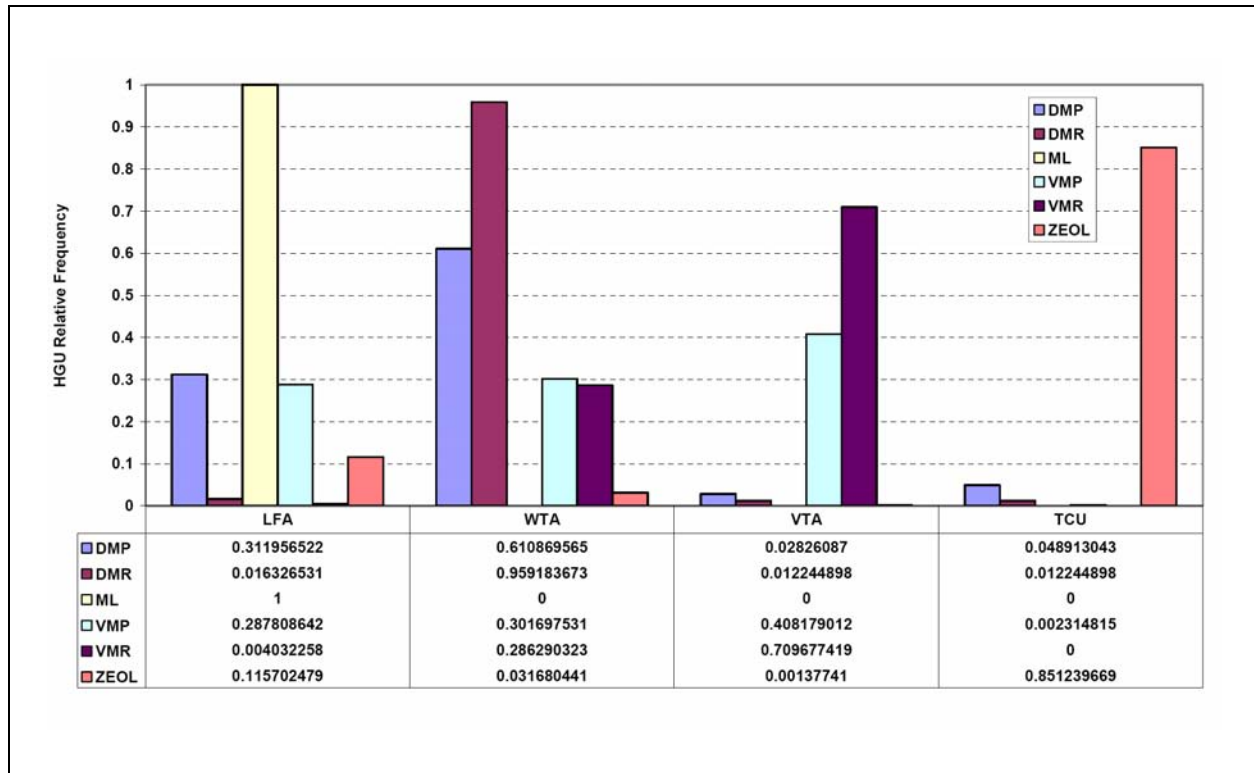


**Figure B.1-1**  
**Bar Chart Showing the Percentage of HGU per RMC**

The strong association between RMCs and HGUs is apparent in all cases, most noticeably between the zeolitic RMC (ZEOL) and the TCU HGU. Table B.1-1 presents a finalized crosswalk between Pahute Mesa HGUs and RMCs based upon the data in Figure B.1-1 and the following interpretations.

In the LFA and WTA HGUs, permeability is controlled by fracture flow. As the two units have similar physical properties and the propensity to develop cooling fractures, the hydraulic properties of the LFA and WTA may be considered equivalent (Prothro and Drellack, 1997). The DMP/R and ML are fractured RMC units; more than 90 percent of these RMC intervals identified in boreholes correspond to the LFA/WTA. Fracture properties assigned to these RMCs may be derived directly from those properties assigned to the LFA and WTA.

The ZEOL RMC is defined as a porous unit analogous to the TCU, with 85 percent correspondence. Fracture permeability comprises a minor component of the unit’s permeability, if at all.

The VMP/R RMC cannot be clearly defined as a porous or fractured unit. This result is reasonable given that vitric units may be vitrophyric (brittle, susceptible to fracturing) or pumiceous (soft, deformable, no fracturing). The distinction between VMP/R permeability data that are representative of porous versus fractured media is not entirely clear. For example, about 40 percent of the VMP corresponds with VTA (pumiceous), and 59 percent with the LFA and WTA. For those permeabilities that correspond to fractures, the fracture properties used to characterize the permeability should be derived from the WTA, shown to contain layered intervals of both stony lava and vitrophyre. This ambiguity is resolved during presentation of the permeability distribution for the VMP/R below.

### **B.1.2 RMC Permeability**

The RMCs are assigned to interval-specific lithologic units in boreholes at Pahute Mesa, and permeabilities have been determined for many of these borehole intervals from aquifer testing. Methods of aquifer testing include single- and multiple-well pumping tests, slug/packer testing, and spinner-tool flow log analysis. The scales of RMC and permeability definition are equivalent; therefore, permeability data can be directly assigned to each of the RMCs. In some cases, the RMC depth interval and aquifer-testing interval are identical. In other cases, aquifer testing was completed over an interval larger than the RMC, so the permeability value is a composite of more than one RMC.

Each RMC permeability ECDF is defined at 10 thresholds between which the linear interpolation of cumulative probability is applied. The minimum and maximum thresholds define, respectively, the lower and upper distribution bounds beyond which permeability is not defined. The threshold values for the DMP/R, VMP/R, and ZEOL units are respectively shown in [Figures B.1-2 through B.1-4](#) and are listed in [Tables B.1-2 through B.1-4](#).

Individually, each ECDF is indicative of a bimodal permeability distribution. A threshold of  $-12.0 \text{ m}^2$  is defined as the transition permeability between porous- and fracture-dominated flow, although the proportion of data below and above the threshold varies between RMCs. From the conceptual interpretation of RMC lithology and hydrogeology, permeability data below the porous-fracture threshold represent either porous or small-scale (less than 1 m length) fracture flow. Above the threshold, permeability data represent large-scale (greater than 1 to 20 m length) fractures. Based



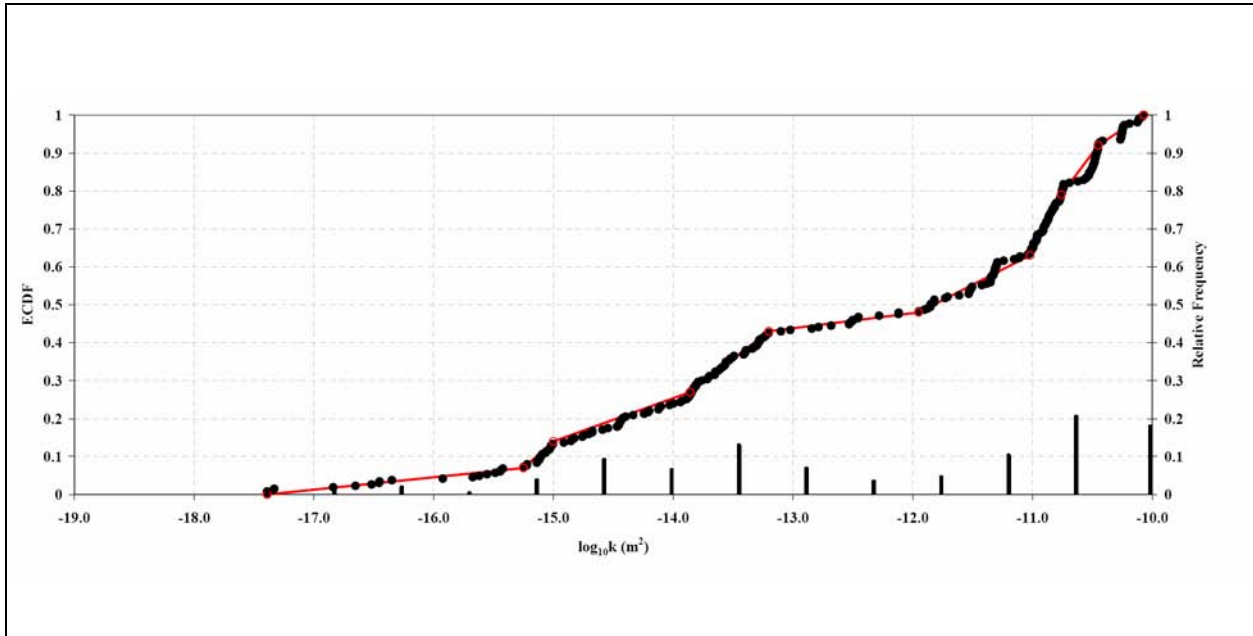


**Figure B.1-2**  
**DMP/R RMC ECDF on y-Axis at Left (black) with Thresholds (red)**  
**and PDF (vertical bars) Shown on y-Axis at Right**  
 Note: See [Table B.1-2](#) for corresponding data.

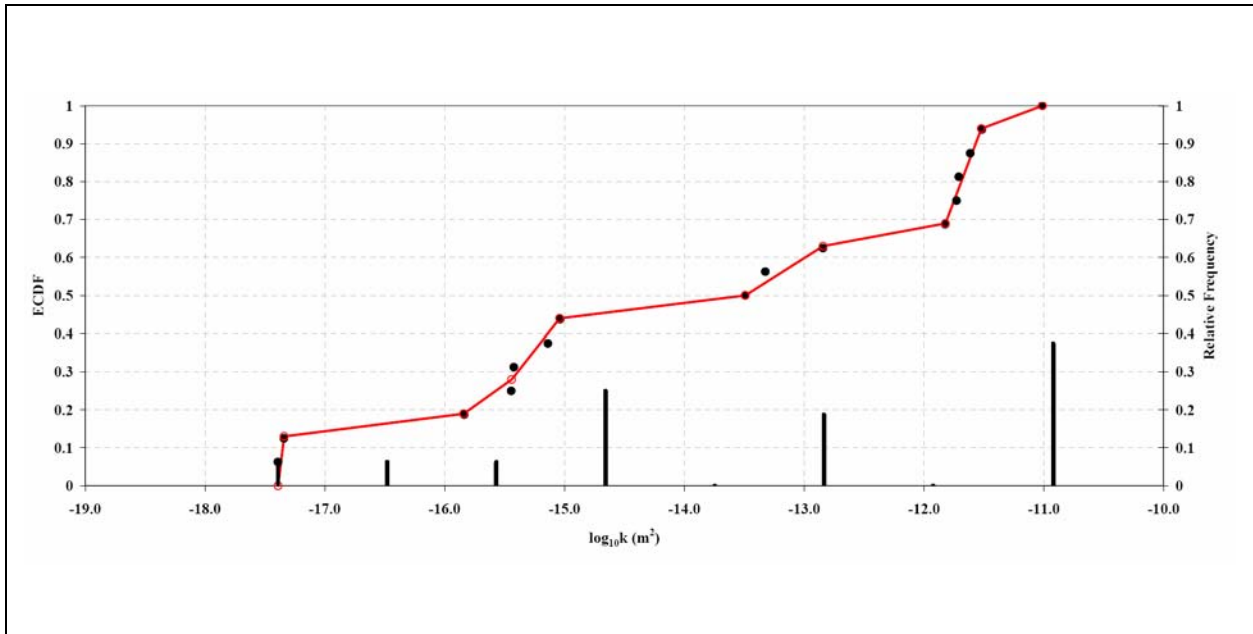


**Figure B.1-3**  
**VMP/R RMC ECDF on y-Axis at Left (black) with Thresholds (red)**  
**and PDF (vertical bars) Shown on y-Axis at Right**  
 Note: See [Table B.1-3](#) for corresponding data.

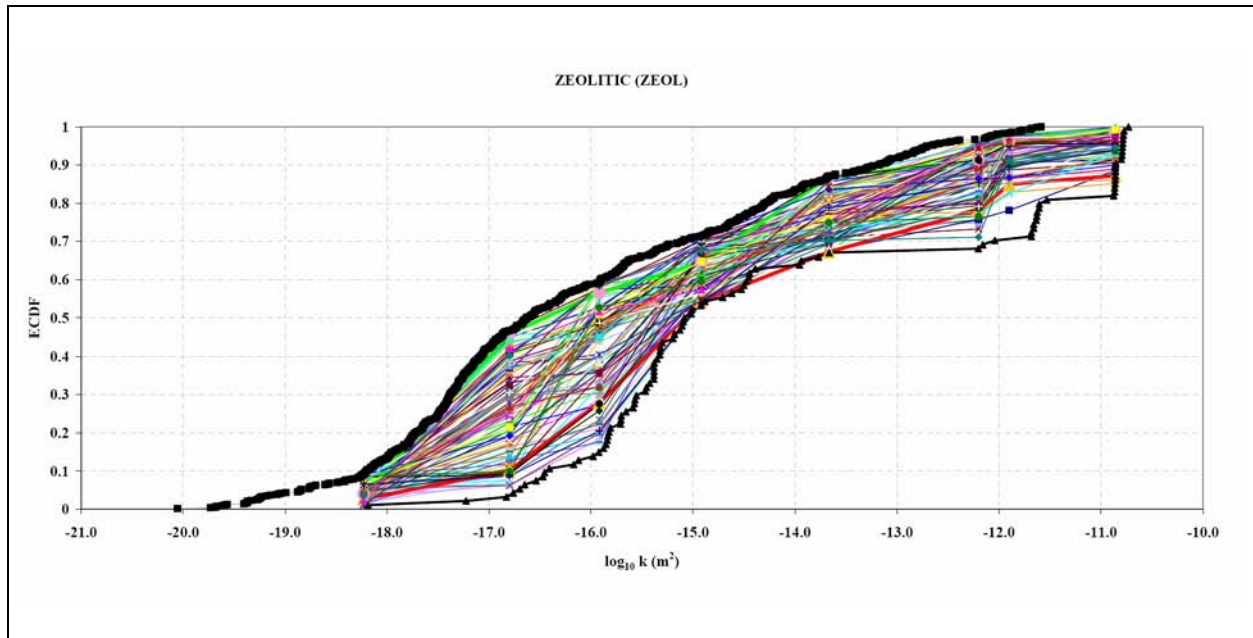


**Figure B.1-4**  
**Permeability ECDF Region for ZEOL RMC (minimum and maximum bounds in black)**  
**and 100 Randomly Generated ECDFs (varied colors)**  
**with Thresholds (colored solid symbols)**

Note: See [Table B.1-4](#) for corresponding data.

**Table B.1-2**  
**ECDF Threshold Descriptors for the DMP/R RMC Including Permeability,**  
**CDF, and Directional Variogram Parameters**

Threshold	Log <sub>10</sub> K (m <sup>2</sup> )	ECDF	Nugget	Integral Range <sup>a,b</sup> (m)	Sill (m/day) <sup>2</sup>	Anisotropy (X:Y:Z) <sup>c</sup>
1	-17.39	0.00	N/A	N/A	N/A	N/A
2	-15.25	0.07	0.0	3	0.065	1:3:3
3	-15	0.14	0.0	3	0.120	1:3:3
4	-13.86	0.27	0.0	3	0.197	1:3:3
5	-13.2	0.43	0.0	3	0.245	1:3:3
6	-11.95	0.48	0.0	20	0.250	4:20:20
7	-11.02	0.63	0.0	20	0.233	4:20:20
8	-10.76	0.79	0.0	20	0.166	4:20:20
9	-10.45	0.92	0.0	20	0.074	4:20:20
10	-10.07	1.00	N/A	N/A	N/A	N/A

<sup>a</sup> The range is in the (Y-) direction of maximum continuity with fracture orientations between 332° and 44° mean dip of 68° (IT, 2001).

<sup>b</sup> The effective range is a factor of three greater than the integral range (approximate correlation length).

<sup>c</sup> Presented as the ratio of the integral ranges.

**Table B.1-3**  
**ECDF Threshold Descriptors for the VMP/R RMC Including Permeability, CDF, and Directional Variogram Parameters**

Threshold	Log <sub>10</sub> K (m <sup>2</sup> )	ECDF	Nugget	Integral Range <sup>a,b</sup> (m)	Sill (m/day) <sup>2</sup>	Anisotropy (X:Y:Z) <sup>c</sup>
1	-17.39	0.00	N/A	N/A	N/A	N/A
2	-17.34	0.13	0.0	1	0.113	1:1:1
3	-15.84	0.19	0.0	1	0.154	1:1:1
4	-15.44	0.28	0.0	1	0.202	1:1:1
5	-15.04	0.44	0.0	1	0.246	1:1:1
6	-13.49	0.44	0.0	1	0.250	1:1:1
7	-12.84	0.63	0.0	1	0.233	1:1:1
8	-11.82	0.69	0.0	20	0.214	4:20:20
9	-11.52	0.94	0.0	20	0.056	4:20:20
10	-11.01	1.00	N/A	N/A	N/A	N/A

<sup>a</sup> The range is in the (Y-) direction of maximum continuity.

<sup>b</sup> The effective range is a factor of three greater than the integral range (approximate correlation length).

<sup>c</sup> Presented as the ratio of the integral ranges.

upon whether a permeability datum falls below or above the threshold, per ECDF, directional scales of spatial correlation are distinctively assigned.

The exact threshold is somewhat ambiguous for the VMP/R given the paucity of the data. However, the assumption of -12.0 m<sup>2</sup> imposes the fracture properties of the LFA and WTA (observed concretely in the DMP/R) on the VMP/R, a valid assumption (from [Table B.1-3](#)).

The exact threshold for the ZEOL is also ambiguous, although for different reason. In this case there are two distinct data sources, one from well-test analyses (as for the other RMCs), and one from indirect measurement of permeability. The former represents well-test-scale measurements, while the latter represents the core-scale and does not consider fractures. These data are from measurements presented by Flint (1998), who indirectly defines core-scale permeability from porosity. To incorporate the effect of both measurement types in ZEOL permeability realizations, a permeability ECDF “region” ([Figure B.1-4](#); [Table B.1-4](#)) is presented rather than a single, unique ECDF. Individual ECDFs, for simulation of individual realizations, are randomly defined from within this region, subject to the constraints that data thresholds are constant for all realizations and that

**Table B.1-4**  
**Minimum- and Maximum-ECDF Threshold Descriptors for the ZEOL RMC Including Permeability, CDF, and Directional Variogram Parameters**

Threshold	Log <sub>10</sub> K (m <sup>2</sup> )	ECDF		Nugget	Integral Range <sup>a,b</sup> (m)	Sill (m/day) <sup>2</sup>		Anisotropy (X:Y:Z) <sup>c</sup>
		Min	Max			Min	Max	
1	-18.19	0.00	0.00	N/A	N/A	N/A	N/A	N/A
2	-16.83	0.01	0.09	0.0	1	0.010	0.082	1:1:1
3	-15.98	0.03	0.47	0.0	1	0.029	0.249	1:1:1
4	-15.56	0.15	0.59	0.0	1	0.128	0.242	1:1:1
5	-15.10	0.53	0.71	0.0	1	0.249	0.206	1:1:1
6	-14.50	0.67	0.87	0.0	1	0.221	0.113	1:1:1
7	-13.77	0.68	0.97	0.0	1	0.218	0.029	1:1:1
8	-12.20	0.70	0.98	0.0	1	0.210	0.020	1:1:1
9	-11.00	0.85	1.00	0.0	20	0.128	0.000	4:20:20
10	-10.73	1.00	1.00	N/A	N/A	N/A	N/A	N/A

<sup>a</sup> The range is in the (Y-) direction of maximum continuity with mean orientation and dip of (12° and 71°) (IT, 2001).

<sup>b</sup> The effective range is a factor of three greater than the integral range (approximate correlation length).

<sup>c</sup> Presented as the ratio of the integral ranges.

thresholds are monotonically increasing per realization. Figure B.1-4 shows each of the 100 randomly generated ECDFs with the region.

Figure B.1-5 presents the RMC permeability ECDFs superimposed for each of the three RMCs. For the ZEOL RMC, the bounded ECDF region is presented rather than a single distribution. Some general observations can be made regarding the individual and pooled data:

- Permeability data are abundant for the devitrified and zeolitized units, providing a high level of certainty in the distribution accuracy. Although data for the vitric units are sparse, the range of the data reflects the range of hydrogeologic variability, from an entirely porous medium to a fractured vitrophyre, which is appropriate in this unit (described in Section B.1.3).
- The pooled PDF (y-axis on the right) shows a bimodal distribution indicative of both porous and fractured media permeability. The porous-fracture threshold is at about -12.0 m<sup>2</sup>. In an analysis of a volcanic aquifer permeability dataset at Yucca Mountain, McKenna et al. (2003) identified an analogous threshold at -12.2 m<sup>2</sup> log<sub>10</sub> permeability.

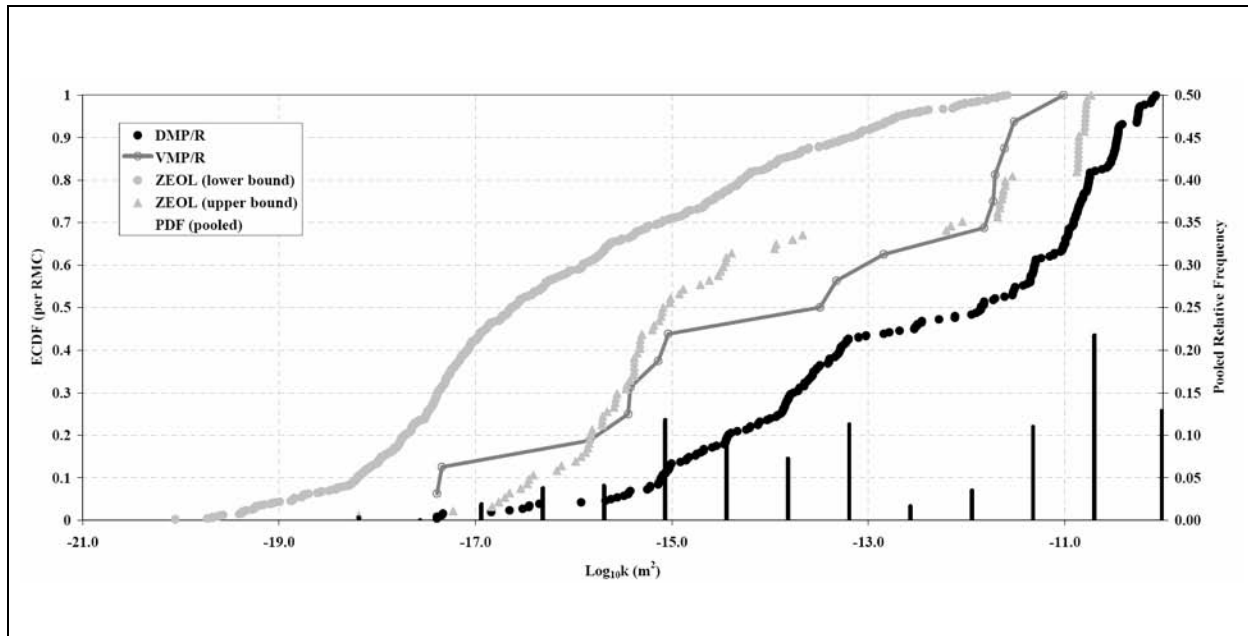


**Figure B.1-5**

**Permeability ECDF (y-axis on left) for Each of the Three RMCs**

Note: For the ZEOL RMC, a bounded ECDF region is presented rather than a single distribution. The pooled permeability PDF (from well-test-derived data) is shown as vertical bars on the y-axis at right.

The observed differences between the distributions are conceptually consistent. For example:

1. About 70 to 95 percent of the ZEOL data are low, between -20.0 and -12.0  $\log_{10} m^2$ , a range appropriate for zeolitized tuff. The percent of the data greater than -12.0  $m^2$  represent sparse fracturing, which is consistent with observed fracture data.
2. The DMP/R distribution is split nearly 50 percent – 50 percent about the porous – fracture threshold at -12.0  $m^2$ , indicative of a fracture-flow dominated unit. Additionally, and appropriately, the largest permeability data in the DMP/R are nearly one order of magnitude greater than that for the ZEOL and VMP/R units.

The assignment of corresponding matrix and fracture properties, as they directionally and spatially vary at each threshold for each RMC ECDF, is described in [Section B.1.3](#).

**B.1.3 Incorporation of Porous Media and Fracture Properties into RMC Permeability**

While the replication (via the sequential indicator method) of the permeability ECDF per RMC honors the data values, the data structure is enforced through replication of the permeability semivariogram, for each permeability threshold, and for each principal direction. Because the

semivariogram structure is assumed (i.e., it is not constructed from measured spatial data), a simple model is assumed. The exponential semivariogram is used to define permeability continuity at each ECDF threshold and in each orientation. The semivariogram model parameters are the nugget, integral range, and sill. The nugget effect is assumed negligible; (1-m<sup>3</sup>) point measurements are assumed accurate. The integral range, representing the continuity of the feature in question at a given threshold, is defined equal to the average length of that feature in a given direction. The variance contribution is directly defined as  $p(1-p)$ , theoretically a function of the cumulative probability  $p$  at a given threshold.

For permeabilities that correspond to porous media or small-scale fractures, the integral range in the direction of maximum continuity is set equal to 3.0 m (Sweetkind and Williams-Stroud, 1996). Because there is no evidence to differentiate this scale with that in the vertical orientation, the integral range in the vertical is assigned the same value. In the direction of minimum continuity, the integral range is set equal to 1.0 m, the length of a sub-gridblock, which effectively removes any spatial correlation in that orientation.

For permeabilities that correspond to large-scale fracture flow, high-permeability strips are simulated that are meant to physically imitate actual fracture features within an analogous volume of rock (i.e., high-permeability linear features preferentially oriented in one or more directions). Again, the sequential indicator method imposes these highly anisotropic features within the gridblock through replication of a user-defined semivariogram at each threshold. At those permeability thresholds greater than -12.0 m<sup>2</sup>, the integral range parameter in each principal orientation is defined to reflect the fracture dimensions. In the direction of maximum continuity, the integral range (Tables B.1-1 through B.1-3) is set equal to the average fracture length identified for the HGU (and, therefore, RMC). There is no evidence to differentiate the average fracture length in the direction of maximum continuity with that in the vertical orientation; therefore, the integral range in the vertical is assigned the same value. In the direction of minimum continuity, the integral range is analogous to the average fracture aperture. Because this average is on the order of millimeters, the integral range in this direction is set equal to 1.0 m, the length of each sub-gridblock. The distance between fractures is therefore spatially uncorrelated within the complete gridblock.

Although the simulation method does not permit the incorporation of additional fracture properties — namely, fracture connectivity, fracture frequency, and flowing interval spacing — it is important to notice that such properties remain useful. For example, in this analysis, flowing interval spacing data are available for some of the RMCs and are used as verification datasets (discussed in [Section B.1.4](#)). If fracture correlation lengths are honored in each principal orientation, then is it reasonable to consider that related fracture properties are reproduced via simulation. Additionally (although not applied in this analysis), post-processing simulation methods (e.g., annealing) may be used to fine-tune the permeability fields to honor additional properties such as fracture connectivity.

#### **B.1.4 Results and Verification**

For each RMC, 100 realizations of permeability are generated for a gridblock-scale domain of 50 by 100 by 100 m with 1 m<sup>3</sup> resolution. [Figure B.1-6](#) shows an arbitrarily selected realization for each of the three RMCs, the differences between which are reflected by both the relative proportion of permeability values at a given value (i.e., color) and the directional length of higher-permeability (fracture) features. While the results can be generally verified by comparing attributes of each permeability block to their respective descriptive statistics in [Tables B.1-2](#) through [B.1-4](#), results are verified more directly through two methods: (1) confirming the approximate reproduction of the measured ECDF by the simulated ECDFs, and (2) confirming the approximate reproduction of the measured directional variograms (at each ECDF threshold) by those simulated. Additionally, direct verification is corroborated by the calculation of (vertical) flowing fracture spacing for the simulated permeability blocks. These measurements have been collected for certain HGUs and, although not incorporated into the simulation method, provide an independent test of how well the method is able to reproduce actual features and flow properties of the media.

##### **B.1.4.1 ECDF Reproduction**

Reproduction of the sample ECDF by a realization indicates that the relative proportion of permeability values within the domain honor those derived from the field data. The simulation method indirectly reproduces the sample ECDF; a measure of error between the sample and simulated ECDF is not incorporated into the algorithm. A comparison of the ECDFs from each realization (of 100 total) is plotted against the sample ECDF for the DMP/R RMC in [Figure B.1-7](#). While the agreement between the measured and simulated thresholds is good for each, the best

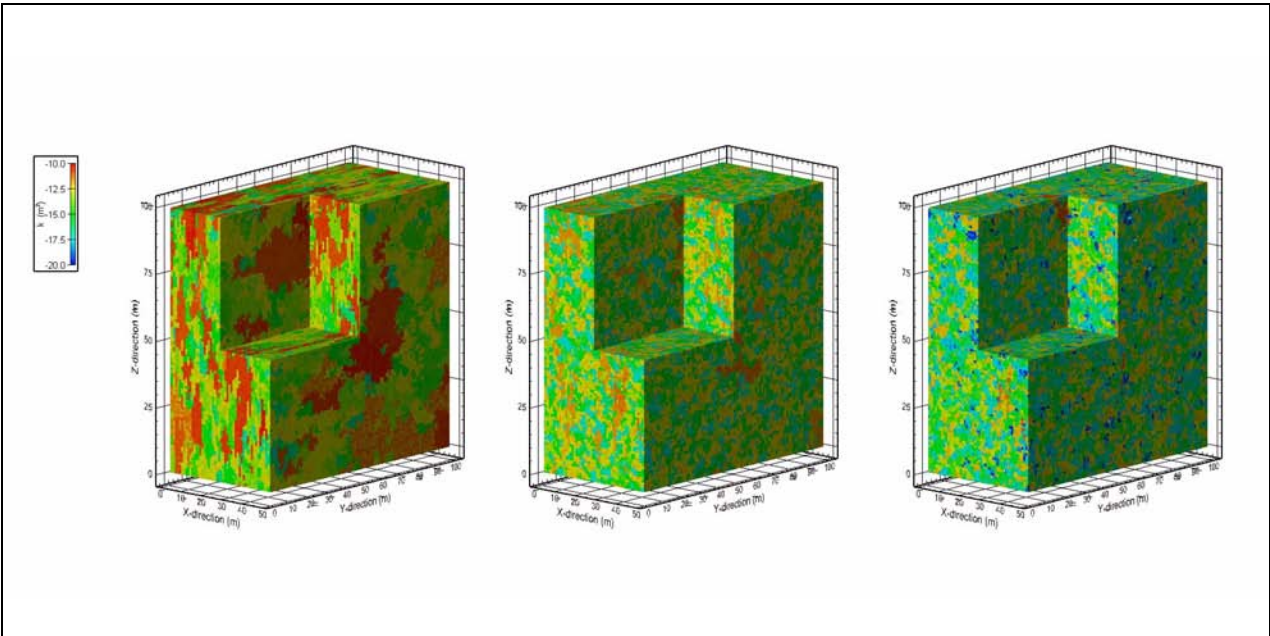


**Figure B.1-6**  
**Selected Permeability Realizations for (from left to right)**  
**the DMP/R, VMP/R, and ZEOL RMCs**  
 Note: Model domains have dimensions 50 by 100 by 100 m with 1-m<sup>3</sup> grid blocks.

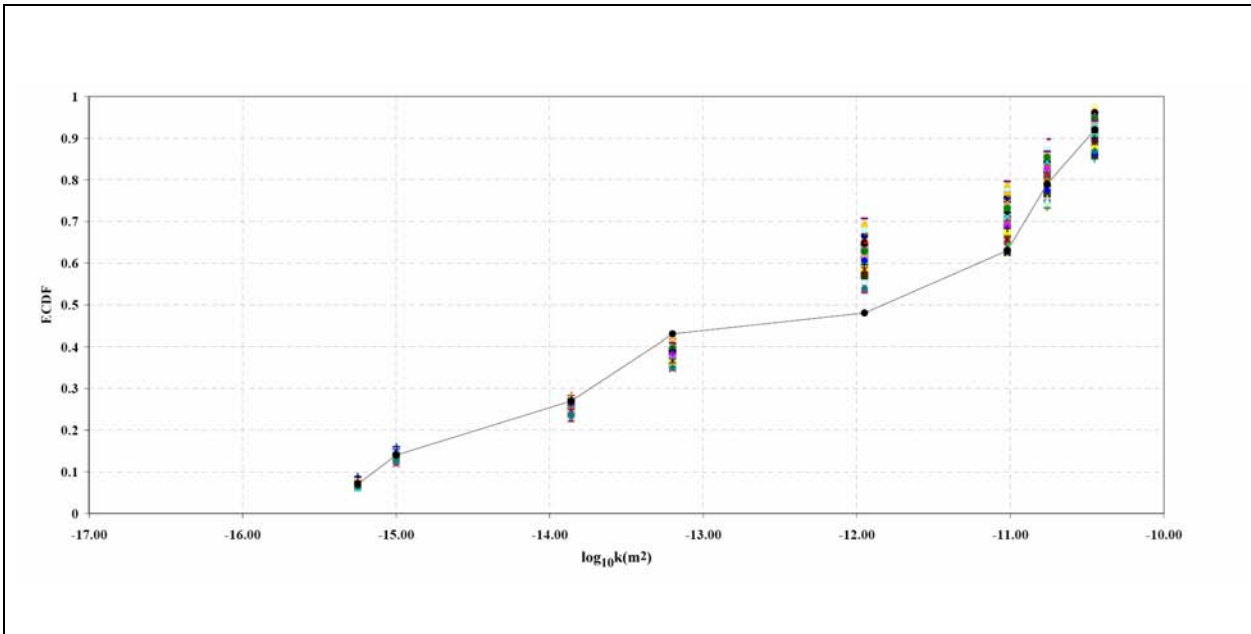


**Figure B.1-7**  
**Comparison of the Discrete ECDFs from (all 100) Realizations of the**  
**DMP/R RMC Plotted against the Sample ECDF Described in [Table B.1-2](#)**



agreement occurs toward the tails of the distribution. The agreement becomes poorer, although remains acceptable, towards the (porous-to-fracture) permeability threshold at  $-12.0 \text{ m}^2$ . This is a result of the discrete change in correlation lengths across the threshold. The sequential indicator method, through enforcement of the variograms on each side of the discrete threshold, cannot accurately reproduce an ECDF to match the discontinuity in correlation lengths. There is a tendency toward smoothing of the monotonically increasing ECDF near the threshold.

#### ***B.1.4.2 Variogram Reproduction***

Reproduction of an input variogram by a realization, for all ECDF thresholds and the three principal directions, indicates that directional correlation lengths are honored across the entire range of permeability values in that simulated gridblock. As part of the determination of each node permeability, the sequential indicator method enforces the input variograms at each ECDF threshold, thus each realization should approximate these variograms when transformed into a given indicator field. [Figure B.1-8](#) shows this is, indeed, the case. For each of 100 VMP/R realizations, the x- and y-direction variograms, for an arbitrarily selected threshold, are plotted against the input variogram. Correlation lengths are well reproduced. Only the sills are slightly variable, but by a negligibly small amount considering that semivariance (y-axis) is a squared unit.

#### ***B.1.4.3 Flowing Fracture Spacing***

Flowing fracture spacing is defined here as the average vertical distance between flowing features, and not simply fracture features. In most cases, flowing interval spacing can be considered significantly greater than fracture spacing (often reported as a frequency). Although not incorporated into the simulation method, this metric is useful for a general assessment of how well the simulated permeability fields compare to field observations.

In the field, measured data are sparse. Kuzio (2004) presents the average distance between flowing features in fractured volcanics at Yucca Mountain, derived from flow-log analysis in multiple boreholes. She reported a lognormal distribution of saturated-zone flowing interval spacing with a (back transformed) mean of 19.5 m and a range from 1 to 500 m. The reported mean fracture spacing is 0.26 m, directly indicating that not all fracture features contributed to flow (e.g., isolated or sealed fractures). However, caveats were presented such as the unknown influence of packers on the vertical

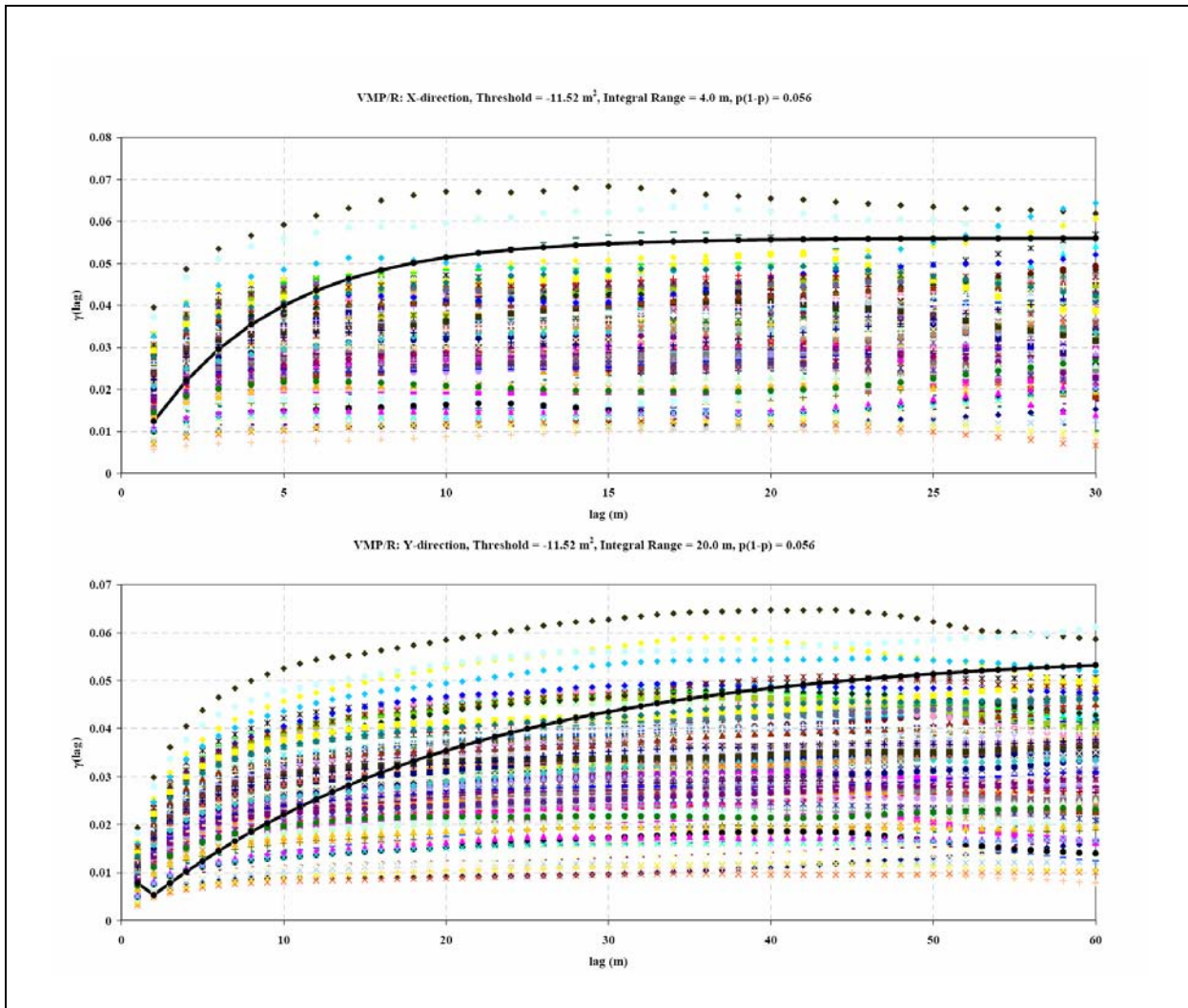


**Figure B.1-8**  
**Comparison of x- and y-Direction Variograms from (100 total) Realizations of the VMP/R RMC Plotted against the Input Variogram at the  $k = -11.52 \text{ m}^2$  Threshold**  
 Note: See [Table B.1-3](#).

distribution of head in the borehole during measurement, and potentially unmeasured vertical flowing features because of the vertical orientation of the borehole. On the contrary to the incongruence observed between fracture and flowing fracture spacing, fracture lengths in the Tiva Canyon tuff were reported from 0.1 to 24.0 m (IT, 2001), with lengths approximately equal to spacing. This reported range of fracture spacing is of the same order as the flowing fracture spacing reported by Kuzio (2004) and suggests that, at least in some cases, fracture and flowing fracture spacing may be nearly equivalent.

Equally important to this analysis, Kuzio (2004) showed the HGU tested (her study included the LFA, VTA, and TCU) and flowing interval spacing to be uncorrelated. This would imply that the mean flowing interval spacing of 19.5 m may be compared with that derived for each of the three RMC-block types realized in this study (i.e., DMP/R, VMP/R, ZEOL). However, Kuzio (2004) acknowledges this result to be significantly impacted by data sparsity. Further, fracture spacing in the RMC permeability realization were explicitly defined through their proportion and correlation length. The VMP/R and ZEOL were primarily designed as porous units, and only the DMP/R was defined as the fracture-flow dominated unit. Lastly, flowing intervals derived from the simulated blocks would in reality be a gross underestimate of the actual because flowing features cannot be differentiated from fracture features. Considering this, in the following analysis it is appropriate only to “identify” flowing intervals in the DMP/R RMC, as flow through these realizations was designed to primarily be through discrete features.

To calculate flowing interval spacing in the (100) DMP/R permeability realizations, a single randomly selected vertical plane (Y-Z orientation) is selected. For each column within the plane, the vertical spacing between flowing intervals was recorded and then averaged per column, resulting in (100 realizations x 50 column “wells” =) 5,000 flowing interval measurements. Fractures were defined as all nodes with permeability greater than  $-12.0 \text{ m}^2$ , and a minimum of 2.0 m was required to define a flowing interval. A histogram of results is shown in [Figure B.1-9](#). Qualitatively speaking, results indicate an approximately lognormal flowing interval distribution with a (back-transformed) mean of 14.3 m, agreeing well with that defined by Kuzio (2004). The range of intervals is from 3 to 100 m, with 100 m being the gridblock height.

#### ***B.1.4.4 Transport Simulations for Upscaling***

##### ***B.1.4.4.1 Introduction***

For each 500,000 node heterogeneous realization of permeability, a steady-state flow model is computed with 0.1 m difference in head over 100 m, prescribed along the principal flow direction. [Figure B.1-10](#) shows a cutout of a DMP simulated permeability field and the resulting heads in the flow model.

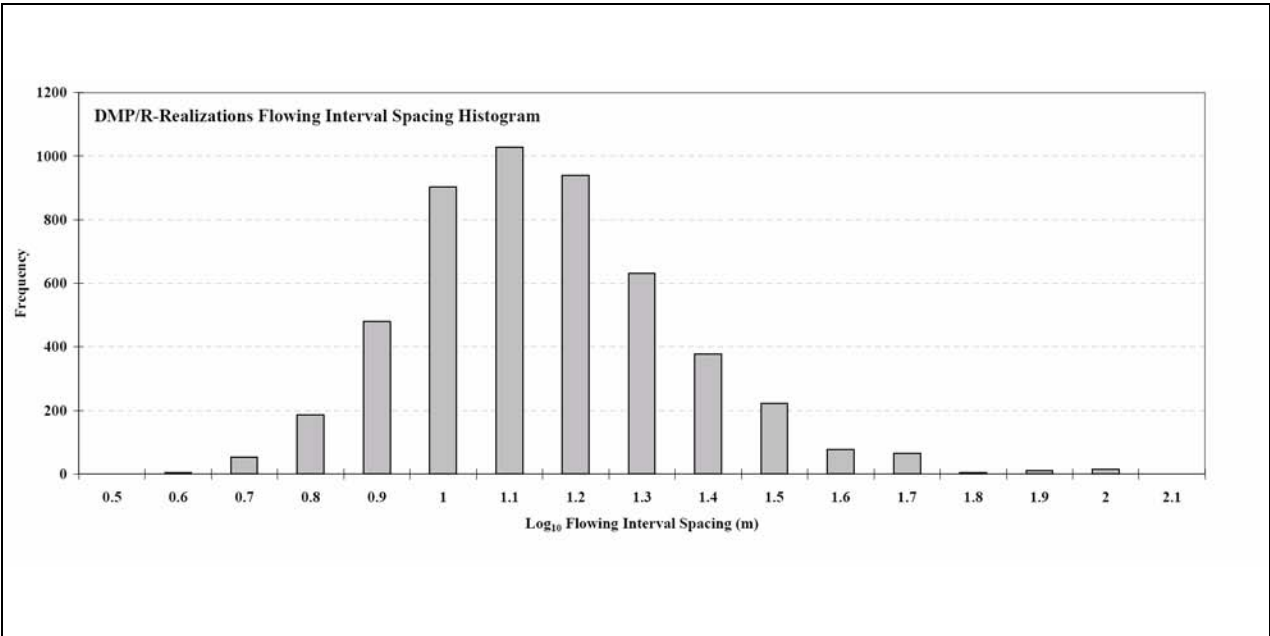


**Figure B.1-9**

**Vertical Flowing Interval Spacing Histogram for 100 DMP/R Permeability Realizations**

Note: Flowing features defined as zone with permeability less than  $-12.0 \text{ m}^2$ .  
 Mean interval is 1.1 m with a range from 0.5 to 2.0 m.

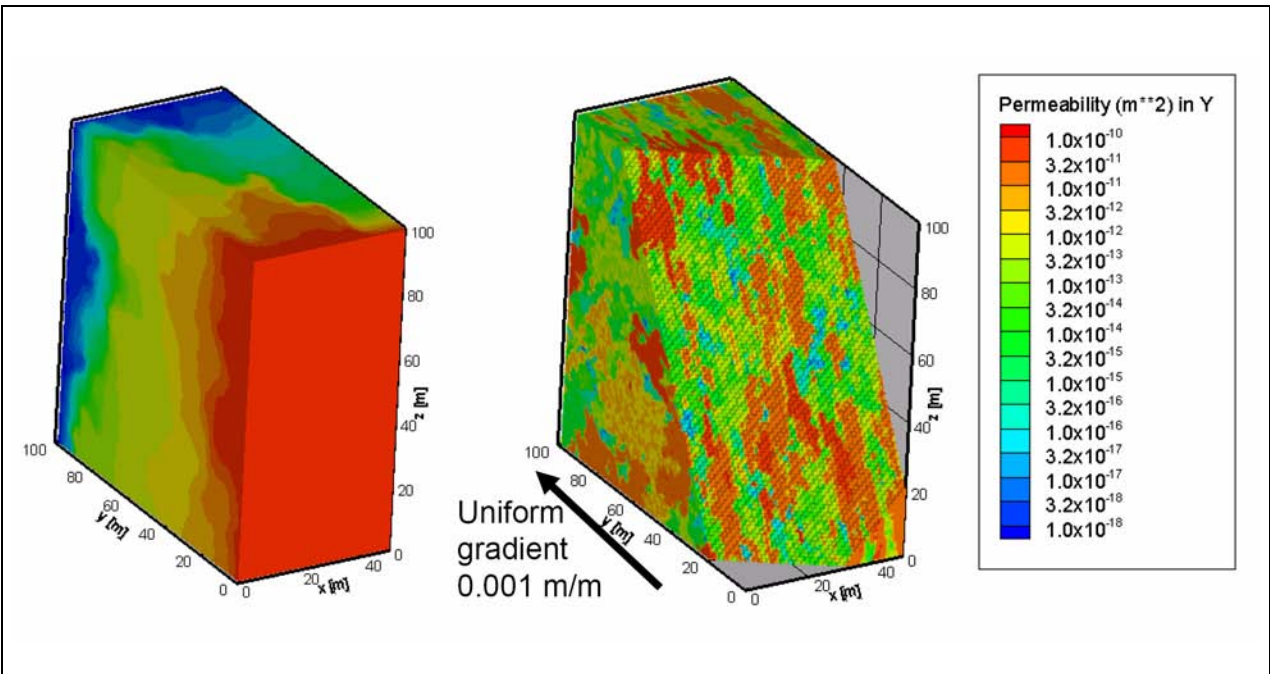


**Figure B.1-10**

**Permeability Distribution and Simulated Head for a DMP Realization**

Note: Heads decrease from red to blue by 0.1 m.

Non-reactive, non-diffusing particles are uniformly distributed across the upgradient boundary. The first 5 m of material into the flow domain is a high-permeability/low-porosity manifold through which particles migrate freely toward high-flux zones. Figure B.1-11 shows particle paths moving through one DMP model domain used in this analysis. The particles migrate out of the manifold into the high-flow zones and through the model. Their departure along the downgradient boundary defines a breakthrough curve that is then used to estimate the Peclet number and the average residence time.

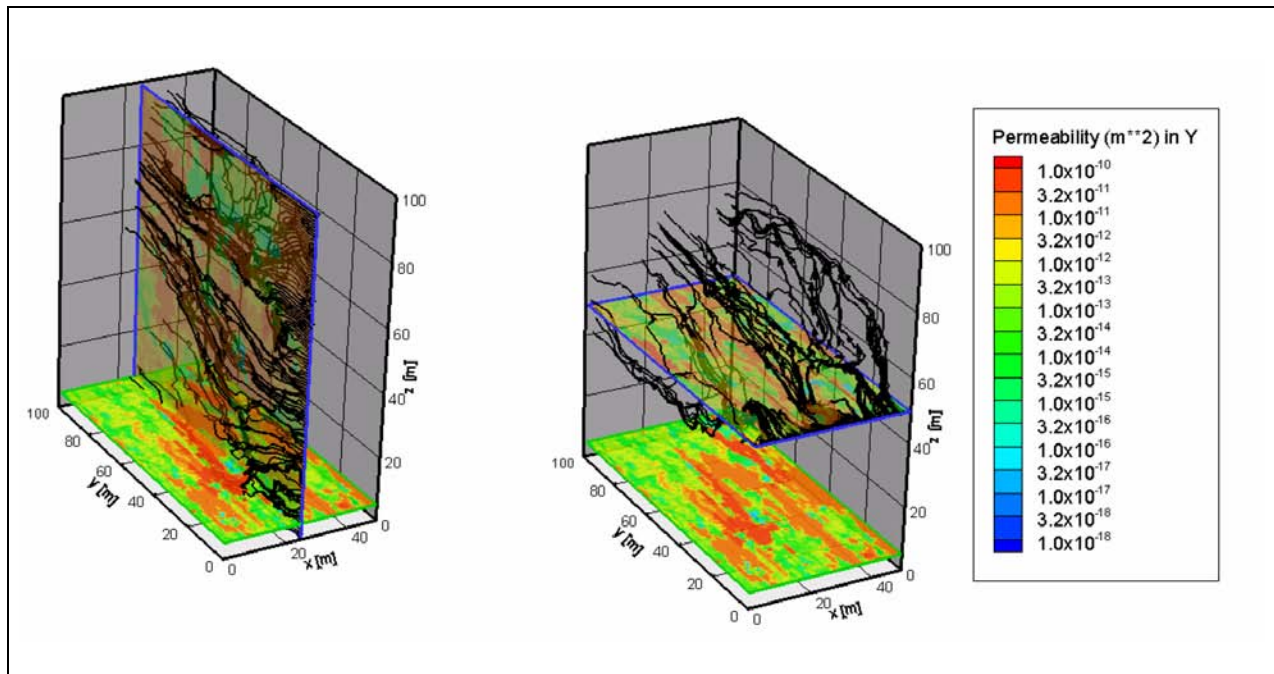


**Figure B.1-11**  
**Simulated Particle Paths in a 3-D DMP Model**

The software package RELAP (Reimus and Haga, 1999) is used for the parameter fitting in these simulations. RELAP is a semi-analytical solute transport model that uses an efficient inverse Laplace transform solution to simulate non-reactive and reactive solute transport in porous and dual-porosity media. The parameter estimation component in RELAP is achieved with a simple exhaustive gridding technique that samples all parameter combinations specified by the user. The RELAP parameter combination that minimizes the sum of the squared residuals between simulated and target values is identified as the best fit. Whereas, exhaustive gridding would be prohibitively costly for large scale models with many parameters, it is efficient and effective for simple models such as this

one, where single upscaled parameters are estimated to match the complex curve generated with the FEHM particle-tracking simulation. The user interface with RELAP entails either entering known parameters or ranges within which to estimate parameters. These parameters include the residence time ( $\tau$ ) which is the distance divided by the average velocity, the Peclet number (Pe), which characterizes dispersion, fracture aperture and spacing, and matrix  $K_d$ .

Figure B.1-12 shows the match between a RELAP transport simulation for a non-reactive, non-diffusing solute (line) and the particle breakthrough curve computed with FEHM particles in the 3-D heterogeneous flow field. The RELAP parameters matched for this flow field are  $Pe = 0.36$  and  $\tau = 770$  hr.

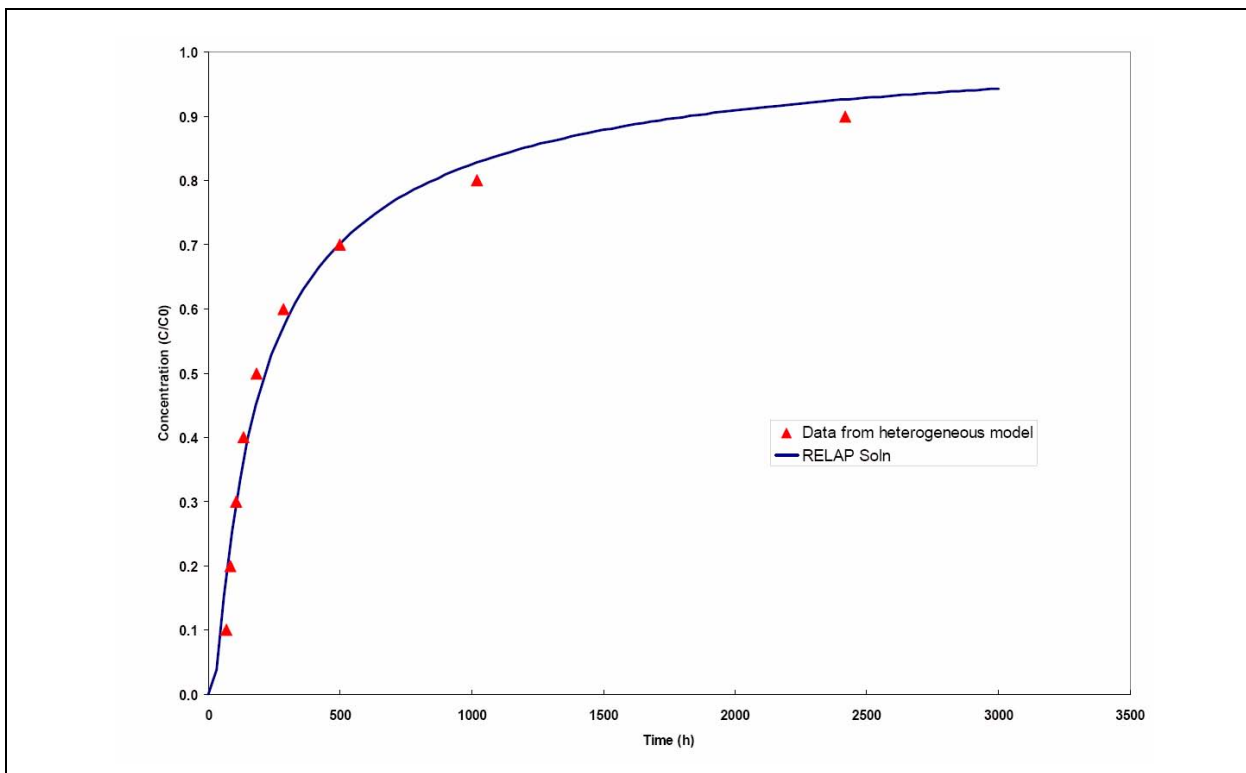


**Figure B.1-12**  
**Fitting the Non-reactive Breakthrough Curve (physical dispersion)**

Note: Symbols represent the breakthrough curve from the heterogeneous domain, particle-tracking simulation. The line is the RELAP match to those data.

The second step in the  $K_d$  upscaling procedure is to simulate particle transport again, but with matrix diffusion and matrix sorption. For all fracture nodes (all nodes in DMP/R models), a

fracture porosity of 1.8E-04 is specified. Then, using the relationship  $s = b/\phi_f$  and the cubic rule (Freeze and Cherry, 1979):

$$b = \sqrt[3]{12ks} \tag{B.1-1}$$

fracture spacing ( $s$ ) and aperture ( $b$ ) are computed based upon the permeability ( $k$ ) of each node. As permeability decreases, so do aperture and spacing for a given fracture porosity. This relationship leads to the convenient behavior that the lower-permeability nodes in the model domain will demonstrate transport characteristics of single matrix porosity material. In other words, with small aperture and spacing, the fracture solute concentration will be in equilibrium with the immobile matrix water as discussed in Section 6.4.1 and shown in Figure 6-7. This is consistent with the conceptual model here, that the fracture flow and transport are associated with the high-permeability nodes.

**B.1.5 Yucca Mountain Project  $K_d$  Distributions**

Tables B.1-5 and B.1-6 relate to YMP  $K_d$  distributions for laboratory fits as shown in SNL (2007).

**Table B.1-5  
Small-Scale Probability Distribution Functions for  $K_d$  in the Saturated Zone Developed  
on the Basis of Laboratory Data from Core Samples  
(Page 1 of 2)**

Species	Unit/Analysis	Distribution	Coefficients Describing Distribution (mL/g)
U	Zeolitic	Truncated Normal	Range = 5-20; $\mu = 12, \sigma = 3.6$
	Devitrified	Truncated Normal	Range = 0-4; $\mu = 2, \sigma = 0.6$
	Alluvium	Cumulative	( $K_d$ , prob) (1.7, 0.) (2.9, 0.05) (6.3, 0.95) (8.9, 1.0)
Np	Zeolitic	Truncated Normal	Range = 0 to 6; $\mu = 2.88, \sigma = 1.47$
	Devitrified	Exponential	Range = 0 to 2; $\mu = 0.69, \sigma = 0.71$
	Alluvium	Cumulative	( $K_d$ , prob) (1.8, 0.) (4.0, 0.05) (8.7, 0.95) (13, 1.0)
Pu	Zeolitic	Beta	Range = 50 to 300; $\mu = 100, \sigma = 15$
	Devitrified	Beta	Range = 50 to 300; $\mu = 100, \sigma = 15$
	Alluvium	Beta	Range = 50 to 300; $\mu = 100, \sigma = 15$
Cs	Zeolitic	Exponential	Range = 4,000 to 42,000; $\mu = 16,942, \sigma = 14,930$
	Devitrified	Truncated Normal	Range = 100 to 1,000; $\mu = 728, \sigma = 464$
	Alluvium	Truncated Normal	Range = 100 to 1,000; $\mu = 728, \sigma = 464$

**Table B.1-5**  
**Small-Scale Probability Distribution Functions for  $K_d$  in the Saturated Zone Developed**  
**on the Basis of Laboratory Data from Core Samples**  
 (Page 2 of 2)

Species	Unit/Analysis	Distribution	Coefficients Describing Distribution (mL/g)
Am	Zeolitic	Truncated Normal	Range = 1,000 to 10,000; $\mu = 5,500$ , $\sigma = 1,500$
	Devitrified	Truncated Normal	Range = 1,000 to 10,000; $\mu = 5,500$ , $\sigma = 1,500$
	Alluvium	Truncated Normal	Range = 1,000 to 10,000; $\mu = 5,500$ , $\sigma = 1,500$
Pa	Zeolitic	Truncated Normal	Range = 1,000 to 10,000; $\mu = 5,500$ , $\sigma = 1,500$
	Devitrified	Truncated Normal	Range = 1,000 to 10,000; $\mu = 5,500$ , $\sigma = 1,500$
	Alluvium	Truncated Normal	Range = 1,000 to 10,000; $\mu = 5,500$ , $\sigma = 1,500$
Sr	Zeolitic	Cumulative	( $K_d$ , prob) (100, 0) (5,000, 0.5) (90,000, 1.0)
	Devitrified	Uniform	Range = 20 to 400
	Alluvium	Uniform	Range = 20 to 400
Th	Zeolitic	Truncated Normal	Range = 1,000 to 10,000; $\mu = 5,500$ , $\sigma = 1,500$ (for a symmetric distribution and a min and max at $\pm 3 \sigma$ )
	Devitrified	Truncated Normal	Range = 1,000 to 10,000; $\mu = 5,500$ , $\sigma = 1,500$ (for a symmetric distribution and a min and max at $\pm 3 \sigma$ )
	Alluvium (same as devitrified)	Truncated Normal	Range = 1,000 to 10,000; $\mu = 5,500$ , $\sigma = 1,500$ (for a symmetric distribution and a min and max at $\pm 3 \sigma$ )
Ra	Zeolitic	Truncated Lognormal	Range = 1,000 to 250,000; $\mu = 100,000$ , $\sigma = 31,420$
	Devitrified	Uniform	Range = 100 to 1,000
	Alluvium	Uniform	Range = 100 to 1,000
Se	Devitrified	Truncated Lognormal	Range = 1 to 50; $\mu = 14.0$ ; $\sigma = 11.2$
	Zeolitic	Truncated Lognormal	Range = 1 to 35; $\mu = 14.3$ ; $\sigma = 7.9$
	Alluvium	Truncated Lognormal	Range = 1 to 50; $\mu = 14.0$ ; $\sigma = 11.2$
Sn	Devitrified	Log Uniform	Range = 100 to 36,700
	Zeolitic	Log Uniform	Range = 100 to 36,700
	Alluvium	Log Uniform	Range = 100 to 36,700
C/Tc/I	Volcanics/Alluvium	Constant	Zero

Source: SNL, 2007

Output DTN: LA0702AM150304.001, Tables 1 and 4.

$\mu$  = Mean

$\sigma$  = Standard deviation



**Table B.1-6**  
**Recommended Composite Distribution for  $K_d$  in Volcanics and Alluvium**

Species	Unit/Analysis	Distribution	Coefficients Describing Distribution (mL/g)
U	Composite (Volcanics)	Cumulative	( $K_d$ , prob) (0, 0.) (5.39, 0.05) (8.16, 0.95) (20, 1.0)
	Alluvium	Cumulative	( $K_d$ , prob) (1.7, 0.) (2.9, 0.05) (6.3, 0.95) (8, 9, 1.0)
Np	Composite (Volcanics)	Cumulative	( $K_d$ , prob) (0, 0.) (0.99, 0.05) (1.83, 0.90) (6, 1.0)
	Alluvium	Cumulative	( $K_d$ , prob) (1.8, 0.) (4.0, 0.05) (8.7, 0.95) (13, 1.0)
Pu	Composite (Volcanics)	Cumulative	( $K_d$ , prob) (10, 0.) (89.9, 0.25) (129.87, 0.95) (300, 1.0)
	Alluvium (Devitrified)	Beta	$\mu = 100$ , range = 50 to 300, $\sigma = 15$
Cs	Composite (Volcanics)	Cumulative	( $K_d$ , prob) (100, 0.) (3,000.59, 0.05) (6,782.92, 1.0)
	Alluvium (Devitrified)	Truncated Normal	range = 100 to 1,000; $\mu = 728$ , $\sigma = 464$
Am/Th/Pa	Volcanics and Alluvium	Truncated Normal	range = 1,000 to 10,000; $\mu = 5,500$ , $\sigma = 1,500$
Sr	Volcanics and Alluvium	Uniform	range = 20 to 400
Ra	Volcanics and Alluvium	Uniform	range = 100 to 1,000
Se	Volcanics	Truncated Lognormal	range = 1 to 35; m = 14.3; s = 7.9
	Alluvium	Truncated Lognormal	range = 1 to 50; m = 14.0, s = 11.2
Sn	Volcanics	Truncated Log Uniform	range = 100 to 36,700
	Alluvium	Truncated Log Uniform	range = 100 to 36,700
C/Tc/I	Volcanics and Alluvium	Constant	Zero

Source: SNL, 2007

Output DTN: LA0702AM150304.001.

Note: Development of the distributions is based on Table B.1-5 of this document and Table C-11 in SNL (2007).

$\mu$  = Mean

$\sigma$  = Standard deviation

Tables B.1-7 through B.1-12 relate to  $K_d$  distributions as shown in Shaw (2003).

**Table B.1-7  
Carbonate Sorption  $K_d$  Ranges**

Radionuclide	Dosch and Lynch (1980)	Stout and Carroll (1992)	Perkins et al. (1998)	Total Range
Cs	Range(4,101)	--	--	Range(4,101)
Sr	Range(5,16)	--	--	Range(5,16)
Eu	Range(1E4,4E5)	--	--	Range(1E4,4e5)
Pu	Range(2E3,7E3)	Range(1E2, 1E4)	275	Range(1E2, 1E4)
Am	Range(2E3,2E4)	Range(2E3,3E5)	Range(150,350)	Range(2E3,3E5)
U	Range(2,132)	Range(1E-5, 0.3)	--	Range(0,132)
Np	--	Range(<1E2, 5E3)	--	Range(<1E2, 5E3)

Source: Shaw, 2003

-- = Not applicable

**Table B.1-8**  
**Summary of Distributions Fit for Pu Sorption Using YMP Data - Minimum and Maximum of Dataset Listed in Parentheses When Different from Distribution**

Rock Type	Water	Exp. Atmos.	Min	Max	Mean	Std Dev	Parameters	Distribution <sup>a</sup>
Vitric	all	all	214	3085	360	362	a1 = 0.6 a2 = 5.4	Beta
Devit	all	all	0	350	55	54	a1 = 0.7 a2 = 3.8	Beta
Zeo	all	all	0	750	240	205	a1 = 0.6 a2 = 1.3	Beta
Vitric	J-13	Air & CO <sub>2</sub>	64	1984 (1810)	704	453	--	Triangular
Vitric	J-13	Air	147	1995 (1810)	763	535	--	Triangular
Vitric	P#1	Air & CO <sub>2</sub>	21	651 (580)	231	148	--	Triangular
Devit	J-13	Air & CO <sub>2</sub>	5.4 (6)	N/A (246)	77	215	m = 72 s = 215	Lognormal
Devit	p#1	Air	4.3 (4.8)	N/A (122)	30	26	b = 26	Exponential
Devit	p#1	CO <sub>2</sub>	--	--	300	--	--	2 Data Points
Zeolitic	J-13	Air & CO <sub>2</sub>	N/A (32)	N/A (516)	265	127	α = 265 β = 70	Logistic
Zeolitic	p#1	Air & CO <sub>2</sub>	0	N/A (739)	89	963	μ = 302 σ = 963	Lognormal

Source: Shaw, 2003

Note: All data fit for these distributions from YMP [1996] DTN: LAIT831341AQ96.001.

<sup>a</sup> See [Appendix C](#) for distribution definitions.

-- = Not applicable

**Table B.1-9**  
**Summary of Distributions Fit for  $N_p$  Sorption Using YMP Data**

Rock Type	Water	Exp. Atmos.	Min	Max	Mean	Std Dev	Parameters	Distribution <sup>a</sup>	Comments
Devit	all	all	0	Inf <sup>b</sup> (30)	1	1	Shift = -3.3	Exponential	--
Vitric	all	all	0	Inf (4)	0.62	0.62	Shift = -2.8	Exponential	--
Zeolite	all	all	0	Inf (41)	2.5	2.5	Shift = -6.7	Exponential	--
Vitric	J-13	Air & CO <sub>2</sub>	0	Inf (3.5)	0.66	0.66	$\beta = 0.66$	Exponential	--
Vitric	P#1	Air & CO <sub>2</sub>	0	Inf (4)	0.48	0.49	$\beta = 0.49$	Exponential	--
Devit	J-13	Air & CO <sub>2</sub>	0	Inf (3.5)	0.48	0.48	$\beta = 0.48$	Exponential	--
Devit	p#1	Air & CO <sub>2</sub>	0	Inf (30)	2.2	2.2	$\beta = 2.2$	Exponential	Temperatures 20-90 °C
Devit	p#1	Air & CO <sub>2</sub>	0	Inf (30)	0.23	0.23	$\beta = 0.23$	Exponential	Temperatures 20-25 °C, Upper 4 valued (>18) rejected.
Zeolitic	J-13	Air & CO <sub>2</sub>	-2.4 (0)	Inf (6.5)	2.3	1.5	$\mu = 4.7$ $\sigma = 1.5$	Lognormal	T=20-25 °C
Zeolitic	J-13	Air & CO <sub>2</sub>	-1.8 (0)	Inf (8.5)	2.4	1.6	$\mu = 4.3$ $\sigma = 1.6$	Lognormal	T = 20-60 °C
Zeolitic	J-13	Air & CO <sub>2</sub>	-1.2 (0)	Inf (13.2)	2.5	1.9	$\mu = 3.8$ $\sigma = 1.9$	Lognormal	T = 20-90 °C
Zeolitic	J-13	Air & CO <sub>2</sub>	-Inf (2)	Inf (13.2)	8.3	3.7	$\mu = 8.3$ $\sigma = 3.7$	Normal	T = 90 °C
Zeolitic	p#1	Air & CO <sub>2</sub>	0	Inf (32)	1.45	1.47	$\beta = 1.47$	Exponential	T = 25-90 °C

Source: Shaw, 2003

Note: Source data for distributions: YMP [1996] DTN: LAIT831341AQ96.001.

<sup>a</sup> See Appendix C for distribution definitions.

<sup>b</sup> Infinity

-- = Not applicable

**Table B.1-10**  
**Summary of Distributions Fit for Sr Using YMP Data**

Rock Type	Water	Exp. Atmos.	Min	Max	Mean	Std Dev	Distribution <sup>a</sup>	Comments
Devit	J-13	Air & CO <sub>2</sub>	0 (24)	Inf (41)	30.8	5.6	Lognormal	T = 20-80 °C
Vitric	J-13	Air & CO <sub>2</sub>	0 (130)	Inf (199)	175	18	Lognormal	T = 20-80 °C
Zeolitic	J-13	Air & CO <sub>2</sub>	Inf (2.4e5)	0 (1.2e4)	1.2e5	1.4e5	Lognormal	T = 20-80 °C

Source: Shaw, 2003

Note: Source data for distributions: YMP [1996] DTN: LAIT831341AQ96.001.

Note: Compare with Table 9-10 for distributions of Conca (2000).

<sup>a</sup> See [Appendix C](#) for distribution definitions.

**Table B.1-11**  
**Summary of Distributions Fit for Cs Using YMP Data**

Rock Type	Water	Exp. Atmos.	Min	Max	Mean	Std Dev	Distribution <sup>a</sup>	Comments
Devit	J-13	Air & CO <sub>2</sub>	0 (124)	Inf (243)	185	46	Lognormal	T = 20-80 °C
Vitric	J-13	Air & CO <sub>2</sub>	0 (506)	Inf (1067)	837	223	Lognormal	T = 20-80 °C
Zeolitic	J-13	Air & CO <sub>2</sub>	4357 (7353)	Inf (4.2e4)	17400	20265	Lognormal	T = 20-80 °C

Source: Shaw, 2003

Source data for distributions: YMP [1996] DTN: LAIT831341AQ96.001.

Compare with Table 9-10 for distributions of Conca (2000).

<sup>a</sup> See [Appendix C](#) for distribution definitions.

**Table B.1-12**  
**Summary of Distributions Fit for U Using YMP Data**

Rock Type	Water	Exp. Atmos.	Min	Max	Mean	Std Dev	Distribution <sup>a</sup>	Comments
Devit	J-13	Air & CO <sub>2</sub>	0	Inf (14.5)	2.28	2.28	Exponential	T = 20-80 °C
Devit	p#1	Air & CO <sub>2</sub>	0	Inf (4.8)	0.87	0.87	Exponential	T = 20-80 °C
Vitric	J-13	Air & CO <sub>2</sub>	0	Inf (4.6)	1.38	1.38	Exponential	T = 20-80 °C
Vitric	p#1	Air & CO <sub>2</sub>	0	Inf (5.8)	1.04	1.04	Exponential	T = 20-80 °C
Zeolitic	J-13	Air & CO <sub>2</sub>	0	Inf (126)	16.5	16.5	Exponential	T = 20-80 °C
Zeolitic	p#1	Air & CO <sub>2</sub>	0	Inf (4.6)	0.79	0.79	Exponential	T = 20-80 °C

Source: Shaw, 2003

Source data for distributions: YMP [1996] DTN: LAIT831341AQ96.001.

Compare with Table 9-10 for distributions of Conca (2000).

<sup>a</sup> See Appendix C for probability distribution definitions.

Tables B.1-13 through B.1-15 relate to  $K_d$  distributions as shown in SNJV (2005).

**Table B.1-13**  
**Distribution Coefficients Statistics and Shape Parameters for**  
**Laboratory Measurement of Radionuclide Sorption on Vitric Tuff**

	Am		Sr		Cs		Np		U		Pu	
	Sample	Fit	Sample	Fit	Sample	Fit	Sample	Fit	Sample	Fit	Sample	Fit
Model Type		Uniform		Weibull		Uniform		Log Logistic		Weibull		Exponential
Number of Samples	8	--	30	--	30	--	400	--	59	--	71	--
Mean (mL/g)	1,354	1,344	148	174	646	644	3.17	1.84	1.89	1.98	516	534
Standard Deviation (mL/g)	398	418	62	21	317	320	29	+infinity	1.70	1.91	472	534
Sample Minimum (mL/g)	860	--	23	--	109	--	0	--	0	--	23	--
Sample Maximum (mL/g)	2,050	--	220	--	1,061	--	526	--	12	--	1,810	--
95% CI Minimum (mL/g)	--	655	--	127	--	118	--	0.03	--	0.06	--	14
95% CI Maximum (mL/g)	--	2,032	--	208	--	1,170	--	8.6	--	7.1	--	1,969
RMS error	--	2.90E-03	--	7.23E-03	--	2.50E-03	--	7.51E-04	--	7.98E-04	--	2.70E-03
<b>Model Shape Parameters</b>												
alpha ( $\alpha$ )	--	--	--	10	--	--	--	1.32	--	1.03	--	--
beta ( $\beta$ )	--	--	--	183	--	--	--	0.54	--	2.00	--	534
gamma ( $\gamma$ )	--	--	--	--	--	--	--	0	--	--	--	--

Source: SNJV, 2005

--- = No applicable data

**Table B.1-14**  
**Distribution Coefficients Statistics and Shape Parameters for**  
**Laboratory Measurement of Radionuclide Sorption on Devitrified Tuffs**

	Am		Sr		Cs		Np		U		Pu	
	Sample	Fit	Sample	Fit	Sample	Fit	Sample	Fit	Sample	Fit	Sample	Fit
Model Type		Exponential		Log Logistic		Exponential		Log Logistic		Log Logistic		Log Normal (2)
Number of Samples	35	--	154	--	159	--	421	--	75	--	118	--
Mean (mL/g)	1,845	1,894	101	101	645	601	19	12	2.51	2.76	125	142
Standard Deviation (mL/g)	1,834	1,894	141	+Infinity	656	590	166.37	+infinity	2.29	4.46	168	237
Sample Minimum (mL/g)	79	--	9	--	10	--	0	--	0	--	6	--
Sample Maximum (mL/g)	12,000	--	1,200	--	3,800	--	2,353	--	15	--	1,900	--
95% CI Minimum (mL/g)	--	48	--	18	--	25	--	0.02	--	0.4	--	8
95% CI Maximum (mL/g)	--	6,986	--	402	--	2,187	--	17.34	--	9.75	--	701
RMS error	--	1.60E-03	--	1.30E-03	--	2.10E-03	--	6.69E-04	--	9.42E-04	--	8.35E-04
<b>Model Shape Parameters</b>												
alpha ( $\alpha$ )	--	--	--	2	--	--	--	1.04	--	2.29	--	--
beta ( $\beta$ )	--	1,894	--	48	--	590	--	0.51	--	1.97	--	--
mu ( $\mu$ )	--	--	--	--	--	--	--	--	--	--	--	4
sigma ( $\sigma$ )	--	--	--	--	--	--	--	--	--	--	--	1
gamma ( $\gamma$ )	--	--	--	12	--	--	--	0	--	0	--	--

Source: SNJV, 2005

-- = No applicable data



**Table B.1-15**  
**Distribution Coefficients Statistics and Shape Parameters for**  
**Laboratory Measurement of Radionuclide Sorption on Zeolitic Tuffs**

	Am		Sr		Cs		Np		U		Pu	
	Sample	Fit	Sample	Fit	Sample	Fit	Sample	Fit	Sample	Fit	Sample	Fit
Model Type		Inverse Gaussian		Weibull		Log Normal (2)		Gamma		Log Normal (2)		Weibull
Number of Samples	25	--	83	--	86	--	430	--	176	--	110	--
Mean (mL/g)	5,204	6,037	39,277	40,278	16,747	17,762	3	3	45	17	260	255
Standard Deviation (mL/g)	7,757	14,863	54,882	65,354	13,710	19,440	2	1	423	22	242	205
Sample Minimum (mL/g)	470	--	1,200	--	2,700	--	0	--	0	--	19	--
Sample Maximum (mL/g)	33,000	--	246,085	--	72,000	--	22	--	9,423	--	2,000	--
95% CI Minimum (mL/g)	--	612	--	1,492	--	3,495	--	1	--	3	--	14
95% CI Maximum (mL/g)	--	42,028	--	221,800	--	67,375	--	6	--	70	--	778
RMS error	--	3.10E-03	--	3.58E-04	--	--	--	3.45E-04	--	3.82E-03	--	1.37E-03
<b>Model Shape Parameters</b>												
alpha ( $\alpha$ )	--	--	--	1	--	--	--	3	--	--	--	1
beta ( $\beta$ )	--	--	--	27,023	--	--	--	1	--	--	--	273
mu ( $\mu$ )	--	5,573	--	--	--	9	--	--	--	2	--	--
lambda ( $\lambda$ )	--	784	--	--	--	--	--	--	--	--	--	--
sigma ( $\sigma$ )	--	--	--	--	--	1	--	--	--	1	--	--

Source: SNJV, 2005

-- = No applicable data

## **B.2.0** REFERENCES

- Conca, J. 2000. *Unsaturated Zone and Saturated Zone Transport Parameters, Yucca Mountain Analysis and Model Report*, ANL-NBS-HS-00019, Rev. 0. Argonne, IL: Argonne National Laboratory.
- Deutsch, C.V., and A.G. Journel. 1992. *GSLIB Geostatistical Software Library and User's Guide*. New York, NY: Oxford University Press.
- Dosch, R.G., and A.W. Lynch. 1980. "Radionuclide Transport in a Dolomite Aquifer, Scientific Basis for Nuclear Waste Management." In *Proceedings of the International Symposium*, held in Boston, Massachusetts, on November 27-30, 1979. New York, NY: Plenum Press.
- Flint, L.E. 1998. *Characterization of Hydrogeologic Units Using Matrix Properties, Yucca Mountain, Nevada*, Water-Resources Investigation Report 97-4243. Denver, CO: U.S. Geological Survey.
- Freeze, A.R., and J.H. Cherry. 1979. *Groundwater*. Prentice Hall, NJ.
- IT, see IT Corporation.
- IT Corporation. 2001. *Underground Test Area Fracture Analysis Report: Analysis of Fractures in Volcanic Rocks of Western Pahute Mesa-Oasis Valley*, ITLV/13052-150. Las Vegas, NV.
- Kuzio, S. 2004. *Probability Distribution for Flowing Interval Spacing*, ANL-NBS-MD-000003 REV. 01. Las Vegas, NV: Yucca Mountain Project.
- McKenna, S.A., D.D. Walker, and B. Arnold. 2003. "Modeling Dispersion in Three-Dimensional Heterogeneous Fractured Media at Yucca Mountain." In *Journal of Contaminant Hydrology*, Vol. 62-63: 577-594.
- Perkins, W.G., D.A. Lucero, and G.O. Brown. 1998. *Column Experiments for Radionuclide Adsorption Studies of Culebra Dolomite: Retardation Parameter Estimation for Non-Eluted Actinide Species*, SAND98-1005. Albuquerque, NM: Sandia National Laboratories.
- Prothro, L.B., and S.L. Drellack, Jr. 1997. *Nature and Extent of Lava Flow Aquifers Beneath Pahute Mesa, Nevada Test Site*, DOE/NV11718B--156. Las Vegas, NV: Bechtel Nevada.

- Reimus, P.W., and M.J. Haga. 1999. *Analysis of Tracer Responses in the BULLION Forced-Gradient Experiment at Pahute Mesa, Nevada*, LA-13615-MS. Los Alamos, NM: Los Alamos National Laboratory.
- Shaw, see Shaw Environmental, Inc.
- SNJV, see Stoller-Navarro Joint Venture.
- SNL, see Sandia National Laboratories.
- Sandia National Laboratories. 2007. *Site-Scale Saturated Zone Transport*, MDL-NBS-HS-000010 REV 03. Las Vegas, NV.
- Shaw Environmental, Inc. 2003. *Contaminant Transport Parameters for the Groundwater Flow and Contaminant Transport Model of Corrective Action Units 101 and 102: Central and Western Pahute Mesa, Nye County, Nevada*, Rev. 0, Shaw/13052-201. Las Vegas, NV.
- Stoller-Navarro Joint Venture. 2005. *Phase II Contaminant Transport Parameters for the Groundwater Flow and Contaminant Transport Model of Corrective Action Unit 98: Frenchman Flat, Nye County, Nevada*, S-N/99205--043. Las Vegas, NV.
- Stout, D.L., and S.A. Carroll. 1992. *A Literature Review of Actinide-Carbonate Mineral Interaction*, SAND92-7328. Albuquerque, NM: Sandia National Laboratories.
- Sweetkind, D.S., and S.C. Williams-Stroud. 1996. Written communication. Subject: *Characteristics of Fractures at Yucca Mountain, Nevada: Synthesis Report*, Administrative Report. Denver, CO: U.S. Geological Survey.
- Warren, R.G. 1994. *Structural Elements and Hydrogeologic Units of the Southwestern Nevada Volcanic Field*, Technical Paper, 19 January. Los Alamos, NM: Los Alamos National Laboratory.
- YMP, see Yucca Mountain Project.
- Yucca Mountain Project. 1996. DTN: LAIT831341AQ96.001. *Radionuclide Retardation Measurements of Batch-Sorption Distribution Coefficients for Barium, Cesium, Selenium, Strontium, Uranium, Plutonium, and Neptunium*, Submittal 12 November.



## **Appendix C**

### **Mechanistic Field-Scale Reactive Transport Modeling**

## **C.1.0 INTRODUCTION**

A significant challenge for CAU-scale radionuclide transport simulation is to obtain a sufficient mechanistic understanding of hydrologic and chemical processes at various scales to develop field-scale parameterizations that accurately address the combined influence of complex and often heterogeneous physical and chemical processes. In groundwater below Pahute Mesa, radionuclide migration from the source areas can potentially occur in volcanic tuffs that are either fractured or unfractured, ultimately to spring discharge areas in Oasis Valley or to the regional carbonate aquifer. The PM CAU-scale transport models rely on particle-tracking-based solute-transport simulations to effectively deal with distributed source locations and the necessary large space and time scales for contaminant migration assessment. The particle-based models are far more efficient than finite-difference or finite-element based models, but require certain linear assumptions about equilibrium chemistry and non-interaction among migrating species. Therefore, in this supplementary analysis, field-scale reactive transport simulations along individual streamtubes created with the 3-D particle-tracking models are conducted to provide support for these assumptions and parameter refinement. This complementary study provides support for simplifying assumptions made in the particle-based analysis, recognizing that this approach would be infeasible for all source-release locations and all uncertainty analyses necessary for the statistical interpretations provided in the body of this report.

This appendix analyzes the reactive transport mechanisms and processes involving radionuclides and colloids in volcanic rocks at Pahute Mesa by considering two specific subsurface tests, TYBO and PURSE. For each of these tests, reactive transport involving multiple radionuclides in the presence of colloids is considered. Whereas the PLUMECALC method (Robinson and Dash, 2005), used in conjunction with particle-tracking results for the Monte Carlo simulations, is capable only of linear sorption chemical reactions, the method described here represents a mechanistic consideration of equilibrium and kinetic sorption of radionuclides onto both colloids and immobile minerals in a dual-porosity formulation that allows diffusion out of fractures into matrix material. The purpose of

the reactive transport simulations is to develop abstractions, and support assumptions invoked in the CAU-scale particle-based transport model. Specifically, these include (1) developing abstractions for colloid-facilitated transport and source functions, (2) addressing assumptions regarding radioactive decay daughter products, and (3) evaluating the scale dependence of radionuclide sorption processes (kinetics versus local equilibrium).

## **C.2.0 FLOW AND TRANSPORT IN FRACTURED ROCK**

### **C.2.1 Background**

Groundwater flow and solute transport in fractured rock have been studied at variable scales from column experiments to field tracer tests (e.g., Grisak et al., 1980; Neretnieks et al., 1982; Moreno et al., 1985; Johns and Roberts, 1991; Keller et al., 1995; Berkowitz and Scher, 1995; Zimmerman and Bodvarsson, 1996; Zyvoloski et al., 1997 and 2007; Wolfsberg et al., 2002; Andersson et al., 2004; Robinson et al., 2007; Dai et al., 2007; and Reimus and Callahan, 2007). In saturated fractured-rock systems, where the primary pathway for groundwater flow and solute transport is through fractures, groundwater in the matrix is considered immobile in dual-porosity conceptual models (Grisak and Pickens, 1980; Tang et al., 1981; Sudicky and Frind, 1982). Thus, although the bulk of the water travels through the fractures, a very large reservoir of water in the matrix can act to store and reduce mobility of contaminants via  $D_m$  (Robinson, 1994). Recent field-scale tracer test interpretations by Reimus and Callahan (2007) highlight the significance of fracture apertures in governing mass transfer between fractures and matrix, particularly when the field-scale fractures in which solutes flow may have larger apertures than those used in laboratory columns.

To study radionuclide transport at field scales in fractured rock without compromising reaction complexity and material heterogeneity, a generalized dual-porosity model (GDPM) (Zyvoloski et al., 2007) was developed for integration with the multicomponent reactive transport simulator of FEHM (Zyvoloski et al., 2003) to simulate in fractured systems the processes of radionuclide decay with daughter products, equilibrium or kinetically controlled sorption, aqueous speciation, radionuclide reactions with colloids, and colloid filtration.

In this appendix, the GDPM is first verified against analytical solutions (Tang et al., 1981) and the particle-tracking solutions (Zyvoloski et al., 2003). Then, streamtubes from the PM flow and transport models and GDPM reactive transport is simulated for releases from the TYBO and PURSE

tests to evaluate transport processes and develop a basis for abstractions and assumptions in the CAU particle-based transport model.

### **C.2.2 Generalized Dual-Porosity Model**

The GDPM provides dual-porosity formulations for both fracture/matrix systems and porous media with heterogeneous materials of contrasting material properties (Zyvoloski et al., 2007). The term “primary porosity” is introduced to represent the medium in which large-scale global flow and transport occurs, while “secondary porosity” is connected locally only to the primary porosity nodes to represent the storage volume, typically of lower permeability. The fundamental principle behind the GDPM method is that secondary nodes are prescribed normal to the primary nodes with user-specified high resolution near the primary nodes and decreasing resolution away from the primary nodes. This enables accurate simulation of diffusive solute fronts moving out of the fractures and into the matrix. The secondary nodes for each primary node are not connected to those for other primary nodes, which means only diffusive transport normal to the fracture is simulated. This leads to a highly efficient numerical scheme for simulating flow and transport in the fracture, diffusive transport into the matrix, and the full suite of reactive processes available in FEHM in both the fractures and the matrix.

#### **C.2.2.1 Validation of GDPM with Column Experiment Data**

Model validation ensures that the model meets its intended requirements in terms of the methods employed and the results obtained. To test whether the GDPM can represent and correctly reproduce the processes considered, it is used to simulate a set of  $^3\text{H}$  laboratory transport experiments, and the results are compared with the observation data and the Relap semi-analytical solution (Reimus et al., 2001). Radionuclide transport experiments through fractured tuffaceous rock were conducted by Ware et al. (2005) at LANL (Figure C.2-1). Two flow rates were employed in the experiments: high flow 2 milliliters per hour (mL/hr) and low flow 0.5 mL/hr. The core length is 13 cm, and the diameter is 6 cm. Assuming the experiment can be represented with a 1-D transport model, the GDPM coupled with PEST (Doherty, 2005) is used to estimate transport parameters for the  $^3\text{H}$  experiments (column number UE-7az-1770), and results are compared with the Relap semi-analytical solution for transport in fractured rock (Figure C.2-2). The estimated  $D_m$  coefficient is  $1.2 \cdot 10^{-9} \text{ m}^2/\text{s}$ ; fracture aperture is 0.48 mm; mean residence times are 4.76 hours and 1.19 hours for the low-flow



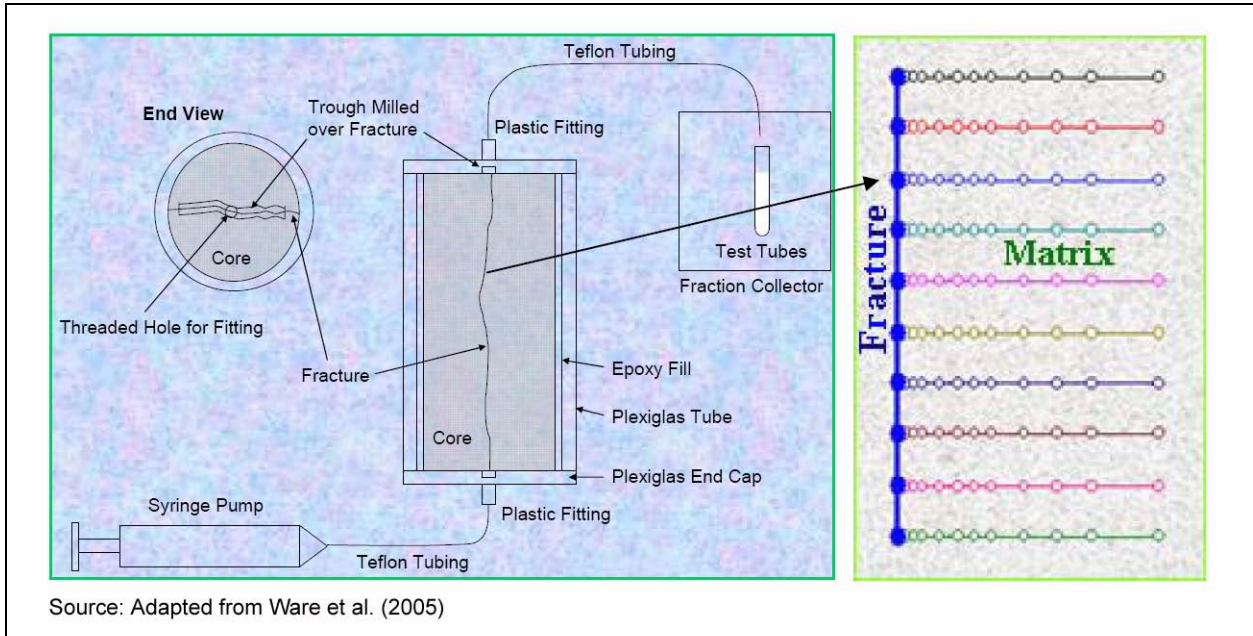


**Figure C.2-1**  
**Schematic Illustration of Column Experiments for Fracture Transport System and the GDPM Grid**

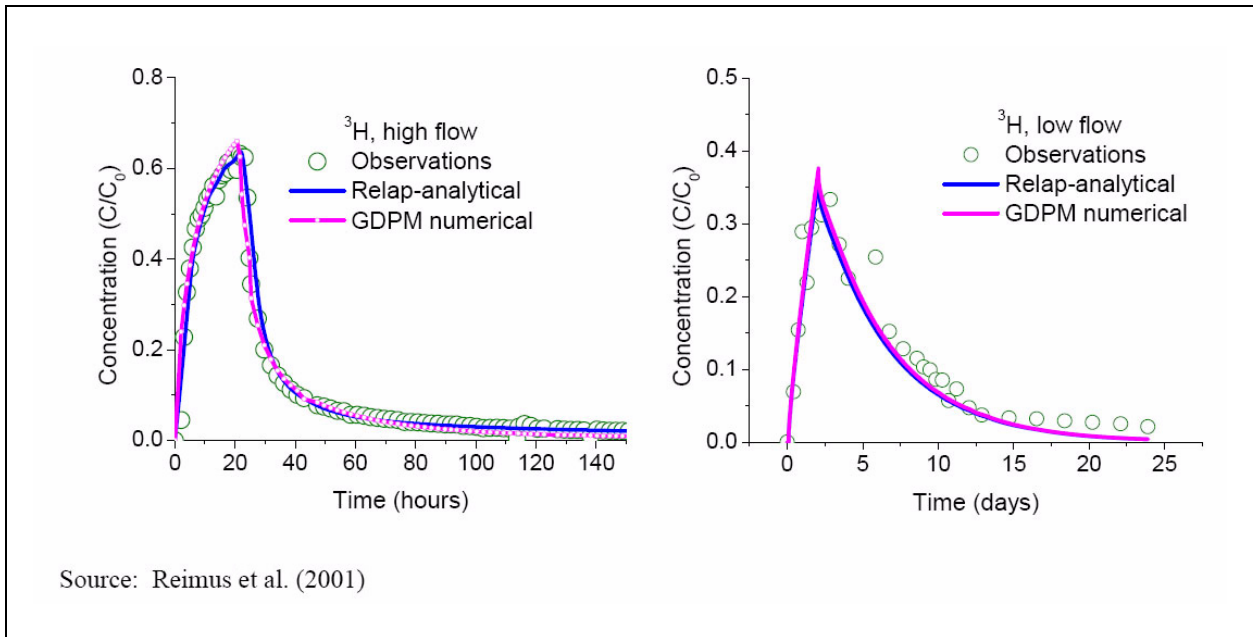


**Figure C.2-2**  
**Comparison of the GDPM against the Relap Semianalytical Solution for Interpreting the Column Experiments Conducted by Ware et al. (2005)**

and high-flow experiments, respectively; and the Peclet number is 1.41 (Table C.2-1). In both experiments, the GDPM and the Relap analytical solution fit the observation data equally well, using the parameters estimated with GDPM and PEST. These results demonstrate that the GDPM compares well with experimental data and with an semi-analytical solution for conservative solute transport in fractured rock.

**Table C.2-1**  
**Inverse Modeling of <sup>3</sup>H Breakthrough Curves from Two Fractured Tuffaceous Rock Experiments**

Parameters	$\tau$ (hr) Low/High	$Pe$	$b$ (mm)	$D_m$ (m <sup>2</sup> /s)
Values	4.76/1.19	1.41	0.048	1.2E-05

Note: Flow rates 0.5 and 2.0 mL/hr.

### C.2.2.2 Verification of the GDPM for Field-Scale Application

To build confidence in the GDPM for field-scale application, the algorithm is first verified against an analytical solution (Tang et al., 1981) and particle-tracking results (Zyvoloski et al., 2003). A synthetic model has been built to confirm the accuracy of the GDPM algorithm by comparison with the analytical and particle-based solutions. The dimensions of the synthetic model are 10 by 20 km in the horizontal directions and 500 m thick (Figure C.2-3). The groundwater flow direction is aligned with the  $x$ -axis with an average pore velocity of 34 m/yr. The conservative tracer with a constant normalized concentration (or particles) is inserted within a single cell (dimension: 100 x 100 x 50 m<sup>3</sup>) on the upstream boundary, and the breakthrough curve at a downstream location (15 km from the inlet) is recorded for comparisons. The transport parameters are longitudinal dispersivity = 100 m, transverse dispersivity = 0.1 m, and  $D_m$  coefficients = 10<sup>-13</sup> m<sup>2</sup>/s or 10<sup>-11</sup> m<sup>2</sup>/s.

Along the central flow line (+ $x$  direction) a 1-D GDPM is extracted and used to compute the concentration breakthrough curve at a node 15 km from the tracer injection node. The GDPM extraction entails developing a 1-D grid along a flow path and preserving the  $x$  component of velocity from the 3-D flow system, assuming there are no  $y$  or  $z$  velocity components in this case. Low matrix diffusion ( $D_m = 10^{-13}$  m<sup>2</sup>/s) and high matrix diffusion ( $D_m = 10^{-11}$  m<sup>2</sup>/s) cases are executed with the GDPM. The comparison against the analytical solutions (Tang et al., 1981) and dual-porosity particle-tracking results (Dash, 2003) is depicted in Figure C.2-4, which shows that the concentration

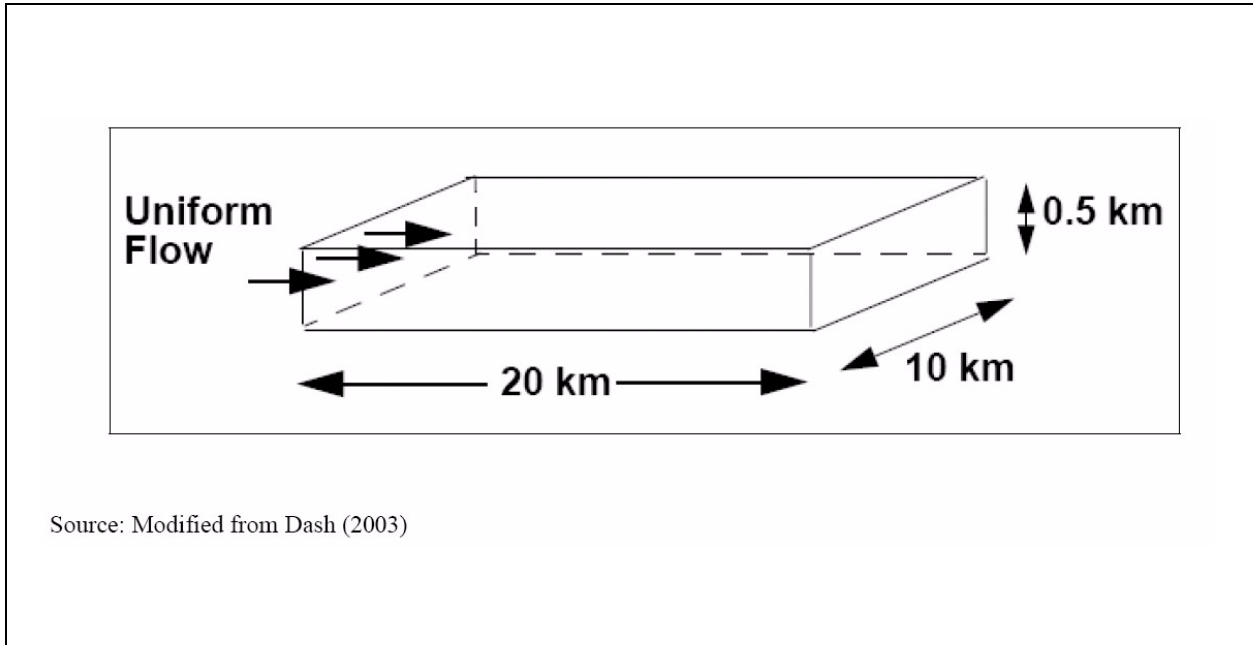


**Figure C.2-3**  
**Model Domain and Flow Boundary Conditions for the Verification of the GDPM Algorithm against Analytical and Particle-Tracking Results Solutions**

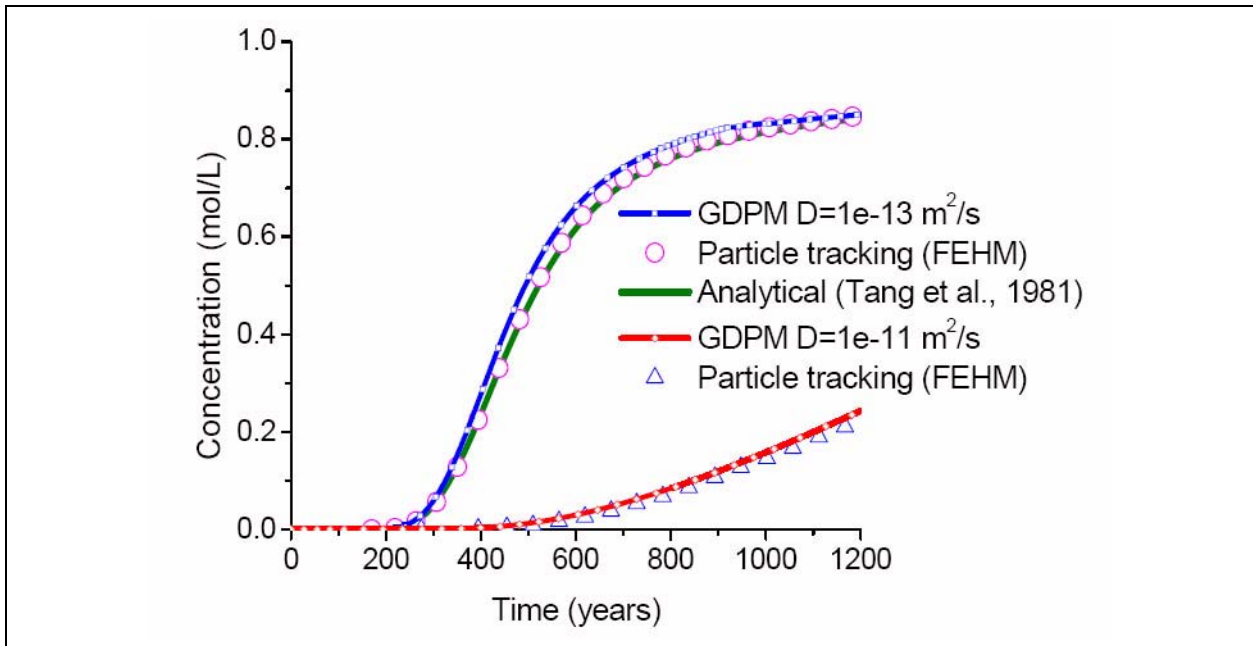


**Figure C.2-4**  
**Comparison of the GDPM against the Particle-Tracking Results for the Synthetic Model of Dash (2003)**

Also shown is Dash's (2003) analytical solution for the lower diffusion rate using Tang et al. (1981).

breakthrough computed from the GDPM match those computed from the analytical solutions and particle-tracking results well.

The GDPM is also verified against dual-porosity particle-tracking methods with two reactive tracers (Np and Pu in the Pahute Mesa flow system). A 5 km-long streamline originating at the TYBO test in the LCCU1-MME flow model was created in which the fracture aperture is 0.001 m and the fracture spacing is 1 m. This process, described in [Section C.4.0](#), involves simulating a single particle path through the 3-D flow system, and then converting the path into a 1-D model with variable grid spacing and cross-sectional area determined by the particle's velocity. In this grid, there are 2,509 fracture nodes and 25,090 matrix nodes with matrix node spacing normal to the primary fracture nodes increasing from 0.001 m near the fracture to 0.4 m. In this example, the  $D_m$  coefficient for the two species is  $5 \times 10^{-11}$  m<sup>2</sup>/s, the longitudinal dispersivity is 10 m, and the transverse dispersivity is 0.1 m. Equilibrium sorption reactions are specified for Np and Pu to immobile matrix minerals for this comparison because the particle-tracking method in FEHM can only simulate the equilibrium reactions (Zyvoloski et al., 2003), while the GDPM method can simulate a much broader set of reaction types. The results from the two methods are plotted in [Figure C.2-5](#), which shows that the computed concentrations at 5 km from the GDPM fits to the results of particle-tracking model for the two reactive tracers. These two verification cases indicate that the GDPM is appropriate for diffusive transport modeling in field-scale fractured rock systems. The modeling approach is limited by the dual-porosity model assumption of parallel plate fractures in which the spacing and aperture are defined by fixed relationships. These relationships abstract the actual complexities of fracture network geometries, orientations, and connectivities, which could result in different surface areas available for  $D_m$  than those developed with parallel plate model assumptions.

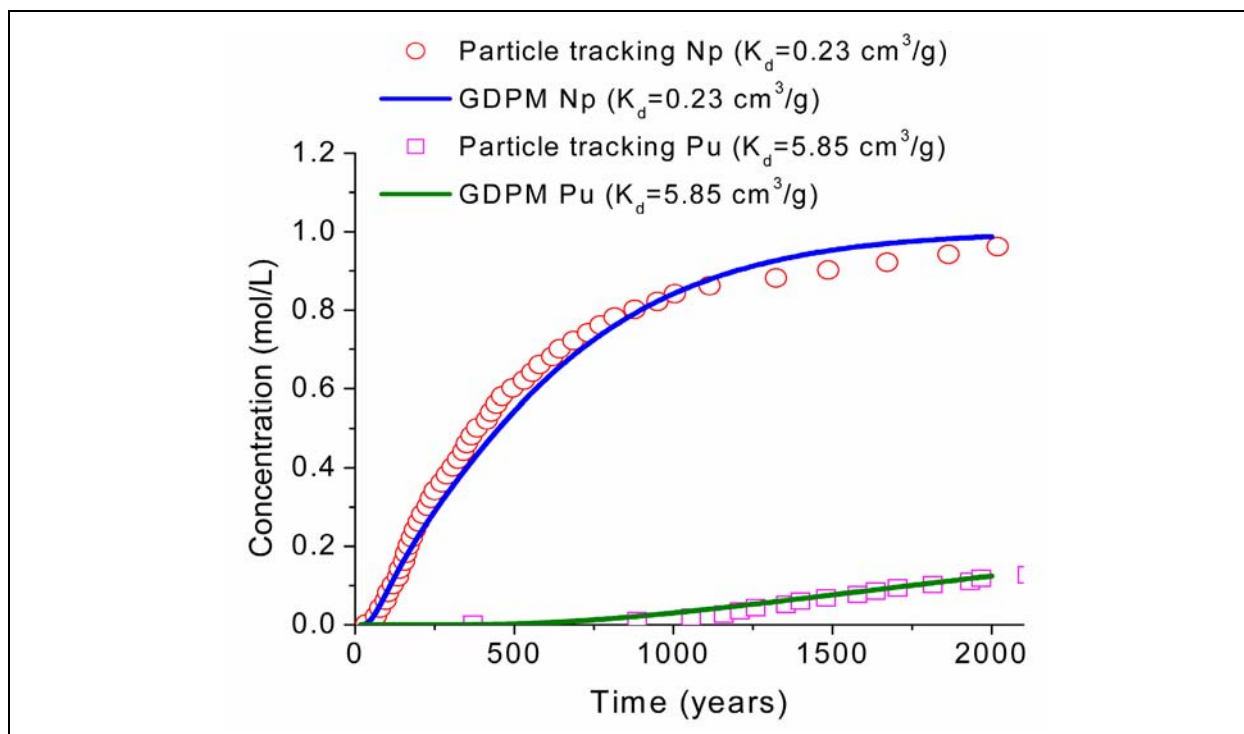


**Figure C.2-5**  
**Comparison of Breakthrough Curves for the GDPM against the Particle-Tracking Method with Reactive Tracers in the Pahute Mesa LCCU1-MME Flow Model with Releases at TYBO**

## C.3.0 RADIONUCLIDE TRANSPORT AND REACTION PROCESSES

### C.3.1 Summary of the Radionuclide Chemical Reactions

To investigate radionuclide (e.g., Pu, Np,  $^3\text{H}$ ,  $^{14}\text{C}$ , Am) transport in fractured and porous media in the PM CAU model, the chemical reaction simulator of FEHM (Zyvoloski et al., 2003) is incorporated into the GDPM to enable consideration of processes such as radionuclide diffusion into the matrix, radionuclide sorption to immobile minerals as well as to mobile colloids, attachment and detachment of colloids on the fracture walls or in porous media, and radionuclide decay chains with daughter products. A schematic diagram for some of the processes and reactions of Pu is illustrated in Figure C.3-1. The detailed description of these reactive transport processes can be found in Wolfsberg et al. (2002). The reactions included in the field-scale simulations are summarized in Table C.3-1.

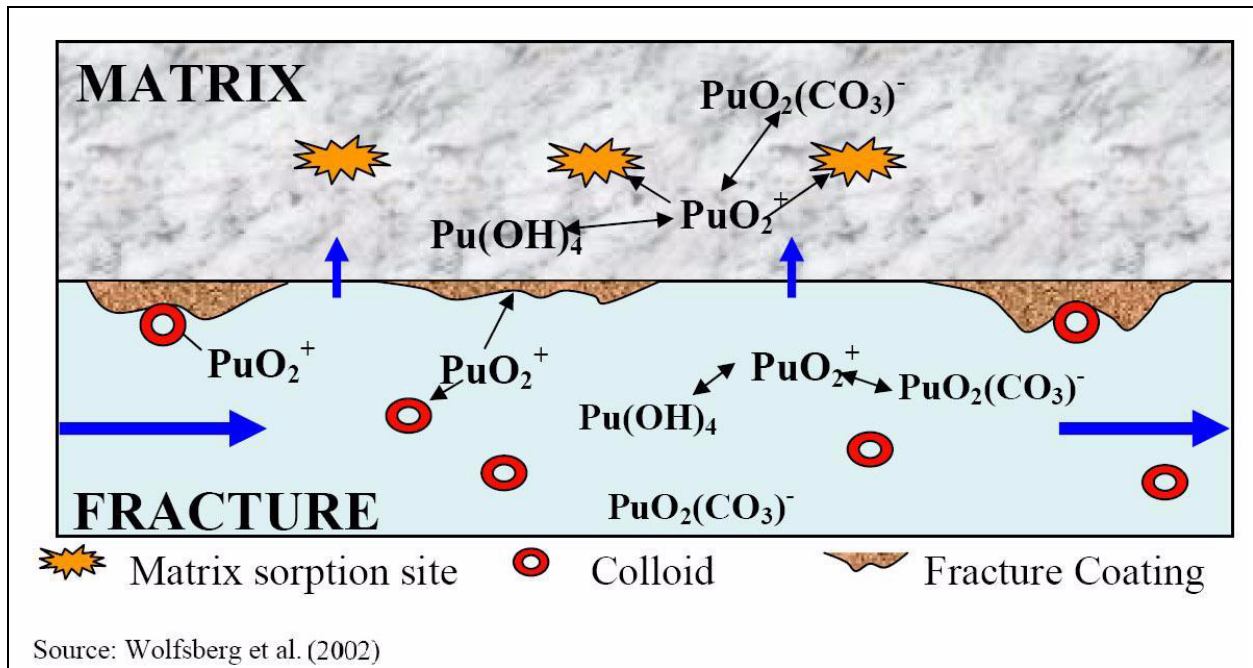


**Figure C.3-1**  
**Conceptual Model of Pu Reactive Transport in Fractures**

**Table C.3-1  
Radionuclide-Related Reactions Included in the Field-Scale Simulations**

<b>I: Radionuclide Sorption to Immobile Minerals</b>	
$^{239}\text{Pu}(\text{aq}) \rightleftharpoons ^{239}\text{Pu}(\text{s})$	
$^{237}\text{Np}(\text{aq}) \rightleftharpoons ^{237}\text{Np}(\text{s})$	
$^{241}\text{Am}(\text{aq}) \rightleftharpoons ^{241}\text{Am}(\text{s})$	
<b>II: Radionuclide Sorption onto Colloids in Fractures</b>	
$^{239}\text{Pu}(\text{aq}) + \text{Col}(\text{aq}) \rightleftharpoons ^{239}\text{Pu-Col}(\text{aq})$	
$^{241}\text{Am}(\text{aq}) + \text{Col}(\text{aq}) \rightleftharpoons ^{241}\text{Am-Col}(\text{aq})$	
<b>III: Colloid Filtration in Fractures</b>	
$^{239}\text{Pu-Col}(\text{aq}) \rightleftharpoons ^{239}\text{Pu-Col}(\text{s})$	
$^{241}\text{Am-Col}(\text{aq}) \rightleftharpoons \text{XO}^{241}\text{Am-Col}(\text{s})$	
$\text{Col}(\text{aq}) \rightleftharpoons \text{Col}(\text{s})$	
<b>IV: Radioactive Decay in Fractures and Matrix</b>	<b>(<math>T_{1/2}</math> = half-life) (years)</b>
$^3\text{H}(\text{aq}) \Rightarrow ^2\text{H}(\text{aq})$	$T_{1/2} = 12.32$
$^{14}\text{C}(\text{aq}) \Rightarrow ^{13}\text{C}(\text{aq})$	$T_{1/2} = 5,730$
$^{241}\text{Pu}(\text{aq}) \Rightarrow ^{241}\text{Am}(\text{aq})$	$T_{1/2} = 14.4$
$^{241}\text{Am}(\text{aq}) \Rightarrow ^{237}\text{Np}(\text{aq})$	$T_{1/2} = 433$
$^{241}\text{Pu-Col}(\text{aq}) \Rightarrow ^{241}\text{Am-Col}(\text{aq})$	$T_{1/2} = 14.4$
$^{241}\text{Am-Col}(\text{aq}) \Rightarrow ^{237}\text{Np}(\text{aq})$	$T_{1/2} = 433$
$^{241}\text{Pu}(\text{s}) \Rightarrow ^{241}\text{Am}(\text{s})$	$T_{1/2} = 14.4$
$^{241}\text{Am}(\text{s}) \Rightarrow ^{237}\text{Np}(\text{s})$	$T_{1/2} = 433$
$^{241}\text{Pu-Col}(\text{s}) \Rightarrow ^{241}\text{Am-Col}(\text{s})$	$T_{1/2} = 14.4$
$^{241}\text{Am-Col}(\text{s}) \Rightarrow ^{237}\text{Np}(\text{s})$	$T_{1/2} = 433$
$^{244}\text{Cm}(\text{aq}) \Rightarrow ^{240}\text{Pu}(\text{aq})$	$T_{1/2} = 18.1$
$^{244}\text{Cm}(\text{s}) \Rightarrow ^{240}\text{Pu}(\text{s})$	$T_{1/2} = 18.1$

Note: These reactions may be considered as either equilibrium or kinetic in the simulations, and the colloid reactive surface area is addressed in [Section C.3.2.3](#).

Note:  $^{239}\text{Pu}$  half-life is  $2.4 \times 10^4$  years.

aq = Aqueous  
s = Solid

### C.3.2 Transport Parameters

#### C.3.2.1 Porosity of Matrix and Fractures

When the GDPM is used to simulate radionuclide transport in fractured rock, two porosities are defined: fracture porosity ( $\phi_f$ ) and matrix porosity ( $\phi_m$ ). Fracture porosity is the primary porosity for flow and solute transport, which is equal to the fracture volume divided by the total volume of the fracture-matrix system. Matrix porosity provides a secondary component of porosity that is equal to the total void volume within the consolidated matrix divided by the total volume of the matrix. The porosity data used here are compiled from publications that report porosity measurements made in Pahute Mesa boreholes or on borehole core samples (Shaw, 2003). The porosity data for the radionuclide transport model are listed in [Table C.3-2](#).

**Table C.3-2**  
**Statistics of the Porosity Data for the GDPM**

RMC	HGU	$\phi_f$	$\phi_m$
DMP	WTA	0.0011	0.14
VMP	VTA	N/A	0.20/0.25
ZEOL	TCU	N/A	0.20/0.33
DMR	WTA	0.0011	0.14
ML	LFA	0.00082	0.16
Carbonate	CA	0.0031	0.05
Siliciclastic	ICU/CCU	0.00005	0.05

Hydrogeologic unit defined in Shaw (2003), BN (2002), and described in [Appendix A](#).

#### C.3.2.2 Matrix Sorption Coefficients

The sorption coefficients of the radionuclides are different for different RMCs. Based on the documented parameter distributions for Pahute Mesa (Shaw, 2003), the means of the sorption coefficients for Am, Np, and Pu are listed in the five main RMCs where the streamline passes through ([Table C.3-3](#)). Note this work was completed before consideration of other sorption coefficient distributions as described in [Section 6.0](#), so differences may exist. It is also assumed that sorption to fracture coating minerals is negligible, relative to the reactions that occur on matrix minerals



**Table C.3-3**  
**Mean Sorption Coefficients for Am, Np, and Pu (cm<sup>3</sup>/g) from Mechanistic K<sub>d</sub> Estimates**  
**(Section 6.0)**

RMC	DMP	VMP	ZEOL	DMR	ML
Am	554	5,150	5,495	365	1,240
Np	0.23	2.4	1.8	0.23	1.23
Pu	5.85	47.9	54.9	1.85	14.2

cm<sup>3</sup>/g = Cubic centimeters per gram

(see Section 6.0). Therefore, a radionuclide must first diffuse out of the fracture to contact the reactive matrix minerals where sorption takes place in this model.

### C.3.2.3 Colloid Load

This study assumes colloid sites are aqueous species that do not diffuse out of fractures into matrix material. Aggregation, buoyancy, and other issues associated with the actual size and shape of individual colloids are not considered; however, the distribution of sizes is considered with respect to estimates of available reactive surface area. Only the concentrations of available reactive sites on colloids are considered. This approximation is warranted for this study due to the low aqueous concentrations of Pu under consideration.

**Colloid site concentration:** Following the assumptions of Wolfsberg et al. (2002), the colloid site concentration  $C_{col}$  (moles sites/L) is defined by:

$$C_{col} = 4\pi r^2 n_c x_n / Av \quad (C.3-1)$$

where  $n_c$  is the colloid particle concentration (particles/L),  $r$  is the particle radius (nm/particle),  $x_n$  is the sorption sites per nm<sup>2</sup> (2.31 sites/nm<sup>2</sup> of goethite was used for the calculation), and  $Av$  is Avogadro's number,  $6.022 \times 10^{23}$  sites/mole sites.

The colloid sizes and the number of colloids per liter groundwater in Pahute Mesa vary from borehole to borehole. By using Equation (C.3-1) and the colloid measurements (size distributions of colloids sampled) in boreholes ER 5-4 #2, Water Well 4A, and UE-5 PW-3 (Reimus et al., 2006a), the naturally occurring colloid site concentrations in Pahute Mesa were computed with a mean of

$2.04 \times 10^{-8}$  moles sites/L and an SD of  $1.40 \times 10^{-10}$ . This distribution takes into account the variety of sizes and respective surface areas in the measured distributions of colloids. Only natural colloids are considered here; there is insufficient supporting information to address test-related colloids.

### C.3.2.4 Rate Constants for Plutonium Sorption onto Colloids

Sensitivity analyses of Pu reactive transport processes indicate that the sorption of Pu onto colloids is kinetically controlled and is one of the most sensitive processes for Pu transport. The equations in Table C.3-1 take the following form to address the statistics of the kinetic rate constants.

$${}^{239}\text{Pu}(aq) + \text{Col}(aq) \xrightleftharpoons[k_r]{k_f} {}^{239}\text{Pu} - \text{Col}(aq) \quad (\text{C.3-2})$$

Based on the previous investigations of Reimus et al. (2006b) and Wolfsberg and Viswanathan (2002), a statistical analysis of their estimated results of forward (sorption) ( $k_f$ ) and reverse (desorption) ( $k_r$ ) rate constants of Equation (C.3-2) was conducted. For different types of colloids such as montmorillonite, zeolite, and silica colloids, the forward and reverse rate constants are quite different. Considering that all these types of colloids exist in Pahute Mesa groundwater, the mean values of the rate constants for the field-scale simulation of  ${}^{239}\text{Pu}$  were used. Experiments for  ${}^{241}\text{Am}$  sorption and desorption rates such as those conducted by Reimus et al. (2006b) for Pu do not exist. Therefore, the Pu forward rate is used for  ${}^{241}\text{Am}$ . Because  ${}^{241}\text{Am}$  has a larger  $K_d$  than Pu (Table C.3-3), the reverse rate, computed as  $k_r = k_f/K_d$ , is smaller than for Pu; 0.002 is used here, based on the  $K_d$  differences of approximately two orders of magnitude (Table C.3-4).

**Table C.3-4**  
**Statistical Results of Forward and Reverse Rate Constants of Pu Sorption onto Colloids**

Parameters	Mean	SD	Minimum	Maximum
Forward Rate Constant (1/hr)	$1.36 \times 10^5$	$3.49 \times 10^5$	10	$1.0 \times 10^6$
Reverse Rate Constant (1/hr)	0.2191	0.4108	0.00018	1.70

Sources: Kersting and Reimus, 2003; Wolfsberg and Viswanathan, 2002

### C.3.2.5 Rate Constants for Colloid Filtration

The processes and mechanisms associated with colloid attachment and detachment to/from fracture walls (filtration) are not fully understood (Wolfsberg et al., 2002). However, both UGTA and YMP have supported studies seeking to quantify parameters associated with colloid filtration processes such as the studies of Reimus et al. (2001 and 2006a), in which filtration parameters are fit for multiple, different, natural colloid types in fractured core experiments in the laboratory. A statistical analysis of previous investigations is presented in [Table C.3-5](#). The mean values of the attachment and detachment rate constants for colloid filtration (listed in [Table C.2-1](#)) were used.

**Table C.3-5**  
**Statistics of Rate Constants of Colloid Attachment and Detachment to/from Fracture Walls**

Parameters	Mean	SD	Minimum	Maximum
Forward Rate Constant (1/hr)	0.0883	0.0757	0.04	0.2
Reverse Rate Constant (1/hr)	0.6231	1.3356	0.00015	3.33

Source: Wolfsberg et al., 2002

## **C.4.0 FIELD-SCALE RADIONUCLIDE REACTIVE TRANSPORT MODELING**

The GDPM is applied for analysis of reactive radionuclide transport from TYBO and PURSE. A stepwise procedure for conducting these simulations is described as follows:

1. Use a steady-state flow field of Pahute Mesa to conduct the 3-D particle-tracking modeling by releasing a particle from the source locations and mapping the time of flight along the streamline of the non-reactive, non-diffusing particle.
2. Convert the particle streamline through the 3-D domain into a high-resolution, 1-D, finite-element model with constant flux of 0.01 kg/s (and varying cross-sectional area – hence, the streamtube concept).
3. For fractured rock zones (DMP, DMR, and ML), assign the fracture porosity to the primary nodes and the matrix porosity to the matrix nodes. For non-fractured media zones (VMP and ZEOL), the primary porosity is the porosity of the matrix porous media, and there are no GDPM nodes. A longitudinal dispersivity of 10 m is applied to all flowing nodes.
4. Simulate reactive, dual-porosity transport for each solute of interest by using the reactive simulator (rxn) of FEHM and the userc input macro (Zyvoloski et al., 2003) for modeling the time-varying source functions. The GDPM provides a dual-porosity representation of interacting fractures and porous media. The diffusive mass transfer between the two media is governed by several factors including fracture and matrix porosities, surface area per unit model volume, diffusion coefficients, and fracture spacing, just as with classic dual-porosity models, but with the capability of taking full advantage of FEHM's rxn module for complex reactions in both the fractures and in the matrix.
5. Analyze the concentration distributions of the radionuclide species for the primary nodes and the secondary nodes.

The transport parameters associated with the simulations described in the next several sections are listed in [Tables C.3-2 through C.3-5](#). These simulations use expected value parameters only. In [Section C.6.0](#), the transport parameters are treated as uncertain, and parameter distributions for CAU transport models are developed. A flux of 0.01 kg/s is used for the streamtube, and 10 m is used for longitudinal dispersivity. The flow model invoked for these transport simulations

is LCCU1-MME. At the time of this study, the LCCU1-MME-TMCM model had not yet been developed.

### C.4.1 TYBO

#### C.4.1.1 TYBO Radionuclide Source Terms

The radionuclide source-release terms are derived from the 100 realizations of the TYBO sources (see Appendix B). These realizations are used to compute the mean of the source-release function for the reactive transport simulations. Figures C.4-1 and C.4-2 present the mean radionuclide source terms from TYBO, which are then scaled for the individual streamtube and used in these reactive transport models.

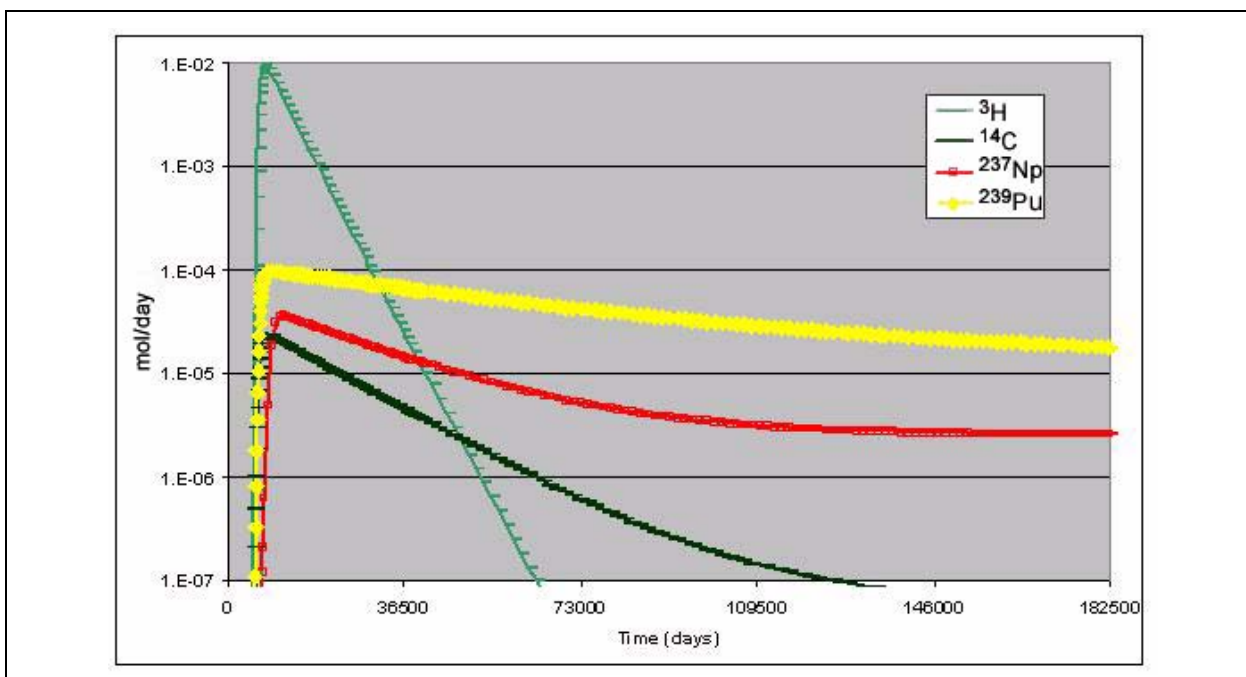


**Figure C.4-1**  
**Mean Radionuclide Source Flux Functions for  $^3\text{H}$ ,  $^{14}\text{C}$ ,  $^{237}\text{Np}$ , and  $^{239}\text{Pu}$  from TYBO**

#### C.4.1.2 Streamtube from TYBO Source Area

The TYBO test is located in southwestern Area 20, near the NTS boundary. The elevation of the working point is about 1,142 m, within the TSA. The TSA consists of a single WTA composed of moderately welded ash-flow tuff. Fractures are well developed in this aquifer and partially filled with

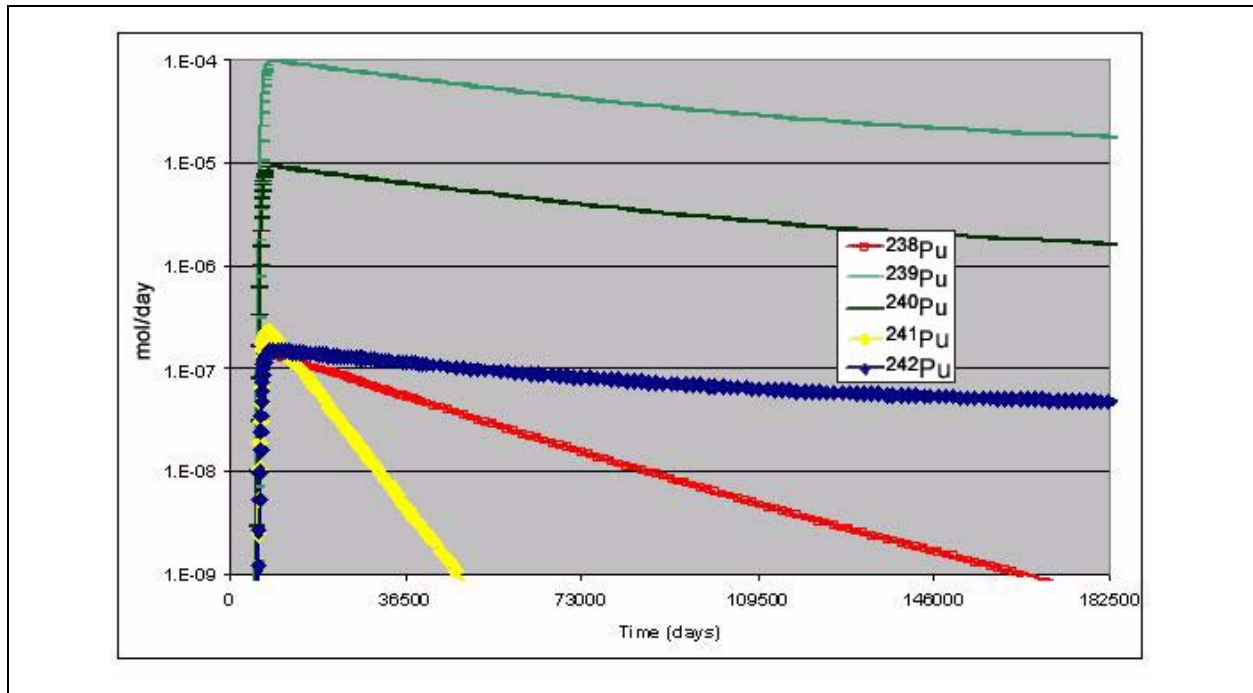


**Figure C.4-2**  
**Mean Radionuclide Source Flux Functions for Pu Isotopes from TYBO**

minerals including quartz, calcite, clay and zeolite. The TSA at this location is saturated and is highly transmissive, but is limited in aerial extent (Wolfsberg et al., 2002). As the TSA dips upward toward the water table, it intersects the BA, a lava flow system extending south of the Moat fault and off of the NTS. The TSA and BA are treated as fractured dual-porosity media.

By using the particle-tracking simulator (sptr) in FEHM, the transport path or streamline for a non-reactive and non-diffusing particle originating at the TYBO working point is first identified, as shown in [Figure C.4-3](#). The path or streamline encounters several material properties in the CAU model including TSA, BA, FCCM, and then into the TMCM subunits before finally heading southwest in the FCA ([Figure C.4-3](#)). The detailed descriptions of these HGUs and the CAU flow paths can be found in [Section 3.0](#).

With a particle path-derived streamline, the finite-element grid for the GDPM is established. [Figure C.4-4](#) presents the schematic illustration of the GDPM numerical model for the heterogeneous fractured and porous rocks. There are 1,230 nodes for the primary porosity in all zones and 12,300 matrix nodes for the secondary porosity in the fracture zones. The GDPM node resolution



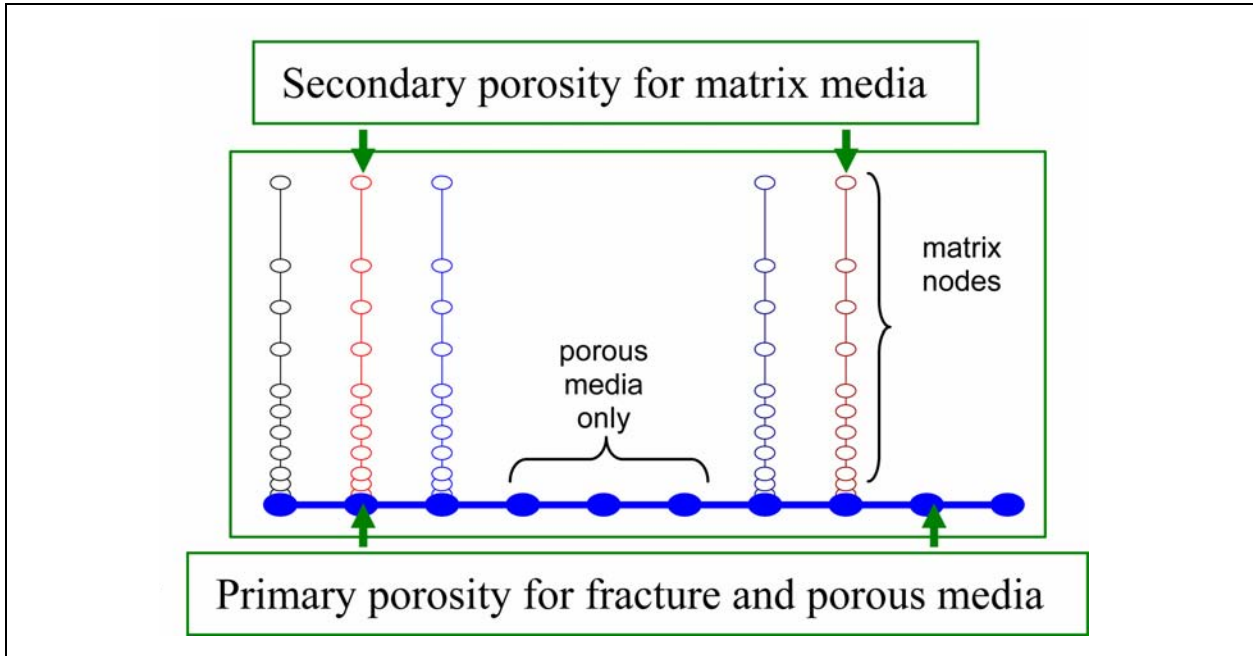


**Figure C.4-4**  
**Schematic Illustration of the GDPM Numerical Model**  
**with Heterogeneous Rock Properties**

Note: The fractured media include primary nodes and secondary matrix nodes, but the porous media include only primary nodes.

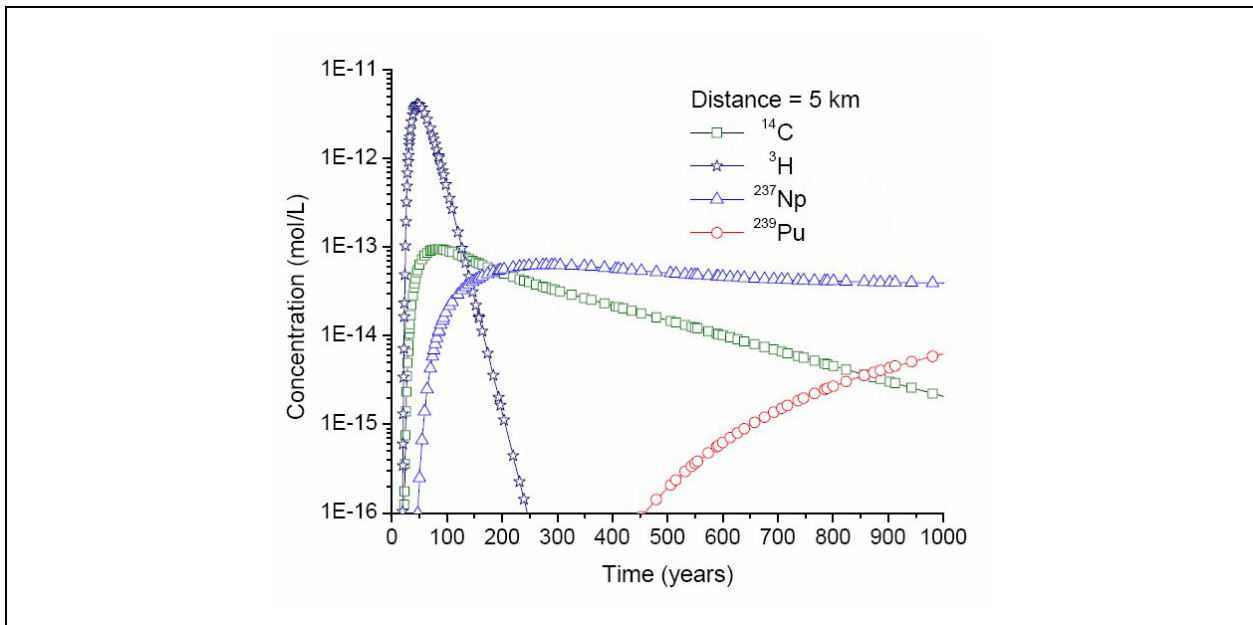


**Figure C.4-5**  
**Computed Concentration Breakthrough Curves for  $^3\text{H}$ ,  $^{14}\text{C}$ ,  $^{239}\text{Pu}$ , and  $^{237}\text{Np}$**   
**at a Distance of 5 km Away from the TYBO Source Location**

Note: It takes about 450 years for  $^{239}\text{Pu}$  to transport to 5 km with a concentration greater than  $10^{-16}$  mol/L.



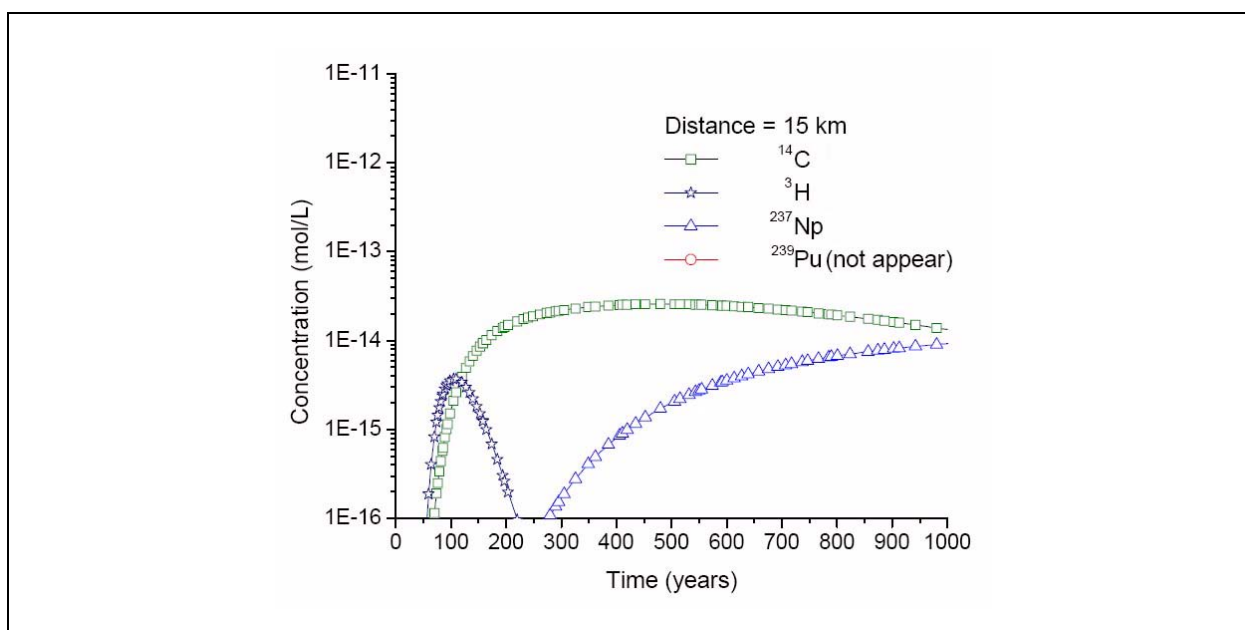


**Figure C.4-6**  
**Computed Concentration Breakthrough Curves for  $^3\text{H}$ ,  $^{14}\text{C}$ ,  $^{239}\text{Pu}$ , and  $^{237}\text{Np}$  at a Distance of 15 km Away from the TYBO Source Location**

Note: Plutonium-239 has not reached to 15 km at 1,000 years. Neptunium-237 reaches to 15 km in about 300 years with a concentration greater than  $10^{-16}$  mol/L.

200 years, while  $^{14}\text{C}$  (half-life 5,280 years) migrates as a conservative species, transporting to about 40 km in 1,000 years. With a small sorption coefficient,  $^{237}\text{Np}$  migrates to a distance of about 28 km in 1,000 years, and Pu transports to a distance about 5 km away from the source area in 1,000 years due to its larger matrix  $K_d$ . The results demonstrate that without colloids, Pu is strongly retarded and cannot transport far from the source area. It is important to note in these simulations that the results are highly conservative due to the 1-D model design. There is no transverse dispersion to spread solutes that would result in lateral spreading and reduced concentrations. Also, the wetted surface area of fractures is probably underestimated substantially. The models emulate a nearly continuous fracture, whereas in reality, fracture networks along a flow path provide increased surface area for diffusion. Uncertainty in the parameters for this field-scale model are addressed in [Section C.6.0](#), providing insight into the role of uncertainty and perhaps scaling.

#### **C.4.1.4 Colloid-Facilitated Radionuclide Transport**

With colloids present (only considering naturally occurring colloids), the sorption of Pu onto colloids occurs as a reactive process competitive with  $D_m$  of the aqueous species and sorption onto immobile

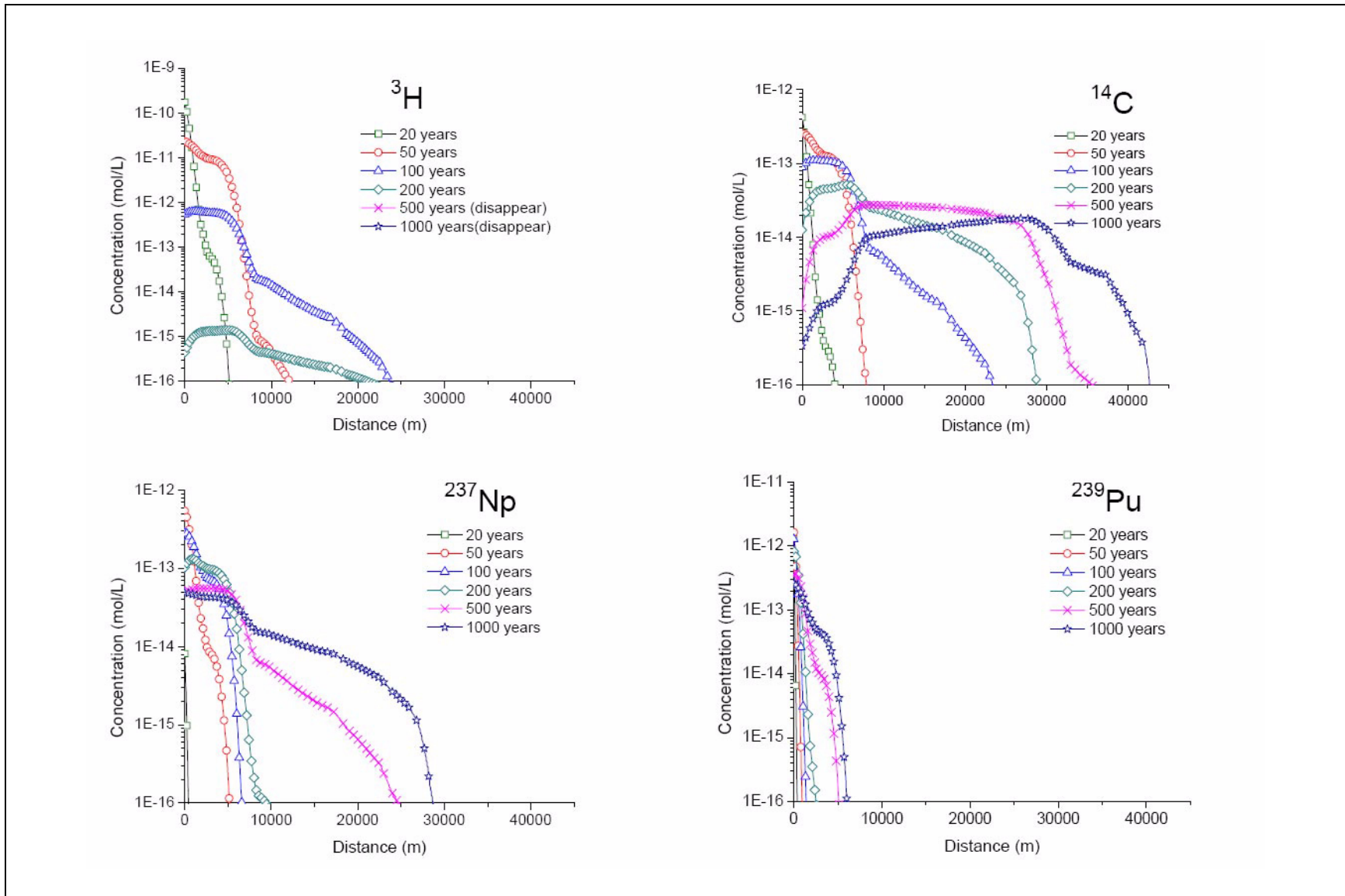


**Figure C.4-7**  
**Radionuclide Concentration Distributions at Different Transport Time**

matrix minerals. The computed concentration breakthrough curves of colloid-facilitated radionuclide transport using the parameters described in the previous section are plotted in Figures C.4-8 and C.4-9 for the nodes at 5 and 15 km, respectively, away from the TYBO source location. In this scenario, the results for  $^3\text{H}$  and  $^{14}\text{C}$  are the same as those in the first scenario. The results show early arrival and much greater concentration of Pu when colloids are present. However, these results are only demonstrative. The assumptions are conservative, with all colloids being highly mobile and large quantities of Pu(aq) available in the source-release function. Section C.6.0 addresses the mobility of the measured colloid load, showing that only a small fraction of that which is measured may be available for field-scale transport.

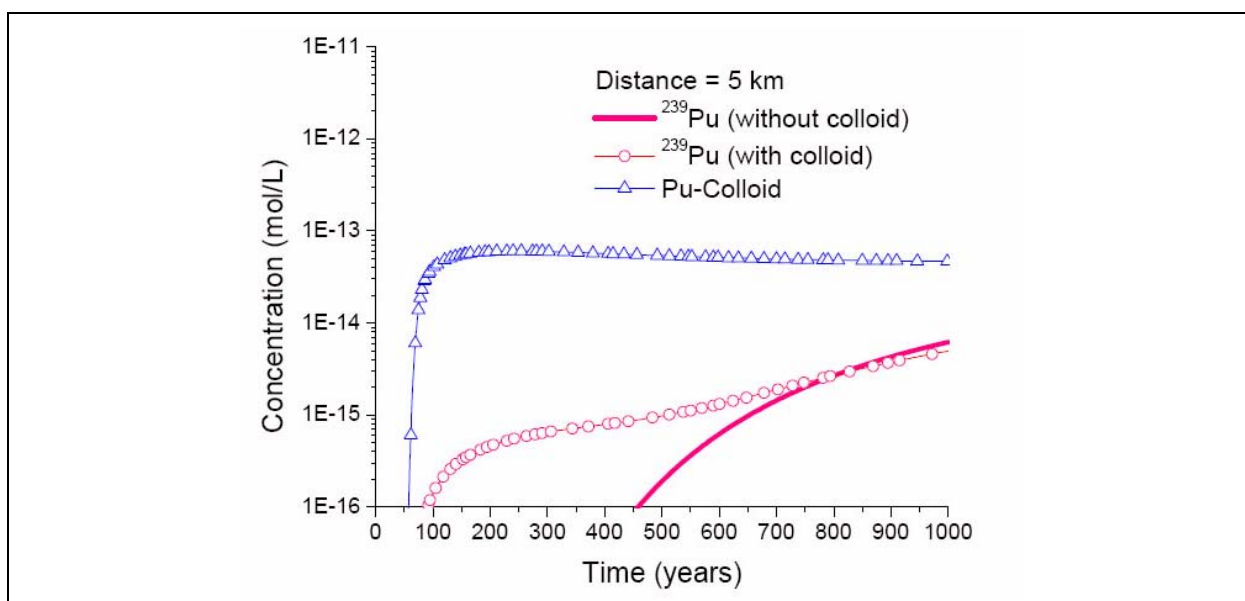


**Figure C.4-8**

**Computed Concentration Breakthrough Curves for  $^{239}\text{Pu}$  at a Distance of 5 km Away from the TYBO Source Location**

Note: First arrivals of Pu-colloid at 5 km occur after 60 years with concentrations exceeding  $10^{-16}$  mol/L. Note the SDWA standard for Pu in groundwater is approximately  $1\text{E-}12$  mol/L, and the mobile colloid load is highly conservative.

Introducing colloids into the reactive transport model has a significant influence on the computed concentrations of Pu. The total concentration of Pu is mainly from Pu-colloid because the forward rate of sorption of Pu onto colloids is so much larger than the reverse rate (Table C.3-4).

Figure C.4-10 plots the concentration distributions along the model domain at different time. In this figure, Pu transports along fractures to a distance of 34 km in 1,000 years, although at low concentrations. At about 8 km, velocities reduce locally in fault. The Pu-colloid plume only

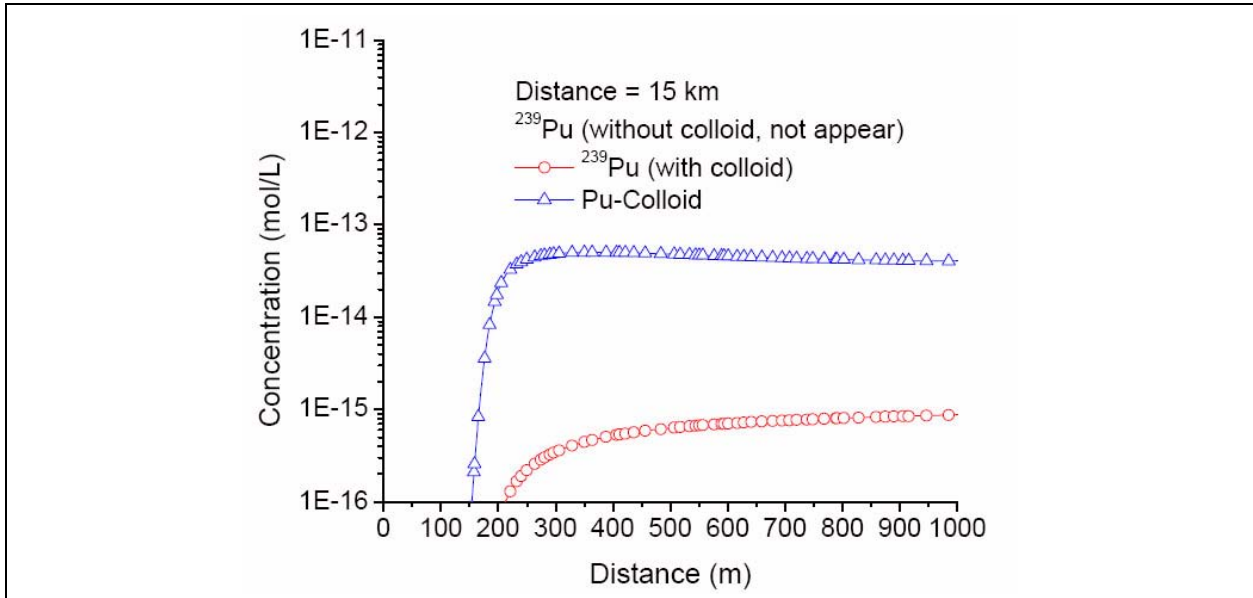


**Figure C.4-9**

**Computed Concentration Breakthrough Curves for <sup>239</sup>Pu at a Distance of 15 km Away from the TYBO Source Location**

Note: First arrivals of Pu-colloid at 15 km occur after 160 years with concentrations exceeding  $10^{-16}$  mol/L. Note the SDWA standard for Pu in groundwater is approximately  $1E-12$  mol/L, and the mobile colloid load is highly conservative.

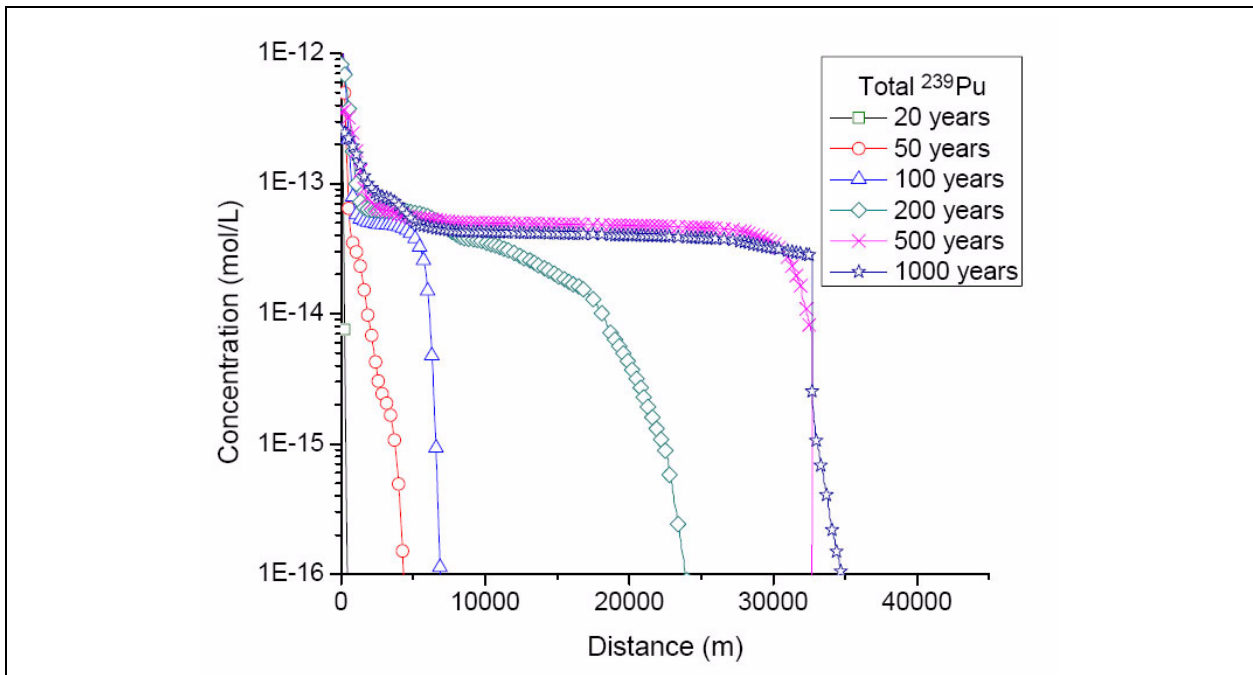


**Figure C.4-10**

**Simulated Total Pu Concentration (Aqueous and Colloidal) Distributions for the Colloid-Facilitated Radionuclide Transport Model at Different Times**

advances beyond the fault after slow migration through the fault zone, after 100 years. The impact of faults and associated reduced velocity with changes from fracture to matrix flow on aqueous species migration is shown later in this appendix for source releases at PURSE.

The calculations presented in [Figures C.4-5](#) through [C.4-10](#) show the simulated migration along the GDPM streamtube, extracted from the 3-D flow field, for non-reactive, reactive, and colloidal species. They highlight the role colloids may play in enhancing mobility of reactive species such as Pu, where sorption becomes competitive between mobile and immobile minerals. Clearly, the results will be highly sensitive to the reaction parameters. [Section C.6.0](#) addresses the sensitivity to these uncertainties.

#### **C.4.1.5 Plutonium Isotopes and Daughter Products**

This section assesses decay and in-growth of radionuclides on their transport from TYBO. The decay and in-growth of radionuclides may have geochemical implications for the migration of radionuclides away from source area. It becomes important to understand the evolution of the radionuclides in terms of effects on their mobility and abundance in the fractures and matrix that are created by decay and in-growth processes. On the other hand, analyzing these decay and in-growth processes may simplify the transport models by determining which in-growth is unimportant.

First, the relative importance of the Pu isotopes transported along the streamline is tested. By including the colloid-facilitated transport of all Pu isotopes and also including decay and in-growth of these isotopes (see [Table C.2-1](#)), the concentration breakthrough curves of aqueous Pu and Pu-colloid for all Pu isotopes are computed ([Figures C.4-11](#) and [C.4-12](#)). The total concentration of Pu is almost the same as the concentration of  $^{239}\text{Pu}$ -colloid, because  $^{239}\text{Pu}$  has a source concentration about two orders of magnitude larger than other Pu isotopes and a very large half-life (about 24,100 years). On the other hand,  $^{241}\text{Pu}$  and other Pu isotopes have relatively short half-lives and much lower source concentration. They contribute little to the total concentration of Pu. These results indicate that  $^{239}\text{Pu}$  can be used as the indicator species for Pu transport simulation, recognizing that the activity of the other isotopes increases with decreasing half-life. However, whereas  $^{241}\text{Pu}$  has an activity nearly 500 times greater than  $^{239}\text{Pu}$ , its simulated concentration is more than 1,000 times lower. Similar arguments hold for the other isotopes.

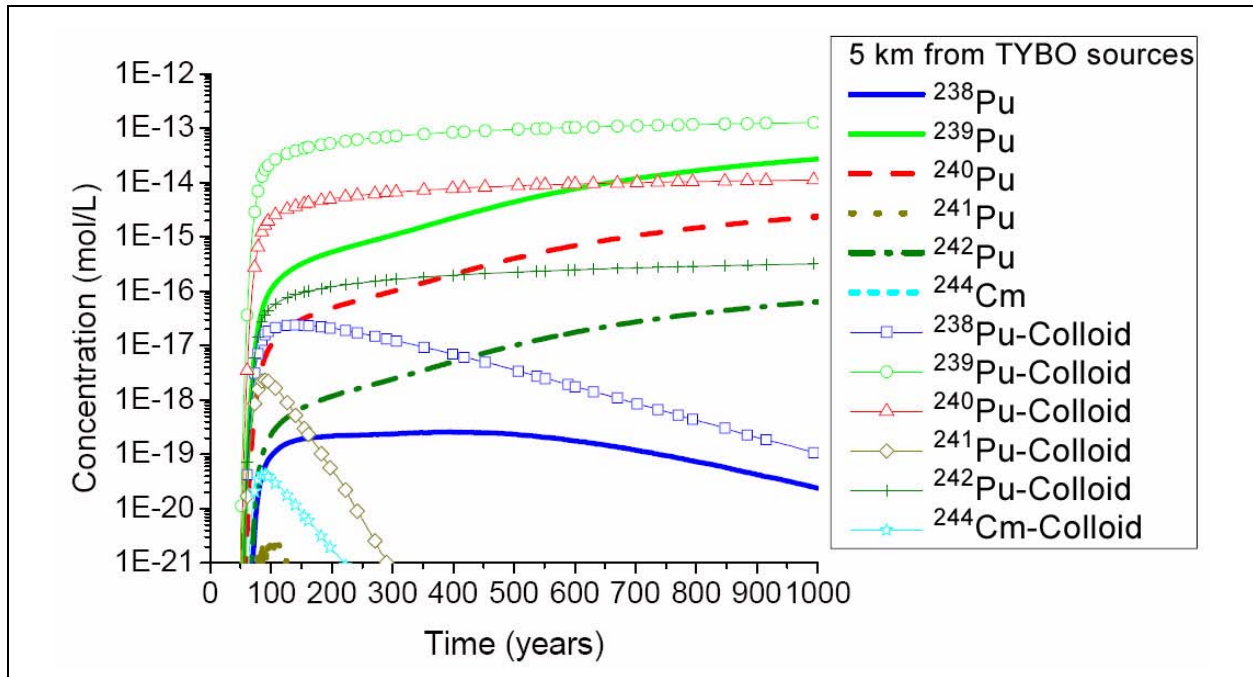


Figure C.4-11

**Concentration Breakthrough Curves of Pu Isotopes for Colloid-Facilitated Transport at 5 km Away from the TYBO Source Area**

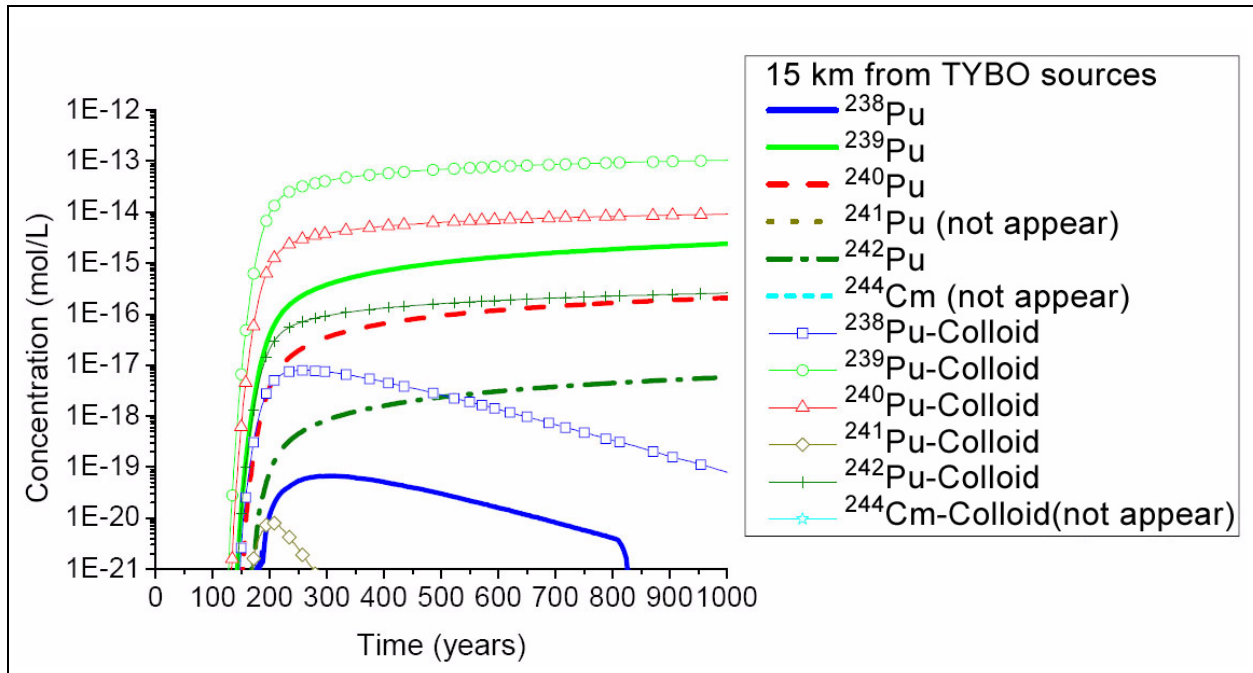


Figure C.4-12

**Concentration Breakthrough Curves of Pu Isotopes for the Colloid-Facilitated Transport at 15 km Away from the TYBO Source Area**

Next, the importance of two decay chains is tested:  $^{241}\text{Pu} \rightarrow ^{241}\text{Am} \rightarrow ^{237}\text{Np}$ , and  $^{238}\text{Pu} \rightarrow ^{234}\text{U}$ . The computed total concentrations of  $^{237}\text{Np}$  in the breakthrough curves considering in-growth are almost the same as those without considering in-growth (Figure C.4-13), indicating that although  $^{241}\text{Pu}$  and  $^{241}\text{Am}$  can transport further from the source location due to colloid-facilitated transport, the decay chain  $^{241}\text{Pu} \rightarrow ^{241}\text{Am} \rightarrow ^{237}\text{Np}$  does not provide a significant component of  $^{237}\text{Np}$  to the total concentration of  $^{237}\text{Np}$  at any location, particularly when considering early arrival. The source concentration of  $^{237}\text{Np}$  is much higher than those of  $^{241}\text{Pu}$  and  $^{241}\text{Am}$ , and  $^{241}\text{Am}$  has a long half-life of 433 years. Thus, there is no significant addition of  $^{237}\text{Np}$  at the leading edge of the plume ahead of aqueous Np migration where Pu and Am might exist due to colloid-facilitated transport.

Figures C.4-14 and C.4-15 show the concentration breakthroughs of Am, Np, Pu, and U for the colloid-facilitated transport model at 5 and 15 km away from TYBO source area, by considering the decay and in-growth processes. In Figures C.4-13 through C.4-15, the Np breakthrough curve occurs sooner than the colloidal Pu and Am curves. Two factors contribute to this simulated behavior. First, the SSM produces earlier entry into the CAU aquifers of Np(aq) than Pu(aq), which is earlier than Am (aq). The staggering of the entries of these species is due to the SSMs accounting of sorption in the source region. Americium has a larger  $K_d$  than Pu, thus leading to a later release from the source region. Only after entering the aquifer in this model can the reactive species sorb to colloids. Second, Pu and Am sorption to colloids is modeled with the same forward kinetic rate (Table C.3-4). However, Am's much larger sorption coefficient enables the immobile minerals to compete more strongly for Am(aq) than for Pu(aq), leading to later arrival times for Am as a colloidal species in these simulations. The impact is minor, as shown in Figure C.4-13, with slightly earlier arrivals of Am when the decay chain is considered as a result of migration of Pu and then the subsequent decay to Am.

## C.4.2 PURSE

This section extends the simulations presented in the previous section, but for source releases at the PURSE test (Figure C.4-3).

### C.4.2.1 Source Terms of PURSE

The radionuclide source-release terms were derived from the 100 realizations of the PURSE test simplified source-release function (Appendix B). These realizations are used to compute the mean of

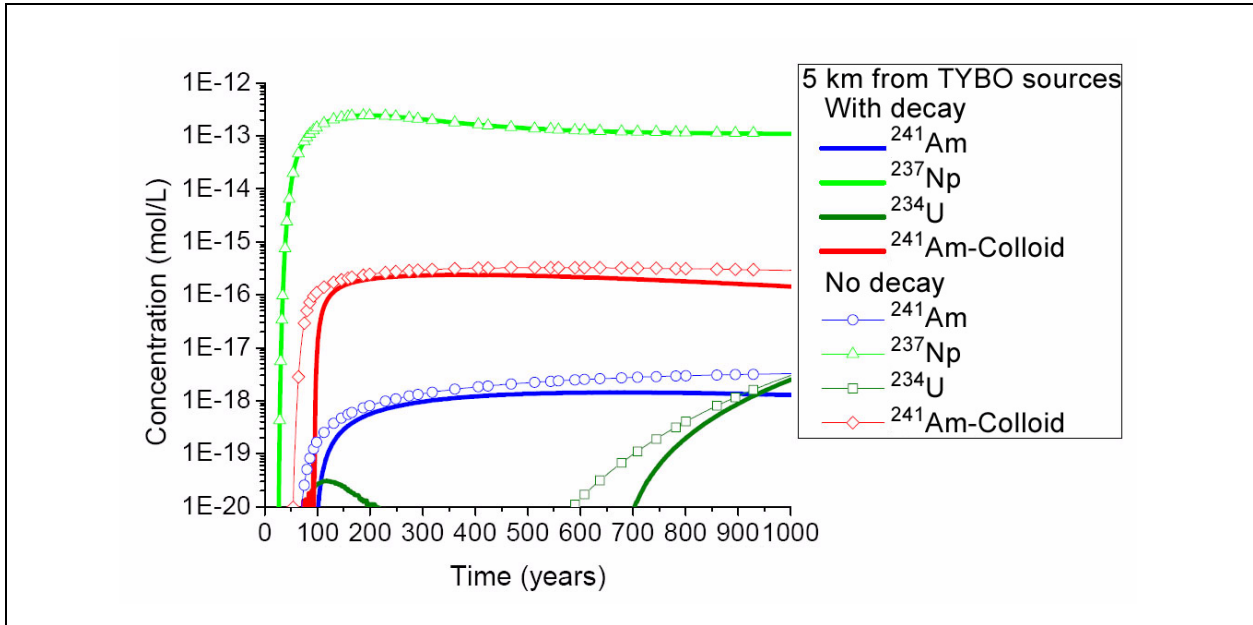


**Figure C.4-13**  
**Concentration Breakthrough Curves of Am, Np, and U for the Colloid-Facilitated Transport at 5 km Away from the TYBO Source Area, by Considering and Omitting the Two Decay Chains**

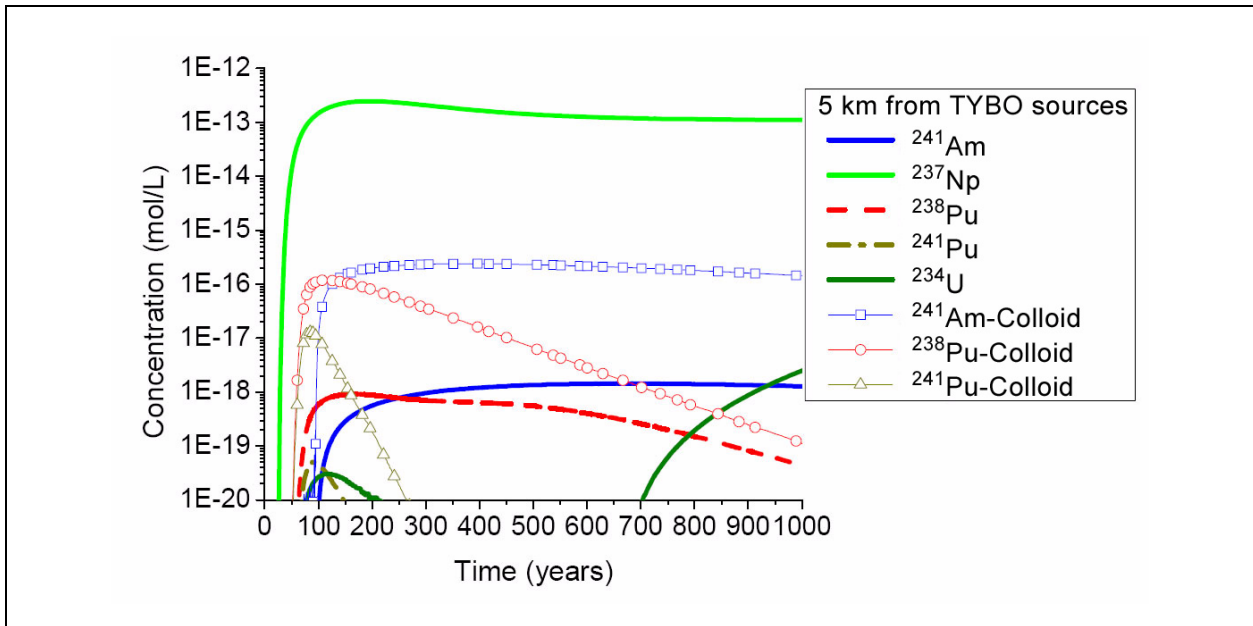


**Figure C.4-14**  
**Concentration Breakthrough Curves of Am, Np, Pu, and U for the Colloid-Facilitated Transport at 5 km Away from the TYBO Source Area, by Considering the Decay and In-growth Processes**



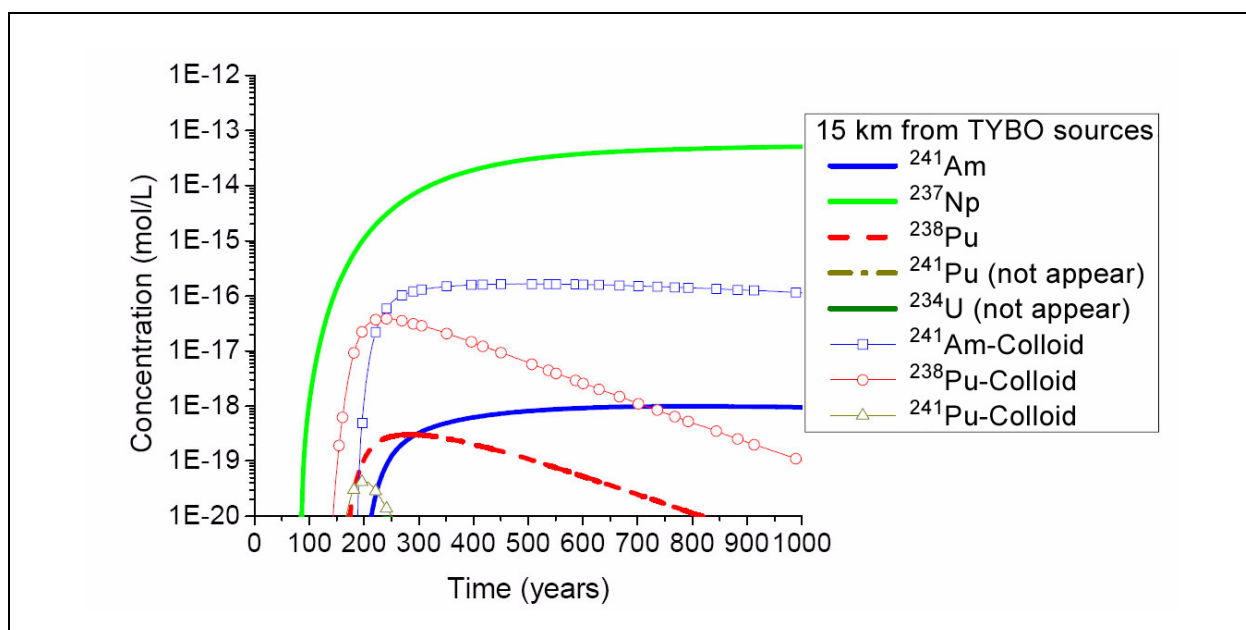


**Figure C.4-15**

**Concentration Breakthrough Curves of Am, Np, Pu, and U for the Colloid-Facilitated Transport at 15 km Away from the TYBO Source Area, by Considering the Decay and In-growth Processes**

the source release function for the GDPM simulations presented here. [Figure C.4-16](#) presents the mean radionuclide source terms for PURSE included in these reactive transport models. As with TYBO, these are scaled by the ratio of the streamtube cross-sectional area to the cross-sectional area of the estimated cavity for the test, computed from maximum unclassified announced yield.

#### **C.4.2.2 Streamline from PURSE Sources Area**

The PURSE test is located in northwestern Area 20 on Pahute Mesa. The elevation of the working point is 1,257 m, within the UPCU, a zeolitic bedded tuff. However, the cavity intersects the highly permeable TCA, a WTA composed of moderately welded ash-flow tuff, which belongs to the DMP RMC. Fractures in the TCA are well developed.

By using the particle-tracking simulator (sptr) in FEHM, the transport path or streamline for a non-reactive and non-diffusing particle originating in the TCA was simulated, shown in [Figure C.4-17](#). The path or streamline encounters several material properties in the CAU model including alternative units of WTA (DMP, in blue), VTA (VMP, in green), TCU (ZEOL, in red) and more (see [Figure C.4-17](#)). The detailed descriptions of these HGUs and the RMCs can be found in

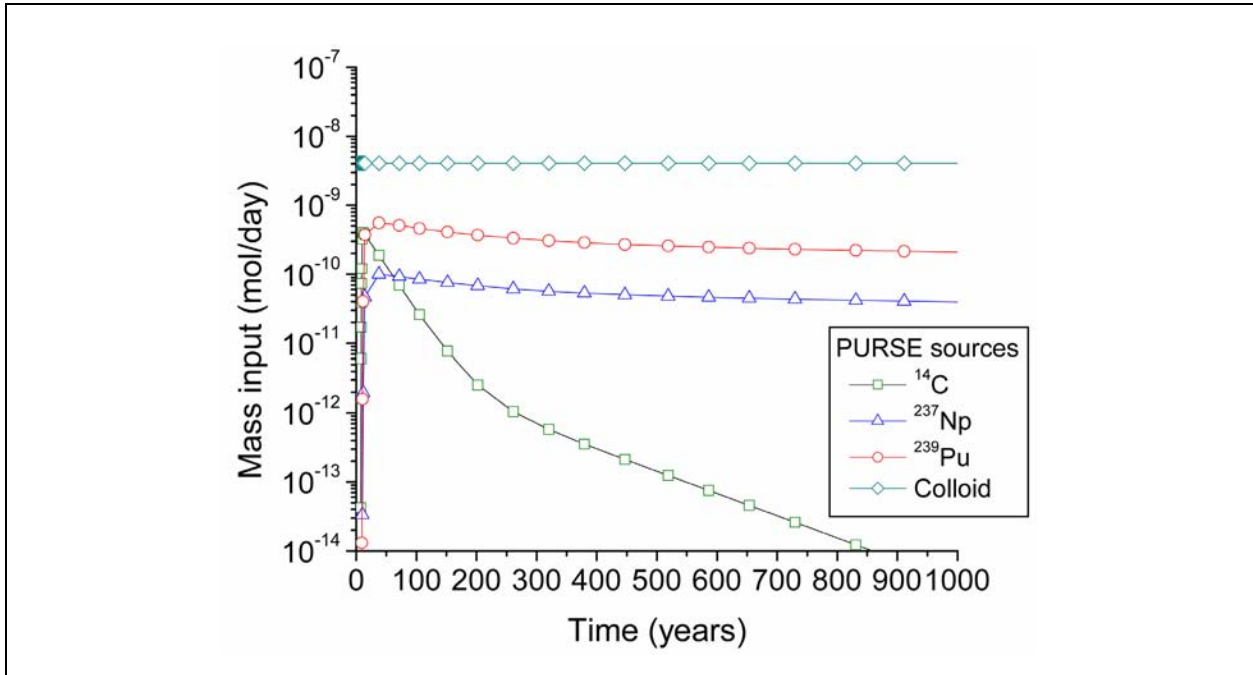


**Figure C.4-16**  
**Mean Radionuclide Source Flux Functions for PURSE**

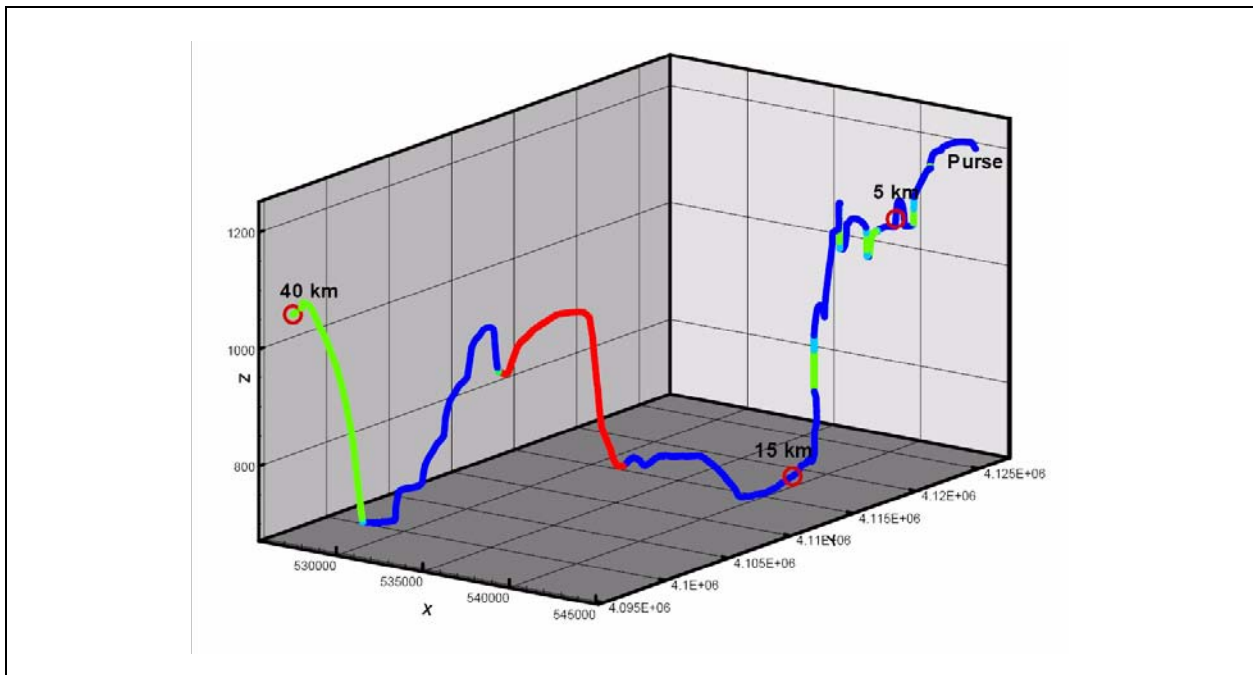


**Figure C.4-17**  
**3-D Streamline for the Non-reactive and Non-diffusing Particle Transport from the PURSE Source Area**

Note: The different colors represent the property zones in the model (WTA/DMP in blue, VTA/VMP in green, and TCU/ZEOL in red).

Section 3.0 and Appendix A. With the particle-derived streamline, a finite-element grid for the GDPM is established. There are 1,146 nodes for the primary porosity of all units, with spacing and cross-sectional area varying according to velocity to preserve streamtube flux and 9,440 matrix nodes for the secondary porosity of fractured units, with spacing increasing from 0.001 m near to the fracture nodes to almost 0.5 at the boundary representing the available matrix volume for the specified fractured porosity. As described above, this streamtube represents a mixed dual-porosity and single-continuum pathway at the field scale for fractured and unfractured zones, respectively.

#### **C.4.2.3 Colloid-Facilitated Radionuclide Transport**

This simulation applies five kinetically controlled reactions to examine the competitive interactions between Pu, colloids, and immobile matrix minerals as Pu sorption onto the rock matrix and colloids, and colloid and Pu-colloid filtration (attachment and detachment processes). Neptunium sorption onto the matrix after diffusion is also considered for comparison (see Table C.3-1). The flow velocity in this area is very low, thus favoring the desorption of Pu from the colloids and sorption of Pu on immobile minerals in the competitive reaction environment. The computed concentration breakthrough curves of  $^{14}\text{C}$  and Np at a distance of 5 km from the PURSE source location are plotted in Figure C.4-18, which shows that it takes about 350 years for  $^{14}\text{C}$  to arrive at a distance of 5 km, and 720 years for Np to arrive at that distance with concentrations greater than  $10^{-18}$  mol/L. This threshold is lower than what was used for TYBO because the source release for PURSE has much lower mass flux for all nuclides as compared to TYBO. Even though colloid-facilitated transport is applicable for Pu, it still cannot transport 5 km from the source location due to the very low flow velocity in this area.

Figure C.4-19 plots the final concentration distributions along the model domain at 1,000 years. In Figure C.4-19,  $^{14}\text{C}$  transports to a distance of about 8 km, Np transports to a distance of about 7 km, and colloidal Pu transports to a distance of about 4 km, all distance defined by the low threshold of  $10^{-18}$  mol/L. The heterogeneity of rock properties has a large impact on radionuclide transport. In fractured rock such as WTA, the radionuclides can transport faster, while in porous matrix such as VTA or VMP, they are sorbed by the matrix and they transport slowly due to large effective porosities. The abrupt changes in  $^{14}\text{C}$  concentration can be attributed to the limited time of release. At this snapshot in time (1,000 years), the concentration increases gradually along the first fractured

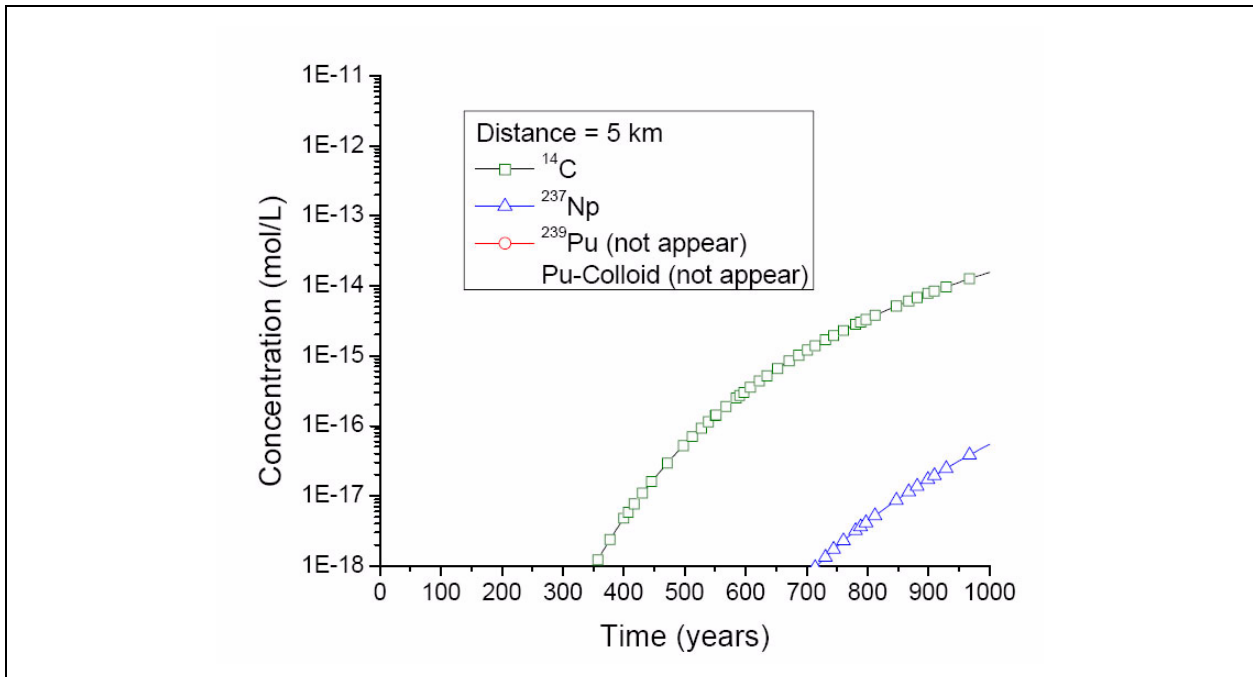


**Figure C.4-18**  
**Concentration Breakthrough Curves of  $^{14}\text{C}$ , Np, and Pu for Colloid-Facilitated Transport at 5 km Away from the PURSE Source Area, by Considering the Decay and In-growth Processes**

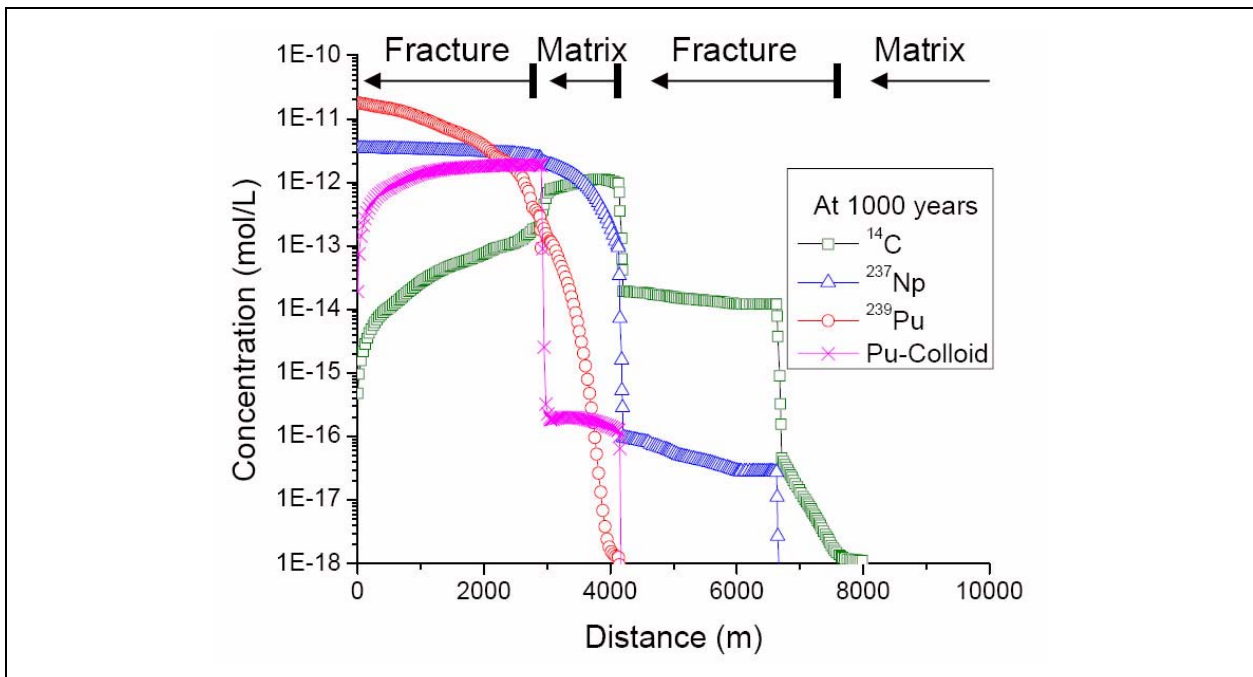


**Figure C.4-19**  
**Final Concentration Distributions for Radionuclide Transport from PURSE along a GDPM Streamtube Model at 1,000 Years**

zone due to diffusion back into the fractures from the matrix in the dual-porosity model. In the matrix-only zone (between about 3,000 and 4,200 m), the majority of the source mass resides. However, this slow flow in the matrix provides a source for migration in the fracture at greater distances, where the concentration is reduced due to  $D_m$ . This behavior at the first transition is not as apparent for Pu(aq) and Np(aq) due to the continuous source release over the entire 1,000-year time frame. However, Np(aq) shows the same behavior at the second matrix-to-fracture transition, where diffusion reduces the concentration in the fractures. The Pu-colloid concentration reduction is due to the slow matrix flow at 3,000 m, which facilitates desorption of Pu from the colloids.

### C.4.3 Summary of Deterministic Transport Simulations

Following the simulations for radionuclide migration from TYBO and PURSE using the parameters tabulated in Section C.3.0, a few points are summarized as:

#### TYBO

1. In these simulations, Pu and Am sorption and desorption onto natural colloid sites are considered (with the same reaction parameters developed for Pu). These are evaluated in a competitive reaction regime where the radionuclides can react with colloid sites, diffuse from fractures into matrix material, and react with immobile minerals. Radionuclide decay and daughter products are considered.
2. Colloid-facilitated transport has an influence on the computed concentrations of Pu and Am. With colloids, Pu and Am can transport further away from the source area. However, they do not migrate as far as conservative species such as  $^{99}\text{Tc}$ ,  $^{129}\text{I}$ ,  $^{36}\text{Cl}$ , and  $^{14}\text{C}$ , as represented by  $^{14}\text{C}$  in these simulations. Americium has a stronger affinity for immobile minerals than Pu, so when both have the same reversible reaction rates with colloids, Am migration is more retarded than Pu.
3. The total concentration of Pu is approximately equal to that of  $^{239}\text{Pu}$  because of its much higher source concentrations and a very large half-life. Plutonium-241 has a relatively short half-life and much lower source concentration, and provides little contribution to the total concentration of Pu. Its concentration is small enough that its higher activity does not become an important consideration, especially at later time.
4. The decay chain  $^{241}\text{Pu} \rightarrow ^{241}\text{Am} \rightarrow ^{237}\text{Np}$  does not provide a significant portion of  $^{237}\text{Np}$  for the total concentration of  $^{237}\text{Np}$  because the source concentration of  $^{237}\text{Np}$  is much higher than those of  $^{241}\text{Pu}$  and  $^{241}\text{Am}$ , Np is relatively mobile compared to the colloid-facilitated species, it releases from the source area sooner than Pu(aq) and Am(aq), and  $^{241}\text{Am}$  has a long half-life of 433 years, thus restricting the amount of Np created within 1,000 years.

5. The variability of rock properties along the flow path has a large impact on radionuclide transport from TYBO. In fractured rock such as WTA, the radionuclides transport faster, while in porous material such as VTA, velocities are lower and sorption to immobile minerals is favored, leading to much slower migration.

### **PURSE**

1. Migration rates from PURSE are lower than from TYBO because the area around the PURSE source consists of high-porosity porous matrix (VTA) with a small hydraulic gradient. In the 1,000-year simulation period, the non-reactive tracer  $^{14}\text{C}$  transports to a distance of 8 km, and the weakly sorbing species  $^{237}\text{Np}$  transports to a distance of about 7 km, based on a low threshold of  $10^{-18}$  mol/L as compared to the  $10^{-16}$  mol/L threshold for TYBO.
2. Plutonium transport processes from PURSE include Pu sorption onto the immobile minerals in the porous matrix, and onto natural colloids, colloid, and Pu-colloid filtration to the fracture walls and matrix in unfractured zones, as modeled with attachment and detachment rates.
3. The simulation results indicate that even though the colloid-facilitated transport is applied to Pu, its migration rates are hindered due to the high sorption of Pu onto the high-porosity matrix and a very low flow velocity in this area, which facilitates desorption of Pu from colloids. The Pu transport bound is about 4 km in 1,000 years.

## **C.5.0 SCALE DEPENDENCE OF RADIONUCLIDE SORPTION: KINETICS VERSUS EQUILIBRIUM**

Radionuclide sorption onto minerals is related to the variability of the sorption coefficients in the rock mineral facies (Zavarin et al., 2004) and the solute transport velocity. Without an applicable upscaling rule, the parameters controlling sorption under field conditions usually are approximated by the values derived from batch or column experiments. There is a need to consider how to characterize the sorption processes from the column scale to those at the scale of the model grid blocks. This is partially addressed in [Section 6.0](#), where heterogeneities in physical and chemical processes at scales smaller than the CAU model grid block are addressed. Here, the sorption formulation is considered as either equilibrium or kinetic controlled, and the scales of applicability are examined. First, the transport parameters for non-reactive and reactive solutes transport in column-scale experiments are estimated. Then the sorption processes (kinetic or equilibrium) at the field scale are tested. A theoretical basis for upscaling the sorption process to effective field-scale sorption parameters is also provided.

### **C.5.1 Identifying Sorption Processes from Column Experiments**

The column-scale fracture transport experiments conducted by Ware et al. (2005) involve seven radionuclides ( $^3\text{H}$ ,  $^{14}\text{C}$ ,  $^{90}\text{Sr}$ ,  $^{137}\text{Cs}$ ,  $^{233}\text{U}$ ,  $^{237}\text{Np}$ , and  $^{239}\text{Pu}$ ) and numerous geologic samples from both the TCU and the LCA in Yucca Flat. The parameter estimates for Yucca Flat volcanic tuffs are assumed to be applicable, at least with regard to trends and processes, to the volcanic tuffs of Pahute Mesa. In this section, by using the experimental data for  $^3\text{H}$ ,  $^{233}\text{U}$  and  $^{237}\text{Np}$ , a stepwise inversion is applied to estimate the transport parameters and fit the multiple experiments simultaneously with PEST (Doherty, 2005). Much more importantly, the radionuclide sorption processes (kinetic or equilibrium) are also identified during the inverse progression. Aqueous Pu migration parameters are not considered in this section because Ware et al. (2005) identified an unplanned colloidal component facilitating Pu migration in the experiments on tuff cores. The Np and U are unaffected by the colloid presence in the experiments.

### Step 1: Estimating the General Transport Parameters from Four Experiments

The first step is to estimate the general transport parameters, including mean residence time ( $\tau$ ), Peclet number ( $Pe$ ), fracture aperture ( $b$ ), and  $D_m$  coefficient of  $^3\text{H}$  by simultaneously fitting the four breakthrough curves of  $^3\text{H}$  from the four experiments on core UE-7az-1770 described by Ware et al. (2005). This core is a fractured volcanic tuff sample from the tuff confining unit of Yucca Flat. Coming from a different CAU, the rock parameters and  $D_m$  coefficient estimated for this sample are not directly used in the PM CAU model; rather, this experiment is used to validate the model and to quantify other parameters such as sorption and colloid-facilitated transport parameters. The effective  $^3\text{H}$  diffusion coefficient is a function of the diffusion coefficient in free solution and the tortuosity of the medium (Rowe et al., 1988). Reimus et al. (1999) reported a  $D_m$  for  $^3\text{H}$  in the range of  $0.7 - 1.2 \times 10^{-9} \text{ m}^2/\text{s}$  for a fractured tuffaceous rock. By considering all other published data (e.g., Gillham et al., 1984; Young and Ball, 1998), the  $^3\text{H}$  diffusion coefficient for this study was bounded in the inverse modeling to a range between  $0.3 \times 10^{-9} \text{ m}^2/\text{s}$  and  $1.2 \times 10^{-9} \text{ m}^2/\text{s}$ .

In this step, the four  $^3\text{H}$  breakthrough curves from two high- and two low-flow experiments are coupled. The ratio of  $\tau$  values is constrained to be exactly the ratio of flow rates between experiments. The basic transport parameters ( $\tau$ ,  $Pe$ , and fracture aperture  $b$ ) and the  $^3\text{H}$  diffusion coefficient are estimated simultaneously. The estimated results are presented in [Table C.5-1](#) and [Figure C.5-1](#). Any one of the experimental curves can be fit better than is shown in these figures, when not constrained to simultaneous inversion of all four experiments. However, individual fits do not preserve invariant rock properties, which amounts to folding other processes not parameterized in the model into the fit parameters. Simultaneous inversion weights each of the experiments equally, finding the best parameters for the tracer and rock material tested.

From a value of  $2.4 \times 10^{-9} \text{ m}^2/\text{s}$  for  $^3\text{H}$  diffusion in water and an estimated of  $1.2 \times 10^{-9} \text{ m}^2/\text{s}$ , a dimensionless tortuosity factor of 0.5 for this tuffaceous core is computed. As described above, the physical properties of the Yucca Flat sample are not used directly in the PM model. The relationship of  $D_m$  to Pahute Mesa rock porosities and the distribution used in the CAU model are discussed in [Section 6.0](#). The mean residence time for high-flow experiments is  $4.76/4 = 1.2$  hr. In each case,  $\tau$ , a parameter that reflects velocity, is most directly related to first arrivals. Each of these experiments are conducted on the same core. The observed results for similar flow rates differ because the input pulse volumes differ in each experiment. These are captured in the numerical simulations. With the



**Table C.5-1**  
**Inverse Modeling of Four <sup>3</sup>H Breakthrough Curves**  
**from Four Fractured Tuffaceous Rock Experiments**

Parameters		Estimated Values	95% Confidence Intervals	
$\tau_{low\ flow}(\text{hr})^{-1}$		4.76	1.06	8.46
$Pe$		1.41	0.98	1.83
$b$ (cm)		0.024	0.016	0.032
<sup>3</sup> H	$Dm$ (m <sup>2</sup> /s)	1.2E-09	0.3E-09	3.2E-09
	$\frac{\phi}{b}\sqrt{D_m}$ (hr <sup>-0.5</sup> )	3.14	--	--

1-  $\tau_{high\ flow}$  constrained to be  $\tau_{low\ flow}/4$

Note: Flow rate 0.5 and 2.0 mL/hr.

-- = Not applicable

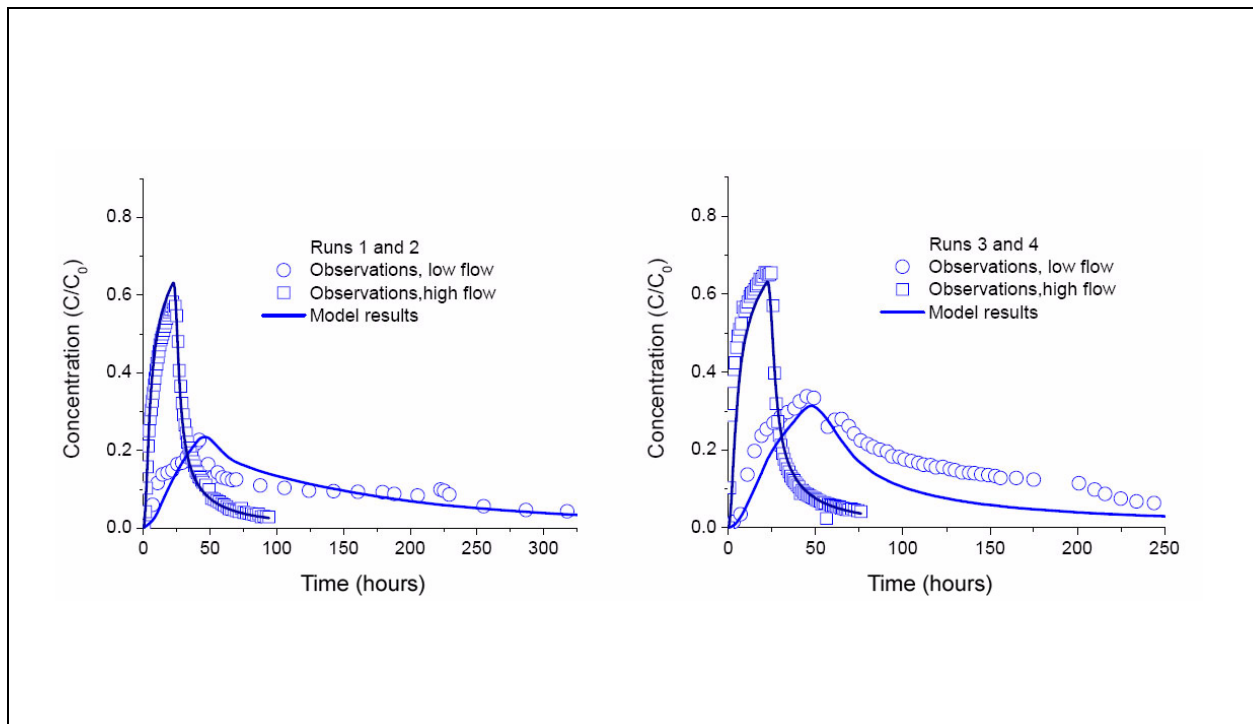


**Figure C.5-1**  
**Fitting Four <sup>3</sup>H Breakthrough Curves from Four Fractured Tuffaceous**  
**Rock Experiments**

$Pe$  values estimated, dispersivity is on the order of the column length. Dispersivities of such scale for laboratory experiments have been documented (e.g., Zhang et al., 2007) and may also be attributed to multidimensional processes in the complex fracture simulated with a 1-D model.

### Step 2: Estimating Neptunium Sorption Parameters from Two Experiments

In the second step, the basic transport parameters ( $\tau$  and  $Pe$ , the ratio of  $\tau$  values is constrained to be exactly the ratio of flow rates between experiments) from Step 1 are fixed, and estimates are computed of the Np diffusion and sorption parameters simultaneously with PEST, considering the two Np breakthrough curves from low- and high-flow experiments (Table C.5-2 and Figure C.5-2). During the inverse processes, the lower and upper bounds for  $D_m$  coefficient of Np as ( $1.0 \times 10^{-11}$ ,  $6.0 \times 10^{-10}$  m<sup>2</sup>/s) are used.

**Table C.5-2**  
**Inverse Modeling of Two Np Breakthrough Curves from Two Fractured Tuffaceous Rock Experiments**

Parameters	Estimated Values (Kinetic)	95% Confidence Intervals		Equilibrium
$D_m$ (m <sup>2</sup> /s)	5.20E-06	3.69E-06	2.15E-05	5.90E-06
$R_m$	8.27	7.13	9.42	6.64
$k_f$ (hr <sup>-1</sup> )	0.14	0.11	0.16	--
$\frac{\phi}{b} \sqrt{D_m} R_m$ (s <sup>-0.5</sup> )	0.46	--	--	0.32

Note: Flow rate 0.5 and 2.0 mL/hr.

-- = Not applicable

To identify the appropriate Np sorption process, the inverse problem under alternative scenarios is solved (e.g., [1] considering an inverse model with kinetically controlled sorption and [2] considering an inverse model with equilibrium sorption). This assessment considers Np sorption only to matrix minerals, not to fracture coating minerals, assuming that diffusion is necessary to bring the reactive solute into contact with immobile reactive surface sites. Although  $D_m$  serves to increase the contact time between solutes and matrix minerals, advective transport in the fractures dominated the critical boundary condition on the diffusion process, hence the importance of kinetics at this scale.

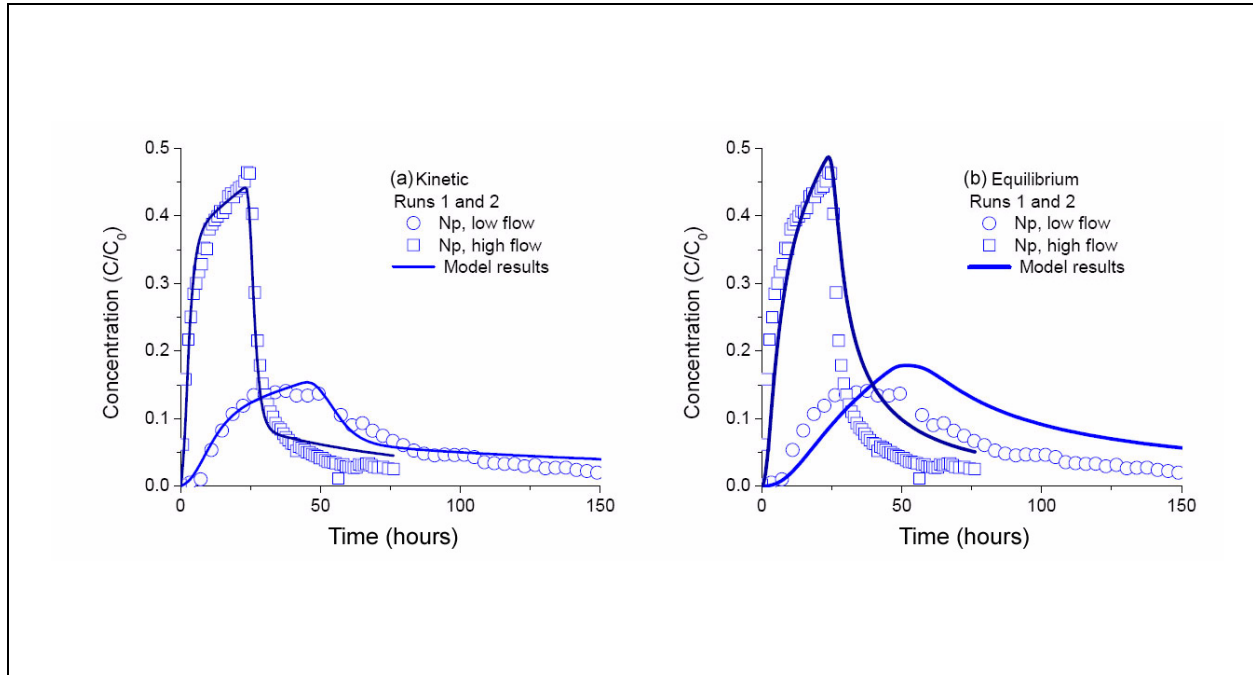


**Figure C.5-2**  
**Fitting Two Np Breakthrough Curves from Two**  
**Fractured Tuffaceous Rock Experiments**

Nonequilibrium Np matrix sorption is clearly demonstrated by the difference in model results relative to the experimental data (Figure C.5-2). The equilibrium model for Np transport cannot be fit to the breakthrough observations, and the objective function values are about 10 times larger than those obtained from kinetic sorption model. Had the early arrivals been properly captured with the equilibrium model, then the peaks would have been much higher than the data.

To confirm the sorption processes, two criteria are used — the *half time* of the sorption reaction ( $t_{1/2}$ ) and Damköhler number ( $D_I$ ) computed with Equations (C.5-1) and (C.5-2) (Hoffman, 1981; Domenico and Schwartz, 1990) — to test whether the sorption can be approximated as an equilibrium or kinetic process:

$$t_{1/2} = \frac{\ln 2}{k_{fm}} = \frac{0.693}{k_{fm}} \quad (C.5-1)$$

$$D_I = \frac{\tau}{1/k_{fm}} = k_{fm} \tau \quad (C.5-2)$$

where  $k_{fm}$  is the forward sorption rate in the matrix. If  $\tau \gg t_{1/2}$  in Equation (C.5-1), the sorption reaction approaches equilibrium; otherwise, if  $\tau \ll t_{1/2}$ , then rate-limited kinetic models are necessary to explain the state of the sorption reaction. The Damköhler number in Equation (C.5-2) represents the ratio of transport time (residence time) to chemical reaction time. If  $D_l \gg 1$ , the sorption reaction rate exceeds the transport rate and therefore the reaction can be considered fast enough to be at equilibrium (often referred as supporting the local equilibrium assumption [LEA]). Conversely, if  $D_l \ll 1$ , the reaction is slower than the transport rate and therefore should be described by kinetics.

Table C.5-2 lists the estimated parameters for the model results shown in Figure C.5-2. The estimated  $k_f$  is  $0.14 \text{ hr}^{-1}$  and the mean residence time ( $\tau$ ) for the high-flow rate experiment is 1.2 hr. Thus,  $t_{1/2} = 4.95 > \tau$ , and  $D_l = 0.168 < 1$ . So, the Np sorption reaction in the high-flow experiment has not yet reached equilibrium. For the low-flow rate experiment the mean residence time ( $\tau$ ) is 4.76 hr. Now,  $t_{1/2} > \tau$  and  $D_l = 0.66 < 1$ . The two criteria indicate that the reaction is still in the kinetic state. However, at the lower flow rate, the reactions are much closer to equilibrium, a trend important to consider when field-scale processes are next evaluated. The kinetic inverse model provides much better fitting to the observation data, and its objective function is about 10 times less than that of equilibrium model. Therefore, the study concludes that the Np sorption reaction in these low- and high-flow experiments is still in the kinetic state.

### **Step 3: Uranium Sorption Parameter Estimates from Two Experiments**

This step uses the same method as Step 2 by fixing the basic transport parameters from Step 1, and estimating the U diffusion and sorption parameters simultaneously with PEST for the two U experiments from Ware et al. (2005). The sorption reaction is assumed to be kinetically controlled. The relevant field and laboratory values of U diffusion coefficients published in the literature (Shackelford, 1991) were used to determine the lower and upper bounds as  $1.0 \times 10^{-11} \text{ m}^2/\text{s}$  and  $6.0 \times 10^{-10} \text{ m}^2/\text{s}$ , respectively. The estimated U diffusion coefficient reached to the upper bound. To test the possible range of this parameter, its upper bound was extended from  $6.0 \times 10^{-10} \text{ m}^2/\text{s}$  to  $1.2 \times 10^{-9} \text{ m}^2/\text{s}$ , and the inverse model was rerun. The model estimated a large U diffusion coefficient of  $9.26 \times 10^{-10} \text{ m}^2/\text{s}$ , but the objective function changed little from the previous value. Therefore, the study accepts  $6.0 \times 10^{-10} \text{ m}^2/\text{s}$  as the U diffusion coefficient estimate from these experiments to be consistent with the published values (Shackelford, 1991).

The above inverse run was based on U kinetic sorption model. To identify the appropriate sorption process for this scale of experiment, the inverse problem is solved with the alternative scenario of considering equilibrium sorption. The objective function from the equilibrium model increases 40 percent to 0.1432 from kinetic model's 0.1021 (Table C.5-3 and Figure C.5-3). Because the equilibrium model cannot get fit breakthrough curves well, the study concludes that the kinetic model is more appropriate, again at this scale. The two testing criteria discussed for Np, the *half time* of the sorption reaction ( $t_{1/2}$ ) and Damköhler number ( $D_I$ ) were also used to test the sorption processes.

**Table C.5-3  
Inverse Modeling of Two U Breakthrough Curves from Two Fractured Tuffaceous Rock Experiments**

Parameters	Estimated Values (Kinetic)	95% Confidence Intervals		Equilibrium
$D_m$ (m <sup>2</sup> /s)	6.0E-10	0.3E-11	2.49E-09	7.39E-11
$R_m$	48.29	1.0	200.69	200.16
$k_f$ (1/hr)	0.488	0.001	2.070	/
$\frac{\phi}{b} \sqrt{D_m} R_m$ (s <sup>-0.5</sup> )	2.936	--	--	0.664

Note: Flow rate 0.5 and 2.0 mL/hr.

-- = Not applicable

The estimated  $k_f$  is 0.488 hr<sup>-1</sup>, and the mean residence time ( $\tau$ ) for the high-flow rate experiment is 1.2 hr. Thus,  $t_{1/2} = 1.42 \gg \tau$ , and  $D_I = 0.586 \ll 1$ . This testing confirms the inverse modeling conclusion that the U sorption reaction in the high flow experiment has not yet reached equilibrium. For the low-flow rate experiment the mean residence time ( $\tau$ ) is 4.76 hr. Now,  $t_{1/2} < \tau$  and  $D_I = 2.32 > 1$ . The two criteria indicate that for the low-flow rate experiment the sorption reaction is close to equilibrium state. Considering the inverse modeling results that the kinetic model provides much better fitting to the observation data when all tests are solved simultaneously, the study concludes that the U sorption reaction in these experiments is best simulated with kinetic model, but that an equilibrium model might be fit well only to the low-flow experiments.

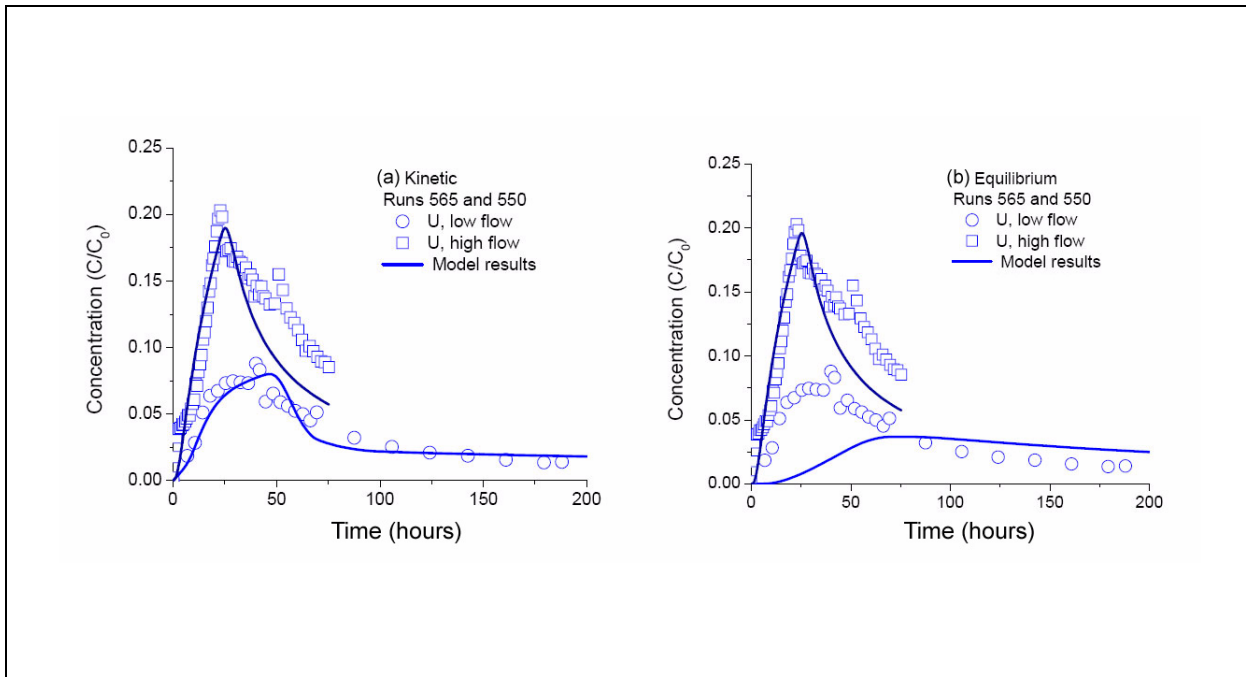


**Figure C.5-3**  
**Fitting Two U Breakthrough Curves from Two Fractured Tuffaceous Rock Experiments under (a) Kinetic and (b) Equilibrium Conditions**

### C.5.2 Identifying Sorption Processes for Field-Scale Modeling

Using the particle-tracking results obtained for the TYBO release in [Section C.3.0](#), the travel time and flow velocity in the streamtube model along the transport path can be computed. [Figure C.5-4](#) shows the computed velocity distribution in the streamtube extracted from the LCCU1-MME flow field. These are the velocities derived from the constant flux, accounting for changes in the cross-sectional area of the streamtube and changes in flowing material porosity. With these velocity data, the residence time at each node in the numerical model ([Figure C.5-5](#)) is computed and compared with the half reaction time for Np sorption, which was calculated with [Equation \(C.5-1\)](#). [Figure C.5-5](#) shows the computed Damköhler number for Np at each numerical model node. Note that the sorption coefficients and the forward rate constants are also scale-dependent, and usually they are increased with increasing scale (Rajaram, 1997). Here, the forward rate constant as listed in [Table C.5-2](#) was fixed to get a conservative estimation of the half reaction time and the Damköhler number. Even with a conservative estimation of the forward rate constant, the computed residence time at each numerical cell is much greater than the half reaction time, and the Damköhler number is much greater than 1, which implies that Np sorption at each node can be estimated with local equilibrium. With the same

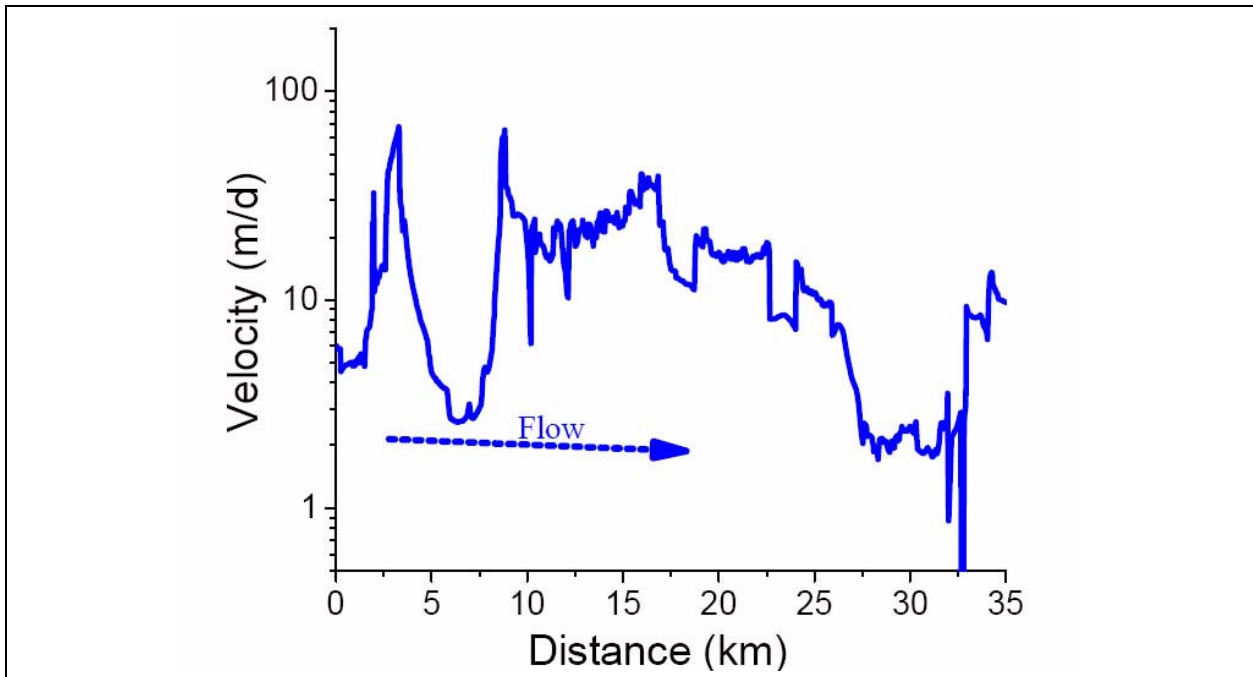


**Figure C.5-4**  
**Flow Velocity Distribution along the 1-D Streamline Starting from the TYBO Source Area**

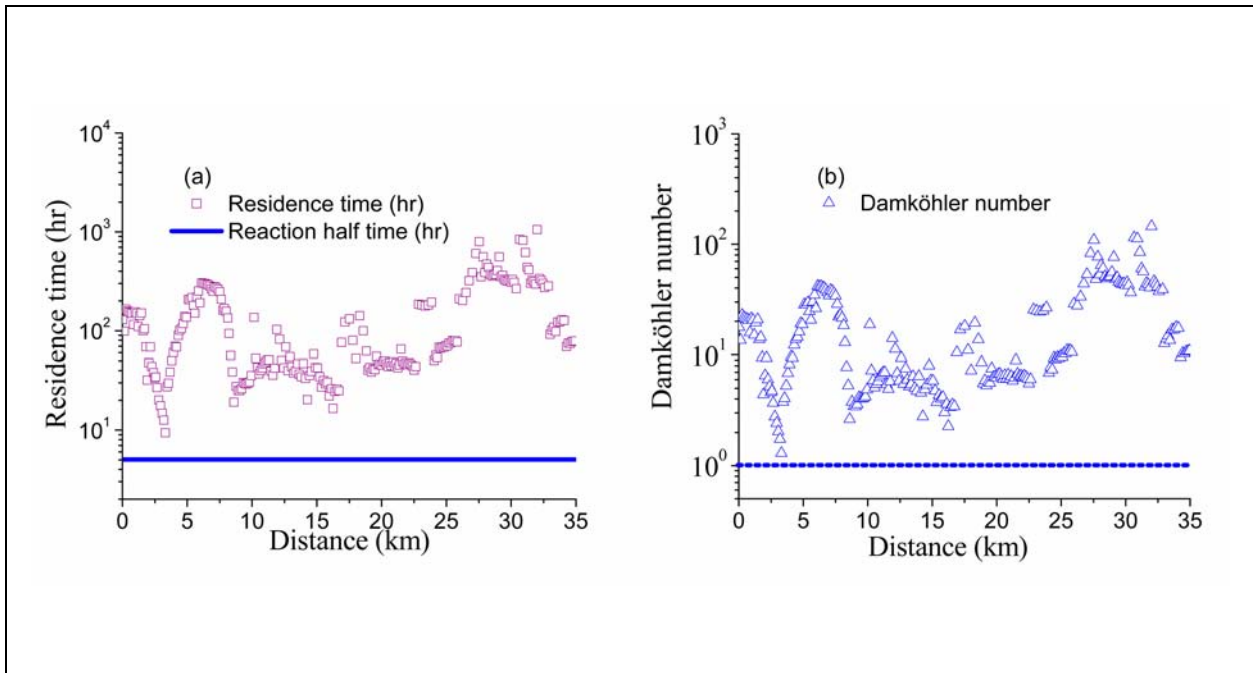


**Figure C.5-5**  
**(a) Computed Residence Time at Each Numerical Node and the Half Reaction Time and (b) Computed Damköhler Number for  $N_p$  Sorption and Transport**

flow velocity field, the half reaction time of the U sorption reaction and the Damköhler number (Figure C.5-6) was also computed. The results also imply that the U sorption at each numerical node can be approximated with local equilibrium conditions in this field site.

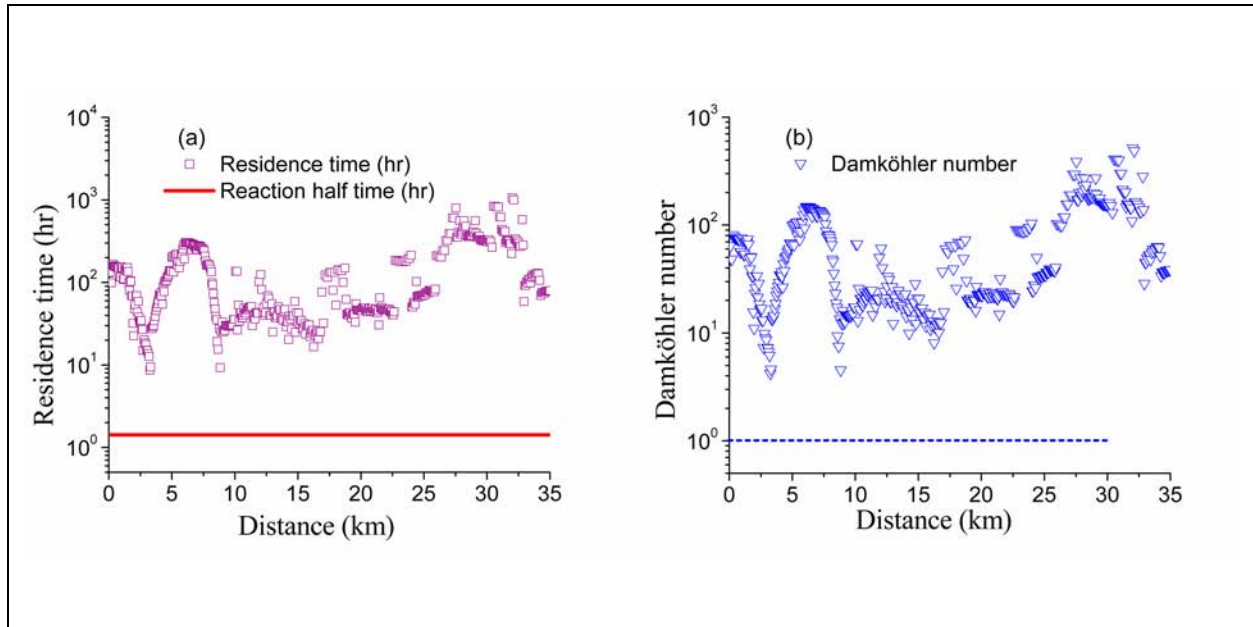


**Figure C.5-6**

**(a) Computed Residence Time at Each Numerical Node and the Half Reaction Time and (b) Computed Damköhler Number for U Sorption and Transport**



## **C.6.0 PU-COLLOID SOURCE REDUCTION: MONTE CARLO SIMULATION**

The release of colloidal radionuclides from source locations has not been addressed in HST studies and is not explicitly accounted for in the simplified source term discussed in this report. Therefore, this section uses the reactive GDPM transport model to estimate a distribution of the fraction of released aqueous Pu that sorbs to colloids and then migrates as a colloidal species. These new release functions are abstractions that represent the source Pu that can migrate as essentially irreversibly sorbed onto colloid. In the PLUMECALC CAU transport model that uses the results of this abstraction, the only parameter affecting this new abstracted species is the colloid retardation factor.

### **C.6.1 Framework of Monte Carlo Simulation**

The GDPM described in [Section C.2.2](#) is used to simulate Monte Carlo realizations of reactive radionuclide transport from TYBO. The framework for conducting the Monte Carlo simulations is described as follows:

1. Extract a streamtube from the 3-D flow model originating at TYBO.
2. Construct a highly discretized GDPM along the streamtube to simulate reactive transport in fractured and porous media.
3. Use the mean TYBO source-release function for  $^{239}\text{Pu}_{(\text{aq})}$ .
4. Develop uncertainty distributions for the following parameters:
  - *Colloid load* (in mol/L reactive sites): The study measures distributions of colloid sizes and concentrations, then reduces that by a fraction determined by percentage of total colloid load estimated to be mobile using a colloid diversity model.
  - *Fracture aperture*, which has large impact on diffusion of aqueous species from fractures to matrix; aqueous species that diffuse out of fractures cannot sorb to colloids, which remain in the fractures. Thus, the mobility of the species depends on the strengths of the two competing processes.

- *Forward rate constant* for Pu + Colloid  $\Leftrightarrow$  PuCol: (Colloids and PuCol do not diffuse out of fractures)
  - *Reverses rate constant* for Pu + Colloid  $\Leftrightarrow$  PuCol
  - *Matrix  $K_d$*  for Pu(aq)  $\Leftrightarrow$  Pu(s) in the matrix after diffusion.
5. Develop 1,000 LHS combination of parameters.
  6. Run 1,000 Monte Carlo simulations.
  7. Calculate the ratio of simulated Pu<sub>total</sub> concentration to a *Perfect Pu Tracer* (no diffusion, no sorption) at 5 km from source. This is called the *Pu Source Reduction Factor*.
  8. Develop a distribution of *Pu Source Reduction Factors*, based on the Monte Carlo results at 5 km (at 1,000 years).

Note that the *Perfect Pu Tracer* is used in this analysis. It represents transport results for a tracer that does not diffuse and does not sorb. The source function for the perfect tracer is the aqueous <sup>239</sup>Pu source release function. Thus, the results for the perfect tracer are as if *all* of the SSM <sup>239</sup>Pu attaches to colloids and migrates with no retardation or filtration. The *Pu Source Reduction Factor* is the ratio of the simulated Pu concentration (colloidal and aqueous), calculated with all competing processes, to the concentration of the *Perfect Pu Tracer*.

## **C.6.2 Parameters Created with Latin Hypercube Sampling**

### **C.6.2.1 Colloid Mobility**

The mobility of colloids has been studied by YMP within the context of colloid diversity (SNL, 2007), where they summarized a cumulative probability distribution for colloid retardation factors (R) to represent filtration, attachment, and detachment processes (Figure C.6-1). About 92 percent of the colloids have a retardation factor larger than 10,000, implying that a large portion of colloids at any location are actually quite immobile in the context of large-scale migration. Note the relationship between  $K_d$  and R in fractures is simply  $R = 1 + K_d$ , where R is unitless and  $K_d$  is in cm<sup>3</sup>/g.

To determine the portion of colloid sample described in Section C.3.0 that would be sufficiently mobile to facilitate radionuclide transport, a sensitivity analysis was conducted of the colloid retardation factor to the transport distance in 1,000 years. Using a streamtube starting from TYBO

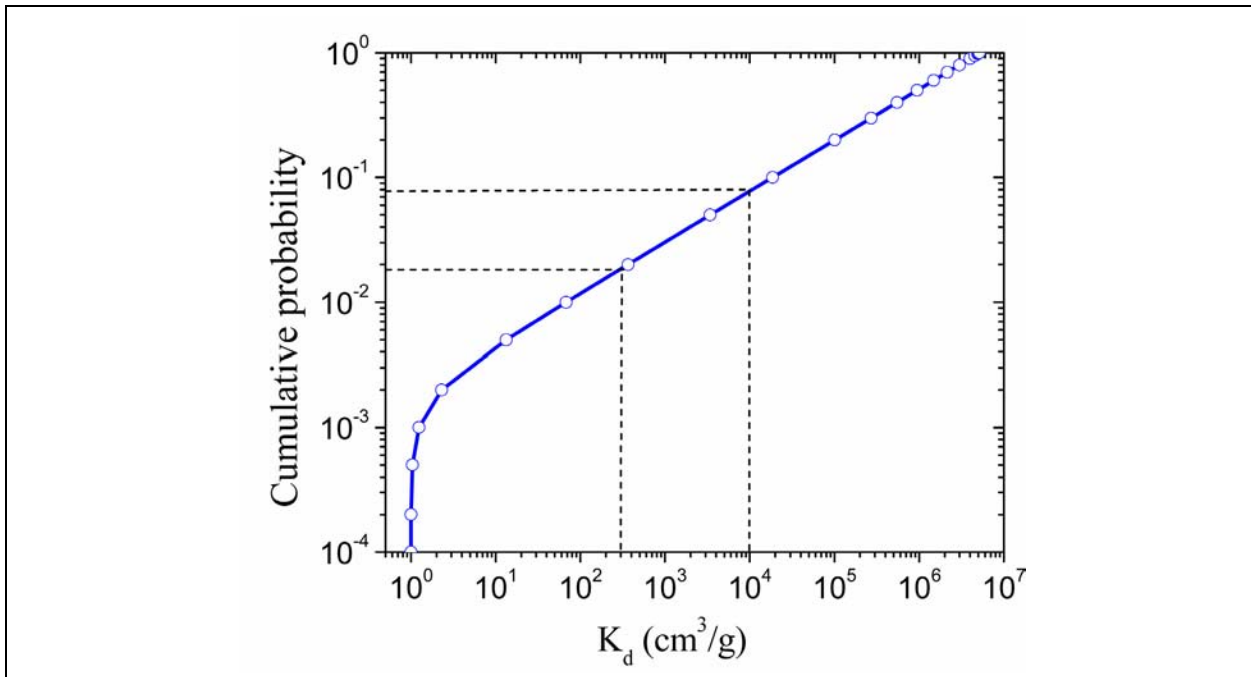


**Figure C.6-1**

**YMP Cumulative Probability Distribution for Colloid Sorption Retardation Factors Converted to Sorption Coefficients**

source within the Topopah Spring WTA, colloid transport is simulated using a source concentration of colloid sites derived in Section C.3.0 ( $2.04 \times 10^{-8}$  moles sites/L). Different colloid retardation factors (converted to  $K_d$ ) were then applied, and the colloid concentration breakthrough was computed at 8 km downgradient from the TYBO source for 1,000 years (Figure C.6-2). The results indicate that only colloids with a  $K_d$  less than  $300 \text{ cm}^3/\text{g}$  can transport to 8 km in 1,000 years, assuming a 0.5 percent of source concentration cutoff value. The study abstracts this result and assumes that colloids mobile to 8 km in 1,000 years can be treated as field-scale mobile colloids affected only by  $K_d$  between 0 and  $300 \text{ cm}^3/\text{g}$ . In fractured rock, the YMP retardation factor,  $R$ , is converted to  $K_d$  by the relationship  $R = 1 + K_d$ . In porous media, the relationship is  $R = 1 + \rho/\phi(K_d)$ , where  $\rho$  is the rock density and  $\phi$  is the matrix porosity. Here, only colloid attachment in the fracture where the bulk density and the porosity cancel is considered.

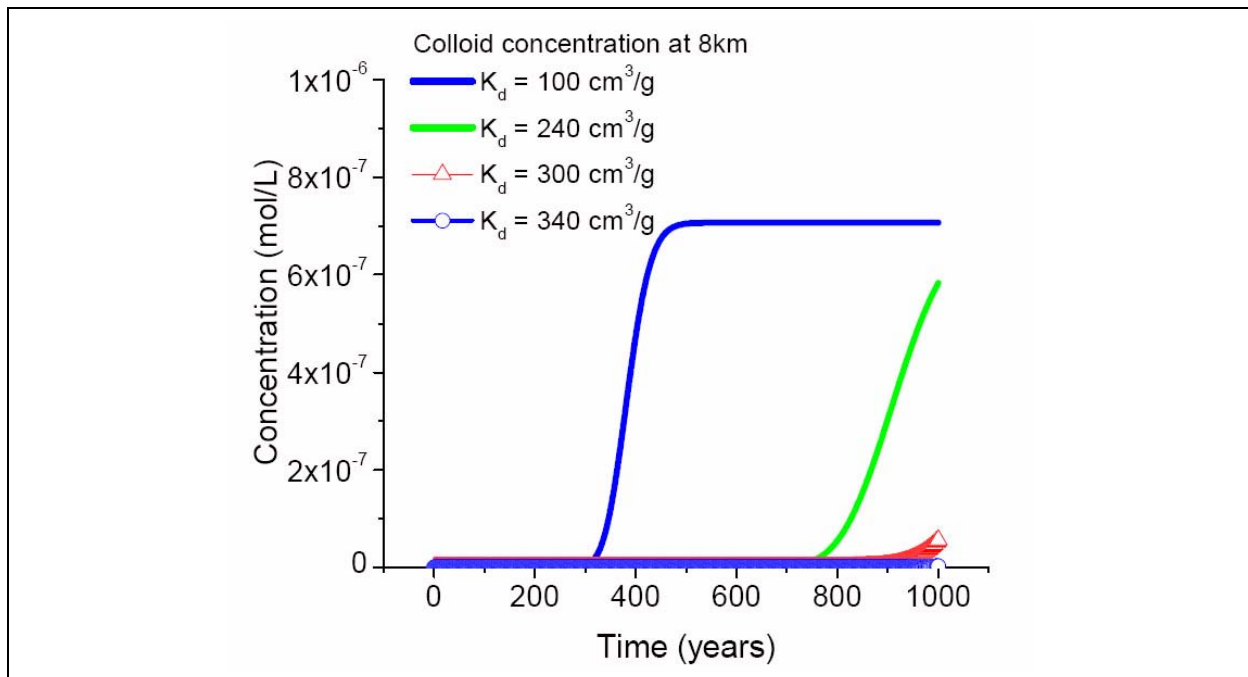


**Figure C.6-2**

**Sensitivity Analysis of Colloid Sorption Coefficient on Field-Scale Mobility**

Note: Lines show breakthrough of colloids in LCCU1-MME flow model at 8 km from TYBO for varying colloid retardation factors (represented as  $K_d$  where  $R = 1 + K_d$  for fractures). For  $R > 300$ , colloids are not sufficiently mobile to 8 km.

From the cumulative probability distribution for colloid sorption coefficients shown in [Figure C.6-2](#), the study found that only 1.5 percent of the colloids have a retardation factor less than 300 and can be treated as field-scale mobile. Then, the effective concentration of colloid sites in Pahute Mesa groundwater is recalculated by multiplying the derived concentration by this reduction factor of 0.015. Therefore, the effective mean concentration is  $3.06 \times 10^{-10}$  moles sites/L. Colloid load uncertainty is addressed by sampling from the uncertain distribution of sites from [Section C.3.0](#) ( $\mu = 2.04 \times 10^{-8}$  M,  $\sigma = 1.40 \times 10^{-10}$ ), and then multiplying the value by 0.0015. The resulting value is then specified for the initial and boundary-inflow concentrations of colloid sites. The distribution is shown in [Figure C.6-3](#).

**C.6.2.2 Monte Carlo Parameters**

Sensitivity analysis of the colloid-facilitated Pu reactive transport models demonstrate that the reactive transport models extracted from the streamtubes are most sensitive to the parameters of (1) colloid load concentrations, (2) Pu-colloid kinetic rate constants (forward and reverse),

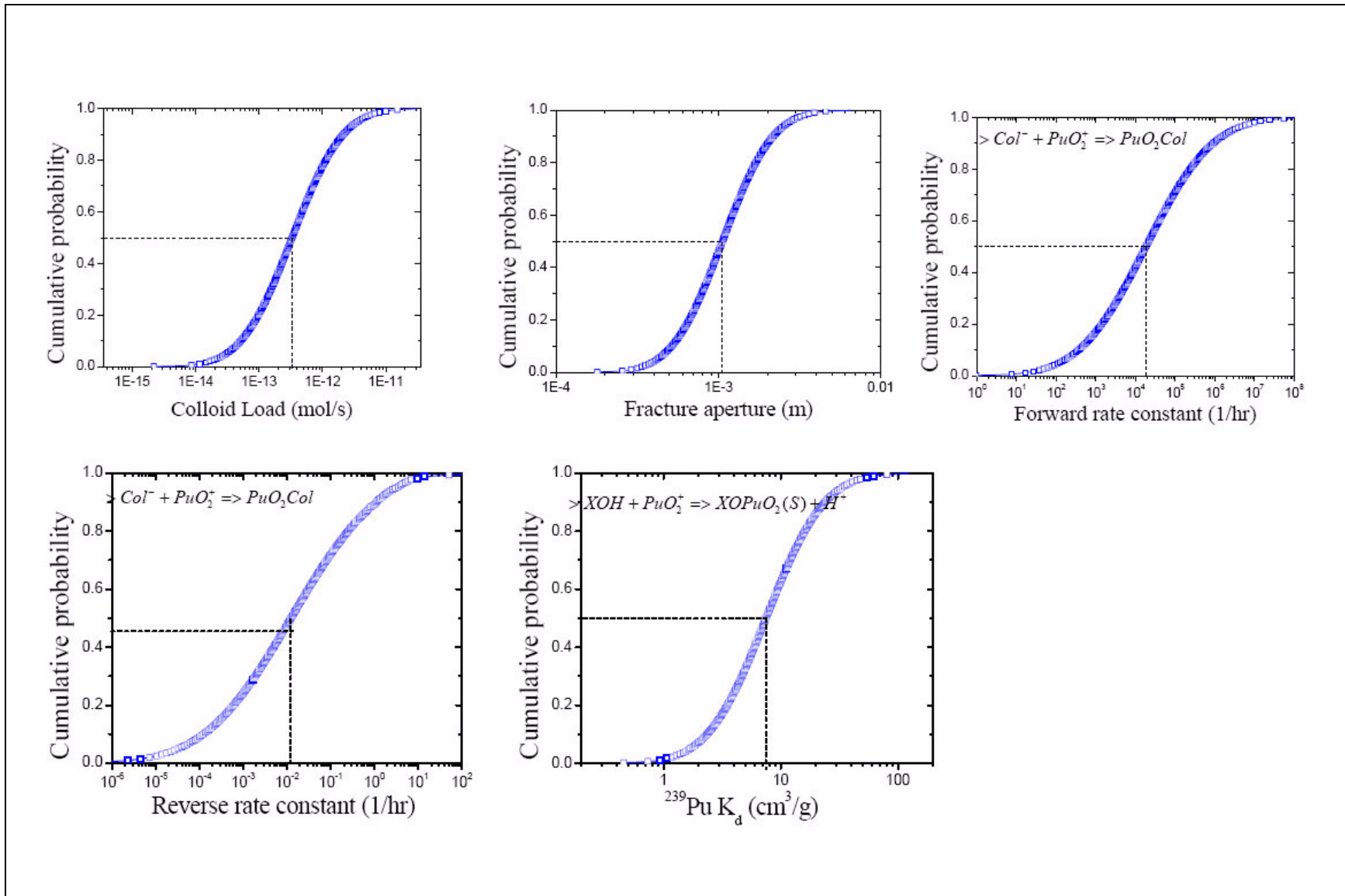


**Figure C.6-3**  
**Distribution of 1,000 Realizations of the Parameters Created with LHS**

(3) Pu matrix sorption coefficient, and (4) fracture aperture. Latin hypercube sampling is applied to create 1,000 realizations of these most sensitive parameters by considering the correlation structures of these parameters (The forward rate constant and reverse rate constant are correlated with a correlation coefficient of 0.95. Other parameters are independent to one another). The statistics of these five parameters from LHS are listed in Table C.6-1. (These parameters were selected before CAU-scale transport modeling as described in Section 7.0. Thus, they are similar but not identical.) The 1,000 realizations of the five most sensitive parameters are plotted in Figure C.6-3. Fracture aperture is treated separately as a discrete distribution.

**Table C.6-1**  
**Statistics of the Five Most Sensitive Parameters**

Parameters	Colloid Load Concentration (ln(mol/s))	Forward Rate Constant (ln(1/hr))	Reverse Rate Constant (ln(1/hr))	Pu Matrix Sorption Coefficient ln(cm <sup>3</sup> /g)	Fracture Aperture ln(m) <sup>a</sup>
	Lognormal	Triangular	Triangular	Normal	Triangular
Mean or Likeliest	2.72	9.9	-6.9	2.02	-6.91
SD	1.0	--	--	0.9	--
Minimum	--	4.6	-13.8	--	-9.21
Maximum	--	18.2	0	--	-5.3

<sup>a</sup> See Section 6.0 for discussion of fracture apertures used in this study.

Note: Forward and reverse rate constants for Pu sorption to colloids are correlated with a constant of 0.9.

Note: These parameters were selected before CAU-scale transport modeling as described in Section 7.0. Thus, they are similar but not identical.

-- = Not applicable

### C.6.3 Results of Monte Carlo Simulations

Monte Carlo simulation is used to predict percentage of the source-release Pu actually mobilized by natural colloids. The reactive transport modeling results provide a distribution of factors for the CAU model to multiply by the aqueous <sup>239</sup>Pu release function to create a new source function for <sup>239</sup>Pu-colloid. This new species is an abstraction of the present reactive transport model results. The Pu cannot desorb from the colloids in the particle-tracking model. Thus, the estimate is for the irreversibly sorbed component of the <sup>239</sup>Pu(aq) release.

In dual-porosity transport modeling with GDPM, particle-tracking models, and analytical solutions, fracture aperture affects  $D_m$  by setting the effective wetted surface for a fixed fracture porosity. For a fixed porosity, wetted surface area increases as fracture aperture decreases, because more fractures are necessary to provide that porosity. On the other hand, fracture aperture is related to fracture porosity through the fracture spacing term, and thus can affect groundwater velocities. Because the GDPM is constructed after sampling groundwater velocities in the CAU flow and transport model, a practical approach implanted here is to create two different GDPMs for fracture porosities of 0.0001 and 0.001 in the 3-D flow model to investigate potential velocities, and then to sample fracture aperture from the distribution in Figure C.6-3 to consider its sensitivity on  $D_m$  only. Although the distribution of fracture apertures developed in Section 6.0 exceeds 1 mm, such large fractures are not considered in this investigation of reactive transport in fractured media. This estimation method approximates the process of generating a new GDPM for each new fracture aperture sampled during Monte Carlo simulation. The computed Pu concentration breakthrough with the first 100 realizations in scenario two ( $b = 0.001$  m) is presented in Figure C.6-4. By using the concentration of the perfect Pu tracer at 5 km to divide into the computed Pu concentrations at 5 km from Monte Carlo simulations, source-reduction factors were derived. The final Monte Carlo simulation results for the source-reduction factors from the two scenarios are presented in Figures C.6-5 and C.6-6.

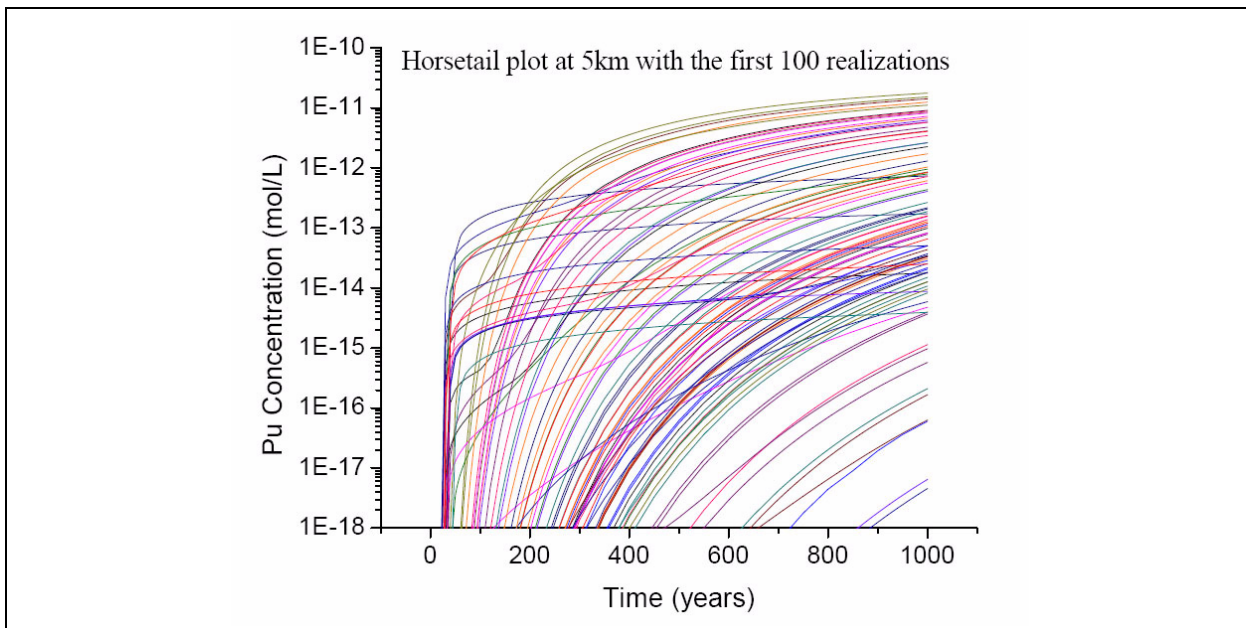


**Figure C.6-4**  
**Simulated Breakthrough Curves of  $^{239}\text{Pu}$  from the First 100 Realizations of the Monte Carlo Simulation of Scenario Two (aperture = 0.001 m) at 5 km**

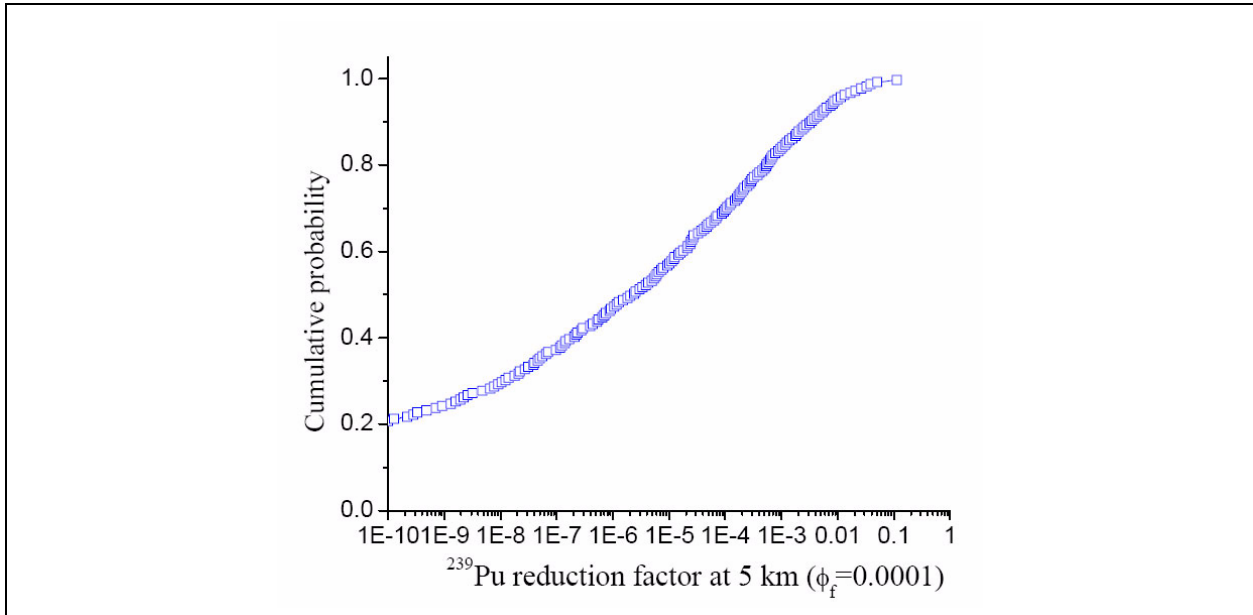


**Figure C.6-5**  
 **$^{239}\text{Pu}$  Source-Reduction Factor ( $f_{sr}$ ) Distribution at 5 km Using a Fracture Porosity of 0.0001 m**

Note: The mean of the factors is 0.23% with an SD of 0.01. The minimum and the maximum of the factors are (~0, 12.85%).

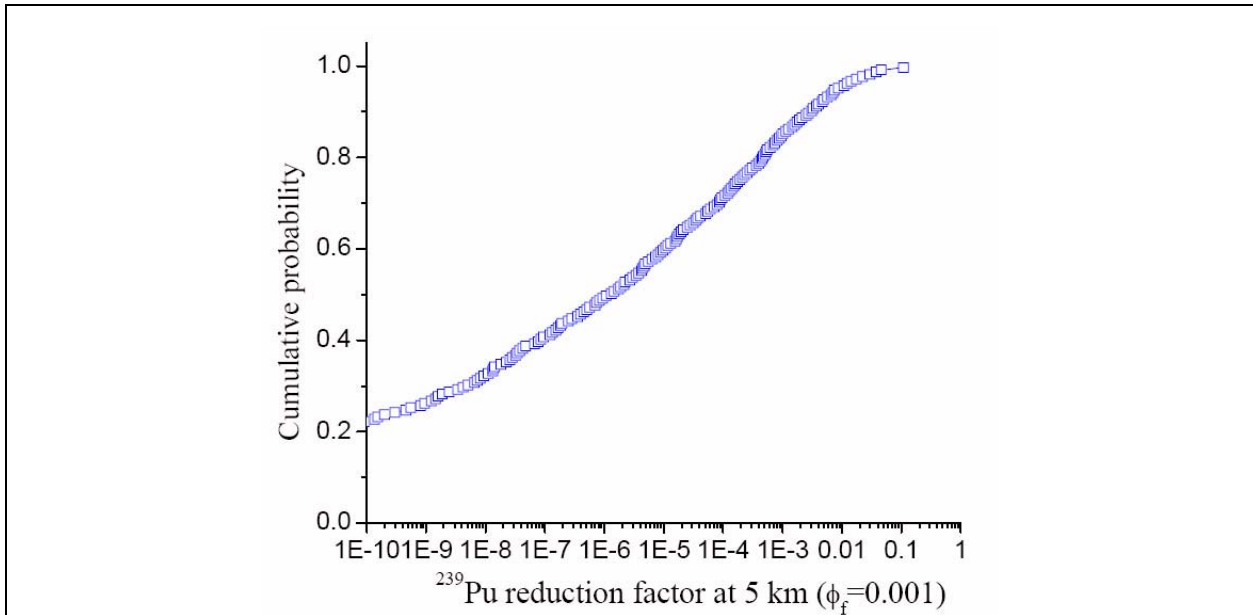


**Figure C.6-6**  
 **$^{239}\text{Pu}$  Source-Reduction Factor ( $f_{sr}$ ) Distribution at 5 km Using a Fracture Porosity of 0.001 m**

Note: The mean of the factors is 0.19% with an SD of 0.009. The minimum and the maximum of the factors are (~0, 11.87%).



**C.6.4 Summary**

To summarize the results from the two scenarios of Monte Carlo simulations, the percentile of the two porosity values is defined as listed in Table C.6-2. Then, by using equations derived by Dai et al. (2007) for computing the composite mean and variance from sub-component statistic data, the composite mean of the <sup>239</sup>Pu reduction factors of the two Monte Carlo simulations is computed as:

$$F_{sr} = \sum_{k=1}^3 P_k f_{srk} \tag{C.6-1}$$

The composite variance of the <sup>239</sup>Pu reduction factors of the two Monte Carlo simulations can be computed as:

**Table C.6-2**  
**Summary of the Two Monte Carlo Simulations with Variable Fracture Porosities**

Monte Carlo (k)	Fracture $\phi_f$	Percentile $P_k$	Monte Carlo Mean Factor $f_{sr}$ (%)	SD $\sigma$	Minimum $f_{sr}$ (%)	Maximum $f_{sr}$ (%)
1	0.0001	0.08	0.2275	0.01055	1.20E-16	12.85
2	0.001	0.92	0.1939	0.00918	1.20E-16	11.87

$$D_l = \frac{\tau}{1/k_{fm}} = k_{fm} \tau \tag{C.6-2}$$

Using Equations (C.6-1) and (C.6-2), the composite mean and variance is calculated as:

$$F_{sr} = 0.2 \text{ percent and } \sigma^2 = 8.77\text{E-}05 \text{ (an SD of 0.0093).}$$

The distribution of the reduction factors at the composite level can be treated as a triangular (or log triangular) distribution with a mean of 0.2 percent and a range (minimum and maximum of the factors) of 0, 12.85 percent.

## C.7.0 REFERENCES

- Andersson, P., J. Byegard, E.L. Tullborg, T. Doe, J. Hermanson, and A. Winberge. 2004. "In Situ Tracer Tests to Determine Retention Properties of a Block Scale Fracture Network in Granitic Rock at the Aspo Hard Rock Laboratory, Sweden." In *Journal of Contaminant Hydrology*, Vol. 70(3-4): 271-297.
- BN, see Bechtel Nevada.
- Bechtel Nevada. 2002. *A Hydrostratigraphic Model and Alternatives for the Groundwater Flow and Contaminant Transport Model of Corrective Action Units 101 and 102: Central and Western Pahute Mesa, Nye County, Nevada*, DOE/NV/11718--706. Las Vegas, NV.
- Berkowitz, B., and H. Scher. 1995. "On Characterization of Anomalous Dispersion in Porous and Fractured Media." In *Water Resources Research*, Vol. 31(6): 1461-1466.
- Dai, Z., A. Wolfsberg, Z. Lu, and P. Reimus. 2007. "Upscaling Matrix Diffusion Coefficients for Heterogeneous Fractured Rocks." In *Geophysical Research Letters*, doi:10.1029/2007GL029332.
- Dash, Z.V. 2003. *Validation Test Plan (VTP) for the FEHM Application Version 2.21*, 10086-Vtp-2.21-00. Los Alamos, NM: Los Alamos National Laboratory.
- Doherty, J. 2005. *PEST Version 9 Users Guide, Model-Independent Parameter Estimation*. Watermark Computing.
- Domenico, P.A., and F.W. Schwartz. 1990. *Physical and Chemical Hydrogeology*. New York, NY: John Wiley and Sons.
- Gillham, R.W., M.L. Robin, D.J. Dytynyshyn, and H.M. Johnston. 1984. "Diffusion of Nonreactive and Reactive Solutes Through Fine-Grained Barrier Materials." In *Canadian Geotechnical Journal*, Vol. 21: 541-550.
- Grisak, G.E. and J.F. Pickens. 1980. "Solute Transport through Fractured Media: 1. The Effect of Matrix Diffusion." In *Water Resources Research*, Vol. 16, No. 4, p.719-730.
- Grisak, G.E., J.F. Pickens and J.A. Cherry. 1980. "Solute Transport Through Fractured Media: 2. Column Study of Fractured Till." In *Water Resources Research*, Vol. 16, No. 4, p.731-739.

- Hoffman, M.R. 1981. "Thermodynamic, Kinetic, and Extrathermodynamic Considerations in the Development of Equilibrium Models for Aqueous Systems." In *Environmental Science & Technology*, Vol. 15: 345-353.
- Johns, R.A., and P.V. Roberts. 1991. "A Solute Transport Model for Channelized Flow in a Fracture." In *Water Resources Research*, Vol. 27: 1797-1808.
- Keller, A.A., P.V. Roberts, and P.K. Kitanidis. 1995. "Prediction of Single Phase Transport Parameters in a Variable Aperture Fracture." In *Geophysical Research Letters*, Vol. 22: 1425-1428.
- Kersting, A.B., and P.W. Reimus, eds. 2003. *Colloid-Facilitated Transport of Low-Solubility Radionuclides: A Field, Experimental, and Modeling Investigation*, UCRL-ID-149688. Livermore, CA: Lawrence Livermore National Laboratory.
- Moreno, L., I. Neretnieks, and T. Eriksen. 1985. "Analysis of Some Laboratory Tracer Runs in Natural Fissures." In *Water Resources Research*, Vol. 21, No. 7, p.951-958.
- Neretnieks, I., T. Eriksen, and P. Tahtinen. 1982. "Tracer Movement in a Single Fissure in Granitic Rock: Some Experimental and Their Interpretation." In *Water Resources Research*, Vol. 18: 849-858.
- Rajaram, H. 1997. "Time and Scale Dependent Effective Retardation Factors in Heterogeneous Aquifers." In *Advances in Water Resources*, 20(4): 217-230.
- Reimus, P.W., and T.J. Callahan. 2007. "Matrix Diffusion Rates in Fractured Volcanic Rocks at the Nevada Test Site: Evidence for a Dominant Influence of Effective Fracture Apertures." In *Water Resources Research*, Vol.43, W07421, doi:10.1029/2006WR005746, 2007.
- Reimus, P.W., A. Abdel-Fattah, S.D. Ware, N. Lu, I. Anghel, and K.S. Kung. 1999. Written communication. Subject: *Progress Report on Colloid Transport and Colloid-Facilitated Plutonium Transport in Fractured Rocks from Pahute Mesa, Nevada Test Site*. Los Alamos, NM: Los Alamos National Laboratory.
- Reimus, P.W., S.D. Ware, N. Lu, A. Abdel-Fattah, K.S. Kung, and M.P. Neu. 2001. *FY 2001 Progress Report on Colloid-Facilitated Plutonium Transport in Fractured Rocks from Pahute Mesa, Nevada Test Site*, ERD.011004.0001. Los Alamos, NM: Los Alamos National Laboratory.
- Reimus, P.W., M. Murrell, A. Abdel-Fattah, E. Garcia, D. Norman, S. Goldstein, A. Nunn, R. Gritz, and B. Martinez. 2006a. *Colloid Characteristics and Radionuclide Associations with Colloids in Near-Field Waters at the Nevada Test Site (FY2005 Progress Report)*, LA-UR-05-8612. Los Alamos, NM: Los Alamos National Laboratory.

- Reimus, P.W., R.L. Hershey, D.L. Decker, S.D. Ware, C. Papelis, S. Earman, A. Abdel-Fattah, M. Haga, D. Counce, S. Chipera, and C. Sedlacek. 2006b. *Tracer Transport Properties in the Lower Carbonate Aquifer of Yucca Flat*, LA-UR-06-0486. Los Alamos, NM: Los Alamos National Laboratory.
- Robinson, B.A. 1994. "A Strategy for Validating a Conceptual Model for Radionuclide Migration in the Saturated Zone Beneath Yucca Mountain." In *Radioactive Waste Management and Environmental Restoration*, Vol. 19: 73-96.
- Robinson, B.A., and Z.V. Dash. 2005. *User's Guide for the PLUMECALC Application, V 2.2*. Los Alamos, NM: Los Alamos National Laboratory.
- Robinson, B.A., A.V. Wolfsberg, H.S. Viswanathan, and P.W. Reimus. 2007. "A Colloid-Facilitated Transport Model with Variable Colloid Transport Properties." In *Geophysical Research Letters*, doi:10.1029/2007GL029625.
- Rowe, R.K., C.J. Caers, and F. Barone. 1988. "Laboratory Determination of Diffusion and Distribution Coefficients of Contaminants Using Undisturbed Clayey Soils." In *Canadian Geotechnical Journal*, Vol. 25: 108-118.
- Shaw, see Shaw Environmental, Inc.
- SNL, see Sandia National Laboratories.
- Sandia National Laboratories. 2007. *Total System Performance Assessment Model/Analysis for the License Application*, MDL-WIS-PA-000005 REV00 APPENDIX C-7. Albuquerque, NM: Sandia National Laboratories.
- Shackelford, C.D. 1991. "Laboratory Diffusion Testing for Waste Disposal - A Review." In *Journal of Contaminant Hydrology*, Vol. 7: 177-217.
- Shaw Environmental, Inc. 2003. *Contaminant Transport Parameters for the Groundwater Flow and Contaminant Transport Model of Corrective Action Units 101 and 102: Central and Western Pahute Mesa, Nye County, Nevada*, Rev. 0, Shaw/13052-201. Las Vegas, NV.
- Sudicky, E.A., and E.O. Frind. 1982. "Contaminant Transport in Fractured Porous Media: Analytic Solutions for a System of Parallel Fractures." In *Water Resources Research*, Vol. 18(6): 1634-1642.
- Tang, D.H., E.O. Frind, and E.A. Sudicky. 1981. "Contaminant Transport in Fractured Porous Media: Analytical Solution for a Single Fracture." In *Water Resources Research*, Vol. 7(3): 555-564.

- Ware, D., A. Abdel-Fattah, M. Ding, P. Reimus, C. Sedlacek, M. Haga, E. Garcia, and S. Chipera. 2005. *Radionuclide Sorption and Transport in Fractured Rocks of Yucca Flat, Nevada Test Site*, LA-UR-05-9279. Los Alamos, NM: Los Alamos National Laboratory.
- Wolfsberg, A., and H.S. Viswanathan. 2002. Written communication. Subject: *Reactive Transport Model Parameters for Flowing Fractures: Parameter Estimation and Comparison with Experimental Data for Colloid-Facilitated Plutonium Transport*. Los Alamos, NM: Los Alamos National Laboratory.
- Wolfsberg, A., L. Glascoe, G. Lu, A. Olson, P. Lichtner, M. McGraw, T. Cherry, and G. Roemer. 2002. *TYBO/BENHAM: Model Analysis of Groundwater Flow and Radionuclide Migration from Underground Nuclear Tests in Southwestern Pahute Mesa, Nevada*, LA-13977. Los Alamos, NM: Los Alamos National Laboratory.
- Young, D.F., and W.P. Ball. 1998. "Estimating Diffusion Coefficients in Low-Permeability Porous Media Using a Macropore Column." In *Environmental Science & Technology*, Vol. 32: 2578-2584.
- Zavarin, M., S.F. Carle, and R.M. Maxwell. 2004. *Upscaling Radionuclide Retardation-Linking the Surface Complexation and Ion Exchange Mechanistic Approach to a Linear  $K_d$  Approach*, UCRL-TR-204713. Livermore, CA: Lawrence Livermore National Laboratory.
- Zhang, F., G.T. Yeh, J.C. Parker, S.C. Brooks, M.N. Pace, Y.-J. Kim, P.M. Jardine, and D.B. Watson. 2007. "A Reaction-Based Paradigm to Model Reactive Chemical Transport in Groundwater with General Kinetic and Equilibrium Reactions." In *Journal of Contaminant Hydrology*, Vol: 92 Issue: 1-2.
- Zimmerman, R.W., and G.S. Bodvarsson. 1996. "Hydraulic Conductivity of Rock Fractures." In *Transport in Porous Media*, Vol. 23: 1-30.
- Zyvoloski, G.A., B.A. Robinson, Z.V. Dash, and L.L. Trease. 1997. *Summary of Models and Methods for the FEHM Application - A Finite-Element Heat- and Mass-Transfer Code*, LA-13307-MS. Los Alamos, NM: Los Alamos National Laboratory.
- Zyvoloski, G.A., B.A. Robinson, Z.V. Dash, and L.L. Trease. 2003. *Summary of Models and Methods for the FEHM Application - A Finite-Element Heat and Mass-Transfer Code*, LA-13307-MS. Los Alamos, NM: Los Alamos National Laboratory.
- Zyvoloski, G.A., B.A. Robinson, and H.S. Viswanathan. 2007. *Generalized Double Porosity: A Method for Representing Spatially Variable Sub-Grid Scale Processes*, LA-UR-07-3486, Los Alamos, NM: Los Alamos National Laboratory.



## **Appendix D**

# **Evaluation of Groundwater Travel Times in the PM-OV Flow System from $^{14}\text{C}$ Data**

As provided Edward Kwicklis, Los Alamos National Laboratory

## **D.1.0 INTRODUCTION**

Groundwater flow directions and mixing in the PM-OV flow system were analyzed by Thomas et al. (2002), Rose et al. (2006), and Kwicklis et al. (2005) using groundwater geochemical and isotopic data from the region. These studies relied on a combination of analytical mixing models that used non-reactive tracers and on inverse geochemical models that used both non-reactive and reactive chemical and isotopic species to identify potential groundwater flow paths and mixing relations. The study by Kwicklis et al. (2005) built on the earlier studies by including additional data adjacent to and south of the PM-OV model domain to constrain the analysis and used the PHREEQC code (Parkhurst and Appelo, 1999) rather than the NETPATH code (Plummer et al., 1994) used in the earlier studies to perform the inverse geochemical modeling. The inclusion of additional data to the south of the PM-OV flow model area enabled the fate of water leaving the PM-OV flow system to be better defined, whereas the use of PHREEQC allowed a more thorough treatment of uncertainty in the flow path analysis than was possible with NETPATH. The inverse geochemical models developed by Kwicklis et al. (2005) form the basis for the groundwater travel time analysis presented in this report.

In Kwicklis et al. (2005), different geographic areas of the flow system were defined based on differences and similarities in the groundwater chemical and isotopic compositions (Figures D.1-1 and D.1-2). The spatial variability of non-reactive tracers such as  $\delta\text{H}$ ,  $\delta^{18}\text{O}$ , Cl and  $\text{SO}_4$  were examined in map view (Figure D.1-3) and in a scatter plot (Figure D.1-4) and analytical mixing models were constructed based on these tracers. These analytical mixing models were then tested with PHREEQC to determine if they were valid when reactive chemical species and isotopes that evolve through water/rock interaction (such as  $\delta^{13}\text{C}$ ) were also considered.

The inverse geochemical models attempt to explain the chemical and isotopic composition at downgradient wells as a function of mixing of groundwater from upgradient areas and water/rock

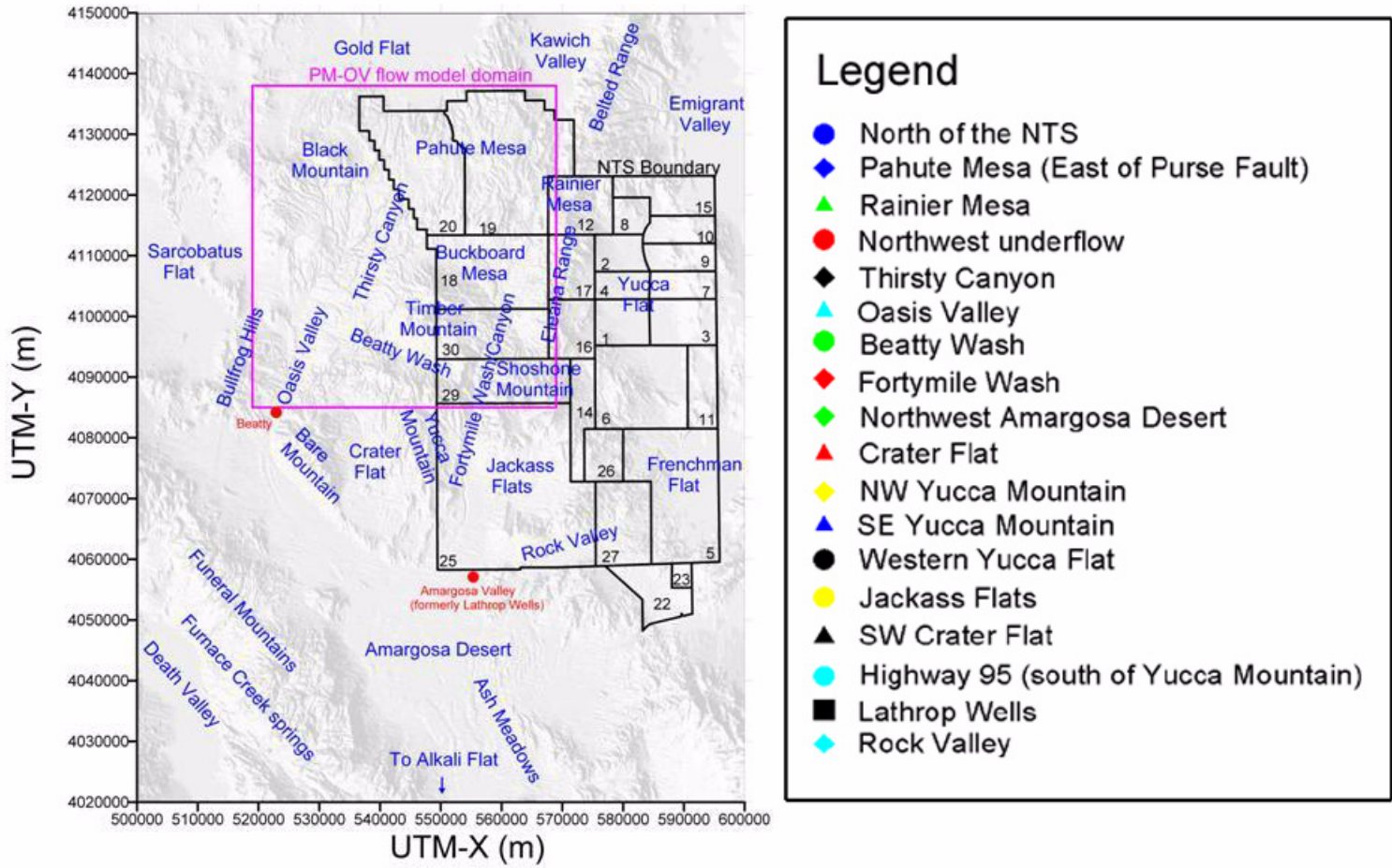


**Figure D.1-1**  
**Topographic Features near the PM-OV Area**



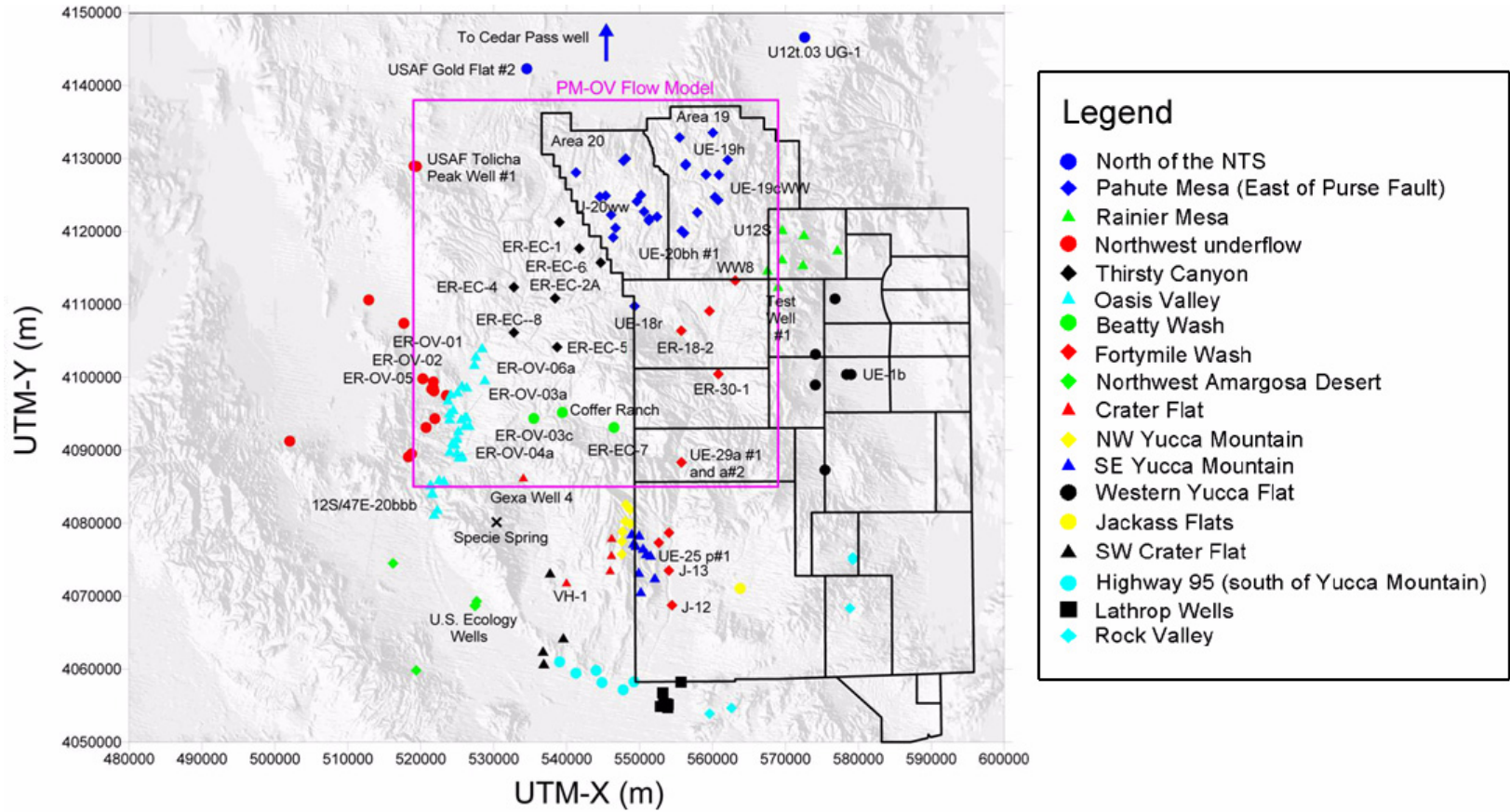


**Figure D.1-2**  
**Well Groups and Key Wells in the PM-OV Flow System**

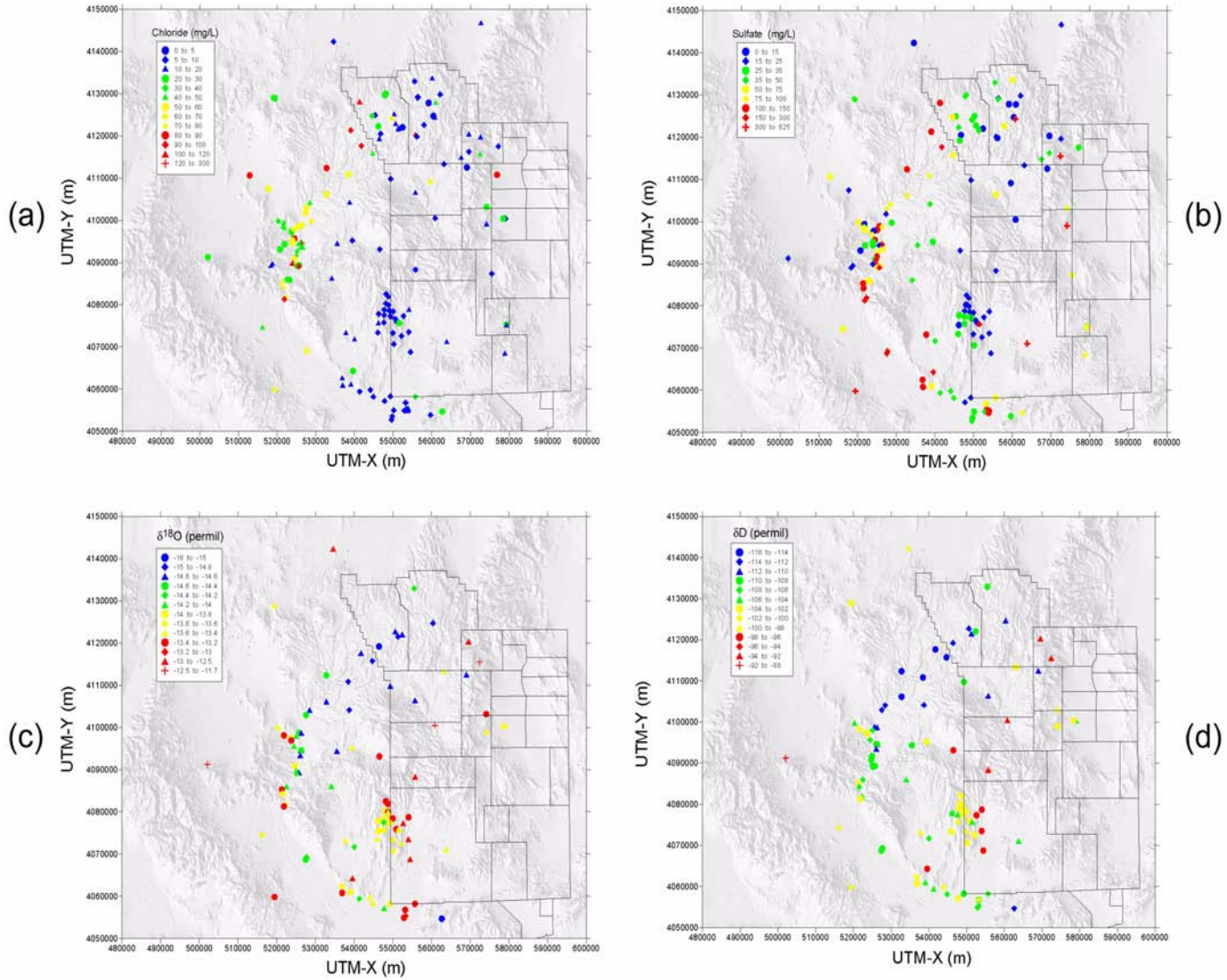
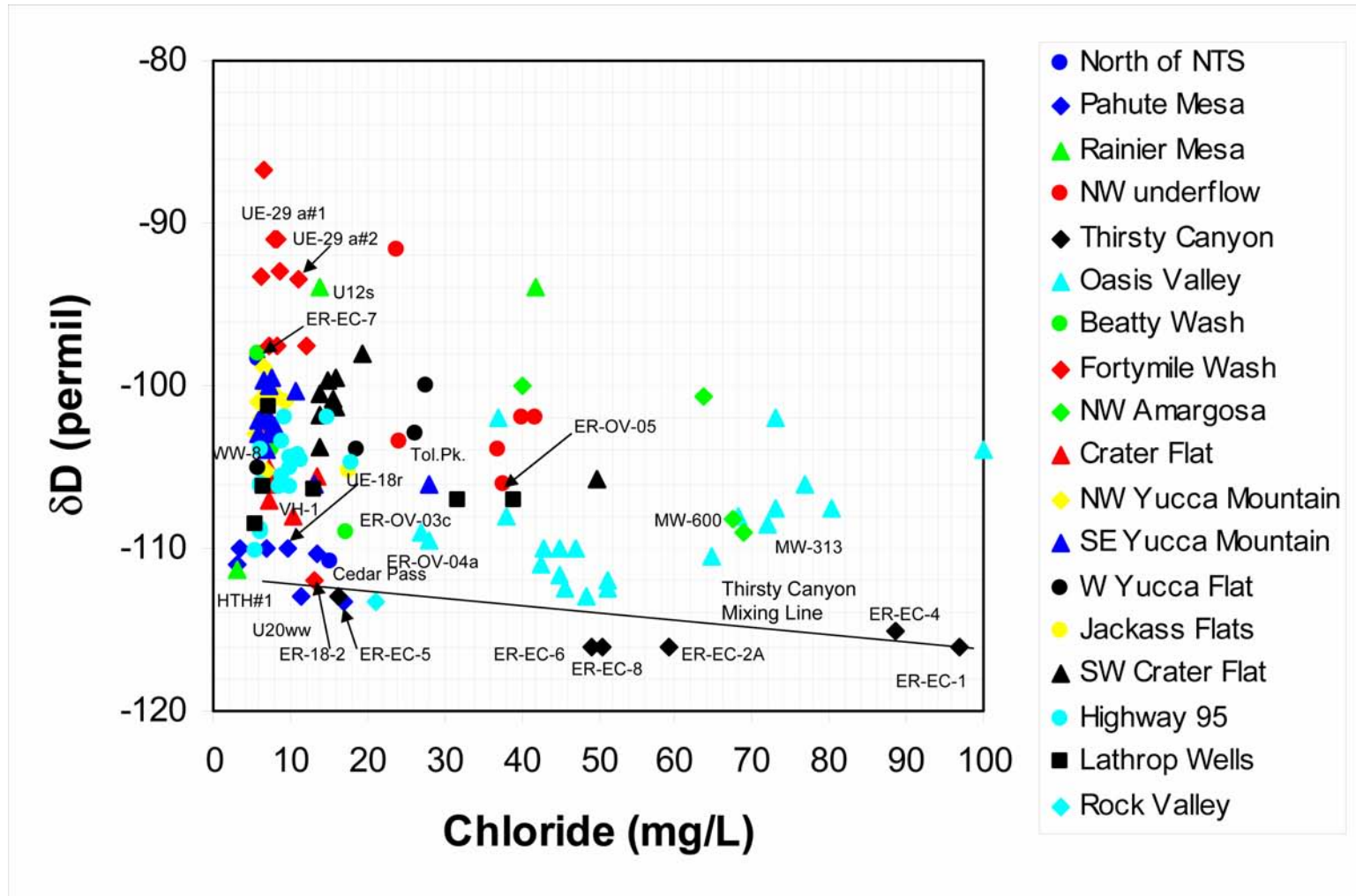


**Figure D.1-3**  
**Tracers Used in the PM-OV Geochemical Modeling Analysis: (a) Chloride, (b) Sulfate, (c)  $\delta^{18}\text{O}$ , and (d)  $\delta\text{D}$**



interactions. For each chemical or isotopic component, the composition at the target well can be expressed as:

$$\text{Target Well} = f_1 \text{ Well \#1} + f_2 \text{ Well \#2} + \dots + f_n \text{ Well \#n} + \text{reactions} \quad (\text{D.1-1})$$

where  $f_i$  are the mixing fractions of groundwater from upgradient wells  $i$  to  $n$  at the target well. The chemical and isotopic components tracked and balanced in the PHREEQC models that form the basis of the travel time calculations presented here include: (1) major cations and anions (Ca, Na, Mg, K, Si, C, S, and Cl); (2) some minor cations and anions (Al, Fe, F, and sometimes Sr); and (3) isotopes ( $\delta\text{H}$ ,  $\delta^{18}\text{O}$  and  $\delta^{13}\text{C}$ ). Thus, one equation of the form of Equation (D.1-1) exists for each component that is tracked in the models, and the mixing fractions and reactions identified by the inverse model must simultaneously balance all of the components that are being tracked at the target well.

The uncertainty in the groundwater chemical compositions that arises because of analytical errors and sampling variability is specified by the user as part of the model input, and is propagated to the PHREEQC results in the form of 95 percent confidence limits and also manifested as model non-uniqueness. Typically, multiple inverse models based on different mixing relationships and different water/rock reactions can be found that explain the groundwater composition at a well. Although the inclusion of multiple chemical and isotopic species as constraints in the models tends to minimize the problem of nonuniqueness, it does not eliminate the problem altogether.

### **D.1.1 Data Limitations**

Groundwater chemical and isotopic data have been collected over several decades from the PM-OV flow system for different purposes by many different investigators and organizations. Typically, complete suites of hydrochemical and isotopic data that were required for the types of analysis employed in this report exist for only a subset of the wells that have been drilled in the study area. This was especially true of the  $^{14}\text{C}$  data, which have only in the last several decades been collected on a routine basis as part of the UGTA Sub-Project. Many of the boreholes drilled as exploratory holes in the 1960s and 1970s as part of the nuclear weapons program were sampled only for major ions. Therefore, relatively few wells (38) exist with  $^{14}\text{C}$  data in the roughly 2,500 km<sup>2</sup> area, for a well density of 0.015 wells/km<sup>2</sup> or 65 km<sup>2</sup> per well.

One of the strengths of using geochemical analysis to understand the PM-OV flow system is that a detailed understanding of the geometry and hydraulic properties of HSUs and structural features is not required to conduct the analysis. This is a valuable strength in an area as geologically complex as the PM-OV flow system. Nonetheless, it is important to recognize the assumptions inherent in the types of analysis presented in this report. The first is that the analysis presented in Kwicklis et al. (2005) and built upon in this report implicitly assumes that a 3-D flow system can be compressed into two dimensions. This assumption, in fact, implies that geographic variability in geochemical compositions is much larger than vertical variability at any location in the flow system. The relatively coherent spatial structure evident in the maps of  $\delta D$ ,  $\delta^{18}O$ , Cl, and  $SO_4$  (Figure D.1-3) despite the different depths at which these samples were taken, suggests that this is a reasonable assumption for these chemical and isotopic species. However, the situation may be different for  $^{14}C$ , which may vary much more strongly with sample depth and the hydrostratigraphic unit than these non-decaying species. It is reasonable to assume that flow within shallow aquifers will be more rapid, and hence, that  $^{14}C$  activities will be higher compared with groundwater sampled from deeper confining units where flow is more stagnant. Therefore, the groundwater travel time analysis based on  $^{14}C$  presented in this report is expected to be more sensitive to the sample depths and the hydraulic properties of the formations sampled than the mixing analysis that preceded it (Kwicklis et al., 2005).

A second important assumption is that the wells involved in the travel time analysis lie directly along a flow path and not at some oblique angle to the flow direction. It would be fortuitous, indeed, if the wells were aligned perfectly with the flow direction. Thus, in most cases, the travel times calculated in this report are “apparent” travel times in the sense that they are taken at some angle to the true flow direction, and hence are longer than the travel times that would be calculated for wells that were perfectly aligned with the flow path.

A third important assumption is that the flow system is in a physical and chemical steady state, so that variations in the chemical and isotopic compositions that are observed today also existed in the past. This implies that neither flow rates or flow directions have changed since groundwater first entered the flow system, or at least that these transients are long-lived compared with the residence times of groundwater in the flow system.

### D.1.2 Carbon-14 Data

Groundwater  $^{14}\text{C}$  data associated with the dissolved inorganic carbon (DIC) component form the principal basis for the residence time and travel time calculations performed in this study. Carbon-14 decreases naturally by radioactive decay and so constitutes a natural clock by which groundwater travel times can be estimated once other processes that can affect its concentration in groundwater are considered. These processes include groundwater mixing and water/rock interactions involving carbon-bearing phases (Glynn and Plummer, 2005). Adjusting groundwater  $^{14}\text{C}$  ages so that they properly consider the effects of water/rock interactions, and modeling groundwater travel times so that they consider the effects of groundwater mixing and water/rock interaction on downgradient groundwater  $^{14}\text{C}$  activities are the two primary goals of this study.

Carbon-14 data are shown in map view in [Figure D.1-5](#) along with the major flow paths determined by Kwicklis et al. (2005) for the PM-OV model area and areas to the south. The processes by which these flow paths were identified are described in detail in Kwicklis et al., 2005 and are summarized briefly in a later section of this report titled “Travel Time Results.” From [Figure D.1-5](#), it can be noted that the  $^{14}\text{C}$  concentrations do not decrease systematically between Pahute Mesa and Oasis Valley or lower Beatty Wash along Flow Paths #1, #2, or #4. The  $^{14}\text{C}$  activities along these flow paths actually increase rather than decrease toward Oasis Valley as a result of the addition of local recharge, groundwater mixing, and possibly the interaction of shallow groundwater with carbon dioxide ( $\text{CO}_2$ ) in the unsaturated zone. Evidence that local recharge may have impacted  $^{14}\text{C}$  activities of groundwater in Oasis Valley is provided by the plot of  $\delta\text{D}$  versus  $\text{Cl}$  ([Figure D.1-4](#)). This plot shows that all of the groundwater from the PM-OV flow system and adjacent areas falls within a triangular region defined by three endmembers: (1) an isotopically light (more negative) but somewhat concentrated groundwater represented by upper Thirsty Canyon groundwater from ER-EC-1 and ER-EC-4; (2) an isotopically light, dilute groundwater represented by groundwater from Pahute Mesa (e.g., U-20 WW); and (3) an isotopically heavy (less negative) dilute groundwater typified by local shallow recharge from Fortymile Canyon at UE-29a #1 and UE-29a #2). A mixing line between Thirsty Canyon groundwater and Pahute Mesa groundwater is also plotted on [Figure D.1-4](#), which shows where Oasis Valley groundwater would plot if it consisted only of these endmembers. [Figure D.1-4](#) shows that groundwater from many of the wells in Oasis Valley plot significantly above the Thirsty Canyon Mixing Line defined by the Pahute Mesa and upper Thirsty Canyon groundwater

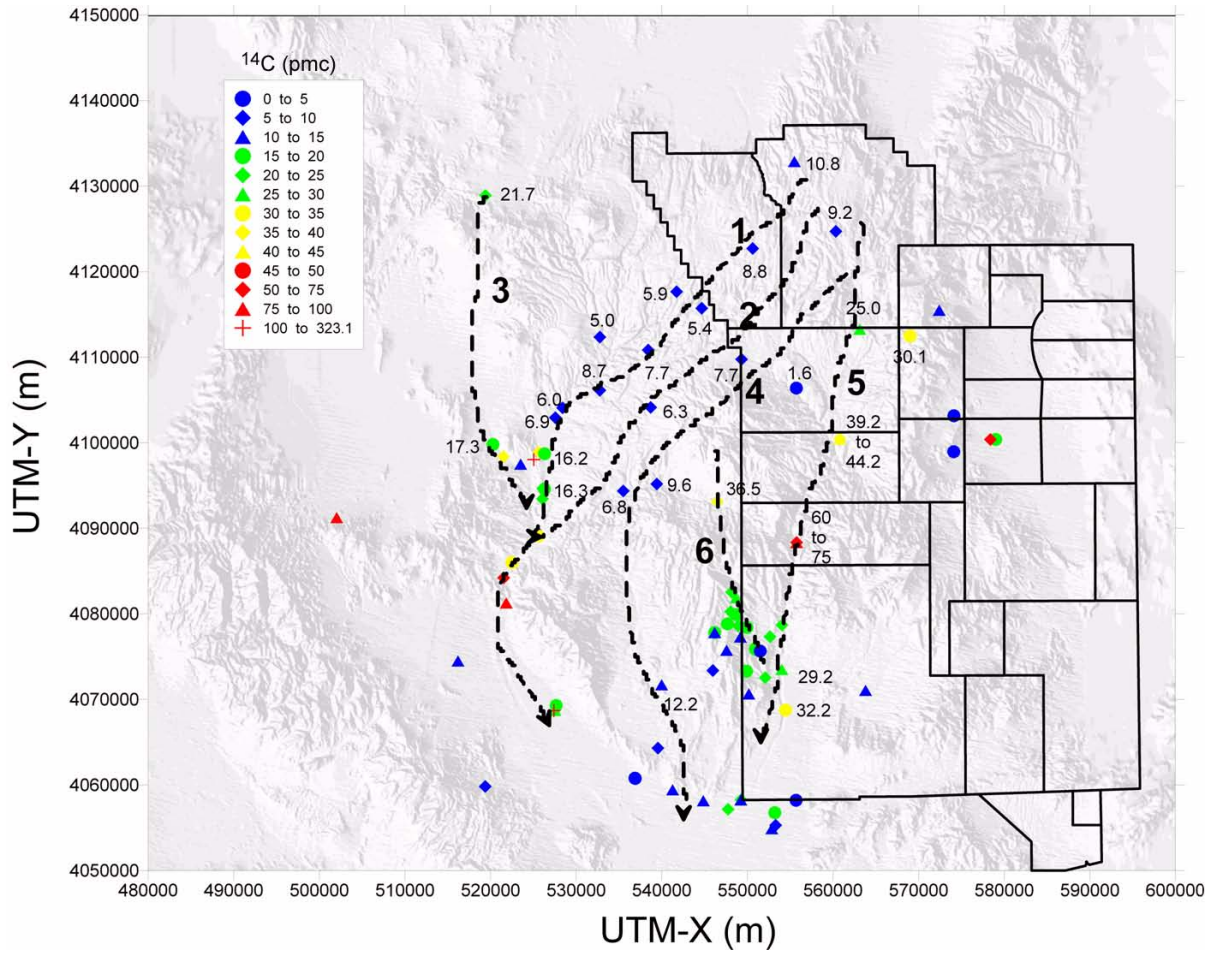


**Figure D.1-5**  
**Map with Groundwater <sup>14</sup>C Data and Flow Paths Interpreted from Groundwater Mixing Model**  
 Source: Kwicklis et al., 2005

endmembers, indicating that they contain a component of dilute, isotopically heavy recharge, as represented by the Fortymile Wash groundwaters.

The possibility that Oasis Valley groundwater may have interacted with soil gas is provided by the plot of  $\delta^{13}\text{C}$  versus inverse alkalinity data (Figure D.1-6), which shows that groundwater in Oasis Valley and the northwest Amargosa Desert is lighter (more negative) in  $\delta^{13}\text{C}$  and has higher alkalinity (lower inverse alkalinity) than upgradient Thirsty Canyon water, suggesting dissolution of isotopically light  $\text{CO}_2$  in the soil zone (White and Chuma, 1987). The mixing of younger water flowing southeast along Flow Path #3 west of Oasis Valley with older water moving along Flow Path #1 may also increase the  $^{14}\text{C}$  activity of groundwater from Pahute Mesa near Oasis Valley (Figure D.1-5). By the time groundwater leaves Oasis Valley into the northwest Amargosa Desert south of Beatty, it has a  $^{14}\text{C}$  activity between 75 to 100 percent modern carbon (pmc) as a result of these processes (Figure D.1-5).

On the eastern side of the Pahute Mesa flow system, groundwater moving southward from Pahute Mesa along Flow Path #5 also lacks evidence for a systematic decrease in  $^{14}\text{C}$  activities that would allow a simple interpretation of travel times along this flow path. The variability in  $^{14}\text{C}$  activity along this flow path results from the addition of local recharge in Fortymile Canyon and Fortymile Wash. The different depths and aquifers from which the groundwater samples were taken (deep in Area 19, shallow in Fortymile Canyon) also probably contributes to some of the observed variability in  $^{14}\text{C}$  activities.

The absence of significant decreases in  $^{14}\text{C}$  activities along most of Flow Paths #1, #2, and #4, combined with the increases in  $^{14}\text{C}$  activities near Oasis Valley, and the variability in  $^{14}\text{C}$  activities along flow Path #5 suggest it may be difficult to get robust estimates of travel time along these flow paths as a whole. The analyses presented in this report therefore focus on obtaining estimates of travel time along specific segments of these flow paths where the data allow meaningful interpretations to be developed.

### **D.1.3 Estimation of Groundwater $^{14}\text{C}$ Ages**

As in other study areas, the primary factor complicating the interpretation of groundwater  $^{14}\text{C}$  ages for Pahute Mesa groundwater is the possible interaction between groundwater and minerals in the rock.



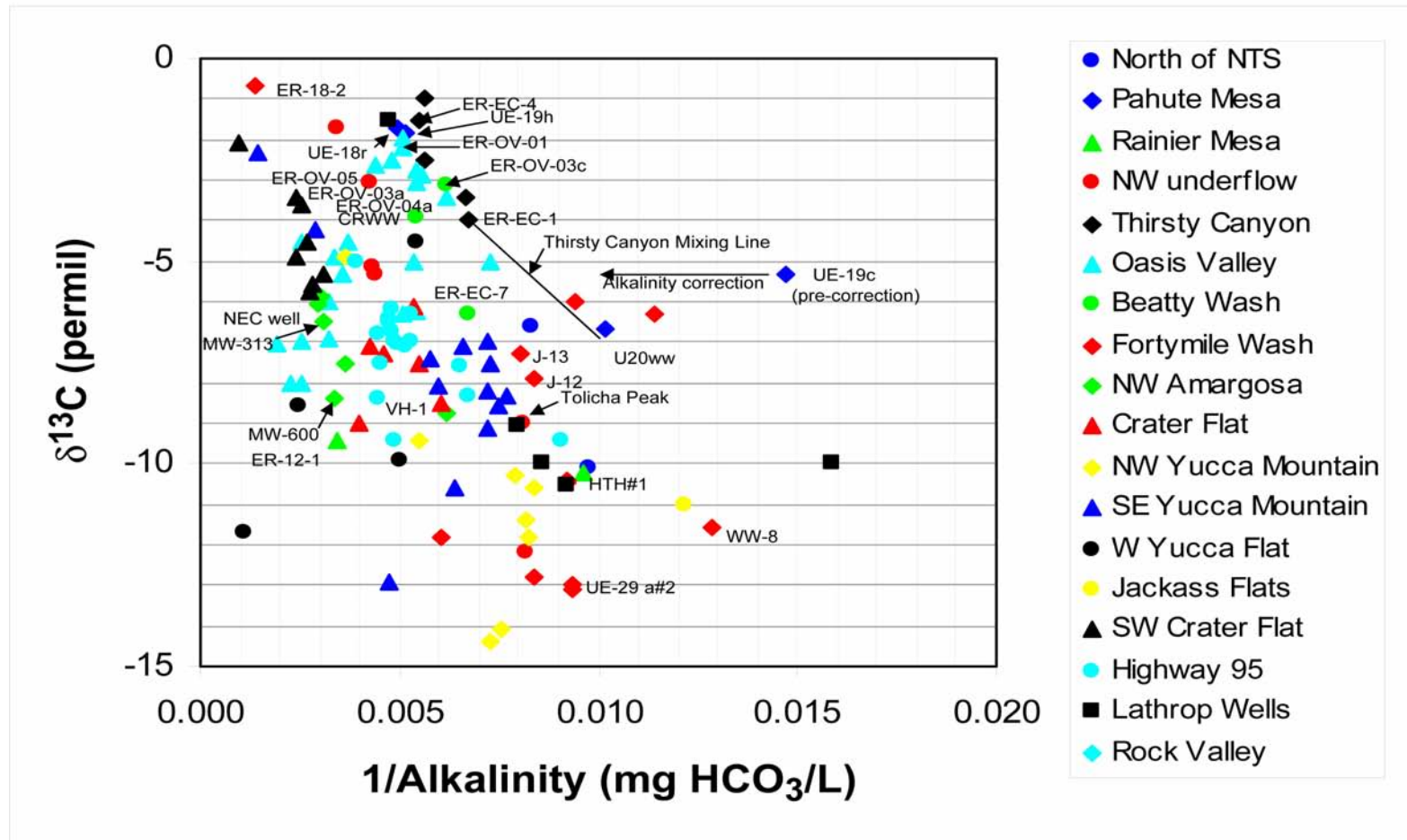
Groundwater  $\delta^{13}\text{C}$  and alkalinity data from PM-OV

Figure D.1-6

Groundwater  $\delta^{13}\text{C}$  and Inverse Alkalinity Data from PM-OV Flow System

These potential interactions include: (1) the dissolution of  $^{14}\text{C}$ -free calcite or dolomite in groundwater, (2) loss of  $^{14}\text{C}$  in groundwater through isotope exchange with calcite (sometimes interpreted as groundwater  $^{14}\text{C}$  loss during calcite recrystallization [Glynn and Plummer, 2005]), and (3) sorption of  $^{14}\text{C}$  (as  $\text{H}^{14}\text{CO}_3^-$ ) onto calcite surfaces (Maloszewski and Zuber, 1991; Sheppard et al., 1998). Each of these processes tends to either lower the  $^{14}\text{C}$  activity in the groundwater and/or retard its movement relative to the groundwater, thus resulting in estimates of groundwater age that are erroneously high or estimates of groundwater velocity that are erroneously low if they are not accounted for in the interpretation. The analyses presented in this report do not attempt to account for the possible sorption of  $^{14}\text{C}$  onto mineral surfaces. However, the near-constant  $^{14}\text{C}$  activities along many of the flow paths suggest that  $^{14}\text{C}$  sorption is not significant or else a more dramatic decrease in  $^{14}\text{C}$  activities along the flow paths would be apparent in [Figure D.1-5](#).

[Figure D.1-7](#) shows groundwater  $^{14}\text{C}$  concentrations as a function of their  $\delta^{13}\text{C}$  compositions. Some interaction of the groundwater in the PM-OV area with carbon-bearing minerals is indicated by the fact that  $^{14}\text{C}$  activities show an overall decrease as  $\delta^{13}\text{C}$  evolves from values typical of soil  $\text{CO}_2$  which initially provides most of the DIC and which has light  $\delta^{13}\text{C}$  (approximately -15 to -10 per mil after fractionation) to values typical of fracture lining carbonate minerals ( $0 \pm 4$  per mil). This trend suggests dilution of  $^{14}\text{C}$  in groundwater through dissolution or exchange with  $^{14}\text{C}$ -free carbonate minerals.

To correct for the first two types of interactions listed above, two commonly utilized analytical correction methods (Clark and Fritz, 1997) are applied to the  $^{14}\text{C}$  data from the PM-OV flow system. The first method uses the downgradient increase in the DIC relative to recharge water to estimate the total fraction of the groundwater DIC that was acquired during recharge. This fraction ( $q_{\text{DIC}}$ ) is calculated as:

$$q_{\text{DIC}} = \text{DIC}_{\text{rech}} / \text{DIC}_{\text{well}} \quad (\text{D.1-2})$$

where the subscripts *rech* and *well* indicate recharge and groundwater at the well under consideration. Groundwater DIC includes dissolved  $\text{CO}_2(\text{aq})$ ,  $\text{HCO}_3^-$ , and  $\text{CO}_3^{2-}$  and is essentially equivalent to alkalinity (the sum of milliequivalents per liter [meq/L]  $\text{HCO}_3^-$  and meq/L  $\text{CO}_3^{2-}$ ) at the pH values typical of groundwater near Pahute Mesa.

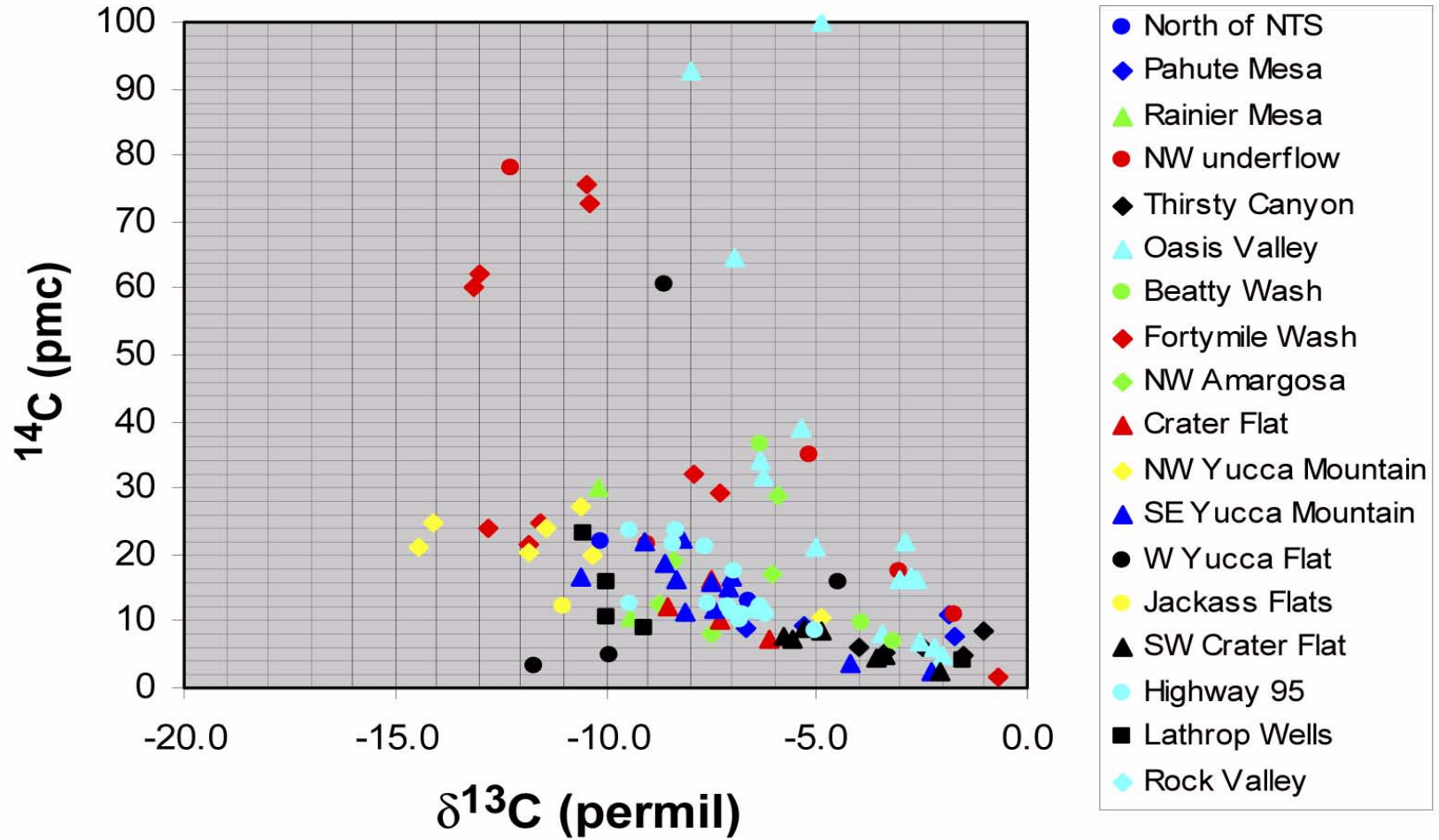


Figure D.1-7

$^{14}\text{C}$  versus  $\delta^{13}\text{C}$  Data from the PM-OV Flow System

Under the assumption that the dissolved calcite was old enough that it essentially has no  $^{14}\text{C}$ , the factor  $q_{DIC}$  represents the dilution of the  $^{14}\text{C}$  originally in the sample at the time of recharge by dissolution of non-radiogenic carbon (mostly  $^{12}\text{C}$ ). This factor is then used to adjust the initial  $^{14}\text{C}$  activity in the decay equation so that the calculated age reflects only the  $^{14}\text{C}$  decrease associated with radioactive decay and not decreases in  $^{14}\text{C}$  caused by water/rock interaction:

$$t_{\text{years}} = (1/\lambda) \cdot \ln(^{14}\text{C}_{\text{rech}} \cdot q_{DIC} / ^{14}\text{C}_{\text{well}}) \quad (\text{D.1-3})$$

where  $t_{\text{years}}$  is the  $^{14}\text{C}$  age in years and  $\lambda$  is the decay constant for  $^{14}\text{C}$  ( $1.21 \times 10^{-4}$  years $^{-1}$ ).

The second correction method uses the differences in the  $\delta^{13}\text{C}$  of recharge and of calcite in the aquifer to estimate an analogous dilution factor:

$$q_{\delta^{13}\text{C}} = (\delta^{13}\text{C}_{\text{well}} - \delta^{13}\text{C}_{\text{calcite}}) / (\delta^{13}\text{C}_{\text{rech}} - \delta^{13}\text{C}_{\text{calcite}}) \quad (\text{D.1-4})$$

Changes in the  $\delta^{13}\text{C}$  of the groundwater since it was recharged, as expressed in the dilution factor  $q_{\delta^{13}\text{C}}$ , reflect the effects of both calcite dissolution and isotope exchange during calcite recrystallization on the  $^{14}\text{C}$  originally in the recharge water. The dilution factor  $q_{\delta^{13}\text{C}}$  is used in an identical manner to  $q_{DIC}$  in Equation (D.1-3).

Equation (D.1-3) with the appropriate dilution factor (either  $q_{DIC}$  or  $q_{\delta^{13}\text{C}}$ ) can be applied and interpreted in several ways. If the recharge composition is defined by sampling shallow groundwater from beneath the recharge area, the measured  $^{14}\text{C}$  activity of the shallow groundwater can be less than atmospheric (or soil-gas) activity because of finite travel times through the unsaturated zone or interaction with calcite in the unsaturated zone. When  $^{14}\text{C}_{\text{rech}}$  is defined by shallow groundwater compositions, the application of Equation (D.1-3) produces ages that are, in fact, groundwater travel times from the recharge area to the downgradient sampling location. Alternatively, the age of the groundwater can be calculated with Equation (D.1-3) if the atmospheric  $^{14}\text{C}$  activity is used in the numerator, provided the dilution factors (either  $q_{DIC}$  or  $q_{\delta^{13}\text{C}}$ ) also incorporate the effects of unsaturated zone processes like the dissolution of pedogenic calcite as well as water/rock interactions in the saturated zone. The latter approach is used in this report by postulating the characteristics of recharge before any water/rock interaction.

To calculate the  $^{14}\text{C}$  dilution factors  $q_{\text{DIC}}$  or  $q_{\delta^{13}\text{C}}$  necessary to correct the groundwater  $^{14}\text{C}$  ages in Pahute Mesa, the compositions of the recharge and mineral end-members were estimated graphically by plotting the groundwater  $\delta^{13}\text{C}$  data against the inverse of the groundwater DIC concentrations (Figure D.1-6). When plotted this way, groundwaters less affected by water/rock interaction should have lighter  $\delta^{13}\text{C}$  values and lower DIC concentrations (higher inverse DIC concentrations) and fall in the lower right corner of the plot, whereas groundwaters more affected by water/rock interaction should have heavier  $\delta^{13}\text{C}$  values and higher DIC concentrations (lower inverse DIC values) and fall in the upper left part of the plot. If the recharge and calcite end-member compositions are relatively uniform, the groundwater data should plot along a roughly linear trend between the recharge and calcite end-members. Although there appears to be a trend for the data set as a whole (Figure D.1-6), it is apparent that considerable scatter would exist around any single trend line that could be drawn through the data. The scatter in these data are assumed to represent the natural variability in  $\delta^{13}\text{C}$  and alkalinity that arises because of differences in vegetation cover, rock type, and climate in the different recharge areas of these groundwaters.

On the whole, the groundwater from the PM-OV model area appears to form a different population than groundwater from the adjacent areas, being heavier in  $\delta^{13}\text{C}$  for a given alkalinity than groundwaters from Yucca Mountain and Crater Flat to the south or groundwater from Yucca Flat to the east. Because flow within the PM-OV model area is the primary focus of this study,  $^{14}\text{C}$  age corrections were made only for groundwater samples from the model area. Using  $\delta^{13}\text{C}_{\text{recharge}} = -11\text{‰}$ ,  $\delta^{13}\text{C}_{\text{calcite}} = +3\text{‰}$ , and  $\text{DIC}_{\text{recharge}}$  of 87 mg/L ( $1/\text{DIC} = 0.0115\text{ L/mg HCO}_3$ ), two estimates of the corrected  $^{14}\text{C}$  ages were made for the PM-OV samples based on Equations (D.1-2) through (D.1-4). These two estimates are compared in Figure D.1-8 against the one-to-one line. On the whole, the  $\delta^{13}\text{C}$ -corrected ages and DIC-corrected ages are in reasonable agreement, although relatively large discrepancies exist for a small number of samples (ER-18-2, ER-12-1, and UE-29a #2).

The average of the  $\delta^{13}\text{C}$ - and DIC-corrected groundwater  $^{14}\text{C}$  ages are shown for each well in map view in Figure D.1-9 superimposed on the flow paths identified in Kwicklis et al. (2005). The groundwater beneath Pahute Mesa in Areas 19 and 20 has a corrected  $^{14}\text{C}$  age of between approximately 11,000 and 18,000 years, indicating a predominantly Pleistocene origin for the groundwater. Groundwater  $^{14}\text{C}$  ages in Thirsty Canyon are also between about 12,000 and 18,000 years, although they do not vary along Flow Path #1 in a systematic manner. Groundwater  $^{14}\text{C}$

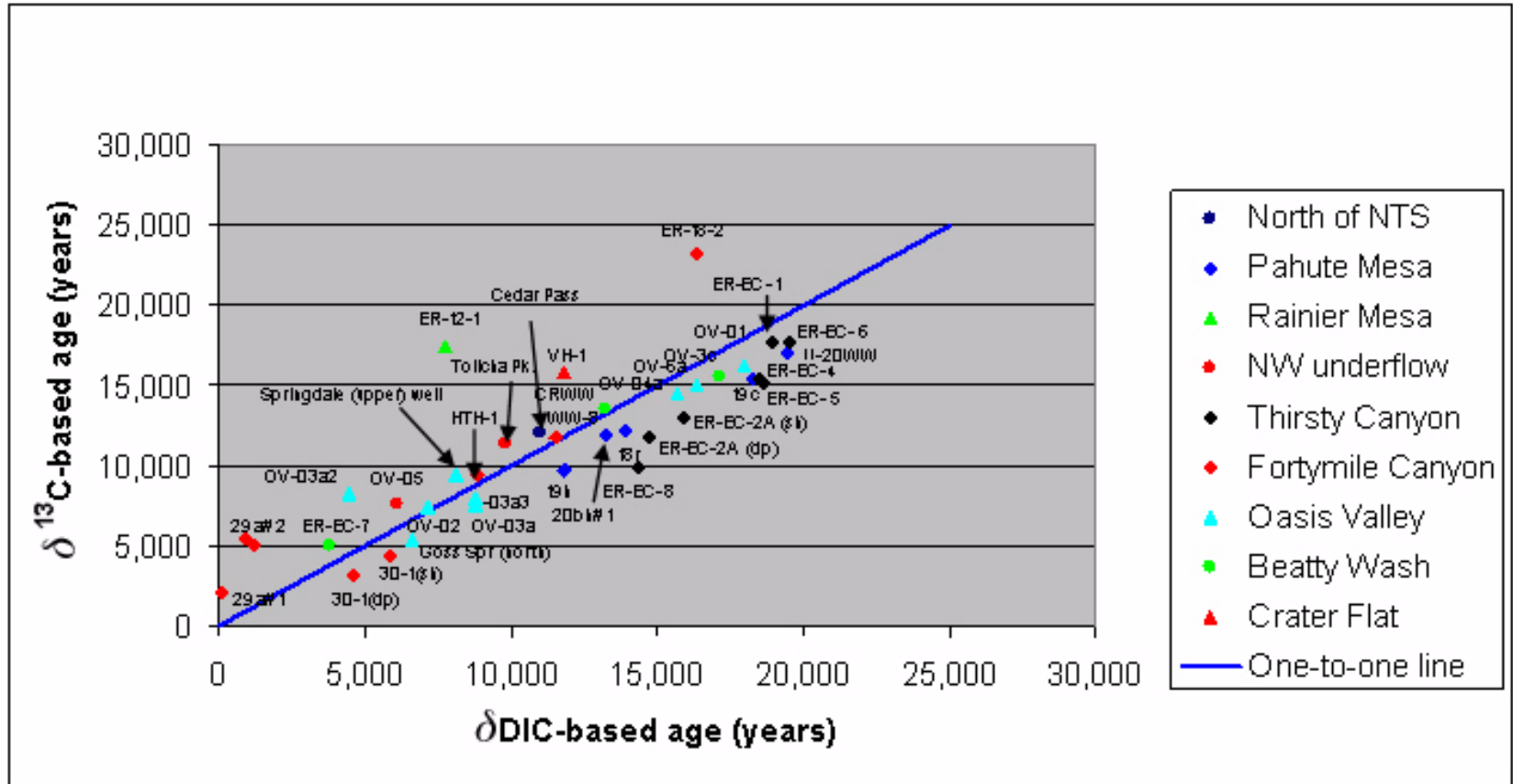
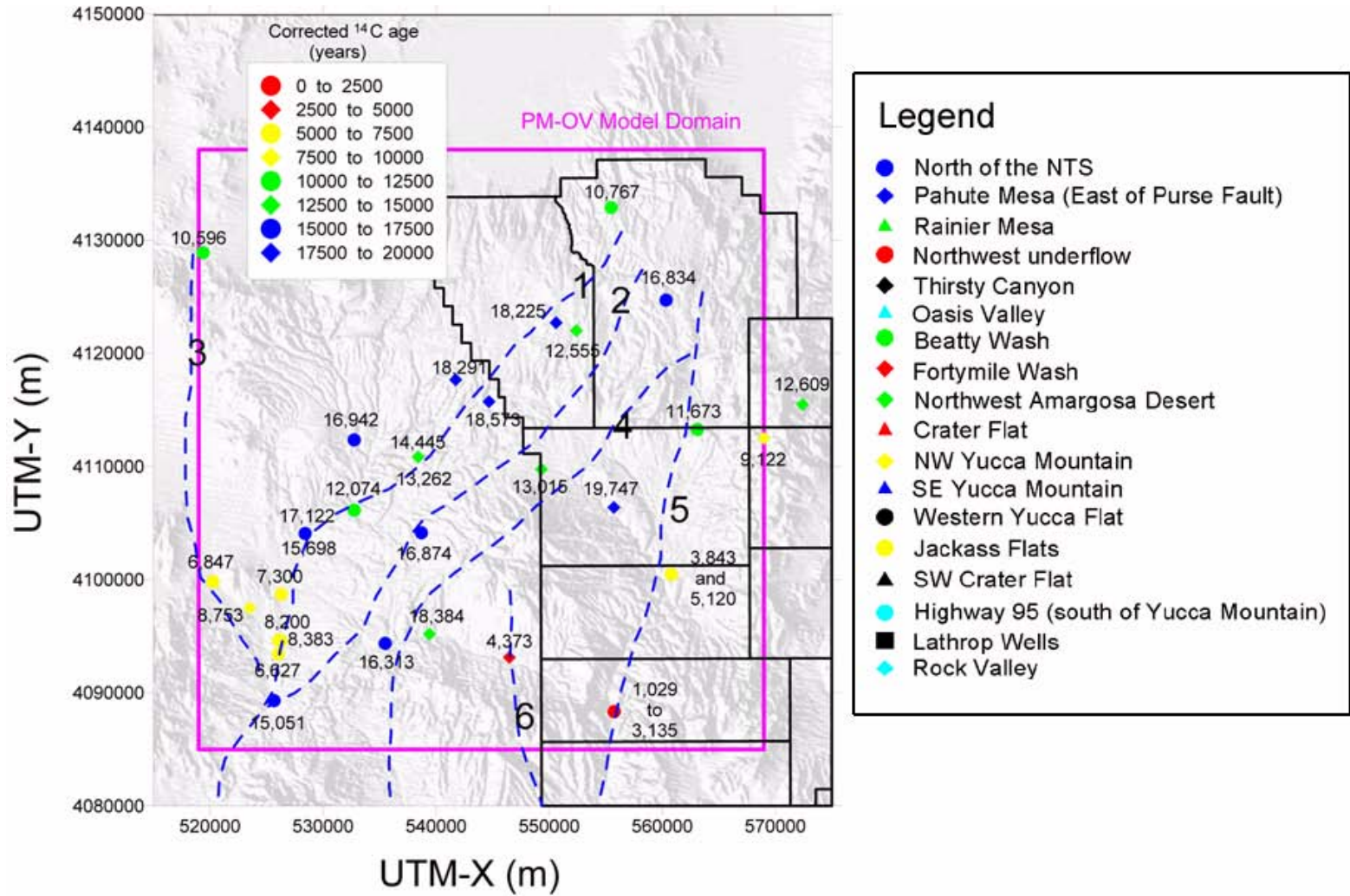


Figure D.1-8  
 Comparison of δ<sup>13</sup>C- and DIC-Corrected Groundwater <sup>14</sup>C Ages



**Figure D.1-9**  
**Average of the  $\delta^{13}\text{C}$ - and DIC-Corrected Groundwater <sup>14</sup>C Ages Superimposed on Flow Paths**

ages generally decrease to between 6,500 to 9,000 years in Oasis Valley, although two nearby wells in the northern part of Oasis Valley (ER-OV-01 and ER-OV-06a) and one well in the southern part of Oasis Valley (ER-OV-04a) have  $^{14}\text{C}$  ages greater than 15,000 years (Figures D.1-8 and D.1-9). Groundwater in the lower part of Beatty Wash southwest of Timber Mountain at ER-OV-03c and the Coffey Ranch Windmill Well (CRWW) has an age of about 16,300 to 18,300 years. This is a surprising result given the much younger ages of shallow groundwater in Fortymile Canyon along Flow Path #5 (about 1,000 to 5,000 years), and may indicate that recharge beneath lower Beatty Wash is relatively insignificant, as inferred from stable isotopes and tracers by Kwicklis et al. (2005). Groundwater at ER-EC-7 in upper Beatty Wash is much younger (about 4,400 years), but this water originates as recharge on Timber Mountain and was interpreted from geochemical modeling to flow southeast through northern Yucca Mountain toward Fortymile Wash along Flow Path #6 (Kwicklis et al., 2005).

#### ***D.1.4 Effects of Unsaturated-Zone Thickness and Sampling Depths on $^{14}\text{C}$ Ages***

In an effort to better understand the variations in groundwater  $^{14}\text{C}$  ages, the average of the  $\delta^{13}\text{C}$ - and DIC-corrected  $^{14}\text{C}$  ages at each well were plotted as a function of unsaturated-zone thickness (depth to water) in Figure D.1-10 and as a function of average depth and range of the sampled interval below the water table in Figure D.1-11. The Pleistocene age of the groundwater beneath Pahute Mesa (and the apparent absence of modern recharge) may be related to the considerable thickness of the unsaturated zone (600 to 700 m) under Pahute Mesa (Figure D.1-10). Most of the Pahute Mesa wells sample the upper few hundred meters of the saturated zone (Figure D.1-11a). The unsaturated-zone thickness beneath the Thirsty Canyon area is more variable, ranging from more than 600 m in the northern part of Thirsty Canyon area at ER-EC-1 to about 100 m at ER-EC-8 in the south. In general, the average depths of the Thirsty Canyon samples below the water table are quite deep, ranging from about 240 m at ER-EC-5 to almost 800 m at ER-EC-2A (deep), and the length of the open intervals are large, particularly at ER-EC-6, ER-EC-1, ER-EC-2A (deep), and ER-EC-5 (Figure D.1-11a).

In contrast, the depths to water at the Oasis Valley wells are generally less than 20 m (ER-OV-03a2 has a depth to water of 49 m) (Figure D.1-10). Additionally, the average depths of the sampled intervals below the water table are generally less than 50 m except at ER-OV-06a (152 m) and ER-OV-03a2 (136 m) and the open interval thickness are small (Figure D.1-11b). The relatively thin



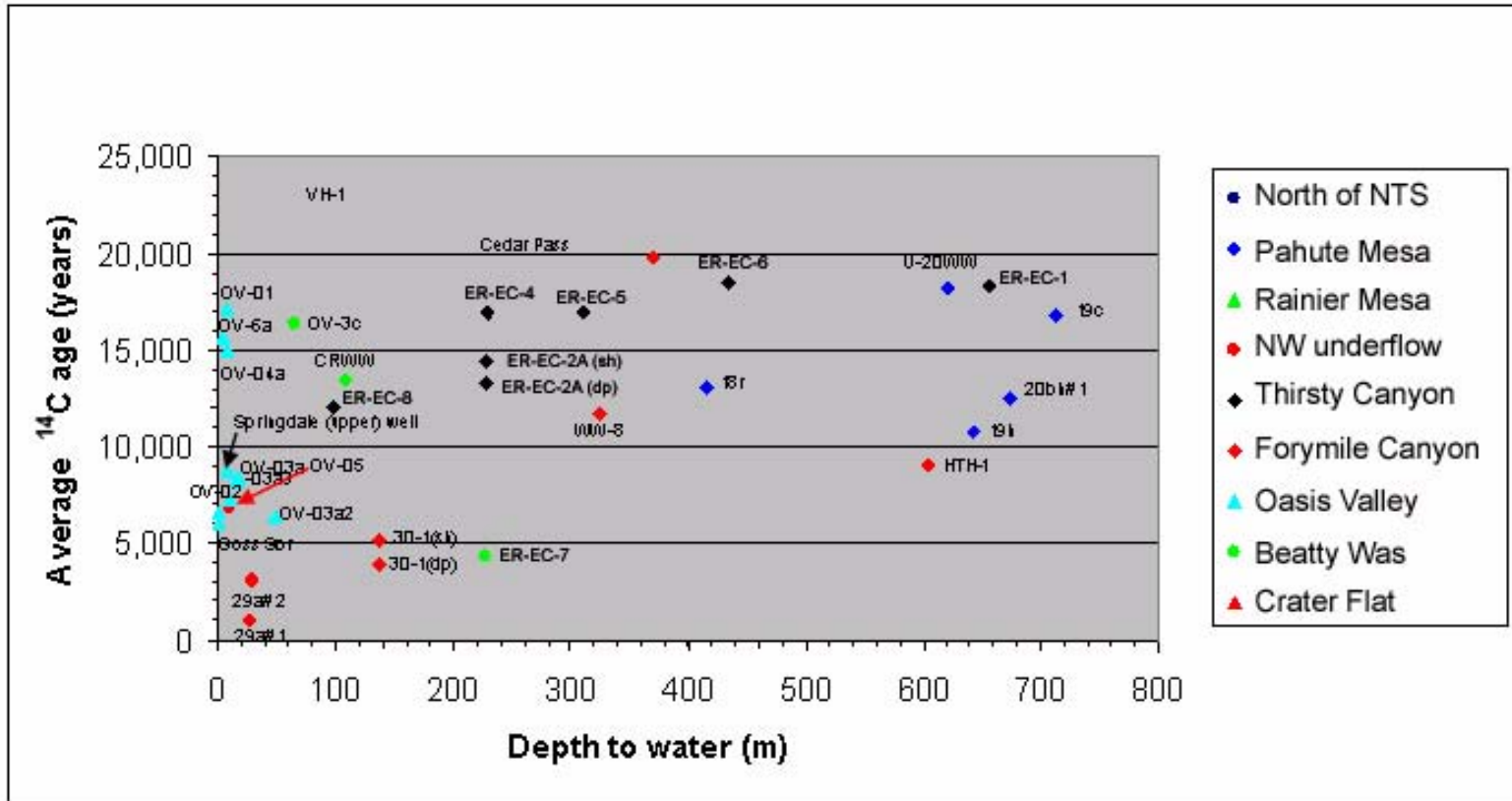


**Figure D.1-10**  
**Average of the  $\delta^{13}\text{C}$ - and DIC-Corrected Groundwater  $^{14}\text{C}$  Ages as a Function of Depth to Water**

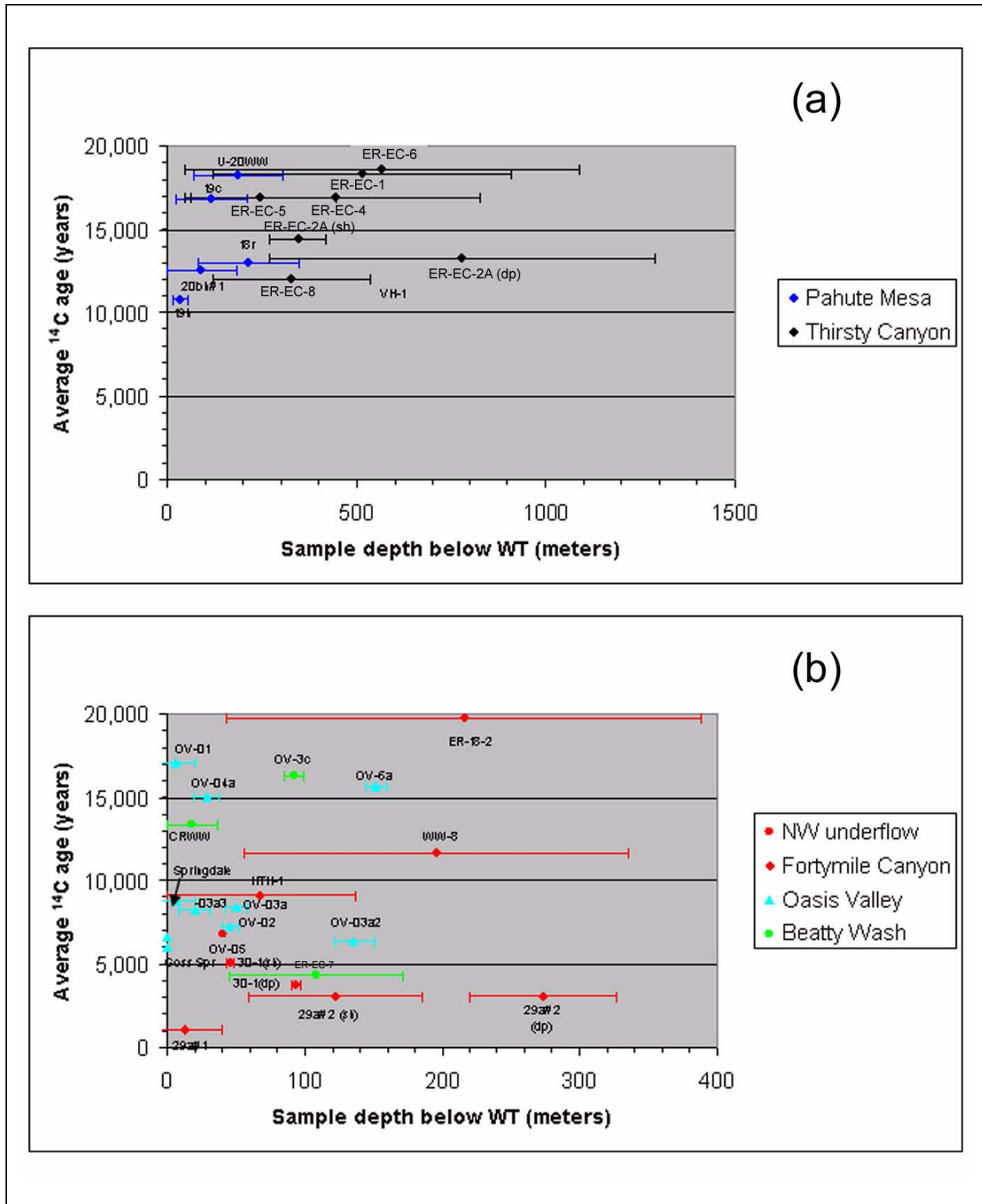


**Figure D.1-11**  
**Average Corrected <sup>14</sup>C Age as a Function of Sample Depth below the Water Table (WT) (a) Pahute Mesa and Thirsty Canyon Wells and (b) Other Wells**

unsaturated zone and shallow sampling depths make it more likely that local recharge flowing at shallow depths would be detected in the Oasis Valley samples, as evident in the plot of  $\delta D$  versus Cl described earlier (Figure D.1-4). This potential recharge could occur south of ER-OV-01 and ER-OV-06a where the depth to water is also small (Figure D.1-10), but where old  $^{14}C$  ages do not appear to reflect the presence of recharge (Figure D.1-8). Local recharge in Oasis Valley north of ER-OV-4a does not have a significant effect on the groundwater  $^{14}C$  age at the well, despite the fact that the depth to water and the average sample depth are both small at ER-OV-4a (Figures D.1-10 and D.1-11b). The old groundwater  $^{14}C$  ages in lower Beatty Wash at ER-OV-03c and the CRWW (greater than 15,000 years) and the inferred absence of significant recharge beneath lower Beatty Wash do not appear to be related to either their unsaturated-zone thickness or the depths of these samples beneath the water table, both of which are small compared with ER-EC-7, where groundwater  $^{14}C$  ages are much younger (Figures D.1-10 and D.1-11b).

In Fortymile Canyon, the depths to water are less than 40 m at UE-29a #1 and UE-29a #2, with samples originating from depths below the water table of 15 to 280 m. Both unsaturated zone thickness and sampling depths are considerably larger at other wells in this sample group that are located in adjacent upland areas (ER-18-2, WW-8, and HTH-1). The considerable range in unsaturated-zone thickness and sample depths relative to the water table may be a factor contributing to the wide range of groundwater  $^{14}C$  ages estimated for this group of wells.

In summary, the thick unsaturated-zones beneath Pahute Mesa, the northern part of Thirsty Canyon, and upland areas adjacent to Fortymile Canyon may contribute to the apparent absence of modern recharge in these areas. For the Thirsty Canyon wells and upland wells included in the Fortymile Wash group, the depths of the samples below the water table may also contribute to their large apparent  $^{14}C$  ages. Most of the Oasis Valley wells and wells immediately to the west of Oasis Valley produce samples from wells where depths to water are small and samples are relatively close to the water table. Samples from these wells would be especially likely to include any local recharge in these locations. In contrast, despite the fact that depths to water are small and the wells sample water close to the water table, groundwater  $^{14}C$  ages from lower Beatty Wash at ER-OV-3c and CRWW demonstrate that little recent recharge take place in this area.

### D.1.5 Groundwater Travel Time Calculations

The groundwater  $^{14}\text{C}$  ages calculated in the previous sections give an overall indication of when groundwater recharge took place, and although some inferences about flow system behavior can be made from these ages, travel times between locations in the flow system cannot be calculated directly from the difference in ages. This is because these  $^{14}\text{C}$  ages reflect not only the upgradient groundwater  $^{14}\text{C}$  activities, but also the effects of groundwater mixing and water/rock interaction. Although the PHREEQC code itself does not directly calculate groundwater travel times, the mixing fractions and water/rock interactions that are identified in the PHREEQC inverse models (Kwicklis et al., 2005) can be used to perform these calculations in a post-processing step external to the code.

Groundwater transit times in this report were calculated in EXCEL using the radioactive decay Equation (D.1-3), together with estimates of the groundwater  $^{14}\text{C}$  activity that results from upgradient mixing ( $^{14}\text{C}_{\text{mix}}$ ) and subsequent  $^{14}\text{C}$  dilution by carbonate reactions ( $q_{\text{DIC}}$ ):

$$t_c = (1/\lambda) \times \ln (^{14}\text{C}_{\text{mix}} \cdot q_{\text{DIC}} / ^{14}\text{C}_{\text{well}}) \quad (\text{D.1-5})$$

This equation is identical to Equation (D.1-3), except that the term  $^{14}\text{C}_{\text{mix}}$  substitutes for  $^{14}\text{C}_{\text{rech}}$  and  $t_c$  represents the composite travel time. Operationally,  $^{14}\text{C}_{\text{mix}}$  is calculated as the  $^{14}\text{C}$  activity that results from mixing the upgradient groundwaters in the proportions identified in the PHREEQC models:

$$^{14}\text{C}_{\text{mix}} = (f_1^{14}\text{C}_1 \text{DIC}_1 + f_2^{14}\text{C}_2 \text{DIC}_2 + \dots + f_i^{14}\text{C}_i \text{DIC}_i) / (f_1 \text{DIC}_1 + f_2 \text{DIC}_2 + \dots + f_i \text{DIC}_i) \quad (\text{D.1-6})$$

where  $f_i$ ,  $^{14}\text{C}_i$ , and  $\text{DIC}_i$  are the mixing fractions,  $^{14}\text{C}$  activities, and DIC concentrations at each upgradient well  $i$  in the mixture.

The  $^{14}\text{C}$  dilution factor  $q_{\text{DIC}} = \text{DIC}_{\text{mix}} / \text{DIC}_{\text{well}}$  can be calculated from the relative increase in DIC that occurs between the upgradient mixture and the downgradient well. This term is also calculated from the PHREEQC output:

$$q_{\text{DIC}} = (f_1 \text{DIC}_1 + f_2 \text{DIC}_2 + \dots + f_i \text{DIC}_i) / (f_1 \text{DIC}_1 + f_2 \text{DIC}_2 + \dots + f_i \text{DIC}_i + \text{DIC}_{\text{carbonate}}) \quad (\text{D.1-7})$$

The groundwater travel times estimated from the  $^{14}\text{C}$  decay Equation (D.1-5) provide an estimate of the average or composite travel time for the mixture to the downgradient well. These estimates can be useful when the upgradient boreholes are close to each other, relative to their distance from the

downgradient well. However, these composite travel times become less meaningful when the upgradient wells in the mixture are widely separated or lie along different trajectories to the downgradient well. Estimates of the travel times from individual upgradient wells to the downgradient well can be obtained from the PHREEQC model results by expressing the composite travel times from the individual models as a function of the mixing fractions and travel times from the individual wells:

$$\begin{aligned}
 f_{1a}t_{t_1} + f_{2a}t_{t_2} + \dots + f_{na}t_{t_n} &= t_{t_a} \\
 f_{1b}t_{t_1} + f_{2b}t_{t_2} + \dots + f_{nb}t_{t_n} &= t_{t_b} \\
 &\vdots \\
 &\vdots \\
 &\vdots \\
 f_{1m}t_{t_1} + f_{2m}t_{t_2} + \dots + f_{nm}t_{t_n} &= t_{t_m}
 \end{aligned}
 \tag{D.1-8}$$

where  $f_{ij}$  is the mixing fraction of well  $i$  ( $i = 1$  to  $n$ ) in model result  $j$  ( $j = a$  to  $m$ ),  $t_{t_i}$  is the travel time from well  $i$  to the downgradient well, and  $t_{t_j}$  is the composite travel time calculated from the radioactive decay equations for model result  $j$ . The equation matrix expresses variations in the composite travel times ( $t_{t_j}$ ) among the model results as a function of the variations of the identified mixing fractions ( $f_{ij}$ ) and the unknown travel times from the individual wells to the downgradient well ( $t_{t_i}$ ). On the right hand side of the equation are the composite travel time  $t_{t_j}$  of the resulting mixture in model  $j$ .

For some sets of inverse models, the number of unique mixing models will be smaller than the number of wells involved in the mixtures, so that the travel times from individual wells to the downgradient well cannot be estimated. Rarely, the number of unique models and the number of upgradient wells in a set of models will be the same, so that travel times from individual wells to the downgradient well can be identified uniquely. Most often, there are many more models than there are wells with non-zero mixing fractions in a set of model results, so that the unknown travel times from the individual wells ( $t_{t_i}$ ) must be estimated by regression rather than by direct inversion of the system of equations. In this study, the regression analyses were done using EXCEL to estimate the slopes in the system of equations (i.e., the values of  $t_{t_i}$ ) along with their 95 percent confidence limits, thus providing the desired estimates of the travel times from individual wells and their uncertainty bounds.

It is also of interest to note that in the special case where only two upgradient sources contribute to the downgradient well, and one of those sources is local recharge for which it can be reasonably assumed that  $t_1 = 0$ , Equation (D.1-5) can be rearranged to find the travel time from the second source to the downgradient well ( $t_2$ ) by removing the  $^{14}\text{C}$  contributed to the downgradient well by the recharge:

$$t_2 = (-1/\lambda) \ln [(^{14}\text{C}_{\text{well}}\text{DIC}_{\text{well}} - f_{\text{rech}}\ ^{14}\text{C}_{\text{rech}}\text{DIC}_{\text{rech}})/f_2\ ^{14}\text{C}_2\text{DIC}_2] \quad (\text{D.1-9})$$

Equation (D.1-9) was used to estimate groundwater travel times for some inverse models where only two mixing components were identified and one of them was a local recharge component.

### D.1.6 Travel Time Results

Because the addition of local recharge causes increases in groundwater  $^{14}\text{C}$  activities near Oasis Valley, it is difficult to extract meaningful travel time estimates when Oasis Valley wells affected by local recharge are used as the downgradient wells in the travel time calculations. Therefore, the focus in this study is the calculation of travel times from Pahute Mesa area wells to wells in Oasis Valley where local recharge does not appear to have impacted the groundwater ages. The Oasis Valley wells where groundwater appears to be largely free of local recharge are identified by their proximity to the Thirsty Canyon Mixing Line in Figure D.1-4. These wells include ER-OV-01, ER-OV-03a, and ER-OV-4a, which appear from these plots to be composed mostly Pahute Mesa and Thirsty Canyon area groundwater. Figure D.1-6 shows these wells lie along a projection of the Thirsty Canyon Mixing Line toward values typical of calcite or dolomite ( $\delta^{13}\text{C} = 0 \pm 3$  per mil,  $1/\text{alkalinity} = 0$ ), suggesting these wells have interacted with carbonate minerals by not with either soil gas, which has a  $\delta^{13}\text{C}$  of -23.7 to -18.0 per mil (White and Chuma, 1987) or with local recharge (exemplified by data from UE-29a #2).

Travel times for the PM-OV flow system are discussed according to the flow paths shown in Figure D.1-5. A detailed discussion of the derivation of these flow paths is provided in Kwicklis et al. (2005). To summarize briefly, these flow paths were derived by constructing a series of geochemical inverse models for wells located at or beyond the downgradient margins of the PM-OV flow model boundaries (i.e., the “target wells”). Candidate wells that could contribute groundwater to the mixed groundwater that is assumed to be present at the downgradient well were selected based scatterplots of conservative species such as  $\delta\text{D}$  and  $\text{Cl}$  (Figure D.1-4) and permitted by the hydraulic

gradient. Once the upgradient groundwater source areas, represented by the candidate wells, were identified, the selected candidate wells became the new target wells and new upgradient candidate wells were chosen based on scatterplots of conservative dissolved species and the hydraulic gradient. Eventually, a network of models is constructed that shows where groundwater at each well in the system originates and the proportions of water contributing to the mixture at the target well (see Figure 15 of Kwicklis et al. [2005] for an example). Based on these quantitative results, interpretative flow paths are then drawn to capture the main directions of groundwater flow identified in the analysis, while remaining true to the general principles that groundwater can only flow from areas of higher hydraulic head to lower hydraulic head, and that flow paths will not cross in two dimensions in a groundwater system at steady state.

#### **D.1.7 Flow Path #1**

A graphical summary of the PHREEQC models that form the basis for Flow Path #1 is shown in [Figure D.1-12](#). On this plot, the results for two sets of inverse models are shown, one set for target ER-EC-6 (shown in red) and one set for target ER-OV-01 (shown in blue). In this, and in similar plots presented later in later sections, the numbers listed adjacent to the arrows connecting different upgradient wells to the target well represent the range in the mixing fractions of the upgradient groundwater at the target well estimated by that set of models. A lower limit of zero indicates that some of the inverse models in the set did not include that particular upgradient well in the mixture, and so it is not a required part of the mixture. The contributions of local recharge components, typically represented by UE-29a #1 or UE-29a #2 groundwater to represent local recharge from ephemeral runoff in a wash, or by ER-EC-7 groundwater to represent recharge on Timber Mountain, are not represented on these maps because the direction of flow from the recharge components is assumed to be vertical.

The PHREEQC inverse model results when ER-EC-6 is the chosen as the target well are shown in [Figures D.1-13a](#) and [D.1-13b](#). PHREEQC identified seven models involving different mixing scenarios and water/rock reactions that would produce the measured groundwater chemistry at ER-EC-6. The horizontal bars in [Figure D.1-13a](#) represent the 95 percent confidence limits in the mixture fractions for each model based on the user-specified uncertainty in groundwater compositions. In these models, groundwater from U-20 WW and ER-EC-1 mixes in roughly equal

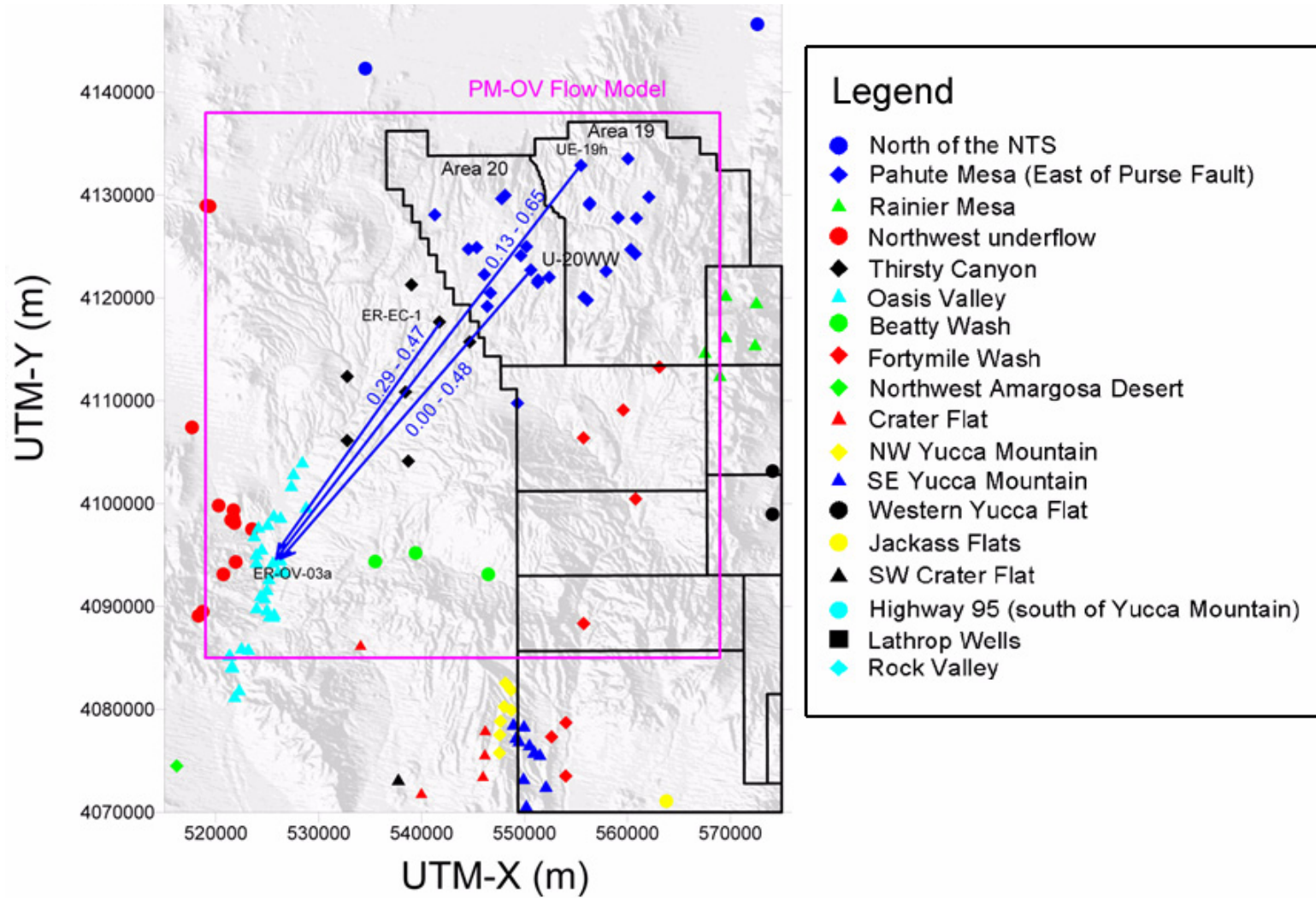


**Figure D.1-12**  
**Map Summarizing Mixing Models for Flow Path #1**



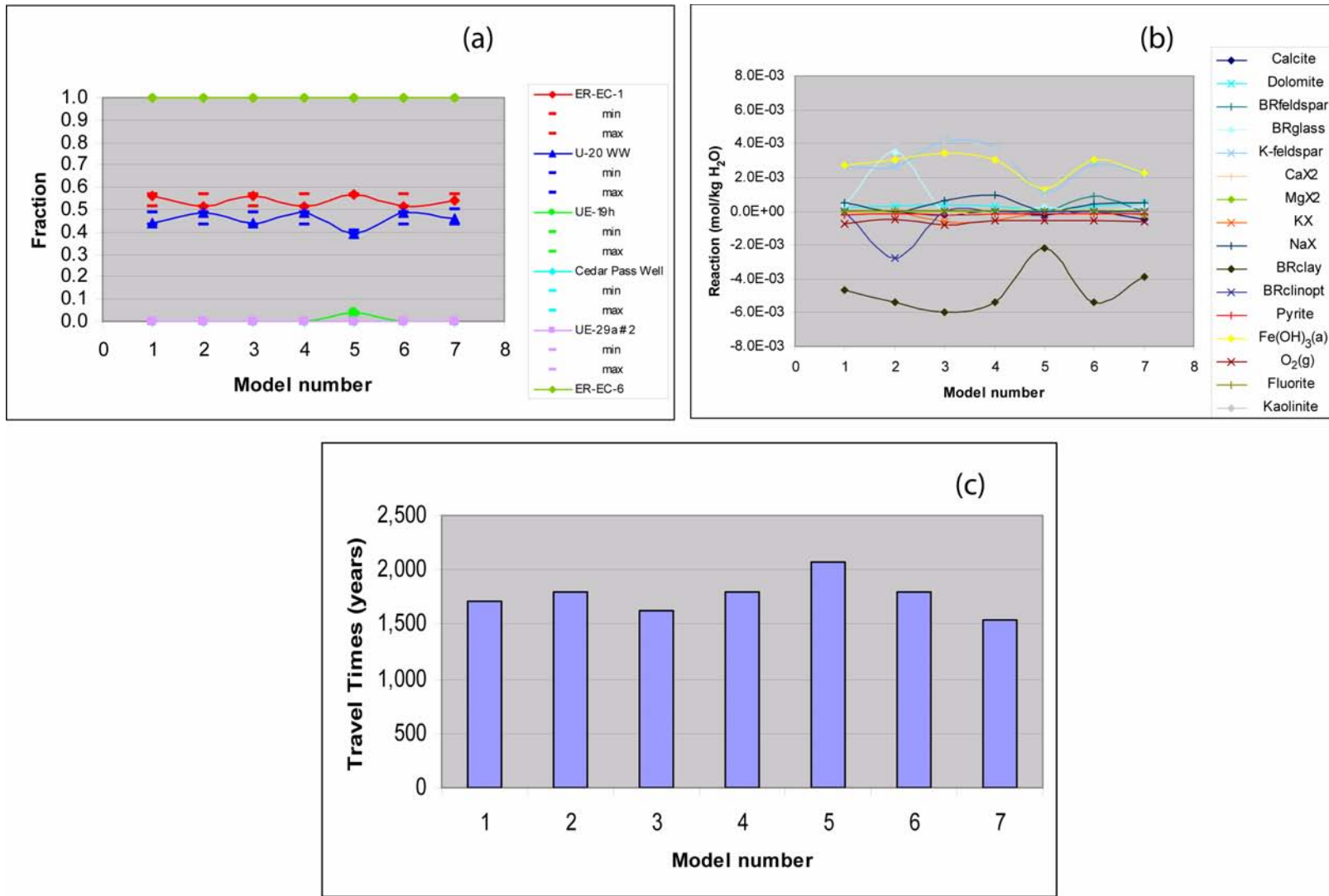


**Figure D.1-13**  
**Inverse Model Results for ER-EC-6: (a) Mixing Fractions, (b) Reactions, and (c) Composite Travel Times**

proportions along with a possible minor contribution from UE-19h. The composite travel times for this set of models calculated using Equation (D.1-5) range from approximately 1,500 to 2,100 years (Figure D.1-13c). Decomposition of the composite travel times for this set of models using Equation (D.1-8) yields travel times from ER-EC-1 (357 years), U-20 WW (3,264 years), and UE-19h (14,528 years), but these travel times have considerable uncertainty associated with them (Table D.1-1). Based on their relative proximity to ER-EC-6, the magnitudes of the travel times from these wells to ER-EC-6 seem reasonable. The longer apparent travel time from UE-19h to ER-EC-6 may be related to the fact that UE-19h samples shallower (and younger) groundwater than other wells included in these models (Figure D.1-11).

**Table D.1-1**  
**Travel Times from Individual Wells to ER-EC-6**

Upgradient Well	Estimated Travel Time (Years)	Lower 95% Confidence Limit (Years)	Upper 95% Confidence Limit (Years)
ER-EC-1	357	-2,196	2,910
U-20 WW	3,264	337	6,191
UE-19h	14,528	4,329	24,726

The second set of models along this flow path involves ER-OV-01 as the target well and widely separated wells to the northeast and northwest as potential contributing wells (Figure D.1-12). Although in most hydrologic settings groundwater mixing among such widely separated areas would be considered unlikely, groundwater flow paths are expected to converge near Oasis Valley because it is a major discharge area for the flow system and flow paths bend toward it as they would toward a pumping well.

Based on the plot of  $\delta^{14}\text{C}$  versus inverse alkalinity (Figure D.1-6), ER-OV-01 is north of the area in Oasis Valley that appears to be affected by local recharge or by water/soil gas interactions. The results for this set of models shows that ER-OV-01 derives most of its water from the vicinity of ER-EC-6, with minor and highly variable contributions from other wells in the mixture (Figure D.1-14). Local recharge, represented by water compositions equivalent to UE-29a #2 groundwater, is no more than 8 percent of the mixture, and is absent in most of the models. The inverse models for ER-OV-01, when considered with the inverse models for ER-EC-6, imply the continuity of a flow path from Area 20 through ER-EC-6 and the Thirsty Canyon area to northern

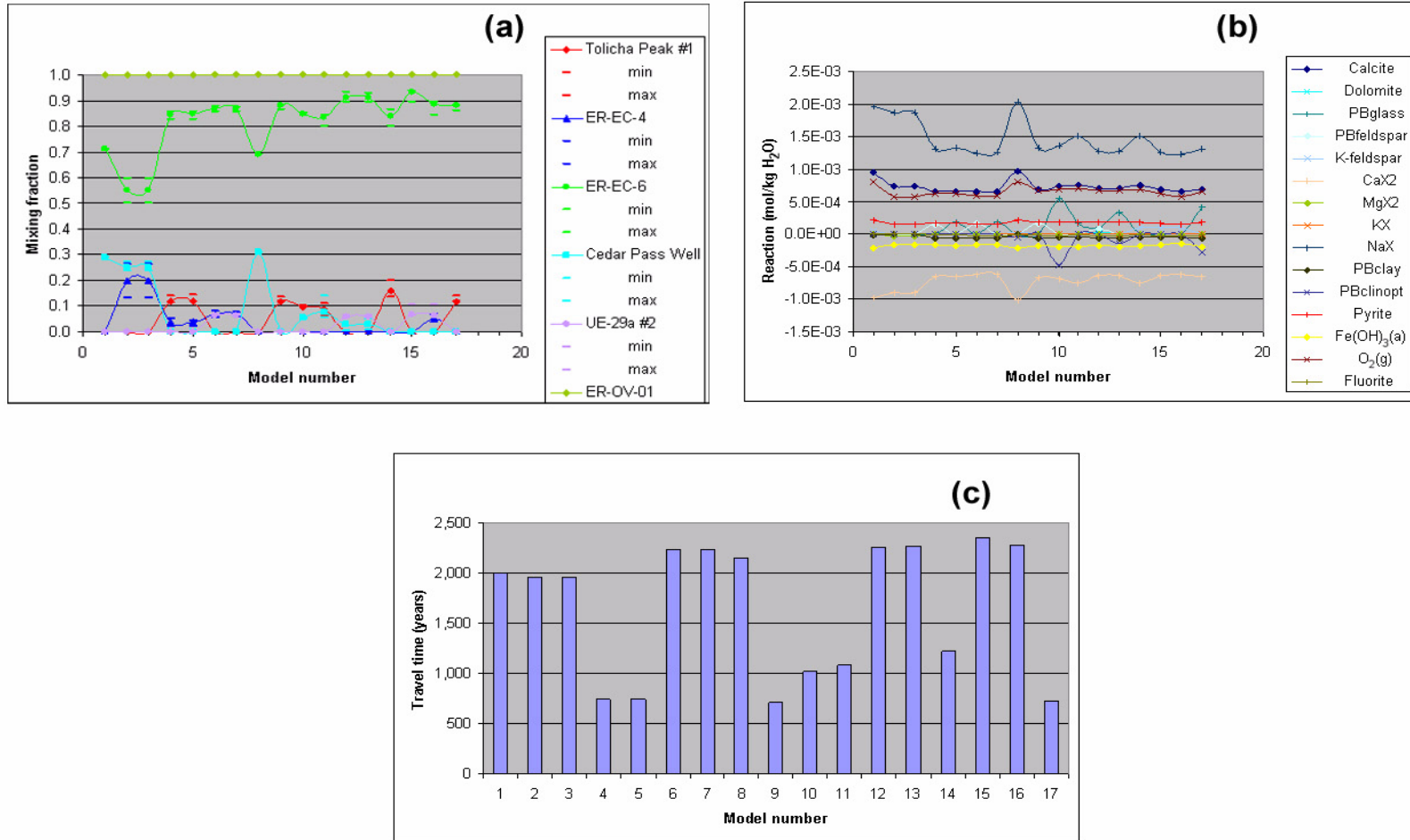


Figure D.1-14

Inverse Model Results for ER-OV-01: (a) Mixing Fractions, (b) Reactions, and (c) Composite Travel Times

Oasis Valley. Composite travel times to ER-OV-01 range from about 700 years to more than 2,300 years (Figure D.1-14c). Decomposition of the composite travel times yields an estimate of the travel time from ER-EC-4 to ER-OV-01 of 867 years and a travel time from ER-EC-6 to ER-OV-01 of -631 years, a physical impossibility. The tight confidence limits on the estimated travel times suggest the mean travel times are relatively well constrained by the available data (Table D.1-2).

**Table D.1-2  
Travel Times from Individual Wells to ER-OV-01**

Upgradient Well	Estimated Travel Time (Years)	Lower 95% Confidence Limit (Years)	Upper 95% Confidence Limit (Years)
Tolicha Peak AFB #1	10,679	9,773	11,586
ER-EC-4	867	693	1,040
ER-EC-6	-631	-764	-498
Cedar Pass Well	8,500	8,172	8,829
UE-29a #2	43,956	42,048	45,863

However, the small differences in the <sup>14</sup>C activities of ER-EC-6 (5.4 pmc), ER-EC-4 (5 pmc), and ER-OV-01 (5 pmc) makes it difficult to extract a meaningful travel time from ER-EC-6 to ER-OV-01 when the complicating effects of other mixing components must also be considered. An additional factor to consider with regard to these short or negative travel times is that ER-EC-4 and ER-EC-6 draw their water from thick, relatively deep open intervals, whereas water from ER-OV-01 was sampled from a thin, shallower interval near the water table (Figure D.1-11). If differences in groundwater age with depth are a factor, the differences in sampling depths and open interval thickness among these wells would tend to favor younger groundwater being sampled at ER-OV-01. This could be a factor contributing the apparently short travel times along Flow Path #1. Nonetheless, short travel times within the Thirsty Canyon area are possible given the available <sup>14</sup>C data.

To determine whether travel times could be estimated for shorter flow path segments along Flow Path #1, the PHREEQC inverse models documented in Kwicklis et al. (2005) were augmented with additional inverse models for ER-EC-2A (both shallow and deep intervals) and for ER-EC-8. The inverse models for ER-EC-2A (shallow interval) indicate that ER-EC-2A groundwater is formed by

mixing water from ER-EC-6 and ER-EC-4 with small amounts of groundwater from U-20 WW or UE-19h (Figures D.1-15a and D.1-15b).

Groundwater from the deep interval of ER-EC-2A also derives most of its groundwater from ER-EC-6 and ER-EC-4, but can derive as much as 25 percent of its groundwater from UE-18r (Figures D.1-16a and D.1-16b). Further downgradient in the Thirsty Canyon area, groundwater from ER-EC-8 can be formed from a two-component mixture of ER-EC-2A (deep) groundwater and UE-19c WW groundwater, or from a three component mixture involving ER-EC-4, ER-EC-2A (shallow) and UE-19c WW (Figures D.1-17a and D.1-17b). Groundwater from ER-EC-1 and ER-EC-6 are not explicitly identified in the ER-EC-8 inverse models as components in ER-EC-8 groundwater, but are indirectly inferred to be components due to their presence in the ER-EC-6 and ER-EC-2A models. Unfortunately, all the models for ER-EC-2A (shallow and deep intervals) as well as the models for ER-EC-8 yielded negative composite travel times. Either groundwater travel times in the Thirsty Canyon area are too short to be resolved with the methods employed here, or other shallower upgradient groundwater with higher  $^{14}\text{C}$  activities is present in the Thirsty Canyon area that has not yet been sampled or identified within the mixed groundwater sampled from the thick, open intervals (Figure D.1-11a).

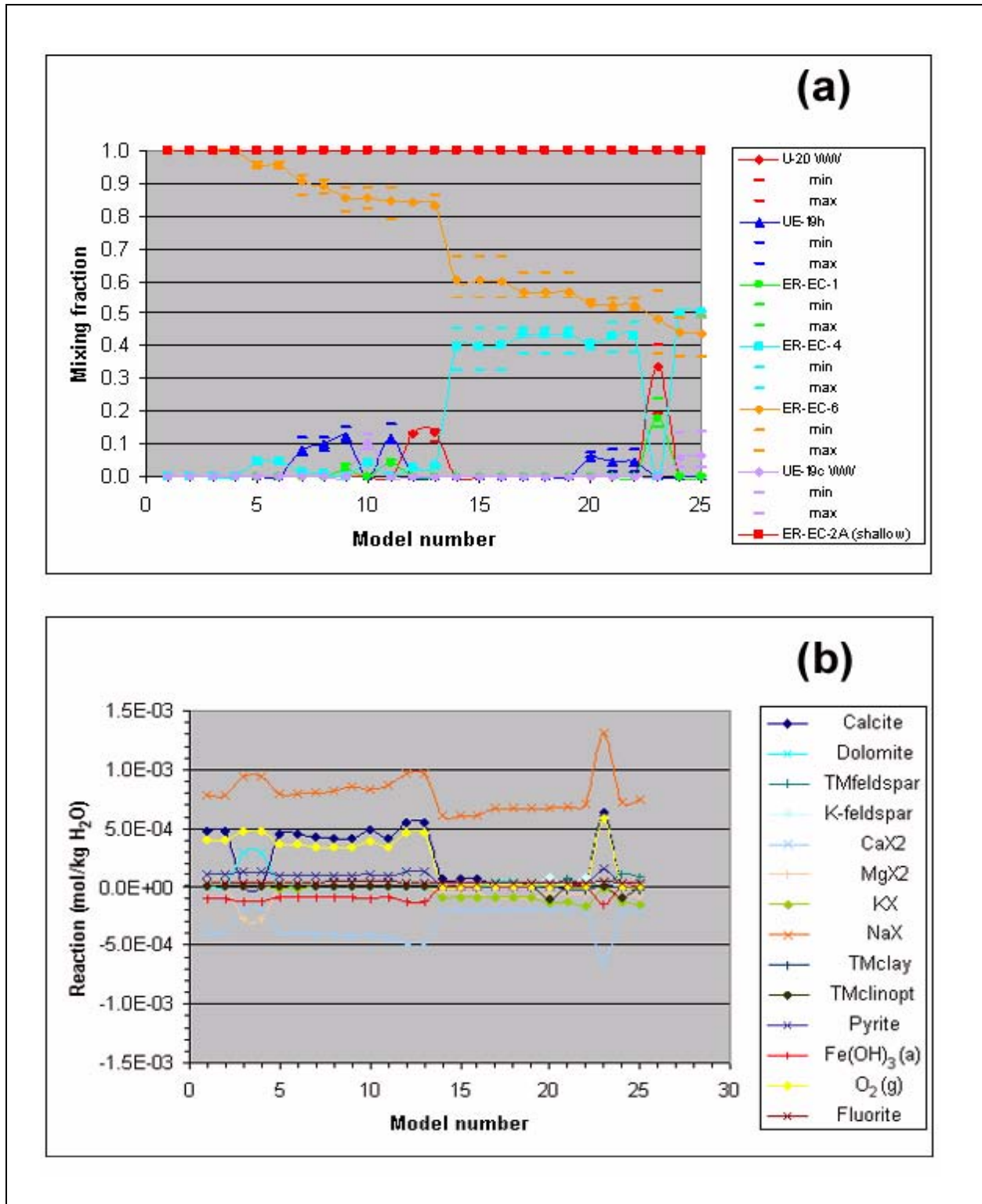


Figure D.1-15

Inverse Model Results for ER-EC-2A (shallow): (a) Mixing Fractions and (b) Reactions

Note: All composite travel times were negative.

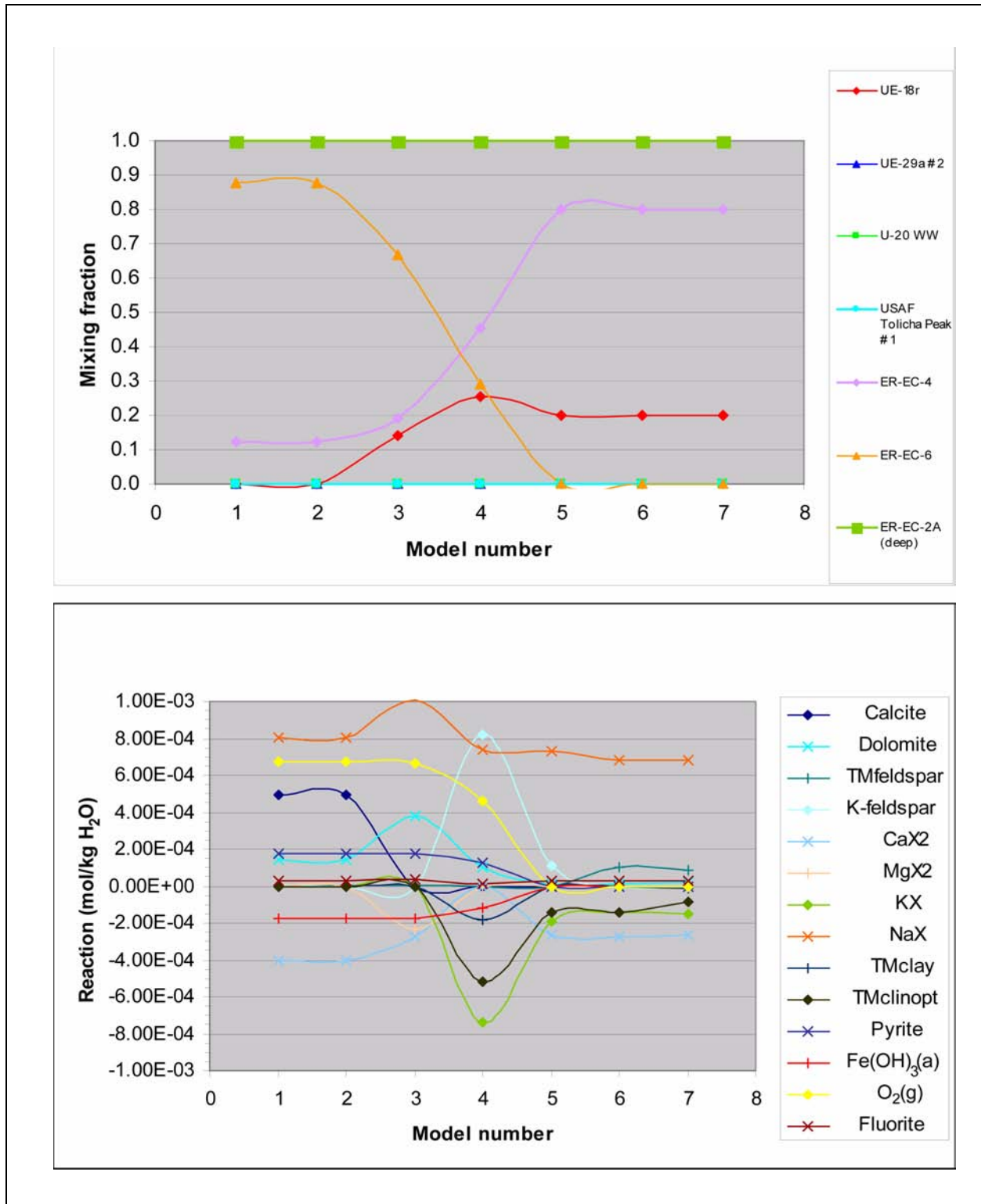


Figure D.1-16

Inverse Model Results for ER-EC-2A (deep): (a) Mixing Fractions and (b) Reactions

Note: All composite travel times were negative.

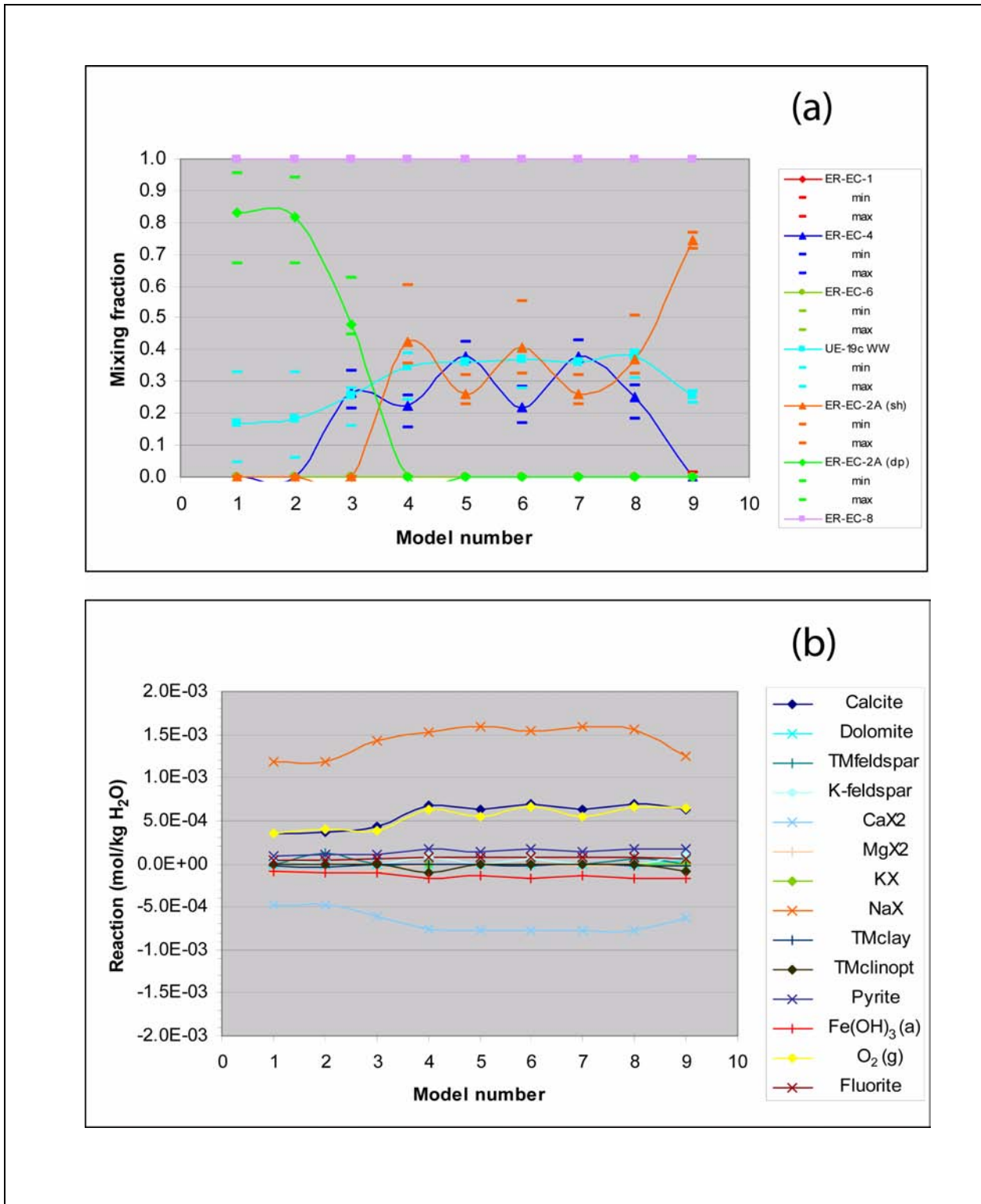


Figure D.1-17

Inverse Model Results for ER-EC-8 (shallow): (a) Mixing Fractions and (b) Reactions

Note: All composite travel times were negative.



### D.1.8 Flow Paths #2 and #4

Flow Paths #2 and #4 follow a similar trajectory from Area 19 southwestward toward Oasis Valley across the northwest perimeter of Timber Mountain (Figure D.1-5) and are based on an overlapping set of PHREEQC models. The main distinction between the two flow paths is that Flow Path #2 continues to flow southwestward toward Oasis Valley after reaching lower Beatty Wash, whereas Flow Path #4 turns southward into Crater Flat after reaching lower Beatty Wash.

The PHREEQC geochemical inverse models that provide the basis for Flow Path #2 are summarized in map view in Figure D.1-18. This sequence of models shows that groundwater from Area 19 flows through the vicinity of UE-18r north of Timber Mountain, around the northwest perimeter of Timber Mountain through the ER-EC-5 area where it mixes with smaller amounts of groundwater flowing south from Area 20 (U-20 WW) and the upper Thirsty Canyon area (ER-EC-1). Groundwater near ER-EC-5 then flows south through lower Beatty Wash near ER-OV-03c and southwestward toward ER-OV-04a in Oasis Valley. Travel times for this sequence of flow path segments and for a model from ER-EC-1 and UE-20 WW directly to ER-OV-04a are discussed in this section.

Inverse model results using UE-18r as the target well identified Area 19 wells UE-19h and UE-19c WW as the source of most of the water at UE-18r (Figures D.1-19a and D.1-19b). Significantly, no groundwater from the Rainier Mesa area (WW-8 or HTH-1) or wells from Area 20 (U-20 WW or UE-20bh #1) were identified as components in the groundwater at UE-18r, despite being included as potential upgradient endmembers in the models. Composite travel times for this set of models range from 1,000 to a little more than 1,200 years (Figure D.1-19c). The small number of models and the lack of variability in the mixing fractions prevent the derivation of meaningful travel time estimates from individual wells to UE-18r.

Working in a downgradient direction toward Oasis Valley, the next set of models involve ER-EC-5 as the target well. Only two models were found for ER-EC-5, and both indicated that approximately 63 percent of the water at ER-EC-5 originated from UE-18r, approximately 28 percent originated from U-20 WW, and approximately 9 percent originated from local recharge represented by UE-29a #2 groundwater (Figures D.1-20a and D.1-20b). The composite travel time for these two models was about 1,700 years (Figure D.1-20c). Travel times from individual wells to ER-EC-5 could not be calculated given the small number of models. Although very small differences exist in the  $^{14}\text{C}$

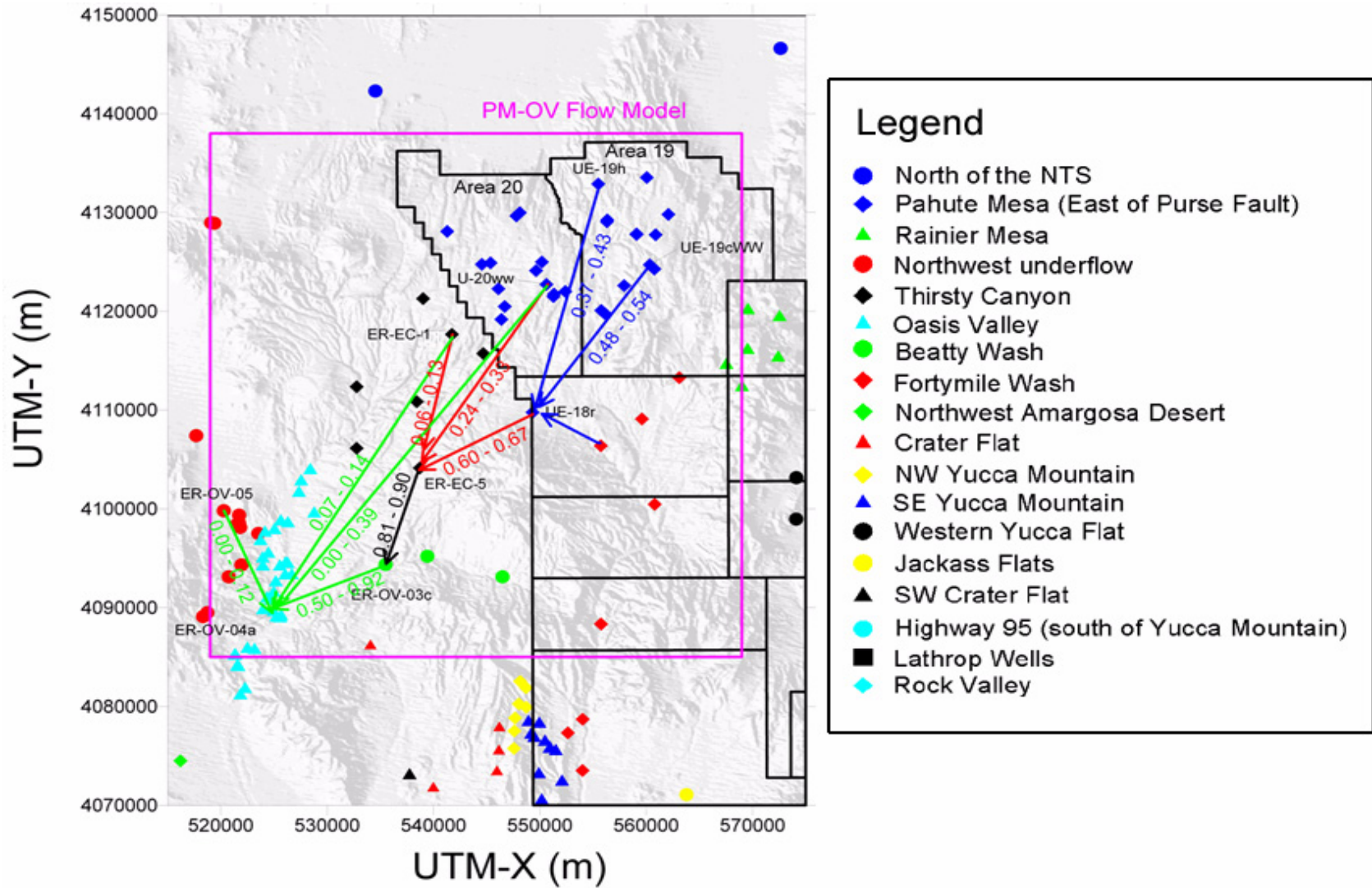


**Figure D.1-18**  
**Map Summarizing Geochemical Inverse Model Results for Flow Path #2**

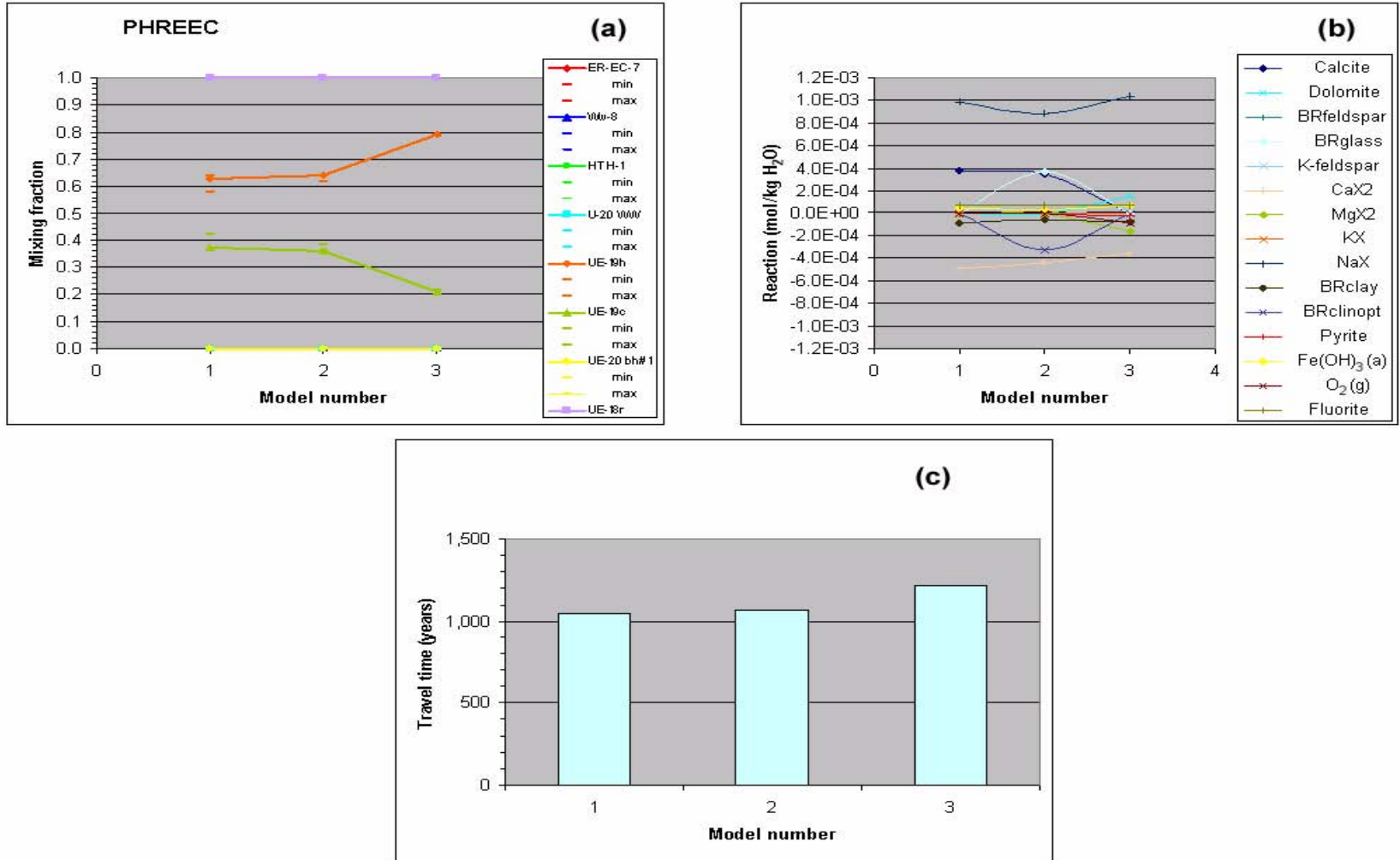


**Figure D.1-19**  
**Inverse Model Results for UE-18r: (a) Mixing Fractions, (b) Reactions, and (c) Composite Travel Times**

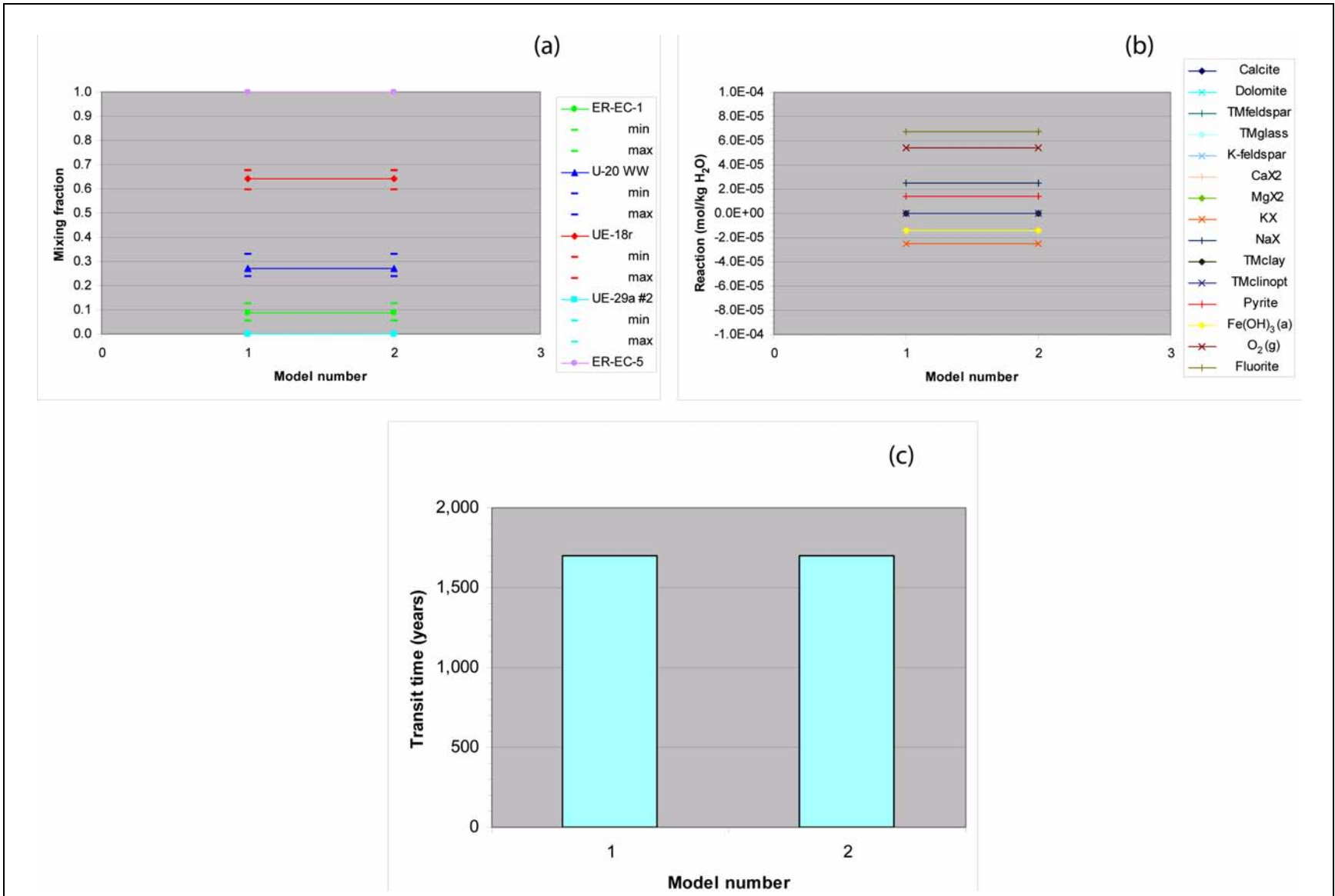


Figure D.1-20

Inverse Model Results for ER-EC-5: (a) Mixing Fractions, (b) Reactions, and (c) Composite Travel Times

activities of the non-recharge component in the mixture (U-20 WW [8.9 pmc] and UE-18r [7.7 pmc]) and the target well (ER-EC-5 [6.3 pmc]), the relative magnitude of the  $^{14}\text{C}$  activities suggests small but positive travel times for the non-recharge components.

The PHREEQC inverse models for ER-OV-03c identified groundwater from ER-EC-5 as the major component in the mixture, along with minor contributions of local recharge represented by water from either UE-29a #2 or ER-EC-7 (Figures D.1-16 and D.1-21a, b, and c). Groundwater from ER-EC-7 water is thought to be derived mostly from recharge on Timber Mountain because of the presence of bomb-pulse  $^3\text{H}$  and  $^{36}\text{Cl}$  in the water (Rose et al., 2006; Kwicklis et al., 2005), yet its relatively old  $^{14}\text{C}$  age of about 4,400 years suggests that, if this is the case, it is a mixture of younger and older recharge. Composite travel times calculated for this set of models ranged from 3,200 to 5,400 years (Figure D.1-21c). Decomposition of the composite travel times resulted in an estimated travel time from ER-EC-5 to ER-OV-03c of about 1,574 years, with lower and upper 95 percent confidence limit of 503 and 2,645 years (Table D.1-3). Mean travel times for the local infiltration to reach the sampling point at ER-OV-03c were about 17,000 years for model in which ER-EC-7 groundwater was assumed to represent local recharge, and 24,000 years in models where UE-29a #2 groundwater was taken as representative of local recharge. In terms of the calculations, the long travel times calculated for the local recharge components are a consequence of the large contrasts in the  $^{14}\text{C}$  activities of the recharge components ( $^{14}\text{C} = 36.5$  and  $60$  pmc for ER-EC-7 and UE-29a #2, respectively) and the ER-OV-03c groundwater ( $^{14}\text{C} = 6.8$  pmc). The physical meaning of these long travel times is more difficult to fathom, but it may reflect a combination of factors including low infiltration rates and a sampling depth at ER-OV-03c of approximately 150 m relative to land surface. As an exploratory calculation, the pore water velocity required for a particle of water to travel 150 m in 20,000 years is 7.5 mm/yr. From the relationship  $q = v \cdot \theta$  where  $q$  is water flux,  $v$  is seepage velocity and  $\theta$  is wetted porosity, and the assumption  $\theta \sim 0.2$ , an estimate for  $q$  of 1.5 mm/yr is obtained. The calculated travel times for the local recharge components thus imply a very small but not unrealistic local infiltration flux, a result consistent with the  $^{14}\text{C}$  age of about 16,300 years estimated earlier for the ER-OV-03c groundwater.

A second approach to interpreting the composite travel times for the ER-OV-03c inverse models is to use Equation (D.1-9), which assumes that local recharge near the target well reaches the well almost instantaneously, so that its contribution of  $^{14}\text{C}$  to the mixed groundwater at the target well can be used

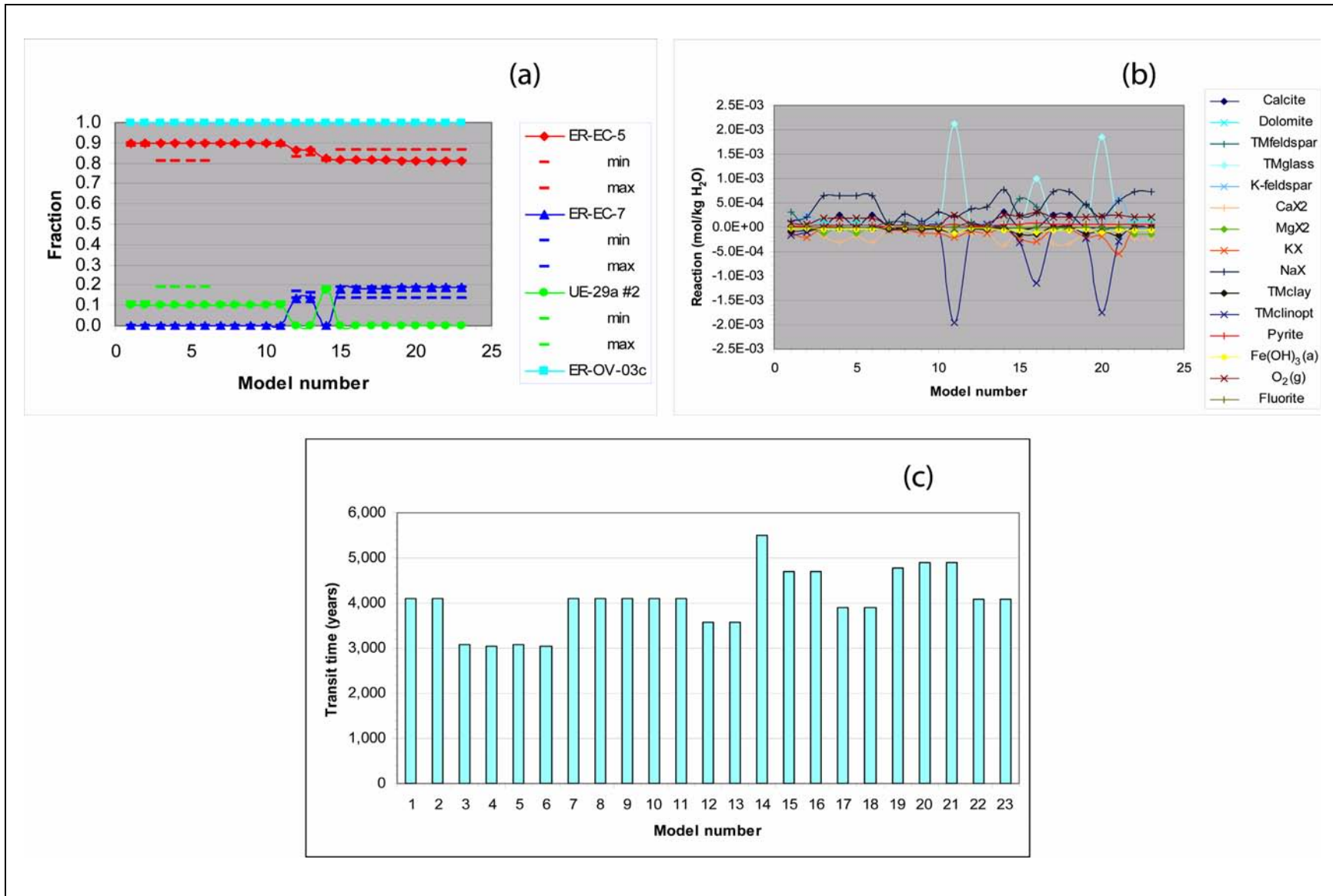


Figure D.1-21

Inverse Model Results for ER-OV-03c: (a) Mixing Fractions, (b) Reactions, and (c) Composite Travel Times

**Table D.1-3**  
**Travel Times from Individual Wells to ER-OV-03c**

Upgradient Well	Estimated Travel Time (Years)	Lower 95% Confidence Limit (Years)	Upper 95% Confidence Limit (Years)
ER-EC-5	1,574	503	2,645
ER-EC-7	16,806	11,736	21,877
UE-29a #2	23,757	14,878	32,636

to adjust the <sup>14</sup>C content of the well so that it reflects only the contribution from the upgradient well. When travel times between ER-EC-5 and ER-OV-03c are estimated using this approach, the estimated travel times range between about 5,000 and 25,000 years (Figure D.1-22). Because of their different assumptions regarding the travel time of recharge, the different approaches to estimating the travel times from ER-EC-5 to ER-OV-03c yield a large range of groundwater travel times. Eliminating the very short travel times of the first method and the very long travel times of the second method provides a truncated range of 1,500 to 5,000 years.

A set of PHREEQC models were constructed for ER-OV-04a and identified groundwater at ER-OV-03c as the dominant component in the mixture (Figures D.1-18 and D.1-23). Individual models for ER-OV-04a all had negative composite travel times except for models involving well ER-OV-05 (Models 9, 12, and 13), suggesting that the groundwater at ER-OV-04a requires a small component of its water from the northwest at ER-OV-05.

Because groundwater at ER-OV-03c was derived primarily from ER-EC-5, and groundwater from ER-EC-5 was derived primarily from UE-18r (Figure D.1-18), groundwater from UE-18r was substituted for the ER-OV-03c mixing component in the ER-OV-04a mixing models. The resulting models indicate that ER-OV-04a receives about 30 to 60 percent of its groundwater from UE-18r (Figure D.1-24), with significant components from U-20 WW, ER-EC-1 and ER-OV-05 and small amounts of local recharge (represented by water from UE-29a #2). Composite travel times for this set of models were between about 1,300 and 2,300 years, but it was not possible to derive meaningful estimates of travel times from the individual wells (Table D.1-4). Mean travel times from UE-18r were about 2,500 years, but travel times from U-20 WW and ER-EC-1 were negative.

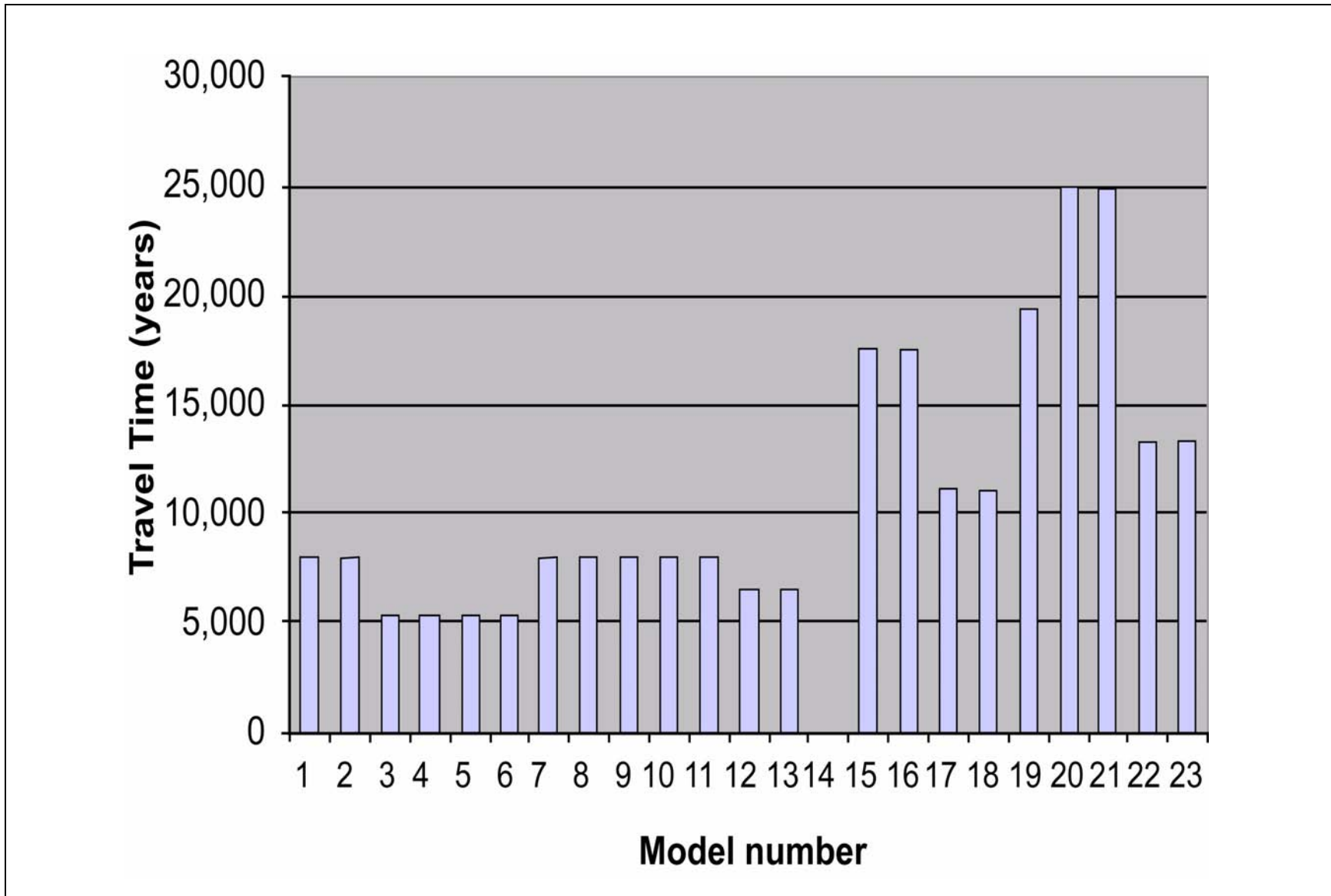


**Figure D.1-22**  
*Travel Times from ER-EC-5 to ER-OV-03c Calculated Assuming Zero Travel Times for Recharge Component to ER-OV-03c*



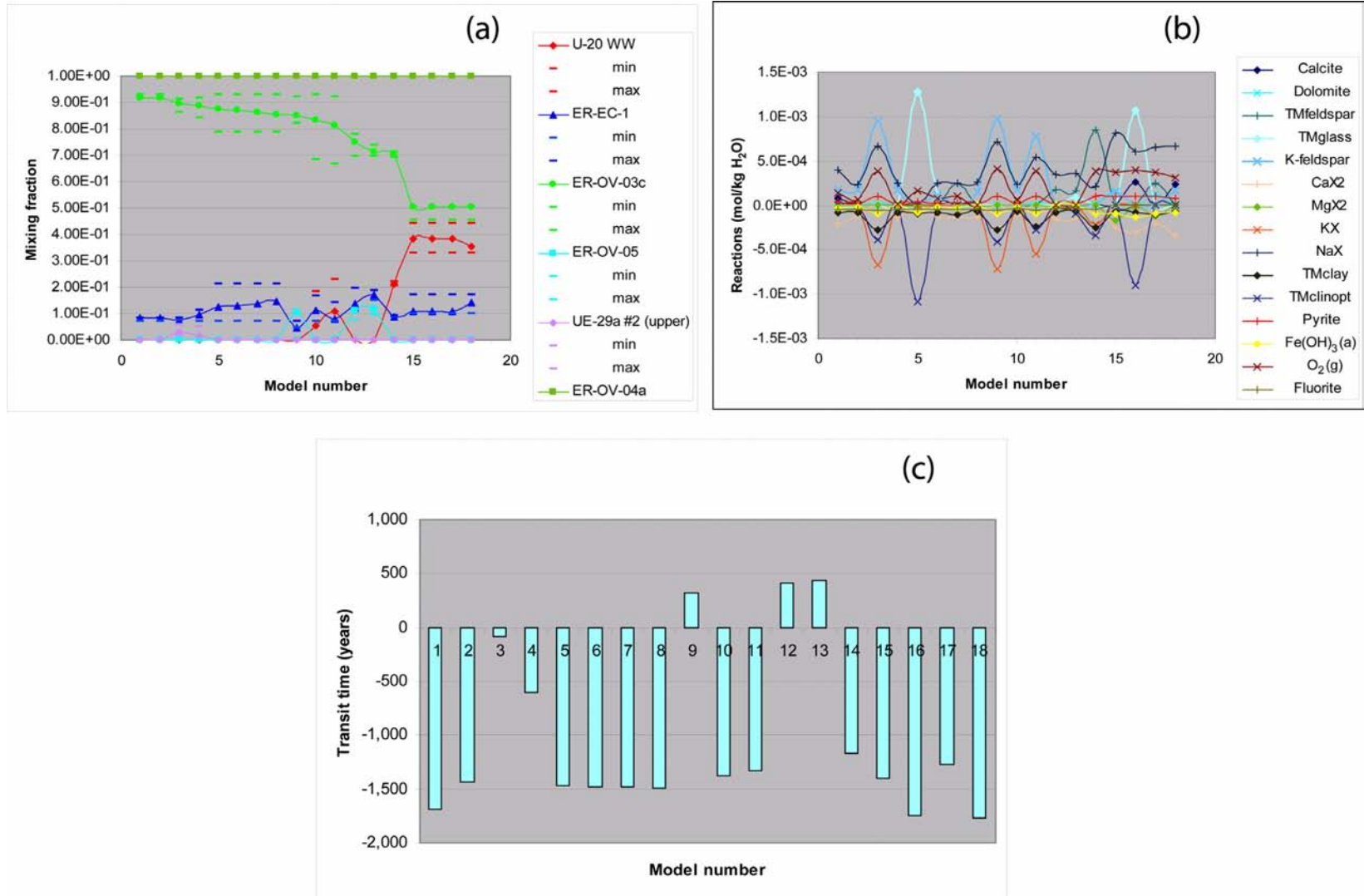


**Figure D.1-23**  
**Inverse Model Results for ER-OV-04a with ER-OV-03c as an Upgradient Source: (a) Mixing Fractions, (b) Reactions, and (c) Composite Travel Times**

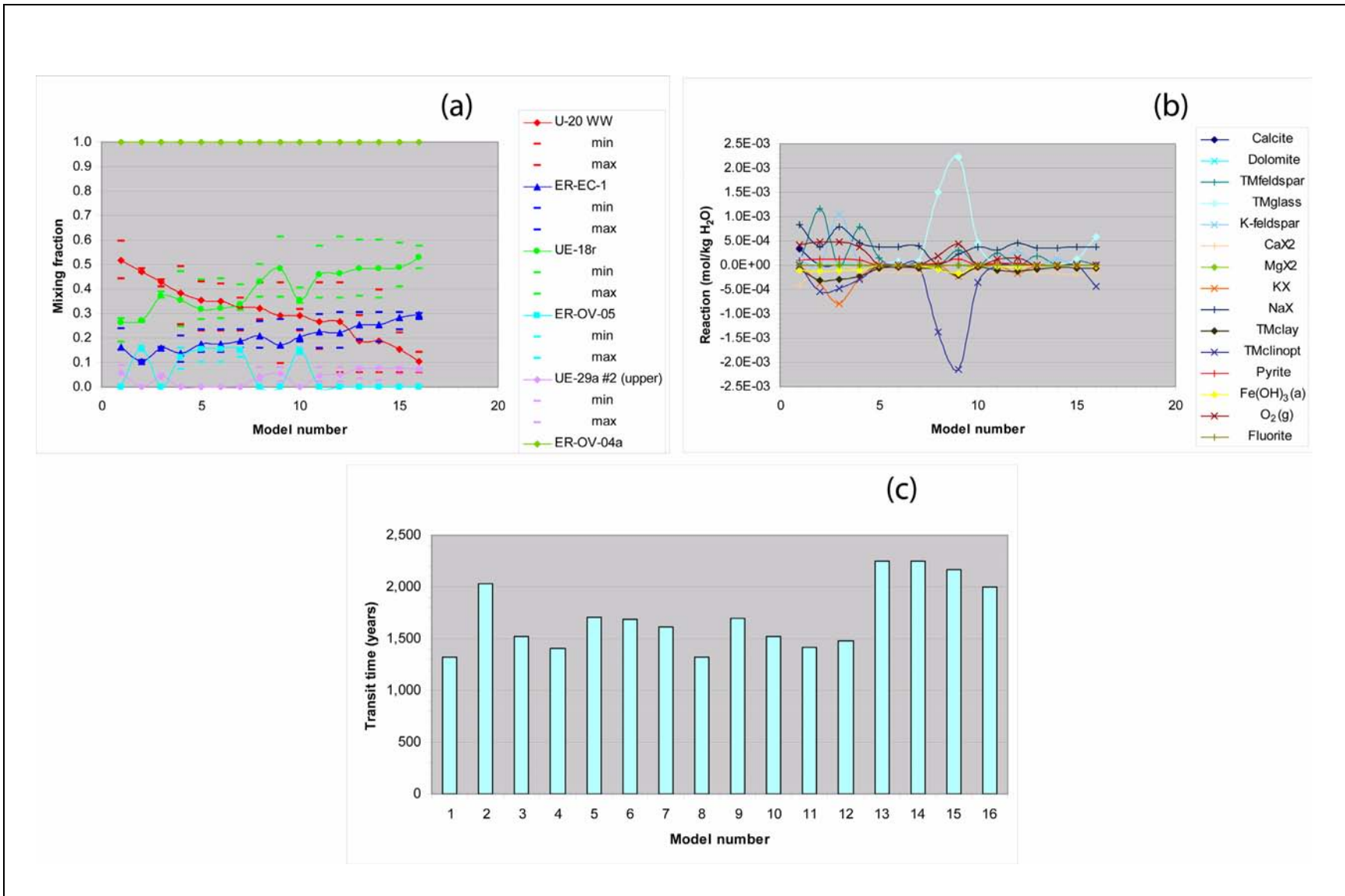


Figure D.1-24

Inverse Model Results for ER-OV-04a with UE-18r as an Upgradient Source: (a) Mixing Fractions, (b) Reactions, and (c) Composite Travel Times

**Table D.1-4**  
**Travel Times from Individual Wells to the CRWW**

Upgradient Well	Estimated Travel Time (Years)	Lower 95% Confidence Limit (Years)	Upper 95% Confidence Limit (Years)
UE-18r	-5,728	-9,777	-1,679
ER-18-2	-30,046	-40,164	-19,928
WW-8	5,824	4,149	7,499
ER-EC-7	14,377	12,201	16,553

The last set of travel times along Flow Path #4 were calculated for inverse models that used the CRWW as the downgradient well (Figure D.1-25). Flow Path #4 is based primarily on inverse models for CRWW and well VH-1 in Crater Flat, which show that VH-1 groundwater originates primarily from groundwater in lower Beatty Wash (Figure D.1-25). Hence, the inverse model results for other wells that we found to contribute water to ER-OV-3c are also shown for this flow path.

The results for the CRWW inverse models indicate that groundwaters can mix and react in several different ways to produce the groundwater at CRWW (Figures D.1-26a and D.1-26b): (1) Models 1 to 4 involve groundwater from the northeast side of Timber Mountain at WW-8 and ER-18-2; (2) Models 9 to 15 involve UE-18r and ER-EC-7 water; and models 5 to 8 are based on mixtures involving groundwater from all four wells. Composite travel times for the CRWW models range from a few tens of years to about 7,400 years (Figure D.1-26c). The models that include ER-18-2 groundwater in the mixture have the shortest calculated travel times because the extremely low <sup>14</sup>C (1.6 pmc) and high DIC concentration (755 mg/L as HCO<sub>3</sub>) significantly lower the <sup>14</sup>C activity of the upgradient mixture. Conversely, the models that involve mixtures of just UE-18r and ER-EC-7 groundwater have composite travel times of about 7,000 years because ER-EC-7 has a <sup>14</sup>C activity of 36.5 pmc, raising the overall <sup>14</sup>C activity in the mixture. Decomposition of the composite travel times from individual upgradient wells to CRWW yielded negative travel times for the UE-18r and ER-18-2 components, but travel times of about 5,824 years and 14,377 years for the WW-8 and ER-EC-7 components (Table D.1-5). There was considerable uncertainty in these estimates.

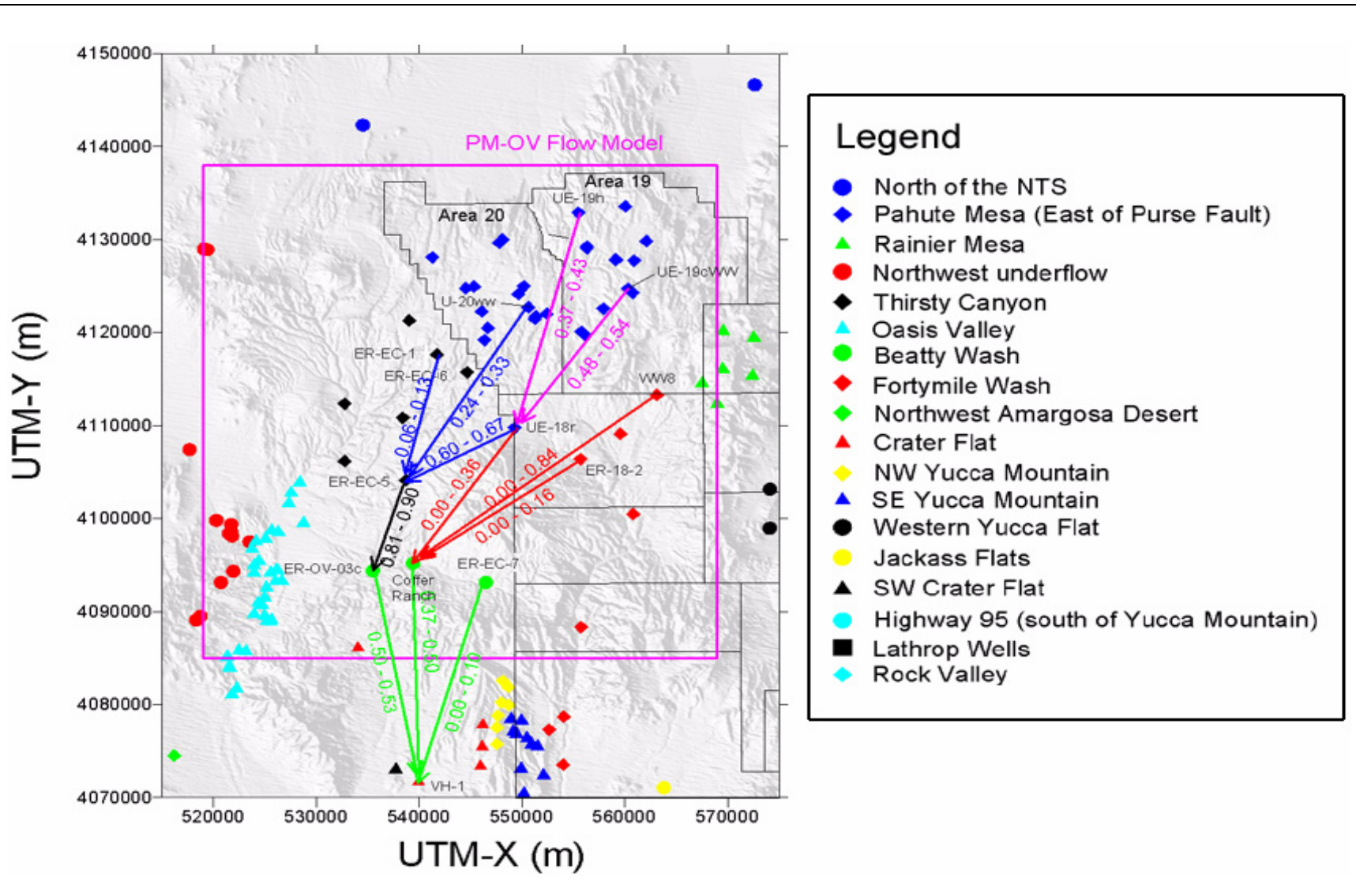


**Figure D.1-25**  
**Map Summarizing Geochemical Inverse Model Results for Flow Path #4**

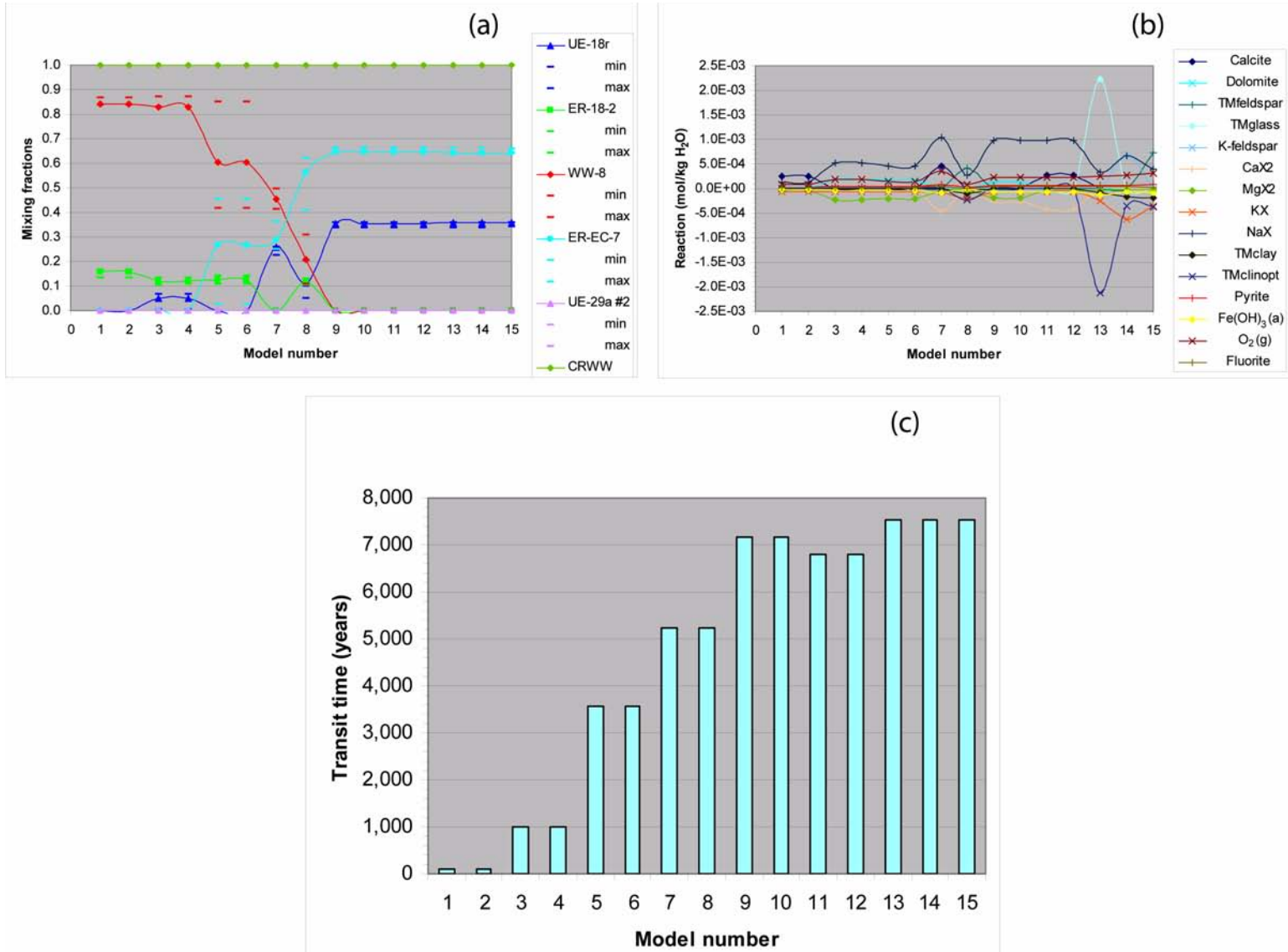


**Figure D.1-26**  
**Inverse Model Results for CRWW: (a) Mixing Fractions, (b) Reactions, and (c) Composite Travel Times**

**Table D.1-5**  
**Travel Times from Individual Wells to ER-OV-04a**

Upgradient Well	Estimated Travel Time (Years)	Lower 95% Confidence Limit (Years)	Upper 95% Confidence Limit (Years)
U-20 WW	-307	-900	286
ER-EC-1	-4,450	-7,665	-1,236
UE-18r	2,474	1,089	3,859
ER-OV-05	11,552	8,713	14,392
UE-29a #2	28,806	20,803	36,810

### **D.1.9 Flow Path #5**

Flow Path #5 extends from the southeast quadrant of Area 19 southward through Fortymile Canyon and Fortymile Wash to the east of Yucca Mountain. Groundwater  $^{14}\text{C}$  activities and ages vary in a non-systematic way along this flow path due to the presence of local recharge, primarily in Fortymile Canyon (Figures D.1-5 and D.1-9). Kwicklis et al. (2005) found that many different mixing and water/rock interaction models could explain the groundwater composition at well J-13 adjacent to Yucca Mountain (Figure D.1-27). One set of models involving groundwater from wells on Buckboard Mesa (WW-8), the Timber Mountain moat (ER-18-2), shallow Fortymile Wash (UE-29a #1) and upper Beatty Wash (ER-EC-7) was analyzed for groundwater travel times. In this set of models, most of the groundwater at J-13 is estimated to come from UE-29a #1 and WW-8, with relatively minor contributions from ER-EC-7 and ER-18-2 (Figure D.1-28a). The composite travel times for the three models that were found range from about 2,000 to a little over 4,000 years (Figure D.1-28c). Travel times from individual upgradient wells to J-13 could not be calculated because of the small number of models that were found.

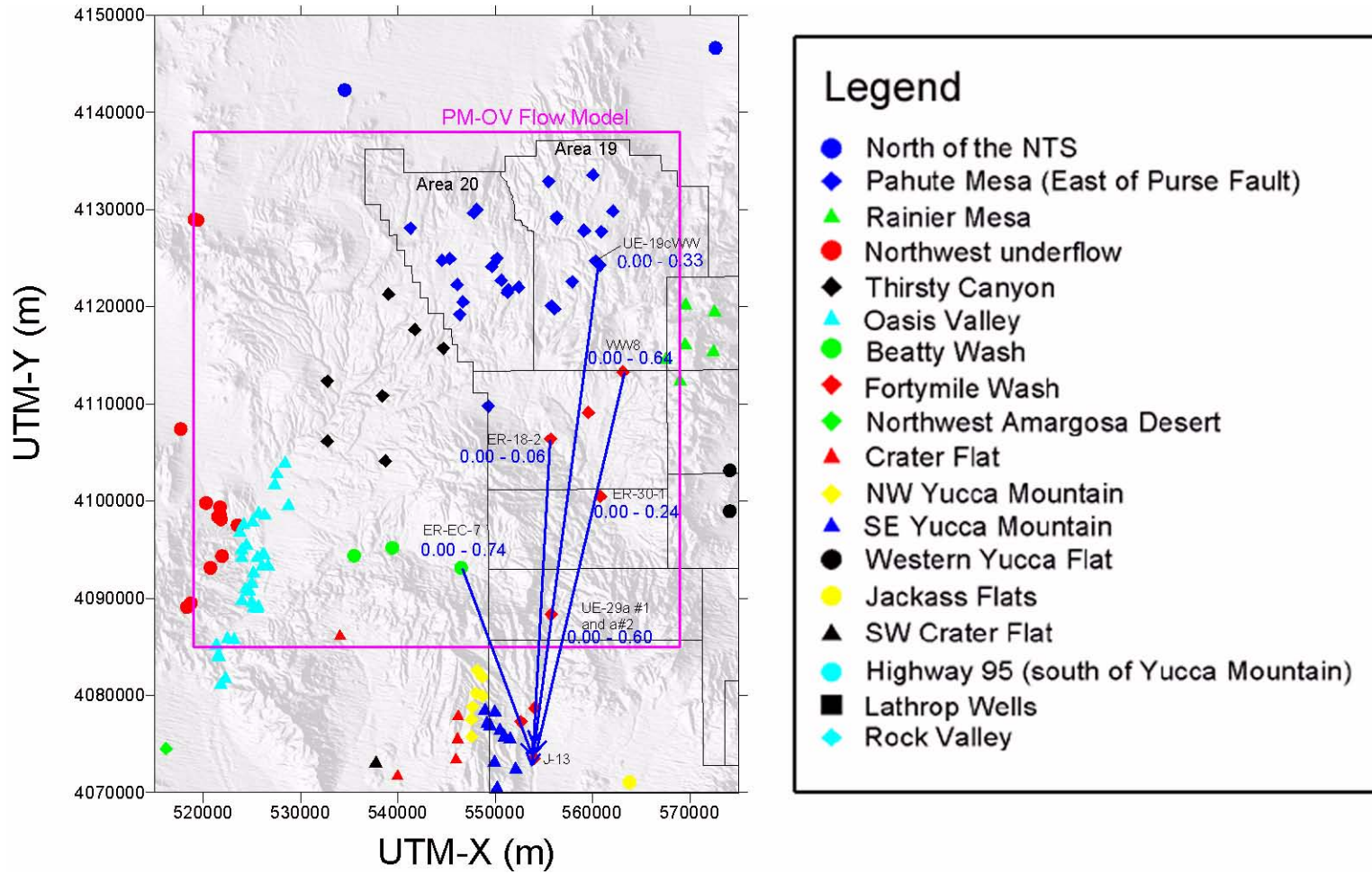


**Figure D.1-27**  
**Map Summarizing Geochemical Inverse Model Results for J-13**

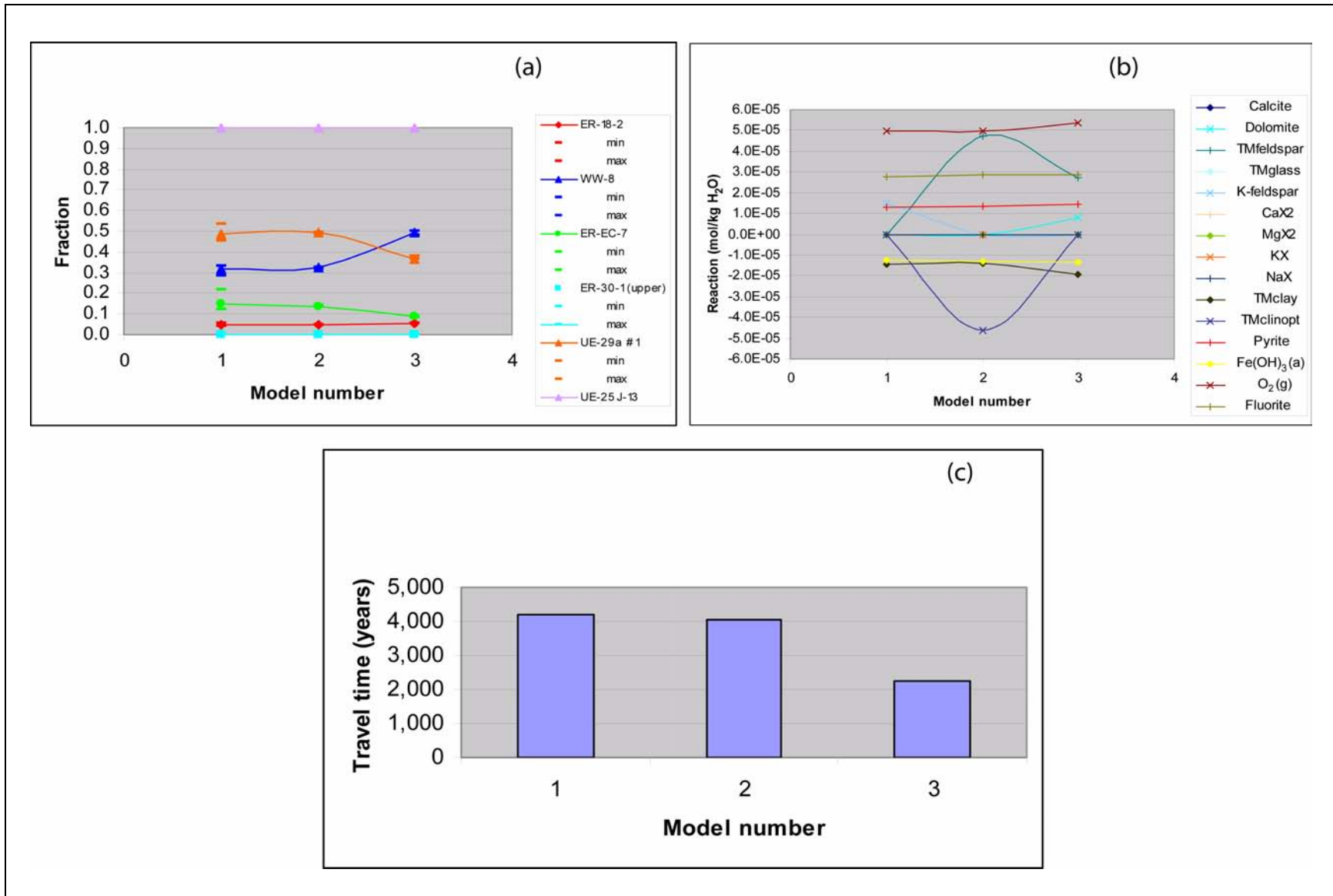
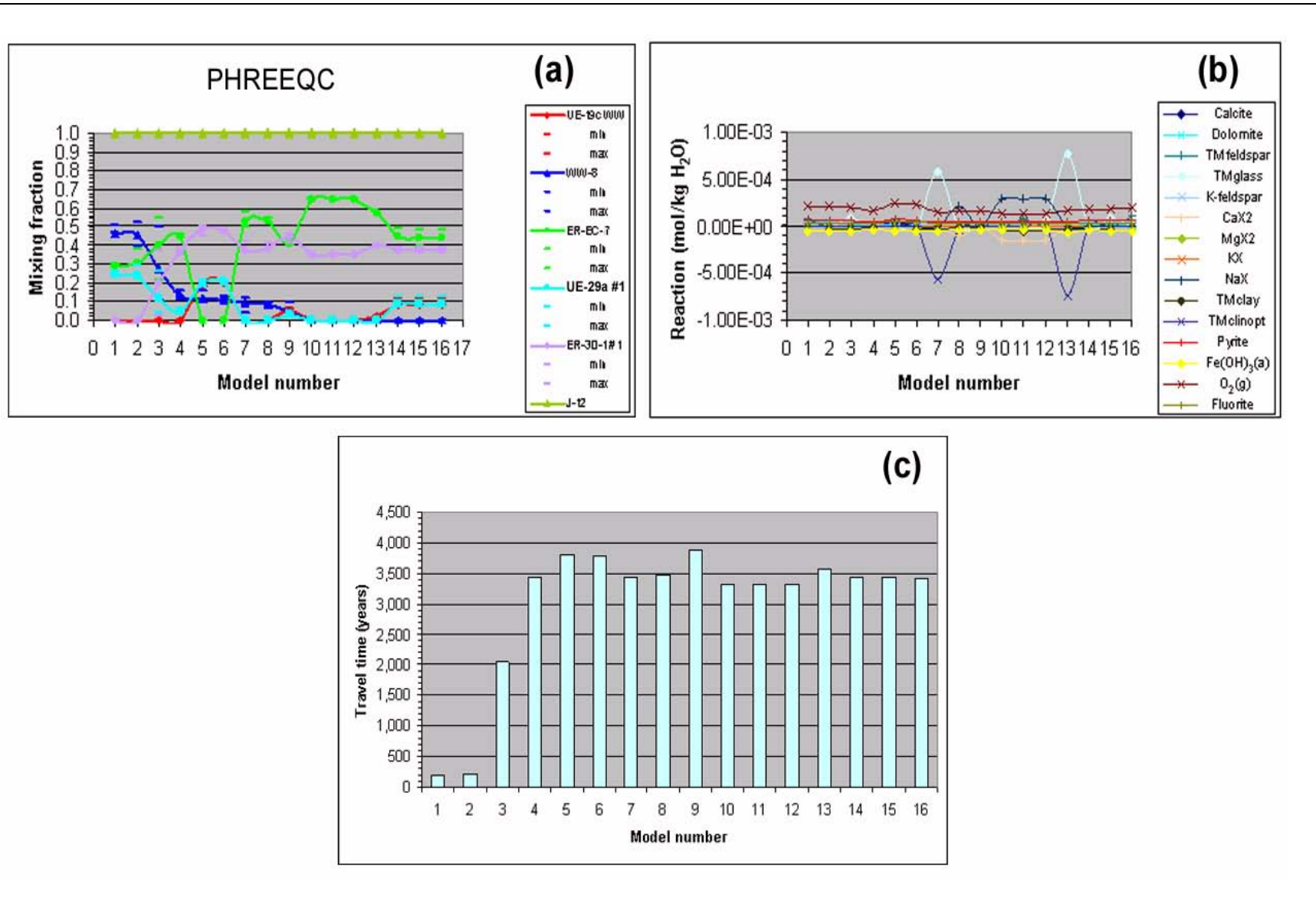


Figure D.1-28

Inverse Model Results for J-13: (a) Mixing Fractions, (b) Reactions, and (c) Composite Travel Times



A set of inverse models was also created for J-12 in Fortymile Wash east of Yucca Mountain. This well is about 5 km south of J-13. Considerable variability in the mixing percentages exists (Figure D.1-29a), with groundwater from all of the upgradient wells potentially found in groundwater at J-12. However, for each mixing component, several models are found that contain none of that component indicating that, while many components could be present at J-13, no one of them by itself is required to be present in order to model the composition of J-13 groundwater. The composite travel times are also quite variable, ranging from a few hundred years in models 1 and 2 to between about 3,000 and 4,000 years for most of the models (Figure D.1-28c). The first two models contain about 45 percent of WW-8 groundwater in the mixture. Smaller travel times are calculated for these models between the groundwater  $^{14}\text{C}$  activity at WW-8 is smaller (25 pmc) than at most of the other wells, and so the upgradient mixture contains less  $^{14}\text{C}$  relative to J-12 ( $^{14}\text{C} = 32.2$  pmc).



**Figure D.1-29**  
**Inverse Model Results for J-12: (a) Mixing Fractions, (b) Reactions, and (c) Composite Travel Times**

## **D.2.0 SUMMARY AND CONCLUSIONS**

Groundwater  $^{14}\text{C}$  ages and travel times between wells were estimated for the PM-OV model domain using groundwater mixing and water/rock interaction models previously developed for the PM-OV flow system. Groundwater ages displayed variability along the previously identified flow paths, and groundwater ages actually decreased near Oasis Valley, where mixing models suggest the addition of small amounts of local recharge. Similar variability was observed along a flow path in Fortymile Canyon, where groundwater appears to be dominated by local recharge.

Small differences in groundwater  $^{14}\text{C}$  activities and  $^{14}\text{C}$  ages along Flow Path #1 extending from southwest Area 20 to Oasis Valley made it impossible to calculate positive travel times for most segments of this flow path. The one flow path segment where positive travel times could be calculated was the segment from U-20 WW to ER-EC-6, where groundwater travel times were estimated to be about 3,264 years (with 95 percent confidence limits of 337 to 6,191 years). The negative travel times estimated for the flow paths segments downgradient of the U-20 WW to ER-EC-6 segment are not attributable to the addition of local recharge, based on mixing models and scatterplots that show no evidence for modern recharge along this flow path north of Oasis Valley. The negative travel times may be reflecting truly fast groundwater flow in the Thirsty Canyon area, or they may reflect the decrease in unsaturated zone thickness and groundwater sampling depths closer to Oasis Valley, which would tend to capture younger water than the deep wells in the northern part of the flow path.

Groundwater from Area 19 was estimated to flow southwestward along Flow Paths #2 and #4 around the northwest side of Timber Mountain where it mixes with groundwater flowing southward from Area 20, and then southwestward through lower Beatty Wash. Some of this water moves from lower Beatty Wash toward Oasis Valley (Flow Path #2), and some of the water moves into northern Crater Flat (Flow Path #4). Groundwater moving from Pahute Mesa Area 19 wells UE-19h and UE-19cWW toward UE-18r in the moat area north of Timber Mountain has a composite travel time of approximately 1,000 to 1,200 years. A composite travel time of about 1,700 years is required for

water flowing from U-20 WW and UE-18r (and local recharge) to reach ER-EC-5. This groundwater then requires between 1,600 and 5,000 years to reach ER-OV-03c in lower Beatty Wash. The flow velocity in this last segment has a large uncertainty associated with it due to the different approaches and assumptions used to estimate the travel time. Groundwater travel times to the CRWW from UE-18r range from a few tens of years to 7,500 years depending on the wells involved in mixing model. Mixtures involving WW-8 and ER-18-2 have the shortest composite travel times (several tens of years), whereas models involving UE-18r and ER-EC-7 have the longest composite travel times.

The persistently negative travel times calculated for various flow path segments along Flow Path #1 in the Thirsty Canyon area of the model point to sampling limitations in which young water in upgradient wells has gone undetected, possibly as a result of mixing with older, deep water in long screened intervals. Conversely, long apparent travel times could result in situations where the upgradient wells sample a shallow aquifer with high  $^{14}\text{C}$  activities and the downgradient well samples a combination of aquifers and confining units with lower  $^{14}\text{C}$  activities over a long screened interval. The effects of sample depth and length of the screened interval could have contributed to the long apparent travel times between upgradient U-20 WW and UE-19h, and downgradient ER-EC-6, and to a lesser extent, between upgradient UE-19h and U-19c WW and downgradient UE-18r (Figure D.1-11).

Inverse models for J-13 and J-12 located east of Yucca Mountain in Fortymile Wash identified many different inverse models involving groundwater from Fortymile Wash, upper Beatty Wash, and even eastern Area 19 on Pahute Mesa (UE-19c WW) as potential contributors to the groundwater at these wells. The composite travel times from the Fortymile Canyon area to J-12 and J-13 were generally on the order of 2,000 to 4,000 years, although a few models were found involving large fractions of WW-8 groundwater that had groundwater travel times on the order of a few hundred years. The shorter travel times for the groundwater with a large WW-8 component is due to the lower  $^{14}\text{C}$  activity at WW-8 compared with most of the other upgradient wells in these models.

## D.3.0 REFERENCES

- Clark, I.D., and P. Fritz. 1997. *Environmental Isotopes in Hydrogeology*. Boca Raton, FL: Lewis Publishers.
- Glynn, P.D., and L.N. Plummer. 2005. "Geochemistry and the Understanding of Ground-Water Systems." In *Hydrogeology Journal*, Vol. 13: 263-287.
- Kwicklis, E.M., T.P. Rose, and F.C. Benedict, Jr. 2005. *Evaluation of Groundwater Flow in the Pahute Mesa - Oasis Valley Flow System Using Groundwater Chemical and Isotopic Data*, LA-UR-05-4344. Los Alamos, NM: Los Alamos National Laboratory.
- Maloszewski, P., and A. Zuber. 1991. "Influence of Matrix Diffusion and Exchange Reactions on Radiocarbon Ages in Fissured Carbonate Aquifers." In *Water Resources Research*, Vol. 27(8): 1937-1945.
- Parkhurst, D.L., and C.A.J. Appelo. 1999. *User's Guide to PHREEQC (Version 2) - A Computer Program for Speciation, Batch-Reaction, One-Dimensional Transport, and Inverse Geochemical Calculations*, Water-Resources Investigations Report 99-4259. U.S. Geological Survey.
- Plummer, L.N., E.C. Prestemon, and D.L. Parkhurst. 1994. *An Interactive Code (NETPATH) for Modeling NET Geochemical Reactions Along a Flow Path*, Version 2.0, Water-Resources Investigations Report 94-4169. Reston, VA: U.S. Geological Survey.
- Rose, T.P., F.C. Benedict, Jr., J.M. Thomas, W.S. Sicke, R.L. Hershey, J.B. Paces, I.M. Farnham, and Z.E. Peterman. 2006. *Geochemical Data Analysis and Interpretation of the Pahute Mesa - Oasis Valley Groundwater Flow System, Nye County, Nevada, August 2002*, UCRL-TR-224559. Livermore, CA: Lawrence Livermore National Laboratory; Reno, NV: GeoTrans Inc. and Desert Research Institute; Denver, CO: U.S. Geological Survey; and Las Vegas, NV: Harry Reid Center for Environmental Studies.
- Sheppard, S.C., K.V. Ticknor, and W.G. Evenden. 1998. "Sorption of Inorganic  $^{14}\text{C}$  on to Calcite, Montmorillonite and Soil." In *Applied Geochemistry*, Vol. 13: 43-47.
- Thomas, J.M., F.C. Benedict, Jr., T.P. Rose, R.L. Hershey, J.B. Paces, Z.E. Peterman, I.M. Farnham, K.H. Johannesson, A.K. Singh, K.J. Stetzenbach, G.B. Hudson, J.M. Kenneally, G.F. Eaton, and D.K. Smith. 2002. *Geochemical and Isotopic Interpretations of Groundwater Flow in the Oasis Valley Flow System, Southern Nevada*, Publication No. 45190. Desert Research Institute.

White, A.F., and N.J. Chuma. 1987. "Carbon and Isotopic Mass Balance Models of Oasis Valley-Fortymile Canyon Groundwater Basin, Southern Nevada." In *Water Resources Research*, Vol. 23(4): 571-582. Washington, DC: American Geophysical Union.



## **Appendix E**

### **Nevada Division of Environmental Protection Comments**

(5 pages)

## NEVADA ENVIRONMENTAL RESTORATION PROJECT DOCUMENT REVIEW SHEET

1. Document Title/Number <u>Phase I Transport Model of Corrective Action Units 101 and 102: Central and Western Pahute Mesa, Nevada Test Site, Nye County, Nevada</u>		2. Document Date <u>September 2008</u>		
3. Revision Number <u>0</u>		4. Originator/Organization <u>Stoller-Navarro</u>		
5. Responsible DOE/NV ERP Project Mgr. <u>Bill Wilborn</u>		6. Date Comments Due <u>December 2008</u>		
7. Review Criteria <u>Full</u>				
8. Reviewer/Organization/Phone No. <u>Chris Andres, NDEP, 486-2850, ext 232</u>		9. Reviewer's Signature _____		
10. Comment Number/ Location	11. Type <sup>a</sup>	12. Comment	13. Comment Response	14. Accept
1) Section ES, Page ES-3, Bullet Point 3		"Exceedance Volume" was not mentioned in the preceding statements as indicated. More importantly, the replacement of the contaminant boundary with the use of exceedance volume has not been accepted by the NDEP. Neither the Pahute Mesa Phase I CAIP nor subsequent letters of documents accepted by NDEP propose the substitution. A change in teh approach from that described in the Phaute Mesa CAIP and FFACO require a written agreement with the NDEP. Until such time as an agreement is written or the FFACO is modified, the exceedance volume approach and model are not within FFACO criteria. Further discussion on this concept needs to occur between NNSA/NSO and the NDEP.	Bulleted item has been changes to define the concept of the exceedance volume and it's relationship to the contaminant boundary that is identified in the FFACO.	A  (EJF)
2) Section ES, Page ES-9, 3 <sup>rd</sup> Full Paragraph, Last Sentence and Other Pages throughout Document		How are uncertainties in estimates from a geochemical study obtained. How are the uncertainties considered in the geochemical verification targets for transport modeling?	Incorrectly labelled as estimated. Geochemical markers for the simulated model are compared to the geochemical markers measured at the well. The text was revised to reflect this change.	A  (EJF)

<sup>a</sup>Comment Types: M = Mandatory, S = Suggested.



## NEVADA ENVIRONMENTAL RESTORATION PROJECT DOCUMENT REVIEW SHEET

Document Title/Number Phase I Transport Model of Corrective Action Units 101 and 102:Revision Number 0Central and Western Pahute Mesa, Nevada Test Site, Nye County, NevadaReviewer/Organization Chris Andres, NDEP, 486-2850, ext 232

10. Comment Number/ Location	11. Type <sup>a</sup>	12. Comment	13. Comment Response	14. Accept
3) Section 3.2.4.1, Page 3-23, Last Paragraph 1 <sup>st</sup> Sentence and Possibly Page ES-26, 7 <sup>th</sup> Bullet		The document states that the UGTA regional groundwater flow model (1997) is used for the boundary conditions. However, in the other CAUs, the Death Valley Regional Groundwater flow model was used for the boundary conditions. How will the possible mismatch of boundary conditions between CAUs be addressed.	Discussion was expanded to note that the DVRFM was not available until near the end of the Pahute Mesa CAU flow model design. Therefore, the UGTA model was retained. Revision of the boundary conditions to reflect conditions synomous with the DVRFM are left as an activity for the phase II CAI. Text was changed to clarify this approach.	A  (EJF)
4) Section 3.2.6 Page 3-35, 2 <sup>nd</sup> Paragraph, 1 <sup>st</sup> Sentence		The document states that in the geochemical verification targets the "comparison is subjective because the model identifies zones of contribution whereas Kwicklis et al (2005) identify mixing ratios of water types associated with specific wells." However, on page 3-37 "geochemical mixing residuals" are grouped into four types. If the comparison is subjective the how can quantitative residuals be obtained? The four types listed use teh terms, "too much flow, not enough flow" and too much local recharge". Will these values be adjusted until some quantitative goal is reached or are they subjective in nature.	The comparison was not subjective. This term has been removed. Comparisons were dreived from simulated geochemical targets derived from the defined zones with those that were calculated from well-to-well measurements. Text have been revised.	A  (EJF)
5) Section 3.4.3, Page 3-68, 1 <sup>st</sup> Paragraph, 8 <sup>th</sup> Sentence		"... have a negligible detrimental (if not positive) impact on head residuals ..." This sentence is not clear and needs to be rewritten.	Sentence has been revised.	A  (EJF)
6) Section 4.1.8.2 Page 4-26, 2 <sup>nd</sup> Paragraph, Last Sentence		"The ranges in Table 4-10 are judgements ..." What is the basis for these judgements?	Incorrect term, this paragraph was supplimented to identify the rationale for partitioning of the radionuclides	A  (EJF)

<sup>a</sup>Comment Types: M = Mandatory, S = Suggested.

## NEVADA ENVIRONMENTAL RESTORATION PROJECT DOCUMENT REVIEW SHEET

Document Title/Number Phase I Transport Model of Corrective Action Units 101 and 102:Revision Number 0Central and Western Pahute Mesa, Nevada Test Site, Nye County, NevadaReviewer/Organization Chris Andres, NDEP, 486-2850, ext 232

10. Comment Number/ Location	11. Type <sup>a</sup>	12. Comment	13. Comment Response	14. Accept
7) Section 6.8.1 Page 6-64 1 <sup>st</sup> Paragraph, 2 <sup>nd</sup> Sentence		How is the uncertainty for the "extrapolation of the parameter beyond the endpoints ..." addressed.	Discussion of the uncertainty approach exceeds the level of detail that is intended for this section.	R  (EJF)
8) Section 6.8.1 Page 6-65, Partial Sentence on top of page		"...briefing description of the data inadequacies for which the distribution is best suited". A statistical distribution is selected based on analyzing the data, not selected for the best description of data inadequacies. Please clarify this sentence.	We took out inadequacies. However, specific distribution types are selected based on there ability to derive a reasonable range of values to accomidate extreme behavior that can skew the normal distribution.	A  (EJF)
9) Section 7.3.4 Page 7-9, 1 <sup>st</sup> Paragraph, 3 <sup>rd</sup> Sentence		This paragraph says it addresses the contaminant boundary ..." but it does not. Please expand on the information given.	Text was revised to indicate that the contaminant boundary was not formally calculated but rather the exceedance volume was used to quantify the new role of this report, which was to quantify model uncertainty	A  (EJF)
10) Section 8.2.4.3 Page 8-22, Figure 8-9		On page 8-19, fifth paragraph, the text discusses the top three parameters for the step-wise regression analysis; however the final R2 term is based on seven parameters. Please explain why all seven parameters are used to obtain the R2 and the conclusion is based on this value. (in the stepwise regression plots for the various models, the plots use seven steps and the text indicates seven variables. Generally the text only discusses the first three most important variables but represents the total variance reduction based on all seven included. Why is the variance reduction based on four additional variables that are not important)	Reference to seven variables was removed. The algorithm used calculated variance of the top seven parameters, however, this is just a formatting convention. The variance of the top parameters is a function of the total parameters space, not just those seven parameters reported.	A  (EJF)

<sup>a</sup>Comment Types: M = Mandatory, S = Suggested.

## NEVADA ENVIRONMENTAL RESTORATION PROJECT DOCUMENT REVIEW SHEET

Document Title/Number Phase I Transport Model of Corrective Action Units 101 and 102:Revision Number 0Central and Western Pahute Mesa, Nevada Test Site, Nye County, NevadaReviewer/Organization Chris Andres, NDEP, 486-2850, ext 232

10. Comment Number/ Location	11. Type <sup>a</sup>	12. Comment	13. Comment Response	14. Accept
11) Section 8.2.7 Page 8-46, 1 <sup>st</sup> Paragraph, 2 <sup>nd</sup> Sentence		"... should include calibration and analysis of combined flow and transport parameters." Are the authors suggesting that a calibration of a combined flow and transport model be considered? If so is there transport information available for the calibration process.	Sentence added to explicitly suggest a role to collect transport data for use in a joint flow and transport calibration.	A  (EJF)
12) Appendix B Page B-9, Table B.1-3		The vertical correlation length is assigned and is the same value as the horizontal correlation length for fracture domain. The use of this large correlation length in the vertical appears to suggest that these are small fractures. Is this the intent of the use of vertical correlation length.	Actually the anisotropy ratio is equal. The VMP/R is conceptually a porous medium with limited fracturing. Flow and transport through this medium is conceptualized as occurring in the rock matrix, not through fractures.	R  (EJF)
13) Figure 1-3 Page 1-10		Blue and black blocks in the legend refer to Frenchman Flat. This document is addressing Pahute Mesa. If reference to Frenchman Flat in the legend is incorrect, the should be changed.	Figure will be corrected.	A  (EJF)
14) Section 3.3.1.2 Page 3-45, 1 <sup>st</sup> Paragraph, Last Sentence		Figure 3-17 should be figure 3-16.	Reference is correct.	R  (EJF)
15) Section 4.1.3 Page 4-13, 1 <sup>st</sup> Paragraph		These two sentences contradict each other concerning the inventory the glass. Please clarify which approach is used.	Text was revised.	A  (EJF)
16) Section 4.2.2 Page 4-30, Bulleted Item, and Figure 4-5		The text indicated LCCU1-TMD and the figure indicates LCCU1-TMD100. Please make this notation consistent.	Figure legend will be corrected.	A  (EJF)

<sup>a</sup>Comment Types: M = Mandatory, S = Suggested.

## NEVADA ENVIRONMENTAL RESTORATION PROJECT DOCUMENT REVIEW SHEET

Document Title/Number Phase I Transport Model of Corrective Action Units 101 and 102:Revision Number 0Central and Western Pahute Mesa, Nevada Test Site, Nye County, NevadaReviewer/Organization Chris Andres, NDEP, 486-2850, ext 232

10. Comment Number/ Location	11. Type <sup>a</sup>	12. Comment	13. Comment Response	14. Accept
17) Page 6-13 Tables 6-2 and 6-3		The column "All" is not defined. Please indicate what value is given in this column.	see Drelleck, 1997	A  (EJF)
18) Section 6.5.3 Page 6-55, 1 <sup>st</sup> Paragraph, Last Sentence		The use of the word "deweighted" is unusual. Please clarify the term.	The sentence was confusing as written and didn't necessarily follow from the previous sentences. Therefore, this sentence was removed for clarity.	A  (EJF)
19) Section 8.2.3 Page 8-9		The last sentence of this section is incomplete and should be rewritten.	Removed the confusing sentence.	A  (EJF)

<sup>a</sup>Comment Types: M = Mandatory, S = Suggested.

## DISTRIBUTION

### Copies

Tim Murphy State of Nevada Nevada Division of Environmental Protection 2030 E. Flamingo Road, Suite 230 Las Vegas, NV 89119-0818	2 Hard copies/2 CDs
W.R. Wilborn Environmental Restoration Project U.S. Department of Energy National Nuclear Security Administration Nevada Site Office P.O. Box 98518, M/S 505 Las Vegas, NV 89193-8518	2 Hard copies/2 CDs
K.C. Thompson Environmental Restoration Project U.S. Department of Energy National Nuclear Security Administration Nevada Site Office P.O. Box 98518, M/S 505 Las Vegas, NV 89193-8518	1 CD
Alicia Tauber Environmental Management Records U.S. Department of Energy National Nuclear Security Administration Nevada Site Office P.O. Box 98518, M/S 505 Las Vegas, NV 89193-8518	1 CD
U.S. Department of Energy Office of Scientific and Technical Information P.O. Box 62 Oak Ridge, TN 37831-0062	1 CD
Southern Nevada Public Reading Facility c/o Nuclear Testing Archive P.O. Box 98521, M/S 400 Las Vegas, NV 89193-8521	1 CD

**Central and Western Pahute Mesa Phase I CAU Transport Model**

---

	<u>Copies</u>
Manager, Northern Nevada FFACO Public Reading Facility c/o Nevada State Library & Archives 100 N. Stewart Street Carson City, NV 89701-4285	1 CD
Naomi Becker Los Alamos National Laboratory, M/S F665 Bikini Atoll Rd., SM30, MS T003 Los Alamos, NM 87545	1 CD
Gayle Pawloski Lawrence Livermore National Laboratory 7000 East Avenue, L-231 Livermore, CA 94550-9234	1 CD
Mavrik Zavarin Lawrence Livermore National Laboratory 7000 East Avenue, L-231 Livermore, CA 94550-9234	1 CD
Bonnie Thompson USGS WRD 160 N. Stephanie Street Henderson, NV 89074	1 CD
Chuck E. Russell Desert Research Institute 755 E. Flamingo Las Vegas, NV 89119	1 CD
Ken Ortego National Security Technologies, LLC P.O. Box 98521, M/S NLV 082 Las Vegas, NV 89193-8521	1 CD
Sigmund Drellack National Security Technologies, LLC P.O. Box 98521, M/S NLV 082 Las Vegas, NV 89193-8521	1 CD

	<u>Copies</u>
Andy Wolfsberg Los Alamos National Laboratory Bikini Atoll Rd., SM30 Drop Pt. 19U, MS T003 Los Alamos, NM 87545	1 CD
Robert Gamble Nye Country Nuclear Waste Repository Project Office 1551 Hillshire Drive M/S 523 Las Vegas, NV 89134	1 CD
Sam Marutzky Stoller-Navarro Joint Venture c/o U.S. DOE P.O. Box 98952 Las Vegas, NV 89193-8952	1 Hard copy w/CD
Greg Ruskauff Stoller-Navarro Joint Venture c/o U.S. DOE P.O. Box 98952 Las Vegas, NV 89193-8952	1 CD
Eugene Freeman Stoller-Navarro Joint Venture c/o U.S. DOE P.O. Box 98952 Las Vegas, NV 89193-8952	1 CD
Bruce Crowe Stoller-Navarro Joint Venture c/o U.S. DOE P.O. Box 98952 Las Vegas, NV 89193-8952	1 CD
Stoller-Navarro Joint Venture Central Files c/o U.S. DOE P.O. Box 98952 Las Vegas, NV 89193-8952	1 Hard copy w/CD